Vinod Singh · Rinku Sharma ·
Man Mohan · Mohan Singh Mehata ·
A. K. Razdan *Editors*

Proceedings of the International Conference on Atomic, Molecular, Optical & Nano Physics with Applications

CAMNP 2019

Springer

Springer Proceedings in Physics

Volume 271

Indexed by Scopus

The series Springer Proceedings in Physics, founded in 1984, is devoted to timely reports of state-of-the-art developments in physics and related sciences. Typically based on material presented at conferences, workshops and similar scientific meetings, volumes published in this series will constitute a comprehensive up-to-date source of reference on a field or subfield of relevance in contemporary physics. Proposals must include the following:

– name, place and date of the scientific meeting
– a link to the committees (local organization, international advisors etc.)
– scientific description of the meeting
– list of invited/plenary speakers
– an estimate of the planned proceedings book parameters (number of pages/ articles, requested number of bulk copies, submission deadline).

Please contact:

For Americas and Europe: Dr. Zachary Evenson; zachary.evenson@springer.com
For Asia, Australia and New Zealand: Dr. Loyola DSilva; loyola.dsilva@springer. com

More information about this series at https://link.springer.com/bookseries/361

Vinod Singh · Rinku Sharma · Man Mohan ·
Mohan Singh Mehata · A. K. Razdan
Editors

Proceedings of the International Conference on Atomic, Molecular, Optical & Nano Physics with Applications

CAMNP 2019

Editors
Vinod Singh
Department of Applied Physics
Delhi Technological University
New Delhi, Delhi, India

Rinku Sharma
Department of Applied Physics
Delhi Technological University
New Delhi, Delhi, India

Man Mohan
Department of Physics
University of Delhi
New Delhi, Delhi, India

Mohan Singh Mehata
Department of Applied Physics
Delhi Technological University
New Delhi, Delhi, India

A. K. Razdan
Laser Science & Tech Centre (LASTEC)
Defence Research and Development
Organization
New Delhi, Delhi, India

Organizing Committee

Chief Patron

Prof. Yogesh Singh, Vice Chancellor, Delhi Technological University (DTU), New Delhi, India

Patron

Prof. S. K. Garg, Pro-Vice Chancellor, DTU

Co-Patron

Prof. R. P. Tandon, University of Delhi, Delhi

President

Prof. Man Mohan, Emeritus Professor, University of Delhi, Delhi

Vice President

Prof. Samsher, Registrar, DTU

Chief Advisor

Prof. Nicholas P. Bigelow, University of Rochester, USA

Chairperson

Prof. Rinku Sharma, Head, Department of Applied Physics, DTU

Convener

Dr. Vinod Singh, Department of Applied Physics, DTU

Co-Conveners

Dr. A. K. Razdan, LASTEC, DRDO, Delhi
Dr. Avnindra Kumar Singh, DDU College, University of Delhi, Delhi
Dr. M. S. Mehata, DTU
Dr. Amrish K. Panwar, DTU

Secretaries

Dr. Yogita Kalra, DTU
Dr. Ajeet Kumar, DTU
Dr. M. Jayasimhadri, DTU

Joint Secretaries

Prof. A. S. Rao, DTU
Dr. Rishu Chaujar, DTU
Dr. Mukhtiyar Singh, DTU

Abstract Review Committee

Dr. M. Jayasimhadri, DTU
Dr. Yogita Kalra, DTU
Dr. Amrish K. Panwar, DTU

Manuscript Review Committee

Prof. Rinku Sharma, DTU
Dr. Vinod Singh, DTU
Dr. M. S. Mehata, DTU
Dr. Bharti Singh, DTU
Dr. Mukhtiyar Singh, DTU
Dr. Renuka Bokolia, DTU
Dr. Richa Sharma, DTU
Dr. Deshraj Meena, DTU

Finance Committee

Dr. Bharti Singh, DTU (Treasurer)
Dr. Renuka Bokolia, DTU
Dr. Richa Sharma, DTU

Local Organizing Committee

Prof. S. C. Sharma, DTU
Dr. Nitin K. Puri, DTU
Mr. Deshraj Meena, DTU
Mr. Yogendra K. Meena, DTU
Dr. Sarita Baghel, DTU
Dr. Kamal Kishor, DTU

Research Committee

Dr. K. P. Singh, IISER, Mohali
Prof. A. K. Shukla, IIT Delhi

Dr. Sidharth Lahon, DU
Dr. Tarun Rawat, DU
Dr. Manoj Malik, DU
Dr. Narendra Singh, DU
Dr. Kriti Batra, IPU
Dr. S. Somorendro Singh, DU
Dr. Arun Goyal, DU
Dr. Sunny Aggarwal, DU

Student Organizing Committee

Mr. Abhishek Bhardwaj, DTU
Mr. Anurag, DTU
Mr. Ashok, DTU
Ms. Umang, DTU
Ms. Priya, DTU
Ms. Suman Dahiya, DTU
Ms. Richa Gautam, DTU
Mr. Mukesh Sahu, DTU
Ms. Anchali Jain, DTU
Ms. Megha Sharma, DTU
Mr. Ankush Dewan, DTU
Ms. Ritika Ranga, DTU
Ms. Pooja Chauhan, DTU
Ms. Harpreet Kaur, DTU
Ms. Deepali, DTU
Mr. Vishal, DTU
Mr. Mayank Dimri, DU
Ms. Dishu Dwara, DU
Ms. Falta Yadav, DU
Mr. Kailash Chandra, DTU
Mr. Bhavya, DTU
Mr. Parful Bhomik, DTU

Preface

The Department of Applied Physics, Delhi Technological University, New Delhi, India, has organized the three days "International Conference on Atomic, Molecular, Optical and Nano Physics with Applications (CAMNP-2019)" during 18–20 December 2019, co-sponsored by LASTEC, DRDO, Delhi. The objective of CAMNP-2019 was to bring prominent scientists and researchers from academia and industry as well as experts from all strata of society under one roof to explore and muster the new horizon of novel technological and industrial developments in the field of science and technology.

The CAMNP-2019 featured a diverse array of research presentations on the theoretical and experimental developments in atomic, molecular, optical, nanoscience and technology. Such studies leave a powerful impact on various industrial applications in information technology, renewable energy, climate change, space technology and biological studies.

The response received against the call of papers for CAMNP-2019 has also been overwhelming. This conference has attracted researchers, scientists and practitioners from academia and industry to exchange ideas and share their valuable experiences. We have received a larger number of research contributions (around 100 invited talks and 260 poster presentations) worldwide. These research contributions represented a wide variety of research topics in all the emerging areas. Indeed, these contributions augmented the knowledge and encouraged many of us to take up these challenging application areas and contribute successfully to research in engineering and applied sciences. A large number of international invited speakers in our technical programme schedule indicated the success of the CAMNP-2019 conference that makes all the organizers extremely proud.

We are thankful to Springer Nature for accepting our proposal of publishing the recommended manuscripts in the Springer Proceedings in Physics. We have received 75 full-length manuscripts for publication in the Springer Proceedings in Physics. Accordingly, a review committee has been constituted for reviewing the manuscripts. After the sufficient and appropriate review cycles, the review committee has recommended 63 manuscripts for publication in the Springer Proceedings in Physics.

The success of this conference has been the collective effort and contribution of the entire organizing team. We are sincerely grateful to Hon'ble Vice Chancellor, DTU, Prof. Yogesh Singh, for his constant support. We would also like to thank Prof. S. K. Garg, Pro-Vice Chancellor and Prof. Samsher, Registrar, and the concerned authorities for their guidance and encouragement. We are also thankful to government (AICTE, MoEF&CC, SERB, DRDO, TEQIP-III, CSIR, BRNS, ICAR) and private agencies for providing financial assistance.

New Delhi, India   Dr. Vinod Singh
                                                                                      Prof. Rinku Sharma
                                                                                       Prof. Man Mohan
                                                                              Dr. Mohan Singh Mehata

Funding Agencies

List of Government Sponsors

Delhi Technological University, New Delhi
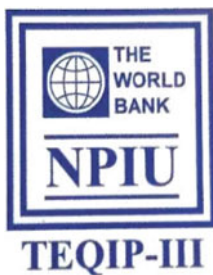
Technical Education Quality Education Programme-III (TEQIP-III)

Laser Science and Technology Centre (LASTEC-DRDO)

All India Council for Technical Education (AICTE)

Ministry of Environment, Forest and Climate Change (MOEF&CC)

Science and Engineering Research Board (SERB)

Defence Research and Development Organization (DRDO)

Indian Council for Agricultural Research (ICAR)

Council of Scientific and Industrial Research (CSIR)

Board of Research in Nuclear Science (BRNS)

List of Private Sponsors

ATOS Instruments Marketing Services (Gold Sponsor)

Laser Spectra Services India Pvt. Ltd.

Hind High Vacuum Company Pvt. Ltd.

Silicom Electronics Pvt. Ltd.

Tushar Scientific Industries

Infrared Optics

Contents

Contributors

Sunny Aggarwal Department of Physics, Shyamlal College, University of Delhi, New Delhi, Delhi, India

Tulika Agrawal Department of Physics, Indian Institute of Technology Madras, Chennai, Tamil Nadu, India

Rachna Ahlawat Department of Physics, Material Science Laboratory, Chaudhary Devi Lal University, Sirsa, Haryana, India

Taslim Ahmad Centre for Nanoscience and Nanotechnology, New Delhi, India

B. L. Ahuja Department of Physics, University College of Science, M. L. Sukhadia University, Udaipur, Rajasthan, India

Mashqoor Alam Centre for Nanoscience and Nanotechnology, New Delhi, India

P. S. Alegaonkar Defence Institute of Advanced Technology (DIAT), Girinagar, Pune, India

Anahat Department of Physics, Hindu College, University of Delhi, Delhi, India

Anjali UIET, Panjab University, Chandigarh, India;
Department of Physics, Panjab University, Chandigarh, India

Annu Molecular Spectroscopy and Biophysics Lab, Department of Physics, Deva Nagri College, Meerut, Uttar Pradesh, India

Ardhendu Saha Department of Electrical Engineering, National Institute of Technology Agartala, Tripura (west), India

Arti Department of Physics, Hindu College, University of Delhi, Delhi, India;
Department of Physics and Astrophysics, University of Delhi, Delhi, India

Aryan Laser-Spectroscopy Laboratory, Department of Applied Physics, Delhi Technological University, Delhi, India

James F. Babb Institute for Theoretical Atomic, Molecular, and Optical Physics (ITAMP), Center for Astrophysics-Harvard & Smithsonian, Cambridge, MA, USA

Kriti Batra University School of Basic and Applied Sciences GGS Indraprastha University, Dwarka, Delhi, India

Umang Department of Applied Physics, Delhi Technological University, New Delhi, India

Ram Bhagat Department of Electrical Engineering, Delhi Technological University, Delhi, India

Shaleen Bhardwaj Molecular Spectroscopy and Biophysics Lab, Department of Physics, Deva Nagri College, Meerut, Uttar Pradesh, India

D. R. Bhaskar Department of Electrical Engineering, Delhi Technological University, Delhi, India

Shubhayan Bhattacharya Department of Physics, Indian Institute of Technology Madras, Chennai, Tamil Nadu, India

Prafulla Chandra Bhowmick Department of Physics and Astrophysics, University of Delhi, Delhi, India

Pooja Bhowmik Department of Physics, University College of Science, M. L. Sukhadia University, Udaipur, Rajasthan, India

Chitra Bhukkal Department of Physics, Material Science Laboratory, Chaudhary Devi Lal University, Sirsa, Haryana, India

Prem B. Bisht Department of Physics, Indian Institute of Technology Madras, Chennai, Tamil Nadu, India

Loknath Biswas Department of Physics, School of Applied Sciences, University of Science and Technology Meghalaya, Ri Bhoi, Meghalaya, India

Darshana Bora Department of Physics, University of Science and Technoloygy, Ri-Bhoi, Meghalaya, India

Nitu Borgohain Department of Physics, University of Science and Technoloygy, Ri-Bhoi, Meghalaya, India

Swati Bugalia Department of Chemistry, University of Rajasthan, Jaipur, India

Garima Chanana University School of Basic and Applied Sciences GGS Indraprastha University, Dwarka, Delhi, India

Asha S. Chaudhari Visnagar, India

Pooja Chauhan Advanced Photonics Simulation Research Laboratory, Department of Applied Physics, Delhi Technological University, New Delhi, India

Rashmi Rai Chauhan LASTEC, DRDO, Delhi, India

Plabita Chetia Department of Physics, University of Science and Technoloygy, Ri-Bhoi, Meghalaya, India

Sanjiv Chettri Department of Physics, School of Applied Sciences, University of Science and Technology Meghalaya, Ri Bhoi, Meghalaya, India

Vikas Choudary Bio-NanoTechnology Lab (H-1), CSIR-CSIO, Chandigarh, India

Anju Dahiya Department of Physics and Astrophysics, University of Delhi, Delhi, India

Suman Dahiya Department of Applied Physics, Delhi Technological University, New Delhi, Delhi, India

Saurabh Daripa Department of Applied Physics, Delhi Technological University, Delhi, India

Jyotshna Das Department of Physics, University of Science and Technoloygy, Ri-Bhoi, Meghalaya, India

Nil Ratan Das LIDAR Division, Laser Science & Technology Centre, DRDO, Metcalfe House, Delhi, India

Dishu Dawra Department of Physics and Astrophysics, University of Delhi, Delhi, India

Argha Debnath Bennett University, Greater Noida, India

Deepak Department of Physics, Hindu College, University of Delhi, Delhi, India

Anju Dhillon Department of Applied Sciences, MSIT, New Delhi, India

Mayank Dimri Department of Physics and Astrophysics, University of Delhi, Delhi, India;
Department of Physics, Deen Dayal Upadhyaya College, University of Delhi, Delhi, India

C. F. Dong Southwestern Institute of Physics, Chengdu, China

Z. Felfli Department of Physics and CTSPS, Clark Atlanta University, Atlanta, GA, USA

K. Fujii Department of Mechanical Engineering and Science, Kyoto University, Kyoto, Japan

Vijayeta Gambhir LASTEC, DRDO, Delhi, India

Ankita Garg Molecular Spectroscopy and Biophysics Lab, Department of Physics, Deva Nagri College, Meerut, Uttar Pradesh, India

Bindiya Goswami Department of Physics, Material Science Laboratory, Chaudhary Devi Lal University, Sirsa, Haryana, India

J. K. Goswamy Department of Applied Sciences (Physics), UIET, Panjab University, Chandigarh, India

M. Goto National Institute for Fusion Science, Gifu, Japan

J. K. Gowsamy UIET, Panjab University, Chandigarh, India

Arun Goyal Department of Physics, Shyamlal College, University of Delhi, Delhi, India

Megha Goyal Department of Physics, Sant Longowal Institute of Engineering and Technology, Longowal, Sangrur, India

Kamal Kumar Gulati LASTEC, DRDO, Delhi, India

Sakshi Gupta LASTEC, DRDO, Delhi, India

R. Gupta Department of Physics & Astrophysics, University of Delhi, Delhi, India; Department of Physics, Hindu College, University of Delhi, Delhi, India

Vishal Gupta Department of Physics, Hindu College, University of Delhi, New Delhi, India

Yuhit Gupta Department of Physics, Sant Longowal Institute of Engineering and Technology, Longowal, Sangrur, India

M. Hasuo Department of Mechanical Engineering and Science, Kyoto University, Kyoto, Japan

Samina Husain Centre for Nanoscience and Nanotechnology, New Delhi, India

Aasim Hussain Department of Physics, JamiaMilliaIslamia, New Delhi, India

Saurabh Inamdar LIDAR Division, Laser Science & Technology Centre, DRDO, Metcalfe House, Delhi, India

Anchali Jain Department of Applied Physics, Delhi Technological University, New Delhi, Delhi, India

Masuma Jannat Department of Physics, University of Science and Technology Meghalaya, Ri-Bhoi, Meghalaya, India

Alok K. S. Jha Department of Physics, Kirori Mal College, University of Delhi, Delhi, India

Valdas Jonauskas Institute of Theoretical Physics and Astronomy, Vilnius University, Vilnius, Lithuania

Foram M. Joshi G. H. Patel College of Engineering and Technology, Vallabh Vidyanagar, Gujarat, India

K. N. Joshipura (Retd) Sardar Patel University, Vallabh Vidyanagar, India

R. K. Kalal High Energy Materials Research Laboratory (HEMRL), Sutarwadi, Pune, India;
Defence Institute of Advanced Technology (DIAT), Girinagar, Pune, India

Monika Kalita Department of Physics, University of Science & Technology Meghalaya, Ri-Bhoi, Meghalaya, India

Ravi Kant Department of Physics, Indian Institute of Technology Delhi, New Delhi, India

D. Kato National Institute for Fusion Science, Gifu, Japan

Surleen Kaur Advanced Photonics Simulation Research Laboratory, Department of Applied Physics, Delhi Technological University, New Delhi, India

Tavneet Kaur Department of Physics, Sant Longowal Institute of Engineering and Technology, Longowal, Sangrur, India

Manpreet Kaur Department of Applied Sciences (Physics), UIET, Panjab University, Chandigarh, India;
Department of Physics, Panjab University, Chandigarh, India

Y. Kawamoto National Institute for Fusion Science, Gifu, Japan

Ayan Khan Bennett University, Greater Noida, India

Maya Khangembam Department of Applied Physics, Delhi Technological University, New Delhi, Delhi, India

S. P. Khanna CSIR-National Physical Laboratory, Dr. K. S. Krishnan Road, New Delhi, India;
Academy of Scientific and Innovative Research (AcSIR), Ghaziabad, India

Manika Khauja Jamia Millia Islamia, New Delhi, India

Kamal Kishor TIFAC-Centre of Relevance & Excellence in Fiber Optics & Optical Communications, Applied Physics Department, Delhi Technological University (Formerly Delhi College of Engineering), New Delhi, Delhi, India

Jurgita Koncevičiūtė Institute of Theoretical Physics and Astronomy, Vilnius University, Vilnius, Lithuania

Pawan K. Kulriya School of Physical Sciences, Jawaharlal Nehru University, New Delhi, India

Ajeet Kumar Advanced Photonics Simulation Research Laboratory, Department of Applied Physics, Delhi Technological University, New Delhi, India

Arvind Kumar High Energy Materials Research Laboratory (HEMRL), Sutarwadi, Pune, India

Ashish Kumar CSIR-National Physical Laboratory, Dr. K. S. Krishnan Road, New Delhi, India;
Academy of Scientific and Innovative Research (AcSIR), Ghaziabad, India

Ashok Kumar Department of Applied Physics, Delhi Technological University, New Delhi, India;
Atma Ram Sanatan Dharma College, University of Delhi, New Delhi, India

Lalit Kumar Department of Physics, Hindu College, University of Delhi, New Delhi, India

Nitesh Kumar LASTEC, DRDO, Delhi, India

P. Kumar Department of Physics, Hindu College, University of Delhi, Delhi, India;
Department of Physics and Astrophysics, University of Delhi, Delhi, India

Parveen Kumar Bio-NanoTechnology Lab (H-1), CSIR-CSIO, Chandigarh, India

Pragati Kumar Department of Electrical Engineering, Delhi Technological University, Delhi, India

Sumit Kumar Department of Physics, Hindu College, University of Delhi, Delhi, India;
Department of Physics and Astrophysics, University of Delhi, Delhi, India

Suresh Kumar UIET, Panjab University, Chandigarh, India

Vikas Kumar Molecular Spectroscopy and Biophysics Laboratory, Deva Nagri College, Meerut, Uttar Pradesh, India

Yogesh Kumar Department of Physics, ARSD College, University of Delhi, New Delhi, India

Puja Kumari Department of Physics, Darbhanga College of Engineering, Darbhanga, India

Sushama Kumari Department of Chemistry, University of Rajasthan, Jaipur, India

Aušra Kynienė Institute of Theoretical Physics and Astronomy, Vilnius University, Vilnius, Lithuania

Siddhartha Lahon Physics Department, Kirori Mal College, University of Delhi, New Delhi, Delhi, India

Kiranmala Laishram LIDAR Division, Laser Science & Technology Centre, DRDO, Metcalfe House, Delhi, India

C. Limbachiya Department of Applied Physics, The M. S. University of Baroda, Vadodara, India

Chetan Limbachiya The Maharaja Sayajirao University of Baroda, Vadodara, India

Roshan Makkar Photonics Division, Society for Applied Microwave Electronics & Engineering Research, IIT Bombay Campus, Powai, Mumbai, Maharashtra, India

Jairam Manam Department of Applied Physics, IIT (ISM), Dhanbad, India

Rekha Mann LASTEC, DRDO, Delhi, India

Brendan M. McLaughlin Centre for Theoretical Atomic Molecular and Optical Physics, Queens University Belfast, Belfast, UK

Mohan Singh Mehata Laser-Spectroscopy Laboratory, Department of Applied Physics, Delhi Technological University, Delhi, India

Shalini Mittal LIDAR Division, Laser Science & Technology Centre, DRDO, Metcalfe House, Delhi, India

Man Mohan Department of Physics and Astrophysics, University of Delhi, Delhi, India;
Department of Physics, Deen Dayal Upadhyaya College, University of Delhi, Delhi, India

S. V. Moharil Department of Physics, R.T.M. Nagpur University, Nagpur, India

S. Morita National Institute for Fusion Science, Gifu, Japan

A. Z. Msezane Department of Physics and CTSPS, Clark Atlanta University, Atlanta, GA, USA

I. Murakami National Institute for Fusion Science, Gifu, Japan

Nabamita Goswami Department of Electrical Engineering, National Institute of Technology Agartala, Tripura (west), India

N. Nakamura Institute for Laser Science, The University of Electro-Communications, Chofu, Tokyo, Japan

Nihal UIET, Panjab University, Chandigarh, India

T. Oishi National Institute for Fusion Science, Gifu, Japan

Amrindra Pal Electronics & Communication Engineering, DIT University, Dehradun, Uttarakhand, India

Rakesh Kumar Pandey Department of Physics, Kirori Mal College, University of Delhi, Delhi, India

Amrish K. Panwar Department of Applied Physics, Delhi Technological University, New Delhi, Delhi, India

Smruti Parikh The Maharaja Sayajirao University of Baroda, Vadodara, India

Poonam Department of Physics, Guru Jambheshwar University of Science & Technology, Hisar, Haryana, India;

Hindu Girls Colloge, Sonipat, Haryana, India;
Department of Applied Physics, Delhi Technological University, New Delhi, Delhi, India

D. Prajapati Shree M. R. Arts & Science College, Rajpipla, India

Gorur Govinda Raju Department of Electrical and Computer Engineering, University of Windsor, Windsor, ON, Canada

Isha Rathi Molecular Spectroscopy and Biophysics Lab, Department of Physics, Deva Nagri College, Meerut, Uttar Pradesh, India

Sonal Rattan Center of Nanoscience, Panjab University, Chandigarh, India

S. S. Rawat CSIR-National Physical Laboratory, Dr. K. S. Krishnan Road, New Delhi, India;
Academy of Scientific and Innovative Research (AcSIR), Ghaziabad, India

A. K. Razdan LIDAR Division, Laser Science & Technology Centre, DRDO, Metcalfe House, Delhi, India

Balesh Ropiaa High Energy Material Research Laboratory, Pune, India

F. B. Rosmej Faculty of Science and Engineering, UMR 7605, Sorbonne University, Paris, France;
Laboratoire Pour L'Utilisation Des Lasers Intenses, Physique Atomique Dans Les Plasmas Denses-PAPD, Ecole Polytechnique, Palaiseau Cedex, France;
Moscow Institute of Physics and Technology-MIPT, Dolgoprudnyi, Russia;
National Research Nuclear University MEPhI (Moscow Engineering Physics Institute), Moscow, Russia

Sanchita Roy Department of Physics, School of Applied Sciences, University of Science and Technology Meghalaya, Ri Bhoi, Meghalaya, India

Ruby Laser-Spectroscopy Laboratory, Department of Applied Physics, Delhi Technological University, Delhi, India

Vijay Kumar Sagar Department of Physics, Indian Institute of Technology Madras, Chennai, India

Lipika Saha Department of Physics, University of Science and Technology Meghalaya, Ri-Bhoi, Meghalaya, India

Rimlee Saikia Department of Physics, Gauhati University, Guwahati, Assam, India

Hardev S. Saini Department of Physics, Guru Jambheshwar University of Science & Technology, Hisar, Haryana, India

Sonakshi Saini Department of Applied Physics, Delhi Technological University, New Delhi, Delhi, India

H. A. Sakaue National Institute for Fusion Science, Gifu, Japan

Rekha Sangtyani High Energy Materials Research Laboratory (HEMRL), Sutar-wadi, Pune, India

Sanoj Kumar Yadav Department of Electrical Engineering, National Institute of Technology Agartala, Tripura (west), India

Tapas Sen Department of Physics, University of Science and Technology Megha-laya, Ri-Bhoi, Meghalaya, India

Saurabh K. Sengar D S College, Aligarh, India

Shahina Shaheen Centre for Nanoscience and Nanotechnology, New Delhi, India

Bhawna Sharma Electronics & Communication Engineering, DIT University, Dehradun, Uttarakhand, India

Manisha Sharma Department of Physics, University of Science and Technology Meghalaya, Ri-Bhoi, Meghalaya, India

Mohit Sharma Department of Physics, Mody University of Science and Tech-nology, Laxmangarh, Rajasthan, India

Mamta Sharma Department of Applied Sciences (Physics), UIET, Panjab Univer-sity, Chandigarh, India

Rahul Sharma Department of Applied Sciences (Physics), UIET, Panjab Univer-sity, Chandigarh, India

Rinku Sharma Department of Applied Physics, Delhi Technological University, Delhi, India

Rohan Sharma Advanced Photonics Simulation Research Laboratory, Department of Applied Physics, Delhi Technological University, New Delhi, India

S. K. Sharma Materials Science Group, Inter-University Accelerator Centre, New Delhi, India

Sakshi Sharma Department of Applied Physics, Delhi Technological University, New Delhi, Delhi, India

Sandeep Sharma Department of Electronics Engineering, Centre for Reliability Sciences and Technology, Chang Gung University, Taoyuan, Taiwan

H. Shekhar Defence Institute of Advanced Technology (DIAT), Girinagar, Pune, India

Himanshu Shekher High Energy Material Research Laboratory, Pune, India

Shumaila Department of Physics, JamiaMilliaIslamia, New Delhi, India

Azher M. Siddiqui Department of Physics, JamiaMilliaIslamia, New Delhi, India

A. Singh Department of Physics, Hindu College, University of Delhi, Delhi, India

A. K. Singh Department of Physics and Astrophysics, University of Delhi, Delhi, India;
Department of Physics, Deen Dayal Upadhyaya College, University of Delhi, Delhi, India

Divya Singh Computational Plasma Dynamics Laboratory, Rajdhani College, University of Delhi, New Delhi, India

Gurvinder Singh School of Biomedical Engineering, University of Sydney, Sydney, NSW, Australia

Gyan Singh Centre for Nanoscience and Nanotechnology, New Delhi, India

Harjot Singh UIET, Panjab University, Chandigarh, India

Mukhtiyar Singh Hindu Girls Colloge, Sonipat, Haryana, India

Narendra Singh Department of Physics, SLC, University of Delhi, Delhi, India

Vartika S. Singh Department of Physics, R.T.M. Nagpur University, Nagpur, India

Vinod Singh Department of Applied Physics, Delhi Technological University, New Delhi, Delhi, India

Murari Mohan Sinha Department of Physics, Sant Longowal Institute of Engineering and Technology, Longowal, Sangrur, India

S. Somorendro Singh Department of Physics and Astrophysics, University of Delhi, Delhi, India

Pankaj Srivastava Nanomaterials Research Group-CNTL (NRG-CNTL), ABV-Indian Institute of Information Technology and Management (ABV-IIITM), Gwalior, Madhya Pradesh, India

R. Srivastava CSIR-National Physical Laboratory, Dr. K. S. Krishnan Road, New Delhi, India;
Academy of Scientific and Innovative Research (AcSIR), Ghaziabad, India

K. Suggs Department of Physics and CTSPS, Clark Atlanta University, Atlanta, GA, USA

I. Sulania Inter University Accelerator Centre, New Delhi, India

C. K. Suman CSIR-National Physical Laboratory, Dr. K. S. Krishnan Road, New Delhi, India;
Academy of Scientific and Innovative Research (AcSIR), Ghaziabad, India

Sanjay Kumar Swami CSIR-National Physical Laboratory, New Delhi, India

Rana Tabassum Centre for Nanoscience and Nanotechnology, Jamia Millia Islamia (A Central University), New Delhi, India

Jayant Teotia Molecular Spectroscopy and Biophysics Lab, Department of Physics, Deva Nagri College, Meerut, Uttar Pradesh, India

D. G. Thakur Defence Institute of Advanced Technology, Pune, India

Twinkle UIET, Panjab University, Chandigarh, India;
Department of Physics, Panjab University, Chandigarh, India

M. Tyagi Department of Physics, Hindu College, University of Delhi, Delhi, India

Pawan K. Tyagi Department of Applied Physics, Delhi Technological University, New Delhi, Delhi, India

Sneha Upadhyay Nanomaterials Research Group-CNTL (NRG-CNTL), ABV-Indian Institute of Information Technology and Management (ABV-IIITM), Gwalior, Madhya Pradesh, India

Ravish Kumar Uppadhayay Molecular Spectroscopy and Biophysics Lab, Department of Physics, Deva Nagri College, Meerut, Uttar Pradesh, India

S. Vadhel Department of Physics, Sardar Patel University, Vallabh Vidyanagar, India

Rajni Vats Department of Physics, Material Science Laboratory, Chaudhary Devi Lal University, Sirsa, Haryana, India

Suram Singh Verma Department of Physics, Sant Longowal Institute of Engineering and Technology, Longowal, Sangrur, India

Vivek Verma Department of Physics, Hindu College, University of Delhi, Delhi, India

M. Vinodkumar V. P. & R. P. T. P. Science College, Vallabh Vidyanagar, India

P. C. Vinodkumar Department of Physics, Sardar Patel University, Vallabh Vidyanagar, India

B. S. Yadav Molecular Spectroscopy and Biophysics Laboratory, Deva Nagri College, Meerut, Uttar Pradesh, India

Falta Yadav Department of Physics and Astrophysics, University of Delhi, Delhi, India

L. Zhang Institute of Plasma Physics, Chinese Academy of Sciences, Anhui, China

Hala Zreiqat School of Biomedical Engineering, University of Sydney, Sydney, NSW, Australia

Chapter 1
X-ray Free Electron Lasers and Atomic Physics in Dense Plasmas

F. B. Rosmej

Abstract The recent evolution to combine high-intensity X-ray Free Electron Lasers XFEL's with high-energy high-intensity optical lasers provides the scientific community with outstanding tools to study matter and radiation under extreme conditions never achieved in laboratories so far. Atomic physics in dense plasmas and X-ray spectroscopy are the key elements for novel studies beyond the current state-of-the art. The self-seeded mode of XFEL's will enable for the first time to combine efficient pumping of atomic states in dense plasmas while resolving the frequency dependence of X-ray absorption and emission line profiles. The perspectives for novel fundamental studies in atomic density matrix theory are discussed. Finally, a new role of atomic physics processes is explored in XFEL-solid matter interaction: Auger electron heating and three-body recombination heating.

1.1 Introduction

Dense plasma atomic physics is concerned with the properties of a statistical system containing many charged particles where the long-range Coulomb forces play an important role in establishing collective phenomena [1]. As density is increased and temperature lowered, the plasma begins exhibiting features characteristic of condensed matter, where short-range as well as long-range forces are important. In this regime, the so-called "strongly coupled many particle Coulomb system",

F. B. Rosmej (✉)
Faculty of Science and Engineering, UMR 7605, Sorbonne University, LULI, case 128, 4 Place Jussieu, Paris Cedex 05, 75252 Paris, France
e-mail: frank.rosmej@sorbonne-universite.fr

Laboratoire Pour L'Utilisation Des Lasers Intenses, Physique Atomique Dans Les Plasmas Denses-PAPD, Ecole Polytechnique, Route de Saclay, 91128 Palaiseau Cedex, France

Moscow Institute of Physics and Technology-MIPT, Institutskii per. 9, Dolgoprudnyi 141700, Russia

National Research Nuclear University MEPhI (Moscow Engineering Physics Institute), Kashirskoe sh.31, 115409 Moscow, Russia

quantum statistics and dynamic effects are important parts in the plasma and the interplay with atomic, molecular and nuclear physics becomes a major issue [2, 3]. Associated with these properties are the emergences of features such as insulator-to-metal transition, order–disorder transition and chemical separation. Microscopic properties of these plasmas depend on phase transitions, which in turn affect the macroscopic properties of the plasma through the rates of elementary and transport processes.

Astrophysical dense plasmas are those which we find in the interiors of white and brown dwarfs, the Sun, neutron stars, and giant planets while laboratory dense plasmas include metals, alloys, semiconductors as well as a large variety of plasmas produced by diamond-anvil cells, metal vaporization, shock-compression, pinches.

Due to the rapid development of powerful laser installations high-energy density laser produced plasmas, strongly coupled plasmas and Warm Dense Matter (matter near solid density while temperatures are of the order of the Fermi energy) became a major top for the high-energy density physics community [4].

Dense strongly coupled plasma and warm dense matter are exotic conditions of matter that are extremely challenging [5–15]: as theory is very difficult experimental studies are therefore indispensable. In most cases X-ray emission from the sample itself provides a unique characterization: opacity is low allowing to record volumetric self-emission of the sample under study. However, interesting matter samples (strongly coupled plasmas, Warm Dense Matter) have typical temperatures of the order of the Fermi energy (typically some 1 eV ... 10 eV). Target self-emission in the X-ray range is therefore not available.

In order to circumvent the absence of the volumetric X-ray self-emission, essentially two methods have been developed. One method employs high-intensity lasers: the interaction with the near solid density matter generates suprathermal electrons that in turn ionize inner atomic shells of the finite temperature target material. Subsequently emitted radiation is in the X-ray spectral range [16–21].

Another method is similar but instead of suprathermal electrons, the pulse of an X-ray Free Electron Laser XFEL is used to generate target X-ray emission [6]. E.g. for K-shell ionization of partially ionized copper and corresponding X-ray K_α- and K_β-emission we have the following description:

$$K^2 L^8 M^x + h\nu_{XFEL} \rightarrow K^1 L^8 M^x + e_{photo}, \tag{1.1.1}$$

$$K^1 L^8 M^x \rightarrow K^2 L^7 M^x + h\nu_{K\alpha}, \tag{1.1.2}$$

$$K^1 L^8 M^x \rightarrow K^1 L^8 M^{x-1} + h\nu_{K\beta}, \tag{1.1.3}$$

where x indicates the ionization degree of the heated sample (e.g., x = 18 for single ionized copper, x = 17 for double ionized copper etc.).

The method of XFEL interaction with matter is extremely challenging due to the tuning capability of XFEL's. This makes XFEL's exceptional tools for fundamental

studies. Moreover, the technological progress in the generation of ultra-short XFEL pluses is impressive and even methods to generate XFEL pulses with durations of the order of a few tens of attoseconds are described [22]. Ultra-short X-ray pulses in femto- and attosecond time domain are very challenging and of rapidly growing interest [23–29]. From the fundamental point of view, Fermi's Golden Rule and Einstein's theory of stimulated emission and absorption (that are almost exclusively used in atomic population kinetics of dense plasmas) may not apply [23–28]. This is particular harmful as X-ray pumping and X-ray induced photoionization are at the heart of almost all X-ray matter interaction.

The most recent evolution at XFEL's installations is the combination of powerful optical laser beams with high intensity XFEL beams. The optical laser allows creating interesting dense matter samples and the XFEL radiation is employed as a probe beam for diagnostic purposes. These combinations of powerful lasers in optical and X-ray spectral range have been realized at the XFEL installations LCLS [30], EU-XFEL [31] and SACLA [32]. Figure 1.1 shows the principle experimental setup of an experiment in dense plasma atomic physics. The dense plasma is created irradiating a target with the optical laser beam (pink color). The XFEL beam is then focused into the dense plasma at a specified time delay relative to the optical laser pulse (note that time delays are of the order of the pulse duration of the optical laser). In order to increase the signal to noise ratio, numerous shots have to be accumulated (typically 1000–100,000 shots). This is realized with a rotating target (in order to provide for each shot a fresh target surface) and a repetition frequency of typically 5–20 Hz, see Fig. 1.1. The link to (1.1.1, 1.1.2, 1.1.3) is as follows: the irradiation of the target with the optical laser results in a material heating where different ionization stages (different values of x in (1.1.1)) are produced by electron collisional ionization in the dense laser produced plasma. The target volumetric X-ray emission is then induced focusing the XFEL beam into the dense plasma. This creates core hole states, that
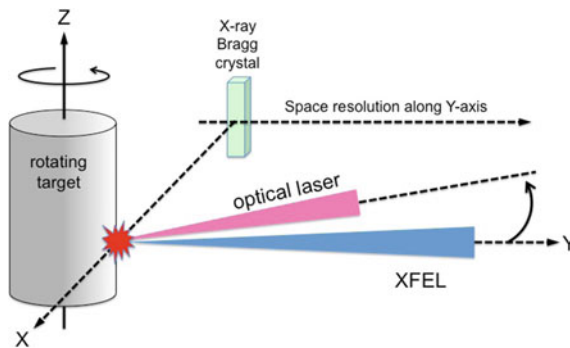
Fig. 1.1 Principle scheme of a pump probe experiment when intense XFEL radiation interacts with dense plasma produced by a powerful auxiliary optical laser. Induced X-ray emission is observed with Bragg crystals to record the X-ray radiation emission of the matter samples under study for the exploration of their properties. The rotating targets allows accumulation of thousands of shots to increase the signal to noise ratio

decay via the characteristic X-ray emission (1.1.2, 1.1.3) and by autoionization. In order to study the material properties at various different densities, the natural density gradient of the laser-produced plasma is employed: at different target distances, we encounter different electron densities. Therefore, the space resolved emission (see Fig. 1.1) provides access to the radiative properties in dependence of the density that is a key element in dense plasma atomic physics.

The experimental scheme demonstrates the need, to determine temperature, density and charge state distribution of the dense laser produced plasma in order to explore the interaction of the XFEL beam with the non-equilibrium dense heated matter sample. X-ray spectroscopy is a unique method to characterize the matter sample. The short time scales, the non-equilibrium radiative emission, the perturbation of the dense matter sample by the XFEL itself are challenging topics and at the forefront of today research to investigate matter at extreme conditions.

In general terms, X-ray radiation from autoionzing states, so-called dielectronic satellite emission turned out to be one of the most unique transitions to respond to the above constraints and to explore new and/or unknown phenomena. For example, Auger electron heating of conduction band electrons and subsequent disintegration of crystalline order has been identified via the satellite emission of L-shell hole states [33]; K-shell hollow ion emission enables intrinsic high time resolution down to the autoionizing time scale of some 10 fs [34, 35] to explore ultra-fast dynamics; X-ray satellite emission induced by direct interaction of XFEL radiation with solids allowed to develop the Atomic-Solid-Plasma model [36] and the novel b-potential method [11] to explore ionization potential depression in dense strongly coupled plasmas. These examples underline the unique and important role of dielectronic satellite emission for the worldwide emerging 4th generation light sources that are nowadays combined with powerful optical lasers. For the recent advances on dielectronic satellite emission the interesting reader may consult the reviews [19, 28, 29, 37, 38] (and references therein).

1.2 Interaction of XFEL Radiation with Atoms in Dense Plamas

The interaction of X-ray photons populates core hole states due to core photo ionization and core excitation. As core hole states are autoionizing, the related atomic physics processes are much more complex as it is usually the case for atoms in hot plasmas. Figure 1.2 shows a schematic diagram for a two level system (levels i and j) that are autoionizing (Auger effect) to explore the various phenomena that are typical for plasma (red color) and XFEL (blue color) related excitation. Due to the autoionizing phenomena, the standard two level system has to be "replaced" by an atomic structure of properly chosen 5 levels (black lines indicated with indexes j, i, m, k, k') at different charge states $(Z, Z + 1)$. The spontaneous radiative decay rate A_{ji} and the autoionzing rates $\Gamma_{jk'}$, Γ_{jk} and $\Gamma_{ik'}$ are represented by black flashes.
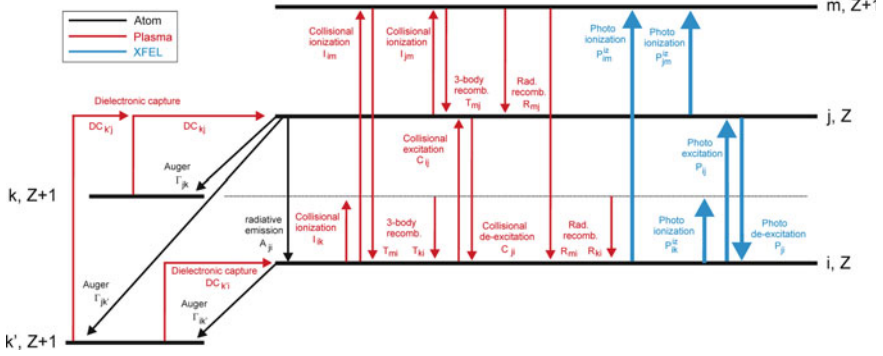
Fig. 1.2 Schematic sketch of some selected elementary processes of atoms in dense plasmas interacting with X-ray Free Electron Laser XFEL radiation. The standard 2-level system (to describe the radiation emission of interest from level (j,Z) to level (I,Z) is represented for autoionizing core hole states by a 5-level atom (black colors) with levels (j, i, m, k, k') at different charge states Z and $Z + 1$. The spontaneous radiative decay rate is indicated by A_{ji} and the autoionizing rates by Γ_{jk}, $\Gamma_{jk'}$ and $\Gamma_{ik'}$. The dense plasma related processes like dielectronic capture DC_{kj}, $DC_{k'j}$ and $DC_{k'i}$, collisional excitation C_{ij}, collisional de-excitation C_{ji}, collisional ionization I_{im}, I_{ik} and I_{jm}, 3-body recombination T_{mi}, T_{ki} and T_{mj} as well as radiative recombination R_{mi}, R_{ki} and R_{mj} are designated in red colors. The interaction of the XFEL with the atom is represented by photo excitation P_{ij}, photo de-excitation P_{ji} and photo ionizations P_{ik}^{iz}, P_{im}^{iz} and P_{jm}^{iz} and designated with blue colors

The various elementary processes of atoms in dense hot plasmas induced by X-ray Free Electron Laser radiation are indicated by red flashes. Due to the kinetic energy of the free electrons in the dense plasma, various elementary population and de-population processes are induced: collisional excitation C_{ij} and de-excitation C_{ji}, collisional ionization I_{ik}, I_{im} and I_{jm}, 3-body recombination T_{ki} T_{mi} and T_{mj}, radiative recombination R_{ki}, R_{mi} and R_{mj} as well as dielectronic capture $DC_{k'j}$, DC_{kj} and $DC_{k'i}$.

The processes induced by the interaction of the XFEL radiation are visualized with blue flashes: photo ionization P_{ik}^{iz}, P_{im}^{iz} and P_{jm}^{iz} (note that the upper index "iz" is introduced for clarity to identify ionization in photo processes) as well as photo excitation P_{ij} and photo de-excitation P_{ji}. We note, that also stimulated radiative recombination processes are encountered. These processes are not relevant for the present discussion and the interesting reader is refereed to [28, 38].

Let us illuminate the various atomic physics processes depicted in Fig. 1.2 with a characteristic example from the physics of hollow ion X-ray emission in dense plasmas [34, 35, 37–39]. Let the upper atomic level correspond to the hollow ion configuration K^0L^3, i.e. (j, Z) = K^0L^3. Because the K^0L^3-configuration can autoionize towards the state K^1L^1, we have (k, Z + 1) = K^1L^1. Moreover, K^0L^3 can also autoionize towards the state K^2, i.e. the transition $K^0L^3 \rightarrow K^2 + e_{Auger}$.

The hollow ion X-ray emission corresponds to the radiative decay $K^0L^3 \rightarrow K^1L^2 + h\nu$, i.e. the lower state $K^1L^2 = $ (i, Z). Also the lower state K^1L^2 is autoionizing, namely towards the state K^2, i.e. (k', Z + 1) = K^2.

Ionization from the configuration K^0L^3 populates the configuration K^0L^2, therefore we have $K^0L^2 = $ (m, Z + 1). The transition from the state (i, Z) = K^1L^2 to the

state $K^0L^2 = (m, Z + 1)$ corresponds therefore to the ionization of a K-shell electron, i.e. the process $K^1L^2 \rightarrow K^0L^2 + e$. Ionization of an L-shell electron corresponds to $K^1L^2 \rightarrow K^1L^1 + e$ (indicated via the blue flash in Fig. 1.2 connecting the states (i, Z) and (k, Z + 1) = dashed black line).

In consequence, excitation corresponds to the transitions (i, Z) $\rightarrow$ (j, Z), de-excitations to (j, Z) $\rightarrow$ (i, Z), ionization to (i, Z) $\rightarrow$ (m, Z + 1), (j, Z) $\rightarrow$ (m, Z + 1) and (i, Z) $\rightarrow$ (k, Z + 1) while recombination corresponds to (m, Z + 1) $\rightarrow$ (i, Z), (m, Z + 1) $\rightarrow$ (j, Z) and (k, Z + 1) $\rightarrow$ (i, Z).

For completeness, let us list the related plasma induced transitions that are indicated with red flashes in Fig. 1.2:

- electron collisional excitation C_{ij}: $K^1L^2 + e(E) \rightarrow K^0L^3 + e(E - \Delta E_{ij})$, where ΔE_{ij} is the excitation energy, i.e. the energy difference between the states K^1L^2 and K^0L^3,
- electron collisional de-excitation $K^0L^3 + e(E - \Delta E) \rightarrow K^1L^2 + e(E)$,
- electron collisional ionization I_{jm}: $K^0L^3 + e(E) \rightarrow K^0L^2 + e(E - \Delta E_{jm})$, I_{im}: $K^1L^2 + e(E) \rightarrow K^0L^2 + e(E - \Delta E_{im})$, I_{ik}: $K^1L^2 + e(E) \rightarrow K^1L^1 + e(E - \Delta E_{ik})$,
- dielectronic capture $DC_{k'j}$: $K^2 + e(E) \rightarrow K^0L^3 + e(E - \Delta E_{k'j})$, DC_{kj}: $K^1L^1 + e(E) \rightarrow K^0L^3 + e(E - \Delta E_{kj})$, $DC_{k'i}$: $K^2 + e(E) \rightarrow K^1L^2 + e(E - \Delta E_{k'i})$,
- radiative recombination R_{mj}: $K^0L^2 + e(E) \rightarrow K^0L^3 + e + h\nu$, R_{mi}: $K^0L^2 + e(E) \rightarrow K^1L^2 + e + h\nu$, R_{ki}: $K^1L^1 + e(E) \rightarrow K^1L^2 + e + h\nu$,
- 3-body recombination T_{mj}: $K^0L^2 + e(E) \rightarrow K^0L^3 + e(E + \Delta E_{mj})$, T_{mi}: $K^0L^2 + e(E) \rightarrow K^1L^2 + e(E + \Delta E_{mi})$, R_{ki}: $K^1L^1 + e(E) \rightarrow K^1L^2 + e(E + \Delta E_{ki})$.

The interest to study the interaction of X-ray Free Electron Laser radiation with atoms to explore new phenomena is manifold and essentially related to a selective increase of atomic populations and to employ the subsequently induced radiative X-ray emission to explore unknown phenomena via spectroscopic methods [6, 19, 28, 37, 40–43]. The XFEL induced atomic population increase is essentially based on two mechanisms:

(1) To induce a high atomic population of an excited level (j, Z) (that would other-wise not be populated, e.g. due to low collisional excitations at low tempera-tures) and to provoke corresponding important radiative decay (A_{ji}) that can then be observed with X-ray spectroscopic methods. This is the basic principle of laser induced fluorescence LIF that is now transferred to X-ray energies, the so-called X-LIF.

(2) To ionize the atom from charge state (Z) to (Z + 1) in order to provoke important population in the charge state (Z + 1) that would otherwise not be populated (e.g. due to dominating recombination processes in low temperature plasmas).

In the overwhelming cases of interest the interaction of XFEL radiation with matter is based on efficient photo ionization and photo excitation rates. In cold matter, even low intensity X-ray sources (such as synchrotrons) provoke observable X-ray emission that serve as a means to study unknown matter properties. This low intensity domain is efficient because other excitation mechanisms are negligible. In dense plasmas, however, the situation is dramatically different. The temperature of

the unbound electrons induces already efficient elementary atomic physics processes (indicated with the red flashes in Fig. 1.2) to provoke X-ray emission. Atomic X-ray radiation induced by XFEL interaction is therefore only efficient if the photon induced ionization and excitation rates are larger compared to the plasma induced rates. This is indicated in Fig. 1.2 by the bold blue flashes compared to the red flashes (not in bold). The detailed analysis of the cross sections shows, that due to particular scaling relations, the manipulation of the atomic populations in the X-ray spectral range is rather specific and requests particular attention. We therefore discuss below the particularities of photo excitation and photoionization in the X-ray spectral range.

1.3   XFEL Induced Rates Versus Plasma Rates

1.3.1   XFEL Pulse Modeling

In order to estimate the efficiency of XFEL induced rates compared to plasma rates let us firstly consider a simplified description of the time and energy dependence of the XFEL radiation that are assumed to be independent from each other and described by the functions $f_{FEL}(t)$ and $\tilde{N}_{FEL}(E)$. The number of photons per volume/time/energy is then given by:

$$\tilde{N}_{FEL}(E, t) = \tilde{N}_{FEL}(E) \, f_{FEL}(t), \qquad (1.3.1)$$

$$\int_{-\infty}^{+\infty} f_{FEL}(t)dt = 1. \qquad (1.3.2)$$

We assume a Gaussian energy dependence to simulate the narrow bandwidth of the XFEL:

$$\tilde{N}_{FEL}(E) = \tilde{N}_0 \, \frac{1}{\sqrt{\pi} \, \Gamma_{FEL}} \, \exp\left(-\frac{(E - E_{FEL})^2}{\Gamma_{FEL}^2}\right), \qquad (1.3.3)$$

$$\Gamma_{FEL} = \delta E/2 \sqrt{\ln 2}. \qquad (1.3.4)$$

E_{FEL} is the central energy of the radiation field, $\tilde{N}_{FEL}(E)$ is the number of photons / volume / energy, $\tilde{N}_0$ is the peak number of photons/volume, δE is the bandwidth. Assuming a Gaussian time dependence the number of photons $N_{tot,\tau}$ per pulse length τ is given by

$$N_{tot,\tau} = \int\limits_{0}^{\infty} dE \int\limits_{volume} dV \int\limits_{-\tau/2}^{+\tau/2} dt\, \tilde{N}_{FEL}(E,t)$$

$$\approx 2Ac\tau\tilde{N}_0 erf\left(\sqrt{\ln 2}\right) \approx 0.761 \cdot Ac\tau\tilde{N}_0. \tag{1.3.5}$$

A is the focal spot area, τ is the XFEL pulse width (FWHM) and erf is the error function defined by

$$erf(x) = \frac{1}{\sqrt{\pi}} \int\limits_{0}^{x} e^{-t^2} \cdot dt. \tag{1.3.6}$$

For estimations, the error function can be approximated by

$$erf(x) \approx \frac{1}{2} - \frac{e^{-x^2}}{2}$$
$$\cdot \left[\frac{0.3480242}{1 + 0.47047 \cdot x} - \frac{0.0958798}{(1 + 0.47047 \cdot x)^2} + \frac{0.7478556}{(1 + 0.47047 \cdot x)^3} \right]. \tag{1.3.7}$$

The laser intensity $\tilde{I}_{FEL}(E,t)$ per bandwidth energy and time interval is related to the photon density $\tilde{N}_{FEL}(E,t)$ via

$$\tilde{I}_{FEL}(E,t)dEdAdt = \tilde{N}_{FEL}(E,t)E \cdot dEdVdt. \tag{1.3.8}$$

Integrating the XFEL radiation over a full width at half maximum FWHM with respect to energy and time, $\overline{I}_{FEL,\delta E,\tau}$ (energy/time/surface) is given by (assuming a Gaussian time dependence):

$$\overline{I}_{FEL,\delta E,\tau} = \int\limits_{-\delta E/2}^{\delta E/2} dE \int\limits_{-\tau/2}^{\tau/2} cdt E \cdot \tilde{N}(E,t)$$

$$\approx 4E_{FEL}c\tilde{N}_0 erf^2\left(\sqrt{\ln 2}\right) \approx 0.579 \cdot c \cdot E_{FEL} \cdot \tilde{N}_0 \tag{1.3.9}$$

or, in convenient units

$$\overline{I}_{FEL,\delta E,\tau} \approx 2.8 \times 10^{-9} \left(\frac{\tilde{N}_0}{cm^3}\right) \left(\frac{E_{FEL}}{eV}\right) \left[\frac{W}{cm^2}\right]. \tag{1.3.10}$$

The number of photons $N_{tot,\tau}$ is related to the intensity $\overline{I}_{FEL,\tau}$ via (d is the focal spot diameter)

$$\overline{I}_{FEL,\tau} = 2 \cdot erf\left(\sqrt{\ln 2}\right) \cdot \frac{N_{tot,\tau} \cdot E_{FEL}}{\pi \tau \cdot d^2/4} \approx \frac{N_{tot,\tau} \cdot E_{FEL}}{\tau \cdot d^2}. \qquad (1.3.11)$$

Let us estimate the intensity $\overline{I}_{FEL,\tau}$ for typical XFEL parameters: for $N_{tot,\tau} = 10^{12}, \tau = 100\,fs, E_{XFEL} = 10\,keV, d = 3\,\mu m$ we have $\overline{I}_{FEL,\tau} \simeq 1.8 \cdot 10^{17}\,W/cm^2$. This example demonstrates, that intensities in excess of 10^{17} W/cm^2 can only be achieved with micro focusing (realized, e.g. with Beryllium lenses) because photon numbers in excess of 10^{13} per pulse are rather difficult to achieve with present XFEL installations. We note, that recently also sub-micro focusing was demonstrated employing a four mirror focusing system in Kirkpatrick-Baez geometry. This allowed reaching focal spot sizes down to 0.05 μm and intensities up to 10^{20} W/cm^2 (achieved at the SACLA XFEL [44]).

1.3.2 Photo Excitation Versus Spontaneous Radiative Decay

In order that photo excitation influences strongly on the upper level population, e.g. to reach a regime of saturated absorption, photo excitation rates need to be larger than the corresponding spontaneous radiative decay rates, i.e.

$$\int_{-\tau/2}^{+\tau/2} dt \int_{\Delta E_{nm}-\delta\tilde{E}/2}^{\Delta E_{nm}+\delta\tilde{E}/2} dE \sigma_{ij}^{abs}(E) c \tilde{N}_{FEL}(E,t) \geq A_{ji}. \qquad (1.3.12)$$

$\sigma_{ij}^{abs}(E)$ is the photo absorption cross section for the transition from level i to level j and A_{ji} is the spontaneous radiative decay rate from level j to level i, $\delta\tilde{E}$ is an effective width for the XFEL interaction with the atomic transition. The photo absorption cross section is given by

$$\sigma_{ij}^{abs}(E) = \frac{E}{4\pi} B_{ij} \, \varphi_{ij}(E). \qquad (1.3.13)$$

B_{ij} is the Einstein coefficient of stimulated absorption that is related to the Einstein coefficient of spontaneous radiative decay according

$$B_{ij} = \frac{4\pi^3 \hbar^3 c^2}{E^3} \frac{g_j}{g_i} A_{ji}. \qquad (1.3.14)$$

$\varphi_{ij}(E)$ is the normalized local absorption line profile:

$$\int_{-\infty}^{+\infty} \varphi_{ij}(E) dE = 1. \qquad (1.3.15)$$

We assume a Gaussian line profile with Full Width at Half Maximum, i.e.

$$FWHM = 2\sqrt{\ln 2}\,\Gamma_G. \tag{1.3.16}$$

and a width parameter (T_i is the ion temperature and M is the ion mass)

$$\Gamma_G = \Delta E_{ij}\sqrt{2kT_i/Mc^2}. \tag{1.3.17}$$

corresponding to a Doppler profile to obtain analytical estimates:

$$\varphi_{ij}(E) = \frac{1}{\sqrt{\pi}\,\Gamma_G} \exp\left[-\left(\frac{E - \Delta E_{ij}}{\Gamma_G}\right)^2\right] \tag{1.3.18}$$

and

$$\frac{4\ln 2}{\delta \tilde{E}^2} = \frac{1}{\Gamma_G^2} + \frac{1}{\Gamma_{FEL}^2}. \tag{1.3.19}$$

If the XFEL photon energy is exactly tuned to the transition energy, e.g. $E_{XFEL} = \Delta E_{ij}$, we obtain the following estimate:

$$I_{FEL} > 2 \cdot 10^5 \Delta E_{ij}^3 \frac{g_i}{g_j} \sqrt{FWHM_{FEL}^2 + FWHM_G^2} \left[\frac{W}{cm^2}\right] \tag{1.3.20}$$

with ΔE_{ij} and $FWHM$ in [eV]. For H-like V Ly$_\alpha$, $\Delta E_{ij} = 5.44$ keV, $g_i = 2$, $g_j = 6$, we obtain $I_{XFEL} = 2 \cdot 10^{17}$ W/cm^2 (assuming $\sqrt{FWHM_{FEL}^2 + FWHM_G^2} = 20$ eV). The relation (1.3.19) indicates an important scaling law (neglecting the Z-dependence of the widths parameters):

$$I_{FEL} \propto Z^6. \tag{1.3.21}$$

Therefore, extremely high brilliance of XFEL's are needed to achieve level saturation for X-ray transitions. Assuming a spot diameter of $d = 3$ µm, pulse length $\tau = 30\,fs$, photon energy $E_{XFEL} = 5.44$ keV and a laser intensity of $\overline{I}_{FEL,\tau} = 2 \cdot 10^{17}$ W/cm^2, a minimum of about $N_{tot,\tau} = 6 \cdot 10^{11}\ photons$ in the XFEL pulse is requested according (1.3.5) to effectively move atomic populations corresponding to the X-ray energy range towards saturation.

1.3.3 Photoionization Versus Plasma Electron Collisional Ionization

In order to change ionic charge state populations by irradiation of matter with XFEL, photo ionization rates need to be larger than corresponding plasma electron ionization rates. In order to obtain analytical estimates, we consider the hydrogen-like approximation for an arbitrary atom/ion with effective charge Z_{eff} and an atomic level with principal quantum number n and energy

$$E_n = \frac{Z_{eff}^2 \cdot Ry}{n^2}, \tag{1.3.22}$$

where $Ry = 13.6057$ eV. For photo ionization this leads to the following relation:

$$\int_{-\tau/2}^{+\tau/2} dt \int_{E_n}^{\infty} dE \sigma_n^{iz}(E) c \tilde{N}_{FEL}(E, t) > n_e I_n. \tag{1.3.23}$$

$\sigma_n^{iz}(E_{FEL})$ is the photo ionization cross section from level n, n_e is the electron density, I_n is the electron collisional ionization rate, c the speed of light. Employing the Kramers classical cross section for the photo ionization [28, 29], i.e.

$$E > E_n: \sigma_n^{iz}(E) = 2.9 \cdot 10^{-17} \frac{E_n^{5/2}}{Z_{eff} \cdot E^3} [\text{cm}^2] \tag{1.3.24}$$

and the Lotz-formula for the electron collisional ionization [28, 29], i.e.

$$I_n = 6 \cdot 10^{-8} \cdot \left(\frac{Ry}{E_n}\right)^{3/2} \cdot \sqrt{\beta_n} \cdot e^{-\beta_n} \cdot \ln\left[1 + \frac{0.562 + 1.4\beta_n}{\beta_n(1 + 1.4\beta_n)}\right] [\text{cm}^3 \text{ s}^{-1}], \tag{1.3.25}$$

$$\beta_n = \frac{E_n}{kT_e} \tag{1.3.26}$$

we obtain the following estimate for a peak intensity given by $I_{FEL} = cE_{FEL}\tilde{N}_0$:

$$I_{FEL} > 3 \cdot 10^{-8} \cdot n_e(\text{cm}^{-3}) \cdot Z_{eff} \cdot \sqrt{\beta_n} \cdot e^{-\beta_n} \cdot \ln\left[1 + \frac{0.562 + 1.4\beta_n}{\beta_n(1 + 1.4\beta_n)}\right]\left[\frac{W}{\text{cm}^2}\right]. \tag{1.3.27}$$

Note, that in (1.3.27) we have assumed $E_{FEL} = E_n + 3\delta E$ ($\delta E \ll E_{FEL}$) for effective photo ionization. For $n_e = 10^{21} cm^{-3}$, $Z_{eff} = 23$, $\beta_n = 2$ (1.3.27) requests $I_{FEL} > 3 \cdot 10^{14}$ W/cm^2.

1.3.4 Photo Ionization Versus Autoionization

In order to create double core hole vacancies (e.g. the hollow ion configuration K^0L^3 discussed in Fig. 1.2) photo ionization rates of inner atomic shells need to be larger than the autoionizing rate of the states K^1L^3 (because hollow ion creation starts from core hole ionization of the K^2L^3 configuration):

$$K^2L^3 + h\nu_{XFEL} \rightarrow K^1L^3 + e_{photo,1}. \tag{1.3.28}$$

As the state K^1L^3 decays by autoionization, i.e.

$$K^1L^3 \rightarrow K^2L^1 + e_{Auger} \tag{1.3.29}$$

population of the hollow ion configuration K^0L^3 according

$$K^1L^3 + h\nu_{XFEL} \rightarrow K^0L^3 + e_{photo,2} \tag{1.3.30}$$

is only efficient, if the photo ionization rate is larger than the autoionizing rate Γ:

$$\int\limits_{-\tau/2}^{+\tau/2} dt \int\limits_{E_n}^{\infty} dE\sigma_{K^1L^3 \rightarrow K^0L^3}^{iz}(E) c\tilde{N}_{FEL}(E,t) > \Gamma_{K^1L^3 \rightarrow K^2L^1}. \tag{1.3.31}$$

Assuming a photon energy E_{FEL} of the XFEL just above threshold we obtain the following estimate:

$$I_{FEL} > 4 \times 10^{-1} \cdot \Gamma \cdot \frac{Z_{eff}^4}{n^3} \left[\frac{W}{cm^2} \right]. \tag{1.3.32}$$

As autoionizing rates scale approximately like $\Gamma \propto Z^0$ (means almost independent of Z in the hydrogenic approximation) the Z-scaling of (1.3.32) is approximately given by

$$I_{FEL} \propto Z_{eff}^4. \tag{1.3.33}$$

Let us consider the photo ionization of the K-shell of Al I (neutral aluminum) as an example: $Z_{eff} \approx 10.8$, n = 1, $\Gamma \approx 10^{14}$ s^{-1}, $I_{FEL} > 5 \times 10^{17}$ W/cm^2. We note that the

competition between the photoionization of inner shells and the autoionization means that the change in atomic populations due to photo ionization is larger compared to the Auger rate that destroys the inner-shell excited autoionizing state.

1.4   Hollow Crystals: Excotic States of Dense Matter Induced by Intense XFEL Irradiation of Solids

According (1.3.9) a typical XFEL intensity at some keV photon energy implies a photon density $\tilde{N}_0$ of the order of solid density:

$$\tilde{N}_0 = \frac{I_{FEL,\delta E,\tau}}{4 \cdot c \cdot erf^2\left(\sqrt{\ln 2}\right) \cdot E_{FEL}} \approx 3.6 \times 10^8 \cdot \frac{I_{FEL,\delta E,\tau}\left(W/cm^2\right)}{E_{FEL}(eV)} \quad \left[1/cm^3\right].$$

(1.4.1)

E.g., for $I_{FEL,\delta E,\tau} = 10^{17}$ W/cm^2 and $E_{FEL} = 2000$ eV we obtain $\tilde{N}_0 = 1.8 \cdot 10^{22}$ cm^{-3}. Therefore, inside the XFEL light pencil there exist a photon for almost every atom in the lattice structure. As X-ray pulse durations are of the order of (or even smaller) the Auger time scale (about 1–10 fs), the irradiation of solids with XFEL results in a sudden photoionization of inner-shells for almost all atoms in the lattice (note, that macroscopic samples are almost immobile on the fs times scale). Consequently, almost every atom is core ionized and therefore transformed to an autoionizing state. This finally results into a massive burst of Auger electrons on a time scale of some 10 fs.

Figure 1.3 schematically illustrates the corresponding evolution. In Fig. 1.3a a high intensity XFEL beam interacts with a solid density crystal. Due to the high intensity almost all core electrons are photo ionized resulting in the formation of an exotic state, a hollow crystal, Fig. 1.3b. Due to the core hole vacancies, the states are autoionizing and decay on the Auger time scale (1–10 fs). This results into the ejection of Auger electrons. Therefore, the hollow crystal is a very short living exotic dense state of matter.

The density of the photoelectrons and the Auger electrons is near solid density, because almost every atom in the lattice structure has a core hole due to photoionization. In consequence, 3-body recombination is effective to recombine the core hole states. These processes are very important for the solid matter heating (to be discussed below).
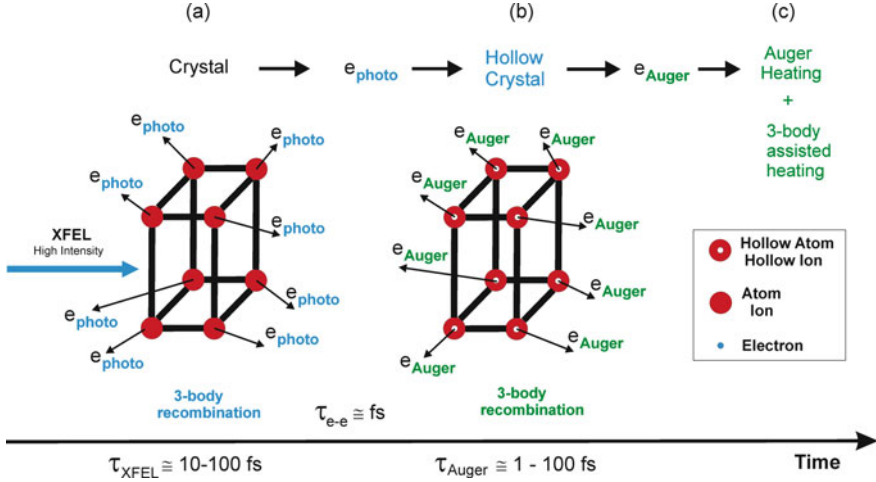
Fig. 1.3 Schematic evolution of XFEL interaction with matter. **a** Interaction with a cold solid, **b** formation of a hollow crystal, **c** Auger and 3-body assisted heating

1.5 Auger Electron Heating and 3-body Recombination Heating

The photoelectrons have kinetic energy E_{photo} given by the difference of the XFEL photon energy E_{XFEL} and the ionization energy E_{core} of the core electron, i.e.

$$E_{photo} = E_{XFEL} - E_{core}. \qquad (1.5.1)$$

The photo electron kinetic energy can therefore be close to zero if the XFEL is tuned exactly to the ionization energy.

This is distinct different for Auger electrons, that have kinetic energies corresponding to the capture energy (see Fig. 1.2). The dielectronic capture energies E_{Auger} are the energy differences between the states before and after autoionization (depicted in Fig. 1.2 by the energy difference between the states (j, Z) and (k, Z + 1), (j, Z) and (k', Z + 1) and (i, Z) and (k', Z + 1)). These capture energies are independent of the photon energy (if the photon energy exceeds the ionization energy for core hole ionization) as they do depend only on the atomic structure. The capture energies of core hole states are of the order of $0.5 \cdot Z_{eff}^2 Ry$ (Z_{eff} is the effective charge seen by the core hole electrons) the Auger electron kinetic energy is therefore very large (and of the order of the core hole ionization energy). Therefore, the kinetic energy of the Auger electrons plays an important role in the material heating.

Auger electron heating has been identified with independent methods in experiments via an analysis of the spectral distribution of the satellite emission originating from the various core hole states [33]. This identification has therefore attributed

an additional new role to the Auger effect, namely a mechanism of direct material heating (apart the usual role as a simple atomic physics process).

The photoelectrons have definite energy (see (1.5.1)) and induce therefore a peak in the electron energy distribution function, i.e. the energy distribution function just after photoelectron ejection is given by

$$F_{photo}(E) \propto \delta\big(E - E_{photo}\big). \qquad (1.5.2)$$

A similar effect is observed for Auger electrons: it is a resonance process and the Auger electron kinetic energy has therefore a definite energy (except the Auger width). We therefore encounter for the electron energy distribution just after Auger electron ejection

$$F_{Auger}(E) \propto \delta\big(E - E_{Auger}\big). \qquad (1.5.3)$$

Due to the high density, Auger electrons as well as photoelectrons equilibrate rapidly (the electron–electron collisional time scale τ_{ee} is of the order of fs for near solid density) among each other and with the "cold" conduction band electrons (fs…10 fs time scale). After equilibration a common "bath" of dense hot electrons is encountered. Subsequently, efficient 3-body recombination from the bath of dense electrons towards the original hole states can take place. The energy released by 3-body recombination is determined by the energy balance between the two continuum electrons with energies E_1 and E_2 that transfer back the energy E to the continuum electron (E_i is the ionization energy)

$$E - E_i = E_1 + E_2. \qquad (1.5.4)$$

Three-body recombination influences therefore on the heating of dense matter.

The importance of 3-body recombination for the material heating is demonstrated in Fig. 1.4 via a 0-dimensional simulation of the XUV-FEL interaction with solid aluminum [6, 45, 46] solving the atomic population equations together with the energy balance equation for an intensity of $I_{FEL} = 10^{16}$ W/cm^2, photon energy of $F_{EEL} = 92$ eV and pulse duration of $\tau = 15$ fs. The solid black curve shows the time evolution of the electron temperature taking into account all atomic physics processes calculated with standard methods of atomic physics [47, 48]. The dashed red curve shows the evolution of the electron temperature when the 3-body recombination rates are reduced by a factor of 10. The green dashed-dot curve shows the electron temperature when the collisional ionization rates are reduced by a factor of 10. The comparison of the red dashed curve and the solid black curves identifies the important role of 3-body recombination as a heating mechanism: suppressing the 3-body recombination by a factor of 10 reduces the maximum temperature considerably. Therefore, turning back the ionization energy to the continuum according (1.5.4) is important for the material heating.

Due to the 3-body recombination into the core hole states, the absorbing ground states are recreated from which further photo absorption in the light pencil can
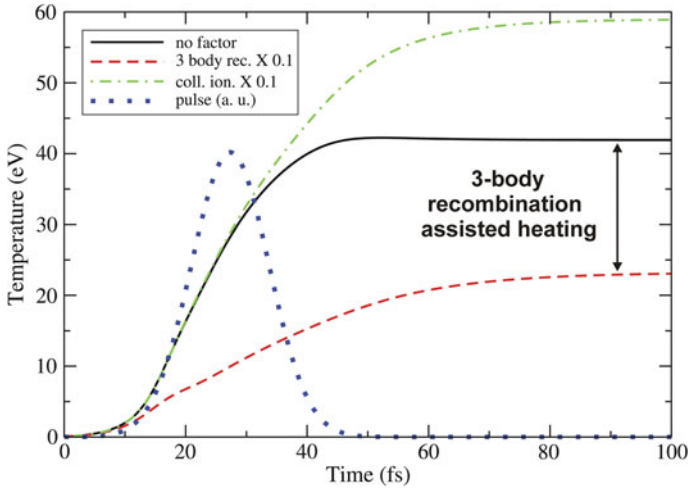
Fig. 1.4 Simulation of the time evolution of the electron temperature in XUV-FEL interaction with solid aluminum (solid black curve). Dashed red curve shows a simulation suppressing the 3-body recombination rates by a factor of 10. The dramatic difference between the red-dashed and solid black curves identifies 3-body recombination as an important mechanism in the material heating. Simulation parameters: $I_{FEL} = 10^{16}$ W/cm^2, $E_{FEL} = 92$ eV, $\tau_{FEL} = 15$ fs

take place. This phenomenon strongly adds to the material heating. In consequence, one atom can even absorb more than one photon during the total period of XFEL interaction. This effect is demonstrated in Fig. 1.5 where it can clearly be seen, that for intensities in excess of about 10^{15} W/cm^2 more than 1 absorption per atom takes place (due to the recreation of absorbing lower states via 3-body recombination and photo de-excitation).

In summary, the well-known processes of photoionization, autoionization and 3-body recombination contribute also directly to the material heating and this attributes a new role to these elementary atomic physics processes for the XFEL induced material heating.

1.6 Seeded XFEL Pumping: Line Profiles in Dense Plasmas

In the overwhelming number of cases, XFEL interaction with matter has been performed so far in the so-called SASE-mode (Self-Amplified Spontaneous Emission mode). This mode is characterized by a bandwidth that usually exceeds the line width of the pumped transition (the bandwidth is typically 0.3% of the photon energy). Therefore, atomic populations might be changed in a drastic manner due to photo absorption and photoionization as discussed above. However, the frequency dependence in the pumping phenomena remained inaccessible up to present days. Therefore strong efforts have been made, to increase the monochromaticity of the
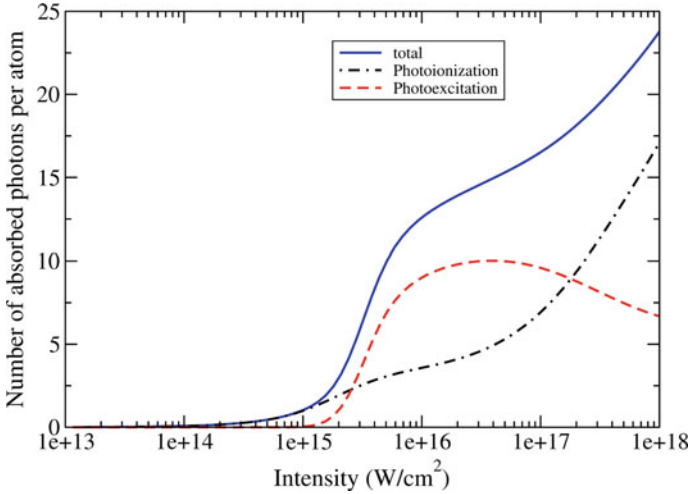
Fig. 1.5 Simulation of the number of absorptions per atom in XUV-FEL interaction with solid aluminum for $E_{FEL} = 92$ eV, $\tau_{FEL} = 15$ fs in dependence of the intensity. The black dashed-dot curve shows the number of absorptions related to the photoionization while the red dashed curve shows the number of absorptions due to photoexcitation. The blue solid curve is the total number of averaged absorptions per atom

XFEL light beam by more than an order of magnitude. These studies resulted in the so-called self-seeded mode [49–51] at XFEL's. Figure 1.6 visualizes the effect of the SASE and self-seeded mode with the X-ray transition $1s7p\,^1P_1 \rightarrow 1s^2\,^1S_0$ of He-like vanadium ions immersed in a dense plasma. The line profile is obtained
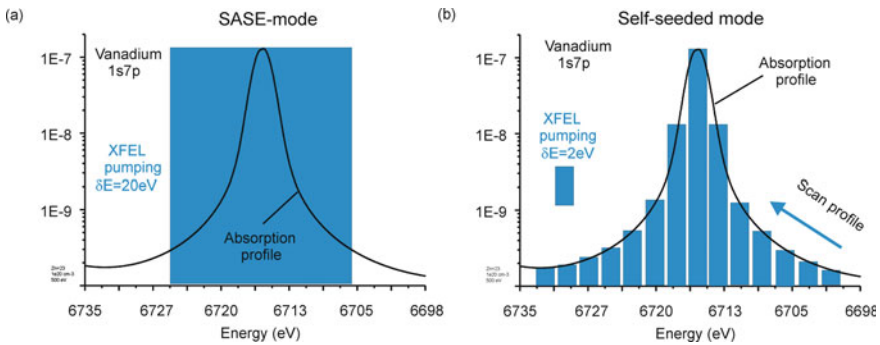
Fig. 1.6 Demonstration of typical X-ray pumping in SASE and self-seeded mode. The pumped transition is $1s^2\,^1S_0 + E_{XFEL} \rightarrow 1s7p\,^1P_1$ in He-like vanadium ($Z_n = 23$). The corresponding He_ζ-line profile of He-like vanadium ions in dense plasmas has been calculated for $n_e = 10^{20}$ cm^{-3}, $kT_e = 500$ eV. It can clearly be seen, that the SASE-mode does not allow pumping the line profile at definite energies. In the self-seeded mode, the bandwidth is about a factor of 10 reduced permitting to scan the line profile from the line wings to the line center

from a Stark broadening simulation for an electron density of $n_e = 10^{20}$ cm^{-3} and an electron temperature of $kT_e = 500$ eV.

Fig. 1.6a demonstrates, that the SASE mode does typically not allow to scan the pumping source with respect to energy over the absorption line profile: the width (indicated with blue rectangle) is too large and integrates changes in absorption over more than 2 orders of magnitude. Figure 1.6b shows the situation for typical parameters in the self-seeded mode [14, 52]. The width of the light beam is sufficiently small to scan the absorption line profile from the line wing to the line center (note, that also important integrations over the bandwidth of $\delta E = 2$ eV are present, however, these integrations are much smaller than those for $\delta E = 20$ eV). This will allow studying the frequency dependence in photoabsorption of ions in dense plasma and has resulted in one of the first beam time proposals and corresponding experimental studies at the LCLS XFEL in high-energy–density science [14, 52].

We note that the simultaneous study of atomic populations and frequency dependence is the most fundamental level in atomic kinetics that is described by the density matrix [28, 29, 53–56]. In dense plasmas, the atomic density matrix equations are given by

$$
\frac{d\tilde{\rho}_{\alpha\beta}}{dt} = -i\omega_{\alpha\beta}\tilde{\rho}_{\alpha\beta} - \frac{i}{\hbar}\sum_{\gamma}\left(V_{\alpha\gamma}\tilde{\rho}_{\gamma\beta} - \tilde{\rho}_{\alpha\gamma}V_{\gamma\beta}\right) + S_{\alpha\beta}
$$
$$
- \left(\frac{\gamma_\alpha}{2} + \frac{\gamma_\beta}{2}\right)\tilde{\rho}_{\alpha\beta} + R_{\alpha\beta} + A_{\alpha\beta} + Q_{\alpha\beta}
$$
. (1.6.1)

$\rho_{\alpha\beta}$ is the density matrix element of the states α and β that is related to the reduced representation according

$$
\tilde{\rho}_{\alpha\beta} = \rho_{\alpha\beta} \cdot \exp\left[-\frac{i}{\hbar}\left(E_\alpha - E_\beta\right)t\right].
$$
(1.6.2)

The diagonal elements $\rho_{\alpha\alpha}$ describe the atomic populations while the non-diagonal elements $\rho_{\alpha\beta}$ are related to coherences. Note, that for the diagonal elements $\tilde{\rho}_{\alpha\beta} = \rho_{\alpha\beta}$. The first term on the right hand side of (1.6.2) is related to the oscillatory behavior of the non-diagonal matrix elements with frequency $\omega_{\alpha\beta} = \frac{1}{\hbar}\left(E_\alpha - E_\beta\right)$, the second term accounts for the mixing of populations $\rho_{\alpha\gamma}$ due to the perturbation potential $V_{\gamma\beta}$ (e.g. the electric plasma microfield). $S_{\alpha\beta}$ is the change of the density matrix in time due to collisions and $\Phi_{\alpha\beta}^{\alpha'\beta'}$ are the matrix elements of the collision operator [48, 54–56]:

$$
S_{\alpha\beta} = \sum_{\alpha'\beta'}\Phi_{\alpha\beta}^{\alpha'\beta'} \cdot \tilde{\rho}_{\alpha'\beta'}.
$$
(1.6.3)

The collision matrix elements $\Phi_{\alpha\beta}^{\alpha'\beta'}$ describe the influence of the density matrix element $\rho_{\alpha'\beta'}$ on the matrix element $\rho_{\alpha\beta}$ due to collisions. The 4th term accounts for the loss of populations due to transitions into quantum states that are not explicitly

included in the set of the density matrix equations, the 5th term describes the inverse process of the 4th term, the 6th term $A_{\alpha\beta}$ describes radiative transitions and the last term accounts for external pumping.

The solution of the set of (1.6.1) demonstrates, that the atomic populations are functions of frequency, i.e.

$$\rho_{\alpha\alpha} = \rho_{\alpha\alpha}(\omega) \tag{1.6.4}$$

and that the non-diagonal elements specify the absorption/emission line profiles [53, 54]. The generalized description via the atomic density matrix is distinct different from the standard collisional-radiative model CRM where the intensity is a simple product of the atomic populations with the line profile, i.e. $I_{\alpha\beta} \propto n_\alpha \cdot A_{\alpha\beta} \cdot \varphi_{\alpha\beta}(\omega)$. In the atomic density matrix theory, populations, coherences and line profiles are treated on a unique footing while in the standard model, only populations are present, line profiles are calculated "externally" from the population kinetics and coherences do not exist.

The self-seeded mode of XFEL's provides therefore access to the most fundamental studies in quantum kinetics and the frequency dependent matrix elements $\rho_{\alpha\beta}(\omega)$ and $\rho_{\alpha\alpha}(\omega)$ in dense plasmas. These studies are currently at its infancy.

1.7 Conclusion

High energy, high intensity optical lasers combined with high intensity short pulse XUV/X-FEL Free Electron Laser radiation provide to the scientific community outstanding tools to investigate matter under extreme conditions never obtained in laboratories so far. X-ray spectroscopy and atomic physics in dense plasmas are key topics for a unique understanding of radiation and matter that range from applications in various domains to the most fundamental level of quantum mechanics in dense finite temperature plasmas. In X-ray spectral range, photo absorption and photoionization are essentially related to atomic core ionization. Because the created core hole states are autoionizing, the characteristic X-ray emission corresponds to dielectronic satellite and hollow ion emission that have outstanding properties to explore matter under extreme conditions. Moreover, it has been demonstrated that the XFEL interaction with solid matter attributes a new role to several elementary atomic physics processes: Auger electron heating and 3-body recombination heating have been identified as important heating mechanisms in the X-ray light matter interaction.

Finally, the recent developments of the self-seeded mode at current XFEL's are discussed that enable challenging studies in dense finite temperature matter: dense plasma atomic physics, quantum kinetics, line profiles, non-equilibrium radiative properties and ultra-fast dynamics. To realize these ambitious undertaking, dense

plasma atomic physics, related quantum kinetics and X-ray spectroscopy have to be developed above the current-state-of-the-art.

References

1. F. Chen, *Plasma Physics and Controlled Fusion*, 2nd edn. (Plenum Press, New York and London, 1984)
2. S. Ichmaru, *Statistical Plasmas Physics: Condensed Plasmas* (Westview Press, Oxford, 2004)
3. W.-D. Kraeft, D. Kremp, W. Ebeling, G. Röpke, *Quantum Statistics of Charged Particle Systems* (Akademie-Verlag, Berlin, 1986)
4. R. Drake, *High-Energy-Density Physics* (Springer, Berlin, 2006)
5. R. Cheng, Y. Lei, X. Zhou, Y. Wang, Y. Chen, Y. Zhao, J. Ren, L. Sheng, J. Yang, Z. Zhang et al., Warm dense matter research at HIAF. Matt. Radiat. Extremes **3**, 85 (2018)
6. B. Deschaud, O. Peyrusse F.B. Rosmej, Simulation of XFEL induced fluorescence spectra of hollow ions and studies of dense plasma effects. Phys. Plasmas **27,** 063303 (2020)
7. F. Dorchies, F. Festa, V. Recoules, O. Peyrusse, A. Benuzzi-Munaix, E. Brambrink, A. Levy, A. Ravasio, M. Koenig, T. Hall, S. Mazevet, X-ray absorption K-edge as a diagnostic of the electronic temperature in warm dense aluminum. Phys. Rev. B **92**, 085117 (2015)
8. F. Graziani, M.P. Desjarlais, R. Redmer, S.B. Trickey, *Frontiers and Challenges in Warm Dense Matter*, vol. 96 (Springer Science & Business, 2014)
9. M. Harmand, A. Ravasio, S. Mazevet, J. Bouchet, A. Denoeud, F. Dorchies, Y. Feng, C. Fourment, E. Galtier, J. Gaudin, F. Guyot, R. Kodama, M. Koenig, H. Lee, K. Miyanishi, G. Morard, R. Musella, B. Nagler, M. Nakatsutsumi, N. Ozaki, V. Recoules, S. Toleikis, T. Vinci, U. Zastrau, D. Zhu, A. Benuzzi-Mounaix, X-ray absorption spectroscopy of iron at multimegabar pressures in laser shock experiments. Phys. Rev. B **92**, 024108 (2015)
10. X. Li, F.B. Rosmej, V.A. Astapenko, V.S. Lisitsa, An analytical plasma screening potential based on the self-consistent-field ion-sphere model. Phys. Plasmas **26**, 033301 (2019)
11. X. Li, F.B. Rosmej, Analytical approach to level delocalization and line shifts in finite temperature dense plasmas. Phys. Lett. A **384**, 126478 (2020)
12. F.B. Rosmej, K. Bennadji , V.S. Lisitsa, Dense plasmas effects on exchange energy shifts in highly charged ions: an alternative approach for arbitrary perturbation potentials. Phys. Rev. A **84**, 032512 (2011)
13. F.B. Rosmej, B. Deschaud, K. Bennadji, P. Indelicato, J.P. Marquès, Study of electric dipole matrix elements of He-like ions for X-ray line shape calculations. Phys. Rev. A **87,** 022515 (2013)
14. F.B. Rosmej (principal investigator), S.H. Glenzer, F. Condamine, E. Galtier, O. Renner, D. Khaghani, *Solving Solar Opacity Problems*. LCLS beam time proposal LR21 (2018)
15. S. Zhang, S. Zhao, W. Kang, P. Zhang, X.-T. He, Link between K absorption edges and thermo-dynamic properties of warm dense plasmas established by an imporved first-principles method. Phys. Rev. B **93,** 115114 (2016)
16. E. Galtier, A. Moinard, F. Khattak, O. Renner, T. Robert, J.J. Santos, C. Beaucourt, P. Angelo, V. Tikhonchuk, F.B. Rosmej, High resolution X-ray imaging of K-alpha volume radiation induced by high intensity laser pulse interaction with a copper target. J. Phys. B: At. Mol. Opt. Phys. **45**, 205701 (2012)

17. S.H. Glenzer, F.B. Rosmej, R.W. Lee, C.A. Back, K.G. Estabrook, B.J. MacCowan, T.D. Shepard, R.E. Turner, Measurements of suprathermal electrons in hohlraum plasmas with X-ray spectroscopy. Phys. Rev. Lett. **81**, 365 (1998)

18. O. Renner, M. Smid, D. Batani, L. Antonelli, Suprathermal electron production in laser-irradiated Cu targets characterized by combined methods of x-ray imaging and spectroscopy. Plasma Phys. Controlled Fusion **58,** 075007 (2016)

19. O. Renner, F.B. Rosmej, Challenges of X-ray spectroscopy in investigations of matter under extreme conditions. Matt. Radiat. Extremes (Rev.) **4**, 024201 (2019)

20. F.B. Rosmej, Hot electron X-ray diagnostics. Lett. J. Phys. B: At. Mol. Opt. Phys. **30**, L819 (1997)

21. M. Smid, O. Renner, A. Colaitis, V. Tikhonchuk, T. Schlegel, F. Rosmej, Characterization of suprathermal electrons inside laser accelerated solid density matter via axially-resolved K-alpha emission. Nat. Commun. **10**, 4212 (2019)

22. Y. Kida, R. Kinjo, T. Tanaka, Synthesizing high order harmonics to generate a sub-cycle pulse in free electron lasers. Appl. Phys. Lett. **109**, 151107 (2016)

23. F.B. Rosmej, V.A. Astapenko, V.S. Lisitsa, Effects of ultrashort laser pulse durations on Fano resonances in atomic spectra. Phys. Rev. A **90**, 043412 (2014)

24. F.B. Rosmej, V.A. Astapenko, V.S. Lisitsa, Scaling laws for ionization of atomic states by ultra-short electromagnetic pulses. J. Phys. B: At. Mol. Opt. Phys. **49**, 025602 (2016)

25. F.B. Rosmej, V.A. Astapenko, V.S. Lisitsa, XUV and X-ray elastic scattering of attosecond electromagnetic pulses on atoms. J. Phys. B: At. Mol. Opt. Phys. **50**, 235601 (2017)

26. F.B. Rosmej, V.A. Astapenko, V.S. Lisitsa, N.N. Moroz, Non-linear resonance scattering of femtosecond X-ray pulses on atoms in plasmas. Phys. Lett. A **381**, 3576 (2017)

27. F.B. Rosmej, V.A. Astapenko, V.S. Lisitsa, X. Li, E. Khramov, Scattering of ultrashort laser pulses on ion-sphere in dense plasmas. Contrib. Plasma Phys. **59**, 189 (2019). https://doi.org/10.1002/ctpp.201800062

28. F.B. Rosmej, V.A. Astapenko, V.S. Lisitsa, *Plasma Atomic Physics* (Springer, Berlin, 2021)

29. Rosmej FB, Astapenko VA, Lisitsa VS, Vainshtein LA (2020b) Dielectronic recombination in non-LTE plasmas. Matter and Radiation at Extremes, submitted

30. LSLS (2021). https://lcls.slac.stanford.edu

31. EU-XFEL 2021. https://www.xfel.eu/

32. SACLA, 2021. http://xfel.riken.jp/eng/

33. E. Galtier, F.B. Rosmej, D. Riley et al., Decay of crystaline order and equilibration during solid-to-plasma transition induced by 20-fs microfocused 92 eV Free Electron Laser Pulses. Phys. Rev. Lett. **106**, 164801 (2011)

34. F.B. Rosmej, R.W. Lee, Hollow ion emission driven by pulsed x-ray radiation fields. Europhys. Lett. **77**, 24001 (2007)

35. F.B. Rosmej, R.W. Lee, D.H.G. Schneider, Fast x-ray emission switches driven by intense x-ray free electron laser radiation. High Energy Density Phys. **3**, 218 (2007)

36. F.B. Rosmej, Ionization potential depression in an atomic-solid-plasma picture. Lett. J. Phys. B: At. Mol. Opt. Phys. **51**, 09LT01 (2018)

37. F.B. Rosmej, X-ray emission spectroscopy and diagnostics of non-equilibrium fusion and laser produced plasmas, in *Highly Charged Ion Spectroscopic Research* ed. by Y. Zou, R. Hutton (Taylor and Francis, 2012), pp. 267–341. ISBN: 9781420079043. http://www.crcnetbase.com/isbn/9781420079050

38. F.B. Rosmej, Exotic states of high density matter driven by intense XUV/X-ray free electron lasers, "Free Electron Laser". In: Varró S (eds) InTech (2012). ISBN 978–953–51–0279–3. The download from the webside is free of charge: https://www.intechopen.com/books/free-electron-lasers/exotic-states-of-high-density-matter-driven-by-intense-xuv-x-ray-free-electron-lasers

39. F.B. Rosmej, R. Dachicourt, B. Deschaud, D. Khaghani, M. Dozières, M. Smîd, O. Renner, Exotic X-ray emission from dense plasmas. J. Phys. B: Rev. Spec. Top. **48,** 224005 (2015). Available online http://iopscience.iop.org/article/. https://doi.org/10.1088/0953-4075/48/22/224005

40. V.A. Boiko, V.A. Vinogradov, S.A. Pikuz, I.Y. Skobelev, A.Y. Faenov, X-ray spectroscopy of laser produced plasmas. J. Sov. Laser Res. **6**, 82 (1985)
41. H.R. Griem, *Principles of Plasma Spectroscopy* (Cambridge University Press, New York, 1997)
42. H.-J. Kunze, *Introduction to Plasma Spectroscopy* (Springer, Berlin, 2009)
43. C. de Michelis, M. Mattioli, Soft X-ray spectroscopic diagnostics of laboratory plasmas. Nucl. Fusion **21**, 677 (1981)
44. H. Mimura, H. Yumoto, S. Matsuyama, T. Koyama, K. Tono, Y. Inubushi, T. Togashi, T. Sato, J. Kim, R. Fukui, Y. Sano, M. Yabashi, H. Ohashi, T. Ishikawa, K. Yamauchi, Generation of 10^{20} Wcm^{-2} hard X-ray laser pulses with two-stage reflective focusing system. Nat. Commun. **5**, 3539 (2014)
45. B. Deschaud, O. Peyrusse, F.B. Rosmej, Generalized atomic physics processes when intense femtosecond XUV- and X-ray radiation is interacting with solids. Europhys. Lett. **108**, 53001 (2014)
46. B. Deschaud, O. Peyrusse, F.B. Rosmej, Atomic kinetics for isochoric heating of solid aluminum under short intense XUV free electron laser irradiation. HEDP **15**, 22 (2015)
47. R.D. Cowan, The theory of atomic structure and spectra (University of California Press, 1981)
48. I.I. Sobelman, L.A. Vainshtein, Excitation of atomic spectra (Alpha Sci. 2006, ISBN 978-1842652336)
49. J. Aman et al., Demonstration of self-seeding in a hard-X-ray free-electron laser. Nat. Photonics **6**, 693 (2012)
50. G. Geloniet al., A novel self-seeding scheme for hard X-ray FELs. J. Mod. Opt. **58,** 1391 (2011). https://doi.org/10.1080/09500340.2011.586473
51. S. Serkez, Soft X-ray self-seeding simulation methods and their application for LCLS, in *Proceedings of FEL2014, Basel*, Switzerland, MOO090 (2014). ISBN 978-3-95450-133-5
52. F.P. Condamine, D. Khaghani, E. Glatier, L. Gournay, O. Renner, E. Cunningham, G. Dyer, M. Greenberg, B. Nagler, H.-J. Lee, S.H. Glenzer, F.B. Rosmej, Self-seeded X-ray laser resonant pumping of highly charged ions in hot dense plasma, in preparation (2020)
53. A.N. Anufrienko, A.L. Godunov, A.V. Demura, Yu.K. Zemtsov, V.S. Lisitsa, A.N. Starostin, M.D. Taran, V.A. Shchipakov, Nonlinear interference effects in Stark broadening of ion lines in a dense plasma. Sov. Phys. JETP **71**, 728 (1990)
54. A.N. Anufrienko, A.E. Bulyshev, A.L. Godunov, A.V. Demura, Yu.K. Zemtsov, V.S. Lisitsa, A.N. Starostin, Nonlinear interference effects and ion dynamics in the kinetic theory of Stark broadening of the spectral lines of multicharged ions in a dense plasma. Sov. Phys. JETP **76**, 219 (1993)
55. V.S. Lisitsa, *Atoms in Plasmas* (Springer, New York, 1994)
56. S.G. Rautian, A.M. Shalagin, *Kinetic Problems of Non-linear Spectroscopy* (North-Holland, 1991)

Chapter 2
Recent Progress on Identifications of Spectral Lines from Tungsten Ions in Low and High Ionization Stages Using Laboratory Plasmas for Fusion Research and Its Application to Plasma Diagnostics

S. Morita, C. F. Dong, D. Kato, T. Oishi, L. Zhang, K. Fujii, M. Goto, M. Hasuo, Y. Kawamoto, I. Murakami, N. Nakamura, and H. A. Sakaue

Abstract Tungsten spectra in visible, vacuum ultra-violet (VUV) and extreme ultra-violet (EUV) wavelength ranges have been studied in LHD, EAST and HL-2A toroidal devices for magnetic-confinement fusion research. Tungsten spectra from low-ionized tungsten ions are observed in VUV and EUV ranges, e.g. W VI at 605.926 Å and W VII at 216.219 Å and 261.387 Å, and Doppler temperature of the W^{5+} ion and edge tungsten influx rate of the W^{6+} ion are analyzed. Ionization stages of unresolved transition array mainly consisting of W^{24+}-W^{33+} ions at 15–70 Å are determined at each small wavelength interval of 0.1 Å based on radial profile measurement. The density profile is analyzed for W^{24+} and W^{27+} ions in addition to highly ionized ions, e.g. W^{44+} and W^{45+}. Several magnetic dipole forbidden lines are observed, e.g. W XXVII and W XXVIII, and the density profile is also analyzed for W^{27+} ions. Contributions are made on tungsten diagnostics for fusion research through the present studies.

S. Morita (✉) · D. Kato · T. Oishi · M. Goto · Y. Kawamoto · I. Murakami · H. A. Sakaue
National Institute for Fusion Science, Toki, Gifu 509-5292, Japan
e-mail: morita@nifs.ac.jp

C. F. Dong
Southwestern Institute of Physics, P.O. Box 432, Chengdu 610041, China

L. Zhang
Institute of Plasma Physics, Chinese Academy of Sciences, Hefei, Anhui 230031, China

K. Fujii · M. Hasuo
Department of Mechanical Engineering and Science, Kyoto University, Kyoto 615-8540, Japan

N. Nakamura
Institute for Laser Science, The University of Electro-Communications, Chofu 182-8585, Tokyo, Japan

2.1 Introduction

In recent fusion research the study on tungsten as impurity atoms and ions are extremely important because the tungsten is used as a divertor material in ITER tokamak. At present behavior of the tungsten has been widely studied in the field of edge and core impurity transports, divertor physics and plasma-wall interaction in addition to physical properties of the solid tungsten. For the purpose the study of tungsten spectra and related atomic physics, e.g. spectral structure, photon emission coefficient and wavelength of spectral lines, is also important for the reliable tungsten diagnostics. Although lots of efforts have been done on the tungsten spectroscopy not only in the fusion device [1, 2] but also in the atomic physics device like EBIT [3, 4], the understanding of the tungsten spectra and atomic database necessary for the analysis are still insufficient. Then, the tungsten spectroscopic study has been energetically done in LHD (NIFS at Toki), EAST (ASIPP at Hefei) and HL-2A (SWIP at Chengdu) toroidal devices for magnetic-confinement fusion research. Recent progresses in these devices on the tungsten study are reported.

Ionization stages of the tungsten ions appeared in these devices are plotted with stripped area in Fig. 2.1 as a function of the tungsten ionization stage. The ionization energy in the vertical axis is equal to the electron temperature of plasmas. The maximum ionization stage which can be produced in the plasma center of the three devices is probably the W^{46+} ion (Table 2.1), while the neutral tungsten atoms and weekly ionized tungsten ions exist in the divertor and peripheral plasma regions, respectively.

Fig. 2.1 Ionization energies, E_i, as a function of tungsten ionization stage. Striped area indicates a range of electron temperatures, T_e, at the whole plasma radial position in LHD NBI discharges under assumption of $T_e = E_i$ and hatched area roughly indicates central electron temperature range of ITER plasmas
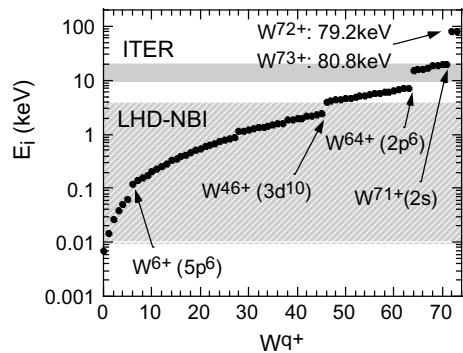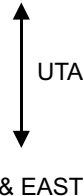
Table 2.1 Electron configurations of tungsten ions. Bold characters show tungsten ions with one or two electrons at the outermost electron orbit, which are useful to tungsten ion density measurement

W^{0} : $1s^2 2s^2 2p^6 3s^2 3p^6 3d^{10} 4s^2 4p^6 4d^{10} 4f^{14} 5s^2 5p^6 4d^6$

W^{6+} : $1s^2 2s^2 2p^6 3s^2 3p^6 3d^{10} 4s^2 4p^6 4d^{10} 4f^{14} 5s^2 5p^6$

W^{12+} : $1s^2 2s^2 2p^6 3s^2 3p^6 3d^{10} 4s^2 4p^6 4d^{10} 4f^{14} 5s^2$

W^{15+} : $1s^2 2s^2 2p^6 3s^2 3p^6 3d^{10} 4s^2 4p^6 4d^{10} 4f^{11} 5s^2$

W^{17+} : $1s^2 2s^2 2p^6 3s^2 3p^6 3d^{10} 4s^2 4p^6 4d^{10} 4f^{11}$

W^{28+} : $1s^2 2s^2 2p^6 3s^2 3p^6 3d^{10} 4s^2 4p^6 4d^{10}$ UTA

W^{38+} : $1s^2 2s^2 2p^6 3s^2 3p^6 3d^{10} 4s^2 4p^6$

W^{44+} : $1s^2 2s^2 2p^6 3s^2 3p^6 3d^{10} 4s^2$

W^{45+} : $1s^2 2s^2 2p^6 3s^2 3p^6 3d^{10} 4s$

W^{46+} : $1s^2 2s^2 2p^6 3s^2 3p^6 3d^{10}$ LHD & EAST

W^{56+} : $1s^2 2s^2 2p^6 3s^2 3p^6$

W^{62+} : $1s^2 2s^2 2p^6 3s^2$ (3p3s-3s^2: 79.91Å)   ITER

W^{63+} : $1s^2 2s^2 2p^6 3s$ (3p-3s: 77.69Å)

W^{64+} : $1s^2 2s^2 2p^6$

W^{70+} : $1s^2 2s^2$ (2p2s-2s^2: 7.12Å)

W^{71+} : $1s^2 2s$ (2p-2s: 7.31Å)

W^{72+} : $1s^2$ (2p2s-1s^2: 0.204Å)

W^{73+} : $1s$ (2p-1s: 0.201Å)

2.2 Tungsten Pellet Injection in LHD

2.2.1 Time Sequence of Tungsten Ionization Stages After Pellet Injection

A small amount of tungsten is injected for tungsten spectroscopy with an impurity pellet [5] accelerated by pressurized He gas in LHD ($3 - 10 \times 10^{16}$ W atoms) and weekly ionized plasma produced by laser blow-off technique [6] in HL-2A ($1 - 4 \times 10^{18}$ W atoms). On the contrary the tungsten ions intrinsically exist in EAST discharges, since the carbon divertor material has been already replaced by the tungsten material [7] for testing the ITER divertor operation.

Figures 2.1a, b show temporal behaviors of electron density and temperature after the tungsten pellet injection in LHD, respectively. As the tungsten pellet has a co-axial structure, i.e. a thin tungsten wire inserted into a graphite tube, the density rise after the pellet injection shown in Fig. 2.1a is mainly brought by carbon ions. The quick drop of the electron temperature seen in Fig. 2.2b is caused by radiation cooling and ionization energy loss due to tungsten ions. The temperature gradually recovers after a few hundred milliseconds of the pellet injection. Then, the ionization of tungsten ions is slowly progresses as shown in Fig. 2.1c–e. The highest ionization stage of tungsten ions in LHD, i.e. W^{45+}, is observed at 1.5 s after the pellet injection. In LHD, therefore, the tungsten spectra from all ionization stages up to W^{45+} ions

Fig. 2.2 Temporal behaviors of **a** electron density, **b** electron temperature and line emissions from **c** low-, **d** middle- and **e** high-ionized tungsten ions after tungsten pellet injection at t = 4.1 s in LHD
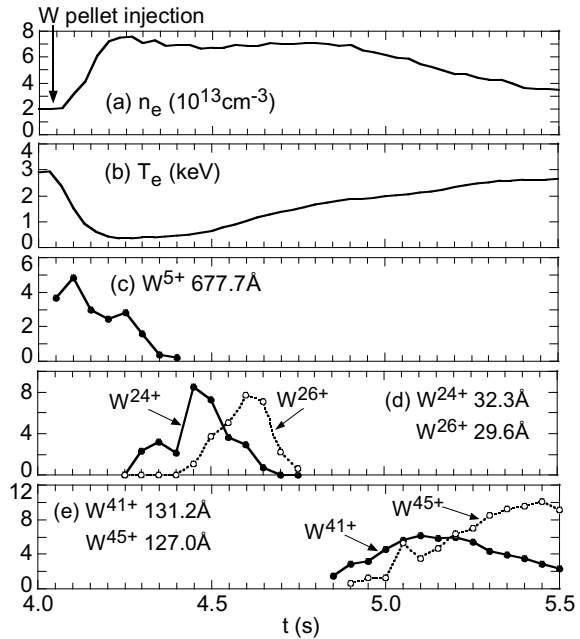
can be measured with sufficient intensities as a function of discharge time after the pellet injection.

2.2.2 Visible W I and W II Spectra from Pellet Ablation Plasmas

When the injected tungsten pellet is ablated by plasma particles, a weakly ionized tungsten plasma called ablation plasma, is first produced along a magnetic flux tube at certain radial location before the tungsten ions expand across the magnetic surface. Visible spectra have been observed from the ablation plasma of which the electron density and temperature are estimated to be $n_e = 5 \times 10^{16}$ cm^{-3} and $T_e = 2.5$ eV, respectively [8]. A typical example is shown in Fig. 2.3 which is taken at the first frame of CCD after the pellet injection. Many tungsten lines are identified on transitions from neutral atoms and singly ionized ions. The strong C II emission at 4267 Å originates in the graphite material of the co-axial tungsten pellet. Although some of lines observed here have been listed in NIST database, several emissions are still unknown. Since the spectra observed here arise from transitions among excited levels reflecting sufficiently high electron collision in the high-density ablation plasma, the line identification is entirely difficult due to the complicated atomic structure at Rydberg states in such atoms and ions. It is noticed here that only WI line at 4009 Å
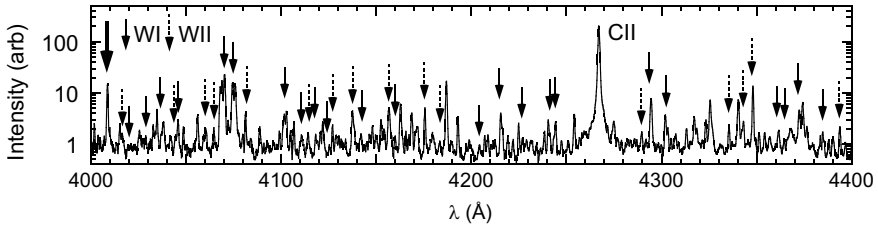
Fig. 2.3 Visible spectrum observed just after the tungsten pellet injection in LHD. The spectra are emitted from low-temperature and high-density ablation plasma made of tungsten pellet itself which is composed of a cylindrical graphite pellet and a co-axially inserted thin tungsten wire

$(5d^4 6s6p\,^7P_4 - 5d^5 6s\,^7S_3)$ can be dominantly observed in fusion plasmas because the line emission among excited levels is quite weak due to the low electron density, e.g. $n_e \sim 1 \times 10^{13}$ cm^{-3} at the plasma edge.

2.3 Low-Ionized Tungsten Ions

2.3.1 Observation of VUV Spectra and Measurement of W^{5+} Ion Temperature

VUV spectra from low-ionized tungsten ions can be observed during ~ 300 ms at low T_e phase after the pellet injection, as seen in Fig. 2.2c. The tungsten spectra have been extensively searched in the VUV range, in particular, between 500 and 1500 Å using a high-resolution 3 m normal incidence spectrometer. As a result, many tungsten lines from W^{3+} to W^{6+} ions are identified, and VUV lines useful for tungsten diagnostics, i.e. isolated line with sufficiently high intensity, are selected from identified tungsten lines [9]. One of the selected lines, W VI at 605.926 Å, is plotted in Fig. 2.4.

Since most of the VUV lines measured in the present study are isolated from other lines because of the high spectral resolution and large wavelength dispersion, the spectral profile can be also examined. In order to precisely analyze the spectral profile the W VI spectrum at 605.926 Å is measured at the second order light. The

Fig. 2.4 Typical example of VUV line emissions with WVI ($6p\,^2P_{3/2} \rightarrow 5d\,^2D_{3/2}$) at 600–635 Å observed during a few hundreds of milliseconds after the tungsten pellet injection in LHD
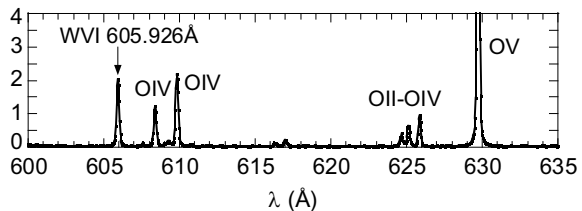
Fig. 2.5 Doppler-broadened
W VI profile measured at
second order of 605.926 Å
shown in Fig. 2.4
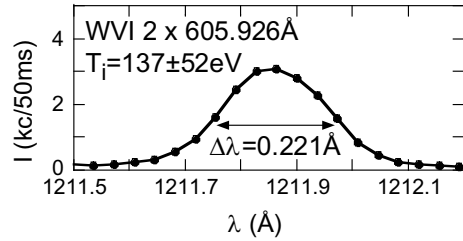
result is shown in Fig. 2.5. It clearly indicates a Dopper-broadened profile with
spectral line width of 0.221 Å, which results in a local ion temperature of 137 eV at
a radial position where the W^{5+} ion exists in the LHD edge plasma.

2.3.2 Observation of EUV Spectra and W^{6+} Ion Influx Analysis

Spectra from low-ionized tungsten ions are also surveyed in HL-2A. Recently, the
tungsten spectra from W^{6+} and W^{7+} ions are newly found in the EUV range [10]. A
typical EUV spectrum with W VII and W VIII lines observed after the tungsten laser-
blow-off injection is shown in Fig. 2.6. In particular, the two W VII lines isolated
from other lines have enough intensity for the analysis. The tungsten ion influx can
be then determined from absolute intensity of the W VII line because the W^{6+} ion
exists in the edge of the main plasma but not in the divertor region. If the tungsten
influx analysis is possible, the total number of tungsten ions entering the main plasma
can be estimated from the influx rate. Therefore, the present study is very important
for a quantitative analysis of the tungsten transport.

In HL-2A discharges after the laser bow-off injection a sudden enhancement of
the plasma-wall interaction sometimes occurs at divertor plate where the tungsten
has been already deposited by the laser blow-off. A typical indication of the enhanced

Fig. 2.6 EUV spectrum at
190–280 Å after tungsten
laser blow-off in HL-2A
discharges. W VII and W
VIII are identified and
indicated with bold
characters
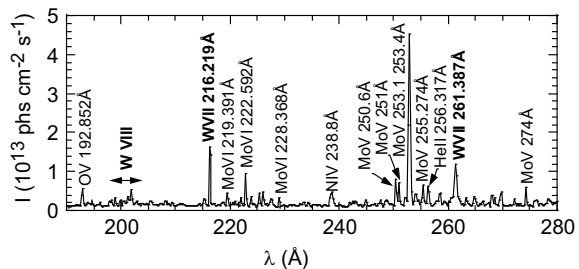
Fig. 2.7 Temporal behaviors of **a** deuterium Balmer-α line (6561 Å) intensity, **b** divertor flux, W VII line (216 Å) intensity and **d** W^{6+} ion influx rate after tungsten laser blow-off. A sudden plasma-wall interaction occurs at t = 0.842 and 0.852 s
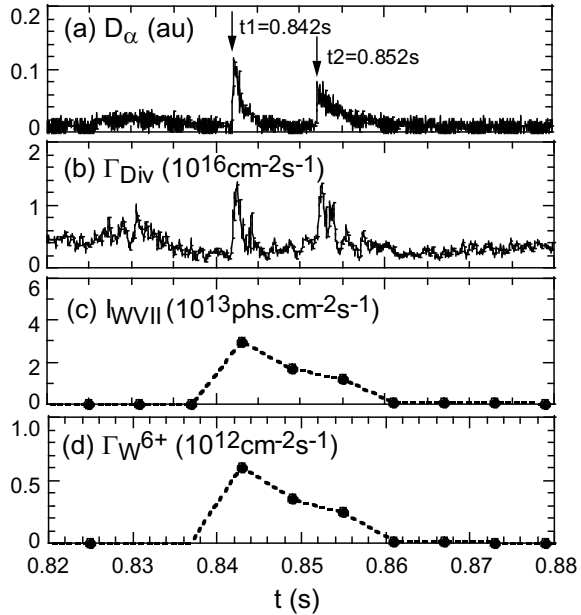
interaction usually appears in deuterium Balmer-α (Dα) light and divertor flux (Γ_{Div}), as seen in Fig. 2.7a and b, respectively. In the figure the sudden increase in the plasma-wall interaction is occurred twice at t = 0.842 and 0.852 s. According to the events the WVII intensity is also enhanced as plotted in Fig. 2.7c.

The impurity influx, Γ_{imp}(ions · s^{-1} cm^{-2}), for A^{q+} ion, can be derived by

$$\Gamma_{imp} = I_{imp} \times (S/XB), \tag{2.1}$$

where I_{imp} (photons · s^{-1} cm^{-2}) is the measured line intensity, S (cm^{-3} s^{-1}) the electron impact ionization rate, X (cm^{-3} s^{-1}) the electron impact ionization rate and B the branching ratio. The coefficient, S/XB, called 'inverse photon efficiency' denotes the number of ionization events per detected photon (ions/photon). In the present analysis the ADAS code [11] is used for deriving the inverse photon efficiency. The result is shown in Fig. 2.7d. The total number of W^{6+} ions, N_{W6+}, can be obtained by integrating the influx rate over the whole plasma surface, i.e. $N_{W6+} = 1.4 \times 10^{15}$. If all W^{6+} ions are fully confined and uniformly distributed in the plasma, we can roughly estimate the tungsten density to be $n_W \sim 10^9$ cm^{-3}. It indicates a reasonable ratio of $n_W/n_e \sim 10^{-4}$ against the electron density.

2.4   Highly Ionized Tungsten Ions

2.4.1   Analysis of Tungsten Unresolved Transition Array

In heavy ions with many orbital electrons huge numbers of spectral lines are emitted in the same wavelength range and highly overlapped each other. It creates a pseudo-continuum spectrum composing of thousands of transitions. In the case of tungsten ions the pseudo-continuum spectrum called unresolved transition array (UTA) appears in the EUV wavelength range of 15–70 Å. It basically arises from W^{17+}–W^{43+} ions. A typical example of the UTA observed from LHD plasmas with relatively low electron temperature of $T_e = 0.94$ keV is shown in Fig. 2.8. The spectrum includes 6 g–4f transitions (W^{24+}–W^{28+}) at 20–25 Å and 5 g–4f (W^{17+}–W^{27+}) transitions and 4d–4f and 5d–4f (W^{17+}–W^{27+}) at 45–70 Å [12]. If C VI and O VIII spectra are compared with each peak in the UTA, we notice all the UTA peak widths are much wider than the spectral resolution of the EUV spectrometer which is equivalent to the C VI and O VIII spectral widths. Therefore, the spectral identification of the UTA is quite difficult even if the UTA spectrum is analyzed with CR model. In LHD, then, a new method to identify the UTA spectra is attempted by measuring the radial profile.

At first all the UTA spectra are divided into a small wavelength unit of ~ 0.1 Å, and then the radial profile is measured at each wavelength unit over the whole wavelength range where the UTA spectra exist [13]. Since the electron temperature in fusion plasmas has a radial profile, the radial profile of the UTA entirely depends on the ionization stage of tungsten ion existing within the small wavelength unit. Therefore, if the radial profile is identical between different two wavelength units, both wavelength units belong to the same ionization stage of tungsten ion. Typical results are shown in Fig. 2.9a, b. The comparison between two wavelength units exhibits an entirely identical profile. When the radial profile of the UTA is analyzed against the electron temperature profile, we can finally determine the ionization stage of the tungsten ion. In the case of Fig. 2.9a, b, the ionization stage is determined to be W^{27+} and W^{24+}, respectively.
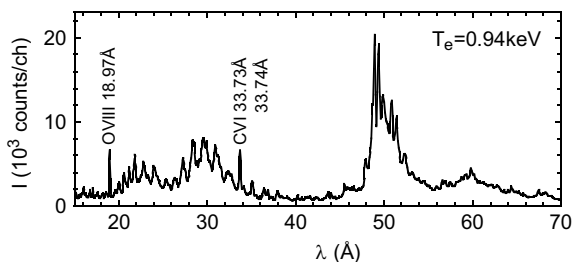
Fig. 2.8 Typical tungsten spectrum with unresolved transition array (UTA) at 15–70 Å observed in LHD. The spectrum at $T_e = 0.94$ keV includes 6 g–4f transitions at 20–25 Å and 5 g–4f transitions from $W^{24+} - W^{28+}$ ions and 4d-4f and 5d-4f transitions at 45–70 Å from $W^{17+} - W^{27+}$ ions

Fig. 2.9 Radial intensity profiles along vertical direction in LHD plasmas of **a** W XXVIII (W^{27+} emissions) measured at 28.38 Å $\leq \lambda \leq$ 28.48 Å (open circles) and 49.24 Å $\leq \lambda \leq$ 49.46 Å (solid triangles) and **b** W XXV (W^{24+} emissions) measured at 32.28 Å $\leq \lambda \leq$ 32.39 Å (open circles) and 47.94 Å $\leq \lambda \leq$ 48.15 Å (solid triangles)
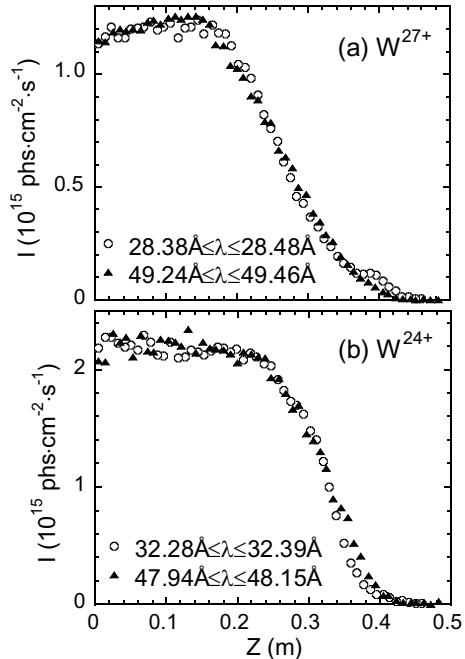
Next, we calculate the density profile of such ions based on the measured radial profile of the UTA spectrum [14]. For the calculation the measured profile in Fig. 2.9 is reconstructed into a local emissivity profile, $\varepsilon(\rho)$, as a function of normalized plasma radius, ρ, through Abel inversion method. The value of ρ is a function of magnetic surfaces for plasma confinement, i.e. $\rho = 0$ at plasma center and $\rho = 1$ at plasma edge, and generally used in the radial transport analysis because the plasma cross section is non-circular and the central plasma position is basically always shifted due to the plasma pressure effect. To obtain the tungsten ion density profile, $n_{Wq+}(\rho)$, photon emission coefficient, f_{PEC}, is necessary in addition to the electron density and temperature profiles which have been precisely measured in the fusion plasma experiment. The relation is expressed by

$$n_{Wq+}(\rho) = \varepsilon(\rho)/[n_e(\rho) \times f_{PEC}(T_e, \; n_e)]. \tag{2.2}$$

We have developed the CR model for analyzing the UTA spectrum where the principal quantum numbers up to $n = 7$ and roughly ten thousands J-resolved fine-structure levels, e.g. 11,753 for W^{24+}, are considered with several electron configurations, e.g. 19 for W^{24+}. Inner-shell excitation and configuration interaction are also included. Therefore, tungsten emission lines more than 100 thousands are taken into account at each wavelength interval. Based on the f_{PEC} calculated from the CR model the W^{24+} ion density profiles are analyzed for different electron temperatures, as shown in Fig. 2.10a. To compare with the result from the present CR model code

Fig. 2.10 Radial profiles of W^{24+} ion density at electron temperatures of 2.19 keV (dashed lines), 1.95 keV (thin solid lines) and 1.82 keV (dotted lines) calculated with photon emission coefficients from **a** CR model and **b** ADAS code. The abscissa indicates normalized radius, i.e. $\rho = 0$ and 1.0 mean plasma center and edge, respectively
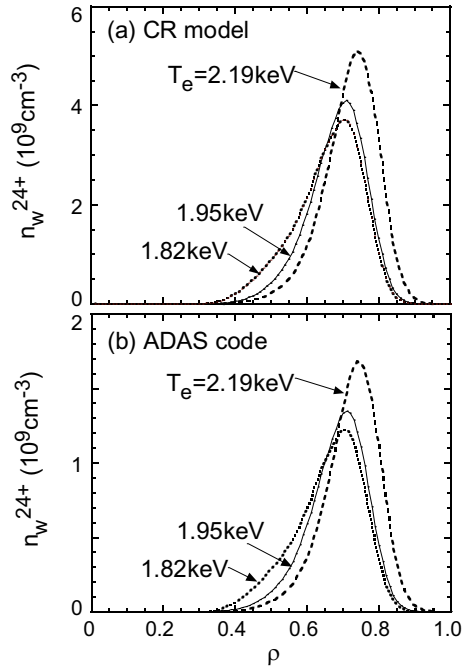
the analysis is also done using the open-ADAS code [15]. The result is plotted in Fig. 2.10b. We notice that the W^{24+} ion density from the CR-model is roughly three times bigger than that from the ADAS code. The photon emission coefficient from the ADAS code seems to be increased by additional consideration on a cascade effect from higher excited levels.

The W^{24+} ion density is also analyzed for different pellet sizes. The result is shown in Fig. 2.11. The W^{24+} density reasonably increases with the pellet size. It indicates the injected tungsten atoms are fully evaporated and confined in the plasma. Then, we can easily estimate the total number of tungsten ions, N_W, staying in the

Fig. 2.11 Radial profiles of W^{24+} ion density at $t = 0.1$ s after pellet injection with different tungsten wire sizes of $60 m^{\phi} \times 1mm^{L}$ (dashed line), $50 m^{\phi} \times 1mm^{L}$ (thin solid line) and $30 m^{\phi} \times 1mm^{L}$ (dotted line) as a function of normalized plasma radius, ρ
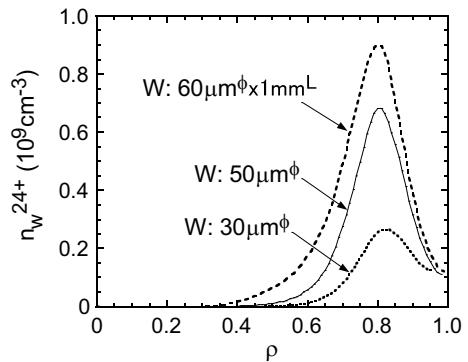
plasma from the tungsten wire size. On the other hand, if we assume the ionization equilibrium for tungsten ions in the LHD plasma, the value of N_W can be also estimated from the analyzed W^{24+} ion density profile shown in Fig. 2.10. When the value of N_W from the tungsten ion density profile is compared with the N_W from the pellet size, a good agreement is unexpectedly obtained for the analysis with the ADAS code. However, the present result does not dismiss the importance of the precise CR model construction. It rather emphasizes further development of the CR model to understand more deeply and exactly the atomic process in many electron systems such as tungsten.

2.4.2 Density Profile Measurement of W^{43+} and W^{45+} Ions

The tungsten spectra in the EUV range have been energetically studied also in EAST device with tungsten divertor. One of the main aims in the EAST tungsten diagnostics is to determine the tungsten density in the central plasma region. For the purpose radial profiles from highly ionized tungsten ions have been observed in EAST discharges. The radial profiles of W XLIV (128.29 Å) from W^{43+} ions and W XLVI (126.998 Å) from W^{45+} ions observed from H-mode discharges with $T_e = 2.9$ keV are shown in Fig. 2.12a [16]. The local emissivity profiles reconstructed from Fig. 2.12a are plotted in Fig. 2.12b. The centrally peaked profiles indicate those ions exist in the central plasma region. The W^{43+} and W^{45+} ion density profiles are analyzed from the

Fig. 2.12 Radial profiles of **a** W XLIV (128.29 Å) and W XLVI (126.998 Å) intensities, **b** W XLIV and W XLVI local emissivity and W^{43+} and W^{45+} ion densities as a function of normalized plasma radius, ρ, observed from EAST plasmas
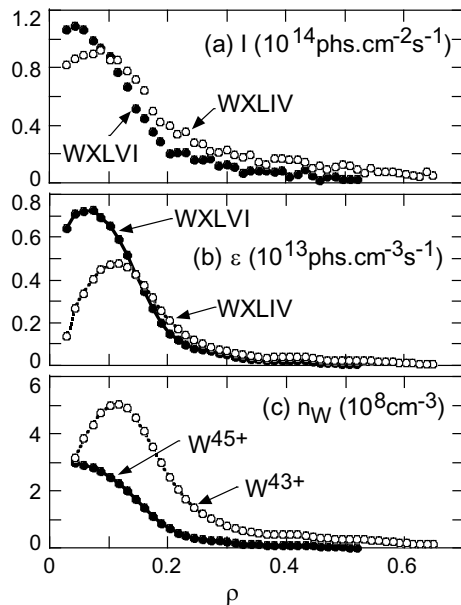
Fig. 2.13 Visible spectrum with tungsten magnetic dipole forbidden transitions (M1) of W XXVII (3337 Å: $4f^2 \, ^3F_4 \to \, ^3F_3$), W XXVII (3357 Å: $4f^2 \, ^3F_4 \to \, ^3G_4$) and W XXVIII (3377 Å: $4f \, ^2F_{7/2} \to \, ^2F_{5/2}$)
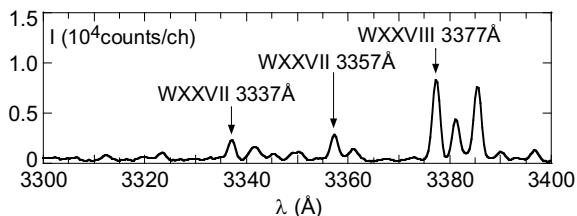
local emissivity profile based on the (2.2) as well as the manner in the density analysis of W^{24+} ions. Here, the values of f_{PEC} are taken from the open-ADAS database [15].

It is found through the analysis that the central density of $W^{43+} - W^{45+}$ ions are distributed in the range of $2 - 6 \times 10^8$ cm^{-3}. It suggests a value of $0.2 - 0.5 \times 10^{-4}$ to the electron density in the plasma center of H-mode discharges. The result indicates the H-mode discharge is still sustainable even at such a relatively high tungsten concentration.

2.5 Observation of M1 Transitions and W^{27+} Density Profile Analysis

The magnetic dipole forbidden line (M1), which is a transition among sub-levels in ground level, has been extensively studied in LHD [17–19]. Recently, the M1 transition is successfully found for tungsten ions in the visible range by injecting a relatively large tungsten pellet to increase the intensity [20–22]. A typical visible spectrum with M1 transitions is shown in Fig. 2.13 in the wavelength range of 3300–3400 Å. Three M1 transitions from W^{26+} and W^{27+} ions are clearly found in the wavelength range. Those are identified as W XXVII $4f^2 \, ^3F_4 \to \, ^3F_3$ (3337 Å), W XXVII $4f^2 \, ^3F_4 \to \, ^3G_4$ (3357 Å) and W XXVIII $4f \, ^2F_{7/2} \to \, ^2F_{5/2}$ (3377 Å). As the W XXVIII M1 intensity at 3377 Å is considerably strong among the three M1 lines, the radial profile measurement is attempted for application to the tungsten diagnostics. Fortunately, the radial profile has been observed with sufficient intensity.

An example of the radial profile of the W XXVIII M1 line is represented in Fig. 2.14a. The hollow intensity profile indicates the W^{27+} ion exists in outer region of the LHD plasma because the central electron temperature is much higher than the ionization energy of the W^{27+} ion. Based on the same manner mentioned above, the W^{27+} ion density profile is analyzed as shown in Fig. 2.14b. A CR model code is developed for the M1 line intensity analysis to obtain the f_{PEC}. In the modeling energy levels, radiative transition rates and electron distorted-wave cross sections are calculated using HULLAC code [23]. A contribution of proton collisions is very important in evaluating the M1 intensity because the transition energy of the M1 transition is very small. Then, cross sections of the proton collision are newly calculated in a semi-classical perturbation approximation. The W^{27+} ion density is thus obtained here, but the value seems to be unexpectedly large, even if we consider

Fig. 2.14 Radial profiles of **a** W XXVIII M1 line (3377 Å) intensity against vertical direction, Z, and **b** W^{27+} ion density against normalized plasma radius, ρ
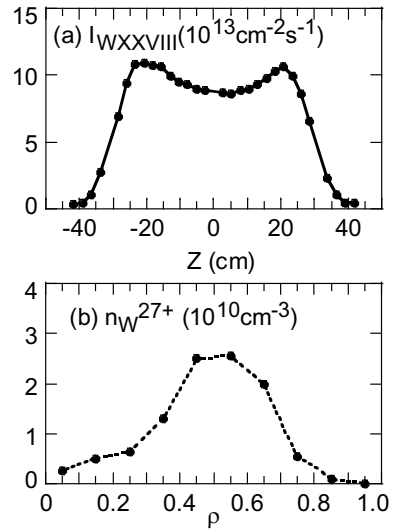
a large tungsten pellet injection and a hollow density profile in which the maximum density position is close to the density peak of $n_W{}^{27+}(\rho)$. The f_{PEC} used in the analysis may be underestimated, while the atomic process related to the M1 intensity is not so simple like an electric dipole transition. Further understanding is necessary on the M1 intensity modeling including the atomic process.

2.6 Summary

Tungsten spectra from weakly and highly ionized tungsten ions have been studied in LHD, EAST and HL-2A fusion devices at visible, VUV and EUV wavelength ranges including unresolved transition array and M1 transition. A method of analyzing the tungsten influx is developed by utilizing newly identified W VII emissions. Radial profiles of the tungsten spectra are observed for deeper understanding of the UTA spectral structure and for the tungsten density diagnostic. The tungsten ion density profiles are successfully obtained for many ionization stages of tungsten ions. The photon emission coefficients necessary for the density determination are also examined by developing the CR modeling code and adopting the ADAS database. Unfortunately, a non-negligible discrepancy is found between the CR models developed here and the experimental result in evaluating the tungsten ion density. However, the inconsistency may encourage the future efforts to more deeply understand the atomic process of tungsten ions with complicated electron configurations.

References

1. S. Morita, C.F. Dong, D. Kato et al., J. Phys. Conf. Series **1289**, 012005 (2019)
2. T. Pütterich, E. Fable, R. Dux et al., Nucl. Fusion **59**, 056013 (2019)
3. H.A. Sakaue, D. Kato, N. Yamamoto et al., Phys. Rev. A **92**, 012504 (2015)
4. M.L. Qiu, W.X. Li, Z.Z. Zhao et al., J. Phys. B **48**, 144029 (2015)
5. K. Zhang, Z.Y. Cui, P. Sun et al., Chin. Phys. B **52**, 065202 (2016)
6. X.L. Huang, S.Morita, T.Oishi et al., Rev. Sci. Instrum. **85**, 11E818 (2014)
7. D. Yao, G. Luo, S. Du et al., Fusion Eng. Des. **98–99**, 1692 (2015)
8. M. Goto, S. Morita, M. Koubiti, J. Phys. B **43**, 144023 (2010)
9. T. Oishi, S. Morita, X.L. Huang et al., Phys. Scr. **91**, 025602 (2016)
10. C.F. Dong, S. Morita, Z.Y. Cui et al., Nucl. Fusion **59**, 016020 (2019)
11. H.P. Summers, The ADAS User Manual version 2.6 (www.adas.ac.uk) 2004
12. S. Morita, C.F. Dong, M. Goto et al., AIP Conf. Proc. **1545**, 143 (2013)
13. Y. Liu, S. Morita, S. Huang et al., J. Appl. Phys. **122**, 233301 (2017)
14. Y. Liu, S. Morita, I. Murakami et al., Jpn. J. Appl. Phys. **57**, 106101 (2018)
15. Open-ADAS. http://open.adas.ac.uk
16. L. Zhang, S. Morita, Z.W. Wu et al., Nucl. Instrum. Meth. A **916**, 169 (2019)
17. R. Katai, S. Morita, M. Goto, J. Quant. Spectr. Radiant. Trans. **107**, 120 (2007)
18. R. Katai, S. Morita, M. Goto, Plasma Fus. Res. **2**, 006 (2007)
19. H.A. Sakaue, N. Yamamoto, S. Morita et al., J. Appl. Phys. **109**, 073304 (2011)
20. D. Kato, M. Goto, S. Morita et al., Phys. Scr. **T156**, 014081 (2013)
21. M. Shinohara, K. Fujii, D. Kato et al., Phys. Scr. **90**, 125402 (2015)
22. K. Fujii, Y. Takahashi, Y. Nakai et al., Phys. Scr. **90**, 125403 (2015)
23. A. Bar-Shalom, M. Klapisch, J. Oreg, J. Quant. Spectr. Radiant. Trans. **71**, 169 (2001)

Chapter 3
Radiative Collisions of Atoms and Ions from Astrophysical to Ultracold Domains

James F. Babb and Brendan M. McLaughlin

Abstract Charge transfer in collisions between atoms and ions is of fundamental interest for many applications. In this paper, radiative charge transfer processes, in which an atom and ion collide and emit radiation in the vibrational continua of the initial and final quasimolecules, are discussed. After a brief historical review and discussions of applications to astrophysics and to ultra-cold collisional energies, two case studies are described.

3.1 Introduction

Charge transfer processes in collisions of atoms and ions are of fundamental importance in describing the dynamics affecting energy transfer in ionized gases and the ionization structure in plasmas. The topic is wide and applications can be found in astrophysics [1–4], atmospheric [5] and space and fusion plasma physics [6–8], for example. The immense literature encompasses experimental and theoretical work across a range of collisional energies from those representative of accelerators down to the recently-of-interest domains representative of ultracold collisions. Charge transfer processes may occur without collisional radiation (*direct charge transfer*), though radiation may be emitted by cascade emission from resulting excited electronic states in product species. The charge transfer processes with the emission of cascade radiation form a subset of charge transfer processes also with wide-ranging applications. Such phenomena are observed in varied astrophysical environments including, comets, planets, and the moon, see [7, 9] for recent perspectives. A notable

J. F. Babb (✉)
Institute for Theoretical Atomic, Molecular, and Optical Physics (ITAMP), Center for Astrophysics-Harvard & Smithsonian, 60 Garden St., MS 14, Cambridge, MA 02138, USA
e-mail: jbabb@cfa.harvard.edu

B. M. McLaughlin
Centre for Theoretical Atomic Molecular and Optical Physics, Queens University Belfast, Belfast BT7 1NN, UK
e-mail: bmclaughlin899@btinternet.com

example is solar wind cometary charge exchange [10], in which cometary neutral molecules transfer charge with a highly charged solar wind ion (such as O^{7+}), followed by cascade line radiation from the resulting ions (O^{6+} and so on) in the X-ray wavelengths. Similarly, EUV radiation may result, such as in the collisions of He^+ with neutrals, resulting in, for example, 58.4 nm line radiation from the $He(2p\ ^1P^o)$ state [11]. Somewhat earlier, EUV radiation resulting from solar wind alpha particles colliding with interstellar atomic hydrogen was investigated [12], He^{2+} and H, where 30.4 nm line radiation from the relaxation of the product $He^+(2p\ ^2P^o)$ levels is prevalent. Charge exchange with cascade line radiation will not be addressed in the present work.

In the present paper, the topic will be further narrowed to *radiative charge transfer* processes involving single electron transfer between an atom and a singly or doubly charged ion. Here, the radiation is continuous, corresponding to the photons emitted in spontaneous emission from the continuum of the initial molecular state of the atom-ion colliders to the final molecular state of the ion-atom product state. By way of introduction, in the present section some examples, taken from the literature and recent calculations, will be presented, and the theoretical formulation of the process will be presented and assessed. In the final section, Sect. 3.2, we will briefly present two case studies of radiative charge transfer.

3.1.1   Early Studies

Closely related to the radiative charge transfer process is the *radiative association* process describing a collision where an atom and an ion collide, emit radiation, and form a molecule, i.e.

$$A + B^+ \rightarrow AB^+ + h\nu. \tag{3.1}$$

In the late 40's and early 50's a quantitative theory of radiative association processes was established [13]. Bates calculated the rate coefficients for several cases, such as for $H^+ + H$ forming H_2^+, for $C^+ + H$ forming CH^+, and for $N^+ + N$ forming N_2^+. Process (3.1) represents spontaneous transitions from the molecular vibrational continuum of the intial atom and ion to a bound molecular ion ("free-bound"). In Bates' formulation the probability of spontaneous emission from the initial quasi-molecule to a bound molecule is integrated along the classical path of the colliding atom and ion and an integration over a Maxwellian velocity distribution yields the rate coefficient for a desired temperature.

Arthurs and Hyslop [14] considered the possibility of "free-free" transitions resulting in radiative charge transfer, namely the process

$$A + B^+ \rightarrow A^+ + B + h\nu, \tag{3.2}$$
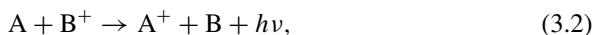
representing transitions between the molecular continua of the initial and final quasi-molecular states. The particular case studied quantitatively was

$$He^{2+} + H \rightarrow He^+ + H^+ + h\nu. \tag{3.3}$$
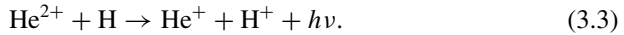
Here the products He^+ and H^+ interact via a purely repulsive potential and in this case the radiative association channel does not exist, but with appropriate modifications Bates' theory could be applied to the case where the final states are not bound.

Evidently, the molecular data for these calculations were all in place at the time (1957), as complementary contemporary work by Bates and collaborators (1953) produced wave functions for the one-electron molecules [15], which were applied to HeH^{2+} to calculate (1956) the energies [16] and (1957) transition dipole moments [17], and the theoretical formulation of Bates [13] for radiative association (free-bound) was extended (1956) to transitions ending in the continuum of the final products (free-free) [18, 19]. Arthurs and Hyslop gave rate coefficients over the range from 250 to 64000 K. It is interesting to note that Dalgarno and Stewart [20] derived the long-range potentials of the $He^{2+} + H$ and $He^+ + H^+$ systems in 1956 and we might imagine that use of these data in the calculations of Arthurs and Hyslop would have allowed the rate coefficient calculation to be carried out precisely to very low temperatures anticipating the boom in ultra-cold collisions to come four decades later (discussed further in Sect. 3.1.3).

Seven years later, in 1965, calculations of rate coefficients for the process

$$He^{2+} + He \rightarrow He^+ + He^+ + h\nu, \tag{3.4}$$
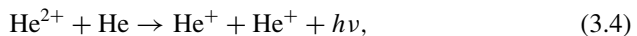
were presented by Allison and Dalgarno [21]. The rate coefficients for reaction (3.4) were calculated from 250 to 16 000 K and were found to be on average 30 times smaller than those for reaction (3.3) (however, see Sect. 3.1.2 below).

In the course of this chronological introduction, we will discuss several calculations that revisited reactions (3.3) and (3.4) using other theoretical approaches. Nevertheless, it is apparent that as early as 1957 a theoretical framework for calculating radiative charge transfer cross sections and rate coefficients was in place. Indeed Arthurs and Hyslop [14] claimed an accuracy of 1% for their calculated rate coefficients.

3.1.2 Further Studies

Interest in radiative charge transfer processes for applications to astrophysics and to thermal gases followed in the 1970's and 1980's, with further astrophysical applications in the 90's.

Notably, Butler, Guberman, and Dalgarno [22] emphasized that when direct charge transfer is unfavorable, radiative charge transfer may be rapid at thermal energies and thereby represents a lower limit to the rate of charge transfer. Using the theory of Bates [13], they calculated the rate coefficients for radiative charge transfer in collisions of $C^{2+} + H$, $C^{3+} + H$, and $N^{2+} + H$.

It is useful to introduce the term *radiative loss* to describe the sum of radiative association and radiative charge transfer processes. Experimental drift-tube studies by Biondi and Johnsen in 1978 established rate coefficients for slow charge-transfer in collisions of the noble gas atoms with noble gas ions; while photons were not detected, the processes could be assigned to radiative charge transfer. The measured data [23] for reaction (3.4) led to some new calculations by Cohen and Bardsley [24], who found rate coefficients about a factor of ten larger than those obtained by Allison and Dalgarno [21]. A further treatment addressing resonances in the collisional process was given by Bardsley et al. [25]. Good agreement with the measured radiative loss rate coefficient at 300 K was achieved, with theory giving 4.2×10^{-14} cm^3/s compared to the measured value [23] of $4.8 \pm 0.5 \times 10^{-14}$ cm^3/s.

With the loss of initial reactants by spontaneous emission treated using a local imaginary potential, the optical potential concept (see, for example [26, p. 184] and [27, p. 291]) was utilized by West, Lane, and Cohen [28] to calculate the cross sections for reaction (3.3), but a comparison to the earlier calculated rate coefficients of Arthurs and Hyslop was not made.

Responding to the drift-tube and spectroscopic measurements of Johnsen [29] in which the radiation emitted in collisions of He$^+$ and Ne was observed, Cooper, Kirby, and Dalgarno [30] used the quantal distorted wave theory to evaluate the cross sections, rate coefficients (at 300 K), and photon emission spectra for the radiative charge transfer process

$$\mathrm{He^+ + Ne \rightarrow He + Ne^+ + } h\nu. \tag{3.5}$$
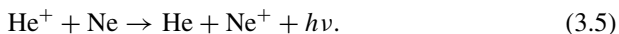
In this system, the possibility of the formation of the molecular ion HeNe$^+$ by radiative association was included in the theoretical analysis. The measured rate coefficients for radiative loss were $1 \pm 0.5 \times 10^{-15}$ cm^3/s at 300 K [23, 29] and $\sim 2 \times 10^{-15}$ cm^3/s at 77 K [29]. The calculated emission spectra for radiative charge transfer and radiative association were similar to those measured by Johnsen. The measured rate coefficients at 300 K for radiative charge transfer and for radiative association, respectively, were $1 \pm 0.2 \times 10^{-15}$ cm^3/s and $0.2 \pm 0.05 \times 10^{-16}$ cm^3/s, while the theoretical analysis found that they were the same and equal to 0.5×10^{-15} cm^3/s, in satisfactory agreement[1] with the measurements given uncertainties in the molecular data used in the calculations. The process (3.5), He$^+$ + Ne, was revisited by Liu et al. (2010) [31] (though no comparison to the earlier theoretical work [30] was made). Liu et al. calculated cross sections and rate coefficients over a range of temperatures for radiative loss, but did not give spectra. Their calculated rate coefficients at 300 K for radiative charge transfer and radiative association, respectively, are about 0.3×10^{-15} cm^3/s and 0.2×10^{-15} cm^3/s , giving a radiative loss of about 0.5×10^{-15} cm^3/s, in agreement with the lower limit of the measurements. On the other hand, according to Liu et al. the radiative loss rate coefficient at 77 K is about 0.6×10^{-15} cm^3/s, or about a factor of 3 less than experiment [29].

---

[1] Note that Cooper et al. quote the radiative association rate coefficient with an exponent of 10^{-15}, while Johnsen gives 10^{-16}; we guess that the experimental value is a typographical error.

Zygelman and Dalgarno [32] related the quantal distorted wave theory [30], optical potential method [28], and the theory of Bates [13] and applied the approach to calculate cross sections, emission spectra and rate coefficients for radiative charge transfer in collisions of He^+ and H [33]. A calculation of radiative charge transfer for applications to modeling the lithium chemistry in the early universe appeared in the 90's where Stancil and Zygelman [34] considered $H^+ + Li$.

3.1.3   Recent Studies: Ultracold Collisions

Motivated by progress in cold hybrid trapping of ions and atoms, calculated cross sections and rate coefficients for radiative charge transfer between atoms and ions are rapidly accumulating, where either species is an alkali-metal or alkaline-earth metal. A calculation of radiative charge transfer rate coefficients ($0.001 < T < 1000$ K) between $Ca^+ + Na$ using the theory of Bates [13] was given in [35]. Since then (2003), numerous calculations have appeared, such as those of cross sections and rate coefficients ($5 < T < 80$ mK) for radiative charge transfer in collisions of Ca^+, Sr^+, Ba^+, and Yb^+ with Rb and Yb^+ with Li using the quantal distorted wave theory [36]. Indeed, a recent review [37, Sec. II.C] focusing on calculations extending to ultralow energies lists references to further systems (spanning the time period 2013–2019) for systems such as $Yb^+ + Rb$, $Yb^+ + Ca$, $Yb^+ + Ca$, $Na^+ + Rb$, etc. That review, focused on ultracold collisions, omits calculations of radiative charge transfer valid at thermal and higher energies, such as those for astrophysical applications, $He^+ + C$ [38], $He^+ + O$ [39], and $H^+ + Na$ [40], and plasma applications, $H^+ + C$ [41], and for the case of reaction (3.5), $He^+ + Ne$, discussed above. Ultralow energy calculations continue, with, for example, Tomza and Lisaj [42] recently reporting radiative charge transfer rate coefficients ($10^{-8} < T < 0.1$ K) in collisions of $Al^+ + Rb$ and $Al^+ + Cs$.

For this brief review, we note two systems for which radiative loss processes were considered experimentally and theoretically. First, in the case of $^{174}Yb^+ + ^{40}Ca$, Rellergert et al. [43] found a reaction rate of the order 2×10^{-10} cm^3/s, which is noticeably larger than typical radiative charge transfer rate coefficients (such as those we discussed above). While the theoretical analysis of [43] supported the claim that radiative loss accounted for the measured rate, subsequent theoretical analysis [44] found that the radiative loss rate coefficients are significantly—five orders of magnitude—lower, at about 1.5×10^{-15} cm^3/s. The large reaction rate is now considered to be due to charge transfer in the presence of a laser-field [45]. Secondly, in the case of $Yb^+ + Rb$, calculations were carried out using the optical potential theory for radiative loss [46, 47]. Additionally, in [46] the quantal distorted wave theory was also applied to obtain radiative charge transfer and radiative association rate coefficients and emission spectra. Both of these independent studies found radiative loss rate coefficients of the order 10^{-14} cm^3/s in agreement with experiment [48] for effective temperatures in the range 0.2–5 K.

Finally, we note the detailed calculations by Mrugała and Kraemer [49] of radiative charge transfer in collisions of He^+ and H_2 from nano-eV to milli-eV collisional energies.

3.2 Two Case Studies

In this section we present two example calculations of radiative charge transfer carried out for astrophysical applications: $He^+ + C$ and $He^+ + Ar$.

3.2.1 The Helium Ion and the Carbon Atom

Carbon monoxide (CO) was observed in Supernova 1987A [50]. The formation and destruction of CO was studied using chemical models and the desirability of further data on the charge transfer of He^+ with carbon was noted [51]. The needed data were obtained by Kimura et al., who calculated direct [52] and radiative [38] charge transfer in collisions of He^+ and C. They found that radiative charge transfer cross sections were unimportant, of the order 10^{-24} cm^2 at a relative energy of 0.001 eV for transitions from the $3\,^2\Pi$ state[2] to the B $^2\Pi$ state, but they neglected the potentially significant $3\,^2\Pi$ to X $^2\Pi$ transition, as well as other doublet and quartet transitions that are allowed for the HeC$^+$ quasimolecule. In order to gauge the importance of these omitted transitions, we calculated potential energies and transition dipole moments of HeC$^+$. These data were used with the optical potential theory to evaluate cross sections and rate coefficients for radiative loss in collisions of He^+ and C. The cross sections for the $3\,^2\Pi$ to X $^2\Pi$ transition were found to more than 4 orders of magnitude larger than those for the $3\,^2\Pi$ to B $^2\Pi$ transition, yielding rate coefficients of the order 10^{-13} cm^3/s at 1000 K [53]. For temperatures less than 2000 K, radiative charge transfer was found to be dominant compared to the previous calculations of direct charge transfer [52].

3.2.2 The Helium Ion and the Argon Atom

The argonium ion (^{36}ArH$^+$) was identified in the Crab Nebula [54] and subsequently detected in other sources [55]. A reaction that might contribute to the formation of the precursor Ar$^+$ is the reaction

$$He^+ + Ar \rightarrow Ar^+ + He + h\nu, \tag{3.6}$$

---
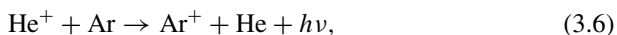
[2] Denoted D $^2\Pi$ in [38].

as direct charge transfer is not significant at thermal temperatures. Charge transfer rate coefficients were determined in drift-tube experiments to be no more than 10^{-13} cm^3/s at 295 K by Johnsen et al. [56] and to be greater than about 2×10^{-14} cm^3/s at 300 K by Jones et al. [57]. In order to test the importance of reaction (3.6) in modeling the chemistry of the argonium ion in astrophysical environments, we used the optical potential theory to evaluate the cross sections and rate coefficients over a range of temperatures [58]. The theoretical values were found to be roughly constant at about 1×10^{-14} cm^3/s from 77 to 500 K, weakly decreasing to 8.3×10^{-15} cm^3/s at 3000 K. The agreement with experiments at 300 K is satisfactory, but the reaction (3.6) does not significantly affect the chemistry of argonium.

References

1. A. Dalgarno, Rev. Mod. Phys. **39**(4), 850 (1967). https://doi.org/10.1103/RevModPhys.39.850
2. D.A. Swartz, Astrophys. J. **428**, 267 (1994). https://doi.org/10.1086/174238
3. J.B. Kingdon, G.J. Ferland, Astrophys. J. Lett. **516**(2), L107 (1999). https://doi.org/10.1086/312008
4. P.C. Stancil, in *Spectroscopic Challenges of Photoionized Plasmas*, *Astronomical Society of the Pacific Conference Series*, vol. 247, ed. by G. Ferland, D.W. Savin (2001), p. 3
5. D.R. Bates, H.S.W. Massey, Proc. R. Soc., London, Ser. A **192**(1028), 1 (1947). https://doi.org/10.1098/rspa.1947.0134
6. B.G. Lindsay, R.F. Stebbings, J. Geophys. Res.: Space Phys. **110**(A12) (2005). https://doi.org/10.1029/2005JA011298
7. K. Dennerl, Space Sci. Rev. **157**(1–4), 57 (2010). https://doi.org/10.1007/s11214-010-9720-5
8. J.M. Muñoz Burgos, M. Griener, J. Loreau, A. Gorbunov, T. Lunt, O. Schmitz, E. Wolfrum, Phys. Plasma **26**(6), 063301 (2019). https://doi.org/10.1063/1.5088363
9. K.D. Kuntz, Astron. Astrophys. Rev. **27**(1), 1 (2019). https://doi.org/10.1007/s00159-018-0114-0
10. T.E. Cravens, Geophys. Res. Lett. **24**(1), 105 (1997). https://doi.org/10.1029/96GL03780
11. V.A. Krasnopolsky, M.J. Mumma, M. Abbott, B.C. Flynn, K.J. Meech, D.K. Yeomans, P.D. Feldman, C.B. Cosmovici, Science **277**, 1488 (1997). https://doi.org/10.1126/science.277.5331.1488
12. M.A. Gruntman, Geophys. Res. Lett. **19**(13), 1323 (1992). https://doi.org/10.1029/92GL01277
13. D.R. Bates, Mon. Not. R. Astron. Soc. **111**(3), 303 (1951). https://doi.org/10.1093/mnras/111.3.303
14. A.M. Arthurs, J. Hyslop, Proc. Phys. Soc., London, Sect. A **70**(12), 849 (1957). https://doi.org/10.1088/0370-1298/70/12/301
15. D.R. Bates, K. Ledsham, A.L. Stewart, Philos. Trans. R. Soc. London, Ser. A **246**(911), 215 (1953). https://doi.org/10.1098/rsta.1953.0014
16. D.R. Bates, T.R. Carson, Proc. R. Soc., London, Ser. A **234**(1197), 207 (1956). https://doi.org/10.1098/rspa.1956.0027
17. A.M. Arthurs, R.A.B. Bond, J. Hyslop, Proc. Phys. Soc., London, Sect. A **70**(8), 617 (1957). https://doi.org/10.1088/0370-1298/70/8/408

18. D.R. Bates, Mon. Not. R. Astron. Soc. **112**, 40 (1952). https://doi.org/10.1093/mnras/112.1.40
19. E.H.S. Burhop, R. Marriott, Proc. Phys. Soc., London, Sect. A **69**(3), 271 (1956). https://doi.org/10.1088/0370-1298/69/3/310
20. A. Dalgarno, A.L. Stewart, Proc. R. Soc., London, Ser. A **238**(1213), 276 (1956). https://doi.org/10.1098/rspa.1956.0220
21. D.C.S. Allison, A. Dalgarno, Proc. Phys. Soc., London **85**(5), 845 (1965). https://doi.org/10.1088/0370-1328/85/5/303
22. S.E. Butler, S.L. Guberman, A. Dalgarno, Phys. Rev. A **16**(2), 500 (1977). https://doi.org/10.1103/PhysRevA.16.500
23. R. Johnsen, M.A. Biondi, Phys. Rev. A **18**(3), 996 (1978). https://doi.org/10.1103/PhysRevA.18.996
24. J.S. Cohen, J.N. Bardsley, Phys. Rev. A **18**(3), 1004 (1978). https://doi.org/10.1103/PhysRevA.18.1004
25. J.N. Bardsley, J.S. Cohen, J.M. Wadehra, Phys. Rev. A **19**(5), 2129 (1979). https://doi.org/10.1103/PhysRevA.19.2129
26. N.F. Mott, H.S.W. Massey, *The Theory of Atomic Collisions*, 3rd edn. (Oxford, London, 1965)
27. L.F. Canto, M.S. Hussein, *Scattering Theory of Molecules, Atoms and Nuclei* (World Scientific, Singapore, 2013)
28. B.W. West, N.F. Lane, J.S. Cohen, Phys. Rev. A **26**(6), 3164 (1982). https://doi.org/10.1103/PhysRevA.26.3164
29. R. Johnsen, Phys. Rev. A **28**(3), 1460 (1983). https://doi.org/10.1103/PhysRevA.28.1460
30. D.L. Cooper, K. Kirby, A. Dalgarno, Can. J. Phys. **62**, 1622 (1984). https://doi.org/10.1139/p84-208
31. X.J. Liu, Y.Z. Qu, B.J. Xiao, C.H. Liu, Y. Zhou, J.G. Wang, R.J. Buenker, Phys. Rev. A **81**(2), 022717 (2010). https://doi.org/10.1103/PhysRevA.81.022717
32. B. Zygelman, A. Dalgarno, Phys. Rev. A **38**(4), 1877 (1988). https://doi.org/10.1103/PhysRevA.38.1877
33. B. Zygelman, A. Dalgarno, M. Kimura, N.F. Lane, Phys. Rev. A **40**(5), 2340 (1989). https://doi.org/10.1103/PhysRevA.40.2340
34. P.C. Stancil, B. Zygelman, Astrophys. J. **472**(1), 102 (1996). https://doi.org/10.1086/178044
35. O.P. Makarov, R. Côté, H. Michels, W.W. Smith, Phys. Rev. A **67**, 042705 (2003). https://doi.org/10.1103/PhysRevA.67.042705
36. H. da Silva, Jr., M. Raoult, M. Aymar, O. Dulieu, New J. Phys. **17**(4), 045015 (2015). https://doi.org/10.1088/1367-2630/17/4/045015
37. M. Tomza, K. Jachymski, R. Gerritsma, A. Negretti, T. Calarco, Z. Idziaszek, P.S. Julienne, Rev. Mod. Phys. **91**(3), 035001 (2019). https://doi.org/10.1103/RevModPhys.91.035001
38. M. Kimura, A. Dalgarno, L. Chantranupong, Y. Li, G. Hirsch, R.J. Buenker, Phys. Rev. A **49**(4), 2541 (1994). https://doi.org/10.1103/PhysRevA.49.2541
39. L.B. Zhao, P.C. Stancil, J.P. Gu, H.P. Liebermann, Y. Li, P. Funke, R.J. Buenker, B. Zygelman, M. Kimura, A. Dalgarno, Astrophys. J. **615**(2), 1063 (2004). https://doi.org/10.1086/424729
40. C. Liu, Y. Qu, J. Wang, Y. Li, R. Buenker, Phys. Lett. A **373**(41), 3761 (2009). https://doi.org/10.1016/j.physleta.2009.08.022
41. P.C. Stancil, J.P. Gu, C.C. Havener, P.S. Krstic, D.R. Schultz, M. Kimura, B. Zygelman, G. Hirsch, R.J. Buenker, M.E. Bannister, J. Phys. B: At. Mol. Opt. Phys. **31**(16), 3647 (1998). https://doi.org/10.1088/0953-4075/31/16/017
42. M. Tomza, M. Lisaj, Phys. Rev. A **101**, 012705 (2020). https://doi.org/10.1103/PhysRevA.101.012705
43. W.G. Rellergert, S.T. Sullivan, S. Kotochigova, A. Petrov, K. Chen, S.J. Schowalter, E.R. Hudson, Phys. Rev. Lett. **107**(24), 243201 (2011). https://doi.org/10.1103/PhysRevLett.107.243201
44. B. Zygelman, Z. Lucic, E.R. Hudson, J. Phys. B: At. Mol. Opt. Phys. **47**(1), 015301 (2014). https://doi.org/10.1088/0953-4075/47/1/015301

45. M. Li, M. Mills, P. Puri, A. Petrov, E.R. Hudson, S. Kotochigova, Phys. Rev. A **99**(6), 062706 (2019). https://doi.org/10.1103/PhysRevA.99.062706
46. E.R. Sayfutyarova, A.A. Buchachenko, S.A. Yakovleva, A.K. Belyaev, Phys. Rev. A **87**(5), 052717 (2013). https://doi.org/10.1103/PhysRevA.87.052717
47. B.M. McLaughlin, H.D.L. Lamb, I.C. Lane, J.F. McCann, J. Phys. B: At. Mol. Opt. Phys. **47**(14), 145201 (2014). https://doi.org/10.1088/0953-4075/47/14/145201
48. C. Zipkes, S. Palzer, L. Ratschbacher, C. Sias, M. Köhl, Phys. Rev. Lett. **105**, 133201 (2010). https://doi.org/10.1103/PhysRevLett.105.133201
49. F. Mrugała, W.P. Kraemer, J. Chem. Phys. **138**(10), 104315 (2013). https://doi.org/10.1063/1.4793986
50. V. Trimble, Rev. Mod. Phys. **60**(4), 859 (1988). https://doi.org/10.1103/RevModPhys.60.859
51. S. Lepp, A. Dalgarno, R. McCray, Astrophys. J. **358**, 262 (1990). https://doi.org/10.1086/168981
52. M. Kimura, A. Dalgarno, L. Chantranupong, Y. Li, G. Hirsch, R.J. Buenker, Astrophys. J. **417**, 812 (1993). https://doi.org/10.1086/173361
53. J.F. Babb, B.M. McLaughlin, J. Phys. B: At. Mol. Opt. Phys. **50**(4), 044003 (2017). https://doi.org/10.1088/1361-6455/aa54f4
54. M.J. Barlow, B.M. Swinyard, P.J. Owen, J. Cernicharo, H.L. Gomez, R.J. Ivison, O. Krause, T.L. Lim, M. Matsuura, S. Miller, G. Olofsson, E.T. Polehampton, Science **342**(6164), 1343 (2013). https://doi.org/10.1126/science.1243582
55. H.S.P. Müller, S. Muller, P. Schilke, E.A. Bergin, J.H. Black, M. Gerin, D.C. Lis, D.A. Neufeld, S. Suri, Astron. Astrophys. **582**, L4 (2015). https://doi.org/10.1051/0004-6361/201527254
56. R. Johnsen, M.T. Leu, M.A. Biondi, Phys. Rev. A **8**, 1808 (1973). https://doi.org/10.1103/PhysRevA.8.1808
57. J.D.C. Jones, D.G. Lister, N.D. Twiddy, J. Phys. B: At. Molec. Phys. **12**(16), 2723 (1979)
58. J.F. Babb, B.M. McLaughlin, Ap. J. **860**(2), 151 (2018). https://doi.org/10.3847/1538-4357/aac5f4

Chapter 4
Multielectron Processes in Ions Formation by Electron Impact

Valdas Jonauskas, Aušra Kynienė, and Jurgita Koncevičiūtė

Abstract Electron-impact double ionization is investigated for the B^+ ion. Influence of the multielectron processes is estimated by considering correlation effects and direct double ionization. Contribution of the emission of the electron from atomic system by scattered or ejected electron following the $1s$ shell ionization is investigated.

4.1 Introduction

Electron-impact ionization and radiative recombination in addition to dielectronic recombination define charge state distribution in collisionally ionized plasma. Direct and indirect ionization by electron impact have to be studied to explain single and multiple ionization. Excitation-autoionization and resonant-excitation double-autoionization processes produce the main contribution to the indirect single ionization. The electron-impact excitation to autoionizing states forms ions in the next ionization stage through Auger transitions. The double Auger decay of the states produced by dielectronic capture leads to single ionization. Influence of the multiple ionization on the charge state distribution can often be neglected in the coronal equilibrium. However, contribution of multiple ionization has to be considered if neutrals or ions in low charge states are suddenly exposed to high electron temperatures [1, 2]. Indirect process for double ionization is determined by ionization and subsequent autoionization. Study of the direct double ionization (DDI) process is more complicated compared to direct single ionization due to complex nature of the four-body Coulomb problem. A kick-off model has been suggested to study DDI process [3]. What is more, triple ionization was explained as a sequence of DDI with subsequent autoionization in the Se^{2+} [4] and Se^{3+} [5] ions. These results have further strength-

V. Jonauskas (✉) · A. Kynienė · J. Koncevičiūtė
Institute of Theoretical Physics and Astronomy, Vilnius University, Saulėtekio av. 3, 10257 Vilnius, Lithuania
e-mail: valdas.jonauskas@tfai.vu.lt

ened our hypothesis that the *additional processes* that we have introduced alongside sequential ionization are important in the multiple ionization.

The main aim of the current work is to demonstrate importance of the multielectron processes for the double ionization by electron impact in the B^+ ion. The study presents analysis of the direct and indirect ionization. The DDI process is studied using a few-step approach [3] which involves ionization-ionization (II), excitation-ionization-ionization (EII), and ionization-excitation-ionization (IEI) processes. The double ionization by electron impact for B^+ was investigated previously using time-dependent close-coupling (TDCC) and distorted-waves (DW) methods [6]. However, the TDCC calculations are more complicated compared to DW [7].

The paper is organized as follows. In Sect. 4.2, the theoretical methods used to calculate cross sections are outlined. In Sect. 4.3, the results are presented and discussed and in Sect. 4.4 some final conclusions are provided.

4.2 Theoretical Approach

Direct and indirect processes have to be considered for the analysis of electron-impact single ionization (SI) from the level i to the level f:

$$\sigma_{if}(\varepsilon) = \sigma_{if}^{CI}(\varepsilon) + \sum_k \sigma_{ik}^{exc}(\varepsilon) B_{kf}. \tag{4.1}$$

Here, ε is the incident electron energy, σ_{if}^{CI} represents the collisional ionization (CI) cross section, σ_{ik}^{exc} corresponds to the electron-impact excitation cross section to the level k of the initial ion. The summation over all final levels f in equation (4.1) produces the total single ionization cross sections for the level i. Electron-impact excitation and CI cross sections are studied using the DW approximation.

The DDI process can be described by a multi-step approach [3–5, 8–10] which includes II, EII, and IEI branches. The same approach was applied to study double and triple Auger processes [11]. The DDI processes are initiated by electron-impact ionization or excitation. The double ionized states are produced when the scattered or knocked out electrons participate in the further ionization. Therefore, this leads to diminished values of the theoretical SI cross sections since the higher ionization stage is created instead of the lower one. Often the negative contribution of the DDI processes to the SI cross sections is not considered since the effect is not large.

The DDI cross sections for the II process are expressed by the equation

$$\sigma_{if}^{DDI(II)}(\varepsilon) = \sum_j \sigma_{ij}^{CI}(\varepsilon) \frac{\sigma_{jf}^{CI}(\varepsilon_1)}{4\pi \bar{R}_{nl}^2}. \tag{4.2}$$

Here ε_1 is the energy of the scattered or ejected electron that participates in the subsequent ionization from the level j of singly ionized ion. Factor $\frac{\sigma_{jf}^{CI}(\varepsilon_1)}{4\pi \bar{R}_{nl}^2}$ determines

the probability of the subsequent ionization from the nl shell, $\bar{R}_{nl}$ is the mean distance of the electrons from the nucleus.

The DDI EII branch includes three sequential transitions - excitation with the subsequent DI:

$$\sigma_{if}^{\text{DDI(EII)}}(\varepsilon) = \sum_{kj} \sigma_{ik}^{\text{CE}}(\varepsilon) \frac{\sigma_{kj}^{\text{CI}}(\varepsilon_1)}{4\pi \, \bar{R}_{nl}^2} \frac{\sigma_{jf}^{\text{CI}}(\varepsilon_2)}{4\pi \, \bar{R}_{n'l'}^2}. \tag{4.3}$$

Here $\varepsilon_1 = \varepsilon - \Delta E_{ik}$, ΔE_{ik} is a transition energy and ε_2 is the energy of the scattered or ejected electron. $\sigma_{ik}^{\text{CE}}(\varepsilon)$ is the electron-impact excitation cross section.

The DDI IEI branch is determined by ionization with subsequent excitation by the ejected or scattered electrons followed by electron-impact ionization

$$\sigma_{if}^{\text{DDI(IEI)}}(\varepsilon) = \sum_{kj} \sigma_{ik}^{\text{CI}}(\varepsilon) \frac{\sigma_{kj}^{\text{CE}}(\varepsilon_1)}{4\pi \, \bar{R}_{nl}^2} \frac{\sigma_{jf}^{\text{CI}}(\varepsilon_2)}{4\pi \, \bar{R}_{n'l'}^2}. \tag{4.4}$$

It should be noted that two different situations for energy distribution between the scattered and ejected electrons after the first ionization process (the first step in II and IEI, the second step in EII) are considered in this work. In one case, the electrons share the excess energy equally. In other case, one of the electrons takes all the excess energy and participates in the further excitation or ionization process. It was demonstrated that one of the electrons tends to take all the excess energy at the lower energies of the incident electron while the electrons share this energy for the higher energies [3].

The scaled cross sections for the excitation are obtained by using equation [12]

$$\sigma_{ij}^{\text{CE*}}(\varepsilon) = \frac{\varepsilon}{\varepsilon + \Delta E_{ij} + \varepsilon_b} \sigma_{ij}^{\text{CE}}(\varepsilon), \tag{4.5}$$

where ε_b - the bounding energy of the electron. The scaling for the direct ionization cross sections is expressed by the equation

$$\sigma_{ij}^{\text{CI*}}(\varepsilon) = \frac{\varepsilon}{\varepsilon + I} \sigma_{ij}^{\text{CI}}(\varepsilon). \tag{4.6}$$

where I is the ionization energy, ε_k - the kinetic energy of the bound electron.

Energy levels, radiative and Auger transition probabilities as well as electron-impact excitation and CI cross sections have been calculated using the Flexible Atomic Code [13]. This code implements the Dirac-Fock-Slater approach. Electron-impact excitation and CI processes are investigated using the distorted-wave (DW) approximation.

4.3 Results

The single ionization threshold of the B^+ ion is 23.35 eV while the energy provided by the NIST equals 25.15 eV [14]. Similar tendency for the FAC ionization thresholds compared to the NIST data was observed for other ions: Se^{2+} [4], Se^{3+} [8], W^{27+} [15], W^{26+} [16], W^{25+} [17]. The first excited configuration is formed by the $2s \rightarrow 2p$ promotion from the ground configuration. The energy levels of the B^+ $2s\,2p$ configuration span from 3.34 to 9.18 eV. For the B^{2+} ion, the theoretical SI threshold of 37.63 is slightly below the NIST recommended value of 37.93 eV. Finally, the theoretical DI threshold of 60.98 eV is lower than the NIST value of 63.08 eV.

Theoretical DI cross sections for the B^+ ion are compared to measurements in Fig. 4.1. The correlation effects are included in the ionization calculations by using configuration interaction method. Furthermore, the electron impact ionization and excitation cross sections for B^+ and B^{2+} are diminished by using the scaling functions (4.5 and 4.6). Two limiting cases of energy distribution of ejected and scattered electrons which participate in the additional ionization process are presented. It has to be noted that the experimental values are underestimated at the higher energies of the incident electron. This demonstrates that some additional processes are important in this energy region. The intermediate distribution of the energies for ejected and scattered electrons occurs at the lower energies.
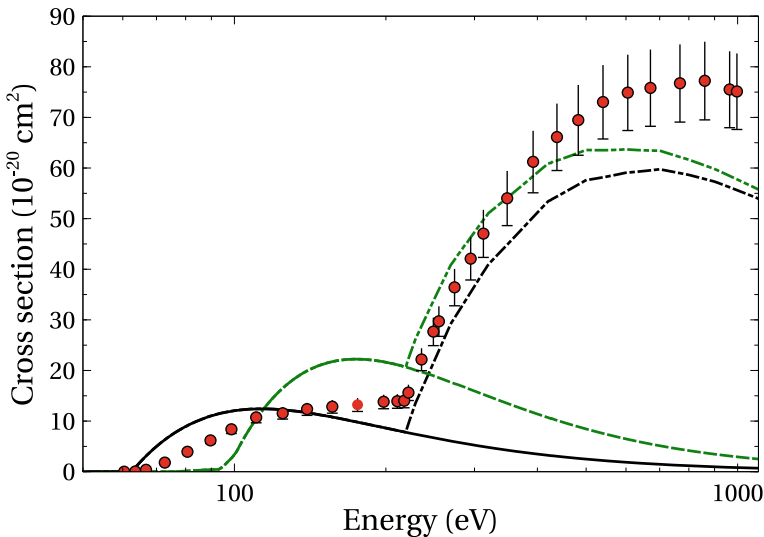
Fig. 4.1 Electron-impact DI of B^+. Solid line (black): DDI cross sections when one of the electrons takes all excess energy; dashed line (green): DDI cross sections when electrons share the excess energy; dot-dashed line (black): cross sections of the indirect process added to the DDI cross sections when one of the electrons takes all the excess energy; dot-dot-dashed line (green): cross sections of the indirect process added to the DDI cross sections when electrons share the excess energy; circles: experiment [18]

The indirect process of double ionization corresponds to ionization from the $1s$ shell with subsequent autoionization. However, the initial $1s$ shell ionization can lead to kick-off of the electron from atomic system by scattered or ejected electrons. This means that autoionization competes with the ionization produced by electron impact. Our data shows that the additional collisional ionization is by four orders of magnitude quicker compared to autoionization. The attosecond laser spectroscopy could be used to observe these differences. Finally, current modelling shows that the kick-off process following the $1s$ shell ionization amounts to ~15% of the cross sections from the indirect process.

4.4 Conclusions

Electron-impact DI is studied for the B^+ ion. The study presents data for direct and indirect processes. Theoretical data underestimate measurements at higher energies of the incident electron. This demonstrates that some additional effects contribute to DI in this energy region. Furthermore, our study shows that single ionization of the $1s$ shell can lead not only to autoionization but also to ejection of the electron from atomic system by scattered or ejected electron.

References

1. A. Müller, Phys. Lett. A **113**(8), 415 (1986)
2. M. Hahn, D.W. Savin, Astrophys. J. **800**(1), 68 (2015)
3. V. Jonauskas, A. Prancikevičius, Š Masys, A. Kynienė, Phys. Rev. A **89**, 052714 (2014)
4. J. Koncevičiūtė, S. Kučas, Š. Masys, A. Kynienė, V. Jonauskas, Phys. Rev. A **97**, 012705 (2018)
5. J. Koncevičiutė, S. Kučas, A. Kynienė, Š Masys, V. Jonauskas, J. Phys. B: At. Mol. Opt. Phys **52**(2), 025203 (2019)
6. M.S. Pindzola, J.A. Ludlow, C.P. Ballance, F. Robicheaux, J. Colgan, J. Phys. B: At. Mol. Opt. Phys **44**(10), 105202 (2011)
7. M.S. Pindzola, F. Robicheaux, S.D. Loch, J.C. Berengut, T. Topcu, J. Colgan, M. Foster, D.C. Griffin, C.P. Ballance, D.R. Schultz, T. Minami, N.R. Badnell, M.C. Witthoeft, D.R. Plante, D.M. Mitnik, J.a. Ludlow, U. Kleiman, J. Phys. B: At. Mol. Opt. Phys **40**(7), R39 (2007)
8. S. Pakalka, S. Kučas, v. Masys, A. Kynienė, A. Momkauskaitė, V. Jonauskas, Phys. Rev. A **97**, 012708 (2018)
9. J. Koncevičiūtė, V. Jonauskas, Phys. Rev. A **93**, 022711 (2016)
10. V. Jonauskas, A&A **620**, A188 (2018)
11. V. Jonauskas, Š. Masys, J. Quant. Spectrosc. Radiat. Transfer **229**, 11 (2019)
12. Y.K. Kim, Phys. Rev. A **64**(3), 032713 (2001)
13. M.F. Gu, Can. J. Phys. **86**, 675 (2008). https://doi.org/10.1139/P07-197
14. A. Kramida, Yu. Ralchenko, J. Reader, and NIST ASD Team, NIST Atomic Spectra Database (ver. 5.7.1), [Online]. Available https://physics.nist.gov/asd [2019, December 20]. National Institute of Standards and Technology, Gaithersburg, MD (2019)
15. V. Jonauskas, A. Kynienė, G. Merkelis, G. Gaigalas, R. Kisielius, S. Kučas, Š Masys, L. Radžiūtė, P. Rynkun, Phys. Rev. A **91**, 012715 (2015)
16. A. Kynienė, Š. Masys, V. Jonauskas, Phys. Rev. A **91**, 062707 (2015)

17. A. Kynienė, S. Pakalka, Š Masys, V. Jonauskas, J. Phys. B: At. Mol. Opt. Phys **49**(18), 185001 (2016)
18. V.P. Shevelko, H. Tawara, F. Scheuermann, B. Fabian, A. Müller, E. Salzborn, J. Phys. B: At. Mol. Opt. Phys. **38**(5), 525 (2005)

Chapter 5
Electron Energy Distribution Functions in Ionized Gases: An Engineering Point of View

Gorur Govinda Raju

Abstract Electron energy distribution functions in low degree ionized gases are of fundamental importance in understanding ionization phenomena in gases and provide a link between theory and measurements. The paper provides a brief historical review of the present state of study in this area, and includes an update of both experimental study of transport phenomena and calculation of the distribution functions. Recent researches in to application of gas discharges in several different areas are briefly included. The need for an analytical expression of the distribution function is pointed out. With this objective a bimodal distribution function is developed and in previous publications its applicability to argon, neon, and xenon have been shown to be successful. In this paper the bimodal distribution is applied to Penning mixtures of neon and argon, and good agreement is obtained between the measured and calculated first ionization coefficients as a function of reduced electric field. Other swarm parameters calculated by this method are also presented for the first time.

5.1 Introduction

Applications underlying the principle of gaseous plasma are many from the common tube lights, sodium vapor lamps, Plasma spray technology developed during 1950s [1], Plasma cutting of metals, and more recent cutting of concrete [2]. Recent applications of cold plasma are in the medical and bio-medical field [3–8].

Computation of electron distribution function as a function of reduced electric field E/N (E = Electric field, N = gas number density) involves various collision cross sections as a function of electron energy. The swarm parameters are the drift velocity (W), diffusion coefficient (D), the characteristic energy D/μ (μ = mobility) and the reduced first ionization coefficient (α/N). The inter-relationships between the cross sections, swarm parameters and electron energy distribution functions are shown in Fig. 5.1.

G. G. Raju (✉)

Department of Electrical and Computer Engineering, University of Windsor, Windsor, ON N9B 3P4, Canada

e-mail: raju@uwindsor.ca
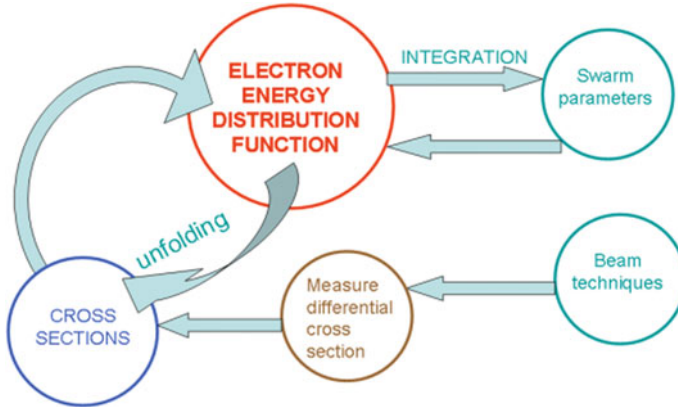
Fig. 5.1 Integration and unfolding procedures with the aid of electron energy distribution functions

The purposes of this paper are:

1. To present a brief review of the success obtained by the use of Boltzmann equation.
2. To present a new method of obtaining analytical expression for energy distribution function and demonstrate its applicability to Penning mixtures.
3. Future challenges.

5.2 Theory

The electron distribution function is calculated using the following methods:

1. Solution of continuity equations. The generation and decay of electrons are calculated using the idea that change of charge in a volume is in accordance with the change of electric current flowing in or out of the volume. The charge particles namely electrons, positive ions, and negative ion densities are represented by partial differential equations with time as the variable. The continuity equations are coupled to Poisson's equation via charge density and the current density is calculated by the equation:

$$J = e\left(N_p W_p - N_n W_n - N_e W_e\right) \qquad (5.1)$$

Subscripts e, p, and n represent electrons, positive ions and negative ions respectively, N the number density (m^{-3}) and W the drift velocity (m/s). Particular success has been achieved in SF_6 and other gases, both in one dimensional and three dimensional analysis [9].

2. Monte Carlo Method.

The Boltzmann equation which, in concise form, is stated as

$$
\frac{d}{d\varepsilon}\left(\frac{e^2 E^2 \varepsilon}{3N Q_M}\frac{df}{d\varepsilon}\right) + \frac{2m}{M}\frac{d}{d\varepsilon}\left(\varepsilon^2 N Q_M\left[f + kT\frac{df}{d\varepsilon}\right]\right)
$$
$$
+ \sum_j \left[(\varepsilon + \varepsilon_j)f(\varepsilon + \varepsilon_j)N Q_j(\varepsilon + \varepsilon_j) - \varepsilon f(\varepsilon)N Q_j(\varepsilon)\right]
$$
$$
+ \sum_j \left[(\varepsilon - \varepsilon_j)f(\varepsilon - \varepsilon_j)N Q_{-j}(\varepsilon - \varepsilon_j) - \varepsilon f(\varepsilon)N Q_{-j}(\varepsilon)\right] = 0 \qquad (5.2)
$$

Here E = Electric field (V/m), e/m and M have their conventional meaning, Q_M is the momentum transfer cross section (m^2), Q is the cross section, subscripts $-j$ and j are the short form of energy levels, $\varepsilon = -j + \Delta j$, and $f(\varepsilon)$ is the electron energy distribution.

The equation is the mathematical expression for the statement that the energy gain from the electric field is equal to the energy loss during both elastic and inelastic collisions. Integration of (5.2) results in a second equation having both differentials and integrals, called integro-differential equation. Closed form solution is not possible and numerical techniques are applied to find the solution. Frost and Phelps, in their epochal paper [10] developed the solution using main frame computing facilities at Westinghouse laboratories. It is appropriate to mention that experimental measurements for measuring low energy inelastic collision cross sections were not developed yet, then, and the method adopted was to calculate the transport coefficients from the electron energy distribution functions and compare them with the measured values. Assumed vibrational and rotational excitation cross sections were modified by a technique known as backward prolongation [11]. The choice of gases studied was dictated by the fact that that the transport coefficients at low values of E/N were available in 1962.

The swarm parameters are defined by the following relationships:

$$
W = -\frac{E}{3N}\left(\frac{2e}{m}\right)^{1/2}\int_0^\infty \frac{\varepsilon}{Q_M(\varepsilon)}\frac{d}{d\varepsilon}\left[\frac{F(\varepsilon)}{\varepsilon^{1/2}}\right]d\varepsilon \qquad (5.3)
$$

$$
D_T = \frac{1}{3N}\int_0^\infty \frac{\varepsilon}{Q_M(\varepsilon)}F(\varepsilon)\,d\varepsilon \qquad (5.4)
$$

$$
\frac{\alpha}{N} = \frac{1}{W}\int_{\varepsilon_i}^\infty \varepsilon^{1/2}Q_i(\varepsilon)F(\varepsilon)\,d\varepsilon \qquad (5.5)
$$

The mean energy of the swarm is given by

$$\bar{\varepsilon} = \frac{\int\limits_0^\infty \varepsilon F(\varepsilon)d\varepsilon}{\int\limits_0^\infty F(\varepsilon)d\varepsilon} \tag{5.6}$$

In (5.3)–(5.6) the symbols are defined as follows:

D_T = radial diffusion coefficient (m²/s); e/m = electron charge to mass ratio; j = specific inelastic process, k_j = rate constant for jth process; (m³/s); $Q_{i\,=}$ ionization cross section (m²); ε = electron energy, ε_i = ionization threshold energy; ε_j = threshold energy for jth process. The distribution is normalized according to

$$\int\limits_0^\infty F(\varepsilon)\,d\varepsilon = 1 \tag{5.7}$$

Substitution of determined electron energy distribution function (EEDF) into (5.3)–(5.7) yields the respective quantity. This operation is identified with the integration part shown in Fig. 5.1. A large number of publications in the literature show very good correspondence between the theoretically calculated swarm parameters and experimentally determined ones [10].

The detailed collision cross section data for calculation of swarm parameters are not necessary for practical engineering purposes where one can tolerate fewer rigors in accuracy for the benefit of speedier calculation, without the knowledge of extensive physics and computational techniques. The early assumptions that the inelastic collisions can be neglected in finding the solution of (5.2) in closed form, given by Morse, Allis and Lamar [9] results in a unimodal distribution function and is found not satisfactory enough.

The starting point for the simplified approach is the derivation of Morse, Allis and Lamar [9] who derived an analytical equation to the electron energy distribution according to:

$$F(\varepsilon) = G\frac{\varepsilon^{1/2}}{\bar{\varepsilon}^{3/2}} \exp\left[-H\left(\frac{\varepsilon}{\bar{\varepsilon}}\right)^{2(p+1)}\right] \tag{5.8}$$

where $\bar{\varepsilon}$ is the mean energy, p is a constant having value of $-1 < p$ and no upper limit seems to exist. G and H are functions given by:

$$G = 2(p+1)\left[\Gamma\frac{5}{4(p+1)}\right]^{3/2} \times \left[\Gamma\frac{3}{4(p+1)}\right]^{-5/2} \tag{5.9}$$

$$H = \left[\Gamma \frac{5}{4(p+1)} \times \frac{1}{\Gamma \frac{3}{4(p+1)}} \right]^{2(p+1)} \tag{5.10}$$

Raju and Hackam [12] have attempted to calculate drift velocity and ionization coefficients by substituting (5.3) and (5.5) into (5.8). For the purpose of integration they approximated the respective cross sections as a function of energy by analytical expressions. In this paper we have used numerical methods to overcome these restrictions and extend the theory to bimodal distribution to fully explore the potential of (5.8).

A bimodal distribution has been shown to be applicable in radio-frequency discharges [13] according to

$$G(\varepsilon) = \gamma F_1(\varepsilon) + (1 - \gamma) F_2(\varepsilon) \tag{5.11}$$

In such a discharge electrons are accelerated to high energies due to collisions at the sheath, and this can produce a species of electrons which has considerably higher energy than the bulk component. The bi-modal energy distribution can maintain a discharge at a much lower bulk temperature due to ionization and excitation produced by the warmer component of the plasma [15].

5.3   Application to Penning Gas Mixtures

Penning gas mixtures are mixtures of two gases A and B in which A has a higher ionization potential than B and an excited level of A that is higher than the ionization potential of B exists. When collisions occur between excited level of A and neutral species of B ionization of the latter occurs with a disproportionate increase of ionization of A. This effect, named after the founder during 1930's, is advantageously used where an increase of ionization in gas is desired as in the case of radiation monitoring. Sakai et al. [14, 15] have calculated the electron swarm properties of this mixture where the ratio of argon in the total concentration varied from 10^{-6} to 10^{-1}. Numerical solution of Boltzmann equation was employed to determine the electron energy distributions.

We have calculated, for the first time the swarm coefficients in this mixture using the bimodal distribution function given by (5.11).

To calculate swarm parameters defined by (5.3)–(5.6) we need just the momentum transfer cross sections and ionization cross sections for the two gases under consideration. Argon exhibits pronounced Townsend Ramsauer effect where as neon exhibits slowly increasing momentum transfer cross sections.

The results for argon, neon and xenon using bimodal distribution functions are given elsewhere [16] and the results for neon are checked in this paper [17] before considering Penning mixtures.

Figure 5.2 shows the calculated distribution functions in mixtures of neon and 0.0001% argon calculated using the bimodal distribution according to (5.11). Figure 5.3 appertains to lower values of the reduced electric field, E/N and Fig. 5.4 appertains to higher values. In these figures the curves are shifted to the right successively by two divisions, for purposes of clarity. The curves are neither Maxwellian nor Druyvesteyn distributions. In the region of ionization the tail of the distribution varies with energy according to a power law.

Fig. 5.2 Electron energy distribution function in Ne + 0.0001% Ar Penning mixtures at low E/N. The curves are successively displaced to the right for the sake of clarity
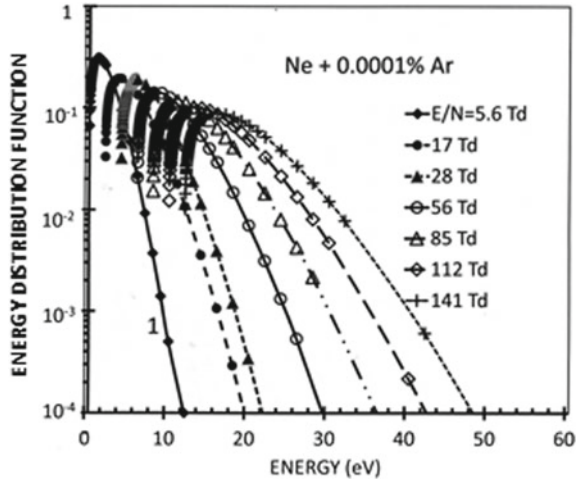
Fig. 5.3 Electron energy distribution function in Ne + 0.0001% Ar Penning mixtures at moderate E/N. The curves are successively shifted to the right for clarity of presentation
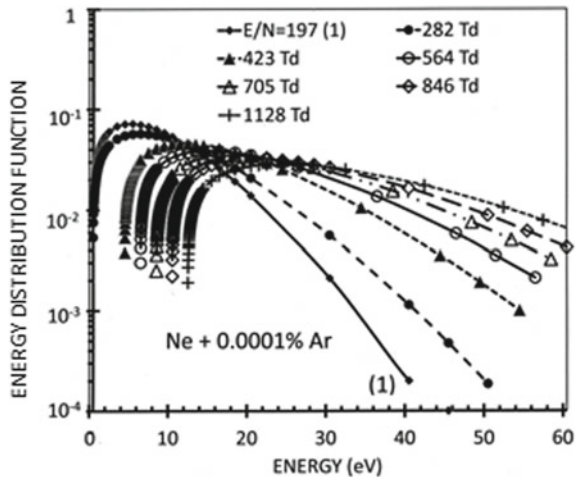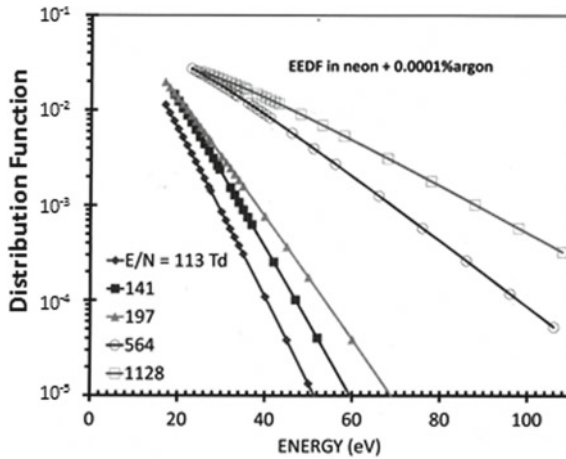
Fig. 5.4 Electron energy distribution function in Ne + 0.0001% Ar Penning mixtures at high E/N. The curves are successively shifted for clarity of presentation
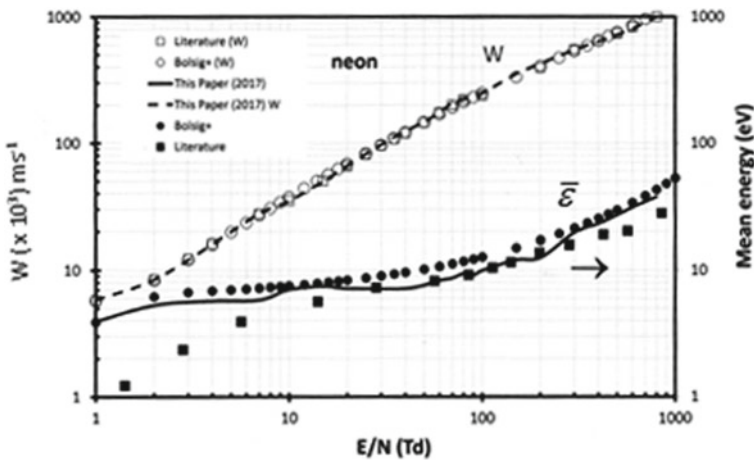
Fig. 5.5 Transport parameters for neon in 100% neon compiled from published literature. Such curves are available from published literature [10, 11] for argon and other gases

5.4 Concluding Remarks

This paper is a first attempt to examine whether there is a way to calculate coefficients by the integration process, by deriving the electron energy distribution functions with a simpler and different approach. It should be understood clearly that the method proposed is not claimed to be more original or more rigorous than the Boltzmann solution. The advantages claimed for the explained procedure are:

Fig. 5.6 First ionization coefficients in Penning mixtures of neon and argon. Both experimental [17] and theoretical (this paper) values are plotted as shown in the legend. Plotted values unless otherwise specified are experimental
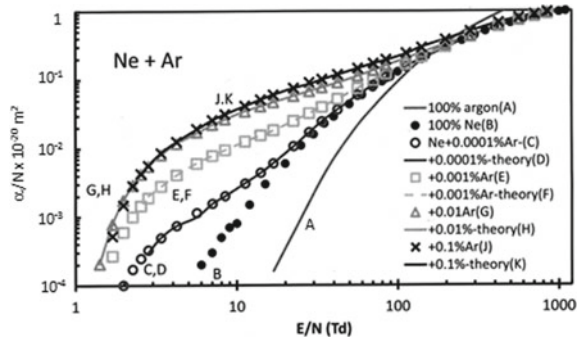
1. It is much simpler to use than the numerical solution of boltzmann equation requiring elaborate collision cross section data and demanding expertise in coding the programs.
2. An analytical expression for energy distribution is necessary for calculation of electron energy distribution functions in non-uniform electric fields, microwave breakdown, breakdown in magnetic fields, and application of plasma science to medical sciences etc., which use the concept of equivalent electric field.
3. The paper highlights some of the challenges in the unfolding procedures for obtaining cross sections from swarm data through the numerical boltzmann solution.

References

1. A. Vardelle, C. Moreau, N.J. Themelis, C. Chazelas, Plasma Chem Plasma Process **35**, 491–509 (2015)
2. J.C. Chamarro, L. Prevosto, E. Cejas, N.J. Milardovich, B.R. Mancinelli, G. Fischfeld, IEEE Trans. Plasma Sci. **47**(6), 2839–2866
3. J. Julak, O. Janouskova, V. Scholtz, K. Holada, Plas. Proc. Polym. **8**, 316–323 (2011)
4. M.J. Gallagher, N. Vaze, S. Gangoli, V.N. Vasilets, A.F. Gutsol, T.N. Milavonova, S. Anandan, D.M. Murasko, A.A. Fridman, IEEE Trans. Plasma Sci. **35**(5), 1501–1510 (2007)
5. S. Khalgagti, *Plasma Assisted Blood Co-agulation*. Reference [1], Chapter 12.2, pp. 81–96
6. H.W. Lee, S.H. Nam, A.-A. Mohamed, G.C. Kim, J.K. Lee, Plasma Processes and Polymers **7**(3–4), (2010)
7. G. Fridman, A. Shereshevsky, M.M. Jost, A.D. Brooks, A. Fridman, A. Gutsol, V. Vasilets, G. Friedman, Plasma Chem. Plasma Process. **27**, 163–176 (2007)
8. A.D. Morris, G.B. McCombs, T. Akan, W. Hynes, M. Laroussi, S.L.J. Tolle, Dent. Hyg. **83**(2), 55–61 (2009)
9. R. Morrow, Properties of Streamers and streamer channels, $SF_{6''}$, Phys. Rev. A **35**(4), 1778 (1987)
10. L.S. Frost, A.V. Phelps, Phys. Rev. **127**(5), 1621–1633 (1962)

11. J. Sherman, Math. Anal. Appl. **1**, 342–334 (1960)
12. G.G. Raju, R. Hackam, J. Appl. Phys. **52**, 3912–3920 (1981)
13. Gupta, N., G. Raju, IEEE Trans. Dielectr. Electr. Insul. **7**, 705–720 (2000). M.J. Brunger, S.J. Buckman, D.S. Newman, Austr. J. Phys. **43**, 665–682 (1990)
14. Y. Sakai, S. Sawada, H. Tagashira, Effect of penning ionization on an electron swarm in Ar/Ne mixtures: Boltzmann equation analysis. J. Phys. D: Appl. Phys. **19**(9), 1741 (1986)
15. Y. Sakai, S. Sawada, H. Tagashira, J. Phys. D: Appl. Phys. **19**(12), 2393–2400 (1986)
16. G. Govinda-Raju, J. Phys. Conf. Ser. **591**, 012032 (2015)
17. J. At. Mol. Nucl. Opt. Phys. University of Delhi, to be published

Chapter 6
Green Synthesis of Silver Nanoparticles Using *Abutilon theophrasti* Leaves and their Photocatalytic Activity for Water Treatment

Ruby, Aryan, and Mohan Singh Mehata

Abstract A new medicinal plant, *Abutilon theophrasti,* was used to synthesize silver nanoparticles (AgNPs) via the green synthesis process. An absorption band of bio-synthesized crystalline AgNPs was observed due to the strong surface plasmon resonance (SPR). The effects of temperature and pH were recorded as changes in the absorption spectrum. The absorption intensity of AgNPs increases with increasing pH, whereas the peak shifts toward a shorter wavelength upon increasing temperature. It was observed that basic pH is more suitable for synthesized nanoparticles. The zeta potential of the colloidal solution revealed that the AgNPs are highly stable. The size of nanoparticles calculated using different techniques is nearly equal to 38 nm. The methyl orange dye degradation in the presence of AgNPs with and without sunlight were disucssed. The results show that the rate of dye degradation was faster under sunlight.

6.1 Introduction

Green synthesis focus on products that provide a minimum hazard to the environment [22]. Moreover, high energy is needed and purification is complex during synthesis; therefore, major challenges currently are the non-poisonous and ecological synthesis of metal nanoparticles [3, 32]. Metallic nanoparticles are synthesized by many processes like chemical and physical methods, also using green synthesis processes [16, 23]. They have many applications in the field of medicine [12, 38], catalysis [39], bio-sensing [19], electronic [25], magnetic, optoelectronic, photoelectrochemical [5], and information storage [30].

Using the green synthesis method, AgNPs can be synthesized using various entities like plants [7, 13, 17, 18, 26], microorganisms [21], and enzymes [8]. Silver shows

---

Ruby and Aryan—both are contributed equally

Ruby · Aryan · M. S. Mehata (✉)
Laser-Spectroscopy Laboratory, Department of Applied Physics, Delhi Technological University, Bawana Road, Delhi 110042, India

antimicrobial and catalytic properties [10], synthesized AgNPs enhance those properties to a higher extent making AgNPs very practical and valuable in the medical field and wastewater management [1, 4, 9, 33]. The current study includes the synthesis of AgNPs with the help of plant leaves of *Abutilon theophrasti.* It is an ethnomedicinal weed plant mainly cultivated for oil and fiber [20]. The leaves, stems, roots, and seeds of the plant exhibit properties like anti-inflammatory, carminative, etc., used to treat rheumatic pains, sprains and dysentery [6].

Azo dyes are commonly used in the textile and paint industries and the primary sources of water pollution. The oxidative reduction technique is an efficient method for reducing such harmful dyes [41]. Nanomaterials like TiO_2 require UV light for their activation [34]; however, AgNPs exhibit strong absorption under natural light, and their high reactivity and selectivity enhance their photocatalytic activity [2]. In recent studies, photocatalytic degradation of methyl orange (MO) is done using AgNPs [15]. Therefore, in the present study, AgNPs were used to degrade MO dye under sunlight, which can be further used for water treatment.

6.2   Materials and Methods

Silver nitrate ($AgNO_3$) and Sodium hydroxide were acquired from S-Aldrich chemical Co. Chemicals were used without further purification. 1 mM of $AgNO_3$ is prepared by adding 17 mg of $AgNO_3$ in 100 mL ultrapure (UP) water. For 0.1 M sodium hydroxide, 40 mg was added in 100 mL UP water. 3.7 mg of methyl orange ($C_{14}H_{14}N_3NaO_3S$) (MO) is added in 100 mL UP water to make a 10^{-4} M concentration solution.

Abutilon theophrasti green leaves were obtained from the Delhi Technological University (DTU) campus, washed under tap and UP water to remove impurities. 5 g of green leaves are chopped and added with 50 ml UP water followed by boiling for 15 min. Whatman filter paper is used for filtration and the extract is kept in a cool and dry place. 5 mL extract was dissolved in 45 mL $AgNO_3$ solution and stirred continuously to ensure the plant extract could uniformly react with a silver salt. The temperature of the reaction was kept constant at 37 °C. Figure 6.1 shows the AgNPs synthesis schematic diagram.
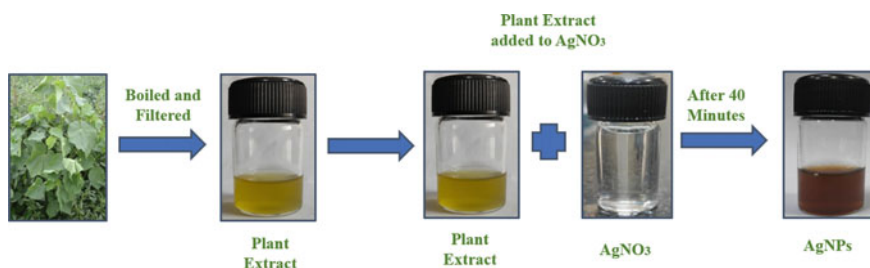
Fig. 6.1 Pictorial representation of silver nanoparticles synthesis

Absorption spectra of AgNPs and dye were recorded with a Lambda- 750 Perkin Elmer spectrometer. XRD was analyzed using BRUKER- D8 advanced and zeta potential was recorded using zeta potential Analyzer from Malvern Panalytical.

6.3   Results and Discussion

The UV–visible absorption spectra of $AgNO_3$, plant extract, and AgNPs are shown in Fig. 6.2. A strong absorption band is observed at around 438 nm as SPR of the AgNPs. The green synthesized nanoparticles depend on physical parameters like temperature and pH.

AgNPs emergence is first confirmed by observing the color change at different reaction times. 5 mL extract was mixed with 45 mL of $AgNO_3$ salt and with time color of the solution was changed from pale yellow to brown and finally into dark brown, confirming the formation of AgNPs as shown in Fig. 6.3a [38]. Formation of silver nanoparticles initiated after 5 min and vigorously increased up to 40 min. The flavonoids and terpenoids present in plants cause Ag ion reduction to AgNPs [14]. Over time, a sharp SPR band was observed, and the peak intensity also increased with time [29]. The absorption maximum of SPR peak was observed at 439 nm, as shown in Fig. 6.3b.

At a highly acidic pH, the biomolecules present in the extract are inactivated hence no reaction take place, which leads to no absorption peak [11]. At a very high basic pH, silver nanoparticles agglomerates and were unstable [37]. Therefore, the absorption spectrum of AgNPs was recorded for pH between 6 and 12 pH, as shown in Fig. 6.4. The SPR peak at pH 6 is at 432 nm having an intensity/absorbance of 0.5. On rising pH from 6 to 12, the SPR peak shifts to 444 nm, and the intensity increases to 0.8. A similar effect was observed in the previous study [27]. The results suggest that alkaline pH is suitable for AgNPs synthesis.

Fig. 6.2 Absorption spectra of plant extract, silver salt, and silver nanoparticles in water
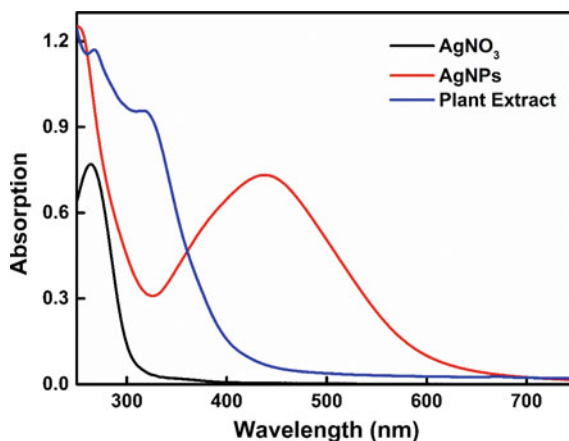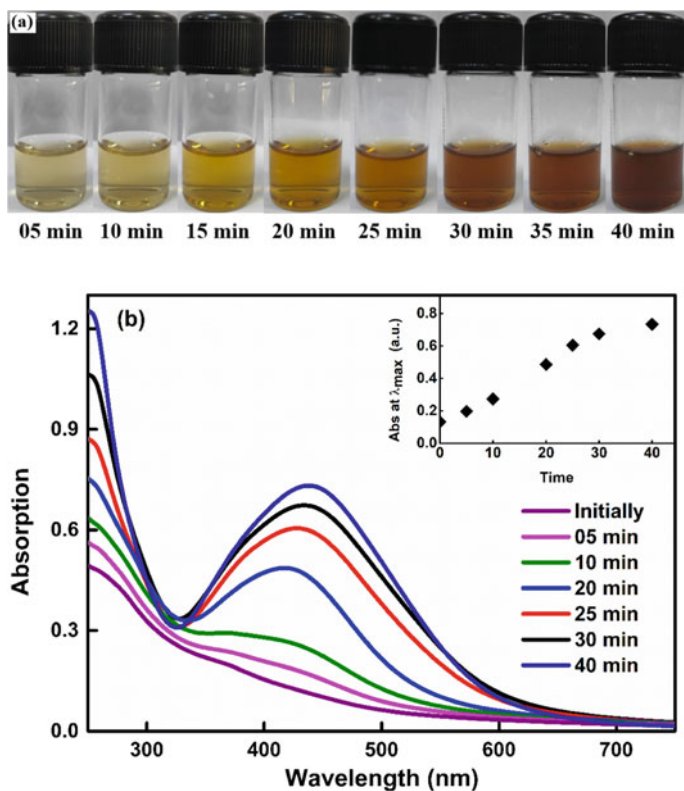
Fig. 6.3 Color change in silver slat plant extract solution with time (**a**) and absorption spectra of AgNPs at various reaction time intervals. Inset (**b**) shows the shift in peak of absorption maximum as a function of time

Fig. 6.4 Absorption spectrum AgNPs at various pH. Inset shows the shift in wavelength at different pH
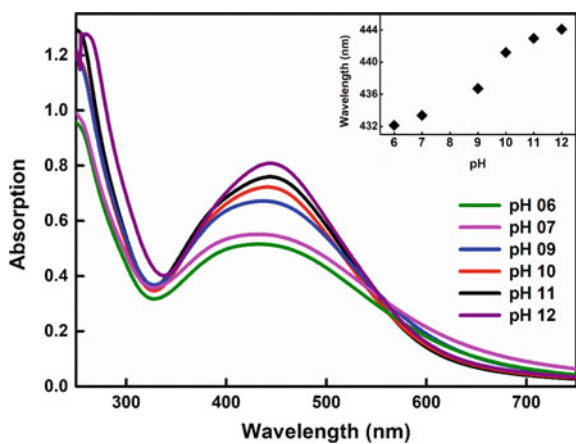
Temperature is a dominating parameter responsible for the shape, size, and morphology of AgNPs. Figure 6.5 shows the temperature effect in the range 10–60 °C on silver nanoparticle synthesis. With temperature increase, SPR peak intensity increases, and wavelength shifts from 440 to 433 nm, i.e., a blue shift occurs, indicating the decrease in particle size [31]. This may be because the faster consumption of reactant and the complete reduction of silver nitrate also occurs fast, causing faster color change [24].

For the XRD measurement, the AgNPs dispersed in water were quoted on glass substrate at room temperature. Figure 6.6 illustrate the XRD pattern of synthesized AgNPs and four major reflection peaks can be observed for (111), (200), (220), and (311) planes at 2θ equal to 38.28°, 44.28°, 64.4°, 77.34° respectively (JCPDS, file No. 04–0783) [36]. AgNPs average crystalline size was determined using Debye's

Fig. 6.5 The absorption spectrum of AgNPs for various reaction temperatures. Inset of (**a**) shows the zoomed peaks of the absorption spectrum and (**b**) the shift in absorption maximum with temperature
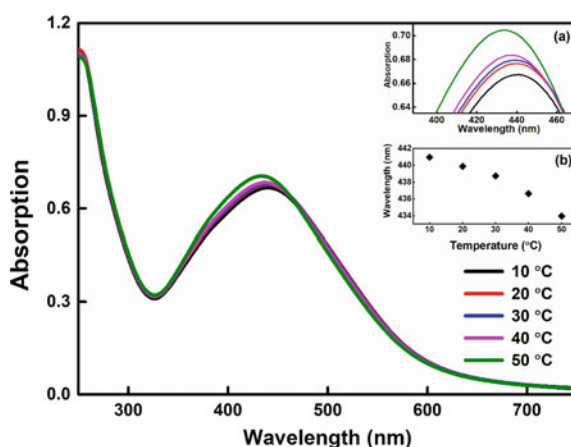
Fig. 6.6 XRD pattern of AgNPs formed using plant extract
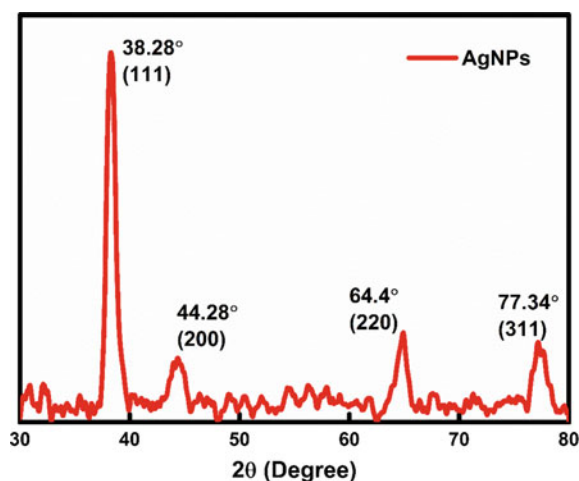
Fig. 6.7 Plot of AgNPs size
distribution
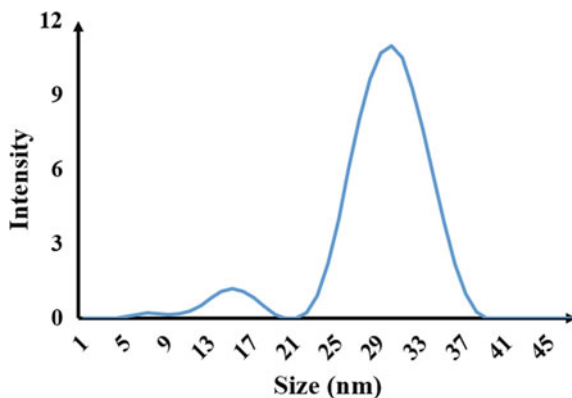
equation $D = 0.9\lambda/\beta\cos\theta$, here D is particles size, λ and β represent wavelength, and FWHM (full-width half maxima). The estimated particle size for peak (111) is 36.9 nm.

Zeta potential is used to determine the nanoparticle's surface charge in colloidal solutions, and the magnitude of zeta potential analyzes its stability. Lower or higher dispersion zeta potential value causes the solution in aggregation or coagulation of AgNPs due to Van der Waals interparticle attraction or repulsion. The magnitude of zeta potential is -27 mV making the colloidal solution highly stable. The calculated average AgNPs size from zeta potential is 36 nm, as shown in Fig. 6.7.

6.4 Methyl Orange Dye (MO) Photocatalytic Degradation

A certain amount of AgNPs (5 mL) was mixed in 45 mL of MO dye solution and stirred for 30 min in dark conditions. Later put into two beakers, one stored in the dark, and another is kept under natural light (sunlight). The absorption maximum of MO is observed at 464 nm and gradually decreases when irradiated with sunlight. The percentage of dye degraded is calculated using $[(C_0\text{-}C_t)/C_0] \times 100$ [28], C_0 and C_t denote concentration initially and at t time interval, respectively. In the dark, 25.4% of the dye is degraded in 35 min and whereas under sunlight, nearly 74% of the dye is degraded in the same reaction time and AgNPs concentration. The color change is shown in Fig. 6.8. Absorption spectra of MO in the dark and under sunlight are shown in Fig. 6.9a, b. Reaction rate constant k is estimated with $\ln(C_t/C_0) = -kt$ [35]. Figure 6.10 shows that dye degradation follows pseudo-first−order kinetics. The k value for dark is 0.0084/min, and under sunlight is 0.0366/min. AgNP's photocatalytic activity in sunlight is due to the excitation of SPR. The Ag conduction electron gets excited and captured by oxygen molecules which produce hydroxyl radicals and are responsible for MO dye degradation [40].

Fig. 6.8 Change in colour of the dye MO, after degradation under sunlight (**a**) and dark conditions (**b**)

(a) Observation under sunlight

After 35 minutes

(b) Observation in dark

After 35 minutes
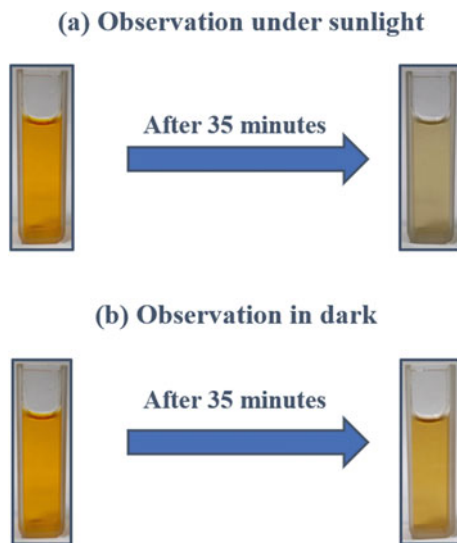
6.5   Conclusion

AgNPs were synthesized with fresh *Abutilon theophrasti* leaves using the green synthesis method. The effects of physical parameters were studied. The absorption spectra show an increase in absorption intensity with increasing pH. While on the increasing temperature, a blue shift in SPR peak is observed, indicating the formation of smaller nanoparticles. XRD analysis shows AgNPs crystalline nature, whereas significant zeta potential value has proven its higher stability. The AgNPs were used to degrade MO dye. The reduction rate of dye is higher under sunlight.

Fig. 6.9 Absorption spectra
of MO dye solution in water
at different reaction times in
the presence of AgNPs under
dark conditions (**a**) and
sunlight (**b**)
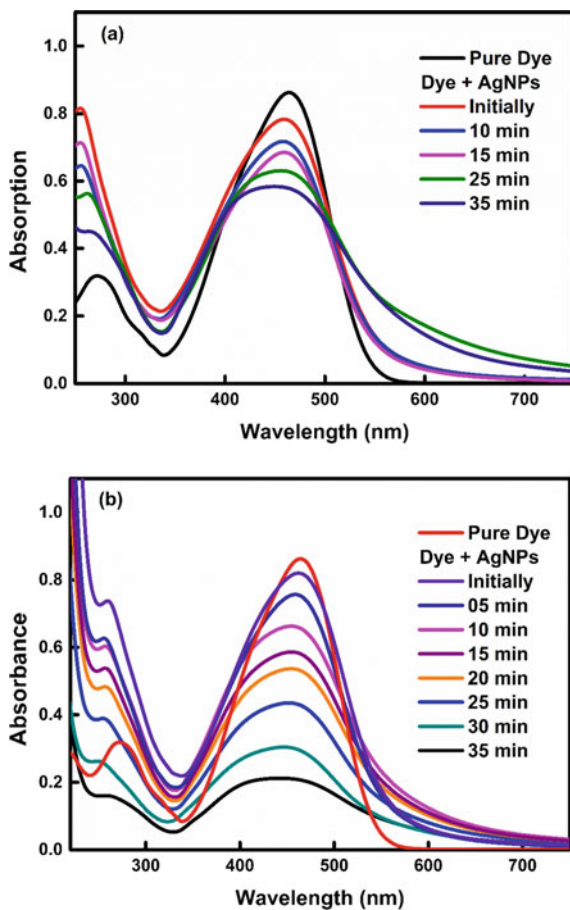
Fig. 6.10 Plots of ln (C_t/C_0)
against reaction time for
reducing MO dye in the
presence of AgNPs in the
dark and under sunlight
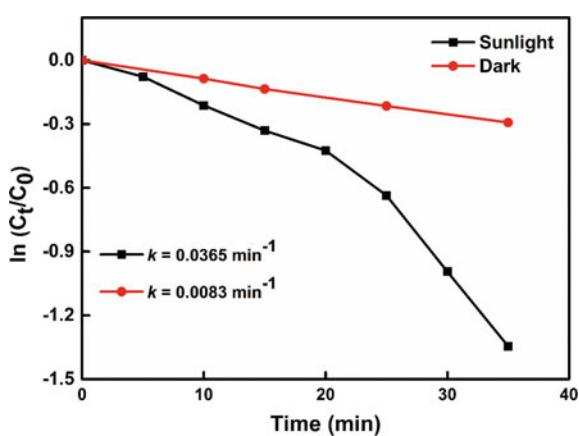
Data availability
All data generated or analysed during this study are included in this article.

Author Contribution
Ruby: Conception and design the study, acquisition of data and drafting the manuscript.

Aryan: Conception and design the study, acquisition of data and drafting the manuscript.

MSM: Resources, funding acquisition, supervision, conception and design of the study, revising and editing the manuscript.

Conflict of interest
The authors declare no competing interest.

Consent to Publish
All authors have approved the paper and agree with its publication.

Ethical approval
This article does not contain any studies with human participants or animals, clinical trial registration or plant reproducibility performed by any authors.

References

1. M.A. Albrecht, C.W. Evans, C.L. Raston, Green chemistry and the health implications of nanoparticles. Green Chem **8**, 417–432 (2006). https://doi.org/10.1039/b517131h
2. S.M. Albukhari, M. Ismail, K. Akhtar, E.Y. Danish, Catalytic reduction of nitrophenols and dyes using silver nanoparticles @ cellulose polymer paper for the resolution of waste water treatment challenges. Colloids Surf. A Physicochem. Eng. Asp. **577**, 548–561 (2019). https://doi.org/10.1016/j.colsurfa.2019.05.058
3. D. Bose, S. Chatterjee, Biogenic synthesis of silver nanoparticles using guava (*Psidium guajava*) leaf extract and its antibacterial activity against *Pseudomonas aeruginosa*. Appl. Nanosci. **6**, 895–901 (2016). https://doi.org/10.1007/s13204-015-0496-5
4. J. Brown, Impact of silver nanoparticles on wastewater treatment, ed. by G. Lofrano, G. Libralato, J. Brown. *Nanotechnologies for Environmental Remediation* (Springer, Cham, 2017) pp. 255–267, https://doi.org/10.1007/978-3-319-53162-5_9
5. N. Chandrasekharan, P.Y. Kainat, Improving the photoelectrochemical performance of nanostructured TiO_2 films by adsorption of gold nanoparticles. J. Phys. Chem. B **104**, 10851–10857 (2000). https://doi.org/10.1021/jp0010029
6. M. Dinu, V. Uivarosi, M.U. Popescu, V. Radulescu, C. Cristina Arama, T.O. Nicolescu, R.V. Ancuceanu, Proximate composition and some physico-chemical properties of *Abutilon theophrasti* (velvetleaf) seed oil. Rev. Chim. **61**, 50–54 (2010)
7. J.L. Gardea-Torresdey, E. Gomez, J.R. Peralta-Videa, J.G. Parsons, H. Troiani, M. Jose-Yacaman, *Alfalfa sprouts*: a natural source for the synthesis of silver nanoparticles. Langmuir **19**, 1357–1361 (2003). https://doi.org/10.1021/la020835i

8. M. Gericke, A. Pinches, Biological synthesis of metal nanoparticles. Hydrometallurgy **83**, 132–140 (2006). https://doi.org/10.1016/j.hydromet.2006.03.019

9. I. Hussain, M. Brust, A.J. Papworth, A.I. Cooper, Preparation of acrylate-stabilized gold and silver hydrosols and gold-polymer composite films. Langmuir **19**, 4831–4835 (2003). https://doi.org/10.1021/la020710d

10. J.E. Hutchison, Greener nanoscience: a proactive approach to advancing applications and reducing implications of nanotechnology. ACS Nano **2**, 395–402 (2008). https://doi.org/10.1021/nn800131j

11. H.M.M. Ibrahim, Green synthesis and characterization of silver nanoparticles using banana peel extract and their antimicrobial activity against representative microorganisms. J. Radiat. Res. Appl. Sci. **8**, 265–275 (2015). https://doi.org/10.1016/j.jrras.2015.01.007

12. S. Jain, M.S. Mehata, Medicinal plant leaf extract and pure flavonoid mediated green synthesis of silver nanoparticles and their enhanced antibacterial property. Sci. Rep. **7**, 15867 (2017). https://doi.org/10.1038/s41598-017-15724-8

13. H. Jiale, L. Qingbiao, S. Daohua, L. Yinghua, S. Yuanbo, Y. Xin, W. Huixuan, W. Yuanpeng, S. Wenyao, H. Ning, H. Jinqing, C. Cuixue, Biosynthesis of silver and gold nanoparticles by novel sundried *Cinnamomum camphora* leaf. Nanotechnology **18**, 105104 (2007)

14. C. Krishnaraj, E.G. Jagan, S. Rajasekar, P. Selvakumar, P.T. Kalaichelvan, N. Mohan, Synthesis of silver nanoparticles using *Acalypha indica* leaf extracts and its antibacterial activity against water borne pathogens. Colloids Surf. B **76**, 50–56 (2010). https://doi.org/10.1016/j.colsurfb.2009.10.008

15. P. Kumar, M. Govindaraju, S. Senthamilselvi, K. Premkumar, Photocatalytic degradation of methyl orange dye using silver (Ag) nanoparticles synthesized from *Ulva lactuca*. Colloids Surf. B **103**, 658–661 (2013). https://doi.org/10.1016/j.colsurfb.2012.11.022

16. A.T. Le, L.T. Tam, P.D. Tam, P.T. Huy, T.Q. Huy, N. Van Hieu, A.A. Kudrinskiy, Y.A. Krutyakov, Synthesis of oleic acid-stabilized silver nanoparticles and analysis of their antibacterial activity. Mater. Sci. Eng. C **30**, 910–916 (2010). https://doi.org/10.1016/j.msec.2010.04.009

17. M.F. Lengke, M.E. Fleet, G. Southam, Biosynthesis of silver nanoparticles by *Filamentous cyanobacteria* from a silver(I) nitrate complex. Langmuir **23**, 2694–2699 (2007). https://doi.org/10.1021/la0613124

18. S. Li, Y. Shen, A. Xie, X. Yu, L. Qiu, L. Zhang, Q. Zhang, Green synthesis of silver nanoparticles using *Capsicum annuum* L. extract. Green. Chem. **9**, 852–885 (2007). https://doi.org/10.1039/b615357g

19. X. Luo, A. Morrin, A.J. Killard, M.R. Smyth, Application of nanoparticles in electrochemical sensors and biosensors. Electroanalysis **18**, 319–326 (2006). https://doi.org/10.1002/elan.200503415

20. N.Z. Mamadalieva, F. Sharopov, J.P. Giraultc, M. Wink, R. Lafont, Phytochemical analysis and bioactivity of the aerial parts of *Abutilon theophrasti* (Malvaceae), a medicinal weed. Nat. Prod. Res. **28**, 1777–1779 (2014). https://doi.org/10.1080/14786419.2014.939080

21. D. Mandal, M.E. Bolander, D. Mukhopadhyay, G. Sarkar, P. Mukherjee, The use of microorganisms for the formation of metal nanoparticles and their application. Appl. Microbiol. Biotechnol. **69**, 485–492 (2006). https://doi.org/10.1007/s00253-005-0179-3

22. M.N. Moore, Do nanoparticles present ecotoxicological risks for the health of the aquatic environment? Environ. Int. **32**, 967–976 (2006). https://doi.org/10.1016/j.envint.2006.06.014

23. U. Nickel, A.Z. Castell, K. Pöppl, S. Schneider, Silver colloid produced by reduction with hydrazine as support for highly sensitive surface-enhanced Raman spectroscopy. Langmuir **16**, 9087–9091 (2000). https://doi.org/10.1021/la000536y

24. J. Park, J. Joo, S.G. Kwon, Y. Jang, T. Hyeon, Synthesis of monodisperse spherical nanocrystals. ChemInform **38**, 1–27 (2007). https://doi.org/10.1002/chin.200733240

25. G. Pető, G.L. Molnár, Z. Pászti, O. Geszti, A. Beck, L. Guczi, Electronic structure of gold nanoparticles deposited on SiOx/Si(100). Mater. Sci. Eng. C **19**, 95–99 (2002). https://doi.org/10.1016/S0928-4931(01)00449-0

26. D. Raju, U.J. Mehta, S. Hazra, Synthesis of gold nanotriangles and silver nanoparticles using Aloe vera plant extract. Trees (Berl. West) **25**, 577–583 (2011). https://doi.org/10.1021/nl015673+

27. S.M. Roopan, M.G. Rohit, A.A. Rahuman, C. Kamaraj, A. Bharathi, T.V. Surendra, Low-cost and eco-friendly phyto-synthesis of silver nanoparticles using *Cocos nucifera* coir extract and its larvicidal activity. Ind. Crops Prod. **43**, 631–635 (2013). https://doi.org/10.1016/j.indcrop.2012.08.013

28. K. Roy, C.K. Sarkar, C.K. Ghosh, Photocatalytic activity of biogenic silver nanoparticles synthesized using potato (*Solanum tuberosum*) infusion. Spectrochim Acta Part A Mol. Biomol. Spectrosc. **146**, 286–291 (2015). https://doi.org/10.1016/j.saa.2015.02.058

29. P.S. Sadalage, R.V. Patil, M.N. Padvi, K.D. Pawar, Almond skin extract mediated optimally biosynthesized antibacterial silver nanoparticles enable selective and sensitive colorimetric detection of Fe^{+2} ions. Colloids Surf. B **193,** 111084 (2020). https://doi.org/10.1016/j.colsurfb.2020.111084

30. O.V. Salata, Applications of nanoparticles in biology and medicine. J. Nanobiotechnol. **2**, 3 (2004). https://doi.org/10.1186/1477-3155-2-3

31. K. Saware, A. Venkataraman, Biosynthesis and characterization of stable silver nanoparticles using *Ficus religiosa* leaf extract: a mechanism perspective. J Clust Sci **25**, 1157–1171 (2014). https://doi.org/10.1007/s10876-014-0697-1

32. A. Sengottaiyan, R. Mythili, T. Selvankumar, A. Aravinthan, S. Kamala-Kannan, K. Manoharan, P. Thiyagarajan, M. Govarthanan, J.H. Kim, Green synthesis of silver nanoparticles using *Solanum indicum* L. and their antibacterial, splenocyte cytotoxic potentials. Res. Chem. Intermed. **42**, 3095–3103 (2016). https://doi.org/10.1007/s11164-015-2199-7

33. V.K. Sharma, R.A. Yngard, Y. Lin, Silver nanoparticles: Green synthesis and their antimicrobial activities. Adv. Colloid Interface Sci. **145**, 83–96 (2009). https://doi.org/10.1016/j.cis.2008.09.002

34. M.K. Singh, M.S. Mehata, Enhanced photoinduced catalytic activity of transition metal ions incorporated TiO_2 nanoparticles for degradation of organic dye: absorption and photoluminescence spectroscopy. Opt. Mater. (Amst.) **109,** 110309 (2020). https://doi.org/10.1016/j.optmat.2020.110309

35. M.K. Singh, M.S. Mehata, Phase-dependent optical and photocatalytic performance of synthesized titanium dioxide (TiO_2) nanoparticles. Optik (Stuttg) **193,** 163011 (2019). https://doi.org/10.1016/j.ijleo.2019.163011

36. R. Singh, S.K. Sahu, M. Thangaraj, Biosynthesis of silver nanoparticles by marine invertebrate (polychaete) and assessment of its efficacy against human pathogens. J. Nanopart. **2014**, 1–7 (2014). https://doi.org/10.1155/2014/718240

37. R. Veerasamy, T.Z. Xin, S. Gunasagaran, T.F.W. Xiang, E.F.C. Yang, N. Jeyakumar, S.A. Dhanaraj, Biosynthesis of silver nanoparticles using mangosteen leaf extract and evaluation of their antimicrobial activities. J. Saudi Chem. Soc. **15**, 113–120 (2011). https://doi.org/10.1016/j.jscs.2010.06.004

38. A. Verma, M.S. Mehata, Controllable synthesis of silver nanoparticles using Neem leaves and their antimicrobial activity. J. Radiat. Res. Appl. Sci. **9**, 109–115 (2016). https://doi.org/10.1016/j.jrras.2015.11.001

39. C. Wang, N.T. Flynn, R. Langer, Controlled structure and properties of thermoresponsive nanoparticle-hydrogel composites. Adv. Mater. **16**, 1074–1079 (2004). https://doi.org/10.1002/adma.200306516

40. L. Wang, F. Lu, Y. Liu, Y. Wu, Z. Wu, Photocatalytic degradation of organic dyes and antimicrobial activity of silver nanoparticles fast synthesized by flavonoids fraction of *Psidium guajava* L. leaves. J. Mol. Liq. **263**, 187–192 (2018). https://doi.org/10.1016/j.molliq.2018.04.151

41. Y. Xu, B. Ren, R. Wang, L. Zhang, T. Jiao, Z. Liu, Facile preparation of rod-like MnO nanomixtures via hydrothermal approach and highly efficient removal of methylene blue for wastewater treatment. Nanomaterials **9**, 10 (2019). https://doi.org/10.3390/nano9010010

Chapter 7
Synthesis of Deformation Resistant Palladium (Pd) Nanoparticle Layer

Saurabh K. Sengar, Vinod Singh, Pawan K. Kulriya, Manika Khauja, and Ashok Kumar

Abstract In this study, a comparison of structural changes on hydrogen loading-deloading cycles in palladium (Pd) nanoparticle layer and Pd thin film has been carried out. Cracks start to appear in the Pd thin film, which grow in size on continuous hydrogen loading-deloading cycles while no such phenomenon is observed in the nanoparticle layer. The XRD studies of the samples suggest that stress is generated in thin films on hydrogenation, which, when released, results in the crack formation. In comparison, due to low interaction with the substrate, nanoparticles are free to expand in all the directions and hence no stress is generated in the nanoparticle layer on being subjected to hydrogen loading deloading cycles. The variation in the XPS core level peak positions, before and after hydrogenation cycles support the inferences drawn from the XRD and SEM analysis of the samples.

7.1 Introduction

The extremely high affinity of hydrogen towards palladium (Pd) makes latter one of the best choices for hydrogen sensing, production and storage applications. In comparison to bulk, thin films of Pd show better properties in terms of increased hydrogen solubility and lower critical temperatures, in addition to being economically viable. However, on repeated hydrogen loading-deloading cycles, Pd thin films

S. K. Sengar (✉)
D S College, Aligarh 202001, India

V. Singh · A. Kumar
Department of Applied Physics, Delhi Technological University, New Delhi 110042, India

P. K. Kulriya
School of Physical Sciences, Jawaharlal Nehru University, New Delhi 110067, India

M. Khauja
Jamia Millia Islamia, New Delhi 110025, India

A. Kumar
Atma Ram Sanatan Dharma College, University of Delhi, New Delhi 110021, India

suffer from stress induced effects which deteriorates their performance. The pressure concentration isotherms of Palladium-hydride exhibit the transition from the α-Pd-Hx to the β- Pd-Hx at the equilibrium pressure. The α-palladium-hydride has low solubility of hydrogen, whereas, β- palladium-hydride is a non-stoichiometric phase. The α- Pd-Hx and the β- Pd-Hx has a lattice mismatch of 3.54% lattice mismatch [1] (11 vol. %) and it leads to the expansion upon hydrogenation. The thin films, which can not expand freely in-plane due to being clamped to the substrate, experience large compressive stresses due to hydrogen induced expansion. Therefore, the substantial compressive in-plane strains [2], microstructural defects [3] and finally substantial plastic deformations [4] are created by the hydrogenation of Pd thin films. The Gremaud et al. have shown that strain generated in Pd thin films clamped to the substrate on hydrogen absorption desorption cycles gets delivered by the generation of a buckle-and-crack network [5]. The process of stress generation and release on hydrogenation of the Pd films is governed by the film-substrate interaction. If film-substrate interaction is relatively weak, the in-plane compressive stresses are released by the formation of so-called buckles [6]. This happens when the hydrogenation stresses dominate over the adhesion forces between the substrate and the film [7]. In fact, in buckled Pd and Pd-Fe thin films, a reasonable trimming of mechanical stresses was observed during hydrogen cycling [8]. Further, a strong adhesion with the substrate is exhibited by the thin films of the metal-hydride. Therefore, the plastic deformations occur along with the elastic deformations, in the absence of an effective stress release. In case of Pd films' having good adhesion with the substrate, rearrangement and pile-up of the material takes place instead of buckling on cycling between the dilute α-phase and fully hydrogenated β-phase. The structural deformation in Pd thin films not only alters their properties but also limits their life time. In the present study, Pd nanoparticles layer and thin film have been deposited on to Si substrate and a comparative study of structural and electronic changes on hydrogen loading-deloading cycles has been discussed.

7.2 Experimental

The nanoparticle layer of Pd has been synthesized by the gas phase synthesis technique, whereas, the Pd thin film has been fabricated by the thermal evaporation technique. The gas phase synthesis system employed for the synthesis of palladium nanoparticles is shown schematically in Fig. 7.1. The primary nanoparticles are generated in the spark generator using the two Pd rods. Each of the Pd rods has a diameter of 3.2 mm. A constant spark frequency of 300 Hz is fixed in the spark generator. In order to carry the nano agglomerates, nitrogen gas (N2) is used as a carrier gas. The nitrogen gas flow rate in the spark generator was 2.6 l/min. The nano agglomerates are then charged by the radioactive Kr-85 neutralizer. Thereafter, a differential mobility analyzer (DMA) is used to select the agglomerates of a mobility equivalent diameter (Dm) of 20 nm. The DMA selects the nanoparticles on the basis of their electrical mobility. The sheath flow and aerosol flow in the DMA
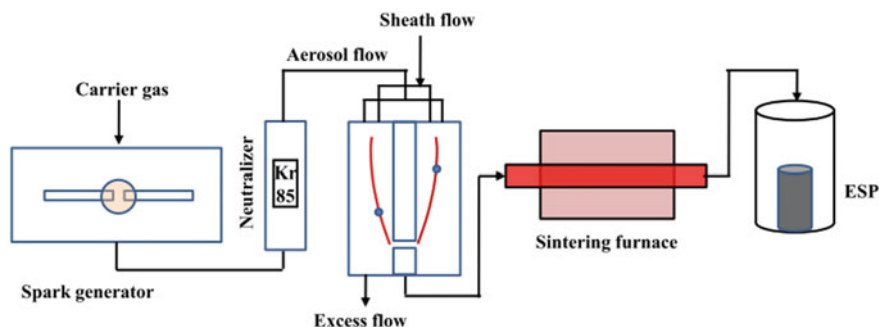
Fig. 7.1 The schematic diagram of the gas phase synthesis system used for the production of Pd nanoparticles

are put at a constant value of 10 and 1 l/m, respectively. The nano agglomerates are sintered in a sintering furnace at a temperature of 500 °C, which results in the formation of the spherical nanoparticles. An electrostatic precipitator (ESP) is taken as a deposition chamber where the nanoparticles are deposited on the desired substrate. A constant aerosol flow of 1 l/min is fixed in the DMA, sintering furnace, and ESP. The Pd thin films are synthesized onto a Si substrate using thermal evaporation at a base pressure of $1 \times 10{-6}$ Torr. A piece of Pd wire having 99.99% purity is used for Pd evaporation. By the quartz crystal monitor, the thickness of the Pd film is fixed at 60 nm. The more details of the gas phase synthesis system can be seen elsewhere [9–13].

The samples were loaded and deloaded with hydrogen in a specially designed gas chamber. Hydrogen was loaded into the sample at a pressure of 1 bar, while it was deloaded by creating vacuum in the system. The glancing angle X-ray diffraction (GAXRD) (Bruker, D8 Advance) comprising of a Cu-Kα X-ray source (energy: 8.0 keV and wavelength: 1.54 Å), is used for the XRD study. The value of the glancing angle is taken as 2°. A Field effect scanning electron microscope (FESEM) (Quanta 3D, FEI) has been used to study the morphology of the Pd nanoparticle layer and thin film. Model-1257, Perkin Elmer USA equipment is used for performing the X-ray photoelectron microscopy (XPS) measurements. Al K_α radiation is used as the excitation source for recording the core level spectra of the samples. C 1 s peak position at 284.6 eV is used as a reference for the binding energy (B.E.) values.

7.3 Results and Discussion

Figure 7.2 shows the XRD patterns corresponding to as-deposited Pd nanoparticle layer and thin film samples. The XRD spectrograph of Pd thin film shows peaks at 2θ (d) values of 40.12° (2.216 Å) and 46.08° (1.84 Å), which correspond to body centred cubic Pd lattice. The XRD spectrograph of Pd nanoparticle layers has peaks

Fig. 7.2 X-ray
diffractogram (XRD) of as
deposited Pd nanoparticle
layer (NP) and thin film (TF)
sample
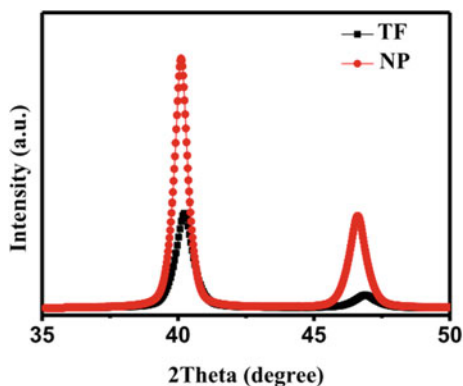
at 2θ (d) values of 40.22° (2.246 Å) and 46.44° (1.84 Å), which also confirms the body centred cubic Pd lattice. The positive shift towards higher 2θ value indicates lattice contraction in the nanoparticles. On decreasing the particle size, a similar lattice contraction is reported in Sn, Ni, and Bi nanoparticles [14, 15]. The observed lattice contraction can be the result of the surface bond contraction [16].

The gas sensing performance of Pd thin films and nanoparticle layers was investigated by measuring the change in resistance of the films and nanoparticle layers on changing the N2 to H2 gaseous environment in a cyclic order. The hydrogen sensing response of a Pd thin film sample on hydrogen loading deloading (HLD) cycles is shown in Fig. 7.3. The electrical resistance of the Pd thin film increases on exposure to hydrogen gas and attains a saturation level after few seconds as shown in Fig. 7.3a. On hydrogen exposure, dissociative adsorption takes place, as hydrogen molecules come near the Pd surface. The adsorbed hydrogen atoms diffuse into the palladium structure, thereby occupying the interstitial lattice sites. This creates the additional electron scattering, which results in the increase in the resistance of the sample. On purging the N2 gas into the system, hydrogen gets removed from the interstitial sites and the resistance of the film again decreases to its initial value. It is also clear from the Fig. 7.3b that on repeating the HLD cycles similar changes in the value of the sample resistance is observed. However, it is evident from the sensing curve of thin film (TF) sample that both the response time and recovery time increase on increasing the number of HLD cycles as shown in the Fig. 7.3b. This indicates that sample is being deteriorated on continuous HLD cycles. The sensing response of nanoparticle layer sample is shown in Fig. 7.3c. On contrary to thin film sample, response and recovery time of nanoparticle layer (NP) sample is not affected with increasing the number of HLD cycles as evident from Fig. 7.3d. The sensing response is stable and reproducible over a number of hydrogen loading–unloading cycles.

To study the effect of hydrogen loading deloading (HLD) cycles on the microstructure of Pd nanoparticle layer and thin film, SEM analysis of the surface morphology was carried out. In the thin film as well as nanoparticle layer samples, hydrogen was loaded and deloaded up to 40 cycles in a specially designed chamber. The SEM micrographs of the as deposited and hydrogenated thin film and nanoparticle samples
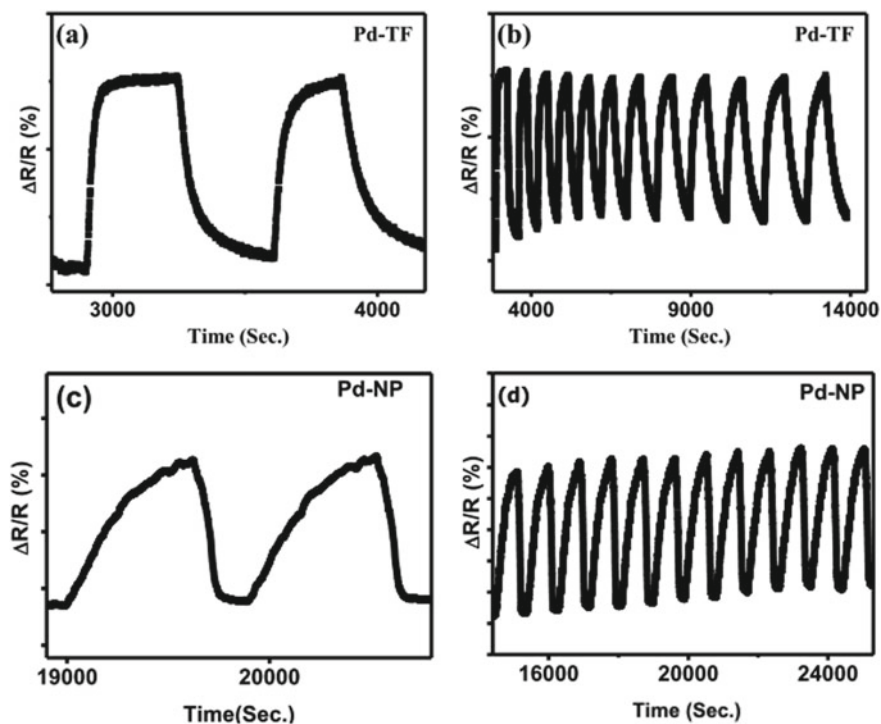
Fig. 7.3 Hydrogen sensing response curves **a**, **b** of Pd thin film (TF) and **c**, **d** Pd nanoparticle (NP) samples for 2 and 12 HLD cycles, respectively

are shown in Fig. 7.4. It can be seen that the as deposited thin film has a smooth surface at the micrometer scale. Cracks start to appear after 20 cycles of hydrogen loading deloading cycles which grow in size and are more clearly visible after 40 cycles. It is interesting to note that in the nanoparticle sample, surface remains smooth and no crack is observable even after 40 cycles. The thin films are not free to expand in all the direction on hydrogen exposure because of the film-substrate interaction, resulting in in-plane stress [2]. The continuous HLD cycles generate stress which dissipates by appearance of buckles and cracks [5]. In the vacuum evaporation techniques, thin films are grown by heterogeneous nucleation of the material on the substrate. In contrast, in the gas phase synthesis technique nanoparticles are formed in the gas phase itself and hence substrate has no role in the growth of nanoparticles; it merely acts as a station where particles are just staying. Due to this the interaction between nanoparticles and substrate is negligible, and hence, the former are free to expand in all the directions without any compressive stress. Nanoparticles expand when they are exposed to hydrogen. Once hydrogen is removed by creating the vacuum in the chamber, particles regain their original configuration. Hence nanoparticle layers will be able to sustain any number of HLD cycles, unlike the thin films which gets deformed only after 40 cycles.
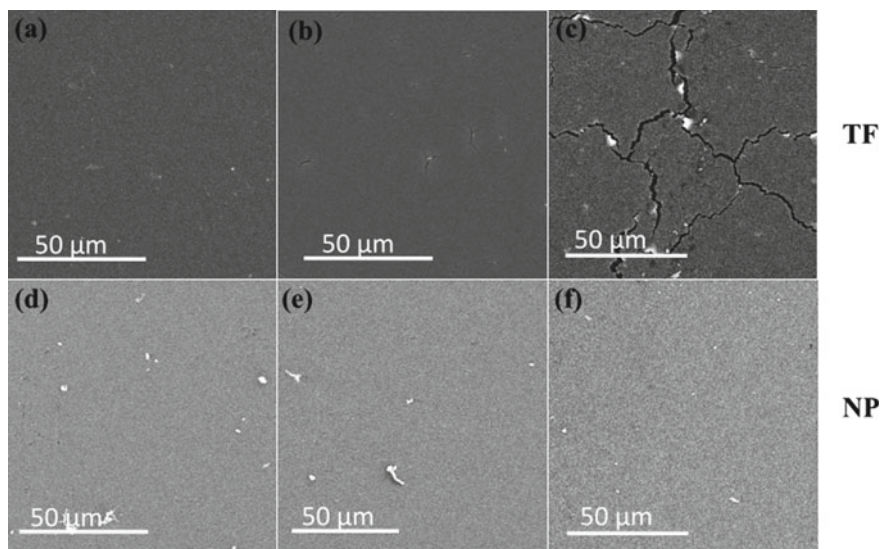
Fig. 7.4 SEM images of Pd thin films (TF) and nanoparticles (NP) before (**a**, **d**); after 20 (**b**, **e**) and after 40 (**c**, **f**) HLD cycles

A XRD study of the Pd nanoparticle layer and thin film samples after 20 and 40 HLD cycles was carried out (Fig. 7.5). In case of Pd thin film hydrogenated for 20 HLD cycles, the (111) XRD peak shifts towards lower 2θ value in comparison to that of as deposited Pd thin film. On further increasing the HLD cycles to 40, the (111) peak shifts to its original position. The above results indicate the strained nature of Pd thin films, hydrogenated for 20 HLD cycles. This behaviour is possibly attributed
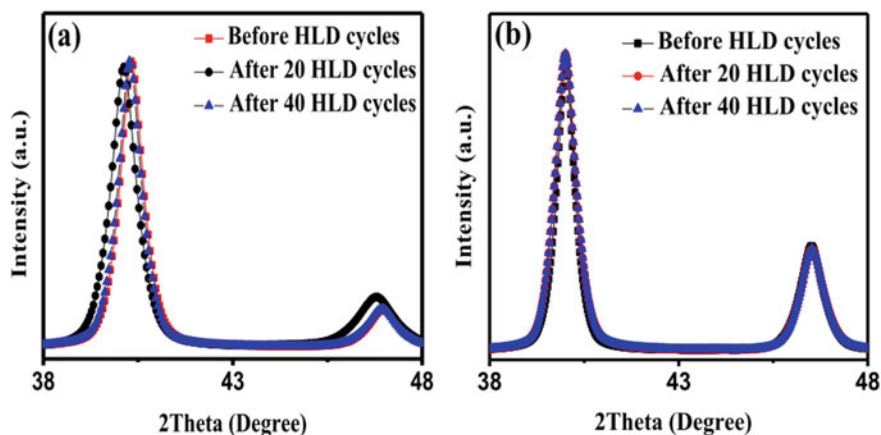
Fig. 7.5 XRD diffractograms of **a** Pd thin films and **b** Pd nanoparticles before and after HLD cycles
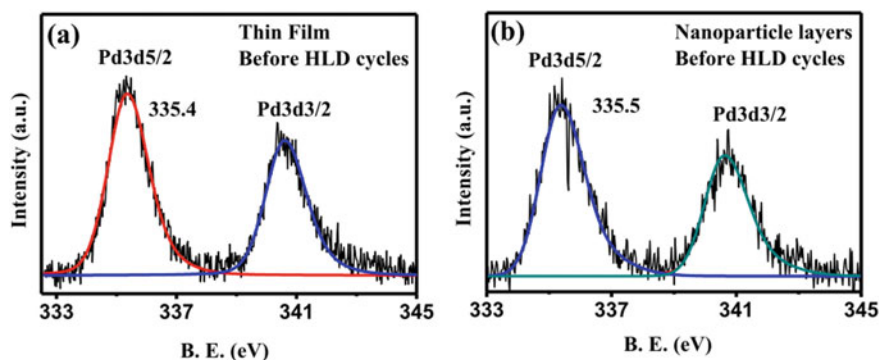
Fig. 7.6 XPS core level binding energy spectra of the as deposited Pd thin film (TF) and nanoparticle layer (NP) samples

by some residual stress build-up and/or irreversibly trapped H upon cycling [5]. It is also clear that after 40 HLD cycles the peak shifts to its original position which indicates that strain has been released. It is interesting to note that in nanoparticle layer, (111) XRD peak remains at its original position even after 40 HLD cycles which implies absence of any accumulated strain. Further, the peak intensity of the nanoparticle layers is nearly same before and after the HLD cycles, which indicates that Pd nanoparticle remains unaffected by HLD cycles.

The XPS analysis of the as deposited and hydrogenated samples (20 and 40 HLD cycles) was also carried out. The XPS core level binding energy spectra of the as deposited Pd nanoparticle layer and thin film samples are presented in Fig. 7.6. In case of Pd thin film, Pd3d5/2 core level binding energy peak occurs at 335.4 eV. These values resemble with the earlier reported bulk values [17–19]. In case of Pd nanoparticle layer, Pd3d5/2 core level peak lies at 335.5 eV. This shows a positive shift of 0.1 eV towards the higher binding energy side. On decreasing the size of Ag, Cu and Sn crystallites in vacuum evaporated thin films, an increase in binding energy has been reported in earlier reports [20–22]. The observed XPS peak shift in Pd nanoparticles can be attributed to the lattice contraction as revealed by the XRD measurements discussed earlier. It is reported that the decrease in the particle size results in the decrease in the lattice parameter, which in turn results in the increase in binding energy [23]. Because of the lattice contraction, the average bond distance is shorter in nanoparticles than in the bulk [24, 25]. The chemical bonding is different at the shorter bond distances, which leads to changes in the core-level binding energies [21]. The XPS Pd3d5/2 peak positions of the hydrogenated Pd film and nanoparticles are shown in Fig. 7.7. In Pd thin film, after 20 HLD cycles, Pd3d5/2 peak position shifts towards lower binding energy by 0.3 eV. On increasing the HLD cycles to 40, it again approaches the binding energy of the as deposited Pd thin film. In case of Pd nanoparticle layer no such behaviour is observed, instead, the Pd3d5/2 peak position remains constant at 335.5 eV. These results can be correlated with the XRD observation of hydrogenated Pd thin film and nanoparticle samples. In Pd thin film

Fig. 7.7 The XPS core-level
Pd3d5/2 peak positions of
the hydrogenated Pd film
(TF) and nanoparticle layer
(NP) sample
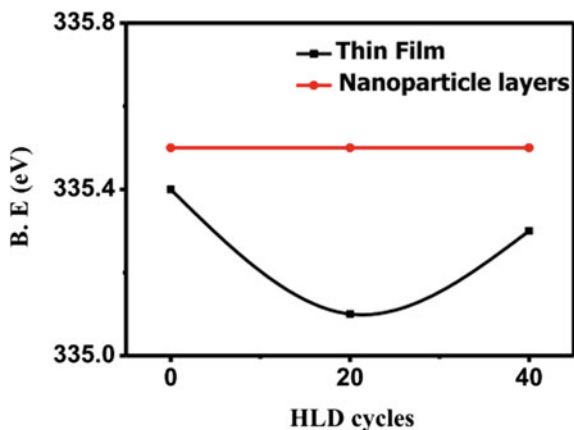
sample, the observed XPS shift in Pd3d5/2, on HLD cycles is consistent with the
lattice variation indicated by (111) XRD peak shift.

The above study suggests that, on hydrogen exposure, due to the substrate-film
interaction, in-plane stress is generated in the film which gets released via crack
formation. In contrast to Pd thin film no residual stress is generated in the Pd nanopar-
ticle sample after HLD cycles. The crack formation in Pd films limits their life time
and performance, and hence they are not suitable for the applications that require
continuous HLD cycles over a long period of time. This shows that Pd nanoparticle
layers can replace the Pd thin films in certain application like sensors, hydrogen
production membranes and storage materials where continuous HLD cycles are
required.

7.4   Conclusions

In contrast to Pd thin film, the nanoparticle layer does not show any crack formation
on being subjected to continuous HLD cycles. XRD along with XPS results suggest
that, in thin films on continuous HLD cycles, residual stress is built up, which, when
released, forms the cracks in the film. The Pd nanoparticle layers may have potential
applications in the field of hydrogen gas sensing, storage and production membranes.

References

1. F.D. Manchester, *Phase Diagrams of Binary Hydrogen Alloys* (ASM International, Materials
   Park, OH, 2000)
2. T.P. Leervad Pedersen, Hydrogen-induced changes of mechanical stress and optical transmis-
   sion in thin Pd films. Thin Solid Films **458**(1–2), 299–303 (2004)

3. A. Pundt, Hydrogen in metals: microstructural aspects. Annu. Rev. Mater. Res. **36**, 555–608 (2006)
4. R. Nowakowski, Atomic force microscopy studies of thin Pd film response to palladium hydride formation and its reaction with oxygen. Langmuir **19**(17), 6750–6758 (2003)
5. R. Gremaud, Hydrogenography of PdHx thin films: influence of H-induced stress relaxation processes. Acta Mater. **57**(4), 1209–1219 (2009)
6. A. Pundt, Adhesion energy between metal films and polymers obtained by studying buckling induced by hydrogen. Acta Mater. **52**(6), 1579–1587 (2006)
7. M.W. Lee, Pressure concentration isotherms of thin films of the palladium-hydrogen system as modified by film thickness, hydrogen cycling, and stress. J. Appl. Phys. **57**(12), 5236 (1985)
8. S. Wagner, Mechanical stress impact on thin $Pd_{1-x}Fe_x$ film thermodynamic properties, Appl. Phys. Lett. **92**, 051914 (2008)
9. S. Sengar, B. Mehta, R. Kumar et al., In-flight gas phase growth of metal/multi layer graphene core shell nanoparticles with controllable sizes. Sci. Rep. **3**, 2814 (2013). https://doi.org/10.1038/srep02814
10. V. Singh, B.R. Mehta, S.K. Sengar, O.M. Karakulina, J. Hadermann, A. Kaushal, Achieving independent control of core diameter and carbon shell thickness in Pd-C core–shell nanoparticles by gas phase synthesis. Nanotechnology **28** (29), 295603 (2017). https://doi.org/10.1088/1361-6528/aa7660
11. V. Singh, B.R. Mehta, S.K. Sengar, P.K. Kulriya, S.A. Khan, S.M. Shivaprasad, Enhanced hydrogenation properties of size selected Pd–C core–shell nanoparticles; effect of carbon shell thickness. J. Phys. Chem. C **119**(25), 14455–14460 (2015). https://doi.org/10.1021/acs.jpcc.5b04205
12. R. Sharma, N. Kodan, V. Singh, S.N. Sharma, O.P. Sinha, Enhanced photoelectrochemical performance of TiO2 photoanode decorated with Pd-carbon core shell Nanoparticles. Renew. Energy **134**, 1232–1239 (2019). ISSN 0960-1481, https://doi.org/10.1016/j.renene.2018.09.061
13. V. Singh, S. Dhall, A. Kaushal, B.R. Mehta, Room temperature response and enhanced hydrogen sensing in size selected Pd-C core-shell nanoparticles: role of carbon shell and Pd-C interface. Int. J. Hydrogen Energy **43**(2), 1025–1033 (2018). ISSN 0360-3199. https://doi.org/10.1016/j.ijhydene.2017.11.143
14. C.Q. Sun, The lattice contraction of nanometre-sized Sn and Bi particles produced by an electrohydrodynamic technique. J. Phys. Condens. Matter **11**(24), 4801 (1999)
15. Z.M. Stadnik, ^{61}Ni Mössbauer study of the hyperfine magnetic field near the Ni surface. Phys. Rev. B **35**(13), 6588–6592 (1987)
16. I. Aruna, B.R. Mehta, L.K. Malhotra, S.M. Shivaprasad, J. Appl. Phys. **104**, 064308 (2008)
17. P. Légaré, XPS investigation of the oxidation of the Al/Pd interface: the Al_2O_3/Pd interface. Surf. Sci. **217**(1–2), 167–168 (1989)
18. J.C. Fuggle, Electronic structure of aluminum and aluminum-noble-metal alloys studied by soft-x-ray and x-ray photoelectron spectroscopies. Phys. Rev. B **16**, 750 (1977)
19. S.K. Sengar, Charge transfer, lattice distortion, and quantum confinement effects in Pd, Cu, and Pd–Cu nanoparticles; size and alloying induced modifications in binding energy, Appl. Phys. Lett. **98**, 193115 (2011)
20. G.K. Wertheim, Noble-and transition-metal clusters: the d bands of silver and palladium. Phys. Rev. B **33**, 5384 (1986)
21. B. Richter, Cluster core-level binding-energy shifts: the role of lattice strain. Phys. Rev. Lett. **93**, 026805 (2004)
22. G.K. Wertheim, Cluster growth and core-electron binding energies in supported metal clusters. Phys. Rev. B **37**, 844 (1988)
23. S.K. Sengar, Size and alloying induced shift in core and valence bands of Pd-Ag and Pd-Cu nanoparticles. J. Appl. Phys. **115**(12), 124301 (2014)
24. S.A. Nepijko, Structural investigation of palladium clusters on γ-AlO3(111)/NiAl(110) with transmission electron microscopy. Langmuir **15**(16), 5309–5313 (1999)

25. M. Klimenkov, The structure of Pt-aggregates on a supported thin aluminum oxide film in comparison with unsupported alumina: a transmission electron microscopy study. Surf. Sci. **391**(1–3), 27–36 (1997)

Chapter 8
Influence of Dense Plasma Environment on the He-α and He-β Transitions of Cl^{15+} Ion

Dishu Dawra, Mayank Dimri, A. K. Singh, Rakesh Kumar Pandey, Alok K. S. Jha, and Man Mohan

Abstract The effect of plasma shielding on the He-α $1s^2\,{}^1S_0 \rightarrow 1s2p\,({}^3P_1^o,\,{}^1P_1^o)$ and He-β $1s^2\,{}^1S_0 \rightarrow 1s3p\,({}^3P_1^o,\,{}^1P_1^o)$ transitions of Cl^{15+} ion embedded in warm-dense plasma environment is investigated. The analytical plasma screening potential of Li et al. [Phys. Plasmas 26, 033,301 (2019)] and uniform electron gas model potential have been incorporated within the multiconfiguration Dirac–Fock method and relativistic configuration interaction technique. It is seen that the excitation energies for the above transitions are red shifted with increasing free electron densities. At lower values of electron temperature, the plasma energy shift becomes more sensitive to the free electron density. The variation in weighted oscillator strengths ratio with plasma densities has also been analyzed. The presently reported results will be of great help in the modelling and diagnostics of laboratory and astrophysical plasmas.

8.1 Introduction

During the past few decades, the investigation of atomic structure properties in warm-dense plasma environment has become an active area of research due to the potential applications in astrophysical systems, laser produced plasmas, plasma spectroscopy, X-ray lasers and inertial confinement fusion [1–4]. In such an environment, the interaction between the bound electrons and atomic nucleus is screened by the neighbouring ions and free electrons. This modified interaction results in continuum lowering and influences the atomic structure and radiative properties of the atoms/ions, while compared with free systems.

The plasma environment can be classified into two types of plasmas namely, strongly and weakly coupled plasma according to the value of the plasma coupling

D. Dawra · M. Dimri (✉) · A. K. Singh · M. Mohan
Department of Physics and Astrophysics, University of Delhi, Delhi 110007, India

M. Dimri · A. K. Singh · M. Mohan
Department of Physics, Deen Dayal Upadhyaya College, University of Delhi, Delhi 110078, India

R. K. Pandey · A. K. S. Jha
Department of Physics, Kirori Mal College, University of Delhi, Delhi 110007, India

strength (Γ), that is defined as the ratio of average electrostatic energy to kinetic energy. The $\Gamma \geq 1$ denotes a strongly coupled plasma case, whereas $\Gamma < 1$ signifies a weakly coupled plasma [5, 6]. In the strongly coupled plasma, the screening of the nuclear Coulomb interaction by the free electrons is depicted by the standard ion sphere model. The ion sphere model relies on the presumption that each ion is enclosed in a spherically symmetric cell enclosing the precise number of electrons to sustain charge neutrality of the system.

Extensive theoretical studies have been performed in the past few years to model the influence of warm-dense plasma environment on the atomic spectroscopic properties of two-electron system by making use of the ion-sphere model. Sil et al. [7, 8] have analyzed the effect of strongly coupled plasma on the electronic structure and radiative properties of He-like ions within the relativistic and non-relativistic framework. The exchange energy shifts between the $1s^2 \rightarrow 1s2p$ ($^3 P_1^o$, $^1 P_1^o$) lines of Al^{11+} ion immersed in dense plasma have been investigated by Li et al. [9] by making use of the self-consistent field method. Rodriguez et al. [10] have used the relativistic detailed configuration accounting method for estimating the influence of plasma shielding in non-hydrogenic ions. Further, atomic structure calculations of two electron ions within the non-relativistic framework in a dense plasma environment have been carried out by Bhattacharya et al. [11] using the Rayleigh–Ritz variation principle in Hylleraas coordinates. Belkhiri et al. [12] have estimated the atomic structure properties of various ions in plasma environment using the Cowan ATomic Structure (CATS) code and Flexible Atomic Code (FAC). Later on, the atomic structure and radiative properties of Al^{11+} and Ar^{16+} ions in warm-dense matter regime have been investigated by Li et al. [13, 14] by making use of the modified general-purpose relativistic atomic structure package (GRASP2K). Chen et al. [15–17] have estimated the influence of hot and dense plasma on the energies and radiative properties of multiply charged ions using both non-relativistic and relativistic methods. Moreover, an analytical formula for the dense plasma screening potential has been developed by Li et al. [18] which was found to be in better agreement with the quantum mechanical self-consistent finite temperature atomic structure calculations. In recent past, Dawra et al. [19] and Dimri et al. [20] have analyzed the plasma shielding effects on the transition energies and radiative properties of He-like Ca^{18+} and Ni^{26+} ions under dense plasma conditions. Thereafter, Singh et al. [21] have studied the plasma screening effects on the atomic structure of He-like ions embedded in strongly coupled plasma.

Although, significant work has been done on He-like ions in dense plasma environment but there is paucity of data for He-like Cl^{15+} ion. Therefore, in the present study, we have presented the excitation energies and transition properties of this ion within the dense plasma environment. For this purpose, the analytical plasma screening (APS) potential of Li et al. [18] and the UEGM potential [2] have been incorporated within the multiconfiguration Dirac–Fock method (MCDF) and the relativistic configuration interaction (RCI) technique, as a modified interaction potential between the nucleus and the electron. Attention has been laid on the He-α $1s^2\ ^1S_0 \rightarrow 1s2p$ ($^3 P_1^o$, $^1 P_1^o$) and He-β $1s^2\ ^1S_0 \rightarrow 1s3p$ ($^3 P_1^o$, $^1 P_1^o$) transitions as these transitions are beneficial for plasma diagnostics.

This paper is structured as follows: In Sect. 2, we have briefly summarized the theoretical models employed in our atomic structure calculations. In Sect. 3 we have presented the discussion of our results. Section 4 deals with the implications of the present work.

8.2   Theoretical Methods

A brief description of the theoretical methods adopted has been presented in this section to depict the influence of plasma shielding using the ion sphere model. The ion sphere model relies on the presumption that the ion is described by a point-like nucleus embedded at the centre of a spherical cavity comprising sufficient electrons to ensure the overall neutrality.

8.2.1   The UEGM and Analytical Plasma Screening (APS) Potentials

The effect of plasma screening on the atomic structure properties has been modeled by using the UEGM potential [2], given by

$$V_{IS}(r, R_0) = -\frac{Z}{r} + \frac{Z - N_b}{2R_0}\left[3 - \left(\frac{r}{R_0}\right)^2\right], \tag{8.1}$$

with

$$R_0 = \left[3N_f/4\pi n_e\right]^{1/3}; N_f = Z - N_b \tag{8.2}$$

where r, N_b, N_f, R_0 and n_e are the radial coordinate of the electron, number of bound electrons, the number of free electrons within the ion sphere, radius of the ion sphere and free electron density.

On the contrary, the analytical plasma screening (APS) potential of Li et al. [18] is given by

$$V^{APS} = -\frac{Z}{r}$$

$$+ \frac{N_f}{R_0} \left[1 + \frac{1}{\left(3 - \frac{b}{\pi}\sqrt{\frac{N_f}{R_0\,T_e}}\right) - 1} - \frac{1}{\left(3 - \frac{b}{\pi}\sqrt{\frac{N_f}{R_0\,T_e}}\right) - 1} \left(\frac{r}{R_0}\right)^{\left(3 - \frac{b}{\pi}\sqrt{\frac{N_f}{R_0\,T_e}}\right) - 1} \right]$$

(8.3)

where b is nearly 2 for the Maxwell–Boltzmann distribution and T_e is the electron temperature.

8.2.2 The UEGM and APS Potentials Incorporated in the MCDF and RCI Methods

In our present study, the fully relativistic MCDF method, revised by Norrington [22] and formerly developed by Grant et al. [23] has been utilized. This method has also been successfully adopted in our previous works [19–21, 24–26]. For considering the influence of warm-dense plasma environment on the spectral properties, the Dirac-Coulomb Hamiltonian containing all the dominant interactions can be written as

$$\hat{H}^{DC} = \sum_{i=1}^{N} \hat{H}_i + \sum_{i=1}^{N-1} \sum_{j=i+1}^{N} \frac{1}{|\hat{r}_i - \hat{r}_j|}$$

(8.4)

where $\hat{H}_i$ is the one-electron Hamiltonian, and is written as

$$\hat{H}_i = c\alpha_i \cdot p_i + \beta mc^2 + V_{IS}(r, R_0).$$

(8.5)

where the first two terms denote the kinetic energy of a bound electron and the final term $V_{IS}(r, R_0)$ represents the modified potential faced by the bound electron present within the ion sphere.

For N-electron system, an atomic state function (ASF) is written as summation of n electronic configuration state functions (CSFs)

$$|\psi_\alpha(\text{PJM})\rangle = \sum_{i=1}^{n} C_i(\alpha)|\gamma_i\,(\text{PJM})\rangle.$$

(8.6)

where the CSFs γ_i(PJM) indicate a particular state having PJM be the parity, total angular momentum and magnetic quantum number, respectively. The expansion mixing coefficients $C_i(\alpha)$ satisfy the relation

$$\left(C_i(\alpha)\right)^{\dagger} C_j(\alpha) = \delta_{ij} \tag{8.7}$$

so that ASFs follow the orthonormality condition, α symbolizes the coupling, orbital occupation numbers, etc. The CSFs are the sum of products of four-component spin-orbitals which are written in the following form

$$\phi_{nkm} = \frac{1}{r} \begin{pmatrix} P_{nk}(r) & \chi_{km}(\Theta, \phi, \sigma) \\ -i\, Q_{nk}(r) & \chi_{-km}(\Theta, \phi, \sigma) \end{pmatrix} \tag{8.8}$$

where n represents the principal quantum number, k denotes the Dirac angular quantum number, $P_{nk}(r)$ and $Q_{nk}(r)$ are large and small components of one-electron radial functions and $\chi_{km}(\Theta, \phi)$ is the spinor spherical harmonic function.

On the contrary, RCI uses a fully relativistic configuration interaction technique in which a self-consistent Dirac–Fock-Slater iteration is carried out on some selected fictitious mean configurations for deriving the local central potential [27]. The relativistic Hamiltonian for the N-electron atom or ion immersed in warm-dense matter regime can be written as

$$\hat{H} = \sum_{i=1}^{N} \hat{H}_D(i) + \sum_{i<j}^{N} \frac{1}{r_{ij}}, \tag{8.9}$$

where the single-electron Dirac-Hamiltonian $\hat{H}_D(i)$ is defined as

$$\hat{H}_D(i) = c\boldsymbol{\alpha} \cdot \boldsymbol{p} + (\boldsymbol{\beta} - 1)c^2 + V_{IS}(r, R_0) \tag{8.10}$$

The ASFs are written as the linear combination of the basis states, ϕ_v, with same symmetries

$$\Psi = \sum_{v} b_v \phi_v \tag{8.11}$$

where diagnolization of the total Hamiltonian yields the mixing coefficients b_v.

The UEGM and APS ion sphere potentials are incorporated within the MCDF and RCI methods and the radial components of the wavefunction satisfy the normalization condition given by

$$\int\limits_{0}^{\infty} \left[P_{nk}^2(r) + Q_{nk}^2(r) \right] dr = 1. \tag{8.12}$$

For higher values of plasma densities, the bound electron wavefunctions may not be equal to 0 outside the ion sphere.

8.3 Results and Discussion

In the present study, the two kinds of ion sphere potentials have been incorporated in to the fully relativistic MCDF method to study the effect of warm-dense plasma environment. The option of 'extended average level' has been utilized for optimizing the orbitals, in which the minimization of the weighted trace of the Hamiltonian matrix takes place. An atomic model of 18 configurations, namely, $1s^2$, $1s2l$ ($l=0$–1), $1s3l$ ($l=0$–2), $1s4l$ ($l=0$–2), $2s^2$, $2s2p$, $2p^2$, $2s3l$ ($l=0$–2) and $2s4l$ ($l=0$–2) has been used generating 57 energy levels. For comparison purposes, parallel calculations have been carried out using the modified RCI by including the above mentioned configuration set as in MCDF. The relativistic contributions from the quantum electrodynamics (QED) and Breit interaction (BI) corrections are considered.

In Table 8.1, we have shown the variation of electron binding energy as a function of plasma density for He-like Cl^{15+} ion at kT $= 600$ eV. The relative variation of electron binding energies for He-like Cl^{15+} ion at different free electron densities within the range $2.0 \times 10^{23} - 1.0 \times 10^{24}$ cm^{-3} has been plotted in Fig. 8.1 using the MCDF and RCI approaches at kT $= 600$ eV. It can be seen that the binding energies are decreasing monotonically with increase in plasma densities. The reason behind this trend is that the strength of the plasma shielding effect on the nucleus by the free electrons increases with increasing free electron density. Moreover, the two theoretical methods are found to be in better agreement with each other.

The transition energies of the lowest 27 fine structure levels of He-like Cl^{15+} ion are tabulated in Table 8.2 using the MCDF method at kT $= 600$ eV and $n_e = 2.0 \times$

Table 8.1 Variation of electron binding energy as a function of plasma density for He-like Cl^{15+} ion at kT $= 600$ eV

n_e	MCDF	RCI	Relative difference (%)	
			MCDF	RCI
0	558.7295	7603.3326		
2.0×10^{23}	539.7254	7344.7752	-3.40131	-3.40058
4.0×10^{23}	534.6472	7275.6866	-4.31019	-4.30924
6.0×10^{23}	531.0591	7226.8754	-4.95238	-4.95121
8.0×10^{23}	528.1884	7187.8251	-5.46617	-5.46481
1.0×10^{24}	525.7548	7154.7228	-5.90173	-5.90017
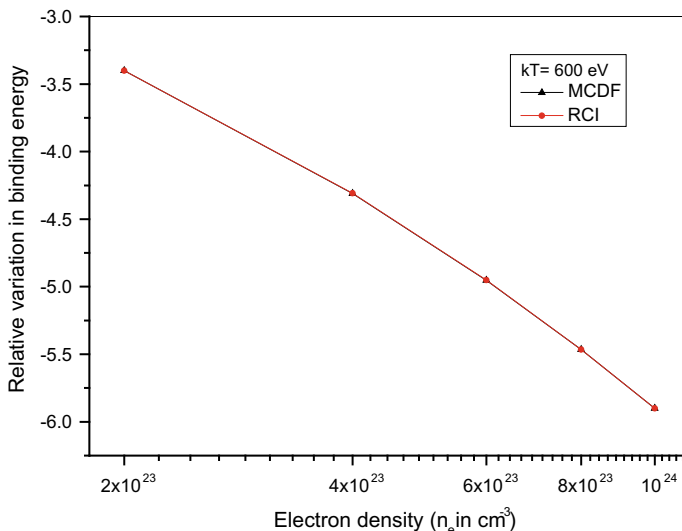
Fig. 8.1 Relative variation in binding energies of Cl^{15+} ion with respect to the free electron densities by the APS potential [18]

10^{23} to 1.0×10^{24} cm^{-3}, respectively. The values for the plasma free case are also given. Moreover, the transition energies for the He-α $1s^2\,^1S_0 \rightarrow 1s2p$ ($^3P_1^o$, $^1P_1^o$) and He-β $1s^2\,^1S_0 \rightarrow 1s3p$ ($^3P_1^o$, $^1P_1^o$) transitions of He-like Cl^{15+} ion are given in Table 8.3 using the MCDF and RCI methods at various plasma densities n_e (cm^{-3}) and electron temperatures kT (eV). It is evident that the reported results for the unscreened He-like Cl^{15+} ion for the He-α $1s^2\,^1S_0 \rightarrow 1s2p$ ($^3P_1^o$, $^1P_1^o$) and He-β $1s^2\,^1S_0 \rightarrow 1s3p$ ($^3P_1^o$, $^1P_1^o$) transitions are in excellent agreement with the National Institute of Standards and Technology (NIST) [28] recommended values of 203.9592, 205.0413, 240.1611 and 240.4585 Ryd, respectively. It is evident that our results from MCDF calculations match well with the RCI ones ensuring the reliability and integrity of our results. One can see that when the effect of hot and dense plasma is considered, the transition energies are found to be red shifted with increasing plasma densities for both the transitions.

In Fig. 8.2, we have displayed the variation of our MCDF and RCI plasma energy shifts for He-α and He-β transitions of Cl^{15+} ion at various kT and n_e values. It has been observed that for a fixed value of kT, the shifts of the transition energies are found to increase with the increasing plasma densities. For instance, our MCDF (RCI) plasma energy shifts for He-β $1s^2\,^1S_0 \rightarrow 1s3p\,^1P_1^o$ transition are nearly 1.96 eV (1.95 eV) and 9.88 eV (9.85 eV) for electron densities 2.0×10^{23} and 1.0×10^{24} cm^{-3} at electron temperature kT = 600 eV, respectively. The plasma energy shifts reported by MCDF method are in excellent agreement with the RCI ones. Also, the plasma energy shifts are decreasing with the increase in kT. For instance, when $n_e = 1.0 \times 10^{24}$ cm^{-3}, the plasma energy shifts for $1s^2\,^1S_0 \rightarrow 1s3p\,^1P_1^o$ transition reported from the MCDF method are nearly 9.88 and 8.78 eV at kT = 600 and 1000 eV, respectively. Such

Table 8.2 Excitation energies (in Ryd) for the lowest 27 levels of Cl^{15+} ion at various plasma densities n_e (cm^{-3}) and electron temperature $kT = 600$ eV using the MCDF method

Key	Level	NIST	n_e					
			0	2.0×10^{23}	4.0×10^{23}	6.0×10^{23}	8.0×10^{23}	1.0×10^{24}
1	$1s^2\,^1S_0$	0.0000	0.0000	0.0000	0.0000	0.0000	0.0000	0.0000
2	$1s2s\,^3S_1$	202.6310	202.4521	202.4177	202.3816	202.3452	202.3086	202.2720
3	$1s2p\,^3P^o_0$	202.9217	203.7332	203.7077	203.6809	203.6537	203.6263	203.5987
4	$1s2p\,^3P^o_1$	203.9592	203.7703	203.7448	203.7179	203.6907	203.6632	203.6356
5	$1s2s\,^1S_0$	204.0000	203.9796	203.9449	203.9087	203.8722	203.8356	203.7992
6	$1s2p\,^3P^o_2$	204.1160	203.9250	203.8993	203.8722	203.8448	203.8171	203.7893
7	$1s2p\,^1P^o_1$	205.0413	204.9090	204.8829	204.8555	204.8277	204.7997	204.7717
8	$1s3s\,^3S_1$	239.7941	239.5859	239.4288	239.2701	239.1116	238.9533	238.7951
9	$1s3p\,^3P^o_0$	240.1497	239.9454	239.8044	239.6616	239.5188	239.3760	239.2331
10	$1s3p\,^3P^o_1$	240.1611	239.9566	239.8155	239.6726	239.5297	239.3868	239.2437
11	$1s3s\,^1S_0$	240.1649	239.9939	239.8334	239.6714	239.5097	239.3483	239.1870
12	$1s3p\,^3P^o_2$	240.2075	240.0025	239.8609	239.7176	239.5742	239.4308	239.2873
13	$1s3d\,^3D_1$	240.4047	240.1965	240.0929	239.9870	239.8807	239.7740	239.6671
14	$1s3d\,^3D_2$	240.4049	240.1967	240.0931	239.9872	239.8808	239.7742	239.6672
15	$1s3d\,^3D_3$	240.4233	240.2148	240.1111	240.0050	239.8985	239.7917	239.6846
16	$1s3d\,^1D_2$	240.4335	240.2256	240.1217	240.0156	239.9090	239.8020	239.6948
17	$1s3p\,^1P^o_1$	240.4585	240.2773	240.1336	239.9880	239.8425	239.6970	239.5515
18	$1s4s\,^3S_1$	252.6110	252.4067	251.9595	251.5088	251.0495	250.5763	250.0831
19	$1s4p\,^3P^o_0$	252.7610	252.5552	252.1315	251.7033	251.2660	250.8142	250.3412
20	$1s4p\,^3P^o_1$	252.7650	252.5600	252.1360	251.7075	251.2700	250.8178	250.3445
21	$1s4s\,^1S_0$	252.7700	252.5805	252.1252	251.6659	251.1974	250.7135	250.2079
22	$1s4p\,^3P^o_2$	252.8000	252.5792	252.1543	251.7247	251.2861	250.8327	250.3578
23	$1s4d\,^3D_1$	252.8680	252.6584	252.2920	251.9199	251.5391	251.1447	250.7300
24	$1s4d\,^3D_2$	252.8680	252.6588	252.2924	251.9202	251.5394	251.1450	250.7302
25	$1s4d\,^1D_2$	252.8800	252.6721	252.3050	251.9321	251.5506	251.1553	250.7396
26	$1s4p\,^1P^o_1$	252.8910	252.6978	252.2673	251.8320	251.3870	250.9263	250.4428
27	$1s4d\,^3D_3$	252.9000	252.6662	252.2993	251.9268	251.5456	251.1508	250.7354

shifts can be estimated in hot and dense plasma experiments, given that the observed spectral lines are very narrow, and Stark shifts and self-absorption do not deform the line profiles over recognition. From Figure, it has been observed that the shifts by the UEGM potential are increasing with increase in plasma densities.

Table 8.3 Transition energies (in Ryd) for the He-α $1s^2\,{}^1S_0 \rightarrow 1s2p$ $({}^3P_1^o,\,{}^1P_1^o)$ and He-β $1s^2\,{}^1S_0 \rightarrow 1s3p$ $({}^3P_1^o,\,{}^1P_1^o)$ transitions of Cl^{15+} ion at various plasma densities n_e (cm^{-3}) and electron temperatures kT (eV)

kT	Transition	n_e					
		0	2.0×10^{23}	4.0×10^{23}	6.0×10^{23}	8.0×10^{23}	1.0×10^{24}
MCDF 600	$1s^2\,{}^1S_0 \rightarrow 1s2p$ ${}^3P_1^o$	203.7703	203.7448	203.7179	203.6907	203.6632	203.6356
	$1s^2\,{}^1S_0 \rightarrow 1s2p$ ${}^1P_1^o$	204.9090	204.8829	204.8555	204.8277	204.7997	204.7717
	$1s^2\,{}^1S_0 \rightarrow 1s3p$ ${}^3P_1^o$	239.9566	239.8155	239.6726	239.5297	239.3868	239.2437
	$1s^2\,{}^1S_0 \rightarrow 1s3p$ ${}^1P_1^o$	240.2773	240.1336	239.9880	239.8425	239.6970	239.5515
MCDF 650	$1s^2\,{}^1S_0 \rightarrow 1s2p$ ${}^3P_1^o$		203.7454	203.7194	203.6929	203.6663	203.6395
	$1s^2\,{}^1S_0 \rightarrow 1s2p$ ${}^1P_1^o$		204.8836	204.8570	204.8300	204.8029	204.7757
	$1s^2\,{}^1S_0 \rightarrow 1s3p$ ${}^3P_1^o$		239.8184	239.6784	239.5384	239.3984	239.2582
	$1s^2\,{}^1S_0 \rightarrow 1s3p$ ${}^1P_1^o$		240.1365	239.9939	239.8513	239.7088	239.5662
MCDF 1000	$1s^2\,{}^1S_0 \rightarrow 1s2p$ ${}^3P_1^o$		203.7485	203.7257	203.7028	203.6796	203.6564
	$1s^2\,{}^1S_0 \rightarrow 1s2p$ ${}^1P_1^o$		204.8867	204.8635	204.8401	204.8166	204.7931
	$1s^2\,{}^1S_0 \rightarrow 1s3p$ ${}^3P_1^o$		239.8311	239.7043	239.5772	239.4501	239.3227
	$1s^2\,{}^1S_0 \rightarrow 1s3p$ ${}^1P_1^o$		240.1494	240.0201	239.8907	239.7612	239.6315
MCDF UEGM	$1s^2\,{}^1S_0 \rightarrow 1s2p$ ${}^3P_1^o$		203.7575	203.7446	203.7316	203.7187	203.7057
	$1s^2\,{}^1S_0 \rightarrow 1s2p$ ${}^1P_1^o$		204.8959	204.8828	204.8697	204.8567	204.8437
	$1s^2\,{}^1S_0 \rightarrow 1s3p$ ${}^3P_1^o$		239.8721	239.7870	239.7013	239.6151	239.5282
	$1s^2\,{}^1S_0 \rightarrow 1s3p$ ${}^1P_1^o$		240.1910	240.1041	240.0167	239.9287	239.8401
RCI 600	$1s^2\,{}^1S_0 \rightarrow 1s2p$ ${}^3P_1^o$	203.8547	203.8295	203.8034	203.7765	203.7495	203.7222
	$1s^2\,{}^1S_0 \rightarrow 1s2p$ ${}^1P_1^o$	204.9624	204.9362	204.9089	204.8810	204.8529	204.8247

(continued)

Table 8.3 (continued)

kT	Transition	n_e					
		0	2.0×10^{23}	4.0×10^{23}	6.0×10^{23}	8.0×10^{23}	1.0×10^{24}
	$1s^2\,{}^1S_0 \to 1s3p\,{}^3P^o_1$	240.0372	239.8966	239.7546	239.6123	239.4699	239.3276
	$1s^2\,{}^1S_0 \to 1s3p\,{}^1P^o_1$	240.3426	240.1992	240.0544	239.9091	239.7639	239.6187
RCI 650	$1s^2\,{}^1S_0 \to 1s2p\,{}^3P^o_1$		203.8302	203.8049	203.7788	203.7525	203.7261
	$1s^2\,{}^1S_0 \to 1s2p\,{}^1P^o_1$		204.9369	204.9104	204.8834	204.8561	204.8287
	$1s^2\,{}^1S_0 \to 1s3p\,{}^3P^o_1$		239.8995	239.7604	239.6210	239.4815	239.3420
	$1s^2\,{}^1S_0 \to 1s3p\,{}^1P^o_1$		240.2021	240.0602	239.9180	239.7757	239.6334
RCI 1000	$1s^2\,{}^1S_0 \to 1s2p\,{}^3P^o_1$		203.8332	203.8112	203.7886	203.7658	203.7430
	$1s^2\,{}^1S_0 \to 1s2p\,{}^1P^o_1$		204.9400	204.9170	204.8935	204.8698	204.8461
	$1s^2\,{}^1S_0 \to 1s3p\,{}^3P^o_1$		239.9121	239.7862	239.6597	239.5331	239.4063
	$1s^2\,{}^1S_0 \to 1s3p\,{}^1P^o_1$		240.2150	240.0864	239.9573	239.8280	239.6986
RCI UEGM	$1s^2\,{}^1S_0 \to 1s2p\,{}^3P^o_1$		203.8421	203.8299	203.8173	203.8046	203.7919
	$1s^2\,{}^1S_0 \to 1s2p\,{}^1P^o_1$		204.9492	204.9363	204.9231	204.9099	204.8967
	$1s^2\,{}^1S_0 \to 1s3p\,{}^3P^o_1$		239.9530	239.8687	239.7835	239.6977	239.6113
	$1s^2\,{}^1S_0 \to 1s3p\,{}^1P^o_1$		240.2565	240.1702	240.0830	239.9952	239.9068

The results of the UEGM are also given

In Tables 8.4, 8.5, 8.6, 8.7, we have reported the transition wavelengths (λ_{ij} in Å), radiative rates (A_{ji} in s^{-1}), oscillator strengths (f_{ij} dimensionless) and line strengths (S in atomic units) at $n_e = 0$ and 2.0×10^{23}, and kT = 600, 650 and 1000 eV from the present MCDF calculations for E1 transitions in He-like Cl^{15+} ion. The results from the UEGM model are given in Table 8.8. The last column gives R, the ratio of velocity and length forms of A-values. The ratio of oscillator strength for resonance-to-intercombination transitions has been plotted in Fig. 8.3 at various kT and n_e values using the MCDF method. The ratio of oscillator strength for these transitions plays a crucial role in characterizing the hot and dense plasmas. For the above calculations, we have chosen two spectral lines $1s^2\,{}^1S_0 \to 1s3p\,{}^1P^o_1$ and $1s^2\,{}^1S_0$
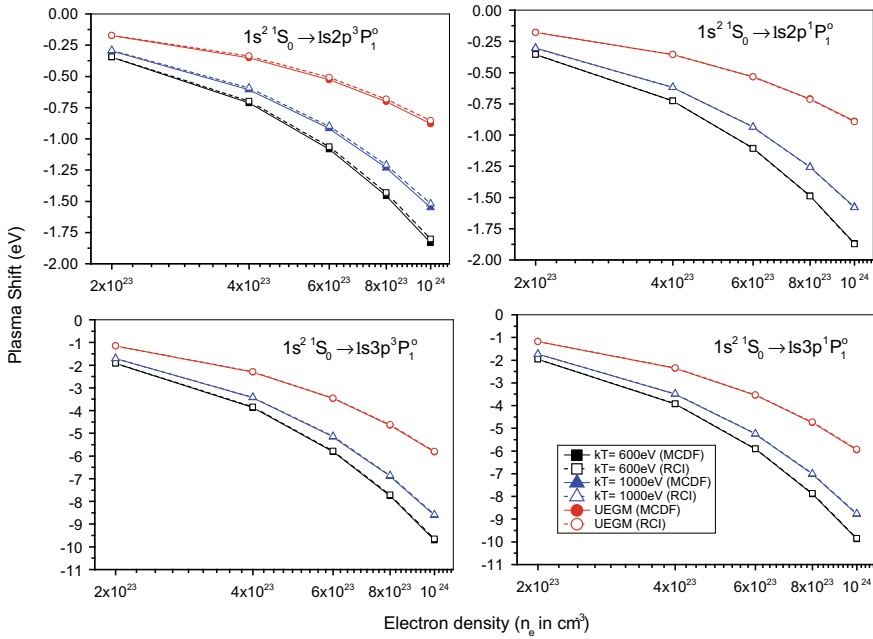
Fig. 8.2 Plasma energy shift for on the He-α $1s^2\,{}^1S_0 \rightarrow 1s2p$ ($^3P_1^o$, $^1P_1^o$) and He-β $1s^2\,{}^1S_0 \rightarrow 1s3p$ ($^3P_1^o$, $^1P_1^o$) transitions of He-like Cl^{15+} ion with respect to the electron density by the APS [18] and UEGM [2] potential

$\rightarrow 1s3p\,{}^3P_1^o$. For a given kT, one can see that the ratio of oscillator strength increases with increasing plasma density. For instance, the influence of plasma on the ratio of oscillator strength is nearly 0.27% and 1.65% for electron densities 2.0×10^{23} and 1.0×10^{24} cm^{-3} at electron temperature kT $= 600$ eV, respectively. At present, these effects are very small to be detected in the experiment, yet further advancements in the detecting equipment will make it possible in the near future.

Table 8.4 Transition wavelengths (λ_{ij} in Å), radiative rates (A_{ji} in s^{-1}), oscillator strengths (f_{ij} dimensionless), and line strengths (S in atomic units) for unscreened case from the present MCDF calculations for E1 transitions in He-like Cl^{15+} ion

i	j	λ_{ij}	A_{ji}	f_{ij}	S	R
1	4	4.47E+00	9.83E+11	8.84E−03	1.30E−04	1.00E+00
1	7	4.45E+00	8.88E+13	7.90E−01	1.16E−02	1.00E+00
1	10	3.80E+00	3.13E+11	2.03E−03	2.54E−05	9.60E−01
1	17	3.79E+00	2.63E+13	1.70E−01	2.13E−03	9.60E−01
1	20	3.61E+00	1.39E+11	8.14E−04	9.67E−06	9.10E−01
1	27	3.61E+00	1.23E+13	7.21E−02	8.57E−04	9.00E−01
2	3	7.11E+02	1.88E+08	4.76E−03	3.34E−02	7.40E−01
2	4	6.91E+02	2.03E+08	1.46E−02	9.94E−02	7.70E−01
2	5	6.19E+02	2.88E+08	2.75E−02	1.68E−01	8.10E−01
2	7	3.71E+02	1.47E+07	3.03E−04	1.11E−03	8.60E−01
2	9	2.43E+01	1.52E+12	4.49E−02	1.08E−02	9.80E−01
2	10	2.43E+01	1.50E+12	1.33E−01	3.19E−02	9.80E−01
2	12	2.43E+01	1.50E+12	2.21E−01	5.30E−02	9.80E−01
2	17	2.41E+01	1.68E+10	1.46E−03	3.47E−04	9.80E−01
2	19	1.82E+01	7.49E+11	1.24E−02	2.22E−03	8.80E−01
2	20	1.82E+01	7.39E+11	3.66E−02	6.58E−03	8.80E−01
2	22	1.82E+01	7.43E+11	6.13E−02	1.10E−02	8.80E−01
2	27	1.81E+01	8.21E+09	4.05E−04	7.25E−05	8.70E−01
3	8	2.54E+01	6.15E+10	1.79E−02	1.49E−03	8.80E−01
3	13	2.50E+01	2.44E+12	6.84E−01	5.63E−02	1.00E+00
3	18	1.87E+01	3.32E+10	5.23E−03	3.22E−04	6.40E−01
3	23	1.86E+01	8.30E+11	1.30E−01	7.94E−03	9.70E−01
4	6	4.35E+03	2.60E+04	2.46E−05	1.06E−03	1.40E+01
4	8	2.54E+01	1.80E+11	1.75E−02	4.40E−03	8.80E−01
4	11	2.52E+01	5.44E+09	1.72E−04	4.27E−05	7.10E−01
4	13	2.50E+01	1.81E+12	1.69E−01	4.19E−02	1.00E+00
4	14	2.50E+01	2.88E+12	4.50E−01	1.11E−01	1.00E+00
4	16	2.50E+01	4.16E+11	6.49E−02	1.60E−02	1.00E+00
4	18	1.87E+01	9.66E+10	5.08E−03	9.41E−04	6.50E−01
4	21	1.87E+01	4.10E+09	7.14E−05	1.32E−05	3.70E−01
4	23	1.86E+01	6.15E+11	3.20E−02	5.89E−03	9.70E−01
4	24	1.86E+01	1.02E+12	8.84E−02	1.63E−02	9.70E−01
4	26	1.86E+01	1.04E+11	9.05E−03	1.67E−03	9.80E−01
5	8	2.56E+01	3.10E+11	1.82E−02	7.66E−03	8.90E−01

(continued)

Table 8.4 (continued)

i	j	λ_{ij}	A_{ji}	f_{ij}	S	R
5	13	2.51E+01	1.21E+11	6.86E−03	2.84E−03	1.00E+00
5	14	2.51E+01	8.55E+11	8.09E−02	3.35E−02	1.00E+00
5	15	2.51E+01	4.36E+12	5.77E−01	2.38E−01	1.00E+00
5	16	2.51E+01	2.35E+11	2.22E−02	9.16E−03	1.00E+00
5	18	1.88E+01	1.64E+11	5.21E−03	1.61E−03	6.60E−01
5	23	1.87E+01	4.09E+10	1.29E−03	3.96E−04	9.70E−01
5	24	1.87E+01	3.05E+11	1.60E−02	4.92E−03	9.70E−01
5	25	1.87E+01	1.48E+12	1.09E−01	3.34E−02	9.70E−01
5	26	1.87E+01	6.46E+10	3.38E−03	1.04E−03	9.70E−01

The last column gives R, the ratio of velocity and length forms of A-values

Table 8.5 Transition wavelengths (λ_{ij} in Å), radiative rates (A_{ji} in s^{-1}), oscillator strengths (f_{ij} dimensionless) and line strengths (S in atomic units) at $n_e = 2.0 \times 10^{23}$ and kT = 600 eV from the present MCDF calculations for E1 transitions in He-like Cl^{15+} ion

i	j	λ_{ij}	A_{ji}	f_{ij}	S	R
1	4	4.47E+00	9.82E+11	8.83E−03	1.30E−04	1.00E+00
1	7	4.45E+00	8.88E+13	7.90E−01	1.16E−02	1.00E+00
1	10	3.80E+00	3.10E+11	2.01E−03	2.52E−05	9.60E−01
1	17	3.79E+00	2.61E+13	1.69E−01	2.11E−03	9.60E−01
1	21	3.61E+00	1.32E+11	7.76E−04	9.23E−06	9.10E−01
1	23	3.61E+00	1.18E+13	6.92E−02	8.23E−04	9.00E−01
2	3	7.06E+02	1.92E+08	4.80E−03	3.35E−02	7.40E−01
2	4	6.87E+02	2.07E+08	1.47E−02	9.95E−02	7.70E−01
2	5	6.15E+02	2.93E+08	2.77E−02	1.68E−01	8.10E−01
2	7	3.70E+02	1.48E+07	3.04E−04	1.11E−03	8.60E−01
2	9	2.44E+01	1.51E+12	4.47E−02	1.08E−02	9.80E−01
2	10	2.44E+01	1.48E+12	1.32E−01	3.18E−02	9.80E−01
2	12	2.43E+01	1.49E+12	2.20E−01	5.29E−02	9.70E−01
2	17	2.42E+01	1.65E+10	1.45E−03	3.45E−04	9.70E−01
2	20	1.83E+01	7.15E+11	1.20E−02	2.17E−03	8.80E−01
2	21	1.83E+01	7.05E+11	3.55E−02	6.43E−03	8.80E−01
2	22	1.83E+01	7.09E+11	5.94E−02	1.08E−02	8.70E−01
2	23	1.83E+01	7.77E+09	3.89E−04	7.03E−05	8.70E−01
3	8	2.55E+01	6.09E+10	1.78E−02	1.50E−03	8.80E−01
3	13	2.50E+01	2.41E+12	6.81E−01	5.62E−02	1.00E+00
3	18	1.89E+01	3.18E+10	5.10E−03	3.17E−04	6.30E−01

(continued)

Table 8.5 (continued)

i	j	λ_{ij}	A_{ji}	f_{ij}	S	R
3	24	1.88E+01	7.97E+11	1.26E−01	7.79E−03	9.70E−01
4	6	4.55E+03	2.27E+04	2.36E−05	1.06E−03	1.50E+01
4	8	2.55E+01	1.79E+11	1.75E−02	4.41E−03	8.80E−01
4	11	2.53E+01	5.39E+09	1.72E−04	4.29E−05	7.00E−01
4	13	2.51E+01	1.79E+12	1.69E−01	4.18E−02	1.00E+00
4	14	2.51E+01	2.86E+12	4.48E−01	1.11E−01	1.00E+00
4	16	2.51E+01	4.13E+11	6.47E−02	1.60E−02	1.00E+00
4	18	1.89E+01	9.28E+10	4.97E−03	9.28E−04	6.40E−01
4	19	1.88E+01	3.96E+09	7.02E−05	1.31E−05	3.60E−01
4	24	1.88E+01	5.90E+11	3.12E−02	5.78E−03	9.70E−01
4	25	1.88E+01	9.77E+11	8.60E−02	1.59E−02	9.60E−01
4	27	1.88E+01	1.01E+11	8.85E−03	1.64E−03	9.80E−01
5	8	2.56E+01	3.07E+11	1.82E−02	7.67E−03	8.90E−01
5	13	2.52E+01	1.20E+11	6.84E−03	2.83E−03	1.00E+00
5	14	2.52E+01	8.48E+11	8.05E−02	3.34E−02	1.00E+00
5	15	2.52E+01	4.32E+12	5.74E−01	2.38E−01	1.00E+00
5	16	2.52E+01	2.33E+11	2.21E−02	9.15E−03	1.00E+00
5	18	1.90E+01	1.57E+11	5.09E−03	1.59E−03	6.50E−01
5	24	1.88E+ 01	3.93E+10	1.25E−03	3.89E−04	9.70E−01
5	25	1.88E+01	2.92E+11	1.55E−02	4.82E−03	9.70E−01
5	26	1.88E+01	1.42E+12	1.06E−01	3.27E−02	9.70E−01
5	27	1.88E+01	6.22E+10	3.30E−03	1.02E−03	9.70E−01

The last column gives R, the ratio of velocity and length forms of A-values

Table 8.6 Transition wavelengths (λ_{ij} in Å), radiative rates (A_{ji} in s^{-1}), oscillator strengths (f_{ij} dimensionless) and line strengths (S in atomic units) at $n_e = 2.0 \times 10^{23}$ and $kT = 650$ eV from the present MCDF calculations for E1 transitions in He-like Cl^{15+} ion

i	j	λ_{ij}	A_{ji}	f_{ij}	S	R
1	4	4.47E+00	9.82E+11	8.83E−03	1.30E−04	1.00E+00
1	7	4.45E+00	8.88E+13	7.90E−01	1.16E−02	1.00E+00
1	10	3.80E+00	3.10E+11	2.02E−03	2.52E−05	9.60E−01
1	17	3.79E+00	2.61E+13	1.69E−01	2.11E−03	9.60E−01
1	21	3.61E+00	1.32E+11	7.76E−04	9.24E−06	9.10E−01
1	23	3.61E+00	1.18E+13	6.92E−02	8.23E−04	9.00E−01
2	3	7.07E+02	1.92E+08	4.79E−03	3.35E−02	7.40E−01
2	4	6.87E+02	2.07E+08	1.47E−02	9.95E−02	7.70E−01
2	5	6.15E+02	2.93E+08	2.77E−02	1.68E−01	8.10E−01

(continued)

Table 8.6 (continued)

i	j	λ_{ij}	A_{ji}	f_{ij}	S	R
2	7	3.70E+02	1.48E+07	3.04E−04	1.11E−03	8.60E−01
2	9	2.44E+01	1.51E+12	4.47E−02	1.08E−02	9.80E−01
2	10	2.44E+01	1.48E+12	1.32E−01	3.18E−02	9.80E−01
2	12	2.43E+01	1.49E+12	2.20E−01	5.29E−02	9.70E−01
2	17	2.42E+01	1.65E+10	1.45E−03	3.45E−04	9.70E−01
2	20	1.83E+01	7.15E+11	1.20E−02	2.17E−03	8.80E−01
2	21	1.83E+01	7.06E+11	3.55E−02	6.43E−03	8.80E−01
2	22	1.83E+01	7.09E+11	5.95E−02	1.08E−02	8.70E−01
2	23	1.83E+01	7.77E+09	3.89E−04	7.03E−05	8.70E−01
3	8	2.55E+01	6.09E+10	1.78E−02	1.50E−03	8.80E−01
3	13	2.50E+01	2.41E+12	6.81E−01	5.62E−02	1.00E+00
3	18	1.89E+01	3.18E+10	5.10E−03	3.17E−04	6.30E−01
3	24	1.88E+01	7.97E+11	1.26E−01	7.79E−03	9.70E−01
4	6	4.55E+03	2.28E+04	2.36E−05	1.06E−03	1.50E+01
4	8	2.55E+01	1.79E+11	1.75E−02	4.41E−03	8.80E−01
4	11	2.52E+01	5.39E+09	1.72E−04	4.29E−05	7.00E−01
4	13	2.51E+01	1.79E+12	1.69E−01	4.18E−02	1.00E+00
4	14	2.51E+01	2.86E+12	4.48E−01	1.11E−01	1.00E+00
4	16	2.51E+01	4.13E+11	6.47E−02	1.60E−02	1.00E+00
4	18	1.89E+01	9.29E+10	4.97E−03	9.28E−04	6.40E−01
4	19	1.88E+01	3.96E+09	7.02E−05	1.31E−05	3.60E−01
4	24	1.88E+01	5.90E+11	3.12E−02	5.78E−03	9.70E−01
4	25	1.88E+01	9.77E+11	8.60E−02	1.59E−02	9.60E−01
4	27	1.88E+01	1.01E+11	8.85E−03	1.64E−03	9.80E−01
5	8	2.56E+01	3.07E+11	1.82E−02	7.67E−03	8.90E−01
5	13	2.52E+01	1.20E+11	6.84E−03	2.83E−03	1.00E+00
5	14	2.52E+01	8.48E+11	8.06E−02	3.34E−02	1.00E+00
5	15	2.52E+01	4.32E+12	5.75E−01	2.38E−01	1.00E+00
5	16	2.52E+01	2.33E+11	2.21E−02	9.15E−03	1.00E+00
5	18	1.90E+01	1.57E+11	5.09E−03	1.59E−03	6.50E−01
5	24	1.88E+01	3.93E+10	1.25E−03	3.89E−04	9.70E−01
5	25	1.88E+01	2.92E+11	1.55E−02	4.82E−03	9.70E−01
5	26	1.88E+01	1.42E+12	1.06E−01	3.27E−02	9.70E−01
5	27	1.88E+01	6.22E+10	3.31E−03	1.02E−03	9.70E−01

The last column gives R, the ratio of velocity and length forms of A-values

Table 8.7 Transition wavelengths (λ_{ij} in Å), radiative rates (A_{ji} in s^{-1}), oscillator strengths (f_{ij} dimensionless) and line strengths (S in atomic units) at $n_e = 2.0 \times 10^{23}$ and kT = 1000 eV from the present MCDF calculations for E1 transitions in He-like Cl^{15+} ion

i	j	λ_{ij}	A_{ji}	f_{ij}	S	R
1	4	4.47E+00	9.82E+11	8.84E−03	1.30E−04	1.00E+00
1	7	4.45E+00	8.88E+13	7.90E−01	1.16E−02	1.00E+00
1	10	3.80E+00	3.11E+11	2.02E−03	2.52E−05	9.60E−01
1	17	3.79E+00	2.61E+13	1.69E−01	2.12E−03	9.60E−01
1	21	3.61E+00	1.33E+11	7.78E−04	9.26E−06	9.10E−01
1	23	3.61E+00	1.18E+13	6.93E−02	8.25E−04	9.00E−01
2	3	7.07E+02	1.92E+08	4.79E−03	3.34E−02	7.40E−01
2	4	6.87E+02	2.07E+08	1.47E−02	9.94E−02	7.70E−01
2	5	6.16E+02	2.92E+08	2.77E−02	1.68E−01	8.10E−01
2	7	3.70E+02	1.48E+07	3.04E−04	1.11E−03	8.60E−01
2	9	2.44E+01	1.51E+12	4.47E−02	1.08E−02	9.80E−01
2	10	2.44E+01	1.49E+12	1.32E−01	3.18E−02	9.80E−01
2	12	2.43E+01	1.49E+12	2.20E−01	5.29E−02	9.70E−01
2	17	2.42E+01	1.65E+10	1.45E−03	3.45E−04	9.70E−01
2	20	1.83E+01	7.17E+11	1.20E−02	2.17E−03	8.80E−01
2	21	1.83E+01	7.07E+11	3.56E−02	6.44E−03	8.80E−01
2	22	1.83E+01	7.11E+11	5.95E−02	1.08E−02	8.70E−01
2	23	1.83E+01	7.79E+09	3.90E−04	7.04E−05	8.70E−01
3	8	2.55E+01	6.09E+10	1.78E−02	1.50E−03	8.80E−01
3	13	2.50E+01	2.42E+12	6.81E−01	5.62E−02	1.00E+00
3	18	1.89E+01	3.19E+10	5.10E−03	3.17E−04	6.30E−01
3	24	1.87E+01	7.99E+11	1.26E−01	7.79E−03	9.70E−01
4	6	4.52E+03	2.32E+04	2.37E−05	1.06E−03	1.50E+01
4	8	2.55E+01	1.79E+11	1.75E−02	4.41E−03	8.80E−01
4	11	2.52E+01	5.40E+09	1.72E−04	4.28E−05	7.00E−01
4	13	2.51E+01	1.79E+12	1.69E−01	4.18E−02	1.00E+00
4	14	2.51E+01	2.86E+12	4.49E−01	1.11E−01	1.00E+00
4	16	2.50E+01	4.13E+11	6.47E−02	1.60E−02	1.00E+00
4	18	1.89E+01	9.31E+10	4.98E−03	9.28E−04	6.40E−01
4	19	1.88E+01	3.97E+09	7.02E−05	1.31E−05	3.60E−01
4	24	1.88E+01	5.92E+11	3.12E−02	5.78E−03	9.70E−01
4	25	1.88E+01	9.79E+11	8.61E−02	1.60E−02	9.70E−01
4	27	1.88E+01	1.01E+11	8.86E−03	1.64E−03	9.80E−01
5	8	2.56E+01	3.07E+11	1.82E−02	7.67E−03	8.90E−01

(continued)

Table 8.7 (continued)

i	j	λ_{ij}	A_{ji}	f_{ij}	S	R
5	13	2.52E+01	1.20E+11	6.84E−03	2.83E−03	1.00E+00
5	14	2.52E+01	8.48E+11	8.06E−02	3.34E−02	1.00E+00
5	15	2.52E+01	4.33E+12	5.75E−01	2.38E−01	1.00E+00
5	16	2.52E+01	2.33E+11	2.21E−02	9.15E−03	1.00E+00
5	18	1.89E+01	1.58E+11	5.09E−03	1.59E−03	6.50E−01
5	24	1.88E+01	3.94E+10	1.26E−03	3.89E−04	9.70E−01
5	25	1.88E+01	2.93E+11	1.56E−02	4.82E−03	9.70E−01
5	26	1.88E+01	1.42E+12	1.06E−01	3.28E−02	9.70E−01
5	27	1.88E+01	6.23E+10	3.31E−03	1.02E−03	9.70E−01

The last column gives R, the ratio of velocity and length forms of A-values

Table 8.8 Transition wavelengths (λ_{ij} in Å), radiative rates (A_{ji} in s^{-1}), oscillator strengths (f_{ij} dimensionless) and line strengths (S in atomic units) at $n_e = 2.0 \times 10^{23}$ from the present MCDF UEGM calculations for E1 transitions in He-like Cl^{15+} ion

i	j	λ_{ij}	A_{ji}	f_{ij}	S	R
1	4	4.47E+00	9.83E+11	8.84E−03	1.30E−04	1.00E+00
1	7	4.45E+00	8.88E+13	7.90E−01	1.16E−02	1.00E+00
1	10	3.80E+00	3.11E+11	2.02E−03	2.53E−05	9.60E−01
1	17	3.79E+00	2.62E+13	1.70E−01	2.12E−03	9.60E−01
1	21	3.61E+00	1.34E+11	7.85E−04	9.33E−06	9.10Ev01
1	23	3.61E+00	1.19E+13	6.98E−02	8.30E−04	9.00E−01
2	3	7.09E+02	1.90E+08	4.78E−03	3.34E−02	7.40E−01
2	4	6.89E+02	2.05E+08	1.46E−02	9.94E−02	7.70E−01
2	5	6.17E+02	2.91E+08	2.76E−02	1.68E−01	8.10E−01
2	7	3.70E+02	1.48E+07	3.03E−04	1.11E−03	8.60E−01
2	9	2.43E+01	1.51E+12	4.48E−02	1.08E−02	9.80E−01
2	10	2.43E+01	1.49E+12	1.32E−01	3.18E−02	9.80E−01
2	12	2.43E+01	1.49E+12	2.20E−01	5.29E−02	9.70E−01
2	17	2.41E+01	1.66E+10	1.45E−03	3.46E−04	9.70E−01
2	19	1.83E+01	7.23E+11	1.21E−02	2.18E−03	8.80E−01
2	21	1.83E+01	7.13E+11	3.58E−02	6.46E−03	8.80E−01
2	22	1.83E+01	7.17E+11	5.99E−02	1.08E−02	8.80E−01
2	23	1.82E+01	7.87E+09	3.93E−04	7.07E−05	8.70E−01

Table 8.8 (continued)

i	j	λ_{ij}	A_{ji}	f_{ij}	S	R
3	8	2.55E+01	6.11E+10	1.78E−02	1.50E−03	8.80E−01
3	13	2.50E+01	2.42E+12	6.82E−01	5.62E−02	1.00E+00
3	18	1.88E+01	3.21E+10	5.12E−03	3.18E−04	6.30E−01
3	24	1.87E+01	8.05E+11	1.27E−01	7.82E−03	9.70E−01
4	6	4.45E+03	2.43E+04	2.41E−05	1.06E−03	1.40E+01
4	8	2.55E+01	1.79E+11	1.75E−02	4.41E−03	8.80E−01
4	11	2.52E+01	5.41E+09	1.72E−04	4.28E−05	7.10E−01
4	13	2.51E+01	1.80E+12	1.69E−01	4.18E−02	1.00E+00
4	14	2.50E+01	2.86E+12	4.49E−01	1.11E−01	1.00E+00
4	16	2.50E+01	4.14E+11	6.48E−02	1.60E−02	1.00E+00
4	18	1.89E+01	9.37E+10	4.99E−03	9.30E−04	6.40E−01
4	20	1.88E+01	3.99E+09	7.04E−05	1.31E−05	3.60E−01
4	24	1.87E+01	5.96E+11	3.13E−02	5.80E−03	9.70E−01
4	25	1.87E+01	9.87E+11	8.65E−02	1.60E−02	9.70E−01
4	27	1.87E+01	1.01E+11	8.89E−03	1.64E−03	9.80E−01
5	8	2.56E+01	3.08E+11	1.82E−02	7.66E−03	8.90E−01
5	13	2.52E+01	1.20E+11	6.85E−03	2.83E−03	1.00E+00
5	14	2.52E+01	8.50E+11	8.07E−02	3.34E−02	1.00E+00
5	15	2.51E+01	4.34E+12	5.75E−01	2.38E−01	1.00E+00
5	16	2.51E+01	2.34E+11	2.21E−02	9.15E−03	1.00E+00
5	18	1.89E+01	1.59E+11	5.11E−03	1.59E−03	6.50E−01
5	24	1.88E+01	3.97E+10	1.26E−03	3.90E−04	9.70E−01
5	25	1.88E+01	2.95E+11	1.56E−02	4.84E−03	9.70E−01
5	26	1.88E+01	1.43E+12	1.06E−01	3.29E−02	9.70E−01
5	27	1.88E+01	6.28E+10	3.32E−03	1.03E−03	9.70E−01

The last column gives R, the ratio of velocity and length forms of A-values

8.4   Conclusion

In this study, the MCDF and RCI methods have been employed incorporating the APS and UEGM potentials to be the modified interaction potentials between the nucleus and the electron. We have studied the effect of plasma screening on the He-α $1s^2\,{}^1S_0 \rightarrow 1s2p$ (${}^3\,P_1^o,\,{}^1\,P_1^o$) and He-β $1s^2\,{}^1S_0 \rightarrow 1s3p$ (${}^3\,P_1^o,\,{}^1\,P_1^o$) transitions of Cl^{15+} ion at various kT and n_e. Moreover, the results for plasma free case are in good agreement with the recommended values from NIST. It has been seen that red shift is found for both the He-α and He-β transitions as the plasma density increases. The plasma energy shift is found to be more sensitive to the free electron density at lower values of electron temperature. We believe that the presently reported results
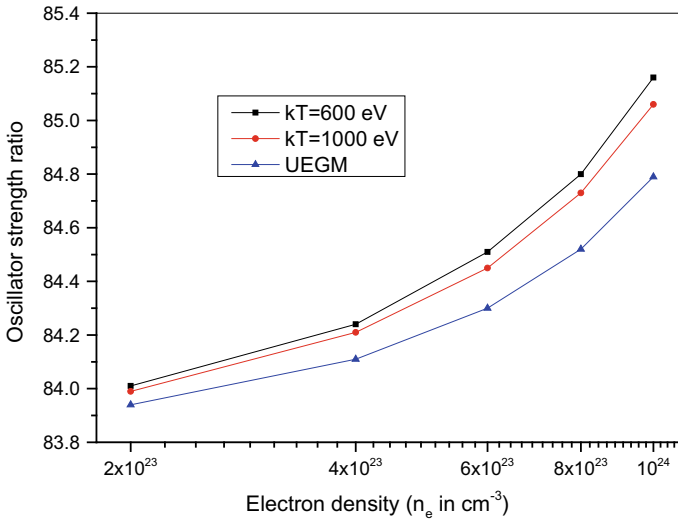
Fig. 8.3 Ratio of oscillator strength for resonance-to-intercombination transitions with respect to the free electron density

will be of great help in the modeling and diagnostics of laboratory and astrophysical plasmas.

References

1. M.S. Murillo, J.Weisheit, S.B. Hansen, M. DharmaWardana, Phys. Rev. E **87**, 063113 (2013)
2. B. Saha, S. Fritzsche, J. Phys. B: At. Mol. Opt. Phys. **40**, 259 (2007)
3. M. Nantel, G. Ma, S. Gu, C.Y. Cote, J. Itatani, D. Umstadter, Phys. Rev. Lett. **80**, 4442 (1998)
4. O. Renner, F. B. Rosmej, Matter Radiat. Extremes **4**, 024201 (2019)
5. S. Ichimaru, Rev. Mod. Phys. **54**, 1017 (1982)
6. M.S. Murillo, J.C. Weisheit, Phys. Rep. **302**, 1 (1998)
7. A. Sil, P. Mukherjee, Int. J. Quantum Chem. **106**, 465 (2006)
8. A. Sil, J. Anton, S. Fritzsche, P. Mukherjee, B. Fricke, Eur. Phys. J. D **55**, 645 (2009)
9. X. Li, Z. Xu, F. Rosmej, J. Phys. B: At. Mol. Opt. Phys. **39**, 3373 (2006)
10. R. Rodriguez, J.M. Gil, R. Florido, Phys. Scr. **76**, 418 (2007)
11. S. Bhattacharyya, J. Saha and T. Mukherjee, Phys. Rev. A **91**, 042515 (2015)
12. M. Belkhiri, C. J. Fontes, M. Poirier, Phys. Rev. A **92**, 032501 (2015)
13. X.-F. Li, G. Jiang, H.-B. Wang, M. Wu, Q. Sun, Phys. Scr. **92**, 075401 (2017)

14. X.-F. Li, G. Jiang, Chin. Phys. B **27**, 073101 (2018)
15. Z.-B. Chen, K. Ma, Y. L. Ma, K. Wang, Phys. Plasmas **26**, 082101 (2019)
16. Z.-B. Chen, J. Quant. Spectrosc. Radiat. Transf. **237**, 106615 (2019)
17. Z.-B. Chen, Radiat. Phys. Chem. **166**, 108508 (2020)
18. X. Li, F. B. Rosmej, V. S. Lisitsa, V. A. Astapenko, Phys. Plasmas **26**, 033301 (2019).
19. D. Dawra, M. Dimri, A.K. Singh, A.K. Jha, S.S. Singh, J. At. Mol. Condensate Nano Phys. **6**, 103 (2019)
20. M. Dimri, D. Dawra, A.K. Singh, A.K. Jha, R.K. Pandey, M. Mohan, Atomic structure and radiative properties of He-like Ni^{26+} ion in dense plasma, Can. J. Phys. (Accepted Manuscript)
21. A.K. Singh, D. Dawra, M. Dimri, A.K. Jha, R.K. Pandey, M. Mohan, Phys. Lett. A. **384**, 126369 (2020)
22. http://amdpp.phys.strath.ac.uk /UK APAP/codes.html
23. I. Grant, J. McKenzie, P. Norrington, M. Mayers, N. Pyper, Comput. Phys. Commun. **21**, 207 (1980)
24. A. Singh, D. Dawra, M. Dimri, A.K. Jha, M. Mohan, Phys. Plasmas **26**, 062704 (2019)
25. A. Singh, M. Dimri, D. Dawra, A.K. Jha, N. Verma, M. Mohan, Radiat. Phys. Chem. **156**, 174 (2019)
26. A. Singh, M. Dimri, D. Dawra, A.K. Jha, M. Mohan, Can. J. Phys. **97**, 436 (2019)
27. M.F. Gu, Can. J. Phys. **86**, 675 (2008)
28. A. Kramida, Y. Ralchenko, J. Reader, NIST ASD Team, NIST Atomic Spectra Database (ver. 5.6.1), [Online]. Available https://physics.nist.gov/asd [2019, June 20]. National Institute of Standards and Technology, Gaithersburg, MD. (2018)

Chapter 9
Fabrication of Ag Thin Film Nano Layered Structure and Its Potential Application as the Supercapacitor Electrode

Saurabh Daripa and Amrish K. Panwar

Abstract Nano layer thin-film of silver (Ag) has been synthesized using a thermal vapor deposition technique on copper (Cu) substrate to study the potential application of silver as a supercapacitor electrode material. X-ray diffraction (XRD) characterization of the deposited film was performed to identify and confirm the proper phase formation of the crystalline materialh. Surface characterization has been performed using atomic force microscopy (AFM) to see the physical structure and skewness of the surface. The surface to volume ratio of the nanolayer structure is quite high and this property can be useful as the electrode material of supercapacitor. The electrochemical performance of the synthesized thin films as supercapacitor electrodes has been studied using Cyclic Voltammetry. The specific capacitance of the supercapacitor was observed to be 14.5 F/g.

9.1 Introduction

Supercapacitor is an energy storage device which exibits high capacity, high power density, excellent cyclability, fast charge–discharge process, and longer life cycle when compared to the traditional batteries or dielectric capacitor [1]. A supercapacitor can play a critical role in spanning the gap between fast charging and longer charger storage [2, 3]. Supercapacitors are a crucial component of several applications like communication devices, electric vehicles, UPS, mobile phones, laser technology, military warheads, and solar cell energy storage, etc. [4, 5].

Usually, supercapacitors consist of a current collector, electrode material, separator, and an electrolyte. Electrochemical Double-Layer Supercapacitor (EDLC) stores charge electrostatically onto the active material. These active materials are designed in such a way that they are electrochemically stable (non-reactive to the electrolyte) and have a high specific surface area [4, 5]. Three factors that influence the double-layer formation are a highly conductive electrode, the high surface area of material, and porosity of the electrode. A good electrode material in a supercapacitor

S. Daripa · A. K. Panwar (✉)
Department of Applied Physics, Delhi Technological University, Delhi 110042, India

device must be highly conductive and should have a high surface area for high charge accumulation onto the surface. The conductivity of the electrode material must be high or else the internal resistance of the supercapacitor device will not be in the permissible range [4, 5].

The specific resistance of Ag thin film is quite low making it a good candidate for the supercapacitor electrode. Separators in a supercapacitor are fixed between the two electrodes to restrict the movement of electrons between the two electrodes. Moreover, the separator should be considerably thin to assure smooth movement of the ions [6].

In this study, the nano-layer thin-film of silver has been deposited on Cu foil using a thermal vapor deposition. X-ray diffraction and atomic force microscopy of deposited Ag film has been carried out to confirm the proper phase formation and surface smoothness of the crystalline material. The electrochemical performance of the Supercapacitor has been studied using Cyclic Voltammetry. Moreover, the egg-shells membrane (ESM) (ion exchange membrane) is used as a separator medium for the electrolyte of Na_2SO_4 [6, 7].

9.2 Experimental

9.2.1 Preparation of Ion Exchange Membrane

Eggshells were dipped in HCL (38% concentration) for 6 h to separate the membrane from the outer calcium layer. Once the outer shell is completely dissolved (6 h), the membrane was carefully cleaned and soaked in DI water for 2 h. The cleaned membrane was then soaked in 1 M Na_2SO_4 solution for 24 h. This soaked eggshell membrane was used as a separator soaked with electrolyte (1 M Na_2SO_4 solution).

9.2.2 Ag Coating on Cu Substrate

A uniform Cu sheet was taken and cleaned with concentrated HCl and DI water to remove any oily residue from the surface. After cleaning the Cu substrate, it was sonicated for 20 min under de-ionized water. This Cu substrate was then dried in a hot air oven.

The Ag film was coated on a Cu substrate by the thermal evaporation technique using the Hind Hi-Vac coating unit. The Cu substrate was placed on the substrate holder and 50 mg of pure silver was kept in the Molybdenum boat. The vacuum pressure of the order of 10^{-5} mbar was attained inside the vacuum chamber. After obtaining the desired vacuum pressure, the Ag coating was done onto the Cu substrate until a thickness of 100 nm. The coating rate was fixed to 5 Å/sec ensuring uniform coating onto the Cu surface.

Fig. 9.1 Components and design used for supercapacitor fabrication
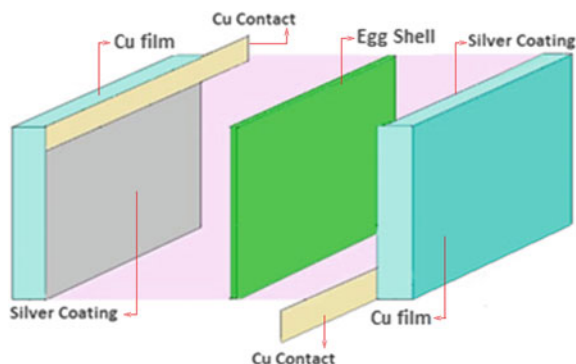
9.2.3 Characterizations

X-ray diffraction (XRD) pattern has been recorded by X'Pert Pro system with wavelength of X-ray,1.54 Å and scan rate of 2°/min. AFM results are obtained using a Witec MultiMode Instrument under tapping mode in using a V-shaped tip. Cyclic voltammetry measurements were carried out with the BioLogics Make VMP3 equipment.

9.2.4 Supercapacitor Fabrication

The soaked egg-shell membrane (separator) was placed between both the Ag coated Cu electrodes in such a way that two electrodes are not shorted. Cu Contacts are made in the electrode before supercapacitor fabrication. Figure 9.1 indicates the fabrication design used in this study.

9.3 Results and Discussion

9.3.1 XRD Pattern Analysis

XRD patterns of the Ag thin film coated on Cu substrate is observed as shown in Fig. 9.2 at room temperature. The observed XRD patterns are compared with the standard XRD pattern of the Ag and Cu. The peaks at 38.2° and 44.3° can be attributed to the planes (111) and (200) for Ag and the peaks at 43.32° and 50.46° can be attributed to the planes (111) and (200) for Cu, respectively. It has been noticed that the proper phase of the face-centered cubic structure of Ag is formed. In-set of Fig. 9.2 shows that the Gaussian fitting of the main peak of silver at the plane
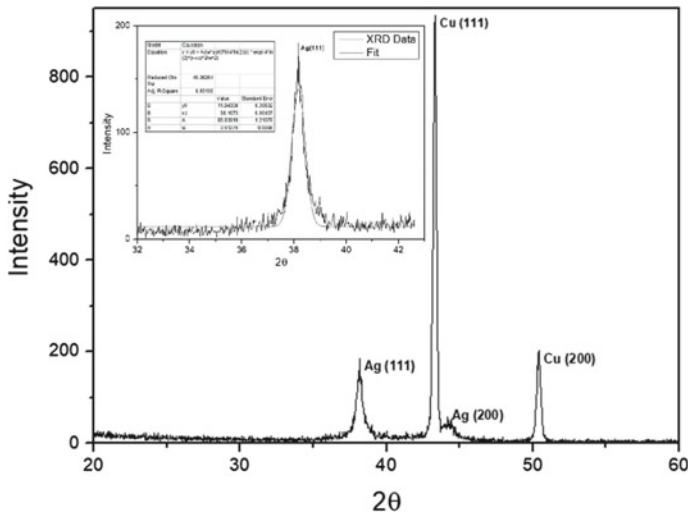
Fig. 9.2 XRD pattern of the silver electrode deposited on a Cu substrate using thermal evaporation technique

(111) is used to determine the average crystalline size. The average crystallite size of 14.35 nm is observed as estimated from Scherrer relation the XRD peaks.

9.3.2 AFM

The surface morphology was studied by atomic force microscopy. The surface texture of the Ag deposited Cu substrate in 3D and distribution of particle size as calculated in AFM analysis is shown in Fig. 9.3a and b, respectively. The Cu and glass substrate was placed inside the reaction chamber of the vapor deposition machine at the same moment. Ag deposited on the glass substrate was used for AFM imaging. Surface texture of the Skewness is represented by SSK, it shows degree of symmetry of the heights of surface with reference to mean plane or base. The sign of SSK relates the peaks for SSK > 0 or valley structures as SSK < 0 covering the surface. This SSK value for the given surface of Ag is measured 2.43613.

9.3.3 Electrochemical Performances

Charge–discharge response of the supercapacitors was observed by CV measurement as shown in Fig. 9.4. The CV data has been measured in the potential range, 0–0.9 V for different scan rates. The distinctive rectangular shape of the CV curve implies
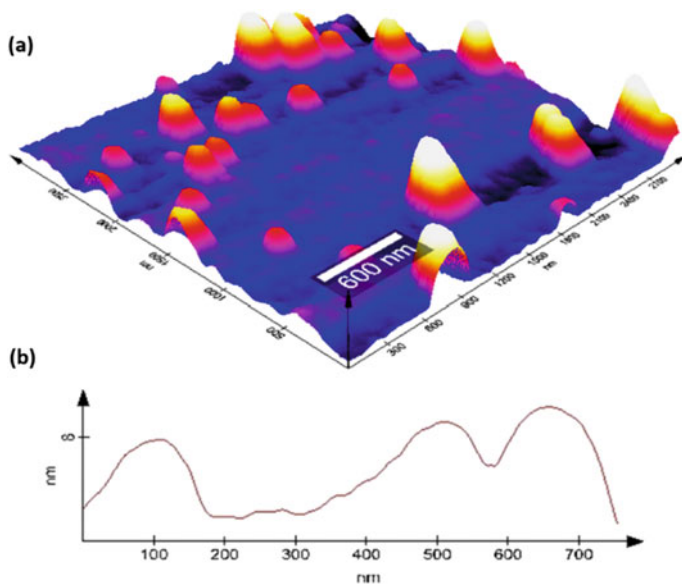
Fig. 9.3 **a** 3D AFM image of the Silver electrode and **b** Average particle size distribution calculated by AFM
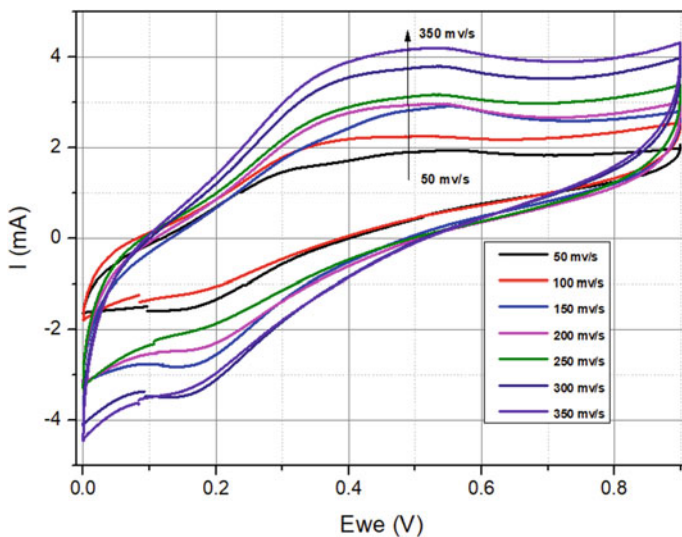
Fig. 9.4 Cyclic voltammetry of the silver electrode of type A supercapacitor

that the charge is accumulated at the electrode-eggshell interface forming an electric double layer [8].

Specific capacitance is estimated using the mass of the silver deposited on the electrode. The mass of silver deposited on the electrode was around 1 mg covered the surface area of one electrode of 9.375 cm^2.

The specific capacitance C$_p$ was calculated using [9, 10];

$$C_p = \frac{A}{(2\mathrm{mk}(v_2 - v_1))}$$

where A, m, k and (v_2–v_1) are area under the CV plot, active material mass, scan rate, and potential gap in CV plot. Therefore in this given design, the specific capacitance is observed to be 14.5 F/g at scan rate of 50 mV/s.

9.4   Conclusion

Supercapacitors are demanding because of their numerous technological advantages like quick charging and discharging processes, exceptional cycle stability, and high power densities. In this study, silver-eggshell based supercapacitor device was fabricated and its electrochemical performance was analyzed using the CV curve. The specific capacitance, 14.5 F/g is measured at a high scan rate of 50 mV/s.

References

1. L. Zhang, X.S. Zhao, Chem. Soc. Rev. **38**, 2520–2531 (2009)
2. W. Zuo, R. Li, C. Zhou, Y. Li, J. Xia, J. Liu, Adv. Sci. **4**, 1600539 (2017)
3. D.P. Dubal, O. Ayyad, V. Ruiz, P. Gomez-Romero, Chem. Soc. Rev. **44**, 1777–1790 (2015)
4. W. Raza, Nano Energy **52**, 441–473 (2018)
5. P. Simon, Y. Gogotsi, Materials for electrochemical capacitors. Nanosci. Technol. 320–329 (2009)
6. E. Taer, Adv. Mater. Res. **896**, 66–69 (2014)
7. Y.M. Shulga, S.A. Baskakov, V.A. Smirnov, N.Y. Shulga, K.G. Belay, G.L. Gutsev, J. Power Sources **245**, 33–36 (2014)

8. H. Yang, S. Kannappan, A.S. Pandian, J.-H. Jang, Y.S. Lee, W. Lu, Nanotechnology **28**, 445401 (2017)
9. S. Zhang, N. Pan, Supercapacitors. Adv. Energy Mater. **5**, 1401401 (2015)
10. T. Chen, L. Dai, Mater. Today **16**, 1–9 (2013)

Chapter 10
Energy Levels, Transition Data and SXRay Spectral Lines in W LXVII

Rinku Sharma and Arun Goyal

Abstract A main ingredient for understanding the influence of Tungsten 'W' as a plasma impurity and its impact on the plasma in experimental investigation is primarily done with the help of the spatially resolved theoretical spectroscopic diagnosis of W ions. In this research article, We have performed calculations for the excitation energies (Ex Ene), wavelength (Tr Wav) and line strengths (LSt) of emitted photon during the transition from upper level to lower level transitions rates and other transition parameters for first fine structure 80 levels of W LXVII by employing fully relativistic Multi-Configuration Dirac-Fock (FR-MCDF) technique. The strong interference effect of Quantum Electrodynamics corrections (QEDC) and Relativistic Breit interaction term (RBIT) in the calculations for energies of levels is observed. Our results, where possible, have been compared with the few previous theoretical calculations, NIST and experimental available results of Ex Ene that are available. The 31 electric dipole (E1) transitions from ground state are Soft X-ray transitions (SXRay) have been computed. In addition, the accurate and new atomic and radiative data of O-like W not available in the research articles is furnished. This dataset which is not published upto the knowledge of the authors can be useful in the field of biophysics, cell biology and astrophysical plasma.

10.1 Introduction

Tungsten (W) has been identified as a main candidate in the fusion research for the plasma facing materials (PFMs) of ITER and succeeding fusion reactor. The focus of experimental study is on the strong radiation emissions of highly ionised W- ions (about W20+ to W50+) in the vacuum Ultraviolet (VUV) to the soft x-ray (SXRay) region in electromagnetic spectra enveloping the thermal range of electrons from about 0.5–5.0 keV.

R. Sharma
Department of Applied Physics, Delhi Technological University, Delhi 110042, India

A. Goyal (✉)
Department of Physics, Shyamlal College, University of Delhi, Delhi 110032, India

The interest in the atomic spectroscopic data of W-ions has increased in the last few years for the reason that designing and buildout of strong magnetic fusion plasma and radiative energy sources. It is well known that W has the highest melting point temperature along the metals in the periodic table, has good thermal conductivity, which does not degenerate too much if temperature is increased, low swelling and low sputtering yield. Owing to these properties and to meet the design requirements for future fusion reactors, the role tungsten impurities in the fusion plasma cannot be avoided. The versatile applications of Tungsten as a PFM requires comprehensive research in areas namely, atomic and plasma physics and development of materials. Thus, the complete and accurate data is needed for the radiative and atomic properties of various ionizations of W-ions (in all stages of ionization) such as transition probabilities (Tr Prob), Transition Wavelengths (Tr Wav) Oscillator Strengths (OSt) collisional and photoionization cross sections (Photo CS) to withstand extreme surrounding environment condition such as high-rise temperatures, excessive thermal loads, high irradiation conditions induced by fast moving high-energy neutron, and high fluencies flux and less-energy plasma [1–5].

Thus, for explanation and analysis, the identification of the spectral emissions from experiments is mandatory; the procedure of interpreting the spectral data should also be partnered by theoretical model computational calculations using atomic data. This analysis helps the extracting of the observed experimental datasets and yields reasonable analysis of the measurement such as electron beam ion trap (EBIT) at Berlin [6–8], Lawrence Livermore National Laboratory (LLNL) [9–12], National Institute of Standards and Technology (NIST) [13–16] as well as ASDEX upgrade tokamak [17–19]. Studies have reported the significance of the radiations emitted from L-shell (n = 2) W- ions i.e. in ionization stages from Li-like to Ne-like and play key role for the computations of ionic temperature and scaled velocity of thermal plasma.

To understand and diagnose the complete plasma parameters in thermodynamic equilibrium (Local and non-local) at high temperatures we need to compute accurate and complete spectroscopic analysis such as Tr Prob, Tr Wav, OSt, Ex Ene and photoionization cross sections (Photo CS) and dataset for collisional excitation-ionization, and recombination. Further, the ground state of O-like ions has an open 2p subshell and the atomic electric dipole transitions will lie in X-ray regime. These SXRay transitions are important in SXRay tomography (SoftXT) in which the internal structure is visualised by imaging tissues in cell to understand the relevant biological problems. As mentioned, the precise and accurate data for W-ions is much needed in the current scenario, but up to our knowledge insufficient experimental observations and computational data is available and is true in the case of O-like W also. Consequently, we have furnished the valid and precise data for lowest 80 fine structure Ex Ene and Electric dipole transition E1 data from ground state. We strongly believe that the dataset computed in this research problem is highly useful to estimate theoretical uncertainties which will be suitable to evaluation of good-resolution radiative and spectroscopic data.

10.2   Theoretical Method

Till date several semi classical and quantum mechanical techniques including the RBIT and QEDC corrections in atomic structure calculations in detailed way are explored and reported in different research works. Here, we have attempted to explore the electron correlation effects and its comparison with the RBIT and QEDC donations. We have evaluated the O like W dataset using fully relativistic General-Purpose Relativistic Atomic Structure Program (GRASP) and Flexible Atomic Code Flexible Atomic Code (FAC) computational codes. The GRASP code was developed by the Grant et al. at Oxford University and recently improvised by Froese Fischer and group so as to execute extensive FR-MCDF calculations. The FAC was expanded by M. F. Gu [20] at Stanford University which exploits the modified MCI Dirac-Hartree-Fock-Slater (MC-DHFS) model, [20] for fast atomic structure calculation and radiative-collisional designing. Detailed and good precision atomic structure calculations including the RBIT and QED effects are important to interpret the complex spectra observed for highly ionised tungsten ions. These studies constitute the strong foundation for the farther convention modelling of the high energy radiation emitted from tokamak plasmas. The idea behind of this research article is to examine and walk through the divergences in the extant of theoretical contributions taken into account by the computational codes.

10.3   Computational Procedure

We begin our calculations taking into account the single double (Si Do) excitations from outermost orbitals 2 s and 2p for the ion in question wherein the configurations, Active Data Set (ADS) in our first part were incorporated as per detailed procedure given below:

$$ADS1 = \{n = 2,\ l = 0(s) \text{ to } 1(p)\}$$
$$ADS2 = ADS1\ +\ \{n = 3,\ l = 0(s) \text{to } 2(p, d)\}$$
$$ADS3 = ADS2\ +\ \{n = 4,\ l = 0(s) \text{to } 3(p, d, f)\}$$
$$ADS4 = ADS3\ +\ \{n = 5,\ l = 0(s) \text{to } 4(p, d, f, g)\}$$
$$ADS5 = ADS4\ +\ \{n = 6,\ l = 0(s) \text{to } 4(p, d, f, g)\}$$

Eventually, in the next part, we have pulled out the configurations which have yielded 10% or more impact on total configuration orbital wave function. The contribution of those configurations having impact less than 10% are excluded so as to reserve the clock time.

10.4 Results and Discussion

10.4.1 Energy Levels

The precise and accurate fine structure energies (Ex Ene) of smallest 80 energy levels involving fine structure corrections related to non-relativistic configurations $2s^22p^4$, $2s2p^5$, $2p^6$, $2s^22p^33l$ (l = s, p, d) and $2s2p^43l$ (l = s, p) are computed using GRASP and FAC code which is listed in Table 10.1. Here, in Table 10.1, the effect of the components in total energy namely, Dirac-Coulomb and RBIT and QEDC is projected discretely. It is evident that the component of RBIT is greater than the component of QEDC for majority of the levels. It is interesting to compare the electron EX Ene and radiative data with the critically compiled NIST data [21] in selected cases and the data for experimentally calculated Ex Ene by Beiersdorfer et al. [21] in Tables 10.1 and 10.2 respectively.

The one important focus of this research work presented here is to estimate the numerical difference of our computed Ex Ene with the dataset available in the other research work which is relevant to the interpretation of precise-resolution radiative data, using the relation,

$$\Delta E = |E_{other} - E_{cal.}| \tag{10.1}$$

The highest variation in reported Ex Ene calculated from GRASP technique with NIST [21] is 0.215 Ryd. for energy state number 6 and with reference to the percentage error difference, the maximum discrepancy is 0.61% for energy state number 2. The greatest difference in our computed GRASP and FAC Ex Ene with the dataset of energies reported by Beiersdorfer et al. [21] is 0.360 and 0.364 resp. for energy state number 12. It is apparent from the percentage error calculations, that our results are consonant with the other experimental and theoretical results available.

10.4.2 Radiative Rates

For E1 transitions, Tr Prob (A_{ji}) and OSt (f_{ij}) are related to LSt (S_{ij}) as mentioned below:

$$A_{ji} = \frac{2.0261 \times 10^{18}}{\omega_j \lambda_{ji}^3} S_{ij} \text{ and } f_{ij} = \frac{303.75}{\lambda_{ji} \omega_i} S_{ij} \tag{10.2}$$

λ_{ij}, ω_i and ω_j denotes wavelength of the photons emitted in units of Å, statistical weight of lower and upper energy states, respectively in the above expression. We have tabulated the accurate transition data of E1 transitions from ground state in Table 10.1. It can be noticed that the results are presented in babushkin gauge only considering the minimum effect of negative energy levels on babushkin gauge in

Table 10.1 Ex Ene (in Ryd.) of lowest 80 fine structure levels of O-like W

Level No	Configurations	Energies (in Ryd.)				FAC	NIST	ΔE
		MCDF						
		DC	Briet	QED	Total			
1	$2s^2\,2p^4\,^3P_2\,^e$	0.000	–	–	0.000	0.000	0.000	–
2	$2s^2\,2p^4\,^1S_0\,^e$	3.865	0.645	−0.001	4.510	4.503	4.538	0.028
3	$2s^2\,2p^4\,^3P_1\,^e$	103.683	−1.030	0.122	102.774	102.883		
4	$2s^2\,2p^4\,^1D_2\,^e$	105.660	−1.620	0.122	104.165	104.273		
5	$2s^1\,2p^5\,^3P_2\,^e$	134.474	−0.167	−1.180	133.131	132.920	132.735	0.211
6	$2s^1\,2p^5\,^1P_1\,^o$	140.500	0.041	−1.180	139.366	139.151	138.968	0.215
7	$2s^2\,2p^4\,^3P_0\,^e$	210.845	−2.250	0.231	208.829	209.049		
8	$2s^1\,2p^5\,^3P_0\,^o$	239.024	−1.180	−1.050	236.793	236.694		
9	$2s^1\,2p^5\,^3P_1\,^o$	242.204	−1.520	−1.050	239.634	239.528		
10	$2p^6\,^1S_0\,^e$	277.767	0.035	−2.340	275.466	274.962		
11	$2s^2\,2p^3\,3s^1\,^3P_2\,^o$	635.717	−0.817	0.178	635.078	635.068		
12	$2s^2\,2p^3\,3s^1\,^1P_1\,^o$	636.358	−0.777	0.178	635.759	635.755		
13	$2s^2\,2p^3\,3p^1\,^3P_1\,^e$	644.688	−0.318	−0.175	644.196	644.056		
14	$2s^2\,2p^3\,3p^1\,^3D_2\,^e$	644.959	−0.483	−0.174	644.302	644.165		
15	$2s^2\,2p^3\,3p^1\,^1P_1\,^e$	674.637	−0.859	−0.139	673.639	673.488		
16	$2s^2\,2p^3\,3p^1\,^3D_3\,^e$	674.655	−0.915	−0.138	673.602	673.525		
17	$2s^2\,2p^3\,3p^1\,^3P_2\,^e$	676.790	−0.812	−0.138	675.840	675.712		
18	$2s^2\,2p^3\,3p^1\,^1S_0\,^e$	678.498	−0.555	−0.138	677.806	677.670		
19	$2s^2\,2p^3\,3d^1\,^3D_2\,^o$	683.503	−0.843	−0.188	682.472	682.303		
20	$2s^2\,2p^3\,3d^1\,^3F_3\,^o$	684.276	−1.010	−0.188	683.078	682.909		
21	$2s^2\,2p^3\,3d^1\,^3P_0\,^o$	684.338	−0.517	−0.188	683.633	683.179		
22	$2s^2\,2p^3\,3d^1\,^3P_1\,^o$	684.367	−0.831	−0.188	683.347	683.462		
23	$2s^2\,2p^3\,3d^1\,^3F_4\,^o$	691.304	−1.170	−0.188	689.945	689.787		
24	$2s^2\,2p^3\,3d^1\,^3P_2\,^o$	692.100	−1.090	−0.188	690.824	690.672		
25	$2s^2\,2p^3\,3d^1\,^3D_3\,^o$	693.405	−1.200	−0.188	692.013	691.857		
26	$2s^2\,2p^3\,3d^1\,^1P_1\,^o$	694.119	−0.975	−0.188	692.955	692.794		
27	$2s^2\,2p^3\,3s^1\,^5S_2\,^o$	738.522	−2.190	0.298	736.627	736.719		
28	$2s^2\,2p^3\,3s^1\,^3S_1\,^o$	739.430	−2.190	0.299	737.541	737.645		
29	$2s^2\,2p^3\,3s^1\,^3D_3\,^o$	741.128	−2.970	0.299	738.455	738.539		
30	$2s^2\,2p^3\,3s^1\,^1D_2\,^o$	741.686	−2.870	0.298	739.113	739.206		
31	$2s^2\,2p^3\,3s^1\,^3P_0\,^o$	743.979	−1.900	0.296	742.377	742.423		
32	$2s^2\,2p^3\,3s^1\,^3P_1\,^o$	744.330	−1.990	0.298	742.633	742.684		
33	$2s^2\,2p^3\,3p^1\,^5P_1\,^e$	747.344	−1.770	−0.053	745.518	745.480		
34	$2s^2\,2p^3\,3p^1\,^3F_2\,^e$	748.218	−2.040	−0.053	746.123	746.084		

(continued)

Table 10.1 (continued)

Level No	Configurations	Energies (in Ryd.)						
		MCDF				FAC	NIST	ΔE
		DC	Briet	QED	Total			
35	$2s^2\ 2p^3\ 3p^1\ {}^3F_3{}^e$	750.136	−2.710	−0.054	747.368	747.326		
36	$2s^2\ 2p^3\ 3p^1\ {}^3P_2{}^e$	752.673	−2.210	−0.056	750.411	750.356		
37	$2s^2\ 2p^3\ 3p^1\ {}^3D_1{}^e$	752.885	−1.680	−0.054	751.153	751.071		
38	$2s^2\ 2p^3\ 3p^1\ {}^3P_0{}^e$	756.296	−1.440	−0.056	754.800	754.705		
39	$2s^1\ 2p^4\ 3s^1\ {}^5P_1{}^o$	765.018	−1.430	−0.980	762.607	762.369		
40	$2s^1\ 2p^4\ 3s^1\ {}^3P_2{}^e$	767.223	−1.320	−0.983	764.922	764.677		
41	$2s^1\ 2p^4\ 3s^1\ {}^3S_1{}^e$	772.384	−0.641	−0.975	770.768	770.482		
42	$2s^1\ 2p^4\ 3s^1\ {}^3D_1{}^e$	773.407	−1.180	−0.956	771.276	771.036		
43	$2s^1\ 2p^4\ 3s^1\ {}^3P_2{}^e$	773.937	−1.150	−0.953	771.834	771.585		
44	$2s^1\ 2p^4\ 3p^1\ {}^5P_2{}^o$	774.520	−0.880	−1.340	772.295	771.980		
45	$2s^1\ 2p^4\ 3p^1\ {}^3D_3{}^o$	774.927	−1.190	−1.340	772.392	772.081		
46	$2s^1\ 2p^4\ 3s^1\ {}^1S_0{}^e$	775.156	−0.484	−0.993	773.679	773.366		
47	$2s^2\ 2p^3\ 3p^1\ {}^3P_1{}^e$	777.546	−2.260	−0.027	775.259	775.243		
48	$2s^2\ 2p^3\ 3p^1\ {}^1D_2{}^e$	777.547	−2.280	−0.017	775.253	775.248		
49	$2s^2\ 2p^3\ 3p^1\ {}^3D_2{}^e$	777.855	−2.210	−0.060	775.589	775.545		
50	$2s^2\ 2p^3\ 3p^1\ {}^1P_1{}^e$	779.141	−2.560	−0.026	776.558	776.526		
51	$2s^2\ 2p^3\ 3p^1\ {}^3D_3{}^e$	779.956	−3.000	−0.021	776.937	776.870		
52	$2s^2\ 2p^3\ 3p^1\ {}^3F_4{}^e$	780.006	−3.100	−0.016	776.886	776.918		
53	$2s^1\ 2p^4\ 3p^1\ {}^3P_0{}^o$	781.726	−0.140	−1.350	780.241	779.650		
54	$2s^1\ 2p^4\ 3p^1\ {}^3P_1{}^o$	781.849	−0.346	−1.340	780.162	779.816		
55	$2s^2\ 2p^3\ 3p^1\ {}^3P_1{}^e$	781.963	−2.240	−0.047	779.679	779.861		
56	$2s^1\ 2p^4\ 3p^1\ {}^3D_1{}^o$	782.279	−0.749	−1.330	780.198	779.884		
57	$2s^1\ 2p^4\ 3p^1\ {}^3F_2{}^o$	782.562	−0.856	−1.330	780.371	780.030		
58	$2s^2\ 2p^3\ 3p^1\ {}^1D_2{}^e$	782.864	−2.450	−0.022	780.394	780.366		
59	$2s^2\ 2p^3\ 3p^1\ {}^3S_1{}^e$	783.943	−1.940	−0.037	781.969	781.911		
60	$2s^2\ 2p^3\ 3p^1\ {}^1D_2{}^e$	784.293	−2.300	−0.020	781.968	781.922		
61	$2s^2\ 2p^3\ 3d^1\ {}^5D_1{}^o$	786.698	−2.100	−0.070	784.531	784.491		
62	$2s^2\ 2p^3\ 3d^1\ {}^5D_0{}^o$	786.973	−2.190	−0.066	784.714	784.619		
63	$2s^2\ 2p^3\ 3d^1\ {}^3F_2{}^o$	787.016	−2.280	−0.069	784.663	784.683		
64	$2s^2\ 2p^3\ 3d^1\ {}^3G_3{}^o$	787.749	−2.560	−0.068	785.119	785.077		
65	$2s^2\ 2p^3\ 3d^1\ {}^3G_4{}^o$	789.467	−3.220	−0.066	786.182	786.135		
66	$2s^2\ 2p^3\ 3d^1\ {}^3D_2{}^o$	790.504	−2.820	−0.077	787.612	787.351		

Table 10.1 (continued)

Level No	Configurations	Energies (in Ryd.)				FAC	NIST	ΔE
		MCDF						
		DC	Briet	QED	Total			
67	$2s^2\ 2p^3\ 3d^1\ ^3F_3^o$	790.513	−3.050	−0.070	787.398	787.547		
68	$2s^2\ 2p^3\ 3d^1\ ^3P_1^o$	791.096	−2.890	−0.080	788.122	788.051		
69	$2s^2\ 2p^3\ 3d^1\ ^3F_2^o$	792.371	−2.160	−0.068	790.144	790.039		
70	$2s^2\ 2p^3\ 3d^1\ ^5D_4^o$	794.016	−2.550	−0.074	791.397	791.360		
71	$2s^2\ 2p^3\ 3d^1\ ^3D_1^o$	794.128	−2.160	−0.075	791.890	791.574		
72	$2s^2\ 2p^3\ 3d^1\ ^5D_3^o$	794.226	−2.550	−0.072	791.604	791.772		
73	$2s^2\ 2p^3\ 3d^1\ ^3D_1^o$	795.825	−2.530	−0.066	793.227	793.154		
74	$2s^2\ 2p^3\ 3d^1\ ^3F_4^o$	796.506	−3.250	−0.071	793.190	793.200		
75	$2s^2\ 2p^3\ 3d^1\ ^3G_5^o$	796.727	−3.340	−0.066	793.320	793.274		
76	$2s^2\ 2p^3\ 3d^1\ ^3D_2^o$	797.037	−2.450	−0.068	794.523	794.071		
77	$2s^2\ 2p^3\ 3d^1\ ^1S_0^o$	797.234	−3.070	−0.070	794.089	794.487		
78	$2s^2\ 2p^3\ 3d^1\ ^1P_1^o$	798.707	−2.980	−0.074	795.649	795.596		
79	$2s^2\ 2p^3\ 3d^1\ ^1F_3^o$	799.004	−3.050	−0.072	795.885	795.854		
80	$2s^2\ 2p^3\ 3d^1\ ^1D_2^o$	799.250	−3.080	−0.071	796.104	796.051		

Table 10.2 Comparison of Ex Ene (in Ryd.) for O-like W

Upper Level	Lower Level	GRASP	FAC	[22]	ΔE$_1$	ΔE$_2$
12	2	631.249	631.252	631.583	0.334	0.331
40	5	631.791	631.757	632.076	0.285	0.319
43	6	632.468	632.434	632.642	0.174	0.208
11	1	635.078	635.068	635.391	0.313	0.323
12	1	635.759	635.755	636.119	0.360	0.364
25	1	692.013	691.857	691.922	0.091	0.065

comparison to coulomb gauge. The authenticity of our results is verified from the unity or near to unity values of length and velocity form (leng/velo) ratios of absorption OSt which is tabulated (leng/velo) in the last column of Table 10.3. It can be deduced from the Table 10.3 that (leng/velo) is unity for almost ten E1 transitions from the ground state whereas leng/velo is near to unity for other listed transitions. It is reported that lowest 31 Electric Dipole transitions for O like W lies in SXRay range.

Table 10.3 Radiative data for O-like W from ground state

Transitions		Tr Wav (in Å)	Tr Prob (in s)	OSt	LSt (in a.u.)	len/vel
i	j					
1	5	6.845	1.0134E+13	7.1179E−02	8.0198E−03	1.00
1	6	6.539	1.8750E+13	7.2110E−02	7.7613E−03	1.00
1	9	3.803	8.9223E+10	1.1606E−04	7.2648E−06	0.83
1	11	1.435	1.1443E+14	3.5321E−02	8.3424E−04	1.00
1	12	1.433	1.8989E+14	3.5093E−02	8.2799E−04	1.00
1	19	1.335	1.3626E+14	3.6421E−02	8.0050E−04	0.98
1	20	1.334	2.8793E+13	1.0755E−02	2.3618E−04	0.99
1	22	1.334	2.7335E+14	4.3725E−02	9.5980E−04	0.98
1	24	1.319	1.0412E+15	2.7160E−01	5.8974E−03	0.99
1	25	1.317	2.3228E+15	8.4539E−01	1.8325E−02	0.99
1	26	1.315	1.2678E+14	1.9721E−02	4.2689E−04	0.97
1	27	1.237	2.4449E+13	5.6093E−03	1.1422E−04	0.98
1	28	1.236	5.0705E+13	6.9627E−03	1.4161E−04	0.99
1	29	1.234	4.3978E+13	1.4056E−02	2.8552E−04	0.97
1	30	1.233	2.3652E+13	5.3900E−03	1.0939E−04	0.98
1	32	1.227	2.7102E+11	3.6707E−05	7.4143E−07	0.92
1	44	1.180	2.1934E+14	4.5783E−02	8.8923E−04	1.00
1	45	1.180	5.4694E+14	1.5979E−01	3.1031E−03	1.00
1	54	1.168	7.0002E+13	8.5910E−03	1.6518E−04	1.00
1	56	1.168	6.4313E+14	7.8920E−02	1.5173E−03	1.00
1	57	1.168	4.5047E+14	9.2089E−02	1.7701E−03	1.00
1	61	1.162	4.7972E+13	5.8220E−03	1.1131E−04	0.97
1	63	1.161	7.5107E+13	1.5187E−02	2.9032E−04	0.98
1	64	1.161	2.6010E+14	7.3544E−02	1.4051E−03	0.99
1	66	1.157	1.4740E+15	2.9582E−01	5.6338E−03	0.98
1	67	1.157	1.4816E+15	4.1651E−01	7.9345E−03	0.99
1	68	1.156	1.5111E+15	1.8173E−01	3.4587E−03	0.98
1	69	1.153	6.4488E+13	1.2859E−02	2.4412E−04	0.99
1	71	1.151	1.9056E+13	2.2699E−03	4.2997E−05	0.96
1	72	1.151	3.2775E+11	9.1159E−05	1.7274E−06	0.94
1	73	1.149	2.2313E+13	2.6488E−03	5.0090E−05	1.00

10.5   Conclusion

The explanation of atomic structure calculations by theoretical models and subsequent assessment of computational predictions by experiment are correlated processes. In this research work the results obtained from GRASP and FAC computational codes have been evaluated and compared in selected case studies with the other work available including spectroscopic analysis of transitions occurring in the O like W. We have tabulated concise transition parameters of W LXVII and fine structure energies for lowest 80 levels. We have also reported the first 31 SXRay transitions and also presented the complete transition data. The integrity of the data set reported in this work is verified by precise values of leng/velo ratio gauge. We confirm that the data detailed in this paper will be beneficial in the interpretation of high-precision atomic calculations of compounded spectra of highly charged W-ions and in modelling of the radiation emission from tokamak plasmas and in cell biology.

References

1. R. Neu et al., Nucl. Fusion **45**, 209 (2005)
2. C. Biedermann, R. Radtke, R. Seidel, T. Pütterich. Phys. Scr., **T134**, 014026 (2009)
3. R. Causey, K. Wilson, T. Venhaus, W.R. Wampler, J. Nucl. Mater. **266–299**, 467 (1999)
4. B. Lipschultz, et al. MIT Plasma Science and Fusion Center, **RR-10–4** (2010)
5. A. Pospieszczyk, *Nuclear Fusion Research* (Springer, Berlin, 2006)
6. C. Biedermann, R. Radtke, R. Seidel, and T. Pütterich. Phys.Scr. **T134**, 014026 (2009)
7. C. Biedermann, R. Radtke, J.L. Schwob, P. Mandelbaum, R. Doron, T. Fuchs, G. Fußmann, Phys. Scr. T **92**, 85 (2001)
8. C. Biedermann, R. Radtke, R. Seidel, and E. Behar. J. Phys. Conf. Ser. **163**, 012034 (2009)
9. S.B. Utter, P. Beiersdorfer, and G.V. Brown. Phys. Rev. A **61**, 030503 (2000)
10. S.B. Utter, P. Beiersdorfer, E. Träbert, Can. J. Phys. **80**, 1503 (2002)
11. P. Neill, C. Harris, A.S. Safronova, S. Hamasha, S. Hansen, U.I. Safronova, P. Beiersdorfer, Can. J. Phys. **82**, 931 (2004)
12. A.S. Safronova, V.L. Kantsyrev, P. Neill, U.I. Safronova, D.A. Fedin, N.D. Ouart, M.F. Yilmaz, G. Osborne, I. Shrestha, K. Williamson, T. Hoppe, C. Harris, P. Beiersdorfer, S. Hansen, Can. J. Phys. **86**, 267 (2008)
13. Y. Ralchenko, J.N. Tan, J.D. Gillaspy, J.M. Pomeroy, and E. Silver. Phys. Rev. A **74**, 042514 (2006).
14. Y. Ralchenko, J. Reader, J.M. Pomeroy, J.N. Tan, J.D. Gillaspy, J. Phys. At. Mol. Opt. Phys. **40**, 3861 (2007)
15. Y. Ralchenko, I.N. Draganic, J.N. Tan, J.D. Gillaspy, J.M. Pomeroy, J. Reader, U. Feldman, G.E. Holland. J. Phys. At. Mol. Opt. Phys. **41**, 021003 (2008)
16. J.D. Gillaspy, I.N. Draganić, Y. Ralchenko, J. Reader, J.N. Tan, J.M. Pomeroy, and S.M. Brewer. Phys. Rev. A **80**, 010501 (2009)
17. T. Pütterich, R. Neu, C. Biedermann, R. Radtke, and the ASDEX Upgrade Team. J. Phys. At. Mol. Opt. Phys. **38**, 3071 (2005)

18. R. Neu, R. Dux, A. Kallenback, T. Pütterich, M. Balden, J.C. Fuchs, A. Hermann, C.F. Maggi, M. O'Mullane, R. Pugno, I. Radivojevic, V. Rohde, A.C.C. Sips, W. Suttrop, A. Whiteford, The ASDEX Upgrade Team. Nucl. Fusion **45**, 209 (2005)
19. R. Neu, K.B. Fournier, D. Bolshukhin, R. Dux, Phys. Scr. T **92**, 307 (2001)
20. M.F. Gu. Can. J. Phys. **86**, 675 (2008). Karol Kozio, Breit and QED contributions in atomic structure calculations of tungsten ions. J. Quant. Spectro. Radiat. Transfer (2020)
21. Kramida A, Ralchenko Yu, Reader J and NIST ASD Team 2014. http://physics.nist.gov/asd
22. P. Beiersdorfer, J.K. Lepson, M.B. Schneider, M.P. Bode. Phys. Rev. A **86**, 012509 (2012)

Chapter 11
To Study Temperature and Hydrostatic Pressure Effect on ORC for a Semi-parabolic 1-D InAs Excitonic System

Suman Dahiya, Siddhartha Lahon, and Rinku Sharma

Abstract   In the present paper, we studied the combined effect of hydrostatic pressure and temperature on ORC for a semi-parabolic 1-D InAs excitonic system is investigated under effective mass approximation and density matrix formalism is used to solve the Eigen function and Eigen energies. Effect of hydrostatic pressure and temperature on the OR has been studied for excitonic as well as without excitonic in the regime of strong confinement. The results showed a blue/red shift with application of hydrostatic pressure/temperature.

11.1   Introduction

As semiconductor nanomaterials have many potential applications in the field of electronics, photonics, and biological etc., hence they are provided with an exceptional consideration from the last few decades [1–4]. These nanostructures, especially quantum dots have been treated with special attention as they possess rare and unique electronic & optical properties. Quantum dots are considered as nano crystalline structures that are grown by using various physical & chemical methods.

Numerous investigations have been carried out to study the nonlinear optical properties of nanostructures under the effect of external factors such as lasers, spin, electric field, temperature etc. [5–8]. Effect of electron–hole correlation in quantum dots is also studied by many authors [3, 9, 10]. But in our sincere belief, there are no studies available on the effect of external factors in InAs semiconductor quantum dots.

In the present paper we carried out an investigation for the study of effect of tempt. and hydrost. pressure on the ORC of a 1-D InAs excitonic system in a semi-parabolic quantum dot. In the first section we present the theory including Hamiltonian, Eigen

S. Dahiya · R. Sharma (✉)
Department of Applied Physics, Delhi Technological University, New Delhi, Delhi 110042, India
e-mail: rinkusharma@dtu.ac.in

S. Lahon
Physics Department, Kirori Mal College, University of Delhi, New Delhi, Delhi 110007, India

functions, Eigen energies etc. In the next section we presented our results. In the final section we concluded our results.

11.2 Theory

Hamiltonian for an excitonic system with semi-parabolic confining potential with effective mass approximation in 1D QDs is given by [3, 8–10]:

$$H_{e1} = \frac{p_h^2}{2m_h^*(P, T)} + \frac{p_e^2}{2m_e^*(P, T)} + V(z_e) + V(z_h) - \frac{e^2}{\varepsilon|z_e - z_h|} \tag{11.1}$$

where $(z_e, z_h > 0)$.

The semi-parabolic potential is:

$$V(z_k) = \begin{cases} \frac{1}{2}m_i^*\omega_0^2 z_k^2, & z_k \geq 0, \\ \infty, & z_k \leq 0 \quad (k = e, h) \end{cases} \tag{11.2}$$

Effective mass of the electron–hole dependent on temperature and pressure for InAs semiconductor is given by [11–13]:

$$m_e^*(P, T) = m_o\left[1 + \frac{7510}{E_g(P, T) + 341} + \frac{15020}{E_g(P, T)}\right]^{-1} \tag{11.3}$$

$$m_h^*(P, T) = \left(0.09 - 0.20 \times 10^{-3}P - 3.55 \times 10^{-5}T\right)m_0 \tag{11.4}$$

$$\text{With } E_g(P, T) = \left[1519 - \frac{0.5405T^2}{T + 204} + 10.7\,P\right] \tag{11.5}$$

Here E_g is in meV, P is in "kbar" and T is in "Kelvin".

The Hamiltonian is segmented into two terms:

$$H_{e1} = H_{r1} + H_{c1} \tag{11.6}$$

$$H_{r1} = \frac{p^2}{2\mu} + \frac{1}{2}\mu\omega_0^2 z_{r1}^2 - \frac{e^2}{\varepsilon(P, T)|z_{r1}|} \tag{11.7}$$

$$and \quad H_{c1} = \frac{P^2}{2M_{T1}} + \frac{1}{2}M_{T1}\omega_0^2 Z_{T1}^2 \tag{11.8}$$

Eigen wavefunction and eigen energies are:

$$\phi_{k1}(Z_{T1}) = N_{k1} \exp\left(-\frac{1}{2}\alpha^2 Z_{T1}^2\right) H_{2k1+1}(\alpha Z_{T1}) \tag{11.9}$$

$$E_{k1} = \left(2k1 + \frac{3}{2}\right)\hbar\omega_0, \quad (k1 = 0, 1, 2, \ldots), \tag{11.10}$$

The nonlinear ORC in 1D semi-parabolic QD given for 2-level system is given as

$$\chi_0^{(2)} = 4\frac{\sigma_s}{\varepsilon_0 \hbar^2} M_{01}^2 \delta_{01} \times \frac{\omega_{01}^2\left(1 + \frac{\sigma_s}{T_2}\right) + \left(\omega^2 + \frac{1}{T_2^2}\right)\left(\frac{T_1}{T_2} - 1\right)}{\left[(\omega_{01} - \omega)^2 + \frac{1}{T_2^2}\right]\left[(\omega_{01} + \omega)^2 + \frac{1}{T_2^2}\right]} \tag{11.11}$$

11.3 Result

IaAs semiconductor material constants have been considered in our calculations where $T_1 = 1\,ps$ and $T_2 = 0.2\,ps$, and $m_e^* = 0.042m_0$, $m_h^* = 0.023m_0$ where m_0 is the mass of a free electron. σ_s is taken as $5 \times 10^{22}\,\mathrm{m}^{-3}$, $\varepsilon_r = 12.53$, and $I = 10^9$ W/m^2 [8, 13].

In Fig. 11.1, results are presented for both of the cases by considering EE as well as WEE on the SHG peaks when the temperature is varied from 10 to 100 K keeping pressure constant at 50 kbar. As we can observe a blue shift in the peaks after increasing the temperature in both the cases but it is more significant in the case of excitonic effect. Also, we can observe peak height is also increasing as temperature is affecting energy band gap.

In Fig. 11.2, we presented the results for EE as well as WEE on the SHG peaks when pressure is varied from 10 to 100 kbar keeping temperature constant at 50 K. A
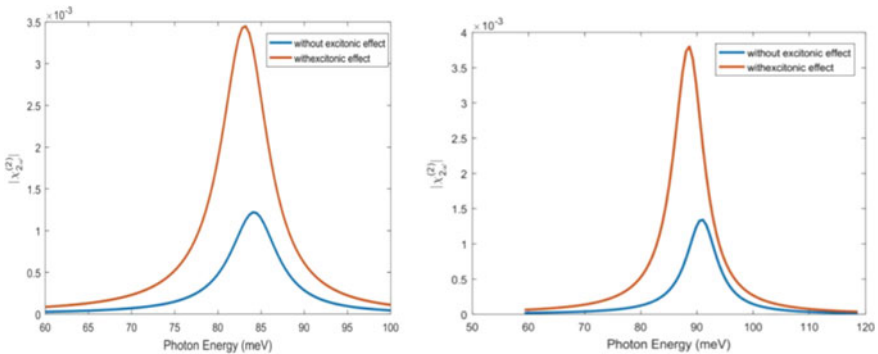
Fig. 11.1 ORC as a function of incident photon energy for T = 10 and 100 K keeping P constant at P = 50 kbar
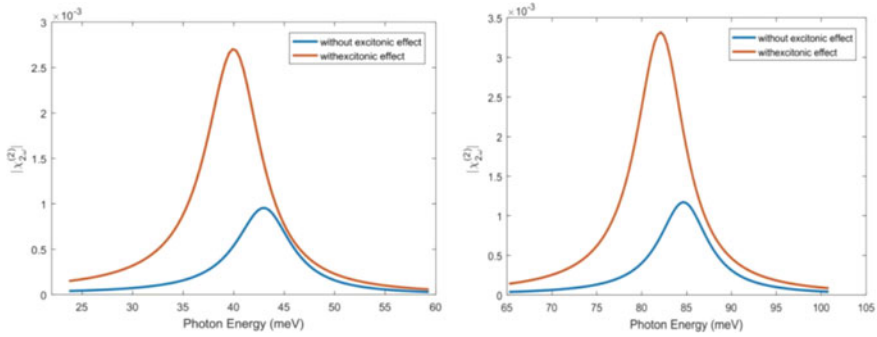
Fig. 11.2 ORC as a function of incident photon energy for P = 10 and 100 kbar keeping T constant at T = 50 K

red shift can be observed with decrease in size of the peaks with increase in pressure as effective is depending on pressure.

11.4 Conclusion

Combined effect of correlation of electron–hole pair with external factors such as temperature, and hydrostatic pressure on ORC in a 1-D semi-parabolic InAs QDs has been studied under effective mass approximation and by using density matrix approach eigen energies and eigenfunction in the regime of strong confinement has been calculated. The results are showing that the ORC is extensively enlarged when electron hole pair correlation has been considered in the QDs. It is also noticed that inclusion of hydrostatic pressure and temperature affected the ORC peak positions in a very significant way as changing the value of temperature and hydrostatic pressure induced a blue shift/red shift.

References

1. O. Salata, J. Nanobiotechnol. **2**, 1–6 (2004)
2. D. Mocatta, G. Cohen, J. Schattner, O. Millo, E. Rabani, U. Banin, Science **332**, 77–81 (2011)
3. D. Bejan, Eur. Phys. J. Plus **132**, 102 (2017)
4. I. Karabulut, H. Safak, M. Tomak, Solid State Commun. **135**, 735 (2005)
5. J.-H. Yuan, Y. Zhang, H. Mo, N. Chen, Z.-H. Zhang, Phys. E **77**, 102 (2016)
6. C.M. Duque, M.E. Mora-Ramos, C.A. Duque, J Nanopart Res. **13**, 6103–6112 (2011)
7. N. Eseanu, Phys. Lett. A **374**, 1278 (2010)
8. Y.-B. Yu, S.-N. Zhu, K.-X. Guo, Phys. Lett. A **175**, 335 (2005)
9. S. Antil, M. Kumar, S. Lahon, A.S. Maan, Opt.—Int. J. Light Electron Opt. **176**, 278–286 (2019)
10. S. Dahiya, S. Lahon, R. Sharma, Phys. E **118** 113918 (2020)

11. C.A. Duque, N. Porras-Montenegro, Z. Barticevic, M. Pacheco, L.E. Oliveira, J. Phys.: Condens. Matter **18**, 1877–1884 (2006)
12. J. Wu et al., Small band gap bowing in In1-xGaxN alloys. Appl. Phys. Lett. **80**, 4741 (2002)
13. I. Vurgaftman, J.R. Meyer, Band parameters for nitrogen-containing semiconductors. J. Appl. Phys. **94**, 3675–3696 (2003)

Chapter 12
Numerical Modeling and Analysis of GAP-Se Chalcogenide Based Rib Waveguide for Nonlinear Applications

Rohan Sharma, Surleen Kaur, Pooja Chauhan, and Ajeet Kumar

Abstract We report a design of rib waveguide composed of $GeSe_2$-As_2Se_3-PbSe and MgF_2 for application in nonlinear photonic devices. We have implemented full vectorial finite element method for modal analysis of the waveguide. The proposed waveguide exhibits nonlinear coefficient of 666.9 W^{-1} km^{-1} and effective mode area of 2.17 μm^2 at 3100 nm pump wavelength source, along with a supercontinuum spectrum spanning 1–10 μm in 7 mm propagation length. Such chalcogenide-based rib waveguides can be fabricated with high control and lower losses enhancing their applications in multitude of electronic process.

12.1 Introduction

Optical waveguides are devices that confine and propagate electromagnetic radiation through them. Among different designs of optical waveguides, the rib waveguides or channel waveguides offer lower fiber coupling loss, lower propagation losses and symmetric mode profiles [1–4]. Rib waveguides composed of nonlinear material exhibiting high nonlinearity have potential uses in diverse fields of telecommunication, sensing, medical imaging and laser technologies [1, 3–9]. Thus, there is an ever-increasing demand for nonlinear optical devices in industry, research, manufacturing and academia.

Silica, fluorides and chalcogenides materials have been analyzed for nonlinear applications due to their high Kerr nonlinearity and response time lesser than 100 fs making them suitable for photonic applications [6, 7, 9, 10]. However, in mid-infrared (M-IR) region, silica waveguides offer higher losses and fail to exhibit supercontinuum generation (SCG) [7]. Chalcogenides offer higher refractive index, lower weight and higher transmission in the M-IR spectrum. Additionally, there are plenty of fabrication techniques to create such waveguides. Both lithographic and deposition techniques can be used to fabricate rib optical waveguides. Some commonly used techniques are thermal nano-imprint lithography, photolithography, sputtering,

R. Sharma (✉) · S. Kaur · P. Chauhan · A. Kumar
Advanced Photonics Simulation Research Laboratory, Department of Applied Physics, Delhi Technological University, New Delhi 110042, India

chemical vapour deposition and ion etching techniques. [2, 3, 11]. Recently, C. Goncalves et al. introduced a novel multicomponent chalcogenide glasses $GeSe_2$-As_2Se_3-PbSe (GAP-Se) [5] for applications in broadband SCG which has been studied as the primary material for the core of the buried rib waveguide in our study. Significant work has been carried by Karim et al. for M-IR SCG with rib waveguide composed of $Ge_{11.5}As_{24}S_{64.5}$ and MgF_2 glass using lower power femtosecond pulses pumped at 3.1 μm producing a spectrum spanning 2–6 μm [4]. Similar studies on the numerical analysis of photonic crystal fiber for SCG has been reported by Chauhan et al. [12, 13].

We report the numerical modeling and analysis of the rib waveguide structure composed of GAP-Se and MgF_2 glasses for nonlinear applications by optimizing waveguide geometry by dispersion engineering. The performance of the waveguide is evaluated by its effective mode area, nonlinearity coefficient and chromatic dispersion curve using COMSOL. To validate the nonlinear behaviour and associated applications, the proposed waveguide is simulated for SCG through injection of secant hyperbolic shaped input femtosecond laser pulse of 85 fs duration with peak power 10 kW in a 7 mm long waveguide using MATLAB. Due to its nonlinear behaviour, such a waveguide in the GAP-Se chalcogenide glass system can be proven effective for nonlinear applications in mid infrared region.

12.2   Waveguide Design

Figure 12.1a depicts the transverse cross section picture of the proposed buried rib waveguide which is parameterized to facilitate control over dispersion during the simulations. The core of the waveguide is GAP-Se chalcogenide glass as shown in blue and the substrate (or cladding) is made of MgF_2 glass as shown in gray. The maximum height of the core is defined by parameter h, the core trench height is defined by parameter b and the width of the core by parameter a. The dimensions of the proposed waveguide are given in Table 12.1.
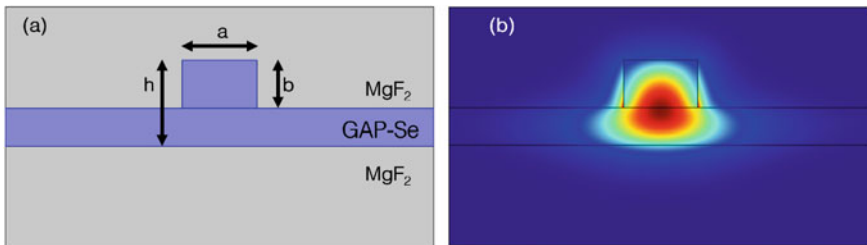
Fig. 12.1   a Cross section of parameterized optical buried rib waveguide with labelled composition. **b** Normalized transverse electric field distribution in waveguide at pump wavelength of 3.1 μm

Table 12.1 Optimized parameters of the proposed GAP-Se chalcogenide-based waveguide

Parameter	a (μm)	b (μm)	h (μm)
Value	1.4	0.9	1.6

12.3 Methodology

To study the linear and nonlinear behavior of the proposed optical waveguide, multiple numerical simulations were performed to evaluate the effective area, effective refractive index, nonlinear coefficient and dispersion profile in the fundamental mode to achieve flat chromatic dispersion curve in the M-IR region. Our simulation is carried out using the Modal Analysis in the Electromagnetic wave frequency domain (EWFD) in the COMSOL Multiphysics® software, which solved the eigenvalue problem for the Maxwell's electromagnetic equations employing full vectorial finite element method (FEM) approach to yield the effective mode index of the fundamental propagating mode as well as the effective mode area at different wavelengths. The wavelength dependent linear refractive indices of GAP-Se and MgF$_2$ glasses have been calculated using the following Sellmeier equation given in Eq. 12.1 are given in Table 12.2 as follows:

$$n^2(\lambda) = A_0 + \sum_{n=1}^{3} \frac{A_n \lambda^2}{\lambda^2 - B_n^2} \tag{12.1}$$

The effective mode area in an optical waveguide is the area occupied by the electric field of the propagating fundamental mode and considers the extension of the mode into the cladding region as well. It is inversely proportional to the nonlinearity index given in Eq. 12.4. Equation 12.2 dictates the formula used to calculate effective mode area in COMSOL [8]:

$$A_{eff} = \frac{\left(\iint_{-\infty}^{\infty} |E(x, y)|^2 dxdy \right)^2}{\iint_{-\infty}^{\infty} |E(x, y)|^4 dxdy} \tag{12.2}$$

Table 12.2 Sellmeier coefficients for GAP-Se and MgF$_2$ with reference mentioned in brackets

Coefficient index	GAP-Se [5]	MgF$_2$ [14]
A_0	−20.6611	0
A_1	28.5635	0.48755708
A_2	10.4782	0.39875031
A_3	–	2.3120353
B_1	0.2312	0.0433840
B_2	90.4186	0.09461442
B_3	–	23.793604

The group velocity dispersion (GVD), also known as waveguide chromatic dispersion, is critical in nonlinear processes as it pertains to the shift of the effective mode index of the waveguide with frequency of incident light. Due to the variation in effective mode index, different spectral components are delayed by different times after propagating a certain distance. For nonlinear applications, it is desirable to achieve near zero dispersion values. Chromatic dispersion (D) depends on the waveguide material composition as well as the geometry and is calculated using the following relation [8]:

$$D = -\frac{\lambda}{c} \frac{d^2 \mathrm{Re}(n_{eff})}{d\lambda^2}$$

(12.3)

where c is the velocity of light in free space, λ is the operating wavelength and $\mathrm{Re}(n_{eff})$ is the real part of the effective mode index. Further, Kerr nonlinearity of an optical waveguide is calculated by a nonlinear coefficient γ which is defined as [8]:

$$\gamma = \frac{n_2 \omega_0}{c A_{eff}}$$

(12.4)

where $n_2 = 7.14 \times 10^{-19}$ m²/W is the nonlinear refractive index for GAP-Se chalcogenide glass taken from Ref. [5]. For the simulation of SCG from the proposed waveguide design, generalized nonlinear Schrodinger wave equation (GNLSE) is emulated in MATLAB using Split-Step Fourier Method. Selection of the laser pump wavelength is based on pump wavelength near ZDW, low pulse width, high peak power and market availability. A secant hyperbolic femtosecond pulse is incident to the medium for the simulation of SCG.

12.4   Results and Discussion

Interesting results are obtained during the variation of the parameters *a, b & h* one-at-a-time (OAT) while keeping others constant. (Fig. 12.2a–c). Selection of the optimum design was based on the chromatic dispersion curve being flat, exhibiting zero dispersion at multiple wavelengths and normal dispersion in M-IR region. In the variational analysis, it is found that the geometrical parameters strongly affect the dispersion characteristics of the waveguide. Increasing core width '*a*' from 1.2 to 1.4 µm as well as increasing core trench height '*b*' from 0.7 to 1.1 µm leads to dispersion curve shifting to positive dispersion region, while increasing core maximum height '*h*' from 1.4 to 1.8 µm shifts the curve to negative dispersion.

The optimized dispersion plot for parameters is displayed in Fig. 12.2d. The dispersion profile shown in Fig. 12.2d exhibits a small positive dispersion region between 3318 and 3684 nm which acts as a potential barrier to an optical soliton and leads to stimulated Raman self-scattering can be fully utilized in the applications of
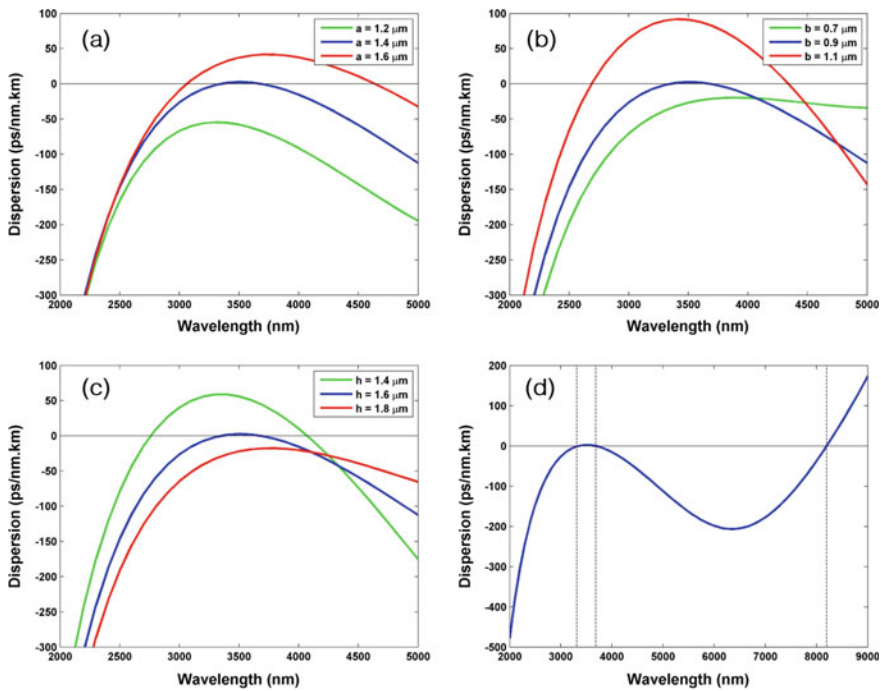
Fig. 12.2 Effect on the chromatic dispersion due to variation of **a** core width, **b** core trench height and **c** core maximum height, **d** chromatic dispersion curve of optimized waveguide with three ZDWs (vertical lines) at 3318, 3684 and 8200 nm

supercontinuum generation. Three zero dispersion wavelengths (ZDW) are encountered at 3318, 3684 and 8200 nm. The anomalous region begins after 8200 nm ZDW towards longer wavelengths.

Further reduction in the core size of the waveguide results in lower mode area and higher nonlinearity at the expense of failing to achieve ZDW, poorer chromatic dispersion curve and exceeding difficulty in fabrication. From Fig. 12.3, it is also observed that the nonlinear coefficient decreases with increasing wavelength, while the effective mode area increases. The proposed waveguide bears the materials and size order that can be fabricated effectively. The optical parameters of the proposed design are given in Table 12.3. The waveguide exhibits a high nonlinearity coefficient of 666.9 W^{-1} km^{-1} and simultaneously nearly zero dispersion of -15.21 ps/nm km at the pump wavelength.

For design validation, the waveguide is simulated for SCG using 85 fs secant hyperbolic pulse of peak power 10 kW at 3100 nm pump wavelength. The spectral evolution of an optical soliton pulse is given in Fig. 12.4. The spectral broadening occurs rapidly in the proposed design starting from 1 mm propagation length and gradually transfers power to longer wavelengths. The normalized intensity supercontinuum spectrum is shown in Fig. 12.5. The waveguide produces a spectrum span-
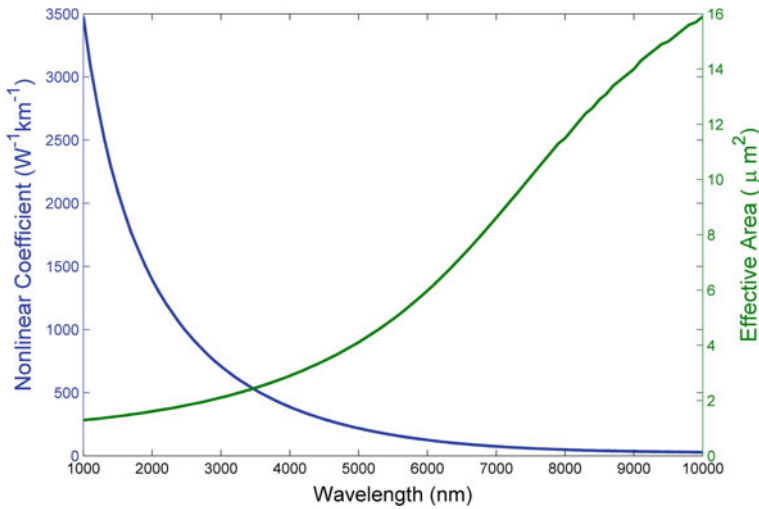
Fig. 12.3 Variation of nonlinear coefficient (blue curve) and effective mode area (green curve) with wavelength

Table 12.3 Waveguide optical characteristic parameters at pump wavelength

Parameter	n_{eff}	A_{eff}	γ	D
Value at $\lambda = 3.1\ \mu m$	2.594	2.17 μm^2	666.9 $W^{-1}\ km^{-1}$	-15.21 ps/nm km
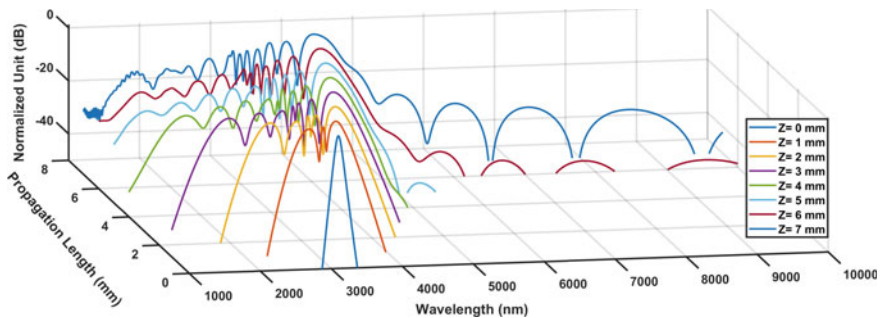
Fig. 12.4 Supercontinuum spectrum inside proposed waveguide at different propagation length

ning 1–10 μm in just 7 mm propagation length. The continuous spectrum is shown till −50 dB power levels. Due to absorption and inhomogeneous frequency dependent dispersive wave propagation, some wavelength regions lack sufficient power. A trade-off has been made to maximize the spectrum with propagation distance while maintaining sufficient optical output power. Since exhibiting SCG is an indication of highly nonlinear behaviour of a waveguide, such a broad spectrum is highly favorable
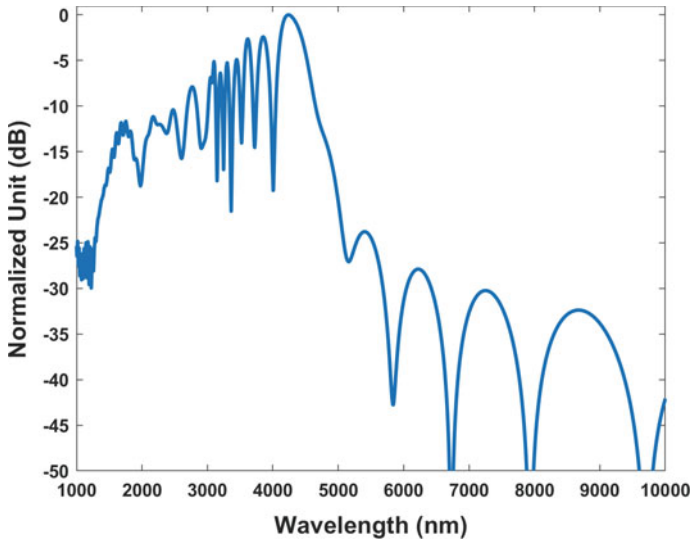
Fig. 12.5 Normalized intensity supercontinuum spectrum at 7 mm propagation

for nonlinear applications in M-IR region including optical coherence tomography, sensing, mid infrared light source and other nonlinear applications.

12.5 Conclusion

We propose a design of buried rib waveguide structure composed of $GeSe_2$-As_2Se_3-PbSe (GAP-Se) and MgF_2 glass for nonlinear optical applications in the M-IR wavelength region. The waveguide offers three zero dispersion wavelengths in the mid-infrared region at 3314, 3684, and 8200 nm, showing low chromatic dispersion of -15.21 ps/nm km, high nonlinear coefficient of 666.9 W^{-1} km^{-1} and low effective mode area of 2.17 μm^2 at 3.1 μm pump wavelength. To validate the nonlinear behaviour, the proposed waveguide is simulated for supercontinuum generation yielding a spectrum spanning 1–10 μm in just 7 mm waveguide length when injected with 85 fs pulse width with peak power 10 kW. Such a waveguide offers potential nonlinear applications in M-IR region such as optical coherence tomography, sensing and broadband light source.

References

1. A. Dutta, B. Deka, P.P. Sahu, *Planar Waveguide Optical Sensors* (Springer Science and Business Media LLC, 2016)
2. N. Takato, M. Yam, M. Kawachi, Low-loss high-silica embedded channel waveguides. Elecrrorl. Lett. **22**, 321–322 (1986)
3. T. Han, S. Madden, D. Bulla, B.L. Davies, Low loss chalcogenide glass waveguides by thermal nano-imprint lithography. Opt. Express **18**(18), 19286–19291 (2010)
4. M.R. Karim, B.M.A. Rahman, Govind P. Agrawal, Mid-infrared supercontinuum generation using dispersion-engineered $Ge_{11.5}As_{24}Se_{64.5}$ chalcogenide channel waveguide. Opt. Express **23**(5), 6903–6914 (2015)
5. C. Goncalves, M. Kang, B. Sohn, G. Yin, J. Hu, D.T.H. Tan, K. Richardson, New candidate multicomponent chalcogenide glasses for supercontinuum generation. Appl. Sci. **2018**(8), 2082 (2018)
6. J.M. Harbold, F.O. Ilday, F.W. Wise, J.S. Sanghera, V.Q. Nguyen, L.B. Shaw, I.D. Aggarwal, Highly nonlinear As-S-Se glasses for all-optical switching. Opt. Lett. **27**, 119–121 (2002)
7. G.P. Agrawal, *Nonlinear Fiber Optics*, 3rd edn. (Academic Press, 2001)
8. G.P. Agrawal, *Applications of Nonlinear Fiber Optics* (Academic Press, 2001)
9. R.E. Slusher, G. Lenz, J. Hodelin, J. Sanghera, L.B. Shaw, I.D. Aggarwal, Large Raman gain and nonlinear phase shifts in high-purity As_2Se_3 chalcogenide fibers. J. Opt. Soc. Am. B **21**, 1146–1155 (2004)
10. J.M. Dudley, G. Genty, S. Coen, Supercontinuum generation in photonic crystal fiber. Rev. Mod. Phys. **78**, 1135–1184 (2006)
11. M. El-Amraoui, G. Gadret, J.C. Jules, J. Fatome, C. Fortier, J. Troles, Microstructured chalcogenide optical fibers from As_2S_3 glass: towards new IR broadband sources. Opt. Express **18**, 26655–26665 (2010)
12. P. Chauhan, A. Kumar, Y. Kalra, Mid-infrared broadband supercontinuum generation in a highly nonlinear rectangular core chalcogenide photonic crystal fiber. Opt. Fiber Technol. **46**, 174–178 (2018)
13. P. Chauhan, A. Kumar, Y. Kalra, T.S. Saini, Design and analysis of photonic crystal fiber in Ga-Sb-S chalcogenide glass for nonlinear applications, in AIP Conference Proceedings 2009, 020047 (2018)
14. M.J. Dodge. Refractive properties of magnesium fluoride. Appl. Opt. **23** (1984)

Chapter 13
Nanodiamonds—Synthesis Techniques, Properties and Applications in Photovoltaics

Sonakshi Saini, Sakshi Sharma, Maya Khangembam, and Vinod Singh

Abstract The age of nanoscience and technology has ushered in a whole range of technological innovations that provide varied real-world applications. The focus of this paper is on nanodiamonds, which continue to gather research interest all over the world, owing to their unique properties that can be tailored as per the specific requirements of the field of application. This paper reviews the various commonly used methods of synthesizing nanodiamonds-namely detonation, CVD and laser ablation techniques, along with their electronic and optical properties as well as their specific application in photovoltaic devices. Although nanodiamonds can serve in diverse possible applications, their inclusion in optoelectronic devices in various forms has reportedly resulted in enhanced efficiencies over traditional silicon solar cells. This paper presents such findings to highlight improvements in energy harnessing capability.

13.1 Introduction

Nanodiamonds (ND) are zero dimensional carbon nanomaterial, approximately 2–8 nm in diameter. They may contain both sp2 and sp3 bonds. They have been studied and developed since many years using various techniques to utilise their unique properties that are being harnessed for real-life applications. They are about 50 times as hard as titanium, hence acting as excellent cutting tools. They are chemically inert, which makes them attractive for biological applications. Nanodiamonds that have small grain sizes display excellent photoluminescence. They can also be used to improve thermal conductivity of a material.

S. Saini · S. Sharma · M. Khangembam · V. Singh (✉)
Department of Applied Physics, Delhi Technological University, New Delhi, Delhi, India
e-mail: vinodsingh@dtu.ac.in

13.2   Synthesis

13.2.1   Detonation Technique

The detonation method is most popularly used for commercial purposes. This technique for fabricating nanodiamonds was first performed by a group of scientists in 1963 in the (then) USSR, including V. V. Danilenko, K. V. Volvov and V. I. Elin. This was an accidental discovery as the scientists were focused on studying the process of synthesis of diamonds by using shock compression method on graphite and carbon black [1]. Empirical and theoretical data has shown that free carbon during detonation process, which is performed in an experimental setup of negative oxygen balance, condenses in a liquid or diamond phase. The rate of graphitization of diamond has been shown to depend strongly on temperature [2].

Detonation technique is carried out in a closed chamber, where the atmosphere is devoid of oxygen. A controlled, explosive mixture of the compounds trinitrotoluene (TNT) and hexogen (RDX) produces a soot, which results in single crystal diamond nanoparticles. The nanodiamond yield depends on the process parameters, including the heating capacity of the coolant used in the detonation chamber. The resultant soot must be purified and treated to get rid of other unwanted carbon species, de-agglomerations and metal impurities present in it. The yield is affected by both external factors related to the detonation process inside the chamber) as well as by internal factors (such as mass, shape, density and chemical composition) [3, 4].

Experimental techniques utilising TEM and XRD indicate a perfect crystalline structure of the diamond nanokernel (grain size of around 5 nm), surrounded by an impurity shell. The grains are unstable and spontaneously form micrometer-sized clusters. An impurity subsystem is formed, which determines the chemical and physical properties of the obtained nanodiamond [5, 6] (Fig. 13.1).

13.2.2   Chemical Vapour Deposition (CVD)

This technique involves the dissociation of a gas precursor, which consists of carbon, on a solid surface, at a moderate temperature between 500 and 1200 °C. If a foreign substrate is used, nucleation occurs for nanodiamonds to be formed. A high concentration of hydrogen gas is used in this process, along with a hydrocarbon gas, such as methane. The primary benefit offered by this technique is that it allows thin films or coatings of diamond nanoparticles of varying grain sizes to be obtained, depending on whether the process conditions are optimum or not. Further, the composition and structure of nanocrystalline diamond (NCD) films formed also vary, depending on nucleation and growth conditions. The resulting film, depending on the grain size and the percentage of sp3/sp2 bonded carbon present, may be poly, nano or ultra-crystalline. This method was first performed at the Argonne National Laboratory by a group of scientists, headed by D. M. Gruen. UNCD (Ultracrystalline nanodiamond)
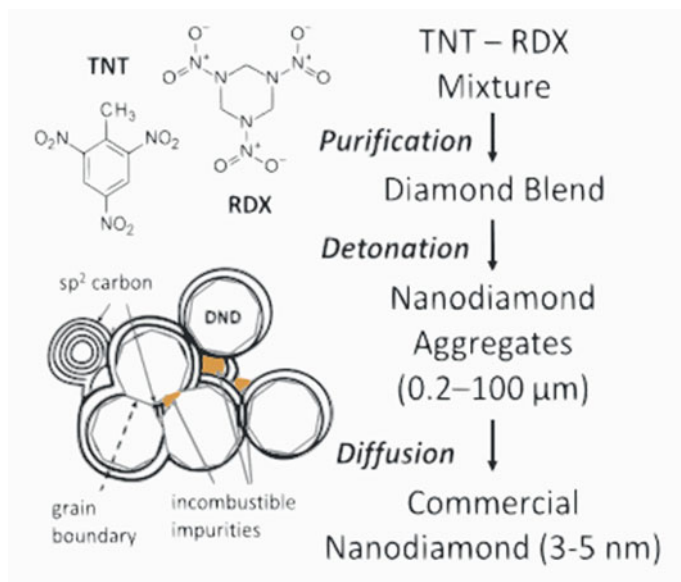
Fig. 13.1 Synthesis of nanodiamonds through detonation technique

thin films possess extremely low grain dimensions and are grown in a hydrogen-poor and argon-rich environment, having a grain size of about 2–5 nm in size [7].

Diamond is also often doped during the CVD process to alter its properties for the desired specific application. Boron is often used as a dopant, particularly for applications in electrochemistry, and is associated with superconductivity in nanodiamond films [8]. Nitrogen may be doped to induce conductivity. Boron and Nitrogen codoped Nanodiamond (BND) has been shown to possess superior current density and peak potential, as compared to only B or N doped nanodiamond, to function as a metal free catalyst having applications for renewable energy [9]. Metals may be used too and depending on the dopant used, the film will display metal-like or semiconducting electrical properties.

PECVD (Plasma Enhanced CVD) method utilises plasma to produce atomic hydrogen and carbon precursors to grow nanodiamonds, by electron impact dissociation processes. This process allows lower substrate temperatures, shorter processing time and greater control over the structure of the film hence produced. The absolute concentrations of atomic hydrogen and neutral radicals produced depends on the plasma pressure. Higher growth rate has been reported when high-pressure plasma is used. Among the PECVD methods currently being used to fabricate nanodiamond films, MWCVD (Microwave Plasma assisted CVD) is one of the most widely used ones. It offers significant advantages, including preventing unwanted carbon deposition in the chamber and lesser contamination of the films. MWCVD is used for both research as well as industrial purposes [10].

Further, thermal CVD, combustion flame assisted CVD and DC jet spray CVD are also used based on specific requirements (Fig. 13.2).

The Pulsed Laser Ablation (PLA) is a method used to produce diamond nanoparticles in a liquid or liquid–solid interfaces, at room temperature and standard pressure conditions. Microcrystalline graphite powder is suspended in a circulating liquid medium, bombarded by laser and the resultant product is then purified to obtain diamond nanopowders. This process also opens the possibility of self-assembly of surface nanostructures [11]. The advantages of using this technique include high reproducibility, high purity and high stability over a range of pH values of the nanodiamonds so obtained, having various applications, especially in nanomedicine (Fig. 13.3).
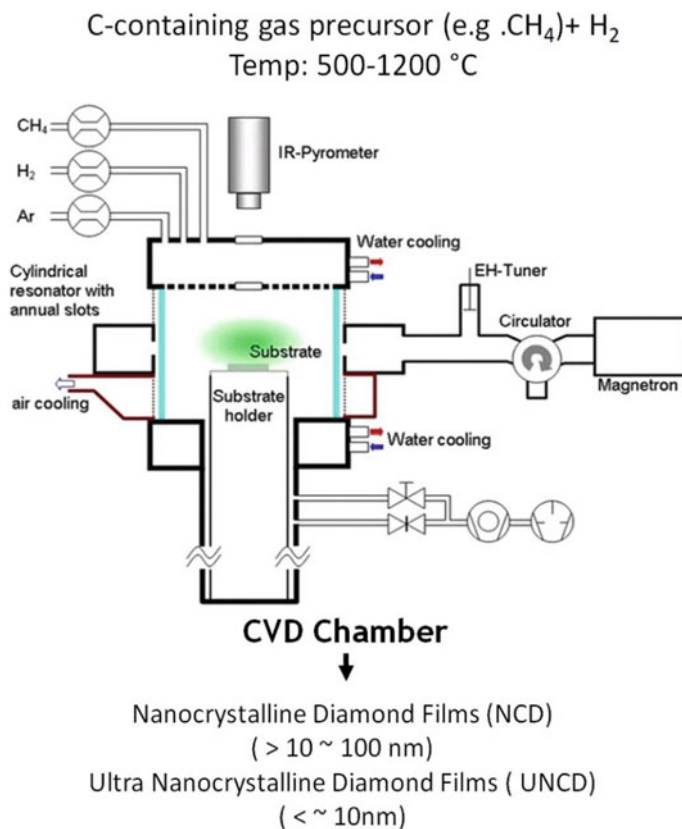
Fig. 13.2 CVD apparatus to produce NCD and UNCD films. From Gottlieb, S., Wöhrl, N., Schulz, S. et al. Simultaneous synthesis of nanodiamonds and graphene via plasma enhanced chemical vapor deposition (MW PE-CVD) on copper. SpringerPlus 5, 568 (2016). Used under CC BY 4.0 license
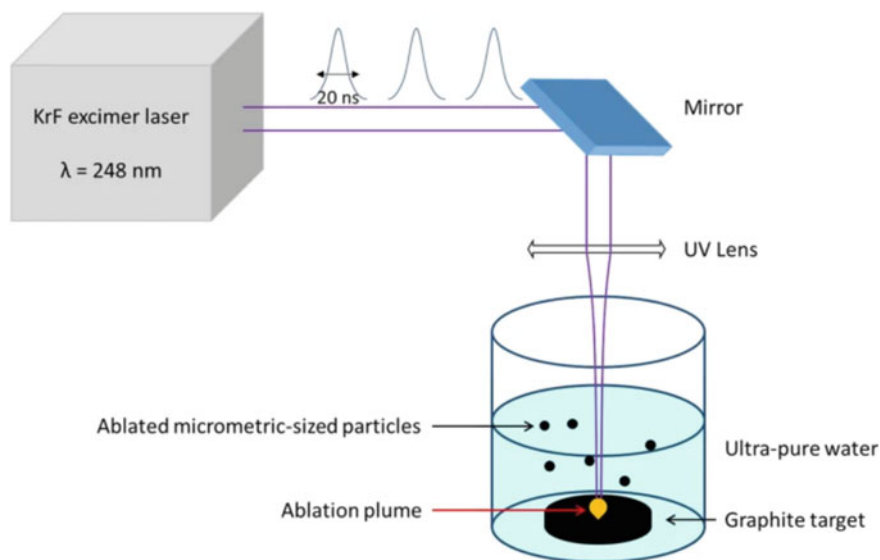
Fig. 13.3 Setup of CPLA process. The UV laser output is focused through a quartz lens (focal length f = 40 cm) and irradiates the pyrolytic graphite target. Ablated particles are suspended in water. From Gorrini, F. et al., 'On the thermodynamic path enabling a room-temperature, laser-assisted graphite to nanodiamond transformation", Sci Rep 6, 35244 (2016). Used under CC BY 4.0 license

13.3 Properties of Nanodiamonds

13.3.1 Electronic

The range of quantum confinement effects in nanodiamonds has long been a source of controversy with studies observing quantum confinement effects in nanodiamonds upto a diameter of 27 and 4 nm, while other studies, done on small nanodiamond particles of diameter less than 1.5 nm, have observed that the effects of quantum confinement persist up to 1 nm, after which the band gap decreases to less than the band gap of bulk diamond and the effects disappear. This was also observed by Raty et al. who calculated the relation between optical bandgap of diamondoids and their sizes using time-dependent and time-independent density-functional theory. They also showed in their calculations that the gap in diamondoids of sizes 1–1.5 nm which is less than bandgap of bulk diamond. QMC and DFT calculations performed confirm that the quantum confinement effects observed disappear when the nanoparticles have size greater than 1 nm [12]. It was also calculated that nanoparticles of sizes up to 1 nm have negative electron affinity and an exciton binding energy that is anomalously small.
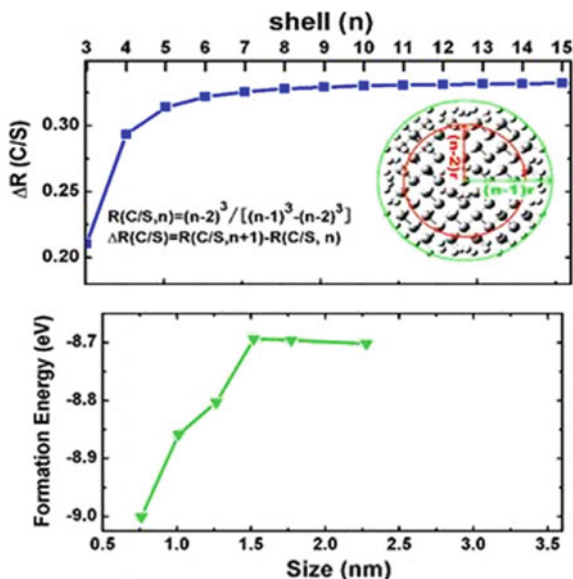
Jiang et al. observed that quantum confinement effects and hence electronic properties observed in nanodiamonds were not only dependent on the total number of atoms but also to the ratio of atoms in the inner core of the cluster to the number of atoms in the outer shell [13]. The ratio of core-to-shell was observed to change fast for nanodiamond clusters having diameter less than 1.5 nm while it saturated for clusters with diameters 1.5 nm and above. Evolution of electronic properties ND clusters smaller than 1.5 nm was found to deviate from the conventional models on quantum confinement (Fig. 13.4).

Both NCD and UNCD films are metallically conductive and their conductivity can be enhanced by various dopants and dopant concentrations. Studies conducted using spectrally resolved photoconductivity and photothermal deflection spectroscopy have revealed that doping with nitrogen atoms leads to enhancement in conductivity caused by broadening of π and π^* states introduced into the band gap by sp2-bonded atoms at the grain boundary. N-type conductivity with mobility values $1.5 \, cm^2 \, V^{-1} \, s^{-1}$ as well as a decrease in thermal activation energy due to nitrogen addition at gas phase has been observed. It is theorised that the observations are due to π-bonded atoms at the grain boundaries causing an increase in the density of states near the Fermi level [14]. Studies on boron doped NCD thin films has shown that for sufficiently high boron concentrations, although initially the NCD film exhibits positive magnetoresistance at ~4 K, it becomes superconductive at a further lower temperature of ~2 K43. Highly nitrogen doped UNCD films have been shown to exhibit high conductivity of around $1.4 \times 104 \, Sm^{-1}$ while negative resistance of upto 22% at 8 T has been observed at the temperatures of 1.28–3.8 K which has been attributed to confinement of electron transport to the grain boundaries [15] (Fig. 13.5).
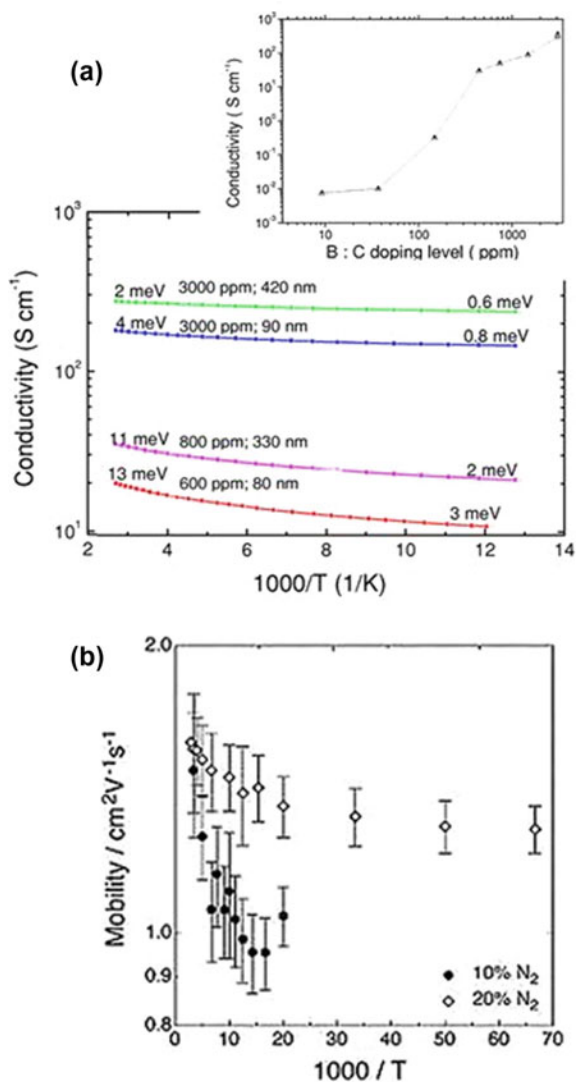
Fig. 13.5 Conductivity in doped nanodiamond films: **a** Electrical conductivity versus (1000/T) of different boron-doped NCD films. The inset is conductivity at room temperature versus different boron:carbon doping ratios. From Nesládek, M. et al., Appl. Phys. Lett. 88, (2006). **b** Hall mobilities versus temperature in a nitrogen-doped UNCD. From Williams, Curat et al., Appl. Phys. Lett., 85, (2004). Reprinted with permission

13.3.2 *Optical*

NDs have highly useful optical properties such as transparency, higher refractive index, greater range of visible wavelength, fluorescence etc. NCD thin films have a greater transparency than UNCD films. Undoped NCD shows a high degree of transparency and an overall lower absorption coefficient while undoped UNCD is highly absorbing. The greater absorption coefficient of UNCD has been suggested to be due to its larger grain boundary volume fraction caused by optical absorption by sp2 carbon at grain boundaries which are present in both UNCDs and NCDs [16]. Addition of nitrogen results in an increase of grain boundary volume fraction as well as sp2 carbon density of states and hence an increase in optical absorption. Similarly, data from Raman spectroscopy has revealed that boron doping in NCD causes optically transparency due to low concentrations of sp2 carbon [17].

Cheng Fu et al. [18] observed exceptional photostability of fluorescent NDs laser excitation of up to 1 MW/cm^2 and that even after immobilization of large biomolecules on its surface the fluorescence brightness remained almost constant. They also found the photostability of nanodiamonds to be size-independent. Studies done on SiV centres in nanodiamonds grown through CVD method have given linewidths as narrow as 325 and 360 MHz and absolute photostability of the emitters even when excited above saturation [19]. Tran and others observed solid-state single-photon emitters embedded in CVD diamond and found it to be optically stable when placed under resonant excitation of low power and observed that the ZPL was blue shifted as the excitation power was increased [20].

The past few decades have seen a tremendous increase of interest in crystal defects in diamond due to their stable nature and interesting optical properties which has led to their consideration for a number of applications. Although most studies about the optical properties of diamond have been done on bulk diamond, colour centres and fluorescence in nanodiamonds has recently become an active research area. Crystal defects in nanocrystals have been observed to show unlimited photostability and low cytotoxicity. The fluorescence from single nitrogen-vacancy centres can be efficiently collected due to photon antibunching almost free of background light and a larger lifetime of the NV centres than that in bulk diamonds, as a result of different surrounding refractive index [21, 22]. Some crystal defects, for example the NV centres, have spin states sensitive to local environmental conditions and thus have the capability to detect locally and thus be used to calculate a number of physical quantities, such as magnetic and electric fields. Fluorescence in nanodiamonds can also be diamond unrelated such as those emitted by the outer surface amorphous carbon layers of the nanodiamond and graphite shells which can emit fluorescence bright enough to suppress fluorescence from the colour centres. Particularly in DNDs this surface fluorescence observed can overshadow the colour-centre fluorescence.

NV centres are the most common defects in diamond due to nitrogen being a prominent impurity. The NV centre can exist as either in its ground state, NV0, with zero phonon line emission wavelength of 575 nm or an anionic state NV– which has a different ZPL wavelength of 638 nm. The NV–state has been observed to be the more prevalent stable ground-state electronic configuration. Production of commercial quantities of NV centres containing nanodiamonds of sizes 100 nm and below has been done by irradiation of the nanodiamonds with He ions or 1–3 meV electrons [23]. Observations in 5-nm detonation nanodiamonds have shown that NV centres emit sporadic luminesce [24]. NV centres have also been observed to emit stable luminescence in nanodiamonds of size greater than 20 nm [25, 26]. These studies suggest that factors such as nitrogen percentage in precursors used and cooling conditions play a role in the incorporation of nitrogen into the core of the nanodiamond and thus the formation of NV centres.

The concentration of electron irradiation produced fluorescent nitrogen-vacancy defects has been found to be independent of the size of nanocrystals. However it has been found that the number of NV–defects in comparison to the number of NV0 decreases as the size of the nanodiamonds produced by the same method is decreased [27]. This is presumably due to the relation between the surface density of electron traps to the size of the nanodiamonds. Recent quantum mechanical simulations done by Hertkorn and Fyta on hydrogen terminated nanodiamonds have shown the possibility of enhancing optical properties of nanodiamonds using NV–centres by charging or shifting the levels of the defect by different methods [28] (Fig. 13.6).

A good possible alternative to NV centres are SiV centres. SiV centres are marked by narrow zero phonon-line (ZPL) (5 nm width) of 738 nm which is a spectral region characterised by weak fluorescence of surrounding diamond as well as high photostability [29]. Neu et al. used microwave-plasma-assisted CVD growth to fabricate high-quality isolated NDs on iridium and have observed the emission of ZPL down to 0.7 in SiV colour centres and single photon count rates as high as 4.8 Mcps at saturation [30].

Fig. 13.6 Graph shows spectra of color centers in FNDs—nitrogen vacancy (NV) and silicon vacancy (SiV). Adapted from Alkahtani et al., Nanophotonics, vol 7, issue 8, (2018)
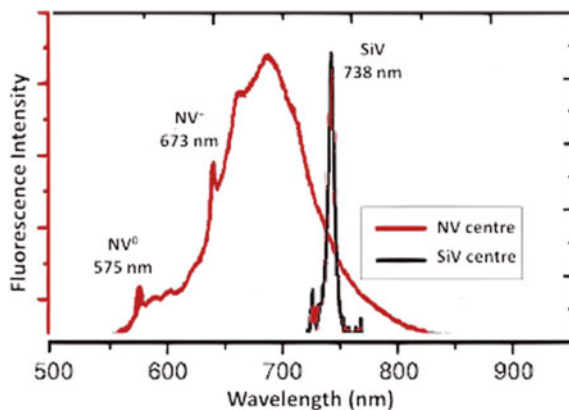
Optically transparent diamond films grown on fused silica at low temperatures by Remes and others were found to be smooth and and shifting of the Raman peak to lower wavenumbers for diamond films deposited on fused silica and to higher wavenumbers for films deposited on borosilicate glass as compared to diamond films grown on silicon (1332 cm^{-1}) was observed [31].

13.4 Applications

13.4.1 Dye Sensitized Solar Cells (DSSCs)

Over the last few years, conventional Silicon solar cells have increasingly begun to be replaced by the hybrid, third generation, Dye sensitized solar cells [32, 33]. The structure of DSSCs consists of a dye (Photosensitizer) sandwiched between two electrodes-working and counter- that consist of FTO/ITO coated glass substrates. The working electrode has a coating of titanium dioxide nanoparticles and the counter electrode has FTO glass coated with Pt acting as cathode [34]. When sunlight falls on the dye, charge carriers are generated in the active area of the solar cell-the electrons from excited dye molecules migrate to the working electrode and circulate around the circuit, constituting electricity. Despite being an efficient cathode material [35], Pt turns out to be costly and scarce. One potential replacement alternative is provided by carbon nanomaterials such as graphene and nanodiamond due to their good conductivity and impressive electro-catalytic action [36, 37]. Nanodiamond's electronic properties can be tailored through modifications in structure and chemical functionalization [38, 39], thus making it a suitable alternative for depositing optically transparent film on FTO.

Brian O'Regan and Michael Gratzel at UC Berkeley are credited with the invention of first DSSCs with nanoporous TiO$_2$ photoanode [32]. These devices exhibited 7% efficiency, due in part to the photoanode that served to increase the dye absorption by increasing the effective surface area of the working electrode. In the years that followed, their rising popularity among researchers-as a result of their cost-effectiveness and simpler light harvesting when contrasted with Si solar cells-led to efficiency improvement in the devices to around 11% [40].

Traditional DSSCs employ TiO$_2$ in photoanode films [41]. Large sized aggregates of these nanoparticles, having dimensions comparable to visible light wavelengths function as light scatterers. Even though TiO$_2$ nanoparticles demonstrate appreciable power conversion efficiency, their ability as scatterers is limited because of relatively small particle size (20 nm). Using Nanodiamond aggregates provides a solution overcoming said limitation [42]. Nanodiamond particles in the form of agglomerates, intermediate aggregates and core aggregates all have sizes on scales of either micrometer or hundreds of nm [43]. For particles having sizes comparable to the incident wavelength, it can be seen that sufficiently large (sub-micrometer)

sized nanodiamond aggregates [44] are able to scatter visible light efficiently [45], resulting in significant enhancement in light harvesting ability of the photoanode.

The same has been empirically seen in the experiment performed by Tafti and Sadeghzadeh [46], and the subsequent observations. In their study, micron sized aggregates had to be disaggregated using tip sonication. In DSSC photoanode, various samples consisting of composite of ND paste in differing wt% (25, 50, 5) with TiO_2 (300, 300, 20 respectively) were fabricated along with an independent ND scattering layer and a standard cell containing TiO_2 only for reference. FESEM and EDAX techniques were employed to study the structure and size of ND aggregates. Of all the samples investigated, the general trend is that presence of ND in electrode film results in improved efficiencies, with the 1-1 composite of ND-TiO_2(300) showing maximum improvement, 74.5% compared to standard TiO_2 cell with no scattering layer. This was also accompanied by a greater optical absorption with increasing ND concentration in the ND-TiO_2 composite. Enhancement in optical absorption of the film sample along with light scattering abilities resulted in significant improvement in light harvesting properties of the cell.

13.4.2   Nanodiamond as Coating Material

One of the setbacks of conventional Silicon based photovoltaic is wearing off and erosion of protective layers on these cells by environmental factors like dust or sand. In the long run, wear caused due to these external factors can reduce the efficiency of these cells. Thus, there arises a need for a material that exhibits mechanical hardness, chemical and radiation stabilities, thermal conductivity and optical transparency so that performance of the cell remains unaffected. Amorphous carbon such as diamond like carbon seems to be a promising material [47, 48]. Controlling refractive index and transmissivity allows thin nanodiamond films to be used as protective layers. Nanocrystalline diamond films with lower grain size and surface roughness, both of which ultimately factor into transmissivity of the film [49], are used to obtain optically transparent films. Study with HFCVD deposited films. Work of Simões et al. [50] consisted of fabricating a nanocrystalline diamond film, deposited over glass substrate that could perform the function of a protective layer in solar cells. Film obtained using HFCVD and characterized by SEM and Spectrophotometric analysis revealed that film had a reduced grain size, which was suggested to be a result of addition of Argon to the gas mixture in HFCVD reactor during fabrication. This in turn, resulted in smoothness of film and good transmissivity. The role of high transmissivity or transmittance becomes important in obtaining a protective film as it means the film can allow passage of light without much impacting its intensity and therefore, has minimal effect on the cell's efficiency. A comparison of transmission percentage of film coated substrate with uncoated glass substrate showed that transmittance of the former suffered significantly. So, this begs further efforts in obtaining a much smoother film with reduced grain size that can prevent excessive light scattering happening in the present case.

High optical transparency and refractive index, among other unique properties of diamond warrant its usage as not just in numerous optoelectronic devices or as a protective coating, but also as Anti-reflective (AR) layer deposited on a substrate. In cells, it is used to reduce unwanted light reflection and thus, enhance efficiency of solar cells. Tafti et al. [51] prepared samples of ND coated FTO glass by spin coating, employing 0.3 wt% concentration of nanodiamond in the suspension. They then analyzed optical properties like (1) reflectance measurement that turned out to be lowest in case of ND on both sides of FTO glass, (2) optical absorption spectra in (300–1100 nm range that showed that by deposition of ND results in, optical absorption in the visible region (above 400 nm) generally improving, with best results shown again in case of ND coated on either side of FTO. This was supposed to be due to lesser reflection of light, which is a primary concern in solar cells. Other parameters that were measured, like the open circuit voltage (Voc), the short circuit photocurrent density (Jsc), electron mobility, were all found to increase compared with standard cell with introduction of ND and in all cases, best performance was shown in the sample cell with both sides of FTO coated with ND. Most importantly, the power conversion efficiency (PCE) of this cell improved the most, 25.7%, compared with standard DSSC.

13.4.3   Nanodiamonds in Organic Photovoltaics

Organic solar cells employing pi-conjugated polymers or fullerene derivatives are considered a feasible for photovoltaic applications [52] due to a number of advantages ranging from solution processability, high optical absorption, controllability of bandgap and thus, electronic behavior by functionalization of organic polymers, to flexibility and cost effectiveness, even for large scale production [53, 54]. However, their drawbacks include low light trapping efficiency due to low charge mobility [55, 56] as well as significant photochemical degradation [57]. Despite the fact that tandem OPVs showed efficiency of around 17% [58], improvements require materials that can improve exciton generation rate, exciton diffusion lengths and chemical and thermal stabilities. One alternative is hybrid OPVs as they showcase the combined benefits of both organic and inorganic materials to obtain improved values of the device power conversion efficiencies (PCE) [59]. Nanodiamonds present a potential candidate in polymer-nanocrystal composites due to its strong UV absorption and conductivity values [60] and improved electron mobility [61].

Hasio et al. [62] undertook the task of fabricating a blend film of poly-3-hexylthiophene (P3HT), [6,6]-phenylC61-butyric acid methyl ester (P3HT:PCBM) and Nanodiamond (ND) that acted as photoactive layer in hybrid solar cell. Spin coating employing a spin speed of 800 rpm was used to deposit the film with varying amounts of nanodiamond, the average diameter of nanodiamond particles produced by Detonation method was 50 nm. TEM image of the hybrid sample showed uniformly dispersed ND particles in the P3HT/PCBM polymer. Absorption spectra of the films obtained by UV–Vis Spectroscopy showed increased optical absorption

as concentration of ND in the P3HT/PCBM/ND active layer was increased. Measurement of device parameters such as Jsc and PCE were found to be clearly higher for the ND containing blended films as opposed to P3HT:PCBM films. Incident photon-to-current conversion efficiency (IPCE), that is a factor in PCE of the device, as displayed in IPCE spectra, revealed higher IPCE values for devices incorporating P3HT:PCBM:NDs than the corresponding values for P3HT:PCBM at a given wavelength. The difference was attributed to an increased rate of exciton generation. Similarly, superior results for thermal stability were obtained in case of ND doped active layer devices.

In another experiment performed by Nagata et al. [63], Fullerene based solar cells were blended with ND to improve efficiency. Here, ND particles acted as p type semiconductor in the 150 nm thick active layer. These Bulk heterojunction solar cells show efficient generation of free, mobile charge carriers and charge transfer at the junction/interface.

Optical properties measured through UV–Vis Spectroscopy by obtaining absorption spectra within 300–800 nm range showed a comparatively higher absorption for thin films with the ND: C60 structure than films without ND at any given wavelength. Further TEM imaging of the film revealed a disordered mixing of ND and C60 at the nanoscopic scale, which posed difficulty in electron and hole transport due to carrier recombination, thus responsible for low conversion efficiency of the thin film. This indicates the need for minimizing defects in the crystalline structure and inclusion of a layer to eliminate carrier recombination (Fig. 13.7).

13.5 Conclusion

Nanodiamonds and nanodiamond films are currently being used in a wide variety of fields, both industrially and for research purposes. The specific technique used for their synthesis depends on various factors, such as the specific application for which they are required, the limitations of cost and apparatus as well as the yield, structure, reproducibility and composition of the final required products.

Potential applications of Nanodiamonds arise from its unique optical and electronic properties as addressed in the paper. Continuous efforts towards efficiency enhancement of traditional photovoltaics and search for more reliable, cost effective alternatives have yielded Nanocarbons, and especially Nanodiamonds as a potential additive in cell components such as dyes, working or counter electrodes and coatings. Their ability to provide a reasonably comparable performance with Silicon solar cells lends them tremendous potential for energy conversion devices.

Fig. 13.7 Absorption spectra of diamond: C60 layer (**a**), Tc-CoPc: ND/C60 and Tc-CoPc/C60 layers (**b**), Tc-CuPc: ND: C60(OH)10–12 and Tc-CuPc:C60(OH)10–12 layers (**c**), © by Akihito Nagata et al. used under CC BY -NC-ND 3.0 license
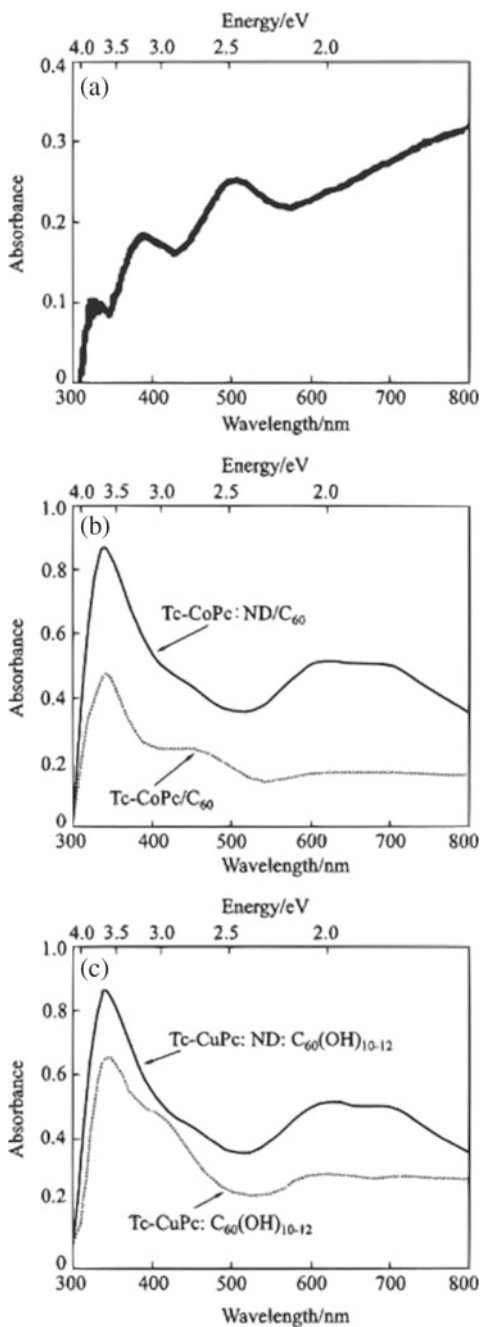
References

1. V.V. Danilenko, On the history of the discovery of nanodiamond synthesis. Phys. Solid State **46**, 595–599 (2004). https://doi.org/10.1134/1.1711431
2. V.Y. Dolmatov, M.V. Veretennikova, V.A. Marchukov, V.G. Sushchev, Currently available methods of industrial nanodiamond synthesis. Phys. Solid State **46**, 611–615 (2004). https://doi.org/10.1134/1.1711434
3. M.L. Terranova, S. Orlanducci, E. Tamburri et al., Polycrystalline diamond on self-assembled detonation nanodiamond: a viable route for fabrication of all-diamond preformed micro-components. Nanotechnology **19**, 415601 (2008). https://doi.org/10.1088/0957-4484/19/41/415601
4. E. Tamburri, S. Orlanducci, G. Reina et al., Nanodiamonds: the ways forward. AIP Conf. Proc. **1667** (2015). https://doi.org/10.1063/1.4922557
5. V.A. Plotnikov, S.V. Makarov, D.G. Bogdanov, A.S. Bogdanov, The structure of detonation nanodiamond particles. AIP Conf. Proc. **1785** (2016). https://doi.org/10.1063/1.4967102
6. S. Kazi, A Review article on nanodiamonds discussing their properties and applications a review article on nanodiamonds discussing their properties and applications. Int. J. Pharm. Sci. Invention **3**, 40–45 (2014)
7. J.E. Butler, A.V. Sumant, The CVD of nanodiamond materials. Chem. Vap. Deposition **14**, 145–160 (2008). https://doi.org/10.1002/cvde.200700037
8. A. Afandi, A. Howkins, I.W. Boyd, R.B. Jackman, Nanodiamonds for device applications: an investigation of the properties of boron-doped detonation nanodiamonds. Sci. Rep. **8** (2018). https://doi.org/10.1038/s41598-018-21670-w
9. Y. Liu, S. Chen, X. Quan et al., Boron and nitrogen codoped nanodiamond as an efficient metal-free catalyst for oxygen reduction reaction. J. Phys. Chem. C **117**, 14992–14998 (2013). https://doi.org/10.1021/jp4044094
10. J.J. Gracio, Q.H. Fan, J.C. Madaleno, Diamond growth by chemical vapour deposition. J. Phys. D: Appl. Phys. **43**, 374017 (2010). https://doi.org/10.1088/0022-3727/43/37/374017
11. B. Kharisov, O. Kharissova, L. Chávez-Guerrero, Synthesis techniques, properties, and applications of nanodiamonds CRC concise Encyclopedia of nanotechnology view project synthesis of phthalocyanine and salen complexes view project. Synth. React. Inorg. Met.-Org. Nano-Metal Chem. **40** (2014). https://doi.org/10.3109/10799890903555665
12. N.D. Drummond, A.J. Williamson, R.J. Needs, G. Galli, Electron emission from diamondoids: a diffusion quantum Monte Carlo study. Phys. Rev. Lett. **95** (2005). https://doi.org/10.1103/physrevlett.95.096801
13. J. Jiang, L. Sun, B. Gao et al., Structure dependent quantum confinement effect in hydrogen-terminated nanodiamond clusters. J. Appl. Phys. **108**, 094303 (2010). https://doi.org/10.1063/1.3503365
14. O.A. Williams, S. Curat, J.E. Gerbi et al., n-type conductivity in ultrananocrystalline diamond films. Appl. Phys. Lett. **85**, 1680–1682 (2004). https://doi.org/10.1063/1.1785288
15. J.J. Mareš, P. Hubík, J. Krištofik et al., Weak localization in ultrananocrystalline diamond. Appl. Phys. Lett. **88**, 092107 (2006). https://doi.org/10.1063/1.2176853
16. M. Nesládek, K. Meykens, L.M. Stals et al., Origin of characteristic subgap optical absorption in CVD diamond films. Phys. Rev. B **54**, 5552–5561 (1996). https://doi.org/10.1103/physrevb.54.5552
17. M. Nesládek, D. Tromson, C. Mer, et al., Superconductive B-doped nanocrystalline diamond thin films: Electrical transport and Raman spectra. Appl. Phys. Lett. **88**, 232111 (2006). https://doi.org/10.1063/1.2211055
18. C.-C. Fu, H.-Y. Lee, K. Chen et al., Characterization and application of single fluorescent nanodiamonds as cellular biomarkers. Proc. Natl. Acad. Sci. **104**, 727–732 (2007). https://doi.org/10.1073/pnas.0605409104
19. U. Jantzen, A.B. Kurz, D.S. Rudnicki, et al., Nanodiamonds carrying silicon-vacancy quantum emitters with almost lifetime-limited linewidths. New J. Phys. **18**, 073036 (2016). https://doi.org/10.1088/1367-2630/18/7/073036

20. T.T. Tran, M. Kianinia, K. Bray, et al., Nanodiamonds with photostable, sub-gigahertz linewidth quantum emitters. APL Photonics **2**, 116103 (2017). https://doi.org/10.1063/1.4998199

21. A. Beveratos, R. Brouri, T. Gacoin et al., Nonclassical radiation from diamond nanocrystals. Phys. Rev. A **64** (2001). https://doi.org/10.1103/physreva.64.061802

22. J. Tisler, G. Balasubramanian, B. Naydenov et al., Fluorescence and spin properties of defects in single digit nanodiamonds. ACS Nano **3**, 1959–1965 (2009). https://doi.org/10.1021/nn9003617

23. O. Shenderova, N. Nunn, T. Oeckinghaus et al., Commercial quantities of ultrasmall fluorescent nanodiamonds containing color centers, in *International Society for Optics and Photonics* ed. by Z. Ul Hasan, P.R. Hemmer, H. Lee, A.L. Migdall (SPIE, 2017), pp. 2–17

24. C. Bradac, T. Gaebel, N. Naidoo et al., Observation and control of blinking nitrogen-vacancy centres in discrete nanodiamonds. Nat. Nanotechnol. **5**, 345–349 (2010). https://doi.org/10.1038/nnano.2010.56

25. O.A. Shenderova, I.I. Vlasov, S. Turner et al., Nitrogen control in nanodiamond produced by detonation shock-wave-assisted synthesis. J. Phys. Chem. C **115**, 14014–14024 (2011). https://doi.org/10.1021/jp202057q

26. I.I. Vlasov, O. Shenderova, S. Turner et al., Nitrogen and luminescent nitrogen-vacancy defects in detonation nanodiamond. Small **6**, 687–694 (2010). https://doi.org/10.1002/smll.200901587

27. L. Rondin, G. Dantelle, A. Slablab et al., Surface-induced charge state conversion of nitrogen-vacancy defects in nanodiamonds. Phys. Rev. B **82** (2010). https://doi.org/10.1103/physrevb.82.115449

28. J. Hertkorn, M. Fyta, Electronic features of vacancy, nitrogen, and phosphorus defects in nanodiamonds. Electron. Struct. **1**, 025002 (2019). https://doi.org/10.1088/2516-1075/ab177b

29. C. Wang, C. Kurtsiefer, H. Weinfurter, B. Burchard, Single photon emission from SiV centres in diamond produced by ion implantation. J. Phys. B: At. Mol. Opt. Phys. **39**, 37–41 (2005). https://doi.org/10.1088/0953-4075/39/1/005

30. E. Neu, D. Steinmetz, J. Riedrich-Möller et al., Single photon emission from silicon-vacancy colour centres in chemical vapour deposition nano-diamonds on iridium. New J. Phys. **13**, 025012 (2011). https://doi.org/10.1088/1367-2630/13/2/025012

31. Z. Remes, Y. Avigal, R. Kalish et al., Structural, optical and electrical properties of nanodiamond films deposited by HFCVD on borosilicate glass, fused silica and silicon at low temperature. Phys. Status Solidi (A) **201**, 2499–2502 (2004). https://doi.org/10.1002/pssa.200405174

32. B. O'Regan, M. Grätzel, A low-cost, high-efficiency solar cell based on dye-sensitized colloidal TiO_2 films. Nature **353**, 737–740 (1991). https://doi.org/10.1038/353737a0

33. M. Grätzel, Recent advances in sensitized mesoscopic solar cells. Acc. Chem. Res. **42**, 1788–1798 (2009). https://doi.org/10.1021/ar900141y

34. K. Sharma, V. Sharma, S.S. Sharma, Dye-sensitized solar cells: fundamentals and current status. Nanoscale Res. Lett. **13** (2018). https://doi.org/10.1186/s11671-018-2760-6

35. M. Graetzel, J.-E. Moser, Solar Energy Conversion (2008), pp. 588–644

36. H. Zhu, J. Wei, K. Wang, D. Wu, Applications of carbon materials in photovoltaic solar cells. Sol. Energy Mater. Sol. Cells **93**, 1461–1470 (2009). https://doi.org/10.1016/j.solmat.2009.04.006

37. J. Chen, B. Li, J. Zheng et al., Role of carbon nanotubes in dye-sensitized TiO_2-based solar cells. J. Phys. Chem. C **116**, 14848–14856 (2012). https://doi.org/10.1021/jp304845t

38. V. Pichot, O. Muller, A. Seve et al., Optical properties of functionalized nanodiamonds. Sci. Rep. **7** (2017). https://doi.org/10.1038/s41598-017-14553-z

39. N. Brown, O. Hod, Controlling the electronic properties of nanodiamonds via surface chemical functionalization: a DFT study. J. Phys. Chem. C **118**, 5530–5537 (2014). https://doi.org/10.1021/jp409236t

40. Y. Chiba, A. Islam, Y. Watanabe et al., Dye-sensitized solar cells with conversion efficiency of 11.1%. Jpn. J. Appl. Phys. **45**, L638–L640 (2006). https://doi.org/10.1143/jjap.45.l638

41. A.K. Chandiran, M. Abdi-Jalebi, M.K. Nazeeruddin, M. Grätzel, Analysis of electron transfer properties of ZnO and TiO_2 photoanodes for dye-sensitized solar cells. ACS Nano **8**, 2261–2268 (2014). https://doi.org/10.1021/nn405535j

42. G.M. Mikheev, A.P. Puzyr', V.V. Vanyukov et al., Nonlinear scattering of light in nanodiamond hydrosol. Tech. Phys. Lett. **36**, 358–361(2010). https://doi.org/10.1134/s1063785010040206

43. A. Pentecost, S. Gour, V. Mochalin et al., Deaggregation of nanodiamond powders using salt- and sugar-assisted milling. ACS Appl. Mater. Interfaces. **2**, 3289–3294 (2010). https://doi.org/10.1021/am100720n

44. A.E. Aleksenskii, V.Y. Osipov, A.Y. Vul' et al., Optical properties of nanodiamond layers. Phys. Solid State **43**, 145–150 (2001). https://doi.org/10.1134/1.1340200

45. O. Williams, Nanodiamond, in RSC Nanoscience & Nanotechnology (2014a). https://doi.org/10.1039/9781849737616

46. M.H. Karimi Tafti, S.M. Sadeghzadeh, Novel use of nanodiamonds as light-scattering material in dye-sensitized solar cells. J. Mater. Sci.: Mater. Electron. **27**, 5225–5232 (2016). https://doi.org/10.1007/s10854-016-4417-5

47. S. Josset, O. Muller, L. Schmidlin et al., Nonlinear optical properties of detonation nanodiamond in the near infrared: effects of concentration and size distribution. Diam. Relat. Mater. **32**, 66–71 (2013). https://doi.org/10.1016/j.diamond.2012.12.001

48. V.G. Litovchenko, N.I. Klyui, Solar cells based on DLC film—Si structures for space application. Sol. Energy Mater. Sol. Cells **68**, 55–70 (2001). https://doi.org/10.1016/S0927-0248(00)00345-7

49. W.S. Choi, K. Kim, J. Yi, B. Hong, Diamond-like carbon protective anti-reflection coating for Si solar cell. Mater. Lett. **62**, 577–580 (2008). https://doi.org/10.1016/j.matlet.2007.06.019

50. R. Simões, V.F. Neto, Nanodiamond coated glass as a protective layer in solar cells. Mater. Today: Proc. **2**, 230–235 (2015). https://doi.org/10.1016/j.matpr.2015.04.027

51. M.H. Karimi Tafti, S.M. Sadeghzadeh, Dye sensitized solar cell efficiency improvement using nanodiamond anti-reflect layer. Opt. Quant. Electron. **48**, 124 (2016). https://doi.org/10.1007/s11082-016-0420-6

52. Y. Liang, Z. Xu, J. Xia et al., For the bright future-bulk heterojunction polymer solar cells with power conversion efficiency of 7.4%. Adv. Mater. **22**, E135–E138 (2010). https://doi.org/10.1002/adma.200903528

53. J. Nelson, Polymer:fullerene bulk heterojunction solar cells. Mater. Today **14**, 462–470 (2011). https://doi.org/10.1016/S1369-7021(11)70210-3

54. N. Yeh, P. Yeh, Organic solar cells: their developments and potentials. Renew. Sustain. Energy Rev. **21**, 421–431 (2013). https://doi.org/10.1016/j.rser.2012.12.046

55. M.M. Mandoc, L.J.A. Koster, P.W.M. Blom, Optimum charge carrier mobility in organic solar cells. Appl. Phys. Lett. **90**, 133504 (2007). https://doi.org/10.1063/1.2711534

56. S. Shoaee, M. Stolterfoht, D. Neher, The role of mobility on charge generation, recombination, and extraction in polymer-based solar cells. Adv. Energy Mater. **8**, 1703355 (2018). https://doi.org/10.1002/aenm.201703355

57. M. Jørgensen, K. Norrman, F.C. Krebs, Stability/degradation of polymer solar cells. Sol. Energy Mater. Sol. Cells **92**, 686–714 (2008). https://doi.org/10.1016/j.solmat.2008.01.005

58. L. Meng, Y. Zhang, X. Wan et al., Organic and solution-processed tandem solar cells with 17.3% efficiency. Science **361**, 1094–1098 (2018). https://doi.org/10.1126/science.aat2612

59. B. Sun, H.J. Snaith, A.S. Dhoot et al., Vertically segregated hybrid blends for photovoltaic devices with improved efficiency. J. Appl. Phys. **97**, 014914 (2005). https://doi.org/10.1063/1.1804613

60. Shenderova O, Gruen D (2006) Ultrananocrystalline Diamond—1st Edition. In: https://www.elsevier.com/books/ultrananocrystalline-diamond/shenderova/978-0-8155-1524-1

61. X.C. Lau, C. Desai, S. Mitra, Functionalized nanodiamond as a charge transporter in organic solar cells. Sol. Energy **91**, 204–211 (2013). https://doi.org/10.1016/j.solener.2013.01.024

62. Y.-J. Hsiao, T.-H. Fang, L.-W. Ji et al., Nanodiamonds embedded in P3HT:PCBM for enhancing efficiency and reliability of hybrid photovoltaics. Electrochem. Solid-State Lett. **15**, K27 (2012). https://doi.org/10.1149/2.006204esl

63. A. Nagata, T. Oku, K. Kikuchi et al., Fabrication, nanostructures and electronic properties of nanodiamond-based solar cells. Prog. Natural Sci.: Mater. Int. **20**, 38–43 (2010). https://doi.org/10.1016/s1002-0071(12)60004-5

Chapter 14
Structural Properties of TiS$_2$/MWCNTs Hybrid Nanostructures

Umang, Vinod Singh, and Rinku Sharma

Abstract Titanium disulphide (TiS$_2$) nanoplates have been prepared by using the solid-state reaction technique and the multiwalled carbon nanotubes (MWCNTs) have been prepared by adopting chemical vapour deposition method using Co:Mo:MgO powder catalyst and acetylene as precursor. The prepared TiS$_2$ nanoplates were further doped with MWCNTs. The structural analysis with single-phase confirmation of TiS2, MWCNTs, and hybrid TiS$_2$ was done through XRD. The diffraction peaks of TiS$_2$ were found to be shifted on higher 2θ value which indicates the lattice contraction caused by doping with MWCNTs. The crystallite size was found to be reduced from 141 to 116 nm as a result of doping with MWCNTs. SEM micrograph of MWCNTs exhibits a well separated cylindrical nano tubes with the length of the order of microns. The AFM of hybrid composite powder shows a perfectly homogeneous structure and well embedded MWCNTs into TiS$_2$ structure. The structural and microstructural properties of TiS$_2$ were found to be enhanced by the means of doping with MWCNTs which shows its better potential applications.

14.1 Introduction

In last few decades, 2D materials have drawn much attention due to providing a range of electrical, optical, and mechanical properties [1]. The 2D transition metal dichalcogenides (TMDCs) have been utilized for several applications such as super-conductors [2], transistors [3], thermoelectric materials [4], electrochemical energy storage [5], supercapacitors [6], photo catalysis [1], and sensing [7] etc. As a general description, these 2D TMDCs can be explained by general formula UX$_2$ (where U as transition metals of IV, V, and VI group elements and X as Chalcogen being explored elements S, Se, Te). These can be prepared with various forms like layered

Umang · V. Singh (✉) · R. Sharma
Department of Applied Physics, Delhi Technological University, Bawana Road, New Delhi 110042, India
e-mail: vinodsingh@dtu.ac.in

R. Sharma
e-mail: rinkusharma@dtu.ac.in

structures, Nanotubes, buckminsterfullerene like nanoparticles and graphene type flakes [8]. These structures have been studied on a large scale due to their structural, electronic & optical effects [9–11]. Among all TMDCs, TiS_2 is one of the most important candidate, used as an active electrode material for Li & Na ion based rechargeable batteries [12] and thermoelectric material [13]. TiS_2 has been used a negative terminal electrode material in Li & Na ion based rechargeable batteries due to a large current capacity, high electronic conductivity, and high reversibility of the intercalation ion reaction [14]. Thus, exploring of TiS_2 as a thermoelectric material can be opened new possibilities of the development of optional energy resources in the present situation of energy crisis in the whole world. The TiS_2 material consists of hexagonal layer of Ti transition metal atom which is packed between two alike sheets of S chalcogen atoms (1/2 of the octahedral sites are fill up with Ti^{4+} and each Ti^+ ion is surrounded by 6 Sulfur ions) and thus forming a basis S–Ti–S [15]. The individual sheets of S–Ti–S were well adjusted by weak vander walls forces & the bond length between Ti–S is about 0.05–2.5 Å and behaves as semiconductor material [16]. Several species such as 3d transition metals and alkali metals enters into the gap between the TiS_2 layers and thus forming a new material known as intercalation compound [12]. This new intercalation compound shows various interesting physical properties and the inter-layer separation can be varied significantly through changing the visitor alkali atom concentration and it has been also observed that super lattices are formed at a particular concentration [16]. The TiS_2 crystal is behaving like n-type semiconductor with high density of conduction ions because of surplus Ti atoms occupy the Van der waals spaces [14]. The working of TiS2 can be refined by maximizing the surface area of TiS_2. Several methods are used to synthesize 2D TMDCs; namely solid-state reaction methods [12], Chemical Vapour Deposition (CVD) [17], Hydrothermal method (Solvothermal) [18], and Chemical Vapour Transport method [19]. Out of all these methods, solid-state reaction method is a very simplest one with easy steps and produces material on mass scale at low cost. TiS_2 is synthesized at a very low temperature using standard solid-state method.

In addition, Carbon nanotubes (CNTs) are the most important segment of nanoscience that has the mass potential to revolutionize the world of science [20]. CNTs are basically rolled over graphene sheets in which carbon atoms are bonded together using strong sp^2 hybridization, having dimensions in the range of 0.4–40 nm in diameter and their length can vary from 0.14 nm to 55.5 cm making them fall under the category of one dimensional nanomaterial [21]. In current manuscript, we have produced TiS_2 nanoplates using the solid-state reaction route and synthesis of multi walled carbon Nanotubes (MWCNTs) is performed using CVD. At last, a composite of TiS_2 nanoplates and MWCNTs is produced. A structural and microstructural analysis is reported on the basis of characterization techniques; namely X-ray diffraction (XRD) and Scanning electron microscopy (SEM).

14.2 Experimental Details

14.2.1 Formation of TiS$_2$ Nanoplates

The 2D TiS$_2$ crystalline material was prepared through solid-state reaction method with the involved steps as shown in Fig. 14.1 [22]. The precursor, 800 mg of fundamental sulfur (99.99 % of Sigma Aldrich) is taken and dissolved into 20 ml of oleylamine (OMA) in a 3-neck round bottom flask. This mixture is heated upto 100 °C for 1 h using magnetic stirring to remove excess moisture present in the solution under the protection of argon gas. The magnetic stirring was switched off so that solution was permitted to cool down at room temperature. After cool down the solution to room temperature, add 2 ml of TiCl$_4$ in the solution with the help of syringe. The colour of the solution immediately changes from orange shade to black. Now this solution again heated to 300 °C for 3 h with the help of magnetic stirring under the protection of argon gas. At the end of the reaction process, heating mental was turned off & the solution was allowed to cool down at room temperature. TiS$_2$ nanoplates were collected through centrifugation and washed with 1:1 ethanol. Finally, the washed powder is annealed under the argon gas at 450 °C for 2 h to remove organic impurities [12].
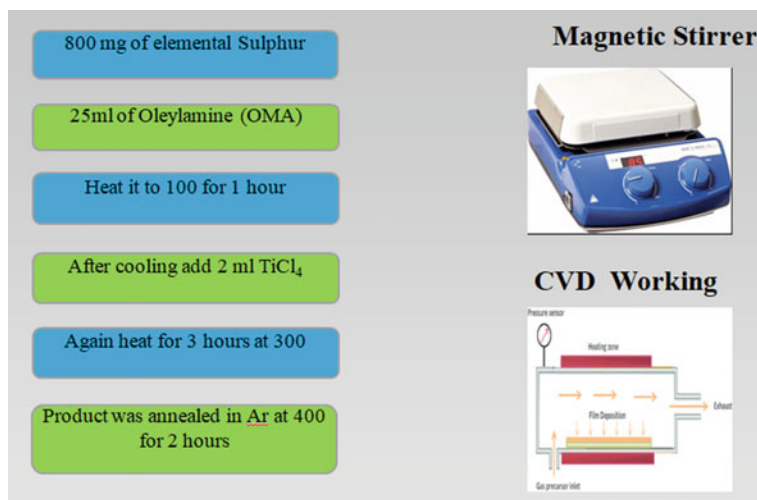
Fig. 14.1 Flow chart for preparation of TiS$_2$
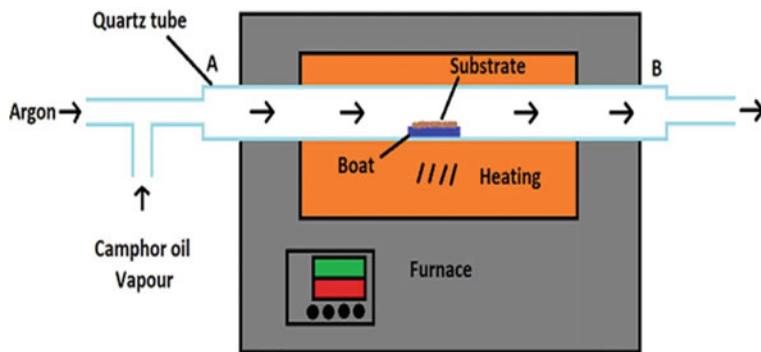
Fig. 14.2 A Schematic of CVD apparatus used for MWCNTs growth

14.2.2 Synthesis of MWCNTs

(a) Preparation of catalyst: The catalyst for the Catalyst thermal CVD process for the synthesis of CNTs was prepared using the sol-gel technique. This technique was chosen over the impregnation technique for preparation due to the formation of smaller and more regular nanoparticles in sol-gel method which gives better performing and high surface area catalyst [23]. 30 ml of deionized water (DI) was taken in a properly clean beaker.

Cobalt (II) nitrate hexahydrate and Ammonium hepta-molybdate were added to the DI water where Co:Mo molar ratio was kept 1:3.5. Magnesium nitrate was added to the solution to provide support for the catalyst constituting to the catalyst support ratio of 15% by weight. Citric acid was added to the solution as a foaming agent (citric acid). This solution was then stirred using ultrasonication for 1 h and then heated at 100 °C for 1 h which led to the formation of a pink gel like substance. This gel was dried in the oven for 2 days at 120 °C and then grinded into very fine particles using pestle and mortar. The procured powered catalyst was then calcinated at 550 °C for 30 min to remove any volatile substances. The prepared catalyst (~2g) was kept in a quartz boat as a substrate which was then placed in the central zone of the split furnace. The volatile input gases and precursor gases were fed to the furnace through port A. After the growth process the by-products were removed using Argon flow through port B.

(b) Growth of CNTs: Constant Argon flow (120 sccm) was given to furnace for 15 min to remove any unwanted substance residing in the environment of the substrate or present in the quartz tube. The temperature of the furnace was then raised to 850 °C while keeping the Argon flow constant. When the constant 850 °C temperature was achieved the precursor gas (Camphor oil vapours) flow was initiated over the substrate using the vapour flow apparatus (as described in Fig. 14.3) along with the constant argon flow. This started the growth deposition process of CNTs and after keeping the continuity of the process of for 45 min the deposition process was halted, precursor flow and heating was turned off keeping the argon flow constant;

Fig. 14.3 An apparatus for camphor vapour flow
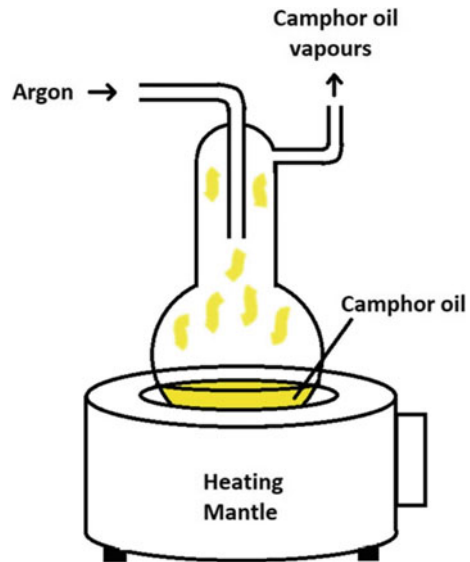
the furnace was the allowed to cool to room temperature which took almost 8 h. After the cooling process, the substrate was collected which have now turned dark in colour denoting the formation of CNTs in the sample.

Finally, the formed TiS$_2$ were mixed with MWCNTs (Co:Mo:MgO metal powder) using mortar and pestle. The mixed powders were grinded for 2 h with the help of ethanol. The fine mixed powder was collected and placed in vacuum furnace at 200 °C for 12 h. Finally, the TiS$_2$/MWCNTs nanocomposite was obtained.

14.3   Results and Discussion

The structural analysis of synthesized TiS$_2$, MWCNTs, and a hybrid composition of both were performed using XRD. A diffraction pattern for the TiS$_2$ powder was recorded in the range of 2θ from 20° to 60° as shown in Fig. 14.4. The results obtained from XRD pattern are nearly close in agreement with the standard JCPDS data for TiS$_2$ material with the reference number ICSD #026861. The diffraction pattern with multiple peaks confirms polycrystalline in nature for TiS$_2$ nanoplates. XRD pattern of TiS$_2$ nanoplates were well indexed with the reflection corresponds to TiS$_2$ planes. The diffraction maxima related to TiS$_2$ set of planes are appeared at 29.575° (100), 34.748° (011), 48.246° (003), and 54.058° (110). All the mentioned peaks related with TiS$_2$ unit cell are marked by '*'.

Moreover, two extra peaks are also observed at 25.467° (101) and 38.081° (112) with the reference number ICSD #202243 which belong to anatase phase of TiO$_2$ and are marked by '#' in Fig. 14.4 [24]. All diffraction peaks correspond to TiS$_2$

Fig. 14.4 X-ray diffraction
spectrum of TiS$_2$ nanoplates
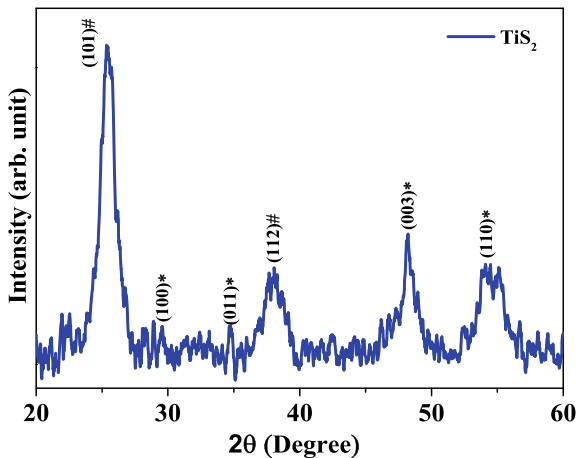
as well as TiO$_2$ were fitted with pseudo-Voigt function to determine peak positions
and FWHM (full-width at half maximum). The calculated interplanar spacings for
various set of planes were calculated using the following expression and listed in
Table 14.1.

$$2d.\mathrm{Sin}(\theta) = n.\lambda \tag{14.1}$$

where 'd' represents the interplanar spacing for a particular set of planes depicted
by respective diffraction maximum observed at the Bragg's angle 'θ'. On the other
hand, 'n' is the order of diffraction taken as ~1 in the present work and 'λ' stands
for wavelength.

The Williamson-Hall plot was used to determine the crystallite size in accom-
panied with microstrain [25]. The following expression of W–H formalism was
used:

Table 14.1 XRD data result for TiS$_2$ and as prepared TiS2/MWCNTs nanocomposites

S. No.	Sample	Related peak	Peak No.	Hkl	2θ (°)	d-spacing (nm)
1	Raw TiS$_2$	TiS$_2$	1	100	29.575	0.30
		TiO$_2$	2	011	34.748	0.26
			3	003	48.246	0.19
			4	110	54.058	0.17
			1	101	25.467	0.35
			2	112	38.081	0.24
2	Mixed sample TiS$_2$/MWCNTs	TiS$_2$	1	100	31.383	0.28
		TiO$_2$	2	011	36.943	0.24
			3	003	48.409	0.19
			4	110	54.278	0.17
			1	101	25.632	0.35

Fig. 14.5 X-ray diffraction spectrum of MWCNTs

$$\beta.\mathrm{Cos}(\theta) = \frac{k.\lambda}{D} + 4.\varepsilon.\mathrm{Sin}(\theta) \qquad (14.2)$$
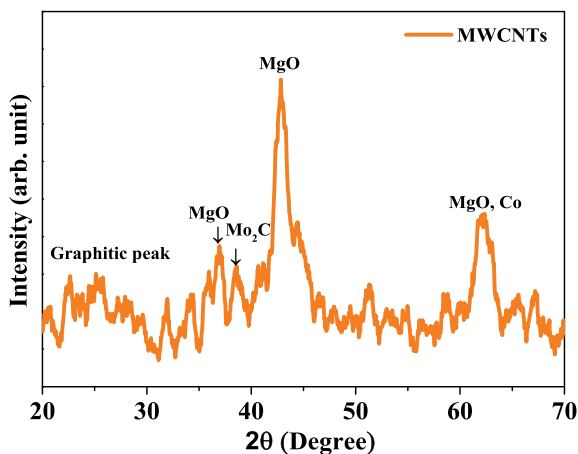
where β is the FWHM of the peak appeared at a particular θ value, k is the structure factor with the numerical value ~0.94, and λ is the wavelength of source of lab-XRD (here, copper K$_\alpha$ is the cathode with wavelength equal to 1.54056 Å). D and ε are the calculated parameters as crystallite size and microstrain; respectively. The TiS$_2$ structure related peaks were employed to determine the crystallite size and microstrain. The value of crystallite size and microstrain for TiS$_2$ are estimated to be 141 nm and 0.0035.

In case of structural analysis of MWCNTs, the recorded diffraction pattern is shown in Fig. 14.5. The peak observed at 2θ value of 38.52° gives an evidence of Mo$_2$C structure.

The peak appeared at 37.0° and 42.84° show the presence of MgO structured cell. These peaks appeared for MgO and Mo$_2$C are in accordance of the previous published results and exhibits the efficient growth of MWCNTs [26, 27]. Thus, in this work, the MWCNTs were produced by taking Co:Mo ratio as 1:3.5.

Now, TiS$_2$ and MWCNTs mixed together using mortar and pestle to study the effect of MWCNTs on TiS$_2$ structured powder. Figure 14.6 exhibits the diffraction pattern recorded in the range from 20° to 70° for a hybrid composite of TiS$_2$ and MWCNTs.

This hybrid composite contains all TiS$_2$ peaks with almost same intensity as recorded for TiS$_2$ powder. As a result of mixing with MWCNTs, TiO$_2$ structure deteriorates as only one peak (101) is observed with comparatively lesser intensity. The peaks in the XRD pattern of hybrid composite were appeared at the 2θ values ~31.383° (100), 36.943° (011), 48.409° (003), and 54.278° (110). These all peaks are related with TiS$_2$ structure and provide a strong support that the intermixing of TiS$_2$ with MWCNTs is not going to destroy its structure. Although two impurity peaks related to anatase TiO$_2$ phase were weaken and one peak has been disappeared in

Fig. 14.6 X-ray diffraction spectra of as prepared TiS$_2$/MWCNTs nanocomposites
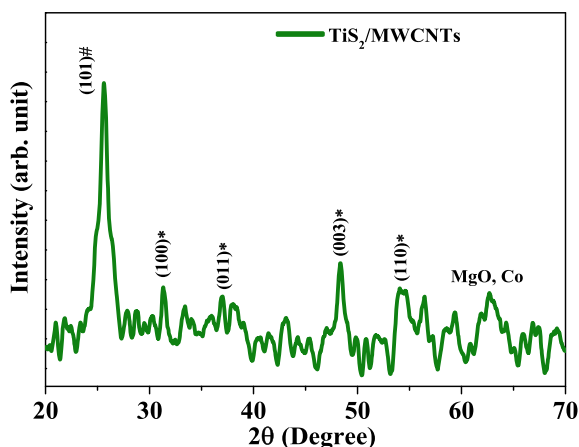
hybrid composite as a result of intermixing with MWCNTs. It should be noted that the diffraction peaks are found to be shifted towards higher 2θ values. This observation implies that the intermixing with MWCNTs results in lattice contraction [28]. On the basis of W–H formalism, the crystallite size and microstrain were deduced using expression (14.2) for XRD data of hybrid composite powder. The crystallite size and microstrain were calculated to be 116 nm and 0.0079; respectively. It may be noted that the crystallite size decreases and microstrain was found to be increased due to the doping of MWCNTs into TiS$_2$ nanoplates. The interplanar spacings were also determined for both TiS$_2$ as well as TiO$_2$ peaks. The diffraction peaks were fitted with pseudo-Voigt profile function to get the values of FWHM and peak position for various peaks. The interplanar spacings for various peaks were calculated by using expression (14.1) and tabulated in Table 14.1. It should be noted that a small reduction was found in the value of interplanar spacings for all diffraction maxima on doping MWCNTs in TiS$_2$ structure which shows the lattice contraction [29, 30].

The microstructural analysis of MWCNTs was performed using SEM. On the other hand, AFM (Atomic Force Microscopy) was employed to study the surface morphology of TiS$_2$ and hybrid composite of TiS$_2$/MWCNTs. Figure 14.7 shows the SEM micrograph of MWCNTs and AFM topography for both TiS$_2$ and MWCNTs doped composite structure of TiS$_2$. SEM micrograph of MWCNTs shows a lateral view at magnification scale 10 μm. Most of the synthesized MWCNTs consists a uniform diameter and length [31]. The synthesized MWCNTs length was found in the micron order. A wide range of particle sizes can be characterized in the same scan, from 1 nm to 10 μm. The SEM image contains well structured nanowires of CNTs. AFM offers high resolution and visualization in 3D images from the tip movement with high resolution.

AFM image of hybrid composite shows the well embedded MWCNTs into TiS$_2$ nanoplates as shown in Fig. 14.7c. A perfectly homogeneous structure of MWCNTs doped TiS$_2$ is described by AFM image.
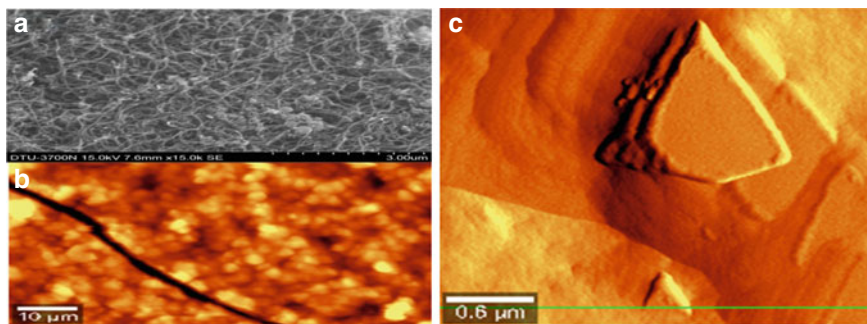
Fig. 14.7 **a** Represents SEM micrograph of MWCNTs, **b** AFM topography of TiS$_2$ nanoplates, and **c** AFM of hybrid composite of TiS$_2$/MWCNTs

14.4 Conclusion

Thin TiS$_2$ nanoplates can be produced using high temperature solution method and the resulting product having nanoscale dimensions. The XRD result confirms the formation of TiS$_2$ nanoplates synthesized through standard solid-state technique. The crystallite size was calculated using W–H plot and found to be 141 nm. On comparing the XRD data of TiS$_2$ with as synthesized TiS$_2$/MWCNTs, we observed that all peaks of TiS$_2$ shifts towards higher 2θ angle due to the lattice contraction. XRD and SEM studies show the formation of well separated cylindrical nanowires of MWCNTs with single phase. The doping of MWCNTs into TiS$_2$ nanoplates induced lattice contraction which is characterized by a reduction in interplanar spacing. A reduction in crystallite size is also observed by doping MWCNTs into TiS$_2$. MWCNTs doped TiS$_2$ may have a better potential application in the area of supercapacitors, energy storage devices like grid storage and super conductors.

References

1. Q.H. Wang, K. Kalantar-Zadeh, A. Kis, J.N. Coleman, M.S. Strano, Electronics and optoelectronics of two-dimensional transition metal dichalcogenides. Nat. Nanotechnol. **7**, 699–712 (2012)
2. F.R. Gamble, B.G. Silbernagel, Anisotropy of the proton spin—lattice relaxation time in the superconducting intercalation complex TaS$_2$ (NH$_3$): structural and bonding implications **2** (1975)
3. B. Radisavljevic, A. Radenovic, J. Brivio, V. Giacometti, A. Kis, Single-layer MoS$_2$ transistors **6** (2011)
4. A. Amara, Y. Frongillo, J. Aubin, S. Jandl, Thermoelectric TiS$_2$, **36** (1987)

5. W. Choi, N. Choudhary, G.H. Han, J. Park, D. Akinwande, Y.H. Lee, Recent development of two-dimensional transition metal dichalcogenides and their applications. Mater. Today **20**, 116–130 (2017)

6. J. Feng, X. Sun, C. Wu, L. Peng, C. Lin, S. Hu, J. Yang, Y. Xie, Metallic few-layered VS_2 ultrathin nanosheets: high two-dimensional conductivity for in-plane supercapacitors. J. Am. Chem. Soc. **133**, 17832–17838 (2011)

7. C. Singhal, M. Khanuja, N. Chaudhary, C.S. Pundir, J. Narang, Detection of chikungunya virus DNA using two-dimensional MoS_2 nanosheets based disposable biosensor. Sci. Rep. **8**, 1–11 (2018)

8. Z. Wei, B. Li, C. Xia, Y. Cui, J. He, J. Xia, J. Li, Various structures of 2D transition-metal dichalcogenides and their applications. Small Methods **2**, 1800094 (2018)

9. J.A. Wilson, F.J. Di Salvo, S. Mahajan, Charge-density waves and superlattices in the metallic layered transition metal dichalcogenides. Adv. Phys. **24**, 117–201 (1975)

10. F.J. Di Salvo, New findings in charge density wave phenomena in layered compounds. Phys. B+ C **105**, 3–8 (1981)

11. K.F. Mak, J. Shan, Photonics and optoelectronics of 2D semiconductor transition metal dichalcogenides. Nat. Photonics **10**, 216–226 (2016)

12. TiS_2 nanoplates A high-rate and stable electrode material for sodium ion batteries _ Elsevier Enhanced Reader.pdf (n.d.)

13. E. Guilmeau, Y. Bréard, A. Maignan, Transport and thermoelectric properties in copper intercalated TiS_2 chalcogenide. Appl. Phys. Lett. **99**, 52107 (2011)

14. Y. Zhou, J. Wan, Q. Li, L. Chen, J. Zhou, H. Wang, D. He, X. Li, Y. Yang, H. Huang, Chemical welding on semimetallic TiS_2 nanosheets for high-performance flexible n-type thermoelectric films. ACS Appl. Mater. Interfaces **9**, 42430–42437 (2017)

15. V.V. Ivanovskaya, G. Seifert, Tubular structures of titanium disulfide TiS_2. Solid State Commun. **130**, 175–180 (2004)

16. M. Mori, K. Ohshima, S.C. Moss, R.F. Frindt, M. Plischke, J.C. Irwin, X-ray study of c-axis parameters in disordered stage II $Ag\chi\ TiS_2$. Solid State Commun. **43**, 781–784 (1982)

17. G. Che, K.B. Jirage, E.R. Fisher, C.R. Martin, H. Yoneyama, Chemical-vapor deposition-based template synthesis of microtubular TiS_2 battery electrodes. J. Electrochem. Soc. **144**, 4296 (1997)

18. F. Wang, F. Li, L. Zhang, H. Zeng, Y. Sun, S. Zhang, X. Xu, S-TiO_2 with enhanced visible-light photocatalytic activity derived from TiS_2 in deionized water. Mater. Res. Bull. **87**, 20–26 (2017)

19. J. Ma, H. Jin, X. Liu, M.E. Fleet, J. Li, X. Cao, S. Feng, Selective synthesis and formation mechanism of TiS_2 dendritic crystals. Cryst. Growth Des. **8**, 4460–4464 (2008)

20. M.S. Dresselhaus, G. Dresselhaus, P.C. Eklund, A.M. Rao, Carbon nanotubes, in Phys. Fullerene-Based Fullerene-Related Mater., Springer, 2000, pp. 331–379

21. M. Endo, S. Iijima, M.S. Dresselhaus, Carbon Nanotubes (Elsevier, 2013)

22. K.H. Park, J. Choi, H.J. Kim, D. Oh, J.R. Ahn, S.U. Son, Unstable single-layered colloidal TiS_2 nanodisks. Small **4**, 945–950 (2008)

23. S.J.H. Rad, M. Haghighi, A.A. Eslami, F. Rahmani, N. Rahemi, Sol–gel versus impregnation preparation of MgO and CeO_2 doped Ni/Al_2O_3 nanocatalysts used in dry reforming of methane: effect of process conditions, synthesis method and support composition. Int. J. Hydrogen Energy **41**, 5335–5350 (2016)

24. H. Tang, K. Prasad, R. Sanjines, P.E. Schmid, F. Levy, Electrical and optical properties of TiO_2 anatase thin films. J. Appl. Phys. **75**, 2042–2047 (1994)

25. S.K. Sharma, V. Grover, A.K. Tyagi, D.K. Avasthi, U.B. Singh, P.K. Kulriya, Probing the temperature effects in the radiation stability of $Nd_2Zr_2O_7$ pyrochlore under swift ion irradiation. Materialia **6**, 100317 (2019)

26. J.A. Phys, Effect of bimetallic Co: Mo/MgO catalyst on the growth efficiency of single-walled carbon nanotubes Effect of bimetallic Co:Mo/MgO catalyst on the growth efficiency of single-walled carbon nanotubes, 225103 (2020)

27. C. Lu, M. Wey, The performance of CNT as catalyst support on CO oxidation at low temperature **86**, 1153–1161 (2007)
28. S.K. Sengar, B.R. Mehta, Govind, Size and alloying induced shift in core and valence bands of Pd-Ag and Pd-Cu nanoparticles, J. Appl. Phys. **115**, 124301 (2014)
29. D. Teich, T. Lorenz, J.-O. Joswig, G. Seifert, D.-B. Zhang, T. Dumitrica, Structural and electronic properties of helical TiS$_2$ nanotubes studied with objective molecular dynamics. J. Phys. Chem. C. **115**, 6392–6396 (2011)
30. M. Parvaz, N. Salah, Z.H. Khan, Optik Photocatalytic properties of TiS$_2$ nanodisc and Sb @ TiS$_2$ nanocomposite for methylene blue dye, 207 (2020)
31. V. Kumar, P.K. Tyagi, Potential application of multi-walled carbon nanotubes/activated carbon/bamboo charcoal for efficient alcohol sensing. J. Alloys Compd. **767**, 215–222 (2018)

Chapter 15
Broadband Spiral Optical Delay on a Silicon Nitride Platform at 1310 nm Wavelength

Bhawna Sharma, Kamal Kishor, Amrindra Pal, Sandeep Sharma, and Roshan Makkar

Abstract Optical delay lines are vital components in integrated optics circuits and systems having numerous applications in optical sensing, beamforming networks, microwave signal processing and optical coherence tomography. In this paper, we have reported spiral optical delay lines on a silicon nitride platform having various advantages such as a wide wavelength range, low bending losses and medium core-clad index contrast. These delay lines are compact in size and covers a footprint of few mm square for a length of approximately 68 cm. Simulations were performed using finite difference method for mode studies and eigen mode expansion method to study propagation along length. Further, different losses were analysed at 1310 nm centre wavelength and an excess loss was calculated to be less than 0.08 dB over the 200 nm bandwidth and propagation loss of 0.018 dB across the length of propagation was accounted.

15.1 Introduction

Delay lines are essential components for photonic devices and systems that have various applications in communication, radar and signal processing [1]. These delay lines can be either electrical or optical. However optical delay lines (ODLs) show

B. Sharma (✉) · A. Pal
Electronics & Communication Engineering, DIT University, Dehradun, Uttarakhand 248009, India

K. Kishor
TIFAC-Centre of Relevance & Excellence in Fiber Optics & Optical Communications, Applied Physics Department, Delhi Technological University (Formerly Delhi College of Engineering), Bawana Road, New Delhi, Delhi 110042, India

S. Sharma
Department of Electronics Engineering, Centre for Reliability Sciences and Technology, Chang Gung University, Taoyuan 33302, Taiwan

R. Makkar
Photonics Division, Society for Applied Microwave Electronics & Engineering Research, IIT Bombay Campus, Powai, Mumbai, Maharashtra, India

various advantages over electrical delay lines such as high speed and wider bandwidth and are recently deployed in various photonic integrated devices and systems [2].

ODLs are also an essential part of optical communication and networking, optical beam forming networks, sensing units, imaging processing units [3], optical coherence tomography [4] etc. In all of these cases, a precisely regulated delay must be imposed between the input and output. This delay can be achieved by either introducing an additional propagation channel or lowering the group velocity of optical signals. In general, adding an extra propagation channel is seen as a convenient method of introducing delay, while lowering group velocity will need complicated circuitry, which is still in its early stages of development [5].

Numerous research groups have deployed various techniques to introduce optical delay for photonic integrated circuits. Some of these are integrated grating delay lines (IGDL) wherein the spatial structure or refractive index parameter undergoes a periodic change mostly by modulating its structural parameters such as waveguide width and height or by modulating its effective refractive index [6], photonic crystal waveguides (PhCWs) based delay [7, 8], micro ring resonators (MRR) consists of cascaded optical ring resonators for obtaining tuneable delay lines mainly in side coupled integrated space sequence of resonators (SCISSSOR) or coupled resonator optical waveguides (CROW) fashion [9–11] and optical waveguide delay lines which are simple length dependent delay structures that can be implemented in various patterns such as serpentine, spiral or meander lines using various material technologies indium phosphide (InP), silicon nitride (Si_3N_4) and silicon on insulator (SOI) [12].

Although PhCWs offer wider bandwidth nevertheless they incur high propagation losses, MRRs on the other hand results in small foot print but in general have narrow bandwidth and bandwidth delay product is relatively small [13]. IGDLs offer compact resonant delay lines but fabrication is rather challenging and insertion loss is also high. Spiral delay lines are most promising candidate as they offer optimal area utilization with low loss, large bandwidth and does not require any external control [14]. Moreover, these delay lines can be easily integrated with other components.

We have recently designed and simulated Archimedean spiral based optical delay lines on silicon nitride platform at 1310 nm central wavelength. These delay lines are very compact in size having a foot print of few mm square and covering a length of 68 cm providing timed delay in the range of nano seconds. Simulation results were calculated and showed good agreement in terms of excess loss and propagation loss across length of propagation. These spiral delay lines when integrated with broadband directional couplers [15, 16] results in a complete chip design.

15.2 Waveguide Design and Modelling

Waveguides used for designing spiral delay lines are based on silicon nitride and silicon dioxide technology also known as Triplex [17]. A channel waveguide wherein

a high index Si_3N_4 core is buried inside low index SiO_2 layer. Schematic for waveguide design can be seen through Fig. 15.1. One of the essential factors while designing waveguides is its mode properties. Single mode waveguides are preferred over multimode waveguides as they offer lower dispersion and attenuation values.

Mode confinement for single mode waveguides requires its core dimensions to be tightly confined so as to allow only single mode to propagate. Mode calculations were performed using the finite difference approach, and simulation results were presented using the fully vectorial mode solver software FIMMWAVE. The simulation for the effective index was carried out at a wavelength of 1210 nm, which is at the lower spectral end of the whole broadband spectrum. For TE and TM modes, the effective index as a function of waveguide width was computed and the results are reported in Fig. 15.2.

Maximum waveguide width for single mode condition can be interpreted from Fig. 15.2. Only fundamental TE and TM modes are propagating in waveguides with widths less than 1.2 µm. As a result, a waveguide width of 1 µm and a thickness of 100 nm is picked, which is less than the single mode cut-off of 1.45.

Fig. 15.1 Illustration of Si_3N_4 buried inside SiO_2
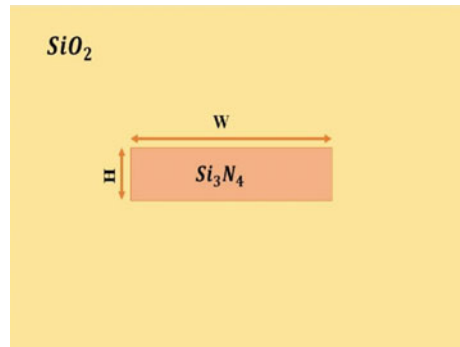
Fig. 15.2 Calculated effective index for TE and TM mode at 1210 nm versus waveguide width
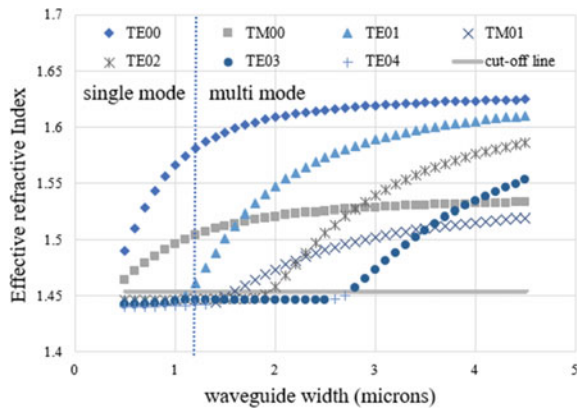
15.3   Spiral Optical Delay Lines

The main setback of length-based delay lines is their compactness and large footprint. We have deployed Archimedean spirals in order to make our optical delay line compact. They are frequently used in chip waveguides as they provide optimal area utilization.

15.3.1   Design of Spiral Delay Line

The designed structure in general consist of 2 interleaved Archimedean shaped spirals one in clockwise direction and other in counter clockwise direction wherein one brings light from outside to inside and the other returns light back from inside to outside.

Moreover, these clockwise and counter clockwise Archimedean spirals are connected via an S shaped bend consisting of 2 semi circles in opposite direction. Figure 15.3a shows the schematic for spiral optical delay line and its zoom in version for starting and ending Archimedean spirals can be seen through (b) and (c).

The total length of this reported spiral structure was accounted to be approximately 68 cm and spacing between two adjacent waveguides in order to avoid coupling was taken as 4 μm.
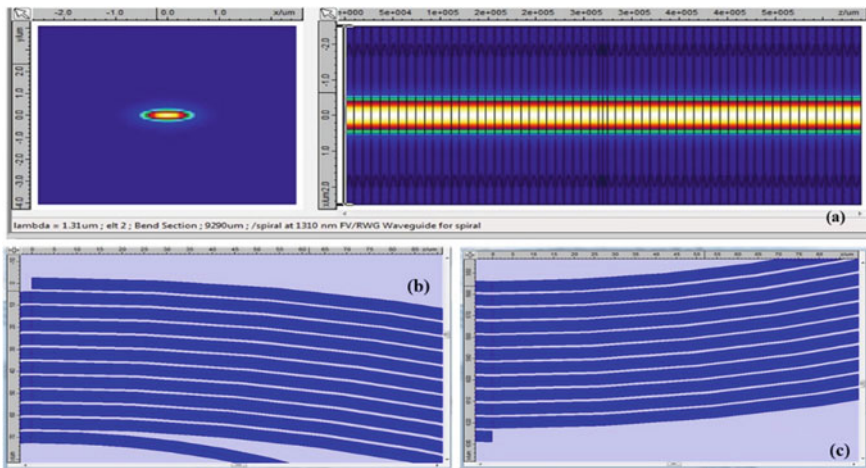
Fig. 15.3   a Transmission of spiral delay line across length at 1310 nm central wavelength **b**, **c** are zoom in view of upper and lower Archimedean spirals of reported delay line

Fig. 15.4 Loss and power transmission across length of propagation at 1310 nm central wavelength
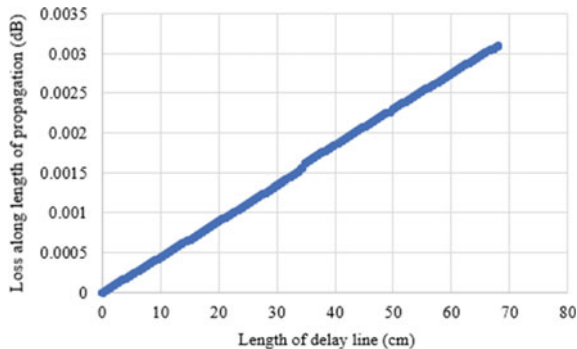
15.3.2 Simulation Results

The accountability of any structure can only be testified by its transmission and loss parameters in general. We have used eigen mode expansion method to calculate optical loss across length of propagation for 1310 nm central wavelength. Figure 15.4 show propagation loss and transmitted power across length of propagation. It can be seen from the plot that propagation loss across length of propagation was calculated to be 0.0031 dB and overall loss across length of propagation was accounted to be 0.0274 dB.

One of the essential parameters of optical delay lines to be used for photonic applications is to have a wider bandwidth. The reported structure is designed keeping such parameters in mind and has broadband bandwidth of more than 200 nm, with a centre wavelength of 1310 nm. The plot for normalized power at output over the entire bandwidth and its corresponding excess loss parameter can be seen through Fig. 15.5. It can also be seen through graph that maximum excess loss over entire 200 nm bandwidth was 0.084 dB.

Since time delay provided by spiral structure is directly dependent on its length parameter. It can then can be calculated by following relation

Fig. 15.5 Normalized power at transmission over 200 nm bandwidth and corresponding excess loss at 1310 nm central wavelength
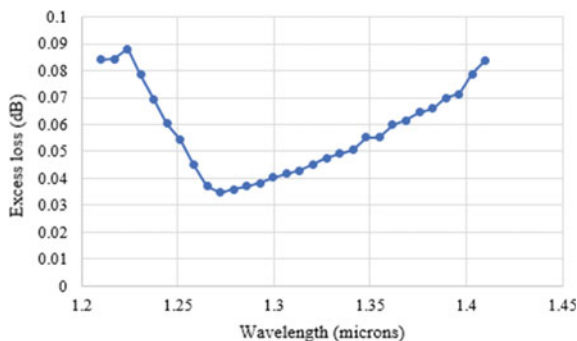
$$t_d = \left(n_g \times L\right)/C \tag{15.1}$$

where t_d is the time delay of the spiral delay line, n_g is the group effective index (1.6212) and the speed of light is denoted as C.

For a delay length (L) of 68 cm and effective group index (n_g) of 1.6212, a delay time of 3.67 ns is reported for this structure at 1310 nm.

15.4   Conclusion

In this work we have designed and simulated spiral optical delay line at 1310 nm wavelength. The waveguides used for designing delay lines were based on buried channel Triplex platform. The reported delay lines were compact, low loss and ultra-broadband in nature. Loss parameters were accounted across length of propagation and also across 200 nm bandwidth and were found to be in good agreement with our structure. These delay lines may be utilised in a variety of optical applications, including optical coherence tomography based on integrated optics.

References

1. A. Melloni, *Photonic Integrated Circuits for Tunable Delay Lines* (n.d.). http://www.polifab.polimi.it
2. J. Webster (ed.), Wiley Encyclopedia of Electrical and Electronics Engineering. Copyright (Wiley, 2014). https://doi.org/10.1016/b978-0-12-395558-6.50025-3
3. J.F. Diehl, J.M. Singley, C.E. Sunderman, V.J. Urick, Microwave photonic delay line signal processing. Appl. Opt. **54**(31), F35 (2015). https://doi.org/10.1364/ao.54.000f35
4. G. Yurtsever, B. Považay, A. Alex, B. Zabihian, W. Drexler, R. Baets, Photonic integrated Mach-Zehnder interferometer with an on-chip reference arm for optical coherence tomography. Biomed. Opt. Express **5**(4), 1050 (2014). https://doi.org/10.1364/boe.5.001050
5. Y. Li, X. Song, Y. Xu, Y.P. Li, Spiral optical delay lines in silicon-on-insulator, in *Optics InfoBase Conference Papers*, 2, 3–5 (2014). https://doi.org/10.1364/ACPC.2016.AF3G.6
6. L. Zhou, X. Wang, L. Lu, J. Chen, Integrated optical delay lines: a review and perspective [Invited]. Chin. Opt. Lett. **16**(10), 1–16 (2018). https://doi.org/10.3788/COL201816.101301

7. O. Watcharakitchakorn, R. Silapunt, Design and modeling of the photonic crystal waveguide structure for heat-assisted magnetic recording. Adv. Mater. Sci. Eng., 2018 (2018). https://doi.org/10.1155/2018/8097841

8. C.J. Chung, X. Xu, G. Wang, Z. Pan, R.T. Chen, On-chip optical true time delay lines featuring one-dimensional fishbone photonic crystal waveguide. Appl. Phys. Lett. **112**(7), 1–6 (2018). https://doi.org/10.1063/1.5006188

9. J. Xie, L. Zhou, Z. Zou, J. Wang, X. Li, J. Chen, Continuously tunable reflective-type optical delay lines using microring resonators. Opt. Express **22**(1), 817 (2014). https://doi.org/10.1364/oe.22.000817

10. F. Liu, Q. Li, Z. Zhang, M. Qiu, Y. Su, Optically tunable delay line in silicon microring resonator based on thermal nonlinear effect. IEEE J. Sel. Top. Quantum Electron. **14**(3), 706–712 (2008). https://doi.org/10.1109/JSTQE.2008.916240

11. S. Chauhan, R. Letizia, Photonic crystal-microring resonators for tunable delay lines (2018). Retrieved from http://arxiv.org/abs/1811.07828

12. S. Stopinski, M. Malinowski, R. Piramidowicz, E. Kleijn, M.K. Smit, X.J.M. Leijtens, Integrated optical delay lines for time-division multiplexers. IEEE Photonics J. **5**(5) (2013). https://doi.org/10.1109/JPHOT.2013.2280519

13. A. Melloni, A. Canciamilla, C. Ferrari, F. Morichetti, L. O'Faolain, T. Krauss, R. De La Rue, A. Samarelli, M. Sorel, IEEE Photonics J. 2(2), 181–194 (2010) https://doi.org/10.1109/JPHOT.2010.2044989

14. B. Wu, Y. Yu, J. Xiong, X. Zhang, Silicon Integrated Interferometric optical gyroscope. Sci. Rep. **8**(1), 1–7 (2018). https://doi.org/10.1038/s41598-018-27077-x

15. B. Sharma, K. Kishor, S. Sharma, R. Makkar, Design and simulation of broadband beam splitter on a silicon nitride platform for optical coherence tomography. Fiber Integr. Opt. **38**(4), 247–257 (2019). https://doi.org/10.1080/01468030.2019.1639001

16. B. Sharma, K. Kishor, S. Sharma, R. Makkar, Broadband SiN directional coupler at 850 nm for optical coherence tomography, in Proceedings SPIE 11105, Novel Optical Systems, Methods, and Applications XXII, 111050V (9 September 2019); https://doi.org/10.1117/12.2529351

17. K. Wörhoff, R.G. Heideman, A. Leinse, M. Hoekman, TriPleX: a versatile dielectric photonic platform. Adv. Opt. Technol. **4**(2), 189–207 (2015). https://doi.org/10.1515/aot-2015-0016

Chapter 16
Robust Half Metallicity in Ti Doped BaSe: A Promising Spintronic Material

Poonam, Hardev S. Saini, and Mukhtiyar Singh

Abstract To investigate the electronic and magnetic properties of $Ba_{88}Ti_{0.12}Se$ compound, the *ab-initio* calculations have been performed using full potential linearized augmented plane wave (FPLAPW) method. The ground state properties of pristine BaSe semiconductor get modified significantly after Ti doping. The $Ba_{0.88}Ti_{0.12}Se$ shows half metallic ferromagnetism at fermi level (E_F) with 100% spin polarization and can be characterised as true half-metallic ferromagnet (HMF). The emergence of half-metallic character in this compound is caused by hybridization between Ti-d and Se-p states. The total magnetic moment is essentially attributed to Ti-d states and negligible magnetic moments originated on other nonmagnetic atoms (Ba and Se). The existence of magnetism along with half-metallic gap makes the compound suitable for spintronic applications.

16.1 Introduction

Spintronics is a modern field of research, used to ameliorate the processing performance and data storage of spin-based devices. It is preferred over conventional electronics due to having several advantages such as non-volatility, improved data processing speed, better transistor density and decreased power consumption etc. The magnetic materials having spin polarization at Fermi level (E_F) with large half-metallic gap and high Curie temperature are the essential requirements for the materials to be used in spintronic devices. In last decade, transition metal (TM) based II–VI and III–V compounds [1–7] have fascinated significant attention of research community because of their tremendous electronic and magnetic properties. These

Poonam · H. S. Saini (✉)
Department of Physics, Guru Jambheshwar University of Science & Technology, Hisar, Haryana 125001, India

Poonam · M. Singh
Hindu Girls Colloge, Sonipat, Haryana 131001, India

Poonam
Department of Applied Physics, Delhi Technological University, New Delhi, Delhi 110042, India

compounds can be described as true half-metallic ferromagnets (HMFs). A number of efforts have been employed by many experimentalists and theoreticians to investigate new HMFs in order to prove the promising candidature of TM doped II–VI semiconductors in spintronic devices [5–10]. Among these, BaSe belonging to II–VI family, is scientifically important compound with extensive uses in microelectronics such as visual displays, light-emitting diodes and transparent conductors etc. [11]. The TM doping in host BaSe semiconductor significantly changes the ground state properties of the resultant compound. Recently, Bahloul et al. [7] studied ground state properties of $Ba_{1-x}Cr_xSe$ (x = 0.25, 0.50 and 0.75) using spin polarised density functional theory (DFT) and found that Cr-d and Se-p states play key role to find out the electronic properties of the present alloys. Also, the electronic structures exhibited by the resultant compounds confirm their HMF behavior. From last decades, the first-principles calculations have been carried out to investigate half-metallicity in various TM doped II–VI compounds namely Ti substituted zinc-blende (ZB) BeS [5], Ti doped MgSe [6], Cr substituted BaTe [8], V doped rock-salt SrO [9] and V doped BaS [10] etc.

In this work, we have investigated the electronics and magnetic properties of $Ba_{0.88}Ti_{0.12}Se$ with the aim that the present compound revealing half metallicity, which may be helpful to make the resultant compound for spintronic devices.

16.2 Methodology

The highly precise all electron FP-LAPW method executed in WIEN2k [12] were employed to forecast the half-metallic ferromagnetism in Ti substituted BaSe at dopant concentration of 12.5%. We used modified Becke-Johnson (mBJ) exchange potential united with GGA correlation [13] to investigate ferromagnetism in $Ba_{0.88}Ti_{0.12}Se$. Energy cutoff of -6 Ry was chosen to separate valance and core states. The muffin-tin radii (R_{MT}) of Ba, Ti and Se were taken as largest possible values so as to accomplish almost touching spheres and to make certain minimum interstitial spacings. The energy and charge convergence criterion were taken to as 10^{-4} Ry and 10^{-2}e, respectively. For k-space integration, 112 k-points were used in the irreducible Brillouin zone (IBZ) for the present compound $Ba_{0.88}Ti_{0.12}Se$.

BaSe is found to be stable in rock-salt structure, where Ba atom is placed at (0, 0, 0) and Se atom at (0.5, 0.5, 0.5) positions. A supercell ($2 \times 1 \times 1$) having 16 atoms was constructed and one Ba site at (0, 0, 0) was replaced by Ti dopant to obtain desired alloy $Ba_{0.88}Ti_{0.12}Se$.

16.3   Results and Discussion

In order to study ground state properties of $Ba_{0.88}Ti_{0.12}Se$ compound, the lattice parameter have been optimized in the vicinity of experimental lattice parameter of the host BaSe [14]. The calculated lattice parameter as listed in Table 16.1.

The total density of states (TDOS) of $Ba_{0.88}Ti_{0.12}Se$ shows unequal distribution of DOS at Fermi level (E_F) for both majority spin channel (MAC) and minority spin channels (MIC) as presented in Fig. 16.1a. The electronic and magnetic properties of present compound have been altered significantly after Ti-doping as predicted in figure and the resultant compound, $Ba_{0.88}Ti_{0.12}Se$ exhibits both metallic as well as semiconducting behaviour for MAC and MIC respectively. Due to the presence of this marvellous behaviour, this compound demonstrate half metallic ferromagnetism and thus useful for spin injection with high efficiency.

The HM gap (E_{HM}) in MIC is found to be 0.80 eV for $Ba_{0.88}Ti_{0.12}Se$ and therefore this compound is accountable to maximize the efficiency of spintronic devices. Half-Metallic Gap (E_{HM}) is an essential striking feature of the half-metallic ferromagnets and useful for studying the half-metallicity. It can be determined by finding the minimum value either of E_F-E_v^{top} or E_c^{bot}-E_F, where, E_v^{top} and E_c^{bot} represent the energy equivalent to maxima of valence band (VB) and minima of conduction band (CB), respectively [2].

Table 16.1 Calculated lattice constant (a), half-metallic gap (E_{HM}), total magnetic moment (M_{tot}) and partial magnetic moments of $Ba_{0.88}Ti_{0.12}Se$

Compounds	a(Å)	E_{HM}(eV)	$M_{Ba}(\mu_B)$	$M_{Se}(\mu_B)$	$M_{Ti}(\mu_B)$	$M_{tot}(\mu_B)$
BaSe	6.593[a]	–	–	–	–	0.0000
$Ba_{0.88}Ti_{0.12}Se$	6.434	0.80	0.0012	−0.0024	1.7382	2.0000

[a]Reference [14]
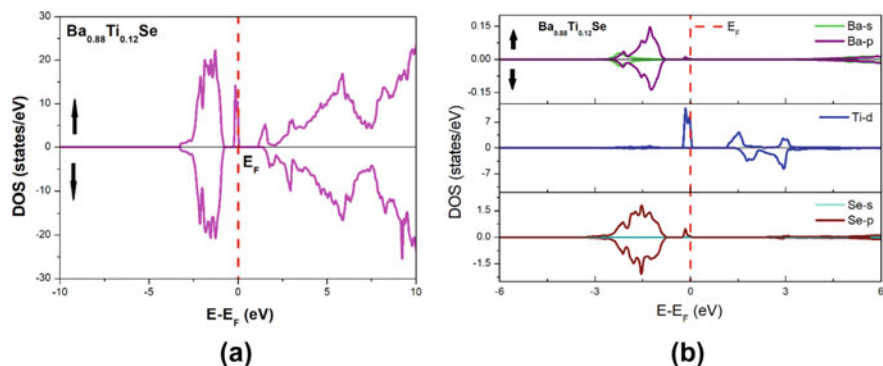
Fig. 16.1 a Total density of states (TDOS) and **b** partial density of states (PDOS) for $Ba_{0.88}Ti_{0.12}Se$ compound
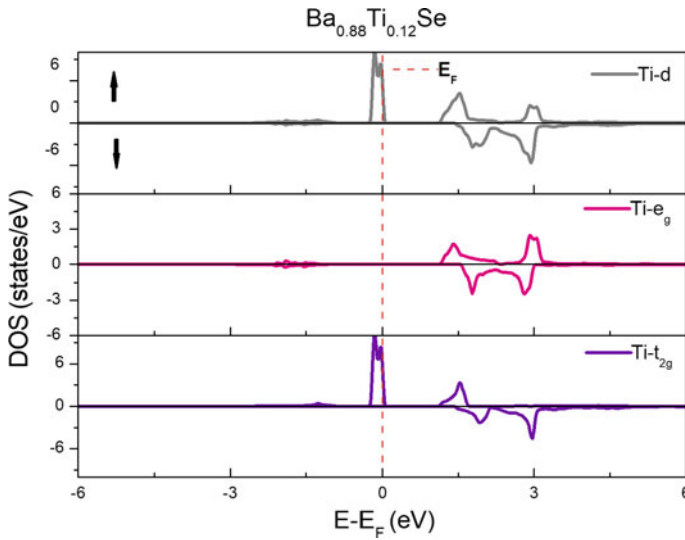
Fig. 16.2 Calculated DOS of Ti-d, e_g and t_{2g} for $Ba_{0.88}Ti_{0.12}Se$ compound

The partial density of states (PDOS) as shown in Fig. 16.1b have been explored in order to analyse the involvement of various states of individual atoms which are in turn responsible for the half metallicity of $Ba_{0.88}Ti_{0.12}Se$ compound. The occurrence of E_{HM} in MIC is a cause of hybridization among Ti-d states and Se-p states, whereas the Ba-s, Ba-p and Se-s states have minor contribution towards both the spin channels.

The emergence of HMF in $Ba_{0.88}Ti_{0.12}Se$ can be interpreted by the theory of crystal field splitting [15], according to which, the octahedral environment of Se-anions splits the Ti-3d states into three-fold degenerate t_{2g} (d_{xy}, d_{zx}, d_{yz}) and doubly degenerate e_g (d_{z2}, d_{x2-y2}) states. The DOS at fermi level is mainly generated due to t_{2g} states as shown in Fig. 16.2. This types of behaviour can be elucidated using both the Zener's p-d exchange model and double exchange mechanism [16, 17].

The total and partial magnetic moments of $Ba_{0.88}Ti_{0.12}Se$ have been calculated as listed in Table 16.1, which shows that the 3d-states of the impurity atom (Ti) contributing essentially in the total magnetic moment whereas the role of Ba and Se atoms is negligible. Also, the integer value computed for total magnetic moment confirms HM behaviour of this material.

To understand the temperament of bands at and near the E_F, the band structures of $Ba_{0.88}Ti_{0.12}Se$ have been analysed along high symmetry directions in the irreducible Brillouin zone as shown in Fig. 16.3. The bands from -2.65 to -0.75 eV in valance band (VB) is due to Se-p and Ba-p states with negligible contribution of Ti-d, Se-s and Ba-s states for both spin channels. The bands in the neighbourhood of fermi level (E_F), are generally due to Ti-d states with very small involvement of Se-p states for MAC while in MIC these states are pushed out towards the conduction band (CB). In MIC, absence of bands at/above the E_F, reveals its semiconducting behaviour.
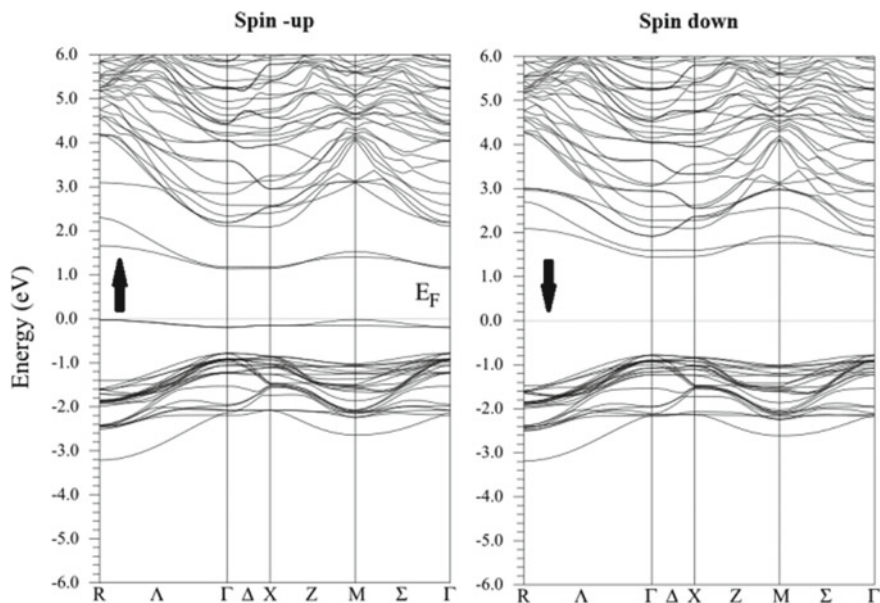
Fig. 16.3 Electronic band structure of $Ba_{0.88}Ti_{0.12}Se$ calculated by using mBJ-GGA (Fermi level set at 0 eV)

Due to the existence of this large value of HM gap, the resultant compound may be considered as a useful material in spintronics.

16.4 Conclusion

Half-metallic ferromagnetic response for $Ba_{0.88}Ti_{0.12}Se$ have been analysed by first-principles calculations with the support of DFT. To further explore electronic and magnetic properties of $Ba_{0.88}Ti_{0.12}Se$ modified Becke-Johenson (mBJ) exchange potential along with GGA correlation has been used. FM nature of the resultant compound is ratified by the integer value of M_{tot}. Also, the computed magnetic moment of Ti comes out to be less than its fundamental value and a very tiny local magnetic moment get genrated on the non-magnetic sites (Ba and Se). The main cause behind half-metallic performance of the material is the hybridization between Ti-d and Se-p states. This material is half-metallic with a significant value of E_{HM} (0.80 eV). Our predicted results reveal the opportunities for exploitation of this material in spintronic and would motivate the experimentalists to build-up this type of materials.

References

1. H.S. Saini, M. Singh, A.H. Reshak, M.K. Kashyap, J. Magn. Magn. Mater. **331**, 1–6 (2013)
2. H.S. Saini, M.K. Kashyap, M. Kumar, J. Thakur, M. Singh, Ali H. Reshak, G.S.S. Saini, J. Alloys Compd. **649**, 184–189 (2015)
3. H.S. Saini, M. Singh, A.H. Reshak, M.K. Kashyap, J. Alloys and Compd. **536**, 214–218 (2012)
4. H.S. Saini, M. Singh, A.H. Reshak, M.K. Kashyap, Comp. Mat. Sci. **74**, 114–118 (2013)
5. H.S. Saini, A.K. Pundir, V. Mehta, Nisha, P. Mehra and M.K. Kashyap, AIP Conf. Proc. **2006**, 030019-1–030019-4(2018).
6. Poonam, H.S. Saini, J. Thakur, A.K. Pundir, M. Singh, M.K. Kashyap, AIP Conf. Proc. **2093**, 020001 1–4 (2019)
7. H. Bahloul, A. Mokaddem, B. Doumi, M. Berber, A. Boudali, J. Supercond. Nov. Magn. https://doi.org/10.1007/s10948-018-4948-5(2018)
8. K. Berriah, B. Doumi, A. Mokaddem, M. Elkeurti, A. Sayede, A. Tadjer, J.P. Araújo, J. Comp. Elec. **17**, 909–919 (2018)
9. M. Berber, B. Doumi, A. Mokaddem, Y. Mogulkoc, A. Sayede, A. Tadjer, J. Electron. Mater. **47**, 449–456 (2018)
10. Z. Addadi, B. Doumi, A. Mokaddem, M. Elkeurti, A. Sayede, A. Tadjer, F. Dahmane, J. Supercond. Nov. Magn. **30**, 917–923 (2017)
11. Z. Feng, H. Hu, Z. Lv, S. Cui, Cent. Eur. J. Phys. **8**(5), 782–788 (2010)
12. P. Blaha, K. Schwarz, G.K.H. Madsen, D. Kvasnicka, J. Luitz, R. Laskowski, F. Tran, L.D. Marks, WIEN2k, An Augmented Plane Wave + Local Orbitals Program for Calculating Crystal Properties (Karlheinz Schwarz, Techn. Universität Wien, Austria, 2018). ISBN 3-9501031-1-2
13. Z. Wu, R.E.Cohen, Phys. Rev. **73**, 235116-1-6 (2006)
14. T.A. Grzybowski, A.L. Ruoff, Phys. Rev. B **27**, 6502–6508 (1983)
15. A. Zunger, Solid state Physics **39**, 377–388 (1986)
16. T. Dietl, H. Ohno, F. Matsukura, J. Cibert, D. Ferrand, Science **287**, 1019–1022 (2000)
17. T. Dietl, Semicond. Sci. Technol. **17**, 377–392 (2002)

Chapter 17
Determination of Atomic Properties of Pm-like Gold

Rinku Sharma and Sunny Aggarwal

Abstract Atomic Structure calculations and properties for Pm-like Gold were studied using different atomic codes. Spectra in these heavy atoms are very extensive and complicated as so many shells are open and so many transitions are possible. Excitation energies (Exc. Ene) for some fine structural levels involving $4f^{14}5s$, $4f^{13}5s^2$, $4f^{14}5p$, $4f^{13}5s5p$ and $4f^{12}5s^25p$ configuration are evaluated within the framework of Flexible Atomic Code (FAC). Two different set of configurations are used and the discrepancies in ground state as well as in transition wavelengths are observed and discussed in this paper. We evaluate transition wavelength (Trans. WavLe), transition probability (Trans. Prob), oscillator strength (OSt) and line strength (LSt) for the various levels. Comparisons are made between our calculated values using FAC and available results from the previous studies and good agreement has been achieved.

17.1 Introduction

Promethium-like sequence (61 electron systems) is a very interesting sequence and therefore studied both theoretically and experimentally for past few decades. There full understanding of this sequence is yet not made as the 4f shell is also open and an accurate atomic data for this sequence is a largely unsolved problem. Different studies contradict over ground state of various Pm-like ions. An reliable atomic properties for Promethium-like ions is needed as it plays vital role in the development of optical clocks in near future [1] and variation of the fine-structural constant [2–4].

Curtis and Ellis [5] in 1980 by using Hartree–Fock method studied theoretically the transition wavelength for $4f^{14}5s$ $^2S_{1/2}$-$4f^{14}5p$ $^2P_{1/2}$ and $4f^{14}5s$ $^2S_{1/2}$-$4f^{14}5p$ $^2P_{3/2}$ transition. They [5] have also calculated the lifetime for the levels belonging to $4f^{14}5p$ configuration. There calculations showed that in Pm-like ions (including Pm-like Au) 5 s-5p doublets were the dominants resonance lines. Theodosiou and

R. Sharma
Department of Applied Physics, Delhi Technological University, New Delhi, Delhi, India

S. Aggarwal (✉)
Department of Physics, Shyamlal College, University of Delhi, New Delhi, Delhi, India

Raftopoulos [6] calculated the energies of the $4f^{14}nl$ (5 s,5p,5d,4f) levels for Pm-like ions (W^{13+}, Ir^{16+}, Au^{18+}, Pb^{21+}, U^{31+}) by executing complete relativistic calculations involving Dirac–Fock approximation. Vilkas et al. [7] used $4f^{13}5s^2$, $4f^{13}5p^2$, $4f^{13}5s5p$, $4f^{12}5s^25p$, $4f^{12}5s5p^2$, $4f^{12}5p^3$ configurations to evaluate the transition wavelength (Trans. WavLe) and lifetimes in Pm-like ions. They showed that for Pm-like Au the ground state is $4f^{14}5s$ $^2S_{1/2}$ and not $4f^{13}5s^2$. Safronova et al. [8] calculated the excitation energies (Exc. Ene) for Pm-like ions (including Pm-like Au) using COWAN, HULLAC and RMBPT codes. Experimentally, datasets are available for Promethium like tungsten and gold using the Electron beam ion trap (EBIT) [9–11] and beam foil spectroscopy [12, 13]. EBIT technique provides a simple spectra containing contribution from few charge states while beam foil spectroscopy yields complex spectra which contain contribution from various charge states. Kobayashi et al. [14] using electron beam ion trap studied the extreme ultraviolet and visible spectra of Pm-like tungsten and gold and also performed collisional-radiative (CR) model calculations. They showed that ground state configuration of Pm-like Au is $4f^{14}5s$ and first excited state is $4f^{13}5s^2$.

In the present research problem, we have employed Flexible Atomic Code (FAC) to calculate energy levels, Trans. WavLe and Trans. Prob in Pm-like Au. The Fac (Flexible Atomic Code), exploits the modified multi-configuration Dirac-Hartree–Fock-Slater (DHFS) method, was developed by M. F. Gu at Stanford University for speed, multi-utility, and collisional-radiative modelling and is based on Dirac equation [15] It is used to calculate accurate and reliable fully relativistic atomic data and transition parameters for highly charged ions. The present study intends not only to extend the previous studies but to provide the detailed atomic data useful in various applications. We used have two different set of configurations and found that ground state is different for both sets in Pm-like Au. We have discussed the discrepancies in present and previous studies.

17.2   Results and Discussion

In Present calculations we have evaluated energy levels (Exc. Ene) and radiative rates using a fully relativistic flexible atomic code (FAC) with a large set of electronic configuration ([Kr]4d10) $4f^{14}5s$, $4f^{13}5s^2$, $4f^{13}5s5p$, $4f^{14}5p$, $4f^{13}5p^2$, $4f^{12}5s^25p$, $4f^{12}5s5p^2$, $4f^{12}5p^3$, $4f^{11}5s^25p^2$, $4f^{11}5s5p^3$, $4f^{10}5s^25p^3$, $4f^{10}5s5p^4$, $4f^{12}5s^25d$, $4f^{12}5s5d^2$, $4f^{13}5d^2$, $4f^{13}5p5d$, $4f^{12}5p5d^2$, $4f^{12}5p^25d$, $4f^{13}5s5d$ which generate 13,160 fine structural levels. Previous studies have not included this much large set of configurations in their study. Our ground state is $4f^{14}5s$ $^2S_{1/2}$ and the first excited state is $4f^{13}5s^2$ $^2F_{7/2}$ with this set of configuration which has also shown by Kobayashi et al. [14]. We tried to calculate the results with the above configurations using General purpose relativistic atomic code (GRASP) code which use MCDF technology which was implementing by Grant et al. [16] and used previously to calculate different parameters for various ions [17–22]. but we are unable to find it due to complex 4f shell behavior. We have presented energy levels of lowest 20

Table 17.1 Energy level (in Rydberg) for the lowest 20 levels calculated with FAC

Level No	Configuration	J	FAC (Rydberg)
0	$4f^{14}5s^1$	½	0
1	$4f^{13}5s^2$	7/2	0.77573
2	$4f^{13}5s^2$	5/2	1.059168
3	$4f^{14}5p^1$	½	3.102206
4	$4f^{13}5s^15p^1$	7/2	3.460468
5	$4f^{13}5s^15p^1$	7/2	3.664446
6	$4f^{13}5s^15p^1$	9/2	3.696742
7	$4f^{13}5s^15p^1$	5/2	3.708774
8	$4f^{13}5s^15p^1$	5/2	3.784068
9	$4f^{13}5s^15p^1$	5/2	3.990743
10	$4f^{13}5s^15p^1$	7/2	4.004742
11	$4f^{13}5s^15p^1$	3/2	4.041614
12	$4f^{12}5s^25p^1$	11/2	4.68517
13	$4f^{12}5s^25p^1$	13/2	4.737384
14	$4f^{12}5s^25p^1$	7/2	4.790259
15	$4f^{12}5s^25p^1$	9/2	4.822333
16	$4f^{14}5p^1$	3/2	4.871896
17	$4f^{12}5s^25p^1$	11/2	4.981975
18	$4f^{12}5s^25p^1$	9/2	4.989113
19	$4f^{12}5s^25p^1$	3/2	5.036973
20	$4f^{12}5s^25p^1$	5/2	5.04375

levels in Table 17.1. A general criterion is to match the calculated results with the critically assessed data published and compiled by NIST. For Pm-like Au, there is no energy level present in the database. In absence of these results other criteria to check reliability of results is to compare calculated results with the other available work and to do convergence test with the different set of configurations. We found a convergence problem when we used other set of configurations ([Kr]$4d^{10}$) $4f^{14}5s$, $4f^{13}5s^2$, $4f^{13}5s5p$, $4f^{14}5p$, $4f^{12}5s^25p$, $4f^{12}5s5p^2$ which generate 429 fine structural levels. The ground state from these configurations is found to be $4f^{13}5s^2\,^2F_{7/2}$ which is different from the ground state mentioned above. The possible explanation can be the instability of $4f$ 14 core owing to the large contribution of $4f$ -core excitations which makes the study of Pm-like Au more difficult and therefore we decided to check the authenticity of our evaluated datasets with the large set of configurations with the other available theoretical and experimental results as suggested by Fischer et al. [23].

In Table 17.2, we have furnished the complete transition data from the lowest energy (ground) state $4f^{14}5s\,^2S_{1/2}$ to other levels performed using fully relativistic FAC. One can see from Table 17.2, the Trans. Prob of two important transitions $4f^{14}5s$

Table 17.2 Transition data from $4f^{14}5s\ ^2S_{1/2}$ to various levels and 2 J for lower level I, upper level 'k', Trans. WavLe 'λ' (in Å), LSt 'S', OSt 'f', Trans. Prob 'A_{ji}' calculated using FAC

Level		λ (in Å)	f_{ij}	$A_{ji}(s^{-1})$	$S_{ij}(au)$
I	K				
0	7	245.3	3.81E−08	7.01E+02	3.81E−08
0	8	240.5	1.88E−07	3.60E+03	1.88E−07
0	9	228.0	1.47E−06	3.14E+04	1.47E−06
0	11	225.1	8.95E−07	2.93E+04	8.95E−07
0	19	180.6	2.86E−03	1.46E+08	2.86E−03
0	3	293.3	4.85E−01	1.87E+10	4.85E−01
0	16	186.8	1.54E+00	7.33E+10	1.54E+00
0	2	859.1	6.36E−15	9.54E−06	6.36E−15

$^2S_{1/2}$—$4f^{14}5p\ ^2P_{1/2}$ and $4f^{14}5s\ ^2S_{1/2}$—$4f^{14}5p\ ^2P_{3/2}$ is large while for $4f^{14}5s\ ^2S_{1/2}$—$4f^{13}5s^2\ ^2F_{7/2}$ it is very small. In Table 17.3, we have presented the comparison between our Trans. WavLe for the transitions $4f^{14}5s\ ^2S_{1/2}$—$4f^{14}5p\ ^2P_{1/2}$, $4f^{14}5s\ ^2S_{1/2}$—$4f^{14}5p\ ^2P_{3/2}$ and $4f^{13}5s^2\ ^2F_{7/2}$—$4f^{13}5s^2\ ^2F_{5/2}$ calculated with FAC with the other available results. The wavelengths listed in Column 'COWAN' and 'HULLAC' are calculated by Safronova et al. [8]. They have given the Trans. WavLe for $4f^{14}5s\ ^2S_{1/2}$—$4f^{14}5p\ ^2P_{1/2}$ and $4f^{14}5s\ ^2S_{1/2}$—$4f^{14}5p\ ^2P_{3/2}$ transitions. For the transition $4f^{14}5s\ ^2S_{1/2}$—$4f^{14}5p\ ^2P_{1/2}$ the variation in our FAC results and results presented by COWAN is about 0.73% while for $4f^{14}5s\ ^2S_{1/2}$—$4f^{14}5p\ ^2P_{3/2}$ transition the difference is 0.61%. The difference between HULLAC and FAC result is 0.92% and 0.09% respectively for the transitions $4f^{14}5s\ ^2S_{1/2}$—$4f^{14}5p\ ^2P_{1/2}$ and $4f^{14}5s\ ^2S_{1/2}$—$4f^{14}5p\ ^2P_{3/2}$. In column 'MR-MP' of Table 17.3, we furnish the results obtained by the multireference Moller-Presset approach (MR-MP) [7]. The variation in our FAC results and MR-MP data for the $4f\ ^{14}5\ s\ ^2S_{1/2}$—$4f\ ^{14}5p\ ^2P_{1/2}$ transition is greater than for the $4f\ ^{14}5\ s\ ^2S_{1/2}$—$4f\ ^{14}5p\ ^2P_{3/2}$ transition (0.6% and 0.35% respectively). The data given under the column 'DF' are the calculations of C. E. Theodosiou and V. Raftopoulos [6] are consistent

Table 17.3 Collation of computed Trans. WavLe (in Å) computed from FAC with other available Trans. WavLe for various transitions

Transition	FAC	CR-model	COWAN	MR-MP	DF	HULLAC
$4f^{14}5s\ ^2S_{1/2}$—$4f^{14}5p\ ^2P_{1/2}$	293.3	289.80[a]	291.15[b]	291.49[c]	290.33[d]	290.58[e]
$4f^{14}5s\ ^2S_{1/2}$—$4f^{14}5p\ ^2P_{3/2}$	186.8	186.63[a]th 186.6[a]exp	185.66[b]	186.14[c]	186.43[d]	186.97[e]
$4f^{13}5s^2\ ^2F_{7/2}$—$4f^{13}5s^2\ ^2F_{5/2}$	321	327.4[a]th 324.39[a]exp				

[a]Reference[14]
[b, e]Reference [8]
[c]Reference [7]
[d]Reference [6]

Table 17.4 Collation of calculated Trans. Prob (in s^{-1}) calculated from FAC with other results

Transition	FAC	CR-model	HULLAC
$4f^{14}5s\ ^2S_{1/2}$—$4f^{14}5p\ ^2P_{1/2}$	1.87E+10	2.0E+10[a]	3.78E+10[e]
$4f^{14}5s\ ^2S_{1/2}$—$4f^{14}5p\ ^2P_{3/2}$	7.33E+10	7.7E+10[a]	2.89E+11[e]

[a]Reference [14]
[e]Reference [8]

for the transition $4f^{14}5s\ ^2S_{1/2}$—$4f^{14}5p\ ^2P_{3/2}$ (0.2%) while for the transition $4f^{14}5s\ ^2S_{1/2}$—$4f^{14}5p\ ^2P_{1/2}$ the deviation is large (1%). The most recent result for the Trans. WavLe of Pm-like Au is presented by kobayashi et al. [14] who presented both experimental and theoretical results for the $4f^{14}5s\ ^2S_{1/2}$—$4f^{14}5p\ ^2P_{1/2}$, $4f^{14}5s\ ^2S_{1/2}$—$4f^{14}5p\ ^2P_{3/2}$ transitions which are given under the column of 'CR model' in Table 17.3. The experimental results projected by them are taken with a compact electron beam ion trap (CoBIT) installed at The University of Electro-Communications in Tokyo. Our FAC Trans. WavLe for both transitions are comparable and consistent with results of Kobayashi et al. [14]. The small variation between our calculated results with various literature studies is due to difference in the CI included.

To explore the cause of little disagreement, we have carried FAC calculations using different set of configurations ([Kr]$4d^{10}$) $4f^{14}5s$, $4f^{13}5s^2$, $4f^{13}5s5p$, $4f^{14}5p$, $4f^{12}5s^25p$, $4f^{12}5s5p^2$ which generate 429 fine structural levels. We face the convergence issue with this set of calculations. We found the Trans. WavLe for the transition $4f^{14}5s\ ^2S_{1/2}$—$4f^{14}5p\ ^2P_{1/2}$ and $4f^{14}5s\ ^2S_{1/2}$—$4f^{14}5p\ ^2P_{3/2}$ are 370 and 260 Å respectively which matches well with the results of Safronova et al. [8] whose RMBPT results are the transitions $4f^{14}5s\ ^2S_{1/2}$—$4f^{14}5p\ ^2P_{1/2}$ and $4f^{14}5s\ ^2S_{1/2}$—$4f^{14}5p\ ^2P_{3/2}$ are 370.9 and 260.9 Å respectively.

In Table 17.4, we have compared A-value for $4f^{14}5s\ ^2S_{1/2}$—$4f^{14}5p\ ^2P_{1/2}$ and $4f^{14}5s\ ^2S_{1/2}$—$4f^{14}5p\ ^2P_{3/2}$ transitions calculated using FAC with the results of Koyabashi et al. [14] and Safronova et al. [8]. For the $4f^{14}5s\ ^2S_{1/2}$—$4f^{14}5p\ ^2P_{3/2}$ transition, the results of Safronova et al. [8] using HULLAC deviates from other calculations by an order of magnitude. For the $4f^{14}5s\ ^2S_{1/2}$—$4f^{14}5p\ ^2P_{1/2}$ transition, our calculated A-value in agreement with the results of Koyabashi et al. [14]. The A-value calculated by Safronova et al. [8] for the transition $4f^{14}5s\ ^2S_{1/2}$—$4f^{14}5p\ ^2P_{1/2}$ differs from Koyabashi et al. [14] and our results by >10%. Table 17.3 shows that for our calculated values A-values are consistent with the recent results of Koyabashi et al. [14] which indicate towards the reliability of our calculated results.

17.3 Conclusion

Motivated by the need of authentic and consistent atomic data for Pm-like Au and due to absence of any large scale study for this ion, we have furnished the detailed and accurate atomic data. For our calculations we have employed complete relativistic Flexible atomic code. We have computed energy levels for lowest 20 levels and detailed radiative data for transition from the ground state. We have taken a large data set of configurations ([Kr]4d^{10}) 4f^{14}5s, 4f^{13}5s^2, 4f^{13}5s5p, 4f^{14}5p, 4f^{13}5p^2, 4f^{12}5s^{2}5p, 4f^{12}5s5p^2, 4f^{12}5p^3, 4f^{11}5s^{2}5p^2, 4f^{11}5s5p^3, 4f^{10}5s^{2}5p^3, 4f^{10}5s5p^4, 4f^{12}5s^{2}5d, 4f^{12}5s5d^2, 4f^{13}5d^2, 4f^{13}5p5d, 4f^{12}5p5d^2, 4f^{12}5p^{2}5d, 4f^{13}5s5d which include single and double excitations. We have confirmed the ground state of Pm-like Au is 4f^{14}5s ^{2}S$_{1/2}$ as suggested by past studies but as we change the set of configurations the ground state changes to 4f^{13}5s^2 2F$_{7/2}$ which is due to configuration interaction. We would like to mention that we have reported some new atomic data which has not been published anywhere in the previous studies which will help experimentalists for their future work. Further, the Pm-like ions are very interesting and complex to deal and more studies on these ions are needed in future.

References

1. J.C. Berengut, V.A. Dzuba, V.V. Flambaum, A, Ong. Phys. Rev. A **86**, 022517 (2012)
2. J.K. Webb, J.A. King, M.T. Murphy, V.V. Flambaum, R.F. Carswell, M.B. Bainbridge, Phys. Rev. Lett. **107**, 191101 (2011)
3. J.C. Berengut, V.A. Dzuba, V.V. Flambaum, Phys. Rev. Lett. **105**, 120801 (2010)
4. J.C. Berengut, V.A. Dzuba, V.V. Flambaum, A. Ong, Phys. Rev. Lett. **106**, 210802 (2011)
5. L.J. Curtis, D.G. Ellis, Phys. Rev. Lett. **45**, 2099 (1980)
6. C.E. Theodosiou, V. Raftopoulos, Phys. Rev. A **28**, 1186 (1983)
7. M.J. Vilkas, Y. Ishikawa, E. Trabert, Phys. Rev. A **77**, 042510 (2008)
8. U.I. Safronova, A.S. Safronova, P. Beiersdorfer, Phys. Rev. A, **88**, 032512 (2013)
9. S. Wu, R. Hutton, Can. J. Phys. **86**, 125 (2008)
10. Z. Zhao, M.L. Qiu et al., J. Phys. B: At. Mol. Opt. Phys. **48**, 115004 (2015)
11. R. Hutton, Y. Zou, J.R. Almandos et al., Nucl. Instrum. Methods B **205**, 114 (2003)
12. E. Trabert, P.H. Heckmann, Z. Phys. D. **1**, 381 (1986)
13. B.M. Jhnson, K.W. Jones et al., Nucl. Instrum. Methods B **202**, 53 (1982)
14. M.F. Gu, Can. J. Phys. **86**, 675–689 (2008)
15. Y. Kobayshi, K. Kubota et al., Phys. Rev. A **92**, 022510 (2015)
16. I.P. Grant, J. McKenzie, P.H. Norrington, D.F. Mayers, N.C. Pyper, Comput. Phys. Common. **21**, 207 (1980)
17. A. Goyal, I. Khatri, N. Singh, S. Aggarwal, A.K. Singh, R. Sharma, Can. J. Phys. **96**, 871 (2018)
18. N. Singh, S. Aggarwal, M. Mohan, Can. J. Phys. **96**, 36 (2017)
19. A.K. Singh, A. Goyal, I. Khatri, S. Aggarwal, R. Sharma, M. Mohan. Atomic data nuclear data tables **109**, 339 (2016)
20. A. Goyal, I. Khatri, S. Aggarwal, A.K. Singh, M. Mohan, Atomic data nuclear data tables, **107**, 406 (2016)
21. I. Khatri, A. Goyal, S. Aggarwal, A.K. Singh, M. Mohan, Atomic data nuclear data tables, **107**, 367 (2016)

22. A. Goyal, R. Sharma, S. Aggarwal, J. Electron Spectrosc. Relat. Phenom. **239**, 146905, (2020)
23. CF Fischer: J. Phys. B: At. Mol. Opt. Phys. **44**, 125001 (2011)

Chapter 18
Energy Transfer from Carbon Dots to Organic Dye

Vijay Kumar Sagar and Prem B. Bisht

Abstract Organic fluorophores and inorganic material such as metal nano-clusters and fluorescent quantum dots (QDs) are reliable and quantitative nanoprobes in bio-imaging and bio-sensing. The excellent water solubility, good biocompatibility, and photostability of carbon based QDs (CBQDs) make them suitable for sensing. The sensing capability of the fluorescent probe was further enhanced by the non-covalent functionalization approach with an organic dye rhodamine 6G (R6G). The nanohybrid (O-f-CD-R6G) indicates the possibility of non-radiative resonance energy transfer (NRET). Steady-state measurements indicate that the spectral overlap between the photoluminescence (PL) spectrum of O-f-CD and the absorption spectrum of the R6G makes them suitable for excited-state energy transfer studies. For Forster resonance energy transfer (FRET), the value of the critical transfer distance (R_0) obtained from the spectral overlap (22 Å) is within the permissible limit. The FRET efficiency was obtained to be 8% at R_0.

18.1 Introduction

Carbon based quantum Å dots (CBQDs) are fluorescent nanoparticles composed carbons with sizes less than 10 nm. The PL of the CBQDs can be assigned to various parameters such as quantum confinement effects, defects, or contribution of surface functional groups. Oxygen functionalized carbon dots (O-f-CDs) was synthesized by solvothermal procedure. The brightness and photostability of oxygen functionalized CDs (O-f-CD) make them suitable for sensing. Due to the high extinction coefficient, high fluorescence quantum yield, good solubility, and excellent photostability rhodamine 6G (R6G) has been widely used as a fluorescent probe in numerous investigations. Noncovalent functionalization is a preferable method to functionalize O-f-CDs without altering its physical or chemical structure. The dipole–dipole interaction between a fluorescent donor and acceptor leads to the possibility of energy transfer. The FÖrster resonance energy transfer (FRET) is a non-radiative energy transfer

V. K. Sagar · P. B. Bisht (✉)
Department of Physics, Indian Institute of Technology Madras, Chennai 600036, India
e-mail: bisht@iitm.ac.in

process. FRET technique has played a significant role in biosensing and solar energy harvesting applications. The nanohybrid has been studied with the steady-state and time-resolved measurements. The FRET based nanohybrid leads to the possibility of dual wavelength fluorescent nanoprobe which can play a vital role in demanding applications of sensing for the real time monitoring of drug-delivery in biological media.

18.2 Materials and Methods

18.2.1 Materials

Rhodamine 6G was purchased from Sigma-Aldrich chemicals. Ethylene glycol purchased from local supplier R. K. Chemicals, Chennai.

18.2.2 Sample Preparation

Oxygen functionalized carbon dots (O-*f*-CDs) was synthesized by solvothermal procedure, respectively [1]. The presence of C, H, and O in ethylene glycol makes it a suitable precursor to synthesize carbon nanomaterials. 20 mL ethylene glycol was heated at 200 °C in Teflon lined autoclave. The nucleation of carbon dots starts at higher temperatures by dehydration of ethylene glycol [2]. A homogeneous solution of the O-*f*-CD was obtained after cooling down to room temperature.

18.2.3 Analytical Methods

The absorption and photoluminescence spectra respectively, were measured using a UV–visible dual-beam spectrometer (Jasco-570) and a spectrofluorometer (Jasco, FP-6600) in front of face geometry. The Fourier transform infrared (FTIR) spectrometer (Jasco, 4100) was used to investigate the functional group attached to the O-*f*-CD. Time-resolved measurements were carried out by using the time-correlated single-photon counting (TCSPC) technique. The excitation source was a picosecond (ps) diode laser (1 MHz, Pil 047 (Advance Photonics System)) with excitation wavelength of 365 nm. The decay profiles were analyzed with the help of a commercial software FAST (Edinburgh Instruments).

Fig. 18.1 FTIR spectrum of
O-*f*-CQDs
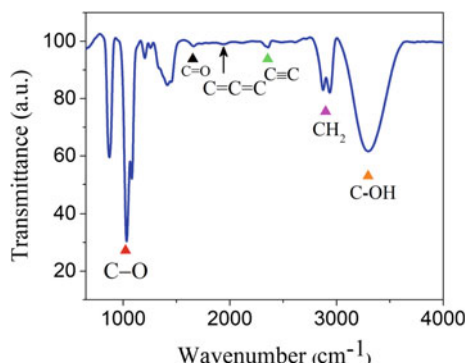
18.3   Results and Discussion

18.3.1   *Characterization of O-**f**-CDs*

FTIR of the as-prepared CD is shown in Fig. 18.1. The dehydration of ethylene glycol at 200 °C leads to the formation of the CD nucleus indicates the C=C bonding.

The presence of various functional groups such as hydroxyl, carboxyl, and carbonyl groups were confirmed. The stretching of C=O and C–OH at 1650 and 3300 cm^{-1} are positioned in the FTIR spectrum.

18.3.2   *Steady-State and Excited State Measurements*

The photoluminescence (PL) spectrum of the as-prepared CDs shows excitation energy-dependent behavior (Fig. 18.2, panel A). The PL peak of the O-*f*-CDs shifts with increasing the excitation wavelength (Fig. 2A). Ding et al. have proposed that the surface defects leads to surface-state related PL [3]. Surface states can be influenced by controlling the degree of oxygen on the surface of CDs, which control the PL. The PL spectrum of O-*f*-CDs ($\lambda_{ex.}$ 350 nm) and absorption spectrum of R6G is shown in panel B.

The PL decay curves of O-*f*-CDs were recorded at different emission wavelengths on excitation at 365 nm. The decay profiles were fitted with the multi-exponential function as follows.

$$I(t) = \sum_{i=1}^{3} \alpha_i e^{-t/\tau_i}$$

Here τ_i are the decay constants along with the corresponding amplitudes α_i.
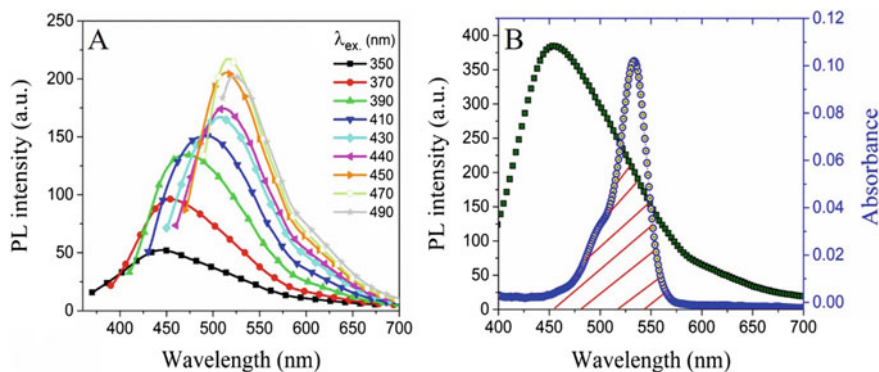
Fig. 18.2 The excitation energy-dependent PL of O-*f*-CDs (panel A). The spectral overlap of the PL of O-*f*-CDs and the absorption spectrum of the R6G (10^{-5} M) is shown in panel B

Table 18.1 Lifetimes and amplitudes of O-*f*-CDs at 365 nm excitation wavelength

$\lambda_{em.}$(nm)	τ(ns)	χ^2	τ_1(ns)	α_1	τ_2(ns)	α_2	χ^2
440	3.51	5.08	1.52	0.41	5.40	0.59	1.08
480	4.19	4.37	1.60	0.37	6.00	0.63	1.18
520	4.45	4.44	1.63	0.30	6.26	0.70	1.16

Both the decay constants increase with the emission wavelength. It was observed that the increase in the PL wavelengths leads to the increment in the PL lifetime parameters (Table 18.1). This rise in the decay lifetimes confirms the existence of localized intermediate energy states (LIES). Consequently, the LIES increase the recombination time of the exciton at 440, 480, and 520 nm emission wavelengths, respectively [4].

18.3.3 *Excited-State Energy Transfer*

The nanohybrid of the O-*f*-CDs and R6G was developed by the non-covalent functionalization procedure. The mixture of the O-*f*-CDs (of fixed concentration) and the variation in the R6G concentrations was stirred at room temperature for 2 h. The spectral overlap between the donor (O-*f*-CDs) emission spectrum and the acceptor (R6G) absorption spectrum is shown in Fig. 2B. The spectral overlap integral ($J(\lambda)$) was calculated to estimate the critical FÖrster radius [5].

$$J(\lambda) = \frac{\int_0^\infty F(\lambda)\varepsilon_A(\lambda)\lambda^4 d\lambda}{\int_0^\infty F(\lambda)d\lambda} \tag{18.1}$$

Here, $\varepsilon_A(\lambda)$ is the molar extinction coefficient of the acceptor and $F(\lambda)$ is the PL of the donor. The critical transfer distance (R_0) between the donor and acceptor pair was obtained using the spectral overlap.

$$R_0^6 = 9.78 \times 10^3 \left[\kappa^2.n^{-4}.Q_D.J(\lambda). \right]^{1/6} \tag{18.2}$$

Here, $\kappa^2 = \left[\vec{d}.\vec{a} - 3\left(\vec{d}.\vec{r}_{da} \right)\left(\vec{a}.r_{da} \right) \right]^2$ is the orientation factor. The transition dipole moments ($\vec{d}$ and $\vec{a}$) correspond to the donor and acceptor systems, respectively. The distance between the FRET pair is represented by $|\vec{r}_{da}|$. Q_D is the donor PL quantum yield and n is the refractive index of the medium. The value of the critical transfer distances and FRET efficiency (η) are given in Table 18.2. The quenching of the donor PL in the FRET pair is as expected due to non-radiative energy transfer from the O-f-CDs to R6G. Figure 3A gives the PL spectra of the O-f-CDs as a function of the R6G concentration.

The determination of the PL quenching of the donor as a function of the acceptor concentration was studied by Stern–Volmer (SV) relation and is shown in Fig. 3B [6]. The SV plot exhibits a linear behavior and was fitted with Eq. 18.3.

$$\frac{F_0}{F} = (1 + K_{SV}[Q]) \tag{18.3}$$

Table 18.2 Donor lifetime, spectral overlap integral, quantum yield, critical transfer distance, and FRET efficiency for O-f-CDs-R6G pair

τ_D(ns)	$J(\lambda)$ $\left(nm^4\ M^{-1}\ cm^{-1} \right)$	Quantum yield	R_0 Å	$\eta_{FRET}(\%)$
4.76	4×10^{13}	0.20	22	8.0
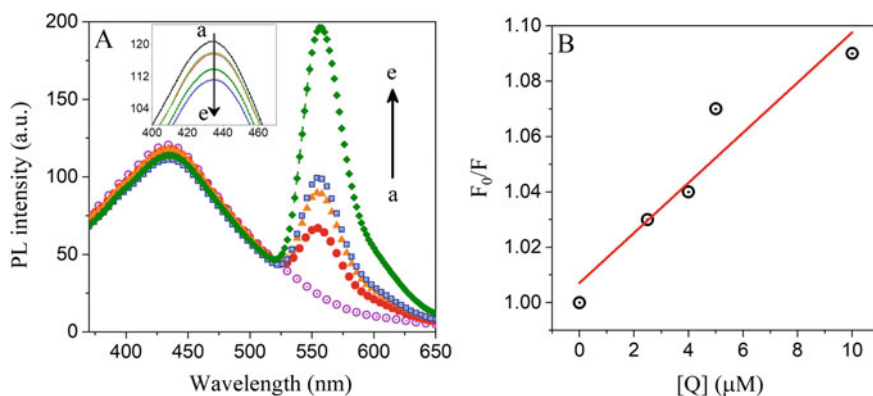
Fig. 18.3 Fluorescence spectra of O-f-CDs (λ_{ex}.350 nm) in presence of varying concentration of R6G acceptor, (a) 0 M, (b) 2.5×10^{-6} M, (c) 4.0×10^{-6} M, (d) 5.0×10^{-6} M and (e) 10×10^{-6} M (panel A). Panel B gives the SV plot

Here, F_0 and F are the PL intensities of the O-f-CDs in the absence and presence of the R6G (acceptor). The value of the quenching constant (K_{SV}) was found to be $9 \times 10^3\ M^{-1}$.

In conclusion, the nanohybrid developed by the noncovalent functionalization of O-f-CDs with R6G leads to non-radiative resonance energy transfer from O-f-CDs to R6G and suggests the capability as a dual wavelength probe for nanosensor based applications.

References

1. S. Hu, R. Tian, Y. Dong, J. Yang, J. Liu, Q. Chang, Modulation and effects of surface groups on photoluminescence and photocatalytic activity of carbon dots. Nanoscale **5**(23), 11665–11671 (2013)
2. J.R. Clifton, W.J. Rossiter, P.W. Brown, Degraded aqueous glycol solutions: pH values and the effects of common ions on suppressing pH decreases. Sol. Energy Mater. **12**(1), 77–86 (1985)
3. H. Ding, S.B. Yu, J.S. Wei, H.M. Xiong, Full-color light-emitting carbon dots with a surface-state-controlled luminescence mechanism. ACS Nano **10**(1), 484–491 (2016)
4. S. Zhu, J. Zhang, S. Tang, C. Qiao, L. Wang, H. Wang, X. Liu, B. Li, Y. Li, W. Yu, X. Wang, H. Sun, B. Yang, Surface chemistry routes to modulate the photoluminescence of graphene quantum dots: From fluorescence mechanism to up-conversion bioimaging applications. Adv. Funct. Mater. **22**(22), 4732–4740 (2012)
5. I. Medintz, N. Hildebrandt (eds.), *FRET—Förster Resonance Energy Transfer* (Wiley-VCH Verlag GmbH & Co. KGaA, 2013)
6. S.R. Bongu, A.V. Veluthandath, B.R.K. Nanda, S. Ramaprabhu, P.B. Bisht, Control over the charge transfer in dye-nanoparticle decorated graphene. Chem. Phys. Lett. **644**, 176–182 (2016)

Chapter 19
Shape and Size Dependence of Noble Metal Nanoparticles on Decay Rates of an Emitter

Tulika Agrawal, Shubhayan Bhattacharya, Gurvinder Singh, Hala Zreiqat, and Prem B. Bisht

Abstract Plasmonics deals with the interaction of the electromagnetic field of an emitter with the noble metal nanoparticles or nanosheets through the evanescent wave coupling. The emitter can either be excited directly by an excitation light or by the evanescent field itself. Excitation through the evanescent field works as a sensor as these fields are sensitive to the surroundings. In this work, the photoluminescence and excited state decay rate of a standard laser dye rhodamine B (RB) has been studied as a function of the shape and size of gold nanoparticles (AuNPs). It has been found that for example, for an octahedral shaped AuNP, the luminescent yield of RB is reduced by a factor of 20 in water. Finite element simulations also show that the localized field of AuNPs changes with their morphology that affects the decay rate of an emitter.

19.1 Introduction

The field of plasmonics has a wide range of applications [1]. Surface plasmons are the collective oscillations of the pool of electrons on the metal surface under the application of the electric field. For nanoparticles these are known as localized surface plasmon resonances (LSPR) [2]. Features like increased surface to volume ratio and a large number of dangling surface bonds make nanoparticles unstable. Hence, they are prone to attach themselves to other particles or functional groups to become stable. Due to an increase in surface to volume ratio, the size and shape effects become significant [2]. It has been seen that the resonance peak shifts with the size of the nanoparticles leading to the shift in the absorption spectrum. The localized electric fields, known as the hot-spots depend on the shape of the nanoparticle. Hence, the phenomenon such as Raman scattering, which is sensitive to the intensity of the

T. Agrawal · S. Bhattacharya · P. B. Bisht (✉)
Department of Physics, Indian Institute of Technology Madras, Chennai, Tamil Nadu 600036, India
e-mail: bisht@iitm.ac.in

G. Singh · H. Zreiqat
School of Biomedical Engineering, University of Sydney, Sydney, NSW 2006, Australia

electric field can use these nanoparticles of appropriate size and shape to enhance the Raman signal [3].

The decay time of the excited state is a fundamental property of a material as it explains not only the energy levels but also how the material behaves in the presence of an external parameter. The changes in the lifetime take place according to the structure of the material and the parameters of the surrounding. The observed lifetime (τ) has the contribution of both the radiative decay rate (k_r) as well as the non-radiative decay rate (k_{nr}) as follows

$$\tau = \frac{1}{k_r + k_{nr}} \tag{19.1}$$

It has been reported that when NPs are brought in contact with an emitter, they tend to quench the photoluminescence (PL) of the emitter [4, 5]. Also, they can influence the quantum yield of the emitter [4, 6]. In this paper, we present the effect of evanescent wave coupling of different shapes of gold nanoparticles (AuNPs) on the PL decay times of a standard organic dye rhodamine B (RB).

19.2   Experiment

Standard organic dye RB was used as received (Aldrich). All the samples were made in high purity distilled (DI) water. AuNPs of various shapes (nanorod and octahedral) were fabricated following the procedure described elsewhere[7, 8]. RB solution of concentration 10^{-5} M was prepared in DI water. A mixture of RB solution and AuNPs colloidal solution with a 1:6 ratio (100 µl of RB solution with 600 µl of AuNPs) was prepared. The samples were made and kept under ambient conditions. UV–Visible absorption spectra for dye, NPs, and its mixture were measured using halogen and deuterium lamp excitation using a spectrophotometer (JASCO, V-570). PL spectra of dye and the mixture were also measured using a home build setup at the excitation wavelength of 405 nm from a laser pointer with a power of <1 mW and a spectrometer (Ocean Optics, HR2000). Lifetimes were recorded for dye and the mixture using time-correlated single-photon counting (TCSPC) technique with an excitation wavelength of 365 nm and at emission wavelengths of 580 and 600 nm. Data were recorded through a software T900 and analyzed with the FAST software (Edinburgh Instruments).

19.3   Simulations

To have an estimate of the strength and distribution of the electric field due to AuNPs, we have performed the simulations on a single AuNP. Figure 19.1 shows the finite element analysis (Comsol Multiphysics) of an individual AuNP. It can be seen that
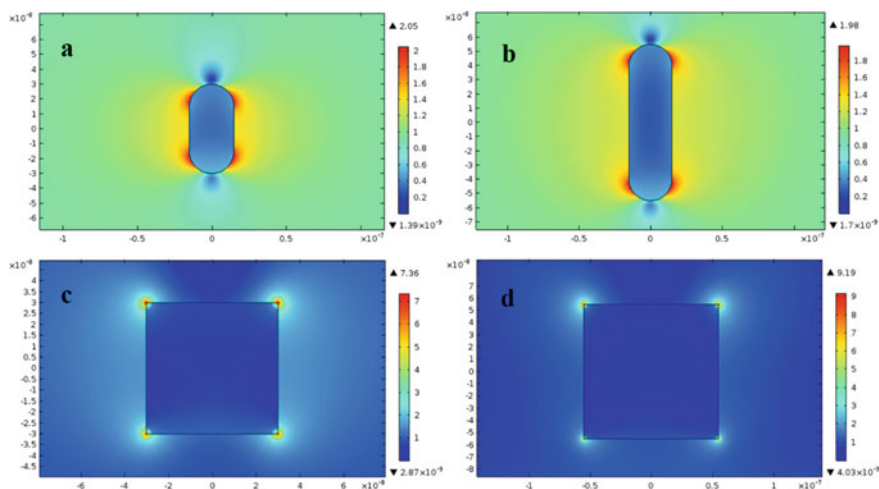
Fig. 19.1 Hotspots of nanorod (**a**, **b**) and nanocube (**c**, **d**) AuNP at 520 nm; **a** height = 60 nm, width = 30 nm; **b** height = 110 nm, width = 30 nm; **c** side = 60 nm; **d** side = 110 nm

Table 19.1 Electric field strength of different shape and size of AuNPs

Shape	Nanorod		Nanocube	
Size	w = 30 nm, h = 60 nm	w = 30 nm, h = 110 nm	s = 60 nm	s = 110 nm
Field strength (V/m)	2.05	1.98	7.36	9.19

for the nanorod, the localized field intensity decrease with size. On the other hand, for nanocube, it increases with size. Table 19.1 gives the field strength for different shapes and size of individual AuNP.

19.4   Results and Discussions

The absorption and PL spectra of dye in combination with various shapes of AuNPs were needed. As shown above, for example for nanorod and nanocube it can be seen that the effect of hotspot is expected to manifest in the spectra. In addition, the size effect is also seen. Experimentally, we observed that there is a drastic change in the PL of dye for nanorod and octahedral shaped AuNPs. Therefore, a detailed study on the two are given.

Figure 19.2 shows the scanning electron microscope (SEM) images of nanorod and octahedral AuNPs prepared by Refs. [7, 8].
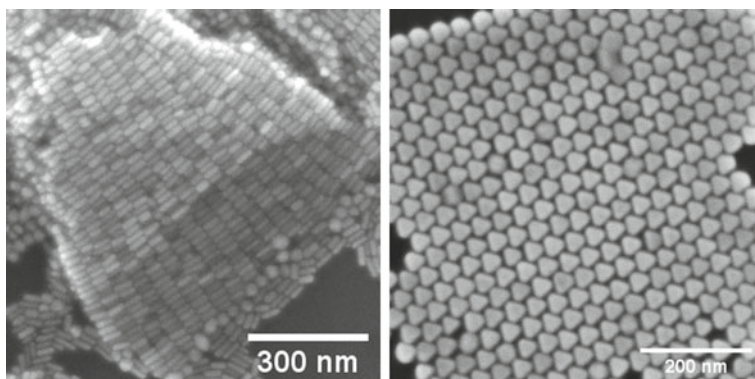
Fig. 19.2 SEM image of nanorod (left) and octahedral (right) AuNPs after drying on silicon wafer

The absorption spectra of nanorod and octahedral shaped AuNPs are shown in Fig. 3a. It can be seen that absorption peak changes with the shape due to the change in the resonance peak and cover a wide range of wavelength. Figure 3b shows the spectral overlap of the absorption and PL spectra of RB.

The emission spectra of the RB on mixing with the AuNPs are shown in Fig. 19.4. The absorption of the mixture follows the same pattern as the absorption of AuNPs without any significant change. The PL spectra show a peak in between 570 and 580 nm (peak of RB is at 578 nm). Quenching in PL by the factor of 20 has been observed. This happens because the absorption of AuNPs mask the PL of RB. Also, there is a red-shift of 2–3 nm in the peak position.

To get a better idea of the effect of AuNPs, the decay time measurements of the RB-AuNP system were carried out. Figure 5a shows the decay profiles of RB on the addition of AuNPs. For nanorod shaped AuNPs, the decay curve fits with a single exponential function. On the other hand, for octahedral, a biexponential behavior is
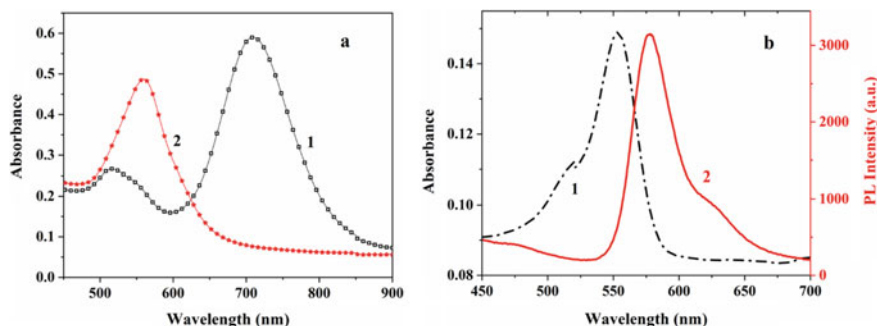
Fig. 19.3 a Absorption of nanorod (1) and octahedral (1) AuNPs in water. **b** Absorption (1) and PL (2) spectra of RB
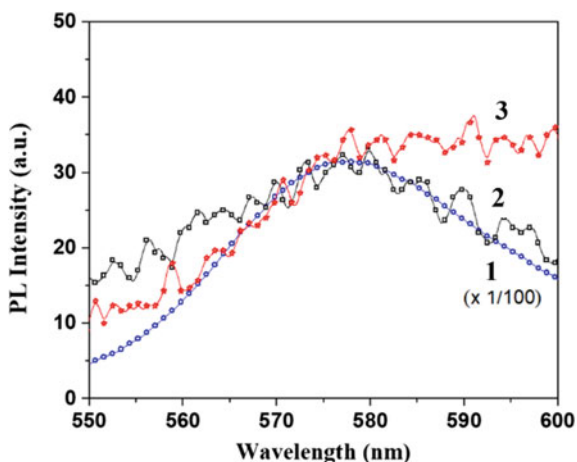
Fig. 19.4 PL of RB without (1) and with nanorod (2) and octahedral (3) shaped AuNPs
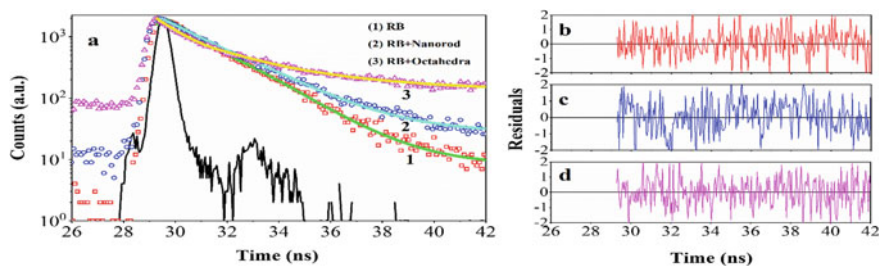
Fig. 19.5 a PL decay profile of RB without (1) and with AuNPs (2 & 3), **b–d** are the residues of the fitted functions. IRF is the instrument response function

observed. Table 19.2 gives an analysis of modifications in the lifetime due to the presence of AuNPs.

We propose this to be because of the charge transfer between RB and octahedral shaped AuNPs.

Table 19.2 Lifetime analysis of RB without and with AuNPs

Sample	$\tau_{1(ns)}$	$\tau_{2(ns)}$	χ^2
RB	1.68 ± 0.12	–	1.03
RB + Nanorod	1.99 ± 0.11	–	1.10
RB + Octahedral[a]	1.02 ± 0.04	3.69 ± 0.15	0.95

[a]The lifetime components have equal weightage

19.5 Conclusions

In conclusion, we studied the effect of AuNPs on the steady-state and PL decay measurements of the standard laser dye RB. PL decay measurements reveal that the lifetime of RB in the presence of AuNPs is dependent on the shape of the NPs. Electric field simulations show that the hotspots at the vicinity of the NPs are dependent on shape and size and hence can modulate the PL behavior of dye molecules near them. It has been also found that the PL of RB is quenched by a factor of 20 when mixed with octahedral AuNPs due to association with their dangling bonds and charge transfer. Since the quantum yield of RB is solvent and temperature-dependent, the lifetime changes take place accordingly.

References

1. A. Polman, Science **322**, 868 (2008)
2. E. Roduner, Chem. Soc. Rev. **35**, 583 (2006)
3. B. Sharma, R.R. Frontiera, A.I. Henry, E. Ringe, R.P. Van Duyne, Mater. Today **15**, 16 (2012)
4. R. Jurga, F. Della Sala, J. Phys. Chem. C **121**, 22361 (2017)
5. E. Dulkeith, A.C. Morteani, T. Niedereichholz, T.A. Klar, J. Feldmann, S.A. Levi, F.C.J.M. van Veggel, D.N. Reinhoudt, M. Möller, D.I. Gittins, Phys. Rev. Lett. **89**, 12 (2002)
6. S. Dey, Y. Zhou, X. Tian, J.A. Jenkins, O. Chen, S. Zou, J. Zhao, Nanoscale **7**, 6851 (2015)
7. S. Bandyopadhyay, G. Singh, W.R. Glomm, Mater. Today Chem. **3**, 1 (2017)
8. P.J. Chung, L.M. Lyu, M.H. Huang, Chem.—A Eur. J. **17**, 9746 (2011)

Chapter 20
Structural, Morphological and Electrochemical Studies of Complex Spinel Titanate $Li_2ZnTi_3O_8$

Anchali Jain, Amrish K. Panwar, and Pawan K. Tyagi

Abstract Complex spinel lithium zinc titanate (LZTO) has been prepared using a simple and facile high-temperature solid-state reaction route followed by calcination at high temperatures in the air atmosphere. Structural analysis was studied using X-ray Diffraction, confirms that the proper phase of LZTO is formed with cubic spinel structure with $P4_332$ space group. Morphological studies are carried by scanning electron microscope and energy dispersive x-rays and it reveals that irregular shape particle in sub-micron range. Electrochemical analysis of synthesized sample has been conducted and electrochemical impedance spectroscopy, galvanostatic charge–discharge and cyclic voltammetry results are observed. Conductivity measurements indicate that the LZTO sample has the resistance and conductivity of the order of $\sim 10^7$ Ω and $\sim 10^{-8}$ S/m respectively. CV results leads to pair of anodic/cathodic peaks of 1.53 V/0.93 V in the range of 0.05–3.0 V (vs. Li//Li$^+$). These results display that synthesized material LZTO acquire the properties of high-energy storage material when applicable as anode.

20.1 Introduction

In today's world research has been shifted from bulk materials to nanomaterials. Presently, Nano-size materials are in demand because they own high surface area, ultimate strength, good conductivity, and many more properties [1]. Apart from all the applications of nanostructured materials in different fields of technology, energy storage devices such as rechargeable batteries show tremendous advancement. Currently, lithium-ion batteries (LIBs) are used in every sector of industries: from electronics to transportation [1]. Nanotechnology in electrode materials provides an approach to increase the energy density, cycle life, safety, and efficiency of LIBs. The performance of LIBs depends on many factors which include electrode/electrolyte interface area. In comparison to bulk materials, nanostructured material exhibits a large surface-to-volume ratio which may enhance the reaction between the surface

A. Jain · A. K. Panwar (✉) · P. K. Tyagi
Department of Applied Physics, Delhi Technological University, New Delhi, Delhi 110042, India
e-mail: amrish.phy@dtu.ac.in

of the electrode and electrolyte. The increase in electrode/electrolyte contact area escalates the diffusion of lithium ions with active material and consequently improves the specific capacities at higher current rates [1, 2].

Nano-sized materials provide a shorter path length for Li-ions in the intercalation/de-intercalation process thus improved the rate capability of batteries [1, 2]. Structural stability is an important factor in the case of batteries during the insertion/extraction process of lithium ions. An electrode material within the nano-range holds its volumetric expansion, and hence shows stable cycle performance at different current rates [2].

In recent past, research and development has been more focused on the synthesis of electrode materials in the nano range. LIBs include anode as negative electrode, cathode as positive electrode, and separator. Traditionally, graphite has been used as an anode electrode because of its low cost, high abundance, and excellent electrochemical properties but its low potential, dendrite formation, and structural instability at higher temperatures hinder the safety of the LIBs [3]. Therefore, there is utmost need for new alternative anode materials to replace the carbonaceous/graphitic anodes. Among them, titanium-based materials such as Li4Ti5O12 show potential due to their "zero stress–strain" characteristics, exhibiting no structural change during insertion/extraction of Li^+ during redox reactions [3, 4]. But Li4Ti5O12 owns a low theoretical capacity (175 mAh g^{-1}) which restricts its use in high energy density LIBs [5]. Moreover, LTO has poor electronic conductivity (~10^{-13} S cm^{-1}) and its high potential (~1.55 V vs. Li/Li^+) limit its practical applications [5, 6]. Here, it has been reported that a new category of cubic spinel material, lithium zinc titanate, $Li_2ZnTi_3O_8$ (LZTO) indicates high theoretical capacity (227 mAh g^{-1}), no structural change, and lower potential (~0.5 V vs. Li/Li^+) [6, 7]. In the LZTO spinel structure, Li^+ and Ti^{4+} occupy octahedral sites in 1:3, and Li^+ and Zn^+ occupy tetrahedral sites in 1:1 [8]. Therefore, LZTO can be described in the formula as $(Li_{0.5}Zn_{0.5})_{tet}[Li_{0.5}Ti_{1.5}]_{oct}O_4$, forming a network of 3D tunnel, providing a multi-channel path for lithium ions insertion and extraction process [8, 9]. Unfortunately, its low electronic conductivity and poor diffusion coefficient limit its applications at a higher current rate [6–9].

To overcome these issues, synthesize of nano-structure lithium zinc titanate (LZTO) has been carried out by solid-state reaction route following the calcinations in the air atmosphere. Physico-chemical analysis of LZTO material is performed using XRD, SEM and EDX analysis. Electrochemical studies of synthesized sample are observed by Cyclic Voltammetry, Electrochemical Impedance Spectroscopy, and Galvanostatic Charge–Discharge.

20.2 Experimental

20.2.1 Synthesis of Material

Solid-state reaction route was used to prepared $Li_2ZnTi_3O_8$ was with calcinations at high temperature. Precursors of TiO_2, Li_2CO_3, and $Zn(CH_3CO_2)_2.2H_2O$ are thoroughly mixed in stoichiometric ratio in a planetary ball mill for and milled for 4 h Then the resulting milled material was first calcined at temperature of 700 °C for 3h followed by 800 °C for another 5 h in air atmosphere.

20.2.2 Characterization of Material

Crystal structure determination was performed using powder X-ray diffraction (XRD, rigaku ultima IV) in the range of diffraction angle (2θ), 10°–90° using $CuK\alpha_1$ source of radiation wavelength, 0.154 nm. The morphological analysis was studied using Scanning Electron Microscopy (SEM, Model: ZEISS EV018) and elemental composition was carried out using energy dispersive x-ray (EDAX) analysis. The electronic conductivity and resistance measurements were carried out with Keithley 6430 source meter. For electrochemical measurements, a CR2016 half-cell assembly was used. To prepare working electrode for testing electrochemical properties homogeneously mixing of active material (LZTO), super P and PVDF (binder) has been mixed in the ratio of 80:10:10, respectively. N-methyl-2-pyrrolidine was used as a solvent for slurry preparation. After mixing, copper foil was used to coat the slurry using doctor blade and it was dried at 120 °C for overnight in a vacuum. Then, electrodes of 16 mm in diameter were punched and further after drying at 60 °C in vacuum oven, it was placed into the MBraun glove box. Half cells (CR2016) were prepared LZTO versus Li metal in Ar filled glove box. Electrochemical testing was performed in a Biologic make VMP3 model cell test system at room temperature. Galvanostatic Charge-Discharge (GCD) and cyclic voltammetry tests was carried out in the potential range of 0.05–3.0 V (vs. Li/Li$^+$). The Electrochemical Impedance Spectroscopy (EIS) was measured with AC pulse signal of 5 mV keeping frequency within 100 KHz to 10 mHz interval.

20.3   Results and Discussion

20.3.1   Structural (XRD) and Morphological (SEM and EDAX) Analysis

XRD pattern of prepared $Li_2ZnTi_3O_8$ nano-material synthesized are shown in Fig. 20.1a. All the intensity peaks of the material are in accordance with cubic spinel system (JCPDS#086-1512) with $P4_332$ space group. All the sharp diffraction peaks show the crystalline nature of synthesized material with no impurity present.

The crystallite size of LZTO was calculated to be 36.78 nm using Scherrer's formula. Using the structure model of $P4_332$ space group, rietveld refinement was performed for structural analysis. The corresponding atomic positions, lattice parameters, and accuracy of the simulation are summarized in Table 20.1. The goodness of fit was found to be 1.80 which indicates the refinement results are acceptable. The lattice constant is found to be a = 8.3693 Å and volume = 586.24 Å^3 after rietveld refinement which is consistent with actual parameters.

Figure 20.2a–c shows the SEM micrographs for LZTO material at different magnifications. It can be observed that particles have an irregular shape in the sub-micron range. Also, slight agglomeration can be seen in the synthesized material. The average
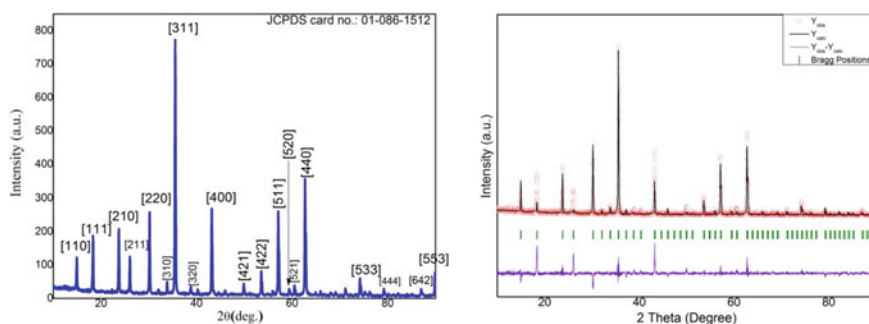
Fig. 20.1 **a** XRD spectra of as synthesized LZTO material, **b** rietveld refinement pattern of LZTO

Table 20.1 Structural parameters result for synthesized $Li_2ZnTi_3O_8$ sample

Site	Atom	x	y	z	Occupancy
8c	Li	0.01131	0.01131	0.01131	0.5
4b	Li	0.62500	0.62500	0.62500	1
12d	Ti	0.38043	0.86957	0.12500	1
8c	Zn	0.01131	0.01131	0.01131	0.5
24e	O	0.93750	0.11142	0.35362	1
8c	O	0.39379	0.39379	0.39379	0.39379
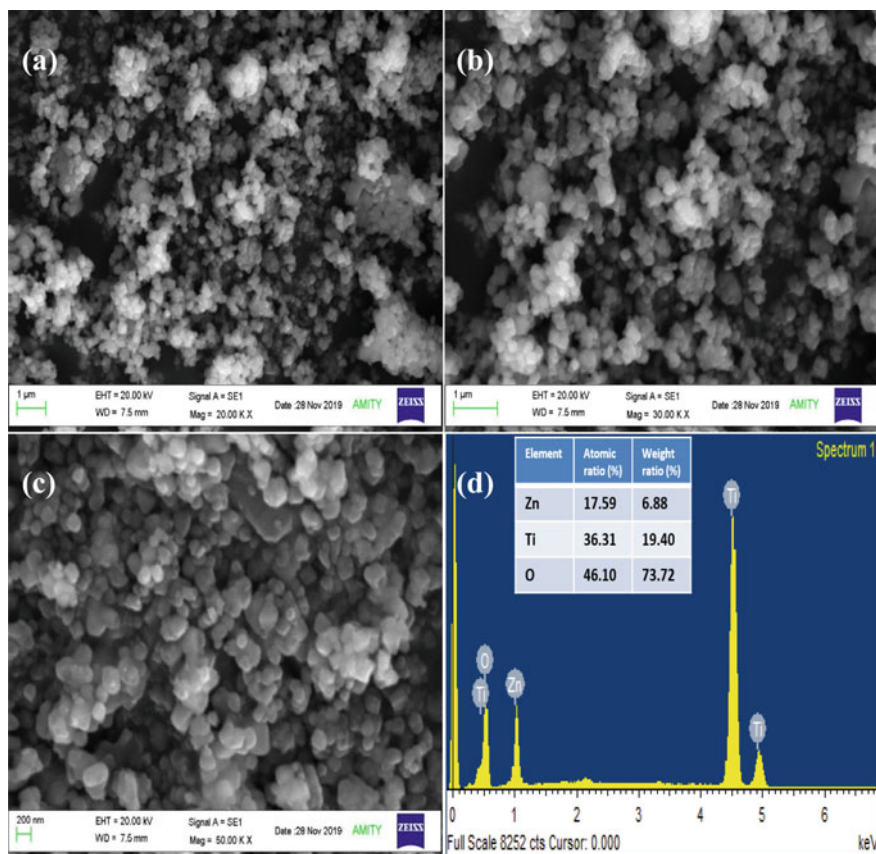
Fig. 20.2 SEM micrographs at different magnifications: **a** 20 K, **b** 30 K, **c** 50 K and **d** EDAX analysis of LZTO material

sizes of particles were calculated in the range of 100–200 nm. The elemental composition has been examined using EDAX analysis as shown in Fig. 20.2d. The table shows the atomic and weight ratio of elements: Zn, Ti, and O attributed to the presence in the synthesized LZTO material.

20.3.2 Electrochemical Analysis

Conductivity measurements: Figure 20.3a displays the I–V curve of synthesized LZTO material from which DC resistance was observed in the order of ~10^7 Ω. The voltage signal range for the data collection was kept from −10 to 10 V. Figure 20.3b illustrates an Arrhenius plot, which is potted between ln (σDC) and reciprocal of
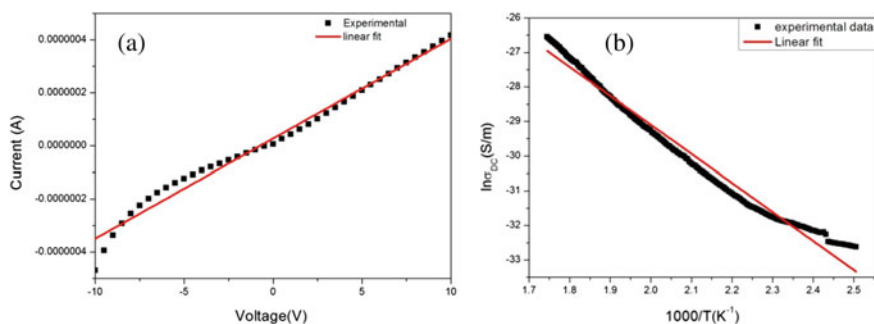
Fig. 20.3 **a** I–V curve of LZTO material, **b** Plot between 1000/T and $\ln\sigma_{DC}$

absolute temperature. The slope of the curve gives the activation energy and dc electrical conductivity is calculated using the Arrhenius equation. The activation energy and electronic conductivity of the sample are found to be in the order of 10^{-4} eV and 10^{-8} S cm^{-1} respectively.

Electrochemical measurements: Cyclic voltammetry (CV) measurements provide information regarding redox reactions within the cell. Figure 20.4a depicts the CV curves of synthesized LZTO material performed in the voltage range of 0.05–3.0 V for a scanning rate of 0.5 mV s^{-1}. A pair of cathodic and anodic peaks in the voltage between 1.0 and 2.0 V is present, associated with the reaction of the Ti^{3+}/Ti^{4+} redox couple [10]. For the subsequent cycles, the cathodic peak shifted towards the higher potential indicating the phase transition from spinel to rock salt structure [11]. Furthermore, a cathodic peak below 0.5V is also observed, related to multiple restorations of Ti^{4+} [11]. Figure 20.4b displays the charge-discharge curves of synthesized electrodes for 20 cycles at current rate of 0.1 C in the potential window of 0.05–3.0 V. The voltage plateaus for charge-discharge curve are following the potentials peaks of voltammogram curves. Galvanostatic charge and discharge capacities are observed
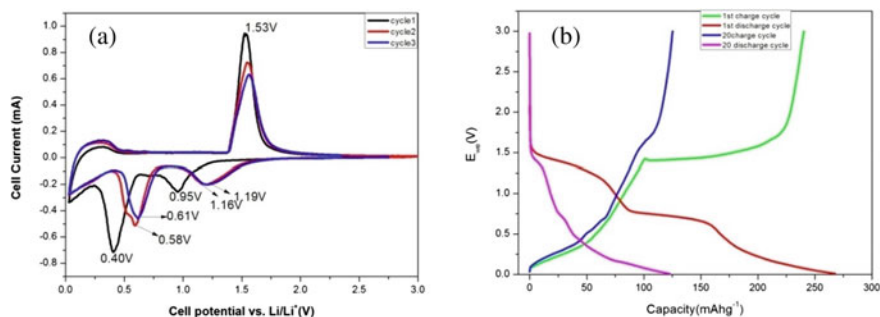
Fig. 20.4 Electrochemical performances of Li$_2$ZnTi$_3$O$_8$ material: **a** Cyclic Voltammogram (CV) of LZTO at scan rate of 0.05 mVs^{-1}, **b** GCD performance recorded in potential range of 0.05–3.0 V
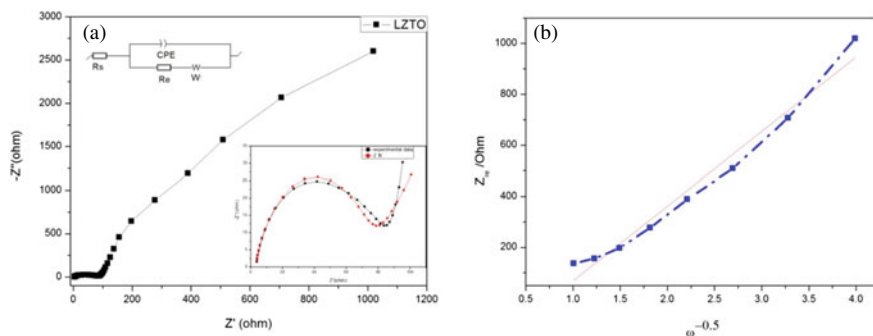
Fig. 20.5 EIS results of $Li_2ZnTi_3O_8$: **a** Nyquist plot recorded at AC amplitude of 5 mV, **b** plot of frequency ($\omega^{-0.5}$) and real of Z' (Zre) in low-frequency region

to be 240.2 mAhg^{-1} and 267.43 mAhg^{-1}, respectively, as recorded at 0.1C for first cycle.

EIS measurements show the mechanism of the charge transfer and Li$^+$ diffusion behavior. Figure 20.5a shows the Nyquist plot of synthesized LZTO material before galvanostatic charge discharge in the frequency range of 100 kHz–10 mHz. Here, curve depicts in high-frequency region, a half circle associated is observed which refers to the charge transfer resistance between electrode and electrolyte interface. Whereas the low frequency region indicates a straight line and it is related to the diffusion of Li$^+$ within active material [12]. The enlarged image of EIS spectra with fitted equivalent circuit diagram is shown in Fig. 20.5a, which includes Re as charge-transfer resistance, Rs as electrolyte resistance, W as Warburg resistance, and CPE as constant phase element. After linear fitting, Re and Rs are 3.013 Ω and 72.82 Ω respectively, which depicts the good electronic conductivity of LZTO material [10–13].

To calculate the diffusion coefficient (D_{Li+}) following equation was used:

$$DLi+ = R^2T^2/2A^2n^4F^4C^2\sigma^2$$

Here DLi+, T, R, A, n, F, and C are diffusion coefficient of Li$^+$ ions (cm^2/s), absolute temperature (K), gas constant (8.3145 J mol^{-1} K^{-1}), surface area of the electrode used (2.0096 cm^2), number of electrons involved in a redox reaction, Faraday constant, and concentration of lithium ions.

Warburg factor (σ) which is related using the following equation:

$$Zre = Re + Rct + \sigma\omega^{-0.5}$$

Figure 20.5b shows the plot between Zre and $\omega^{-0.5}$. From the above equations diffusion coefficient (DLi +) was found to be approx. 10^{-17} cm^2 s^{-1}.

20.4 Conclusion

In this study, we have successfully used a high-temperature solid-state reaction route to prepare nano-structured Li2ZnTi3O8 sample and testing of anode is performed for LIBs. XRD and SEM results show the formation of crystalline nanoparticles. Conductivity measurements show that the LZTO sample has higher conductivity concerning other titanate materials which improve its electrochemical performances. Electrochemical results show that it has a reasonable discharge plateau as well as high capacity which make it a suitable material for electric vehicle (EVs) applications.

References

1. C. Jiang, E. Hosono, H. Zhou, Nanomaterials for lithium ion batteries. Nanotoday **1**(4), 28–33 (2006). https://doi.org/10.1016/S1748-0132(06)70114-1
2. S. Goriparti, E. Miele, F. Angelis, E. Fabrizio, R.P. Zaccaria, C. Capiglia, Review on recent progress of nanostructured anode materials for Li-ion batteries. J. Power Sources **257**, 421–423 (2013). https://doi.org/10.1016/j.jpowsour.2013.11.103
3. C.P. Sandhya, B. John, C. Gouri, Lithium titanate as anode material for lithium-ion cells: a review. Ionics **20**, 601–620 (2014). https://doi.org/10.1007/s11581-014-1113-4
4. B.V. Babu, K.V. Babu, G.T. Aregai, L.S. Devi, B.M. Latha, M.S. Reddi, K. Samatha, V. Veeraiah, Structural and electrical properties of $Li_4Ti_5O_{12}$ anode material for lithium-ion batteries. Results Phys. **9**, 284–289 (2018).https://doi.org/10.1016/j.rinp.2018.02.050
5. G.N. Zhu, Y.G. Wang, Y.Y. Xia, Ti-based compounds as anode materials for Li-ion batteries. Energy Environ. Sci. **5**, 6652–6667 (2012).https://doi.org/10.1039/C2EE03410G
6. Z. Li, Y. Cui, J. Wu, C.Q. Du, X. Zhang, Z.Y. Tang, Synthesis and electrochemical properties of lithium zinc titanate as an anode material for lithium ion batteries via microwave method. RSC Adv. **6**, 39209–39215 (2016). https://doi.org/10.1039/c6ra05244d
7. F. Qie, Z. Tang, Cu-doped $Li_2ZnTi_3O_8$ anode material with improved electrochemical performance for lithium-ion batteries. Mater. Express **4**(3), 221–227 (2014). https://doi.org/10.1166/mex.2014.1166
8. Y.R. Wu, J. Pan, S. Ren, Y. Xie, C. Yue, T.F. Yi, Review and prospect of $Li_2ZnTi_3O_8$-based anode materials for Li-ion battery. Ionics **25**, 373–397 (2019). https://doi.org/10.1007/s11581-018-2818-6
9. H. Tang, L. Zanb, Z. Tang, Predominant electronic conductivity of $Li_2ZnTi_3O_8$ anode material prepared in nitrogen for rechargeable lithium-ion batteries J. Electroanal. Chem. **823**, 269–227 (2018). https://doi.org/10.1016/j.jelechem.2018.06.025
10. T. Liu, H. Tang, J. Liu, Y. Pu, J. Zhang, Z. Lu, W. Li, Z. Tang, F. Ding, Improved electrochemical performance of $Li_2ZnTi_3O_8$ using carbon materials as loose and porous agent Electrochim. Acta **259**, 28–35 (2018). https://doi.org/10.1016/j.electacta.2017.10.139
11. B. Chen, C. Du, Y. Zhang, R. Sun, L. Zhou, L. Wang, A new strategy for synthesis of lithium zinc titanate as an anode material for lithium ion batteries. Electrochim. Acta **159**, 102–110 (2015). https://doi.org/10.1016/j.electacta.2015.01.206
12. Y. Xu, Z. Hong, L. Xia, J. Yang, M. Wei, One step sol–gel synthesis of $Li_2ZnTi_3O_8$/C nanocomposite with enhanced lithium-ion storage properties. Electrochim. Acta **88**, 74–78 (2013). https://doi.org/10.1016/j.electacta.2012.10.044

13. H. Tang, Z. Tang, Effect of different carbon sources on electrochemical properties of Li$_2$ZnTi$_3$O$_8$/C anode material in lithium-ion batteries. J. Alloys Compd. **613**, 267–274 (2014). https://doi.org/10.1016/j.jallcom.2014.06.050

Chapter 21
Conductivity and Structure Correlation in $Gd_2Zr_2O_7$ Pyrochlore for Oxide Fuel Cell Technology

Sushama Kumari, S. K. Sharma, Pawan K. Kulriya, Vinod Singh, and Swati Bugalia

Abstract Energy production using solid oxide fuel cells (SOFCs) technology is the most promising highly efficient and cost-effective clean source of energy to reduce the greenhouse gas emissions and the fossil fuel use. However, novel oxide-ion electrolytes having low operating temperature and high ionic conductivity at the intermediate temperatures is desired. The fluorite type structured materials can accept relatively large amount oxygen vacancy, could be promising candidate for intermediate temperatures oxide-ion electrolytes. Here, conductivity and structure correlation in $Gd_2Zr_2O_7$ pyrochlore prepared using standard solid state reaction technique is presented. Structure, micro-structure and conductivity of the as-prepared highly dense $Gd_2Zr_2O_7$ pyrochlore are investigated using XRD, SEM and impendence spectroscopy techniques. Structural analysis confirms that $Gd_2Zr_2O_7$ consists of single-phasic pyrochlore structure. SEM micrograph exhibits spherical shaped well separated grain having distinct grain-boundaries with a very compact in structure. The variation in ac conductivity of $Gd_2Zr_2O_7$ with frequency shows a dispersive behaviour of ac conductivity which is similar for both the temperatures (475 °C and 500 °C). Further, the impedance analysis of $Gd_2Zr_2O_7$ provides conductivity values are 1.04×10^{-3} $(\Omega m)^{-1}$ and 2.13×10^{-3} $(\Omega m)^{-1}$ at temperature of 475 °C and 500 °C, respectively. The observation of high value of conductivity in the moderate temperature range confirms the utilization of pyrochlore structured materials in SOFCs industry.

S. Kumari · S. Bugalia (✉)
Department of Chemistry, University of Rajasthan, Jaipur 302004, India

S. K. Sharma
Materials Science Group, Inter-University Accelerator Centre, New Delhi 110067, India

P. K. Kulriya
School of Physical Sciences, Jawaharlal Nehru University, New Delhi 110067, India

V. Singh
Department of Applied Physics, Delhi Technological University, Delhi 110042, India

21.1 Introduction

Fluorite structured oxides with low activation energy, low thermal expansion coefficient, high ionic conductivity, comparatively larger melting point, better thermal strength, and very good radiation stability have a wide range of applications in different industries [1]. These unique characteristics of fluorite structured materials proves them a most relevant candidates for the high-temperature thermal barrier coating material [2], disposal of high level radioactive waste, structural material for the incineration of highly radioactive trans-uranium radio-nuclides in the futuristic nuclear reactor [3–11], combustion of methane [12], energy storage [13], and gas sensor [14] etc. In addition, these materials also have potential for utilization as electrolytes for solid-state electrochemical fuel cells [15]. The fuel cell is device based on electro-chemical energy conversion phenomenon that produces electricity from the hydrogen gas. Since, hydrogen is the fuel in the fuel cell therefore; main by-product of the electricity generated using fuel cell is water and heat. It is worth to mention here that fuel cell is unique device which can not only provide power for very large systems like a utility power station and passenger vehicles but also used in very small system like a personal computer. Due to its versatile nature and several benefits over conventional combustion-based technologies, it is being utilised for various purposes such as transportation, material handling, stationary, portable, and for providing emergency backup power to electric instruments. In comparison to other source of energy, it also few advantages like high efficiency (>50%), very low emission, doesn't need charging and produce power along with thermal energy as long as fuel is there.

Generally, fuel cell is the comprising of two electrodes namely negative electrode (or anode) and positive electrode (or cathode) which are sandwiched between an electrolyte. Anode is exposed to the fuel whereas and cathode is remained in air. At the positive electrode, molecular hydrogen is dissociated into atomic hydrogen and electrons via catalyst which moved towards the cathode. On the other hand the protons migrate through the electrolyte to the cathode. A combination of protons happens with oxygen and the electrons which results in a production of water and heat. The electrons pass through an external circuit which generates electricity. Among various types of fuel cells, solid oxide fuel cells (SOFCs) are very attractive due to two major advantages: most efficiently energy conversion with a least emission of pollutants. But, the most important issues associated with the development of fuel cell technology include selection of fuel, the development of advance materials in the fuel-cell stack, solid electrolytes of SOFCs etc. Siemens Westinghouse and Rolls-Royce designed and fabricated a SOFCs with an operating temperature in the range of 850–1000 °C which is quite high. Therefore, the components of the stack of SOFCs should to be made-up of ceramic and high temperature metal alloys. Because of very high efficiencies and easily integration with gas turbines, a large-scale stationary application can be fulfilled by using such kind of fuel cells. But for mini-industries, which works without coalescence with a heat engine and the operation of these industries is performed at low temperature, there is need for the

low temperature SOFCs Such types of SOFCs are known as intermediate temperature (IT) range (500–750 °C) fuel cells. This requires development of advance materials and stack geometries to be used in SOFCs. This also offers cost effective economical system and helps in the reduction in degradation rate of stack and system parts. The yttria-stabilized zirconia was investigated but its operational temperature around 1073–1273 K, is too high and low ionic conductivity. Thus, this put a limit on the choice of relevant electrode and interconnects materials [16]. Therefore, reducing the operational temperature along with large value of ionic conductivity at the IT range is a major challenge to search for novel oxide-ion electrolytes [17].

Oxide ion conductor which plays an important role for the applications like oxygen pump and oxygen sensors are also proposed for solid oxide fuel cell. Among various materials, oxides with fluorite type structure ceramic are potential candidates because the fluorite type structure can accept relatively large amount oxygen vacancy. Polycrystalline pyrochlore structure with general formula A$_2$B$_2$O$_7$ oxides have fluorite type structure and exhibits excellent electrical properties in the IT range and could be a potential solid electrolyte for IT range SOFCs applications. These materials doped with required specific impurities can also fulfil the distinct electrical conductivity necessity of both the electrode as well as electrolyte. In addition, one can also minimized the thermal, mechanical, and chemical mismatches by using the same host material for the electrolyte as well as the electrodes [18]. Basically, pyrochlore structure is advanced structure of fluorite structure with more specific ordering of cations and anions. Its general formula is A$_2$B$_2$O$_7$, where any trivalent rare-earth atom is located at A cationic-site and any tetravalent transition metal can occupy the B cationic-siteand this superstructure is belonging to *Fd-3 m* space group with cubic structure. In contrast to fluorite structure, the pyrochlore superstructure has two different types of cations (A and B) and three types of oxygen sites as well as the absence of one-eighth of oxygen ion. This special structural configuration with inherent oxygen vacancy gives rise to its enhanced ionic conductivity. In this manuscript, correlation between structural and conductivity is presented for the application of pyrochlore structured ceramic for an IT range for SOFCs applications.

21.2 Experimental Details

The pyrochlore composition Gd$_2$Zr$_2$O$_7$ were prepared through simplest physical route i.e., standard solid-state method. The stoichiometric weight of raw materials Gd$_2$O$_3$ and ZrO$_2$ were mixed using agate mortar and pestle by grinding for eight hours. After that, cylindrical pellets of the powder were prepared and heated at 1250 °C for 36 h. The structural phase confirmation was done using X-ray diffraction (XRD) system consists of a Bruker D8-advanced diffractometer coupled with a Cu K-α source ($\lambda = 0.15406$ nm) and Göbel mirror. From XRD, the recorded diffraction data shows a mixed impurity phase, therefore, the pellets were crushed into fine powder and re-grinded for four hours using agate mortar and pestle. Again, this fine powder was converted into cylindrical pellets and heated at 1400 °C for

48 h which is followed by a final heating at 1500 °C for 50 h. The density of the finally prepared pellets was calculated using density measurement set-up working on Archimedes' principle. The density was measured as 88% of its theoretical density. The micro-structural analysis of the prepared material was performed using scanning electron microscope (SEM) titled as MIRA-II, TESCA system. Finally, the prepared single-phasic pellets of $Gd_2Zr_2O_7$ was characterized by impedance analyzer for AC impedance measurements. These AC impedance measurements were performed by making capacitor like set of this cylindrical pellet as the pellet was polished with silver paste on its opposite circular faces. The parameters were recorded in a frequency range starting from 10^2 to 10^6 Hz at 475 °C and 500 °C at by computer-controlled impedance analyzer having model name as HIOKI IM-3570 IMPEDANCE ANALYZER. This manuscript is the extended satellite work of our previous published results on dielectric studies on $Gd_2Zr_2O_7$ [19].

21.3 Results and Discussion

21.3.1 Structural and Micro-Structural Studies

The recorded diffraction data of finally sintered pellet is shown in Fig. 21.1. The diffraction pattern contains two types of XRD peaks; one set is low intensity peaks and another set is high intensity peaks. The low intensity peaks appeared because of pyrochlore super-structural ordering, are marked by asterisk '*' in Fig. 21.1.

These pyrochlore phasic peaks are observed at the peak position of $2\theta \sim 14.4°$ (111), 28.0° (311), 37.1° (331), 44.7° (511), and 51.2° (531). Further, the high intensity peaks observed at $2\theta \sim 29.4°$ (222), 34.0° (400), 48.8° (440), 58.0° (622), and 60.7° (444). The detailed structural analysis performed using Rietveld refinement of this diffraction pattern, was reported in our previous published results [19]. The

Fig. 21.1 Diffraction pattern recorded for finally sintered $Gd_2Zr_2O_7$ pyrochlore. It shows formation of ordered pyrochlore structure of $Gd_2Zr_2O_7$ pyrochlore
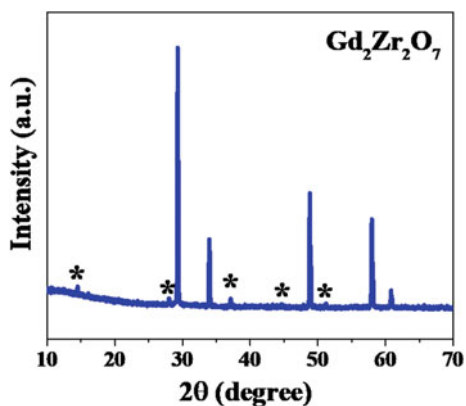
Fig. 21.2 A SEM micrograph recorded for finally sintered Gd$_2$Zr$_2$O$_7$
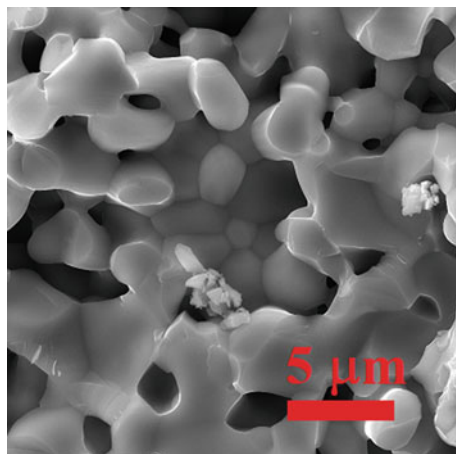
observation of these minor intensity peaks with odd miller indices clearly shows a presence of pyrochlore structure in the finally sintered pellets. It is concluded that the XRD analysis of finally sintered Gd$_2$Zr$_2$O$_7$ pellets strongly claims the single phasic pyrochlore structure in the prepared materials. Figure 21.2 shows a SEM image of finally sintered pellet of Gd$_2$Zr$_2$O$_7$. The SEM micrograph shows a highly dense material that supports the calculated 88% density of the compact pellet. This SEM image shows a very well evolved spherical compact grains with clearly visible grain-boundaries as a result of three stages heat treatment. The smooth surface morphology is observed in this SEM image. The grain size was also calculated from this SEM micrograph and observed as ~1 μm.

21.3.2   AC Conductivity Analysis

From the experimentally obtained AC impedance parameters; namely, capacitance, dissipation factor, impedance, and phase angle, the ac conductivity was calculated through the following relation,

$$\sigma_{ac} = \omega \cdot \varepsilon_o \cdot \varepsilon_r \cdot \tan(\delta) \tag{21.1}$$

where, σ_{ac} represents the ac conductivity, $\varepsilon_r, \varepsilon_o, \omega = 2\pi f$, and $\tan(\delta)$ are the relative permittivity, dielectric permittivity in vacuum, the angular frequency, and dielectric loss, respectively.

The trend in the values of ac conductivity with respect to frequency in the range of 100 Hz to 1 MHz at the temperature of 475 °C and 500 °C is presented in Fig. 21.3. The variation in ac conductivity as a function of frequency clearly shows

Fig. 21.3 A variation in ac
conductivity as a function of
frequency for finally sintered
$Gd_2Zr_2O_7$
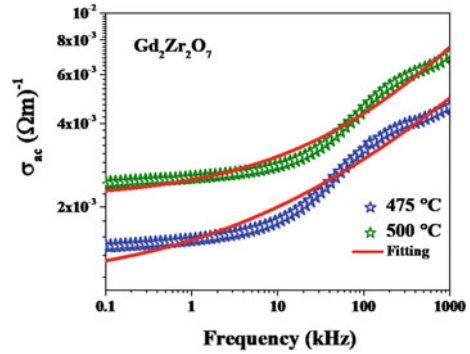
an increasing trend only in high frequency range. The observed values of ac conductivity in lower frequency range are almost independent from varying input signal. This frequency-independent region in low frequency range can be characterized as dc conductivity and is observed for both temperatures. The variation in ac conductivity with frequency is called dispersive behaviour of ac conductivity. On studying the temperature effect on ac conductivity, the temperature does not induce any change in dispersive behaviour of ac conductivity.

The derived values of ac conductivity (shown in Fig. 21.3) with respect to frequency were fitted with *Jonscher's power law*:

$$\sigma_{ac} = \sigma_{dc} + A \cdot \omega^n \tag{21.2}$$

where, σ_{ac} and σ_{dc} represent the ac and dc conductivity, respectively. Furthermore, both parameters, 'A' and 'n' temperature-dependent pre-exponential parameter and frequency exponent factor, respectively.

Table 21.1 shows the all-calculated parameters obtained from the fitting of frequency dependent ac conductivity using relation (21.2). The dc conductivity increases on increasing temperature as usual. The pre-exponential parameter 'A' depends on temperature and gives an information of the polarization in the material [20]. On the other hand, frequency exponent parameter (n) contains the information regarding degree of inter ion-lattice interaction and the deviation from Debye behaviour of oxides. The value of 'n' varies from '0' to '1'. The highest value of 'n' shows a perfectly Debye behaviour (means no interaction between the charge carriers and lattice framework) exhibited by the material. Furthermore, the value of

Table 21.1 The fitted parameters from *Jonscher's power law*

Calculated parameters	$Gd_2Zr_2O_7$ (σ_{ac} vs f) at 475 °C	$Gd_2Zr_2O_7$ (σ_{ac} vs f) at 500 °C
σ_{dc} $(\Omega m)^{-1}$	1.04×10^{-3}	2.13×10^{-3}
'A'	2.5×10^{-5}	5.7×10^{-5}
'n'	0.39	0.31

'n' decreases with increasing temperature as the thermal energy driven ion-lattice interaction dominates at higher temperature [21].

As expected, the increasing value of 'n' shows an increasing carrier to lattice interaction in present studies and larger 'A' value at 500 °C represents the larger value of thermally driven conductivity.

This higher value of ionic conductivity at moderate temperature range is really good for the application of pyrochlore structured materials in SOFCs industry. In literature survey, the ionic conductivity of various materials reported as: $4.0\ (\Omega m)^{-1}$ for $CeO_2 -10$ mol% Sm_2O_3 at 700 °C [22] and $3.6\ (\Omega m)^{-1}$ for $CeO_2 -10$ mol% Gd_2O_3 at 700 °C [23], and $3.79 \times 10^{-2}\ (\Omega m)^{-1}$ scandia-stabilized zirconia (ScSZ) at 560 °C [24]. The conductivity of non-stoichiometric pyrochlore structured materials were also reported for $Nd_{1.6}Zr_{2.4}O_{7.2}$ as $1.78\ (\Omega m)^{-1}$ at 700 °C and $0.343\ (\Omega m)^{-1}$ at 560 °C [25] and for stoichiometric pyrochlore composition $Gd_2Zr_2O_7$ as $0.41\ (\Omega m)^{-1}$ at 700 °C [26]. The comparison of measured conductivity of $Gd_2Zr_2O_7$ in IT range with all above-mentioned reported values of conductivity for various materials shows a better candidate for application of SOFCs.

21.4   Conclusion

The present manuscript reports a structural, micro-structural and conductivity analysis of $Gd_2Zr_2O_7$ pyrochlore composition. The $Gd_2Zr_2O_7$ pyrochlore composition was synthesized through standard solid-state method with different heating protocol. XRD results shows that the prepared pellets of $Gd_2Zr_2O_7$ consists of single-phasic pyrochlore structure. SEM micrograph shows multiple spherical grains which are well separated by grain-boundaries and very compact in structure. The impedance analysis of $Gd_2Zr_2O_7$ provides a conductivity values: $1.04 \times 10^{-3}\ (\Omega m)^{-1}$ at 475 °C and $2.13 \times 10^{-3}\ (\Omega m)^{-1}$ at 500 °C. The comparison of its conductivity with published results for various oxides provides complete evidence regarding its strong candidature as a material used in SOFCs in IT range.

References

1. M.A. Subramanian, G. Aravamudan, G.V. Subba Rao, Oxide Pyrochlores—a review. Prog. Solid State Chem. **15**, 55 (1983)
2. R. Vassen, X. Cao, F. Tietz, D. Basu, D. Stöver, Zirconates as new materials for thermal barrier coatings. J. Am. Ceram. Soc. **83**, 2023 (2004)

3. R. Kaur, M. Gupta, P.K. Kulriya, S.S. Ghumman, Phase analysis and reduction behaviour of Ce dopant in Zirconolite. J. Radioanal. Nucl. Chem. **322**, 183 (2019)

4. P.K. Kulriya, T. Yao, S.M. Scott, S. Nanda, J. Lian, Influence of grain growth on the structural properties of the nanocrystalline $Gd_2Ti_2O_7$. J. Nucl. Mater. **487**, 373 (2017)

5. P.K. Kulriya, F. Singh, A. Tripathi, R. Ahuja, A. Kothari, R.N. Dutt, Y.K. Mishra, A. Kumar, D.K. Avasthi, Setup for in-situ X-ray diffraction study of swift heavy ion irradiated materials. Rev. Sci. Instrum. **78**, 113901 (2007)

6. P.K. Kulriya, R. Kumari, R. Kumar, V. Grover, R. Shukla, A.K. Tyagi, D.K. Avasthi, In-Situ high temperature irradiation setup for temperature dependent structural studies of materials under swift heavy ion irradiation. Nucl. Instru. Methods Phys. Res. Sect. B Beam Interact. Mater. Atoms **342**, 98 (2015).

7. A. Kumar, P.K. Kulriya, S.K. Sharma, V. Grover, A.K. Tyagi, V.K. Shukla, Structural and compositional effects on the electronic excitation induced phase transformations in $Gd_2Ti_{2-Y}Zr_yO_7$ Pyrochlore. J. Nucl. Mater. **539**, 152278 (2020)

8. S.K. Sharma, V. Grover, R. Shukla, A. Hussain, A. Mishra, R.C. Meena, P.K. Kulriya, Evidence of improved tolerance to electronic excitation in nanostructured $Nd_2Zr_2O_7$. J. Appl. Phys. **129**, (2021)

9. J. Lian, S.V. Yudintsev, S.V. Stefanovsky, L.M. Wang, R.C. Ewing, Ion beam irradiation of U-, Th- and Ce-doped Pyrochlores. J. Alloys Compd. **444–445**, 429 (2007)

10. S.K. Sharma, V. Grover, A.K. Tyagi, D.K. Avasthi, U.B. Singh, P.K. Kulriya, Probing the temperature effects in the radiation stability of $Nd_2Zr_2O_7$ Pyrochlore under swift ion irradiation. Materialia **6**, 100317 (2019)

11. R. Kumari, P.K. Kulriya, V. Grover, R. Shukla, K. Saravanan, S. Mohapatra, A.K. Tyagi, Radiation stability of $Gd_2Zr_2O_7$: effect of stoichiometry and structure. Ceram. Int. **42**, 103 (2016)

12. J.M. Sohn, M.R. Kim, S.I. Woo, The catalytic activity and surface characterization of $Ln_2B_2O_7$ (Ln=Sm, Eu, Gd and Tb; B=Ti or Zr) with Pyrochlore structure as novel CH_4 combustion catalyst. Catal. Today **83**, 289 (2003)

13. H. Yamamura, H. Nishino, K. Kakinuma, Ac conductivity for $Eu_2Zr_2O_7$ and $La_2Ce_2O_7$ with Pyrochlore-type composition. Nippon Seramikkusu Kyokai Gakujutsu Ronbunshi **112**, 553 (2004)

14. P.K. Kulriya, M. Kumar, J. Singh, D.K. Avasthi, Hydrogen pressure dependent in-situ electrical studies on Pd/C nano-composite. Int. J. Hydrogen Energy **42**, 3399 (2017)

15. J. Garcia-Barriocanal, A. Rivera-Calzada, M. Varela, Z. Sefrioui, M.R. Díaz-Guillén, K.J. Moreno, J.A. Díaz-Guillén, E. Iborra, A.F. Fuentes, S.J. Pennycook, C. Leon, J. Santamaria, Tailoring disorder and dimensionality: strategies for improved solid oxide fuel cell electrolytes. ChemPhysChem **10**, 1003 (2009)

16. D.J.L. Brett, A. Atkinson, N.P. Brandon, S.J. Skinner, Intermediate temperature solid oxide fuel cells. Chem. Soc. Rev. **37**, 1568 (2008)

17. Z.G. Liu, J.H. Ouyang, Y. Zhou, X.L. Xia, Electrical conductivity of Samarium-Ytterbium Zirconate ceramics. Electrochim. Acta **54**, 3968 (2009)

18. O. Porat, C. Heremans, H.L. Tuller, Phase stability and electrical conductivity in $Gd_2Ti_2O_7$-$Gd_2Mo_2O_7$ solid solutions. J. Am. Ceram. Soc. **80**, 2278 (1997)

19. S.K. Sharma, H.S. Mohanty, D.K. Pradhan, A. Kumar, V.K. Shukla, F. Singh, P.K. Kulriya, Structural, dielectric and electrical properties of Pyrochlore-type $Gd_2Zr_2O_7$ ceramic. J. Mater. Sci. Mater. Electron. (2020)

20. B. Harihara Venkataraman, K.B.R. Varma, Frequency-dependent dielectric characteristics of ferroelectric $SrBi_2Nb_2O_9$ ceramics. Solid State Ionics **167**, 197 (2004).

21. A. Peláiz-Barranco, M.P. Gutiérrez-Amador, A. Huanosta, R. Valenzuela, Phase transitions in ferrimagnetic and ferroelectric ceramics by Ac measurements. Appl. Phys. Lett. **73**, 2039 (1998)

22. T. Kudo, H. Obayashi, Mixed electrical conduction in the fluorite-type $Ce_{1-x}Gd_xO_{2-x/2}$. J. Electrochem. Soc. **123**, 415 (1976)

23. M. Mogensen, N.M. Sammes, G.A. Tompsett, Physical, chemical and electrochemical properties of pure and doped Ceria. Solid State Ionics **129**, 63 (2000)
24. V.V. Lakshmi, R. Bauri, Phase formation and ionic conductivity studies on Ytterbia co-doped Scandia stabilized Zirconia ($0.9ZrO_2$–$0.09Sc_2O_3$–$0.01Yb_2O_3$) electrolyte for SOFCs. Solid State Sci. **13**, 1520 (2011)
25. P. Anithakumari, V. Grover, C. Nandi, K. Bhattacharyya, A.K. Tyagi, Utilizing non-stoichiometry in $Nd_2Zr_2O_7$ Pyrochlore: exploring superior ionic conductors. RSC Adv. **6**, 97566 (2016)
26. A.J. Burggraaf, T. Van Dijk, M.J. Verkerk, Structure and conductivity of Pyrochlore and Fluorite type solid solutions. Solid State Ionics **5**, 519 (1981)

Chapter 22
Identification of Different Phases and Thermal Analysis of Mn Doped Cadmium Oxide Nano-rods

Chitra Bhukkal, Bindiya Goswami, and Rachna Ahlawat

Abstract The subject of present study is to identify different phases present in pure and Maganese (Mn) doped cadmium oxide (CdO) nanocrystallites. In this regard, Mn doped CdO samples were synthesized by 'co-precipitation' route. When dopant concentration is kept constant, then structural and optical parameters of doped cadmium oxide are modified by proper calcination. The thermal analysis of $Cd(OH)_2$ observed by DTA curve exhibited a prominent peak at 200 °C owing to recrystallization of cadmium oxide. XRD profile demonstrated the mixed phases of $Cd(OH)_2$ and cubic CdO. TEM analysis examined the agglomerated nanoparticles with random shape and sizes for pure CdO sample. Different rods like nanostructures were exhibited in Mn doped CdO sample with an average diameter of ~38 nm. The optical absorbance has been shifted towards visible portion efficiently due to doping and as a result band gap energy is also decreased. Further, it is elaborated that such rod like nanostructure would be useful for futuristic optoelectronics appliances like photodiodes (PDs), as transparent electrodes (TE), catalysts, solar cells (SC), phototransistors (PTs), and gas sensors.

22.1 Introduction

Oxide semiconductor nanomaterial belongs to II–VI group has several wonderful functions in various photonic devices, e.g. energy efficient windows, flat panel displays, heat reflectors, and photovoltaic cells [1, 2]. Recently, the fabrication of oxide semiconductors from II–VI series is explored as the advanced research area because of their supreme structural, and optoelectronic properties [3, 4]. Such nanomaterials are in great demand due to their above said properties and zero dimensional quantum confined material formation. These diverse properties (physical and chemical) related to such nanopowder are pertinent to be size dependent. Upto now, among the different metal oxides, pure CdO nanocrystals and its thin films ate prominently

C. Bhukkal (✉) · B. Goswami · R. Ahlawat
Department of Physics, Material Science Laboratory, Chaudhary Devi Lal University, Sirsa, Haryana 125055, India

researched out because (i) it is an important n-type semiconductor for modern electronics, (ii) Being an fundamental element for the synthesis of sulfide, selenides, and telenides after completion of their reaction with appropriate material. (iii) Also, fantastic optical and electrical properties are obtained after tailoring the stoichiometry, size and shape of the particles, [5–8]. The oxide nanomaterials embedded with luminescent centers of transition metals generate many opportunities for researcher. Therefore, such doped oxides frequently utilized in advanced disciplines like dye sensitizer solar cells, catalysis, optoelectronic and gas sensor technologies. In this decade, considerable attempts have been employed to tailor the internal crystalline arrangement and structural behavior of the metal oxides by suitable doping of proper element which authorizes the particular function of nanomaterials that is coordinated with the selected application. Nanomaterials based on transition metal doped CdO provide high hydrothermal stability, large surface to volume ratio and different oxidation states [9–11]. Due to these characteristics, they exhibit unique electrical, optical and magnetic behavior. In the present work, a significant attention is paid to Mn doped CdO nano-rods for its broad range of applications in photonics and many more [12, 13]. In the present study, we have adopted chemical co-precipitation route that is easier and economically cheaper technique for the synthesis of nanocrystallites in abundance. Considering various application of CdO nanostructures in different optoelectronics devices, we have synthesized pure and Mn doped CdO nanocrystallites to control the structural parameters and optical band gap energy.

22.2 Experimental Details

22.2.1 Sample Preparation

For sample preparation, we have purchased the main chemicals like cadmium acetate dihydrate $\{Cd(CH_3COO)_2.2H_2O\}$ and sodium hydroxide (NaOH) from Sigma Aldrich with high purity. About 0.2 M cadmium acetate dihydrate and 0.075 M sodium hydroxide has been mixed in a big glass beaker and magnetically stirred at normal temperature approximately 60 min. In second beaker, manganese acetate tetrahydrate $\{C_4H_6 \ MnO_4.4H_2O\}$ were liquefied in 100 ml of double purified water and stirred upto half an hour at the room temperature. The content of second container was poured into the first beaker drop wise by a glass burette. Then, reaction between precursors has been started and after that the solution color was suddenly disappeared. When chemical reaction was completed, precipitates were formed which were quarantined for 24 h. We have washed these precipitates many times with double distilled water and then filtered. Using an air oven, the precipitates were dried at 120 °C for 300 min. This dried solid was further calcined in a programmable furnace at 750 °C for 2 h. The calcined sample of both pure CdO and Mn doped CdO was grounded to fine powder using the Agate pestle-mortar and then examined by the subsequent characterization tools like TG–DTA, XRD, SEM, UV–Vis absorption, etc.

22.2.2   Characterization Tools

The prepared samples were evaluated by complementary useful techniques. In this direction, XPERT-PRO X-ray diffractometer was operated at 50 kV and 45 mA to observe the X-ray diffraction (XRD). In the device, Cu Kα radiation with wavelength 1.5406 Å was being used in the step size of 2° angle. We have further observed Fourier Transform Infrared (FTIR) spectrum of the sample which is analyzed with 400 spectrophotometer (from Perkin Elmer) in the prescribed range of 400–4000 cm^{-1}. Moreover, the nanocrystalline behavior of the sample is further verified on Hitachi-4500 TEM device with high resolution. The absorbance was observed by Perkin Elmer Lambda 750 UV-Vis-NIR spectrophotometer in 200–800 nm range.

22.3   Results and Discussion

22.3.1   TG–DTA (Thermal) Analysis

Figure 22.1 exhibits the TG curve and DTA analysis of Mn doped CdO obtained after centrifugation and drying the precipitates in oven. It is observed that the weight loss of the nanocrystallites exhibited four step degradation of weight losses at the offset temperatures: 90° (15%), 220 °C (35%), 350 °C (12%) and 730 °C (3%). The initial decay noticed from 25 to 90 °C which could be credited to removal of water molecules adsorbed on upper surface of sample.

The second stage weight loss (30%) occurred between 160 and 220 °C which may be assigned to phase change to cubic CdO (from hexagonal $Cd(OH)_2$) and removal of acetates, carbonates etc. The third stage of weight loss 12% between 250 and 350 °C predicted the improved crystallinity of the prepared sample. Further, minimum weight loss of (3%) observed in final stage between 700 and 750 °C, indicated complete appearance of cubic CdO as well as removal of $Cd(OH)_2$ hexagonal

Fig. 22.1 Thermal analysis of Mn doped CdO nanocrystallite
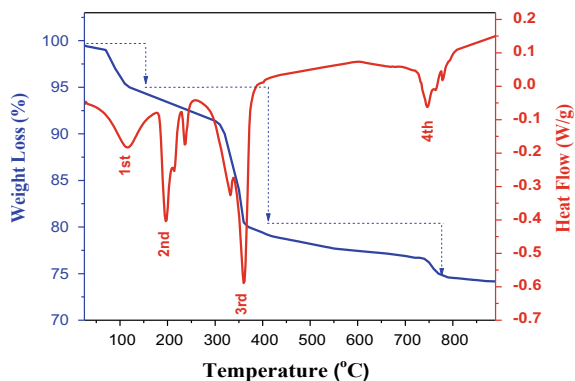
structure. In prepared sample, the DTA curve shows main endothermic peak at 200 °C along with three minor peaks at 45, 296 and 730 °C. The major peak noticed at 200 °C has 237.85 J/g enthalpy value which confirmed that the prepared powder absorb heat at the particular temperature corresponding to start of the decomposition of $Cd(OH)_2$ into CdO while the small peak at 45 °C evolved due to the exhaustion of adsorbed water. Moreover, other prominent peaks found at 296° and 730 °C in DTA graph are in the support of the phase transformation from cadmium hydroxide to cubic CdO nanocrystallite [16]. It is further insured there was negligible mass decay observed greater than 750 °C temperature which notify the preparation of CdO nanocrystallite.

22.3.2 Phase Identification by XRD

The calcined sample of pure and Mn doped cadmium oxide (CdO) has many diffraction peaks which are well indexed to combined phases of hexagonal $Cd(OH)_2$ and cubic CdO as predicted in Fig. 22.2. In both XRD patterns, the small diffraction peaks observed at 2θ ~23.39°, 30.22°, 38.07°, 43.70°, 52.28° are well matched to hexagonal $Cd(OH)_2$ phase having miller indices (001), (100), (101), (002), (102) and well matched with the relevant JCPDS card no. 31–0228. Furthermore, diffraction peaks appeared at 2θ ~32.86°, 38.25°, 55.13°, 65.78° and 69.20° are attributed for (111), (200) and (220) indices for the cubic symmetry of CdO nanocrystallite. These peaks of diffraction are analogous to standard data card (JCPDS card: 05-0640) as observed in pure and Mn doped CdO nanocrystallites. One may notice the slight change in prominent peak (111) appeared at 32. 86° in pure CdO and at 32.82° in Mn doped CdO as displayed separately in Fig. 2c. The width of all peaks in the prepared sample established the evolution of nanocrystallite and occurrence of fine peaks in
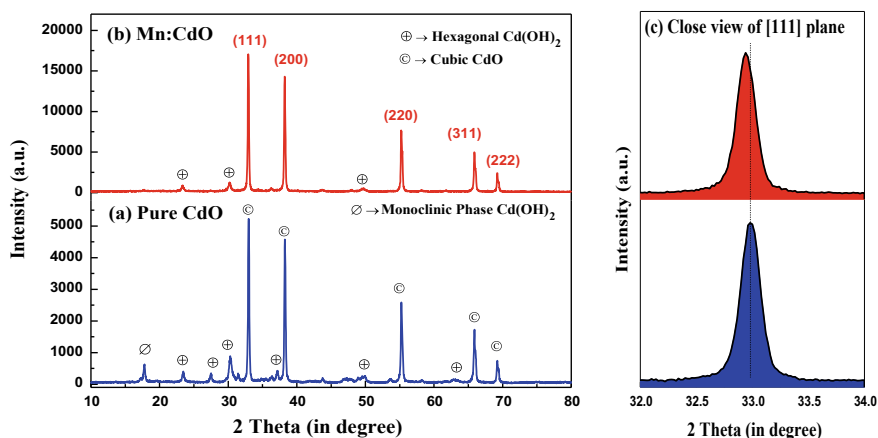
Fig. 22.2 XRD pattern of **a** pure, **b** Mn doped CdO nanocrystallites, **c** Close view of [111] plane within 32–34°

the X-ray diffraction image determined crystalline nature of the prepared material. The FWHM (full width at the half maxima) is denotd by 'β' for most prominent peak that is employed to determine the crystalline size (D) using Debye–Scherrer's equation:

$$\text{Average crystalline size(D)} = \frac{0.94\lambda}{\beta \cos\theta} \tag{22.1}$$

In (22.1), 'λ' is the radiation wavelength (Cu) being used in XRD, and 'θ' is angle at which rays were diffracted obeying Bragg's condition. The average crystalline size for pure and Mn doped CdO is estimated as ~43 and 38 nm, respectively. The dopant has diminished the crystallinity and FWHM of prepared sample and consequently size is also decreased. The lattice parameter is determined using the standard (hkl) value of the dominant plane.

Using standard Bragg's condition, the inter planner spacing 'd' is found to increase slightly i.e. 0.2711 to 0.2718 nm due to doping and therefore lattice constant 'a' is also increased. We have found 'a' = 0.4707 nm for pure cubic phase of CdO and 0.4694 nm for Mn doped sample. As a result, the unit cell volume 'V_c' is estimated as = 102.3Å^3 for pure CdO and = 107.5Å^3 for Mn doped CdO sample. These results confirm the efficient doping process in which Mn with smaller ionic radii has replaced successfully the Cd ion from its lattice site. From XRD profile, the variation in peak intensities and peak width 'β' of the material predicted that the prepared sample is strongly crystallized in a particular direction i.e. along (111) reflection plane of cubic crystalline phase as depicted in Fig. 22.2c. The monoclinic phase is almost disappeared in doped sample; however, the hexagonal phase is still present in the sample but with negligible intensity. The XRD results are well agreed with the thermal analysis and similar to other authors [14, 15].

22.3.3   Fourier Transform Infrared Spectroscopy: (FTIR)

In present study, Fig. 22.3 exhibits IR Spectra of pure and Mn doped CdO nanopowder calcined at 750 °C. In the 400–4000 cm^{-1} spectral region, there are many symmetric, asymmetric and also bending vibrations of various molecule/groups present in nano-material. The whole spectrum is divided mainly into three regions. The widest region is from 3600 to 3200 cm^{-1} in which H–O-H vibrations are executed by both samples. Also small peaks at 2900 and 2350 cm^{-1} have been appeared in pure CdO sample which are completely omitted in doped sample as shown in Fig. 22.3b.

Second important region is assigned to most fundamental precursor i.e. COO$^-$ available in both samples. Finally, the finger print region of Metal–Oxygen is found below 1000 cm^{-1} which contains few wide and fine peaks belongs to bending as well as stretching vibrations of Cd–O. The complete description of peak and their assignments are tabulated below in Table 22.1.

Fig. 22.3 XRD pattern of **a** pure, **b** Mn doped CdO nanocrystallites
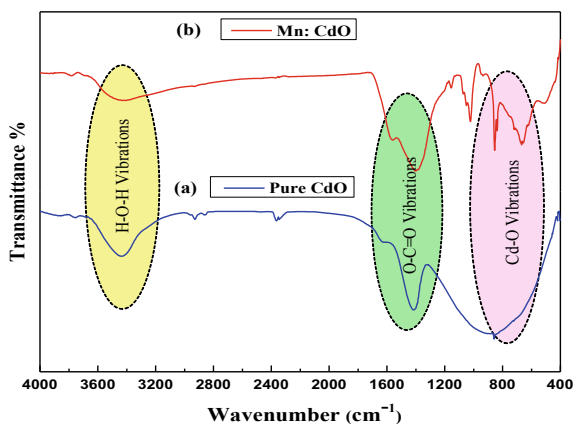
Table 22.1 FTIR analysis of pure and Mn doped CdO nanocrystallites

Wavenumber (cm^{-1})	Different group assignments
3412	Attributed to stretching vibrations of absorbed water molecule (OH$^-$)
1560	Assigned to bending vibration of water present on the surface of cadmium
1406	Attributed to acetate complex (COO-) with symmetric vibration
1024	C = O bending vibration
857	Due to Cd–OH group having bending vibrations
670	May be assigned to Cd–O bond present in the complex
425	Assigned to O–Cd–O bond available in prepared sample

22.3.4　Uv–Vis Absorption and Band Gap Energy (E_g)

For pure and Mn doped CdO nanocrystallites, absorbance and corresponding band gap energy was performed by UV-Vis-NIR Spectrophotometer. The absorbance of presented sample is investigated in 200–800 nm range of wavelength as displayed in Fig. 22.4a. For observation, a pre-decided weight percentage of nanopowder has been dispersed in ethanol solvent with the help of ultrasonic instrument and its optimum absorbance is obtained in the UV–Visible portion of the spectra. In pure CdO sample, the most prominent absorption peak is evolved at 261 nm due to excitonic absorption. In Mn doped CdO sample, a strong and broad optical absorption band is obtained between 350 and 550 nm. The peak at 350 nm is assigned to host while peak at 550 nm would be present due to Mn ions. One may notice that the absorbance peak has been shifted towards visible region due to doping in Fig. 22.4a. From the analysis, it is clear that the maximum absorbance is significantly modified due to doping which is also compared with other reports available in literature [16, 17].
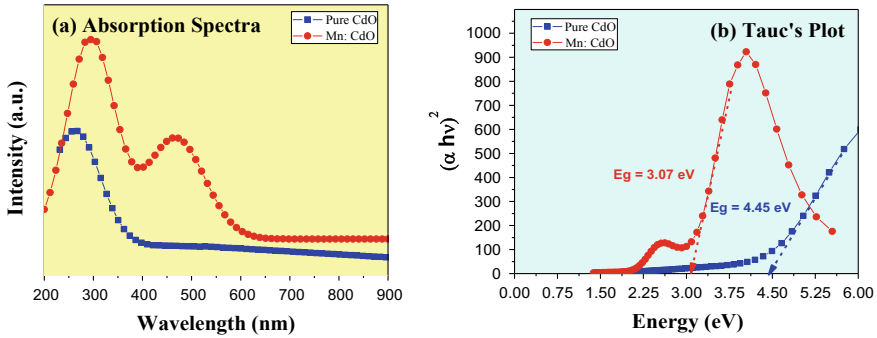
Fig. 22.4 Observed absorbance spectra (**a**) and corresponding Tauc's plot (**b**) for pure and Mn doped CdO nanocrystallites

22.3.5   Band Gap Energy (E_g)

When a dopant is inserted in a nanomaterial, it significantly changes the band gap of the material owing to crystal distortions. It is worth mentioning that the pure CdO has direct allowed transitions which could be determined by the co-relation of the falling optical energy ($h\nu$) and coefficient of the absorbance (α) as follows:

$$(\alpha h\nu)^{1/n} = A(h\nu - Eg) \tag{22.2}$$

In above relation, the main role is played by exponent 'n' which is an integer depends on transition probability and can have few set values attributed to possible transitions. For example, if it is n = ½, imples the direct allowed transition; when 'n' = 2 gives indirect allowed; whereas 'n' = 3/2 is used for forbidden direct and when 'n' = 3 it denotes indirect forbidden transition. In this direction, we have draw a graph between optical energy (hν) on x-axis and $(\alpha h\nu)^2$ on y-axis. One may notice that the linear portion of the graph verifys the optical transition as radiative corresponding to n = ½ as depicted in Fig. 22.4b. By extrapolating the straight region of the graph on energy axis x = 0, we have obtained directly the bangap energy (E_g) = 4.45 eV for pure CdO that is quite higher than undoped CdO [18]. This may be due to presence of hexagonal cadmium hydroxide. This observation may also be correlated with Moss- Burstein (MB) mechanism in which the dopant ion has generated the possible change in the free electron density of the sample which shift the Fermi level and as a result band gap value changed significantly [19, 20]. However, in Mn doped CdO sample, band gap energy is decreased upto 3.07 eV due to existence different impure energy levels between C.B. and V.B. of CdO [19]. These features make the prepared nanocrystalline sample useful for functional applications in optics.

22.3.6 TEM Analysis

The crystalline morphology of pure and Mn doped CdO (annealed at 750 °C) has been investigated through transmission electron microscopy (TEM). The crystallinity and densification of both the samples is improved due to the applied calcination process. In the pure CdO micrograph, nanoparticles are merged together due to large crystalline size and high surface energy. As a result, formation of much larger nano-clusters has been take place simultaneously. Therefore in Fig. 22.5a, one may observe nanoparticles with random shape and sizes. Interestingly, a sharp change in Mn doped CdO sample (in Fig. 22.5b) is observed where rod like nanostructures is evolved. Cluster formation has also been visible in this micrograph due to calcination. For the present study, we have estimated the distribution of all nanocrystallites sample with the help of Image - J software and the draw a bar graph as shown in the Fig. 22.5c and d. This plot is generally called the histogram that exhibits period of occurrence in percentage versus corresponding size of nanocrystallites. In Fig. 22.5e, a magnified image of a single nano-rod along with a spherical CdO crystallite is displayed which has diameter ~40 nm. Figure 22.5f, another close micrograph with sufficient resolution has been shown in which small nanocrystallites (~7 nm) are trapped uniformly with spherical morphology. This morphology is appeared to be most steady form of the prepared nanopowder.

22.4 Conclusions

Pure and Mn doped CdO rod like nanocrystallites are successfully prepared via the chemical co-precipitation methodology. The presence of mixed phases in pure and Mn doped CdO has been revealed by XRD study. The nanoparticle size is found ~43 and 38 nm with high crystallinity and densification. In FTIR spectrum, COO^- band was present at 1410 cm^{-1} and Cd–O band was appeared at 425 cm^{-1}. Two broad absorbance bands in Mn doped CdO are assigned to host and dopant in the UV–Visible region. The bandgap energy is calculated ~4.45 and 3.07 eV, respectively using famous Tauc's Plot. TEM analysis highlighted the rod like morphology. We expect that this type of nanostructures might be interest for application in solar energy converter and photo catalytically reactors.
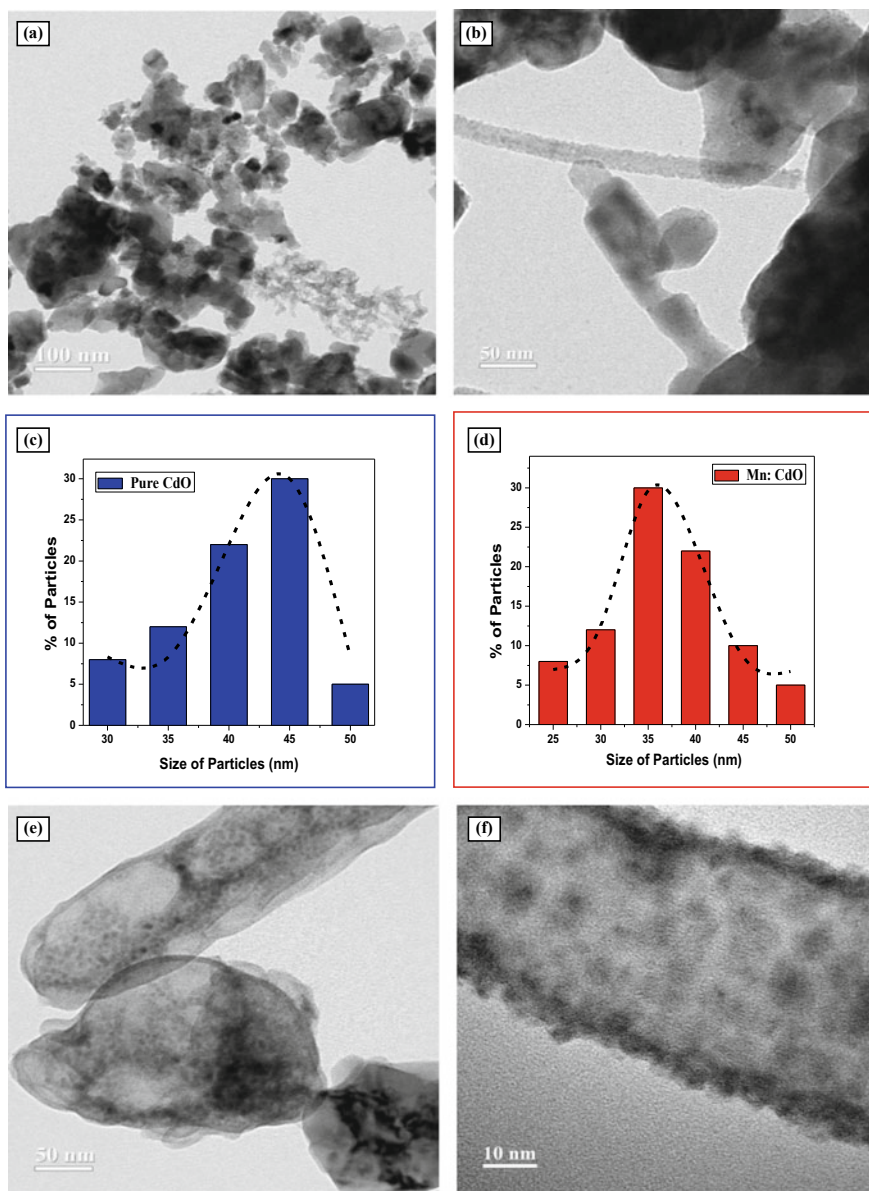
Fig. 22.5   TEM micrographs for **a** pure and **b** Mn doped CdO nanocrystallites, **c** histogram of pure CdO, **d** histogram for Mn doped CdO, **e** Close view of nano-rod structure, **f** Magnified image of Mn doped cdO nano-rod

References

1. S.V. Nistor, L.C. Nistor, M. Stefan, D. Ghica, G. Aldica, J.N. Barascu, Cryst. Growth Des. **11**, 5030–5038 (2011)
2. M. Stefan, S.V. Nistor, D. Ghica, Cryst. Growth Des. **13**, 1350–1359 (2013)
3. R.A. McBride, J.M. Kelly, D.E. McCormack, J. Mater. Chem. **13**, 1196–1201 (2003)
4. S. Music, D. Dragcevic, S. Popovic, J. Alloys Compd. **429**, 242–249 (2007)
5. M. Wang, Y. Zhou, Y. Zhang, S.H. Hahn, E.J. Kim, Cryst. Eng. Comm. **13**, 6024–6026 (2011)
6. S.V. Nistor, D. Ghica, M. Stefan, I. Vlaicu, J.N. Barascu, C. Bartha, J. Alloys Compd. **548**, 222–227 (2013)
7. F. Demoisson, R. Piolet, F. Bernard, Cryst. Growth Des. **14**, 5388–5396 (2014)
8. A. Fakhri, S. Behrouz, M. Pourmand, J. Photochem. Photobiol. B **149**, 45–49 (2015)
9. N. Thovhogi, E. Park, E. Manikandan, M. Maaza, A. Gurib-Fakim, J. Alloys Comp. **655**, 314–320 (2016)
10. A. Fakhri, R. Khakpour, J. Lumin. **160**, 233–237 (2015)
11. D. Ghica, M. Stefan, C. Ghica, G.E. Stan, ACS Appl. Mater. Int. **6**, 14231–14238 (2014)
12. M. Stefan, D. Ghica, S.V. Nistor, A.V. Maraloiu, R. Plugaru, Appl. Surf. Sci. **16**, 30345 (2016)
13. S.V. Nistor, D. Ghica, M. Stefan, L.C. Nistor, J. Phys. Chem. C **117**, 22017–22028 (2013)
14. C. Bhukkal, M. Chauhan, R. Ahlawat, Physica B **582**, 411973 (2020)
15. R. Aydin, B. Sahin, Ceramics Int. **43**, 9285–9290 (2017)
16. A.A. Dakhel, Sol. Energy **83**, 934–939 (2009)
17. S. Kose, F. Atay, V. Bilgi, I. Akyuz, Int. J. Hydrogen Energy **3452**, 52–60 (2009)
18. A.B. Khatibani, S.M. Rozati, Z.A. Hallaj, Mater. Sci. Semicond. Proc. **16**, 980–986 (2013)
19. N. Manjula, A.R. Balu, Optik Int. J. Light Electron. Opt. **130**, 464–472 (2017)
20. R. Vettumperumal, S. Kalyanaraman, R. Thangavel, Superlattices Microstruct. **83**, 237–250 (2015)

Chapter 23
Slow Optical Soliton in a Three-Level Multiple Quantum Well Under Electromagnetically Induced Transparency

Manisha Sharma, Lipika Saha, Tapas Sen, Masuma Jannat, and Nitu Borgohain

Abstract In this article, we present a theoretical investigation of slow optical soliton propagation in a three-level multiple quantum well system under electromagnetically induced transparency (EIT) window. A weak probe laser pulse and a strong control laser beam are applied to interact with the quantum well system through a cascade-type excitation scheme to form the EIT window. EIT facilitated the quantum well system with lowering the linear absorption and enhancing the nonlinear susceptibility leading to Kerr nonlinearity. Under the EIT scheme, the Kerr nonlinearity of the system is found to be as large as 10^{-11} m^2/V^2 at probe wavelength $9.28\,\mu$m. A delicate balance between the Kerr nonlinearity and the dispersion supports the generation of a fundamental optical soliton in the multiple quantum well system. The soliton has propagated at a very low group velocity of the order 10^5 m/s which is almost 1000 times smaller than the speed of light in free space. This investigation may have potential applications in optoelectronic and photonic devices.

23.1 Introduction

In the past few years, the electromagnetically induced transparency (EIT) and its related effects are highly studied in different optical media [1–5], as they offer immense applicability in nonlinear optics. EIT is a technique, by virtue of which the effects of a medium on a propagating beam of light can be eliminated, i.e., an initially opaque medium can be made transparent. The concept of EIT was first observed by Harris et al. in 1990 in a Λ-type atomic system of strontium vapour, using high pulsed laser [1]. Thereafter EIT was studied widely, not only in atomic systems but also in semiconductor quantum wells (SQWs) for the enhancement of Kerr nonlinearity, lowering the group velocity, soliton generation, and many more [5–8]. The optical devices based on SQWs are exceedingly popular because of their

M. Sharma (✉) · L. Saha · T. Sen · M. Jannat · N. Borgohain
Department of Physics, University of Science and Technology Meghalaya, Ri-Bhoi, Meghalaya 793101, India

inherent advantages over atomic systems. SQWs offer large electric dipole moment and desirable device designing, by tuning their dimension structures as their transition levels, dipole moments, thus nonlinear coefficients, etc. can be engineered as required by tuning their structure dimension. These advantages of SQWs support researchers to achieve large Kerr nonlinearities under different EIT schemes. For example, Hamedi et al. in 2015 proposed the switching feature of EIT-based slow light Kerr nonlinearity enhancement systems in QWs [9], Raheli in 2018 also have shown that large Kerr nonlinear indices can be achieved in an asymmetric semiconductor three-coupled-quantum-well (TCQW) structure based on intersubband transitions [10].

Lowering of group velocity is another EIT related phenomena, which was first observed in lead vapour in 1991 by Field et al. [11]. In 2009, Ma et al. [12] have reported the slow down factor of group velocity inside a GaAs/AlGaAs multiple quantum well (MQW) in a transient regime to be $\sim 2.10 \times 10^3$ under an EIT condition. In 2017, Vafapour and Alaei demonstrated the increased Q-factor in metamaterials under classical electromagnetically induced transparency (Cl-EIT) leads to large group index which is efficient for plasmonic sensing, optical switching, and slow light device designing [13].

In past few decades, the optical solitons in different nonlinear media has gained significant attention due to their potential applications in information processing, optical communications, and optical computing [6, 14–16]. Formation of optical solitons is attributed by delicate balance between dispersion and nonlinearity induced by the electromagnetic fields. In most of the recent works, the role of EIT enhanced Kerr nonlinearity has studied in details to investigate the generation and propagation of solitons in SQWs [14–17]. Yang et al. in 2008 have reported that the nature of the soliton i.e. bright or dark could be controlled by the ratio of dipole moments of inter-sub band transition (ISBT) [14]. Zhu and Huang in 2011 have reported the realization of coupled slow-light soliton pairs with very low generation power in QW systems [16].

Thus, in view of above reports, we have investigated the enhancement of Kerr nonlinearity to facilitate the propagation of optical soliton at very low group velocity in a three-level SQW. The system undertaken for investigation may be used for wide applications in optoelectronics and photonics.

23.2 Mathematical Model and Governing Equations

In this study, we adopt a symmetric three-level multiple quantum well (MQW) system as shown in Fig. 23.1a. The MQW system is comprises of 40 symmetric 10 nm n-doped InGaAs wells with 10 nm barriers of AlInAs [17]. In this system, a weak probe pulse and a strong control laser beam are employed to interact in a cascade type configuration. The transition energies of the probe and the control lasers are $E_{21} \sim 129 MeV$ and $E_{32} \sim 160 MeV$, with dipole matrix element $z_{21} = 2.34 nm$ and $z_{32} = 2.64 nm$, respectively, which are shown in Fig. 23.1b. The probe pulse
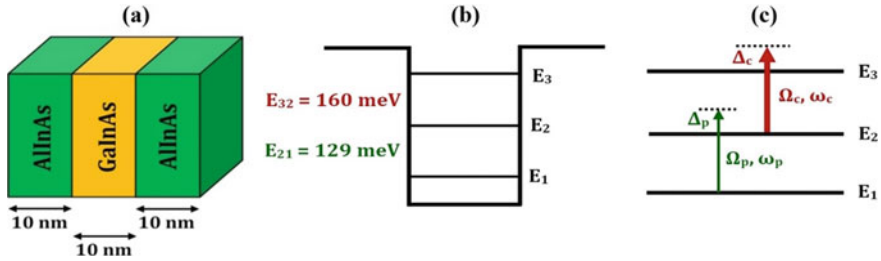
Fig. 23.1 **a** Schematic band structure of a single period of the multiple quantum well adopted for the present study, **b** energy level diagram, and **c** the cascade transition in the quantum well, are presented

with angular frequency ω_p couples the $|1\rangle \rightarrow |2\rangle$ transition and the control beam with angular frequency ω_c couples the $|2\rangle \rightarrow |3\rangle$ transition which are depicted in Fig. 23.1c.

The Hamiltonian of the system presented above is given by

$$\hat{H} = \sum_{i=1}^{3} \hbar\omega_i |i\rangle\langle i| - \hbar\left\{\Omega_p e^{-i\omega_p t}|3\rangle\langle 1| + \Omega_c e^{-i\omega_c t}|3\rangle\langle 2| + c.c.\right\} \tag{23.1}$$

where, Ω_p and Ω_c are probe and control Rabi frequencies described as $\Omega_p = \frac{\mu_{21}\varepsilon_c}{\hbar}$ and $\Omega_c = \frac{\mu_{32}\varepsilon_c}{\hbar}$, respectively.

The equations of motion using density matrix approximation are given as

$$\dot{\tilde{\rho}}_{21} = i\Delta_p \tilde{\rho}_{21} - i\Omega_p(\tilde{\rho}_{22} - \tilde{\rho}_{11}) + i\Omega_c^*\tilde{\rho}_{31} - \frac{\gamma_{21}\tilde{\rho}_{21}}{2} \tag{23.2}$$

$$\dot{\tilde{\rho}}_{32} = i\Delta_c \tilde{\rho}_{32} - i\Omega_c(\tilde{\rho}_{22} - \tilde{\rho}_{33}) - i\Omega_p^*\tilde{\rho}_{31} - \frac{\gamma_{32}\tilde{\rho}_{32}}{2} \tag{23.3}$$

$$\dot{\tilde{\rho}}_{31} = i(\Delta_p + \Delta_c)\tilde{\rho}_{31} - i\Omega_c\tilde{\rho}_{11} - i\Omega_p\tilde{\rho}_{32} + i\Omega_c^*\tilde{\rho}_{31} - \frac{\gamma_{31}\tilde{\rho}_{31}}{2} \tag{23.4}$$

where Δ_p and Δ_c are the intersubband transition detunings and, γ_{21}, γ_{31} and γ_{32} are the decay rates. The optical susceptibility can be segregated into linear and nonlinear parts as the following expression: $\chi_P = \chi^{(1)}(\omega_p) + \chi^{(3)}|E_P|^2$, where we restrict our study to third-ordered terms and neglect the higher orders. The linear and nonlinear (or third order) susceptibilities at probe frequency can be written as:

$$\chi^{(1)} = -\frac{N|\mu_{21}|^2 D_p(0)}{\hbar\varepsilon_0 D(0)}, \tag{23.5}$$

$$\chi^{(3)} = \frac{N|\mu_{21}|^4(|\Omega_c|^2 + |D_p(0)|^2)D_p(0)}{\hbar\varepsilon_0 D(0)|D(0)|^2}, \tag{23.6}$$

where N is the carrier density, $D_p(\omega) = \omega + \Delta_p + \Delta_c + i\frac{\gamma_{31}}{2}$, and $D(\omega) = \left(\omega + \Delta_p + \Delta_c + i\frac{\gamma_{31}}{2}\right)\left(\omega + \Delta_p + \Delta_c + i\frac{\gamma_{21}}{2}\right) - |\Omega_c|^2$.

Following the standard methodology described in [20] we can have the propagation constant of the probe pulse expressed as

$$K = \frac{\omega}{c} - \frac{\alpha D_p(\omega)}{D(\omega)} \tag{23.7}$$

where, $\alpha = \frac{N\omega_p|\mu_{12}|^2}{2c\hbar\varepsilon_0}$. The K($\omega$) can be expressed in Taylor's series, around the central frequency of probe pulse ($\omega = 0$) as follows:

$$K(\omega) = K(0) + K_1(0)\omega + \frac{1}{2}K_2(0)\omega^2 + ..., \tag{23.8}$$

where $K_n(0)s$ are given by $K_n(0) = \frac{d^n K}{d\omega^n}\Big|_{\omega=0}$. Thus we have

$$K(0) = -\frac{\alpha D_p(0)}{D(0)} \tag{23.9}$$

$$K_1(0) = \frac{1}{C} - \frac{\alpha}{D(0)} + \frac{\alpha D_p(0)\left(2\Delta_p + \Delta_c + i\frac{\gamma_{31}}{2} + i\frac{\gamma_{21}}{2}\right)}{\{D(0)\}^2} \tag{23.10}$$

$$K_2(0) = \frac{2\alpha\left(2\Delta_p + \Delta_c + i\frac{\gamma_{31}}{2} + i\frac{\gamma_{21}}{2}\right)}{\{D(0)\}^2}$$
$$- \frac{2\alpha\left(2\Delta_p + \Delta_c + i\frac{\gamma_{31}}{2} + i\frac{\gamma_{21}}{2}\right)\left(\Delta_p + \Delta_c + i\frac{\gamma_{31}}{2}\right)}{\{D(0)\}^3} \tag{23.11}$$
$$+ \frac{2\alpha D_p(0)}{\{D(0)\}^2}$$

Physically, $K(0) = \phi + i\alpha/2$, in which the real and imaginary parts depict the phase shift and absorption coefficient, respectively, while $K_1(0) = \frac{dK(\omega)}{d\omega}\Big|_{\omega=0}$ relates the group velocity as expressed by $V_g = \text{Re}\left[\frac{1}{K'(0)}\right]$. The higher order term $K_2(0) = \frac{d^2 K(\omega)}{d\omega^2}\Big|_{\omega=0}$ represents the group velocity dispersion (GVD) of the probe pulse, responsible for changes in the pulse shape during propagating and additional loss or gain of the probe field intensity.

For the investigation of pulse propagation dynamics in the system, we take the following Nonlinear Schrödinger equation for the envelope $\tilde{\Omega}_p$ [20]

$$i\frac{\partial \tilde{\Omega}_p}{\partial \xi} - \frac{1}{2}\beta_2(0)\frac{\partial^2 \tilde{\Omega}_p}{\partial T^2} + W\left|\tilde{\Omega}_p\right|^2\tilde{\Omega}_p e^{-\alpha z} = 0 \tag{23.12}$$

where $W = \alpha \left(\frac{|\Omega_c|^2 + |D_p(0)|^2}{|D(0)|^2} \right) \frac{D_p(0)}{D(0)}$. We choose the set of parameters of the MQW system in such a way that $a \approx 0$; so that $e^{-\alpha z} = e^{-2\alpha z} = 1$. In general, the nonlinear effect balances the GVD in order to preserve the shape of the probe field throughout the propagation in the MQW. Now, we are in a position to investigate the linear and nonlinear susceptibilities and study the soliton generation dynamics in the MQW system.

23.3 Results and Discussions

In order to proceed with the study, we have taken the following fitting parameters: $N = 6 \times 10^{23} m^{-3}$, $\omega_p = 19.59 \times 10^{13} s^{-1}$, $\mu_{21} = 37.44 \times 10^{-29} mC$ and decay terms are $\gamma_{21} = 7.59 \times 10^{12} s^{-1}$ and $\gamma_{31} = 3.79 \times 10^{12} s^{-1}$. The imaginary part of $\chi^{(1)}$ in (23.5) represents the linear absorption. From Fig. 23.2, it is seen that when the control field $\Omega_c = 0$ around the probe field is zero (i.e. $\Delta_p = 0$) a high absorption peak is observed. When $\Omega_c > 0$, the absorption peak splits into two separate peaks of comparatively low intensity which depicts the creation of EIT window. With further increase of Ω_c, the EIT window becomes wider. The reduction in the absorption peak is due to the effect of quantum destructive interference, which is driven by the strong control beam. The real part of $\chi^{(1)}$ represents the linear dispersion or refractive index, which is depicted in Fig. 23.3. From Fig. 23.3 it is seen that $\text{Re} \chi^{(1)}$ profile changes from positive to negative value as Δ_p changes from negative to positive. With the increase of Ω_c, the behaviour of the $\text{Re} \chi^{(1)}$ changes at around $\Delta_p = 0$ which changes from negative to positive indicating the change in group velocity from anomalous dispersion to normal dispersion region.

In Fig. 23.4, we plot the variation of $\text{Re} \chi^{(3)}$ with respect to Δ_p for different control field Rabi frequencies Ω_c, at resonance (i.e., $\Delta_c = 0$). From Fig. 23.4, it is evident that, for OFF set control field ($\Omega_c = 0$) the $\text{Re} \chi^{(3)}$ possess a single peak around the

Fig. 23.2 Profile of imaginary part of $\chi^{(1)}$ with normalized probe detuning for different control Rabi frequency Ω_c, **a** $\Omega_c = 0$, **b** $\Omega_c = 10\ ps^{-1}$, **c** $\Omega_c = 20\ ps^{-1}$ and **d** $\Omega_c = 30\ ps^{-1}$
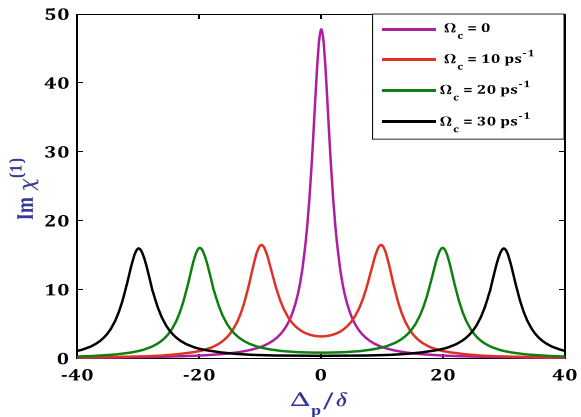
Fig. 23.3 Variation of real part of $\chi^{(1)}$ with normalized probe detuning for different control Rabi frequency Ω_c, **a** $\Omega_c = 0$, **b** $\Omega_c = 10\ ps^{-1}$, **c** $\Omega_c = 20\ ps^{-1}$ and **d** $\Omega_c = 30\ ps^{-1}$
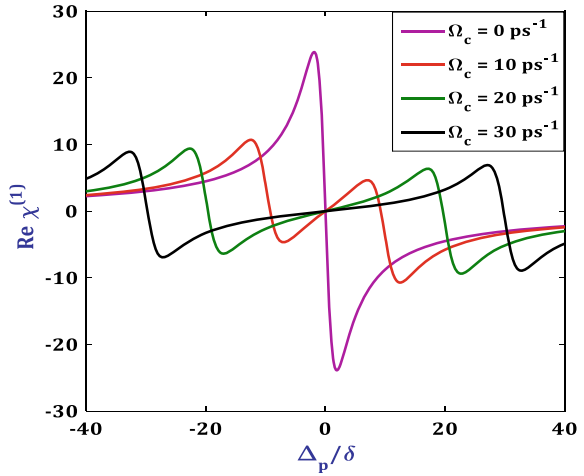
Fig. 23.4 Variation of real part of $\chi^{(3)}$ with normalized probe detuning for different control Rabi frequency Ω_c, **a** $\Omega_c = 0$, **b** $\Omega_c = 10\ ps^{-1}$, **c** $\Omega_c = 20\ ps^{-1}$ and **d** $\Omega_c = 30\ ps^{-1}$
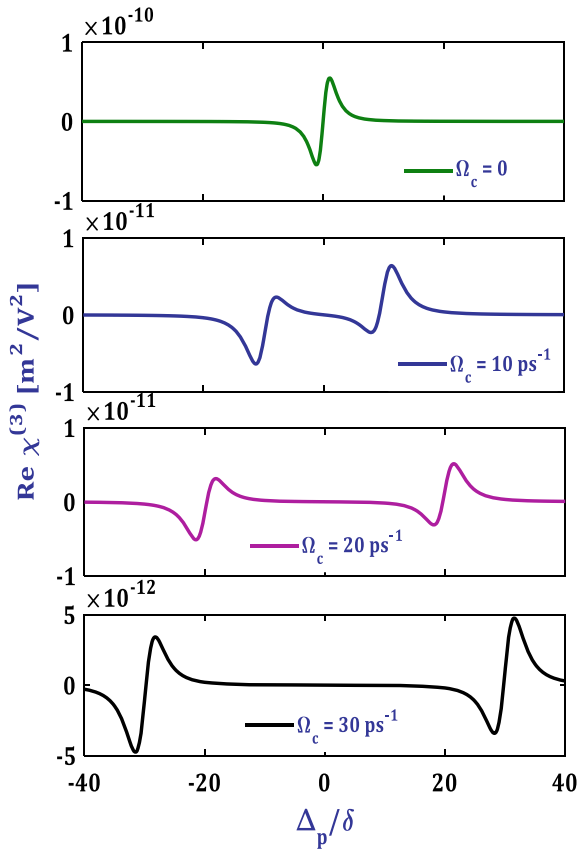
zero probe detuning point ($\Delta_p = 0$), whereas for finite value of Rabi frequencies $\Omega_c > 0$, another peak appears. It is seen from the Fig. 23.4 that, with the increase of control field Rabi frequency $\Omega_c = 0, 10, 20$ and $30\,ps^{-1}$, the separation between the peaks increases. The important result drawn from the figure is that, the MQW system posses a very large third-order susceptibility leading to Kerr-nonlinearity within EIT window is found to be ~10^{-11} m²/V².

At this point, a comparison of $\chi^{(3)}$ values identified in different materials and the quantum well adopted in present study is noteworthy which is present in Table 23.1. From Table 23.1, it is seen that, the value of $\chi^{(3)}$ identified in the present MQW system possesses much higher value as compared to the other materials.

Next, to observe the influence of Δ_c on nonlinear susceptibility, we depict the variation of $\mathrm{Re}\chi^{(3)}$ with respect to Δ_c which is plotted in Fig. 23.5. From the Fig. 23.5 it is seen that, at $\Delta_c = 0$, the profile of is anti-symmetric around zero probe detuning ($\Delta_p = 0$). This anti-symmetric behaviour of $\mathrm{Re}\chi^{(3)}$ changes for any finite value of Δ_c which can be realized easily from the $\mathrm{Re}\chi^{(3)}$ profiles for $\Delta_p = \pm25\,ps$. The $\mathrm{Re}\chi^{(3)}$ profiles shows opposite behaviour for $\Delta_c < 0$ and $\Delta_c > 0$.

Table 23.1 Comparison of values of $\chi^{(3)}$ for different materials

Sl. No.	Materials	$\chi^{(3)}m^2V^{-2}$	λ (μm)	Ref.s
1	TiO$_2$ bulk crystal	5×10^{-21}	0.613	[19]
2	CDS film	1.1×10^{-17}	0.590	[20]
3	InAs/GaAs quantum dots	1.54×10^{-14}	4.000	[21]
5	GaInAs QW	1×10^{-11}	9.280	Present work

Fig. 23.5 Variation of real part of $\chi^{(3)}$ with normalized probe detuning for different control frequency Δ_c, **a** $\Delta_c = -25\,ps^{-1}$, **b** $\Delta_c = 0$, and **c** $\Delta_c = 25\,ps^{-1}$, and with constant $\Omega_c = 30\,ps^{-1}$
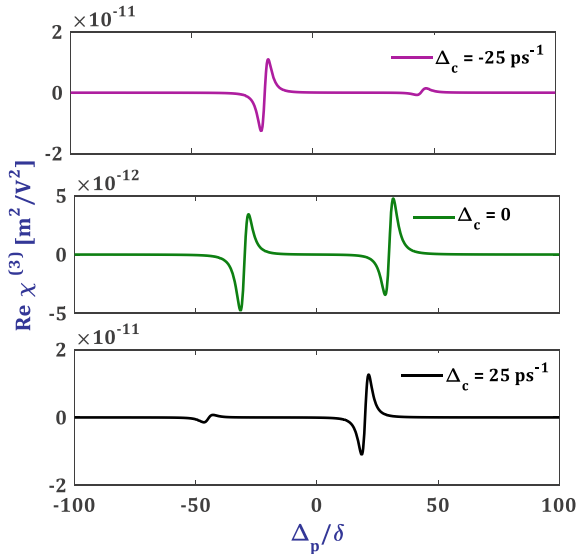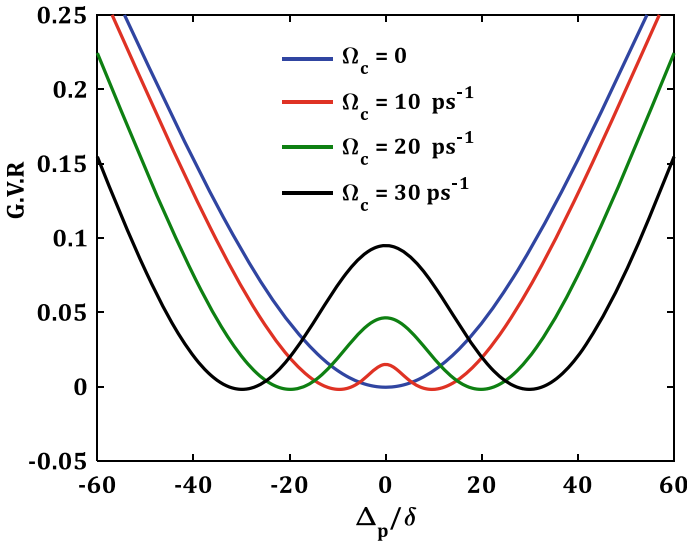
Fig. 23.6 Variation of group velocity ratio (GVR or $\frac{V_g}{c}$) of the probe field with normalized probe detuning for different values of Ω_c, **a** $\Omega_c = 0$, **b** $\Omega_c = 10\ ps^{-1}$, **c** $\Omega_c = 20\ ps^{-1}$ and **d** $\Omega_c = 30\ ps^{-1}$. The detuning of control field is kept at zero ($\Delta_c = 0$)

We now proceed to investigate the group velocity of the probe field. We plot the Group Velocity Ratio (GVR) $\frac{V_g}{c}$ with respect to Δ_p, for different values of Ω_c in Fig. 23.6. At $\Omega_c = 0$, the group velocity initially decreases, reaches the minimum and then increases, with Δ_p. For $\Omega_c > 0$, initially $\frac{V_g}{c}$ decreases but posses a bulge around $\Delta_p = 0$, thereafter it increases with increase in Δ_p. The height of bulge leaps up with increase in Ω_c. From Fig. 23.6, it is seen that at the points of minimum $\frac{V_g}{c}$ the group velocity of the probe field slows down to ~10^3 times smaller than the velocity of light in free space $\left(\frac{V_g}{c} \sim 10^{-3}\right)$.

In Fig. 23.7, we depict the variation of $\frac{V_g}{c}$ with respect to probe detuning under the effect of control detuning (Δ_c) at constant Ω_c. From Fig. 23.7 we observe that the hump appears in negative side of Δ_p for negative values of control detuning Δ_c. The hump moves towards positive values of Δ_p as Δ_c is tuned further positive values.

At this stage, we present the dynamics of soliton generation and propagation in the MQW. To proceed with we consider the NLSE (23.12) of the probe pulse. The Eq. (23.12) contains complex coefficients of K_2 and W, therefore in general, it does not support the shape-preserving distortion free optical solitons. Thus, choose the system parameters in such a way that the real parts of the complex parameters are greater than its imaginary counterparts i.e. $|W_r| > |W_i|$ and $|K_{2r}| > |K_{2i}|$, such that we can take $W = W_r + iW_i \approx W_r$ and $K_2 = K_{2r} + iK_{2i} \approx K_{2r}$. The product ($K_{2r}$, W_r) determines the nature of the soliton. We get bright soliton when ($K_{2r}.W_r < 0$) and dark soliton when ($K_{2r}.W_r > 0$). For the present investigation, we choose the same system parameters as adopted previously, and choose the probe detuning at
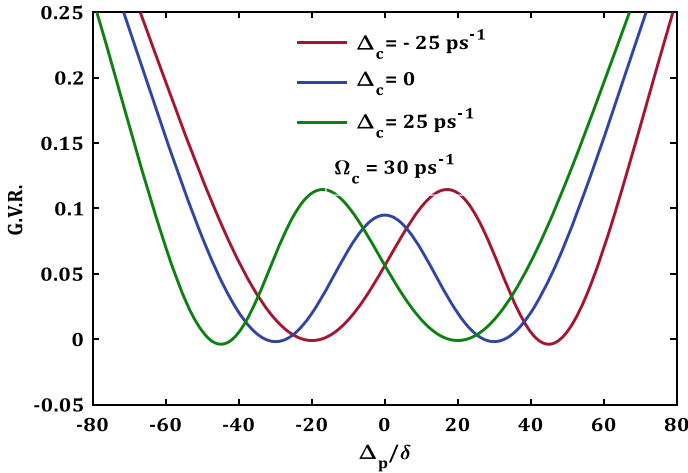
Fig. 23.7 Variation of the group velocity of the probe field (normalized to c) with normalized probe detuning for different values of Δ_c: **a** $\Delta_c = -25\ ps^{-1}$, **b** $\Delta_c = 0$, and **c** $\Delta_c = 25\ ps^{-1}$, and with constant $\Omega_c = 30\ ps^{-1}$

$\Delta_p = 1.05 \times 10^{13} s^{-1}$(corresponding to probe wavelength 9.28 µm) and control Rabi frequency $\Omega_c = 6 \times 10^{13} s^{-1}$. The values GVD and nonlinear coefficient obtained are $K_2 = (1.00 + i0.30) \times 10^{-22} m^{-1} s^2$ and $W = (-2.67 - i0.53) \times 10^{-24} m^{-1} s^2$. Thus it is clear that the imaginary parts of the complex coefficients are indeed much smaller than their corresponding real parts and therefore, Eq. (23.12) would support soliton solutions. $K_{2r}.W_r < 0$ further indicates the soliton to be the bright one. Employing standard procedure [22], the expression of the soliton solution is obtained as

$$\Omega(z, \tau) = \Omega_{po} sech(\tau) e^{-\frac{i\left(|W_r||\Omega_{po}|^2 z\right)}{2}}, \tag{23.13}$$

where z, and $\tau (= T/T_0)$ are the distance, and temporal distribution of the soliton, respectively. T_0 is the temporal width, related to full width at half maximum of the pulse as $T_{FWHM} = 1.76 T_0$. The Ω_{po} is the amplitude that leads to the peak power of the soliton defined by $\Omega_{po} = \frac{1}{\tau_0}\sqrt{|\beta_{2r}|/|W_r|}$. For a 100 ps soliton we identified $\Omega_{po} = 0.034 \times 10^{12} s^{-1}$. In order to check the stable propagation of the soliton we present the result of numerical simulation on soliton wave shape Ω_p versus time τ and distance z by taking (23.13) as depicted in Fig. 23.8. From Fig. 23.8 it is clear that soliton is robust and fairly stable during propagation through the MQW. Thus the result of numerical simulation shows excellent agreement with the exact solution of (23.13).
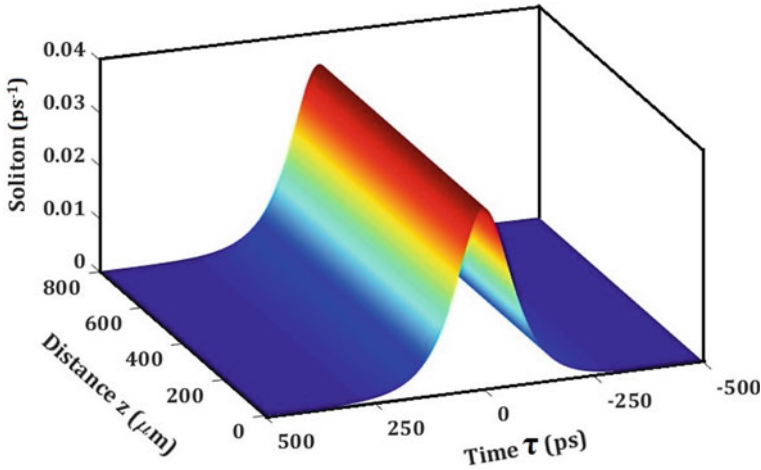
Fig. 23.8 Shape-preserving soliton propagation through MQW. The profile of intensity Ω_p with respect to τ and z, is obtained by solving NLSE (23.12) numerically

23.4 Conclusion

To conclude, we have theoretically investigated the third-order susceptibility in a symmetric three-level MQW nanostructure, where a weak probe and a strong control lasers are employed to interact in a ladder-type configuration. We have identified the existence of giant thrd-order nonlinearity in this system. The peak of Re $\chi^{(3)}$ is found to be $\sim 10^{-11} m^2/V^2$ at 9.28 μm wavelength. We have found that the nonlinearity can be enhanced by tuning the EIT window. In this quantum well structure, the probe field can be slowed down to group velocity $\sim$ 1000 times lesser than that of light speed in free space. By solving the NLSE numerically, we have demonstrated the possibilities of generation and stable propagation of slow optical solitons in the quantum well system. The present investigation affirms that the system can be used in several applications in photonics and optoelectronics and promises potential applications in all optical switching and other information processes.

References

1. S.E. Harris, J.E. Field, A. Imamoglu, Phys. Rev. Lett. **64**, 1107 (1990)
2. S.E. Harris, Phys. Today **50**, 36 (1997)
3. J.P. Marangos, J. Mod. Opt. **45**, 471–503 (1998)

4. G.Q. Yang, P. Xu, J. Wang, Y. Zhu, M.S. Zhan, Phys. Rev. A **82**, 045804 (2010)
5. W. Yan, T. Wang, X.M. Li, Y.J. Jin, Appl. Phy. B **108**, 515 (2012)
6. W.X. Yang, J.M. Hou, R.K. Lee, Phys. Rev. A **77**, 033838–033847 (2008)
7. S.G. Kosionis, A.F. Terzis, E. Paspalakis, J. Appl. Phys. **109**, 084312 (2011)
8. C. Zhu, G. Huang, Phys. Rev. B **80**, 235408 (2009)
9. H.R. Hamedi, M.R. Mehmannavaz, Physica E **66**, 309–316 (2015)
10. A. Raheli, Phys. Wave Phenom. **26**, 182–190 (2018)
11. J.E. Field, K.H. Hahn, S.E. Harris, Phy. Rev. Lett. **67**, 3062 (1991)
12. S.M. Ma, H. Xu, B.S. Ham, Opt. Exp. **17**, 14902 (2009)
13. Z. Vafapour, H. Alaei, Plasmonics **12**, 479 (2017)
14. W.X. Yang, R.K. Lee, Europhys. Lett. **83**, 14002 (2008)
15. S. Swetanshumala, S. Konar, A. Biswas, Appl. Phys. B **111**, 53–64 (2013)
16. C. Zhu, G. Huang, Opt. Exp. **19**, 23364–23376 (2011)
17. K.L. Vodopyanovt, G.B. Serapiglia, E. Paspalakis, C. Sirtorit, C. C. Phillips, in *8th International Symposium on "Nanostructures: Physics and Technology"* (St. Petersburg, Russia, 2000)
18. N. Borgohain, M. Belic, S. Konwar, Annal. Phys. **361**, 107 (2015)
19. T. Okamoto, H. Koizumi, M. Haraguchi, M. Fukui, A. Otomo, Opt. Mat. Express **3**, 1504 (2013)
20. S. Sauvage, P. Boucaud, F. Glotin, R. Prazeres, J.M. Gerad, V. Thierry, Phys. Rev. B **59**, 9830 (1999)
21. T. Ning, Y. Zhou, H. Shen, H. Lu, Z. Sun, L. Cao, D. Guan, D. Zhang, G. Yang, J. Phys. D. Appl. Phys. **40**, 06705 (2007)
22. G.P. Agrawal, *Nonlinear Fiber Optics* (Academic Press, New York, 2006)

Chapter 24
Structural, Magnetic and Optical Study of Transition Element Doped Bismuth Ferrite

Arti, Anahat, Sumit Kumar, P. Kumar, and Vivek Verma

Abstract Enhanced structural and optical properties of pure and manganese (Mn) doped bismuth ferrite has been studied using sol–gel method as preparation technique. The scanning electron microscope analysis showed that Mn doping decreases grain size. M-H loops shows modified magnetic properties with Mn doping. The values of dielectric constants $\varepsilon' = 63.68$ and $\varepsilon'' = 12.47$ of BFO are seen to be enhanced with increase in manganese content and is maximum for $BiFe_{0.8}Mn_{0.2}O_3$ sample. The observed behaviour of ferroelectric P-E loops shows modification with increase in manganese content in BFO samples. The modified ferroelectric behaviour may results in better response of I-V characteristics i.e. dark current which leads good response in photocurrent values. Mn doping leads to the narrowing of the band gap of $BiFe_xMn_{1-x}O_3$ as evaluated from U-V visible response. Pure and Mn doped bismuth ferrite exhibited modification in leakage current from I-V characteristics, which may results in better photovoltaic response. Mn doping in BFO shows modified behavior in various properties, which makes BFO a better material for various applications.

24.1 Introduction

In recent years, due to lacking of energy resources and increasing demands of this era, natural resources of energy is the great way of harvesting energy. Solar energy is one of the most demanding natural resource of energy. From solar energy, light energy can be harvested through various techniques. One of the technique we are studying is the Photovoltaic effect. Due to unique features of $BiFeO_3$ (BFO) i.e. appropriate band gap value (~2.73 eV) and self induced polarization, it plays very crucial role in the research areas of photovoltaic, photocatalytic and in optoelectronic devices. Multiferroic is class of materials which exhibit both ferroic properties simultaneously. BFO is a multiferroic material with its unique properties, which has applications in memory

Arti (✉) · Anahat · S. Kumar · P. Kumar · V. Verma
Department of Physics, Hindu College, University of Delhi, Delhi, India

Arti · S. Kumar · P. Kumar
Department of Physics and Astrophysics, University of Delhi, Delhi, India

devices for storing data, sensors, photovoltaics and spintronics [1]. BFO has attracted attention not only because of its magneto electric coupling but also due to its good optical properties. The materials have good ferroelectric behaviour and low value of band gap are known and being used nowadays for good photovoltaic response, because the spontaneous polarization separates the photo generated electron–hole pairs produces internal electric field and thus, enhanced the photovoltaic properties. In ferroelectric materials polarization leads self-induced polarization. It is the advantage of this self-induced polarization that PV effect in ferroelectric materials requires no p–n junction. The silicon based photovoltaic cells, have limitation of diffusion in junction based solar cell and due to their high cost. Further improvement in efficiency of solar cells is very limited. Photovoltaic effect in $BiFeO_3$ perovskite solar cell and modification in efficiency can be optimized by doping with suitable elements in bismuth ferrites and their composites with suitable magnetic and ferroelectric materials [2]. In this work Bismuth ferrite (BFO) and manganese doped Bismuth ferrite samples are prepared using sol–gel method. Increasing doping of Mn content enhanced the following properties i.e. ferroelectric, magnetic and optical properties, and also the increased content of manganese shows effect on crystal structure and decreased impurities [3].

24.2 Experimental Method

Low temperature synthesis of Pure and manganese doped BFO samples has been done by sol–gel method. In this method Bismuth nitrate $[Bi(NO_3)_3 \cdot 5H_2O]$, iron nitrate $[Fe(NO_3)_3 \cdot 9H_2O]$, and manganese acetate $[Mn(CH_3COO)_2 \cdot 4H_2O]$, were added for making gel according to stoichiometry amount [4]. All the nitrates were allowed for stirring maintaining the magnetic stirring, to make a homogeneous solution. Oxalic acid is then added as complexing agent in the precursor solution. Then obtained solution was allowed to heat for obtaining gel. During heating the amount of gases released and the gel coverts to powder. Powder was then grinded well and sintered at 500 °C for 4 h for phase formation. Further pellets were made for making measurements of different powder samples.

24.3 Results and Discussion

24.3.1 Structural Properties

Figure 24.1 shows XRD spectra of pure and Mn doped BFO samples. From Fig. 24.1 it can be observed that all pure and doped BFO samples exhibits polycrystalline behaviour.
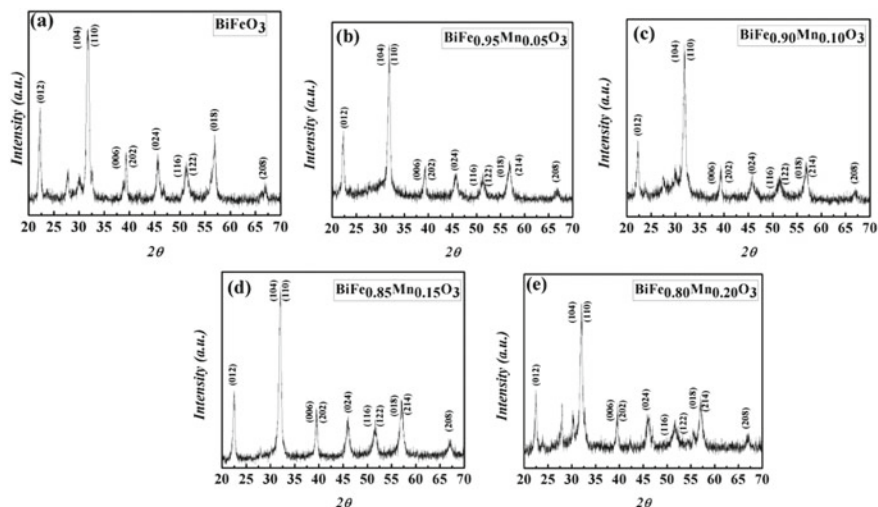
Fig. 24.1 XRD spectra of pure and doped samples of BFO

Apart from the main $BiFeO_3$ peaks few minor peaks belonging to $Bi_{25}FeO_{29}/Bi_2O_3$ are visible in the 2θ range between 25 and 30. The plane (1 0 4), (1 1 0) and (0 0 6), (2 0 2) shown in the Figure are showing the peaks of all the samples which are merging from doublet peak to singlet peak with increase in Mn content may cause change in the structure. This structural transition in the ceramics may be due to substitution of Fe^{3+} cations with Mn^{2+} cations. The variation in structural parameter for R3c space group is observed with Mn substitution. It can depict from Table 24.1 that higher the Mn content for $x = 0.05$ to 0.20 induce larger unit cell volume. Thus the shifting of peaks (104) and (110) towards lower angles (Fig. 24.1), may be due to structural transition to orthorhombic from rhombhohedral structure. Due to lager radii of Mn and its substitution at B-site Fe cation which has smaller radii, the cationic radius of B-site increases. The value of tolerance factor 't' gives the reason for change in cationic radius. With doping content of Mn the value of tolerance factor is increasing as shown in Table 24.1. Tolerance factor for $BiFe_{1-x}Mn_xO_3$ is given by, $t = R_A + R_O/1.44(R_B + R_O)$, where R_A is the effective ionic radii of Bi^{3+}, R_B is the effective radii of Fe^{3+}, and R_O is the effective radii of O^{2-} ions. If 't < 1', the

Table 24.1 Tolerance factor, crystallite size and grain size of samples

Sample name	Tolerance factor (t)	Crystallite size (d) (nm)	Grain size (SEM) (nm)
$BiFeO_3$	0.88729	12.7	81.30
$BiFe_{0.95}Mn_{0.05}O_3$	0.89337	17.9	59.45
$BiFe_{0.90}Mn_{0.10}O_3$	0.89958	18.8	54.73
$BiFe_{0.85}Mn_{0.15}O_3$	0.90584	16.2	50.60
$BiFe_{0.80}Mn0_{.20}O_3$	0.93023	21.6	48.63
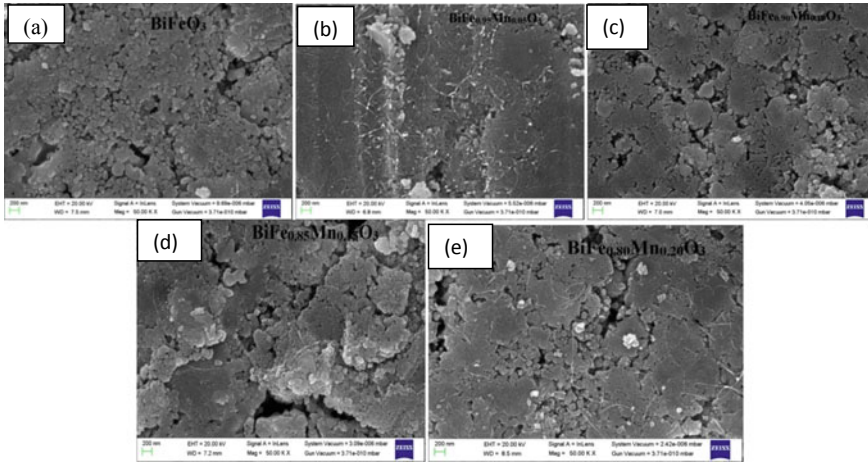
Fig. 24.2 SEM micrographs of pure and doped BFO samples

strain induces lattice distortion because the strain acts on the bond of BFO i.e. Fe–O and Bi-O bonds which leads phase change such as orthorhombic or tetragonal. This corresponds the phase transition from rhombohedral to orthorhombic with increase in manganese content in bismuth ferrite. This leads to suppression of rhombohedral phase and may results new crystallographic phases [5]. This change in crystal structure of $BiFe_{1-x}Mn_xO_3$ ceramics may affect its various properties, which will be useful for various applications. SEM micrographs of pure and doped BFO samples has been shown in Fig. 24.2. Distribution and average size of grain for all the samples has been calculated using Image j software. Grain size decreases with increase in doping content of Mn in BFO (~81.30 nm to 48.63 nm). The decrease in grain size is may be due to different ionic radii of Mn^{2+} and Fe^{3+}. Another reason for grain size decrement is may be because of Kirkendal effect [6].

24.3.2 Ferroelectric Studies

P-E loops for pure and doped BFO ceramics has been shown in Fig. 24.3. It is observed that the polarization (P) and coercivity (E_c) enhanced with doping content of Mn in BFO. This modification in the ferroelectric properties is may be due to decrease in grain size and phase transformation. Pure BFO sample shows lossy nature with small value of polarization (0.3804 $\mu C/cm^2$) which leads to large leakage current. With increase of Mn content in BFO, the value of polarization increases up to the value of Ps = 5.95 $\mu C/cm^2$, for Mn = 0.15. It could not be measured the P-E loop hysteresis behavior for the sample Mn = 0.20 due to its high leakage behavior. This change in polarization value with doping content of Mn is may be due to lattice distortion of BFO samples [7, 8].
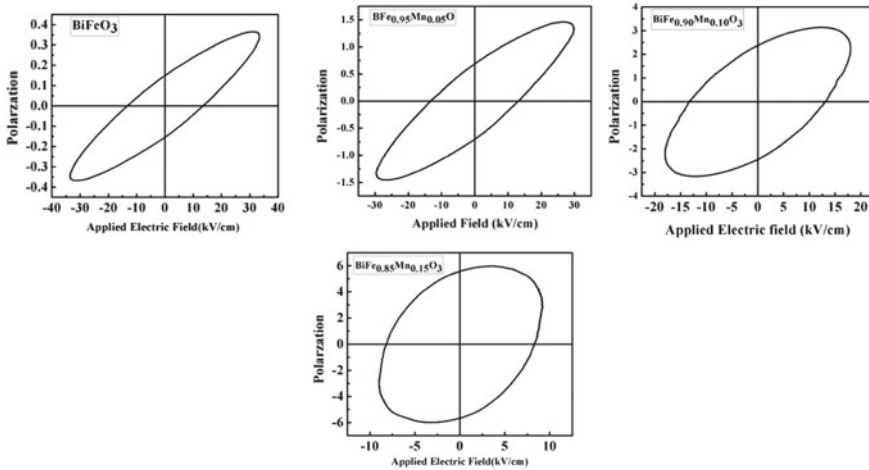
Fig. 24.3 Room temperature P-E loops for pure and doped BFO samples

24.3.3 Dielectric Properties

Dielectric properties of prepared samples of pure and Mn doped BFO has been studied. The value of dielectric constants both real and imaginary parts increases with Mn content in BFO as shown in the Table 24.2. With increasing value of frequency the dielectric constant, both parts of permittivity (real and imaginary) of pure and doped BFO ceramics decreases and at higher frequencies permittivity becomes independent. Thus, low frequency dispersion seen in the results may be due to Maxwell–Wagner effect or interfacial polarization which satisfies Koop's theory. Secondly, at low frequency, hopping of electron is not possible due of lack of energy, so to give sufficient energy the frequency of electric field has been increased and then at some point electrons get sufficient energy for hopping from Fe^{+2} to Fe^{+3} ions. Due to hopping of ions the conductivity of dielectrics increases with frequency, and hence

Table 24.2 Magnetic, dielectric, ferroelectric properties for pure and doped BFO samples

Sample name	Magnetization (M_s)	Dielctric constant				Ferroelectric properties	
		1000 Hz		10^5 Hz		Polarization P_s ($\mu C/cm^2$)	Coercivity E_c (kV/cm)
		ε'	ε''	ε'	ε''		
$BiFeO_3$	0.1581	63.28	5.21	51.30	2.64	0.357	13.001
$BiFe_{0.95}Mn_{0.05}O_3$	0.1746	81.66	26.52	62.48	3.74	1.363	13.258
$BiFe_{0.90}Mn_{0.10}O_3$	0.1614	116.81	152.22	60.89	10.13	2.682	13.222
$BiFe_{0.85}Mn_{0.15}O_3$	0.1647	122.41	169.27	44.11	10.13	3.749	8.317
$BiFe_{0.80}Mn_{0.20}O_3$	0.1676	159.16	497.37	57.69	27.17	–	–

decrements occur in dielectric constant. The dielectric constant and loss tangent of BFMnO is larger at low frequencies. This can be ascribed to Oxygen vacancies created by the substitution of Mn for Fe ions. Since Mn can be stable in two ionic state (Mn^{2+} and Mn^{3+}) which can create oxygen vacancies in the compound. Dielectric losses decrease with increase in frequency and similar is the case with loss tangent [9, 10].

24.3.4 Magnetic Properties

Table 24.2 diminutive enhancement in magnetization for pure and doped BFO ceramics. Weak ferromagnetic behaviour has been exhibited by the prepared ceramics of pure and doped BFO. Pure BFO exhibits G-type antiferromagnetic behaviour. Enhanced magnetic properties of all the BFO samples may be due to Mn doping and decrease in average particle size. Tilt in octahedral and formation of canted structure may be due to lager ionic size of manganese than iron. So Fe–O-Fe bond angle and Fe–O length has been affected due to the presence of manganese ions in BFO. Thus enhanced magnetization results following this phenomenon explained above [11, 12].

24.3.5 FTIR

FTIR spectra of Pure and doped BFO has been shown in the Fig. 24.4. The changes (molecular and chemical) in BFO structure as reported above due to changes in Fe–O due to doping of any other element are shown by FTIR spectra. The broad absorption peaks below 1000 cm^{-1} shows the vibrations of bonds Bi–O or Fe–O. In this work we observed peak near 565.33 due to the vibrations of Fe–O and Bi–O groups. The broad peak near 560 cm^{-1} is at may be due to Fe–O and Bi-O stretching of FeO_6 and BiO_6 octahedral [22]. The low intensity peak near 2929.43 cm^{-1} in the samples may also be due to the vibrations (-OH) groups. Another broad weak absorption peaks near 111.85 and 1672 cm^{-1} may be due to the groups of citric, tartric and oxalic acid. The observed IR peaks at 1370 cm^{-1} may shows the bending vibration of C–H. Mn concentration increases small amount of splitting in some of the peaks near 565.23 and 111.85 cm^{-1} and 1370.11 cm^{-1}. The splitting of absorption peaks for some of the samples may be due to the distortion in BFO caused by structural transition produced by Mn substitution, can also be verified by XRD spectra [13–15].

Fig. 24.4 FTIR spectra of pure and doped BFO samples
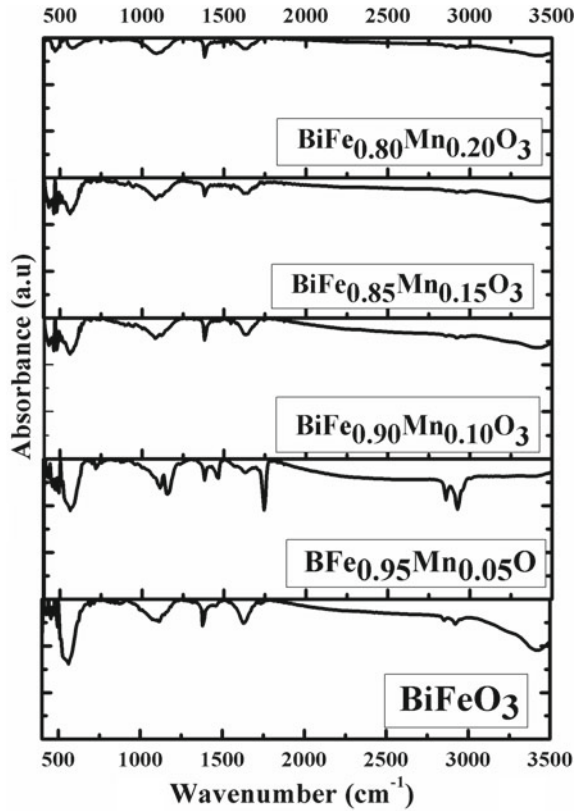
24.3.6   Photovoltaic Properties

24.3.6.1   Band-Gap

The band-gap of pure and magnese doped samples of BFO were studied in the UV–vis wavelength range of 400–600 nm. The corresponding energy band gap of pure and doped samples has been calculated from Tauc's relation for direct band gap. The estimated bandgap values were estimate ~2.37–2.00 eV for $BiFe_{1-x}Mn_xO_3$ samples. Decrement in energy band gap values has been observed increase in manganese content in BFO. This narrowing of band gap is may be due to modification n the value of lattice constants and particle size which leads alteration of the band structure of BFO [16–18].
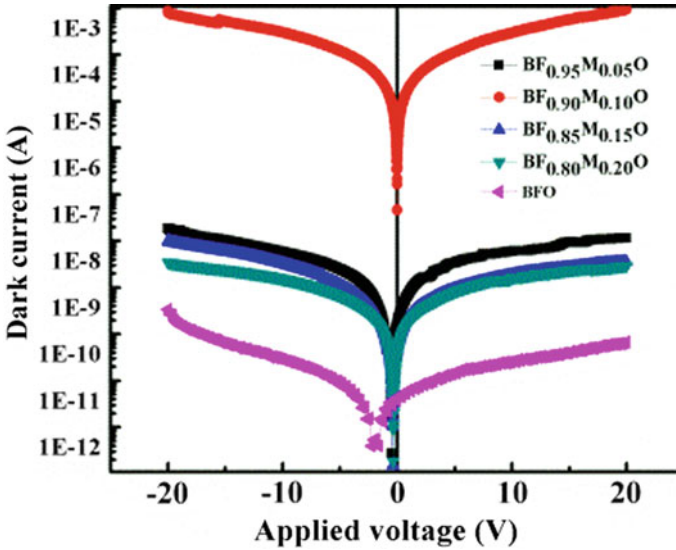
Fig. 24.5 I-V characteristics of Pure and doped BFO samples

24.3.6.2 I-V Characteristics

Figure 24.5 shows the studies of I-V characteristics of bismuth ferrite (BFO) and manganese doped bismuth ferrite samples. Room temperature measurements of dark current has been done for pure and doped BFO samples at room temperature. Leakage current for pure BFO is $I_{dark} = 2.12 \times 10^{-8}$A, and leakage current increases with increase in Mn content in BFO. It can be verified by P-E loops or ferroelectric data which shows lossy behavior. The observed P-E loops shows the consistency with the leakage current behaviour of samples. This leakage current phenomenon can be understood on the basis of some phenomenon such as bulk limited Poole–Frenkel emission (PF) mechanism, or interface-limited Schottky emission, the bulk-limited space-charge-limited conduction (SCLC) mechanism,. This lowering of leakage current values implies good ferroelectric response, and more inherent polarization in the sample which is beneficial for good photovoltaic properties [19–22].

24.4 Conclusion

Low temperature pure and Manganese doped BFO powders has been synthesized by sol–gel method. In this work the structural, electric, magnetic and optical are studied. The phase transition and structural deformation from pervoskite rhombohedral to orthorhombic phase was shown by XRD pattern and other parameters calculated from XRD. Modification in ferroelectric and magnetic properties has been observed

which were in agreement with XRD and SEM data. The modified electrical properties results in lowering of band gap and leakage current as compared to pure BFO with increase in Mn content. Enhanced optical response of BFO with Mn doping can be beneficial for photovoltaic applications in ferroelectric materials.

References

1. A. Manzoor, A.M. Afzal, N. Amin, M.I. Arshad, M. Usman, M. N. Rasool, M. F. Khan, Article in Ceramics International (2016). https://doi.org/10.1016/j.ceramint.2016.04.083
2. M. Alexe, D. Hesse (2011). https://doi.org/10.1038/ncomms1261
3. H.M. Xu, H. Wang, J. Shi, Y. Lin, Photoelectrochemical performance observed in Mn-doped BiFeO$_3$ hetero structured thin films. Cewen Nan Nanomaterials **6**, 215 (2016)
4. *Preparation and Characterization of Bismuth Ferrite Nanoparticle Using Sol–Gel Method*. https://www.researchgate.net/publication/325012631. https://doi.org/10.22214/ijraset.2018.4299
5. V. Srinivas, A.T. Raghavender, K. Vijaya Kumar Volume (2016), Article ID 4835328, 5 pages https://doi.org/10.1155/2016/4835328
6. B. Dhanalakshmi, K. Pratap, B. Parvatheeswar Rao, P.S.V. Subb Rao. 193–201, 676 (2016). https://doi.org/10.1016/j.jallcom.2016.03.208
7. Nisha, D.K. Shukla, S. Kumar, Ferroelectric and dielectric properties of Mn doped BiFeO3 bulk ceramics. AIP Conf. Proc. **2006**, 030037 (2018)
8. J.Z. Huang, Y. Shen, M. Li, C.W. Nan, J. Appl. Phys. **110**, 094106 (2011)
9. C. Elissalde, J. Ravej, Mater. Ceram. Int. **39**, 8527 (2013)
10. S. Godara, B. Kumar, Ceramic Intern. **41**, 6912 (2015)
11. C.T. Munos, J.P. Rivera, H. Schmid, Ferroelectrics **55**, 235 (1984)
12. J.P. Tae, C. Georgia, J.V. Arthur, M.R. Arnold, S.W. Stanislaus, Nano. Lett. **7**, 766 (2007)
13. M.M. Kumar, A. Srinivas, S.V. Suryanarayana, J. Magn. Magn. Mater. **188**, 203 (1998)
14. R. Mazumder, P.S. Devi, D. Bhattacharya, P. Choudhury, A. Sen, M. Raja, Appl. Phys. Lett. **91**, 3 (2007)
15. Y. Hu, L. Fei, Y. Zhang, J. Yuan, Y. Wang, H. Gu, J. Nanomater. **2011**, 6
16. D. Suastiyanti, Ismojo, Int. J. Eng. Sci. (IJES) **5**, 114–117 (2016)
17. H.M. Xu, H. Wang, J. Shi, Y. Lin, Cewen Nan Nanomaterials **6**, 215 (2016)
18. R.Q. Guo, L. Fang, W. Dong, F.G. Zheng, M.G. Shen, J. Phys. Chem. C, **114**, 21390 (2010)
19. F. Gao, X.Y. Chen, K.B. Yin, S. Dong, Z.F. Ren, F. Yuan, T. Yu, Z.G. Zou, J.M. Liu, Adv. Mater. **19**, 2889 (2007)
20. Y.L. Pei, C. Zhang, J. Alloy. Compd. **570**, 57 (2013)
21. H. Yang, M. Jain, N.A. Suvorova, H. Zhou, H.M. Luo, D.M. Feldmann, Q.X. Jia, Appl. Phys. Lett. **91**, 072911 (2007)
22. G.W. Pabst, L.W. Martin, Y.H. Chu, R. Ramesh, Appl. Phys. Lett. **90**, 072902 (2007)

Chapter 25
Investigation of Magneto-conductance Transition Effect in Copper Phthalocyanine Thin Films: Electrical Impedance Study

S. S. Rawat, Ashish Kumar, Sanjay Kumar Swami, R. Srivastava, S. P. Khanna, and C. K. Suman

Abstract We report room temperature measurement of magneto-conductance (MC) and magneto-photoconductance (MPC) in copper phthalocyanine thin film. Single layer device was investigated at different angles between the magnetic field lines and the normal of device surface. The reported reduction in the negative MC as the applied bias voltage was enhanced may be due to minority charge injection at high voltage regions (bipolar). MC at 1 and 5 V were found to be -2.73 and 4.09% at $0º$ (100 mT) whereas at $90º$ (100 mT) were found to be -7.15 and 8.79%, respectively. The data suggests an anisotropic effect in MC. A similar behaviour was observed for MPC. The device shows single relaxation phenomena observed in impedance spectroscopy.

25.1 Introduction

There is a huge scope in phthalocyanine based organic semiconductors because of their low cost, high absorption coefficient, high thermal and chemical stabilities, in-addition to roll-to-roll ease of manufacturing processing. These materials find regular use in organic solar cells, transistors, photodetectors and gas sensors [1–4]. A number of development have been seen in the area of organic electronics but the discovery of magneto-conductance (MC) effect in organic semiconductor devices is latest one [5, 6]. Here, the current passing through such kind of device where organic thin film is sandwiched between two conducting electrodes can be appreciably altered by an external applied magnetic field. MC is defined as $\frac{\Delta J}{J} = \frac{J(B) - J(0)}{J(0)}$, where J(B) and J(0) are the value of current density in the presence and absence of an external applied magnetic field, respectively. Similarly the MC can be varied in response to

S. S. Rawat · A. Kumar · S. K. Swami · R. Srivastava · S. P. Khanna · C. K. Suman (✉)
CSIR-National Physical Laboratory, Dr. K. S. Krishnan Road, New Delhi 110012, India
e-mail: sumanck@nplindia.org

S. S. Rawat · A. Kumar · R. Srivastava · S. P. Khanna · C. K. Suman
Academy of Scientific and Innovative Research (AcSIR), Ghaziabad 201002, India

the applied temperature, voltage, and sample thickness [7]. Spin mixing plays a very important role in the magnetic field induced MC. There is a hyperfine field which is generated from protons of hydrogen nuclei of the organic semiconductor responsible for mixing of spin states. An applied magnetic field should be greater than hyperfine fields which is responsible for the change in singlet and triplet ratios [8, 9].

Copper phthalocyanine (CuPc) is one of the derivatives based on the addition of copper to the parent/base compound of phthalocyanine. It is widely used in opto-electronic applications as a p-type organic semiconductor [10–13]. CuPc has been explored widely by researchers to understand the underlying phenomenon behind its MC behavior [14, 15]. In general, there are few models which have been proposed to explain the MC phenomenon in organic materials namely, polaron pair [16, 17], bipolaron [18, 19], exciton model [20, 21] etc. However, origin of MC is still under debate in scientific community. Since bipolaron model can be used in both unipolar and bipolar device, so this model has been used for CuPc based device [14]. The two polarons with opposite spin approaches to form bipolaron due to less energy having a doubly occupied site [14, 18] whereas polarons with same spins are blocked due to Pauli's Exclusion Principle. Application of external magnetic field spin blocking is enhanced, resulting into negative MC. The decrease in bipolaron formation can improve the current, resulting into positive MC [22].

In order to understand the behaviour of our device, it is essential to explore the charge carrier transport mechanism of thin film of CuPc material. In this paper, we have studied the electrical and angle dependent magnetic field effects on the CuPc single layer device under light and dark conditions.

25.2 Experimental Details

The CuPc device was fabricated on patterned commercial ITO coated transparent glass substrates. These substrates were properly cleaned in sequence with soap solutions, deionized water, acetone, iso-propanol for 15 min in ultrasonic bath and then placed for 30 min in hot oven at 120 °C for drying. After cleaning successfully, UV-O_3 treatment was performed in glove box in inert atmosphere of N_2 gas. CuPc thin films were deposited by thermally evaporating powder of CuPc under a vacuum of 10^{-6} Torr. Using a deposition rate of ~0.2 Å/s, 100 nm thick layers of CuPc were deposited. Al contact of 120 nm was deposited at deposition rate ~1–2 Å/s by thermal evaporation under a good vacuum of 10^{-6} Torr.

The device structure of diode is following:

$$Device : ITO/CuPc(\sim 100\,nm)/Al(\sim 120\,nm)$$

Electrical properties were analyzed by Keithley source meter (2420) and impedance spectroscopy by Solartron, model SI 1260. A small 100 mV alternating

current signal was applied as an electrical perturbation on DC bias to study the resistive and capacitive behavior of device. Magnetic field effect of device was measured by DC electromagnet of 10" pole diameter (Bruker) in which device was kept.

25.3 Results and Discussions

The schematic structure and energy level diagram of single layer CuPc diode have been shown in Fig. 25.1a and b. The device structure was designed in such a way that hole is injected through low energy barrier whereas the electron must face high energy barrier. The energy barrier between ITO to HOMO of CuPc is 0.4 eV and Al to LUMO is 0.7 eV [23, 24]. Therefore, the hole can be easily injected from ITO to CuPc thin film and on the other hand the electron from aluminium will not inject easily due to high energy barrier. At the same time, it is possible to inject both the carrier into the thin film at high bias voltage. Figure 25.2 presents the current density voltage (J-V) characteristics plotted on log–log scale of single layer CuPc diode at different temperatures. At low voltage region; current density linearly depends on applied voltage (J α V) that indicates ohmic region of transport. At high voltage region; J α V^2 which describes space charge limited current (SCLC) region [25, 26]. Within the SCLC region; the relation of current density and voltage is [27]

$$J = \frac{9\varepsilon\mu V^2}{8d^3},\tag{25.1}$$

where $\varepsilon = 3.19 \times 10^{-11}$ F/m [28], d = 100 nm and μ are dielectric permittivity, thickness of CuPc thin film and mobility of charge carrier, respectively. The mobility has been estimated in SCLC region where the linear fit of current density and voltage have the slope equal to two (m ~ 2). Mobility is found to be 3.19×10^{-8}, 4.01×10^{-8}, 4.34×10^{-8}, 6.65×10^{-8}, 9.19×10^{-8} m^2/Vs for temperature 300, 320, 340, 360 and 380 K respectively. The mobility increases with the increase in temperature. The
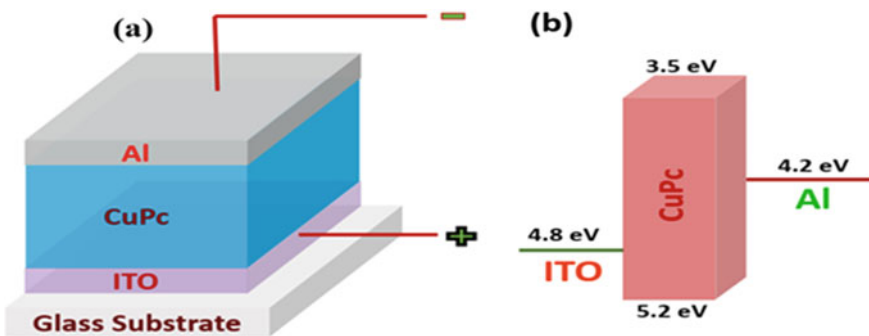
Fig. 25.1 **a** Schematic device structure: ITO/CuPc/Al, **b** device electronic energy level diagram
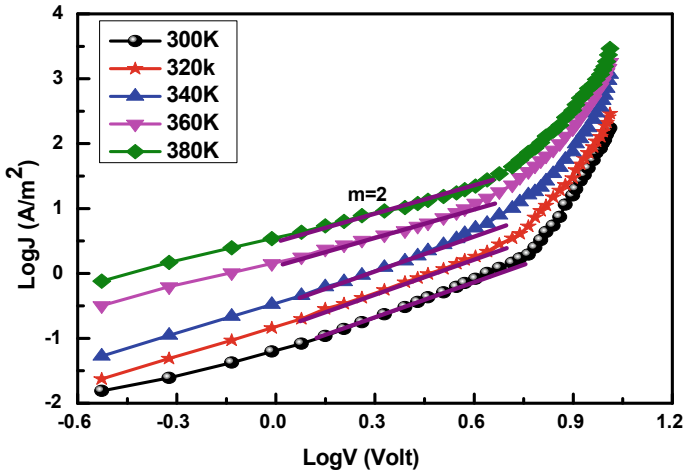
Fig. 25.2 J-V characteristics plotted on log–log scale of single layer CuPc diode at different temperature

increase in mobility with temperature may be attributed to the increase of hopping rate with temperature. The intrinsic transport properties of CuPc thin film have a significant effect of temperature and electric filed. At the same time the magnetic field shows the effect of singlet to triplet spin state conversion through inter system crossing phenomena. The magnetic field effect may be well understood by the MC characterization of the device. The MC is shown in Fig. 25.3a and b at 0º and 90º angle between the magnetic field (B) and electric field (E) of device bias under dark. The non-Lorentzian function can well explain the nature of the MC graph. The empirical non-Lorentzian function of MC [6] is
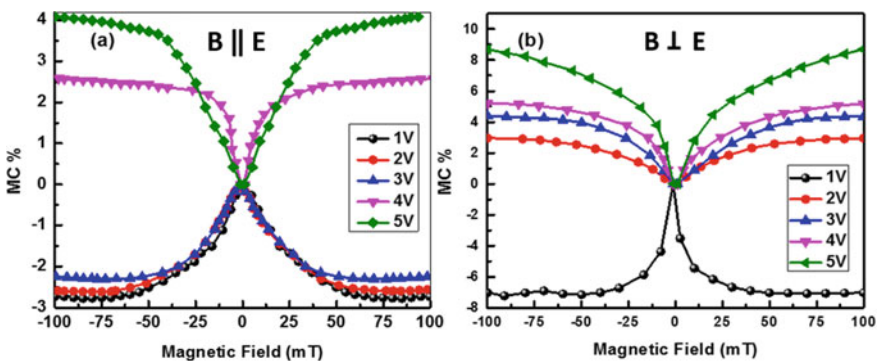
Fig. 25.3 a MC versus an external applied magnetic field for various voltages for 0º angle, **b** MC versus an external applied magnetic field for various voltages for 90º angle

$$MC(B) = MC_\infty \frac{B^2}{(B_0 + |B|)^2} \tag{25.2}$$

where MC_∞ and B_0 are the MC at infinity magnetic field and the full width at half maxima (FWHM).

MC values were found to be -2.73 and 4.09% for 1 and 5 V at 100 mT respectively under dark for 0° angle. The corresponding FWHM values were estimated to be ~35 and ~33 mT for 1 and 5 V, respectively. In comparison, MC values were -7.15 and 8.79% for 1 and 5 V at 100 mT respectively for 90° angle. The corresponding FWHM were observed ~32 and ~36 mT for 1 and 5 V, respectively. The reduction in the negative MC as the applied bias voltage was enhanced may be due to minority charge injection at high voltage regions (bipolar). The data suggests an anisotropic effect in MC. This may be due to filling of traps at low voltage region and minority charge injection at high voltage region [29].

Figure 25.4a and b show MPC effect under 10 mW/cm^2 and 20 mW/cm^2 at 0° angle between B and E. MC values were 2.51 and 7.95% for 1 and 5 V at 100 mT under 10 mW/cm^2 light illumination. The corresponding FWHM value were ~20 and ~37 mT for 1 and 5 V, respectively. The MC value were 1.21 and 10.92% for 1 and 5 V at 100 mT under 20 mW/cm^2 light illumination. The corresponding FWHM values were ~15 and ~32 mT for 1 and 5 V, respectively. Positive MC is observed in light at different bias may be exciton formation in the materials and hence bipolar conduction is taking place. The population of singlet states is increased by applying external magnetic field as singlet states have a larger possibility to dissociate than the triplet states [30]. More the polarons participate in dissociation and then, recombination rate is decreased due to magnetic field, hence MPC is increased [31–33].

Figure 25.5a and b show variation of the real and imaginary part of the AC impedance as a function of frequency of the device measured at forward bias voltages.
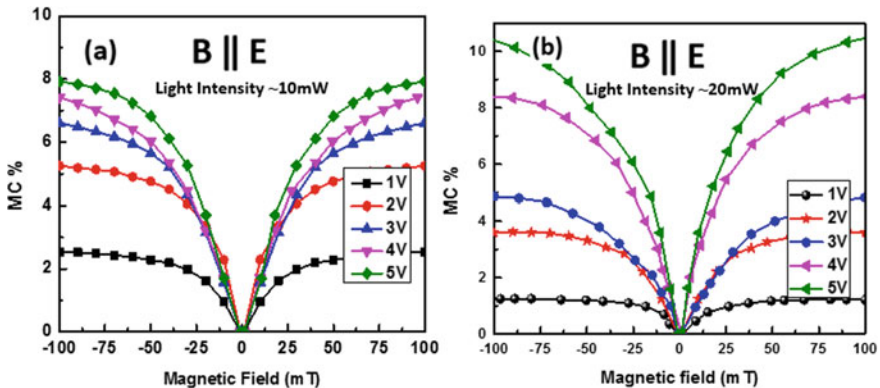
Fig. 25.4 **a** MC versus an external applied magnetic field for various voltages at 0° angle under light 10 mW/cm^2, **b** MC versus an external applied magnetic field for various voltages at 0° angle under light 20 mW/cm^2
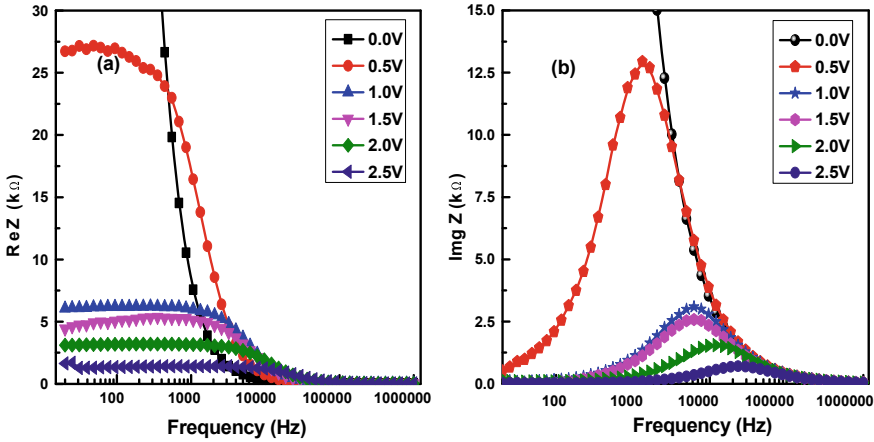
Fig. 25.5 **a** Frequency dependent real part of impedance at forward bias voltage, **b** Frequency dependent imaginary part of impedance at forward bias voltage

The total impedance of a device may be represented as the combination of real and imaginary part of AC impedance in the complex notation as in (25.3)

$$Z(f) = \mathrm{Re}Z(f) + \mathrm{Img}Z(f)$$
$$= \left[Rs + \frac{R_b}{1 + \omega^2 R_b^2 C_b^2} \right] - i \left[\frac{\omega R_b^2 C_b}{1 + \omega^2 R_b^2 C_b^2} \right] \tag{25.3}$$

where the sum of contact (R_s) and bulk (R_b) resistance of the device is equal to the real part of the impedance. The low frequency dependent real part of impedance represents the bulk and interface resistance. The high frequency dependent real part of impedance represents the contact resistance of a device which is caused by the ITO and aluminum electrodes [34]. The bulk resistance of a device is decreased as increasing the voltage whereas contact resistance remains constant approximately equal to 66 Ω [13]. The decrease of bulk resistance with increase of forward bias voltage is attributed to the increase of injected charge carriers and traps filling in the thin films. The decrease of number of traps increases the possibilities of carriers flow in the device. The imaginary part of impedance first increases and reaches maxima before starts decreasing at all applied bias as shown in Fig. 25.5b. The frequency at maxima of imaginary value is called relaxation frequency. When the bias voltage of the device is increased then the relaxation frequency is increased [35]. The relaxation time corresponding to the relaxation frequency represents the dynamics of carrier relaxation with built in and applied bias electric field in the device. The Cole–Cole plot of the device has been shown in Fig. 25.6a at different bias voltages. The Cole–Cole curves are almost semicircle at all applied bias and the center of the circle lies on the real axis. The nature of the experimental data graphs can be well modeled as a single parallel RC circuit with a contact resistance (R_s) in series. The calculated
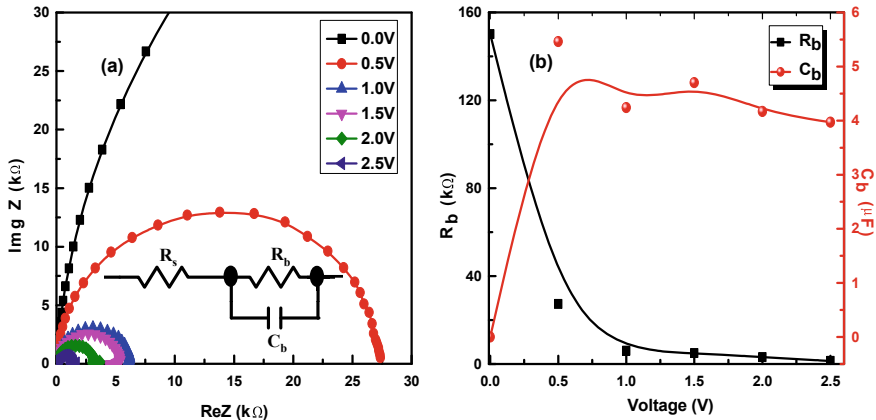
Fig. 25.6 a Cole–Cole curves of device at different applied voltage, **b** Bulk resistance and bulk capacitance for different applied voltage

contact resistance of a device is approximately constant 66Ω as already estimated from Fig. 25.6a. The bulk resistance and capacitance of the device was calculated from the Cole–Cole graphs. The maximum value of bulk resistance measured at 0 V is ~ 150.17 kΩ and the capacitance at the same bias is ~ 0.11 nF. There is decrease in bulk resistance and increase in bulk capacitance with increase of bias voltage as shown in Fig. 25.6b.

25.4 Conclusion

The reported reduction in the negative MC as the applied voltage was enhanced may be due to minority charge injection at high voltage regions (bipolar). The data suggests an anisotropic effect in MC. The increase in mobility of charge carrier with temperature may be attributed to the increase of hopping rate with temperature. It was found that bulk resistance of device was reduced with increase of bias voltage.

References

1. A. Farooq, K.S. Karimov, N. Ahmed, T. Ali, M. Khalid Alamgir, M. Usman, Copper phthalocyanine and metal free phthalocyanine bulk heterojunction photodetector. Phys. B Condens. Matter, 457, 17–21 (2015). https://doi.org/10.1016/j.physb.2014.09.032

2. C. Feng et al. Copper phthalocyanine based hybrid p-type permeable-base transistor in vertical architecture. Appl. Phys. Lett. **88**(20), (2006). https://doi.org/10.1063/1.2204653

3. M. Bouvet, G. Guillaud, A. Leroy, A. Maillard, S. Spirkovitch, F.G. Tournilhac, Phthalocyanine-based field-effect transistor as ozone sensor. Sensors Actuators, B Chem. **73**(1), 63–70 (2001). https://doi.org/10.1016/S0925-4005(00)00682-1

4. C.W. Chu, V. Shrotriya, G. Li, Y. Yang, Tuning acceptor energy level for efficient charge collection in copper-phthalocyanine-based organic solar cells. Appl. Phys. Lett. **88**(15), 2004–2007 (2006). https://doi.org/10.1063/1.2194207

5. J.Y. Song, N. Stingelin, A.J. Drew, T. Kreouzis, W.P. Gillin, Effect of excited states and applied magnetic fields on the measured hole mobility in an organic semiconductor. Phys. Rev. B 1–5 (2010). https://doi.org/10.1103/PhysRevB.82.085205

6. F.L. Bloom et al., Correspondence of the sign change in organic magnetoresistance with the onset of bipolar charge transport. Appl. Phys. Lett. 263302 (2008). https://doi.org/10.1063/1.3059555

7. J.D. Bergeson, V.N. Prigodin, D.M. Lincoln, A.J. Epstein, Inversion of magnetoresistance in organic semiconductors. Phys. Rev. Lett. 067201, 1–4 (2008). https://doi.org/10.1103/PhysRevLett.100.067201

8. W. Wagemans, A.J. Schellekens, M. Kemper, F.L. Bloom, P.A. Bobbert, B. Koopmans, Spin-spin interactions in organic magnetoresistance probed by angle-dependent measurements. Phys. Rev. Lett. 196802, 1–4 (2011). https://doi.org/10.1103/PhysRevLett.106.196802

9. M. Cox, M.H.A. Wijnen, G.A.H. Wetzelaer, M. Kemerink, P.W.M. Blom, B. Koopmans, Spectroscopic evidence for trap-dominated magnetic field effects in organic semiconductors. Phys. Rev. B 155205, 1–7 (2014). https://doi.org/10.1103/PhysRevB.90.155205

10. H. Peisert et al., Order on disorder: copper phthalocyanine thin films on technical substrates. J. Appl. Phys. **90**(1), 466–469 (2001). https://doi.org/10.1063/1.1375017

11. Z. Ahmad, M.H. Sayyad, K.S. Karimov, CuPc based organic-inorganic hetero-junction with Au electrodes. J. Semicond. **31**(7), (2010). https://doi.org/10.1088/1674-4926/31/7/074002

12. F.T. Reis et al., Characterization of ITO/CuPc/AI and ITO/ZnPc/Al structures using optical and capacitance spectroscopy. Synth. Met. **138**(1–2), 33–37 (2003). https://doi.org/10.1016/S0379-6779(02)01284-5

13. Y. Liu, A. Liu, Z. Hu, W. Liu, F. Qiao, Impedance spectroscopy studies on CuPc/n-Si hybrid solar cell. J. Phys. Chem. Solids **73**(5), 626–629 (2012). https://doi.org/10.1016/j.jpcs.2011.12.025

14. L. Chen, Y. Lei, Q. Zhang, Z. Xiong, Negative magnetoconductance effects in amorphous copper phthalocyanine thin film: trap-assisted bipolaron formation. J. Mater. Chem. C 12056–12060 (2015). https://doi.org/10.1039/c5tc01908g

15. W. Jia, Q. Chen, Y. Chen, L. Chen, Z. Xiong, Magneto-conductance characteristics of trapped triplet-polaron and triplet-trapped polaron interactions in anthracene-based organic light emitting diodes. Phys. Chem. Chem. Phys. **18**(44), 30733–30739 (2016). https://doi.org/10.1039/c6cp06322e

16. S. Karabunarliev, E.R. Bittner, Spin-dependent electron-hole capture kinetics in luminescent conjugated polymers. Phys. Rev. Lett. **90**(5), 4 (2003). https://doi.org/10.1103/PhysRevLett.90.057402

17. K. Tandon, S. Ramasesha, S. Mazumdar, Electron correlation effects in electron-hole recombination in organic light-emitting diodes. Phys. Rev. B: Condens. Matter Mater. Phys. **67**(4), 1–19 (2003). https://doi.org/10.1103/PhysRevB.67.045109

18. P.A. Bobbert, T.D. Nguyen, F.W.A. Van Oost, B. Koopmans, M. Wohlgenannt, Bipolaron mechanism for organic magnetoresistance. Phys. Rev. Lett. **99**(21), 1–4 (2007). https://doi.org/10.1103/PhysRevLett.99.216801

19. M.N. Bussac, L. Zuppiroli, Bipolaron singlet and triplet states in disordered conducting polymers. Phys. Rev. B **47**(9), 5493–5496 (1993). https://doi.org/10.1103/PhysRevB.47.5493

20. V.N. Prigodin, J.D. Bergeson, D.M. Lincoln, A.J. Epstein, Anomalous room temperature magnetoresistance in organic semiconductors. Synthetic Metals **156**, 757–761 (2006). https://doi.org/10.1016/j.synthmet.2006.04.010

21. T. Universiteit, E. Document, D. Version, Magnetism and molecular materials: investigating magnetic field effects in organic semiconductors," no. 2015, (2019)

22. M. Li, *Interaction between Charge-transfer States Studied by Magnetic Field Effects* (2016)

23. S. Noh, S. Kim, J. Yang, C. Lee, J.Y. Kim, Investigation into the thermal annealing effect on the photovoltaic properties of organic solar cells based on CuPc/C60 heterojunctions. J. Korean Phys. Soc. **53**(3), 1551–1555 (2008). https://doi.org/10.3938/jkps.53.1551

24. F.J. Lim, K. Ananthanarayanan, J. Luther, G.W. Ho, Influence of a novel fluorosurfactant modified PEDOT: PSS hole transport layer on the performance of inverted organic solar cells. J. Mater. Chem. **22**(48), 25057–25064 (2012). https://doi.org/10.1039/c2jm35646e

25. V. Rani, A. Sharma, P. Kumar, B. Singh, S. Ghosh, Charge transport mechanism in copper phthalocyanine thin films with and without traps. RSC Adv. **7**(86), 54911–54919 (2017). https://doi.org/10.1039/c7ra08316e

26. P.W.M. Blom, M.J.M. De Jong, J.J.M. Vleggaar, Electron and hole transport in poly(p-phenylene vinylene) devices. Appl. Phys. Lett. **68**(23), 3308–3310 (1996). https://doi.org/10.1063/1.116583

27. Z.B. Wang, M.G. Helander, M.T. Greiner, J. Qiu, Z.H. Lu, Carrier mobility of organic semiconductors based on current-voltage characteristics. J. Appl. Phys. **107**(3), (2010). https://doi.org/10.1063/1.3305341

28. R.D. Gould, D.C. electrical measurements on evaporated thin films of copper phthalocyanine. Thin Solid Films **125**(1–2), 63–69 (1985). https://doi.org/10.1016/0040-6090(85)90396-7

29. F.L. Bloom, W. Wagemans, M. Kemerink, B. Koopmans, Separating positive and negative magnetoresistance in organic semiconductor devices. Phys. Rev. Lett. **99**(25), 1–4 (2007). https://doi.org/10.1103/PhysRevLett.99.257201

30. M. Wohlgenannt, X.M. Jiang, Z.V. Vardeny, Spin-dependent exciton formation rates in π-conjugated oligomers and polymers. Phys. B Condens. Matter **338**(1–4), 318–322 (2003). https://doi.org/10.1016/j.physb.2003.08.012

31. S.J. Lee, S.B. Lee, S.C. Yoon, E.Y. Choi, C.S. Yoon, Role of geminate polaron-pair recombination on magnetoconductance in P3HT and PC71BM bulk-heterojunction organic solar cells. Org. Electron. **63**, 384–391 (2018). https://doi.org/10.1016/j.orgel.2018.08.005

32. W.S. Huang, Z.R. Xu, B. Hu, T.F. Guo, J.C.A. Huang, T.C. Wen, Magnetoconductance responses of triplet polaron pair charge reaction in hyperfine coupling regime. Appl. Phys. Lett. **103**(25), 1–5 (2013). https://doi.org/10.1063/1.4852755

33. J. Kalinowski, W. Stampor, Magnetic hyperfine modulation of charge photogeneration in solid films of Alq 3. Chem. Phys. Lett. **378**, 380–387 (2003). https://doi.org/10.1016/j.cplett.2003.07.010

34. Y. Zhang, L. Li, S. Yuan, G. Li, W. Zhang, Electrical properties of the interfaces in bulk heterojunction organic solar cells investigated by electrochemical impedance spectroscopy. Electrochim. Acta **109**, 221–225 (2013). https://doi.org/10.1016/j.electacta.2013.07.152

35. M. Ramar, S.S. Rawat, R. Srivastava, S.K. Dhawan, C.K. Suman, Impact of cross linking chain of N, N'-bis(napthalen-l-yl)-N, N'-bis(phenyl)-benzidine on temperature dependent transport properties. Adv. Mater. Lett. **7**(10), 783–789 (2016). https://doi.org/10.5185/amlett.2016.6305

Chapter 26
Structural Investigations of Dy^{3+} Doped Cubic Gd$_2$O$_3$ Nanopowder via Rietveld Refinement

Rajni Vats and Rachna Ahlawat

Abstract Pechini type sol–gel technique was utilized for the synthesis of Dy^{3+} doped Gd$_2$O$_3$ cubic nanopowder. Sol–gel is not just an economical technique for the fabrication of nanomaterial; it also provides great control over particle size and morphology. The prepared nanopowder was calcined at a temperature of 650.0 °C for 8 h at an annealing rate of 2.0 °C/min. Structural properties of prepared sample are discussed at length which has been investigated with different complementary characterization techniques including XRD, FTIR and HRTEM etc. XRD peaks confirmed cubic crystalline phase of Gd$_2$O$_3$ with Ia-3 space group symmetry. Inter planar spacing, crystallite size, microstrain, texture coefficient and degree of preferred orientation were computed for the powdered sample and are discussed in detail. Rietveld refinement was also carried out to determine the lattice parameters more precisely. Presence of Gd-O vibrations in the FTIR spectra further confirmed the crystalline phase of the sample. Presence of bright rings in SAED pattern indicated the polycrystalline nature of the synthesized nanopowder.

26.1 Introduction

Nanomaterials are studied extensively for their enhanced electrical and optical properties and vast applications in various fields namely electronics, display devices, lasing, white LEDs, magnetic resonance imaging etc. In recent years, the demand to produce advance materials has increased with enhanced electrical, optical and catalytic properties which may find potential applications in diverse fields. In this respect, role of pure and doped rare earth oxides (RE$_2$O$_3$) becomes important due to their vast applications in almost every field i.e. from photonics, electronics, environment, cosmetics, to medical field etc. Gd$_2$O$_3$, due to its large band gap, less phonon energy, large refractive index, good thermal and chemical stability has been established as an excellent host for many lanthanide ions. Also, its ionic radii being similar to Lanthanides, makes it suitable host for the Lanthanide ions. Lanthanide

R. Vats (✉) · R. Ahlawat
Department of Physics, Material Science Laboratory, Chaudhary Devi Lal University, Sirsa, Haryana 125055, India

ions possess unique electronic configurations, suitably doping such ions in nanopowders can lead to remarkable changes in their luminescence properties. Europium, as a lanthanide has been explored immensely, but properties of Dysprosium doped rare earth oxides are yet to be completely analyzed to fully utilize this Lanthanide [1, 2].

These days, researchers are trying to manufacture such nanomaterials which are not just technologically important but environment friendly and cost effective too. Moreover, the synthesis mechanism, annealing condition etc. also play vital role in modifying the electrical and optical properties of the nanopowders. There are many synthesis techniques available for the preparation of nanomaterials such as chemical vapor deposition [3], sol–gel method [4], pulsed laser ablation [5–8] and sputtering techniques [9, 10], molecular beam epitaxy [11, 12], etc. Except sol–gel, all other techniques require sophisticated instrumentation which influences the production cost of the nanomaterials. Sol–gel, on the other hand is not just economical, but also a very simple method to meet the requirements. Doping with a suitable dopant can also modulate the optical and electrical properties of the nanomaterials that would be frequently utilized in diverse photonic appliances.

In the present work, $Gd_2O_3:Dy^{3+}$ nanopowder was prepared by Pechini type sol–gel method [11]. Then the prepared sample was annealed at a temperature of 650.0 °C for 8 h at 2.0 °C/min rate. Further, the synthesized sample has been investigated for its structural study via XRD, FTIR, HRTEM and EDAX analysis. Rietveld analysis is also employed to compute the precise structural parameters which will enhance overall performance of the prepared nanopowder.

26.2 Experimental

26.2.1 Synthesis

Sol–gel is a well-known technique for the production of nanopowders with great control over particle size and ensures better homogeneity. It requires relatively low temperature for synthesis. Therefore, in the present study, nanopowder of $Gd_2O_3:Dy^{3+}$ (4.0 mol %) has been synthesized by Pechini type sol–gel method. Figure 26.1 gives pictorial diagram of the synthesis process. Nitrate salts of the precursors i.e. Gadolinium nitrate hexahydrate [Gd $(NO_3)_3.6H_2O$] and Dysprosium nitrate hydrate [Dy $(NO_3)_3.xH_2O$], were obtained from sigma Aldrich with a purity of 99.90%. Anhydrous citric acid [$C_6H_8O_7$] and ethylene glycol [$C_2H_6O_2$] were acquired from Central drug house and Sisco Research Laboratory, respectively. Proportionate amount of aqueous salts of precursors were taken in a conical flask and stirred at approximately 50 °C for 1/2 h. Citric acid was taken in a burette and added gradually to the precursor solution to form a metal-citrate complex. Addition of ethylene glycol initiated trans-esterification process of metal citrate complex and resulted into a polymer complex. The general reaction for the formation of the nanopowder is represented below:
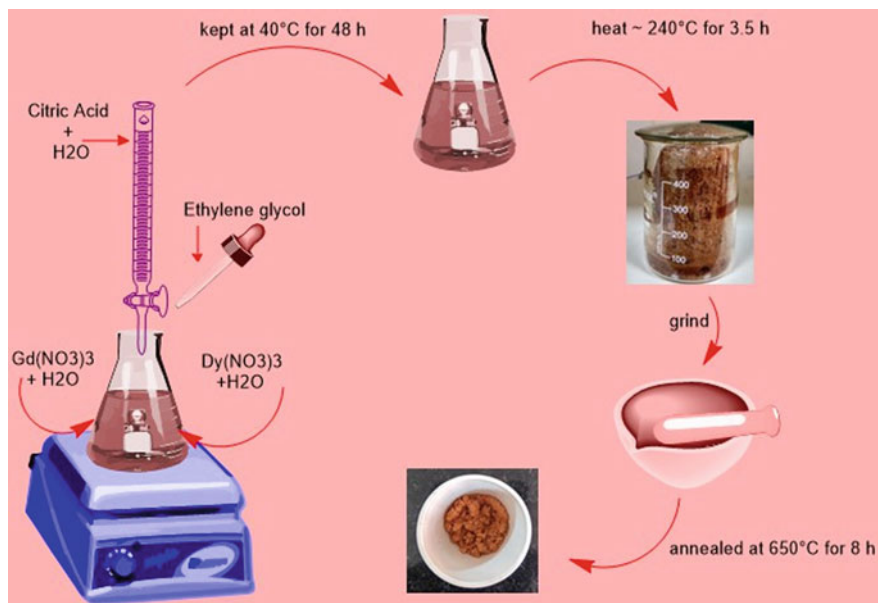
Fig. 26.1 Scheme of the fabrication of Gd$_2$O$_3$:Dy^{3+} nanopowder

$$xY(NO_3)_3 + yDy(NO_3)_3 + HO-\underset{\underset{CH_2COOH}{|}}{\overset{\overset{CH_2COOH}{|}}{C}}-COOH + \underset{\underset{CH_2OH}{|}}{CH_2OH} \longrightarrow Y_xO_3{:}Dy_y + \text{reaction byproducts}$$
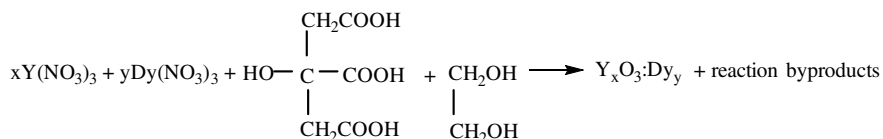
A transparent solution was obtained, that was further stirred for 4 h till the gelation point was reached. This transparent gel was then maintained to a 40 °C temperature for 48 h for completion of the polymerization process. In the meantime, the gel was thickened and ready for the further heat treatment.

The dense gel was further dried at 240.0 °C for $3\frac{1}{2}$ h, resulting into a chocolate brown puffy scoop. This soft puffy scoop was then grinded in an agate pestle-mortar to a fine powder. The granulated powder was calcined at 650.0 °C for 8 h (rate 2.0 °C/min) in the VULCAN 3–130 programmable air furnace which was further characterized for its structural investigation.

26.2.2 Characterizations

The prepared nanopowder was characterized for its structural study via XRD, FT-IR and HRTEM instruments. XRD characterizations of the prepared nanopowder were executed on Rigaku Miniflex-II diffractometer using Cu Kα radiation ($\lambda =$

0.154 nm) in $10° \le 2\theta \le 80°$ range at room temperature. A Perkin Elmer Spectrometer (Spectrum Two) was used to record the FT-IR spectra of the prepared sample, in 4000–400 cm^{-1} range, using KBr pallets. Tecnai G2 20 (FEI) S-Twin TEM instrument is used to take HRTEM images of the sample.

26.3   Results and Discussion

26.3.1   XRD Analysis

XRD profile was used to ensure the phase purity in the crystalline sample and is represented in Fig. 26.2a. Cubic crystalline phase of Gd_2O_3 bearing Ia-3 space group symmetry was confirmed with the XRD analysis as per JCPDS-00-012-0797. The reflection peaks at 19.88°, 28.36°, 32.94°, 47.30° and 56.18° corresponds to 211, 222, 400, 440 and 622 planes of cubic Gd_2O_3 [13, 14]. The interplanar spacing, crystallite size and microstrain have been computed using following equations, respectively [15]:

$$d_{spacing} = \frac{\lambda}{2\sin\theta} \tag{26.1}$$

$$\text{Debye-Scherrer equation}: D = k\lambda/(\beta_{hkl}\cos\theta) \tag{26.2}$$

$$\text{W-H equation}: \beta_{hkl}\cos\theta = \frac{k\lambda}{D} + 4\epsilon\sin\theta \tag{26.3}$$

where, $k = 0.9$, is the shape factor, $\lambda = 0.154$ nm, is the monochromatic X-ray source wavelength, D is the crystallite size, β_{hkl} represents FWHM of the XRD peaks, ϵ is microstrain and θ represents the diffraction angle. The average crystallite size of
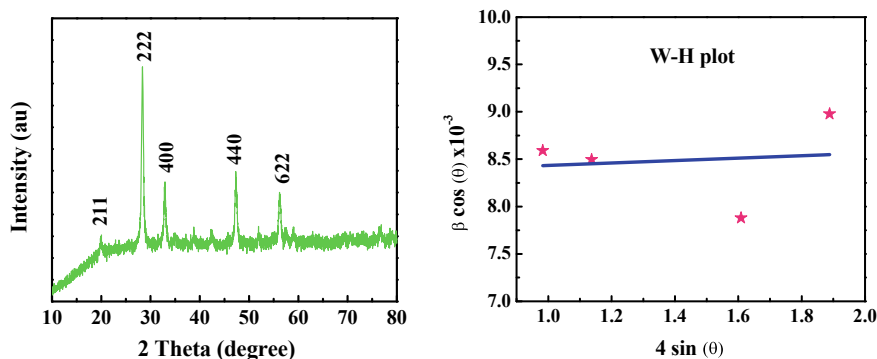
Fig. 26.2   **a** XRD profile, **b** W–H plot of Gd_2O_3:Dy^{3+} nanopowder

the powdered sample, as measured from Debye–Scherrer equation and W–H plot [Fig. 26.2a] are 16.38 nm and 16.68 nm, respectively. The calculated crystallite size are in close agreement. Microstrain present in the sample is of the order of 0.13×10^{-3}.

Physical properties like strength, chemical reactivity, deformation behavior etc. of the materials are greatly influenced by the material texture [16, 17]. Therefore in this regard, texture coefficient and degree of preferred orientation of the sample was also determined by making use of the following equation [18]:

$$TC(hkl) = \frac{n\left[\frac{I(hkl)}{I_0(hkl)}\right]}{\sum_{i=1}^{n}\left[\frac{I(hkl)}{I_0(hkl)}\right]} \tag{26.4}$$

$$\sigma = \sqrt{\sum_{n}\frac{1}{n}(TC_i - TC_{io})^2} \tag{26.5}$$

where, TC (hkl) represents the texture coefficient for the plane with miller indices (hkl); I (hkl) and I$_o$ (hkl) are the intensities of the (hkl) plane of Gd$_2$O$_3$ nanopowder and bulk Gd$_2$O$_3$ as described in the JCPDS card-00-012-0797, respectively. The total number of peaks of diffraction are represented by n. The computed values of texture coefficient are tabulated in Table 26.1 along with the degree of preferred orientation. A greater than 1 value of texture coefficient, indicates high planar density toward that particular plane. From the Table 26.1, it is clear that plane 440 is more preferred over the other planes [19].

The lattice parameter was determined from Nelson- Riley plot (N-R) and Bradley-Jay (B-J) plot, shown in Fig. 26.3a, b, respectively. The measured values of the lattice parameter are stated in their respective figures. Rietveld refinement (using FULL-PROF) was also performed to view the structural changes of the sample. A pseudo voigt peak was selected for the refinement. Rietveld profile of the nanocrystalline powder is shown in Fig. 26.3c. From the Rietveld profile, it is clear that observed and calculated profiles are well matched. The results of the Rietveld analysis have been indexed in Table 26.2. As Dy^{3+} ion (0.912 Å) has smaller ionic radii as compared to Gd^{3+} ion (0.938 Å), lattice parameter and cell volume of the prepared sample are slightly reduced as compared to pure Gd$_2$O$_3$. The goodness of fit (GOF) parameter is

Table 26.1 Structural parameters of Gd$_2$O$_3$:Dy^{3+} nanopowder

2 Theta (Degree)	hkl plane	Intensity (au)	d-spacing (Å)	Texture coefficient (TC)	Degree of preferred orientation (σ)
28.36	222	4117.3	3.1363	0.9815	0.0169
32.94	400	1477.27	2.7099	1.0061	
47.30	440	1719.35	1.9154	1.0247	
56.18	622	1242.82	1.6319	0.9876	
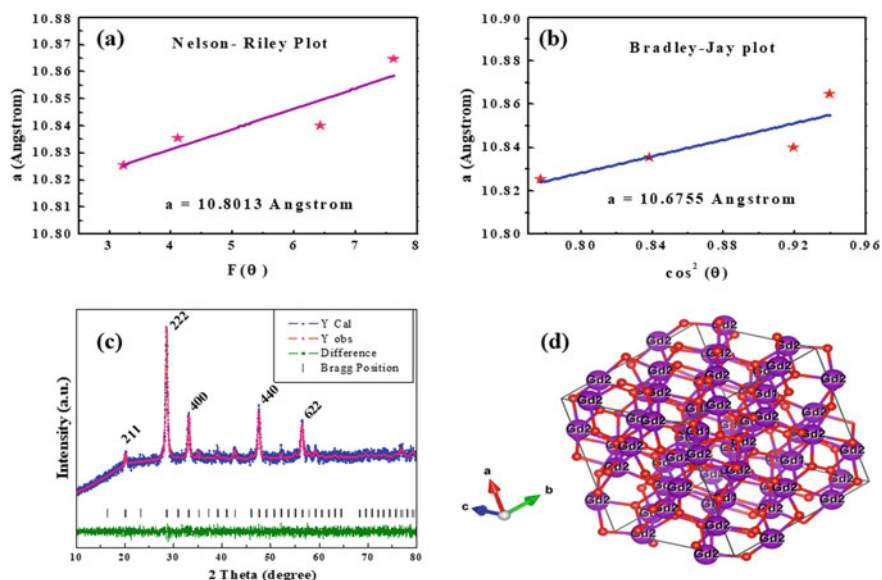
Fig. 26.3 **a** Nelson–Riley, **b** Bradley-Jay plot, **c** Rietveld profile of the Gd_2O_3:Dy^{3+} (4.0 mol%) annealed at 650 °C for 8 h and **d** Structure of pure cubic Gd_2O_3

Table 26.2 Refined structural parameters of Dy^{3+} doped Gd_2O_3 nanopowder

Sample	Atomic positions	Unit Cell parameters	Parameters
Gd_2O_3:Dy^{3+} (650 °C for 8 h)	Gd (−0.02976, 0.0, 0.25) (0.25, 0.25, 0.25) Dy (−0.02976, 0.0, 0.25) (0.25, 0.25, 0.25) O (0.39333, 0.15025 0.38201)	a = b = c = 10.8090 Å $\alpha = \beta = \gamma = 90°$ Density ρ = 7.891 g/cm^3 volume of unit cell = 1262.858 Å^3	R_p = 3.40 R_{wp} = 4.26 R_{exp} = 2.34 χ^2 = 3.31 GOF = 1.8

close to 1, which also indicates a good fit [20–22]. The latttice parameter computed by different methods are in good agreement. The structure of cubic Gd_2O_3 is depicted in Fig. 26.3d. In cubic Gd_2O_3 oxygen atom occupies the C1 symmetry site, while Gd atom occupies S6 and C2 symmetry site [23, 24].

26.3.2 FTIR Analysis

FTIR spectroscopy is a very useful tool to identify the various functional groups in the powdered sample. The FT-IR spectra of annealed sample of Gd_2O_3:Dy^{3+} (4.0 mol %) are presented in Fig. 26.4. In the FTIR spectra, vibrations of Gd-O are confirmed with the two sharp peaks at 567 cm^{-1} and 478 cm^{-1} [25, 26]. Also, a small broad band at 3432 cm^{-1} was observed in the prepared sample, which may be due to stretching
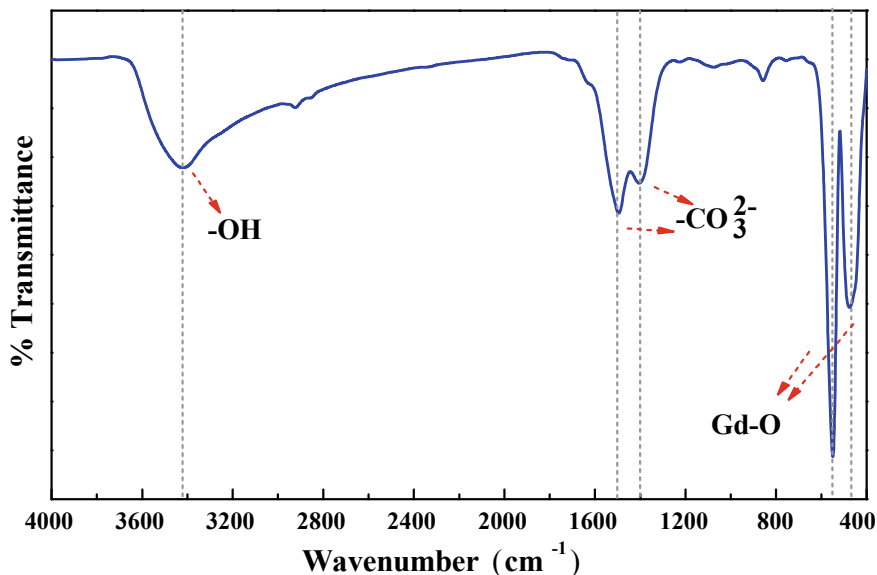
Fig. 26.4 FTIR analysis of Gd_2O_3:Dy^{3+} (4.0 mol %) annealed at 650°C for 8 h

vibrations of –OH group [27]. The two small peaks at 1503 cm^{-1} and 1402 cm^{-1} can be ascribed to CO_3^{2-} group which could be present due to organic compounds used in the synthesis process [28]. Presence of sharp Gd-O peaks in the prepared sample further confirms the cubic phase of Gd_2O_3.

26.3.3 HRTEM

HRTEM is an imaging tool for producing direct images of materials at nanoscale with high resolution up to 0.10 nm and large scale magnification. The dark field HRTEM image of the synthesized nanopowder in 100 nm resolution is displayed in Fig. 26.5a. The image shows nanocrystalline particles with size in 13 nm- 18 nm range. The particle size measured from XRD data are in close agreement with the HRTEM results. SAED pattern gives relevant information about the crystalline nature of the sample. A thin metallic strip is inserted to block the path of the electron beam. A small aperture in the metallic strip allows only a specific selected area of the sample to be examined by the electron beam. Thus only selected specific area contributes to the SAED pattern. Figure 26.5b illustrates selected area electron diffraction (SAED) profile of Dy^{3+} doped Gd_2O_3 sample. The bright rings present in the SAED pattern suggest polycrystalline nature of the synthesized nanopowder. Energy dispersive X-ray analysis (EDAX) gives information about the elemental composition of the sample. Figure 26.5c represents the EDAX spectra of the prepared sample. There
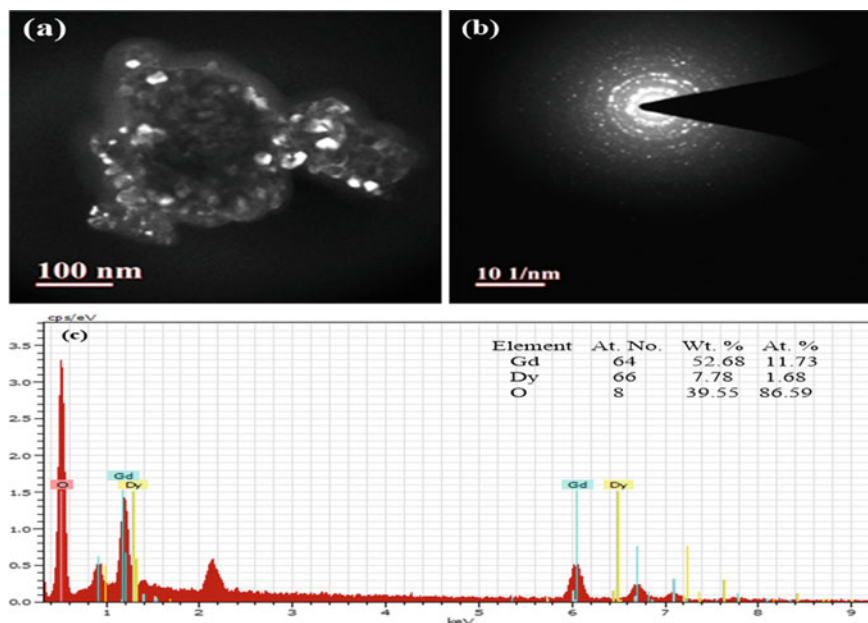
Fig. 26.5 **a** Dark field HRTEM image, **b** SAED pattern and **c** EDAX spectra of $Gd_2O_3:Dy^{3+}$ (4.0 mol%) annealed at 650°C for 8 h

is presence of Dy peaks along with Gd and O elements in the EDAX spectra of the synthesized sample, which confirm that dopant Dy ion is present in significant amount in the prepared sample.

26.4 Conclusion

The cubic $Gd_2O_3:Dy^{3+}$ nanopowders were successfully synthesized by the cost effective Pechini type sol–gel technique. XRD Analysis suggested cubic crystalline phase of the Gd_2O_3 in the prepared sample. Various structural parameters including interplanar spacing, crystallite size, texture coefficient, microstrain etc. are computed for the nanopowder. Particle size greatly affects the properties of nanomaterials. Therefore its precise measurement is important. Particle size computed by Debye–Scherrer equation, W–H plot are in well agreement with the HRTEM results. The Rietveld analysis was also performed to evaluate the structural parameters of the prepared nanopowder. Lattice parameter and cell volume of the prepared sample are slightly reduced due to smaller ionic radii of Dy^{3+} ions in comparison to Gd^{3+} ions. Lattice parameter as measured by Nelson–Riley plot and Rietveld analysis are in good agreement. Sharp Gd-O vibrations in FTIR spectra further confirmed the crystalline phase in synthesized nanopowders. Bright spotty rings present in the

SAED pattern also confirmed the crystalline nature of the powdered sample. EDAX spectra suggested that Dy ion is suitably doped in the cubic Gd$_2$O$_3$. These polycrystalline cubic nanopowders can be used potentially in various fields such as photonics, catalyst, display devices etc.

References

1. T. Selvalakshmi, S. Sellaiyan, A. Uedono, A. Chandra Bose, RSC Adv. **4**, 34257 (2014)
2. D. Li, W. Qin, P. Zhang, L. Wang, M. Lan, P. Shi, Opt. Mater. Express **7**, 329 (2017)
3. K. Xu, R. Ranjith, A. Laha, H. Parala, A.P. Milanov, R.A. Fischer, E. Bugiel, J. Feydt, S. Irsen, T. Toader, C. Bock, D. Rogalla, H.J. Osten, U. Kunze, A. Devi, Chem. Mater. **24**, 651 (2012)
4. H. Guo, X. Yang, T. Xiao, W. Zhang, L. Lou, J. Mugnier, Appl. Surf. Sci. **230**, 215 (2004)
5. Z. Liu, H. Deng, D. Chen, Ceram. Int. **45**, 13235 (2019)
6. F. Chen, M. Chen, C. Yang, J. Liu, N. Luo, G. Yang, D. Chen, L. Li, Phys. Chem. Chem. Phys. **17**, 1189 (2015)
7. A. Dougherty, C. Harper, F. Iskandar, I. Arif, G. Dougherty, J. Sci. Adv. Mater. Devices **3**, 419 (2018)
8. M. Mishra, P. Kuppusami, S. Ramya, V. Ganesan, A. Singh, R. Thirumurugesan, E. Mohandas, Surf. Coatings Technol. **262**, 56 (2015)
9. S. Maidul Haque, R. De, S. Tripathi, C. Mukherjee, A.K. Yadav, D. Bhattacharyya, S.N. Jha, N.K. Sahoo, Appl. Opt. **56**, 6114 (2017).
10. C. A. Lopez-Lazcano, G. G. Martínez-Falomir, and J. L. Almaral-Sánchez, Mater. Sci. Semicond. Process. **111**, 105005 (2020).
11. K.R. Khiangte, J.S. Rathore, S. Das, R.S. Pokharia, J. Schmidt, H.J. Osten, A. Laha, S. Mahapatra, J. Appl. Phys. **124**, (2018)
12. J. Wang, J. Hao, Y. Zhang, H. Wei, J. Mu, Physica E **80**, 185 (2016)
13. R.K. Tamrakar, D.P. Bisen, I.P. Sahu, N. Brahme, J. Radiat. Res. Appl. Sci. **7**, 417 (2014)
14. E.M. Goldys, K. Drozdowicz-Tomsia, S. Jinjun, D. Dosev, I.M. Kennedy, S. Yatsunenko, M. Godlewski, J. Am. Chem. Soc. **128**, 14498 (2006)
15. S. Som, S.K. Sharma, J. Phys. D. Appl. Phys. **45**, 415102 (2012)
16. O. Engler, V. Randle, *Introduction to Texture Analysis: Macrotexture, Microtexture, and Orientation Mapping*, 2nd edn (CRC Press, 2009)
17. U.F. Kocks, C.N. Tomé, H.R. Wenk, *Texture and Anisotropy: Preferred Orientations in Polycrystals and Their Effect on Materials Properties* (Cambridge University Press, 2000).
18. B. Choudhury, A. Choudhury, Mater. Chem. Phys. **131**, 666 (2012)
19. M. Kumar, A. Kumar, A.C. Abhyankar, A.C.S. Appl, Mater. Interfaces **7**, 3571 (2015)
20. S. Delice, M. Isik, N.M. Gasanly, Optik (Stuttg). **158**, 237 (2018)
21. T. R. Jeena, A. Moses Ezhil Raj, and M. Bououdina, Mater. Res. Express **4**, (2017).
22. H. Guo, N. Dong, M. Yin, W. Zhang, L. Lou, S. Xia, J. Phys. Chem. B **108**, 19205 (2004)
23. A. N. Kislov and A. F. Zatsepin, J. Phys. Condens. Matter **31**, (2019).
24. J. Yin, C. Li, D. Chen, J. Yang, H. Liu, W. Hu, Y. Shao, Phys. Chem. Chem. Phys. **19**, 5366 (2017)
25. S.A. Hindocha, L.J. McIntyre, A.M. Fogg, J. Solid State Chem. **182**, 1070 (2009)
26. J.G. Kang, B.K. Min, Y. Sohn, Ceram. Int. **41**, 1243 (2015)
27. J. Chandradass, M. Balasubramanian, D.S. Bae, H. Kim, Mater. Manuf. Process. **27**, 1290 (2012)
28. N. Dhananjaya, H. Nagabhushana, B.M. Nagabhushana, B. Rudraswamy, S.C. Sharma, D.V. Sunitha, C. Shivakumara, R.P.S. Chakradhar, Spectrochim. Acta Part A Mol. Biomol. Spectrosc. **96**, 532 (2012)

Chapter 27
Simple and Efficient Approach to Fabricate Fe₃O₄/CNT Based Electrode for Supercapacitor Application

Twinkle, Manpreet Kaur, Anjali, Rahul Sharma, Harjot Singh, Vikas Choudary, Sonal Rattan, Nihal, J. K. Gowsamy, Parveen Kumar, and Suresh Kumar

Abstract In this work ferric oxide (Fe_3O_4) based carbon nanocomposite were studied as anode material for supercapacitor applications. A comparison between the structural, optical and electrochemical properties of carbon nanotube (CNTs) and their composites with different ratio of Fe_3O_4 are reported. The synthesized nanohybrids are characterized via X-ray diffractometry (XRD), Energy dispersive X-ray spectrometry (EDS), UV–Vis, Fourier transformed infrared spectroscopy (FTIR) and scaning field electron microscopy (SEM). The cyclic voltammetry was employed to study electrochemical supercapacitor performance of the hybrid.

27.1 Introduction

In this modern era, the demand of energy storage devices is increasing at very high rate for various industrial and domestic applications. There are various types of storage device such as batteries, capacitors and supercapacitors. Among these researchers show huge interest in supercapacitors because of their short charging/discharging capacity, long life cycle and high energy density [1]. Supercapacitors have mainly two types, one is, electric double-layer capacitors (EDLCs), in which the energy is stored in the form of non-faradic process and charge separation occur between electrode and electrolyte. The second type is pseudocapacitor, which store energy in the form of reversible redox faradaic reaction at solid electrode surface [2]. In EDLC,

Twinkle (✉) · M. Kaur · Anjali · R. Sharma · H. Singh · Nihal · J. K. Gowsamy · S. Kumar
UIET, Panjab University, Chandigarh 160025, India

Twinkle · M. Kaur · Anjali
Department of Physics, Panjab University, Chandigarh 160014, India

V. Choudary · P. Kumar
Bio-NanoTechnology Lab (H-1), CSIR-CSIO, Chandigarh 160030, India

S. Rattan
Center of Nanoscience, Panjab University, Chandigarh 160025, India

carbon based electrodes materials are preferred. The energy density of supercapacitor depend upon the specific area of the working electrode material [3]. Graphene, carbon nanotubes (CNTs) and mesoporous carbons have been widely researched due to their unique mechanical, electrical and chemical properties [4–6]. In context to energy storage, carbon based nano materials have gained interest due to their high electrochemical double layer capacitor performance too [2, 7]. Among all these materials, CNTs played best performance as a supercapacitor material [8]. Since their emergence in 1991, carbon nanotubes (CNTs) have gained tremendous interest all over the globe [9, 10]. Owing to their excellent physiochemical properties, many reports have been published on the advanced applications of CNTs in numerous fields [11–13].

Similarly compared with other progress metal oxide materials, Fe_3O_4 is highly attractive on account of its high hypothetical explicit limit (347 F/g), huge potential window (1.2–0.25 V) and low toxicity [14]. However, the use of Fe_3O_4 experiences its low conductivity [15, 16]. Maximum capacity of carbon nanotubes for supercapacitor applications is still to be fully harnessed. In this study we made an effort to enhance the supercapacitor properties of CNTs on hybridization with magnetite nanoparticles.

27.2 Materials and Method

27.2.1 Materials

MWCNTs with a purity level of more than 95%, diameter $\sim$ 50 nm and 10–30 μm average length were purchased from SRL, India. Sulphuric acid (H_2SO_4), HNO_3, Ferric Chloride ($FeCl_3$) and Ferrous sulphate (Fe_2SO_4) were purchased from Merk, India.

27.2.2 Methods

The iron oxide (Fe_3O_4) were prepared by already reported method [17, 18]. Firstly, we prepared 0.5 M solution of $FeSO_4$ and $FeCl_3$ separately in deionised water. These two solutions having Fe^{2+} and Fe^{3+} ions were mixed in a ratio of 1:2 (v/v) under magnetic stirring condition. Afterwards, 3 M NaOH solution was added to the blend under consistent magnetic stirring conditions. The reaction resulted in the formation of black-brownish precipitates of Fe_3O_4 nanoparticles. Carboxyl functionalization MWCNTs or acid oxidation of carbon nanotubes was carried out via chemical acid oxidation method [13]. Firstly, MWCNTs was reacted with H_2SO_4/HNO_3 (3:1, v/v ratio) for 4 h. After the completion of this reaction, oxidized carbon nanotubes were dissolved in de-ionized water and vacuum filtered. Afterwards, 20% and 10% solution of Fe_3O_4 dissolved in NMP solution were added to functionalized CNTs [12].

27.2.3 Electrochemical Measurements

1 M potassium hydroxide solution was utilized as an electrolyte. Electrode was prepared by sonicating 8% of active material, 1% polyvinylidene fluoride and 1% of activated carbon black dissolved in N-Methyl-2-pyrrolidone and sonicated for few minutes to form thick slurry. This slurry mixture was then coated on graphite foil and dried over-night at 60 °C in hot air oven.

27.3 Results and Discussion

X-ray diffraction (XRD) is utilized to investigate the inter-planer spacing and analyze the structure of MWCNTs. The diffracto-grams have been recorded utilizing Rigaku Miniflex-600 X-beam diffractometer utilizing Cu Kα as trademark frequency 1.54 Å at working voltage 40 kV. XRD pattern has been recorded for CNTs and Fe$_3$O$_4$/CNT in 2θ range from 5° to 70°. An XRD spectrum of MWCNTs has been presented in Fig. 27.2. The strongest diffraction peak for all samples was found around 2θ = 25.85°, which was labelled as (002) Compared to typical graphite, 2θ = 26.5°, this peak shows a downwards shift in diffraction angle, which demonstrated the expansion in interlayer spacing [14]. Figure 27.2 shows the XRD pattern of the CNT/Fe$_3$O$_4$ nanocomposite. The spectrum showed a sharp peak at 37.68° with (200) plane. The peaks at 2θ = 26.52°, 33.9°, 51.40°, 54.63°, 61.51° and 65.49° corresponds to (110), (101), (211), (220), (130) and (301) of Fe$_3$O$_4$ crystal planes (Fig. 27.1).

FESEM was used to study the surface morphology of Fe$_3$O$_4$/CNT and CNT (Fig. 27.3). The structural attributes of the films were visible at magnification of 25,000 × and 5 kV accelerating voltage. The scanning electron micrographs clearly confirms the presence of Fe$_3$O$_4$ nanoparticles present on CNTs. Figure 27.4 shows the EDS spectra of Fe$_3$O$_4$/CNT, which demonstrated the presence of Fe, O and C atoms in the nanocomposite. The relative wt. percentage of the elements is shown in Table 27.1.

The UV–Vis spectroscopic results of pure Fe$_3$O$_4$ nanoparticles is shown in Fig. 27.5a, whereas the UV–Vis spectra of pure CNT and CNT/Fe$_3$O$_4$ (in 10% and 20% ratio) composite CNT is shown in Fig. 27.5b. The band gap (Eg) is calculated using the Tauc plot. The graph of $(\alpha h\upsilon)^2$ vs. hυ is shown in the inset Fig. 27.5. By extrapolating the graph to hυ-axis, the value of Eg is calculated. The Eg value of pure Fe$_3$O$_4$ and CNT came out to be 5.30 and 5.32 eV, respectively. The values of Eg in case of 10% and 20% Fe$_3$O$_4$ composites CNT is 5.36 and 5.29 eV, respectively. The band gap increased in case of 10% Fe$_3$O$_4$ doped CNT and decreased in case of 20% Fe$_3$O$_4$ doped CNT with respect to pure Fe$_3$O$_4$ and CNT. Thus there is a red shift in case of CNT/ Fe$_3$O$_4$ (10%) and blue shift in case of CNT/ Fe$_3$O$_4$ (20%).

The FTIR spectrum of pure Fe$_3$O$_4$ is shown in Fig. 27.6a. The peak at 588 cm^{-1} and 780 cm^{-1} corresponds to Fe–O vibrational bond [15]. The peak at 880 cm^{-1} is due to the C–Cl stretching which might be due to the presence of chloride ions of FeCl$_3$.
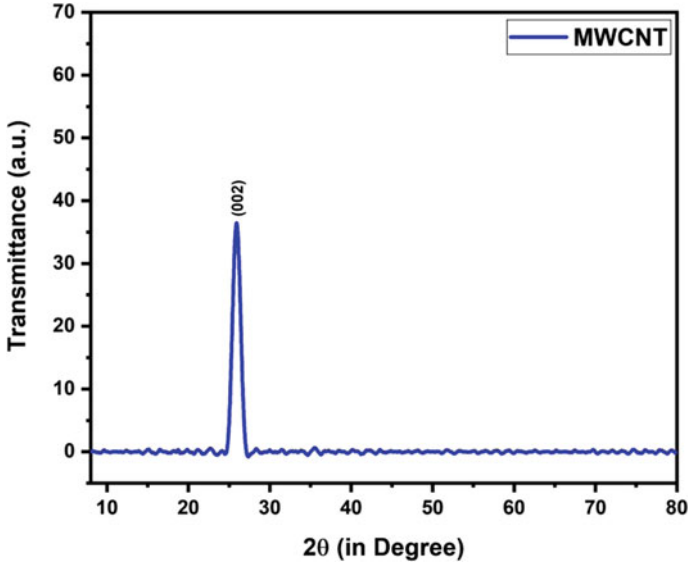
Fig. 27.1 Figure XRD pattern of Carbon nanotubes
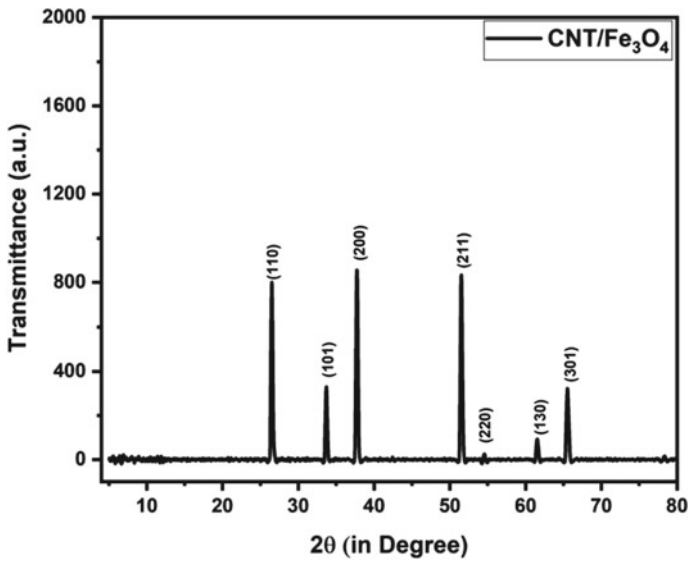
Fig. 27.2 XRD spectra of Fe_3O_4/CNT
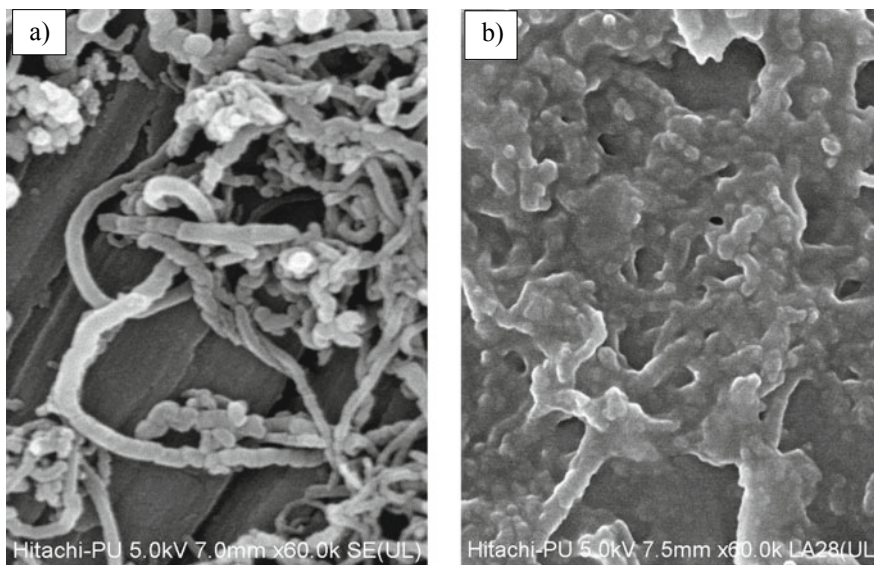
Fig. 27.3 FESEM images of **a** CNT and **b** composite material of Fe$_3$O$_4$/CNT
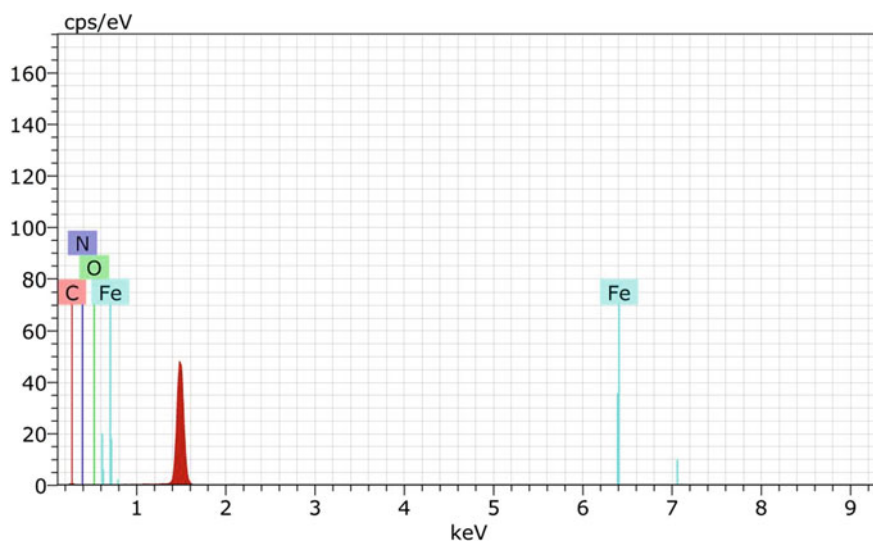
Fig. 27.4 EDS spectra of Fe$_3$O$_4$/CNT

Table 27.1 Relative wt. % of elemental analysis

Element	Series	Unn. C norm. C Atom. C Error (3 Sigma)			
		[wt.%]	[wt.%]	[at.%]	[wt.%]
Carbon	K-series	45.47	45.47	53.13	28.45
Oxygen	K-series	41.83	41.53	36.70	30.77
Iron	K-series	3.41	3.41	0.86	1.38
Nitrogen	K-series	9.30	9.30	9.32	16.27
Total		100.00	100.00	100.00	
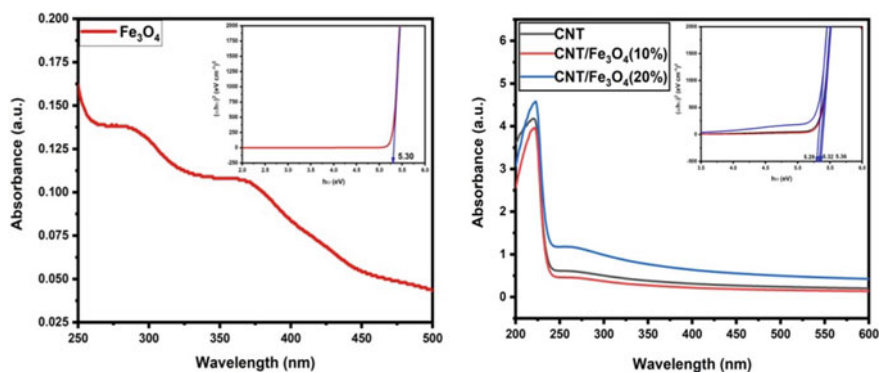
Fig. 27.5 UV–vis spectra of Fe_3O_4 and composite Fe_3O_4/CNT
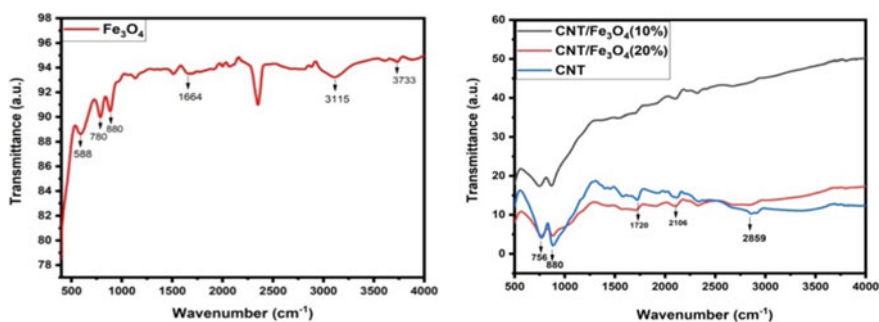
Fig. 27.6 FTIR spectra of Fe_3O_4 and composite Fe_3O_4/CNT

The peaks at 1664 cm^{-1}, 3115 cm^{-1} and 3733 cm^{-1} are due to the hydroxyl group [16]. The FTIR spectra of pure CNT and Fe_3O_4 (in 10 and 20% ratio) composition CNT is shown in Fig. 27.6b. It can be observed from the spectra that the intensity of transmittance get increased with doping of Fe_3O_4 in CNT. The increase is more in the case of 10% Fe_3O_4 doped CNT as compared to that of 20% Fe_3O_4 doped CNTs.

The peaks at 756 cm^{-1} ^{1} corresponds to M–O (metal –oxide) bending. Whereas, the peaks at 1720 cm^{-1} and 2106 cm^{-1} corresponds to C=O stretching.

Supercapacitor charateristics of the nanocomposites was studied using electrochemical workstation with Ag/AgCl as reference electrode, platinum as counter electrode and active material as working electrode. 1 M KOH was used as electrolyte. Figure 27.7 show cyclic voltammetry graph at different scan rate (current v/s potential). Specific capacitance may be evaluated using 27.1:

$$C = \frac{\int_{Va}^{Vb} I\,dv}{mv(Vb - Va)} \tag{27.1}$$

where I (A) discharge current, m (mg) is mass loaded on working electrode, C specific capacitance (F/g), v (mV/s) is scan rate, V$_a$ and V$_b$ are low and high voltages respectively [18]. Figure 27.7 shows cyclic voltammetry graph at different scan rate with different composition of Fe$_3$O$_4$. Specific capacitance was analysed in 0.7 V window voltage. Figure 27.7 (a) shows CV of CNT based electrode 7 (b) and (c) shows CV graph of 10% and 20% Fe$_3$O$_4$/CNT Fe$_3$O$_4$/CNT respectively. 10% Fe$_3$O$_4$
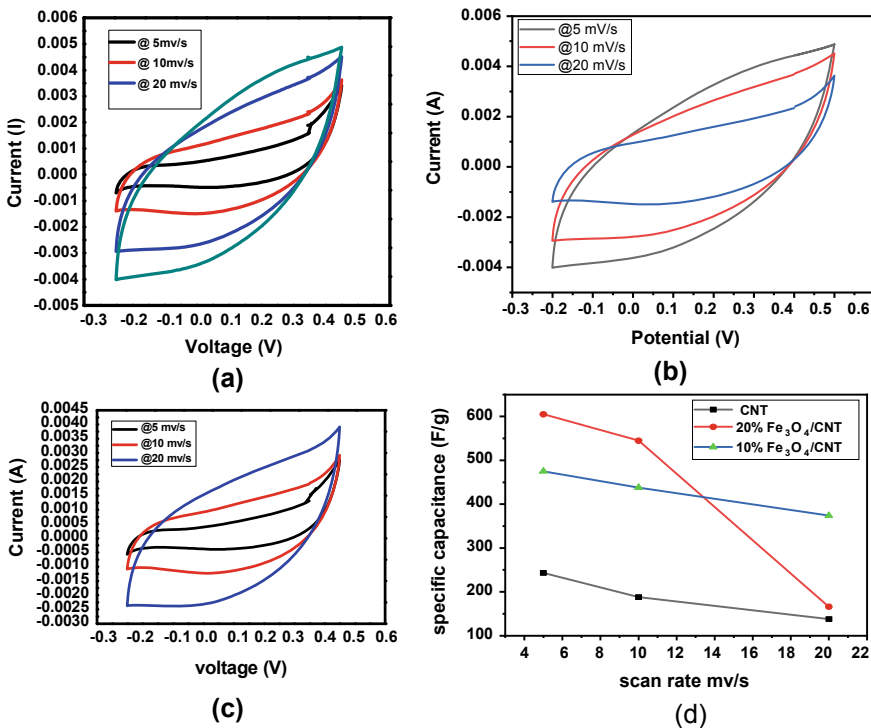
Fig. 27.7 Cyclic voltammetry graph at different scan rate **a** CNT **b** 20% Fe$_3$O$_4$/CNT **c** 10% Fe$_3$O$_4$/CNT **d** scan rate versus specific capacitance

Table 27.2 Specific capacitance at different scan rate of composite materials

Scan rate (mV/s)	CNT (f/g)	20%@Fe_3O_4/CNT (F/g)	10%@Fe_3O_4/CNT (F/g)
5	243	605	475
10	188	545	438
20	138	166	375

Table 27.3 Variation of Specific Capacitance w.r.t Cycle number

No of cycle	CNT (F/g)	20%@Fe_3O_4/CNT (F/g)
1st	243	605
10th	217	525

doping in CNT showed higher value of specific capacitance. The results are compiled in table 27.2. 20% Fe_3O_4/CNT composite showed higher specific capacitance value of 605 F/g, calculated by equation (i) at 5 mV/s. Specific capacitance for CNT and 20% Fe_3O_4/CNT at 1st and 10th cycle is shown in Table 27.3. The results were favourable for the use of Fe_3O_4/CNT for supercapacitor applications [18–21]. The specific capacitance variation, Vs, for cycle number for CNT and 20% Fe_3O_4/CNT is presented in Fig. 27.8. From Fig. 27.8, it is observed that specific capacitance of CNT decreases from 243 F/g to 200 F/g for 3rd cycle after that the specific capacitance increases linearly. The retention after 10th cycle at 5 mV/s for CNT is 89%. In
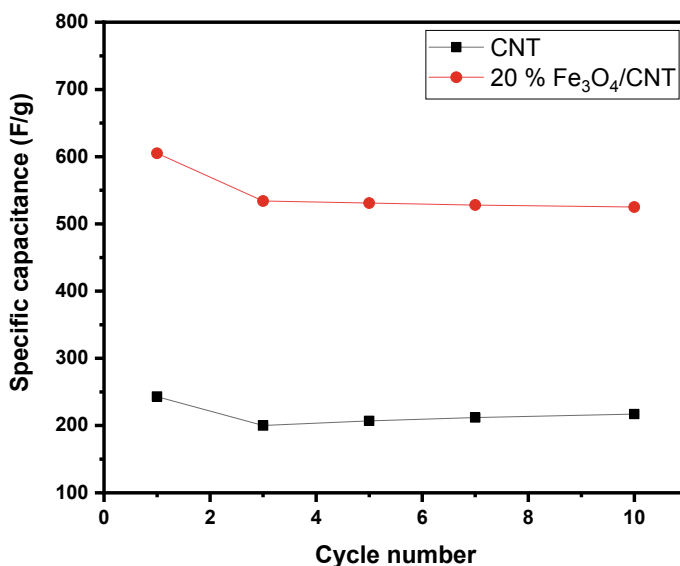
Fig. 27.8 Variation of Specific capacitance versus cycle number for CNT and 20% Fe_3O_4/CNT

case 20% Fe$_3$O$_4$/CNT retention was 86% after 10th cycle at 5 mV/s. The specific capacitance after doping of Fe$_3$O$_4$ in CNT is increases but retention is decreased.

27.4 Conclusion

In this report, we prepared carbon nanotubes Fe$_3$O$_4$ nanoparticles hybrid for improving supercapacitor applications. The nanocomposites was prepared via co-precipitation technique. UV–Vis and FTIR spectra confirmed the carbon nanotube functionalization and CNT/ Fe$_3$O$_4$ nanocomposite formation. FESEM confirmed that growth of Fe$_3$O$_4$ nanoparticles on carbon nanotubes. EDS analysis also ascertained the formation of nanohybrid. Fe$_3$O$_4$/CNT composite materials showed considerable improvement in supercapacitor performance.

References

1. B. Kim, H. Chung, W. Kim, "High-performance supercapacitors based on vertically aligned carbon nanotubes and nonaqueous electrolytes," Nanotechnology **23**(15), 155401 (Apr 2012)
2. L. Zhang, X.S. Zhao, Carbon-based materials as supercapacitor electrodes. Chem. Soc. Rev. **38**(9), 2520–2531 (2009)
3. M. Beidaghi, C. Wang, Micro-supercapacitors based on interdigital electrodes of reduced graphene oxide and carbon nanotube composites with ultrahigh power handling performance. Adv. Funct. Mater. **22**(21), 4501–4510 (2012)
4. S.A. Bansal, S. Singh, A. Srivastava, A.P. Singh, S. Kumar, "Covalent attachment of 2D graphene oxide (GO) sheets with poly allylamine (PAA) for enhanced mechanical performance: theoretical and experimental study." Polymer (Guildf). **213**, 123195 (Jan 2021)
5. E. Zalnezhad et al., Tribo-mechanical properties evaluation of HA/TiO2/CNT nanocomposite. Sci. Rep. **11**(1), 1867 (2021)
6. V. Khanna, V. Kumar, S. Anil Bansal, "Mechanical properties of aluminium-graphene/carbon nanotubes (CNTs) metal matrix composites: advancement, opportunities and perspective." Mater. Res. Bull. p 111224 (Jan 2021)
7. X. Li, B. Wei, Supercapacitors based on nanostructured carbon. Nano Energy **2**(2), 159–173 (2013)
8. C. Niu, E.K. Sichel, R. Hoch, D. Moy, H. Tennent, High power electrochemical capacitors based on carbon nanotube electrodes. Appl. Phys. Lett. **70**(11), 1480–1482 (1997)
9. D. Kumar, S.A. Bansal, N. Kumar, P. Jindal, "Two-step synthesis of polyurethane/multi-walled carbon nanotubes polymer composite to achieve high percentage particle reinforcement for mechanical applications." J. Compos. Mater., p. 002199832199945 (Mar 2021)
10. I.B. Dogru, M.B. Durukan, O. Turel, H.E. Unalan, Flexible supercapacitor electrodes with vertically aligned carbon nanotubes grown on aluminum foils. Prog. Nat. Sci. Mater. Int. **26**(3), 232–236 (2016)
11. R. Raccichini, A. Varzi, S. Passerini, B. Scrosati, The role of graphene for electrochemical energy storage. Nat. Mater. **14**(3), 271–279 (2015)

12. Twinkle, M. Kaur, J.K. Gowsamy, P. Kumar, S. Kumar, "Synthesis and characterization of CNT/PVDF paper for electronic and energy storage applications." Emergent Mater. **3**(2), 181–185 (Apr 2020)
13. Twinkle, K. Singh, S.A. Bansal, S. Kumar, "Graphene oxide (GO)/Copper doped Hematite (α-Fe2O3) nanoparticles for organic pollutants degradation applications at room temperature and neutral pH." Mater. Res. Express. **6**(11) (Sep 2019)
14. V.D. Nithya, N. Sabari Arul, "Progress and development of Fe_3O_4 electrodes for supercapacitors." J. Mater. Chem. A. Royal Soc. Chem. **4**(28), 10767–10778 (2016)
15. H. Wang, Z. Xu, H. Yi, H. Wei, Z. Guo, X. Wang, One-step preparation of single-crystalline Fe2O3 particles/graphene composite hydrogels as high performance anode materials for supercapacitors. Nano Energy **7**, 86–96 (2014)
16. I. Nedkov, T. Merodiiska, L. Slavov, R.E. Vandenberghe, Y. Kusano, J. Takada, Surface oxidation, size and shape of nano-sized magnetite obtained by co-precipitation. J. Magn. Magn. Mater. **300**(2), 358–367 (May 2006)
17. S.H. Chaki, T.J. Malek, M.D. Chaudhary, J.P. Tailor, M.P. Deshpande, "Magnetite Fe_3O_4 nanoparticles synthesis by wet chemical reduction and their characterization." Adv. Nat. Sci. Nanosci. Nanotechnol. **6**(3) (Sep 2015)
18. S. Kumar, I. Kaur, K. Dharamvir, L.M. Bharadwaj, Controlling the density and site of attachment of gold nanoparticles onto the surface of carbon nanotubes. J. Colloid Interface Sci. **369**(1), 23–27 (2012)
19. H. Bin Zhang, G.D. Lin, Z.H. Zhou, X. Dong, T. Chen, "Raman spectra of MWCNTs and MWCNT-based H2-adsorbing system." Carbon N. Y. **40**(13), 2429–2436 (2002)
20. M. Sharma, R. Sharma, Zn-ion batteries: ZnMn2O4as cathode material. Mater. Today: Proc. **26**, 3378–3385 (2019)
21. Y. Wu, Y. Wei, J. Wang, K. Jiang, S. Fan, Conformal Fe 4 sheath on aligned carbon nanotube scaffolds as high-performance anodes for lithium ion batteries. Nano Lett. **13**(2), 818–823 (2013)

Chapter 28
Effect of Gd^{3+} Substitution on Luminescence Characteristics of GdVO$_4$

Puja Kumari and Jairam Manam

Abstract The sequence of GdVO$_4$: Dy^{3+}, Eu^{3+} yellowish white emitting nanosized phosphors were successfully made by simple co-precipitation route. The effect of doping and co-doping on photoemission of GdVO$_4$ matrix were investigated by their structural and optical characterizations. The tetragonal phase formation having space group I41/amd (141) has been confirmed via X-ray diffraction (XRD) study. The morphology of the prepared polycrystalline material has been checked by field emission scanning electron microscope (FESEM) study and nanoparticles formation observed. All the transitions related to Dy^{3+} and Eu^{3+} ions were found present in emission profiles. The emission spectra leaded by $^4F_{9/2} \rightarrow {}^6H_{13/2}$ followed by $^4F_{9/2} \rightarrow {}^6H_{15/2}$ of Dy^{3+} ions and $^5D_0 \rightarrow {}^7F_2$ of Eu^{3+} ions. CIE plot showed the color co-ordinates lying in near white region and its application in display devices.

28.1 Introduction

Luminescent inorganic material substituted with lanthanide ions has versatile applications in conventional, novel, and emerging display devices. Rare earth orthovanadates can exhibit both down-conversion and up-conversion in microcrystalline and nanocrystalline forms under ultraviolet (UV) and infrared (IR) excitations depending upon the doped lanthanide ions and crystal environment provided by the host [1, 2]. The selection of dopants depends upon the applicability of the material. Rare earth doped materials have huge applications in various sectors including plant development, medical identification, optical thermometers, lighting, clean energy, displays and many more [3–5]. Energy saving and clean energy are the fields in which researchers are paying attentions worldwide. Invention of LEDs has solved the issues because of the low energy ingesting, extraordinary luminous proficiency, and environment pleasant features [6–8]. The available WLEDs are lacking with red

P. Kumari (✉)
Department of Physics, Darbhanga College of Engineering, Darbhanga 846005, India

J. Manam
Department of Applied Physics, IIT (ISM), Dhanbad 826004, India

factor because they are mostly as involves of a blue-InGaN chip and yellow emitting $Y_3A_{l5}O_{12}:Ce^{3+}$ powders which resulted into low color rendering index (CRI < 80) and high corelated color temperature (CCT > 7000 K) [9]. Addition of Eu^{3+} ions which is well known for its red emission band related to $^5D_0 \rightarrow {}^7F_2$ transition can overcome the deficiency in red component. Meanwhile, Dy^{3+} ions are capable to emit sharp blue and yellow lines because of their $^4F_{7/2} \rightarrow {}^6H_{15/2}$, $^6H_{13/2}$ transitions. The appearance of emission bands of any lanthanide ions depends strongly upon crystal symmetry provided by the host matrix and occupation of dopants to the available symmetry sites. Substitution of Gd^{3+} ion in $GdVO_4$ host with Eu^{3+} and Dy^{3+} can bring a change in spectroscopic performance of $GdVO_4$ due to the crystal field provided by the host and energy transfer between perturbed energy levels of substituents. With these expectations this study has been made. The study gives a brief detail about the optical characteristics of studied samples.

28.2 Experimental

A series of $GdVO_4$ doped with Eu^{3+} and Dy^{3+} have been prepared by low temperature co-precipitation method. The oxide precursors including dysporsium oxide (Dy_2O_3), europium oxide (Eu_2O_3), gadolinium oxide (Gd_2O_3), and high purity (99.99%) ammonium meta vanadate (NH_4VO_3) were taken in calculative amount. Oxide precursors were converted into nitrate by adding HNO_3 drop wise followed by heating at 60 °C. The solution of NH_4VO_3 was made in 0.5 M/L of NaOH through continuous stirring for adjusting the pH of the solution followed by the addition of nitrates with a continuous rate of 1 drop/3 s at 60 °C. The pH was maintained at 9 throughout the reaction. The white precipitate has been formed after 1 h of stirring. The formed precipitate was filtered and dried at 80 °C for 5 h. The prepared powder was further annealed at 500 °C for 2 h before different characterizations. The reaction for $GdVO_4$: x mol% Dy^{3+} can be written as:

$$NH_4VO_3 + (1-x)Gd(NO_3)_3 + xDy(NO_3) \rightarrow Dy_x : Gd_{1-x}VO_4 + NH_4^+ + 9NO_3^-$$
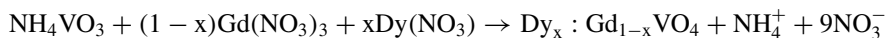
After the optimization of Dy^{3+} doping (up to 1 mol% doping) Eu^{3+} is added as co-dopant.

28.3 Result and Discussions

Figure 28.1a shows the XRD pattern of $GdVO_4$ with tetragonal phase structure with space group *I4₁/amd (141)* (JCPDS File No. 72–0277). All the diffraction lines well matched with the JCPDS File No. 72–0277 and no extra peaks other than $GdVO_4$ appeared. The crystallite size of the prepared samples is calculated via adopting Debye–Scherrer procedure reported elsewhere [10].
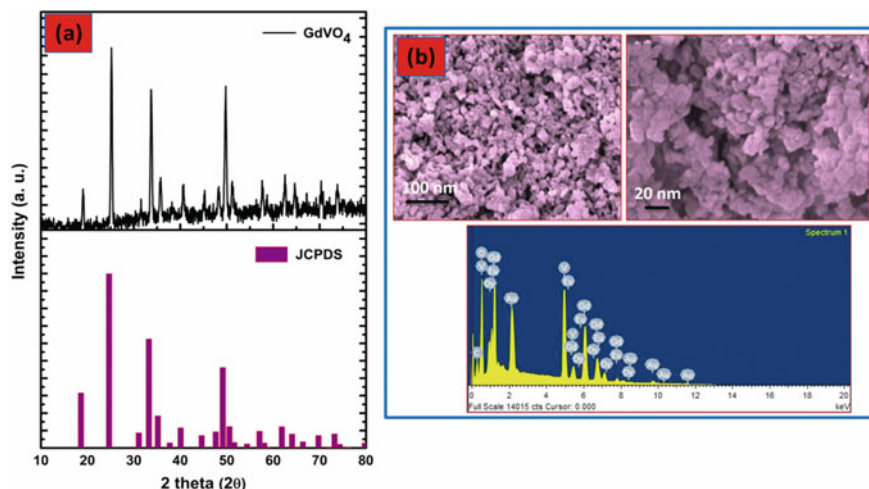
Fig. 28.1 **a** XRD profile of GdVO₄ along with JCPDS, **b** FESEM images of GdVO₄: Dy³⁺, Eu³⁺ and corresponding EDX

The calculated crystallite sizes from Debye-Scherer method are in the range of 20–60 nm. Figure 28.1b demonstrates the FESEM images and EDX spectra of prepared phosphor. Images have particle sizes in the range of 50–150 nm. Since the prepared material is polycrystalline in nature therefore, one particle contains many crystallites hence the particle size is comparatively larger than the crystallite size. To determine the elemental composition in the prepared sample electron dispersive X-ray spectroscopy has been performed. The lower part of Fig. 28.1b shows EDX spectrum which confirmed the presence of all elements: Gd, V, O, Dy and Eu. The presence of C element is due to the carbon paper used for the dispersion of the sample for recording the images.

The variation of Dy³⁺ concentration in GdVO₄ host resulted into the variation in intensity of emission peaks at 485 and 575 nm. The highest intensity is shown for the 1 mol% concentration of Dy³⁺ ion after that due to concentration quenching, there is a fall in intensity appeared. Figure 28.2 depicts the excitation and emission results of GdVO₄: 1 mol% Dy³⁺ and with co-dopant x mol% Eu³⁺ respectively. The excitation spectrum (Fig. 28.2a) monitored at 575 nm, consists of a prominent peak located at 310 nm associated with the V–O charge transfer band of VO_4^{3-} group. Along with this there are some peaks of relatively low intensities also appeared beyond 350 nm owing to the *ff* transitions of Dy³⁺ ions. The higher absorption coefficient of VO_4^{3-} (10^3–10^5 cm⁻¹) compared to Dy³⁺ ions led to domination of this band compare to inter band transfer of dysprosium ion. Figure 28.2b shows emission spectra of Dy³⁺ and Eu³⁺ co-doped GdVO₄ phosphor monitored at the excitation wavelength 310 nm. It consists of two main distinct peaks at 485 and 575 nm which are related to $^4F_{9/2} \rightarrow {}^6H_{15/2}$, $^6H_{13/2}$ transitions of Dy³⁺ ions, respectively, and $^5D_0 \rightarrow {}^7F_J$ (J = 1, 2, 4) transitions of Eu³⁺ ions [10, 11]. With the alteration of dopant
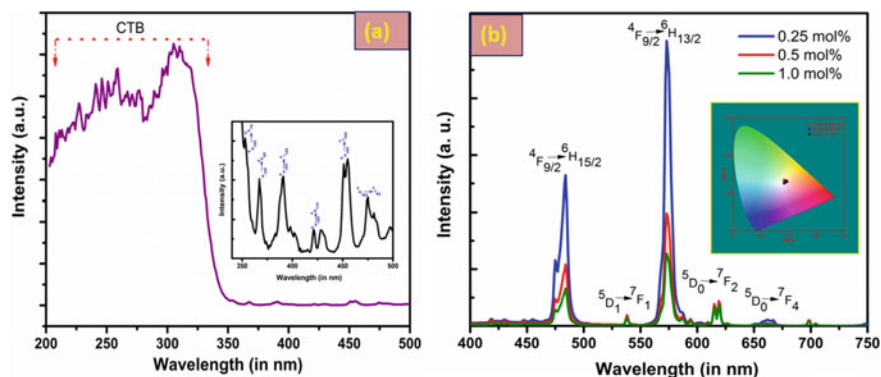
Fig. 28.2 **a** Photoluminescence excitation spectrum, **b** PL emission spectra of $GdVO_4$: 1% Dy^{3+}, x% Eu^{3+} **Inset**: CIE plot

concentration, the variation in intensities are only observed without any change in emissive nature. The peak at 575 nm which is more prominent compare to the peak appeared at 485 nm, reports about the occupation of non-centro symmetry site of Dy^{3+} ion in $GdVO_4$ host. The absence of emission band due to vanadate group depicts the complete transfer of excitation energy and it acts as opaque when orthovanadates are doped with lanthanide ions and excited by UV source. The blue emission band is attributed to $^4F_{9/2} \rightarrow {}^6H_{15/2}$ magnetic dipole transition and the intense yellow emission is designated to $^4F_{9/2} \rightarrow {}^6H_{13/2}$ electric dipole transition. The small emission peaks at 538, 620 and 662 nm are appeared, because of the $^5D_0 \rightarrow$ $^7F_1, {}^7F_2$ and $^7F_4$ transitions of Eu^{3+} ions. These transitions in electronic bands of Eu^{3+} ions are due to magnetic dipole, electric dipole and electric quadrupole transitions. The $^4F_{9/2} \rightarrow {}^6H_{13/2}$ electric dipole transition is hypersensitive to the surroundings, and therefore it is very effective for the crystallographic investigating [12]. Eventually, enhancing Eu^{3+} ions enhance the $^5D_0 \rightarrow {}^7F_2$ band intensity with the subsequent decrement of 575 nm band ($^4F_{9/2} \rightarrow {}^6H_{13/2}$: Dy^{3+}). The above happens owing to the potential energy transfer from Dy^{3+} to Eu^{3+} ions. This outcome demonstrates that an appropriate concentration of Eu^{3+} ions can overcome the inadequacy in red component in $GdVO_4$: 1 mol% Dy^{3+} phosphor. The colour coordinates calculated from Go CIE software were found to be (0.37, 0.40), (0.37, 0.38) and (0.39, 0.39) for varying concentration of Eu^{3+} ions which are very close to the chromaticity of standard white light.

28.4 Conclusion

Substitution of Gd^{3+} ion in $GdVO_4$ with Dy^{3+} and Eu^{3+} ions were studied by synthesizing the samples by a low temperature wet chemical route and luminescent characteristics were probed in detail. Phase formation and tetragonal crystal structure

has been confirmed by XRD study. FESEM images exhibited nano particle formation which were below 100 nm. All the transitions related to Dy^{3+} and Eu^{3+} were present in the emission spectra. The calculated color coordinates demonstrated its application in solid state lighting.

References

 1. Z. Xia, Z. Xu, M. Chen, Q. Liu, Dalton Trans. **45**, 11214 (2016)
 2. J. Grigorjevaite, A. Katelnikovas, ACS Appl. Mater. Interfaces **8**, 31772 (2016)
 3. Y. Jin, J. Zhang, S. Lü, H. Zhao, X. Zhang, X. Wang, J. Phys. Chem. C **112**, 5860 (2008)
 4. X. Shi, J.-G. Li, Q. Zhu, X. Li, X. Sun, J. Alloys Compd. **695**, 1984 (2017)
 5. S. Gai, C. Li, P. Yang, J. Lin, Chem. Rev. **114**, 2343 (2014)
 6. J. Chen, N. Zhang, C. Guo, F. Pan, X. Zhou, H. Suo, X. Zhao, E.M. Goldys, ACS Appl. Mater. Interfaces **8**, 20856 (2016)
 7. X. Huang, Nat. Photonics **8**, 748 (2014)
 8. G. Li, J. Lin, Chem. Soc. Rev. **43**, 7099 (2014)
 9. J. Zhong, D. Chen, Y. Yuan, L. Chen, H. Yu, Z. Ji, Chem. Eng. J. **309**, 795 (2017)
10. P. Kumari, P.K. Baitha, J. Manam, Indian J. Phys. **89**, 1297 (2015)
11. B.K. Grandhe, V.R. Bandi, K. Jang, S. Ramaprabhu, S.S. Yi, J.H. Jeong, Electron. Mater. Lett. **7**, 161 (2011)
12. A.S. de Oliveira et al., J. Lumin. **227**, 117500 (2020)

Chapter 29
Effect of Doping on Structural and Luminescence Behavior of Calcium Aluminates

Bindiya Goswami and Rachna Ahlawat

Abstract In the present study, pure and Sm^{3+} doped $CaAl_2O_4$ nanophosphor has been prepared via modified sol–gel Procedure. The X-ray powder diffraction method supported monoclinic phase of crystalline structures in the prepared samples. Average size of nanocrystalline was determined as 10 and 6 nm with the help of Debye–Scherrer formula that is in fair agreement with Williamson–Hall analysis. Full width at half maximum (FWHM) of the deflection peaks grown due to doping and as a result, decrease in nanocrystalline size noticed. SEM examined powdered morphology of the prepared sample with high crystallinity and further existence of the fundamental constituents (Ca, Al, O and Sm) has been confirmed by the EDAX analysis. Doping of Sm^{3+} ion influenced the UV–Vis absorption efficiently that causes a decrease in bandgap energy may be due to increased defects states. It is observed that Sm^{3+} has strongest emission at 568 nm which mainly took up symmetry centre lattice site. These spinel aluminates are significantly noticed in material science because of their utilization as long lived photo-luminescence particularly in visible region.

29.1 Introduction

Alkaline earth metal oxides fused with aluminium oxide are used as refractory oxides in the steel manufacturing industry and adhesive materials in cement productions houses since long times. Alkaline earth aluminates MAl_2O_4 (where M = Ca, Ba, Zn, Mg) doped with various kind of metal ions (M^+, M^{2+} and M^{3+}) and rare earth ions show intense luminescent properties [1, 2]. They are widely used in material science because of their fundamental characteristic i.e. luminescence in visible region. Calcium aluminates belong to the category of ternary metal oxides has versatile properties, like better chemical, melting, and mechanical persistence. In addition, they also have fantastic magnetic, electrical and optical properties that make them worthy for implement as photocatalyst, sensor, in displays, and bio-imaging etc. Recently, the group Calcium aluminates $CaAl_2O_4$ have gained attention as a modest,

B. Goswami (✉) · R. Ahlawat
Department of Physics, Material Science Laboratory, Chaudhary Devi Lal University, Sirsa, Haryana 125055, India

secure, anti-radiation and non-polluting host of the rare earth luminescence materials [3, 4]. In literature, studies on rare earth ion doped different hosts have acquire much notice of experimental physicists for the adjustment of the electronic configuration of dopant ions so that modification in emissions from UV–Visible-infrared region could be proceed as per requirement [5–7].

Now a day, white luminescence emitting diodes (WLEDS) have come out as an important category of lighting tools and manifest high prospective for renewal of standard igniting sources such as luminous and fluorescent lamps. When $CaAl_2O_4$ is doped by different rare earth elements such as Eu, Nd, Yb, Dy etc. it has luminescence in different region of electromagnetic spectra. The rare earth ions (RE^{3+}) are doped in $CaAl_2O_4$ host because this is excellent host due to its chemical, thermal and mechanical stability [8]. In the present study, Sm^{3+} has been adopted because it was rarely studied by the researcher in past specially its optical properties in green region. It is investigated that Sm^{3+} ion in the UV region has dense excitation lines and emits in 550–600 nm range (green to red region). Citrate sol–gel technique was used to prepare the samples because citrate sol–gel is a cost-effective method and the nanoparticles formed by this method are homogenously dispersed. This paper explained the synthesis procedure, structural details and optical behavior of undoped and Sm^{3+} doped $CaAl_2O_4$ nanophosphor.

29.2 Experimental

29.2.1 Synthesis Route: Citrate Sol–Gel

The familiar citrate sol–gel procedure was used to integrate the pure and 0.5 wt% of Sm^{3+} doped $CaAl_2O_4$ powder samples. The definite amount of $Ca(NO_3)_2.4H_2O$ (99%), $Al(NO_3)_3.9H_2O$ (97.8%) and the mild citric acid (CA) $C_8H_8O_7.H_2O$ (with 99% purity) is dissolved in double distilled water to prepare the host material $CaAl_2O_4$ with Ca: Al ratio as 1:2. By adding 1 ml ethylene glycol $[CH_2(OH).CH_2(OH)]$ in citric acid, we have obtained a mixed solution which is used as chelating agent. Further, Sm^{3+} doped $CaAl_2O_4$ was prepared by adding up 0.5 wt % of $Sm(NO_3)_2$ (99%) into the prepared host material in a separate vessel. For both sample, molar ratio of calcium (Ca) and citric acid (CA) was retained its value as 1:0.75. With the help of magnetic stirrer, we have constantly stirring the solution until the gel was not formed by keeping constant temperature (~70 °C). An air oven is used to dry the gel for 3 h at 240 °C. The powder was kept in a programmable furnace for 2 h and calcinated at 800 °C and further grounded using a pestle and mortar.

29.2.2 Measuring Tools

The prepared powdered sample was examined using different operating techniques. XPERT PRO X-ray diffractometer has been used to determine structure and phase development, samples with the typical radiation (Cu Kα) of wavelength 1.5406 Å in distinct 2º ranges which was functioned at 45 kV and 40 mA. FTIR spectrosocpy of the prepared samples in KBr pellets form were attained at ordinary room temperature with the help of Perkin Elmer spectrum 2 spectrophotometer. Surface morphology were analyzed by NOVA NANOSEM 450 attached with the EDS i. e. energy dispersion spectroscopy. Lambda 750 UV–Vis spectrophotometer was operated to observe absorption spectra and Perkin Elmer LS 55 fluorescence spectrometer was adopted to explore the emission spectra.

29.3 Results and Discussions

29.3.1 Phase Analysis Using XRD

For present study, XRD sequence of pure and Sm^{3+} doped $CaAl_2O_4$ powder samples are displayed in Fig. 29.1. In the current study, we have examined the crystalline behavior and phase identification of synthesized samples (treated at 800 °C temperature) and the single-phase aluminates with spinel structure are obtained. Figure 29.1 conveyed the results of x-ray powder diffraction pattern of pure $CaAl_2O_4$ synthesized by citrate sol–gel method. This diffractogram exhibits diffraction peaks in accordance with the JCPDS PDF #53-0191 which confirmed monoclinic phase with the space group *P21*/n [9]. Besides, the predominant peak at 2θ ~29.25°, few weak peaks are also spotted at 2θ ~29.25°, 35.98° and 39.48° in XRD profile of $CaAl_2O_4$. The crystallographic unit cell parameters are obtained 'a' = 0.8699 nm 'b' = 0.8212 nm, 'c' = 1.5207 nm, β = 90.1584° [10]. In Sm^{3+} doped $CaAl_2O_4$ sample, the crystalline structure is almost matched to $CaAl_2O_4$ crystalline phase, without generating any other types of impurity phase.

It is revealed from Fig. 29.1b that Sm^{3+} doped $CaAl_2O_4$ nanopowder has monoclinic crystalline phase with prominent diffraction peaks appeared at 2θ ~29.28°, 39.48°, 43.38° and 47.48°. These results demonstrated that the Sm^{3+} ion incorporated into the $CaAl_2O_4$ monoclinic structure to form a stable and efficient nanophosphors. In addition, the diffraction peaks are shifted to a higher diffraction angle as the sample was doped with Sm^{3+} ions due to change in its ionic radii as compared to Ca^{2+}. In the present study, the average nanocrystalline size (D) has been computed for both samples corresponding to the most dominating XRD peak. We have used (220) as the favored orientation for estimation of the size using Debye–Scherrer's formula as specified below:
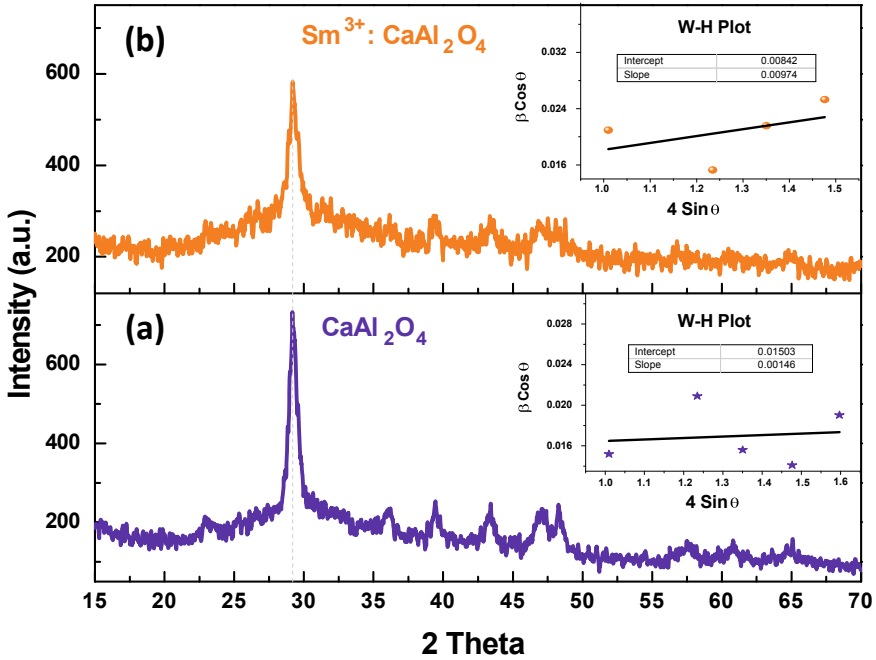
Fig. 29.1 XRD sequence of **a** pure and **b** Sm^{3+} doped $CaAl_2O_4$ powder samples

$$D_{D-S} = \frac{0.94\lambda(nm)}{\beta_{hkl}Cos\theta_{hkl}} \qquad (29.1)$$

In above formula, 'D' is the average size in the unit of nm, 'λ', is designated as wavelength of x-ray, β is generally known as full width at half maxima (FWHM) and the diffraction angle is given as 'θ'. One may notice that the FWHM of the peaks seems to increase in doped sample and the crystallinity of the sample becomes worse after doping. The nanocrystalline size is found 10 and 6 nm, respectively for pure and Sm^{3+} doped $CaAl_2O_4$ nanopowder. It is concluded that Sm doped $CaAl_2O_4$ has a stable crystalline phase which will enhances its optical performances so that the nanopowder could be used in advanced optoelectronic appliances.

Micro-Strain Analysis (ε): The present micro-strain and nanocrystalline size generates peak expansion in XRD profiles. With the help of W–H plot, we can able to understood the mechanism of strain effect for both the samples [10]. The computation of micro-strain is done using the following Williamson-Hall formula specified by (29.2):

$$\beta_{hkl}Cos(\theta)_{hkl} = \frac{0.94\lambda}{D} + 4\varepsilon Sin(\theta)_{hkl} \qquad (29.2)$$

In this equation, ε represents micro-strain and the symbol 'D' illustrated average nanocrystalline size that is estimated in normal direction to upper surface of corresponding sample. Inset of Fig. 29.1a and b illustrates the graph amid $4 \, \text{Sin}(\theta)_{hkl}$ and $\beta \text{Cos}(\theta)_{hkl}$. Micro-strain has been obtained as 1.46×10^{-3} and 9.74×10^{-3} respectively for undoped and Sm^{3+} doped samples approximated from slope of the fitted line. One may also get the crystalline size by the intercept of the straight line graph around 12 ± 0.5 nm and 8 ± 0.5 nm. The size from W–H analysis is obtained slightly higher than Debye-Schere formula probabiliy due to microstrain.

29.3.2 Vibrational Analysis by FTIR

The attachment environment of pure and Sm^{3+} doped $CaAl_2O_4$ powder samples has been explored by the famous Fourier transform infrared spectroscopy at room temperature. We have observed FTIR spectra of pure and Sm^{3+} doped $CaAl_2O_4$ within 400–4000 cm^{-1} spectral region which is depicted in Fig. 29.2. This spectra display many rigorous high-pitched, intermediate and wide IR absorption bands that are studied with extreme efforts. In both samples, the absorption band focusing at 3443 cm^{-1} can be allocated to anti-symmetric or symmetric modes of H-OH group
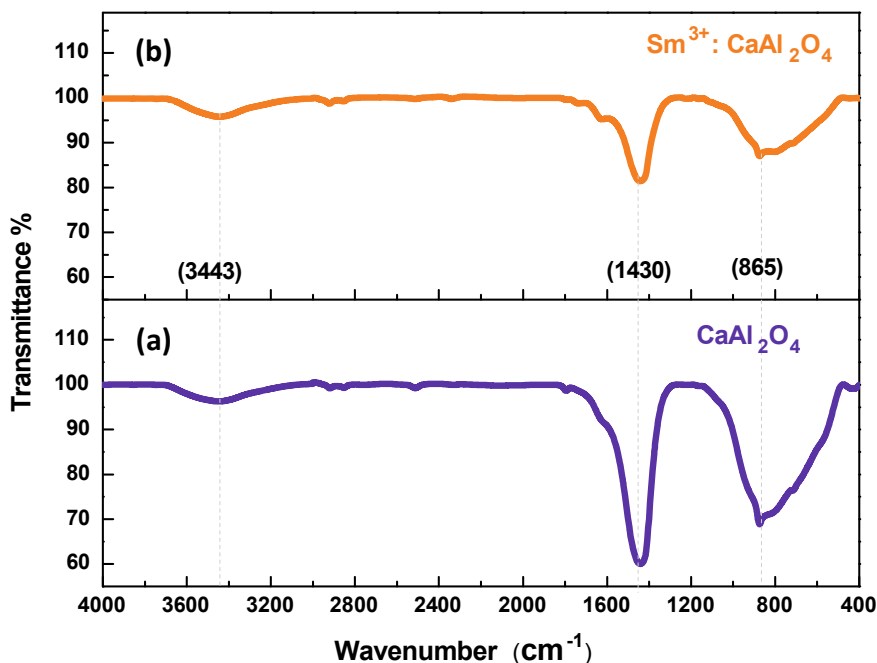
Fig. 29.2 FTIR spectrum of **a** pure and **b** Sm^{3+} doped $CaAl_2O_4$ powder samples

devoted to stretching vibrational. It is happening may be due to humidity in air injected into samples throughout KBr pellet formation [11].

A sharp band at 1430 cm^{-1} is related to amide group and at 865 cm^{-1}, vibration of nitrate groups exist [12]. In literature, the IR transmittance at 865 cm^{-1} is also correlated to stretching frequency of the group AlO_4. Also, bands below 800 cm^{-1} are initiated by metal-oxide (M–O) groups which are slightly shrinks in doped sample [13]. Therefore, when Ca^{2+} ions were replaced by Sm^{3+}, it is observed that FTIR spectra of $CaAl_2O_4$ lattice structure remains unchanged except only slight decrease in crystallinity which is also consistent with XRD result.

29.3.3 Surface Analysis by Scanning Electron Microscope (SEM)

Figure 29.3 displays the SEM images of pure and Sm^{3+} doped $CaAl_2O_4$ nanopowder having 0.5 mol % Sm^{3+} ion. The powder morphology is in the shape of small grainy structure which is interlinked with each other to form bigger particles. As a result, slight agglomeration was observed in both the samples which are attributed to the annealing conditions.
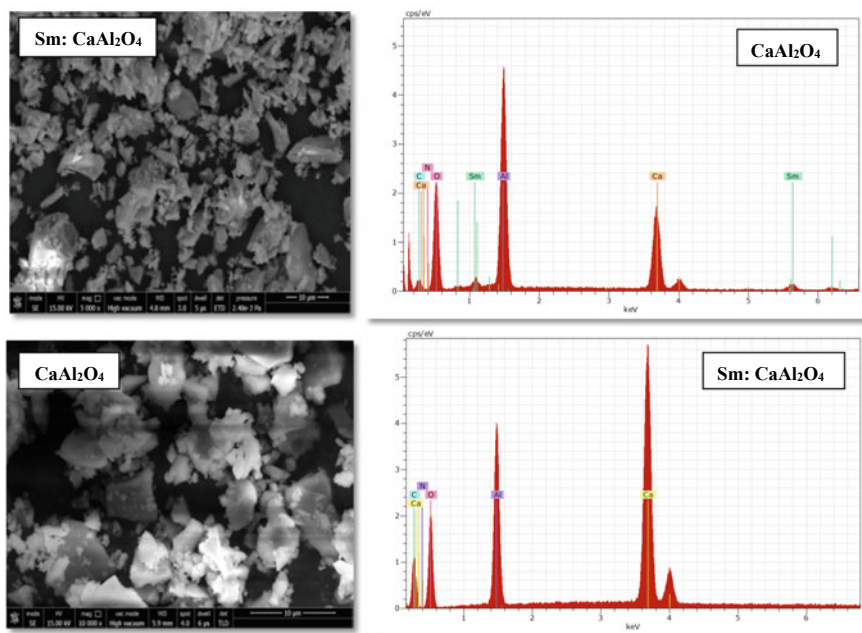
Fig. 29.3 SEM images and EDX of pure and Sm^{3+} doped $CaAl_2O_4$ powder samples

The elemental profile was certified by the EDX procedure. Figure 29.3 also illustrates the EDX spectra of the pure and Sm^{3+}: $CaAl_2O_4$. In pure or undoped sample, the presence of Ca, O, Al, C and N from cores and outside shell which are having weight percentage (wt%) as 49.10, 11.71, 25.33, 11.89 and 1.97%, respectively. In Sm^{3+} doped sample, wt% is obtained as 40.77, 18.57, 24.78, 7.07, 6.26 and 1.54%, respectively. One may notice that Sm peaks are small while peaks of Ca, O and Al elements are intensified due to the low concentration of samarium ions.

29.3.4 Optical Analysis by Uv–Vis Spectroscopy (UV–Vis.)

The UV–Visible absorption spectra were benefitted to tally morphologies and band gap energies of samples. Figure 29.4 depicts the UV–Vis absorption spectrum of pure and Sm^{3+} doped $CaAl_2O_4$ powder samples. Absorption spectra of processed samples having band at 215 and 260 nm, respectively are assigned to the transition from valence band to conduction band due to grouping of AlO_6 anion in $CaAl_2O_4$ [14].
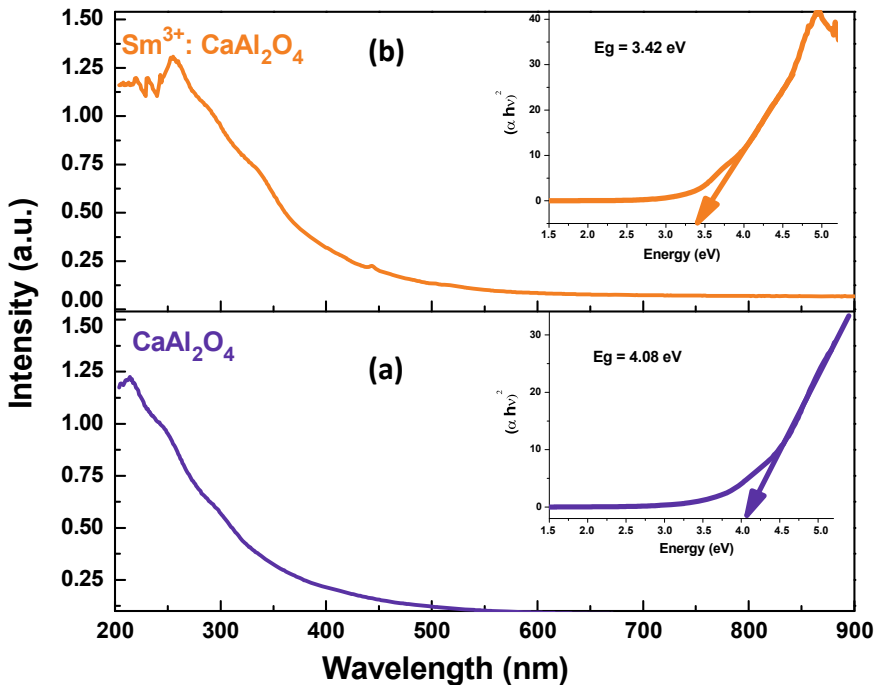
Fig. 29.4 Optical absorption spectra and Band gap energy of pure and Sm^{3+} doped $CaAl_2O_4$ nanopowder

In present study, absorbance is being used to find out the E_g i.e., band gap energy of the processed samples. We have operated the standard Tauc's relation: $(\alpha h\nu)^{1/n}$ = R $(h\nu - Eg)$, which correlate the instance energy of falling photon $(h\nu)$ with the coefficient of absorption (α). In above equation, 'R' indicates a constant and the exponent n = 1/2. As given in inset of Fig. we have plotted a graph between $(\alpha h\nu)^2$ verses $(h\nu)$ and direct band gap energy of the specimen can also be predicted by extrapolating straight region of graph on the $h\nu$ axis where $\alpha = 0$. Consequently, estimated bandgap energy for the pure and Sm^{3+} doped $CaAl_2O_4$ samples samples is estimated as ~4.08 eV and 3.42 eV, respectively.

29.3.5 Emission Spectra Analysis by Fluorescence Spectroscopy (FL):

Emission spectra of the prepared samples energized by 255 nm UV light demonstrate the identical profile with five peaks as exposed in Fig. 29.5. Luminescence characteristics also be elucidated in terms of electronic transition of the Sm^{3+} system. In the present study, different bands are obtained at 475, 568, 621, 657 and 754 nm. All the luminescence intensities were tested in the same condition. It is pertinent to mention here that luminescence intensity has been boosted with the Sm^{3+} doping due to increasing number of luminescence centers [15]. All the emission lines are originated from $^4G_{5/2}$ of Sm^{3+} to its lower multiplex of ^6H_j (j = 5/2, 7/2, 9/2, 11/2, 13/2) in which the $^4G_{5/2} \rightarrow {}^6H_{7/2}$ emission peak at 568 nm is the strongest one [16].
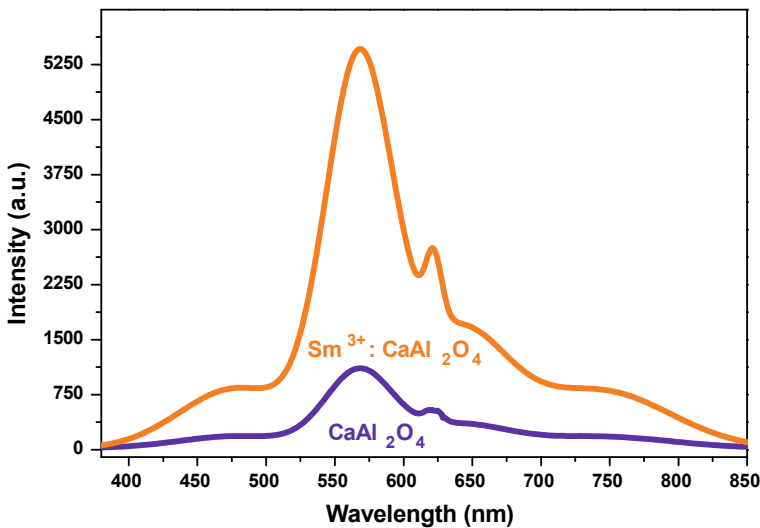
Fig. 29.5 Fluroscence spectra of pure and Sm^{3+} doped $CaAl_2O_4$ nanopowder

This strong peak is mainly arising from the magnetic dipole transition [17]. Therefore sm^{3+} doped $CaAl_2O_4$ will be good potential green phosphors. In Fig. 29.5, emission for $^4G_{5/2} \rightarrow {}^6H_{7/2}$ transition is stronger than $^4G_{5/2} \rightarrow {}^6H_{9/2}$ therefore mostly sm^{3+} took up the symmetry centre lattice site [18].

29.4   Conclusions

The pure and Sm^{3+} doped $CaAl_2O_4$ samples are synthesized by simple citrate sol–gel method. In doped sample, injection of Sm^{3+} in $CaAl_2O_4$ arrangement was obtained due to replacement effect on either at the Ca^{2+} or Al^{3+} sites. Crystallinity and particle morphology of the obtained sample is significantly affected by the Sm^{3+} doping. SEM evaluated that the topography or morphology of the obtained sample is not dependent on the amount/concentration of dopant Sm^{3+}. With doping of Sm^{3+} ion, the absorbance results displayed that bandgap energy is decreased. The red shift in absorption spectra predicted that the Sm^{3+} ions significantly modified the band gap of the host $CaAl_2O_4$. In PL, various emission peaks were attributed to $^4G_{5/2}$ of sm^{3+} to its lower multiplex of ^6H_j (j = 5/2, 7/2, 9/2, 11/2, 13/2) transition at 475, 568, 621, 657 and 754 nm, respectively.

References

1. M.H. Lee, W.S. Jung, Ceram. Int. **42**, 3113 (2016)
2. C. Li, J. Lin, J. Mater. Chem. **20**, 6831 (2010)
3. X. Zhang, W. Zhang, Y. Li, C. Li, Dyes Pigments **140**, 150 (2017)
4. A. Escudero, A.I. Becerro, C. Carrillo-Carrion, N.O. Nunez, M.V. Zyuzin, M. Laguna, Nanophotonics **6**, 881 (2017)
5. A. Escudero, C.C. Carrión, M.V. Zyuzin, W.J. Parak, Top. Curr. Chem. **374**, 48 (2016)
6. N. Kiran, A.P. Baker, G. Wang, J. Mol. Struct. **1129**, 211 (2017)
7. A.K. Vishwakarma, M. Jayasimhadri, J. Lumin. **176**, 112 (2016)
8. Q. Li, Y. Yuan, T. Wei, Y. Li, Z. Chen, X. Jin, Y. Qin, W. Sun, Sol. Energy Mater. **130**, 426 (2014)
9. B. Mothudi, O. Ntwaeaborwa, J. Botha, H. Swart, Physica B **404**, 4440 (2009)
10. X. Zhang, H. Dong, Z. Mei, Optoelectron. Adv Mater.-Rapid Comm. **4**, 28 (2010)
11. P. Li, Q. Peng, Y. Li, et al., Adv. Mater. **21**, 1945 (2009)
12. S. Mahamuda, K. Swapna, M. Venkateswarlu, A.S. Rao, S.L. Shakya, G.V. Prakash, J. Lumin. **154**, 410 (2014)
13. Y. Zhiping, D. Hongyan, L. Pengfei, H. Chuncai, L. Xiaoshuang, W. Can, L. Fachun, J. Rare Earths **32**, 404 (2014)
14. R. Yu, H.M. Noh, B.K. Moon, B.C. Choi, J.H. Jeong, H.S. Lee, K. Jang, S.S. Yi, J. Lumin. **145**, 717 (2014)

15. K. Swapna, S. Mahamuda, A. Srinivasa Rao, S. Shakya, T. Sasikala, D. Haranath, G. Vijaya Prakash, Spectrochim. Acta Part A Mol. Biomol. Spectrosc. **125**, 53 (2014)
16. R. Yu, H.M. Noh, B.K. Moon, B.C. Choi, J.H. Jeong, H.S. Lee, K. Jang, S.S. Yi, J. Lumin. **152**, 133 (2014)
17. Z. Wang, P. Li, Z. Yang, Q. Guo, J. Lumin. **132**, 1944 (2012)
18. A.K. Vishwakarma, M. Jayasimhadri, J. Lumin. **117**, 176112 (2016)

Chapter 30
Novelty of Light Scattering Technique over Other Conventional Techniques for Characterization of Bio-Particles

Sanchita Roy, Loknath Biswas, and Sanjiv Chettri

Abstract Light scattering is an important tool which can be employed to investigate various particulate matters of different types and sizes. Light scattering techniques has found its importance in diverse fields like atmospheric monitoring, meteorology, LIDAR, nano-science issues etc. The scattered light is always encoded with information about the morphology of the particles. Usually, bio-chemical methods are employed for characterizing particle of biological origin; however, light scattering technique is a non-invasive and non-destructive tool that can always be used as an efficient tool for such investigations. The results obtained from light scattering experiments can be further compared with theoretical results obtained by using important light scattering theories like the Mie-theory, T-matrix theory and DDA etc. for comparative analyses. The data analyses give better interpretation of the results. In this paper, we present the novelty of using the scattering technique for characterizing *Escherichia coli* or *E. coli.*

30.1 Introduction: Light Scattering Theory

We know that light is able to travel through any medium and interacts according to the properties of the matter and the medium through which it passes. Light is scattered by almost all objects in this Universe. All matter is composed of discrete electric charges, that is, electrons and protons. The scattering of light may be thought of as the redirection of light that take place when an electromagnetic (EM) wave is incident on a particle, it interact with the particle and the electrons orbiting from the surface of the particles. The electrons are disturbed periodically with the frequency (v_0). This frequency is same as the electric field of the incident wave. Fractional energy of these excited charges is reradiated in all direction as electromagnetic (EM) energy and result in secondary radiation which is the scattered light. Light scattering and its applications is very much important to examine the interaction between light and matter.

S. Roy (✉) · L. Biswas · S. Chettri
Department of Physics, School of Applied Sciences, University of Science and Technology
Meghalaya, Ri Bhoi, Meghalaya 793101, India

When the light beam is incident on a material, the amount and angular distribution of the light scattered by the particles depends upon different parameters such as the size, shape, refractive index, type of particle, composition etc. [1, 2]. Light scattering technique is the technique of extracting information about objects by observing and analysing the light which is scattered by the object. The polarization state of the scattered light is related to that of incident light by a matrix, known as Mueller matrix. The matrix consists of 16 elements in the matrix and each of the elements of the matrix has its significant meaning. The scattering angle dependence on 16 elements of the scattering matrices can be measured by light scattering technique. With the help of the light scattering technique, we can obtain the vital information about the size of the scatterers, its shape, refractive index, optical parameters of the scattering particles like absorption, permittivity, isotropy as well as information about its surfaces like smoothness, roughness, porosity etc. The scattering law does not depend on the size of the particles but it depends on the ratio a/λ, where 'a' is the size of the particle and 'λ' is the wavelength of the incident light. The size parameter in the study of light scattering can be defined as $x = ka = 2\pi a/\lambda$, where 'k' is the wave vector. The ratio of the index of the scatterer to the index of the surrounding media is called relative refraction index. Among other light scattering theories, the Mie theory provides an exact analytical solution of Maxwell equation for spherical particles and T matrix approach can be adopted for non-spherical particles of different types [1–4]. The scattered light intensity that corresponded to the S_{11} and S_{12} element of the scattering matrix was detected using light scattering theories. By quantifying the S_{11} and S_{12} element of Mueller matrix, we could measure the volume scattering function $\beta(\theta)$ and the degree of linear polarization $P(\theta)$ [3, 4].

All the numerical techniques for computing electromagnetic scattering by non-spherical particles mostly fall into two broad categories, Differential and Integral. Differential methods compute the scattered field by solving the vector wave equation in the frequency or time domain, whereas, Integral equation methods are based on volume or surface integral corresponding to Maxwell's equation [2, 3, 5, 6]. Some of approaches are used for such non-spherical particles are Separation of Variables Methods, Finite Difference Time Domain Method, Finite Element Method, Method of Moments or Volume Integral Equation Method, T-Matrix Method etc. [2, 5, 7].

30.1.1 Importance of Light Scattering in Biological Sciences

This technique finds great importance in various scientific fields like atmospheric science, astrophysics, Nanoscience and nanotechnology, oceanography, colloidal chemistry, light detection and ranging (LIDAR) systems, environmental monitoring, visibility and haze, climate modelling and most importantly on bioscience and biomedical sciences etc. Areas of interest mostly hold for colloids, aerosol, hydrosols, bio-particles, macromolecules, astrophysical particles etc. [3, 8–12]

Biological cells can be considered as dielectric objects with a given refractive index distribution [13]. Light scattering tool, being non-destructive and non-invasive,

provide us with an efficient way for studying cell morphology as well as the nature of scattering and its sources [8, 13]. The high sensitivity of light scattering signals to even weak changes in tissue morphology, as well as the unique tool to visualize unstained tissue in vivo, has found its importance in optical scatter based bio-sensing and imaging process [14, 15]. The importance of laser light scattering for characterizing biological particles was realised long time back [16] and still continues to find its importance.

In order to infer about different properties of bio-particles, like bacteria, usually bio-chemical methods are used which are invasive ones. The analysis of this information may be adopted for non-invasive diagnostics for a better insight, and development of new and novel optical methods [17]. The application of optical methods in basic biomedical research as well as clinical applications is emerging as one of the new technological paradigms. This bio-photonics union is suitable for the recent significant advancement of photonics and biotechnologies worldwide. Erstwhile, it addresses various issues related to health, environment and other challenges faced by human society [17]. Again, light scattered from bio-particles, particularly polarised light, carries information about the optical, geometrical, and even cryptic properties of such bio-particles [5, 7, 8, 10, 12]. It is noteworthy to mention that by using novel light scattering codes, light scattering simulations serves as an efficient tool for studying cell morphology of bioparticles and also the nature of the scattering.

It is important to mention that the studies of such organic molecules may also be utilized in interpretation of data obtained from Astrophysical studies on the presence of organic molecules in stellar and interstellar medium. Astrobiologists have been working to find a clue to relate life with planets other than earth in extra-terrestrial region and interstellar region. A trace of bacterial presence was also reported in some leading journals [17–19]. Thus, we may get indication of finding life on other spaces, based on light scattering studies. This gives possibilities of presence of particles of biological origin in space other than terrestrial region.

As reported by many, the practices of scattering and absorbing electromagnetic radiation finds its importance in various fields of science and technology that aim to study the structure and properties of inhomogeneous media. The theoretical models, experimental measurement procedures, and data interpretation methods which are based on the phenomenon of light scattering have been highly explored and developed by experts in various disciplines [20–25]

In view of the great diversity and complexity in structure of biological particles, the most complex step of a study and investigation is regarding the development of adequate optical models of scattering and absorption of light. In this paper, we present the importance of using the non-destructive light scattering technique for characterizations used in biological and biomedical sciences. We also present a modelling of *E. coli* using light scattering.

30.2 Experimental Methods and Analyses for Light Scattering Interpretation

Escherichia coli, also known as *E. coli* is a gram-negative, facultative anaerobic, rod shaped coliform bacterium of the genus *Escherichia* that is commonly found in the lower intestine of warm-blooded organisms [26]. The bacterium can be grown and cultured easily and inexpensively in a laboratory setting [26]. It has been expansively investigated for over 60 years. Most strains of *E. coli* are not harmful to their hosts; however, more and more newly discover strains are contributing into existing population through mutations and evolution. Some can cause severe disease also [26–30]. *E. coli* are a short rod-like bacterium length and diameter measurements varied from approximately 50–250 nm and from 5 to 25 nm respectively. With monodisperse sample the theoretical analysis were carried out for *E. coli*. Because of this, it has been possible to make meaningful interpretation of the scattered light based on single scattering [12, 29, 30].

30.2.1 Materials and Methods of Culture of E. coli and Analysis

The *E. coli* bio-particle having strain ATCC-9637 sample was prepared in the laboratory of Department of Biotechnology, University of Science and Technology Meghalaya. We diluted the samples with Glutaraldehyde to keep the morphology of cells intact. We obtained minimum cells concentration so that we get the single scattering. From cultured *E. coli* we performed the UV–Visible spectroscopic analysis, EDX analysis and SEM analysis. These analyses were performed as a requirement for generating the theoretical plot using the popular light scattering theories, that is, T-matrix approach and Mie theory.

UV–vis spectroscopy was performed in order to obtain the non-resonant absorption which was found at an angular range beyond 540 nm. Non- resonant absorption was more pronounced at around 632.8 nm. So this important parameter of wave length of the laser light was used in theoretical program to model the scattering profiles. We also carried the EDX of *E. coli* sample to know the elemental composition of the bio-particles (Fig. 30.1). We found presence of three elements namely; Oxygen, Sodium and Chlorine are found to be present in the *E. coli* sample, which are usually present in organic molecules or samples of biological origin. From Fig. 30.1, we can see that Oxygen is present in large amount in the *E. coli* sample as compared to other elements in the sample. This ensured the purity of the samples chosen for our investigations.

In biological science, Scanning Electron Microscopy (SEM) can be used for finding the morphology the particles. Figure 30.2a shows the SEM image of the sample which was prepared and discussed in Sect. 30.2.1. Figure 30.2(b) and (c) are the SEM image of *E. coli* which we are collected from internet sources [31–33] for
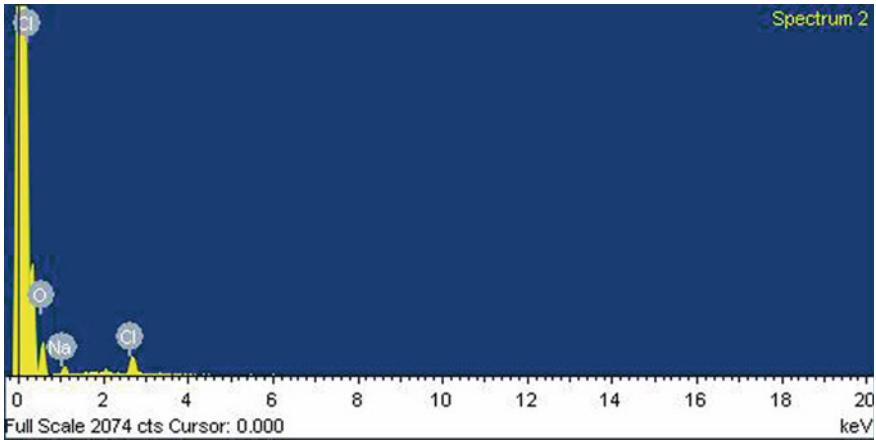
Fig. 30.1 EDX spectrum of *Escherichia Coli*

Fig. 30.2 a SEM image of *E. coli* at magnification of X3500 for sample 1; **b** SEM image of *E. coli* at magnification of X 18,000 for sample 2; **c** SEM image of *E. coli* at magnification of X 15,000 for sample 3

a comparative study. We collected SEM images from internet sources because we wanted to carry out the theoretical light scattering investigation on similar species of bio-particles. This step was followed because of the interest to carry out a qualitative study on *E. coli* bio-particle by modelling of light scattering.

30.3 Investigation and Analysis of *E. coli*

The *E. coli* bio-particle sample was used to generate the size and size distribution and overall morphology of the bio-particles. The SEM image portrays spheroid shape of *E. coli* particles, shown in Fig. 30.2a, b & c respectively. It must be noted that the images of sample 2 & 3 respectively were collected from internet sources and shown in Fig. 30.2b and c [31, 32]. The theoretical approach for determining degree of the linear polarization $P(\theta)$ and volume scattering function $\beta(\theta)$ was carried out using

Table 30.1 Parameters used for the data analysis of *E. coli* (Sample 1, 2 and 3)

Parameters	Value (Sample 1)	Value (Sample 2)	Value (Sample 3)
Particle size distribution	Normal (Gaussian)	Normal (Gaussian)	Normal (Gaussian)
Modal radius (*E. coli*) in μm	0.5	0.6	0.5
Minimum particle radius (μm)	0.37	0.4	0.4
Maximum particle radius (μm)	0.75	0.8	0.8
Shape of the particle	Spheroid	Elongated Spheroid	Elongated Spheroid
Particle refractive index of *E–coli* at 632.8 nm	1.38 + i000	1.38 + i000	1.38 + i000
Aspect ratio (d/l)	0.42	0.44	0.27

java based software **TUScat1.3_2** and **Miescat.c** [34, 35] respectively. It is based on T-matrix approach and Mie theory respectively. The parameters that were included are listed in the Table 30.1. The size distribution graphs of each samples of *E. coli* is presented in Fig. 30.3a, b and c respectively.

30.3.1   Escherichia Coli *Sample 1*

The particles were found to be having modal radius of 0.50 μm [22]. From the same SEM image, we see that the sample of *E. coli* has Gaussian distribution. It is also observed from Fig. 30.2b and c, that the SEM images exhibits an elongated spheroid shapes having a size distribution. The theoretical plots for determining the degree of linear polarization $P(\theta)$ and volume scattering function $\beta(\theta)$ was carried out following the same process as discussed in Sect. 30.3. The parameters used are tabulated in Table 30.1.

30.3.2   Escherichia Coli *Sample 2*

The *E. coli* bio-particle (sample 2) was used to generate the size and size distribution and overall morphology of the bio-particles. In this case, the SEM image portrays elongated spheroid shape of *E. coli* particles, shown in Fig. 30.2b. The particles were found to be having modal radius of 0.60 μm [22]. From SEM image we see that the sample of *E. coli* has Gaussian distribution. The theoretical plots for determining the degree of linear polarization $P(\theta)$ and volume scattering function $\beta(\theta)$ was carried out as discussed in Sect. 30.4. The parameters used are tabulated in Table 30.1.
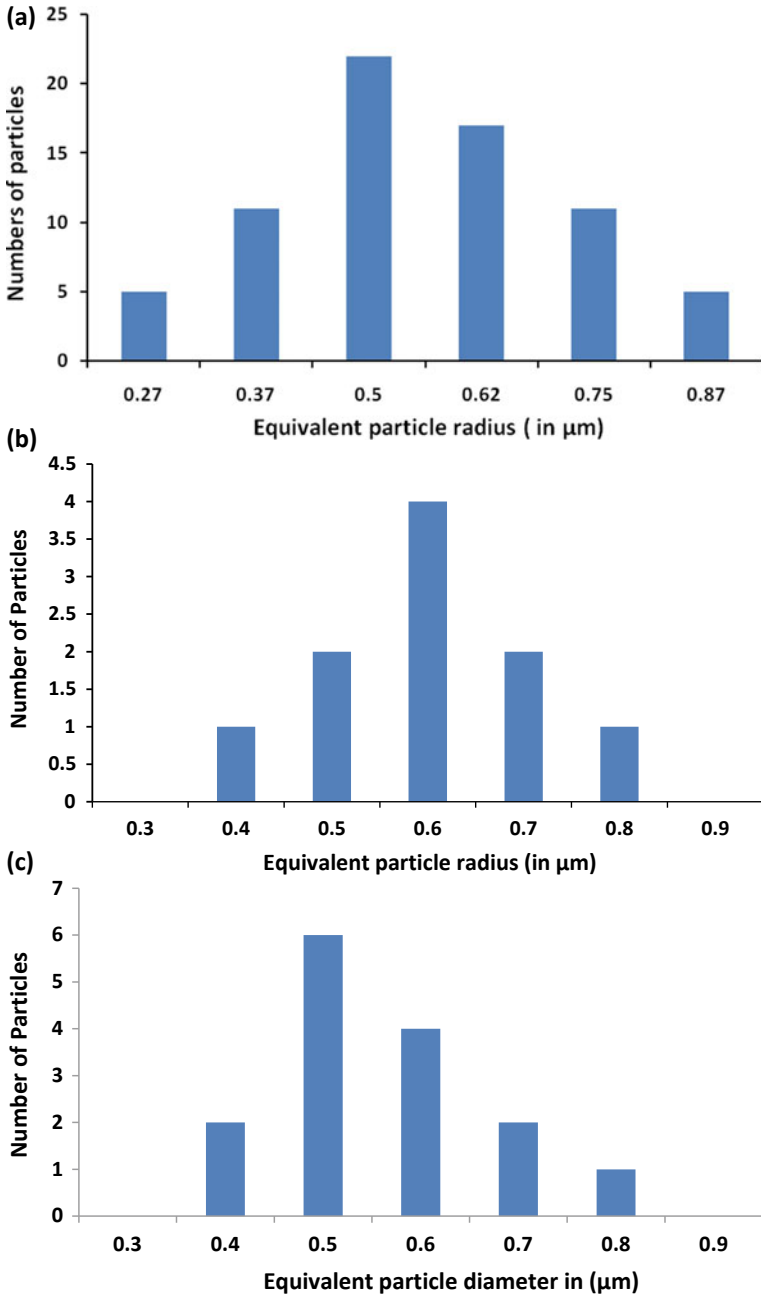
Fig. 30.3   a Size distribution graph of *E. coli* (sample 1), **b** Size distribution graph of *E. coli* (sample 2), **c** Size distribution graph of *E. coli* (sample 3)

30.3.3 Escherichia Coli *Sample 3*

In this case also, the SEM image portrays elongated spheroid shape of *E. coli* particles, shown in Fig. 30.2c. The particles were found to be having modal radius of 0.50 μm. The parameters used for generating the theoretical plots are tabulated in Table 30.1.

30.4 Results and Discussions

The theoretical plots for volume scattering function $\beta(\theta)$ are shown in Figs. 30.4, 30.6 and 30.8 respectively for $\lambda = 632.8$ nm and that of degree of linear polarization $P(\theta)$ are shown in Figs. 30.5, 30.7 and 30.9 respectively for the same wavelength [4, 5, 22]. The particle modal radius was incorporated into the theoretical program to generate Mie plots whereas aspect ratio was incorporated to generate T matrix plots. Both $\beta(\theta)$ and $P(\theta)$ were expressed in arbitrary units (a.u). Figure 30.4 shows the significant profile of volume scattering function $\beta(\theta)$ and Fig. 30.5 shows the degree of linear polarization $P(\theta)$ [4]. Both the profiles depend upon size and size distribution and the composition of the particles. It is observed that both the T-matrix and Mie plot exhibits the forward scattering lobe. From Fig. 30.4 it is found that theoretical volume scattering profile shows a smooth profile for both Mie theory and T- matrix and shows inflection at some of the scattering angles. This variation observed throughout the angular range due to size distribution of the assemblage of randomly oriented bio-particles in the sample 1, of *E. coli*. Again, $\beta(\theta)$ at $\lambda =$
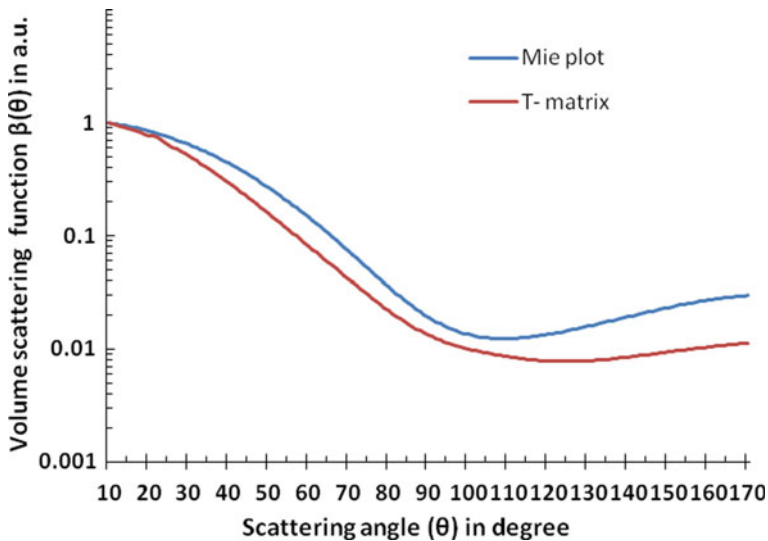
Fig. 30.4 Volume scattering function $\beta(\theta)$ of *E. coli* (sample 1) at $\lambda = 632.8$ nm
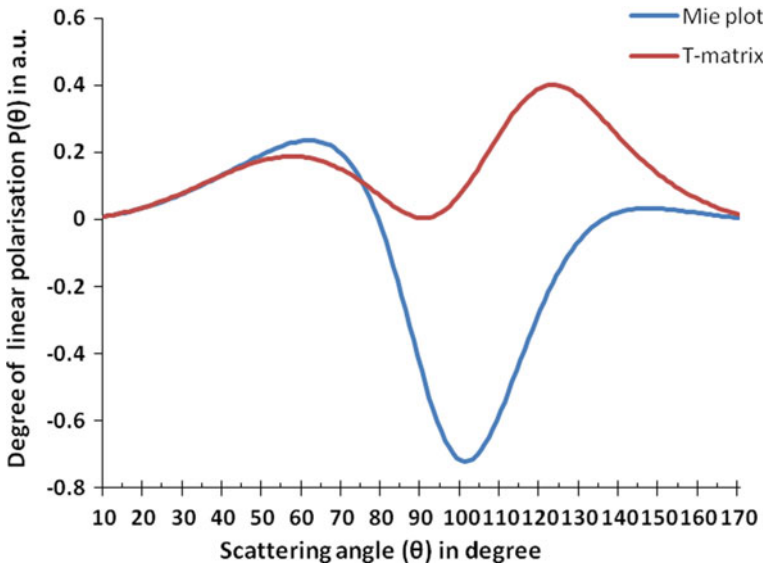
Fig. 30.5   Degree of linear polarisation $P(\theta)$ for *E. coli* (sample 1) at $\lambda = 632.8$ nm

632.8 nm shows slightly decreased value in profile from approximately $\theta = 10°$ to 110° for Mie plot and from $\theta = 10°$ to 123° for T-matrix. The value become more pronounced for $\beta(\theta)$ from $\theta = 110°$ to 170° respectively for both the plots. The overall deviation between both the theoretical plots may be attributed to following reasons,

i.   Presence of size and size distribution function.
ii.   Minimal effect of shape and shape distribution function.
iii. Incorporation of only one size parameter or aspect ratio for generating the theoretical profile for both T-matrix and Mie plot.
iv.   Possible changes of cell morphology in sample 1.

From Fig. 30.5, it is clearly observed that Mie plot shows a huge deviation when compared with T-matrix particularly beyond 80°. Beyond 80°, T-matrix exhibits positive branch. However Mie plot exhibits negative branch at about 135°.

The overall deviation between the theoretical plots was probably due to following reasons,

i.   Strong dependence of polarization on size and shape of the particles. While generating the Mie plot we used the shape of the particle as spherical but in T-matrix we used it as elongated spheroidal.
ii.   The reason of obtaining negative branch plot was because of the reason that the parallel intensity of polarised light getting dominated over the perpendicular intensity of the polarised light.
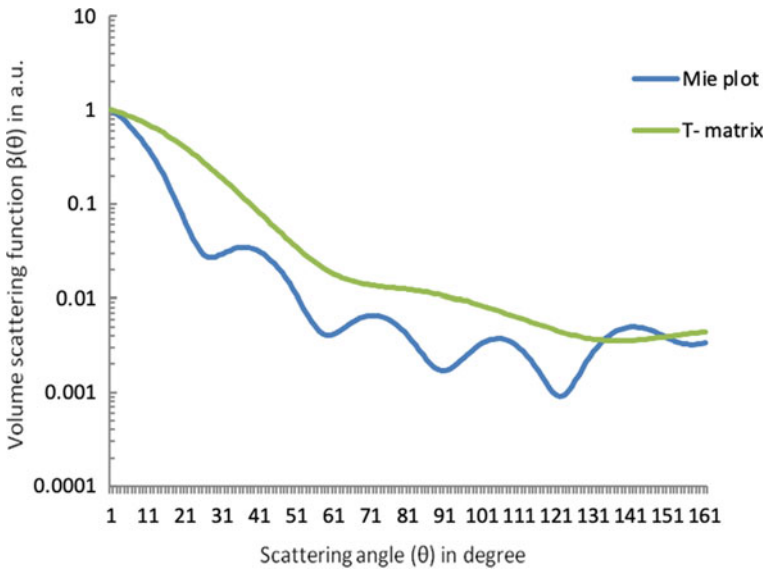
Fig. 30.6 Volume scattering function β(θ) of *E. coli* (sample 2) at λ = 632.8 nm
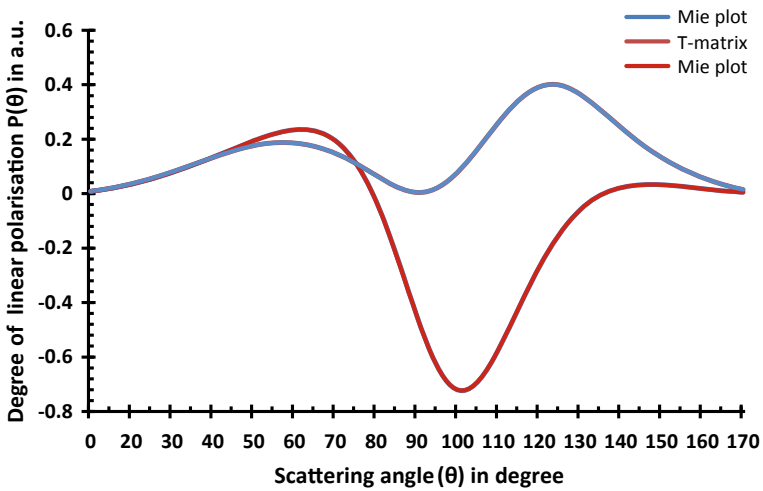
Fig. 30.7 Degree of linear polarisation $P(\theta)$ for *E. coli* (sample 2) at λ = 632.8 nm

iii.   Presence of size and size distribution function.
iv.   Incorporation of only one size parameter for generating the scattering profile.

Figure 30.6 shows the significant profile of volume scattering function $\beta(\theta)$ and Fig. 30.7 shows the degree of linear polarization $P(\theta)$ for sample 2 [4]. Both Mie and T-matrix showed similar trend of scattering profiles. However, Mie oscillations
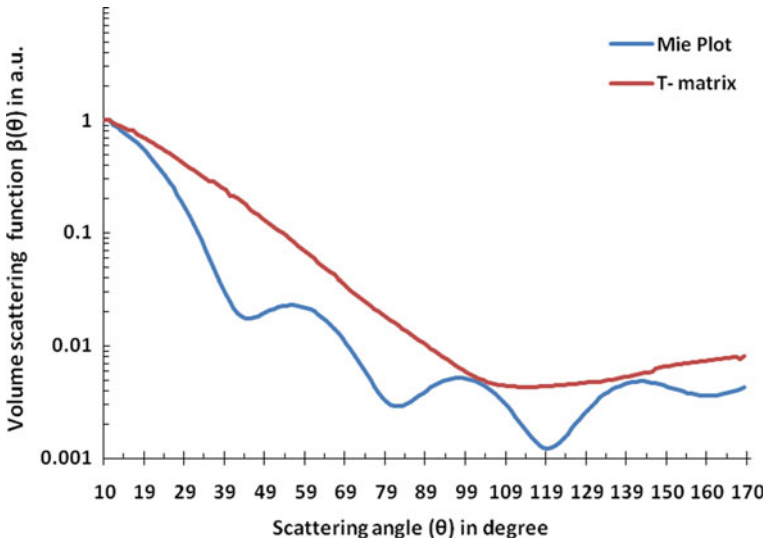
Fig. 30.8 Volume scattering function $\beta(\theta)$ of *E. coli* (sample 3) at $\lambda = 632.8$ nm
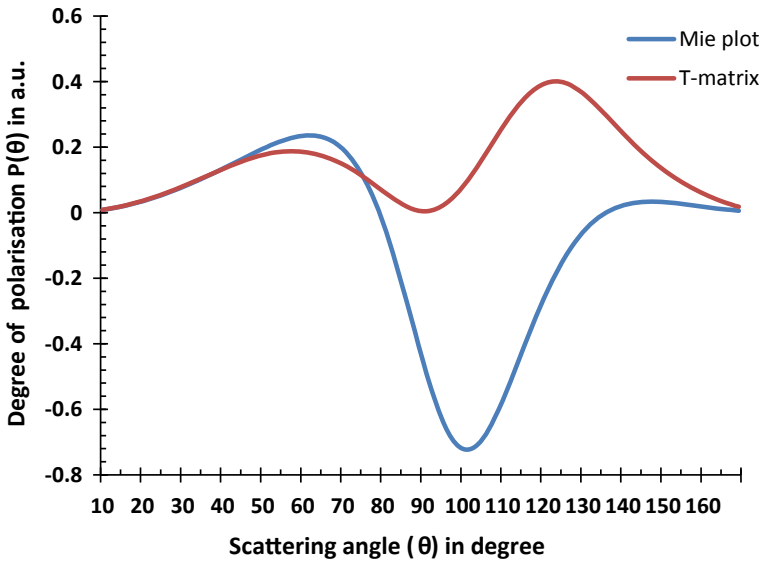
Fig. 30.9 Degree of linear polarisation $P(\theta)$ for *E. coli* (sample 2) at $\lambda = 632.8$ nm

were present in the Mie plot because of presence of comparatively narrow size distribution as shown in Fig. 30.3b. The T-matrix plot was found to be smooth. The overall deviation between the theoretical plots was probably because of the same reasons presented for the scattering profile for sample 1 cited in the same heading. From the Fig. 30.7, it is clearly observed that Mie plot shows a huge deviation as compared with T-matrix. T-matrix plot mostly shows a positive branch and Mie plot show alternate positive and negative branch throughout the angular range. The reason possibly may be due to the following reasons:

i.   The parallel intensity dominates over perpendicular intensity of polarised light in all the negative branches observed.
ii. Presence of size and size distribution function.
iii. Minimal presence of shape and shape distribution.
iv. Incorporation of only one size parameter for generating the theoretical profile for both T-matrix and Mie plot.
v.   Ignoring the imaginary part of refractive index in the input parameter while generating the theoretical plot.

Both Mie and T-matrix plots showed similar trend in Fig. 30.8. However, Mie oscillation was present in the Mie plot because of presence of narrow size distribution. The T-matrix plot was found to be smooth. The measured degree of linear polarisation $P(\theta)$ for non-spherical randomly oriented particles represented is shown in Fig. 30.9. From the figure it is clearly observed that Mie plot shows a huge deviation with T-matrix plot. T-matrix shows a positive branch only and Mie plot show initially a positive branch followed by a negative branch along the angular range. The overall deviation between the theoretical plots for both $\beta(\theta)$ and $P(\theta)$ may be attributed to the familiar reasons already discussed for *E. coli* sample 2 in Sect. 30.4.

Our results show a significant unique theoretical profile of *E. coli* for all the three different samples at a wavelength of 632.8 nm. The reason why one sample was cultured and the other two taken from the samples cultured by other researchers [31, 32] was to verify how fruitfully the same light scattering theories can be applied to different *E. coli* samples. The results indicated that we always obtain a distinct signature while considering Mie theory or T-matrix approach individually. It is also observed that the degree of linear polarization of all the three samples follows the similar trend [4]. For randomly oriented particles, as can be seen from the SEM images Fig. 30.2a, b & c, we know that Mie theory can be applicable [3] and for non-spherical particles, T-matrix approach is considered to be a better theory [2]. However, in this paper, we have shown how both the theoretical approaches lead to a distinct scattering profile (as obtained for all the samples). This means, it is very essential to make a proper selection of theory (either Mie theory or T-matrix) to obtain the scattering profile of the randomly oriented bio-particles, with due consideration of all the necessary input parameters in the theoretical program [34, 35]. The experimental light scattering data for the same nature of samples will provide a better insight to see which theory fits best for the experimental results. Thus, experimentation is also a necessary step forward, to validate the choice of proper theory. In this paper, we also report how, without involving a non-invasive technique we can use light scattering

tool to quantify the morphology of *E. coli* bio-particles. This is an advantage over other conventional techniques which are mostly invasive ones, which are otherwise used to characterize bio-particles.

30.5 Conclusions

In our work we carried out the light scattering investigations on *E. coli* based on light scattering theories namely, Mie theory and T-matrix theory. We generated the significant theoretical profile by using the information from SEM image of *E. coli* sample which we cultured in laboratory as mentioned in Sect. 30.2.1. Also, we generated the theoretical profile of collected SEM images from internet source [31, 32]. Since our particles were actually elongated spheroid type, having random-orientation, we expected the scattering profiles generated with the above-mentioned theories to be similar since many researchers reported that for randomly oriented non-spherical particles the particles behave as equivalent spheres [4, 36, 37]. But in our studies we found fairly disagreement between the profiles obtained from Mie theory and T-matrix theory for morphological characterization. The deviations between both the theoretical plots were more pronounced for the $P(\theta)$ component.

By generating all the elements of Mueller matrix other than the first two elements, S_{11} and S_{12}, we can obtain complete morphological characterization. In our future work, we wish to carry out a real light scattering experiment to generate experimental scattering profiles corresponding to all the matrix elements using a light scattering setup. Finally, we want to carry out comparative analyses of experimental data, theoretical data and also with the stimulated result where we expected to incorporate the size distribution function as well. In this paper, we have reported how and why it is necessary to make a proper choice of scattering theory to characterize bio-particles like, *E. coli.*. Most importantly, we have observed how light scattering tool has an advantage over other characterization tool for bio-particles for its morphological characterization, such as size, shape etc. of the bio-particles.

References

1. M.I. Mishchenko, J.W. Hovenier, L.D. Travis, *Light Scattering by Nonspherical Particles: Theory, Measurements, and Applications* (Academic Press, California, San Diego, 2000)
2. C.F. Bohren, D.R. Huffman, *Absorption and Scattering of Light by Small Particles* (Wiley, New York, 1983)
3. Y.-L. Xu, J. Opt. Soc. Am. A, **20**(11), 2093–2105 (2003)

4. S. Roy et al., Study of ZnO nanoparticles: antibacterial property and light depolarization property using light scattering tool. J. Quant. Spectrosc. Radiat. Transfer **118**, 8–13 (2013)
5. S. Roy et al., J. Quant. Spectrosc. Radiat. Transfer **112**, 1784–1791 (2011)
6. M.I. Mishchenko et al., Overview of scattering by nonspherical particles. in *Light Scattering by Nonspherical Particles: Theory, Measurements, and Applications*, ed. by M.I. Mishchenko, J.W. Hovenier, L.D. Travis (Academic Press, 2000), pp. 29–60
7. S. Sharma, D.J. Somerford, *Light Scattering by Optically Soft Particles: Theory and Applications* (Praxis Publishing, Chichester, UK, 2006)
8. M.S. Quintby- Hunt, A.J. Hunt, Proc. SPIE **925**, 288–295 (1988)
9. Y. Takano, K.N. Liou, J. Atmos. Sci. **52**, 818–837 (1995)
10. Y.-L. Xu, J. Opt. Soc. Am. A **20**(11), 2093–2105 (2003)
11. S. Roy et al., J. Quant. Spectrosc. Radiat. Transfer **118**, 8–13 (2013)
12. N.N. Boustany, S.A. Boppart, V. Backman, Annu. Rev. Biomed. Eng. (2010). https://doi.org/10.1146/annurev-bioeng-061008-124811
13. S. Tanev et al., Simulation tools solve light-scattering problems from biological cells, the finite-difference time-domain approach helps develop optical methods for noninvasive biomedical diagnostics. Optiwave (2004)
14. B.J. Berne, Acc. Chem. Res. **6**, (1973)
15. N.G. Khlebtsov et al., *Light-Tissue Interaction: in the Handbook of Optical Biomedical Diagnostics*, vol. 1, 2nd edn (SPIE Digital Library, 2016)
16. W. Sun et al., Appl. Opt. **41**(27), 5728 (2002)
17. K. Rauf et al., Study of putative microfossils in space dust from the stratosphere. Int. J. Astrobiol. **9**(3), 183–189 (2010)
18. O. Muñoz et al., Experimental determination of scattering matrices of dust particles at visible wavelengths: the IAA light scattering apparatus. J. Quant. Spectrosc. Radiat. Transfer **111**, 187–196 (2010)
19. C. Wickramasinghe, Bacterial morphologies supporting cometary: a reappraisal. Int. J. Astrobiol. **10**, 25–30 (2011)
20. M. Xu, A. Katz, *Light Scattering Reviews 3 Light Scattering and Reflection* (Praxis Publishing Ltd, Chichester, UK, 2008)
21. M.I. Mishchenko et al., J. Quant. Spectrosc. Radiat. Transfer **55**(5), 535–575 (1996)
22. S. Roy, G.A. Ahmed, Monte Carlo simulation of light scattering from size distributed sub-micron spherical CdS particles in a volume element. Optik-Int. J. Light Electron. Opt. **122**, 1000–1004 (2011)
23. L. Kolokolova, L. Nagdimunov, D. Mackowski, J. Quant. Spectrosc. Radiat. Transfer **204**, 138–143 (2018)
24. O. Dubovik et al., J. Quant. Spectrosc. Radiat. Transfer **224**, 474–511 (2019)
25. V.V. Tuchin, L.V. Wang, D.A. Zimnyakov, *Optical Polarization in Biomedical Applications* (Springer Science and Business Media LLC, 2006)
26. From Wikipedia sources, https://en.wikipedia.org/wiki/Escherichia_coli
27. A. Katz et al., IEEE, **9**(2), (2003)
28. B.R. Jennings, V.J. Morris, J. Colloid Interface Sci. **49**(1), 89–97 (1974)
29. A.N. Shvalov et al., J. Quant. Cell Sci. **41**(1), 41–45 (2000)
30. Credit: Rocky Mountain Laboratories, NIAID, NIH. Source from http://en.wikipedia.org/wiki/Image:EscherichiaColi_NIAID
31. From https://medicalxpress.com/news/2015-11-specific-gut-bacteria-severe-diarrhea.html,2005
32. A.N. Shvalov et al., Cytometry **41**(1), 41–50 (2000)
33. A. Gogoi et al., Development of TUSCAT: a software for light scattering studies on spherical, spheroidal and cylindrical particles. J. Quant. Spectrosc. Radiat. Transfer **112**(17), 2713–2721 (2011)
34. S. Roy, G.A. Ahmed, Computation of Mueller scattering matrices of spherical particles with a Gamma size distribution. J. Opt. **39**(2), 76–81 (2010)

35. H. Volten et al., Laboratory measurements and T-matrix calculations of the scattering matrix of rutile particles in water. Appl. Opt. **38**(24), 5232–5240 (1999)
36. T.H. Waterman, Polarization of marine light fields and animal orientation. Proc. SPIE **925**, 431–437 (1988)
37. Y.-L. Xu, Scattering Mueller matrix of an ensemble of variously shaped small particles. J. Opt. Soc. Am. A **20**(11), 2093–2105 (2003)

Chapter 31
Reduced Graphene Oxide-Copper Nanocomposites Synthesis via Green Chemistry

Anjali, Sonal Rattan, Rahul Sharma, Twinkle, Manpreet Kaur, Harjot Singh, Nihal, Mamta Sharma, Suresh Kumar, and J. K. Goswamy

Abstract The graphene-based nanocomposites have recently attracted much attention in the fields of energy storage devices such as supercapacitor and battery, sensor, photo catalytic and optoelectronics applications. In this paper, graphene oxide (GO) is synthesized via a standard modified hummer's method, reduced graphene oxide and copper nanoparticles (CuNPs) reduction has been carried out by green chemistry using neem leaves broth. Study the optical, structural properties as well as the electrical response of GO, rGO, CuNPs and rGO-CuNPs. Synthesis of nanocomposite was accomplished by using eco-friendly solvents, cost-effective and without toxic chemicals.

31.1 Introduction

Presently days graphene and graphene-based nanocomposites are accomplish more exploration enthusiasm for a few properties, for example, a two-dimensional (2D) mono layer carbon material has sp^2 hybridization, high surface area, magnificent electrical conductivity, high mechanical strength, thermal conductivity, noteworthy biocompatibility and simplicity of functionalization [1, 2]. Graphene based materials exhibit prevalent electrochemical and optical properties, just as the capacity of graphene to adsorb an assortment of metal nanoparticles, metal oxides nanoparticles, conductive polymers, and biomolecules atoms through a π–π stacking cooperation as well as electrostatic association, which make them perfect materials for building

Anjali (✉) · S. Rattan · R. Sharma · Twinkle · M. Kaur · H. Singh · M. Sharma · S. Kumar · J. K. Goswamy
Department of Applied Sciences (Physics), UIET, Panjab University, Chandigarh 160 025, India

Anjali · Twinkle · M. Kaur · H. Singh · S. Kumar
Department of Physics, Panjab University, Chandigarh 160 014, India

S. Rattan · S. Kumar
Centre for Nanoscience and Nanotechnology, Panjab University, Chandigarh 160 025, India

Nihal
UIET, Panjab University, Chandigarh, India

vitality energy storage device, sensors, optoelectronics device, photo catalytic and so forth [3]. Honorable metallic nanoparticles have indicated extraordinary likely consideration because of their restricted surface plasmon reverberation (LSPR) and one of a kind electrical, surface and optical properties. NPs of alkali and respectable metals for example Ag, Au, Cu, Pd and Pt have expansive retention band in visible zone of electromagnetic solar spectrum [4, 5]. Out of these metals, copper has remarkable properties like electrical, electrochemical and promising competitor due to the natural abundance, it is utilized as energy storage, in sensors, electronic gadgets, photonic gadgets and heat transfer fluid properties and so forth [6].

Physical, chemical and biological methods are being utilized for delivering nanostructures having various sizes, shapes, harmfulness and synthesis expense. In physical strategy, enormous amount of the material is squandered. The synthetic method reduction of GO is recognized as the most suitable method for preparing graphene in bulk quantities but the reducing agents used, for example, hydrazine hydrate (HH) and sodium borohydride are poisonous and hazardous. As a result, persistent undertakings have been coordinated towards the optimization and improvement of environment friendly reducing agents for GO reduction [7, 8]. The chemical compositions of products in green method reduce or eliminate the use of toxic chemicals. In this method, number of reducing agent like a plant leaves and roots, citric fruit, seeds (sunflower seed, green gram, black gram), bacteria and algae. Plant leaves extract reduction is a one of the promising route, easy to handle and another remarkable advantages in the invulnerability of human body against different bacterial, contagious and viral diseases. Neem is an excellent reducing agent because easily availability, present biomolecules such as terpenoids, flavonoids responsible for the reduction.

In this paper, we have contributed an environment friendly, un-harmful and minimal effort blend technique and through a novel course reduction of graphene (rGO), copper nanoparticles (NPs) utilizing neem leaves extract.

31.2 Characterization Techniques

UV–Visible and FTIR spectrum examination have been done by using a double-beam spectrophotometer (Shimadzu, UV-2600) and Shimadzu IR IRAffnity-1S, respectively. The samples were dispersed in de-ionized (DI) water in quartz cuvette of path length 10 mm. I-V characteristics were carried in voltage scan range of from -1 V to $+ 1$ V. XRD characterization of the powder samples was performed using a Bruker D8 Advance X-ray diffractometer using Cu K_a with wavelength1.54 Å. Electrical response of the nanocomposite has been studied using a Keithley source meter.

31.3 Materials and Method

The copper acetate monohydrate reagent grade was obtained from Merck Life Science Private Limited, India. Graphite flakes, H_2SO_4 (sulfuric acid), H_3PO_4 (ortho-phosphoric acid), $KMnO_4$ (potassium permanganate), H_2O_2 and HCl were obtained from Sigma Aldrich, India. For the complete procedure of synthesis and washing used deionized water.

31.3.1 Preparation of Neem Leaves Extract

The fresh neem leaves were washed number of times with DI. 20 g of washed neem leaves were taken and finely chopped into small pieces and mixed in 100 mL of DI water. The mixture was then boiled at 60 °C for 30 min and settled at the room temperature (1–2 h). The schematic of the process is shown in Fig. 31.1. Finally, the solution was filtered using Whatsmann filter paper. The neem leaves broth was stored at freezer (2–3 months) for further uses [5].

(a) Preparation of neem leaves extract

Neem leaves paste + Deionized water → Boil at 60°C at 30 min → Neem leaves extract

(b) Formation of copper nanoparticles

Cu solution → After 30-45 min → CuNPs
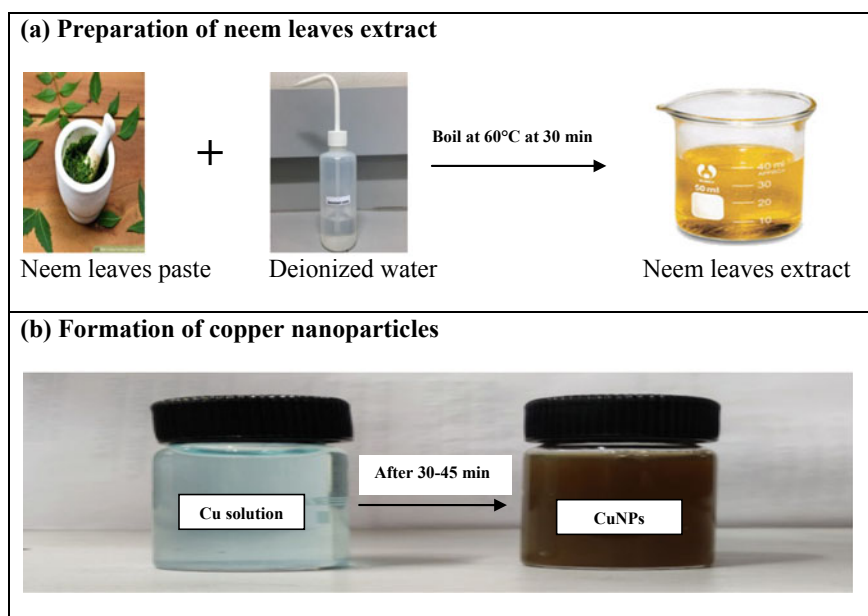
Fig. 31.1 Represents the preparation of neem leave extract and copper nanoparticles

31.3.2   Synthesis of GO and rGO

Graphene oxide (GO) was prepared standard improved Hummer's method by graphite flakes [9]. Graphene oxide was reduced by using neem leaves extract as a reducing agent. 10 mg of GO powder was dispersed in 20 mL of DI (0.5 mg·mL^{-1}). Next, 2 mL of neem leaves extract was added to this solution and stirred with a magnetic stirrer for 30 min at 60 °C. The reduced product was filtered and washed with ethanol followed by washing with water 3 times, respectively, and dried at 60 °C for 24 h.

31.3.3   Synthesis of Copper Nanoparticles

1 mM copper acetate monohydrate was dissolved in 2 mL DI was taken and magnetically stirred for 25 min obtaining a light sky blue coloured solution. After 25 min, 5 ml of neem broth was added to the solution and stirred at 70 °C. The light sky blue colour of solution turned to dark brown, which indicated complete synthesis of CuNPs (the digital camera images are shown in Fig. 31.1).

31.3.4   Synthesis of RGO-CuNPs Nanocomposite

The nanocomposite of rGO-CuNPs was set up by blending 5 mL of rGO solution with 1 mL of CuNPs (5:1(v:v)) and ultrasonicate for 5 min. Filter the prepared sample by vaccum pump using PVDF filter paper. Dry sample for 2–3 h in oven and stored.

31.4   Results and Discussion

31.4.1   Optical Properties

The absorbance peak of graphene oxide and graphene were observed at 228 nm and 265 nm respectively. The results are shown in Fig. 2b and c respectively. The wavelength shift confirmed the reduction of graphene oxide and absorbance peak show at 260 nm [10]. UV/Vis examination of CuNPs is represent in Fig. 2a. The absorption peak of CuNPs was observed at 513 nm, it can be attributing to the surface plasma resonance (SPR) of Cu^0 nanoparticles. The absorbance expanded with increment in the response time. The overall intensity of absorption is very small before addition of plant extract. However, upon reduction of Cu^{2+} ions with neem extract because the three times enhancement in the SPR absorption. The brown color indicates the formation of copper nanoparticles [11, 12]. The UV–Vis spectrum of
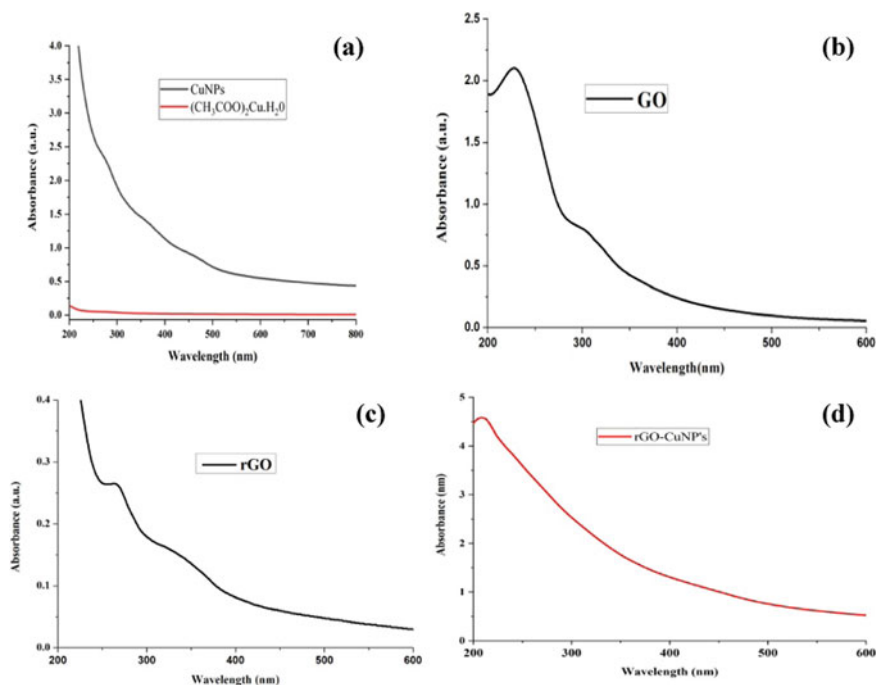
Fig. 31.2 UV/Vis spectra of **a** CuNPs **b** GO **c** rGO **d** rGO-CuNPs

CuNPs is shown in Fig. 2a. The size of nanoparticles was confirmed by particle size distribution. The rGO-CuNPs nanocomposite displays the optical absorbance peak at 210 nm as shown in Fig. 2d.

31.4.2 Structural Properties

FTIR spectrum of GO, rGO and rGO-CuNPs is shown in Fig. 31.3. The difference between the peak position of GO and rGO indicate the complete reduction of graphene. The generally balanced out with capping specialists, for example, surfactants, polymers. Be that as it may, they got here are steady due to in situ bio-capping by the neem leaves broth. rGO-CuNPs analysis was carried out to investigated the strong stretching transmittance peaks at 666.83 cm^{-1}, 1529.85 cm^{-1}, 1665.91 cm^{-1}, 1710.85 cm^{-1}, 1992.91 cm^{-1}, 2138.74 cm^{-1} and 2228.95 cm^{-1} corresponding to nitro (N–O), carboxylic (C $=$ O) and thiocyanate (S-C $=$ N) functional compound respectively. The absorption peak at 3609.85 cm^{-1}, 3746.77 cm^{-1} 3173.86 cm^{-1} correspond to free alcohol (O–H) and alkene (C-H) compound separately [13, 14]. The vibrational groups represented to be these conceivable bioactive present (flavonoids, terpenoids and protein compound) in neem leaves broth, these
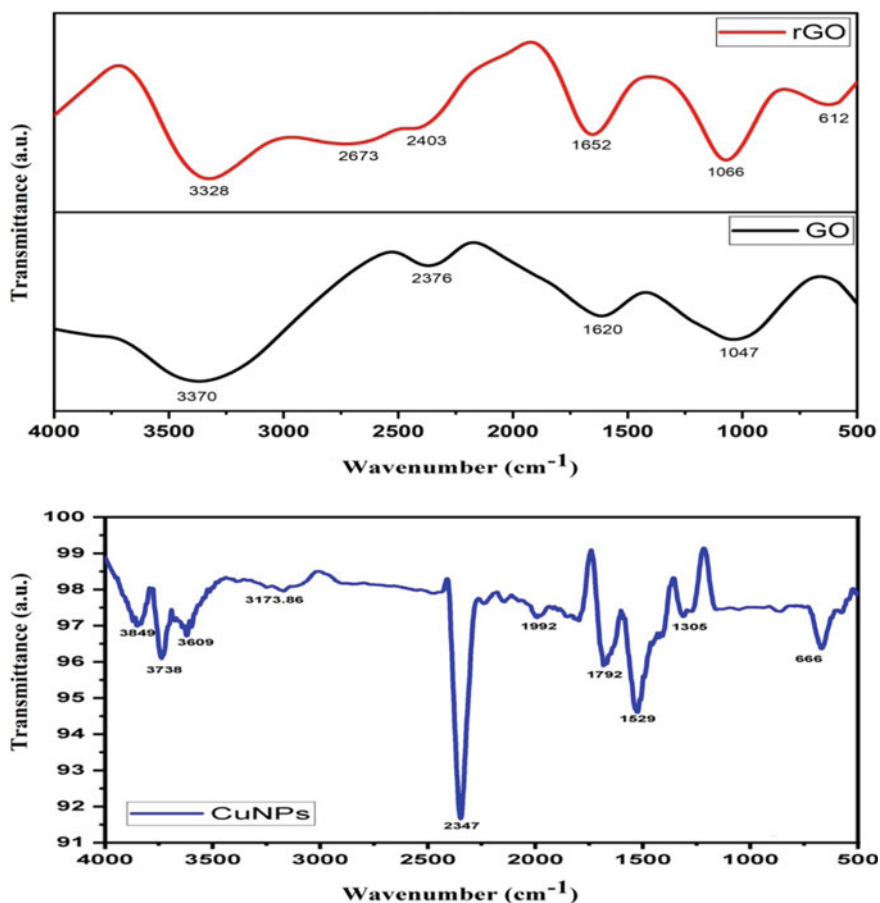
Fig. 31.3 FTIR spectrum of **a** GO **b** rGO **c** CuNPs

bioactive manage reduction of metal nanoparticles. Group of free carboxylate examined in proteins, it exhibit strength to bind the metal nanoparticles and make them stable The terpenoids and flavonoids compound are complete reduction, surface protection and stability of copper nanoparticles [14].

XRD spectra of GO, rGO, CuNPs and rGO-CuNP nanocomposite investigated at 2θ range 5–70 º in Fig. 31.4. GO, rGO shows a sharp peak at (001) and (002) plane respectively. GO plane (001) shift to (002) it identified a reduction of rGO. The CuNPs and rGO-CuNPs shown a sharp peak at (111), (002), (022) and (110), (101), (200), (211), (220), (130), (301) plane respectively. The plane shows reflection for investigated distance between graphene layers and more narrow peaks for all plane show more crystallite. The nanocomposite of rGO-CuNPs shown occurrence of diffraction peaks at 2θ = 26.52°, 33.9°, 51.40°, 54.63°, 61.51° and 65.49° corresponds to (110), (101), (211), (220), (130) and (301) planes, respectively [10,
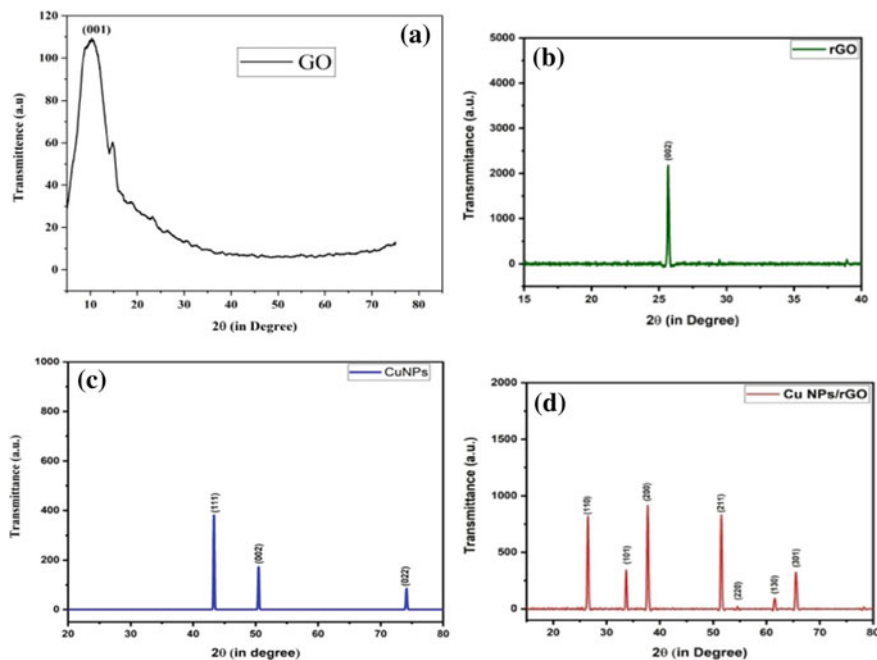
Fig. 31.4 XRD of **a** GO **b** rGO **c** Cu NPs (d) rGO-Cu NP nanocomposite

11]. The Schherer's equation used for calculating the average crystallite size (D) of nanocomposites:

$$D = \frac{K\lambda}{\beta \cos\theta}$$

where, the calculated value of average crystallite size (D) of rGO, CuNPs and rGO-CuNP nanocomposite comes out to be 27 nm, 67.4 nm and 131.15 nm respectively.

31.4.3 Current-Voltage (I/V) Characteristics

The binary copper nanoparticles perform better electronic conductivity comparison to hybrid nanocomposite and reduced graphene oxide represent in Fig. 31.5. The electronic conductivity of rGO-CuNP nanocomposite is not high because of the presence of oxygen containing functional groups. The conductivity can be enhanced using higher concentration of CuNPs in the nanocomposite.
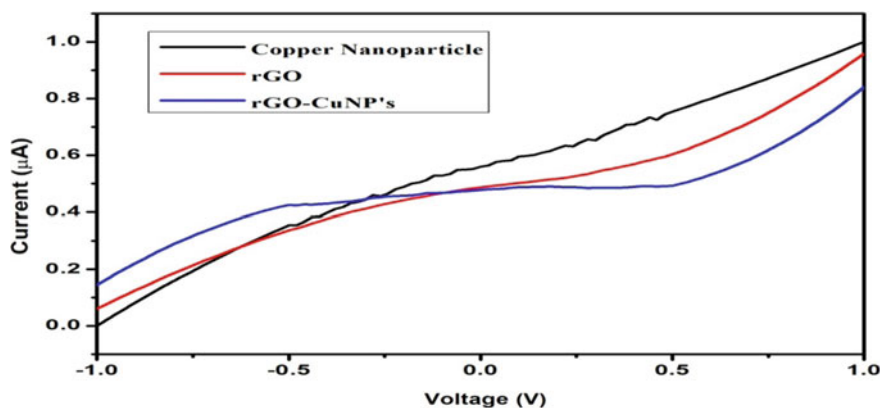
Fig. 31.5 I/V Characteristic of CuNPs, rGO and rGO-CuNPs

31.5 Conclusion

The analysis of this paper appears a properly synthesized of CuNPs and reduction of rGO via green method using neem leaves extract. The average particle size of rGO, CuNPs and rGO-CuNPs are 27 nm, 67.7 nm and 131.15 nm respectively. The electrical response of CuNPs is high with respect to other. The composite can be used in future for supercapacitor, battery, sensors and photocatalysis applications.

References

1. A.K. Geim, Science **324**, 1530–1534 (2009)
2. A.K. Geim, K.S. Novoselov, Nat. Mater **6**, 183–219 (2007)
3. K. Ostrikov et al., Adv. Phys. **62**, 113–224 (2013)
4. Y. Yang et al., Mater. Today **16**, 365–373 (2019)
5. A.J.K. Goswamy, M. Sharma, AIP publishing (2020)
6. S. Tatur, M. Maccarini, R. Barker, A. Nelson, G. Fragneto, Lang **29**, 6606–6614 (2013)
7. S. Stankovich et al., Carbon **45**, 1558–1565 (2007)
8. Z.J. Fan et al., ACS Nano **5**, 191–198 (2011)
9. W.S. Hummers, R.E. Offeman, J. Am. Chem. Soc. **80**, 1339 (1958)
10. S. Rattan, S. Kumar, J.K. Goswamy, Materials (2019)
11. S. Yallappa et al., SpectrochimicaActa Part A: Mole. Biomole. Spectroscopy **110**, 108–115 (2013)
12. B. Blessy et al., Int. J. ChemTech. Res. **7**, 1544–1547 (2015)
13. B. Ajitha, Y.A.K. Reddy, P.S. Reddy, Spectrochim. Acta **121**, 164–172 (2014)
14. Y.H. Kim, D.K. Lee, B.G. Jo, J.H. Jeong, Y.S. Kang, Colloids Surf., A **284**, 368–371
15. W. Yu, H. Xie, L. Chen, Y. Li, C. Zhang, Nanoscale Res. Lett. **4**, 465–470 (2009)

Chapter 32
Stand-Off Detection of DNT Isomers by Raman Spectroscopy with Nanosecond Time-Gating

Rashmi Rai Chauhan, Kamal Kumar Gulati, Sakshi Gupta, Nitesh Kumar, Rekha Mann, and Vijayeta Gambhir

Abstract A mobile platform-based stand-off detection system for chemicals and explosive materials, based on Raman Spectroscopy with nanosecond time-gating was tested for isomers identifications located up to a distance of 30 m. Laser based nanosecond time-gated Raman Spectroscopy experiments were conducted for detection and identification of isomers of Di-nitrotoluene (DNT) at a standoff distance of up to 30 m. A back-scattered stand-off Raman spectroscopy set-up using a nano-second pulsed laser, receiving telescope and ICCD (Intensified Charge Couple Device) coupled spectrograph was employed to detect and identify the samples. The second harmonic of Nd:YAG laser at 532 nm wavelength:, 4 ns Pulse duration, & 10 Hz Rep Rate was used as an excitation source. ICCD coupled Spectrometer with reflection telescope were used to collect and record the weak Raman signals. Standoff experiments for isomers identification were carried out with different number of accumulations and gratings (300lines/mm and 1800 lines/mm grating) to achieve Raman spectra at different resolutions. Isomer samples 2,4- DNT and 2,6- DNT and their mixtures were recorded for identification with appreciable signal to noise ratio. 2,4 and 2,6 DNT were mixed in 50:50 ratio and identified from up to 30 m. Thus Time Gated Raman spectroscopy is an reliable method for identification & distinguishing chemical samples and isomers in mixture form.

32.1 Introduction

Due to the increased instances of use of bombs for terrorist attacks globally, there is a need for detection of toxic and explosive substances. The detection of explosives and precursors for detection of unexploded ordnance, forensic applications and security screening is of great need [1]. Explosive contamination identification is done

R. R. Chauhan · K. K. Gulati · S. Gupta · N. Kumar · R. Mann (✉) · V. Gambhir
LASTEC, DRDO, Delhi 110054, India
e-mail: mann_rekha@lastec.drdo.in

R. R. Chauhan
e-mail: rashmirai@lastec.drdo.in

through surface scan of suspicious objects. Since 2,4-DNT and 2,6-DNT are degradation products of trinitrotoluene (TNT), which is used for landmine production, so their mixture analysis is required to be investigated. One reported approach of isomer identification is to separate different components before detection [2]. DNT isomer identification and detection from very short distance/ point detection has been reported using UV detection after micro chromatographic separation, coupled with SERS [3].

Raman spectroscopy technique involves analysis of inelastically scattered light from the material when monochromatic light interacts with material. Raman spectroscopy has ability to provide unique set of vibrational frequencies which provides information about the molecular structure and sample composition [4, 5]. Raman technique is instantaneous and provides a 'finger print of the molecule [6, 7]. For collection and recording of the back scattered Raman signal, ICCD coupled spectrograph along with 100 mm collection optics was used. Raman spectroscopic technique is non-destructive and highly selective. Generally Raman spectra from standoff distance has background interference and very low intensity. To overcome this problem gate width and time delay in ICCD were introduced to open it only at a time to receive the back-scattered Raman signal from the isomers mixture samples. High gain in intensifier was used to get better signal to noise ratio (SNR) and to boost the received Raman signal from isomers mixture samples.

This paper is reporting DNT isomer identification using nanosecond time gated Raman Spectroscopy, at a distance of 30 m for the first time to the best of our knowledge. This study also becomes relevant to evaluate the remains of post blast detection of explosives.

32.2 Instrumentation and Experimental Procedure

To carry out the experiment for detection of DNT isomers, Time gated Raman spectroscopic system was used. The instrumentation as depicted in Fig. 32.1, consists of nano-second frequency doubled Nd:YAG laser (make Quantel, model Brilliant-B) with 532 nm wavelength as source. The laser operating at 10 Hz and pulse duration ~4 ns excites the sample to produce the Raman spectra. The Raman signals of isomers (along with ambient light and Rayleigh signals) are collected by co-axially aligned 100 mm receiving reflective telescope. The Rayleigh light is quite strong, to block this light notch filter at 532 nm with long pass was used, just before the scattered photons enter the optical fiber bundle. The fiber bundle then transmits these signals to Spectrograph (Andor, SR-303i) which has ICCD (Andor, iStar) coupled for the purpose of time gating and intensifying the Raman signals. The slit width of the spectrograph was kept at 20 μm. Time delay was calculated based on the sample distance and gate width of the order of pulse duration was used as detailed in earlier paper [8]. In the present work detection and identification was carried out up to 30 m from instrument in laboratory conditions. Grating of 300 lines/mm was used to record the Raman spectra of DNT isomers separately and 50:50 ratio isomer mixture.
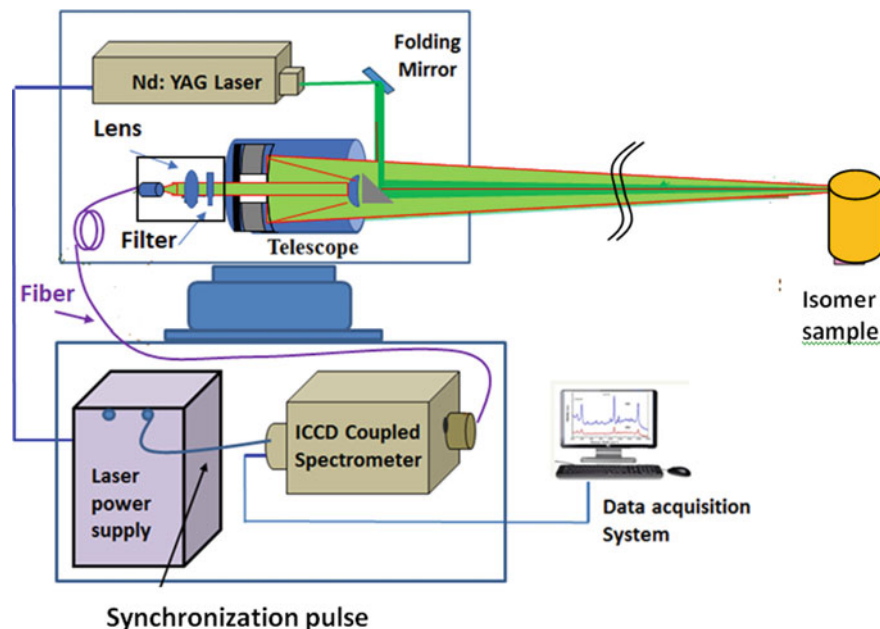
Fig. 32.1 Schematic of Time Gated Raman spectrometer

Further, grating of 1800 lines/mm were also used to resolve the Raman spectra of DNT isomers. Raman spectra with different no. of pulses were also recorded to resolve the DNT isomers spectra present in mixture. To identify the isomers in the mixture at 30 m distance 500 pulses accumulation gave sharp and intensified peaks.

32.3   Results and Discussion

Raman spectra of DNT isomers and isomer mixture (50: 50 ratio) were recorded at a standoff distance of 2 m for reference and at 30 m for identification and detection. Recorded Raman spectra of 2, 4-DNT from 30 m using different gratings is shown in Fig. 32.2.

A Raman spectra of 2,4-DNT is characterized by a very strong peak at ~ 1350 cm^{-1} for NO$_2$ symmetric stretching, wo bands at 1514 & 1607 cm^{-1} for asymmetric and aromatic NO$_2$ stretching respectively. One band at 1147 cm^{-1} for methyl H-C-H bending & one band at 830 cm^{1}are observed in Fig. 2A. The peak at 2940 cm^{-1} observed due to he asymmetric C-H vibration of the CH$_3$ group [9–11]. Peak observed at 3100 cm^{-1} for aromatic C-H stretching vibration.

All the peaks observed at low resolution (Fig. 32.2a) are observed with sharpness and good intensity at high resolution with grating of 1800 lines/mm at 500 pulses (Fig. 32.2b). Thus sharp splitting of peaks is observed at high resolution. Similarly
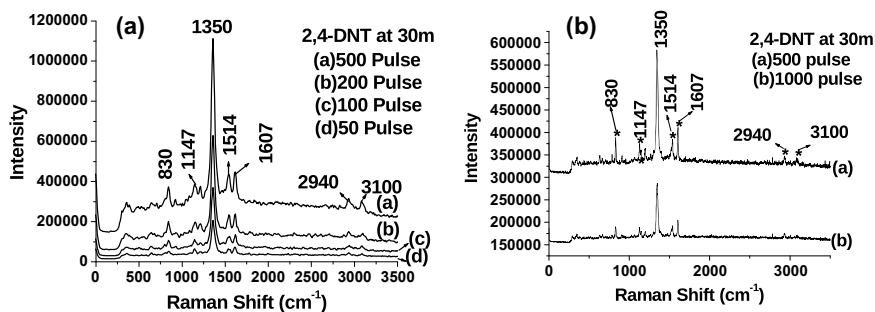
Fig. 32.2 Recorded Raman Peaks of 2,4-DNT at 30 m using grating **a** 300 lines/mm **b** 1800 lines/mm

in Raman spectra of 2,6-DNT depicted in Fig. 32.3 [12], at high resolution using grating of 1800 lines/mm and with 500 pulses, sharp splitting of broad peak around 796 cm^{-1} in to 796 and 844 cm^{-1} (Fig. 32.3a) and splitting of broad band around 1204 cm^{-1}in to three sharp peaks at 1078, 1138 and 1204 cm^{-1} occur at 30 m standoff distance (Fig. 32.3b).

Thus as observed from Figs. 32.2 and 32.3 for 2.4-DNT & 2,6-DNT sharp splitting of peaks occur at 500 pulses at high resolution (grating of 1800 lines/mm) at 30m standoff distance.

In 50:50 ratio of isomer mixture distinguishing peaks due to 2,4-DNT at 1607, 1147 cm^{-1} and of 2,6-DNT at 580, 796 &1204 cm^{-1} recorded up to 30 m at low resolution (gratings 300 lines/mm) (Fig. 32.4a). Reference Raman spectra (Fig. 32.5) of DNT isomers and isomer mixture (in 50:50 ratio) at a distance of 2 m using grating 300 lines/mm, showed all the peaks as were observed in low resolution spectra at 30 m.

On increasing the resolution (grating 1800 lines/mm) an additional peak at 1078 from 2,6-DNT start appearing in mixture at 30 m (Fig. 32.4b). So single broad peak appearing aroud1147 cm^{-1} splits in to two sharp low intensity peaks at 1078 cm^{-1}
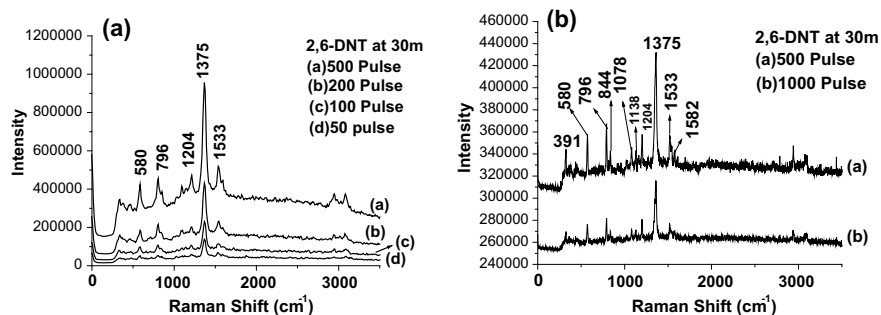
Fig. 32.3 Recorded Raman Peaks of 2,6-DNT at 30 m using grating **a** 300 lines/mm **b** 1800 lines/mm
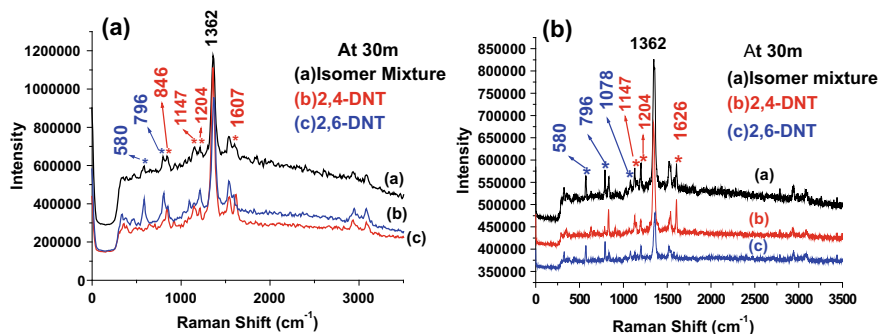
Fig. 32.4 Recorded Raman Peaks of DNT isomers and isomer mixture at 30 m using grating **a** 300 lines/mm **b** 1800 lines/mm

Fig. 32.5 Reference Raman Peaks of DNT isomers and isomer mixture at 2 m using grating 300 lines/mm
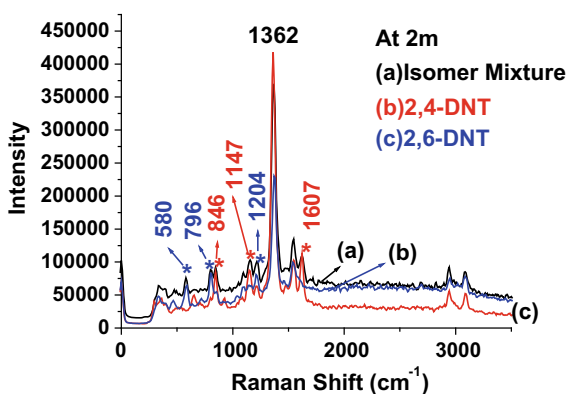
for 2,6-DNT & 1147 cm^{-1} of 2,4-DNT at high resolution. NO$_2$ symmetric stretch peak at ~ 1362 cm^{-1} for mixture is observed for both low and high resolution, which is mix of 2,4-DNT at 1350 cm^{-1} and 2,6-DNT at 1375 cm^{-1}. Thus to identify the isomers in the mixture at 30 m distance 500 pulses accumulation along with grating of 1800 lines/mm gave sharp and intensified peaks, which leads to standoff isomer mixture identification within a minute. At longer standoff distance (more than 30 m) detection and identification of different isomers will be explored in future work.

A mobile platform-based stand-off detection system based on Raman Spectroscopy with nanosecond time-gating was used for detection and identification of isomer samples up to 30 m distance. Thus experimental results show that detection and identification of several isomers is possible using time gated Raman spectroscopy in standoff mode. Detected and identified isomer mixture of DNT may also be relevant to evaluate the remnants of post blast detection of nitro-aromatic explosives.

References

1. L. Nagli, M. Gaft, Y. Fleger, M. Rosenbluch, Opt. Mater. **30**, 1747–1754 (2008)
2. S. Roland, H. Bettermann, K. Kleinermann, Appl. Spectrosc. **51**(11), 1644–1647 (1997)
3. B. Zachhuber, C. Carrillo-Carrion, M. Bartolome, S. Suau, B. Lendi, J of Raman Spectroscopy **43**(8), 998–1002 (2012)
4. S.K. Sharma, P.G. Lucey, M. Ghosh, H.W. Hubble, K.A. Horton, Spectrochimica Acta Part A, **59**, 2391–240 7 (2003)
5. J.H. Alison, L. Bernhard, Trends Anal. Chem. **28**(11), 1235–1242 (2009)
6. I. Nissinen, J. Nissinen, P. Keranen, J. Kotamovaara, Sens. Actuators, B Chem. **241**, 1145–1152 (2017)
7. G. Mogilevsky, l. Borland, M. Brickhouse, W. Augustus,. Int. J. Spectro. pp. 12 (2012), Article ID 808079.
8. Kamal Kumar Gulati, S. Gulia, T. Gambhir, N. Kumar, V. Gambhir, M.N. Reddy, Defence Science Journal, 6(4), 342–34, (2019),.
9. W.O. Rivera, A thesis submitted in partial fulfillment of the requirements for the degree of Master of Science in chemistry University of Puerto Rico Mayaguez Campus (2008)
10. J.M. Sylvia, J.A. Janni, J.D. Klein, K.M. Spencer, Anal. Chem. **72**, 5834–5840 (2000)
11. F. Gao, W.F. Liu, Z.H. Meng, P.F. Su, Z. X. Li, M.H. Wang, Propellants Explos. Pyrotech. **44**(1–9), (2019)
12. E.D. Emmons, J.A. Guicheteau, A.W. Fountain, S.D. Christe-sen, Appl. Spectrosc. **66**, 636–643 (2012)

Chapter 33
Study of Sodium Storage and Diffusion Over Phosphorene Using Density Functional Theory

Sneha Upadhyay and Pankaj Srivastava

Abstract Phosphorene is modeled and investigated using first principles calculations employed by density functional theory. Sodium (Na) is adsorbed over phosphorene at various adsorption sites and an extensive comparison is done between them. Na is chemisorbed at all sites and significant charge transfer happens between phosphorene and Na. Electronic properties before and after adsorption demonstrates that phosphorene undergoes semiconducting to metallic transition. Anisotropic diffusion pattern of Na is ascertained over phosphorene surface with activation energy of 0.5 eV in armchair and 0.1 eV in zigzag direction. Phosphorene shows small change in lattice parameters at higher concentration of Na and becomes more metallic in nature. The specific capacity of 315.54 mAh/g was calculated for fully sodiated surface. Based on the high capacity and low diffusion barrier values, phosphorene can be predicted suitable for Na storage application.

33.1 Introduction

Phosphorene is a well-known material, which is the two- dimensional (2D) form of phosphorus. Bulk phosphorus is found in three forms, red-phosphorus, white-phosphorus and black-phosphorus [1]. Among three of these, black-phosphorus has the highest stability. The phosphorene studied here is the 2D counterpart of black-phosphorus [2–4]. It has gained a lot of attention among 2D materials because it sports various properties which cannot be found in other 2D materials [5, 6]. Being direct bandgap semi-conductor is one of such properties. Presence of foreign materials or employing stress affects its electronic property. Thus, phosphorene is exhaustively researched for application in areas like sensing and storage etc [7–14].

S. Upadhyay (✉) · P. Srivastava
Nanomaterials Research Group-CNTL (NRG-CNTL), ABV-Indian Institute of Information Technology and Management (ABV-IIITM), Gwalior, Madhya Pradesh 474015, India
e-mail: sneha@iiitm.ac.in

P. Srivastava
e-mail: pankajs@iiitm.ac.in

Energy is a fast developing area of research interest. From the efforts to generate energy in a pollution free mode to the storage of energy for all time continuous supply, researchers are paying a lot of attention towards this field. Lithium ion batteries are very popular for energy storage and its supply for portable devices much because of its capability to store high energy in small volume [15, 16]. This advantage comes with some severe limitations such as high cost, effect of humidity which leads to rare but harmful occurrence of battery burst-out and limited resources of lithium [17–19]. One of the alternatives extensively studied nowadays is sodium- ion battery [20, 21]. This can revolutionize the energy storage field because of the cheap availability of sodium (Na) resource and thus lowered battery cost [22–25].

The first step towards the challenge of developing Na- ion battery is finding suitable anode material since the commercially used graphite cannot be utilized due to the large size of Na- ions compared to Li- ions [26–28]. Graphene also poses same difficulty due to the small size of adsorption site [29–31]. Many other 2D materials are being studied to find suitable anode such as stanene, [32] $NbSe_2$,[33] Mo_2C, [34] VS_2,[35] and Cu_2Si, [36]. Here, in this work, we do the basic studies of Na adsorption and diffusion over phosphorene monolayer to find out the associated properties such as the structural and electronic properties, specific capacity and activation energy. At the end of studies, it can be predicted that phosphorene is found suitable in Na- ion batteries anode application.

33.2 Computational Details

The computational analysis was performed on the simulator ATK-VNL [37]. The DFT [38, 39] study included GGA [41] exchange correlation and PBE [40] pseudopotential. The density mesh cut-off energy was taken 150 Ryd and $1 \times 10 \times 10$ k-point sampling was used. Van der Waals (vdW) forces were corrected using Grimme DFT-D2 [41] and DZP basis set was included. The maximum value of interaction range was taken 15 Å and the maximum force of convergence during optimization was set to be 0.05 eV/Å.

Beginning with optimization process, structural stability of phosphorene is studied followed by its basic electronic properties comprising of band structure and density of states (DOS). Further, the adsorption of Na over phosphorene is studied. The energy of adsorption (E_{ads}) [42] is given by,

$$E_{ads} = \frac{E_{Na+P} - nE_{Na} - E_P}{n} \tag{33.2.1}$$

where, E_{Na+P} is the total energy of phosphorene with Na adsorbed over it, E_P is total energy of pristine phosphorene, E_{Na} is total energy of Na atom in molecular configuration and n is the total number of Na atoms adsorbed. For finding specific capacity (C) [43] multiple sodium adsorptions is done and the corresponding capacity

is calculated by,

$$C = \frac{Fnv}{M} \qquad (33.2.2)$$

where, F, n, v and M are Faradey's constant (26.801 Ah/mol), total number of Na atoms per formula unit of electrode material, valence electron number (for Na, v = 1) and molecular mass (g/mol) of the electrode material respectively. To analyse the diffusion of Na over the phosphorene, Climbing Image Nudged Elastic Band (CI-NEB) [44, 45] approach is adopted. The activation energy (E_a) vs reaction coordinate along a certain path is plotted and the maximum value of activation energy is known as the diffusion barrier faced by Na over that path.

33.3 Results and Calculations

33.3.1 Structural Properties

The phosphorus unit cell has orthorhombic lattice structure and space group 64 cmca with the wyckoff position 8f (0, 0.10168, 0.08056) [46]. Phosphorene unit cell can be obtained from phosphorus unit cell by removing the atoms above and below the monolayer. The lattice parameters of the phosphorene unit cell after energy optimization are Δa = 2.13 Å, b = 4.38 Å, c = 3.31 Å, where Δa represents the puckered width of monolayer [47]. To avoid interaction among layers 24 Å vacuum padding is done in x-direction. The bond lengths and the bond angles of P in phosphorene are 2.24 Å and 96.3351° in planar and 2.56 Å and 102.095° in puckered direction respectively.

33.3.2 Na Adsorption

In beginning, to find the most suitable and thermodynamically stable site, Na is tried to be adsorbed at various possible sites. All of these sites are shown in Fig. 33.1. These sites are nominated as hollow site (H), triangular site (Tr), top site (T) and bridge sites (B1 and B2). The figure shows these sites in non-optimized condition. The adsorption energy, optimized vertical height of adsorption, bond lengths of Na-P bonds and charge transferred from Na for all sites are provided in the Table 33.1. Among all of these sites, H-site shows the highest stability due to maximum adsorption energy |1.908 eV| which indicates strongest binding. This fact can also be validated by looking at adsorption height which is minimum (1.964 Å) in case of hollow site. The sites other than H-site are not the stable sites because they transform to hollow site when they are optimized. So, for rest of our study, only hollow site will
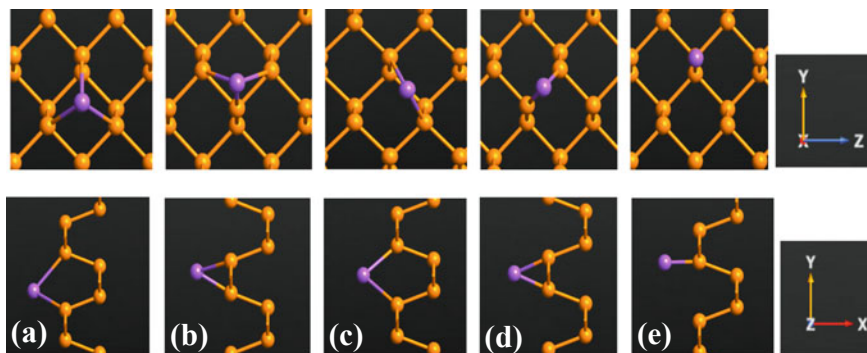
Fig. 33.1 Phosphorene with Na adsorbed over it, front and cross sectional view; **a** hollow (H); **b** traingular (Tr); **c** Bridge1 (B1); **d** Bridge2 (B2); **e** Top (T). The rightmost image shows the axis system

Table 33.1 Adsorption energy (E_{ads}), optimized vertical height of Na over phosphorene (Δh_{opt}), Na-phosphorene bond distance (Δd) and the total charge transferred from Na (ΔQ_{Na})

Site	E_{ads}(eV)	Δh_{opt} (Å)	Δd (Å) Na-P	ΔQ_{Na} |e|
H	−1.908	1.964	1.98, 1.95 & 1.95	0.165
Tr	−1.836	2.063	1.92, 1.98 & 1.97	0.161
T	−1.890	1.966	2.00, 2.02 & 2.03	0.174
B1	−1.418	2.542	2.02 & 2.02	0.175
B2	−1.828	2.116	2.52 & 2.52	0.26

be considered. How adsorption gets affected due to height at which Na is placed over phosphorene surface is analysed and the results are shown in Fig. 33.2. It gives the values of adsorption energy (E_{ads}) and optimized vertical height (Δh_{opt}) corresponding to different heights (h). The interaction between Na and phosphorene is maximum near height 0.75 Å and 2 Å since at these points E_{ads} and Δh_{opt} has
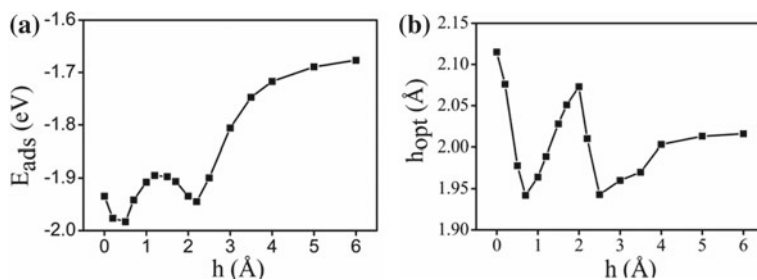
Fig. 33.2 Na is adsorbed at different heights over phosphorene. **a** Adsorption energy (E_{ads}) and **b** Optimized vertical height of Na over phosphorene

lowest value. Na does not get adsorbed at phosphorene after 6 Å and thus do not form bonds.

33.3.3   Electronic and Storage Properties

The electronic properties include the band structure and DOS calculations of pristine as well as Na adsorbed phosphorene. Figure 33.3a, b shows the band structure and DOS plots respectively. The band structure indicates that phosphorene has direct bandgap with a bandgap value of 0.8 eV which is in accordance with the previous work [48]. This bandgap can also be seen in corresponding DOS plot. When Na is adsorbed, Fermi level gets shifted inside the conduction band. Hence, it acquires metallic properties. This transition from semiconducting to metallic nature is a positive trait for electrode application and it can be attributed to the significant charge transferred between them. In Table 33.1, the charge transferred from Na to phosphorene after adsorption is given.

To illustrate the storage properties, multiple atoms of Na are adsorbed over phosphorene surface in different concentrations till the structure is completely full (or is not able to adsorb more Na atoms). The final configuration can be represented as Na_xP_{1-x}, where, $x = 0.0625, 0.125, 0.25, 0.375$ and 0.5. These values of x correspond to the configurations Na_4P_{64}, Na_8P_{64}, $Na_{16}P_{64}$, $Na_{24}P_{64}$ and $Na_{32}P_{64}$ respectively. With the varying concentrations of Na, we study how the properties of phosphorene changes. The band structure plot which has been shown in Fig. 33.4a, shows that the configurations are metallic in nature. We already saw in Fig. 33.3 that presence of Na makes phosphorene metallic in nature and here, we see that metallicity increases with increase in number of Na atoms adsorbed. This fact is also backed up by DOS
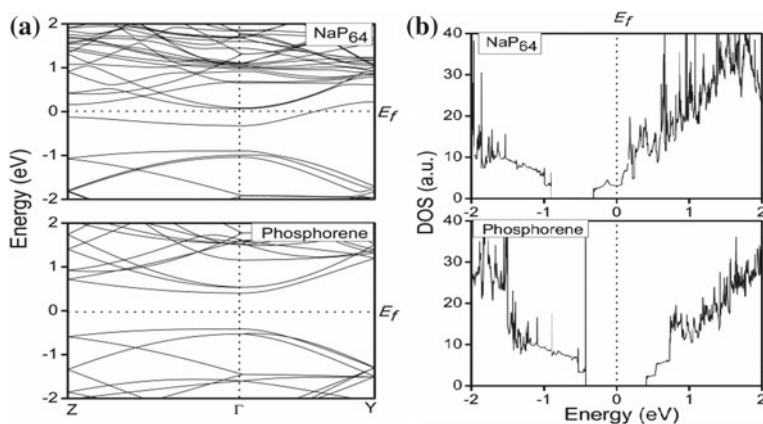
Fig. 33.3 a Bandstructure and **b** DOS of pristine phosphorene and single Na doped phosphorene.
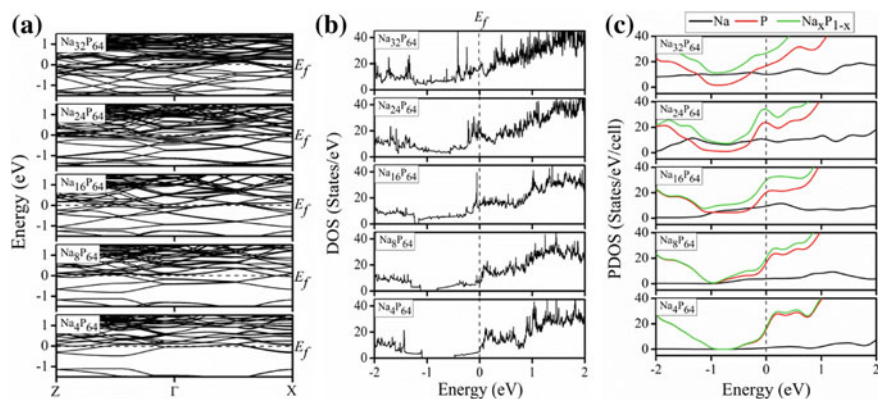
Fig. 33.4 **a** Bandstructure, **b** DOS and **c** PDOS of multiple Na adsorbed over phosphorene (Na_xP_{1-x}) at different Na concentrations (x)

calculation given in Fig. 33.4b. More and more energy states can be seen accumulated near fermi level as the number of Na atoms increase. The pristine phosphorene can be seen having no energy state near fermi level, since it is semi-conducting in nature.

The projected DOS (PDOS) shown in Fig. 33.4c represents the cooperation of the monolayer and Na atoms in the energy states. At lower concentrations of Na, the part contributed by Na is quite low but increases significantly as the number of Na atoms increase. At higher Na concentrations, the Na contribution surpasses the phosphorene contribution at some energy levels as can be seen in conduction band side of the diagram. This mutual effect of phosphorene and Na are responsible for the metallicity. The specific capacity is calculated for $Na_{32}P_{64}$ configuration and it comes out to be 315.54 mAh/g. This value is high compared to the capacities of stanene, [32, 49] $NbSe_2$,[33] Mo_2C, [34] and VS_2, [35]. Table 33.2 mentions the optimized heights of Na atoms over the phosphorene. The charge transferred from Na to phosphorene is higher due to presence of multiple Na atoms and their corresponding energy states. The change in lattice parameter in the direction of adsorption (axis which contains vacuum) shows small change occurring after even multiple adsorptions. It is a desirable property, as negligible expansion ensures that the electrode will remain

Table 33.2 Optimized vertical height of the adsorbed layer (Δh_{opt}), charge transferred from Na to phosphorene (ΔQ_{Na} |e|) and percentage change in lattice parameter in the direction of vacuum (%l.pm.)

	Na_4P_{64}	Na_8P_{64}	$Na_{16}P_{64}$	$Na_{24}P_{64}$	$Na_{32}P_{64}$
Δh_{opt} (Å)	1.845	2.100	2.290	2.334, 4.577	2.242, 4.059
ΔQ_{Na} |e|	0.525	0.358	0.204	0.233	0.260
%l.pm	3.48	1.73	3.20	9.22	6.38

intact after Na intercalation—deintercalation. So phosphorene will not pulverize opposite to what happens in its bulk counterpart due to large volumetric expansion.

33.3.4   Diffusion Properties

For proper functioning of battery, there must be a smooth transport of Na ions and electrons between electrodes so that the ion electron would combine leading to redox reaction. The CI-NEB method helps in plotting activation energy values corresponding to the path coordinates and gives value of diffusion barrier. Na will move faster if it faces smaller diffusion barrier and vice versa. The paths identified for Na diffusion is shown below in Fig. 33.5(i). Path-I is along the armchair direction and path-II is along zigzag direction. Path II consists of four sub paths named as a, b, c, d in the direction from left to right. The path-III is the diagonal path. The activation energy plots for the corresponding paths are shown in Fig. 33.5(ii) for zigzag, Fig. 33.6 (i) for armchair and Fig. 33.6(ii) for diagonal path. The armchair and diagonal directions offer 0.526 eV and 0.525 eV energy barriers respectively. The paths a, b, c, d in zigzag direction offer 0.103 eV, 0.108 eV, 0.103 eV and 0.106 eV of energy barriers respectively. These path evaluations suggest that Na can move easily in zigzag direction as compared to armchair and diagonal direction. The minimum energy that Na needs to possess to diffuse is 0.1 eV which is quite low compared to the diffusion barriers in case of stanene, [32] germanene [32] and comparable to the diffusion barrier of $NbSe_2$,[33] VS_2,[35] and Cu_2Si [36].
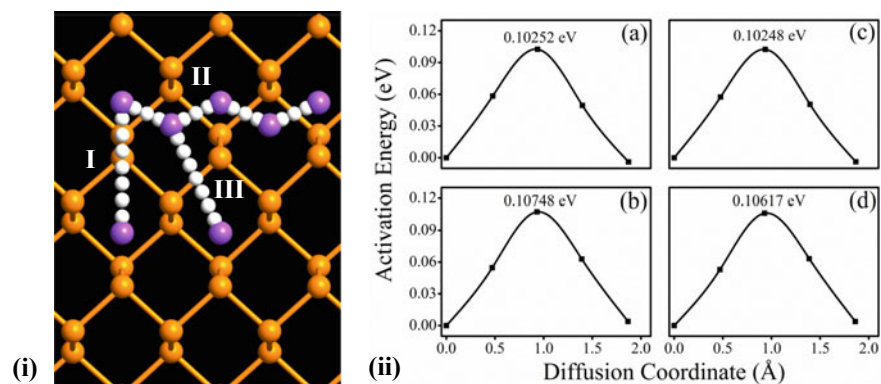
Fig. 33.5   (i) Various paths (I, II, III) of Na diffusion; (ii) Activation energy (E_a) plot along zigzag path over phosphorene surface
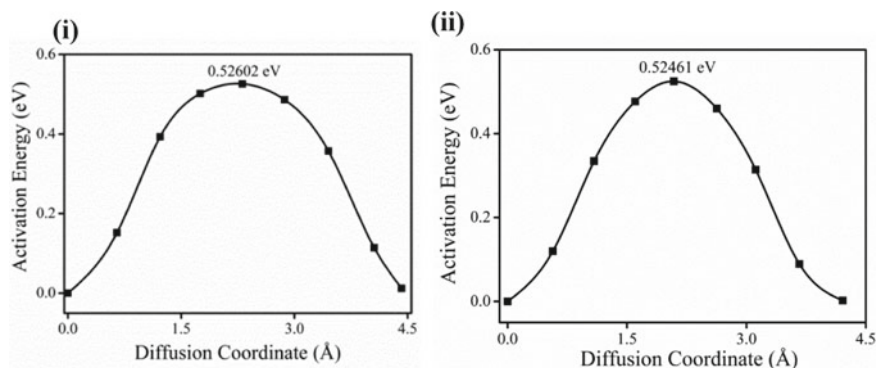
Fig. 33.6 Activation energy (E_a) plot along (i) armchair path (path I) and (ii) diagonal path (path III) over phosphorene surface

33.4 Conclusion

The Na adsorption provides major insights regarding change in phosphorene properties. The single Na adsorption can induce metallicity in phosphorene as can be seen by band structure and DOS properties. It includes significant charge transfer between Na and phosphorene. The multiple Na adsorptions provide detail about Na storage property of phosphorene and the corresponding specific capacity calculated is 315.54 mAh/g. The diffusion of Na is anisotropic in nature with activation energy of 0.5 eV in armchair and 0.1 eV in zigzag direction. Based on these extensive studies, Na storage application in Na ion batteries is probably the best predicted application for phosphorene.

References

1. A. Khandelwal, K. Mani, M. H. Karigerasi, I. Lahiri, Mater. Sci. Eng. B Solid-State Mater. Adv. Technol. **221**, 17 (2017)
2. M. Akhtar, G. Anderson, R. Zhao, A. Alruqi, J.E. Mroczkowska, G. Sumanasekera, J.B. Jasinski, Npj 2D Mater Appl. **1**, 1 (2017)
3. P. Yasaei, B. Kumar, T. Foroozan, C. Wang, M. Asadi, D. Tuschel, J.E. Indacochea, R.F. Klie, A. Salehi-Khojin, Adv. Mater. **27**, 1887 (2015)
4. Z. Guo, H. Zhang, S. Lu, Z. Wang, S. Tang, J. Shao, Z. Sun, H. Xie, H. Wang, X.F. Yu, P.K. Chu, Adv. Funct. Mater. **25**, 6996 (2015)
5. Y. Jing, X. Zhang, Z. Zhou, Wiley Interdiscip. Rev. Comput. Mol. Sci. **6**, 5 (2016)
6. S. Bagheri, N. Mansouri, E. Aghaie, Int. J. Hydrogen Energy **41**, 4085 (2016)

7. K.P.S.S. Hembram, H. Jung, B.C. Yeo, S.J. Pai, S. Kim, K.R. Lee, S.S. Han, J. Phys. Chem. C **119**, 15041 (2015)
8. J. Sun, H.W. Lee, M. Pasta, H. Yuan, G. Zheng, Y. Sun, Y. Li, Y. Cui, Nat. Nanotechnol. **10**, 980 (2015)
9. A. Yang, D. Wang, X. Wang, D. Zhang, N. Koratkar, M. Rong, Nano Today **20**, 13 (2018)
10. M. Lalitha, Y. Nataraj, S. Lakshmipathi, Appl. Surf. Sci. **377**, 311 (2016)
11. H. ping Zhang, A. Du, Q. Bin Shi, Y. Zhou, Y. Zhang, and Y. Tang, J. CO2 Util. **24**, 463 (2018)
12. H. Ping Zhang, W. Hu, A. Du, X. Lu, Y. Ping Zhang, J. Zhou, X. Lin, Y. Tang, Appl. Surf. Sci. **433**, 249 (2018)
13. W. Zhou, H. Zou, X. Xiong, Y. Zhou, R. Liu, F. Ouyang, Phys. E Low-Dimensional Syst. Nanostruct. **94**, 53 (2017)
14. C. Chowdhury, S. Karmakar, A. Datta, ACS Energy Lett. **1**, 253 (2016)
15. A. Opitz, P. Badami, L. Shen, K. Vignarooban, A.M. Kannan, Renew. Sustain. Energy Rev. **68**, 685 (2017)
16. M. Armand, J.M. Tarascon, Nature **451**, 652 (2008)
17. J.B. Goodenough, Y. Kim, Chem. Mater. **22**, 587 (2010)
18. J.M. Tarascon, Nat. Chem. **2**, 510 (2010)
19. X. Sun, H. Hao, F. Zhao, Z. Liu, Environ. Sci. Technol. **52**, 2827 (2018)
20. M.D. Slater, D. Kim, E. Lee, C.S. Johnson, Adv. Funct. Mater. **23**, 947 (2013)
21. P.K. Nayak, L. Yang, W. Brehm, P. Adelhelm, Angew. Chemie - Int. Ed. **57**, 102 (2018)
22. J.Y. Hwang, S.T. Myung, Y.K. Sun, Chem. Soc. Rev. **46**, 3529 (2017)
23. S.W. Kim, D.H. Seo, X. Ma, G. Ceder, K. Kang, Adv. Energy Mater. **2**, 710 (2012)
24. Q. Bai, L. Yang, H. Chen, Y. Mo, Adv. Energy Mater. **8**, 1 (2018)
25. M. Lao, Y. Zhang, W. Luo, Q. Yan, W. Sun, S.X. Dou, Adv. Mater. **29** (2017)
26. Y. Okamoto, J. Phys. Chem. C **118**, 16 (2014)
27. Y. Wen, K. He, Y. Zhu, F. Han, Y. Xu, I. Matsuda, Y. Ishii, J. Cumings, C. Wang, Nat. Commun. **5**, 1 (2014)
28. D.P. Divincenzo, E.J. Mele, Phys. Rev. B **32**, 2538 (1985)
29. L. David, R. Bhandavat, G. Singh, D. E. T. Al, 1 (2014)
30. Y.X. Wang, S.L. Chou, H.K. Liu, S.X. Dou, Carbon N. Y. **57**, 202 (2013)
31. R. Sun, Q. Wei, Q. Li, W. Luo, Q. An, J. Sheng, D. Wang, W. Chen, L. Mai, A.C.S. Appl, Mater. Interfaces **7**, 20902 (2015)
32. B. Mortazavi, A. Dianat, G. Cuniberti, T. Rabczuk, Electrochim. Acta **213**, 865 (2016)
33. Y. Lv, X., Wei, W., Sun, Q., Huang, B., Dai, J. Phy. D Appl. Phys. **50**, 235501 (2017)
34. Y. Yu, Z. Guo, Q. Peng, J. Zhou, Z. Sun, J. Mater. Chem. A **7**, 12145 (2019)
35. D.B. Putungan, S.H. Lin, J.L. Kuo, A.C.S. Appl, Mater. Interfaces **8**, 18754 (2016)
36. X. Sun, S. Wu, K.N. Dinh, Z. Wang, J. Solid State Chem. **274**, 265 (2019)
37. (n.d.).
38. W. Hohenberg, P., Kohn, Phys. Rev. **136**, B864 (1964)
39. L. J. Kohn, W., Sham, Phys. Rev. **140**, A1133 (1965).
40. M. Perdew, J.P., Burke, K., Ernzerhof, Phys. Rev. Lett. **77**, 3865 (1996)
41. S. Grimme, J. Comput. Chem. **27**, 1787 (2006)
42. P. Upadhyay, S., Srivastava, Mater. Chem. Phys. **241**, 122381 (2020)
43. Y. Zhou, M. Zhao, Z.W. Chen, X.M. Shi, Q. Jiang, Phys. Chem. Chem. Phys. **20**, 30290 (2018)
44. H. Henkelman, G., Uberuaga, B.P., Jónsson, J. Chem. Phys **113**, 9901 (200)
45. H. Henkelman, G., Jónsson, J. Chem. Phys. **113**, 9978 (2000)
46. A. Brown, S. Rundqvist, Acta Crystallogr. **19**, 684 (1965)
47. A. Sibari, A. El Marjaoui, M. Lakhal, Z. Kerrami, A. Kara, M. Benaissa, A. Ennaoui, M. Hamedoun, A. Benyoussef, O. Mounkachi, Sol. Energy Mater. Sol. Cells **180**, 253 (2018)
48. A. Carvalho, M. Wang, X. Zhu, A. S. Rodin, H. Su,, A.H. Castro Neto, Nat. Rev. Mater. **1**, (2016)
49. B. Huang, Z. Pan, X. Su, L. An, J. Power Sources **395**, 41 (2018)

Chapter 34
Plasmonic Probing of Refractive Index Variations Using MWCNT@Ta$_2$O$_5$ Core–shell Nanoparticles

Rana Tabassum and Ravi Kant

Abstract Refractive index is an extremely important optical variable commonly used for material characterization as well as to monitor numerous hysic–chemical and biological processes. In this work, the implementation of a nanomaterial based blueprint to measure refractive index of solutions has been described utilizing core–shell nanoparticles incorporating multi–walled carbon nanotubes (MWCNTs) as core encompassed with a surrounding shell of tantalum (v) oxide (Ta$_2$O$_5$). The study benefits from the well–established significance of MWCNTs and Ta$_2$O$_5$ in the sensor technology. The MWCNTs@Ta$_2$O$_5$ core–shell nanoparticles have been synthesized in solution phase using pulsed laser ablation technique taking sucrose solutions of different refractive index values in the range 1.33–1.36 as the synthesizing solvent. The study of absorption spectra of these core–shell nanoparticles synthesized in solvents having different refractive index values reveals a red shift in the peak absorption wavelength. The refractive index sensitivity of core–shell nanoparticles is found to be superior to various earlier published reports, which supports their utility as refractive index sensing framework. In this perspective, this work widens the scope of nanoparticles for refractive index monitoring applications at both laboratory and industrial scales.

34.1 Introduction

Refractive index is one of the most significant properties of a material which is used to decide its optical behaviour and the ensuing characterization. An understanding of the refractive index of a material is crucial from the perspective of designing optical systems, for instance, sensors, photodetectors and optical communication devices. Moreover, keeping a track on the variations in the refractive index of solutions turn

R. Tabassum (✉)
Centre for Nanoscience and Nanotechnology, Jamia Millia Islamia (A Central University), New Delhi 110025, India
e-mail: rtabassum1@jmi.ac.in

R. Kant
Department of Physics, Indian Institute of Technology Delhi, New Delhi 110016, India

out to be important for monitoring various biological processes, clinical analyses and pharmaceutical procedures [1–3]. Further, an optical sensor is characterized by studying its response towards solutions of different refractive indices, which is subsequently used for its calibration. The indicated points outline the necessity for the development of a sensitive and analytically powerful strategy to quantify refractive index and study its variations in physico–chemical and biological processes.

Nanostructured materials of different shapes including particles, rods, wires, tubes, fibers, flakes and flowers among others have been extensively employed for a variety of applications in myriad scientific and industrial processes. Nanostructured materials have aspect ratio higher than that of bulk nanolayers, and therefore, turn out to be immensely important for a variety of applications, in particular, sensing [4–7]. This follows from the fact that the higher aspect ratio of nanostructured materials significantly enhances the extent of interaction between them and the analyte to be sensed. This results in the generation of an improved sensing signal which brings about better sensing performance manifested in terms of higher sensitivity and limit of detection. From that perspective, core–shell nanoparticles present themselves as highly versatile and beneficial nanostructured platform for a variety of sensing applications. As the name suggests, core–shell nanoparticles comprise of a central core of one material surrounded by a spherical shell of another material, and thus, combine the properties of both the constituent materials to evolve into a more useful nanostructured material with tailored properties. These core–shell nanoparticles are frequently employed for sensing applications of a variety of physical parameters, chemicals and biological analytes utilizing different sensing platforms [8]. In addition to this, core–shell nanoparticles of different materials are being used for a lot of other exciting applications, such as solar energy utilization [9], catalysis [10] and bioimaging applications [11].

In this work, we report the synthesis of core–shell nanoparticles comprising of multi–walled carbon nanotubes (MWCNTs) as central core having a metal oxide shell of tantalum (v) oxide (Ta_2O_5) configured as MWCNTs@Ta_2O_5 and investigate their application as refractive index sensing platform. Both MWCNTs and Ta_2O_5 are frequently used for sensing applications in a wide variety of areas [8, 12–15]. The core–shell nanoparticles have been synthesized using pulsed laser ablation technique in sequential manner. Here, the laser ablation of MWCNTs entities in glucose solutions of varying refractive index values is carried out initially. Using this ablated solution of MWCNTs entities as the solvent, the laser ablation of Ta_2O_5 is carried out so that Ta_2O_5 particles accumulate around the MWCNTs entities in the form of a shell, resulting in the formation of MWCNTs@Ta_2O_5 core–shell nanoparticles. The MWCNTs@Ta_2O_5 core–shell nanoparticles have been synthesized using sucrose solutions of different refractive index values in the range 1.33–1.36. The absorption spectra of all of these synthesized solutions of MWCNTs@Ta_2O_5 core–shell nanoparticles have been studied using UV–Visible spectroscopy. A red shift of 6 nm in the peak absorption wavelength is obtained, when the refractive index of synthesizing solvent is varied from 1.33 to 1.36. By extracting the values of peak absorption wavelength and plotting them as a function of refractive index, the calibration curve

of the MWCNTs@Ta$_2$O$_5$ core–shell nanoparticles as refractive index sensing framework has been plotted. Thereafter, their analytical performance for refractive index monitoring applications is figured out by calculating the refractive index sensitivity.

34.2   Experimental Details

Pulsed laser ablation technique was used to synthesize MWCNTs@Ta$_2$O$_5$ core–shell nanoparticles in aqueous medium. In addition to facilitating the synthesis of well–dispersed nanoparticles having high degree of chemical purity and stability, the laser ablation technique enables an efficient control over the size and dimensionality of the nanostructured entities to achieve the desired size distribution. Further, to synthesize core–shell nanoparticles using this technique, pulsed laser ablation is carried out in two steps in a sequential manner. First, the laser ablation of the entity comprising of the core is carried out in deionizing water/buffer solution. Thereafter, using this solution as the solvent, the laser ablation of the second material constituting the shell is performed. In this way, core–shell nanostructures are synthesized using sequential pulsed laser ablation technique [8].

To initiate the synthesis process of MWCNTs@Ta$_2$O$_5$ core–shell nanoparticles using pulsed laser ablation technique, first, the suspension of MWCNTs of a definite amount was taken in deionized water in a beaker. Thereafter, light from Q–switched Nd:YAG laser ($\lambda = 1.064$ μm) was focused on this suspension of MWCNTs using a convex lens to initiate their ablation and consequently obtain laser–ablated MWCNTs entities. Afterwards, using this nano–colloidal suspension of laser–ablated MWCNTs as solvent, the laser ablation of Ta$_2$O$_5$ was carried out in an identical manner. During this ablation process, Ta$_2$O$_5$ particles started absorbing laser light, the emission of which resulted in the accumulation and consequent adsorption of the Ta$_2$O$_5$ particles around the MWCNTs entities forming a shell around them. These emitted Ta$_2$O$_5$ entities get adsorbed on the pre–prepared MWCNTs nanostructures forming a shell around them. With this, the laser synthesis process of MWCNTs@Ta$_2$O$_5$ core–shell nanoparticles is accomplished. These core–shell nanoparticles were filtered through nano–sized filter paper to remove any traces of impurities. To investigate their refractive index sensing properties, MWCNTs@Ta$_2$O$_5$ core–shell nanoparticles were synthesized using glucose solutions of varying refractive index values in an identical manner.

34.3   Results and Discussion

The core–shell nanoparticles of MWCNTs@Ta$_2$O$_5$ synthesized in glucose solutions of different refractive index values using sequential pulsed laser ablation technique were examined as refractive index sensing platform through study of their absorption

Fig. 34.1 Absorbance spectra of MWCNTs@Ta$_2$O$_5$ core–shell nanoparticles prepared in sucrose solutions of different refractive indices as solvent in the range 1.33–1.36
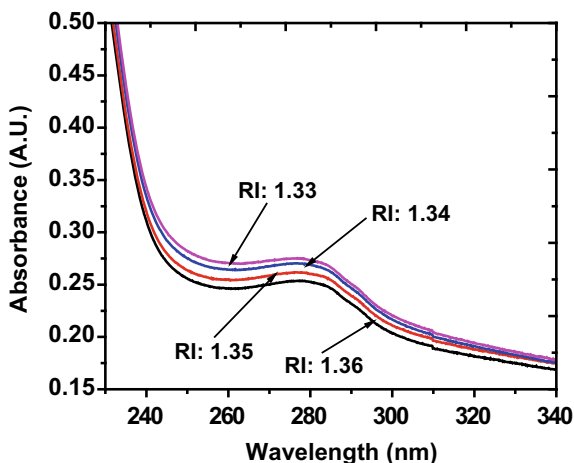
spectra. Figure 34.1 shows the absorption spectra of the MWCNTs@Ta$_2$O$_5$ core–shell nanoparticles obtained using UV–Vis spectrophotometry for different refractive index of the synthesizing solvent ranging from 1.33 to 1.36. The refractive index of the synthesizing solvent has been varied in steps of 0.01 to incorporate even minute variations in the refractive index. As is observed from Fig. 34.1, the absorption spectra move from lower to higher wavelength regime as the refractive index of synthesizing solvent is varied from 1.33 to 1.36, i.e., a red shift in the absorption spectra is attained.

To provide a clearer view of shift attained in peak absorption wavelength and deduce the analytical performance of the MWCNTs@Ta$_2$O$_5$ core–shell nanoparticles as refractive index sensing platform, numeric values of the peak absorption wavelength were extracted from the absorption spectra of the core–shell nanoparticles shown in Fig. 34.1. These values were plotted as a function of the refractive index of the synthesizing solvent as displayed in Fig. 34.2 to deduce the calibration plot of the sensing layout. As is evident from Fig. 34.2, a red shift of approximately 6 nm is attained in peak absorption wavelength as the refractive index of the synthesizing solvent is varied from 1.33 to 1.36. The standard deviation in the measurement of peak absorption wavelength has been incorporated by the inclusion of error bars in Fig. 34.2. The error bars have been added using a method described in [4, 8]. Further, the calibration curve of the refractive index sensing framework constituted by MWCNTs@Ta$_2$O$_5$ core–shell nanoparticles. In depicted Fig. 34.2 follows the following equation

$$\lambda_{abs}(nm) = -9820.30 + 14806.55(RI) - 5425(RI)^2 \qquad (34.1)$$

which is obtained by fitting the data points corresponding to peak absorption wavelengths via a polynomial function. The significance of (34.1) is that it can be used to ascertain the value of peak absorption wavelength at an unknown refractive index value.

Fig. 34.2 Plot showing variation of peak absorption wavelength extracted from absorption spectra of MWCNTs@Ta_2O_5 core–shell nanoparticles as a function of refractive index of the synthesizing solvent
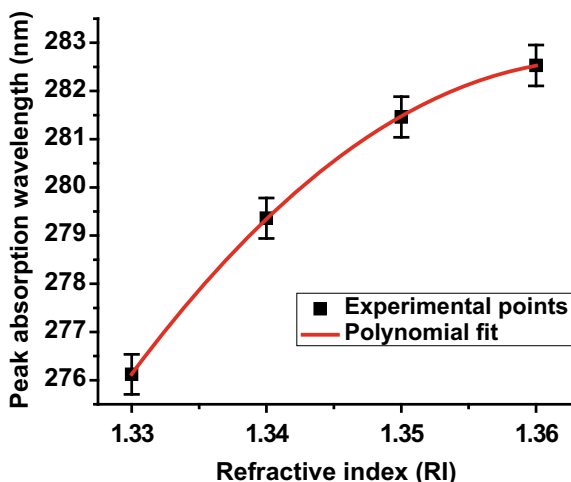
The refractive index sensitivity of the MWCNTs@Ta_2O_5 core–shell nanoparticles were determined by differentiating the equation of the calibration curve with respect to refractive index [12, 15]. The values of refractive index sensitivity obtained in this manner are plotted in Fig. 34.3 as a function of refractive index of the synthesizing solvent. It is observed from Fig. 34.3 that the refractive index sensitivity of the MWCNTs@Ta_2O_5 core–shell nanoparticles decreases with an increase in refractive index of the synthesizing solvent. The maximum value of refractive index sensitivity attained is 375.42 nm/RIU at a refractive index value of 1.33.

The achieved value of refractive index sensitivity is compared with some of the earlier reported studies utilizing different sensing methodologies. This comparative overview is presented in Table 34.1.

Fig. 34.3 Variation of refractive index sensitivity of MWCNTs@Ta_2O_5 core–shell nanoparticles as a function of refractive index of the synthesizing solvent
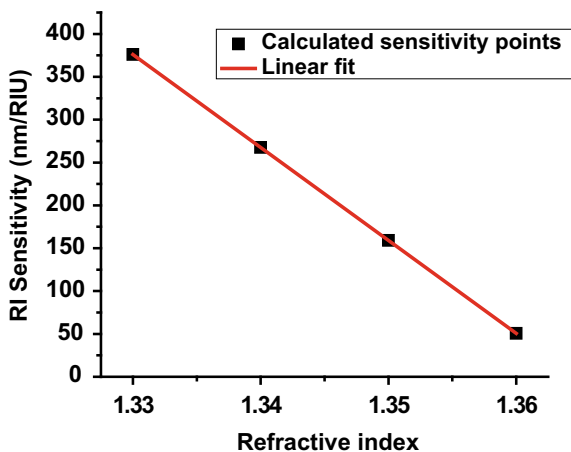
Table 34.1 Comparison of refractive index sensitivity achieved in present study with several earlier published studies

Sensing scheme	RI sensitivity (nm/RIU)	Selected RI range	Reference
Plasmon–based sensor using immobilized ensembles of Au nanospheres	200	1.33–1.36	[16]
S–tapered shaped fiber with Ag mirror on end facet	268.8	1.332–1.387	[2]
Au nanorods–chip based sensor	297	1.335–1.365	[17]
Chiral plasmonic nanostructures and circular dichroism	310	1.32–1.44	[18]
MWCNT@Ta$_2$O$_5$ core–shell nanoparticles	372	1.33–1.36	This work

From Table 34.1, it is clear that the refractive index sensitivity of present study is better as compared to several of the earlier reported studies. This highlights the significance of the present study for refractive index monitoring applications.

34.4 Conclusion

To conclude, a successful attempt of monitoring refractive index variations in liquid medium has been carried out using core–shell nanoparticles constituted by MWCNTs@Ta$_2$O$_5$. The MWCNTs@Ta$_2$O$_5$ core–shell nanoparticles have been synthesized using pulsed laser ablation technique in sequential manner where first the laser ablation of MWCNTs (constituting the core) has been carried out followed by laser ablation of Ta$_2$O$_5$ which accumulate around MWCNTs in the form of surrounding shell to constitute MWCNTs@Ta$_2$O$_5$ core–shell nanoparticles. Their refractive index sensing properties has been explored through study of their absorption spectra obtained for different refractive index values in the range 1.33–1.36 of the synthesizing solvent. The refractive index sensitivity of MWCNTs@Ta$_2$O$_5$ core–shell nanoparticles follows a declining trend with increase in refractive index of the synthesizing solvent with maximum value achieved being 375.42 nm/RIU at a refractive index value of 1.33. The reported results support the promising utility of MWCNTs@Ta$_2$O$_5$ core–shell nanoparticles as an efficient platform for refractive index sensing applications.

References

1. D. Wang, J. Tong, B. Jin, Y. Wang, M. Zhang, Optical fiber liquid refractive index sensor based on Fresnel reflection of anti–Stokes light. Sens. Actuators, A **279**, 140–144 (2018)
2. C. Chen, R. Yang, X.-Y. Zhang, W.-H. Wei, Q. Guo, X. Zhang, Y.-Q. Ning, Y.-S. Yu, Compact refractive index sensor based on an S–tapered fiber probe. Opt. Mater. Express **8**(4), 919–925 (2018)
3. Y.C. Tan, W.B. Ji, V. Mamidala, K.K. Chow, S.C. Tjin, Carbon–nanotube–deposited long period fiber grating for continuous refractive index sensor applications. Sens. Actuators, B **196**, 260–264 (2014)
4. R. Kant, R. Tabassum, B.D. Gupta, Integrating nanohybrid membranes of reduced graphene oxide: chitosan: silica sol gel with fiber optic SPR for caffeine detection. Nanotechnology **28**, 195502 (2017)
5. R. Kant, R. Tabassum, B.D. Gupta, Xanthine oxidase functionalized Ta_2O_5 nanostructures as a novel scaffold for highly sensitive SPR based fiber optic xanthine sensor. Biosens. Bioelectron. **99**, 637–645 (2018)
6. R. Kant, B.D. Gupta, Recent advances in surface plasmon resonance based fiber optic chemical and biosensors utilizing bulk and nanostructures. Opt. Laser Technol. **101**, 144–161 (2018)
7. D. Zhang, C. Zhang, J. Liu, Q. Chen, X. Zhu, C. Liang, Carbon–encapsulated metal/metal carbide/metal oxide core–shell nanostructures generated by laser ablation of metals in organic solvents. ACS Appl. Nanomater. **2**, 28–39 (2019)
8. R. Tabassum, R. Kant, Laser–ablated core–shell nanostructures of MWCNT@Ta_2O_5 as plasmonic framework for implementation of highly sensitive refractive index sensor. Sens. Actuators, A **309**, 112028 (2020)
9. W. Li, A. Elzatahry, D. Aldhayan, D. Zhao, Core–shell structured titanium dioxide nanomaterials for solar energy utilization. Chem. Soc. Rev. **47**, 8203–8237 (2018)
10. Y. Kim, R. Ma, D.A. Reddy, T.K. Kim, Liquid–phase pulsed laser ablation synthesis of graphitized carbon–encapsulated palladium core–shell nanospheres for catalytic reduction of nitrobenzene to aniline. Appl. Surf. Sci. **357**, 2112–2120 (2015)
11. N. Venkatesha, Y. Qurishi, H.S. Atreya, C. Srivastava, ZnO coated $CoFe_2O_4$ nanoparticles for multimodal bio–imaging. RSC Adv. **6**, 18843–18851 (2016)
12. R. Kant, R. Tabassum, B.D. Gupta, A highly sensitive and distinctly selective d–sorbitol biosensor using SDH enzyme entrapped Ta_2O_5 nanoflowers assembly coupled with fiber optic SPR. Sens. Actuators, B **242**, 810–817 (2017)
13. B. Wang, K. Ni, P. Wang, Q. Ma, W. Tian, L. Tan, A CNT–coated refractive index sensor based on Michelson interferometer with thin–core fiber. Opt. Fiber Technol. **46**, 302–305 (2018)
14. R. Kant, B.D. Gupta, Fiber–optic SPR based acetylcholine biosensor using enzyme functionalized Ta_2O_5 nanoflakes for Alzheimer's disease diagnosis. IEEE J. Lightwave Technol. **36**, 4018–4024 (2018)
15. R. Kant, Surface plasmon resonance based fiber–optic nanosensor for the pesticide fenitrothion utilizing Ta_2O_5 nanostructures sequestered onto a reduced graphene oxide matrix. Microchim. Acta **187**(8), 11p (2020)
16. B. Doherty, M. Thiele, S. Warren-Smith, E. Schartner, H. Ebendorff-Heidepriem, W. Fritzsche, M.A. Schmidt, Plasmonic nanoparticle–functionalized exposed core fiber–an optofluidic refractive index sensing platform. Opt. Lett. **42**(21), 4395–4398 (2017)
17. L.P.F. Peixoto, J.F.L. Santos, G.F.S. Andrade, Plasmonic nanobiosensor based on Au nanorods with improved sensitivity: a comparative study for two different configurations. Anal. Chim. Acta **1084**, 71–77 (2019)
18. Y. He, K. Lawrence, W. Ingram, Y. Zhao, Circular dichroism based refractive index sensing using chiral metamaterials. Chem. Commun. **52**, 2047–2050 (2016)

Chapter 35
Towards Detection of Flavonoid Quercetin Using Ta$_2$O$_5$ Nanoparticles Embedded rGO and Chitosan Matrix

Ravi Kant and Rana Tabassum

Abstract Quercetin is a flavonoid which forms a chief constituent of various fruits and beverages. It plays a pivotal role in human body by acting as an antioxidant. Its excess, however, can cause kidney problems and DNA impairment. This study outlines a nanocomposite based approach to detect and quantify quercetin making use of tantalum (v) oxide (Ta$_2$O$_5$) nanoparticles and reduced graphene oxide (rGO) embedded in supporting network of biopolymer chitosan as the sensing framework, which has been synthesized via chemical route. The absorption spectra obtained for various concentration values of quercetin ranging from 1–10 µM have been used to characterize the sensing framework. A red shift in the peak absorption wavelength has been observed for a change in quercetin concentration from 1 to 10 µM, from which the sensitivity of the sensing network has been determined. Limit of detection of the nanocomposite sensing arrangement is calculated to be 280 nM. The proposed sensing strategy offers synthesis and operational simplicity. In view of these advantages, the attained analytical parameters favours the applicability of the nanocomposite arrangement for quercetin detection in food and medicinal samples.

35.1 Introduction

Quercetin is a naturally occurring flavonoid which is found abundantly in a variety of herbs, fruits and vegetables [1, 2]. Chemically, quercetin is represented as 2–(3,4–dihydroxyphenyl)–3,5,7–trihydroxychromen–4–one. It possesses superior anti–oxidant properties, and therefore, is an important compound for medicine and nutrition [3]. It has been found in several studies that quercetin suppresses the growth of cancerous cells. It, thus, exhibits anticancer activities by acting as an efficient scavenger of radicals against oxidative cell damage [4]. Further, quercetin is found to

R. Kant
Department of Physics, Indian Institute of Technology, Delhi, India

R. Tabassum (✉)
Centre for Nanoscience and Nanotechnology, Jamia Millia Islamia (A Central University), New Delhi, Delhi 110025, India
e-mail: rtabassum1@jmi.ac.in

347

manifest anti–inflammatory and anti–allergic properties in addition to its role in physiological systems such as cardiovascular protection [5]. However, an excess amount of quercetin in human body can result in various physiological disorders such as kidney problems and DNA impairment [5], which highlights the significance of sensitive, swift and accurate detection of quercetin. Generally, the detection of quercetin is carried out by electrochemical, spectrophotometry and chromatographic techniques. These methods, however, suffer from various drawbacks such as involvement of harsh and poisonous chemicals and use of expensive instrumentation. Moreover, these methods turn out to be time consuming and require highly skilled personnel to carry out experimentation and data analysis. The indicated facts substantiate the necessity for the development of a simple, sensitive and cost–effective detection strategy for quercetin.

In recent years, nanostructured materials of a variety of shapes including particles, rods, wires, tubes, flakes and flowers have piqued considerable attention in numerous scientific and industrial processes due to their amazing properties which make them immensely suitable for functionalization of biomolecules for sensing applications [6–9]. Such nanomaterials manifest higher surface–to–volume ratio in comparison to bulk nanolayers. This significantly increases the extent of interaction between the functionalized nanomaterial and the sensing analyte, and thus, culminates in the generation of an improved sensing signal. This results in considerable improvement in the sensing performance.

In this work, we present a nanomaterial–based protocol for the detection of quercetin using sensing platform involving tantalum (v) oxide (Ta_2O_5) nanoparticles embedded in a polymeric and supporting network of reduced graphene oxide (rGO) and chitosan. Ta_2O_5 is a high index metal oxide which is frequently used for sensing of gases, chemicals and biomolecules [7–11]. rGO exhibits high surface–to–volume ratio and provides an excellent interface for functionalization of biomolecules, which turn out to be immensely beneficial for biosensor implementation. The significance of rGO in detection of quercetin has been established through various studies reported in the literature [1, 5, 12]. Biopolymer chitosan provides supporting network and mechanical strength to the sensing arrangement [13–15]. The sensing network is synthesized using chemical method and its quercetin sensing properties are investigated through the study of absorption spectra obtained corresponding to different concentrations of quercetin. A red shift of ~ 64 nm in the peak absorption wavelength is obtained when the concentration of quercetin is varied from 1–10 μM. By extracting the peak absorption wavelength values and plotting them as a function of quercetin concentration, the calibration curve of the sensing framework is deduced and its sensitivity towards quercetin detection is explored.

35.2   Experimental

The sensing platform for quercetin detection comprises of Ta$_2$O$_5$ nanoparticles embedded in a layer of rGO and chitosan matrix which was synthesized using chemical method. First, Ta$_2$O$_5$ nanoparticles were synthesized using chemical method as described in [16]. In a common synthesis process, first, 3.0 g of Ta$_2$O$_5$ powder was grinded in a mortar agate for about 10 min. The obtained Ta$_2$O$_5$ powder was dissolved in 100 ml deionized water under constant stirring. While being stirred, 10 ml of 30% H$_2$O$_2$ solution was added dropwise to Ta$_2$O$_5$ solution. The addition of H$_2$O$_2$ solution was performed under conditions of continuous stirring at 300 rpm and heating at a temperature of 60 ℃ for 6 h. Further, few drops of sodium hydroxide were also added to this solution in order to maintain a constant pH of the resulting solution. The solution thus obtained was ultrasonicated for approximately 30 min which represented the solution of Ta$_2$O$_5$ nanoparticles.

Nano–colloidal suspension of rGO was prepared by dispersing a calculated amount of GO in 100 ml deionized water. This GO suspension was ultrasonicated for 10 min. The rGO suspension was obtained from the nano–colloidal suspension of GO by reducing it chemically by treatment with hydrazine hydrate. Thereafter, the obtained rGO suspension was added to the chitosan solution prepared in acetate buffer. This resulted in the synthesis of rGO–chitosan matrix. The solution of Ta$_2$O$_5$ nanoparticles prepared earlier was added to this nano–colloidal suspension of rGO and chitosan while being stirred at 200 rpm on a magnetic stirrer for 3 h. This resulted in the encapsulation of Ta$_2$O$_5$ nanoparticles into the rGO and chitosan matrix. The resulting solution was filtered using filer paper having nano–sized pores to remove any impurity left during the synthesis process. The obtained filtrate represented the solution of Ta$_2$O$_5$ nanoparticles embedded in rGO and chitosan matrix which is used as sensing framework for quercetin detection in this study. The entire synthesis process of Ta$_2$O$_5$ nanoparticles embedded in rGO and chitosan matrix is summarized in schematic form in Fig. 35.1.

35.3   Results and Discussion

The performance of Ta$_2$O$_5$ nanoparticles embedded in rGO and chitosan matrix as quercetin detection layout was examined through the study of UV–Visible absorption spectra. For this purpose, quercetin solutions of different concentrations, namely, 1, 2, 5 and 10 μM were prepared by dissolving appropriate amount of quercetin in phosphate buffer. The absorption spectra of all these quercetin samples taken in Ta$_2$O$_5$ nanoparticles embedded rGO and chitosan matrix solution are shown in Fig. 35.2. The occurrence of peak in the absorption spectrum displayed in Fig. 35.2 confirms the reaction between quercetin and the sensing framework comprising of Ta$_2$O$_5$ nanoparticles embedded in rGO and chitosan matrix. The wavelength at which maximum
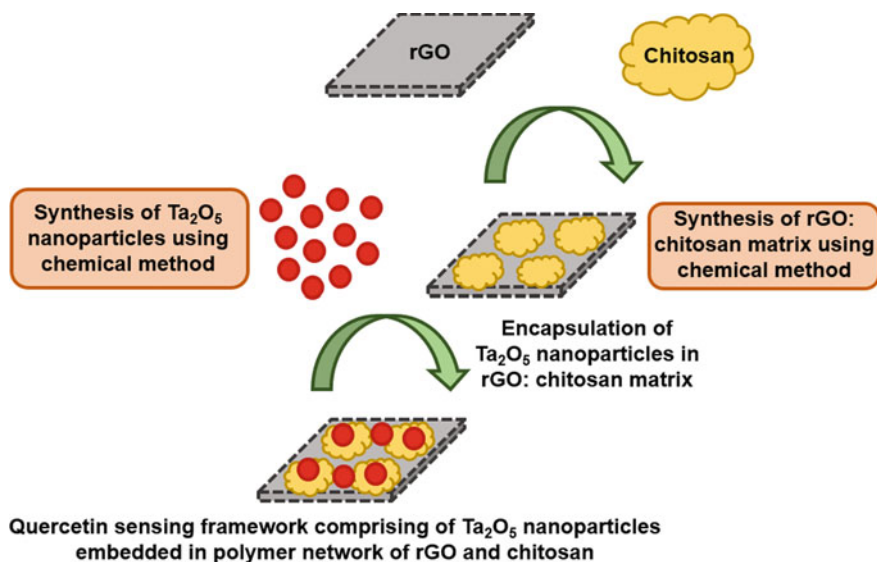
Fig. 35.1 Schematic representing the synthesis process of Ta_2O_5 nanoparticles embedded in rGO and chitosan matrix as quercetin detection layout using chemical method

Fig. 35.2 Absorption spectra for quercetin solutions having concentrations in the range 1–10 μM obtained using Ta_2O_5 nanoparticles embedded rGO and chitosan matrix as the sensing platform
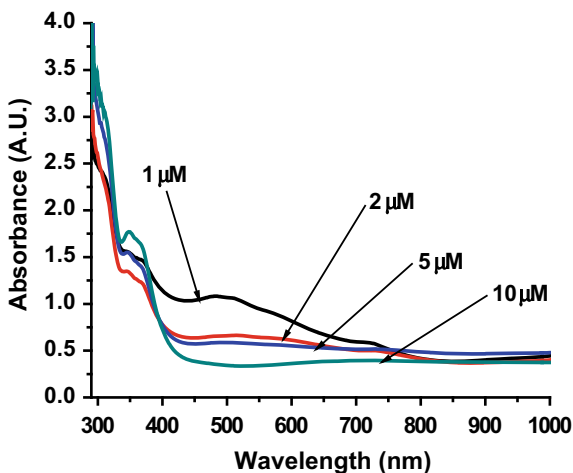
absorbance in the absorption spectrum is observed is termed as the peak absorption wavelength. It is observed from Fig. 35.2 that the peak absorption wavelength corresponding to different concentrations of quercetin shift from lower concentration region to that of higher concentration region. This implies that a red shift in the peak absorption wavelength is achieved as the concentration of quercetin is varied from 1 to 10 μM.

Fig. 35.3 Calibration plot showing the variation of peak absorption wavelength as a function of quercetin concentration
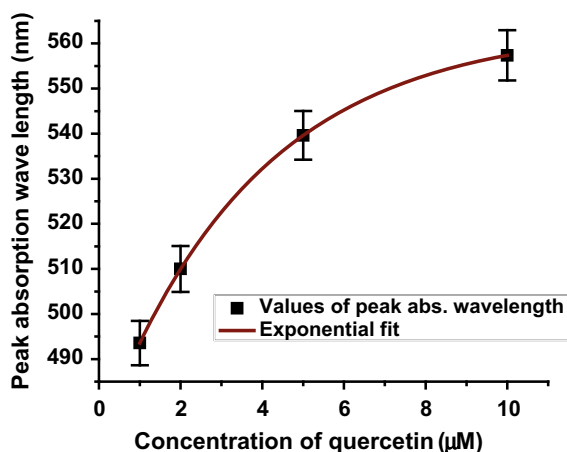
To provide a clearer view of the attained shift in peak absorption wavelength and to quantitatively gauge the sensing performance of Ta$_2$O$_5$ nanoparticles embedded rGO and chitosan matrix for quercetin detection, the values of peak absorption wavelength were extracted from the absorption spectra of Fig. 35.2 and plotted against the quercetin concentration. This plot is displayed in Fig. 35.3. In this figure, the experimentally obtained points of peak absorption wavelengths corresponding to different concentrations of quercetin are represented by solid squares. As is evident from Fig. 35.3, the peak absorption wavelength increases with an increase in the concentration of quercetin. This is in accordance with the observed red shift in peak absorption wavelength in the absorption spectra of Fig. 35.2. Moreover, the amount of this red shift is ascertained to be 64 nm.

The impact of statistical variation in the measurement of peak absorption wavelength is incorporated by plotting error bars in Fig. 35.3 using a method described in [9, 13]. Further, the data points corresponding to peak absorption wavelengths (λ_{abs}) are fitted using the following equation

$$\lambda_{abs}(nm) = 563.693 - 91.635 \times \exp(-0.2672 \times Conc.(\mu M)) \qquad (35.1)$$

where *'Conc.'* represents the concentration of quercetin in μM. The (35.1) is referred to as the calibration equation of the quercetin sensing framework constituted by Ta$_2$O$_5$ nanoparticles embedded rGO and chitosan matrix. The utility of the calibration equation follows from the fact that it can be used to estimate the value of peak absorption wavelength at an unknown concentration of quercetin. Moreover, the mathematical differentiation of the calibration equation is used to determine the sensitivity of the sensing platform under consideration [8, 9].

Fig. 35.4 Variation of sensitivity of Ta_2O_5 nanoparticles embedded rGO and chitosan matrix as quercetin sensing platform as a function of the concentration of quercetin
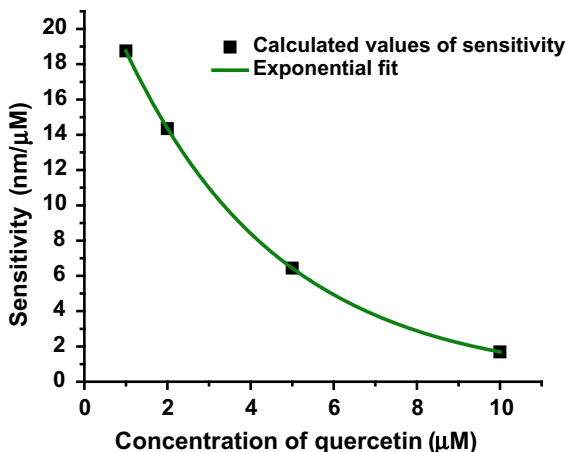
The sensitivity of Ta_2O_5 nanoparticles embedded rGO and chitosan matrix as quercetin sensing framework was determined by differentiating the calibration equation described by (35.1). The calculated values of sensitivity are plotted as a function of quercetin concentration in Fig. 35.4.

It may be noted that since the calibration plot follows an exponential trend, its differentiation leading to the determination of sensitivity also results in an exponential equation given by

$$Sensitivity \ (nm/\mu M) = 24.485 \times \exp(-0.267 \times Conc.(\mu M)) \qquad (35.2)$$

As evident from Fig. 35.4, the sensitivity of Ta_2O_5 nanoparticles embedded rGO and chitosan matrix as quercetin sensing framework decreases with an increase in the concentration of quercetin. This implies that the sensing framework is well–suited for lower concentrations of quercetin. This supports the applicability of the nanostructured sensing framework for quercetin detection in various food and medicinal samples, where the concentration of quercetin is generally low.

Another important performance parameter, limit of detection (LOD) of the nanostructured sensing framework is calculated using the formula [16, 17]

$$LOD = \frac{\Delta\lambda}{S_{C=\min}} \qquad (35.3)$$

where, $\Delta\lambda$ represents the standard deviation in the measurement of peak absorption wavelength and $S_{C=min}$ represents the sensitivity near minimum concentration of the analyte being investigated. For the present case, $\Delta\lambda$ (as calculated from Fig. 35.3) comes out to be 5.251 nm, and $S_{C=min}$ is determined to be 18.75 nm/μM from Fig. 35.4. These values result in an LOD of 280 nM for quercetin using the nanostructured sensing framework constituted by Ta_2O_5 nanoparticles embedded rGO and

Table 35.1 Comparative overview of performance parameters of the proposed nanostructured sensing layout comprising of Ta_2O_5 nanoparticles embedded in rGO and chitosan matrix with several other studies published earlier

Sensing scheme	Working range	LOD	Reference
Electrochemical based on graphene	10–100 μmol.L^{-1}	3.6 nmol.L^{-1}	[1]
MIP and electropolymerization of poly (para–aminobenzoic acid) on Pd NP–porous graphene–CNT composite	0.01–0.50 μM	5.0 nM	[18]
Electrochemical using MIP and nanohybrid modified electrode	10.5–700 μM	0.06 μM	[19]
Electrochemical based on graphene quantum dot/Au NP nanocomposite	0.01–6.0 μM	2.0 nM	[20]
Ta_2O_5 nanoparticles embedded in rGO and chitosan matrix	1.0–10 μM	280 nM	This study

chitosan matrix. The achieved LOD value is compared with some of the earlier reported LOD values utilizing a variety of sensing techniques in Table 35.1.

From Table 35.1, it may be noted that the LOD value for quercetin achieved in this study stands a par with the commonly used sensing strategies. This supports the promising utility of the Ta_2O_5 nanoparticles embedded rGO and chitosan matrix as sensing layout for quercetin sensing applications in commercial food and medicinal samples.

35.4 Conclusion

To conclude, this study reports the chemical synthesis of Ta_2O_5 nanoparticles embedded in rGO and chitosan matrix using chemical method and discusses its utility for detection of flavonoid quercetin. The Ta_2O_5 nanoparticles embedded rGO and chitosan matrix has been characterized for quercetin detection through study of absorption spectra taken for different concentration values of quercetin in the range 1–10 μM. A red shift amounting to 64 nm has been observed in the peak absorption wavelength for the considered concentration range of quercetin. The sensitivity of the proposed nanostructured sensing layout has been calculated and is observed to decrease in an exponential manner with quercetin concentration. The LOD of the nanostructured sensing framework has been determined to be 280 nM. The reported sensing strategy for quercetin offers synthesis and operational simplicity. Moreover, the achieved analytical attributes of the nanostructured sensing layout prove its applicability for quercetin detection in various food and medicinal samples.

References

1. M. Arvand, M. Anvari, A graphene–based electrochemical sensor for sensitive detection of quercetin in foods. J. Iran. Chem. Soc. **10**, 841–849 (2013)
2. B. Xu, L. Yang, F. Zhao, B. Zeng, A novel electrochemical quercetin sensor based on Pd/MoS$_2$– ionic liquid functionalized ordered mesoporous carbon. Electrochim. Acta **247**, 657–665 (2017)
3. K. Pliuta, A. Chebotarev, A. Koicheva, K. Bevziuk, D. Snigur, Development of a novel voltammetric sensor for the determination of quercetin on an electrochemically pretreated carbon–paste electrode. Anal. Methods **10**, 1472–1479 (2018)
4. M. Muti, K. Gencdag, F.M. Nacak, A. Aslan, Electrochemical polymerized 5–amino–2– mercapto–1,3,4–thiadiazole modified single use sensors for detection of quercetin. Colloids Surf., B **106**, 181–186 (2013)
5. Z. Zhang, S. Gu, Y. Ding, M. Shen, L. Jiang, Mild and novel electrochemical preparation of β– cyclodextrin/graphene nanocomposite film for super–sensitive sensing of quercetin. Biosens. Bioelectron. **57**, 239–244 (2014)
6. N. Venkatesha, Y. Qurishi, H.S. Atreya, C. Srivastava, ZnO coated CoFe$_2$O$_4$ nanoparticles for multimodal bio–imaging. RSC Adv. **6**, 18843–18851 (2016)
7. R. Kant, R. Tabassum, B.D. Gupta, A highly sensitive and distinctly selective d–sorbitol biosensor using SDH enzyme entrapped Ta$_2$O$_5$ nanoflowers assembly coupled with fiber optic SPR. Sens. Actuators, B Chem. **242**, 810–817 (2017)
8. R. Kant, Surface plasmon resonance based fiber–optic nanosensor for the pesticide fenitrothion utilizing Ta$_2$O$_5$ nanostructures sequestered onto a reduced graphene oxide matrix. Microchim. Acta **187**(8), 11p (2020)
9. R. Tabassum, R. Kant, Laser–ablated core–shell nanostructures of MWCNT@Ta$_2$O$_5$ as plasmonic framework for implementation of highly sensitive refractive index sensor. Sens. Actuators A: Phys. **309**, 112028 (2020)
10. A. Hosoki, M. Nishiyama, H. Igawa, A. Seki, Y. Choi, K. Watanabe, A surface plasmon resonance hydrogen sensor using Au/Ta$_2$O$_5$/Pd multi–layers on hetero–core optical fiber structures. Sens. Actuators, B Chem. **185**, 53–58 (2013)
11. R. Kant, B.D. Gupta, Fiber–optic SPR based acetylcholine biosensor using enzyme functionalized Ta$_2$O$_5$ nanoflakes for Alzheimer's disease diagnosis. IEEE Journal of Lightwave Technology **36**, 4018–4024 (2018)
12. Z. Yao, X. Yang, X. Liu, Y. Yang, Y. Hu, Z. Zhao, Electrochemical quercetin sensor based on a nanocomposite consisting of magnetized reduced graphene oxide, silver nanoparticles and a molecularly imprinted polymer on a screen–printed electrode. Microchim. Acta **185**(1), 70 (2018)
13. R. Kant, R. Tabassum, B.D. Gupta, Integrating nanohybrid membranes of reduced graphene oxide: chitosan: silica sol gel with fiber optic SPR for caffeine detection. Nanotechnology **28**, 195502 (2017)
14. R. Kant, B.D. Gupta, SPR based fiber optic quercetin biosensor utilizing rGO: PPy: chitosan nanocomposite network. Frontiers in Optics (OSA Technical digest) paper JW4A.69 (2017)
15. R. Kant, B.D. Gupta, SPR based optical biosensor for acetylcholine utilizing enzyme entrapped Ta2O5 nanoflowers assembly encapsulated in chitosan and rGO matrix. Optical Sensors and Sensing Congress (OSA Technical digest) paper JTh2A.20 (2019)
16. R. Kant, R. Tabassum, B.D. Gupta, Xanthine oxidase functionalized Ta$_2$O$_5$ nanostructures as a novel scaffold for highly sensitive SPR based fiber optic xanthine sensor. Biosens. Bioelectron. **99**, 637–645 (2018)
17. I.M. White, X. Fan, On the performance quantification of resonant refractive index sensors. Opt. Express **16**(2), 1020–1028 (2008)
18. L. Yang, B. Xu, H. Ye, F. Zhao, B. Zeng, A novel quercetin electrochemical sensor based on molecularly imprinted poly (para–aminobenzoic acid) on 3D Pd nanoparticles–porous graphene–carbon nanotubes composite. Sens. Actuators, B Chem. **251**, 601–608 (2017)

19. W. Zhang, L. Zong, G. Geng, Y. Li, Y. Zhang, Enhancing determination of quercetin in honey samples through electrochemical sensors based on highly porous polypyrrole coupled with nanohybrid modified GCE. Sens. Actuators, B Chem. **257**, 1099–1109 (2018)
20. J. Li, J. Qu, R. Yang, L. Qu, P.B. Harrington, A sensitive and selective electrochemical sensor based on graphene quantum dot/gold nanoparticle nanocomposite modified electrode for the determination of quercetin in biological samples. Electroanalysis **28**, 1322–1330 (2016)

Chapter 36
Optimization Study of Nozzle End Grid Size Impact on the Pressure Drop and Maximum Velocity of a Rocket Motor

Balesh Ropiaa, R. K. Kalal, Himanshu Shekher, and D. G. Thakur

Abstract In the present study, numerical simulation was carried to study the effect of opening size of nozzle end grid and nozzle on pressure drop and maximum velocity of a rocket motor. The nozzle end grid size was varied from 40 to 80% opening and nozzle peripheral opening was varied from 0 to 6 mm. Total 35 cases were evaluated. In all cases maximum pressure was observed at the inlet and maximum velocity was found invariant. The maximum drop of pressure is observed at 2–4 mm peripheral opening for various cases. The study has shown that a prior optimization study involving geometrical parameters of grid and nozzle will help in a safe working with rocket motor.

36.1 Introduction

Rocket motor is used to deliver payload to required target. It consists of several important components i.e. head end, motor casing, nozzle end, propellant etc. All components have their specific purpose. Rocket motors are designed for specific maximum pressure for safe working. On suitable ignition of propellant, propellant burning surface regresses resulting in the formation of high volumes of gas in the combustion chamber. As the gases passes through the chamber and exit from the nozzle, thrust is generated which eventually moves the rocket motor in the opposite direction of gas exit. Nozzles are generally designed to achieve the required pressure inside the combustion chamber.

In rocket motor, chamber pressure (P_c) and burning surface area (A_b) are correlated [1–4]. The prediction shows that the pressure–time and thrust- time profiles follows the burning surface pattern [5]. Prediction of the expected internal behavior of a given solid-propellant rocket motor under transient conditions is very important. As prediction gives expected pressure rise in rocket motor which will be useful for

B. Ropiaa (✉) · R. K. Kalal · H. Shekher
High Energy Material Research Laboratory, Pune, India

D. G. Thakur
Defence Institute of Advanced Technology, Pune, India

initial design of rocket motor. The factors that affects the performance of rocket needs detailed research. The initial pressure produced during rocket motor firing needs a detailed experimental and numerical study. A simulation study with different divergent angle and Mach number for supersonic rocket nozzle was carried out by Sudhakar et al. [6]. A number of parameters i.e. pressure, temperature and velocity for convergent divergent nozzle was analysed. Similar study of C-D nozzle using Ansys Fluent by changing geometric parameters is carried out by Raut [7].

In literature, inadequate CFD investigation of initial pressure rise in multi-propellant grain solid rocket motor is available. Reported literature discusses about propulsion and the effect of propellant geometry on performance of rocket motor. Even though it is well known that grids that are used to support the grains are the major contributors to the initial development of pressure, as they obstruct the flow of gases, the effect of obstruction by nozzle end (NE) grid and the peripheral opening of the grid is not adequately addressed.

In present study, numerical analysis was carried to investigate rocket motor pressure rise by NE grid and peripheral opening (space between motor casing inner diameter and grid outer diameter). A cartridge loading of cluster of 7 grains is taken for simulation. Grid is designed as circular openings supported by cross bars. In physics these bars are used to strengthen the grid. The grid openings were varied, studied for 40, 50, 60, 70 and 80% opening in conjunction with peripheral openings varying from zero peripheral opening, 1, 2, 3, 4, 5 and 6 mm. Important Flow properties like pressure and velocity were investigated in detail and geometric modifications are suggested based for the optimum peripheral and NE grid opening. Total 35 cases were numerically solved for detailed study on pressure and velocity.

36.2   CFD Methodology and Implementation

36.2.1   Geometric Modelling

Complete rocket motor having nozzle with detail grid geometry is modelled initially in CATIA software. For the current simulation only nozzle part along with detail grid is considered as it is evident form literature that the nozzle is mainly responsible for maintaining pressure in rocket motor. The total length of the propellant grains is less than 1000 mm. As there is no appreciable difference of pressure at head end and nozzle end in short length motor [5]. Hence for ease of numerical analysis only nozzle is modelled and nozzle end pressure is calculated.

The nozzle geometry parameters are shown in Fig. 36.1b and are given in Table 36.1. The computed throat diameter (D_t) 77 mm for nozzle. This dimension is suitable to maintain required ~7 MPa in the rocket motor. The selected exit diameter (D_e) is 210 mm for analysis purpose.

(a)

(b)
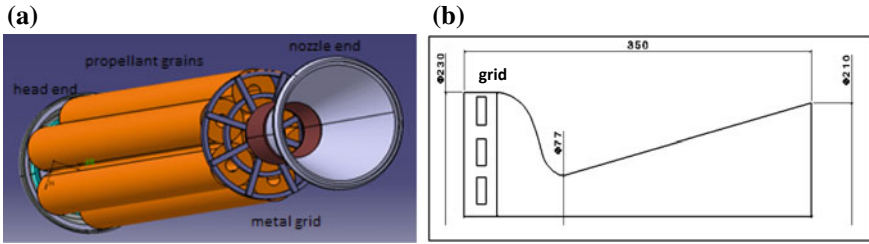
Fig. 36.1 **a** Rocket motor assembly with cluster of 7 grains, **b** Dimensions of NE along with NE grid.

Table 36.1 Design parameters of rocket motor

Inlet diameter (D_i)	230 mm
Throat diameter (D_t)	77 mm
Exit diameter (D_e)	210 mm
Exit pressure (P_e)	1 atm

36.2.2 Simplification of Grid Geometry

The grid shown in Fig. 36.2 is not truly axisymmetric due to equally spaced cross bars. To simplify the problem, an equivalent area of eight bars is added to these circular rings to make model symmetrical. Total percentage opening is maintained constant and the geometry is made axisymmetric. Figure 36.3 shows simplified geometry without bars (Fig. 36.4).

Fig. 36.2 Nozzle end with ribs
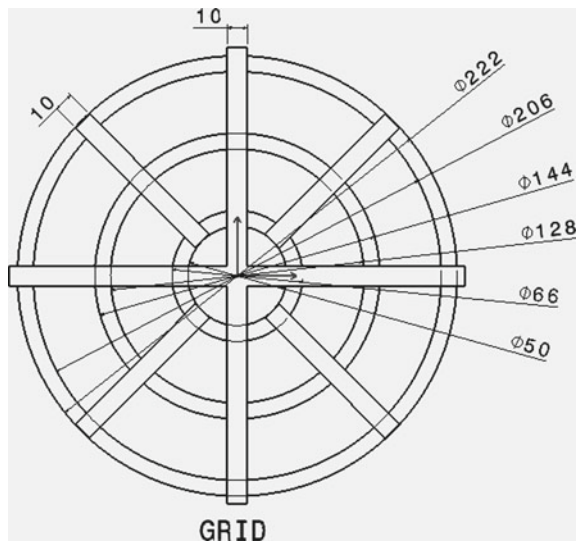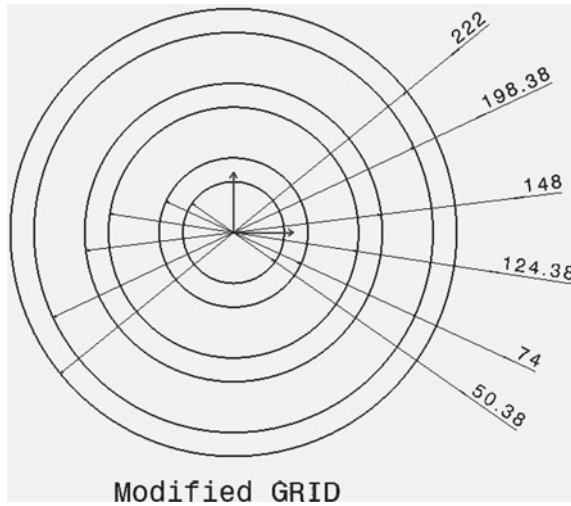
GRID

Fig. 36.3 Modified grid with no ribs
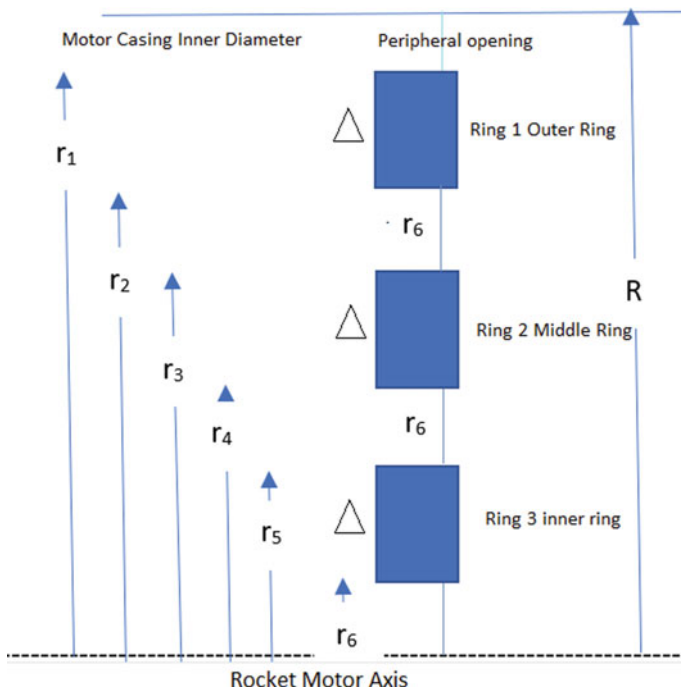
Fig. 36.4 Dimensions of rings of grid

Analyses were performed for different percentage openings of the NE grid. A mathematical approach is developed for different peripheral opening and % opening of NE grid. In this calculation the distance between the two circular rings are assumed constant.

Taking R as inner diameter of motor casing.

r_1 outer diameter of outer ring.

r_2 inner diameter of outer ring.

r_3 outer diameter of middle ring.

r_4 inner diameter of middle ring.

r_5 outer diameter of inner ring.

r_6 inner diameter of inner ring.

and $\Delta = r_1 - r_2 = r_3 - r_4 = r_5 - r_6$.

$r_6 = r_2 - r_3 = r_4 - r_5$.

so $r_1 = 3r_6 + 3\Delta$.

$r_2 = 3r_6 + 2\Delta$.

$r_3 = 2r_6 + 2\Delta$.

$r_4 = 2r_6 + \Delta$.

$r_5 = r_6 + \Delta$.

Now C = percentage area of blocking can be given as

$$C = \frac{\left[\left(r_1^2 - r_2^2\right) + \left(r_3^2 - r_4^2\right) + \left(r_5^2 - r_6^2\right)\right]}{R^2}$$

Now substituting different values equation becomes

$$C = \frac{\Delta[(6r_6 + 5\Delta) + (4r_6 + 3\Delta) + (2r_6 + \Delta)]}{R^2}$$

$$R^2 C = \Delta(12r_6 + 9\Delta) \tag{36.1}$$

For case of 4 mm peripheral opening.

Here $r_1 = 111$ mm.

So $r_1 = 111 = 3r_6 + 3\Delta$

$r_6 = \left(\frac{111}{3} - \Delta\right)$ Put this in (36.1).

So, equation becomes.

$$3\Delta^2 - 444\Delta + R^2 C = 0 \tag{36.2}$$

By using (36.2), for various peripheral opening and different percentage opening different equation is achieved. By solving these equations various dimensions of grid can be obtained and modelling of the different NE grid for each case is done. These cases are numerically solved to get the various parameters.

36.2.3 Calculations for Effective Percentage Opening and Dimensions of Grid

In combustion chamber, most space is occupied by propellant grain. Propellant grain causes main obstacle for flow of combustion gases. After propellant grain other obstacle is caused by NE grid. For analysis, here assumption is made that propellant grain and NE grid are always in contact. Due to contact of propellant grain the flow area on NE grid reduces. Combustion generates continuously free and due to this NE grid opening increases.

The percentage effective opening of grid is calculated by (36.3)

$$\%Effective\ opening = \left[1 - \frac{V_p}{V_c}\right] \times \%Opening\ of\ the\ grid \qquad (36.3)$$

where

V_p = Propellant volume in rocket motor
V_c = Rocket motor volume

36.2.4 Boundary Conditions

In this study, the equilibrium of reactions is assumed and all major species achieved from NASA-CEA model is taken for calculations and given at inlet. The injection temperature is 2398 K we got from NASA-CEA software. Inlet is 10 mm prior of NE grid.

In Fig. 36.5 shows boundary conditions of a 2D model of nozzle.
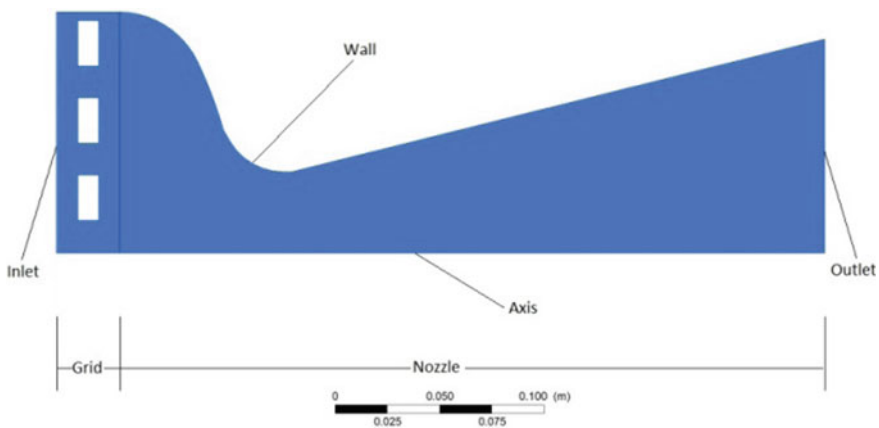
Fig. 36.5 Boundary conditions

36.2.5   *Regressive Boundary Model*

In rocket motor, solid propellant geometry is changing continuously due to the combustion and form combustion products. This variation in geometry is called surface regression. Surface regression between solid propellant grain and gases is modelled which are fuel–air mixture as shown in Fig. 36.6. The grain is tubular type so the grain half section is shown in Fig. 36.6, which show how the propellant surface burn. On combustion, the solid propellant burns and the boundary regresses.

On burning surface regression the oxidizer and reactant gases leaves in opposite direction with velocity V_g. As the density of propellant ρ_p is higher than the density of the gaseous oxidiser and reactant mixture, ρ_g, the velocity of this mixture is greater than the burning rate. Thus, mass conservation is approximated and is used for calculation. By offsetting the grain at every time step, a new surface of the propellant is exposed and is calculated numerically.

The calculated mass flow rate (m) at each step by offsetting the grain dimension is given below.

$$m \doteq \rho_p \, A_b \, \dot{r}_b$$
$$where$$
$$\rho_p = \text{density of Propellant}$$
$$A_b = \text{burn area of propellant}$$
$$r_b = \text{burn rate of propellant}$$

The mass flow rate input (time dependent boundary condition) is shown in the Fig. 36.7.
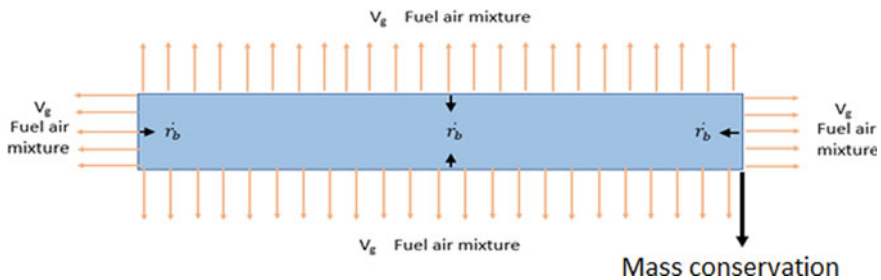
Fig. 36.6 Surface regression model
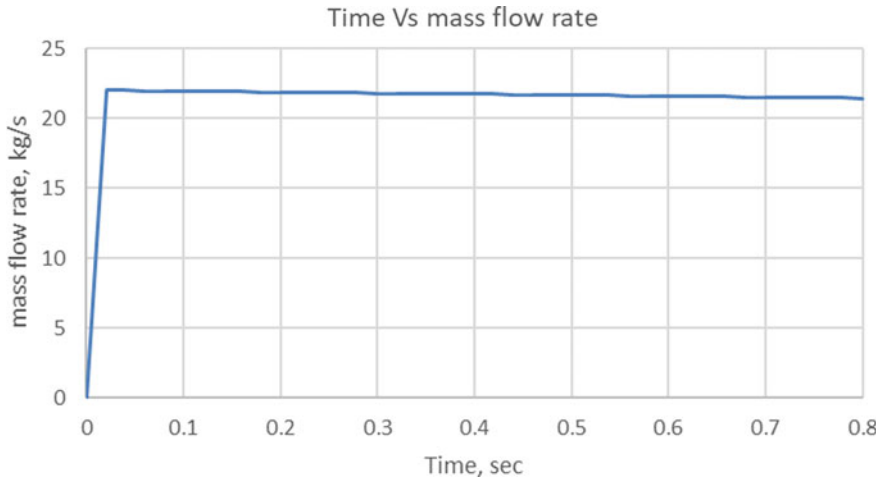
Fig. 36.7 Mass flow rate input vs time

36.2.6 Solution

The shear-stress transport (SST) k- ω model is used as it gives near-wall interactions more accurately than any other model. This model is used to give robust and accurate results. For different grid opening conditions of nozzle the CFD analysis is performed.

36.2.7 Analysis Procedure

The solver settings used for all the types of grid openings (as given in Table 36.2) is summarized as below.

36.3 Result and Discussion

a.   **Pressure drop across the rocket motor**

In rocket motor pressure rise plays a very important role for safe working. All rocket motor is designed for specific maximum pressure. It is very important to study the factor which affect the rocket motor pressure rise. In present study, effect of various peripheral opening and various % openings of NE grid on maximum pressure rise is studied. The numerical solutions are run for various peripheral opening of nozzle i.e. no peripheral, 1, 2, 3, 4, 5 and 6 mm and for various % opening of NE grid i.e. 40%, 50%, 60%, 70% and 80%. All percentage of NE grid opening were analysed for every instance of peripheral opening in order to evaluate the optimized

Table 36.2 Summery of the solver settings for numerical analysis.

Procedure	Details
Problem Setup General-Solver	Type: Density based Velocity: Absolute Time: Transient 2-D space: Axisymmetric
Models	Energy: On Viscous: SST, K-ω (2 eqn.)
Materials	Fluid: mixture of species from NASA-CEA software Density: Ideal Gas Viscosity: Constant
Boundary conditions	Inlet: Mass flow rate Inlet Initial Gauge Pressure (Pa): 0 Outlet: Pressure Outlet Gauge Pressure(Pa): 0 Inlet: thermal on temperature as constant 2389 K
Reference Values	Compute from: Inlet Reference Zone: Diffused
Initialization	Compute from Inlet
Solution	Solution Controls – Courant Number = 5 Run Calculation: Enter the Number of iterations, Press calculation

value of their combined effect. A total 35 cases are solved. The pressure contour results for a 4 mm peripheral opening at various grid percentage opening is shown in Fig. 36.8.

With 4 mm peripheral opening.

From above figure it can be seen that maximum pressure is recorded at inlet. The results of the maximum pressure rise in rocket motor for various peripheral opening are given in the Table 36.3 for all cases.

The variation of the pressure along the axis to the inner diameter of motor at inlet is given as under for various peripheral openings is given as under in Fig. 36.9.

From the Fig. 36.9 it is evident that the maximum pressure is higher at the axis at inlet (0 mm in y direction at inlet) for the cases i.e. 6 mm peripheral opening (PO), 5 mm PO, 3 mm PO (9.7334 MPa, 9.0709 MPa, 9.0113 MPa). It is because, as the peripheral opening increases the flow area at the other opening (distance between the circular rings) will decrease and the reduced flow area will cause the pressure rise at inlet following conservation of energy. Also it is shown in Fig. 36.9 that for the 2 mm and 4 mm PO, the pressure curve from nozzle inlet to the periphery along the axis of the motor is fluctuating in nature. The fluctuating distribution is in line with the physics which basically result in a pressure rise at grid obstruction lies and drop at the opening. It can also be observed that the nozzle opening of 2 mm and 4 mm
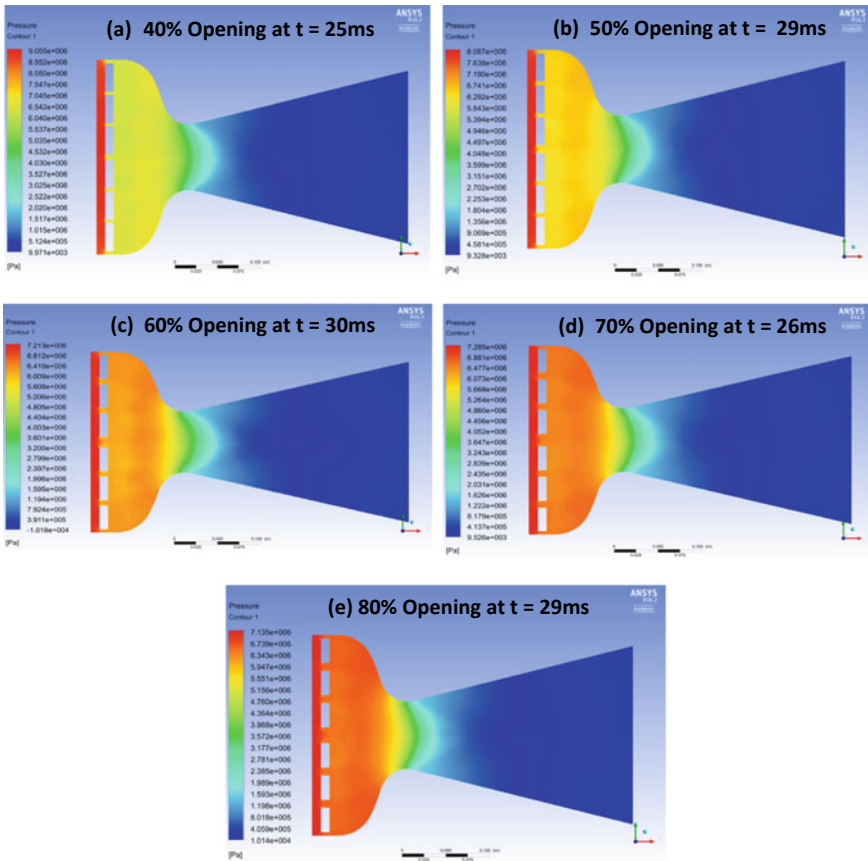
Fig. 36.8 4 mm peripheral opening pressure contours for various percentage opening of grid **a** 40% opening, **b** 50% opening, **c** 60% opening, **d** 70% opening, **e** 80% opening

Table 36.3 Results of maximum pressure rise for various peripheral and grid opening

Peripheral opening	Maximum pressure (P_{max} -MPa) for various grid opening				
	40% grid opening	50% grid opening	60% grid opening	70% grid opening	80% grid opening
W/o peripheral opening	8.9190	8.2490	7.9000	7.6170	7.4190
1 mm	8.7453	7.9464	7.5625	7.3236	7.1645
2 mm	8.6607	7.8653	7.2366	6.9707	6.6442
3 mm	9.0113	8.1049	7.5641	7.3363	6.8486
4 mm	8.9100	8.0880	7.5030	7.3080	7.1570
5 mm	9.0709	8.1980	7.7213	7.4135	7.1776
6 mm	9.7334	8.5919	7.9256	7.5180	7.1494
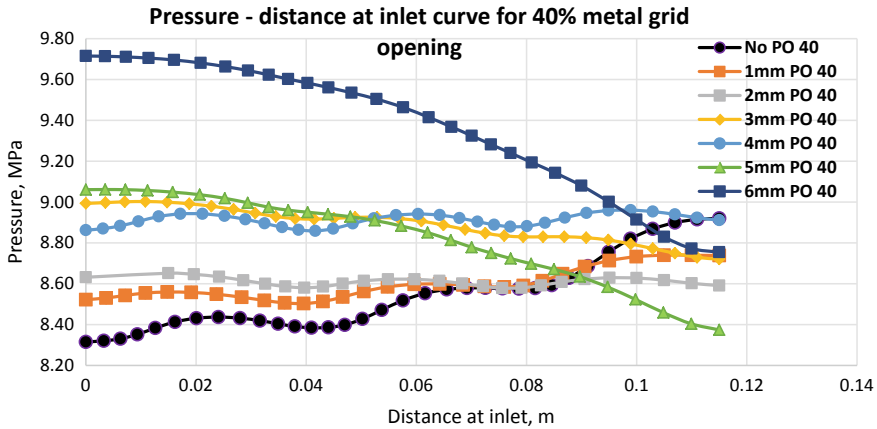
Fig. 36.9 Pressure—distance at inlet curve for 40% grid opening

has negligible effect on this pressure distribution. At 3 mm peripheral opening less fluctuating effect is there. The pressure is continuously reducing as we are moving towards motor inner diameter. This is due to fact that at 3 mm peripheral opening there is good passage is available for gas flow at periphery and at other openings also sufficient passage is available for flow of gases. Similarly, for other cases i.e. no PO and 1 mm PO the maximum pressure is observed at the periphery of the motor i.e. at the last point on inlet.

From Table, it can be seen that at 2 mm periphery opening value, the value of maximum pressure is relatively minimum among all the cases. This is due to fact that grid is optimize at 2 mm periphery opening and flow area at other opening is also optimize. While the maximum pressure is almost same for 3 mm and 4 mm PO cases except 80% NE case where the variation is more (7.1570 MPa for 4 mm PO and 6.8486 MPa for 3 mm PO case). Among all the cases highest maximum pressure value of 9.7334 MPa is observed for 6 mm PO which is because of more peripheral opening. If peripheral opening is increases, then flow area at other opening will reduce and the rise of the maximum pressure can be seen. So we can see that for no peripheral opening the maximum pressure position is at inner diameter of motor and for 5 mm and 6 mm peripheral opening the maximum pressure position is at axis of motor.

In Fig. 36.10 the variation of the pressure along the length of the nozzle is shown for 4 mm peripheral opening and various percentage grid opening. Form this Fig. 36.10 it can be seen that for all percentage of grid openings, the maximum pressure is observed at inlet of the rocket motor (before the grid) and after that the drop of pressure is observed along the length of the nozzle. This drop of pressure is continuous till the nozzle exit. At nozzle exit the pressure is equal to atmosphere pressure. With increase of percentage opening, maximum pressure value is decreasing and nature of the pressure drop is same.
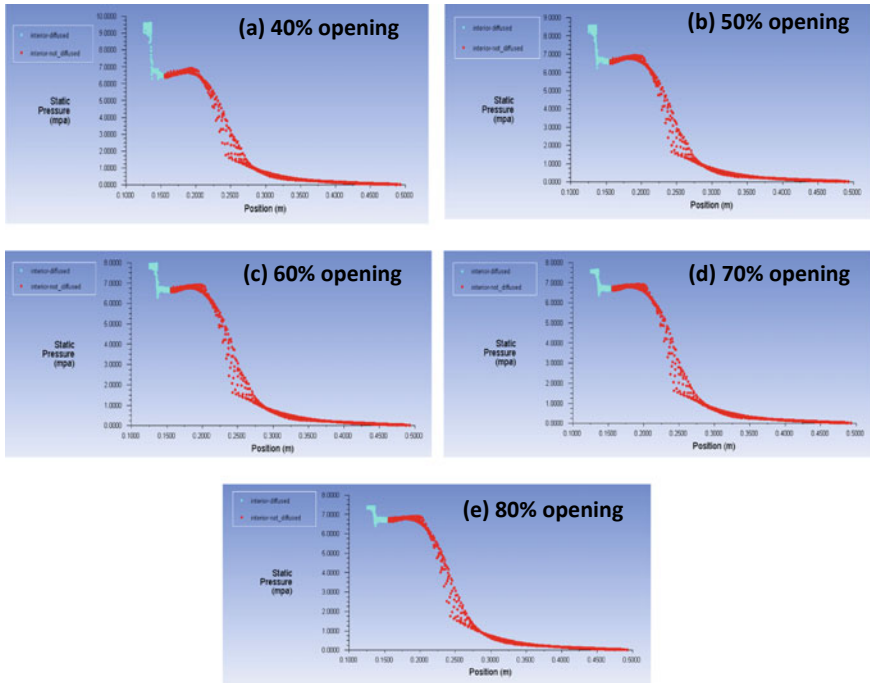
Fig. 36.10 4 mm peripheral opening pressure contours for various % opening of grid along the length of nozzle **a** 40% opening, **b** 50% opening, **c** 60% opening, **d** 70% opening, **e** 80% opening

b. **Velocity distribution of the gases across the rocket motor**

From the Fig. 36.11 below it is evident that velocity is maximum at the outlet of nozzle. The minimum value of velocity is observed at inlet of the nozzle where the analysed pressure is maximum meeting the law of conservation of energy. The velocity at inlet for all cases varying in between 200 m/s to 600 m/s.

Maximum velocity values obtained in the analysis are shown Table 36.4. It is found that the flow is chocked at nozzle and attained supersonic velocity increasing continuously till divergent end of nozzle and to the outlet. As the length of the nozzle is same in all cases the maximum velocity value is almost same for all cases. This can be observed from the maximum velocity values listed in Table 36.4. The maximum velocity value is 2117.25 m/s and the minimum velocity value is 2111.91 m/s. The percentage difference is only 0.22% which is very less. From the above results of the maximum velocity, it is clear that it is not affected much by the % opening of the NE grid and peripheral opening in the motor casing. But at inlet velocity value is ranging from 200 to 600 m/s.

4mm PO 40 velocity

4mm PO 50 velocity

4mm PO 60 velocity

4mm PO 70 velocity

4mm PO 80 velocity
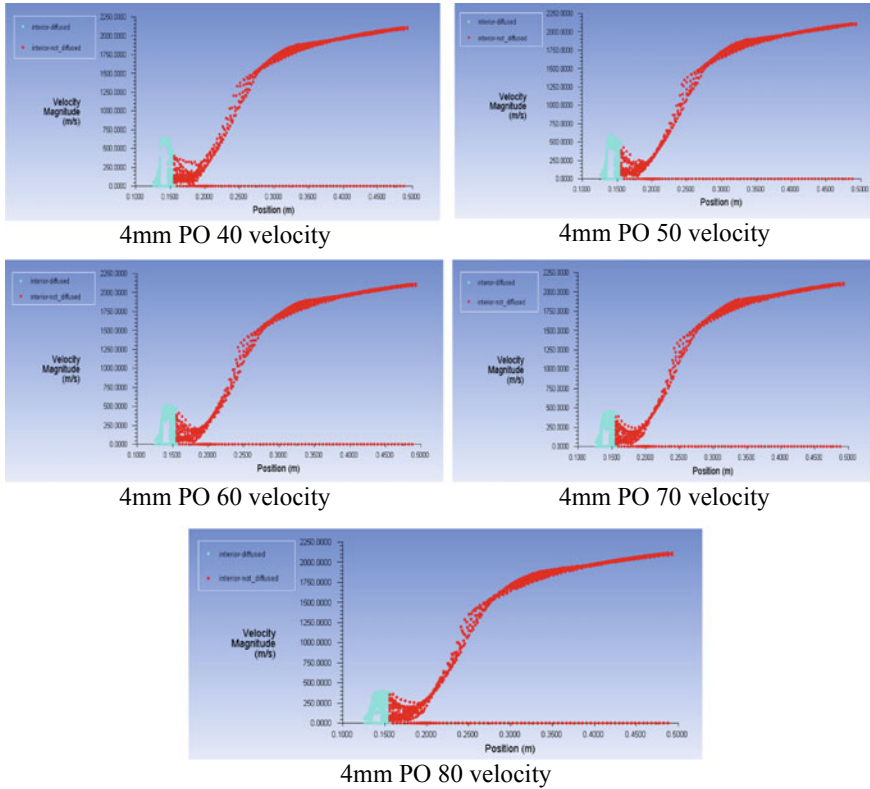
Fig. 36.11 4 mm peripheral opening velocity contours for various % opening of grid along the length of nozzle **a** 40% opening, **b** 50% opening, **c** 60% opening, **d** 70% opening, **e** 80% opening

Table 36.4 Maximum velocity variation in rocket motor

Maximum velocity (observed at outlet of nozzle)				
Peripheral opening	40% grid opening	50% grid opening	60% grid opening	70% grid opening	80% grid opening
No peripheral	2112.37	2115.69	2116.92	2114.31	2114.75
1 mm	2114.26	2113.38	2113.33	2114.53	2115.7
2 mm	2114.23	2111.91	2115.03	2117.19	2115.87
3 mm	2115.45	2115.58	2115.81	2114.6	2114.76
4 mm	2114.49	2115.22	2115	2114.1	2117.25
5 mm	2116.39	2115.74	2114.23	2115.74	2116.41
6 mm	2115.54	2115.04	2116.36	2115.02	2113.97

36.4   Conclusion

From this study, it can be concluded that peripheral opening is playing a very important role in the rocket motor along with percentage opening of the NE grid. The maximum pressure value is found at inlet of the grid. The drop of pressure is continuously observed with higher percentage opening of the grid. The maximum pressure was inversely proportional to peripheral opening till 2 mm PO and then linearly increasing. This is due to the increase of peripheral opening, the flow area at the other circular rings will decrease and this reduction in flow area will cause the increase of maximum pressure. The maximum drop of pressure is observed at 2–4 mm peripheral opening for various cases. Similarly, the velocity is found minimum at inlet and maximum at outlet, in line with law of conservation of energy, and isn't affected largely by both peripheral and grid opening. Hence a prior optimization study involving geometrical parameters of grid and nozzle need to be carried in detail for designing a safe working rocket motor.

References

1. G. Sutton, O. Biblarz, Rocket propulsion elements. Rocket Propulsion Elements. **45–75**(417–53), 520–526 (2001). https://doi.org/10.1017/CBO9781107415324.004
2. B. Zeller, Solid propellant grain design. In *Solid Rocket Propulsion Technology*, pp. 35–84 (1993). http://linkinghub.elsevier.com/retrieve/pii/B9780080409993500072
3. R.I. Reis, W.K. Shimote, L.C. Pardini, Anomalous behavior of a solid rocket motor nozzle insert during static firing test. J. Aerospace Technol. Manage. São José dos Campos, **8**(4), 483–490 (Oct–Dec 2016)
4. N. Gligorijević, M.A. Boulahlib, S. Živković, S. Subotić, S. Kozomara, M. Nikolić, Solving an irregular burning problem in a small rocket motor. Sci. Tech. Rev. **64**(2), 3–13 (2014)
5. B.M. Andre Jaumotte, B. Fraeijs de Veubeke, J. Vandenkerckhove, Rocket Propulsion, Elsevier Publishing Company, Amsterdam, London, New York, Princeton, pp. 1–858 (1960)
6. B.V.V. Naga Sudhakar, B. Purna, C. Sekhar, P.N. Mohan, T. Ahmad, Modeling and simulation of convergent-divergent nozzle using computational fluid dynamics. Int. Res. J. Eng. Technol. (IRJET). **03**(08) (Aug-2016) www.irjet.net p-ISSN: 2395–0072
7. N.D. Raut, A CFD analysis and study on effect over mach of rocket c-d nozzle by varying its geometric parameters. Int. J. Mech. Prod. Eng., ISSN: 2320–2092, **4**(3) (Mar 2016)

Chapter 37
Thermo-Physical Properties and Combustion Wave of Nitramine Based Composite Propellant Compositions

R. K. Kalal, H. Shekhar, P. S. Alegaonkar, Rekha Sangtyani, and Arvind Kumar

Abstract Thermo-physical properties have a significant role in propellant combustion and heat transfer studies of propulsion systems. Some of these properties are also essential for designing and simulation purposes. This paper, discusses experimental determination of the thermo-physical properties of nitramine based composite propellants compositions and effects of percentage variation in nitramine component on these properties. These properties are determined as per ASTM standard (flash technique) in the temperature range of RT to 100^0C. As the nitramine (RDX) to ammonium perchlorate (AP, oxidizer) ratio increases thermal diffusivity decreases whereas thermal conductivity and specific heat increases. These changes in thermal properties lead to variation in combustion behaviour, which is clearly observed in combustion wave pattern and visible in photographic images of burning surface of propellant.

37.1 Introduction

A solid propellant contains oxidizer and fuel as ingredients. It is capable to burn without external supply of air or other oxidizers. After suitable ignition, solid propellants generate combustion products at high-temperature, which have an applications in propulsion. Solid propellants are used to generate propulsive thrust for different applications such as missiles, space vehicles, guns and air-breathing propulsion systems. Applications of solid propellants in various propulsion system depends on their combustion behaviour and other fundamental properties. Combustion behaviour of propellants are studied by using thermo-physical properties namely thermal diffusivity, specific heat and thermal conductivity, burning surface temperature, combustion wave propagation during burning etc.. For better understanding of model for

R. K. Kalal (✉) · R. Sangtyani · A. Kumar
High Energy Materials Research Laboratory (HEMRL), Sutarwadi, Pune 411021, India

R. K. Kalal · H. Shekhar · P. S. Alegaonkar
Defence Institute of Advanced Technology (DIAT), Girinagar, Pune 411057, India

combustion of propellant and heat transfer studies, thermo-physical properties of propellants have a significant role for said studies and development of simulation model. These properties are experimentally determined by ASTM and ISO standard based methods such as flash technique, guarded hot plate method, hot disc technique. Embedded thermocouple techniques are used to experimental determination of surface temperature and combustion wave propagation, and video graphic method specifically, high speed imaging method is used for propellant regression rate measurement and phenomenon related to surface reaction studies during combustion.

Presently, nitramine based composite propellants, which contains either RDX or HMX, are favourable choice of researchers and propulsion system developers having the advantage such as higher energetic, smokeless burning nature, lower temperature sensitivity, combustion products with lower molecular weight etc. The combustion phenomenon for ingredients of these compositions have been explained and documented elsewhere. But these propellant composition's ignition and combustion modelling requires thermal parameters of ingredient materials and composition's as a temperature function [1–5].

Thermal properties discussed above are well reported for ammonium perchlorate (AP) and RDX [6–13] but lacking in mutual agreement. Hence a thorough investigation for effect of systematically partial replacement of AP by RDX in propellant composition, on thermo-physical properties of propellant and combustion behaviour are under taken during this study. This paper focuses on thermo-physical properties measurement in temperature range of RT to 100 ^{0}C, combustion wave and burning surface temperature determination with embedded micro thermocouple and flame structure for RDX contain propellant at ambient pressure. An effect of systematic variation in RDX to AP content percentage on thermo-physical properties, combustion wave, burning surface temperature and its combustion flame structures are also elaborated.

37.2 Experimental

37.2.1 Composition Ingredients and Sample Preparation

RDX based composite propellant compositions are selected for this study. Oxidizer AP is gradually decreased and RDX with the same %wt is added in compositions. Detailed compositions under study are given in Table 37.1.

A disc type sample is cut from a prepared propellant sheet for thermo-physical measurement. This disc is 12.5–12.7 mm in diameter and 1.5–2.5 mm thick whereas for combustion wave and flame structure sample is a strand having dimensions 6 × 6 x 60 mm.

Table 37.1 Propellant composition ingredients

Composition (% wt)	Sample 1	Sample 2	Sample 3
Binder	16	16	16
AP (100–250 μm)	80	74	68
RDX (5 μm)	0	6	12
Al (15 μm)	4	4	4
% of RDX to AP Ratio	0	8.11	17.65

37.2.2 Experimental Determination of Thermo-Physical Properties

Thermal parameters of current interest are determined with ASTM E1461 based flash method. In the present study, Thermo-physical properties are measured simultaneously using Flashline- 3000, Anter make, equipment with variable temperature up to 100^0C. The disc type sample is coated with colloidal graphite spray for the non-contact measurement. This coating increases the surface emissivity of sample and leads to improved IR absorbtion and emission. Figure 37.1 shows the sample before and after graphite coating. The coated sample is placed in sample holder and one side of the sample is irradiated by a small duration xenon source energy. IR detector at back end of sample record the thermal signature other end surface of sample with time by non-contact means [14–16]. This data was further processed and thermal diffusivity of sample under test is computed. Thermal diffusivity of a sample with uniform thickness L, as per parker model, is mathematically expressed as under

$$\alpha = \frac{1.38L^2}{\pi^2 t_{1/2}} \tag{37.1}$$

This system is used in differential mode for specific heat determination. A reference sample, Vespel, was used for specific heat determination. A well-known relation between thermal parameters enable to compute the thermal conductivity of material with additional input of density of the material.

Fig. 37.1 Propellant sample before and after graphite coating
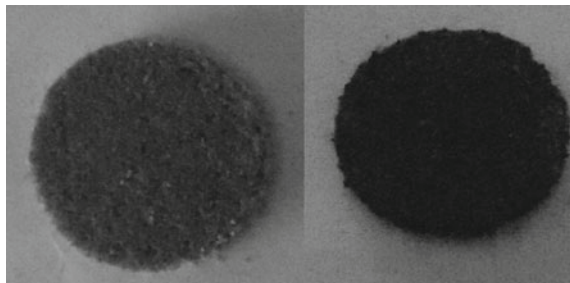
$$\lambda = \alpha\, C_p \rho \qquad\qquad (37.2)$$

37.2.3 Determination of Combustion Wave and Flame Structure

A field experimental setup is prepared to record the internal combustion wave propagation of propellant, burning surface temperature determination, flame structure and dispersion during combustion. A schematic arrangement for the experimental set up is presented in Fig. 37.2. Strand type propellant sample's, all surfaces are inhibited with silicon grease. Then it is dried at ambient temperature for 24 h. Inhibited surfaces ensures the layer by layer burning pattern of the propellant strand. Propellant strand sample of ~60 mm length is inserted two C-type (W-5% Rh and W-26% Rh) thermocouples at 30–35 mm distance. The diameter of thermocouples wire is ~ 75 micro meters. A steady stand is used for mounting the propellant strand vertically as shown in Fig. 37.2. A power supply with 24 V, 5A DC rating is used for ignition of propellant strand. Nichrome wire is coiled around upper end of propellant strand is supplied a 4–5A current for igntion. Embedded thermocouple's output is recorded on DL750P recorder. Temperature data are recorded at 1 kHz sampling rate. High speed camera (AOS-trivit make) is arranged nearby (~2 m distance) the propellant burning site to record flame structure images during the experiments. High speed videos are grabbed with 1000 frames per seconds speed and 12 X optical zoom. All the combustion wave experiments are performed at ambient conditions.
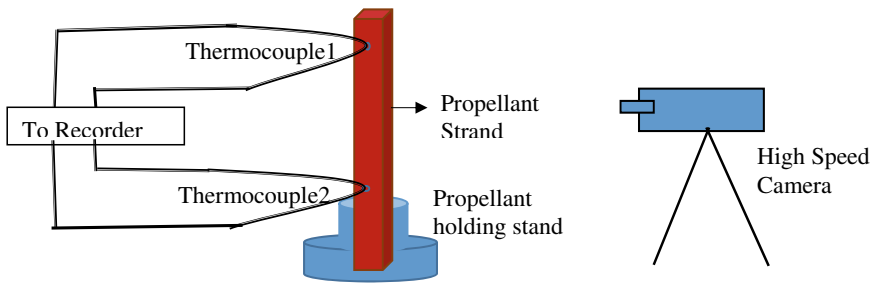
Fig. 37.2 Schematic of field experimental arrangement (not as per scale)

37.3 Results and Discussion

37.3.1 Analysis of Thermo-Physical Properties

Measured thermo-physical properties from RT to 100 ^{0}C are shown in Fig. 37.3. Data are graphically represented in this figure. Also computed errors for measured parameters are shown with error bars. Measurement for these properties were performed, at a particular temperature, for five samples of each compositions.

Estimated error for thermal diffusivity is $\leq \pm 4\%$, thermal conductivity is $\leq \pm 5\%$ and specific heat is $\leq \pm 5\%$. Table 37.2 summarises the thermal properties of RDX and AP ingredients [5, 9, 11–13, 20]. Different researcher have reported these data and variation is found in values.

AP has higher thermal conductivity and specific heat than RDX. But systematic reduction in the AP and subsequently enhancement in the RDX for propellant have altered thermal behaviour. Experimental data shows that increase in the % RDX, reduces thermal diffusivity (Fig. 37.3a) which follows the ingredients thermal
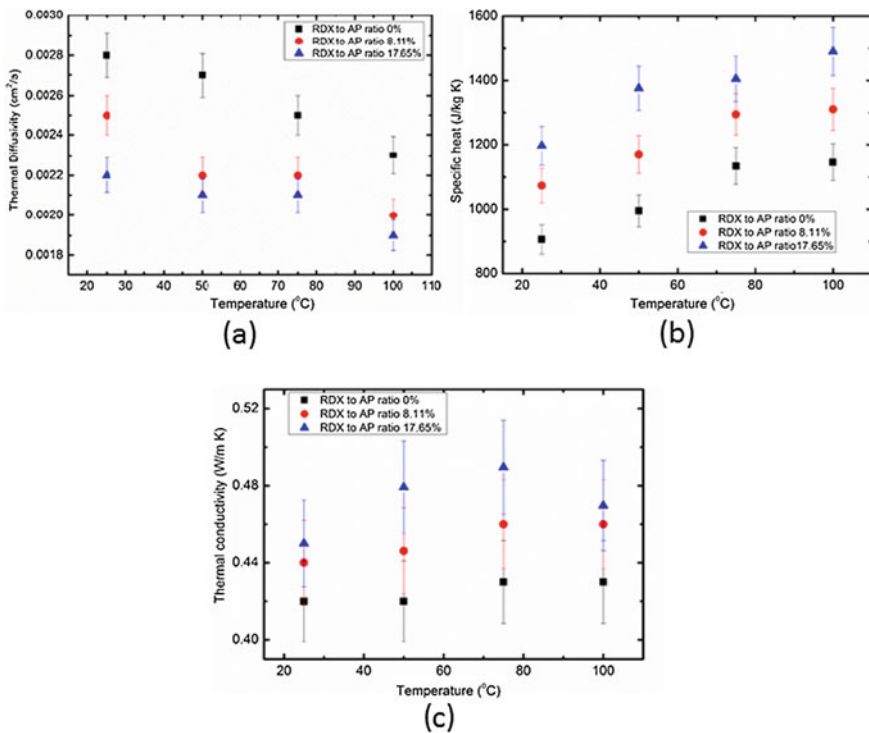
Fig. 37.3 Thermal properties of variable RDX to AP ratio **a** thermal diffusivity (cm^2/s) **b** specific heat (J/kg K) and **c** thermal conductivity (W/m K)

Table 37.2 Thermo-physical properties of AP and RDX

Parameters	AP	RDX
Thermal Diffusivity (cm^2/s)	0.0019–0.0025	0.0011–0.0013
Specific Heat (J/kg-K)	1296–1421	1045–1254
Thermal conductivity (W/m–K)	0.29–0.42	0.19–0.27
Density (g/cc)	1.950	1.806

parameters trends. But increment in this ratio increses specific heat (Fig. 37.3b) and thermal conductivity (Fig. 37.3c). It may be due the different thermal interaction between binder, RDX and AP. Also, the smaller size of RDX particles ~5 μm occupies the gap between coarse AP particles ~100–250 μm and brings the crystalline particles closer in the binder continuum. Effect of variation in the thermo-physical properties is also observed in the combustion behaviour, wave and flame structure of the propellant.

At room temperature thermal diffusivity of 0% RDX content composition is 0.0028 cm^2/s, specific heat is 906 J/kg-K, and thermal conductivity is 0.42 W/m–K. After addition of 6% RDX in composition and removal of similar quantity of AP, thermal diffusivity decreases to 0.0025 cm^2/s but specific heat increases to 1073 J/kg-K and thermal conductivity increases to 0.44 W/m–K. The % variation in thermal diffusivity is observed is 10.7% and thermal conductivity is 4.5% which are lesser than % variation in specific heat i.e.18.4%. Similar explanation can be applied for higher % of RDX compositions. Also with temperature, variation in these parameters is observed. Propellant burning rate is more susceptible to specific heat as compared to thermal conductivity [21]. A correlation can be establish between these data and burning rate of the compositions.

37.3.2 Combustion Wave at Ambient Conditions

Burning rate and recorded temperature–time data are used to convert it into temperature-distance profile with established mathematical model [17–19]. Combustion wave (Temperature –distance) for compositions under study are shown in Fig. 37.4. Propellant burning surface is ascertained by using the Sabadell model [19]. Slope $(dT/dx)_s$ temperature-distance profile in condensed phase signifies heat transfer rate in solid substance. Slope $(dT/dx)_s$ is higher for higher RDX content i.e. it is higher for 17.65% RDX to AP ratio. It confirms heat release at the burning surface is higher for 12% RDX content i.e. sample 3. Average surface temperature for propellants under study is found between 450–520 °C, whereas flame temperature is ~1100 °C at ambient conditions. Data are analogous to reported nitramine contained composite propellants [1, 3, 17–19]. There is not much effect of higher RDX content on measured burning surface temperature. It is found approximately of the same
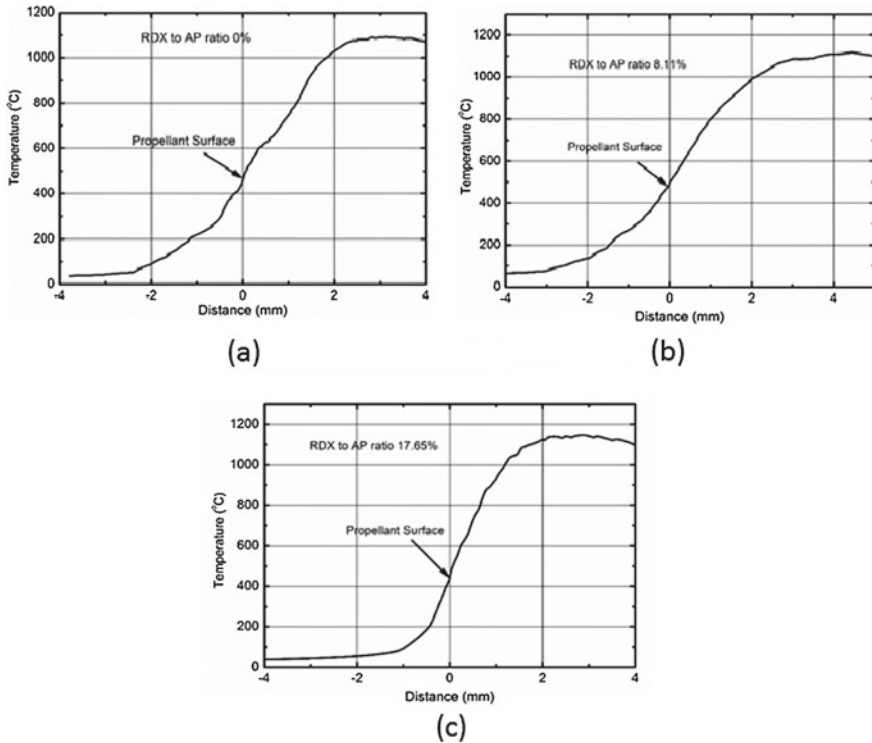
Fig. 37.4 Combustion wave for **a** 0% RDX to AP ratio **b** 8.11% RDX to AP ratio **c** 17.65% RDX to AP ratio

order for different propellant composition under study. Gas phase slope (above the propellant surface) $(dT/dx)_g$ also have increasing trend with increase in the RDX percentage. It indicates that energy content in the gas phase has been increased [22].

37.3.3   Flame Spreading Analysis at Ambient Conditions

High speed videos were captured/grabbed during the combustion of the compositions. Images of established combustion are generated with the help of imaging software. Flame structures for compositions under studies are shown in Figs. 37.5 and 37.6.

All these flame structures shows a luminous structures at the boundaries of propellant burning surface. It is silicon grease burning along with the propellant. Lateral burning of the propellant surface prevented by this layer. Flame front have poor surface propagation and the flame is projecting out for all compositions.
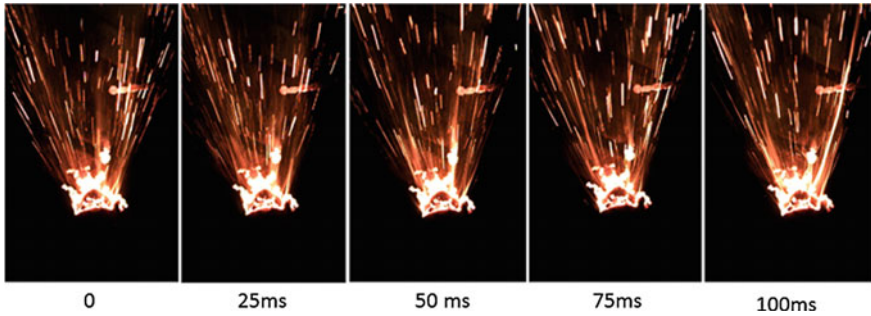
Fig. 37.5 Flame spreading for 0% RDX to AP ratio composition propellant
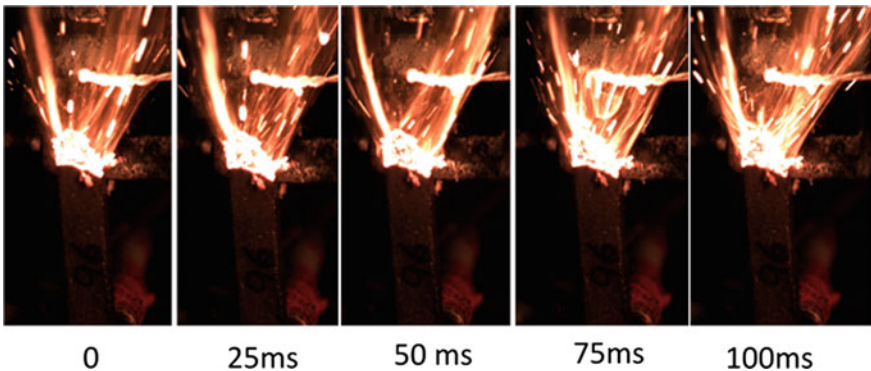
Fig. 37.6 Flame spreading for 8.11% RDX to AP ratio composition propellant

A glowing zone, which attribute premixed flame is visible in all images. It is observed for all propellant compositions. Melt layer of RDX and binder is evident in RDX contain propellants. During experiments, it is observed that all propellant burning surface have many star like luminous sparks while combustion, it can be attributed to the aluminium particles combustion (which is 4% for compositions under study) at the propellant surface. These particles leaves the surface and complete combustion takes place out of the propellant surface. 0% RDX composition (Sample1, Fig. 37.5) have lower gaseous content and flame spread angle. Increase in the RDX 6% (Sample 2, Fig. 37.6) have higher gaseous content and flame spread angle. A further increase in RDX to 12% (Sample 3, Fig. 37.7), generates a thinner flame with lower gas content and flame spread angle. Increased RDX percentage, oxygen balance shifts towards fuel rich direction more and combustion wave not generated properly. Incomplete combustion and successive air added combustion is predicted. Hence thinner flame is observed and It have lower spread angle at higher RDX percentage. Luminous intensity (glow) is also increases with increase in the RDX percentage in the composition up to 6% but for higher RDX percentage i.e. 12% it decreases due to incomplete combustion at atmospheric conditions.
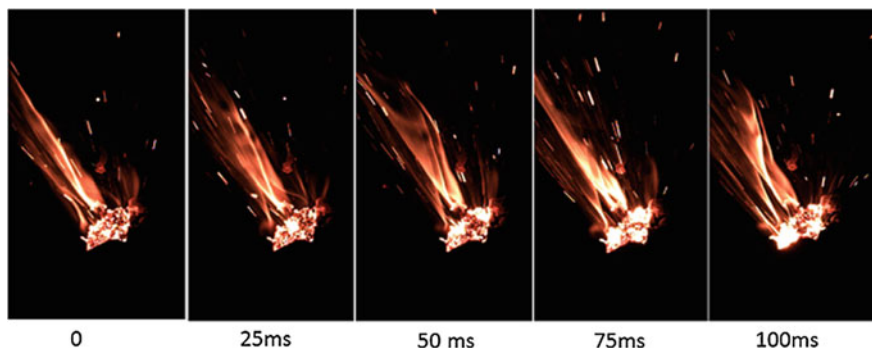
Fig. 37.7 Flame spreading for 17.65% RDX to AP ratio composition propellant

37.4   Conclusions

This studies reveals that increase in RDX percentage reduces thermal diffusivity, whereas increases specific heat and thermal conductivity. It may alter the combustion mechanism of nitramine, specifically RDX contain composite propellants. Flash method used in measurement provides repeatable data for these heterogeneous compositions and errors found in measurement are <5%. Higher specific heat values, for higher RDX contain, will leads to lower burning rate of the composition. Burning surface temperature for the compositions is found 450–520 °C. Heat energy generated at the propellant burning surface is increasing with increase in the RDX contain in propellant. A diffusion type flame structure is produced by these propellant and burning behaviour is entirely changed as compared to homogeneous compositions i.e. NC-NG and nitramine propellants. These experimental data are significant for advance understanding of combustion phenomenon at lower pressure.

References

1. W.H. Hsieh, W.Y. Li, Prop. Expl. Pyrotech **23**, 128–136 (1998)
2. K. K. Kenneth, A. L. Thomas, W. H. Hsieh, Mat. Res. Soc. Symp. Proc., **296** (1993)
3. J. Duterque, G. Lengellet, J. Propulsion, **6**(6) (1990)
4. D.M. Parr, T.P. Parr, Proceedings of the 20th JANNAF Combustion Subcommittee Meeting, Vol. I., 281–291, (CPIA pub 1983), p. 383
5. D.M. Parr, T.P. Parr, J. Energ Mat **17**, 001–047 (1999)
6. M.D. Brigitta, Lawrence Livermore Laboratory report number UCRL-51319 Rev.l., 31 July 1974
7. R.L. Shoemaker, J.A. Stark, R.E. Taylor, High temperatures-high pressures, 9th ETPC Proceedings, **17**, 429–435 (1985)

8. B.B. Stokes, D.W. Booth, R.E. Askins, Proceedings of the 22nd JANNAF Combustion Subcommittee Meeting, Vol. II., (CPIA pub1985), p. 97
9. W.A. Rosser, S.H. Inami, H. Wise, AIAA J **4**, 663 (1966)
10. Y.S. Touloukian, R.W. Powell, C.Y. Ho, P.G. Klemens, Thermal physical Properties of Matter, Vol. 2. Thermal Conductivity, Non-metallic Solid (IFI/Plenum, New York 1970)
11. M.S. Miller, ARL-TO-1319, (Mar 1997)
12. J.T. Rogers, Defense Corporation, Control No. 20-P-26 Series B, (Aug 1962)
13. B.D. Smith, M.S. Ramsburg, J.M. Harrison, U.S. Naval Weapons Laboratory report, TR-2475, (Sept 1970)
14. W. Parker, R. Jenkins, C. Butler, G. Abbott, J. Appl. Phys. **32**, 1679–1684 (1961)
15. L.M. Clark, R.E. Taylor, J. Appl. Phys. **46**, 714 (1975)
16. J.A. Cape, G.W. Lehman, J. Appl. Phys. **34**, 1909 (1963)
17. M.S. Miller, BRL-MR-3819, Ballistics Research Laboratory, Aberdeen Proving Ground, MD (Mar 1990)
18. D.A. Alspach, G.M. Hall, AIAA-91–2192, AIAA/SAE/ASME, 27th Joint Propulsion Conference, June 24–26, Sacramento, CA6 (1991)
19. A.J. Sabadell, J. Wenograd, M. Summerfield, AlAA J. **3**(9), 1580–1584 (1965)
20. C. Zanotti, A. Volpi, in: Nonsteady burning and combustion stability of solid propellants ed. by L.D. Luca, E.W. Price, M. Summerfield. Progress in Astronautics and aeronautics, vol 143, AIAA (1992), ISSN 0079–6050, pp 145–192
21. M. Shusser, N.S. Cohen, F.E.C. Culick, Acta Astronaut. **58**, 617–621 (2006)
22. Y. Yano, K. Miyata, N. Kubota, Prop. Expl. Pyrotech **12**, 137–140 (1987)

Chapter 38
Investigation of Modulation Instability in a Multiple Quantum Well Nanostructure Under EIT Window

Darshana Bora, Plabita Chetia, Jyotshna Das, and Nitu Borgohain

Abstract In this paper we present a theoretical investigation of modulation instability (MI) in a three-level symmetric double quantum well (QW) nanostructure under electromagnetically induced transparency (EIT) window. We employed a weak probe pulse along with a strong control beam in the QW system in a Λ-type of excitation scheme. Using density matrix approximation, we deduced the first- and third-order susceptibility expressions. We found the flexibility in the adjustment of the magnitude of nonlinear susceptibility and group velocity dispersion of the probe field by the control field Rabi frequency, under EIT window. We have investigated the dynamics of MI, which is not only a function of nonlinearity and dispersion but also the input power. The control field parameter has enormous control over MI gain and frequency broadening. At constant input power the gain and the bandwidth of MI varies with control field Rabi frequency. By tuning the control field intensity to a suitable value the probe pulse can be made stable against modulation instability.

38.1 Introduction

The modulation instability (MI) is a fundamental nonlinear phenomenon which is observed in diverse fields like fluid dynamics, plasma physics, nonlinear optics [1–4], etc. MI refers to an exponential growth of weak perturbations of a continuous wave resulting from interplay between the dispersion and the nonlinearity. Due to MI, in time domain, the wave disintegrates during propagation, leading to filamentation of pulse trains and in spectral domain, it results the generation of frequency sidebands around the central frequency of the pump pulse. From its discovery [5] in optical fibers, MI has been studied extensively, due to their potential applications in frequency generation, optical switching and laser techniques. MI is also responsible for the formation of both spatial and temporal solitons. MI is one of the major factors that limits the transmission capacity of long-haul optical communication

D. Bora (✉) · P. Chetia · J. Das · N. Borgohain
Department of Physics, University of Science and Technoloygy, Ri-Bhoi, Meghalaya 793101, India

system. It can also be used to generate chains of short optical pulses for high bit data transmission [6].

Recently, several nonlinear optical phenomena originating from quantum coherent and interference, such as, electromagnetically induced transparency (EIT), quantum coherent control [7], quantum information processing [8–12], gain without inversion (GWI) [13, 14], slow light, Kerr nonlinearity, optical soliton etc., have been studied extensively in semiconductor quantum wells (SQW). The devices based on SQWs possess intrinsic properties like large optical dipole moments, high nonlinear coefficients and wide adjustable parameter that offer large flexibility in device design. Though, the study of MI in QWs still rare, but recently, the effects of higher-order dispersion and nonlinearity on MI in SQWs have been studied [15, 16]. In this article we have studied the effect of control field intensity on MI gain spectrum of a weak probe field, results of which may have important applicability in nonlinear optics.

38.2   Theoretical Model and Governing Equations

We adopted a three-level symmetric multiple quantum well (MQW), which comprises of 40 coupled well periods, each with two GaAs wide wells of thickness 92 Å which are separated by AlGaAs barrier of 30.9 Å as shown in Fig. 38.1. This MQW was first introduced by Fejer et al. [8] in 1989. A weak probe pulse of angular frequency ω_p is applied to drive the $|1\rangle \rightarrow |3\rangle$ transition, where as a strong control laser beam of angular frequency ω_c employed to drive the $|2\rangle \rightarrow |3\rangle$ transition, in a Λ-type configuration, which is depicted in Fig. 38.2. The system adopted in this study can be designed to have energies $\varepsilon_1 = 38$ meV, $\varepsilon_2 = 152$ meV and $\varepsilon_3 = 342$ meV. The electric field employed in the MQW can be expressed as,

Fig. 38.1 Schematic diagram of a single period of the multiple quantum well, adopted for this investigation
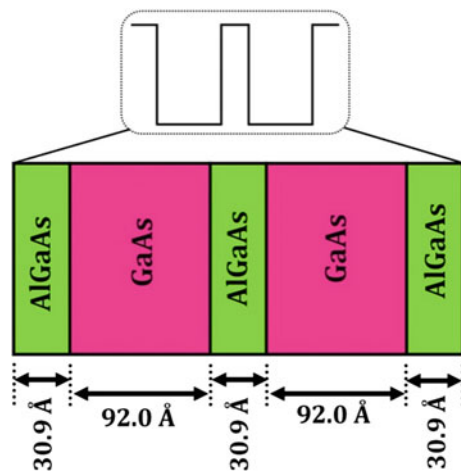
Fig. 38.2 Energy level diagram and the Λ-type excitation scheme of the quantum wellsystem
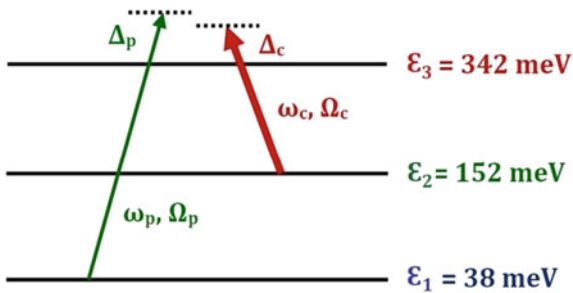
$$\vec{E} = \hat{e}_p E_p e^{-i\omega_p t} + \hat{e}_c E_c e^{-i\omega_c t} + c.c, \tag{38.1}$$

where $\hat{e}_p$ and $\hat{e}_c$ are unit vectors towards polarization direction of the probe field E_p and control field E_c, respectively. ω_p and ω_c are the angular frequencies of the E_p and E_c, respectively. In a Schrödinger picture the semi-classical Hamiltonian of the MQW can be expressed as,

$$
\begin{aligned}
H = \sum_{i=1}^{3} \hbar\omega_i |i\rangle\langle i| &- \hbar\big[\Omega_p e^{-i\omega_p t}|3\rangle\langle 1| + \Omega_c\, e^{-i\omega_c t}|3\rangle\langle 2| \\
&+\Omega_p^* e^{i\omega_p t}|1\rangle\langle 3| + \Omega_c^* e^{i\omega_c t}|2\rangle\langle 3|,
\end{aligned} \tag{38.2}
$$

where Ω_p and Ω_c are half Rabi frequencies of pump and control field respectively, which defined as $\Omega_p = \frac{\mu_{31}E_p}{\hbar}$ and $\Omega_c = \frac{\mu_{32}E_c}{\hbar}$ respectively. $\mu_{mn} = \langle m|z|n\rangle$ are the dipole matrix elements for the transitions $|m\rangle \to |n\rangle$. We adopted the density matrix formalism to describe the rate equations of these states [12–14], which are as follows:

$$\frac{\partial}{\partial t}\tilde{\rho}_{11} = -i\Omega_p\tilde{\rho}_{13} + i\Omega_p^*\tilde{\rho}_{31} \tag{38.3a}$$

$$\frac{\partial}{\partial t}\tilde{\rho}_{22} = -i\Omega_c\tilde{\rho}_{23} + i\Omega_c^*\tilde{\rho}_{32} - \gamma_2\tilde{\rho}_{22} \tag{38.3b}$$

$$\frac{\partial}{\partial t}\tilde{\rho}_{33} = i\Omega_p\tilde{\rho}_{13} - i\Omega_p^*\tilde{\rho}_{31} + i\Omega_c\tilde{\rho}_{23} - i\Omega_c^*\tilde{\rho}_{32} - \gamma_3\tilde{\rho}_{33} \tag{38.3c}$$

$$\frac{\partial}{\partial t}\tilde{\rho}_{21} = i\left(\Delta_p - \Delta_c\right)\tilde{\rho}_{21} - i\Omega_p\tilde{\rho}_{23} + i\Omega_c^*\tilde{\rho}_{31} - \frac{1}{2}\gamma_{12}\tilde{\rho}_{21} \tag{38.3d}$$

$$\frac{\partial}{\partial t}\tilde{\rho}_{31} = i\Omega_p\tilde{\rho}_{11} - i\Omega_p^*\tilde{\rho}_{33} + i\Omega_c\tilde{\rho}_{21} - \frac{1}{2}\gamma_{13}\tilde{\rho}_{31} + i\Delta_p\tilde{\rho}_{31} \tag{38.3e}$$

$$\frac{\partial}{\partial t}\tilde{\rho}_{32} = i\Omega_p\tilde{\rho}_{12} + i\Omega_c\tilde{\rho}_{22} - i\Omega_c\tilde{\rho}_{33} - \frac{1}{2}\gamma_{23}\tilde{\rho}_{32} + i\Delta_c\tilde{\rho}_{32} \tag{38.3f}$$

These equations are supplemented under adiabatic frame work, $|\Omega_p| \ll |\Omega_c|$, where $\tilde{\rho}_{11} = 1$, $\tilde{\rho}_{22} \simeq \tilde{\rho}_{33} = 0$. Here Δ_p and Δ_c are the detuning defined as, $\Delta_p = \omega_p - \omega_{31}$ and, $\Delta_c = \omega_c - \omega_{32}$, ω_{mn} being the angular frequency of a resonant transition between the states $|m\rangle \rightarrow |n\rangle$. Taking Fourier transformation in (38.3d) and (38.3e), we have $\beta_{21}^{(1)} = \frac{\Lambda_p \Omega_c^*}{D(\omega)}$ and $\beta_{31}^{(1)} = -\frac{\Lambda_p D_p(\omega)}{D(\omega)}$, where β_{21} and β_{31} are the Fourier transforms of $\tilde{\rho}_{21}$ and $\tilde{\rho}_{31}$. $D_p(\omega) = \left(\omega + \Delta_p - \Delta_c + i\frac{\Upsilon_{21}}{2}\right)$ and $D(\omega) = \left(\omega + \Delta_p + i\frac{\Upsilon_{31}}{2}\right)\left(\omega + \Delta_p - \Delta_c + i\frac{\Upsilon_{21}}{2}\right) - \Omega_c^2$. By applying inverse Fourier transform, solution of the 38.3d and 38.3c are evaluated as $\tilde{\rho}_{21} = \frac{\Omega_p \Omega_c^*}{D(\omega)}$ and $\tilde{\rho}_{31} = -\frac{\Omega_p D_p(\omega)}{D(\omega)}$.

The induced polarization of a medium due to the probe field is defined as, $P = \varepsilon_0 \chi_p E_p$, where, ε_0 is the permittivity in vacuum and χ_p is the optical susceptibility of the MQW. The polarization due to probe field is expressed as, $P = ND = N\mu_{31}\tilde{\rho}_{31}^{(1)}$, where D is the dipole moment operator and N is the electron concentration. From the above relations the expression for optical susceptibility can be obtained as

$$\chi_p = \frac{N|\mu_{13}|^2}{\varepsilon_0 \Omega_p \hbar} \tilde{\rho}_{31} \tag{38.4}$$

Using the following relations, $\tilde{\rho}_{11} \simeq \tilde{\rho}_{11}^{(0)} \simeq 1$, and $|\tilde{\rho}_{11}|^2 + |\tilde{\rho}_{22}|^2 + |\tilde{\rho}_{33}|^2 = 1$, (38.4) can be recasted as,

$$\chi_p = \frac{N|\mu_{13}|^2}{\varepsilon_0 \Omega_p \hbar}\left[\tilde{\rho}_{31}^{(1)} - \tilde{\rho}_{31}^{(1)}\left(|\tilde{\rho}_{22}|^2 + |\tilde{\rho}_{33}|^2\right)\right] \tag{38.5}$$

The optical susceptibility can be divided into linear and non linear parts as the following expression: $\chi_p = \chi^{(1)} + \chi^{(3)}|E_p|^2$. Thus, the linear and third order susceptibility can be written as,

$$\chi^{(1)} = -\frac{N|\mu_{13}|^2 D_p(0)}{\hbar\varepsilon_0 D(0)}, \tag{38.6a}$$

$$\chi^{(3)} = \frac{N|\mu_{13}|^4}{\hbar^3\varepsilon_0}\frac{(|\Omega_c^*|^2 + |D_p(0)|^2)D_P(0)}{|D(0)|^2 D(0)}. \tag{38.6b}$$

We are now in a position to examine the results of the first-order or linear and third-order or nonlinear susceptibilities under an EIT condition, which are executed by employing numerical simulation.

38.3   Linear and Kerr-Susceptibilities

In this section we investigate the properties of linear and Kerr (nonlinear) suscepti-
bilities of the MQW. For our investigation, we have adopted the following system
parameters: $N = 5 \times 10^{23} \text{m}^{-3}$, $\varepsilon_0 = 8.85 \times 10^{-12} C^2 N^{-1} m^{-2}$, $\mu_{13} = 1.184 \times 10^{-29}$ mC, $\gamma_{21} = 0.05 \times 10^{12} s^{-1}$ and $\gamma_{13} = 0.11 \times 10^{12} s^{-1}$. We first focus on
the linear or first-order susceptibilities which lead to the EIT phenomena. From
the profile of $Im \chi^{(1)}$ as depicted in Fig. 38.3a, it is evident that when the control
field is not applied, i.e. $\frac{\Omega_c}{\delta} = 0$, the probe field at resonance $\left(\frac{\Delta_p}{\delta} = 0 \right)$ is largely
absorbed, appearing an absorption peak. Here δ represents a normalizing term with
value $1.0 \times 10^{12} s^{-1}$ which we have used throughout the results. When the control
field is switched ON i.e. when $\Omega_c = 2.0 \text{ ps}^{-1}$ the absorption peak splits into two sepa-
rate peaks which indicate the EIT window formation. With further increase of Ω_c the
splitting of the peaks become wider which indicate the increase of the EIT window.
In Fig. 38.3b we plot the real part of $\chi^{(1)}$ which indicates the linear dispersion and
the refractive index of the system. In this figure, it is seen that Re $\chi^{(1)}$ changes from
positive to negative values as Δ_p changes from negative to positive, at zero control
field situation. With the increase of Ω_c, the scenario of Re $\chi^{(1)}$ profile changes from
negative to positive values around the probe resonance $\left(\frac{\Delta_p}{\delta} = 0 \right)$. The separation
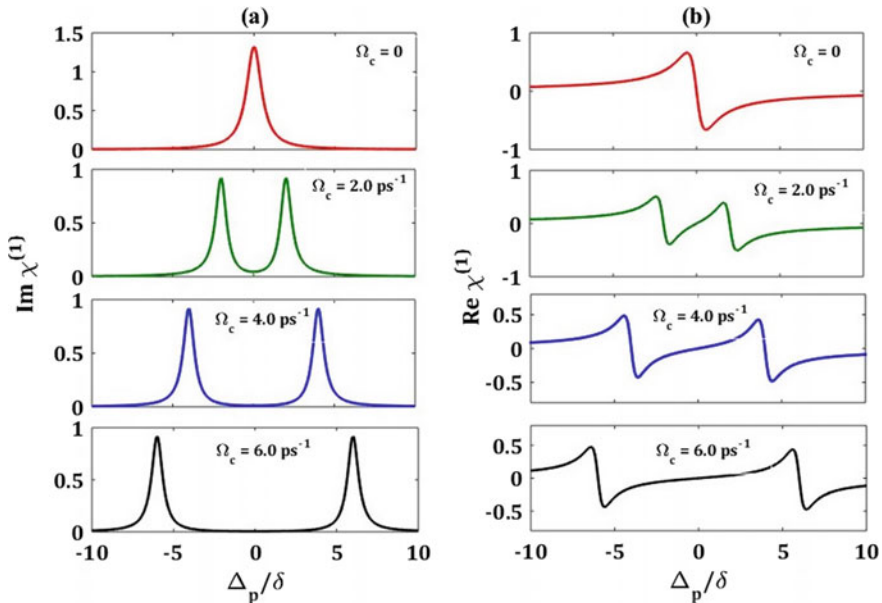
Fig. 38.3 Profile of linear susceptibility v/s probe detuning. **a** Represents the imaginary part of the
susceptibility. **b** Represents the real part of the susceptibility. Values of Rabi frequency of the pump
laser are $\Omega_c = 0$, $\Omega_c = 2.0 ps^{-1}$, $\Omega_c = 4.0 ps^{-1}$, and $\Omega_c = 6.0 ps^{-1}$

Fig. 38.4 Variation of $\chi^{(3)}$ for different Ω_c. **a** Real part of $\chi^{(3)}$ at $\Omega_c = 0$. **b** Real part of $\chi^{(3)}$ at $\Omega_c = 2.0\,ps^{-1}$ **c** Real part of $\chi^{(3)}$ at $\Omega_c = 4.0\,ps^{-1}$ **d** Real part of $\chi^{(3)}$ at $\Omega_c = 6.0\,ps^{-1}$
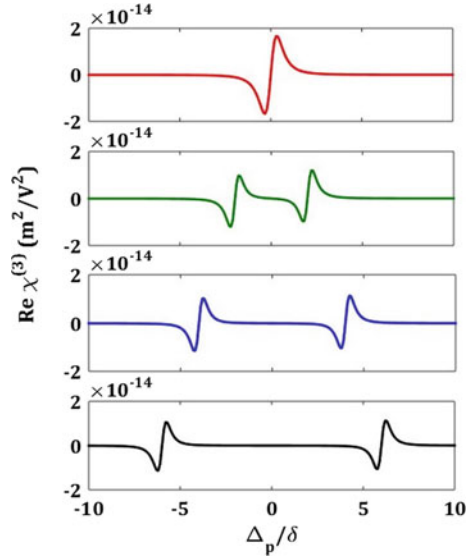
between the peaks in this case also increases with the increase of Ω_c, indicating a change in group velocity dispersion. The negative slope for the case $\frac{\Omega_c}{\delta} = 0$ indicates the change in group velocity dispersion from normal to anomalous dispersion regime, whereas the positive slope in other case indicates the group velocity dispersion which changes from anomalous to normal dispersion regime. Thus by tuning the control Rabi frequency to a suitable value, the dispersion can shift to a suitable value.

We now carry on the examination of the higher order susceptibilities. In Fig. 38.4 we plotted the variation of the real part of the third-order nonlinear susceptibility $(Re\chi^{(3)})$, that leads to the Kerr nonlinearity, as a function of probe detuning $\frac{\Delta_p}{\delta}$ with a variation of control field Ω_c, at resonance $(i.e.\,\Delta_c = 0)$. From the different curves in Fig. 38.4, it is clear that by tuning the value of Rabi frequency of the control field the peak value of $\chi^{(3)}$ can be shifted to different probe frequencies. Thus a desired nonlinearity can be selected just by tuning the probe detuning to a suitable value. Moreover, the value of $\chi^{(3)}$ is still found to possess a very high value within the EIT window.

38.4   Dispersion and Nonlinear Schrödinger Equation

The evolution of the probe electric field in the MQW is governed by Maxwell's wave equation is given by,

$$\left(\nabla^2 - \frac{1}{c^2}\frac{\partial^2}{\partial t^2}\right)\vec{E}(\vec{r}, t) = \frac{1}{\varepsilon_0 c^2}\frac{\partial^2}{\partial t^2}\vec{P}(\vec{r}, t), \tag{38.7}$$

where c is the light speed in vacuum. Under a slowly varying envelope approximation, the above equation reduces to a first order equation described as,

$$\frac{\partial \Omega_p}{\partial Z} + \frac{1}{C}\frac{\partial \Omega_p}{\partial t} = i\,\kappa\,\tilde{\rho}_{31} = i\,\kappa\left[\tilde{\rho}_{31}^{(1)} - \tilde{\rho}_{31}^{(1)}\left(|\tilde{\rho}_{22}|^2 + |\tilde{\rho}_{33}|^2\right)\right], \tag{38.8}$$

where $\kappa = \frac{N|\mu_{13}|^2\omega_P}{2\hbar\varepsilon_0 c}$. Taking Fourier transformation of the linearized version of (38.8) we get.

$$\frac{\partial \Lambda_p}{\partial Z} - i\left\{\frac{\omega}{C} - \kappa\frac{D_p(\omega)}{D(\omega)}\right\}\Lambda_p = \frac{\partial \Lambda_p}{\partial Z} - i K(\omega)\Lambda_p = 0 \tag{38.9}$$

where, $K(\omega) = \frac{\omega}{c} - \kappa\frac{D_p(\omega)}{D(\omega)}$. Taylor series expansion of $K(\omega)$ is given as.

$$K(\omega) = K(0) + K_1(0)\omega + \frac{1}{2}K_2(0)\omega^2 + \frac{1}{6}K_3(0)\omega^3 + \ldots, \tag{38.10}$$

here, $K(0)$ indicates the linear phase-shift, while $K_1(0)$ is related to the group velocity. K_2 describes the group velocity dispersion (GVD) of the probe field which causes spreading of the field during propagation of the pulse.

Under a retarded frame, the nonlinear evolution equation is casted in the form of a nonlinear Schrödinger equation (NLSE) which is given by [16]

$$\frac{\partial \Omega_p}{\partial Z} - \frac{1}{2}K_2\frac{\partial^2\Omega_p}{\partial t^2} + W|\Omega_P|^2\Omega_P = 0, \tag{38.11}$$

where W represents a third order nonlinear term related to the nonlinearity of MQW system, and is given by, $W = \left[\kappa D_p(0)\frac{|\Omega_c^*|^2 + |D_P(0)|^2}{D(0)|D(0)|^2}\right]$. The above NLSE is to be used for formulation of modulation instability in the QW system under the effect of dispersion and non-linearity.

38.5 Dynamics of Modulation Instability

We consider a steady state solution of $\Omega_p(\xi, t) = \left[\sqrt{p_0} + a(\xi, t)\right]e^{i\omega p_0\xi}$ of the (38.11), which reduces the equation to following form.

$$i\frac{\partial a}{\partial \xi} - \frac{1}{2}K_2\frac{\partial^2 a}{\partial T^2} + W\sqrt{p_0}(a + a^*) = 0, \tag{38.12}$$

where $\sqrt{p_0}$ is the amplitude of the continuous wave and $a(\xi, t)$ is a small perturbation to that amplitude. Consider the general solution of (38.12), consist of two sideband plane waves described by.

$$a(Z, T) = Ue^{i(K\xi - \Omega T)} + Ve^{-i(K\xi - \Omega T)}, \tag{38.13}$$

where K and Ω are wave vector and frequency shift, respectively. U and V are the amplitudes of the perturbed field. Substituting (38.13) into (38.12) we get a homogeneous equation for U and V written in matrix form as below

$$\begin{bmatrix} -K + \frac{\Omega^2 K_2}{2} + Wp_0 & Wp_0 \\ Wp_0 & K + \frac{\Omega^2 K_2}{2} + Wp_0 \end{bmatrix}\begin{bmatrix} U \\ V \end{bmatrix} = 0 \tag{38.14}$$

The MI gain $g(\Omega)$ at any frequency Ω is defined as $g(\Omega) = 2Im(K)$. The spectrum of theMI gain is expressed as

$$g(\Omega) = \sqrt{4K_2\Omega^2 Wp_0 - \Omega^4 K_2^2} \tag{38.15}$$

The maximum frequency $\Omega_{max} = \sqrt{\frac{2p_0 W}{K_2}}$ at maximum gain leads to $g_{max} = 2Wp_0$, and the critical frequency is given by.

$$\Omega_{critical} = \sqrt{\frac{4Wp}{K_2}}. \tag{38.16}$$

Now we proceed to investigate the MI characteristics of the probe pulse under an EIT window. Before proceeding to the investigation of MI, it is noteworthy to select a suitable probe frequency at which absorption is negligible, as well as, the dispersion and the nonlinearity are large. Therefore, first we select the probe detuning at $\Delta_p = 1.0\text{ps}^{-1}$, which corresponds to the probe wavelength at $4.07\mu m$. Figure 38.5 shows that when we applied the probe field at frequency $\omega_p = 462.8ps^{-1}$ without the control field, the probe field is initially highly absorbed inside the MQW. At this point, the absorption is found to be 0.319. To reduce this absorption we applied a suitable control field $\Omega_c = 6.0ps^{-1}$ for which EIT window is created, resulting a reduction of absorption as low as 0.0058 (at $\Delta_p = 1.0\text{ps}^{-1}$), which is found to be 55 times lesser than the former.

Under the system parameters mentioned in previous section, the group velocity dispersion (GVD) and nonlinear coefficient (W) at the selected probe detuning at $\Delta_p = 1.0ps^{-1}$, are found to be 2.80×10^{-21} m^{-1}s^2 and 4.87×10^{-22} m^{-1}s^2, respectively. Taking into consideration these values, we plot the MI gain with respect
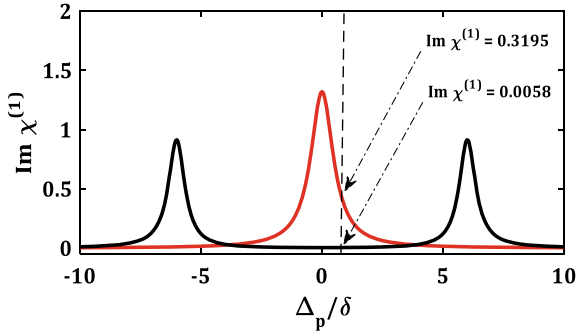
Fig. 38.5 Profile of imaginary part of the linear susceptibility with respect to the normalized probe detuning for control Rabi frequencies $\Omega_c = 0$ (red), and $\Omega_c = 6$ ps^{-1}(black). Normalization term used here is $\delta = 1$ ps^{-1}. Vertical dashed line cuts the $Im\chi^{(1)}$ curves at values 0.319 and 0.0058, indicating that at probe detuning $\Delta_p/\delta = 1.0$, absorption reduces by 55 times when a suitable control field $\Omega_c = 6$ ps^{-1} is applied

to frequency shift (Ω) for an increasing range of power, as shown in Fig. 38.6. Figure 38.6 depicts that the MI growth increases with increase of power in a linear fashion. The width of the frequency shift also grows linearly with power.

We now investigate how the growth of MI is affected by different control field Rabi frequencies (Ω_c). In Fig. 38.7, we depict MI gain as a function of power and frequency shift for different values of Ω_c ($\Omega_c = 0.2$ps^{-1}, 0.4ps^{-1}, 0.6ps^{-1}, 1.7ps^{-1}, 1.9ps^{-1} and 2.3ps^{-1}). Figure 38.7a shows the linear growth of the MI gain for the case of $\Omega_c = 0.2 ps^{-1}$. It is seen from the figure that, the MI growth is analogous to that of Fig. 38.6, also the bandwidth increases with the increase of power. For a slight

Fig. 38.6 The gain spectra of the modulation instability as a function of frequency and normalized power p_0
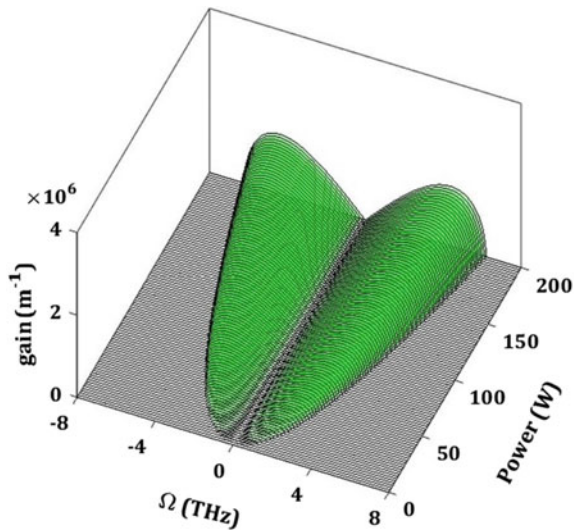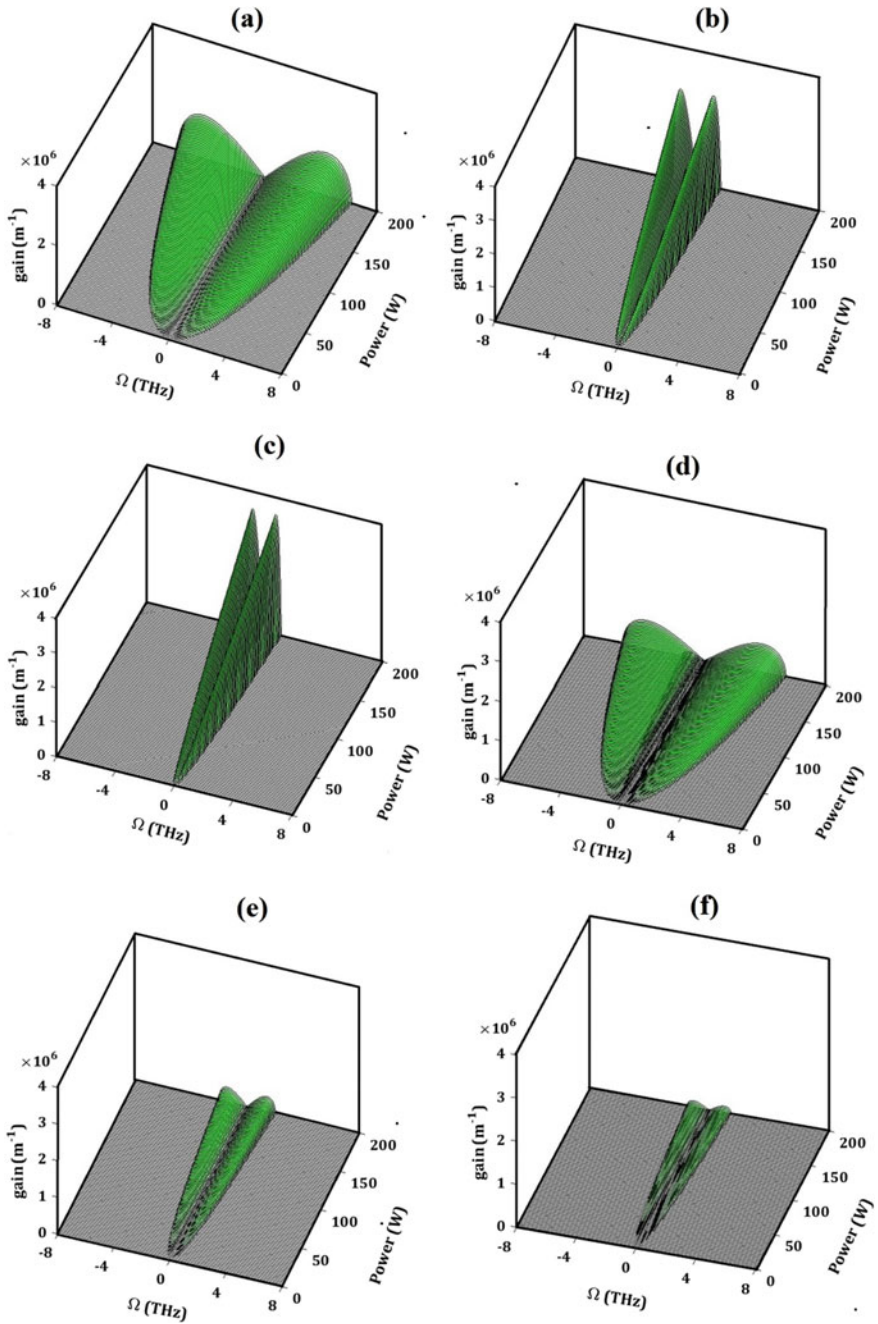
Fig. 38.7 MI gain spectra as functions of power and frequency shift at different control Rabi frequencies **a** $\Omega_c = 0.2\,\text{ps}^{-1}$, **b** $\Omega_c = 0.4\,\text{ps}^{-1}$, **c** $\Omega_c = 0.6\,\text{ps}^{-1}$, **d** $\Omega_c = 0.8\,\text{ps}^{-1}$, **e** $\Omega_c = 1.9\,\text{ps}^{-1}$, and **f** $\Omega_c = 2.3\,\text{ps}^{-1}$

increase of $\Omega_c(=0.4 \text{ ps}^{-1})$, the gain shows a different behavior, which is depicted in Fig. 38.7b. For $\Omega_c = 0.4 \text{ ps}^{-1}$, the height of the gain increases, whereas the bandwidth decreases. For the case of $\Omega_c = 0.6 \text{ ps}^{-1}$, the height of the gain increases more, but decreases in the bandwidth as compared to the case of $\Omega_c = 0.4 \text{ ps}^{-1}$, which is depicted in the Fig. 38.7c. At $\Omega_c = 1.7 \text{ ps}^{-1}$, as shown in Fig. 38.7d, it results a drastic decay in the gain height, but spreading in frequency shift increases. With further increase in Ω_c, (1.9 ps^{-1} and 2.3 ps^{-1}) the gain as well as spreading of frequency shift both decreases to minimum, which are depicted in Fig. 38.7e, and f. From the above results it is clear that, a significant effect of MI can be found for lower values of the control Rabi frequency, whereas, for the higher values the effect of MI is smaller. Thus, the control Rabi frequency has a great control over the MI gain of the probe pulse, along with EIT.

38.6 Conclusion

In conclusion, we include the summery of the results obtained from present systemic investigation, where we adopted a three-level MQW system, in which a probe pulse is used to investigate the nonlinear susceptibilities, linear dispersions as well as modulation instabilities, under the effect of the frequency of a control laser beam. By following density matrix approximation, we have obtained the expression for first and third-order susceptibilities. We have adjusted the control field Rabi frequency to manage the magnitude of nonlinearity and group velocity dispersion of the probe field. We identified the existence of large third-order susceptibility of the order of $10^{-15} \text{m}^2/\text{v}^2$. The investigation of MI under an EIT window reveals that the both the gain and frequency bandwidth of MI can be modulated as desired by tuning the frequency of the control field.

References

1. T.B. Benjamin, J.E. Feir, J. Fluid Mech. **27**, 417 (1967)
2. Y.H. Ichikawa, T. Suzuki, T. Taniuti, J. Phys. Soc. Jpn. **34**, 1089 (1973)
3. G.P. Agrawal, *Nonlinear Fiber Optics*, 5th edn. (Academic Press, California, 2013)
4. V.E. Zakharov, L.A. Ostrovsky, Physica D **238**, 540 (2009)
5. A. Hasegawa, Opt. Lett. **9**, 288–290 (1984)
6. F.K. Abdullaev, S.A. Darmanyan, J. Garnier, Progress in Opt. **44**, 303–307 (2002)
7. M.D. Lukin, Rev. Mod. Phys. **75**, 457–472 (2003)
8. M.M. Fejer, S.J.B. Yoo, R.L. Byer, Phys. Rev. Lett. **62**, 1041–1044 (1989)
9. M.D. Lukin, Yelin, M. Fleischhauer, Phys. Rev. Lett. **84,** 4232–4235 (2000)

10. M. Fleischhauer, M.D. Lukin, Phys. Rev. Lett. **84**, 5094–5097 (2000)
11. A. Chen, Opt. Exp. **19**, 11944–11950 (2011)
12. G.B. Serapiglia et al., Phys. Rev. Lett. **84**, 1019–1022 (2000)
13. M.O. Scully, M.S. Zubairy, *Quantum Optics* (Cambridge University Press, NY, 1997)
14. M.D. Frogley et al., Nat. Mat. **5**, 175–178 (2006)
15. S. Swetanshumala, S. Konar, A. Biswas, Appl. Phys. B **111**, 53–64 (2013)
16. N. Borgohain, S. Konar, J. Appl. Phys. **119**, 213103 (2016)

Chapter 39
Fabrication of Polyaniline Nanospheres as a Good Electrode Material in Supercapacitors

Gyan Singh, Mashqoor Alam, Taslim Ahmad, Shahina Shaheen, Yogesh Kumar, and Samina Husain

Abstract Herein we fabricate and synthesize Polyaniline Nanospheres (PANI$_{NS}$) via simple oxidative polymerization of Aniline, HCl, APS as an oxidant and *TX-100* as a non-ionic surfactant. It is expected that the specific capacitance of Polyaniline (PANI) should change as the morphology of PANI changes due to increase in the porosity of the structure and an enhanced surface area. The diameter of the synthesized PANI$_{NS}$ is in the range of 500–780 nm. The structural morphology PANI$_{NS}$ is investigated by FESEM, FTIR and XRD respectively. To study the behavior of PANI$_{NS}$ for electrochemical properties, CV is done at scan rates of 10, 50, 100 mV/s. The calculated PANI$_{NS}$ have a specific capacity of 589 Fg^{-1} in 0.1 M H_2SO_4 solution at 10 mV/s. The present nanospheres morphology of PANI projects to be one of the good candidates for its application as supercapacitor electrode.

Abbreviation

PANI$_{NS}$	Polyaniline Nanospheres
APS	Ammonium Persulfate.
FE-SEM	Field-Emission Scanning Electron Microscopy.
FT-IR	Fourier Transform Infrared Spectroscopy.
XRD	X-ray powder diffraction.
CV	Cyclic Voltammetry.
PVDF	Polyvinyledene Fluoride.
TX-100	Triton X-100.
C$_{sp}$	Specific Capacitance.
V	Potential window.
M	Mass.

Y. Kumar
Department of Physics, ARSD College, University of Delhi, New Delhi 110021, India

G. Singh · M. Alam · T. Ahmad · S. Shaheen · S. Husain (✉)
Centre for Nanoscience and Nanotechnology, Jamia Millia Islamia, New Delhi 110025, India
e-mail: shusain3@jmi.ac.in

NMP   N-Methyl-2-pyrrolidone.
DI   Deionized water.

39.1   Introduction

In response to the changing global landscape, efforts are being made to develop
economical and environment friendly lightweight energy-storage devices that are
sustainable and suitable for power sources such as supercapacitors. One such energy
storage device is a pseudo-supercapacitor that have emerged with the potential to
assist advances in energy-storage materials. In contrast to conventional capacitors,
pseudo-supercapacitors possess much higher energy densities which stores charges
faradaically. This faradaic process allows them to show greater capacitance and
energy densities than the other capacitive devices. It is envisaged that good capaci-
tive behaviour arises through oxidation/reduction reactions occurring on the surface
as well in the bulk material. The oxidation/reduction mechanisms are powerful
reversible reactions because no changes in a structural elements like phase and
crystallinity appear during these reactions.

Polyaniline (PANI), in the category of conducting polymers are the ideal candi-
date materials for pseudocapacitors because they possess good oxidation/reduction
reaction potential, conductivity, facile synthesis method and favorable environmental
durability [1–5]. They have capacitance values 10,000-times higher in comparison
to those of electrolytic capacitors; $\leq$ 12,000 F at working voltages of 1.2 V. Their
specific capacitance can also show a drastic change as their morphology changes
because their aspect ratio changes.

The choice of the electrode material has a remarkable impact on its specific capac-
itance, rate performance, power capability and stability of a pseudocapacitor [6].
Also, electrolyte plays an important role in deciding the enhanced and improved
electrochemical properties of any supercapacitor. Some recent research papers have
indicated that 0.1 M H_2SO_4 is a strong electrolyte, and that the specific capacitance
of the pseudocapacitive material can be greatly improvised using it. Therefore, using
H_2SO_4 with an effective specific area could establish a conducting network in the
capacitive system.

Herein, we report Polyaniline nanospheres ($PANI_{NS}$) as an electrode material
obtained through simple chemical oxidative polymerization method in the presence
of surfactant Triton (TX-100), which is neutral (nonionic) surfactant. TX-100 is a
surface-active agent that provides porosity and a good surface area in the 0.1 M
H_2SO_4 electrolyte. Two electrode electrochemical system is used to evaluate the
performance of the as-synthesized $PANI_{NS}$.

39.2   Experimental

39.2.1   Materials

Aniline (99.5%), Sodium hydroxide (NaOH) (99%), Triton (TX-100) (99%), Ammonium Persulfate (APS) (98%), Sulfuric Acid (H_2SO_4) (99.99%), N-Methyl-2-pyrrolidone (NMP) (98%), Acetylene Black (%) and Polyvinyledene Fluoride (PVDF) (98%). All the chemicals were analytical grade and were used without further purification.

39.2.2   Synthesis of Polyaniline Nanospheres (PANI$_{NS}$)

PANI$_{NS}$ were synthesized by a simple chemical oxidative polymerization method. In the synthesis process, 25 mM Aniline, 25 mM NaOH and 0.70 mM TX-100 were dispersed in 20 ml DI water for 30 min. with constant magnetic stirring at room temperature. The reaction mixture was then cooled for 10 min. in an ice bath. 20 ml oxidizing solution containing 25 mM APS was now added drop wise to the above reaction mixture and stirred for 1 min. The resultant precipitation was kept untouched at room temperature for 12 h. Finally, the resultant was washed with DI water and ethanol until the color of the material is neutral. Lastly, the as-synthesized PANI$_{NS}$ was heated for 24 h at 60^0C.

39.2.3   Characterization Analysis

The morphology of the synthesized PANI$_{NS}$ material was analyzed with the FE-SEM, ZEISS. The structures of PANI$_{NS}$ were characterized by XRD (Rigaku) and FT-IR (JASCO FT-IR 410 Spectrophotometer).

The Electrochemical performance such as CV, was evaluated using Potentiostat (CHI604E). The working electrode of PANI$_{NS}$ was made using a mixture of 80 wt. % PANI$_{NS}$ (active material), 10 wt. % Acetylene black and 10 wt. % PVDF. The material was dispersed in NMP to form slurry with proper viscosity. It was then drop casted onto graphite sheet, which was used as current collector. The graphite sheet was finally dried at 80^0 C for 24 h in an oven.
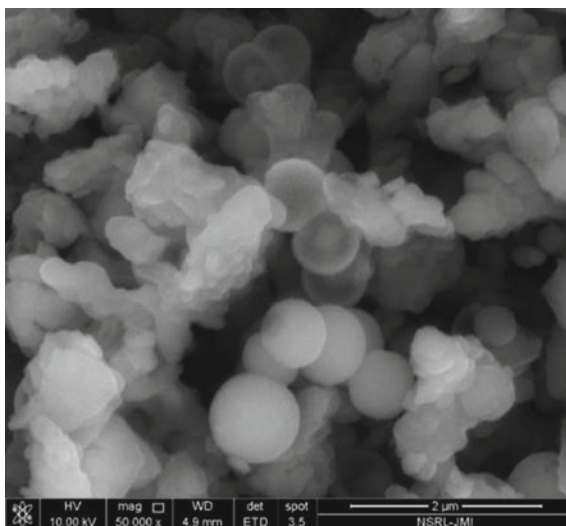
39.3 Results and Discussions

39.3.1 FESEM Analysis

The synthesized PANI$_{NS}$ obtained by simple chemical oxidative polymerization method in the presence of TX-100. The morphology via FE-SEM is shown in Fig. 39.1. Spheres of PANI$_{NS}$ can be observed clearly from the FESEM image. PANI$_{NS}$ are observed with average diameter in the range of 500–780 nm.

39.3.2 FTIR Analysis

To analyse the chemical structure of PANI$_{NS}$, the material is evaluated through FTIR in the range (500–2500 cm^{-1}) (Fig. 2a). Five characteristic peaks can be seen. The peak at 1583 cm^{-1} is due to quinoid ring deformations of the aromatic ring. C = C the peak at 1498 cm^{-1} and the band at 1300 cm^{-1} due to C-N and C = N stretching of benzene rings and aromatic amines respectively. The aromatic C-H bending band contributes to peak at 1130 cm^{-1} and peak at 826 cm^{-1} is attributed to the out of plane deformation of C-H in the 1,4 substituted benzene rings [7–10]. No peak was observed for Triton. Therefore, it can be said that TX-100 surfactant has no effect on the structure of PANI.
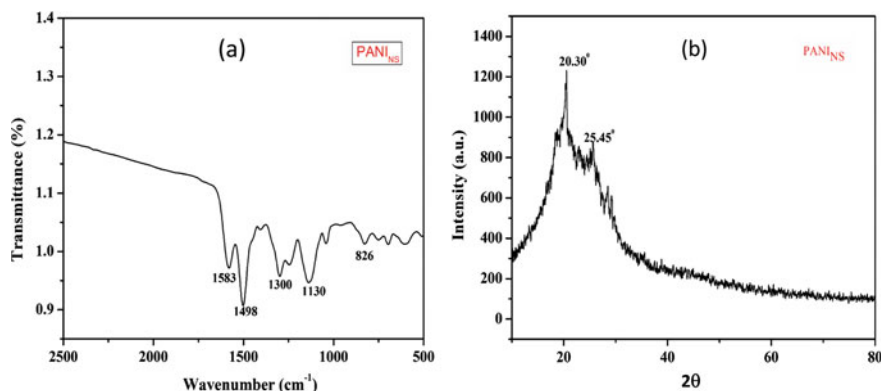
Fig. 39.2 a FTIR spectra and **b** XRD pattern of PANI$_{NS}$

39.3.3 XRD Analysis

Figure 39.2b shows the XRD pattern of synthesized PANI$_{NS}$ of a highly crystalline material with 2θ centred at 20.30° and 25.45° corresponding to the (hkl) plane (011) and (110) respectively [11, 12].

39.3.4 Electrochemical Measurements of PANI$_{NS}$ as an Electrode Material for Supercapacitor

The electrochemical performance was carried out in a two-electrode system at room temperature using aqueous 0.1 M H$_2$SO$_4$ electrolyte solution to analyze the Cyclic Voltammetric (CV) performance of the PANI$_{NS}$.

39.3.4.1 CV Analysis

Figure 39.3 represents CV for PANI$_{NS}$ electrode in the two-electrode cell setup in the potential window of 0–0.8 V. The measurements have been performed in 0.1 M H$_2$SO$_4$ solution. The performance of PANI$_{NS}$ as a good electrode material is evaluated at sweep rates 10, 50,100 mV/s.

The specific capacitance (C$_{sp}$) of the PANI$_{NS}$ is calculated using the following formula:

$$C_{sp} = \frac{1}{m \times V \times \Delta V} \int Iv.dv \qquad (39.1)$$
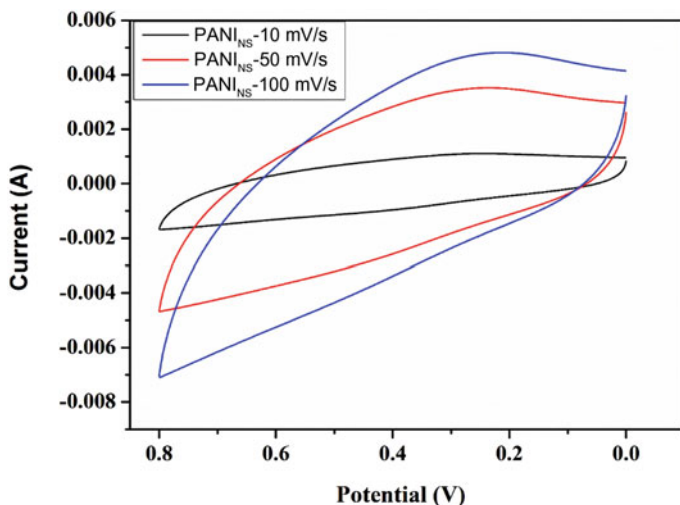
Fig. 39.3 CV curves of PANI$_{NS}$ measured at 10,50,100 mV/s scan rates

where C$_{sp}$ is the specific capacitance in Fg^{-1}, m is the mass of the single electrode material (PANI$_{NS}$) deposited on the graphite sheet, v is the sweep rate in mV/s and ΔV is the potential window, and I is the current obtained in the CV curves. PANI$_{NS}$ CV curve was carried out at different sweep rate in 0.1 M H$_2$SO$_4$ aqueous electrolyte solution. H$_2$SO$_4$ as an electrolyte plays an important role in enhancing the electrochemical performance of the material [13].

PANI$_{NS}$ electrode exhibits an increase in C$_{sp}$ with decreasing scan rate because of the ceaseless movement of SO4^{-2} ions through the PANI$_{NS}$ electrodes. Also, SO4^{-2} ions cater an important role for an enhanced electrochemical functioning of PANI$_{NS}$ electrodes. At low scan rate, there is more accumulation of the SO4^{-2} ions to the electrode because they take more take time to penetrate the electrode/electrolyte ions.

PANI$_{NS}$ CV curve (Fig. 39.3) at scan rates 10, 50,100 mV/s shows a larger integrated area then the reported PANI microspheres [14] which confesses it to be a better pseudocapacitor. Also, the integral area of CV curve increases with increasing sweep rates. The figure shows the quasi-rectangular shape of the CV curves. This study confirms the good capacitive nature of the cell. The shape of the CV curves indicates an oxidation/reduction reaction indicating the pseudocapacitor property of the material [15].

Table 39.1 shows the C$_{sp}$ decreases with an increase in the sweep rates. The maximum C$_{sp}$ of PANI$_{NS}$ is 589 F g^{-1} at 10 mV/s and. While at 50, 100 mV/s scan rates, C$_{sp}$ ~ 337.9 F g^{-1} and 220.7 F g^{-1} are observed respectively. This means that at high scan rates, the charges of H$_2$SO$_4$ electrolyte are able to reach to the surface of the material and as the ions of H$_2$SO$_4$ get into deeper pores of the spheres at lower sweep, it decreases the specific capacitance. Therefore, PANI$_{NS}$ electrode material is able to exhibit a well enhanced C$_{sp}$ in a H$_2$SO$_4$ aqueous electrolyte solution.

Table 39.1 Specific Capacitance (C_{sp}) for PANI$_{NS}$

S. no	Scan rate (mV/s)	Specific Capacitance (C_{sp}) of PANI$_{NS}$
1	10	589.0 F g^{-1}
2	50	337.9 F g^{-1}
3	100	220.7 F g^{-1}
4	Retention rate	37.47%

39.4 Conclusion

The synthesis of PANI$_{NS}$ was successfully carried out through a facile approach. This approach is quite an easy, inexpensive and scalable method to produce uniform PANI$_{NS}$. Because of their nanoscale size, they possess a high surface area and reasonable conductivity. We can infer that nanospheres of PANI are able to give remarkable material with specific capacitance of 589 F g^{-1} at 10 mV/s which could be useful for electrode material applications in pseudocapacitors.

References

1. L. Li, H. Song, Q. Zhang, J. Yao, X. Chen, Effect of compounding process on the Structure and electrochemical properties of ordered mesoporous carbon/polyaniline composites as electrodes for supercapacitors. J. Power Sour. **187**, 268–274 (2009)
2. S.-W. Woo, K. Dokko, H. Nakano, K. Kanamura, Incorporation of polyaniline into macropores of three-dimensionally ordered macroporous carbon electrode for electrochemical capacitors. J. Power Sour. **190**, 596–600 (2009)
3. B.C. Kim, J.S. Kwon, J.M. Ko, J.H. Park, C.O. Too, G.G. Wallace, Preparation and enhanced stability of flexible supercapacitor prepared from Nafion/polyaniline nanofiber. Synth. Met. **160**, 94–98 (2010)
4. Y. Zhao, H. Wei, M. Arowo, X. Yan, W. Wu, J. Chen, Y. Wang, Z. Guo, Electrochemical energy storage by polyaniline nanofibers: high gravity assisted oxidative polymerization versus rapid mixing chemical oxidative polymerization. Phys. Chem. Chem. Phys. **17**, 1498–1502 (2015)
5. G. Singh, Y. Kumar, S. Husain, "High charge retention and optimization of polyaniline–titanium dioxide nanoparticles composite nanostructures for dominantly stable pseudocapacitive nature." J. Energy Storage **31**, 101660 (2020)
6. Y. Liu, Z. Chen, L. Yang, T. Li, X. Lv, User preference heterogeneous network selection in less subjective ways. Wirel. Pers. Commun. **76**, 813–828 (2014)
7. C.Q. Zhou, J. Han, R. Guo, Synthesis of polyaniline hierarchical structures in a dilute sds/hcl solution: Nanostructure-covered rectangular tubes. Macromolecules **42**, 1252–1257 (2009)
8. J. Han, G.P. Song, R. Guo, Nanostructure-based leaf-like polyaniline in the presence of an amphiphilic triblock copolymer. Adv. Mater. **19**, 2993–2999 (2007)
9. Z.M. Zhang, M.X. Wan, Y. Wei, Highly crystalline polyaniline nanostructures doped with dicarboxylic acids. Adv. Funct. Mater. **16**, 1100–1104 (2006)
10. S. Pang et al., Facile synthesis of polyaniline nanotubes with square capillary using urea as template. Polymers **9**(10), 510 (2017)
11. S. Siddiqui, Z.N. Siddiqui, Copper Schiff base functionalized polyaniline (Cu-SB/PANI): a highly efficient polymer based organometallic catalyst for the synthesis of 2-amino chromene derivatives. Appl. Organomet. Chem. **33**(10), 5161 (2019)

12. S.H. Kazemi et al., Polyaniline–ionic liquid derived ordered mesoporous carbon nanocomposite: synthesis and supercapacitive behavior. RSC Adv. **5**(84), 69032–69041 (2015)
13. H. Zhu, S. Peng, W. Jiang, Electrochemical properties of PANI as single electrode of electrochemical capacitors in acid electrolytes. Sci. World J. (2013)
14. Z. Li, J. Hu, Y. Li, J. Liu, Ce3+-doped polyaniline hollow microspheres as electrode material of supercapacitor. Chem. Select **3**(24), 6737–6742 (2018)
15. J.Y. Wang, C.M. Yu, S.C. Hwang, K.C. Ho, L.C. Chen, Sol. Energy Mater. Sol. Cells **92**(2), 112–119 (2008)

Chapter 40
Safe, Efficient and Portable Power Generation in Oxide Based Hydroelectric Cells by Water Splitting

Parveen Kumar, Sumit Kumar, Arti, and Vivek Verma

Abstract Hydroelectric cell is a new green source of energy which uses only water for electricity generation without any harmful effects to the environment. Lithium doped magnesium ferrites and tin oxide samples were prepared by solid state sintering method for the green energy production. The XRD pattern of the magnesium lithium ferrite (MLFO) sample confirmed the spinel phase formation and for the SnO_2 sample, the pattern exhibited tetragonal structure without any impurity. Surface morphology of MLFO and SnO_2 sample was observed by using Scanning Electron Microscopy (SEM) which confirmed the porous nature of the samples with randomly oriented crystalline nature. Adsorption of water and its splitting process over the surface of metal oxides plays key role in production of electricity. The creation of metal–oxygen or metal-hydroxyl bonds are due to thermodynamic driving force and results in dissociation of water molecules in ions (H_3O^+, OH^-). These ions move towards respective electrodes. Hydroelectric cell having diameter 5 cm was designed for both the samples using silver and zinc plates as electrodes. The MLFO cell produced 17.0 mA of highest peak current and highest peak voltage of 950 mV with highest output power with value 16.15 mW whereas for the SnO_2 cell showed a maximum current and voltage of 72.1 mA and 981 mV respectively with maximum output power of 70.7 mW.

40.1 Introduction

Cost-effectively clean and sustainable energy production systems derived from renewable, rich sources like wind, water and sun will be highly valuable for the society [1]. In 2016, green electrical energy was generated by water molecule dissociation on the metal oxides surface using Hydroelectric Cells (HEC). So HEC is one of the sources of green electrical energy which uses only few drops of water to

P. Kumar (✉) · S. Kumar · Arti · V. Verma
Department of Physics, Hindu College, University of Delhi, Delhi, India

P. Kumar · S. Kumar · Arti
Department of Physics and Astrophysics, University of Delhi, Delhi, India

401

produce electricity without any harmful by–products. The hydroelectric cell works on the principle on adsorption of water molecule in the oxide samples followed by its splitting into (OH^-, H_3O^+) ions. Furthermore the process of water adsorption can be explained by two phenomenon; (a) chemical adsorption (chemisorption) and (b) physical adsorption (physisorption) [2]. Water dissociates on surface is due to reaction at facet edges as well as defect sites present in the oxide samples [3]. The lattice sites defects along with oxygen deficit surfaces plays key role for splitting of water molecule [4]. Construction of well-built chemisorption bonds on various ionic surfaces is another distinct feature of H_2O adsorption as a result of which molecular adsorbed H_2O can be stable also at normal temperature [5]. In this work, we reported the preparation, structural analysis and green electrical power generation by oxide based hydroelectric cells.

40.2   Experimental Method

The oxide samples of $Mg_{1-t}Li_tFe_2O_4$ (MLFO) ($0.0 \leq t \leq 0.3$) and SnO_2 were prepared by using solid state sintering method. Stoichiometric amount of MgO, Fe_2O_3 and Li_2CO_3 were taken and mixed. Then dry and wet (distilled water) grinding of powder samples was done for 8 h. After that powders were presintered for 5 h at 750 °C in ambient atmosphere. Then pellets of diameter 5 cm were formed by using hydraulic press. Then these pellets were finally sintered at 1050 °C for 5 h. Similarly, precursor powder of SnO_2 was taken as initial material. The obtained powder was grinded in a pestle mortar for 30 min and pre sintered for 4 h at 600 °C. After that obtained presintered sample powders were again grinded for 4 h and pressed into pellets having diameter 5 cm followed by final sintering at 700 °C for 5 h. Obtained polycrystalline pellets were fixed on zinc plates and comb pattern silver coating was done on other face for study of hydroelectric properties as shown in Fig. 40.1. A digital multimeter was used to measure voltage (mV) and current (mA) generated by each HEC.

Fig. 40.1   HEC of oxide material with zinc and silver electrodes
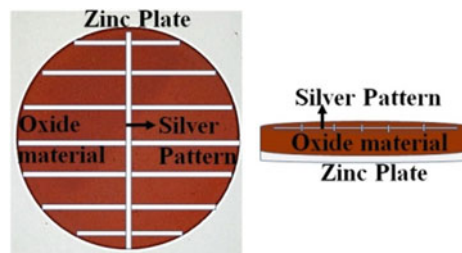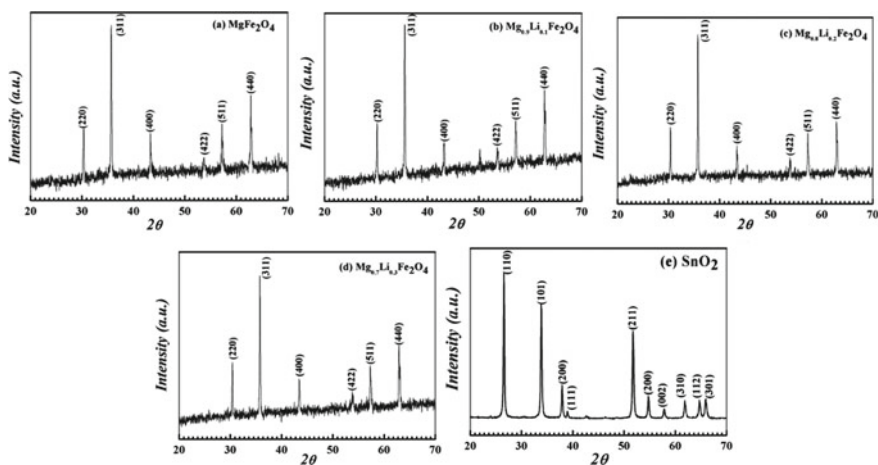
Fig. 40.2 XRD pattern of $Mg_{1-t}Li_tFe_2O_4$ samples **a** t = 0.0, **b** t = 0.1, **c** t = 0.2, **d** t = 0.3 and **e** SnO_2 sample

40.3 Results

40.3.1 XRD Analysis

Figure 40.2a–d confirms the XRD pattern of $Mg_{1-t}Li_tFe_2O_4$ (0≤ t ≤0.3) samples. This XRD pattern shows the same peak positions which are stated in JCPDS file no. (73–1720). It also confirms the Fd $\bar{3}$ m space group with inverse-spinel phase formation. There is decrease in lattice parameter values from 8.38 Å to 8.37 Å which signifies the inclusion of Li^+ ions in the $MgFe_2O_4$. Figure 40.2e shows the XRD pattern of SnO_2 sintered at 700 ℃. This XRD pattern of SnO_2 gives the same peak positions which are stated in JCPDS file no. (41–1445), which correspond to the tetragonal rutile structure of SnO_2 along with P42/mnm space group.

40.3.2 Scanning Electron Microscopy

SEM pictures of the sintered pellets for the $Mg_{1-t}Li_tFe_2O_4$ (0≤ t ≤0.3) samples are shown in Fig. 40.3a–d. It can be seen from the images that the grains of $Mg_{1-t}Li_tFe_2O_4$ samples are closely packed and homogeneous in nature. All the samples have dissimilar grain dimension distribution. This can be explained on the basis of variation in growth rate of all samples for the formation of their individual phases. The average grain size of the pure $MgFe_2O_4$ sample is found to be about 3–4 µm. We can also see that observe densification increases with increase in doping amount of lithium in $MgFe_2O_4$. Figure 40.3e shows the SEM image of finally sintered SnO_2 pellets. It
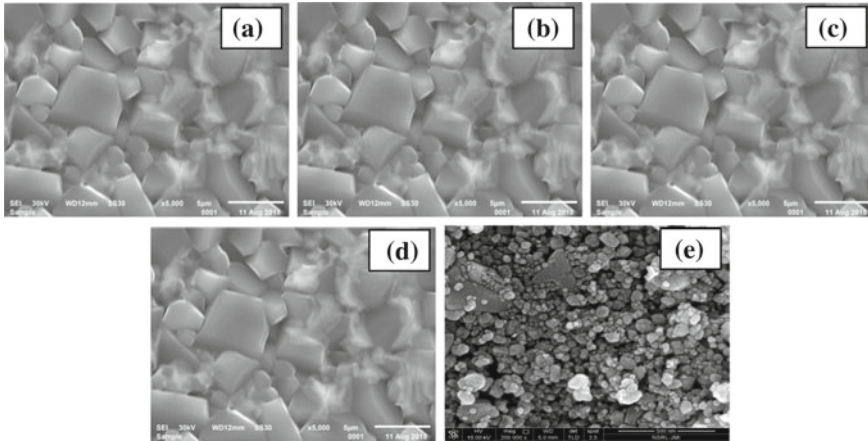
Fig. 40.3 SEM pictures of $Mg_{1-t}Li_tFe_2O_4$ samples **a** t = 0.0, **b** t = 0.1, **c** t = 0.2, **d** t = 0.3 and **e** SnO_2 sample

can be seen that the sample exhibit arbitrarily oriented excellent crystalline structure. The average grain size is found to be around 65 nm. Also it can be stated from the SEM image that SnO_2 sample has porous in nature.

40.3.3 Hydroelectric Properties

The hydroelectric cell (HEC) works on the principle on adsorption of water molecule in the oxide samples followed by its splitting into (OH^-, H_3O^+) ions and their conduction. When H_2O molecules approach towards the oxide surface, instantly H_2O molecules split into ions (H_3O^+, OH^-) [6]. These ions move towards their respective electrodes and following reactions take place which are shown by equations (40.1–40.3).

$$4H_2O \rightarrow 2H_3O^+ + 2OH^- \tag{40.1}$$

$$Zn + 2OH^- \rightarrow Zn(OH)_2 + 2 \text{ electrons} \tag{40.2}$$

$$2 \text{ electrons} + 2H_3O^+ \rightarrow 2H_2O + H_2 \tag{40.3}$$
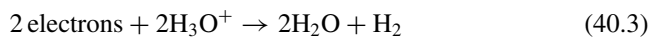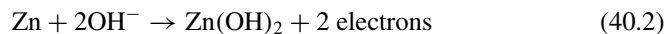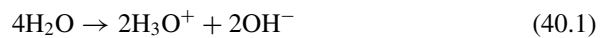
Generally voltage generated between these electrodes is 0.98 V which results in set up of electric field between cathode and anode. This electric field results in additional movement of ions (H_3O^+, OH^-) in oxide and ferrite medium.

Table 40.1 Voltage, current and power values for MLFO and SnO_2 samples

S.No	Sample	Maximum voltage (mV)	Maximum current (mA)	Maximum power (mW)
1	$MgFe_2O_4$	1000	2.47	2.46
2	$Mg_{0.9}Li_{0.1}Fe_2O_4$	883	8.18	6.94
3	$Mg_{0.8}Li_{0.2}Fe_2O_4$	950	17.0	16.15
4	$Mg_{0.7}Li_{0.3}Fe_2O_4$	939	16.67	15.7
5	SnO_2	981	72.1	70.7

The Oxygen defects also play a key role in dissociation of water molecule [7]. After spray with few millilitre deionized water, voltage (mV) and current (mA) for all samples have been observed with MLFO and SnO_2 cells for analyzing their hydroelectric properties. The $Mg_{0.8}Li_{0.2}Fe_2O_4$ cell produced peak current of 17.0 mA and peak voltage of 950 mV along with a highest output power 16.15 mW whereas for the SnO_2 cell showed a peak current of 72.1 mA and the voltage was found to be 981 mV with maximum output power of 70.7 mW as given in Table 40.1. From the observations, we can see that fast decrement in current with time. This fast decrement in the current is the most important barrier. Further research is essential to resolve this problem. It can be seen that lithium doping enhanced the response of current in the samples as shown in Table 40.1. This happens because of divalent Magnesium ions are replaced by monovalent lithium ions which results in creation of oxygen (O_2) vacancies due to charge imbalance in the doped compounds [8]. Maximum current is exhibited by SnO_2 sample.

40.4   Conclusion

Polycrystalline $Mg_{1-t}Li_tFe_2O_4$ (0.0$\leq$ t $\leq$0.3) samples along with SnO_2 samples were prepared by solid state sintering method. Their surface morphology was studied by using SEM pictures and with Li substitution there is decrease in grain size in polycrystalline ferrite samples. In SnO_2 sample it can be observed randomly oriented fine crystalline structure. Voltage (mV), current (mA) and power (mW) generation has been explored for all hydroelectric cells. Highest power was found in case of magnesium ferrite with 0.2 doped sample (16.15 mW). SnO_2 based hydroelectric cells also exhibited promising results as maximum power generated by this cell is 70.7 mW.

References

1. C. Acar et al., Int J Energy Res **40**(11), 1449–1473 (2016)

2. F. Pourfayaz, et al., 130, 625–629 (2008)
3. M.L. Hair, *Infrared Spectroscopy in Surface Chemistry* (Dekker, New York, 1967)
4. R.K. Kotnala, et al., J. Phys. Chem. C, **122,** 18841–18849 (2018)
5. R.L. Kurtz, V.E. Henrich, Phys. Rev. B **26**, 6682 (1982)
6. R.K. Kotnala, J. Shah, Int. J. Energy Res **40**, 1652–1661 (2016)
7. V. Verma et al., Solid State Commu **149**, 1726–1730 (2009)
8. P. Kharbanda, et al., Heliyon, **5**, e01151 (2019)

Chapter 41
Theoretical Investigation of Various Inelastic Cross Sections for e⁻—CO Scattering

S. Vadhel, D. Prajapati, M. Vinodkumar, C. Limbachiya, and P. C. Vinodkumar

Abstract In this work, we present an inelastic cross-sectional (IECS) data of electron interaction with carbon monoxide (CO), that include discrete electronic excitation cross sections (ECS), resonance parameters and ionization cross sections (ICS) along with rate coefficients of excitation and ionization. Here, the low energy calculations below the threshold (Ionization value) of the target are computed by using R-matrix formalism employing Quantemol-N. Beyond ionization threshold the spherical complex optical potential (SCOP) formalism is employed. The ICS derived from the total IECS using a complex scattering potential-ionization contribution (CSP-ic) method is found to be in good agreement with the ICS data generated by Binary Encounter Bethe (BEB) formalism. Results from the close-coupling model give us prominent resonances for three different states $^2\Sigma^+(^2A_1)$, $^2\pi(^2B_1, {}^2B_2)$, $^2\Sigma^-\ (^2A_2)$.

41.1 Introduction

Our universe consist of ample amount of carbon monoxide (CO) after the simplest hydrogen molecule. One of the special characteristic of CO is its large binding energy that gives rise to many electronically excited states. Apart from this, e-CO study is significant to understand its role in CO lasers [1], to investigate CO plasma in presence of electrical discharge [2], to understand its role in magneto hydrodynamics power generation [3], to probe the processes in the atmosphere of Mars and Venus and more interestingly infrared emission from CO in the atmosphere of these planets [4] and

S. Vadhel · P. C. Vinodkumar
Department of Physics, Sardar Patel University, Vallabh Vidyanagar 388120, India

D. Prajapati
Shree M. R. Arts & Science College, Rajpipla 393145, India

M. Vinodkumar (✉)
V. P. & R. P. T. P. Science College, Vallabh Vidyanagar 388120, India

C. Limbachiya
Department of Applied Physics, The M. S. University of Baroda, Vadodara 390001, India
e-mail: cglimbachiya-apply@msubaroda.ac.in

comets [5] and finally in the modelling of space craft entry in the atmosphere of these planets [3]. According to the literature survey, electron impact ECS study for e-CO study is carried out experimentally by [6–8] and theoretically by [9–12]. In contrast, the electron impact ICS are reported experimentally [13–18] by many groups and but theoretically [19, 20] by few groups. Reviews related to resonances are reported by Schulz [21], Gibson et al. [22]. They derived $^2\pi$ resonance present in CO. Itikawa [23] has reported review article on e-CO scattering which includes almost all types of scattering cross sections. Different groups have reported different cross sections in different energy regimes. The relevance of present study is that we are reporting many IECS from 0.01 to 5 keV energy in this paper.

41.2   Theoretical Methodology

We particularly emphasis here on inelastic channels of e-CO scattering. To encompass major inelastic processes, the range of incident energy is taken from 0.01 to 5 keV. Lacking a single theoretical formalism for such wide energy range, we adopt here two different approaches: (i) R-matrix [24–27] and (ii) SCOP formalisms which are well described in our earlier publications [3, 28–31]. For generating total ICS of CO we used Binary-encounter-Bethe (BEB) [32] and CSP-ic [33–35] method. In the next subsections, we explain briefly these theoretical formalisms. Before we get into the specifics of theoretical approaches, we'll go through the target model, which is a key element of our low energy calculations.

41.2.1   Target Properties

CO is a triply bonded linear molecule (see Fig. 41.1). Target properties are generated by self-consistent field (SCF) calculations using modules GAUSPROP and DENPROP [24] of Quantemol-N. The present calculated ground state energy of CO is −112.82 Hartree, which is theoretically in good accord with −112.85 Hartree reported by Dora and Tennyson [36]. The first excitation energy of 6.23 eV is slightly lower than the value of 6.31 eV predicted by [36] and also the experimental value of 6.32 eV reported by Nielsen et al. [37]. The rotational constant of CO is obtained as $1.93011\,cm^{-1}$ and is in excellent agreement with $1.93128\,cm^{-1}$ reported in CCCBDB

Fig. 41.1 Schematic diagram of carbon monoxide molecule
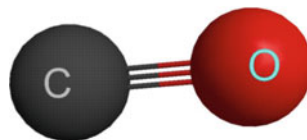
Table 41.1 Properties of carbon monoxide

Properties (unit)	Present work	Others works
Ground state of CO (H)	−112.82	−112.85 [36]
First excitation energy (eV)	6.23	6.31 [36], 6.32 [37]
Ionization potential (eV)	14.014	14.01 [3]
Dipole moment (Debye)	0.112	0.099 [3]
Rotational constant of CO (cm^{-1})	1.93011	1.93128 [3, 38]

[38] and Jain and Baluja [3]. The dipole moment of CO obtained as 0.112 D, which is about 13% higher than 0.099 D reported by Jain and Baluja [3] (Table 41.1).

41.2.2   R-matrix: Low Energy Formalism (Below Threshold)

In the R-matrix formalism [24] the configuration space is split into the inner region (0~(10–15) a.u) and the outer region which is up extended to 100 a.u. The trial wave function in the inner region is described as.

$$\psi_k^{N+1}(x_1 \ldots x_{N+1}) = A \sum_{ij} a_{ijk} \phi_i^N(x_1, \ldots x_N) u_{ij}(x_{N+1}) + \sum_i b_{ik} X_i^{N+1}(x_1 \ldots x_{N+1})$$

(41.1)

In (41.1), ψ_k^{N+1} represents wave function for N-target electron plus one scattering electron, A represents anti-symmetrized operator, a_{ijk} and b_{ik} are variational parameters, ϕ_i^N represents i^{th} target state's wave function and u_{ij} denotes the continuum orbital of scattering electron [39]. At the R-matrix boundary, L^2 function has zero amplitude and summation is performed X_i for N + 1 electrons. Because of permanent dipole moment of CO, we need to apply Born correction [40] for the incorporation of partial waves for angular momentum l > 4. The outer region asymptotic solution is done by expressing the R-matrix on the boundary given by Gailitis [41]. The K-matrix contains all physical observables and we extract T-matrix from K-matrix which is used to compute various cross sections. The eigenphase sum(ρ) we get from diagonalization of K-matrix, and this eigenphase sum help us to find position as well as width of the resonance by fitting them to BW (Breit-Wigner) profile [42] using the RESON program.

41.2.3   High Energy Formalism (Ionization Thresold to 5 keV)

Close coupling (CC) formalism (R-matrix) is very complex beyond 20 eV, so we used the quantum mechanical SCOP approach which is well explained in [3, 28–31]. The Optical Potential is written as.

$$V_{opt}(r, E_i) = V_R(r, E_i) + i V_I(r, E_i) \qquad (41.2)$$

where E_i stands for incident electron energy of electrons. In (41.2), V_R is for the real part of potential which includes the static potential, exchange potential and polarization potential. The imaginary potential V_I is also termed as absorption potential V_{ab}, takes care of total loss of flux scattered by inelastic channels. The total IECS can be written as the first part represents the TICS and the second part represents the sum of all electronic ECS. Thus by definition this inequality leads the CSP-ic (Complex Scattering Potential—ionization contribution) method. The ratio of energy-dependent ICS to IECS is defined as R(E_i), such that $0 \leq R(E_i) \leq 1$. A full description of the CSP-ic method can be found in earlier publications [33–35].

$$Q_{inel}(E_i) \geq Q_{ion}(E_i) \qquad (41.4)$$

$$R(E_i) = \frac{Q_{ion}(E_i)}{Q_{inel}(E_i)} \qquad (41.5)$$

$$Q_{inel}(E_i) = Q_{ion}(E_i) + \sum Q_{exe}(E_i) \qquad (41.3)$$

41.2.4   Binary-Encounter-Bethe Model (for Total ICS)

This BEB method was developed by Kim and Rudd [32]. Here, we used the same method for deriving total ICS by using (41.6). Various parameters used in (41.6) are obtained from our R-matrix calculation, like Kinetic energy (U), binding energy (B) and electron occupation number (N), where b = T/B, u = U/B, $S = 4\pi\, a_0^2 N R^2/B^2$, $a_0 = 5.292$ Å, R = 13.61 eV, T is incident energy and a_0 is bohr radius.

$$\sigma_{BEB} = \frac{S}{b + u + 1}\left[\frac{lnb}{2}\left(1 - \frac{1}{b^2}\right) + 1 - \frac{1}{b} - \frac{lnb}{b + 1}\right] \qquad (41.6)$$

41.3 Results and Discussion

Main results of the various inelastic process of electron scattering with CO over energy range 0.01eV–5 keV are presented in this section. We reported here vertical electronic excitation energies, eigenphase diagram, various cross sections and rate coefficients. For eigenphase sum and electron impact excitations cross sections we used the R-matrix [24] method below threshold energy with inner region radius 10 a.u. CSP-ic [33–35] and BEB [32] methods are used for extracting TICS (total ICS) and SCOP [3, 28–31] formalism used for extracting total IECS.

41.3.1 Vertical Electronic Excitation Energies for Carbon Monoxide Molecule

The VEEE (vertical electronic excitation energies) of carbon monoxide are extracted using Quantemol-N for low energy calculation. Present energies calculated using two different basis sets DZP and 6-311G, which is from ground state to 15 eV excitation cut-off are shown in Table 41.2.

Table 41.2 The ground state energy (in Hartree), Vertical electronic excitation energies (in eV) of CO calculated using DZP and 6-311G Basis sets

States	Present		Theo. [36]	Exp. [37]
	DZP	*6-311G*		
$1\,^1\Sigma^+$	−112.82	−112.73	−112.85 [36] −112.77 [43]	−113.377 [44]
$1\,^3\pi$	6.23	6.47	6.31	6.32
$1\,^1\pi$	9.00	8.90	8.83	8.51
$1\,^3\Sigma^+$	9.04	7.95	8.39	8.51
$1\,^3\Delta$	9.68	8.83	9.23	9.36
$1\,^3\Sigma^-$	10.08	9.23	9.60	9.88
$1\,^1\Sigma^-$	10.29	9.56	9.97	9.87
$1\,^1\Delta$	10.30	9.63	10.00	10.23
$2\,^3\pi$	13.06	11.75	12.29	–
$2\,^3\Sigma^+$	13.87	13.15	12.09	10.40
$2\,^1\pi$	14.47	13.79	13.72	–
$2\,^1\Sigma^+$	14.65	14.28	13.76	10.78
$3\,^3\pi$	14.86	14.67	–	–

Theoretical value derived by Dora et al. [36] and Jain and Norcross [43], experimental value derived by Nielsen et al. [37]
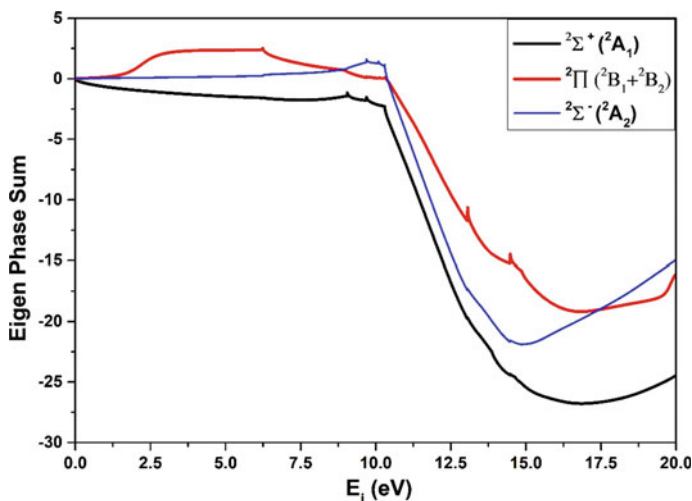
Fig. 41.2 Eigenphase sum for e-CO, where black line represent $^2\Sigma^+$ symmetric state, red line represent $^2\pi$ symmetric state, blue line represent $^2\Sigma^-$ symmetric state of c_{2v} point group

41.3.2 Eigenphase Diagram

The eigenphase diagram for CO target is presented in Fig. 41.2. Eigenphase study is important to confirm resonances and their positions which has significance in low energy regimes. Here we identified 3 doublet scattering states ($^2\Sigma^+(^2A_1)$, $^2\pi(^2B_1$, $^2B_2)$, $^2\Sigma^-$ ($^2A_2$)) of the e-CO system. All the three scattering states ($^2\Sigma^+$, $^2\pi$ $^2\Sigma^-$) show resonances at three different positions as evident from the eigenphase diagram. As shown in Fig. 41.2, the eigenphase of $^2B_1$ and $^2B_2$ symmetry results are the same so we combined them and represented them as $^2\pi$ symmetry of the CO molecule. This $^2\pi$ resonance is well predicted by many theoretical [3, 36, 45] and experimental studies [22]. The $^2\Sigma^+(^2A_1)$ state shows structure/resonance at 9.05, 9.70 and 10.3 eV, the $^2\Sigma^-$ ($^2A_2$) state shows structures at 9.69, 10.09 and 10.30 eV and the $^2\pi(^2B_1$, $^2B_2$) state shows structures at 6.24, 13.06 and 14.48 eV.

41.3.3 Electronic Excitation Cross Sections

In inelastic channel, electronic excitations are totally dominated below the ionization threshold. In Fig. 41.3, we plotted ECS for e—CO scattering using the DZP basisset. There are eight notable excitation states for CO from the ground state ($X^1\Sigma^+$) to $^3B_1$, $^3B_2$, $^1B_1$, $^1B_2$, $^3A_1$, $^3A_1$, $^3A_2$, and $^3A_2$. Here ($^3B_1$, $^3B_2$), ($^1B_1$, $^1B_2$), $^3A_1$, ($^3A_1$, $^3A_2$) and $^3A_2$ can be represented in linear symmetry as $^3\pi$, $^1\pi$, $^3\Sigma^+$, $^3\Delta$ and $^3\Sigma^-$ respectively. It is clear from the Fig. 41.3, that maximum contribution comes from the triplet π state which indirectly shows the presence of $^2\pi$ state as predicted
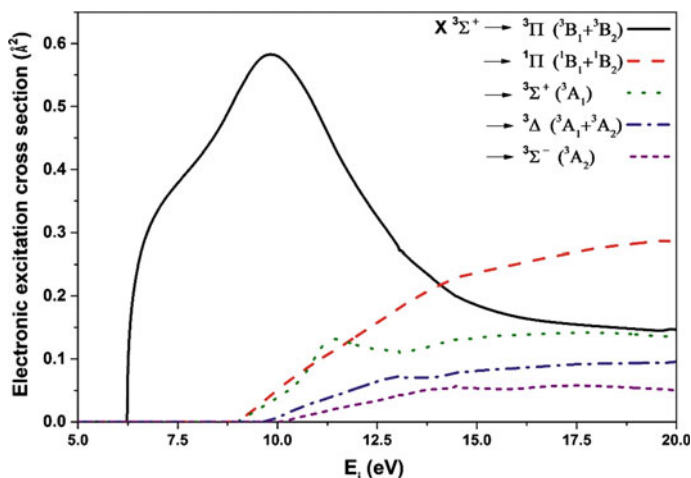
Fig. 41.3 Electron impact ECS for e-CO, where $X^1\Sigma^+$, represents ground state, solid line represents the $^3\pi$, dash line represents the $^1\pi$, dot line represents the $^3\Sigma^+$, dash-dots line represents the $^3\Delta$ and short dash line represents the $^3\Sigma^-$,

earlier. We can see $X^1\Sigma^+ \rightarrow {}^3\pi$ transition originate at 6.23 eV and reaches peak value at around 10 eV before diminishing. The same qualitative features are observed in many experimental [6–8] and theoretical [9–12] studies.

41.3.4 Total Ionization Cross Section (ICS)

The total ICS are important input for many areas of applied interest like astrochemistry [46], modelling of plasma, calibration of mass-spectrometer and ionization chamber etc. Here, we have employed the CSP-ic [33–35] and Binary-Encounter-Bethe (BEB) [32] methods for computing and comparing ICS data. In BEB method, we need typical three basic parameters as listed in Table 41.3 like kinetic energy (U),

Table 41.3 Parameters used in BEB method; molecular orbits (M. O.), average kinetic energy (U), binding energy (B) and orbital occupation number (N) for CO

M.O	U (eV)	B (eV)	N
$1A_1$	794.61	−562.76	2
$2A_1$	436.52	−310.80	2
$3A_1$	77.30	−41.82	2
$4A_1$	70.40	−21.72	2
$5A_1$	44.00	−15.16	2
$1B_1$	54.17	−17.21	2
$1B_2$	54.17	−17.21	2
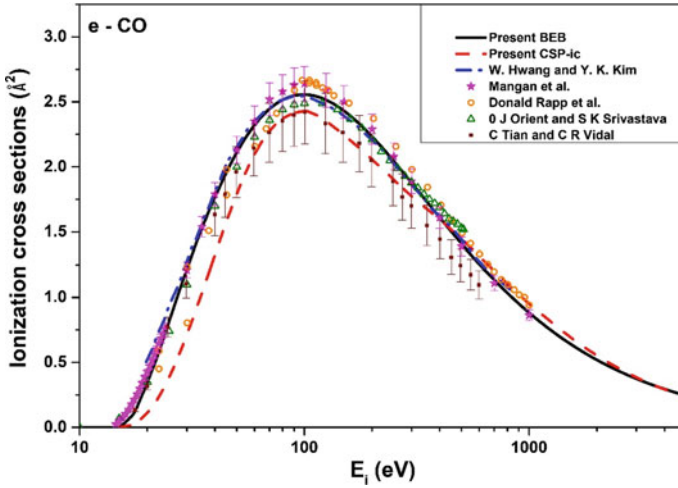
Fig. 41.4 ICS for e-CO, solid line represents the present BEB, dash line represents the present CSP-ic, dash-dots line represents the Hwang and Kim [19], while stars, circles, triangles and square represents Mangan et al. [13], Rapp et al. [14], Orient and Srivastava [47] and Tian and Vidal [16] respectively

binding energy (B) and orbital occupation number (N). In Fig. 41.4, we plotted total ICS for e-CO system which is found in good agreement with present CSP-ic data and other experimental [13, 14, 16, 47] as well as theoretical [19] data.

Figure 41.5, shows all three cross sections due to inelastic channels. We present total ECS (Q_{exe}), total ICS (Q_{ion}) and total IECS (Q_{inel}) obtained using SCOP [3, 28–31] formalism. Present calculated cross sectional data for carbon monoxide are listed in Table 41.4.

41.3.5 Scattering Rate Coefficients

In Figs. 41.6 and 41.7, electron impact rate coefficients are plotted with respect to kinetic temperature of the electrons. In total excitation rate coefficient found to increase drastically after the 7000°K as seen from Fig. 41.6 and ionization rate coefficients increase after 8500°K as shown in Fig. 41.7. These data are useful for atmospheric modeling (For more details [48]).
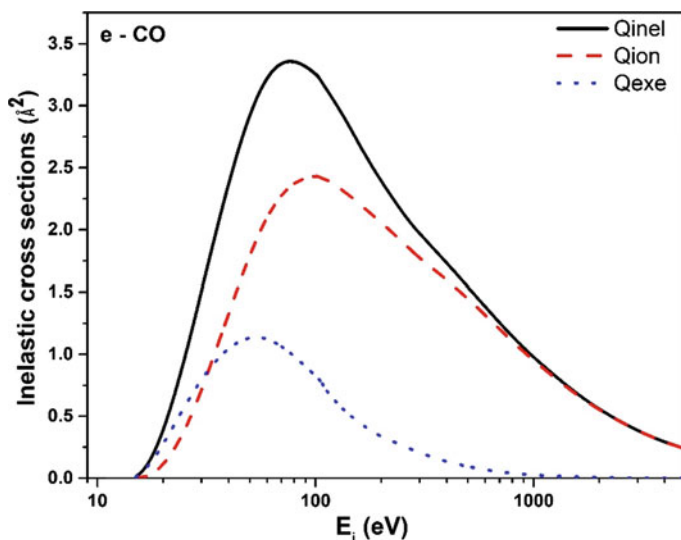
Fig. 41.5 IECS for e-CO, where Q_{exe} represents total ECS, Q_{ion} represents total ICS, Q_{inel} represents total IECS

41.4   Conclusion

The inelastic scattering data for e-CO system has been computed in the present work over a wide energy range. Target properties (Table 41.1), electronic excitation energies (Table 41.2), eigen phase sum (Fig. 41.2), discrete electronic ECS (Fig. 41.3), total ICS (Fig. 41.4), total IECS (Fig. 41.5) and along with total excitation and ionization rate coefficient (Figs. 41.6 and 41.7) are reported for CO. Using the RESON program, we found structures (resonances) in three different states like $^2\Sigma^+$, $^2\pi$, $^2\Sigma^-$ as shown in Fig. 41.2. The calculated vertical electronic excitation energies find good accord with data available in literature. The TICS computed using CSP-ic and BEB methods show good agreement with the data available in literature. The rate coefficients for excitation and ionization for the first time to the best of our knowledge. The reported data show overall good agreement with other theoretical and experimental data available in the literature.

Table 41.4 Total ionization, excitation and IECS of e-CO scattering

Ei (eV)	Q_{ion} (Å²)	Q_{exe} (Å²)	Q_{inel} (Å²)	Ei (eV)	Q_{ion} (Å²)	Q_{exe} (Å²)	Q_{inel} (Å²)	Ei (eV)	Q_{ion} (Å²)	Q_{exe} (Å²)	Q_{inel} (Å²)
15	0.001	0.011	0.012	100	2.56	0.525	3.249	1000	0.88	0.026	0.950
20	0.34	0.276	0.387	200	2.24	0.338	2.402	1500	0.65	0.011	0.697
30	1.22	0.795	1.509	300	1.88	0.202	1.973	2000	0.52	0.006	0.550
40	1.77	0.831	2.374	400	1.61	0.133	1.737	2500	0.44	0.003	0.454
50	2.11	1.046	2.923	500	1.41	0.093	1.542	3000	0.38	0.002	0.384
60	2.32	1.131	3.221	600	1.26	0.068	1.389	3500	0.33	0.001	0.331
70	2.45	1.122	3.340	700	1.14	0.051	1.261	4000	0.30	0.001	0.291
80	2.52	1.062	3.355	800	1.04	0.040	1.145	4500	0.27	0.001	0.262
90	2.55	0.983	3.316	900	0.95	0.032	1.030	5000	0.25	0.001	0.255
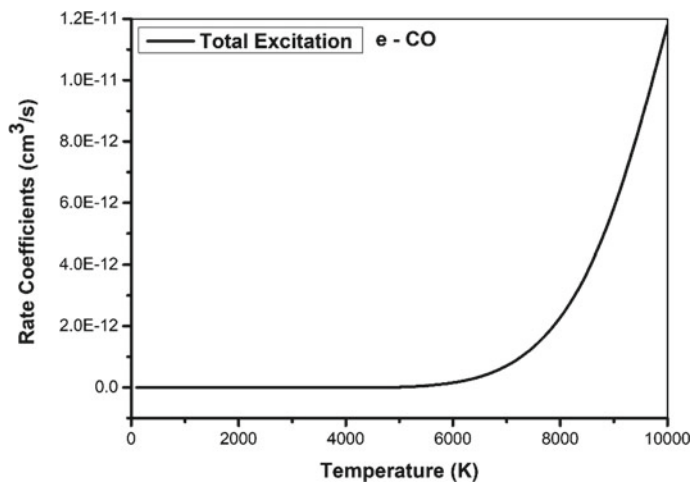
Fig. 41.6 Total excitation rate coefficients of carbon monoxide
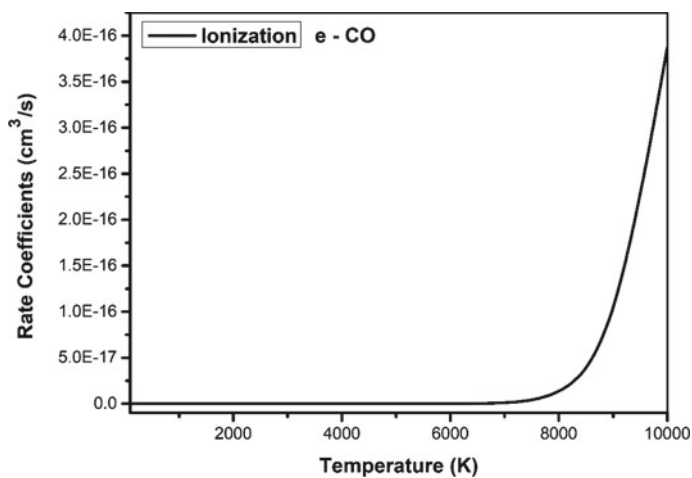
Fig. 41.7 Total ionization rate coefficients of carbon monoxide

References

1. G. Haddad, H. Milloy, Aust. J. Phys. **36**(4), 473 (1983)
2. T. Wang, Q. Cheng, Opt. Laser Technol. **33**(7), 475 (2001)
3. A. Jain, K. Baluja, Phys. Rev. A **45**(1), 202 (1992)
4. L. Campbell, M. Allan, M. Brunger, J. Geophys. Res. Space Phys. **116**(A9) (2011)
5. L. Campbell, M. Brunger, Plasma Sources Sci. Technol. **22**(1), 013002 (2012)
6. D.S. Newman, M. Zubek, G.C. King, J. Phys. B At. Mol. Phys. **16**(12), 2247 (1983)
7. J.P. Polley, T.L. Bailey, Phys. Rev. A **37**, 733 (1988)
8. A.G. Middleton, M.J. Brunger, P.J.O. Teubner, J. Phys. B: At., Mol. Opt. Phys. **26**(11), 1743 (1993)
9. C.A. Weatherford, W.M. Huo, Phys. Rev. A **41**, 186 (1990)
10. L.A. Morgan, J. Tennyson, C.J. Gillan, Comput. Phys. Commun. **114**(1), 120 (1998)
11. M.T. Lee, I. Iga, L. Brescansin, L. Machado, F. Machado, J. Mol. Struct. (Theochem) **585**(1–3), 181 (2002)
12. R. Riahi, P. Teulet, N. Jaidane, A. Gleizes, Eur. Phys. J. D **56**, 67 (2010)
13. M. Mangan, B. Lindsay, R. Stebbings, J. Phys. B: At., Mol. Opt. Phys. **33**(17), 3225 (2000)
14. D. Rapp, P. Englander-Golden, J. Chem. Phy. **43**(5), 1464 (1965)
15. C. Tian, C.R. Vidal, Phys. Rev. A **59**, 1955 (1999)
16. C. Tian, C. Vidal, J. Phys. B: At., Mol. Opt. Phys. **31**(4), 895 (1998)
17. Y. Chung, J. Korean Phys. Soc. **41**(5), 682 (2002)
18. J. Gavin, M. Ortiz, J. Campos, Int. J. Mass Spectrom. **219**(2), 351 (2002)
19. W. Hwang, Y.K. Kim, M.E. Rudd, J. Chem. Phy. **104**(8), 2956 (1996)
20. M. Vinodkumar, C. Limbachiya, H. Bhutadia, J. Phys. B: At., Mol. Opt. Phys. **43**(1), 015203 (2009)
21. G.J. Schulz, Rev. Mod. Phys. **45**, 423 (1973)
22. J.C. Gibson, L.A. Morgan, R.J. Gulley, M.J. Brunger, C.T. Bundschu, S.J. Buckman, J. Phys. B: At. Mol. Opt. Phys. **29**(14), 3197 (1996)
23. Y. Itikawa, J. Phys. Chem. Ref. Data **44**(1), 013105 (2015)
24. J. Tennyson, Phys. Rep. **491**, 29 (2010)
25. M. Vinodkumar, H. Desai, P. Vinodkumar, RSC Adv. **5**(31), 24564 (2015)
26. M. Vinodkumar, C. Limbachiya, A. Barot, N. Mason, Phys. Rev. A **86**(1), 012706 (2012)
27. M. Vinodkumar, C. Limbachiya, K. Joshipura, N. Mason, Eur. Phys. J. D **61**(3), 579 (2011)
28. D. Prajapati, H. Yadav, M. Vinodkumar, C. Limbachiya, P. Vinodkumar, Mol. Phys. **117**(14), 1838 (2019)
29. D. Prajapati, H. Yadav, P. Vinodkumar, C. Limbachiya, A. Dora, M. Vinodkumar, Eur. Phys. J. D **72**(12), 210 (2018)
30. A. Barot, D. Gupta, M. Vinodkumar, B. Antony, Phys. Rev. A **87**, 062701 (2013)
31. M. Vinodkumar, H. Bhutadia, C. Limbachiya, K. Joshipura, Int. J. Mass Spectrom. **308**(1), 35 (2011)
32. Y.K. Kim, M.E. Rudd, Phys. Rev. A **50**(5), 3954 (1994)
33. M. Vinodkumar, C. Limbachiya, M. Barot, M. Swadia, A. Barot, Int. J. Mass Spectrom. **339**, 16 (2013)
34. M. Vinodkumar, K. Korot, C. Limbachiya, B.K. Antony, J. Phys. B: At., Mol. Opt. Phys. **41**(24), 245202 (2008)
35. M. Vinodkumar, H. Bhutadia, R. Dave, B. Antony, Indian J. Phys. **85**(12), 1761 (2011)
36. A. Dora, J. Tennyson, K. Chakrabarti, Eur. Phys. J. D **70**(10), 197 (2016)
37. E.S. Nielsen, P. Jo/rgensen, J. Oddershede, J. Chem. Phy. **73**(12), 6238 (1980)
38. R.D. Johnson III, cccbdb. nist. gov (2015)
39. A. Faure, Comput. Phys. Commun. **144**, 224 (2002)
40. S.I. Chu, A. Dalgarno, Phys. Rev. A **10**(3), 788 (1974)
41. M. Gailitis, J. Phys. B: At. Mol. Phys. **9**(5), 843 (1976)
42. J. Tennyson, C.J. Noble, Comput. Phys. Commun. **33**(4), 421 (1984)

43. A. Jain, D. Norcross, Phys. Rev. A **45**(3), 1644 (1992)
44. B.J. Ransil, Rev. Mod. Phys. **32**(2), 239 (1960)
45. D.W. Norcross, N.T. Padial, Phys. Rev. A **25**(1), 226 (1982)
46. W. Zhou, L. Wilkinson, J.W. Lee, D. Heathcote, C. Vallance, Mol. Phys. 1–10 (2019)
47. O. Orient, S. Strivastava, J. Phys. B: At. Mol. Phys. **20**(15), 3923 (1987)
48. J. Singh, K. Baluja, G. Longiany, Pramana **88**(5), 76 (2017)

Chapter 42
Modelling Novel Organic Molecule 2-(4-Ethylbenzylidene) Malononitrile (EBM) for Nonlinear Optical (NLO) Applications

Garima Chanana and Kriti Batra

Abstract Research for the identification of novel donor-bridge-acceptor organic molecules for applications in optoelectronic and photonic device development has recently gained momentum. Benzylidenemalononitrile derivatives exhibit large molecular nonlinearities and are therefore suitable candidates for Non-linear Optical (NLO) applications. In this study, we report for the first time a detailed theoretical study of molecular structure and spectra (Vibrational and UV-Visible) of 2-(4-ethylbenzylidene) malononitrile (EBM) molecule using Density Functional Theory (DFT) method. B3LYP and CAM-B3LYP functional and standard basis set 6-311++G(d,p) have been employed for our calculations. The calculated structure and spectra are compared with available experimental results. The optical properties such as mean and anisotropic polarizability and first-order hyperpolarizability are also computed and compared for both functionals. The charge distribution within the molecule is analyzed using Mulliken and Natural Bond Order (NBO) analysis. The results offer promising applications in identifying NLO active materials for technological applications.

42.1 Introduction

Identification of efficient Nonlinear Optical (NLO) materials for application in the development of photonic and optoelectronic devices, optical data storage, high-speed information processing, data transmission, and optical communication has emerged as an important area of research in recent years [1]. Earlier research indicates that malononitrile molecules and their derivatives can be used to design ultrasensitive molecular photonic devices [2]. Recent research by Priyadharshini et al. [3] synthesized a novel benzylidenemalononitrile derivatives called 2-(4-ethylbenzylidene) malononitrile (EBM) and reported its experimental optical properties. Their results reveal that the EBM molecule is a promising candidate for NLO applications. In

G. Chanana · K. Batra (✉)
University School of Basic and Applied Sciences GGS Indraprastha University, Dwarka, Delhi 110078, India

view of this it becomes essential to perform theoretical modelling of EBM molecule so that its NLO applications can be understood. In the present work we have reported molecular modelling of EBM molecule using Density Functional Theory (DFT) with the help of B3LYP and CAM-B3LYP functionals and test the validity of obtained theoretical results in comparison with experimentally available data.

42.2   Theory

Organic molecules exhibiting large non-linear responses are ideal candidates for NLO active materials as they have high optical damage threshold and ultrafast response time. For the organic molecule 2-(4-ethylbenzylidene) malononitrile (EBM), the experimental structure and optical properties have been experimentally reported [3]. We study the molecular structure, vibrational motion, and optical properties of EBM molecule from a theoretical standpoint and report the validity of different theoretical density functionals (B3LYP and CAM-B3LYP) by comparing the calculated results with experimental results. We also perform charge distribution analysis using Mulliken population analysis and Natural Bond Orbital (NBO) Analysis to identify the charge distribution and its localization within the molecule.

42.2.1   Molecular Structure Using Density Functional Theory

The molecular geometry of EBM is optimized using DFT algorithm encoded in Gaussian 16 Software package [4]. For DFT calculations we employed B3LYP and CAM-B3LYP functionals to estimate the molecular geometry. These functionals model the electron correlation energy contribution to the total molecular energy. Both of these functionals are hybrid functionals i.e. they include a weighted mixture of Hartree–Fock exchange with DFT exchange–correlation to model electron correlations. B3LYP (E_{xc}^{B3LYP}) is a three-parameter functional developed by Becke [5] defined as:

$$E_{xc}^{B3LYP} = 0.2E_x^{HF} + 0.80E_x^S + 0.72E_x^{88} + 0.81E_C^{VWN} + 0.19E_C^{LYP} \quad (42.1)$$

where E_x^{HF} is the Hartree–Fock exact exchange contribution, E_x^S is the Slater functional, E_x^{88} is the Becke B88 exchange functional, E_C^{LYP} is the LYP correlation functionals for non-local correlation and E_C^{VWN} is the VWN correlation functional for local correlation.

For B3LYP functional, the contribution of E_x^{HF} and E_x^{88} remains constant throughout the interelectronic separation of two electrons. The long-range exchange potential due to B3LYP functional is known to scale as $\frac{-0.2}{r}$ instead of the exact value $\frac{-1}{r}$. This potential deficiency can be improved by introducing range separation of the

interelectronic repulsion term using Ewald split:

$$\frac{1}{r} = \frac{1 - \mathrm{erf}(\mu r)}{r} + \frac{\mathrm{erf}(\mu r)}{r} \tag{42.2}$$

where $\mu = 0.33$ and r is the interelectronic separation. This functional was introduced by Yanai et al. [6], where the first and second term models the short-range and long-range interaction respectively. This results in an increased contribution of HF exchange for long interelectronic separations. However, for small interelectronic separations the Becke exchange functional dominates. As a result, the exchange potential scales as $\frac{-0.65}{r}$. Thus, CAM-B3LYP provides an improved method to model the asymptotic exchange potential of the molecule. Many previous theoretical studies emphasize the use of the long-range asymptotic potential for reliable modelling of the optical properties of a molecule [7]. The asymptotic behavior is crucial for satisfying the ionization potential (IP) theorem in DFT which connects HOMO energy to the IP; it leads to unoccupied eigenvalues of improved interpretability, and as a consequence allows for higher accuracy in the prediction of various response properties [8] which are the focus of our study for EBM molecule.

42.2.2 Optical Properties

The molecular response to the external electric field can be estimated from the accurate prediction of the optical properties of the molecule. These include dipole moment (μ), polarizability (α), and hyperpolarizability (β) of the molecule. These properties also determine the strength of molecular interaction involved in various scattering processes. When a molecule is exposed to a single monochromatic optical oscillating field of frequency ω and static field (E_o), the perturbation ($H^{(1)}$) can be expressed as:

$$H^{(1)} = E_o\left(e^{i\omega t} + e^{-i\omega t} + 1\right) \tag{42.3}$$

The components of polarizability and hyperpolarizability tensor of the molecule can then be estimated using Time-Dependent Hartree-Fock (TDHF) formalism [9]:

$$\alpha(\mp\omega; \pm\omega) = -\operatorname{Tr}(H^{(1)}D(\pm\omega)) \tag{42.4}$$

$$\beta(\mp\omega; 0, \pm\omega) = -\operatorname{Tr}\left(H^{(1)}D(\pm\omega, 0)\right) \tag{42.5}$$

where $D(\pm\omega)$ and $D(\pm\omega, 0)$ are the first and second-order density matrix calculated from ground state coefficients using DFT and TDHF method, $H^{(1)}$ is the perturbed Hamiltonian and $\alpha(\mp\omega; \pm\omega)$ and $\beta(\mp\omega; 0, \pm\omega)$ are the polarizability and hyperpolarizability of the molecule calculated for external field frequency ω. For each functional, the ground state coefficients calculated are different, resulting in distinct

first and second-order density matrix. This difference in density matrices ultimately predicts different frequency-dependent properties for both functionals. The net isotropic polarizability (α), anisotropic polarizability ($\Delta\alpha$) and hyperpolarizability (β) can be computed using the following formulas:

$$\alpha = \frac{\alpha_{xx} + \alpha_{yy} + \alpha_{zz}}{3} \tag{42.6}$$

$$\Delta\alpha = 2^{-\frac{1}{2}} \left[\left(\alpha_{xx} - \alpha_{yy}\right)^2 + \left(\alpha_{yy} - \alpha_{zz}\right)^2 + (\alpha_{zz} - \alpha_{xx})^2 + 6\alpha_{xx}^2 \right] \tag{42.7}$$

$$\beta = \left[\left(\beta_{xxx} + \beta_{xyy} + \beta_{xzz}\right)^2 + \left(\beta_{yzz} + \beta_{yyy} + \beta_{yxx}\right)^2 + \left(\beta_{zxx} + \beta_{zyy} + \beta_{zzz}\right)^2 \right]^{\frac{1}{2}} \tag{42.8}$$

where α_{xx}, α_{yy} and α_{zz} are the polarizability components and β_{xxx}, β_{xyy}, β_{xzz}, β_{yzz}, β_{yyy}, β_{yxx}, β_{zxx}, β_{zyy}, β_{zzz} are the hyperpolarizability components and the subscript (x, y, z) indicates the axis along which the component is defined.

In addition to the above properties, we also study the excited states of the molecule using Time-Dependent Density Functional Theory (TD-DFT). The excitation wavelength (λ_1) and oscillator strength (f_i) for three excited states are used to simulate UV-Vis spectra of EBM molecule according to the relation:

$$\epsilon(\lambda) = \left(1.30629274 \times 10^8\right) \frac{f_i}{10^7/3099.6} \cdot \exp\left[-\left(\frac{1/\lambda - 1/\lambda_1}{1/3099.6}\right)^2 \right] \tag{42.9}$$

where $\epsilon(\lambda)$ is the absorbance corresponding to external exciting wavelength λ.

42.2.3   Population Analysis

Atomic charges in molecules is a fundamental concept which although itself is not an experimentally observable quantity but can be related to many other important observables like dipole moment, electric potentials, etc. These charges within the molecule can be determined from orbital wavefunctions. We explore two such methods of atomic charge estimation in the molecule: Mulliken analysis and Natural Bond Orbital Analysis. Mulliken analysis can be performed using the density and overlap matrix obtained during DFT calculations. The density matrix ($D_{\mu v}$) is defined in terms of coefficients of doubly occupied molecular orbitals for a closed-shell system $C_{\mu i}$ (for μth basis of ith molecular orbital) as:

$$D_{\mu v} = 2 \sum_i C_{\mu i} C_{v i}^* \tag{42.10}$$

where $C_{\nu i}^*$ is the conjugate coefficient of νth basis of ith molecular orbital.

The population matrix ($P_{\mu\nu}$) in terms of density and overlap matrix is defined as:

$$P_{\mu\nu} = D_{\mu\nu} S_{\mu\nu} \tag{42.11}$$

where $D_{\mu\nu}$ and $S_{\mu\nu}$ are density and overlap matrix of the basis function, respectively. For each atom X, within the molecule having atomic charge Z_X, the partial charge (Q_X) is defined as:

$$Q_X = Z_X - GAP_X \tag{42.12}$$

where GAP_X is the gross atomic population. Natural bonding orbital analysis provides insights about the hyper conjugative interactions occurring within the molecule using second-order perturbation theory. The interactions result in loss of occupancy from localized Lewis type NBO orbitals to empty non-Lewis orbitals. For each donor (i) and acceptor (j) the orbital stabilization energy $E^{(2)}$ calculated from second-order perturbation theory is given by:

$$E^{(2)} = \Delta E_{ij} = -\frac{q_i F_{ij}^2}{\varepsilon_j - \varepsilon_i} \tag{42.13}$$

where ΔE_{ij} is the energy shift due to stabilization interaction between the donor(i) and acceptor (j), q_i is the donor orbital occupancy, ε_i and ε_j are donor and acceptor orbital energy values and F_{ij} is Fock matrix elements. The magnitude of $E^{(2)}$ values signifies the strength of the interaction between donor and acceptor orbitals. A larger value of $E^{(2)}$ implies intensive conjugative interactions between donor and acceptor orbitals.

42.2.4   Molecular Vibrations

Vibrational spectroscopy has emerged as an important investigatory method to understand the structure and dynamics of molecules. Determining the vibrational modes of a molecule requires the computation of second-order energy derivatives in cartesian coordinates. The energy derivatives are transformed from cartesian to internal coordinates and then diagonalized. The eigenvalues thus obtained are the vibrational frequencies of the molecule. The transformation of coordinates is valid only for optimized structure and hence the vibrational frequencies are determined only for optimized molecular structure. The infrared intensity (I^{IR}) of the molecule can be determined from the determination of derivatives of dipole moment (dμ/dQ) as [10]:

$$I^{IR} = \frac{N\pi}{3c} \left| \frac{d\mu}{dQ} \right| \tag{42.14}$$

where N is the number density, c is the velocity of light, μ is the electric dipole moment and Q is the normal model coordinate of the molecule. Since both functionals (B3LYP and CAM-B3LYP) will yield different molecular energy and dipole moment, therefore they will predict different vibrational frequencies and intensity for the same molecule.

42.3 Computational Details

Geometrical optimization was performed on the molecular structure of 2-(4- ethyl-benzylidene) malononitrile (EBM) ($C_{12}H_{10}N_2$) to obtain minimum energy structure using Density Functional Theory and B3LYP and CAM-B3LYP exchange-correlation functional along with 6-311++G(d,p) basis set. No geometry constraints were applied during the optimization process. Using the same level of theory, frequency calculations were performed on an optimized EBM molecule structure to ensure no imaginary frequencies occur for optimized geometry. The theoretically obtained optimized parameters were compared with the experimentally available X-ray diffraction data. DFT and TDHF calculations have also been performed to estimate the dipole moment, polarizability and first hyperpolarizability of the title molecule. We also simulate the UV-Visible spectra of EBM using B3LYP and CAM-B3LYP functionals. To further analyze the partial charge assignment on each atom Mulliken population analysis and Natural Bond Orbital (NBO) analysis have also been performed. All the calculations were performed using Gaussian 16 software package and corresponding results were visualized using GaussView 06 Software [11].

42.4 Results and Discussion

42.4.1 Molecular Structure

The optimized ground state molecule geometry of the EBM molecule showed that the molecule belongs to C_1 point group symmetry. The optimized molecular structure is shown in Figure 42.1. The optimized molecular geometric parameters including bond length and bond angles, calculated using B3LYP and CAM-B3LYP functional and 6-311++G(d,p) basis set along with experimental results are reported in Table 42.1. From the calculated optimized parameters, we observe that DFT calculations predict slightly longer bond lengths than experimental values. This difference arises because the experimental parameters were obtained for the molecule in solid-state; however, theoretical calculations were performed for the isolated molecule in the gaseous phase.
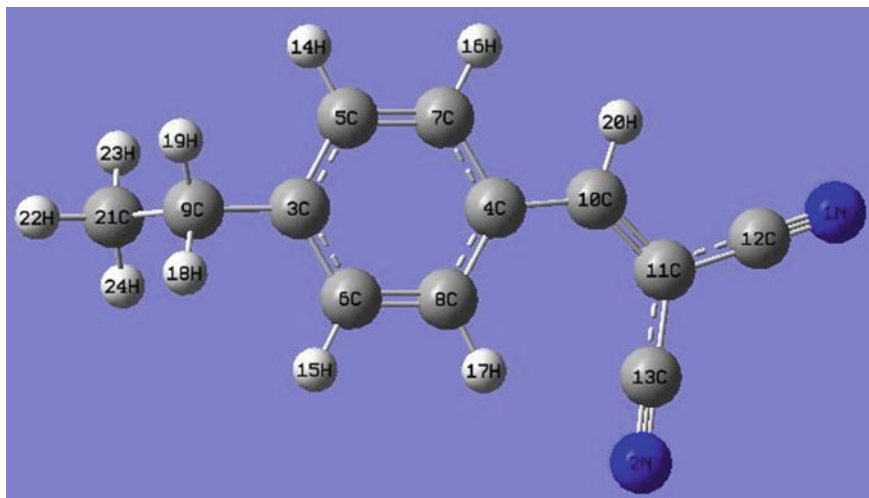
Fig. 42.1 Molecular structure of 2-(4-ethylbenzylidene) malononitrile (EBM)

The average absolute error $\left(\left| \frac{Theo.BondLength - Exp.BondLength}{No.of\ Bonds} \right| \right)$ between theoretical and experimental values of bond angles and bond lengths is listed in Table 42.2. From the table, it is evident that CAM-B3LYP gives less absolute error in comparison to B3LYP results. This result is indicative of the fact that the molecular structure is better modelled using CAM-B3LYP than B3LYP functional.

42.4.2 Optical Properties

We report the ground state static dipole moment, polarizability and hyperpolarizability values for EBM molecule in Table 42.3 calculated using B3LYP and CAM-B3LYP functionals. We also report the UV-Visible spectrum calculated using TDDFT to identify the excitations occurring within the molecule. We observe that the net electric dipole does not change appreciably with the change in functional. However, the magnitude of μ_x decreases for CAM-B3LYP calculation while μ_y and μ_z increases. This is observed because the variation in calculated exchange energy leads to variation in the charge distribution within the molecule. A similar trend is observed in polarizability and hyperpolarizability components (α_{xx}, α_{yy}, α_{zz}, β_x, β_y and β_z) where there is a decrease in the magnitude of x components but a slight increase in the magnitude for y and z components while moving from B3LYP to CAM-B3LYP. This behavior in static optical properties of ground-state calculations for EBM molecule is observed because electron density distribution due to CAM-B3LYP functional decreases along x plane and increases along y and z planes as compared to B3LYP electron density distribution.

Table 42.1 Calculated and experimental bond parameters of EBM molecule

Parameters	Exp. [1]	Calc	
		B3LYP	CAM-B3LYP
Bond length (Å)			
C21-C9	1.465	1.5403	1.5043
C9-C3	1.521	1.5096	1.5096
C3-C6	1.375	1.4027	1.4027
C3-C5	1.378	1.4001	1.4001
C5-C7	1.367	1.3865	1.3865
C7-C4	1.374	1.4101	1.4101
C4-C8	1.387	1.4101	1.4101
C4-C10	1.439	1.4488	1.4488
C8-C6	1.363	1.3861	1.3861
C10-C11	1.340	1.3646	1.3646
C11-C12	1.432	1.4313	1.4313
C11-C13	1.433	1.4277	1.4277
C12-N1	1.136	1.1558	1.1557
Bond angle (°)			
C21-C9-C3	113.6	112.66	112.66
C6-C3-C5	116.5	118.00	118.00
C6-C3-C9	124.7	120.90	120.90
C5-C3-C9	118.7	121.07	121.07
C7-C5-C3	121.3	120.84	120.84
C5-C7-C4	122.2	121.26	121.26
C7-C4-C8	116.6	117.80	117.80
C7-C4-C10	118.4	116.88	116.88
C8-C4-C10	125.0	125.31	125.32
C6-C8-C4	120.9	120.41	120.41
C8-C6-C3	122.5	121.66	121.66
C11-C10-C4	131.2	131.68	131.68
C10-C11-C12	120.6	119.17	119.17
C10-C11-C13	124.4	125.36	125.37
N1-C12-C11	178.8	179.7	179.7
N2-C13-C11	178.0	178.9	178.9

Table 42.2 Average absolute error in bond lengths and bond angles for EBM molecule

	B3LYP	CAM-B3LYP
Bond lengths (Å)	0.0203	0.0175
Bond angle (°)	0.1131	0.1112

Table 42.3 Linear and nonlinear optical properties of EBM molecule

Property	B3LYP	CAM-B3LYP
μ_x (Debye)	7.54946	7.54188
μ_y (Debye)	0.150270	0.158475
μ_z (Debye)	2.14734	2.17312
μ (Debye)	7.85035	7.85032
α_{xx} (10^{-24} esu)	35.8873	35.8243
α_{yy} (10^{-24} esu)	12.9002	12.9023
α_{zz} (10^{-24} esu)	27.0229	27.0784
α (10^{-24} esu)	25.2701	25.2683
$\Delta\alpha$ (10^{-24} esu)	24.6487	24.6445
β_x (10^{-30} esu)	−29.1207	−29.0354
β_y (10^{-30} esu)	−1.75514	−1.79253
β_z (10^{-30} esu)	−23.4073	−23.5091
β (10^{-30} esu)	37.40317	37.40248

Figure 42.2 reports the variation of frequency-dependent polarizability of molecule with the wavelength of the external electric field. From the plots of isotropic (α) and anisotropic ($\Delta\alpha$) polarizability, we observe that change in functional from B3LYP to CAM-B3LYP leads to no change in α and $\Delta\alpha$ in the wavelength range 400–700 nm but a change in the range 100–350 nm. The peak response of α is observed at 300 nm predominately due to α_{xx} and α_{zz} components of polarizability. Thus, at 300 nm wavelength, the dipole moment change with the external electric field is maximum for the x- and z- components of the molecule which results in a large first-order response of the molecule. We also observe that at 300nm, the peak polarizability ($\alpha, \alpha_{xx}, \alpha_{zz}$) is positive for CAM-B3LYP functional and negative for B3LYP functional. This reveals that the change in dipole moment is in direction of electric field for polarizability components calculated using CAM-B3LYP functional; however, the change in dipole moment is in the direction opposite to the electric field for polarizability components calculated using B3LYP functional. Thus, the frequency-dependent response of the molecule is highly sensitive to the functional selected for DFT calculations.

Figure 42.3 depicts the frequency-dependent hyperpolarizability of EBM molecule as a function of the wavelength of external electric field. The hyperpolarizability response of the molecule w.r.t external oscillating field gave a sharp increase below 100 nm wavelength. The hyperpolarizability components predicted using CAM-B3LYP functional at 100 nm is consistently lower than the B3LYP calculated values.

EBM molecule consists of a donor ethyl moiety of low ionization potential and acceptor nitrile moiety of relatively high electron affinity. When this molecule is exposed to the external field, intra-molecular charge transfer occurs from donor to acceptor group, which results in peak electronic excitations in the UV-Visible absorption spectra of the molecule. The excitation energies and oscillator strength
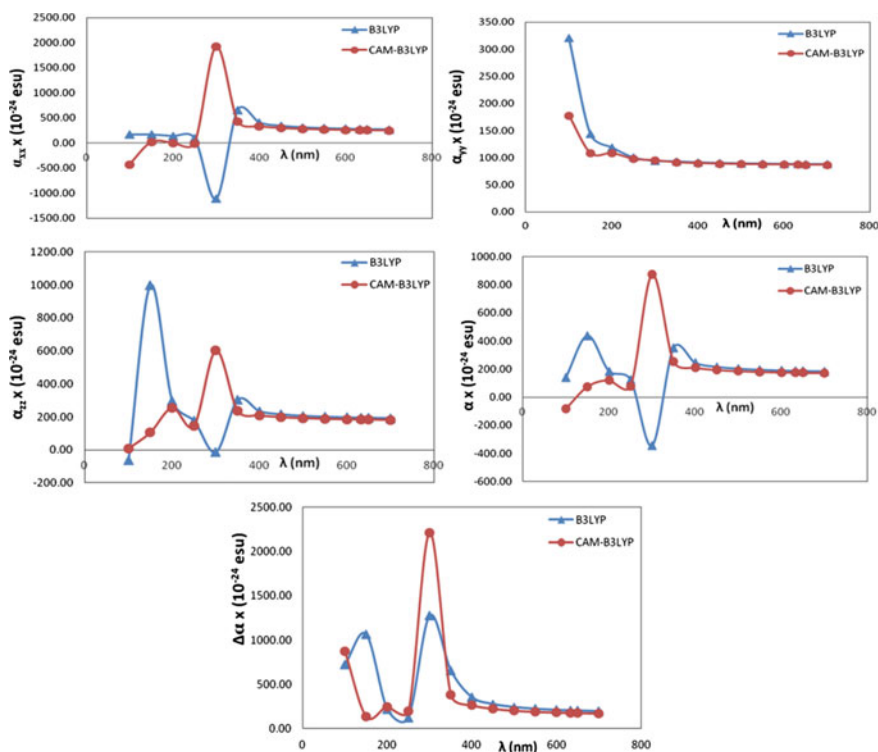
Fig. 42.2 Frequency dependent polarizability (α_{xx}, α_{yy}, α_{zz}, α, $\Delta\alpha$) of 2-(4-ethylbenzylidene) malononitrile (EBM) molecule calculated using B3LYP and CAM-B3LYP functionals and 6-311++G(d,p) basis set

calculated for three excited states are reported in Table 42.4 and are used to simulate the UV-Visible spectrum in accordance with (42.9).

From Fig. 42.4, we observe the peak electronic excitation wavelengths at 316.40 and 299.37 nm for B3LYP and CAM-B3LYP functionals, respectively. During the excitation, the molecule undergoes distortion in the electron cloud and thus inducing large polarizability within the molecule. Both functionals predict large molecular polarizability of components at 300 nm as discussed above. However, the UV excitation wavelength calculated using CAM-B3LYP is much closer to 300 nm than the B3LYP excitation wavelength. CAM-B3LYP functional includes long-range HF exchange, which helps to model the intra-molecular charge transfer within the molecule more efficiently than B3LYP functional.

As a result of this inclusion of long-range HF exchange, CAM-B3LYP functional models molecular polarizability of the molecule better than B3LYP.
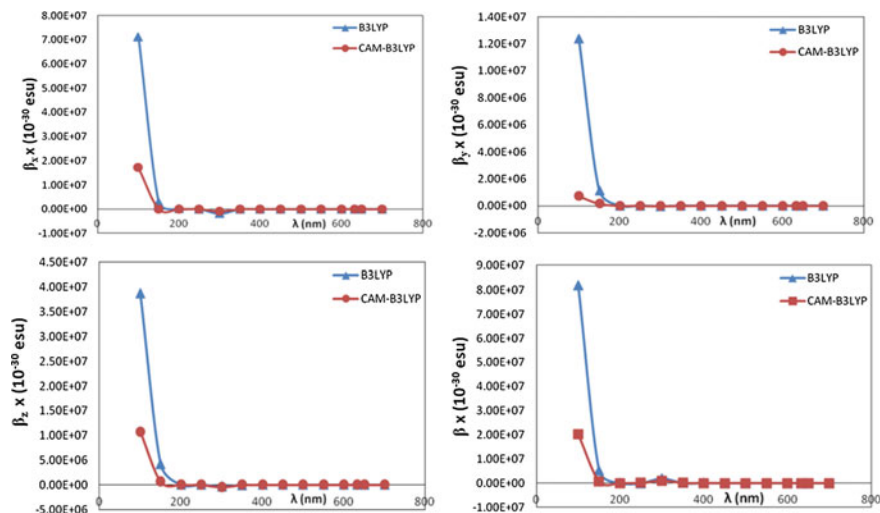
Fig. 42.3 Frequency dependent hyperpolarizability (β, β_x, β_y and β_z) of 2-(4-ethylbenzylidene) malononitrile (EBM) molecule calculated using B3LYP and CAM-B3LYP functionals and 6-311++G(d,p) basis set

Table 42.4 Excitation wavelength (λ_1) and oscillator strength (f_1) of EBM molecule

Excited state		B3LYP		CAM-B3LYP	
	λ_1	f_1	λ_1	f_1
	(nm)		(nm)	
1	316.40	0.7363	299.37	0.7877
2	301.39	0.0399	270.94	0.0201
3	233.27	0.0357	211.42	0.1216

Fig. 42.4 UV–visible spectrum of 2-(4-ethylbenzylidene) malononitrile (EBM) molecule calculated using B3LYP and CAMB3LYP functionals and 6-311++G(d,p) basis set
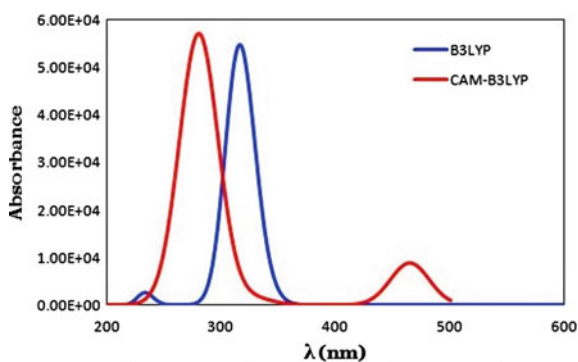
42.4.3 Population Analysis

The charge distribution of the molecule has been calculated using the Mulliken population analysis technique using two hybrid DFT functional B3LYP and CAM-B3LYP in combination with 6-311++G(d,p) basis set and the results are reported in Figure 42.5. We observe that change in the functional from B3LYP to CAM-B3LYP resulted in different charge distribution on three carbon atoms (C11, C8, C6). The charge distribution on all the other atoms remains the same. The atomic charge on C11 atom is calculated to be increased from 1.803e for B3LYP functional to 1.804e for CAM-B3LYP functional where e is the electronic charge (1e = 1.602 × 10^{-19} coulombs). However, the atomic charge on C8 and C6 decreases. This behavior is observed due to the variation in the calculated molecular orbital coefficients with changes in functional selected, which results in different density matrices for different functionals and ultimately different atomic charges (ref. 10–12).

A detailed NBO analysis of the title compound has been performed to analyze the interaction between donor and acceptor orbitals which ultimately provides useful insights about the intra-molecular charge transfer and delocalization interactions. The results of NBO analysis are reported for 25 donor-acceptor orbitals and their corresponding occupancy and stabilization energy in Table 42.5. The donor and acceptor orbitals considered in this study are of σ, σ *, π, π *, 1-centre core pair (CR), 1-centre valence lone pair (LP)(n) and Rydberg (RY*) type. The loss of occupancy from donor to acceptor is referred to as "delocalization correction" to the natural Lewis structure.

From the NBO analysis of the EBM molecule reported in Table 42.5, we observe maximum value of stabilization energy (E^2) for charge transfer π*(C4-C7) → π* (C3-C5) and π*(C4-C7) → π*(C6-C8) bond orbital interaction. This indicates the delocalization of the electron cloud which makes the benzene ring of the molecule highly polarized. The maximum electron density distribution is observed

Fig. 42.5 Mulliken charge distribution of 2-(4-ethylbenzylidene) malononitrile (EBM) molecule calculated using B3LYP and CAMB3LYP functionals and 6-311++G(d,p) basis set

Table 42.5 Second-order perturbation theory analysis of Fock matrix in NBO basis corresponding to the intramolecular bonds of EBM molecule

Donor (i)	Occupancy		Acceptor	Occupancy	$(E^2)^a$ (kcal/mol)		E(j) − E(i)(a.u.)		F(i,j)^b(a.u.)	
	B3LYP	CAM-B3LYP	B3LYP	CAM-B3LYP	B3LYP	CAM-B3LYP	B3LYP	CAM-B3LYP	B3LYP	CAM-B3LYP
σ(N1-C12)	1.99439	1.99423	σ*(C11-C12) 0.03411	0.03456	7.07	6.95	1.55	1.54	0.094	0.093
τ(N1-C12)	1.96175	1.96296	π*(C10-C11) 0.21369	0.20586	7.59	7.70	0.35	0.35	0.048	0.048
σ(N2-C13)	1.99377	1.99356	σ*(C11-C13) 0.03861	0.03918	7.14	6.99	1.55	1.54	0.095	0.094
τ(N2-C13)	1.95752	1.95883	π*(C10-C11) 0.21369	0.20586	8.32	8.46	0.36	0.35	0.051	0.051
π(C3-C5)	1.60844	1.61057	π*(C4-C7) 0.40534	0.40274	25.43	25.50	0.27	0.27	0.075	0.074
π(C3-C5)	1.60844	1.61057	π*(C6-C8) 0.27300	0.27538	17.04	16.78	0.29	0.28	0.064	0.063
π(C4-C7)	1.60469	1.60898	π*(C3-C5) 0.32774	0.32742	17.13	17.17	0.29	0.29	0.064	0.064
π(C4-C7)	1.60469	1.60898	π*(C6-C8) 0.27300	0.27538	19.25	19.02	0.29	0.29	0.069	0.068
π(C4-C7)	1.60469	1.60898	π*(C10-C11) 0.21369	0.20586	23.50	24.25	0.27	0.27	0.075	0.075
π(C6-C8)	1.66914	1.66809	π*(C3-C5) 0.32774	0.32742	22.59	22.43	0.29	0.29	0.073	0.072
π(C6-C8)	1.66914	1.66809	π*(C4-C7) 0.40534	0.40274	18.50	18.08	0.28	0.28	0.065	0.064

(continued)

Table 42.5 (continued)

Donor (i)	Occupancy		Acceptor	Occupancy		$(E^2)^a$(kcal/mol)		$E(j) - E(i)$(a.u.)		$F(i,j)^b$(a.u.)	
π (C10-C11)	1.96847	1.82231	τ (N1-C12) 0.08314	0.08049	19.69	20.08		0.41	0.40	0.082	0.082
π (C10-C11)	1.96847	1.82231	τ (N2-C13) 0.01045	0.07667	18.54	19.37		0.41	0.40	0.081	0.080
π (C10-C11)	1.96847	1.82231	π^* (C4-C7) 0.40534	0.40274	8.99	9.26		0.32	0.31	0.051	0.019
σ(C11-C13)	1.97307	1.97259	σ^* (N2-C13) 0.01045	0.01060	8.03	7.65		1.67	1.66	0.104	0.101
CR(1)N(1)	1.99958	1.99957	RY*C12 0.1664	0.01691	7.29	7.15		15.08	15.07	0.297	0.294
CR(1)N(1)	1.99958	1.99957	RY*C13 0.1678	0.01705	7.23	7.09		15.04	15.03	0.237	0.293
LP(1)N(1)(n)	1.97033	1.97028	RY*C12 0.1664	0.01691	18.41	17.67		1.54	1.52	0.149	0.147
LP(1)N(1)(n)	1.97033	1.97028	σ^* (C11-C12) 0.03411	0.03456	11.36	11.75		1.00	1.00	0.095	0.097
LP(1)N(1)(n)	1.97033	1.97028	RY*C13 0.1678	0.01705	17.78	17.33		1.50	1.49	0.146	0.144
LP(1)N(1)(n)	1.97033	1.97028	σ^*(C11-C13) 0.03861	0.03918	11.35	11.67		1.00	1.01	0.095	0.097
π^* (C4-C7)	0.40534	0.40274	π^* (C3-C5) 0.32774	0.02513	200.75	214.73		0.02	0.01	0.083	0.082
π^* (C4-C7)	0.40534	0.40274	π^* (C6-C8) 0.27300	0.27538	216.15	214.77		0.01	0.01	0.082	0.080
π^* (C10-C11)	1.46847	0.20586	τ (N1-C12) 0.08314	0.08049	11.13	11.42		0.09	0.10	0.077	0.076

(continued)

Table 42.5 (continued)

Donor (i)	Occupancy		Acceptor	Occupancy		$(E^2)^a$(kcal/mol)	E(j) − E(i)(a.u.)		F(i,j)^b(a.u.)	
π^* (C10-C11)	1.46847	0.20586	τ (N2-C13) 0.01045	0.07667	11.62	13.56	0.10	0.09	0.081	0.081

$^a E^2$ is the stabilization energy due to hyperconjugative interactions
^{b}F(i,j) is the Fock matrix element between i and j orbital
^{c}LP(n)A is a valence lone pair orbital (n) on A atom

for CR1(N1) and σ(N1-C12) bond orbital. The N1 lone pair of the molecule acts as a donor and contributes significantly to the stabilization of the molecule through n $\rightarrow$ σ* and n $\rightarrow$ RY* interactions with $E^{(2)}$ values ranging from 11.35 to 18.41 kcal/mol. In addition to the lone pair interaction, $\pi \rightarrow \pi$* interaction between C-C bonds also contributes appreciably to the stabilization of the molecule with stabilization energies of the range 8.99–25.43 kcal/mol. Thus, we infer that maximum stabilization energy is obtained from π* $\rightarrow \pi$* stabilization interaction. The second leading cause of delocalization interactions were due to $\pi \rightarrow \pi$* and N1 lone pair interactions (n$\rightarrow$ σ* and n $\rightarrow$RY* interactions). Among all reported interactions, the movement of electrons from $\sigma \rightarrow \sigma$* orbital resulted in the least stabilization energy. Thus, different bond orbitals contribute differently to the stabilization of the molecule.

42.4.4 Molecular Vibrations

Figure 42.6 shows the calculated vibrational spectra of the EBM molecule. The experimental FT-IR spectra for EBM molecule was reported [3] to exhibit CN vibration at 2223.92 cm^{-1}. In our calculations, two CN vibrational modes were obtained for both B3LYP functional and CAM-B3LYP functional. For B3LYP, they correspond to peak at wavenumbers 2320.78 and 2333.72 cm^{-1} and for CAM-B3LYP the corresponding peaks were obtained at 2320.68 and 2333.6368 cm^{-1}. Both functionals overestimate the actual vibrational mode frequency of the molecule. However, CAM-B3LYP predicts a slightly lower value of harmonic vibrational frequency. Experimental ethyl group vibrational modes were reported at 2974.23 and 2877.79 cm^{-1}. Calculated DFT spectra predicted 5 ethyl vibrational modes at 3099.09, 3096.23,

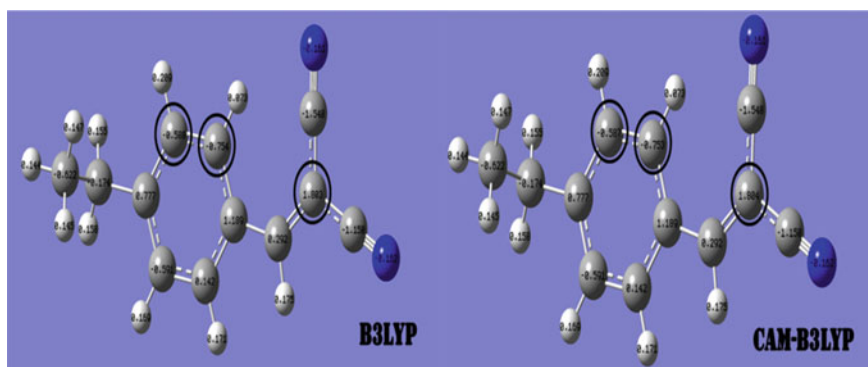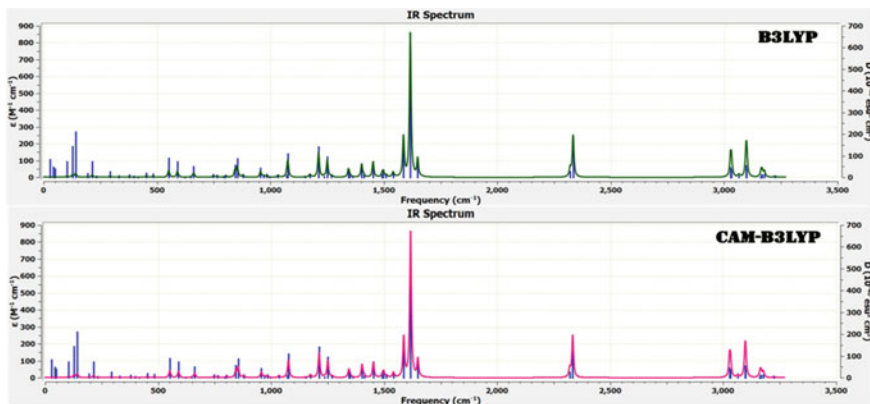**Fig. 42.6** Infrared spectrum of 2-(4-ethylbenzylidene) malononitrile (EBM) molecule calculated using B3LYP and CAM-B3LYP functionals and 6-311++G(d,p) basis set

3064.24, 3031.90 and 3027.68 cm^{-1} for B3LYP functional and 3099.03, 3096.16, 3064.19, 3031.87 and 3027.64 cm^{-1} for CAM-B3LYP.

Like CN vibrations, for ethyl group stretching vibrational frequencies predicted using CAM-B3LYP functional is lower than its B3LYP counterpart. Experimentally aromatic CH stretching vibration was reported [3] at 3037.89 cm^{-1}. In our calculation we observed 5 Aromatic CH stretching vibrational modes at 3223.62, 3176.85, 3166.9792, 3162.60 and 3158.6024 cm^{-1} for B3LYP functional and 3223.61, 3176.91, 3167.04, 3162.65 and 3158.65 cm^{-1}. In contrast to CN and ethyl group vibrations, aromatic CH stretching vibrations showed an increase in the frequency of vibrational modes calculated using CAM- B3LYP functional.

Thus, improved asymptotic exchange potential of CAM-B3LYP functional altered the calculated vibrational frequency modes of the EBM molecule slightly indicating that exchange energy does play an important role in the estimation of the vibrational frequency of the molecule. From our results, we infer that although both functionals predict higher vibrational frequencies for CN, CH, and ethyl vibrational modes, frequencies predicted using CAM-B3LYP were closer to experimental frequencies than those calculated using B3LYP functional. We also observe that IR intensity was calculated to be maximum for CN vibrations than for aromatic CH stretching vibrations indicating that vibrations in the attached substituent groups (CN and ethyl group) were accompanied by a larger change in dipole moment than ring CH bond vibrations.

42.5 Conclusion

In this work, we performed a detailed analysis of EBM molecular structure and its properties using two different hybrid functionals B3LYP and CAM-B3LYP in conjunction with 6-311++G(d,p) basis set. We studied the effect of different functionals in modelling the molecular structure and properties and found that CAM-B3LYP gives better estimate of molecule structure, UV-Visible and Infrared spectra than B3LYP functional and is therefore better suited to perform theoretical modelling of exchange-correlation energy of EBM molecule. Our analysis of functionals is crucial to test the validity of DFT methods in predicting molecular structure and properties. Amongst the molecular properties, the optical properties of EBM molecule are of significant importance due to its high optical nonlinearity which paves way for its NLO applications in the field of photonic device development, fast data transfer, electro-optical modulation, and telecommunication.

References

1. E. Garmire, Opt. Express **21**(25), 30532 (2013)
2. M. Jazbinsek, U. Puc, A. Abina, A. Zidansek, Appl. Sci. **9**(5), 882 (2019)
3. A. Priyadharshini, S. Kalainathan, J. Phys. Chem. Solids **123**, 59 (2018)
4. M.J. Frisch et al. Gaussian 16, Revision A.3 (2016)
5. A.D. Becke, J. Chem. Phys **98**, 5648 (1993)
6. T. Yanai, D.P. Tew, N.C. Handy, Chem. Phys. Lett. **393**, 51 (2004)
7. A.J. Garza, G.E. Scuseria, S.B. Khan, A.M. Asiri, Chem. Phys. Lett. **575**, 122 (2013)
8. E. Kraisler, Isr. J. Chem. (2020)
9. H. Sekino, R.J. Bartlett, J. Chem. Phys. **85**, 976 (1986)
10. D. Porezag, M.R. Pederson, Phys. Rev. B **54**, 7830 (1996)
11. GaussView06, R. Dennington, T.A. Keith, J. M. Millam, Semichem Inc., Shawnee Mission, KS, (2016)

Chapter 43
Vibrational (FT-IR and FT-Raman) Spectroscopic Investigations, NLO, NBO and MEP Analysis of 1,4-Dibromo-2,5-Dimethoxybenzene by DFT

Jayant Teotia, Annu, Isha Rathi, Shaleen Bhardwaj, Ravish Kumar Uppadhayay, and Ankita Garg

Abstract The FT-IR spectra of 1,4-dibromo-2,5-dimethoxybenzene is recorded in the region 4000–400 cm^{-1} and FT-Raman is recorded in the region 3500–100 cm^{-1}. The observed frequencies are matched with the density functional theory (DFT) calculations using Gaussian software. The detailed vibrational assignments are calculated using VEDA program. DFT is also used to calculate non-linear optical (NLO) properties and natural bond analysis (NBO). The entropy, enthalpy and heat capacity are calculated at different temperatures. Mulliken charge distribution along with molecular electrostatic potential (MEP) surfaces are also characterized. Reduced density gradient (RDG) analysis is carried out to study non covalent interactions of the molecule.

43.1 Introduction

Benzene substituted molecules have been studied by many researchers as they have many applications in various fields. Hexa-substituted benzene compounds have been utilized as high performing solar cells as they are soluble, have thermal stability and hole mobility [1]. Donor-σ-acceptor benzene derivative have good application in photovoltaic devices [2]. Halogen substituted benzene molecules have various synthetic and analytic applications [3]. A new class of bis-chalcone embedded benzenes are found to have third-order nonlinear optical applications [4]. D. Mahadevan et al., perform vibrational and electronic studies on 1-bromo-3-fluorobenzene and also calculated thermodynamic properties at different temperatures [5]. M. Govindarajan et al., perform vibrational and electronic studies on chlorobenzene using HartreeFock (HF) and density functional theory (DFT) [6]. Valerie J. Eaton et al., performed detailed study of in-plane vibrations of benzene and

J. Teotia · Annu (✉) · I. Rathi · S. Bhardwaj · R. K. Uppadhayay · A. Garg
Molecular Spectroscopy and Biophysics Lab, Department of Physics, Deva Nagri College, Meerut, Uttar Pradesh 250002, India

fluorobenzenes [7]. G. Raja et al., studied FT-IR, FT-Raman and DFT calculations on hexafluorobenzene [8]. Keeping these applications and importance of benzene and its derivatives in view, the present work deals with detailed vibrational (FT-IR and FT-Raman) spectroscopic analysis of 1,4-dibromo-2,5-dimethoxybenzene (1,4-DB-2,5-DMB). The selected compound is of biological importance and no computational work on 1,4-DB-2,5-DMB have been reported so far.

43.2   Experimental Details

The molecule 1,4-dibromo-2,5-dimethoxybenzene was purchased from Sigma Aldrich chemicals, USA and is used as such. The FT-Raman spectra of 1,4-DB-2,5-DMB is recorded in the region 3500–100 cm^{-1}. The IR spectrum of the molecule is recorded in the region 4000–400 cm^{-1}.

43.3   Computational Details

The molecular structure of 1,4-DB-2,5-DMB in the ground state is computed by density functional theory (DFT) method with Gaussview and Gaussian09 program. The basis set used for 1,4-DB-2,5-DMB is B3LYP/6-311++G(d,p). This basis set employs Becke's parameter [9] (B3) and electron correlation functional of Lee, Yang, and Parr (LYP) [10] functions. A basis set describes the orbitals within a system mathematically and thus approximates the total electronic wavefunction and is used to perform the theoretical calculation [11]. The basis set at DFT level is used to compute optimized structural parameter, subsequent normal coordinates and vibrational frequencies. The VEDA program [12] is used to calculate vibrational assignments on the basis of Total Energy Distribution (TED). The thermodynamic parameters, electric dipole moment (μ), the non-linear optical (NLO) properties like the isotropic polarizability (α) and first hyperpolarizability (β) of the molecule are also calculated by DFT. Reduced density gradient analysis was carried out using multiwfn program to study non covalent interaction [13].

43.4   Results and Discussion

43.4.1   Molecular Geometry and Structural Parameters

The structure along with the numbering of atoms of 1,4-DB-2,5-DMB is shown in Fig. 43.1. The molecule 1,4-DB-2,5-DMB has 20 atoms and belongs to the point group C_S. The total vibrational modes of the 20 atoms are 54, out of which 35 are
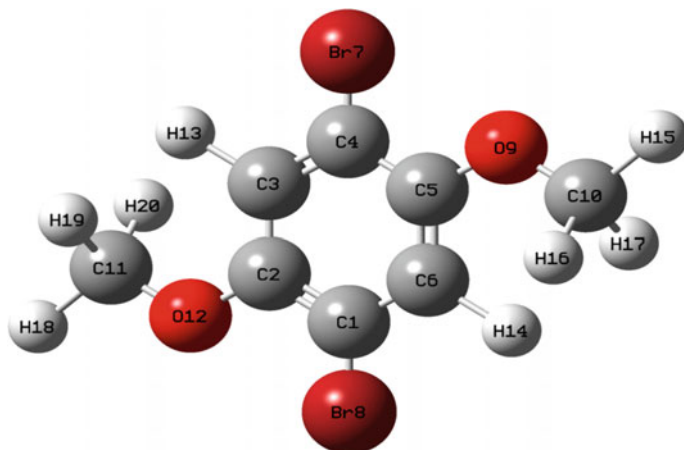
Fig. 43.1 Molecular structure of 1,4-DB-2,5-DMB along with the numbering of atoms

in plane modes and 19 are out of plane modes. The bond lengths and bond angles of optimized 1,4-DB-2,5-DMB calculated at B3LYP/6-311++G(d,p) basis set are shown in Table 43.1. The bond lengths between C–Br are larger than between other atoms.

43.4.2 Normal Coordinate Analysis for 1,4-Dibromo-2,5-Dimethoxybenzene

Various vibrational modes and the subsequent normal coordinate analysis can be described using normal coordinate analysis. There are 20 atoms in 1,4-DB-2,5-DMB molecule and is expected to exhibit 54 normal vibrational modes having 68 standard internal coordinates and 14 redundancies as defined in Table 43.2 [14]. Internal coordinates obtained from local symmetry coordinates is defined in Table 43.3 [15].

43.4.3 Vibrational Analysis

The combined observed and theoretical FTIR and FT-Raman spectra of 1,4-DB-2,5-DMB are shown in Figs. 43.2 and 43.3 respectively. The experimental and computational vibrational assignments of 1,4-DB-2,5-DMB are presented in the Table 43.4. VEDA program [12] is used to assign vibrational modes as all the modes cannot be assigned by just experimental knowledge. These assignments can be done by visualization of the atoms also but potential energy distribution (PED) analysis describes the contribution of movements of atoms in a group more accurately. This analysis has

Table 43.1 Computed bond lengths and bond angles of 1,4-dibromo-2,5-dimethoxybenzene

Bond length (Å) (Å)	B3LYP/6-311G++(d, p) (Å)	Bond angle (°)	B3LYP/6-311G ++(d, p)
C3–C2	1.398	C3–C2–C1	118.8
C4–C3	1.389	C2–C1–Br8 C6C1–Br10	119.7
C1–Br8	1.909	C6–C1–C2	121.3
C2–C1	1.399	O12–C2–C1	117.8
C2–O12	1.358	O12–C2–C3	117.9
C6–C1	1.389	C5–C4–C3	118.6
C3–H13	1.08	H13–C3–C2	120.8
C6–C5	1.398	H13–C3–C4	120.5
C4–Br7	1.909	C4–C3–C2	124.2
C5–C4	1.399	Br7–C4–C3	121.3
C5–O9	1.358	Br7–C4–C5	118.8
C6–H14	1.08	C5–C6–C1	124.2
O12–C11	1.422	C4–C5–O9	117.9
O9–C13	1.422	C6–C5–O9	117.9
C10–H17	1.095	C6–C5–C4	119.7
H15–C10	1.095	H14–C6–C1	120.8
H16–C10	1.088	H14–C6–C5	118.6
H18–C11	1.095	C11–O12–C2	120.5
H19–C11	1.095	C10-O9-C5	118.7
H$_2$0–C11	1.088	H16–C10–O9	111.3
		H15–C10–O9	118.7
		H17–C10–O9	111.3
		H16–C10–H15	105.5
		H17–C10–H16	109.6
		H17–C10–H15	109.3
		H18–C11–O12	109.3
		H19–C11–O12	111.3
		O12–C11–H$_2$0	111.3
		H18–C11–H19	105.5
		H18–C11–H$_2$0	109.6
		H19–C11–H$_2$0	109.3

Table 43.2 Internal coordinates for 1,4-dibromo-2,5-dimethoxybenzene

No. (i)	Symbol	Type	Definition
Stretching			
1–6	r_i	C_2C	C2–C1, C3–C2, C4–C3, C5–C4, C6–C5, C1–C6
7–8	R_i	C_2–Br	C4–Br7, C1–Br8
9–10	Q_i	C–H	C3–H13, C6–H14
11–16	Q_i	C–H(CH_3)	C11–H18, C11–H19, C11–H20, C10–H16, C10–H15, C10–H17
17–20	P_i	C–O, O–C	C11–O12, C2–O12, C5–O9, C10–O9
Bending			
21–26	β_i	B ring	C3–C2–C1, C4–C3–C2, C5–C4–C3, C6–C5–C4, C1–C6–C5, C2–C1–C6
27–30	α_i	C–C–Br	C3–C4–Br7,C5–C4–Br7,C2–C1–Br8, C6–C1–Br8
31–34	σ_i	C–C–H	C4–C3–H13,C2–C3–H13,C5–C6–H14,C1–C6–H14
35–38	δ_i	C–C–O	C3–C2–O12,C1–C2–O12,C6–C5–O9,C4–C5–O9
39–40	ρ_i	C–O–C	C2–O12–C11,C5–O9–C10
41–46	ν_i	H–C–O	H18–C11–O12,H19–C11–O12,H20–C11–O12,H15–C10–O9, H16–C10–O9, H17–C10–O9
47–52	λ_i	H–C–H	H18–C11–H19,H19–C11–H20,H18–C11–H20,H17–C10–H16, H15–C10–H16, H15–C10–H17
Out of plane bending			
53–54	ω_i	C–Br	Br8–C1–C2–C6, Br7–C4–C3–C5
55–56	π_i	C–H	C2–C4–C3–H13 ,C5–C1–C6–H14
57–58	Σ_i	C–O	O12–C2–C3–C1, O9–C5–C4–C6
59–60	Φ_i	O–C	O9–C10–C5–C4(C6), O12–C11–C2–C3(C1)
Torsion			
61–66	τ_i	t ring	C4–C3–C2–C1, C5–C4–C3–C2, C6–C5–C4–C3, C1–C6–C5–C4, C2–C1–C6–C5, C3–C2–C1–C6
67–68	τ_i	t C–OCH₃	(C3–C1)C2–O12–C11(H18,H19,H20),(C4,C6)C5–O9–C10(H15,H16,H17)

Table 43.3 Local symmetry co-ordinates for 1,4-dibromo-2,5-dimethoxybenzene

No.(i)	Symbol	Definition
1–6	CC	$r_1, r_2, r_3, r_4, r_5, r_6$
7–8	CBr	R_7, R_8
9–10	CH	Q_9, Q_{10}
11–12	CH_3 ss	$(Q_{13} + Q_{12} + Q_{11})/\sqrt{3}, (Q_{16} + Q_{15} + Q_{14})/\sqrt{3}$
13–14	CH_3 ips	$(2Q_{11} + Q_{12} + Q_{13})/\sqrt{6}, (2Q_{14} + Q_{15} + Q_{16})/\sqrt{6}$
15–16	CH_3 ops	$(Q_{12}-Q_{13})/\sqrt{2}, (Q_{15}-Q_{16})/\sqrt{2}$
17–20	CO	$P_{17}, P_{18}, P_{19}, P_{20}$
21	R trigd	$(\beta_{21}-\beta_{22}-\beta_{23}-\beta_{24}-\beta_{26} + \beta_{25})/\sqrt{6}$
22	R symd	$(2\beta_{23}-\beta_{21}-\beta_{22} + 2\beta_{26}-\beta_{24}-\beta_{25})/\sqrt{12}$
23	R asymd	$(\beta_{24}-\beta_{25} + \beta_{21}-\beta_{22})/2$
24–27	CH	$(\alpha_{27}-\alpha_{28})/\sqrt{2},(\alpha_{29}- \alpha_{30})/\sqrt{2},(\alpha_{31}- \alpha_{32})/\sqrt{2}, (\alpha_{33}- \alpha_{34})/\sqrt{2}$
28–29	bCO	$(\delta_{35}-\delta_{36})/\sqrt{2},(\delta_{37}-\delta_{38})/\sqrt{2}$
30–31	Boc	ρ_{39}, ρ_{40}
32–33	CH_3 sb	$(-\nu_{41}-\nu_{42}-\nu_{43} + \lambda_{47} + \lambda_{48} + \lambda_{49})/\sqrt{6},(-\nu_{44}-\nu_{45}-\nu_{46} + \lambda_{50} + \lambda_{51} + \lambda_{52})/\sqrt{6}$
34–35	CH_3 ipb	$(-\lambda_{47}-\lambda_{48}-2\lambda_{49})/\sqrt{6},(-\lambda_{50}-\lambda_{51}-2\lambda_{52})/\sqrt{6}$
36–37	CH_3 opb	$(\lambda_{47}-\lambda_{48})/\sqrt{2}, (\lambda_{50}-\lambda_{51})/\sqrt{2}$
38–39	CH_3 ipr	$(2\nu_{41}-\nu_{42}- \nu_{43})/\sqrt{6}, (2\nu_{44}-\nu_{45}- \nu_{46})/\sqrt{6}$
40–41	CH_3 opr	$(\nu_{42}- \nu_{43})/\sqrt{2}, (\nu_{45}- \nu_{46})/\sqrt{2}$
42–43	ω CBr	ω_{53}, ω_{54}
44–45	ω CH	π_{55}, π_{56}
46–47	ω CO	Σ_{57}, Σ_{58}
48–49	ω OC	Φ_{59}, Φ_{60}
50	t R trigd	$(\tau_{63}-\tau_{64} + \tau_{61}-\tau_{62} + \tau_{65}-\tau_{66})/\sqrt{6}$
51	t R symd	$(\tau_{64}-\tau_{63} + \tau_{61}-\tau_{66})/\sqrt{2}$
52	t R asymd	$(2\tau_{62}-\tau_{61}-\tau_{63} + 2\tau_{65}-\tau_{64}-\tau_{66})/\sqrt{12}$
53–54	t OCH_3	τ_{67}, τ_{68}

a correlation with the position, shape and intensity of the bands obtained in IR and Raman spectrum. Table 43.4 shows detailed contributions of PED greater than 10%. The 54 vibrational modes are shown in Table 43.4, out of which 35 in plane modes are denoted by A′ and 19 out of plane modes are denoted by A″. The computational wavenumbers are overestimated and are thus multiplied by scaling factor 0.9613 to match experimental results.
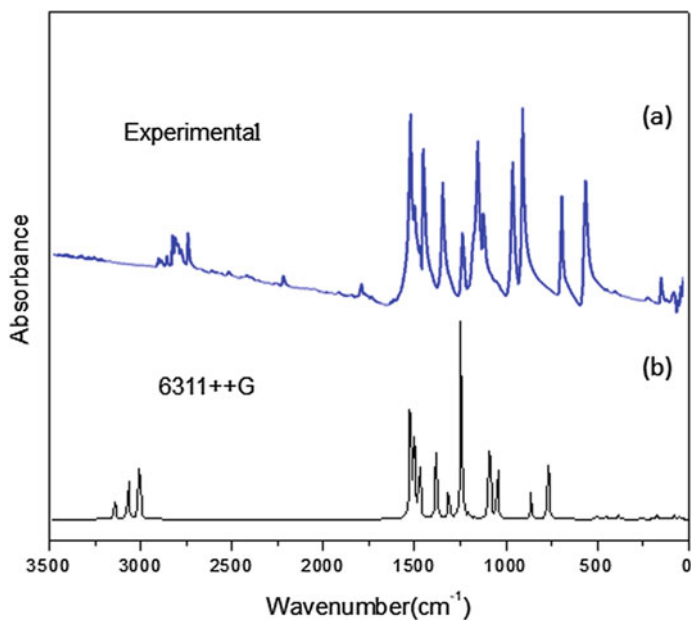
Fig. 43.2 FT-IR spectra of 1,4-dibromo-2,5-dimethoxybenzene **(a)** observed **(b)** calculated at B3LYP/6-311++G(d,p)
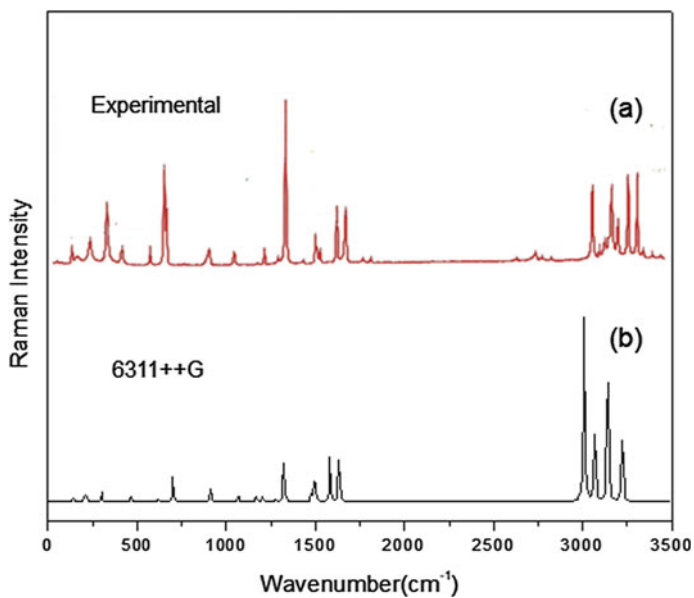
Fig. 43.3 FT-Raman spectra of 1,4-dibromo-2,5-dimethoxybenzene **(a)** observed **(b)** calculated at B3LYP/6-311++G(d,p)

Table 43.4 The computed and experimental FT-IR and FT-Raman vibrational frequencies of 1,4-DB-2,5-DMB along with potential energy distribution using DFT/B3LYP/6311++G(d,p)

Species	Experimental		Computational DFT B3LYP/6311++G (d,p)		Vibrational assignments PED (>10%)
	FT-IR	FT-Raman	Unscaled	Scaled	
A′	3099(w)	3087(vw)	3223	3098	$\nu(C_3\text{-}H_{13})(47) +$ $\nu(C_6\text{-}H_{14})(52)$
A′	3068(w)	3069(s)	3221	3096	$\nu(C_3\text{-}H_{13})(52) +$ $\nu(C_6\text{-}H_{14})(47)$
A′	3023(w)	3024(m)	3141	3020	$\nu_{as}(C_{10}\text{-}H_{15})(92)$ *Methyl*
A′			3140	3019	$\nu_{as}(C_{11}\text{-}H_{18})(92)$ *Methyl*
A″		2967(w)	3069	2950	$\nu_{as}(C_{10}\text{-}H_{16})(50) +$ $\nu_{as}(C_{10}\text{-}H_{17})(50)$ *Methyl*
A″	2945(m)	2940(m)	3068	2949	$\nu_{as}(C_{11}\text{-}H_{19})(50) +$ $\nu_{as}(C_{11}\text{-}H_{20})(50)$ *Methyl*
A′	2905(m)		3008	2892	$\nu_s(C_{10}\text{-}H_{16})(24) +$ $\nu_s(C_{10}\text{-}H_{17})(24) +$ $\nu_s(C_{11}\text{-}H_{19})(22) +$ $\nu_s(C_{11}\text{ - }H_{20})(22)$ *Methyl*
A′	2844(m)	2844(m)	3007	2891	$\nu_s(C_{10}\text{-}H_{16})(22) +$ $\nu_s(C_{10}\text{-}H_{17})(22) +$ $\nu_s(C_{11}\text{-}H_{19})(24) +$ $\nu_s(C_{11}\text{ - }H_{20})(24)$ *Methyl*
A′		1594(w)	1633	1570	$\nu(C_1\text{-}C_6)(25) +$ $\nu(C_5\text{-}C_4)(21) +$ $\beta(C_6\text{-}C_5\text{-}C_4)(10)$
A′	1493(vs)	1550(m)	1582	1521	$\nu(C_2\text{-}C_3)(23) +$ $\nu(C_5\text{-}C_4)(27) +$ $\beta(C_5\text{-}C_4\text{-}C_3)(10)$
A′	1476(m)		1523	1464	$\beta(H_{13}\text{-}C_3\text{-}C_2)(16) +$ $\beta(H_{14}\text{-}C_6\text{-}C_1)(15) +$ $\beta(H_{17}\text{-}C_{10}\text{-}H_{16})(11) +$ $\beta(H_{20}\text{-}C_{11}\text{-}H_{19})(11)$
A′	1460(w)		1504	1446	$\beta(H_{17}\text{-}C_{10}\text{-}H_{16})(27) +$ $\beta(H_{20}\text{-}C_{11}\text{-}H_{19})(27)$
A′		1442(w)	1502	1444	$\beta(H_{17}\text{-}C_{10}\text{-}H_{16})(19) +$ $\beta(H_{20}\text{-}C_{11}\text{-}H_{19})(18)$
A″	1438(s)		1494	1436	$\beta(H_{15}\text{-}C_{10}\text{-}H_{17})(37) +$ $\beta(H_{16}\text{-}C_{10}\text{-}H_{15})(37)$
A″			1493	1435	$\beta(H_{18}\text{-}C_{11}\text{-}H_{20})(37) +$ $\beta(H_{19}\text{-}C_{11}\text{-}H_{18})(37)$ *Twisting*

(continued)

Table 43.4 (continued)

Species	Experimental		Computational DFT B3LYP/6311++G (d,p)		Vibrational assignments PED (>10%)
	FT-IR	FT-Raman	Unscaled	Scaled	
A′			1479	1422	$\beta(H_{15}\text{-}C_{10}\text{-}H_{17})(17) +$ $\beta(H_{16}\text{-}C_{10}\text{-}H_{15})(17) +$ $\beta(H_{17}\text{-}C_{10}\text{-}H_{16})(11) +$ $\beta(H_{18}\text{-}C_{10}\text{-}H_{20})(17)$
A′			1473	1416	$\beta(H_{13}\text{-}C_{3}\text{-}C_{2})(10) +$ $\beta(H_{15}\text{-}C_{10}\text{-}H_{17})(10) +$ $\beta(H_{16}\text{-}C_{10}\text{-}H_{15})(10) +$ $\beta(H_{17}\text{-}C_{10}\text{-}H_{16})(14) +$ $\beta(H_{18}\text{-}C_{11}\text{-}H_{20})(10) +$ $\beta(H_{19}\text{-}C_{11}\text{-}H_{18})(10) +$ $\beta(H_{20}\text{-}C_{11}\text{-}H_{19})(14)$
A′	1358(s)		1381	1328	$\nu(C_{6}\text{-}C_{1})(21) +$ $\nu(C_{4}\text{-}C_{3})(21) +$ $\nu(C_{3}\text{-}C_{2})(12) +$ $\nu(C_{6}\text{-}C_{5})(11)$
A′	1293(vs)		1322	1270	$\nu(C_{1}\text{-}C_{6})(10) +$ $\nu(C_{4}\text{-}C_{3})(14) +$ $\nu(O_{9}\text{-}C_{5})(24) +$ $\nu(O_{12}\text{-}C_{2})(24)$
A′	1275(m)		1313	1262	$\nu(C_{1}\text{-}C_{6})(20) +$ $\nu(C_{4}\text{-}C_{3})(20) +$ $\nu(C_{2}\text{-}C_{3})(22) +$ $\nu(C_{6}\text{-}C_{5})(21)$
A′	1214(vs)		1278	1229	$\beta(H_{13}\text{-}C_{3}\text{-}C_{2})(36) +$ $\beta(H_{14}\text{-}C_{6}\text{-}C_{1})(37)$
A′	1185(m)	1180(vw)	1245	1196	$\nu(O_{9}\text{-}C_{5})(15) +$ $\nu(O_{12}\text{-}C_{2})(15) +$ $\beta(C_{2}\text{-}C_{3}\text{-}C_{4})(12) +$ $\beta(H_{13}\text{-}C_{3}\text{-}C_{2})(11) +$ $\beta(H_{14}\text{-}C_{6}\text{-}C_{1})(17)$
A′			1206	1159	$\tau(H_{16}\text{-}C_{10}\text{-}O_{9}\text{-}C_{5})(17) +$ $\tau(H_{17}\text{-}C_{10}\text{-}O_{9}\text{-}C_{5})(17) +$ $\tau(H_{19}\text{-}C_{11}\text{-}O_{12}\text{-}C_{2})(17) +$ $\tau(H_{20}\text{-}C_{11}\text{-}O_{12}\text{-}C_{2})(17)$
A′			1202	1155	$\tau(H_{16}\text{-}C_{10}\text{-}O_{9}\text{-}C_{5})(16) +$ $\tau(H_{17}\text{-}C_{10}\text{-}O_{9}\text{-}C_{5})(16) +$ $\tau(H_{19}\text{-}C_{11}\text{-}O_{12}\text{-}C_{2})(16) +$ $\tau(H_{20}\text{-}C_{11}\text{-}O_{12}\text{-}C_{2})(16)$

Table 43.4 (continued)

Species	Experimental		Computational DFT B3LYP/6311++G (d,p)		Vibrational assignments PED (>10%)
	FT-IR	FT-Raman	Unscaled	Scaled	
A″			1169	1124	$\tau(H_{15}\text{-}C_{10}\text{-}O_9\text{-}C_5)(36) +$ $\tau(H_{16}\text{-}C_{10}\text{-}O_9\text{-}C_5)(10) +$ $\tau(H_{17}\text{-}C_{10}\text{-}O_9\text{-}C_5)(10)$
A″			1168	1123	$\tau(H_{18}\text{-}C_{11}\text{-}O_{12}\text{-}C_2)(36) +$ $\tau(H_{19}\text{-}C_{11}\text{-}O_{12}\text{-}C_2)(10) +$ $\tau(H_{20}\text{-}C_{11}\text{-}O_{12}\text{-}C_2)(10)$
A′	1064(s)		1089	1047	$\nu(O_9\text{-}C_{10})(16) +$ $\nu(O_{12}\text{-}C_{11})(16) +$ $\beta(H_{13}\text{-}C_3\text{-}C_2)(11) +$ $\beta(C_5\text{-}C_6\text{-}C_1)(10) +$ $\beta(C_5\text{-}C_4\text{-}C_3)(13)$
A′	1022(vs)	1033(vw)	1067	1026	$\nu(C_5\text{-}C_4)(10) +$ $\nu(O_9\text{-}C_{10})(33) +$ $\nu(O_{12}\text{-}C_{11})(33)$
A′			1046	1005	$\nu(O_9\text{-}C_{10})(22) +$ $\nu(O_{12}\text{-}C_{11})(22) +$ $\beta(C_5\text{-}C_6\text{-}C_1)(22)$
A′	861(s)	904(vw)	912	876	$\nu(C_5\text{-}C_6)(14) +$ $\beta(C_4\text{-}C_5\text{-}C_6)(15)$
A″			862	828	$\tau(H_{13}\text{-}C_1\text{-}C_2\text{-}C_3)(41) +$ $\tau(H_{14}\text{-}C_6\text{-}C_1\text{-}C_2)(42)$
A″			840	807	$\tau(H_{13}\text{-}C_3\text{-}C_2\text{-}C_1)(22) +$ $\tau(H_{14}\text{-}C_6\text{-}C_1\text{-}C_2)(21) +$ $\tau(C_4\text{-}C_5\text{-}C_6\text{-}C_1)(15) +$ $\tau(C_2\text{-}C_3\text{-}C_4\text{-}C_5)(16) +$ $\tau(C_6\text{-}C_5\text{-}C_4\text{-}C_3)(14)$
A′	760(s)		767	737	$\nu(O_9\text{-}C_5)(17) +$ $\nu(O_{12}\text{-}C_2)(17) +$ $\beta(C_2\text{-}C_3\text{-}C_4)(11)$
A″			710	682	$\tau(H_{13}\text{-}C_3\text{-}C_2\text{-}C_1)(22) +$ $\tau(H_{14}\text{-}C_6\text{-}C_1\text{-}C_2)(22) +$ $\gamma(O_{12}\text{-}C_3\text{-}C_1\text{-}C_2)(14) +$ $\gamma(O_9\text{-}C_4\text{-}C_6\text{-}C_5)(14)$
A'		679(s)	700	673	$\nu(C_5\text{-}C_4)(22) +$ $\beta(C_2\text{-}C_3\text{-}C_4)(11) +$ $\beta(C_5\text{-}C_4\text{-}C_3)(28)$

(continued)

Table 43.4 (continued)

Species	Experimental		Computational DFT B3LYP/6311++G (d,p)		Vibrational assignments PED (>10%)
	FT-IR	FT-Raman	Unscaled	Scaled	
A″	637(vw)		653	627	$\gamma(Br_8\text{-}C_6\text{-}C_2\text{-}C_1)(15) + \gamma(Br_7\text{-}C_3\text{-}C_5\text{-}C_4)(15) + \gamma(O_{12}\text{-}C_3\text{-}C_1\text{-}C_2)(29) + \gamma(O_9\text{-}C_4\text{-}C_6\text{-}C_5)(28)$
A′		607(vw)	620	596	$\beta(O_9\text{-}C_5\text{-}C_6)(26) + \beta(O_{12}\text{-}C_2\text{-}C_1)(18)$
A′	499(vw)		501	482	$\nu(Br_7\text{-}C_4)(10) + \nu(Br_8\text{-}C_1)(10) + \beta(O_{12} + C_2 + C_1)(11) + \beta(C_{10}\text{-}O_9\text{-}C_5)(17) + \beta(C_{11}\text{-}O_{12}\text{-}C_2)(17)$
A′		463(vw)	467	449	$\beta(C_4\text{-}C_3\text{-}C_2)(14) + \beta(C_4\text{-}C_5\text{-}C_6)(12)$
A″	441(w)		452	434	$\tau(H_{14}\text{-}C_6\text{-}C_1\text{-}C_2)(13) + \tau(C_4\text{-}C_5\text{-}C_6\text{-}C_1)(26) + \tau(C_5\text{-}C_4\text{-}C_3\text{-}C_2)(13) + \gamma(Br_8\text{-}C_6\text{-}C_2\text{-}C_1)(10) + \gamma(Br_7\text{-}C_3\text{-}C_5\text{-}C_4)(10)$
A″	393(vw)	388(w)	389	374	$\tau(C_5\text{-}C_4\text{-}C_3\text{-}C_2)(10) + \gamma(O_{12}\text{-}C_3\text{-}C_1\text{-}C_2)(23) + \gamma(O_9\text{-}C_4\text{-}C_6\text{-}C_5)(21)$
A′	350(w)		386	371	$\nu(Br_7\text{-}C_4)(24) + \nu(Br_8\text{-}C_1)(24) + \beta(C_{10}\text{-}O_9\text{-}C_5)(18) + \beta(C_{11}\text{-}O_{12}\text{-}C_2)(18)$
A′		300(vw)	302	290	$\beta(C_{10}\text{-}O_9\text{-}C_5)(25) + \beta(C_{11}\text{-}O_{12}\text{-}C_2)(25)$
A″			256	246	$\tau(H_{15}\text{-}C_{10}\text{-}O_9\text{-}C_5)(19) + \tau(H_{18}\text{-}C_{11}\text{-}O_{12}\text{-}C_2)(20) + \tau(H_{19}\text{-}C_{11}\text{-}O_{12}\text{-}C_2)(10) + \tau(H_{20}\text{-}C_{11}\text{-}O_{12}\text{-}C_2)(10)$
A″			255	245	$\tau(H_{15}\text{-}C_{10}\text{-}O_9\text{-}C_5)(10) + \gamma(Br_8\text{-}C_6\text{-}C_2\text{-}C_1)(19) + \gamma(Br_7\text{-}C_3\text{-}C_5\text{-}C_4)(19)$
A′		212(vw)	213	205	$\nu(Br_7\text{-}C_4)(32) + \nu(Br_8\text{-}C_1)(32) + \beta(C_5\text{-}C_6\text{-}C_1)(11)$

Table 43.4 (continued)

Species	Experimental		Computational DFT B3LYP/6311++G (d,p)		Vibrational assignments PED (>10%)
	FT-IR	FT-Raman	Unscaled	Scaled	
A″			200	192	$\tau(C_4\text{-}C_5\text{-}C_6\text{-}C_1)(15)$ + $\tau(C_5\text{-}C_4\text{-}C_3\text{-}C_2)(16)$ + $\gamma(Br_8\text{-}C_6\text{-}C_2\text{-}C_1)(15)$ + $\gamma(Br_7\text{-}C_3\text{-}C_5\text{-}C_4)(15)$
A′			175	168	$\beta(O_9\text{-}C_5\text{-}C_6)(28)$ + $\beta(O_{12}\text{-}C_2\text{-}C_1)(29)$ + $\beta(C_{10}\text{-}O_9\text{-}C_5)(10)$ + $\beta(C_{11}\text{-}O_{12}\text{-}C_2)(10)$ *Rocking*
A″			160	154	$\tau(C_2\text{-}C_3\text{-}C_4\text{-}C_5)(12)$ + $\tau(C_3\text{-}C_4\text{-}C_5\text{-}C_6)(16)$ + $\tau(C_{10}\text{-}O_9\text{-}C_5\text{-}C_4)(13)$ + $\tau(C_{11}\text{-}O_{12}\text{-}C_2\text{-}C_3)(16)$ + $\gamma(O_9\text{-}C_4\text{-}C_6\text{-}C_5)(14)$
A′			144	138	$\beta(Br_7\text{-}C_4\text{-}C_3)(43)$ + $\beta(Br_8\text{-}C_1\text{-}C_6)(43)$
A′			142	136	$\beta(Br_7\text{-}C_4\text{-}C_3)(22)$ + $\beta(Br_8\text{-}C_1\text{-}C_6)(22)$ + $\beta(C_5\text{-}C_6\text{-}C_1)(12)$ + $\beta(O_9\text{-}C_5\text{-}C_6)(11)$ + $\beta(O_{12}\text{-}C_2\text{-}C_1)(16)$ *Rocking*
A″			90	87	$\tau(C_{10}\text{-}O_9\text{-}C_5\text{-}C_4)(39)$ + $\tau(C_{11}\text{-}O_{12}\text{-}C_2\text{-}C_3)(36)$
A″			78	75	$\tau(C_3\text{-}C_4\text{-}C_5\text{-}C_6)(10)$ + $\tau(C_{10}\text{-}O_9\text{-}C_5\text{-}C_4)(25)$ + $\tau(C_{11}\text{-}O_{12}\text{-}C_2\text{-}C_3)(20)$ + $\gamma(Br_8\text{-}C_6\text{-}C_2\text{-}C_1)(13)$ + $\gamma(Br_7\text{-}C_3\text{-}C_5\text{-}C_4)(13)$
A″			48	46	$\tau(C_4\text{-}C_5\text{-}C_6\text{-}C_1)(15)$ + $\tau(C_5\text{-}C_4\text{-}C_3\text{-}C_2)(19)$ + $\tau(C_6\text{-}C_5\text{-}C_4\text{-}C_3)(34)$ + $\tau(C_{10}\text{-}O_9\text{-}C_5\text{-}C_4)(13)$ + $\tau(C_{11}\text{-}O_{12}\text{-}C_2\text{-}C_3)(12)$

Unit in cm^{-1}. *Abbreviations* ν—stretching, ν_s—symmetric stretching, ν_{as}—asymmetric stretching, γ—out of plane bending, β—in plane bending, τ—torsion, w—weak, vw—very weak, m—medium, s—strong, vs—very strong. Scale factor: 0.9613

43.4.3.1 Methoxy Group Vibrations

The methoxy group is electron donating and lone pair in oxygen increase electron density due to resonance effect in conjugated ring. This along with hydrogen bonding effects wave numbers corresponding to methoxy group and can shift the position of

bending and stretching modes of CH within methyl group [16]. The vibrations of the two methoxy groups involves the vibrations of the methyl groups. In symmetric stretching, all the three C–H bonds in methyl group stretch in phase and observed around 2920 ± 80 cm^{-1} [17]. In Table 43.4, the symmetric stretching of methyl group is observed at 2905 and 2844 cm^{-1} in the IR spectrum and 2844 cm^{-1} in the Raman spectrum. In the asymmetric methyl stretching, all the C–H do not stretch in phase and observed around 3020 ± 30 cm^{-1} [18, 19]. In Table 43.4, the asymmetric methyl stretching is observed at 3023 and 2945 cm^{-1} in the IR spectrum. The C-OCH$_3$ stretching is observed at 1293 cm^{-1} in the IR spectrum.

43.4.3.2   C–C Vibrations

The C–C stretching vibrations of the ring are observed in the region 1625–1430 cm^{-1} [20]. The carbon–carbon stretching vibrations for 1,4-DB-2,5-DMB are observed at 1594 and 1550 cm^{-1} in the Raman spectrum and at 1493 cm^{-1} in the IR spectrum which is in accordance with the literature [21]. The C–C stretching is also observed at 1358 cm^{-1} in the IR spectrum. The in-plane C–C bending mode is observed at 463 cm^{-1} in the Raman spectrum.

43.4.3.3   C–H Vibrations

The molecule 1,4-dibromo-2,5-dimethoxybenzene has two H atoms at third and sixth position of benzene ring. Thus there will be two C–H vibrational modes of each stretching, in-plane bending and out-of-plane bending [22]. The C–H stretching is usually observed from 3100 to 3000 cm^{-1}. This is not fingerprint region and thus these bands are not affected by substituent bromo and methoxy groups. The C–H vibrations are observed at 3099 and 3068 cm^{-1} in the IR spectra and at 3087 and 3069 cm^{-1} in the Raman spectrum as shown in Table 43.4. A very strong in-plane C-H bending mode for both H atoms is observed at 1214 cm^{-1} in the IR spectrum.

43.4.3.4   C–Br Vibrations

The molecule 1,4-dibromo-2,5-dimethoxybenzene has two Br atoms at first and fourth positions of benzene ring. The C–Br vibrations are influenced by other atoms and groups. According to the literature [17], the strong C–Br stretching modes are observed in the region 650–485 cm^{-1}. Mooney et al. [23, 24] observed that the C–halogen (Cl, Br, I) vibrations are obtained in the range 1129–480 cm^{-1}. The C–Br stretching is observed at 499 cm^{-1} in the IR spectrum. The in-plane C–Br bending mode for both Br atoms is not observed in experimental spectrum but observed at 136 cm^{-1} in DFT calculation. The out of plane bending C–Br vibrations are observed at 441 and 637 cm^{-1} in the IR spectrum.

43.4.4 Natural Bond Orbital (NBO)

Natural bond orbital study of the compound helps in understanding molecular wave function by providing insights on conjugative interaction, intra-molecular charge transfer interaction, bond order, Lewis acid/base interactions, etc. [25]. Second-order perturbation approach is used to find delocalizing interactions. Larger the value of E (2), larger will be the interaction between donor and acceptor electrons. In the present study, NBO analysis of 1,4-DB-2,5-DMB was carried out by density functional theory using 6-311++G(d,p) basis set. The interaction between the lone pair Br7, Br8, O9, C10, C11, O12 with anti-bonding orbital σ* is shown in Table 43.5. From the Table 43.5, it is observed that LP (2) O12 corresponding to the anti-bonding σ*(2) C1-C2 leads to strong delocalization with a stabilization energy value as 23.66 kJ/mol [26].

43.4.5 Thermodynamic Properties

The thermodynamic functions such as entropy, heat capacity and enthalpy can be computed along with the study of IR and Raman spectra of the molecules. The various thermodynamic functions of 1,4-dibromo-2,5-dimethoxybenzene were computed by DFT/B3LYP at 6-311++G(d, p) level from 100 to 1000 K temperature by taking a rigid rotor harmonic oscillator approximation for one mole of the perfect gas at one atmospheric pressure. Table 43.6 shows that the value of thermodynamic functions increases with rise in temperatures because as the temperature increases, the molecular vibrational intensities also increase [27]. Figure 43.4 shows a correlation plot corresponding to these thermodynamic functions at different temperatures [28]. The thermodynamic parameters (rotational constants, zero-point vibrational energy, thermal energy and dipole moment) of 1,4-DB-2,5-DMB at 298.15 K is listed in Table 43.7.

$$ddH = H(T) - H(0)\left[\text{enthalpy content(kJ mol}^{-1})\right]$$

43.4.6 Non-linear Optical Properties

The feasibility of a molecule for various applications can be obtained by non-linear optical studies [29, 30]. The DFT calculations are performed at B3LYP/6-311++G(d,p) basis set to obtain first order hyperpolarizability β_{total}, mean polarizability $\langle\alpha\rangle$ and anisotropy of the polarizability $\Delta\alpha$ for 1,4-DB-2,5-DMB. In the presence of external electric field F, the charge density and the energy of the molecular system will change. The field dependent energy E(F) can be expanded by Taylor

Table 43.5 Second order perturbation study of Fock matrix in NBO basis related to intra-molecular bonds of 1,4-DB-2,5-DMB

Donor NBO(i)	ED/e	Energy E(i)	Acceptor NBO(j)	Energy E(j)	E(2) kcal/mol	E(j)-E(i) (a.u.)	F(i,j) (a.u.)
σ (1) C1–Br8	1.98723	−0.72200	σ*(1) C2–C3	0.488	2.60	1.21	0.050
			σ*(1) C5–C6	0.488	2.20	1.21	0.046
σ (1) C2–O12	1.98937	−0.84829	σ*(1) C2–C1	0.49171	0.88	1.34	0.031
			σ*(1) C6–C1	0.49171	0.78	1.34	0.029
			σ*(1) C3–C4	0.49171	4.87	1.34	0.073
σ (1) C4–Br7	1.98723	−0.72201	σ*(1) C3–C2	0.48799	2.20	1.21	0.046
			σ*(1) C5–C6	0.48799	2.60	1.21	0.050
σ (1) C5–O9	1.98935	−0.84803	σ*(1) C1–C6	0.49197	4.87	1.34	0.073
			σ*(1) C4–C3	0.49197	0.78	1.34	0.029
			σ*(1) C4–C5	0.49197	0.87	1.34	0.031
σ (1) O9–C10	1.97990	−0.88191	σ*(1) C1–C6	0.48809	4.30	1.37	0.069
			σ*(1) C4–C5	0.49809	7.86	1.38	0.093
			σ*(1) C6–C10	0.30809	0.62	1.19	0.024
σ (1) C11–O12	1.97988	−0.88159	σ*(1) C1–C2	0.48841	7.87	1.37	0.093
			σ*(1) C4–C3	0.48841	4.30	1.37	0.069
			σ*(1) C3–C11	0.30841	0.62	1.19	0.024
LP (1) Br7	1.99479	−1.00273	σ*(1) C4–C3	0.48727	1.58	1.49	0.044
			σ*(1) C5–C4	0.49727	1.39	1.50	0.041
LP (2) Br7	1.96715	−0.33602	σ*(1) C4–C3	0.49398	3.95	0.83	0.051
			σ*(1) C5–C4	0.49398	4.24	0.83	0.053

(continued)

Table 43.5 (continued)

Donor NBO(i)	ED/e	Energy E(i)	Acceptor NBO(j)	Energy E(j)	E(2) kcal/mol	E(j)-E(i) (a.u.)	F(i,j) (a.u.)
LP (3) Br7	1.90423	−0.33568	σ*(2) C3–C4	−0.05568	13.22	0.28	0.060
LP (1) Br8	1.99479	−1.00271	σ*(1) C2–C1	0.49729	1.39	1.50	0.041
			σ*(1) C6–C1	0.48729	1.58	1.49	0.044
LP (2) Br8	1.96714	−0.33601	σ*(1) C2–C1	0.49399	4.24	0.83	0.053
			σ*(1) C6–C1	0.49399	3.95	0.83	0.051
LP (3) Br8	1.90426	−0.33567	σ*(2) C1–C2	−0.05567	13.48	0.28	0.059
LP (2) O9	1.73072	−0.37599	σ*(2) C5–C6	−0.03599	17.27	0.34	0.070
LP (1) C10	1.97483	−0.41118	σ*(1) C1–C6	0.48882	1.05	0.90	0.028
			σ*(1) C5–O9	0.17882	2.56	0.59	0.035
LP*(2) C10	0.29282	−0.12553	σ*(2) C2–C1	−0.05553	0.62	0.07	0.010
			σ*(2) C6–C5	−0.03553	20.32	0.09	0.065
LP (1) C11	1.97484	−0.41120	σ*(1) C2–O12	0.1788	2.55	0.59	0.035
			σ*(1) C3–C4	0.4888	1.05	0.90	0.028
LP (2) O12	1.73087	−0.37596	σ*(2) C1–C2	−0.05596	23.66	0.32	0.080

where E(2) is stabilization energy; E(j)-E(i) is Energy difference of donor(i) and acceptor (j) NBO orbitals; F(i,j) is Fock matrix element between orbitals of i and j NBO

series in the components of uniform electric field F and field free energy E (0) (i, j and k denote x, y and z components):

$$E(F) = E(0) - \sum_i \mu_i F_i - 1/2 \sum_i \sum_j \alpha_{ij} F_i F_j - 1/6 \sum_i \sum_j \sum_k \beta_{ijk} F_i F_j F_k + \cdots$$

where F_i is the field component in the i direction, μ_i, α_{ij} and β_{ijk} are the dipole moment, polarizability and the first order hyperpolarizability components, respectively. Kleinman symmetry reduces first order hyperpolarizability components from 27 to 10 [31]. The standard formula of the above-mentioned parameters in terms of

Table 43.6 Calculation of entropy(S), heat capacity (Cp) and enthalpy change (ddH) at different temperatures at B3LYP/6-311G++(d,p) level for 1,4-DB-2,5-DMB

T (K)	S (J/mol K)	Cp (J/mol K)	ddH (kJ/mol)
100	305.951	74.138	5.007
150	339.845	93.855	9.22
200	369.32	111.754	14.364
250	396.106	128.819	20.382
298.15	420.136	144.323	26.962
300	421.031	144.897	27.23
350	444.495	159.675	34.85
400	466.701	172.959	43.172
450	487.765	184.703	52.12
500	507.77	194.972	61.618
550	526.781	203.891	71.595
600	544.861	211.612	81.987
650	562.069	218.291	92.739
700	578.463	224.072	103.801
750	594.097	229.087	115.133
800	609.025	233.45	126.699
850	623.294	237.256	138.469
900	636.952	240.589	150.417
950	650.04	243.518	162.521
1000	662.598	246.102	174.763

where T—temperature (K), S—entropy (J mol^{-1} K^{-1}), Cp—heat capacity at constant pressure (kJ mol^{-1} K^{-1}).
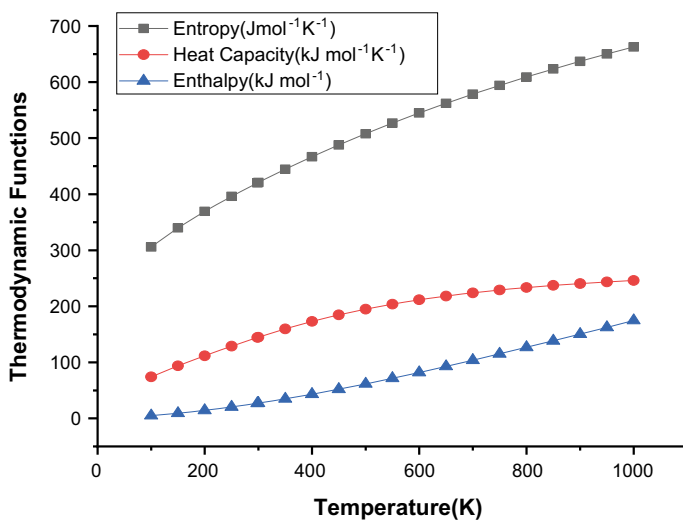
Fig. 43.4 Thermodynamic functions correlations graph for 1,4-DB-2,5-DMB

Table 43.7 Calculated thermodynamic parameters of 1,4 dibromo-2,5-dimethoxybenzene

Parameter	B3LYP 6311++G(d,p)
Zero-point vibrational energy (kJ/mol)	90.58010
Rotational constants (GHz)	0.78177
	0.26620
	0.19909
Thermal energy (kJ/mol)	
Total	98.503
Translational	0.889
Rotational	0.889
Vibrational	96.725
Specific heat (cal/mol^{-1} K^{-1})	
Total	44.243
Translational	2.981
Rotational	2.981
Vibrational	38.281
Entropy (cal/mol^{-1} K^{-1})	
Total	115.097
Translational	42.931
Rotational	33.317
Vibrational	38.848
Dipole moment (Debye)	
μ_x	−0.0003
μ_y	−0.0002
μ_z	0.0000
Total	0.0004

x, y, z components are given as:

$$\mu = \left(\mu_x + \mu_y + \mu_z\right)^{1/2}$$
$$\langle \alpha \rangle = \left(\alpha_{xx} + \alpha_{yy} + \alpha_{zz}\right)/3$$
$$\Delta\alpha$$
$$= \left\{1/2\left[\left(\alpha_{yy} - \alpha_{zz}\right)^2 + \left(\alpha_{xx} - \alpha_{yy}\right)^2 + \left(\alpha_{zz} - \alpha_{xx}\right)^2 + 6\alpha_{xz}^2 + 6\alpha_{yz}^2 + 6\alpha_{xy}^2\right]\right\}^{1/2}$$
$$\beta_{total} = \left[\left(\beta_{xxx} + \beta_{xyy} + \beta_{xzz}\right)^2 + \left(\beta_{yyy} + \beta_{xxy} + \beta_{yzz}\right)^2 + \left(\beta_{zzz} + \beta_{xxz} + \beta_{yyz}\right)^2\right]^{1/2}$$

The calculated polarizabilities α and hyperpolarizabilities β in atomic mass units (a.u.) for 1,4-DB-2,5-DMB is shown in Table 43.8. The component α_{yy} of polarizability has the maximum negative value while components α_{xz} and α_{yz} have zero values. All the calculated components of hyperpolarizability are negative except β_{yyy} and $\beta_{yzz.}$

Table 43.8 Non-linear optical parameters of 1,4-DB-2,5-DMB

Parameters	B3LYP/6-31++G (d, p)
Molecular polarizability (a.u)	
α_{xx}	−74.43
α_{xy}	−2.13
α_{yy}	−105.55
α_{xz}	0.00
α_{yz}	0.00
α_{zz}	−98.20
Mean polarizability <α>	−92.73
Anisotropic polarizability $\Delta\alpha$	28.41
Hyperpolarizability (a.u)	
β_{xxx}	−0.0048
β_{xxy}	−0.0061
β_{xyy}	−0.0038
β_{yyy}	0.0015
β_{xxz}	0.0000
β_{xyz}	0.0000
β_{yyz}	0.0000
β_{xzz}	−0.0001
β_{yzz}	0.0004
β_{zzz}	0.0000
β_x	−0.0087
β_y	−0.0042
β_z	0.0000
β_{Total}	0.0096

43.4.7   Mulliken Charge Distribution

Interpretation of atomic charges helps in understanding the reactive nature of molecules to be studied. Mulliken charge distribution of 1,4-DB-2,5-DMB having 20 atoms was studied using DFT/B3LYP method at 6311++G(d,p) level. Figure 43.5 shows the plot between Mulliken charge and atoms present. Figure 43.5 clearly shows that the carbon atoms C1 and C4 attached to Br and carbon atoms C10 and C11 attached to O in the benzene ring have negative charge, while atoms C3 and C6 have maximum positive charge. All the hydrogen present in the molecule are positively charged as hydrogen is an acceptor of electrons [32].
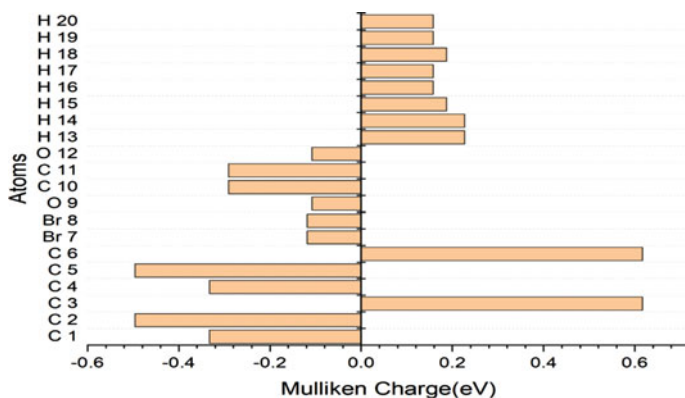
Fig. 43.5 Mulliken charge distribution of 1,4-DB-2,5-DMB

43.4.8 Molecular Electrostatic Potential and Surface Contour Map Analysis

Molecular behavior and interaction with each other along with three-dimensional charge distributions within the molecule can easily be understood by Molecular electrostatic potential (MEP) surfaces. Number of electrons can be derived on the basis of electrostatic potential. When the electrostatic potential is high it denotes relative lack in number of electrons and vice versa. The lowest electrostatic potential energy and highest electrostatic potential energy in its three-dimensional format is represented by red and blue colour respectively as shown in Fig. 43.6 and its corresponding two-dimensional contour map is depicted in Fig. 43.7. Increase in presence of number of electrons can be found in the area of low potential. However, absence in the number of electrons clearly represents areas of high potential [33, 34]. The DFT method at B3LYP/6-311++G(d,p) illustrates the theoretical electrostatic potential map. The extension of the positive and negative electrostatic potential around various groups gives the same conclusion about the nature of the intra-molecular charge transfer as found by the orientation of the molecular dipole moment [35].

43.4.9 Reduced Density Gradient (RDG) Analysis

Reduced density gradient along with non-covalent index (NCI) index helps in better understanding of non-covalent interactions occurring within a molecule. Using multi wave-functional analyser program multiwfn, RDG iso-surface have been obtained in Fig. 43.8 and interactive graphic display of the molecules can be viewed as a coloured scatter plot using VMD program as shown in Fig. 43.9 [13, 36, 37]. It is clear from the scatter graph that the blue colour indicates region of strong attraction while red colour depicts region of strong repulsion. It is clear from the figure that
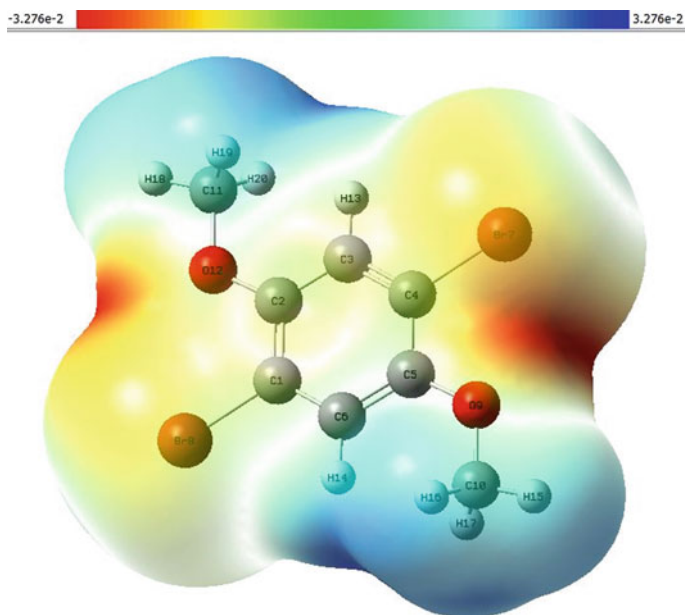
Fig. 43.6 Molecular electrostatic potential (MEP) surfaces in 3D computed at the B3LYP/6-311++G(d,p) level

the prominent RDG spike occurs showing repulsive interaction corresponding to the electron densities 0.0125 a.u and 0.0210 a.u.

43.5 Conclusion

The vibrational FT-IR and FT-Raman spectral study of 1,4-dibromo-2,5-dimethoxybenzene is an attempt to showcase the importance of benzene substituted molecules. The vibrational assignments along with PED for 1,4-dibromo-2,5-dimethoxybenzene has been discussed in detail. The structural parameters, Mulliken charge distribution, RDG analysis, NBO and non-linear optical properties along with thermodynamic parameters are determined and analyzed by DFT. The study of polarizability and hyperpolarizability shows that the molecule is a potential non-linear optical material.
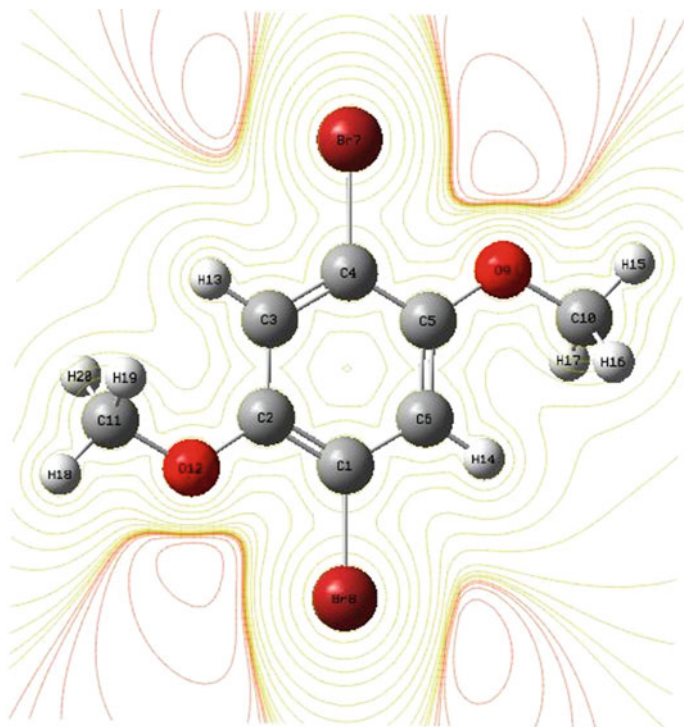
Fig. 43.7 MEP contour map representation of 1,4-DB-2,5-DMB in 2D

Fig. 43.8 RDG iso-surface of 1,4-DB-2,5-DMB
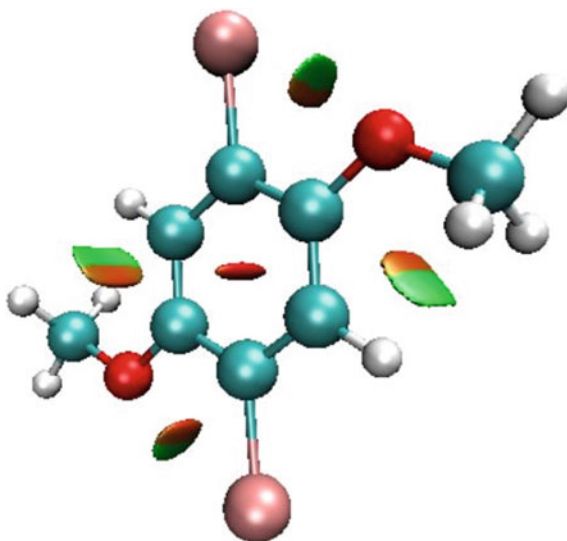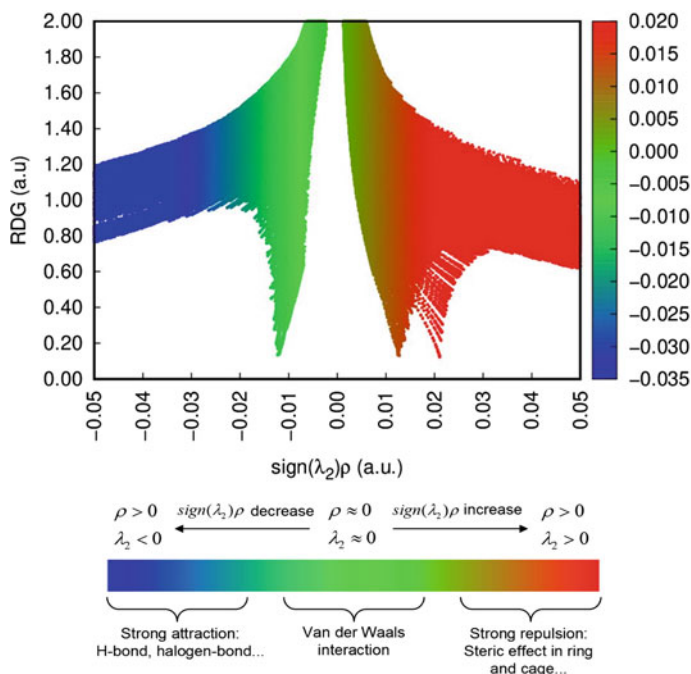
Fig. 43.9 Scatter graph for 1,4-DB-2,5-DMB molecule

References

1. Y. Liu, C. Tao, G. Xie, J. Van Der Velden, S. Marras, Z. Luo, X. Zeng, A. Petrozza, C. Yang, Dye. Pigment. **163**, 267 (2019)
2. M.H. Kim, M.J. Cho, K.H. Kim, M.H. Hoang, T.W. Lee, J. Il Jin, N.S. Kang, J.W. Yu, D.H. Choi, Org. Electron. **10**, 1429 (2009)
3. N.J. Hales, H. Heaney, J.H. Hollinshead, S.V. Ley, Tetrahedron **51**, 7755 (1995)
4. P. Poornesh, K. Ravi, G. Umesh, P.K. Hegde, M.G. Manjunatha, K.B. Manjunatha, A.V. Adhikari, Opt. Commun. **283**, 1519 (2010)
5. D. Mahadevan, S. Periandy, M. Karabacak, S. Ramalingam, Spectrochim. Acta Part A Mol. Biomol. Spectrosc. **82**, 481 (2011)
6. M. Govindarajan, M. Karabacak, V. Udayakumar, S. Periandy, Spectrochim. Acta Part A Mol. Biomol. Spectrosc. **88**, 37 (2012)
7. V.J. Eaton, D. Steele, J. Mol. Spectrosc. **48**, 446 (1973)
8. G. Raja, K. Saravanan, S. Sivakumar, Rasayan J. Chem. **8**, 37 (2015)
9. A.D. Becke, J. Chem. Phys. **98**, 5648 (1993)
10. C. Lee, W. Yang, R.G. Parr, Phys. Rev. B **37**, 785 (1998)
11. J.B. Foresman, M.J. Frisch, *Exploring Chemistry with Electronic Structure Methods* (Gaussian Inc., Pittsburgh, PA, 1996)
12. M.H. Jamróz, Spectrochim. Acta - Part A Mol. Biomol. Spectrosc. **114**, 220 (2013)
13. T. Lu, F. Chen, J. Comput. Chem. **33**, 580 (2012)
14. S. Jeyavijayan, M. Arivazhagan, Spectrochim. Acta Part A Mol. Biomol. Spectrosc. **81**, 466 (2011)
15. S. Jeyavijayan, M. Arivazhagan, Indian J. Pure Appl. Phys. **48**, 869 (2010)

16. M. N and J. Prabakar, J. Theor. Comput. Sci. **2**, 1 (2015)
17. V. Sortur, J. Yenagi, J. Tonannavar, V.B. Jadhav, M.V. Kulkarni, Spectrochim. Acta Part A **71**, 688 (2008)
18. A. Virdi, V.P. Gupta, A. Sharma, Cent. Eur. J. Chem. **2**, 456 (2004)
19. U. John, K.P.R. Nair, Spectrochim. Acta—Part A Mol. Biomol. Spectrosc. **60**, 2337 (2004)
20. V. Udayakumar, S. Periandy, M. Karabacak, S. Ramalingam, Spectrochim. Acta—Part A Mol. Biomol. Spectrosc. **83**, 575 (2011)
21. A. Altun, K. Gölcük, M. Kumru, J. Mol. Struct. Theochem. **637**, 155 (2003)
22. V. Krishnakumar, V. Balachandran, T. Chithambarathanu, Spectrochim. Acta—Part A Mol. Biomol. Spectrosc. **62**, 918 (2005)
23. E.F. Mooney, Spectrochim. Acta **19**, 877 (1963)
24. E.F. Mooney, Spectrochim. Acta **20**, 1021 (1964)
25. M. Khalid, M.A. Ullah, M. Adeel, M. Usman Khan, M.N. Tahir, A.A. C. Braga, J. Saudi Chem. Soc. **23**, 546 (2019)
26. S. Muthu, A. Prabhakaran, Spectrochim. Acta—Part A Mol. Biomol. Spectrosc. **129**, 184 (2014)
27. R. Zhang, B. Du, G. Sun, Y. Sun, Spectrochim. Acta—Part A Mol. Biomol. Spectrosc. **75**, 1115 (2010)
28. P. Govindasamy, S. Gunasekaran, Spectrochim. Acta—Part A Mol. Biomol. Spectrosc. **149**, 800 (2015)
29. Y. Shen, X. Li, J. Ye, Y. Qiu, Comput. Theor. Chem. **1163**, 112535 (2019)
30. R.T. Ulahannan, V. Kannan, V. Vidya, K. Sreekumar, J. Mol. Struct. **1199**, 127004 (2020)
31. D.A. Kleinman, Phys. Rev. **128**, 1761 (1962)
32. M. Elanthiraiyan, B. Jayasudha, M. Arivazhagan, Spectrochim. Acta Part A Mol. Biomol. Spectrosc. (2014)
33. M. Drissi, N. Benhalima, Y. Megrouss, R. Rachida, A. Chouaih, F. Hamzaoui, Molecules **20**, 4042 (2015)
34. E. Kose, A. Atac, F. Bardak, J. Mol. Struct. (2018)
35. C. Bheema Lingam, S.P. Tewari, Comput. Theor. Chem. **1020**, 151 (2013)
36. J. Priscilla, D. Arul Dhas, I. Hubert Joe, S. Balachandran, Chem. Phys. **536**, 110827 (2020)
37. W. Humphrey, A. Dalke, K. Schulten, J. Mol. Graph. (1996)

Chapter 44
Vibrational Spectral Studies, Thermodynamic Investigations and DFT (NLO, NBO, MEP) Computation of Benzene Derivative

Annu, B. S. Yadav, Jayant Teotia, Ravish Kumar Uppadhayay, Isha Rathi, and Vikas Kumar

Abstract The present work deals with combined experimental and theoretical analysis of 1,2,4,5-tetrachloro-3-nitrobenzene (TCNB). The FT-IR and FT Raman vibrational spectra of the said molecule is analysed in between 4000–400 cm^{-1} and 3500–100 cm^{-1}, respectively. The theoretical calculations have been performed by the help of Gaussian 09 program in which density functional theory is utilised to compute various parameters. These frequencies with appropriate basis sets are matched with experimental frequencies. The detailed vibrational assignments are carried out using VEDA program. The density functional theory (DFT) calculations of TCNB are performed to calculate thermodynamic functions and polarisabilities. The molecular electrostatic potential (MEP) surfaces have also been computed. Natural Bond Orbital (NBO) analysis is done using DFT to check the steadiness of TCNB compound. Reduced density gradient (RDG) analysis is carried out for the iso-surface of the molecule.

44.1 Introduction

Since time immemorial, benzene and its derivatives have ruled the chemical industry. Nitrobenzene derivatives are important sources for various nucleophilic and electrophilic ring substitution reactions. Substituted nitrobenzene derivatives have found its widespread use in the field of pharmaceutical companies. Chloronitrobenzenes are used as an intermediate in various reduction reactions and in the manufacturing of antioxidants, colorants, rubber chemicals, dyes, herbicide, insecticide and oil additives. Dapsone, a drug used for leprosy and malaria treatment, is obtained from 4-chloronitrobenzene. Nitrochlorobenzenes have toxic effects as it causes skin allergies and lowers Hb level of blood. Benzene derivatives are said to have hazardous effect on the environment. Terrachlor, a fungicide, is obtained by chlorination of chloronitrobenzene and has found its use in agrochemical industry [1–4]**.** Due to the versatile

Annu (✉) · B. S. Yadav · J. Teotia · R. K. Uppadhayay · I. Rathi · V. Kumar
Molecular Spectroscopy and Biophysics Laboratory, Deva Nagri College, Meerut, Uttar Pradesh 250002, India
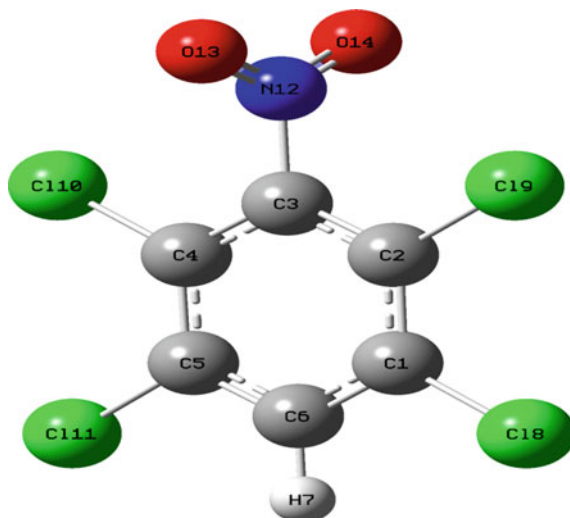
nature of nitrobenzene, the current work deals with the examination of FT-IR and
FT-Raman spectra of TCNB. The geometrical structure of TCNB molecule is shown
in the Fig. 44.1. The experimental and DFT computed IR and Raman spectrum are
compared in this study. The optimized ground state geometries are obtained by DFT
calculations using B3LYP/ccpvdz and 6-311G++(d, p) basis sets. Parr and Becke's
three parameter exact exchange-functional (B3) has been used for DFT calculations
as they predict best results [5, 6].

44.2 Experimental Details

TCNB compound sample was obtained online from Merck India. Using KBr pellets,
the infra-red spectrum of the TCNB molecule is observed with the help of the
PerkinElmer Spectrum 3 FT-IR spectrometer within range of 4000–400 cm^{-1}. The
FT-Raman spectra of TCNB is recorded on BRUKER IFS from 3500 to 100 cm^{-1}.

44.3 Computational Details

Using GAUSSIAN 09 software, DFT calculations have been carried out for TCNB
[7] and the corresponding vibrational assignments are studied using VEDA program
and Gauss view 6 [8]. To match computational and experimental frequencies, scaling
factor of 0.9613 has been used. With the help of DFT, the structure is optimized at two
different B3LYP levels. The variation of thermodynamic functions with temperature,

different kinds of polarizabilities of TCNB are evaluated using DFT. Molecular electrostatic potential (MEP) surfaces showing contour have also been also computed. Natural Bond Orbital interpretation is done using DFT to check the steadiness of the molecule. Reduced density gradient (RDG) analysis is carried out using multiwfn program to study non covalent interaction [9].

44.4   Result and Discussion

44.4.1   Molecular Geometry

The geometrical parameters such as bond length and bond angle of the titled molecule, employing B3LYP levels and using ccpvdz and 6-311++ G (d,p) basis sets are shown in Table 44.1 and are optimized using density functional theory. The measured

Table 44.1   Computed bond length and bond angle of TCNB using B3LYP levels

Bond length (Å)	B3LYP/ccpvdz	B3LYP/6-311G++	Bond angle	B3LYP/ccpvdz	B3LYP/6-311G++
Cl8-C1	1.739	1.739	C3-C2-C1	118.0	118.0
C2-C1	1.403	1.400	C6-C1-C2	120.2	120.2
C6-C1	1.394	1.390	Cl8-C1-C2	121.1	121.1
C2-Cl9	1.732	1.732	C6-C1-Cl8	118.7	118.7
C3-C2	1.397	1.393	Cl9-C2-C1	121.8	121.8
N12-C3	1.484	1.488	H7-C6-C1	119.6	119.6
C4-C3	1.397	1.393	C1-C6-C5	120.8	120.8
Cl10-C4	1.732	1.732	C4-C3-C2	122.8	122.8
Cl11-C5	1.739	1.739	N12-C3-C4	118.6	118.6
C5-C4	1.403	1.400	C3-C2-Cl9	120.2	120.2
C6-C5	1.394	1.390	N12-C3-C2	118.6	118.6
C6-H7	1.083	1.081	C5-C4-C3	118.0	118.0
N12-O13	1.225	1.217	Cl10-C4-C3	120.2	120.2
N12-O14	1.225	1.217	C3-N12-O13	116.6	116.6
			C3-N12-O14	116.6	116.6
			Cl10-C4-C5	121.8	121.8
			C6-C5-C4	120.2	120.2
			Cl11-C5-C4	121.1	121.1
			Cl11-C5-C6	118.7	118.7
			H7-C6-C5	119.6	119.6
			C13-N12-O14	126.8	126.9

amount of bond angles and bond lengths are almost equal for both the basis sets. The molecular structure of TCNB can be drawn using GAUSSIAN 09 W [7]. The NO_2 group and Cl atoms are electronegative in nature, which results in resonance structure and accumulation of electronic charge at this site. The bond lengths of both N–O are equal in the nitro group and found to be 1.225 and 1.217 Å using B3LYP/ccpvdz and B3LYP/6-311++G (d,p) methods respectively. The electron density at the ring carbon atoms decreases by substitution of electronegative chlorine atoms. For both the basis sets, the bond length of C–Cl ranges from 1.732 to 1.739 Å. The C–Cl bond lengths (C4-Cl10 and C2-Cl9) near the nitro group are shorter than the other two which are farther from nitro group. Table 44.1, clearly implies that the bond length of C–H is 1.083 Å at B3LYP/ccpvdz and 1.081 Å at B3LYP/6-311++G (d,p). The C–C bond length vary in between 1.394 and 1.403 Å at B3LYP/ccpvdz basis set and within 1.389–1.399 Å at B3LYP/6-311++G (d,p) basis set. The bond angles C3-C4-Cl10 and C3-C2-Cl9 are 120.20° in both basis sets and bond angles C6-C5-Cl11 and C6-C1-Cl18 are 118.70° in both basis sets. C3-C4-Cl10 and C3-C2-Cl9 have greater bond angles as compared to C6-C5-Cl11 and C6-C1-Cl18 due to vicinity of nitro group.

44.4.2   Normal Coordinate Analysis

The vibrational mode of a compound along with their frequencies and the normal coordinate can be easily calculated and described at length using normal coordinate analysis. The position of the atoms from the origin of the molecule is described by standard internal coordinates. Here 49 coordinates having thirteen redundancies for TCNB is defined as shown in Table 44.2. The linear combinations of the internal coordinates gives local symmetry coordinates which are shown in Table 44.3 [10].

44.4.3   Vibrational Interpretation

The experimental and theoretical FTIR and Raman spectra of TCNB have been illustrated in Figs. 44.2 and 44.3 respectively. The experimental and computational vibrational assignments of TCNB can be seen in Table 44.4. The Raman and IR spectra for most of the modes are complimentary to each other. With the help of suitable scaling factor, it can be seen that the experimental and the computed frequencies are in accordance with each other. Using PED for different intensities, the frequency shifts of the bands of TCNB molecule have been analysed. This has been done by the help of Gaussview 6 and VEDA program [11].

Table 44.2 Internal coordinates of TCNB

Number	Symbol	Type	Definition
Stretching			
1–6	r_i	C–C	C1-C2,C1-C6,C2-C3,C3-C4,C4-C5,C5-C6
7	Q_i	C–H	C6-H7
8–11	P_i	C–Cl	C4-Cl10,C5-Cl11,C1-Cl8,C2-Cl9
12	q_i	C–N	C3-N12
13–14	R_i	N=O	N12-O13,N12-O14
Bending			
15–20	β_i	B ring	C2-C1-C6,C1-C6-C5,C6-C5-C4,C5-C4-C3,C4-C3-C2, C3-C2-C1
21–22	α_i	C–C–H	H7-C6-C1, H7-C6-C5
23–30	ρ_i	C–C–Cl	C6-C1-Cl8,Cl11-C5-C6,C2-C1-Cl8,C1-C2-Cl9, Cl9-C2-C3,Cl10-C4-C3, Cl10-C4-C5, Cl11-C4-C5
31–32	ω_i	C–N=O	O14-N12-C3, O13-N12-C3
33	λ_i	O–N–O	O13-N12-O14
34–35	σ_i	C–C–N	N12-C3-C2, N12-C3-C4
Out of plane bending			
36	π_i	C–H	H7-C6-C5-C1
37–40	θ_i	C–Cl	Cl10-C4-C5-C3,Cl11-C5-C4-C6,Cl8-C1-C2-C6,Cl9-C2-C3-C1
41	δ_i	N–O	C3-N12-O13-O14
42	γ_i	C–N	N12-C3-C2-C4
Torsion			
43–48	T_i	t ring	C3-C2-C1-C6,C2-C1-C6-C5,C1-C6-C5-C4,C6-C5-C4-C3,C5-C4-C3-C2,C4-C3-C2-C1
49	T_i	tNO$_2$	C4(C2)-C3-N12-O13(O14)

Table 44.3 Local symmetry coordinates of TCNB molecule

Number	Representation	Definition
1–6	CC	$r_1, r_2, r_3, r_4, r_5, r_6$
7	CH	Q_7
8–11	CCl	P_8, P_9, P_{10}, P_{11}
12	CN	q_{12}
13–14	NO	R_{13}, R_{14}
15	B ring	$(\beta_{15}-\beta_{16}-\beta_{17}-\beta_{18} + \beta_{19}-\beta_{20})/\sqrt{6}$
16	B ring	$(-\beta_{15}-\beta_{16} + 2\beta_{17}- \beta_{18} -\beta_{19} + 2\beta_{20})/\sqrt{12}$
17	B ring	$(\beta_{15}-\beta_{16} + \beta_{18}-\beta_{19})/2$
18	Bch	$(\alpha_{21}-\alpha_{22})/\sqrt{2}$
19–22	BCCl	$(\rho_{23}-\rho_{24})/\sqrt{2}, (\rho_{25}-\rho_{26})/\sqrt{2}, (\rho_{27}-\rho_{28})/\sqrt{2}, (\rho_{29}-\rho_{30})/\sqrt{2}$
23	CNO_2 bending	$(\sigma_{34}-\sigma_{35})/\sqrt{2}$
24	NO_2 rocking	$(\omega_{31}- \omega_{32})/\sqrt{2}$
25	NO_2 scissoring	$(2\lambda_{33}- \omega_{31}- \omega_{32})/\sqrt{6}$
26	π CH	π_{36}
27–30	θ CCl	$\theta_{37}, \theta_{38}, \theta_{39}, \theta_{40}$
31	CNO_2 oopb	δ_{41}
32	NO_2 oopb	γ_{42}
33	τ ring	$(T_{43}-T_{44} + T_{45}-T_{46} + T_{47}-T_{48})/\sqrt{6}$
34	τ ring	$(T_{43}-T_{45} + T_{46}-T_{48})/2$
35	τ ring	$(-T_{43} + 2T_{44}-T_{45}-T_{46} + 2T_{47}-T_{48})/\sqrt{12}$
36	τ NO_2	T_{49}

Oopb—Out of plane bending

44.4.3.1 C–H Vibrations

In substituted benzenes, the vibrations for in plane bending and out of plane bending can be seen within range of 1290–990 cm^{-1} and 990–740 cm^{-1} respectively [12–17]. All values are in sync with the computed data. The Raman counterpart of C–H stretching is seen at 3076 cm^{-1} and at 3123 cm^{-1} in the IR spectrum which is in accordance with the theoretically computed values.

44.4.3.2 C–C Vibrations

The C–C stretching vibrations in vibrational spectra are observed in between 1599 and 1399 cm^{-1}. The C–C stretching of TCNB corresponding to FT-IR and FT-Raman spectrum are observed at 1213 and 1473 cm^{-1} and 1300, 1368 and 1571 cm^{-1} respectively. The FT-IR and FT-Raman ring in plane bending modes are observed at
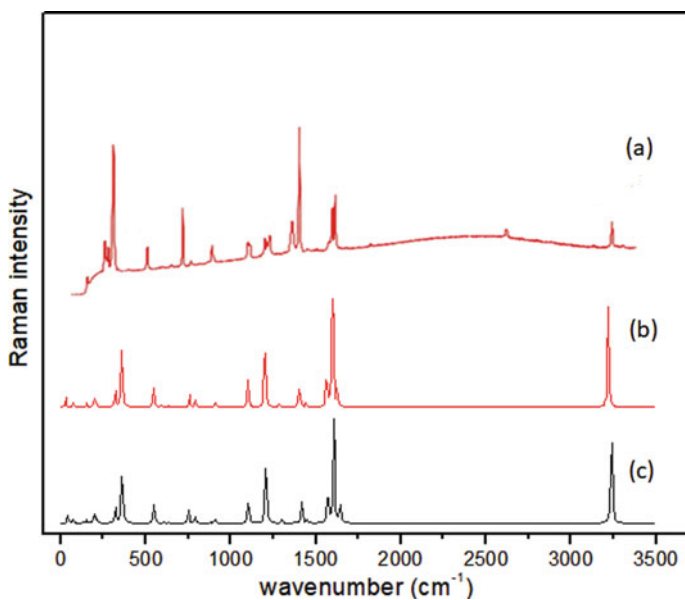
Fig. 44.2 Vibrational Raman spectra of TCNB **(a)** experimental, **(b)** theoretically computed at B3LYP/ ccpvdz, **(c)** theoretically computed at B3LYP/6-311++G(d,p)
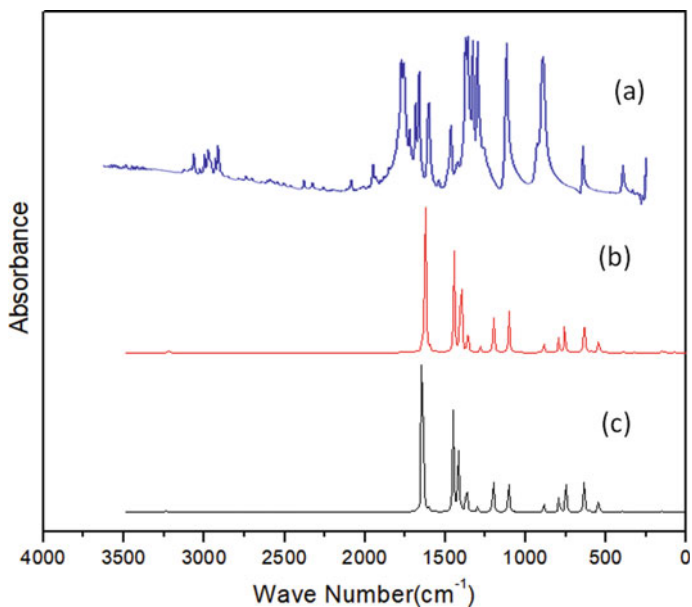
Fig. 44.3 FT-IR spectra of TCNB **(a)** experimental, **(b)** theoretically computed at B3LYP/ccpvdz, **(c)** theoretically computed at B3LYP/6-311++G(d,p)

Table 44.4 Probable vibrational assignments of TCNB computed theoretically and experimentally

Observed		Theoretical (DFT/B3LYP) ccpvdz 6-311++G(d,p)				Probable vibrational assignments (>10%)
FT-IR	FT-RAMAN	Unscaled	Scaled	Unscaled	Scaled	
3676(w)						O/C
3173(w)						O/C
3133(w)						O/C
3123(w)	3076(m)	3238	3112	3219	3093	νC_6-$H_7(100)$
3081(w)						O/C
3027(w)						O/C
2971(w)						O/C
1623(vw)						O/C
1599(w)	1568(s)	1643	1579	1626	1563	$\nu_{as}O_{13}$-$N_{12}(50) +$ $\nu_{as}O_{14}$-$N_{12}(50)$
1535(vs)	1547(m)	1605	1543	1597	1534	$\nu_{as}C_1$-$C_6(26) +$ $\nu_{as}C_3$-$C_2(22) +$ $\nu_{as}C_4$-$C_3(16) +$ $\nu_{as}C_6$-C_5 (19)
1524(vs)	1473(w)	1571	1510	1564	1503	νC_5-$C_4(41) +$ βC_1-C_6-$C_5(14) +$ βC_4-C_3-$C_2(16)$
1498(m)						O/C
1470(s)						O/C
1458(m)						O/C
1451(s)	1415(w)					O/C
1406(s)	1375(vs)	1449	1392	1443	1387	βH_7-C_6-$C_1(34) +$ βC_5-C_4-$C_3(18)$
1355(vw)	1337(m)	1416	1361	1403	1348	$\nu_s O_{13}$-$N_{12}(39) +$ $\nu_s O_{14}$-$N_{12}(39) +$ βO_{14}-N_{12}-$O_{13}(13)$
1298(m)		1368	1315	1362	1309	νC_1-$C_6(17) +$ νC_3-$C_2(20) +$ νC_4-$C_3(22) +$ νC_6-$C_5(15)$
1266(w)						O/C
1226(vs)	1213(m)	1300	1249	1282	1232	νC_1-$C_6(26) +$ νC_3-$C_2(21) +$ νC_4-$C_3(21) +$ νC_6-$C_5(26)$
1215(vs)						O/C
1190(vs)						O/C

<div align="right">(continued)</div>

Table 44.4   (continued)

Observed		Theoretical (DFT/B3LYP) ccpvdz 6-311++G(d,p)				Probable vibrational assignments (>10%)
FT-IR	FT-RAMAN	Unscaled	Scaled	Unscaled	Scaled	
1168(vs)	1193(w)	1207	1160	1201	1154	νC_6-C_5(16) + νC_5-C_4(23) **_Ring breathing_**
1138(w)		1199	1152	1195	1149	βH_7-C_6-C_1(58)
1026(vs)	1097(w)	1102	1059	1100	1057	νCl_9-C_2(10) + νCl_{10}-C_4(10) + βC_1-C_6-C_5(20) + βC_4-C_3-C_2(36)
880(w)	900(w)	908	872	910	875	νN_{12}-C_3(25) + βO_{14}-N_{12}-O_{13}(33)
858(vs)		884	850	884	850	τH_7-C_6-C_1-C_2(77) + τC_1-C_6-C_5-C_4(11)
849(vs)		881	846	877	843	νCl_9-C_2(17) + νCl_{10}-C_4(17) + νCl_8-C_1(19) + νCl_{11}-C_5(19) + βC_6-C_5-C_4(10)
	792(w)	790	759	792	761	βN_{12}-C_3-C_4(22) + γO_{14}-C_3-O_{13}-N_{12}(48)
	741(m)	749	720	756	727	νC_5-C_4(12) + βO_{14}-N_{12}-O_{13}(38)
662(m)	688(vw)	723	695	686	660	βO_{13}-N_{12}-C_3(32) + τC_5-C_4-C_3-C_2(10) + γN_{12}-C_2-C_4-C_3(35)
	637(vw)	634	610	633	609	νCl_9-C_2(18) + νCl_{10}-C_4(18) + νCl_8-C_1(16) + νCl_{11}-C_5(16) + γO_{14}-C_3-O_{13}-N_{12}(15)
		604	581	591	568	βO_{13}-N_{12}-C_3(12) + τH_7-C_6-C_1-C_2(16) + τC_1-C_6-C_5-C_4(28) + τC_6-C_5-C_4-C_3(10) + γCl_8-C_2-C_6-C_1(11) + γCl_{11}-C_4-C_6-C_5(11)
	546(w)	600	577	579	556	γCl_8-C_2-C_6-C_1(25) + γCl_{11}-C_4-C_6-C_5(25) + γCl_{10}-C_3-C_5-C_4(18) + γCl_9-C_3-C_1-C_2(18)
		547	526	545	524	νCl_9-C_2(16) + νCl_{10}-C_4(16)

(continued)

Table 44.4 (continued)

Observed		Theoretical (DFT/B3LYP) ccpvdz 6-311++G(d,p)				Probable vibrational assignments (>10%)
FT-IR	FT-RAMAN	Unscaled	Scaled	Unscaled	Scaled	
		524	504	523	503	βCl_9-C_2-C_1(19) + βCl_{10}-C_4-C_5(19) + βCl_8-C_1-C_6(20) + βCl_{11}-C_5-C_6(20) + γO_{14}-C_3-O_{13}-N_{12}(15) ***Ring rocking***
466(w)	451(vw)					O/C
418(vw)						O/C
378(vw)	363(vs)	400	384	395	379	βO_{13}-N_{12}-C_3(37) + τC_5-C_4-C_3-C_2(14) + γCl_{10}-C_3-C_5-C_4(17) + γCl_9-C_3-C_1-C_2(17)
350(w)	347(w)	360	346	359	345	νCl_8-C_1(16) + νCl_{11}-C_5(16) + βC_1-C_6-C_5(16) ***Ring breathing***
	328(w)	339	326	332	319	γCl_8-C_2-C_6-C_1(22) + γCl_{11}-C_4-C_6-C_5(22) + γCl_{10}-C_3-C_5-C_4(27) + γCl_9-C_3-C_1-C_2(27)
		325	312	324	311	νN_{12}-C_3(27) + βC_4-C_3-C_2(29)
		319	306	319	306	νCl_9-C_2(11) + νCl_{10}-C_4(11) + νCl_8-C_1(13) + νCl_{11}-C_5(13) + βC_6-C_5-C_4(20) + βC_5-C_4-C_3(18)
	220(vw)	213	204	212	204	βCl_9-C_2-C_1(25) + βCl_{10}-C_4-C_5(25) + βCl_8-C_1-C_6(20) + βCl_{11}-C_5-C_6(20)
		212	204	208	200	βO_{13}-N_{12}-C_3(11) + τC_1-C_6-C_5-C_4(15) + γCl_8-C_2-C_6-C_1(14) + γCl_{11}-C_4-C_6-C_5(14) + γCl_{10}-C_3-C_5-C_4(10) + γCl_9-C_3-C_1-C_2(10) + γN_{12}-C_2-C_4-C_3(14)
		200	192	199	192	βCl_9-C_2-C_1(37) + βCl_{10}-C_4-C_5(37)

Table 44.4 (continued)

Observed		Theoretical (DFT/B3LYP) ccpvdz 6-311++G(d,p)				Probable vibrational assignments (>10%)
FT-IR	FT-RAMAN	Unscaled	Scaled	Unscaled	Scaled	
		195	187	194	187	$\beta C_1\text{-}C_6\text{-}C_5(10) +$ $\beta Cl_8\text{-}C_1\text{-}C_6(40) +$ $\beta Cl_{11}\text{-}C_5\text{-}C_6(40)$
		154	148	153	147	$\beta N_{12}\text{-}C_3\text{-}C_4(65) +$ $\gamma O_{14}\text{-}C_3\text{-}O_{13}\text{-}N_{12}(17)$
		131	126	129	124	$\tau C_1\text{-}C_6\text{-}C_5\text{-}C_4(11) +$ $\gamma Cl_8\text{-}C_2\text{-}C_6\text{-}C_1(20) +$ $\gamma Cl_{11}\text{-}C_4\text{-}C_6\text{-}C_5(20) +$ $\gamma Cl_{10}\text{-}C_3\text{-}C_5\text{-}C_4(15) +$ $\gamma Cl_9\text{-}C_3\text{-}C_1\text{-}C_2(15) +$ $\gamma N_{12}\text{-}C_2\text{-}C_4\text{-}C_3(15)$
		72	69	71	69	$\tau C_5\text{-}C_4\text{-}C_3\text{-}C_2(42) +$ $\gamma N_{12}\text{-}C_2\text{-}C_4\text{-}C_3(30)$
		69	67	69	66	$\tau C_1\text{-}C_6\text{-}C_5\text{-}C_4(17) +$ $\tau C_6\text{-}C_5\text{-}C_4\text{-}C_3(56) +$ $\tau C_5\text{-}C_4\text{-}C_3\text{-}C_2(18)$
		40	38	29	28	$\tau O_{13}\text{-}N_{12}\text{-}C_3\text{-}C_2(98)$

Unit in cm^{-1} Abbreviations ν—stretching, ν_{as}—asymmetric stretching, ν_s—symmetric stretching, β—in plane bending, γ—out of plane bending, τ—torsion, vs—very strong, s—strong, m—medium, w—weak, vw—very weak, O/C—Overtone/combination. Scale factor: 0.9613

849 and 1097 cm^{-1} respectively as shown in Table 44.4. The theoretical computed C–C vibrational modes by B3LYP/6-311++G (d,p) matches with observed data.

44.4.3.3 C–N Vibrations

In this study, the C–N stretching modes of TCNB can be seen at 880 cm^{-1} in FT-IR and 900 cm^{-1} in Raman spectrum. The assignments of C–N in-plane bending vibrations for Raman spectrum are seen at 154 and 792 cm^{-1} and vibrations corresponding to out-of-plane bending are visualized at 72 and 212 cm^{-1} [15].

44.4.3.4 C–Cl Vibrations

The impact of the C–Cl vibrations is significant and lowers the molecular symmetry as chlorine molecules are heavier and electronegative [18–21]. The vibrations corresponding to C–Cl stretching have greater strength within 745–575 cm^{-1} range[22–31]. The vibrations for C–Cl stretching can be seen within 350, 849 and 1026 cm^{-1} in the FT-IR band and at 347, 637 and 1097 cm^{-1} in the Raman band of TCNB. The corresponding in plane bending is observed at 220 cm^{-1} in the Raman spectra.

C–Cl out-of-plane bending vibration can be seen at 378 cm^{-1} in the IR spectrum and at 328, 363 and 546 in the Raman spectrum which is in agreement with the literature [26]. Thus the experimental values matches with the theoretical DFT computed frequencies.

44.4.3.5 NO$_2$ Vibrations

Due to the placement of NO$_2$ group in TCNB, the asymmetric stretching can be seen in between 1565 and 1490 cm^{-1} and symmetric NO$_2$ vibrations at 1370–1300 cm^{-1} which clearly shows that the asymmetric stretching values are greater as compared to symmetric ones [17, 18]. In TCNB the mode for asymmetric stretching of NO$_2$ can be observed within range of 1568 and 1599 cm^{-1} in the FT-IR spectrum whereas in the Raman spectrum the values can be seen in between 1337 and 1355 cm^{-1} which is in accordance with computed data. The symmetric stretching of NO$_2$ group for the compound is assigned at 1355 and 1337 cm^{-1} in the FT-IR and FT-Raman spectrum respectively. The nitro in plane bending modes for IR spectrum can be seen at 378, 662 and 880 cm^{-1} while for the Raman spectrum these values are observed at 363, 688, 741 and 990 cm^{-1}. Thus these deformation vibrations matches with the literature [18, 19].

44.4.4 Thermodynamic Parameters

Several thermodynamic parameters along with the minimum energy of TCNB were obtained by DFT using ccpvdz and 6-311++G(d,p) sets as shown in Table 44.5. Temperature plays an important role in understanding the thermodynamic functions. Table 44.6 clearly shows that with rise in temperature, the thermodynamic parameters increases because with rise in temperature the vibrational intensities of the molecule also increases and is illustrated in Fig. 44.4 [27, 28]. where

Cp is the heat capacity in kJ mol^{-1}K^{-1} at constant pressure.
S is entropy in J mol^{-1}K^{-1}.
ddH = H(T) − H(0) in kJ mol^{-1}.
T is temperature in Kelvin.

44.4.5 Natural Bond Orbital Analysis

The inter-linkage in between donor Lewis-type and acceptor non-Lewis natural bond orbitals is observed while analysing natural bond orbitals. Second-order perturbation approach is used to find delocalizing interactions. The large value of E(2) shows the greater extent of interaction occurring for electron acceptor and electron donor. NBO analysis at the B3LYP/6-311++G(d,p) level has been performed on TCNB

Table 44.5 Calculated thermodynamic parameters of TCNB

Parameter	B3LYP/ccpvdz	B3LYP/6-311++G(d,p)
Zero-point vibrational energy (kJ/mol)	39.988	39.688
Rotational constants (GHz)	0.575	0.576
	0.447	0.449
	0.262	0.262
Thermal energy (kJ/mol)		
Total	47.536	47.294
Translational	0.90	0.90
Rotational	0.90	0.90
Vibrational	46.0	45.517
Specific heat (cal/mol^{-1} K^{-1})		
Total	41.297	45.517
Translational	2.981	2.981
Rotational	2.981	2.981
Vibrational	35.335	35.551
Entropy (cal/mol^{-1} K^{-1})		
Total	112.640	113.623
Translational	42.553	42.553
Rotational	32.833	32.825
Vibrational	37.254	38.244
Dipole moment (Debye)		
μ_x	0.0000	0.0000
μ_y	−3.5431	−3.5470
μ_z	0.0000	0.0000
Total	3.5431	3.5470

that helps in studying the intramolecular rehybridization and shows how the electron density is delocalized in TCNB. The interaction between the lone pair Cl8, Cl9, Cl10, Cl11, O13 and O14 with antibonding orbital σ* is shown in Table 44.7 which clearly implies that LP(3)O13 corresponding to the antibonding σ*(N12–O14) leads to strong delocalizing with stabilization energy175.14 kJ/mol [29].

44.4.6 Molecular Polarizability Calculation

Using finite field approach, the non-linear optical (NLO) properties such as the anisotropic polarizability and the mean polarizability of TCNB can be determined by analysing the IR and Raman vibrational modes and using B3LYP/ccpvdz and B3LYP/6-311++G(d,p) basis sets, as shown in Table 44.8. The larger is the value

Table 44.6 Variation of thermodynamic functions at different temperature for TCNB

T (K)	S (J/mol.K)	Cp (J/mol.K)	ddH (kJ/mol)
100	325.857	93.419	6.109
150	368.971	120.244	11.471
200	406.786	143.245	18.071
250	440.979	163.59	25.752
298.15	471.319	181.113	34.058
300	472.441	181.749	34.394
350	501.7	197.961	43.894
400	529.093	212.36	54.16
450	554.855	225.064	65.102
500	579.158	236.21	76.64
550	602.138	245.953	88.7
600	623.912	254.46	101.215
650	644.58	261.889	114.128
700	664.231	268.389	127.388
750	682.947	274.091	140.953
800	700.8	279.111	154.786
850	717.857	283.544	168.854
900	734.177	287.475	183.132
950	749.816	290.973	197.595
1000	764.821	294.097	212.223
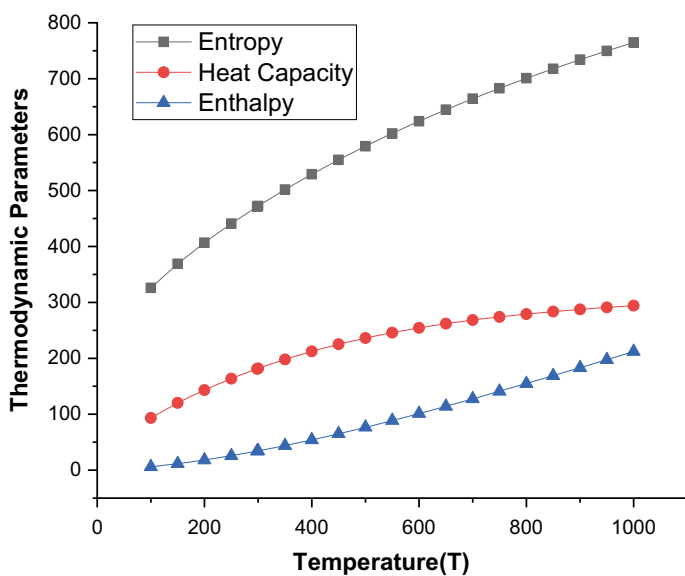
Fig. 44.4 Correlation plot of the thermodynamic functions of 1,2,4,5 -TC-3-NB

Table 44.7 Second order perturbation theory analysis of TCNB

Donor NBO(i)	ED/e	Energy E(i)	Acceptor NBO(j)	Energy E(j)	E(2)[a]kcal/mol	E(j)−E(i)[b](a.u.)	F(i,j)[c](a.u.)
σ(C1-Cl8)	1.98698	−0.76803	σ*(C2-C3)	0.49197	2.38	1.26	0.049
			σ*(C5-C6)	0.50197	2.07	1.27	0.046
σ(C2-Cl9)	1.98592	−0.77374	σ*(C1-C2)	0.48626	0.54	1.26	0.023
			σ*(C1-C6)	0.50626	2.28	1.28	0.048
			σ*(C3-C4)	0.48626	2.68	1.26	0.052
			σ*(C3-N12)	0.20626	0.57	0.98	0.021
σ(C3-N12)	1.98530	−0.84085	σ*(C1-C2)	0.47915	1.61	1.32	0.042
			σ*(C2-C3)	0.48915	0.80	1.33	0.029
			σ*(C3-C4)	0.48915	0.80	1.33	0.029
			σ*(C4-C5)	0.47915	1.61	1.32	0.042
σ(C4-Cl10)	1.98592	−0.77374	σ*(C2-C3)	0.48626	2.68	1.26	0.052
			σ*(C3-N12)	0.20626	0.57	0.98	0.021
			σ*(C4-C5)	0.48626	0.54	1.26	0.023
			σ*(C5-C6)	0.50626	2.28	1.28	0.048
σ(C5-Cl11)	1.98698	−0.76803	σ*(C1-C6)	0.50197	2.07	1.27	0.046
			σ*(C3-C4)	0.49197	2.38	1.26	0.049
σ(N12-O13)	1.99527	−1.14436	σ*(C3-N12)	0.20564	0.77	1.35	0.029
σ(N12-O14)	1.99230	−0.49965	σ*(C3-N12)	0.85035	0.77	1.35	0.029
			σ*(C2-C3)	0.49035	1.33	0.99	0.033
			σ*(C3-C4)	0.49035	1.33	0.99	0.033
			σ*(N12-O14)	−0.16965	6.98	0.33	0.051

(continued)

Table 44.7 (continued)

Donor NBO(i)	ED/e	Energy E(i)	Acceptor NBO(j)	Energy E(j)	E(2)ᵃkcal/mol	E(j)−E(i)ᵇ(a.u.)	F(i,j)ᶜ(a.u.)
LP(1)Cl8	1.99204	−0.97385	σ*(C1-C2)	0.48615	1.27	1.46	0.039
			σ*(C1-C6)	0.50615	1.59	1.48	0.043
LP(2)Cl8	1.96587	−0.35707	σ*(C1-C2)	0.48293	4.95	0.84	0.058
			σ*(C1-C6)	0.50293	4.20	0.86	0.054
LP(3)Cl8	1.91347	−0.35549	σ*(C1-C2)	−0.05707	15.17	0.30	0.066
LP(1)Cl9	1.99292	−0.97577	σ*(C1-C2)	0.48423	1.47	1.46	0.042
			σ*(C2-C3)	0.48423	1.39	1.46	0.040
LP(2)Cl9	1.96136	−0.36005	σ*(C1-C2)	0.47995	4.52	0.84	0.055
			σ*(C2-C3)	0.48995	5.29	0.85	0.060
			σ*(N12-O14)	−0.17005	0.57	0.19	0.011
LP(3)Cl9	1.91044	−0.35700	σ*(C1-C2)	−0.057	15.36	0.30	0.067
LP(1)Cl10	1.99292	−0.97577	σ*(C3-C4)	0.48423	1.39	1.46	0.040
			σ*(C4-C5)	0.48423	1.47	1.46	0.042
LP(2)Cl10	1.96136	−0.36005	σ*(C3-C4)	0.48995	5.29	0.85	0.060
			σ*(C4-C5)	0.47995	4.52	0.84	0.055
			σ*(N12-O14)	−0.17005	0.57	0.19	0.011
LP(3)Cl10	1.91044	−0.35700	σ*(C3-C4)	−0.047	15.08	0.31	0.067
LP(1)Cl11	1.99204	−0.97385	σ*(C4-C5)	0.48615	1.27	1.46	0.039
			σ*(C5-C6)	0.50615	1.59	1.48	0.043
LP(2)Cl11	1.96588	−0.35707	σ*(C4-C5)	0.48293	4.95	0.84	0.058
			σ*(C5-C6)	0.50293	4.20	0.86	0.054

(continued)

Table 44.7 (continued)

Donor NBO(i)	ED/e	Energy E(i)	Acceptor NBO(j)	Energy E(j)	E(2)[a]kcal/mol	E(j)−E(i)[b](a.u.)	F(i,j)[c](a.u.)
LP(3)Cl11	1.91347	−0.35549	σ*(C5-C6)	−0.04549	13.97	0.31	0.064
LP(1)O13	1.98064	−0.84231	σ*(C3-N12)	0.19769	3.85	1.04	0.058
			σ*(N12-O14)	0.39769	3.31	1.24	0.058
LP(2)O13	1.88102	−0.33195	σ*(C3-C4)	−0.05195	1.48	0.28	0.020
			σ*(C3-N12)	0.19805	13.13	0.53	0.075
			σ*(N12-O14)	0.39805	18.74	0.73	0.106
LP(3)O13	1.40971	−0.31494	σ*(N12-O14)	−0.17494	175.14	0.14	0.141
LP(1)O14	1.98064	−0.84231	σ*(C3-N12)	0.19769	3.85	1.04	0.058
			σ*(N12-O13)	0.39769	3.31	1.24	0.058
LP(2)O14	1.88102	−0.33195	σ*(C3-C4)	−0.05195	1.48	0.28	0.020
			σ*(C3-N12)	0.19805	13.13	0.53	0.075
			σ*(N12-O13)	0.39805	18.74	0.73	0.106

[a]E(2) means energy of hyperconjugative interactions(stabilization energy)
[b]Energy difference between donor and acceptor i and j NBO orbitals
[c]F(i, j) is the Fock matrix element between i and j NBO orbitals

Table 44.8 Molecular polarizabiltiy for TCNB

Molecular polarizability (AU)	B3LYP/ccpvdz	B3LYP/6-311++G (d, p)
α_{xx}	-98.1938	-98.0338
α_{xy}	-0.0002	0.0003
α_{yy}	106.2934	106.3868
α_{xz}	0.0002	0.0004
α_{yz}	0.000	0.0000
α_{zz}	-103.9284	-104.3197
Mean dipole polarizability $<\alpha>$	-102.8052	-102.9134
Anisotropic polarizability $\Delta\alpha$	7.213	7.534

of polarizability α, larger will be the NLO activity of the molecule sample [32]. It is related to intra-molecular charge transfer and electron cloud movement from electron donor to electron acceptor groups. The titled compound is suitable for further investigation of NLO properties.

44.4.7 Reduced Density Gradient (RDG)

With the help of reduced density gradient analysis and non-covalent index, non-covalent interactions occurring within a molecule can be studied. Multiwfn program helps in producing the iso-surfaces of TCNB (Fig. 44.5) and thus scatter graph of RDG can be visualised [9]. Figure 44.6 shows the curve plot between reduced density gradient(s) on the y-axis and product of second eigenvalue (λ_2) of Hessian matrix with electron density (ρ) on the x-axis and can be defined as

$$s(r) = \frac{|\nabla\rho(r)|}{2kF\rho(r)}$$

where s(r) is the reduced density gradient, $\rho(r)$ is electron density and k_f is the Fermi momentum. Here, spikes in the red region suggests the region (sign($\lambda 2$)$\rho > 0$) of strong repulsion showing steric effect and the green region indicates the region of van der Waals interaction (sign($\lambda 2$)ρ is nearly 0) [31].

44.4.8 Molecular Electrostatic Potential (MEP) Analysis

In a molecule, 3D charge distributions can be shown using MEP which determines how molecules interact with each another. A high electrostatic potential tells about

Fig. 44.5 RDG isosurface of TCNB
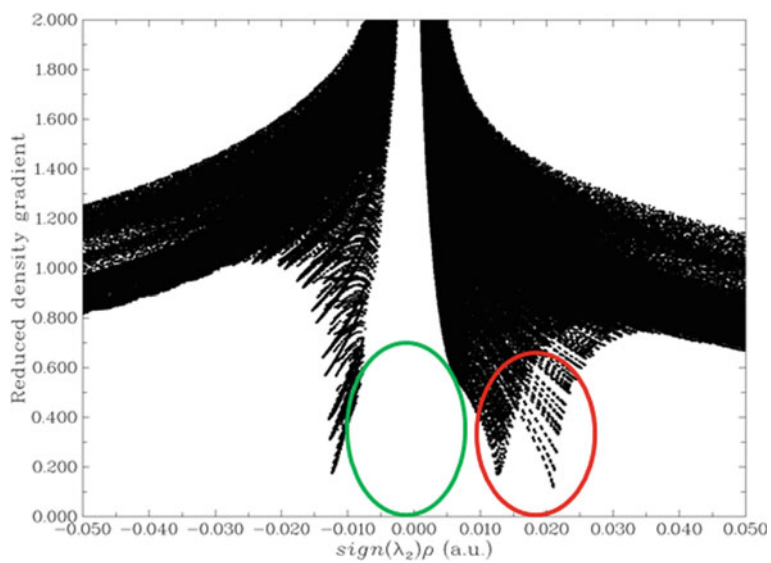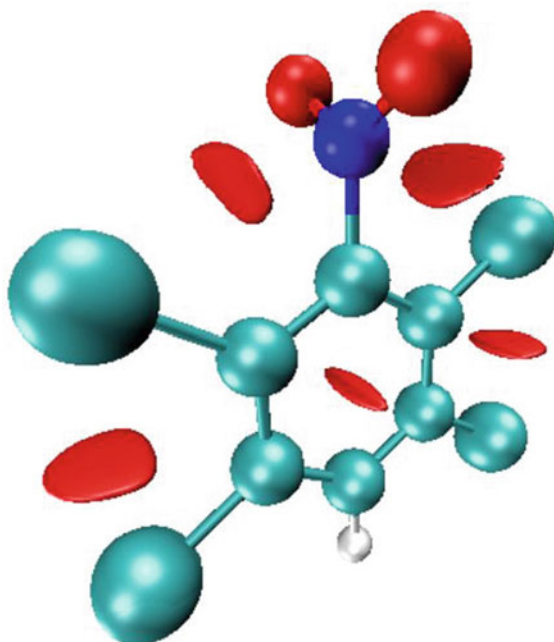
Fig. 44.6 RDG scatter plot of TCNB
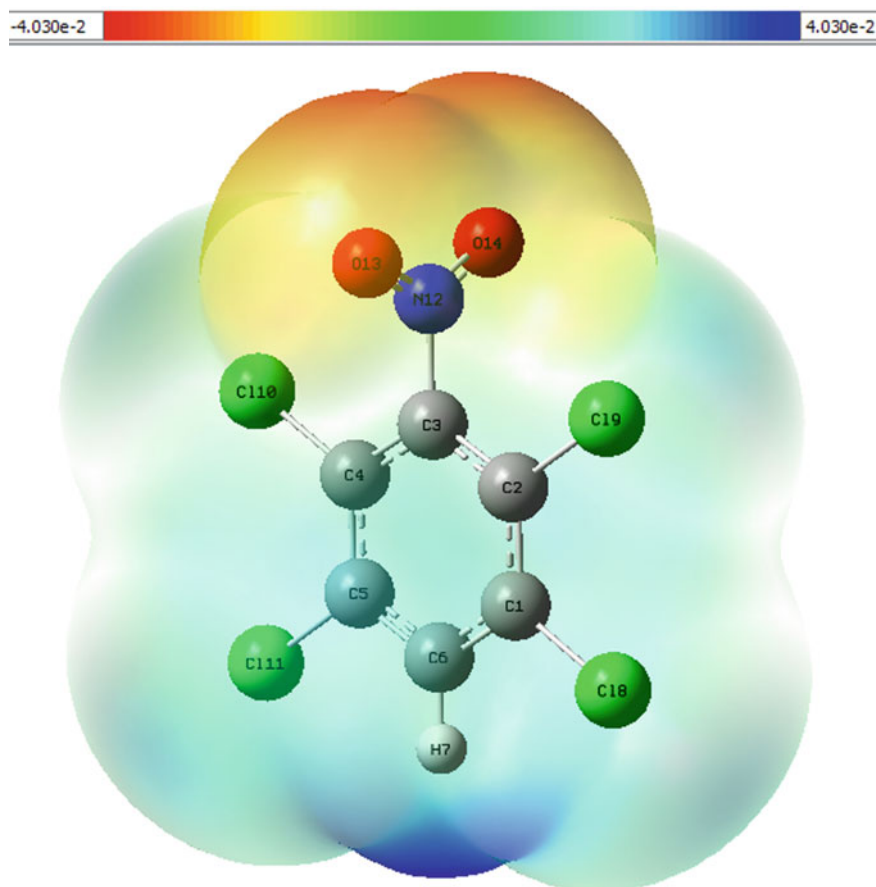
Fig. 44.7 MEP of TCNB molecule

the dearth of electrons and vice-versa. The lowest and highest electrostatic potential energy is indicated by red and blue colour respectively and illustrated in Fig. 44.7. Theoretically, MEP can be easily described using DFT at B3LYP/6-311++G(d,p). Low potential areas implies excess of electrons whereas high potential areas have scarcity of electrons [33]. The electrostatic potential surfaces increase from red to blue from -4.030×10^{-2} to 4.030×10^{-2} (au) [32].

44.4.9   Surface Contour Map Analysis

By plotting a contour around the TCNB molecule, all the molecular electrostatic potential surfaces can be visualized. The red region has excess of electrons while
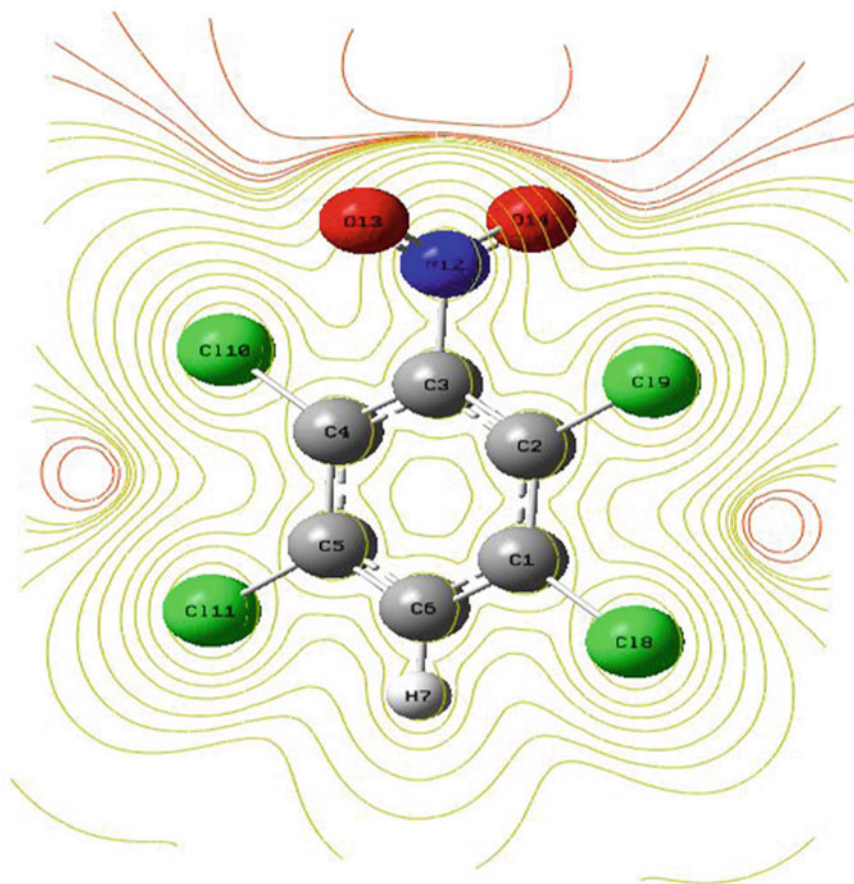
Fig. 44.8 MEP contour map of TCNB

the yellow region has dearth of electrons. The contour map indicates that in nuclear position, the positive electrostatic region is dominant and vice versa as shown in Fig. 44.8 [34].

44.5 Conclusion

The structural parameters and detailed frequency assignments for TCNB using vibrational spectra have been analyzed using two different basis sets {ccpvdz and 6311++(d,p)} at B3LYP level. The influence of NO_2 and Cl atom to the various vibrational frequencies of TCNB was studied. The computed and observed values of the vibrational frequencies are in accordance with each other on using a suitable

scaling factor. Various thermodynamic functions, molecular polarisability/ hyper-polarisability, dipole moment along with MEP, NBO, RDG and normal coordinate analysis for TCNB have been discussed in detail thereby making the compound suitable for studies of photoemissions, NLO properties and as an intermediate in various reactions.

References

1. G. Booth, Ullmann's Encycl. Ind. Chem. **24**, 301 (1988)
2. R.E. Kadunce, G.L. Lamoureux, J. Label. Compd. Radiopharm. **12**, 459 (1976)
3. B.J. Brabin, T.A. Eggelte, M. Parise, F. Verhoeff, Drug Saf. **27**, 633 (2004)
4. K. Błaziak, W. Danikiewicz, M. Mąkosza, Molecules **25** (2020)
5. A.D. Becke, Phys. Rev. A **38**, 3098 (1988)
6. C. Lee, W. Yang, R.G. Parr, Phys. Rev. B **37**, 785 (1988)
7. M.J. Frisch, G.W. Trucks, H.B. Schlegel, G.E. Scuseria, M.A. Robb, J.R. Cheeseman, G. Scalmani, V. Barone, B. Mennucci, G.A. Petersson, H. Nakatsuji, M. Caricato, X. Li, H.P. Hratchian, A.F. Izmaylov, J. Bloino, G. Zheng, J.L. Sonnenberg, M. Hada, M. Ehara, K. Toyota, R. Fukuda, J. Hasegawa, M. Ishida, T. Nakajima, Y. Honda, O. Kitao, H. Nakai, T. Vreven, J.A. Montgomery, J.E. Peralta, F. Ogliaro, M. Bearpark, J.J. Heyd, E. Brothers, K.N. Kudin, V.N. Staroverov, R. Kobayashi, J. Normand, K. Raghavachari, A. Rendell, J.C. Burant, S.S. Iyengar, J. Tomasi, M. Cossi, N. Rega, J.M. Millam, M. Klene, J.E. Knox, J.B. Cross, V. Bakken, C. Adamo, J. Jaramillo, R. Gomperts, R.E. Stratmann, O. Yazyev, A.J. Austin, R. Cammi, C. Pomelli, J.W. Ochterski, R.L. Martin, K. Morokuma, V.G. Zakrzewski, G.A. Voth, P. Salvador, J.J. Dannenberg, S. Dapprich, A.D. Daniels, Ö. Farkas, J.B. Foresman, J.V. Ortiz, J. Cioslowski, D.J. Fox, Gaussian **09** (2009)
8. GaussView, Version 6, Dennington, Roy; Keith, Todd A.; Millam, John M. Semichem Inc., Shawnee Mission, KS, Gaussian (2016)
9. T. Lu, F. Chen, J. Comput. Chem. **33**, 580 (2012)
10. S. Jeyavijayan, M. Arivazhagan, Indian J. Pure Appl. Phys. **48**, 869 (2010)
11. M. H. Jamróz, Spectrochim. Acta - Part A Mol. Biomol. Spectrosc. **114**, 220 (2013)
12. M. Rogojerov, G. Keresztury, B. Jordanov, Spectrochim. Acta Part A **61**, 1661 (2005)
13. C.S. Hiremath, J. Yenagi, J. Tonannavar, Spectrochim. Acta Part A Mol. Biomol. Spectrosc. **68**, 710 (2007)
14. V. Arjunan, I. Saravanan, P. Ravindran, S. Mohan, Spectrochim. Acta Part A Mol. Biomol. Spectrosc. **74**, 642 (2009)
15. V. Krishnakumar, V. Balachandran, Spectrochim. Acta Part A **61**, 1001 (2005)
16. V. Krishnakumar, V. Balachandran, Spectrochim. Acta Part A Mol. Biomol. Spectrosc. **61**, 1811 (2005)
17. N. Sundaraganesan, S. Ayyappan, H. Umamaheswari, B.D. Joshua, Spectrochim. Acta Part A **66**, 17 (2007)
18. A. Kovacs, G. Keresztury, V. Izvekov, Chem. Phys. **253**, 193 (2000)
19. V. Arjunan, S. Mohan, J. Mol. Struct. **892**, 289 (2008)
20. N. Sundaraganesan, B. Anand, B.D. Joshua, Spectrochim. Acta Part A **65**, 1053 (2006)
21. D.S. Annama.J, Daizy.P, Abdullah K.I, Keresztury .G, J. RAMAN Spectrosc. **31**, 1067 (2000)
22. D. Sajan, I.H. Joe, V.S. Jayakumar, J. Phys. Conf. Ser. **28**, 123 (2006)
23. R.K. Goel, S.K. Gupta, S.N. Sharma, Pramana **11**, 541 (1978)
24. S. Gunasekaran, P. Abitha, Indian J. Pure Appl. Phys. **43**, 329 (2005)
25. V. Mukherjee, K. Singh, N.P. Singh, R.A. Yadav, Spectrochim. Acta Part A Mol. Biomol. Spectrosc. **73**, 44 (2009)
26. J.S. Singh, Pramana **70**, 479 (2008)

27. R. Zhang, B. Du, G. Sun, Y. Sun, Spectrochim. Acta Part A Mol. Biomol. Spectrosc. **75**, 1115 (2010)
28. P. Govindasamy, S. Gunasekaran, Spectrochim. Acta Part A Mol. Biomol. Spectrosc. **149**, 800 (2015)
29. S. Muthu and A. Prabhakaran, Spectrochim. Acta Part A Mol. Biomol. Spectrosc. **129**, 184 (2014)
30. B.S. Yadav, R. Saran, Mater. Sci. Res. **3**, 103 (2006)
31. J. Priscilla, D. Arul Dhas, I. Hubert Joe, S. Balachandran, Chem. Phys. **536**, 110827 (2020)
32. E. Kose, A. Atac, F. Bardak, J. Mol. Struct. (2018)
33. M. Drissi, N. Benhalima, Y. Megrouss, R. Rachida, A. Chouaih, F. Hamzaoui, Molecules **20**, 4042 (2015)
34. S. Premkumar, A. Jawahar, T. Mathavan, M. Kumara Dhas, A. Milton Franklin Benial, Spectrochim. Acta. A. Mol. Biomol. Spectrosc. **138**, 252 (2015)

Chapter 45
First Principles Study of the Electronic Structure, Charge Density Contours and Fermi Surfaces of Zirconium-Based Weyl Semi-Metals ZrX (X = S, Se, and Te)

Yuhit Gupta, Murari Mohan Sinha, and Suram Singh Verma

Abstract Weyl Semimetals have substantial applications in spintronics, quantum computation, and electronic industry. Therefore, to get a physical insight behind the electronic applications of these Weyl semimetals, the electronic band structure, total as well as partial phonon density of states, Fermi surfaces and charge density contours related to Zirconium based Weyl semimetals ZrX (X = S, Se and Te) are investigated and discussed in the present report using generalized gradient approximations by employing density functional theory. From the calculated values of bulk modulus B_o and its derivative with respect to change in pressure values B_o', it is found that ZrS possesses the highest value of B_o and B_o' among all. This confirms that ZrS has least compressibility. The Fermi surfaces of ZrX are composed of two bands traversing along with M-L directions of the Brillouin zone. The bonding characteristics are determined by using the electronic charge density contours in the (110) plane of crystallography. The present calculation suggests the ionic and polar-covalent bonding in the WSMs, which is found to be in consistent with the electro-negativity difference values.

45.1 Introduction

Weyl Semi-Metals (WSMs) are formed when two elements: one from the transition elements and another from chalcogen elements combine in the definite proportion of 1:1 to form a *WC-type* crystal structure [1]. These materials possess many stupendous properties such as large magneto-resistance, ultra-high mobility of fermions, exceptional Weyl nodes, Fermi-arcs, transport properties, and massless fermions [2]. The massless fermions present in the Weyl semimetals further find many applications in the manufacturing of super lenses and scanning tunneling microscopes in the field of the electronics industry [3]. The presence of exclusive states of electron

Y. Gupta (✉) · M. M. Sinha · S. S. Verma
Department of Physics, Sant Longowal Institute of Engineering and Technology, Longowal, Sangrur 148106, India

density, new discovered topological states of surface, and applications in the high-speed quantum computers and shape-memory devices has involved the concentration of various researchers and scientists globally towards these materials [4].

In addition to the numerous applications of Weyl semimetals, various efforts has been made to understand properties related to the crystal structure and characteristics of electronic bands of WSMs, after the discovery of Weyl fermions [5]. Experimental discovery of fermions with their three components in WSM 'MoP' (Molybdenum Phosphide) by angle-resolved photoemission spectroscopy in the electronic structure reveals many unconventional fermions in material science [6]. The Quantum design method was used to measure magnetic conveyance and resistive hall measurements of ZrTe [7].

Weyl semimetal ZrTe was found to be a system with high mobility of charge carrier and possess a 3D-complex Fermi surface [8]. The combination of three degenerate nodal points and Weyl fermions in ZrTe with WC-type crystal structure was investigated theoretically by applying approximation of generalized gradient (GGA) of Perdew-Burke-Ernzerhof (PBE) type with Open MX software package [7]. The superconducting properties of Weyl semimetals such as ZrS and ZrTe were explored at the ambient condition of temperature by Gupta et al. [9] by implementing the theory based on density functional known as density functional theory (DFT). Besides, the various number of properties related to the crystal structure, electronic structure, and superconducting properties of ZrX have been investigated, but the theoretical study of Fermi surfaces and charge density contours of Weyl semimetals ZrX are very scarce.

As the study of Fermi surfaces is of utmost importance for characterizing the thermal, electronic, magnetic, and optical properties of materials. Therefore, in this work, the systematic investigation of the electronic structure, Fermi surfaces, and charge density contours for ZrX are calculated and discussed with available results.

45.2   Computational Method

The calculations related to electronic band structure were made under DFT [10, 11] using the QUANTUM ESPRESSO software package [12]. The interaction of outer electrons, nuclei as well as inner electrons of the constituent atoms was determined by pseudo-potentials of the norm-conserving type under the framework of GGA of PBE [13, 14]. The occupation distribution was selected by the smearing of Marzari Vanderbilt [15]. For investigating the parameters like as such as Bulk modulus and its pressure derivative, electronic band structures, the electron density of states, Fermi surfaces, and charge density contours of ZrS, ZrSe, and ZrTe, the kinetic energy cut off 120 *Ry.*, 90 *Ry.* and 60 *Ry.* were found to be sufficient in our earlier study [9] respectively. These value of cut off energies were found to be enough to fully converge the systems. Similar to our earlier study [9] the Monkhrost Pack [16] mesh of k-points with order of $8 \times 8x12$, $16 \times 16x9$ and $17 \times 17x10$ were used to perform the integration over the first Brillouin zone of ZrS, ZrSe, and ZrTe respectively.

Previously calculated values of the lattice constant of '*a*' = 3.482 Å, '*c*' = 3.479 Å [9] for ZrS and '*a*' = 3.792 Å, '*c*' = 3.884 Å [9] are used designed for investigating the other parameters like as Bulk modulus and its derivative with respect to pressure, electronic band structures, the electron density of states, Fermi surfaces and charge density contours of ZrS and ZrTe. For finding the structure related parameters such as the values of lattice constants (*a and c*), B_o and $B_o{}'$ of ZrSe, the energy versus volume data of ZrSe was built-in to Birch-Murnaghan's equation of state (EOS) of third order, [17] that can be written as follows:

$$E(V) = E_o + \frac{9V_o B_o}{16} \left\{ \left[\left(\frac{V_o}{V} \right)^{\frac{2}{3}} - 1 \right]^3 B_o{}' + \left[\left(\frac{V_o}{V} \right)^{\frac{2}{3}} - 1 \right]^2 \left[6 - 4 \left(\frac{V_o}{V} \right)^{\frac{2}{3}} \right] \right\}.$$

45.3   Results and Discussion

The investigation and comparison of structural, electronic, Fermi surfaces and charge density contours of ZrX ((X = S, Se, and Te) have been made using density functional theory, and are discussed below:

45.3.1   Structural Properties

The binary WSMs ZrX have a hexagonal (WC-type) crystal structure [18]. The Bravais lattice has space group $P\,\bar{6}\,m2$ with its primitive cell of one formula unit. Consequently, the primitive unit cell of WSM contains a total number of two atoms, in which transition metal atom Zirconium 'Zr' is located at Wyckoff position 1a (0, 0, 0) and chalcogen atom '*X*' at *1d* (1/3,2/3,1/3) site. Since WSMs possess the crystal structure like that of Molybdenum Phosphide (*MoP*) [19]. Therefore, the current WSMs also possess the symmetry around rotation (C_{3z}), and symmetries of mirror (M_y and M_z). The crystal structure of the unit cell of all the three WSMs is shown in Fig. 45.1.

The calculated values of lattice constants of *ZrSe* are calculated to be $a = 3.594$ Å, and $c = 3.659$ Å, which are consistent with the earlier reported theoretical and experimental results [7] with a variation of less than 1.5%. This small variation may be due to the type of pseudo-potential used in present calculations. Moreover, the calculated values of volume ($Å^3$), B_o, $B_o{}'$ of ZrS, ZrSe, and ZrTe are presented in Table 45.1. along with the available theoretical results.

Bulk modulus is an important structural parameter, as it gives the information about the ability of a solid to hold out changes in volume under compression. Therefore, it is also considered a measure of the incompressibility of a solid and is equal to the applied pressure divided by the change in the relative deformation. Therefore the

Fig. 45.1 Crystal structure of ZrX, where X = S/Se/Te
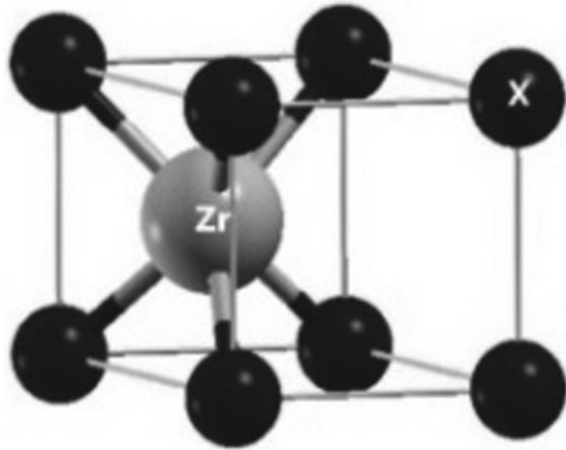
Table 45.1 Calculated structural parameters of ZrX (X = S, Se, and Te) Weyl semimetals

Weyl semimetal	$V_o(\text{Å}^3)$	B_0(GPa)	$B_o{}'$
ZrS	36.56	133.3	4.35
	35.42[a]	–	–
ZrSe	40.98	113.2	4.29
ZrSe$_{0.90}$	39.47[b]	–	–
ZrTe	48.40	94.9	4.30
	47.25[c]	–	–

[a][20]
*[b][7]
*[c][21–23]

Bulk modulus of all the three Weyl semimetals are calculated and presented in Table 45.1. By comparing the values of volumes of all WSMs with each other, one finds V_o (ZrS) < V_o (ZrSe) < V_o (ZrTe) but the Bulk modulus follows the opposite trend as B_o (ZrS) > B_o (ZrSe) > B_o (ZrTe). This is according to the fact that the volume increases then the value of bulk modulus decreases and vice-versa. Moreover as the volume increases, the compressibility increases, and hence bulk modulus decreases.

The study of derivative of bulk modulus with resepct to pressure is also an important parameter to determine the thermoplastic parameters [19] of Weyl Semimetals, therefore, the pressure derivative of bulk modulus for all the three Weyl semimetals are calculated and presented in Table 45.1. It can be observed from Table 45.1, that $B_o{}'$ also follows a similar trend that of the bulk modulus. The values of the derivative of bulk modulus with respect to the pressure are reported for the first time. It is obvious from Table 45.1 that ZrS has the highest value of $B_o{}'$ in all the three WSMs, therefore is a highly thermo-plastic material.

45.3.2   Electronic Band Structure and Density of States

To elucidate the electronic characteristics, the electronic band structure, electron density of states have been calculated for ZrS, ZrSe, and ZrTe and are shown in Fig. 45.2a, c, e respectively. From the electronic band structure of ZrX, it is observed that valence bands and conduction band present in the vicinity of Fermi energy level,

Fig. 45.2 Electronic bands and density of states for **a, b** ZrS; **c, d** ZrSe; and **e, f** ZrTe

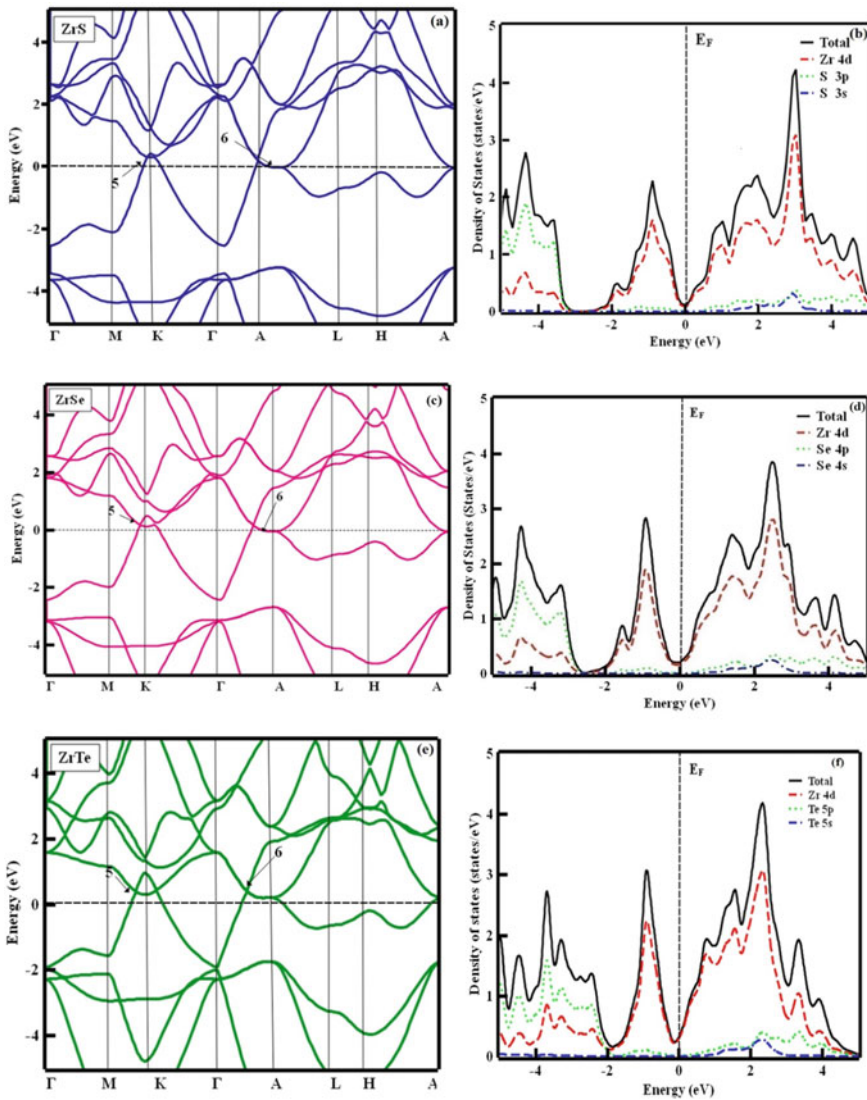such as band traversing along 'Γ-A' direction and are nearly same to that of similar structured *TaN* topological semimetal [24]. One different feature that is observed in ZrX than that of observed in *TaN* is the presence of inversion of conduction band around the high symmetry direction K-directions, which is not observed in *TaN*. This inversion of the band may be due to the presence of d electrons of '*Zr*' atom. Moreover, our calculated band structure of ZrTe is found to be in great consistency with that reported earlier [16], which strengthens the reliability of our calculated electronic band structure for other Weyl semimetals such as ZrS and ZrSe.

The computed density of states (DOS) (total as well as partial) for all the three Weyl Semimetals are presented in Fig. 45.2b, d, f. The combined analysis of electronic band structure in the company of the density of states of *ZrS*, it can be noticed that the bands below the Fermi level from -5.0eV to -3.5 eV is characterized by the 'p' states of 'S' atom, while the bands present in the neighbourhood of Fermi energy states are mainly due to 'd' state of 'Zr' atom. The 's' state of 'S' atom also shows minute interaction with 'p' and 'd' states of 'S' and 'Zr' respectively. Moreover, the semi-metallic nature is confirmed from the very small value of their number density of states present at the Fermi energy states for ZrS i.e. $N(E_F) = 0.121$ states/eV.

The calculated electronic band structure for ZrSe is like that of ZrS except that bands are slightly shifted towards the Fermi level. This slight shift can be noticed from the density of states of ZrSe. The peaks in the energy range from -5.0eV to -2.0 eV arise due to the delocalization of the 'p' state of 'Se' atom. The major contribution at the Fermi level is due to the' states of 'Zr'. The calculated number of density of states at the Fermi level is $N(E_F) = 0.203$ states/eV. This small value of $N(E_F)$ indicates further the semi-metallic character of ZrSe.

Furthermore, the electronic band structure for ZrTe is like that of ZrS and ZrSe. From the density of states of ZrTe, it is analysed that there exist numerous peaks in the region from -5.0 to -2.5 eV lower than the Fermi level which is because of the 'p' states of Te atom. The presence of electronic bands at E_F are because of the interaction of 'd' states of 'Zr' and 'p' states *of* 'Te'. The bands in the environs of Fermi energy level are because of the 'd' states of 'Zr'. The evaluated number density of electronic states at the Fermi energy level is $N(E_F) = 0.349$ states/eV. The observed number density of electronic states at the Fermi energy level follow the trend as ZrS < ZrSe < ZrTe. This increase in the density of states may be due to the increase in the distance of the outermost electron from the nucleus of the chalcogen atom.

45.3.3 Fermi Surfaces

To investigate the distribution of electrons in solids, the allowed energy values of electrons is the prerequisite condition. Fermi surfaces describe the acceptable energy values of electrons in solids and are of significant value as they play an important role in predicting the physical properties related to thermal, magnetic, optical characteristics of materials. Through the study of the electron bands of ZrX, it is analyzed that

the bands traversing or touching the Fermi energy play their significant role, these bands also play their important role in Fermi surfaces. Therefore, in the present report, the Fermi surfaces for the Weyl semimetals ZrX are calculated for only these bands and discussed in detail.

For ZrS, ZrSe and ZrTe, it is found that only two bands, named the band '5' and band '6' are touching/traversing the Fermi energy level for each Weyl semimetal (shown in Fig. 45.3a–c, d–f, and g–i respectively) therefore, corresponding to these two bands, two Fermi surfaces are calculated for each Weyl semimetal and third Fermi surface is obtained by merging the two. The three Fermi surface sheets for each Weyl semimetals are shown in Fig. 45.3. The band 5th is contributing to the formation of hole pocket at 'K' *point* and band 6th is responsible for the presence of electron pocket along 'T-L' direction for each Weyl semimetal. The third Fermi surface for each Weyl semimetal is the merged Fermi surface. The energy range for band 5th and 6th for ZrS are -2.5571 eV to 0.0762 eV and -0.0442 eV to 3.1067 eV;
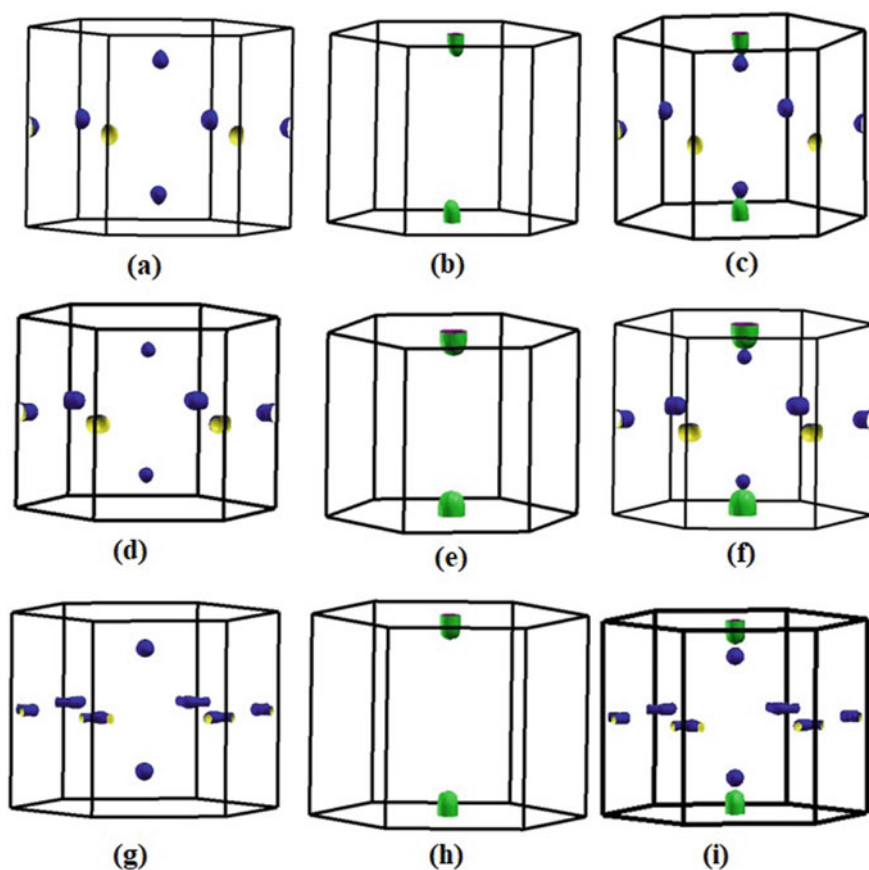
Fig. 45.3 Fermi surfaces of Weyl semimetals **a–c** ZrS; **d–f** ZrSe; and **g–i** ZrTe

and for ZrSe are -2.445 eV to 0.1684 eV and -0.0669 eV to 2.5774 eV; and for ZrTe are -2.1702 eV to 0.0883 eV and -0.05 eV to 2.1091 eV respectively. As it can be observed from the figures of Fermi surfaces that the observed difference in the topology of the Fermi surface occurs, this is because of the change in occupancy of bands. Also, the variation in the color of Fermi surfaces occurs because of the change in the electron speed [25].

45.3.4 Charge Density Contours

To envisage the character of the bond character, charge transfer, and bonding properties of various compounds, the charge density contours play very dominant contribution. The charge density contours which are also known as the distribution of energy Eigenvalues corresponding to each wave vector, provide a vital tool for determining the possibility of an electron being present at a site. Henceforth to elucidate the binding mechanism among the atoms of WSMs, the charge density contour calculations for the three WSMs along (110) planes are described in Fig. 45.4

The two-dimensional charge density contours along (110) plane and variation of charge density with distance from the atomic site ($\Delta n(r)$) for all the three WSM i.e. ZrS, ZrSe, and ZrTe are illustrated in Fig. 45.4a–c. The range of charge density values for ZrS, ZrSe and ZrTe are from 0.0014 to 0.1705 e/Å^3, 0.0014 to 0.1259 e/Å^3 and 0.0015 to 0.0796 e/Å^3 respectively. In all the charge density contours of ZrS,

Fig. 45.4 Charge density contours along (110) plane; $\Delta n(r)$ denotes the change of electron density of **(a)** ZrS, **(b)** ZrSe and **(c)** ZrTe

Table 45.2 Bonding characteristics of ZrX (X = S, Se, and Te)

Atoms	Zr	S	Se	Te
Linus Pauling electro-negativity	1.33	2.58	2.55	2.10
Electro-negativity difference and type of bonding	$D_{Zr\text{-}S}$ 1.25(*ionic*)	$D_{Zr\text{-}Se}$ 1.22 (*ionic*)	$D_{Zr\text{-}Te}$ 0.77(*polar-covalent*)	

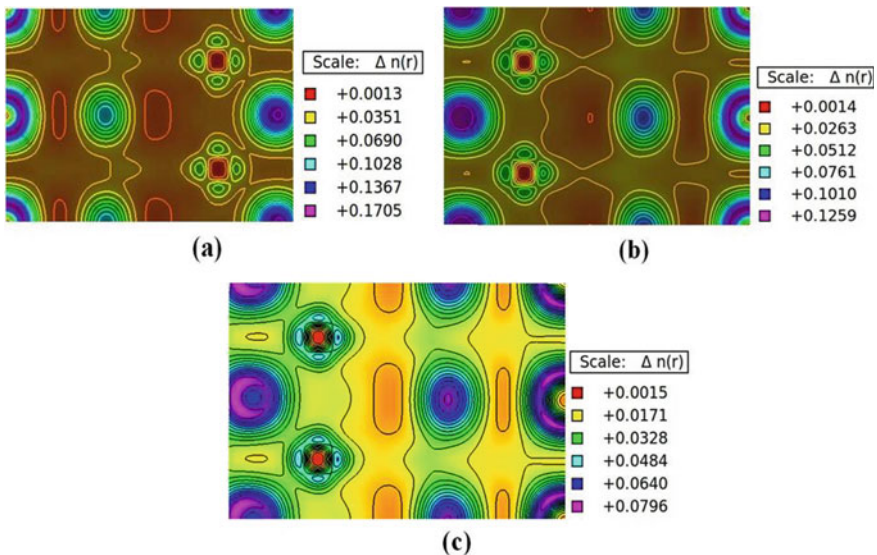ZrSe, and ZrTe, the purple-colored region assigns the high concentration of charge of chalcogen (X = S, Se, and Te) atom and the red-colored region assigns the low concentration of charge of 'Zr' atom. It represents that the charge moves from purple to red region. From the charge density calculations, it is concluded that the domain of 'X' atom is more in comparison to the 'Zr' atom, this is because of the high value of electro-negativity of 'X' atoms in comparison to 'Zr' atom. Since it is according to the fact that more the electro-negativity of an atom more electrons will be attracted to that atom. In the charge density contours of ZrS and ZrSe, the spherical shape of charge density contours indicates the ionic character of the compounds, while the distorted spherical outline of charge density contours of separated atoms of ZrTe describes the polar covalent bonding. These findings of contour calculations are consistent with the values of the electronegativity difference shown in Table 45.2.

From the Table 45.2, it is inferred that for all ZrS, ZrSe, and ZrTe, the electro-negativity difference lies in the range of $0.4 < D < 1.7$ favors the polar covalent behavior of the materials [26, 27].

45.4 Conclusion

A systematic theoretical investigation on the structural parameters, electronic band structures, the electron density of states, Fermi surfaces, and charge density contours of Weyl semimetals in hexagonal (WC-type) crystal is made by implementing the DFT. The computed electronic bands and small values of electron density of states of ZrS, ZrSe, and ZrTe show their semi-metallic character. The calculated Fermi surfaces for all Weyl semimetals gives a physical insight of the electronic band structure. Also, the calculated charge density contour calculations for ZrS, ZrSe, and ZrTe describe the ionic and polar-covalent bonding, which is further found to be consistent with the electro-negativity difference values.

References

1. G. Orlygsson, B. Harbrecht, J. Am. Chem. Soc. **123**(18), 4168 (2001)
2. C. Bai, Y. Yang, K. Chang, Sci. Rep. **6**, 21283 (2016)

3. A. G. Grushin, J. H. Bardarson, Phys. Rev. B **91**, 121109 (2015)
4. B. Yan and C. Felser C, Annu. Rev. Condens. Matter Phys **8**(1) 337 (2017)
5. H. Weyl, Z. Phys. **56**, 330 (1929)
6. B.Q. Lv, Z.L. Feng, Q.N. Xu, X. Gao, J.Z. Ma, L.Y. Kong, P. Richard, Y.B. Huang, V.N. Strocov, C. Fang, H.M. Weng, Y.G. Shi, T. Qian, H. Ding, Nature **546**, 627 (2017)
7. H.Weng, C. Fang, Z. Fang, X. Dai, Phys. Rev. B **94**, 165201 (2016)
8. W.L. Zhu, J.B. He, S. Zhang, D. Chen, L. Shan, Z.A. Ren, G.F. Chen, Condensed matter material science. Phys. Rev. B **101**, 245127 arXiv:1707.00942 (2020)
9. Y. Gupta, M.M. Sinha, S.S. Verma, Phys. C **577**, 1353714 (2020)
10. P. Hohenberg, W. Kohn, Phys. Rev. B **136**, 384 (1964)
11. W. Kohn, L.J. Sham, Phys. Rev. A **140**, 1133 (1965)
12. P. Giannozzi. S. Baroni, N. Bonini, C. Matteo, R. Car[6], C. Cavazzoni, D. Ceresoli, G.L. Chiarotti, M. Cococcioni, I. Dabo, A.D. Corso, S. Gironcoli, S. Fabris, G. Fratesi, R. Gebauer, U. Gerstmann, C. Gougoussis, A. Kokalj, M. Lazzeri, L.M. Samos, N. Marzari, F. Mauri, R. Mazzarello, S. Paolini, A. Pasquarello, L. Paulatto, C. Sbraccia, S. Scandolo, G. Sclauzero, A.P. Seitsonen, A. Smogunov, P. Umari, R.M. Wentzcovitch J. Phys. **21**, 395502 (2009)
13. J.P. Perdew, K. Burke, M. Errnzerhop, Phys. Rev. Lett **77**, 3865 (1996)
14. N. Troullier, J.L. Martins, Phys. Rev. B **43**, 1993 (1991)
15. N. Marzari, D.Vanderbilt, A.D. Vita. M.C.Payne, Phys. Rev. Lett **82**, 3296 (1999)
16. H. Monkhrost, J. Pack, Phys. Rev. B **13**, 5188 (1976)
17. F. Birch, J. Appl. Phys. **9**, 279 (1938)
18. R.P. Steiger, E.D. Cater, HighTemp. **2**, 398 (1970)
19. P.K. Singh, A. Dwivedi, Indian J. Pure AP Phy. **50**, 734 (2012)
20. R. Susstrunk, S.D. Huber, Science **349**, 47 (2015)
21. H. Hahn, B. Harder, U. Mutschke, P. Ness, Zur Kristall-struktur einiger Verbindungen und Phasen des SystemsZirkon/Schwefel. J. Inorganic Gener. Chem. **292**, 82 (1957)
22. H. Wiedemeier, H. Goldman, J. Less Common Met. **116**, 389 (1986)
23. H. Hahn, P. Ness, Über das Syst. Zirkon/Selen **302**, 37 (1959)
24. H. Weng, C. Fang, Z. Fang, X. Dai, Phys. Rev. B **69**, 241202 (2016)
25. Y. Gupta, M.M. Sinha, S.S. Verma, Phil. Mag. (2020). https://doi.org/10.1080/14786435.2020.1792570
26. griffin.ucsc.edu/teaching/11Q1–155/Lecture%2017.pdf
27. M.N. Rassol, Hussaina, A.J. Muhammad, A. Khan, J. Magn. Magn. Mater **426**, 421 (2017)

Chapter 46
Energy Levels and Oscillator Strengths of Sulphur Like Cr Useful in Astrophysical Plasma

Falta Yadav, Prafulla Chandra Bhowmick, and Narendra Singh

Abstract Energy levels and oscillator strength are reported for the lowest 188 fine-structure levels of sulphur like Cr ion. In this paper, we have used Configuration Interaction method through CIV3. The relativistic effects are included using Breit-Pauli approximation by adding mass-correction, Darwin, Spin-orbit terms to the non-relativistic Hamiltonian. For electric dipole allowed transitions, we have also modified the diagonal elements of hamiltonian matrix before the calculations of the oscillator strengths. Our calculated energies are very close agreement with the NIST data. Exact identification of most of the levels become very difficult due to strong mixing between several fine structure levels. We estimated new oscillator strength and energy levels data where no other experimental and theoretical results are available.

46.1   Introduction

Chromium element is very essential for studies of Astrophysical plasma, as many of the lines are frequently observed from various ionization stages. So these lines are very helpful in understanding Astrophysical plasmas like density, temperature and chemical composition. The sulphur like isoelectronic sequence has been the subject of attention due to its application in Astrophysical plasmas. Several authors have been carried out Relativistic calculations for energy levels of Sulphur like ions [1–4]. Energy levels have been presented in the ground state configuration of Sulphur like ions by Biemont et al. [3]. Theoretical energy levels were presented for 47 low lying levels of Sulphur like ions for z is greater than 18 by Chou et al. [5]. There has been a noticeable interest resulting in experimental and theoretical work in past years about the atomic properties of Cr IX ion, which is a fair indication of their importance in the Astrophysics and atomic physics [6].

F. Yadav (✉) · P. C. Bhowmick
Department of Physics and Astrophysics, University of Delhi, Delhi 110007, India

N. Singh
Department of Physics, SLC, University of Delhi, Delhi 110032, India

In our present work, we presented energy levels and oscillator strengths for electric dipole allowed transitions with the lowest-lying 188 fine-structure levels of Cr IX. Our configuration basis, Energy levels of Cr IX belonging to the configurations $(1s^2 2s^2 2p^6)\, 3s^2 3p^4$, $3s3p^5$, $3p^6$, $3s^2 3p^3 3d$, $3s3p^4 3d$, $3s^1 3p^3 3d^2$, $3s^2 3p^3 4s$ and $3s^2 3p^3 4d$. The energies for most of the Fine-structure levels belonging to the $3s^1 3p^3 3d^2$ and $3s^1 3p^4 3d$ are reported. These results are reported for the first time to the best of our knowledge. These levels are essential for diagnosis of spectra obtained by Hinode spacecraft [7], which was recently observed the transition belonging to these levels. We also fine tune the configuration interaction coefficients using the experimental energies. The Relativistic effects are included in the Breit-Pauli Hamiltonian [8]. The Darwin and mass-correction terms shift the energies of levels while the Spin-orbit term introduces fine structure splitting. Our presented energies are in good agreement with the NIST (National Institute of Standards and Technology) and other available theoretical results, giving the assurance of our Configuration Interaction wave functions.

46.2   Method

The configuration interaction was used to calculate the wave function in addition to ab initio energy levels. In this method, the linear combination of single configuration state functions are represented as extending configuration wave function of the hamiltonian and is given by Glass and Hibbert[8], Hibbert [9].

$\psi(LSJ) = \sum_0^M a_i \phi_i (LSJ)$, where ϕ_i is one electron radial wave function and a_i is the expansion coefficient was determined by the eigen vector component of the diagonalised hamiltonian matrix with matrix elements $H_{ji} = <\phi_j | H | \phi_i >$.

In our present work, Hamiltonian (H) consists of non-relativistic terms and the relativistic terms that include mass-correction, darwin and spin-orbit terms as implemented in CIV3 program [9].

In this the radial wavefunction for configuration interaction is given by,

$$P_{nl}(r) = \sum_{i=1}^{k} C_{inl} X_{inl}(r)$$

where X_{inl} is the eigen vector determined by the diagonalizing Hamiltonian,

$$X_{inl} = [\frac{(2\epsilon)^{I_{inl}+.5}}{(2I_{inl})!5}] r^{I_{inl}} \exp(-\epsilon_{inl} r)$$

Oscillator strength is defined as [7]:

$$f_{ji} = \frac{2\delta E}{3g_j} | < \psi_i | \sum_{p=1}^{N} r_p | \psi_j > |^2$$

Table 46.1 Radial wave-functions parameter of CrIX

Cr orbitals	Expansion coefficients	Power of r	Exponents
3s	0.12541	1	23.64560
	0.00067	1	34.90930
	−0.43973	2	9.80173
	0.07440	2	20.47840
	0.80906	3	5.14404
	0.46410	3	4.41516
	−0.29057	3	8.71525
3p	−0.36104	2	10.12360
	−0.02683	2	17.81550
	0.67691	3	4.79243
	0.45863	3	4.15261
	−0.11495	3	8.37201
3d	0.99558	3	4.37047
	0.00587	3	7.77096
4s	0.09312	1	17.69277
	−0.34885	2	8.48733
	0.99314	3	4.26784
	−1.40000	4	2.87584
4p	0.43558	2	12.19553
	−2.72185	3	3.86551
	2.98529	4	3.88453
4d	0.47272	3	4.91492
	−1.06401	4	2.26486
4f	5.75608	3	174.92507
	1.00000	3	2.34813
5s	0.06449	1	17.48288
	−0.23626	2	8.60223
	0.87120	3	3.96379
	−2.16702	4	2.66197
	2.06011	5	2.14909
5p	0.38421	2	3.08477
	−3.83305	3	2.94636
	3.00833	4	4.18583
	1.41635	5	1.86622
5d	0.39251	3	4.90992
	−5.97733	4	1.58830
	6.46988	5	1.78586
5f	3.71935	4	3.95979
	0.04105	4	8.01671
	0.00188	5	10.36780
	−3.97496	5	5.67567

(continued)

Table 46.1 (continued)

Cr orbitals	Expansion coefficients	Power of r	Exponents
5g	0.99920	5	1.80743
	0.00103	5	2.78801
6s	0.00574	1	30.11401
	−6.00052	2	0.70436
	29.18487	3	0.96064
	−45.52483	4	0.96020
	24.76138	5	1.02325
	−2.92685	6	3.51393
6p	0.95093	2	0.64495
	−6.89309	3	1.38487
	14.65819	4	1.37726
	−9.74981	5	1.38697
	0.54476	6	7.13854
6d	8.51503	3	6.20938
	3.78424	3	6.12032
	0.28204	4	10.51820
	−18.49657	4	7.29757
	8.68023	5	7.31500
	−2.68379	6	7.08827
6f	1.70149	4	0.50566
	0.00002	4	5.15571
	0.00001	5	6.13960
	−0.02537	5	2.02838
	−0.94472	6	1.00747
6g	5.19807	5	1.31085
	0.06269	5	2.33011
	−5.79279	6	1.43703
7s	0.02615	1	22.66804
	−4.31048	2	1.69449
	2.80355	3	3.49671
	−21.70683	4	1.05991
	11.16025	5	1.94050
	14.81340	6	1.25108
	0.05900	7	15.63781
7p	0.11809	2	4.43043
	−0.46493	3	3.28932
	−26.66817	4	0.89607
	1.89756	5	3.06518
	19.92076	6	1.44686
	7.61148	7	1.08703

Table 46.2 optmization (Cr)

Orbitals	Eigenvalue minimized	Term	Configuration
3p	$3s^2 3p^4$	^1S	$3s^2 3p^4$
3p	$3s^2 3p^4$	^1S	$3s^2 3p^4$
3d	$3s^2 3p^3 3d$	^3P	$3s^2 3p^3 3d$
4s	$3s^2 3p^3 4s$	^3S	$3s^2 3p^3 4s$
4p	$3s^2 3p^3 4p$	^3P	$3s^2 3p^4, 3s^2 3p^3 4p$
4d	$3s^2 3p^3 4d$	^1D	$3s^2 3p^3 3d, 3s^2 3p^3 4d$
4f	$3s^2 3p^3 4f$	^7F	$3s^2 3p^3 4f$
5s	$3s^2 3p^3 5s$	^3S	$3s^2 3p^3 4s, 3s^2 3p^3 5s$
5p	$3s^2 3p^3 5p$	^3P	$3s^2 3p^3 4p, 3s^2 3p^3 5p$
5d	$3s^2 3p^3 5d$	^3D	$3s^2 3p^3 3d, 3s^2 3p^3 4d, 3s^2 3p^3 5d$
5f	$3s^2 3p^3 5f$	^3P	$3s^2 3p^3 4f, 3s^2 3p^3 5f$
5g	$3s^2 3p^3 5g$	$3D$	$3s^2 3p^3 3d, 3s^2 3p^3 5g$
6s	$3s^2 3p^3 6s$	^3S	$3s^2 3p^3 4s, 3s^2 3p^3 5s, 3s^2 3p^3 6s$
6p	$3s^2 3p^3 6p$	^3P	$3s^2 3p^4, 3s^2 3p^3 4p, 3s^2 3p^3 5p, 3s^2 3p^3 6p$
6d	$3s^2 3p^3 6d$	^3D	$3s^2 3p^3 3d, 3s^2 3p^3 4d, 3s^2 3p^3 5d, 3s^2 3p^3 6d$
6f	$3s^2 3p^3 6f$	^3P	$3s^2 3p^4, 3s^2 3p^3 4f, 3s^2 3p^3 5f, 3s^2 3p^3 6f$
6g	$3s^2 3p^3 6g$	^3D	$3s^2 3p^3 3d, 3s^2 3p^3 5g, 3s^2 3p^3 6g$
7s	$3s^2 3p^3 7s$	^3S	$3s^2 3p^3 4s, 3s^2 3p^3 5s, 3s^2 3p^3 6s, 3s^2 3p^3 7s$
7p	$3s^2 3p^3 7p$	^3P	$3s^2 3p^4, 3s^2 3p^3 4p, 3s^2 3p^3 5p, 3s^2 3p^3 6p, 3s^2 3p^3 7p$

and

$$f_{ji} = \frac{2\delta E}{3g_j} | < \psi_i | \sum_{p=1}^{N} \nabla_p | \psi_j > |^2$$

where g_j is known as statistical factor.

$$\delta E = E_i - E_j$$

Above equations represent the sum of dipole matrix elements over electron co-ordinates. The results obtained from both equations are identical for exact wave function but it may vary for approximate wave functions.

Firstly, we have taken the non-relativistic hamiltonian for optimization of orbitals. The 1s, 2s, 2p, 3s and 3p orbitals are taken Hartree-Fock orbitals of Cr IX from Clemmenti and Roetti [10], while 3s and 3p orbitals re-optimized on $3s^2 3p^4 (^1S)$ for better results of ground states. Similarly, 3d to 7s orbitals optimised on different states where the optimised parameters of the radial wave-functions are shown in Tables 46.1 and 46.2.

Table 46.3 Energy levels of CrIX related to the ground state

Index	Configuration	Term	NIST (RYD)	CIV3 (RYD)	Percentage
1	$3s^2(^1S)3p^4$	$^3P_2$	0.0000	0.000000	96
2	$3s^2(^1S)3p^4$	$^3P_1$	0.07127	0.070570	98
3	$3s^2(^1S)3p^4$	$^3P_0$	0.0870	0.083874	95
4	$3s^2(^1S)3p^4$	$^1D_2$	0.2759	0.275057	95
5	$3s^2(^1S)3p^4$	$^1S_0$	0.6092	0.612776	95
6	$3s^1(^2S)3p^5$	$^3P_2$	2.1785	2.184259	75
7	$3s^1(^2S)3p^5$	$^3P_1$	2.2355	2.233347	74
8	$3s^1(^2S)3p^5$	$^3P_0$	2.26157	2.261574	74
9	$3s^1(^2S)3p^5$	$^1P_1$	2.7845	2.734454	47
10	$3s^23p^3(^4S)3d^1$	$^5D_0$		2.739794	97
11	$3s^23p^3(^4S)3d^1$	$^5D_1$		2.741541	96
12	$3s^23p^3(^4S)3d^1$	$^5D_2$		2.744810	96
13	$3s^23p^3(^4S)3d^1$	$^5D_3$		2.750067	96
14	$3s^23p^3(^4S)3d^1$	$^5D_4$		2.758708	96
15	$3s^23p^3(^2D)3d^1$	$^3D_2$		2.990240	48
16	$3s^23p^3(^2D)3d^1$	$^3D_3$		2.995760	50
17	$3s^23p^3(^2D)3d^1$	$^3D_1$		3.001344	51
18	$3s^23p^3(^2D)3d^1$	$^3F_2$		3.083040	76
19	$3s^23p^3(^2D)3d^1$	$^1S_0$		3.086611	96
20	$3s^23p^3(^2D)3d^1$	$^3F_3$		3.105094	79
21	$3s^23p^3(^2D)3d^1$	$^3F_4$		3.133548	82
22	$3s^23p^3(^2D)3d^1$	$^3G_3$		3.310777	95
23	$3s^23p^3(^2D)3d^1$	$^3G_4$		3.321402	94
24	$3s^23p^3(^2D)3d^1$	$^3G_5$		3.335596	97
25	$3s^23p^3(^2D)3d^1$	$^1G_4$		3.404211	94
26	$3s^23p^3(^2P)3d^1$	$^1D_2$		3.451813	73
27	$3s^23p^3(^2P)3d^1$	$^3P_0$		3.610666	72
28	$3s^23p^3(^2P)3d^1$	$^3D_1$		3.614078	57
29	$3s^23p^3(^2P)3d^1$	$^3F_3$		3.626316	79
30	$3s^23p^3(^2P)3d^1$	$^3F_4$		3.630771	79
31	$3s^23p^3(^2P)3d^1$	$^3F_2$		3.631241	72
32	$3s^23p^3(^2P)3d^1$	$^3P_1$		3.632164	72
33	$3s^23p^3(^2P)3d^1$	$^3D_2$		3.653801	53
34	$3s^23p^3(^2P)3d^1$	$^3P_2$		3.685693	75
35	$3s^23p^3(^2P)3d^1$	$^3D_3$		3.701616	57
36	$3s^23p^3(^2P)3d^1$	$^1F_3$		3.938627	58
37	$3s^23p^3(^2D)3d^1$	$^3P_2$	4.1418	4.134823	62
38	$3s^23p^3(^2D)3d^1$	$^3S_1$		4.140357	53
39	$3s^23p^3(^2D)3d^1$	$^3S_1$		4.174960	43
40	$3s^23p^3(^2D)3d^1$	$^3P_0$		4.194052	57

(continued)

Table 46.3   (continued)

Index	Configuration	Term	NIST (RYD)	CIV3 (RYD)	Percentage
41	$3s^2 3p^3(^2D)3d^1$	$^1P_1$		4.216268	36
42	$3s^2 3p^3(^4S)3d^1$	$^3D_3$	4.3268	4.332721	45
43	$3s^2 3p^3(^4S)3d^1$	$^3D_2$	4.3702	4.372507	43
44	$3s^2 3p^3(^4S)3d^1$	$^3D_1$	4.3992	4.398719	44
45	$3s^2 3p^3(^2D)3d^1$	$^1D_2$	4.4954	4.496758	73
46	$3s^2 3p^3(^2D)3d^1$	$^1F_3$	4.6270	4.627032	58
47	$3s^2 3p^3(^2P)3d^1$	$^1P_1$		4.960947	90
48	$(^1S)3p^6$	$^1S_0$		5.049203	59
49	$3s^1 3p^4(^4P)3d^1$	$^5D_4$		5.205091	99
50	$3s^1 3p^4(^4P)3d^1$	$^5D_3$		5.205196	98
51	$3s^1 3p^4(^4P)3d^1$	$^5D_2$		5.208750	98
52	$3s^1 3p^4(^4P)3d^1$	$^5D_1$		5.212985	99
53	$3s^1 3p^4(^4P)3d^1$	$^5D_0$		5.215828	99
54	$3s^1 3p^4(^4P)3d^1$	$^5F_5$		5.438807	99
55	$3s^1 3p^4(^4P)3d^1$	$^5F_4$		5.458221	98
56	$3s^1 3p^4(^4P)3d^1$	$^5F_3$		5.471719	98
57	$3s^1 3p^4(^4P)3d^1$	$^5F_2$		5.480739	98
58	$3s^1 3p^4(^4P)3d^1$	$^5F_1$		5.486250	99
59	$3s^1 3p^4(^4P)3d^1$	$^5P_1$		5.619336	99
60	$3s^1 3p^4(^4P)3d^1$	$^5P_2$		5.639510	99
61	$3s^1 3p^4(^4P)3d^1$	$^5P_3$		5.667903	99
62	$3s^1 3p^4(^4P)3d^1$	$^3D_1$		5.951700	46
63	$3s^1 3p^4(^4P)3d^1$	$^3F_4$		5.961240	90
64	$3s^1 3p^4(^4P)3d^1$	$^3P_0$		5.971419	59
65	$3s^1 3p^4(^4P)3d^1$	$^3P_1$		5.989932	55
66	$3s^1 3p^4(^4P)3d^1$	$^3F_3$		5.994484	86
67	$3s^1 3p^4(^4P)3d^1$	$^3P_2$		6.015352	28
68	$3s^1 3p^4(^4P)3d^1$	$^3F_2$		6.026347	56
69	$3s^1 3p^4(^2D)3d^1$	$^3D_2$		6.052716	34
70	$3s^1 3p^4(^2D)3d^1$	$^3D_3$		6.066590	44
71	$3s^1 3p^4(^2D)3d^1$	$^3G_3$		6.163574	97
72	$3s^1 3p^4(^2D)3d^1$	$^3G_4$		6.172766	98
73	$3s^1 3p^4(^2D)3d^1$	$^3G_5$		6.183321	98
74	$3s^1 3p^4(^2D)3d^1$	$^3F_2$		6.476387	91
75	$3s^1 3p^4(^2D)3d^1$	$^3F_3$		6.486116	91
76	$3s^1 3p^4(^2D)3d^1$	$^3F_4$		6.495097	90
77	$3s^1 3p^4(^2D)3d^1$	$^1P_1$		6.630719	63
78	$3s^1 3p^4(^2D)3d^1$	$^3S_1$		6.640118	96
79	$3s^1 3p^4(^2D)3d^1$	$^1G_4$		6.647747	98
80	$3s^1 3p^4(^2D)3d^1$	$^1D_2$		6.702203	46

(continued)

Table 46.3 (continued)

Index	Configuration	Term	NIST (RYD)	CIV3 (RYD)	Percentage
81	$3s^13p^4(^2P)3d^1$	$^3D_1$		6.733770	58
82	$3s^13p^4(^2P)3d^1$	$^3D_3$		6.752178	54
83	$3s^13p^4(^2P)3d^1$	$^3D_2$		6.774863	34
84	$3s^13p^4(^2S)3d^1$	$^3D_1$		6.798314	74
85	$3s^13p^4(^2S)3d^1$	$^3D_2$		6.810675	67
86	$3s^13p^4(^2S)3d^1$	$^3D_3$		6.821734	63
87	$3s^13p^4(^2D)3d^1$	$^1F_3$		6.886455	74
88	$3s^13p^4(^2P)3d^1$	$^3P_0$		7.013569	69
89	$3s^13p^4(^2P)3d^1$	$^3P_1$		7.036445	68
90	$3s^13p^4(^2P)3d^1$	$^3F_4$		7.109948	97
91	$3s^13p^4(^2P)3d^1$	$^3F_3$		7.121387	91
92	$3s^13p^4(^2P)3d^1$	$^3F_2$		7.128292	85
93	$3s^13p^4(^2P)3d^1$	$^3P_2$		7.167289	45
94	$3s^13p^4(^2P)3d^1$	$^1F_3$		7.267976	81
95	$3s^23p^3(^4S)4s^1$	$^5S_2$		7.276267	96
96	$3s^13p^4(^2S)3d^1$	$^1D_2$		7.294305	70
97	$3s^13p^4(^4P)3d^1$	$^3D_3$		7.403644	41
98	$3s^13p^4(^4P)3d^1$	$^3D_1$		7.410854	33
99	$3s^23p^3(^4S)4s^1$	$^3S_1$	7.4812	7.428128	95
100	$3s^13p^4(^4P)3d^1$	$^3D_2$		7.443035	40
101	$3s^13p^4(^2D)3d^1$	$^3P_1$		7.537274	46
102	$3s^13p^4(^2D)3d^1$	$^3P_0$		7.546416	48
103	$3s^13p^4(^2P)3d^1$	$^3P_2$		7.574604	45
104	$3s^23p^3(^2D)4s^1$	$^3D_1$	7.708	7.708441	93
105	$3s^23p^3(^2D)4s^1$	$^3D_2$	7.711	7.711739	92
106	$3s^23p^3(^2D)4s^1$	$^3D_3$	7.7264	7.722117	96
107	$3s^23p^3(^2D)4s^1$	$^1D_2$	7.7889	7.790176	92
108	$3s^23p^3(^2P)4s^1$	$^3P_0$		7.997857	96
109	$3s^23p^3(^2P)4s^1$	$^3P_1$		8.004037	93
110	$3s^23p^3(^2P)4s^1$	$^3P_2$		8.019923	89
111	$3s^23p^3(^2P)4s^1$	$^1P_1$	8.0356	8.085309	91
112	$3s^13p^4(^2P)3d^1$	$^1P_1$		8.106427	69
113	$3p^5(^2P)3d^1$	$^3P_0$		8.230237	64
114	$3p^5(^2P)3d^1$	$^3P_1$		8.246921	64
115	$3p^5(^2P)3d^1$	$^3P_2$		8.279115	63
116	$3s^13p^4(^2D)3d^1$	$^1S_0$		8.321457	61
117	$3p^5(^2P)3d^1$	$^3F_4$		8.440393	62
118	$3p^5(^2P)3d^1$	$^3F_3$		8.456255	61
119	$3s^13p^4(^2P)3d^1$	$^1D_2$		8.460875	78
120	$3p^5(^2P)3d^1$	$^3F_2$		8.476667	61

(continued)

Table 46.3 (continued)

Index	Configuration	Term	NIST (RYD)	CIV3 (RYD)	Percentage
121	$3s^1 3p^3 (^5 S) 3d^2$	$^5 D_4$		8.541361	74
122	$3s^1 3p^3 (^5 S) 3d^2$	$^5 D_3$		8.544474	74
123	$3s^1 3p^3 (^5 S) 3d^2$	$^5 D_1$		8.549182	75
124	$3s^1 3p^3 (^5 S) 3d^2$	$^5 D_0$		8.550393	75
125	$3s^1 3p^3 (^5 S) 3d^2$	$^5 D_2$		8.550697	75
126	$3s^1 3p^3 (^3 D) 3d^2$	$^5 G_2$		8.683663	61
127	$3s^1 3p^3 (^5 S) 3d^2$	$^5 G_3$		8.686590	62
128	$3s^1 3p^3 (^5 S) 3d^2$	$^5 G_5$		8.689958	63
129	$3s^1 3p^3 (^5 S) 3d^2$	$^5 G_6$		8.692446	67
130	$3p^5 (^2 P) 3d^1$	$^3 D_3$		8.701837	59
131	$3p^5 (^2 P) 3d^1$	$^3 D_2$		8.710122	59
132	$3p^5 (^2 P) 3d^1$	$^3 D_1$		8.710975	59
133	$3s^1 3p^3 (^5 S) 3d^2$	$^5 P_1$		8.719765	48
134	$3s^1 3p^3 (^5 S) 3d^2$	$^5 P_2$		8.732956	48
135	$3s^1 3p^3 (^5 S) 3d^2$	$^5 F_5$		8.734438	45
136	$3s^1 3p^3 (^5 S) 3d^2$	$^5 F_1$		8.737977	50
137	$3s^1 3p^3 (^5 S) 3d^2$	$^5 F_2$		8.747155	49
138	$3s^1 3p^3 (^5 S) 3d^2$	$^5 P_3$		8.748496	47
139	$3s^1 3p^3 (^5 S) 3d^2$	$^5 F_3$		8.757289	50
140	$3s^1 3p^3 (^5 S) 3d^2$	$^5 F_4$		8.762536	42
141	$3s^1 3p^3 (^5 S) 3d^2$	$^5 G_4$		8.792918	40
142	$3p^5 (^2 P) 3d^1$	$^1 F_3$		8.821935	64
143	$3p^5 (^2 P) 3d^1$	$^1 D_2$		8.846817	68
144	$3s^1 3p^3 (^3 P) 3d^2$	$^5 G_6$		8.962516	78
145	$3s^1 3p^3 (^3 P) 3d^2$	$^5 G_3$		9.029069	61
146	$3s^1 3p^3 (^3 P) 3d^2$	$^5 G_2$		9.031702	60
147	$3s^1 3p^3 (^3 D) 3d^2$	$^5 F_5$		9.048878	38
148	$3s^1 3p^3 (^3 P) 3d^2$	$^5 G_4$		9.054955	38
149	$3s^1 3p^3 (^3 D) 3d^2$	$^5 F_1$		9.057889	75
150	$3s^1 3p^3 (^3 D) 3d^2$	$^5 F_2$		9.061665	70
151	$3s^1 3p^3 (^3 D) 3d^2$	$^5 F_3$		9.065799	68
152	$3s^1 3p^3 (^3 P) 3d^2$	$^5 G_5$		9.075090	36
153	$3s^1 3p^3 (^3 D) 3d^2$	$^5 F_4$		9.080241	39
154	$3s^1 3p^3 (^5 S) 3d^2$	$^5 S_2$		9.219064	81
155	$3s^1 3p^3 (^5 S) 3d^2$	$^3 F_4$		9.276607	34
156	$3s^1 3p^3 (^5 S) 3d^2$	$^3 F_3$		9.294551	35
157	$3s^2 3p^3 (^4 S) 4d^1$	$^5 D_0$		9.307908	74
158	$3s^2 3p^3 (^4 S) 4d^1$	$^5 D_1$		9.309177	82
159	$3s^1 3p^3 (^5 S) 3d^2$	$^3 F_2$		9.309204	34
160	$3s^2 3p^3 (^4 S) 4d^1$	$^5 D_2$		9.311645	93
161	$3s^2 3p^3 (^4 S) 4d^1$	$^5 D_3$		9.313588	93
162	$3s^2 3p^3 (^4 S) 4d^1$	$^5 D_4$		9.317151	95

(continued)

Table 46.3 (continued)

Index	Configuration	Term	NIST (RYD)	CIV3 (RYD)	Percentage
163	$3s^13p^3(^3P)3d^2$	$^5D_0$		9.318258	55
164	$3s^13p^3(^3P)3d^2$	$^5D_1$		9.320555	55
165	$3s^13p^3(^3P)3d^2$	$^5D_3$		9.344851	59
166	$3s^13p^3(^3D)3d^2$	$^3D_1$		9.350707	31
167	$3s^13p^3(^3D)3d^2$	$^3D_2$		9.360723	28
168	$3s^23p^3(^4S)4d^1$	$^3D_2$	9.372	9.371849	82
169	$3s^23p^3(^4S)4d^1$	$^3D_3$	9.376	9.371850	91
170	$3s^13p^3(^3P)3d^2$	$^5D_4$		9.372457	67
171	$3s^23p^3(^4S)4d^1$	$^3D_1$	9.378	9.373528	93
172	$3s^13p^3(^3D)3d^2$	$^3D_3$		9.396213	30
173	$3s^13p^3(^3D)3d^2$	$^3G_4$		9.399884	81
174	$3s^13p^3(^3D)3d^2$	$^3G_5$		9.401281	84
175	$3s^13p^3(^3D)3d^2$	$^5F_5$		9.535132	46
176	$3s^13p^3(^5S)3d^2$	$^3P_0$		9.561390	40
177	$3s^13p^3(^3D)3d^2$	$^5G_6$		9.584799	49
178	$3s^13p^4(^4P)4s^1$	$^5P_3$		9.603936	82
179	$3s^13p^4(^4P)4s^1$	$^5P_2$		9.627864	71
180	$3s^13p^4(^4P)4s^1$	$^5P_1$		9.640243	65
181	$3s^13p^4(^4P)4s^1$	$^3P_1$		9.819480	76
182	$3s^13p^4(^4P)4s^1$	$^3P_0$		9.840375	79
183	$3s^23p^3(^4S)4p^1$	$^3P_0$		10.067927	62
184	$3s^23p^3(^2D)4p^1$	$^3F_4$		10.404458	88
185	$3s^23p^23d^1(^4F)4s$	$^{15}F_4$		10.965089	75
186	$3s^23p^23d^1(^4F)4s$	$^{15}F_5$		10.999900	80
187	$3s^23p^3(^4S)4f^1$	$^5F_5$		11.086604	77
188	$3s^23p^3(^4S)5g^1$	$^5G_6$		12.282009	100

46.3 Results

The lowest 188 fine-structure levels of Cr IX with respect to ground level are shown in Table 46.3, where theoretical results compared with the experimental energies which are compiled in the NIST database [11–13]. There is a good agreement of our tabulated results with data listed in NIST data and other available results. Our results agree within 0.8% deviation from the NIST data except the level $3s^23p^4(^3P_2)$ with 0.9% ,$3s^23p^4(^3P_1)$ with 3.0% and $3s^13p^5(^1P_1)$ with 2.0% deviations as shown in Table 46.3. That means the levels of agreement with the NIST data were found to depends on the level of mixing configurations between various levels. From the table titled "Leading percentage", we first give the percentage of the basis state corresponding to the level's name. Next, the second-largest percentage together with related that basis state and so on.

Table 46.4 Oscillator strengths in length and velocity gauges

Lower Conf.	Terms	Upper conf.	Terms	Wavelength	f_L	f_v	$\frac{f_L}{f_v}$
$3s^2(^1S)3p^4$	$^1D_2$	$3s^23p^3(^2P)4s^1$	$^1P_1$	2.2483282	$0.59807D-01$	$0.61212D-01$	0.98
$3s^1(^2S)3p^5$	$^3P_1$	$3s^13p^4(^2P)3d^1$	$^3D_2$	3.8665498	$0.60964D-01$	$0.58485D-01$	1.04
$3s^23p^3(^2P)3d^1$	$^3P_1$	$3s^13p^4(^2P)3d^1$	$^3P_2$	4.9672905	$0.57446D-01$	$0.55640D-01$	1.03
$3s^23p^3(^4S)3d^1$	$^3D_1$	$3s^13p^4(^4P)3d^1$	$^3D_2$	5.7666037	$0.60578D-01$	$0.59911D-01$	1.01
$3s^1(^2S)3p^5$	$^3P_1$	$3s^13p^4(^2P)3d^1$	$^3P_2$	3.2876154	$0.24180D+00$	$0.23797D+00$	1.02
$3s^2(^1S)3p^4$	$^3P_2$	$3s^23p^3(^2D)4s^1$	$^3D_2$	2.2771055	$0.27543D-01$	$0.26696D-01$	1.03
$3s^2(^1S)3p^4$	$^3P_2$	$3s^23p^3(^2P)4s^1$	$^3P_2$	2.1895494	$0.35459D-01$	$0.34173D-01$	1.04
$3s^2(^1S)3p^4$	$^1D_2$	$3s^23p^3(^2D)3d^1$	$^3P_2$	4.5495039	$0.62446D-02$	$0.63027D-02$	0.99
$3s^2(^1S)3p^4$	$^1D_2$	$3s^23p^3(^2D)4s^1$	$^1D_2$	2.3366252	$0.14672D+00$	$0.15411D+00$	0.95
$3s^23p^3(^4S)3d^1$	$^5D_2$	$3s^13p^4(^4P)3d^1$	$^5F_2$	6.4171040	$0.59216D-01$	$0.56773D-01$	1.04
$3s^13p^4(^4P)3d^1$	$^5F_2$	$3s^13p^3(^3D)3d^2$	$^5F_2$	4.9037593	$0.14623D-01$	$0.15030D-01$	0.97
$3s^23p^3(^2D)3d^1$	$^3D_2$	$3s^13p^4(^4P)3d^1$	$^3F_2$	5.7831966	$0.31223D-01$	$0.30473D-01$	1.02
$3s^23p^3(^2D)3d^1$	$^3F_2$	$3s^13p^4(^2D)3d^1$	$^3D_2$	5.9130896	$0.17310D-01$	$0.17427D-01$	0.99
$3s^23p^3(^2P)3d^1$	$^1D_2$	$3s^13p^4(^2D)3d^1$	$^1D_2$	5.4024260	$0.14641D+00$	$0.14192D+00$	1.03
$3s^23p^3(^2P)3d^1$	$^3F_2$	$3s^13p^4(^2S)3d^1$	$^3D_2$	5.5229805	$0.46637D-01$	$0.46823D-01$	1.00
$3s^23p^3(^2P)3d^1$	$^3P_2$	$3s^13p^4(^2P)3d^1$	$^3P_2$	5.0436629	$0.12247D+00$	$0.12074D+00$	1.01
$3s^23p^3(^4S)4s^1$	$^5S_2$	$3s^13p^4(^4P)4s^1$	$^5P_2$	7.4672653	$0.22052D-01$	$0.22143D-01$	1.00
$3s^2(^1S)3p^4$	$^3P_2$	$3s^23p^3(^2D)4s^1$	$^3D_3$	2.2740464	$0.74162D-01$	$0.77662D-01$	0.95
$3s^13p^4(^4P)3d^1$	$^5F_2$	$3s^13p^3(^5S)3d^2$	$^5G_3$	5.4774852	$0.41162D-01$	$0.42112D-01$	0.98
$3s^23p^3(^4S)3d^1$	$^3D_3$	$3s^13p^4(^2P)3d^1$	$^3P_2$	5.4152661	$0.86742D-01$	$0.88307D-01$	0.98
$3s^1(^2S)3p^5$	$^3P_2$	$3s^13p^4(^2D)3d^1$	$^1F_3$	3.7344253	$0.11319D-01$	$0.11240D-01$	1.01
$3s^23p^3(^2P)3d^1$	$^3P_2$	$3s^13p^4(^4P)3d^1$	$^3D_3$	4.7230304	$0.13034D-01$	$0.13470D-01$	0.97
$3s^23p^3(^4S)3d^1$	$^5D_3$	$3s^13p^4(^4P)3d^1$	$^5F_3$	6.4507365	$0.49657D-01$	$0.49258D-01$	1.01
$3s^13p^4(^4P)3d^1$	$^5F_3$	$3s^13p^3(^3D)3d^2$	$^5F_3$	4.8858141	$0.16279D-01$	$0.16877D-01$	0.96
$3s^23p^3(^2P)3d^1$	$^3F_3$	$3s^13p^4(^2S)3d^1$	$^3D_3$	5.4953667	$0.31486D-01$	$0.32526D-01$	0.97
$3s^13p^4(^4P)3d^1$	$^5D_3$	$3s^13p^3(^5S)3d^2$	$^5F_4$	4.9362750	$0.43186D-01$	$0.45390D-01$	0.95
$3s^13p^4(^4P)3d^1$	$^5D_3$	$3s^13p^3(^5S)3d^2$	$^5G_4$	4.8944714	$0.11418D-01$	$0.12015D-01$	0.95
$3s^23p^3(^2P)3d^1$	$^3F_4$	$3s^13p^4(^2D)3d^1$	$^1F_3$	5.3936409	$0.34557D-01$	$0.36067D-01$	0.96
$3s^23p^3(^2D)3d^1$	$^3G_3$	$3s^13p^4(^2D)3d^1$	$^3G_4$	6.1355936	$0.12970D-01$	$0.13356D-01$	0.97
$3s^23p^3(^4S)3d^1$	$^5D_4$	$3s^13p^4(^4P)3d^1$	$^5F_4$	6.5035874	$0.32223D-01$	$0.33434D-01$	0.96
$3s^13p^4(^4P)3d^1$	$^5F_4$	$3s^13p^3(^3D)3d^2$	$^5F_4$	4.8481261	$0.16791D-01$	$0.16376D-01$	1.03
$3s^23p^3(^2D)3d^1$	$^1G_4$	$3s^13p^4(^2D)3d^1$	$^1G_4$	5.4138446	$0.21476D+00$	$0.22234D+00$	0.97
$3s^13p^4(^4P)3d^1$	$^5F_4$	$3s^13p^3(^5S)3d^2$	$^5G_5$	5.4336102	$0.41263D-01$	$0.41759D-01$	0.99
$3s^23p^3(^4S)3d^1$	$^5D_4$	$3s^13p^4(^4P)3d^1$	$^5F_5$	6.5506888	$0.15430D+00$	$0.14698D+00$	1.05
$3s^23p^3(^2D)3d^1$	$^3G_4$	$3s^13p^4(^2D)3d^1$	$^3G_5$	6.1357423	$0.10556D-01$	$0.10512D-01$	1.00
$3s^13p^4(^4P)3d^1$	$^5F_5$	$3s^13p^3(^5S)3d^2$	$^5G_6$	5.3970329	$0.45952D-01$	$0.46111D-01$	1.00
$3s^2(^1S)3p^4$	$^3P_0$	$3s^23p^3(^2D)4s^1$	$^3D_1$	2.3031437	$0.71928D-01$	$0.70749D-01$	1.02
$3s^2(^1S)3p^4$	$^3P_0$	$3s^23p^3(^2P)4s^1$	$^3P_1$	2.2171273	$0.93340D-01$	$0.94753D-01$	0.99
$3s^1(^2S)3p^5$	$^1P_1$	$(^1S)3p^6$	$^1S_0$	7.5861281	$0.88045D-01$	$0.87285D-01$	1.01
$3s^23p^3(^2P)3d^1$	$^3D_1$	$3s^13p^4(^2P)3d^1$	$^3P_0$	5.1652702	$0.12147D+00$	$0.11905D+00$	1.02
$3s^23p^3(^2P)3d^1$	$^3P_1$	$3s^13p^4(^2P)3d^1$	$^3P_0$	5.1931054	$0.34138D-01$	$0.33961D-01$	1.01
$3s^23p^3(^2D)3d^1$	$^3S_1$	$3s^13p^4(^2D)3d^1$	$^3P_0$	5.1555178	$0.13162D+00$	$0.12826D+00$	1.03
$3s^1(^2S)3p^5$	$^3P_1$	$3s^13p^4(^4P)4s^1$	$^3P_0$	2.3083915	$0.47889D-01$	$0.47949D-01$	1.00

(continued)

Table 46.4 (continued)

Lower Conf.	Terms	Upper conf.	Terms	Wavelength	f_L	f_v	$\frac{f_L}{f_v}$
$3s^1(^2S)3p^5$	$^3P_0$	$3s^13p^4(^2D)3d^1$	$^1P_1$	4.0190925	$0.34068D-01$	$0.35757D-01$	0.95
$3s^1(^2S)3p^5$	$^3P_0$	$3s^13p^4(^2D)3d^1$	$^3S_1$	4.0104652	$0.25047D+00$	$0.25904D+00$	0.97
$3s^1(^2S)3p^5$	$^3P_0$	$3s^13p^4(^2P)3d^1$	$^3D_1$	3.9264823	$0.17692D+00$	$0.18413D+00$	0.96
$3s^23p^3(^2P)3d^1$	$^3P_0$	$3s^13p^4(^2P)3d^1$	$^3D_1$	5.6226086	$0.11598D+00$	$0.11620D+00$	1.00
$3s^23p^3(^2P)3d^1$	$^3P_0$	$3s^13p^4(^2P)3d^1$	$^3P_1$	5.1258402	$0.14685D+00$	$0.14239D+00$	1.03
$3s^1(^2S)3p^5$	$^3P_0$	$3s^13p^4(^2D)3d^1$	$^3P_1$	3.3284681	$0.61561D+00$	$0.59831D+00$	1.03
$3s^1(^2S)3p^5$	$^3P_0$	$3s^13p^4(^4P)4s^1$	$^3P_1$	2.3233947	$0.12379D+00$	$0.12242D+00$	1.01
$3s^2(^1S)3p^4$	$^3P_1$	$3s^23p^3(^2D)4s^1$	$^3D_1$	2.2991318	$0.33603D-01$	$0.32449D-01$	1.04
$3s^2(^1S)3p^4$	$^3P_1$	$3s^23p^3(^2P)4s^1$	$^3P_1$	2.2134092	$0.15830D-01$	$0.15535D-01$	1.02
$3s^1(^2S)3p^5$	$^3P_1$	$3s^13p^4(^2D)3d^1$	$^3S_1$	3.9847761	$0.29302D+00$	$0.30125D+00$	0.97
$3s^1(^2S)3p^5$	$^3P_1$	$3s^13p^4(^2P)3d^1$	$^3D_1$	3.9018546	$0.40661D-01$	$0.41845D-01$	0.97
$3s^23p^3(^2P)3d^1$	$^3P_1$	$3s^13p^4(^2P)3d^1$	$^3D_1$	5.6615795	$0.23050D-01$	$0.23324D-01$	0.99
$3s^23p^3(^2P)3d^1$	$^3D_1$	$3s^13p^4(^2P)3d^1$	$^3P_1$	5.1307458	$0.56659D-01$	$0.54696D-01$	1.04
$3s^23p^3(^2P)3d^1$	$^3P_1$	$3s^13p^4(^2P)3d^1$	$^3P_1$	5.1582092	$0.64708D-01$	$0.62313D-01$	1.04
$3s^23p^3(^4S)3d^1$	$^3D_1$	$3s^13p^4(^4P)3d^1$	$^3D_1$	5.8281967	$0.16596D+00$	$0.16077D+00$	1.03
$3s^1(^2S)3p^5$	$^1P_1$	$3s^13p^4(^2P)3d^1$	$^1P_1$	3.2688158	$0.33864D+00$	$0.35442D+00$	0.96
$3s^1(^2S)3p^5$	$^3P_1$	$3s^13p^4(^4P)4s^1$	$^3P_1$	2.3147495	$0.36920D-01$	$0.36672D-01$	1.01
$3s^2(^1S)3p^4$	$^3P_1$	$3s^23p^3(^2D)4s^1$	$^3D_2$	2.2981363	$0.52452D-01$	$0.53041D-01$	0.99
$3s^2(^1S)3p^4$	$^3P_1$	$3s^23p^3(^2P)4s^1$	$^3P_2$	2.2089871	$0.40996D-01$	$0.42437D-01$	0.97
$3s^1(^2S)3p^5$	$^3P_2$	$3s^13p^4(^2D)3d^1$	$^1P_1$	3.9492085	$0.11055D-01$	$0.11015D-01$	1.00
$3s^1(^2S)3p^5$	$^3P_2$	$3s^13p^4(^2D)3d^1$	$^3S_1$	3.9408783	$0.27993D+00$	$0.28700D+00$	0.98
$3s^23p^3(^2P)3d^1$	$^3D_2$	$3s^13p^4(^2P)3d^1$	$^3P_1$	5.1910117	$0.14681D+00$	$0.14473D+00$	1.01
$3s^23p^3(^2P)3d^1$	$^3P_2$	$3s^13p^4(^2P)3d^1$	$^3P_1$	5.2406139	$0.24881D-01$	$0.25904D-01$	0.96
$3s^1(^2S)3p^5$	$^3P_2$	$3s^13p^4(^4P)4s^1$	$^3P_1$	2.2998677	$0.37323D-01$	$0.37481D-01$	1.00

Most of the levels show very strong mixing in our calculations. For e.g.; we found that the strong mixing is present in the $^3D_2$ level of $3s^23p^3(^2D)3d$ with 48% of the $3s^23p^3(^2D)3d(^3D_2)$ and 39% of the $3s^23p^3(^4S)3d(^3D_2)$ level. That levels belonging to the $3s^13p^4(^2D)3d$ configurations have been presented for the first time. This spectrum belonging to the configuration has so many stronger mixing. Two ^3P symmetries are belonging to the configuration, one is due to $3s^13p^4(^2P)3d(^3P)$(level 88-89) and other due to $3s^13p^4(^2D)3d(^3P)$(level 101–102). That means ^3P symmetry (level 88–89) of $3s^13p^4(^2P)3d(^3P)$ has a strong mixing with ^3P symmetry of $3s^13p^4(^2D)3d(^3P)$(level 101–102). Similarly, ^3D symmetry of $3s^13p^4(^2P)3d(^3D)$(level 81-83) shows very strong mixing with ^3D symmetry of $3s^13p^4(^2D)3d(^3D)$(level 69–70) i.e. it is hard to recognize the levels. Therefore, the spectrum belonging to $3s^13p^43d$ configuration is very elaborated and needs further investigation.

To provide useful data to Astrophysics and also gain an additional understanding of the Atomic Structure calculations [10]. Accurate oscillator strengths are important for determining modeling, radiation loss and Astrophysical plasmas. We have also presented the oscillator strengths for the transitions of the states of CrIX as shown

in Table 46.4. We presented the oscillator strengths in both the length and velocity formulations. One can see that there is a close agreement between the length of f_L and the velocity f_v forms in most of our results. A little difference between velocity and length forms for few transitions, can be due to possible cancellations of dipole integrals and oversight of very faraway configurations.

46.4   Conclusion

In this paper, excitation energies and oscillator strengths are calculated for Cr IX using program CIV3. The lowest 188 fine-structure levels are listed in the Table 46.3. Energies for most of the levels belonging to $3s^2 3p^4 3d^1$ and $3s^1 3p^3 3d^2$ configurations and many of the other levels have been calculated for first time. In most of the cases, our calculated energy levels are compared very well with the NIST data although some energy levels inconsistencies are shown in the Table 46.3. The agreement between length and velocity form of oscillator strength reflects the quality of wavefunction for present calculations. This way, CIV3 method helped us to predict a new data which will form a basis for future work.

References

1. H.S Chou, Chin. J. Physiol. **38**, 914 (2000)
2. E.B. Saloman, Y.K. Kim, At. Data Nucl. Data Tables **41**, 339 (1989)
3. E. Biemont, J.E Hansen, Phys. Scr. **34**, 116 (1986)
4. E.B. Saloman, Y.K. Kim, Phys, Rev. A **38**, 577 (1988)
5. H.S. Chou, J.Y. Chang, Y.H. Chang, K.N. Huang, At. Data Nucl. Tables **62**, 77 (1996)
6. G. Del Zanna, P.J. Storey, H.E. Mason, A and A **514** (2010)
7. Annual Report of National Institute for fusion science (2010–2011)
8. R. Glass, A. Hibbert, Comput. Phys. Comm. **16**, 19 (1978)
9. A. Hibbert, Comput. Phys. Commun. **9**, 141 (1975)
10. E. Clementi, C. Roetti, At. Data Nucl. Data Tables **14**, 177 (1974)
11. L.A. Svenssion, Phys. Scr. **4**, 111 (1971)
12. L.A. Svensson, J.O. Ekberg, Ark. Fys **37**, 65 (1968)
13. J. Sugar, C. Corliss, J. Phys. Chem. Ref. Data, **14**(2), 1 (1985)

Chapter 47
Evolution of Plasma Wave Oscillations in Terahertz Frequency Regime in the Wake of Ultra-Short Laser Irradiation on Air Plasma

Divya Singh

Abstract Plasma is a fourth state of matter consisting of electron, ions and neutrals depending on the extent of ionization. Inherently plasma remains in thermal equilibrium with uniform exchange rate of plasma species however with the exposure of intense laser pulse through the plasma set up oscillations in the plasma leading to the energy transfer from laser to plasma medium. The oscillation propagates in the form of a plasma wave which dies out further in the plasma. The analysis of the field oscillations of plasma wave for different laser pulse profiles is done with the effect of external DC magnetic field and damping forces of plasma species. If theses oscillations are brought in the THz frequency range by proper tailoring of laser pulses, this will open up a new avenue for the development of THz radiation sources.

47.1 Introduction

Plasma being a fourth state of matter is highly interesting and evolving field of study because of the capacity of holding high electrical powers regardless of the breakdown of plasma altogether with the complicated plasma species dynamics, which further involved in giving rise to several interesting phenomenon. It is important to note that the plasma parameters like plasma density, plasma frequency, non-linear excited fields possess a long varied range that makes it suitable for wide range of applications. Out of all the much talked applications of plasma such as nuclear fusion reactors, accelerators, radiation sources etc. we will focus on the development of radiation sources emitting in terahertz frequency range. Development of THz sources has been a much evolved research field in the last few decades due to their employability in several applications such as imaging, material characterization, topography, tomography, short distance communication etc. This is the reason why, Interaction

D. Singh (✉)

Computational Plasma Dynamics Laboratory, Rajdhani College, University of Delhi, New Delhi 110015, India
e-mail: dsingh@rajdhani.du.ac.in

of high intense lasers with gas or solid targets has been studied extensively for developing high power tunable THz radiation sources. Gas targets such as air plasma serve better than the solid targets because there is no material damage at high power of lasers. Indeed, laser plasma interaction has tremendous application such as laser induced fusion [1, 2], acceleration [3], THz radiation sources etc. The first signal of THz frequency range is observed by Cook et al. [4] and later by Hamster et al. [5, 6]. They explained the mechanism of THz emission in their experiments based on the ponderomotive force caused radial acceleration of the ionized electrons. The quality and characterization of THz sources is decided by few key factors which are maximum field amplitude of emitted radiation, frequency bandwidth and conversion efficiency of the mechanism, therefore entire research is about to realize the experiments in order to achieve envisioned THz radiation sources of tunable amplitude and frequency. Indeed, the usage of two color laser enables generation of asymmetric electron dynamics in the photo-induced plasma and therefore THz generation. Other groups had proposed the use of beating of two co-propagating super-Gaussian laser in place of conventional Gaussian lasers because of better amplitude of emitted THz [7, 8]. Wang and coworkers performed theoretical as well as simulation studies to support emission of powerful terahertz by usage of chirped [9] and few cycle laser pulses [10]. Jha et al. [11] had reported THz emission from laser wakefield with Gaussian laser in the magnetized plasma. On the other hand, Sheng et al. [12] applied an approach of mode conversion where large amplitude plasma wakefield in the presence of axial density gradient plasma produces radiation at the plasma frequency (ω_p). So far, it is observed that all the schemes of wakefield excitation have not discussed weakly ionized collisional plasma. We here present an analytical scheme of terahertz emission based on the propagation of super intense short duration laser pulses through uniform density magneto-collisional plasma where ions are fixed. It will be interesting to study the laser plasma interaction for THz generation with employment of different profile of lasers. As it is important to learn that laser profile play a major role in the generation of nonlinearity in the plasma, Hence, I propose in the present paper to analyze the mechanism of THz emission from laser wakefield in the weakly ionized plasma with propagation of skew Cosh-Gaussian lasers.

47.2　Plasma Wave Oscillations on Laser Irradiation

The linearly polarized laser propagates in the z direction of weakly ionized air plasma (collisional frequency—ν among plasma species) of uniform density ρ_0. A magnetic field B is applied transversely to the laser field as well as laser propagation. The Cosh-Gaussian laser profile is presented as $\vec{E} = E_{oL}e^{i(kz-\omega t)}\hat{y}$, where $E_{oL} = E_L \cosh^n\left(\frac{ys}{b_w}\right)e^{-\left(\frac{ys}{b_w}\right)^2}$,$n$, s, ω and k are laser field amplitude, laser order, skewness index, laser frequency and wave number respectively. A specific index of n, s brings asymmetry in the laser shape which is known as skewness. A sharp skewness due to asymmetric intensity of Cosh-Gaussian laser helps setting up large

amplitude plasma oscillations eventually responsible for radiation emission. In order to understand plasma oscillations setup by laser irradiation, we perform a study for lasers of various index $n = 1, 2$ and $s = 0, 0.5, 1.0, 1.5, 2.0$ where b_w is the beamwidth of the laser. The plasma electron dynamics is specified by equation of motion given as $m \frac{\partial \vec{v}}{\partial t} = F_{EM} + F_D$ where $F_{EM} = -e[\vec{E} + \frac{1}{c}\{\vec{v} \times \vec{B}\}]$ is electromagnetic Lorentz force; $F_D = -mv\vec{v}$ is damping force. Above equation of motion is solved to different orders of plasma electron velocities components $\vec{v}_x^{(0)}, \vec{v}_z^{(0)}, \vec{v}_y^{(0)}, \vec{v}_x^{(1)}, \vec{v}_y^{(1)}, \vec{v}_z^{(1)}$ respectively. The damping forces and Lorentz force which introduces cyclotron oscillations (frequency $\omega_c = \frac{eB}{mc}\hat{x}$,) to plasma electrons henceforth establishes the nonlinearity in the plasma dynamics which further give rise to different orders of nonlinear density perturbations ($\rho_x^{(1)}, \rho_y^{(1)}, \rho_z^{(1)}$) computed using equation of continuity $\frac{\partial \rho}{\partial t} + \vec{\nabla}.(\rho_0 \vec{v}) = 0$ where ρ_0 is the ambient plasma density. Finally, the plasma oscillation along with density fluctuations drives various components of nonlinear plasma current densities evaluated as $\vec{J} = -\rho e \vec{v}$ such as, $J_x^{(1)} = 0$, $J_y^{(1)} = \rho_0 e^2 \frac{i\omega(\omega+iv)}{(\omega-k\vec{v}_y^{(0)})} \frac{E}{m\omega'}$ and $J_z^{(1)} = \rho_0 e^2 \frac{\omega_c E}{m\omega'}$, where $\omega' = [(\omega+iv)^2 - \omega_c^2]$. In the next section, it is discussed that how generated nonlinear current densities are responsible for excitation of electromagnetic fields in THz frequency regime in the magnetized plasma.

47.3 Excitation of Electromagnetic Fields in the Plasma

Using the time dependent Maxwell's $\vec{\nabla} \times \vec{E}_{Ex} = -\frac{1}{c}\frac{\partial \vec{B}_{Ex}}{\partial t}; \vec{\nabla} \times \vec{B}_{Ex} = \frac{4\pi}{c}\vec{J} + \frac{1}{c}\varepsilon\frac{\partial \vec{E}_{Ex}}{\partial t}$, we evaluate excited electric ($\vec{E}_{Ex}$) and magnetic ($\vec{B}_{Ex}$) fields inside plasma. It is considered that the laser pulse evolves quasi-statically during its propagation through plasma therefore electromagnetic fields are assumed to be quasistatic i.e. time independent. The Maxwell's equations are transformed and solved to the moving laser frame with coordinates $\xi = z - v_g t$, v_g is group velocity of laser.

$$\left\{ \frac{\partial^2}{\partial \xi^2} + \frac{4\pi \rho_0 e^2}{mc^2} \right\} \vec{E}_{Exz} = -\frac{k_p^2 m}{e}\left[\omega_c v_y^{(0)} - v v_z^{(1)}\right] \tag{47.1}$$

where, k_p is plasma wave number. Horizontal component ($E_{Exz} = E_z$) of excited wakefield is obtained from (47.1) with boundary condition $\{\xi = 0, \vec{E}_{Exz} = 0 \& \xi = L/2, \vec{E}_{Exz} = 0\}$; L is the laser pulse length. Further, vertical ($E_{Exy} = E_y$) component of excited field which actually serve as a terahertz field component is obtained and calculated as follows,

$$E_{Exy} = -\frac{1}{k_p^2}\frac{(\omega - k v_y^{(0)})}{\omega}\frac{\partial^2 \vec{E}_{Exz}}{\partial \xi \partial y} - \frac{mv}{e}v_y^{(1)} \tag{47.2}$$

$$\vec{E}_{THz} = \vec{E}_{Exy} = \frac{1}{ik_p^2} \frac{(\omega + iv)E_{oL}}{\omega'} \times$$

$$\left[\left\{ \begin{array}{l} \dfrac{k_p \omega_c (\omega - k v_y^{(0)})}{\omega} \dfrac{(\omega^2 - \omega_c^2 + iv\omega)}{(i\omega - v)^2} (\sin k_p \xi - \tan \dfrac{k_p L}{4} \cos k_p \xi) \times \\ \left[\dfrac{ns}{b_w} \tanh \left(\dfrac{ys}{b_w} \right) - \dfrac{2ys}{b_w^2} \right] \end{array} \right\} - k_p^2 v \right]$$

$$(47.3)$$

There is no x-component of excited electric field ($\vec{E}_x = 0$) in the plasma.

47.4 Discussion

The main approach used in the present paper is to employ skew Cosh-Gaussian laser for combination of index and skewness parameters (n = 1, 2 and s = 0, 0.5, 1.0, 1.5, 2.0) for the maximized field excitation in the plasma. It is interesting to note that order-n of laser loses its significance for s = 0 which corresponds to the Gaussian laser. Figure 47.1 depicts the longitudinal excited plasma wakefield for different profile skew Cosh-Gaussian lasers where magenta color represents Gaussian laser (s = 0), blue and green color corresponds to first and second order of laser respectively. It is observed that larger field amplitude are emitted when skew Cosh-Gaussian lasers are employed in place of Gaussian laser when laser frequency matches with plasma
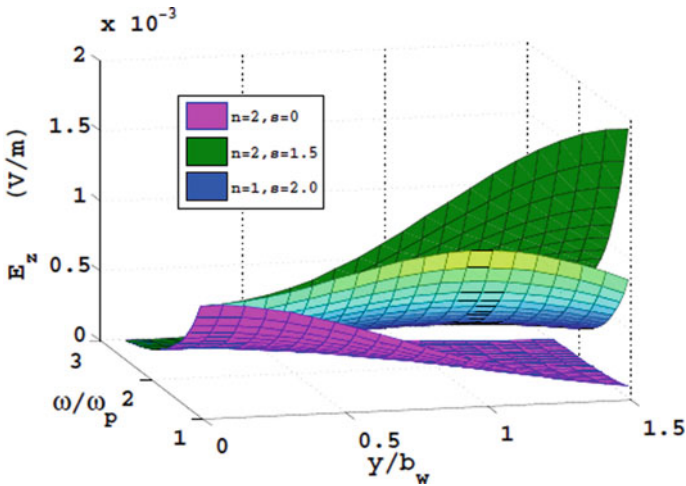
Fig. 47.1 3D visualization of behavior of horizontal excited field with normalized frequecy and normalized beam width for index (n) and skewness parameter (s) when $\omega = 2.4 \times 10^{14}$ rad/s, $\omega_p = 2.0 \times 10^{13}$ rad/s, y = 0.5b_w, $E_0 = 5.0 \times 10^8$ V/m, $b_w = 0.01$ cm and L = 0.5λ_p

frequency ($\omega/\omega_p = 1$). It is evident from Fig. 47.1 that the excited field amplitude decays with departure from the condition that ω is not equal to ω_p. It is already shown mathematically from 47.1 that, the horizontal excited field is responsible for evolution of transverse electromagnetic fields which is emitted as THz radiation.

The visualization of behavior of horizontal excited field with normalized beam width of laser in plasma is due to the maximized magnitude of nonlinear force at particular transverse distance—y. This particular y is different for Gaussian laser as well as for different order skew Cosh-Gaussian lasers. Gaussian laser gives better field amplitude for on axis propagation i.e. $y = 0$ whereas Cosh-Gaussian lasers are suitable when y is in the range from $1.0b_w$ to $1.5b_w$. However second order laser provides largest magnitude of excited field which is followed by first order laser. Therefore, Cosh-Gaussian lasers serve better than the normal Gaussian laser in view of terahertz emission from plasma excited fields.

For further understanding, the variation of normalized THz field amplitude with normalized propagation distance in the plasma is shown from Figs. 47.2 and 47.3. It is evident from both figures that the transverse fields are progressive and periodic in nature and amplitude of THz field is sufficiently good for Gaussian laser ($s = 0$) and drops for skew Cosh-Gaussian laser for combinations of laser index -n and skewness parameters—s except two particular set (Fig. 47.2 $n = 1$, $s = 2.0$ and Fig. 47.3 $n = 2$, $s = 1.5$) known as critical set of parameters. This rapid enhancement of the THz field amplitude for critical set is attributed to the excitation of large amount of nonlinear plasma currents. Therefore, it is obvious from Fig. 47.2 that critical parameter set $1(n = 1, s = 2.0)$ and from Fig. 47.3 that critical parameter set $2(n = 2, s = 1.5)$ are the most suited skewness parameter of Cosh-Gaussian laser pulse in order to obtain large amplitude of THz radiation than Gaussian laser. Since, most of the available lasers have Gaussian profile however there are optical shapers in experimental optics
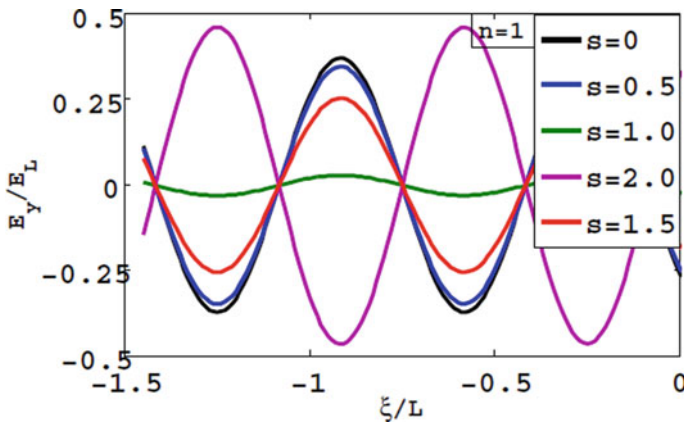
Fig. 47.2 Normalized THz field with normalized propagation distance of laser in plasma for $n = 1$ and various skewness parameter (s) when $\omega = 2.4 \times 10^{14}$ rad/s, $\omega_p = 2.0 \times 10^{13}$ rad/s, $y = 0.5b_w$, $E_0 = 5.0 \times 10^8$ V/m, $b_w = 0.01$ cm and $L = 0.5\lambda_p$
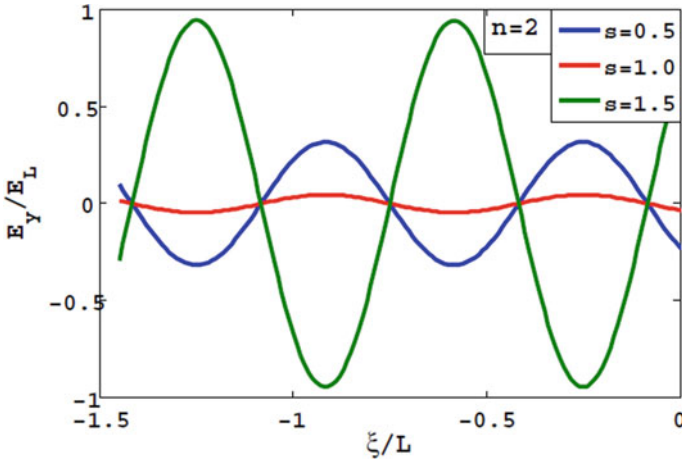
Fig. 47.3 Normalized THz field with normalized propagation distance of laser in plasma for $n = 2$ and various skewness parameter (s) when $\omega = 2.4 \times 10^{14}$ rad/s, $\omega_p = 2.0 \times 10^{13}$ rad/s, $y = 0.5b_w$, $E_0 = 5.0 \times 10^8$ V/m, $b_w = 0.01$ cm and $L = 0.5\lambda_p$
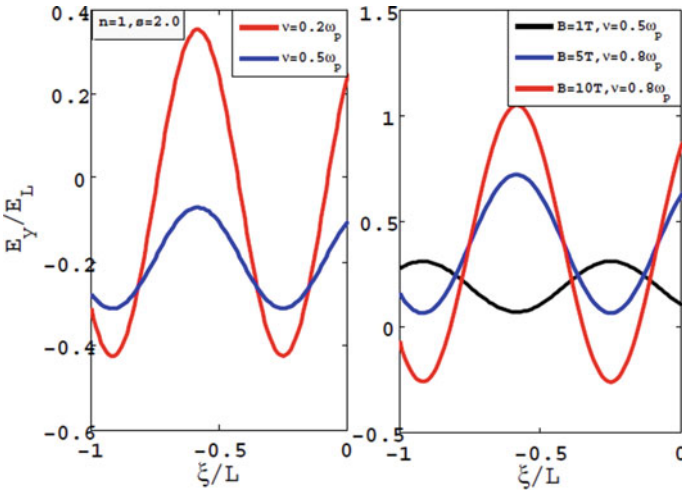
Fig. 47.4 Collision dependent variation of Normalized THz field amplitude with normalized propagation distance of laser in magnetized plasma for skewness parameter ($n = 1$, $s = 2$), when $\omega = 2.4 \times 10^{14}$ rad/s, $\omega_p = 2.0 \times 10^{13}$ rad/s, $y = 0.5b_w$, $E_0 = 5.0 \times 10^8$ V/m, $b_w = 0.01$ cm and $L = 0.5\lambda_p$

to shape different order Cosh-Gaussian laser pulses. However second order ($n = 2$) laser is more suitable than first order ($n = 1$) laser.
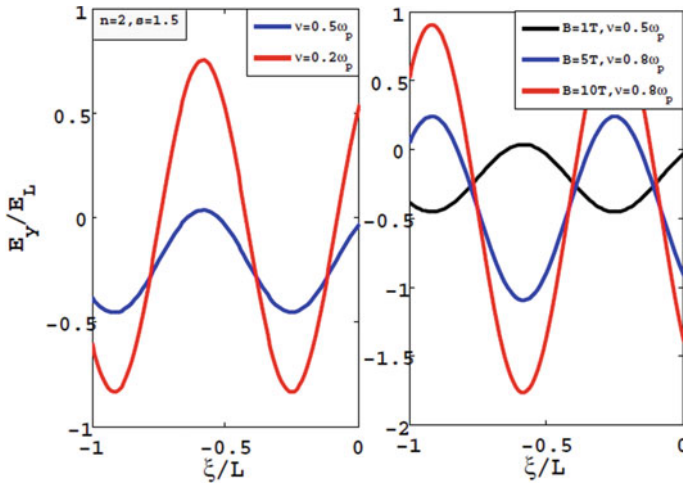
Fig. 47.5 Collision dependent variation of Normalized THz field amplitude with normalized propagation distance of laser in magnetized plasma for skewness parameter ($n = 2$, $s = 1.5$) when other parameters are same as the Fig. 47.4

To illustrate the impact of collision amongst plasma species and external magnetic field on emitted transverse field, Figs. 47.4 and 47.5 are plotted to depict the variation of THz field with normalized laser propagation distance. For the first order laser, Fig. 47.4a shows amplitude variation dependence on collision frequency range from $0.2\omega_p$ to $0.5\ \omega_p$ with simultaneous enhancement effect of external transverse magnetic field of strength 1 to 10 T in Fig 47.4b. This maximum normalized amplitude of THz field is attributed to the large nonlinear plasma currents which strongly depend on the laser pulse shape, collision frequency and magnetic field. The graph with red line corresponds to $\nu = 0.2\omega_p$ (plasma may be approximated as less collisional) gives maximum amplitude whereas slight increase in collisional frequency corresponds to $\nu = 0.5\omega_p$ (corresponds to blue line) results sharp decay in the field amplitude. Comparative graphs are plotted for different collision rate $\nu = 0.5\omega_p$, $0.8\omega_p$ as well as magnetic field B = 1, 5 and 10 T are consistent. The decay in the field amplitude due to collisions may be reasoned due to the loss of energy and momentum. The field amplitude decay may be supplemented by employment of external magnetic field of strength upto 10 T. Hence it is obvious from the respective Fig. 47.4 (critical parameter set 1; $n = 1$, $s = 2.0$) and Fig. 47.5 (critical parameter set 2; $n = 2$, $s = 1.5$) that the slight increase in the collision frequency lead to a sharp decay in the amplitude of THz field.

Thus, similar dependence of THz field amplitude on collision and magnetic field is observed for first and second order Cosh-Gaussian lasers for their respective critical set of parameters. It is important to note that second order laser gives better enhancement in the THz field amplitude than first order. From the above discussion it is clear that the skew Cosh-Gaussian lasers have been proven as potential lasers for efficient mechanism of THz emission in collisional plasma.

Many schemes of terahertz radiation generation have neglected the collisional effects. However, it is very important to talk about the collisions in experimental plasma based THz radiation generation schemes. Though mostly, experimental plasma is weakly collisional ($\nu < \omega_p$). In the present discussion, very low collision frequency regimes are considered ranging from $\nu = 0.2\,\omega_p$ to $0.8\,\omega_p$ (Figs. 47.4 and 47.5). This regime is also weakly collisional but our findings show that these even low electron neutral collisions affects the emission of THz radiation drastically. Therefore it is very important to study collisions in the mechanism as fraction of collision frequency may alter the entire mechanism, that's why employment of skew Cosh-Gaussian laser in presence of magnetic field is highly suggested.

On the other hand it is considered that these large amplitude plasma wave oscillations are excited with a different dispersion relation. Therefore, a plasma wave and an EM wave having different dispersion relation cannot be inter-convertible. But, numerical studies have shown the evidences of such conversion around the plasma frequency from the excited fields in inhomogeneous plasma [13] with relativistic effects [14].

47.5 Conclusions

It is concluded that the study performed on the evolution of THz radiation in the wake of skew cosh-Gaussian laser propagating in a weakly ionized magnetized collisional plasma with two sets of critical parameters i.e. $n = 1$, $s = 1.5$ and $n = 2$, $s = 1.0$ are quite potential to give rise to transverse electromagnetic fields from excited plasma field, which are emitted in terahertz frequency range. Here we tried to point out that maximum THz radiations are emitted when skew Cosh-Gaussian lasers of critical parameters are used than Gaussian laser in presence of weakly collisional effects of magnetized plasma.

References

1. C. Deutsch, H. Furukaw, K. Mima, M. Murakami, K. Nishihara, Phys. Rev. Lett. **77**, 2883–2886 (1996)
2. H. Hora, Laser part. Beams **23**, 441–451 (2004)
3. U. Teubner, P. Gibbon, Rev. Mod. Phys. **81**, 445–473 (2009)
4. D.J. Cook, R.M. Hochstrasser, Opt. Lett. **25**, 1210 (2000)
5. H. Hamster, A. Sullivan, S. Gordon, W. White, R.W. Falcone, Phys. Rev. Lett. **71**, 2725 (1993)
6. H. Hamster, A. Sullivan, S. Gordon, R.W. Falcone, Phys. Rev. E **49**, 671 (1994)
7. D. Singh, H.K. Malik, Phys. Plasmas **21**, 083105 (2014)
8. D. Singh, H.K. Malik, Plasma Sourc. Sci. Tech. **24**, 045001 (2015)
9. W.-M. Wang, Z.-M. Sheng, H.-C. Wu, M. Chen, C. Li, J. Zhang, K. Mima, Opt. Expr. **16**, 16999 (2008)
10. W.-M. Wang, S. Kawata, Z.M. Sheng, Y.T. Li, J. Zhang, Phys. Plasmas **18**, 073108 (2011)
11. P. Jha, A. Saroch, R.K. Mishra, Europhys. Lett. **94**, 15001 (2011)

12. Z.M. Sheng, K. Mima, J. Zhang, H. Sanuki, Phys. Rev. Lett. **94**, 095003 (2005); Z.M. Sheng, K. Mima, J. Zhang, Phys. Plasmas **12**, 123103 (2005)
13. Z.-M. Sheng et al., Phys. Rev. E **69**, 025401 (2004)
14. R. Gill, D. Singh, H.K. Malik, J. Theoret. Appl. Phys. **11**, 103–108 (2017)

Chapter 48
Efficient Supercontinuum Generation in Lead Silicate PCF Employing Tan-Hyperbolic Gaussian Pulses

Check for updates

Monika Kalita, Rimlee Saikia, Mohit Sharma, and Nitu Borgohain

Abstract In this paper, we have theoretically investigated an efficient generation of supercontinuum in photonic crystal fiber by the aid of tan-hyperbolic Gaussian pulses of peak power 100 W, pulse duration 50 fs, launched at 1.55 μm wavelength. It is found that the generated spectra are asymmetric, and composed of oscillatory structure, indicating prominant domination of self-phase modulation. The spanning of the spectra increases with the increase of the tan-hyperbolic parameter Ω_0. With increase of Ω_0, the steepness of the temporal pulses increases in tailing edges, which results in the asymmetric growth of the spectra extending more towards the longer wavelength region. The results may have potential application in photonic devices.

48.1 Introduction

Optical supercontinuum (SC) generation is a phenomenon that leads to the generation of broadband spectrum which occurs owing to the propagation of a narrowband pulse through nonlinear media [1–5]. During propagation, the broadening of the pulse has contributions from various nonlinear phenomena such as self-phase modulation (SPM), cross-phase modulation (XPM), Modulation Instability (MI), soliton generation, etc. [3–5]. Among these, the dominant phenomenon is the SPM, by virtue of which an optical pulse propagating in a medium inflicts a phase modulation on itself leading to broadening of the pulse spectrum. The physical origin of the phenomenon can be understood from the fact that being an intensity-dependent effect, SPM results in an intensity-dependent phase shift that produces an oscillation in the pulse, causing

M. Kalita · N. Borgohain (✉)
Department of Physics, University of Science & Technology Meghalaya, Ri-Bhoi, Meghalaya 793101, India

R. Saikia
Department of Physics, Gauhati University, Guwahati, Assam 781014, India

M. Sharma
Department of Physics, Mody University of Science and Technology, Laxmangarh, Rajasthan 332311, India

to a broadband spectrum (or SC) at the output. Apart from this, SC is also resulted from the generation of new frequencies due to other higher-order nonlinear effects such as self-steepening, Raman scattering, etc. [4–7]. The effect of dispersion of the medium also plays a vital role in the spreading of the output pulse.

The SC generation has been vastly studied in various nonlinear media like conventional optical fibers, silica waveguides, chalcogenide waveguides, etc. [8, 9], but researchers have shown keen interest mostly in the photonic crystal fibers (PCFs). The popularity of the PCFs for SC generation rose due to two important facts: the existence of a customizable dispersive profile using dispersion engineering [2–5, 10–12] and the existance of large nonlinearity. In general, the SC generation in these nonlinear media is being investigated by employing either 'sec-hyperbolic' or 'Gaussian' pulses. The temporal profiles of these pulses are having not much notable difference, and the results of SC in both cases are almost similar. A few years back, the effect of non-Gaussian pulses on SC generation also has been investigated by few researchers [13–15]. They reported interesting results of spectral broadening due to SPM by using non-Gaussian pulses such as 'sinh-Gaussian' as well as 'cosh-Gaussian'. Thus, in view of the above results, we have investigated the SC generation in lead silicate PCFs by employing 'tanh-Gaussian' pulses.

48.2 PCF Properties

To study the propagation dynamics of the optical pulses, first we proceed with the designing of a PCF made up of lead silicate glass. The cross-section of the proposed fiber is demonstrated in Fig. 48.1. The fiber cladding is composed of eight rings of hexagonally arranged air holes of diameter $d_1 (= 1.6\,\mu\text{m})$, along with a small centrally placed air hole of diameter $d_2 (= 1.2\,\mu\text{m})$. To maintain an adequate index contrast, an additional round of air holes of diameter d_1 is designed at the periphery, which provides a tightly confined optical field at the center of the PCF. A typical mode field at $1.55\,\mu\text{m}$ wavelength is demonstrated in Fig. 48.1. In the designed PCF, the effective nonlinear coefficient (γ) of the designed fiber, which plays an important role in self-phase modulation, is calculated as $\gamma = 923\,\text{W}^{-1}\,\text{km}^{-1}$ at the pump wavelength $1.55\,\mu\text{m}$.

Employing the method of finite difference time domain (FDTD) the linear optical properties of the designed fiber have been investigated. The sum of waveguide dispersion and material dispersion gives the total dispersion $D_C(\lambda)$ of the fiber i.e., $D_C(\lambda) = D_M(\lambda) + D_W(\lambda)$ and is mathematically expressed by $D_C(\lambda) = -\frac{\lambda}{c}\frac{d^2 n_{eff}}{d\lambda^2}$, where λ is operating wavelength, c is the speed of light, $n_{eff} = \frac{\lambda}{2\pi}\beta$ is the effective refractive index of the fiber, n_{eff} is the effective refractive index of the fundamental mode and β is the propagation constant.

An important property of the designed fiber is that it simultaneously possesses a low value of anomalous dispersion as well as a large nonlinear coefficient. The higher-order dispersion coefficients β_n s at $1.55\,\mu\text{m}$ wavelength is found to be: $\beta_2 =$
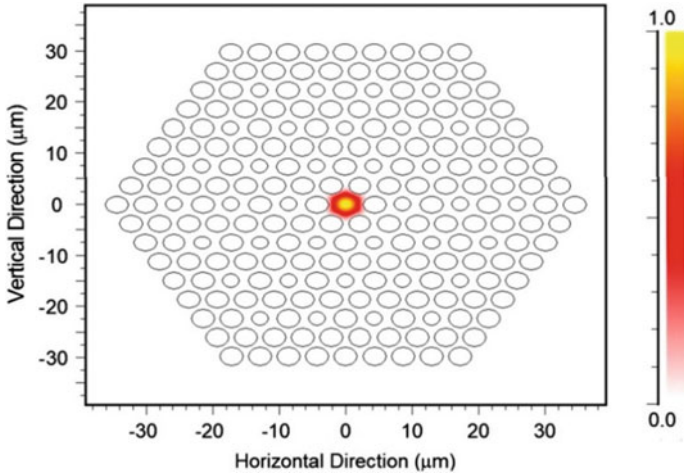
Fig. 48.1 Cross-section of the designed PCF and transverse mode profile at $z = 0$, where $d_1 = 1.6\,\mu$m, and $d_2 = 1.2\,\mu$m

$-4.26594\,\text{ps}^2/\text{km}$, $\beta_3 = 1.45625 \times 10^{-2}\,\text{ps}^3/\text{km}$, $\beta_4 = -1.12520 \times 10^{-5}\,\text{ps}^4/\text{km}$, $\beta_5 = 4.46556 \times 10^{-8}\,\text{ps}^5/\text{km}$, $\beta_6 = -6.26561 \times 10^{-10}\,\text{ps}^6/\text{km}$, $\beta_7 = 1.56481 \times 10^{-11}\,\text{ps}^7/\text{km}$, $\beta_8 = -3.02525 \times 10^{-13}\,\text{ps}^8/\text{km}$, $\beta_9 = 5.81231 \times 10^{-15}\,\text{ps}^9/\text{km}$ and $\beta_{10} = -2.5646 \times 10^{-16}\,\text{ps}^{10}/\text{km}$, where β_n is the nth order of the Taylor series expansion of the propagation constant around the central frequency ω_0.

48.3 Analysis of the Tanh-Gaussian Pulse

To investigate the spectral broadening in the designed PCF, we employed a tanh-Gaussian pulse, which is expressed as

$$A(z, t) = A_0 e^{-\frac{(1+iC)\tau^2}{2}} \left[1 - \tanh^m(\Omega_0 \tau) \right], \tag{48.1}$$

where the parameter Ω_0 is associated with tanh part, A_0 is a constant which defines the power of the pulse and C is the chirp. The parameter 'm' controls the degree of sharpness, although, for our convenience, we take $m = 1$, and $C = 0$ throughout our investigation. In Fig. 48.2 we have depicted the pulses given by (48.1) for different tanh factor Ω_0. It is seen that, for non-zero tanh-parameter ($\Omega_0 > 0$), the tanh-Gaussian pulses possess steepening at the trailing edges. For comparison, we plot the profile of Gaussian pulse, for which $\Omega_0 = 0$. It is evident from the figure that the intensity of tanh-Gaussian pulses peaked slightly away from $\tau = 0$ position, which distinguishes these pulses from the Gaussian counterpart. In addition, the steepness of the tanh-Gaussian pulses also increases with an increase in the value of Ω_0.
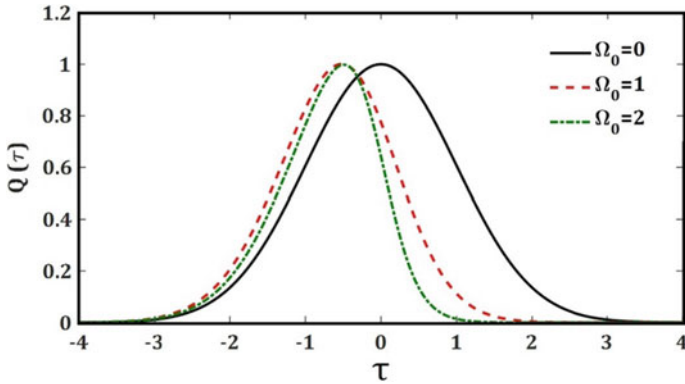
Fig. 48.2 Profile of tanh-Gaussian pulses at different values of tanh factor Ω_0 at normalized intensity

Next, we proceed to the analysis of the frequency shift [5] of the tanh-Gaussian pulses. In Fig. 48.3, we plot the frequency shift of the pulses for different tanh-parameters ($\Omega_0 = 0\,to\,2$). Profile for $\Omega_0 = 0$ corresponds to the Gaussian pulse. It is observed from Fig. 48.3 that, for the Gaussian pulse the leading edge is red-shifted while the trailing edge experiences blueshifting. On analyzing the tanh-Gaussian pulses we observe that it experiences both redshift as well as blue shift simultaneously. For smaller values of $\Omega_0(= 1)$ the leading edge pulse undergoes both red- as well as blueshifted. The trailing edge of the pulse follows blue shifting and a small portion is being red-shifted. As the tanh-parameter increases $\Omega_0(= 2)$ the simultaneous red- and blueshifting on both leading and trailing edges becomes more prominent.
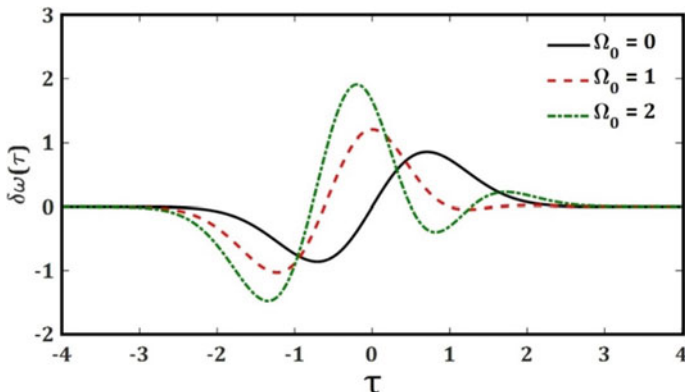
Fig. 48.3 Variation of nonlinear frequency shift ($\delta\omega$) of tanh-Gaussian pulses of different values of Ω_0

48.4   Numerical Modeling for Spectral Broadening in PCF

The nonlinear Schrödinger equation (NLSE) [5] can be used to describe the propagation of optical pulse in the PCF, and the same can be written in a retarded frame as

$$\frac{\partial}{\partial z}A(z, T) = -\frac{\alpha}{2}A(z, T) + \sum_{j \geq 2}\frac{i^{j+1}}{j!}\beta_j\frac{\partial^j}{\partial T^j}A(z, T)$$

$$+ i\left(1 + \frac{i}{\omega}\frac{\partial}{\partial T}\right)A\int_{-\infty}^{\infty}R(T')\left|A(z, T - T')\right|^2 dT' \qquad (48.2)$$

here, α represents the fiber loss, $\beta_j\left(= \frac{d^j\beta}{d\omega^j}\right)$ is the dispersion coefficient of different order (j) at the central frequency ω_0. $R(T)$ gives the nonlinear response function which includes the contribution of delayed Raman response as well as the instantaneous electronic response. The same can be written as, $R(T) = (1 - f_R)\delta(T) + f_R h_R(T)$, $f_R = 0.1$ for lead silicate PCF and $h_R(T)$ is calculated using $h_R(T) = \frac{\tau_1^2 + \tau_2^2}{\tau_1\tau_2^2}e^{\left(-\frac{T}{\tau_2}\right)}\sin\left(\frac{T}{\tau_1}\right)$, with $\tau_1 = 5.5$ fs and $\tau_2 = 32$ fs. Using the *split-step Fourier method* the nonlinear Schrödinger equation is solved, the details of which can be found elsewhere [3–5].

48.5   Supercontinuum Generation

We now proceed to examine the supercontinuum generation by tanh-Gaussian pulses in the designed PCF. We take a 12 cm long PCF and inject the pulses with peak power of 100 W, 50 fs FWHM (full width at half maxima) pulse duration, pumped at 1.55 µm wavelength. Due to the small length of the fiber, the fiber loss will be insignificant, thus neglected. For the sake of comparison, first, we launch a Gaussian pulse ($\Omega_0 = 0$). The spectral evolution of the SC for the Gaussian pulse is depicted in panel (a) of Fig. 48.4. From Fig. 48.4a it is clear that the spectrum of the Gaussian pulse, at the fiber end, achieves a wide span of ~ 1.64 µm. The spectrum develops multiple oscillations around the pumping wavelength, which is the signature of SPM induced spectral broadening. The spectrum smoothly extends towards the longer wavelength side, due to the effect of higher-order dispersions and nonlinear effects. Next, we plot the spectral profile of tanh-Gaussian pulse for $\Omega_0 = 1$, which is depicted in panel (b) of Fig. 48.4. From the Fig. 48.4b it is seen that, with an increase of the tanh parameter Ω_0, the spectrum achieves a spanning of ~ 2.12 µm, which is quite larger than the Gaussian counterpart. In this case also, the spectrum is found to be asymmetric around the pumping wavelength, and composed of more numbers SPM induced oscillations. The extension of the spectrum towards the longer wavelength side may be caused by many effects: steepening of the pulse at the trailing edge,
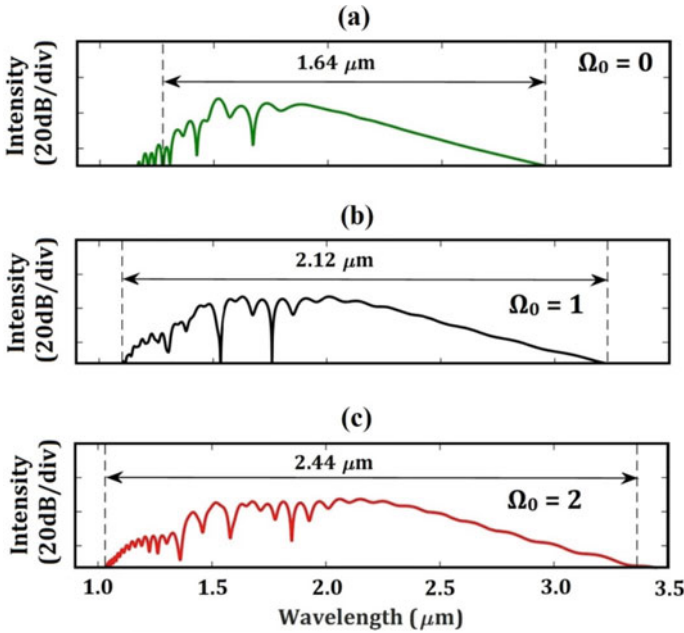
Fig. 48.4 Spectral profiles of the supercontinuum of Gaussian and tanh-Gaussian pulses

the dispersive effect due to the higher-order dispersion terms as well as nonlinear effects. The SC spectrum of tanh-Gaussian pulse for $\Omega_0 = 2$ is plotted in panel (c) of Fig. 48.4. From the figure, it is evident that with further increase of tanh factor Ω_0 the spectral broadening increases up to a spanning of $\sim 2.44\,\mu$m. Like the previous case, a large number of oscillations due to SPM dominates the spectrum, and steepening of the pulse, as well as dispersion of the medium, extends the spectrum more towards the longer wavelength region, resulting in an asymmetric spectral broadening. From Fig. 48.4a, and c, it is seen that for tanh-Gaussian pulses with $\Omega_0 = 2$, the generated SC spectrum is about 1.5 times wider than the Gaussian counterpart. In addition, with $\Omega_0 = 2$, we achieved almost a flat-top spectra for a range of wavelength $\sim 1.50 - 2.50\,\mu$m.

48.6 Conclusion

In conclusion, present a theoretical investigation on the SPM dominated SC generation in lead silicate PCFs by employing tanh-Gaussian pulses of peak power 100 W, pulse duration 50 fs, pumped at $1.55\,\mu$m wavelength. Results show that the generated spectra of the tanh-Gaussian pulses are associated with SPM induced oscillatory structures around the pumping wavelength. The spectra are also found to be extended towards the longer wavelength regions due to steepening present in the

temporal profile of the tanh-Gaussian pulses. It is also observed that the SC broadening increases with the increase of the tanh factor Ω_0. The SC spectrum for the case of $\Omega_0 = 2$ is found to be about 1.55 times wider than its Gaussian counterpart. These results may have potential applicability in the optical devices for supercontinuum sources.

References

1. J.K. Ranka, R.S. Windeler, A. Stentz, Opt. Lett. **25**, 25–27 (2000)
2. P. Russell, Science **299**, 358–362 (2003)
3. J.M. Dudley, G. Genty, G. Coen, Rev. Mod. Phys. **78**, 1135–1184 (2006)
4. J.M. Dudley, J.R. Taylor, *Supercontinuum Generation in Optical Fibers*, 1st edn. (Cambridge University Press, UK, 2010)
5. G.P. Agarwal, *Nonlinear Fiber Optics*, 4th edn. (Academic Press, New York, 2006)
6. R.A. Martinez et al., Opt. Lett. **43**, 296 (2018)
7. M.L. Ferhat, L. Cherbi, *Proceedings Volume 9886, Micro-Structured and Specialty Optical Fibres IV*, 98860C (2016)
8. N. Singh et al., Light: Sci. Appl. **7**, 17131 (2018)
9. S. Dai, Y. Wang, X. Peng, P. Zhang, X. Wang, Y. Xu, Appl. Sci. **8**, 707 (2018)
10. F. Begum, Y. Namihira, T. Kinjo, S. Kaijage, Electron. Lett. **46**, 1518–1520 (2010)
11. B. Barviau, B. Kibler, A. Kudlinski, A. Mussot, G. Millot, A. Picozzi, Opt. Exp. **17**, 7392 (2009)
12. J. Leagsgaard, S. Barkou, K. Hougaard, M. Nielsen, J. Jensen, A. Bjarklev, Mat. Res. Soc. Symp. Proc. **797** (2004)
13. S. Konar, S. Jana, Opt. Commun. **236**, 7 (2004)
14. N. Borgohain, S. Konar, J. Nanophoton. **9**, 093098 (2015)
15. N. Borgohain, M. Sharma, S. Konar, Optik **127**, 1630 (2016)

Chapter 49
Calculations of Total Ionization Cross-Sections for Electron Impact on H_2SO_4

Smruti Parikh, Chetan Limbachiya, and K. N. Joshipura

Abstract The present study investigates the total ionization cross-section, Q_{ion} for the electron collisions with Sulfuric acid (H_2SO_4), which has been identified as key component in aerosol formation over energy range from ionization potential (IP) to 5000 eV. For the calculation of total inelastic cross-section, Q_{inel} Spherical Complex Optical Potential (SCOP) method is used. The Q_{ion}, is then calculated using a semi-empirical approach, called the Complex Spherical Potential-ionization contribution (CSP-ic). We have studied Q_{ion} using various models employed for molecular charge density.

49.1 Introduction

The main human-caused sulfur-containing compound, sulfur dioxide (SO_2) is directly emitted into the Earth's atmosphere and by the atmospheric oxidation of SO_2, sulfuric acid (H_2SO_4) is produced [1]. Isotopic and geological evidence indicates that the water in liquid form was earlier present on all the planets of our solar system. Moreover, the clouds made up of H_2SO_4 and H_2O solution are present in the atmosphere of Venus [2]. Furthermore, geological study suggests that Mercury, Venus, Earth and Mars were volcanically active in their earlier time period. The typical component of volcanic degassing is sulfur dioxide, which is soluble in water and by oxidizing it can form sulfuric acid (H_2SO_4) [2]. In the atmospheric nucleation, this H_2SO_4 has been identified as the key component [3, 4]. The major source of atmospheric aerosol particles are atmospheric nucleation and successive growth of newly formed particles. These aerosol particles are part of the climate of our Earth [5]. The aerosol particles scatter the sunlight and lowers the temperature. Also, aerosols present in the troposphere can alter the dimensions of the cloud particles, and hence modify the characteristics of clouds of absorbing and reflecting the sunlight,

S. Parikh (✉) · C. Limbachiya
The Maharaja Sayajirao University of Baroda, Vadodara 390001, India

K. N. Joshipura
(Retd) Sardar Patel University, Vallabh Vidyanagar 388120, India

Table 49.1 Ionization potentials [8]

Target	IP (eV)	Target	IP (eV)	Target	IP (eV)
H	13.60	S	10.36	O	13.62
P	10.48	H_2SO_4	12.40	H_3PO_4	11.72

which in turn affects the Earth's energy budget. The most remarkable impact of these aerosols is damaging of stratospheric ozone layer [6].

The molecules present in the atmosphere are impacted by the secondary electrons generated by the cosmic ray particles and radiations from the sun. Hence, electron-interactions with atmospheric molecules is the dominant natural phenomenon in the atmosphere. Ionization is the most basic channel in all the inelastic processes which opens for the energy above the ionization potential of the molecules and ionization cross-sections of electron collisions with atmospheric compounds are very important in many applied fields of sciences, like plasma sciences, astrophysics, biomedical researchs, radio sciences, industrial fields, etc. [7].

For the present study, the target we choose here is H_2SO_4, because of its importance in atmosphere of Earth as well as other planets. Lack of theoretical and experimental investigations for this molecule encouraged us to carry out this study. In this present work, the data of the ionization cross-section, Q_{ion} for electron collision with H_2SO_4 has been reported for the energy from the molecular IP to 5 keV. For this calculation, we have used CSP-ic (Complex Scattering Potential-ionization contribution) method. Since this is the first attempt to study the electron interactions with H_2SO_4, we have computed the Q_{ion} using various models. These models include Independent Atom Model (IAM) using atomic as well as molecular properties. Moreover, we have carried a study to understand the dependence of Q_{ion} on the molecular IP and the molecular size through number of target electrons (N) by evaluating Q_{ion} for H_3PO_4 which is having same number of electrons (N = 50) as H_2SO_4 and comparing with cross sections of H_2SO_4. In Table 49.1 we show ionization potential of the target atom/molecules [8].

49.2 Theoretical Methodology

Total ionization cross-section, Q_{ion}, for the electron interaction with H_2SO_4 molecule is calculated using SCOP method as mentioned in our earlier publications [9, 10]. The e-molecule scattering potential is defined as,

$$V(r, E_i) = V_R(r, E_i) + V_I(r, E_i) \tag{49.1}$$

Here the real term V_R consists of potentials to describe static, electron exchange and polarization effects caused by electron impact on the molecule. The imaginary term V_I corresponds to absorption potential which takes care of the lost flux of

electrons leading to inelastic effects. Various model potentials have been used to represent these effects and to construct the complex potential which is then used as input for solving the Schrödinger equation and the total inelastic cross-sections are then computed using the partial wave analysis [9, 10] such that,

$$Q_{inel}(E_i) = Q_{ion}(E_i) + \sum Q_{exc}(E_i) \qquad (49.2)$$

Here, $\sum Q_{exc}$ represent all allowed electronic excitation cross-sections, which gradually reduce at higher energies above the IP [11, 12]. Thus, we can have

$$Q_{inel} \geq Q_{ion} \qquad (49.3)$$

The Complex Scattering Potential-ionization contribution (CSP-ic) method [13] is developed on the basis of (3) and is applied to derive the total ionization cross-section from Q_{inel} by defining a ratio $R(E_i)$ which depends on energy,

$$R(E_i) = \frac{Q_{ion}(E_i)}{Q_{inel}(E_i)} \qquad (49.4)$$

such that,

$$R(E_i) = \begin{cases} 0, & E_i < I \\ R_P, & E_i = E_P \\ 1, & E_i \gg I \end{cases} \qquad (49.5)$$

where, E_P is the energy at which calculated Q_{inel} gains its maximum value. The particular form of the ratio as a continuous function of energy is developed by us,

$$R(E_i) = 1 - C_1 \left[\frac{C_2}{U + a} + \frac{\ln U}{U} \right] \qquad (49.6)$$

where, C_1, C_2 and a are target specific parameters. The detailed CSP-ic method can be found in our earlier publications [13–15].

49.3 Results and Discussion

In the present section, the results of total ionization cross-sections (Q_{ion}) for the gaseous H_2SO_4 molecule on collision with electrons for energy ranging from circa ionization threshold to 5000 eV have been reported along with Q_{inel} and $\sum Q_{exc}$. There are no previous results available for this molecule for comparison. Hence, we have adopted various models to study the e^- - H_2SO_4 scattering and the results are shown in Fig. 49.1. The Q_{ion} of H_2SO_4 are evaluated using different approximate

Fig. 49.1 Present Q_{ion} for
e^-- H_2SO_4 collision. Red
line: IAM with atomic IP,
Green line: IAM with
molecular IP
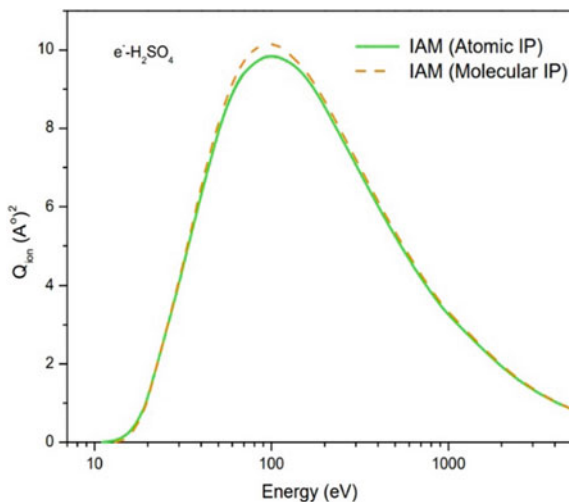
models, viz, Independent Atom model (IAM) with atomic ionization potential (IP)
and molecular IP for constituent atoms are shown.

An interesting feature observed in Fig. 49.1 is that the cross-sections for IAM
with atomic IP's and with molecular IP's are close to each other. One of the reasons
may be due to the fact that IP's of the constituent atoms i.e. H (IP = 13.60 eV), S (IP
= 10.36 eV), O (IP = 13.62 eV) and H_2SO_4 molecule (IP = 12.40 eV) do not differ
much except for S. Particularly the IP of Oxygen and Hydrogen have values close
to IP of H_2SO_4. IP of S is lower to IP of H_2SO4. When we add the cross-section
of constituent atoms, the contribution of O is significantly more than that of S. For
ready perusal we provide cross section data for e-H_2SO_4 collision using the IAM
using the molecular properties in Table 49.2.

In Fig. 49.2 we show our result of e-H_2SO_4 for Q_{inel}, Q_{ion} and $\sum Q_{exc}$. We have
compared our target molecule with other molecule, H_3PO_4 whose number of elec-
trons is same as that of H_2SO_4 (N = 50). We have plotted the Q_{ion} for H_2SO_4 and
H_3PO_4 molecules as shown in Fig. 49.2. The Q_{ion} are very sensitive to ionization
potential of the target molecule. It can be seen that our calculated data and the data
of Mozejko et al. [16] for H_3PO_4 show good matching with each other. The cross-
sections for both the molecules seem to follow the same path. One of the reasons
is their IP's are comparable to each other (11.72 eV for H_3PO_4 and 12.40 eV for
H_2SO_4) and the number of electrons are also same.

Hence, it can be now noted that our Q_{ion} depends not only on ionization potential
of the target molecule, but also the size of the target molecule that is number of
electrons since the molecular charge cloud serves as the scatterer.

Table 49.2 Q_{inel}, Q_{ion} and ΣQ_{exc} in $(A°)^2$ for e^--H_2SO_4 collision

Energy (eV)	Q_{inel}	Q_{ion}	ΣQ_{exc}
12.4 (IP)	0	0	0
20	3.07	1.07	2.00
40	11.26	6.48	4.78
60	13.88	9.12	4.76
80	14.12	10.00	4.11
100	13.61	10.14	3.46
150	11.92	9.63	2.28
200	10.30	8.73	1.57
500	5.70	5.34	0.36
1000	3.41	3.31	0.10
2000	1.94	1.91	0.02
3000	1.36	1.35	0.01
4000	1.04	1.03	0.00
5000	0.85	0.84	0.00

Fig. 49.2 Total cross-sections of H_2SO_4 and H_3PO_4. Solid line: present Q_{ion} of H_2SO_4; dash line: Mozejko et al. Q_{ion} for H_3PO_4; dot line: present Q_{ion} of H_3PO_4; short dash dot line: present Q_{inel} of H_2SO_4 and dash dot dot line: present ΣQ_{exc} of H_2SO_4
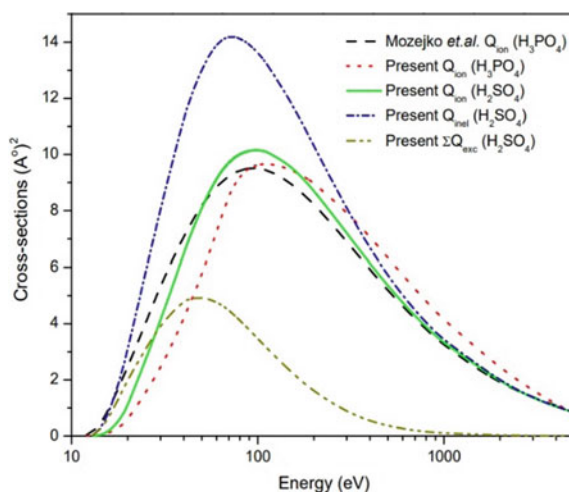
49.4 Conclusion

In this work results on computation of ionization probability through Q_{ion} is reported for electron interactions with H_2SO_4, which is a key element in atmospheric nucleation. We used the quantum mechanical approach, SCOP to compute Q_{inel} and obtained Q_{ion} using the (CSP-ic) formalism. We have studied the Q_{ion} using various models employed for molecular charge density viz., Independent Atom Model (IAM) with atomic and molecular IP's. We have shown Q_{ion} for H_2SO_4 and H_3PO_4 molecules

and it can be seen that our calculated data for H_3PO_4 is in good matching with available data of Mozejko et al. [16]. The Q_{ion} are very sensitive to ionization potential of target molecule and its size in terms of number of electrons ($N = 50$). As the IP of the target molecule increases, the peak value of Q_{ion} shifts towards high energy regime. Also, as the size of target decreases, the peak value of Q_{ion} also decreases. This observation can be seen in most of the targets.

References

1. J.H.Seinfeld et.al., Int. J. Mass Spect. **231**, 17–30 (2004)
2. K. McGouldrick, O.B.Toon, D.H.Grinspoon, Planet. Space Sci. **59**, 934–941 (2011)
3. Yao et al., Science **361**, 278–281 (2018)
4. M. Sipilä et al., Science **327**, 1243–1246 (2010)
5. U. Lohmannn, J. Frichter, Atmos. Chem. Phys. **5**, 715–737 (2005)
6. https://www.nasa.gov/centers/langley/news/factsheets/Aerosols.html
7. M. Swadia, Y. Thakar, M. Vinodkumar, C. Limbachiya, Eur. J. D **71**(4), 85 (2017)
8. D.R. Lide, *CRC Handbook of Chemistry and Physics* (CRC Press, Boca Raton FL2005, 1993–1994)
9. M. Vinodkumar, C. Limbachiya, A. Barot, N. Mason, Phys. Rev. A **87(1)**, 012702 (2013)
10. Y. Thakkar et al., Planet. Space Sci. **168**, 95–103 (2019)
11. A. Zecca, G.P. Karwasz, R.S. Brusa, Cz.Szmytkowski, J. Phys. B **24**, 2747 (1991)
12. A. Zecca, G.P. Karwasz, R.S. Brusa, Cz. Szmytkowski, J. Phys. Rev. A **45**, 2777 (1992)
13. K.N. Joshipura, B.G. Vaishnav, C.G. Limachiya, Pramana **66**(2), 403 (2006)
14. K.N. Joshipura, M.Vinodkumar, C.G.Limbachiya, B.K. Antony, Phys. Rev. A **69**, 022705 (2004)
15. K.N. Joshipura, N.J. Mason, *Atomic Molecular Ionization by Electron Scattering* (Cambridge University Press, 2019)
16. P. Mozejko, L. Sanche, Radiat. Phys. Chem. **73**, 77 (2005)

Chapter 50
Excitation-Emission Matrix Based Characterization and Detection of Fluorescent Compounds

Nil Ratan Das, Saurabh Inamdar, Kiranmala Laishram, Shalini Mittal, and A. K. Razdan

Abstract Laser Induced Fluorescence (LIF) is known to be a very sensitive and important tool for characterization for chemicals, bio-chemicals and biological tissues. Most of the spectra are quite similar and it will be very difficult to identify them on the basis of single excitation wavelength. Excitation-Emission Matrix (EEM) involves scanning of excitation for a broad spectral range and fluorescence emission is detected for each excitation wavelength. This three dimensional matrix data contains all the features of the given specimen. In most of the samples EEM features are visibly quite similar as a whole and the specific features are hidden in database, therefore, each EEM needs to be analyzed meticulously, point to point for accurate identification. A few features are dependent on excitation wavelengths and varies in various specimen. The importance of having a rich dataset is that, it will provide specific features available for classification, which indeed are not available using single excitation wavelength. In this work, we have taken Tramadol and Tyrosine having very similar fluorescence emission spectra for the EEM analysis. Since both the spectra are quite similar, it is very difficult to identify the chemicals on the basis of single excitation wavelength. But using a 3D matrix profile one can go for more detailed analysis of the same. This paper reports the characterization and detection of chemicals having similar spectra using EEM.

50.1 Introduction

There are numerous methodologies available worldwide for characterization and detection of chemicals, bio-chemicals and drugs such as Mass Spectroscopy (MS) [1], Fourier transform infrared spectroscopy (FTIR) [2], Raman Spectroscopy [3], Ion Mobility Spectroscopy (IMS) [4], Colourimetry [5] etc. Each technique has its own advantages and disadvantages. Laser Induced Fluorescence (LIF) is known to be a very sensitive and important tool for characterization and detection of chemicals, bio-chemicals and drugs as most of the bio-chemicals, proteins and drugs

---

N. R. Das (✉) · S. Inamdar · K. Laishram · S. Mittal · A. K. Razdan
LIDAR Division, Laser Science & Technology Centre, DRDO, Metcalfe House, Delhi 110054, India

are fluorescent in nature. Fluorescence spectroscopy has evolved during the last few decades in different forms by utilizing new theoretical and technical decisions. Researchers all over the world are extensively exploiting various fluorescence spectroscopy methods such as steady state/time resolved fluorescence, synchronous and Excitation-Emission Matrix (EEM) spectroscopy for chemical, biochemical and biological tissue characterization [6, 7].

EEM are developed using scanning of excitation wavelength for a broad spectral range and fluorescence emission is detected as a function of the intensity vs. wavelength of the emission for each excitation wavelength.

50.2   Experimental

Sample Preparation: Tramadol Hydrochloride (100 mg/2 ml), Quinine ($\geq$98%, Sigma), L-Tyrosine (99%, SRL) and L-Tryptophan (99%, SRL) were used for this work. Tramadol hydrochloride was diluted in deionized water (D/W) to obtain a sample to solvent ratio of 20 mg/10 ml. Powder sample (Quinine/L-Tyrosine/L-Tryptophan) was dissolved in the appropriate solvent (D/W or ethanol) approximately in the ratio of 20 mg powder in 10 ml solvent.

Fluorescence Measurements
Fluorescence measurements were performed on fluorescence spectrometer, Edinburg nF900. The prepared liquid sample was filled in a polished quartz cuvette and fluorescence emission has been measured at λ_{ex} 270 nm. The EEMs were collected at the excitation wavelengths (λ_{ex}) from 230 to 350 nm with a constant interval of 10 nm, and emission wavelengths (λ_{em}) from 250 to 550 nm with an interval of 2 nm. Both the excitation and emission slits were set at 5 nm, and the scan speed at 1200 nm/min.

50.3   Results and Discussion

Figure 50.1a shows the fluorescence emission spectra of Tramadol (302 nm) and Tyrosine (306 nm) at λ_{ext} 270 nm. As it can be seen that both spectra are quite similar, it will be very difficult to identify the chemicals on the basis of single excitation wavelength. EEM of diluted Tramadol is shown in Fig. 50.1b and that of Tyrosine is shown in Fig. 50.1c. The features are hidden in the EEM profile and can be extracted and classified using Artificial Neural Network (ANN) based classifier.

Similarly, the fluorescence emission spectra of Quinine and Tryptophan at λ_{ext} 270 nm is shown in Fig. 50.2a which will be very difficult to identify using single excitation wavelength. EEM of diluted Quinine is shown in Fig. 50.2b and that of Tryptophan is shown in Fig. 50.2c.
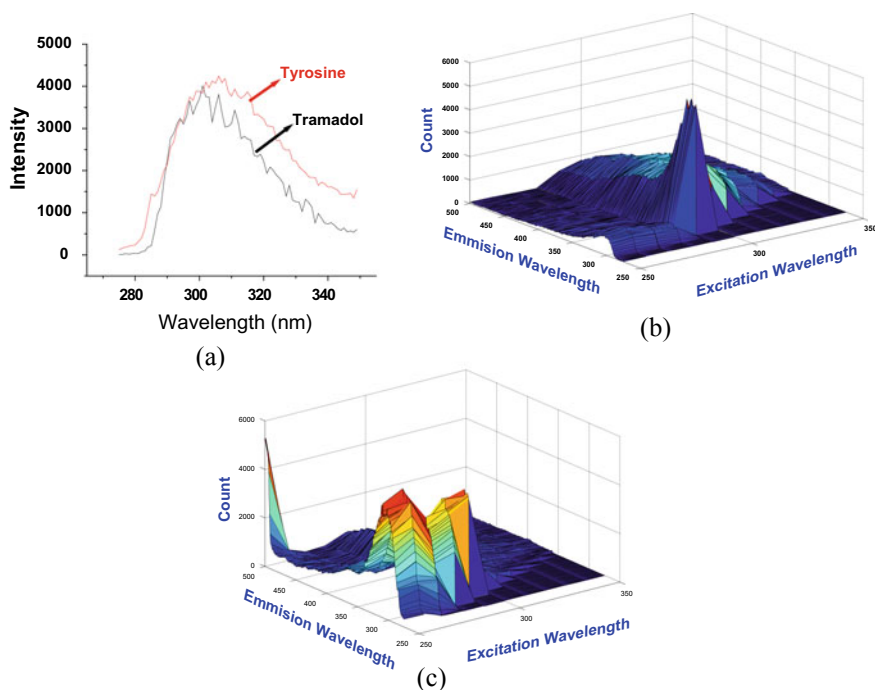
Fig. 50.1 **a** Fluorescence emission spectra of Tramadol (301 nm) and Tyrosine (306 nm) at λ_{ext} 270 nm, **b** *EEM of Tramadol and* **c** *EEM of Tyrosine*

50.4 Data Analysis and Classification

The EEM database library has been stored and an ANN based classifier has been developed for classification of unknown sample (Fig. 50.3). The database has been divided in to three parts: Training database for Validation and Testing database. The ANN has been trained with a predefined and labeled training database. The rest of the data utilized for validation and testing of network. The ANN parameters has been tuned accordingly for best possible outcome.

ANN consist of Input layer, Hidden layers and Output layer.

The database has been generated by numbers of experimentations with previously known samples, e.g. Tramadol, Tyrosine, Quinine and Tryptophan.

- Training dataset will train the network and 70% of total data can be used as training data.
- Remaining 30% dataset can be used for 15% testing and 15% Validation of the network.

Network accuracies for test data can be calculated accordingly.

(a)

(b)

(c)
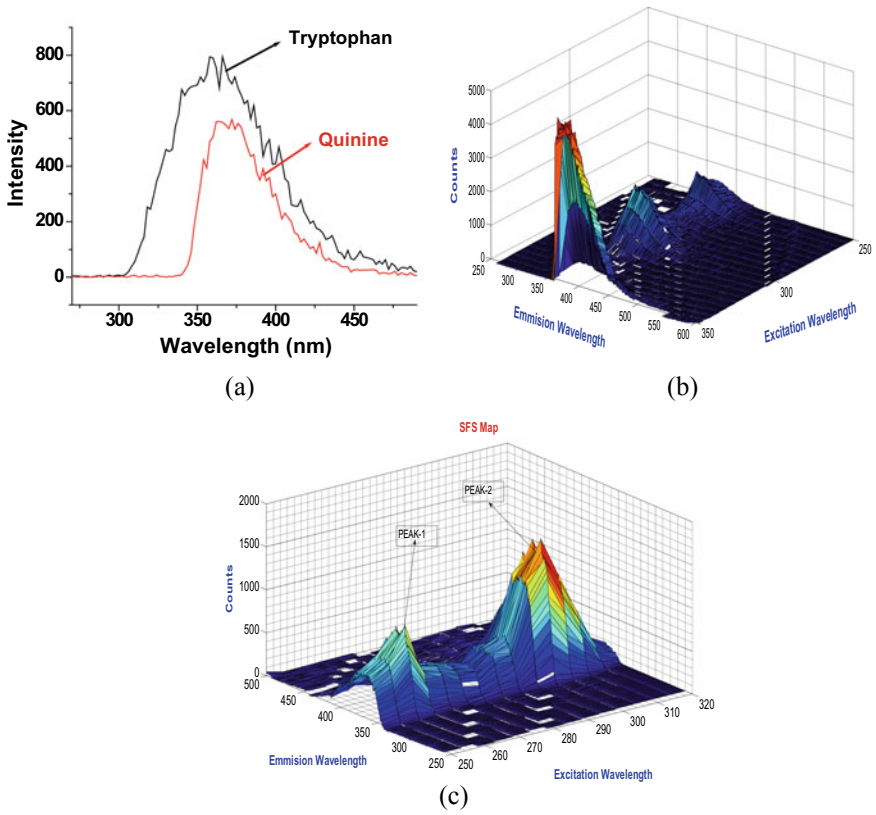
Fig. 50.2 **a** Fluorescence emission spectra of Quinine (around 362 nm) and Tryptophan (around 355 nm) at λ_{ext} 270 nm, **b** *EEM of Quinine and* **c** *EEM of Tryptophan*
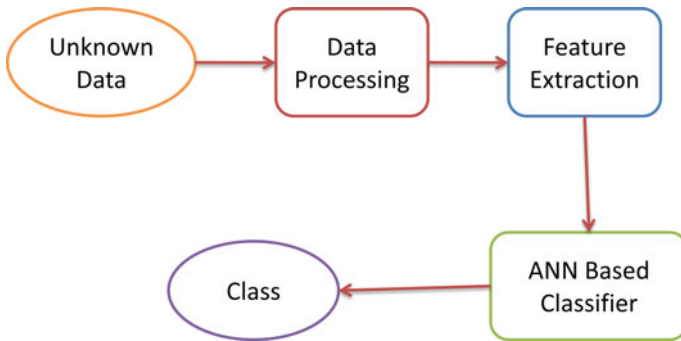
Fig. 50.3 Classification scheme

Table 50.1 Percentage accuracies on test data

Agent/class	Number of sample dataset	Percentage classification accuracy (%)	Number of hidden layer
Tramadol Quinine Tyrosine Tryptophan	100 100 100 100	91.11	10
Tramadol Quinine Tyrosine Tryptophan	200 200 200 200	97.77	10
Tramadol Quinine Tyrosine Tryptophan	500 500 500 500	98.22	10

50.5 Results

Table 50.1 shows the ANN is tuned and achieved accuracies of the order of greater than 90%.

Table 50.1 indicates the identification probability of above mentioned samples. With growing training dataset the probability of identification increases, as more and more knowledge fed to the network. For 500 dataset of each samples the percentage accuracies increases up to 98.22%. The number of hidden layers is fixed in all results.

50.6 Conclusion

Using EEM spectroscopy, we could classify Tramadol, Tyrosine, Quinine and Tryptophan with high classification accuracy. The classification was very difficult using single excitation wavelength based fluorescence spectroscopy. Artificial Neural Network (ANN) based classifier is able to identify the unknown sample with accuracies of the order of 90% or higher.

References

1. I. Ojanpera, M. Kolmonen, A. Pelander, Current use of high-resolution mass spectrometry in drug screening relevant to clinical and forensic toxicology and doping control. Anal. Bioanal. Chem. **403**, 1203–1220 (2012)
2. K.L. Andrew Chan, S.G. Kazarian, Detection of trace materials with Fourier transform infrared spectroscopy using a multi-channel detector. Analyst **131**, 126–131 (2006)
3. E. Deconinck, P.-Y. Sacre, P. Courselle, J.O. De Beer, Chromatography in the detection and characterization of illegal pharmaceutical preparations. J. Chrom. Sci., **51**(8) 791–806 (2013)
4. N. Haghpazir, Application of an ion mobility spectrometry for the determination of tramadol in biological samples. J. Food Drug Anal. **22**(4) 500–504 (2014)
5. S. Hamidi, Drug detection in biological specimens: recent colorimetric methods. Bioanalysis **10**(3), 127–130 (2018)
6. K.R. Grigoryan, H.A. Shilajyan, Fluorescence 2D and 3D spectra analysis of tryptophan, tyrosine and phenylalanine. Proc. Yeveran State Univ. Chem. Biol. **51**(1), 3–7 (2017)
7. Ts. Genova, E. Borisova, Al. Zhelyazkova, O. Semyachkina-Glushkovskaya, N. Penkov, M. Keremedchiev, B. Vladimirov, L. Avramov, Excitation-emission matrices (EEMs) and synchronous fluorescence spectroscopy (SFS) investigations of gastrointestinal tissues. Proc. SPIE **9447**, 94470X (2015)s
8. MATLAB Neural Network Toolbox user's guide

Chapter 51
Theoretical Electron Scattering Studies with Plasma Important Atoms: Tantalum and Molybdenum

Foram M. Joshi, Asha S. Chaudhari, Pooja Bhowmik, and K. N. Joshipura

Abstract Ionization by electron impact is one of the key processes in plasmas. Due to sputtering of wall materials various kinds of ion impurities exist in fusion plasmas. In order to control impurities in plasmas, it is vital to investigate the atomic processes of the elemental Tantalum and Molybdenum atoms which are of engineering importance. Major use of Tantalum is in the production of electronic components. Theoretical computations on Molybdenum are of importance due to diverter studies in quite a few experimental facilities. In this framework, the paper reports ionization cross sections by electron scattering with atomic tantalum and molybdenum in free and solid phases. Currently we find out total ionization cross sections Q_{ion}. The spherical complex (optical) potential formalism SCOP is used to determine the elastic and inelastic cross sections. Then CSP-ic methods is developed to obtain ionization cross sections Q_{ion} from calculated inelastic cross-sections Q_{inel}. This ionization cross sections are studied as a function of incident electron energies.

51.1 Introduction

Ionization by electron impact is one of the key processes in plasmas. Due to sputtering of wall materials various kinds of ion impurities exist in fusion plasmas. In order to control impurities in plasmas, it is vital to investigate the atomic processes of the elemental Tantalum and Molybdenum atoms which are of engineering importance

F. M. Joshi (✉)
G H Patel College of Engineering and Technology, Vallabh Vidyanagar 388120, India

A. S. Chaudhari
Shri Parikh D D Kanya Vidyalaya, Visnagar 384315, India

P. Bhowmik
Department of Physics, University College of Science, M. L. Sukhadia University, Udaipur, Rajasthan 313001, India

K. N. Joshipura
(Formerly) Sardar Patel University, Vallabh Vidyanagar 388120, India

[1]. Mo is found in numerous oxidation states in minerals as it does not appear naturally as a free metal. It has the sixth highest melting points of any element. Generally, molybdenum compounds are sparsely water soluble. Molybdenum is widely used to make alloys and super alloys as it is very hard. Molybdenum containing enzymes are the very common bacterial catalysts as it breaks the chemical bonds in the process of nitrogen fixation. Its extreme temperature tolerance makes Molybdenum most suitable to produce military protective clothing, parts of aircraft, industrial motors etc.

Tantalum is a dense and easily manufactured metal. It conducts both heat and electricity very well. It is used to produce metal powder to make electronic components of capacitors and resistors. Also, it is used in various industrial and medical products. It is used in the radiation shielding of spacecraft and satellites. Apart from solar radiation the shielding is exposed to solar wind of electrons and protons.

So to study the electron interactions with solids it is desirable to have basic cross section data of the targets in free or gaseous phase. For none of these two target atoms, experimental data for the electron impact ionization seem to be available, and hence free-atom calculations are also carried out presently.

Thus we have enough inspiration for studying these atomic targets. The present paper employs our theoretical method known as 'Complex Scattering Potential—ionization contribution' (*CSP-ic*) method to obtain total ionization cross sections Q_{ion} of electron scattering with atomic Molybdenum and Tantalum, at energies from ionization threshold (I) to 2000 eV.

51.2   Theoretical Methodology

In the present paper we have used the spherical Complex Potential methodology, extended for ionization contribution [2–5] to calculate different total cross sections of numerous atomic and molecular targets by electron and positron impact. In our previous publications [2–5], we have effectively calculated various types of electron impact cross sections for atomic and molecular targets using the approach SCOP and CSP-*ic*. In the present theoretical computations basic input parameters are charge density of the target atoms, bond length and ionization potential. We have obtained total (complete) cross sections Q_T which is a addition of total elastic cross sections Q_{el} and total inelastic cross sections Q_{inel}. Thus

$$Q_T(E_i) = Q_{el}(E_i) + Q_{inel}(E_i) \tag{51.1}$$

And

$$Q_{inel}(E_i) = \sum Q_{ion}(E_i) + \sum Q_{exc}(E_i) \tag{51.2}$$

where, E_i depicts the incident electron energy.

Now we theoretically extricate the ionization cross sections Q_{ion} from the total inelastic cross sections Q_{inel} which are resulting from a complex scattering potential. Here Variant CSP-*ic* method is employed, which is developed in the recent year along with the well-established CSP-*ic*, to obtain Q_{ion} besides other cross sections for these targets at energies E_i from ionization potential to about 2 keV. The quantity $\Sigma Q_{ion}(E_i)$ in (51.2) shows the sum total of all the ionization cross sections of the target. For ease we denote the first term just by Q_{ion}. The quantity $\Sigma Q_{exc}(E_i)$ is the byproduct of the process, which is the summated total electronic excitation cross sections.

With this background let us outline how the total ionization cross sections Q_{ion} of electron scattering from atomic targets are deduced from Q_{inel} using complex potential formalism. We have modified the original absorption model, by considering the threshold energy parameter Δ of the absorption potential V_{abs} as a gradually varying function of incident energy around ionization potential as discussed in [1–4]. In Brief, a primary calculation is done with a fixed value $\Delta = I$, but the variable Δ screens the absorption potential in the target charge-cloud zone and it is proven in previous studies. Thereafter we solve the Schrödinger equation with modified absorption potential, to obtain the complex phase shifts δ_l for several partial waves l by usimg the variable phase approach [6]. All the total cross sections viz, elastic (Q_{el}), inelastic (Q_{inel}) and total (complete) (Q_T) are produced from the S-matrix as per the standard equations [7].

Now, electron impact ionization links to many open channels whereas the electronic excitation comes from a small number of discrete scattering channels. So the ionization channel becomes dominating increasingly as the incident energy exceeds I, consequently making Q_{ion} the main contributor to Q_{inel}.

From (51.2),

$$Q_{inel}(E_i) \geq Q_{ion}(E_i) \tag{51.3}$$

Now, there is no accurate way to extract Q_{ion} from Q_{inel}. But an acceptable estimate has been developed by beginning with a ratio function,

$$R(E_i) = \frac{Q_{ion}(E_i)}{Q_{inel}(E_i)} \tag{51.4}$$

The first ever valuation of ionization with to excitation processes was made for water molecules by Turner et al. [8]. The complex potential calculations consist of ionization contribution in the inelastic cross section. In order to infer this contribution, we have created a method based on the (51.4). In our *CSP-ic* method, the energy dependency of this ratio is represented by the following relation [2–5].

$$R(E_i) = 1 - C_1 \left[\frac{C_2}{U+a} + \frac{\ln U}{U} \right] \tag{51.5}$$

where

$$U = E_i/I \tag{51.6}$$

Equation (51.5) involves three dimensionless parameters C_1, C_2 and a, which are computed by enforcing three conditions on the ratio function $R(E_i)$ as deliberated in our publications [2–5]. In Brief, $R = 0$ at the ionization threshold and the ratio takes up asymptotic value $R' \approx 1$ at high energies normally above 1000 eV. The third condition on R comes from its behaviour at the peak of Q_{inel} and is expressed in the following manner.

$$R(E_i) \begin{cases} = 0, \, for \, E_i \leq I \\ = R_p, \, at \, E_i = E_p \\ = R', \, for \, E_i \gg E_p \end{cases} \tag{51.7}$$

Here, E_p is the incident energy at which the calculated inelastic cross section Q_{inel} becomes maximum, while $R_p \approx 0.7$ is the value of the ratio R, where the incident energy takes up the value of peak energy. The choice of this value is approximate but physically reasonable. The peak energy is an incident energy where the predominant discrete excitation cross sections are diminishing, and the ionization cross section is growing fast. This implies that the R_p value should be above 0.5 but still below 1. This behaviour is credited to the faster drop of the second term ΣQ_{exc} in (51.2). An exact theoretical calculation of R_p is not possible, but we can try to see the effect of a small change in this value. The choice of R_p in (51.7) is not thorough and it introduces ambiguity in the final results. From (51.6) at high energies, the ratio R' approaches to unity which is physically supported by the rapidly decreasing excitation cross sections in that energy region. We impose the three conditions on the ratio R to calculate the three parameters of (51.5) and take $R_p = 0.70$ initially. The parameters are determined iteratively. Thus we derive the Q_{ion} from the computed Q_{inel} by (51.4). The method of complex potential paired with ionization contribution to inelastic scattering as described above presents the different total cross sections Q_T.

In the free or gas phase, the incident electron having energy just above the first ionization energy can eject a valance electron from the atom, and both the electrons can move out freely [9]. But in a condensed form, the situation is complicated. Here the ionization effectively can occur only after the incident energy E_i goes above the ionization threshold I by a value equal to the energy band gap by E_{gap} (Fig. 51.1).

Various input properties of the targets are shown in Table 51.1.

51.3 Results and Discussion

It is apt to compute the electron impact ionization cross sections of Mo and Ta atoms in the same theoretical formulation. The current calculation is also crucial in view of the energy range in which ionization is taking place along with elastic scattering as well as electronic excitations.

For Tantalum

$E_{gap} = 2.2$ **eV**

IP = 7.54 eV

Δ = IP+ E_{gap}

= 7.54+2.2

=9.74 eV
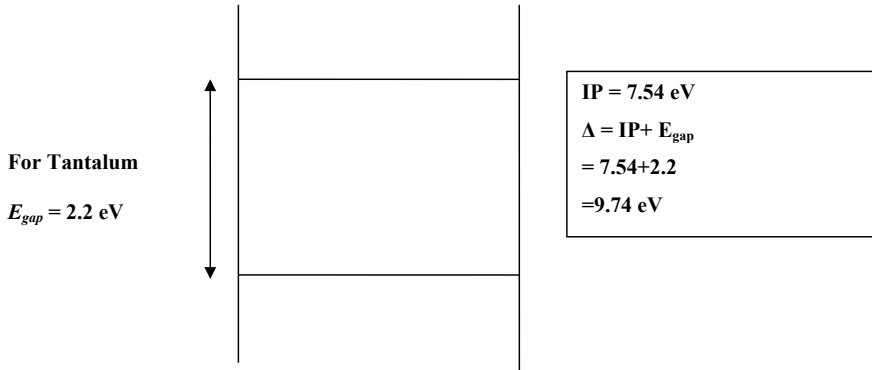
Fig. 51.1 Calculation of effective threshold energy for metallic phase

Table 51.1 Various input properties of the present targets

Property	Mo (free)	Mo (solid)	Ta (free)	Ta (solid)
First ionization energy (eV)	7.09	10.26	7.54	9.74

51.3.1 Molybdenum

Theoretical computations on Molybdenum are of importance due to diverter studies in quite a few experimental facilities, where a spectroscopic determination of impurity influx from the molybdenum surface is needed.

When we compare free and metallic phases, the charge density of metallic phase is redistributed due to metallic bonding. Besides the effective ionization threshold is higher than in the free atom case. Consequently, Q_{ion} for metallic Molybdenum are lower than those of free atoms as shown in Fig. 51.2. We construct total spherical complex potential with well-known model potentials, and absorption potential is chosen to be variable-delta Vabs [2–5]**.** In our calculations we have adopted the Vabs with varying Δ, and the corresponding results are denoted as 'variable Δ'. Alternatively, we also adopt the fixed delta at first threshold ionization energy Δ = I) as shown in the Fig. 51.2. Electron impact cross sections of Mo in solid is calculated using the method presented in Sect. 51.2 which falls slightly below both the calculations for free Mo. The results are also compared with BEB model [10], which is higher than the present result. Their peak in ionization cross section occure around 40 eV, while our calculation gives a peak in ionization cross sections at 25 eV. The reason behind this discrepancy is not understood. There is no experimental data on free Mo for comparison. The byproduct of CSP-ic method ΣQ_{exc} for free atoms is also shown in the Fig. 51.2.
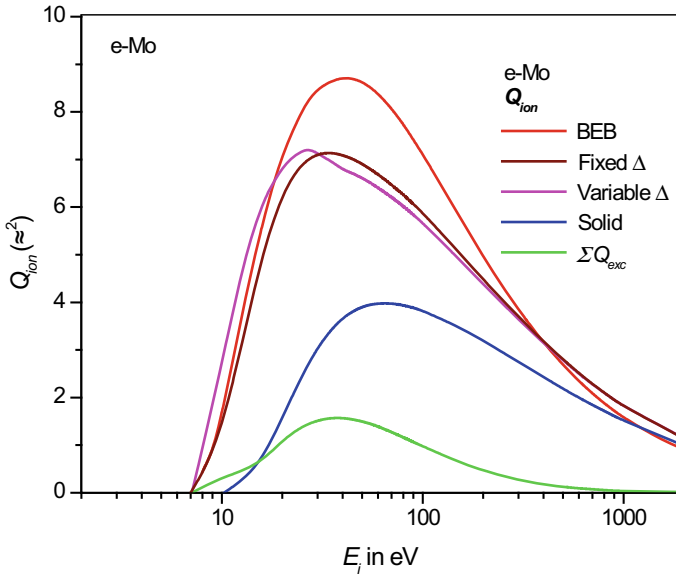
Fig. 51.2 Electron impact ionization scattering cross sections of atomic Mo and Mo in Solid Black solid curve: present Q_{ion} with fixed delta, pink solid curve: present Q_{ion} with variable delta, Red solid curve: BEB [10], Blue solid curve: Q_{ion} for Mo in Solid, Green solid curve: present ΣQ_{exc}

51.3.2 Tantalum

In Fig. 51.3, the upper curve to total ionization cross sections of free atomic Ta compared to the lower curve is total ionization cross sections for solid Ta. The current calculations show that the SCOP paired with variant *CSP-ic* method is a useful means for determining ionization cross sections. We have successfully done a first initiation to obtain Q_{ion} from Q_{inel} using our method called *CSP-ic* for Tantalum atom in free and metallic phases. Due to sparse experimental data for these atomic targets, researchers have to rely solely on theoretical calculations as the input to their codes.

51.4 Conclusions

Here we have reported our theoretical cross sections of electron collisions with two atomic species Mo and Ta for which there are no experimental measurements so far. The present method needs fewer computational efforts than conventional methods, the expanse of work is by no means insignificant. We believe that, in view of small ionization thresholds the atomic ionization peaks would not be so small as indicated by the results in Fig. 51.2. Our atomic cross sections are in an overall agreement
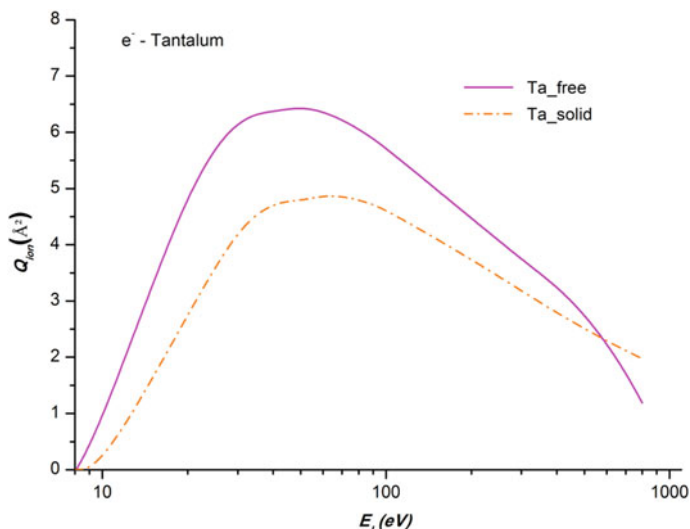
Fig. 51.3 Total ionization cross sections (in Å^2) with free and solid cases for Ta atom Purple solid curve – Ta free for Q_{ion}; Orange dash dot – Ta solid for Q_{ion}

in terms of shape with the BEB theory, which is known for its successes in many cases. Further, the present method with chosen $R_p = 0.70$ has also met with success in a number of atomic targets. Results for solid phase of Ta are perhaps the first in literature. It would be interesting to examine the neighbor atom W (tungsten) as against Ta.

References

1. N.R. Badnell, T.W. Gorczyca, M.S. Pindzola, H.P. Summers, J. Phys. B: At. Mol. Opt. Phys. **29**, 3683 (1996)
2. A.S. Chaudhari, F.M. Joshi, M.Pindariya, K.N. Joshipura, P. Bhowmik, J. Atomic Mol. Condens. Nano Phys. **5**, 205 (2018)
3. S.H. Pandya, F.A. Shelat, K.N. Joshipura, B.G. Vaishnav, Int. J. Mass Spectrom. **323–324**, 28 (2012)
4. K. N. Joshipura, N.J. Mason, *Atomic Molecular Ionization by Electron Scattering: Theory and Applications* (Cambridge University Press, 2019)
5. K.N. Joshipura, H. Kothari, F. Shelat, P. Bhowmik, N. Mason, J. Phys. B: At. Mol. Opt. Phys. **43**, 135207 (2010)
6. F. Calogero, *Variable Phase Approach to Potential Scattering* (Academic, New York, 1974)
7. C.J. Joachain, *Quantum Collision Theory* (North Holland, Amsterdam, 1984)
8. J.E. Turner, H.G. Paretzke, R.N. Hamm, H.A. Wright, R.H. Richie, Radiat. Res. **92**, 47 (1982)
9. F.M. Joshi, K.N. Joshipura, A.S. Chaudhari, in *AIP Conference Proceedings*, vol 1728 (2016), pp. 020186. https://doi.org/10.1063/1.4946237
10. D.K. Kwon, Y. Rhee, Y.K. Kim, Int. J. Mass Spectrom. **245**, 26 (2005)

Chapter 52
Lattice Dynamic and Thermoelectric Properties of ScPtBi in Topological Phase: A DFT Approach

Megha Goyal, Tavneet Kaur, and Murari Mohan Sinha

Abstract Half-Heusler materials have led to the observation of excellent transport properties, indicating their potential as new thermoelectric (TE) materials. In the present work, first-principle calculations have been performed to calculate structural and lattice dynamic properties of *ScPtBi*. The calculations were carried out using Density functional theory (DFT). In addition to this, Boltzmann transport theory has been used to calculate transport properties of *ScPtBi* to check the thermoelectric performance of the material. It is worth mentioning that TE performance of half-Heusler *ScPtBi* is found to be comparable to that of Bi_2Te_3. The maximum value of Seebeck coefficient ($-163\,\mu V/K$) is negative, indicating the n-type doping in *ScPtBi*. The calculated values of lattice thermal conductivity are 23.96 and 5.99 W/mK at 300 and 1200 K, making it a potential thermoelectric material.

52.1 Introduction

Recent studies show a great interest in the family of Heusler compounds due to their exciting electronic, optical, magnetic, mechanical and dynamical properties [1–3]. Half-Heusler compounds are having 18 valence electrons and are favorable thermoelectric materials due to their small bandgap [4, 5]. The dimensionless figure of merit (ZT) is a significant parameter that describes the thermoelectric efficiency of a material and is given by,

$$ZT = \frac{S^2\sigma T}{\kappa}$$

where S represents the Seebeck coefficient, σ is electrical conductivity and κ is the sum of electrical and lattice thermal conductivity.

For a potential thermoelectric material, ZT should be high. The high value of ZT can be achieved by enhancing the Seebeck coefficient and decreasing thermal

M. Goyal (✉) · T. Kaur · M. M. Sinha
Department of Physics, Sant Longowal Institute of Engineering and Technology, Longowal, Sangrur 148106, India

conductivity. But both these factors are interconnected: Seebeck coefficient is high when the carrier concentration is low, resulting in low electrical conductivity and hence low thermal conductivity. Thus, the optimal value of ZT is attained when carrier concentration is between insulators and metals [6].

Some of the half Heusler alloys exhibit semi-metallic behavior due to band inversion at zone center high symmetric point when the spin-orbital coupling is included, which is similar as seen in topological semi-metal *HgTe* [7, 8]. The elastic, electronic, thermodynamic, and thermoelectric transport properties of *TaCoSn* were computed by Haque et al. [9] and reported the value of ZT to be 0.73, showing that it is a promising material for thermoelectric device. Ding et al. [10] also informed that the thermoelectric properties of half Heusler alloys are comparable to Bi_2Te_3, which is well known thermoelectric material.

This work reports the first principle calculation of structural and lattice dynamical properties of *ScPtBi* using density functional theory (DFT). The structural properties include the computation of cell parameter (a_0), which describes the geometry of the unit cell, and the Bulk modulus (B), which indicates the hardness of a material. Phonon dispersion curve and phonon density of state are also plotted, and the zone center frequencies have been computed, which proves *ScPtBi* to be dynamically stable. Additionally, the transport properties of *ScPtBi* are calculated by employing the Boltzmann transport equation, which proves *ScPtBi* to be comparable thermoelectric material to Bi_2Te_3. These calculations prove *ScPtBi* to be a promising thermoelectric material.

52.2 Computational Detail

In this work, calculations of structural and vibrational properties have been performed using Density functional theory. The plane wave pseudo-potential method is employed by using Quantum Espresso code [11]. The Perdew–Zunger (pz) [12] with local density approximation (LDA) is chosen as the exchange–correlation functional. The relativistic effect has been considered to incorporate spin-orbital coupling (SOC) for analyzing the topological phase in *ScPtBi*.

The crystal structure of *ScPtBi* is relaxed by performing set of *scf* calculations. The convergence is achieved by Davidson diagonalization method with 1×10^{-8} Ry energy convergence threshold and kinetic energy cutoff of 80 Ry. The Kohn–Sham equation was solved by employing Monkhrost-Pack [13] of $7 \times 7 \times 7$ k-mesh. The q-mesh of $4 \times 4 \times 4$ is used to calculate eight dynamical matrices with density functional perturbation theory (DFPT). The thermoelectric properties are calculated by BoltzTraP code [14] which is based on Boltzmann transport theory and constant relaxation time approximation. Here, the relaxation time of 10^{-14} s is taken for the calculations of the transport properties.

52.3 Result and Discussion

52.3.1 Structural Properties

Half-Heusler compounds have XYZ chemical formula. The X and Y denotes transition metals and Z is a heavy element. It exists in the face-centered cubic phase and has a space group F43m (# 216). The crystal structure of *ScPtBi* is shown in Fig. 52.1 and is generated by using XcrySDen [15]. The Sc atom occupies Wyckoff site at 4a (0, 0, 0), Pt at 4b (0.25, 0.25, 0.25) and Bi at 4c (0.5, 0.5, 0.5).

The optimized lattice constant is obtained by calculating total energy at different volumes around the equilibrium cell volume. The ground state is computed by fitting the data to the Birch 3rd order equation [16].

The optimized value of the lattice constant is 6.49 Å which is in agreement with the experimental value of 6.59 Å [17]. The computed values of structural are listed in Table 52.1. The high value of bulk modulus indicates that *ScPtBi* is ductile in nature. The pressure derivative of Bulk modulus (B′) illustrates the effect of pressure on the hardness of the material. The calculated value of B′ is greater than 4; hence, ScPtBi is getting stiffer on pressure [19].

Fig. 52.1 Conventional crystal structure of half-Huesler ScPtBi
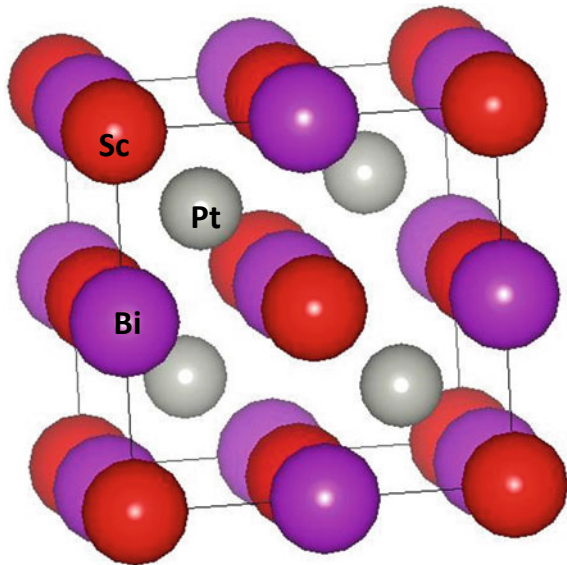
Table 52.1 Calculated structural properties of ScPtBi

	Present	Other theoretical works[a]	Experimental[b]
Lattice constant (a_0 in Å)	6.53	6.47	6.56
Bulk Modulus (B in GPa)	116.0	–	–
Pressure derivative of Bulk modulus (B')	5.04	–	–

[a][18]
[b][17]

52.3.2 Lattice Dynamical Properties

Dynamical structural stability is an essential factor of a crystal that can be deduced from the phonon dispersion curve. Figure 52.2 show phonon dispersion curve along high symmetry direction in Brillouin zone and phonon density of state of *ScPtBi*. The unit cell of *ScPtBi* consists of three atoms therefore, total nine modes of vibrations are possible. Out of which, three are acoustical and the remaining six are optical modes of vibration. As it can be seen from Fig. 52.2a the phonon frequencies are positive within entire Brillouin zone demonstrate that *ScPtBi* is dynamically stable [20, 21]. The computed zone center frequency of the highest optical mode is 207.29 cm^{-1}. The spin orbital coupling has significantly increased the values of zone center frequency of *ScPtBi* which is already discussed in our previous work [21].

Figure 52.2b illustrates the partial and total phonon density of state of *ScPtBi*. As the atomic mass of Scandium is less than the mass of platinum and bismuth, it shows main contribution in optical phonon modes, whereas the acoustical modes are comprised of Pt and Bi. It can also be seen from PDOS that, there is a huge frequency gap between higher and lower optical modes due to large difference in the masses of Sc and Pt.

52.3.3 Thermoelectric Properties

The thermoelectric transport properties assist us in estimating the thermoelectric efficiency of the material. Figure 52.3 shows the variation of thermoelectric properties i.e., Seebeck Coefficient, Electrical conductivity, electronic thermal conductivity and the figure of merit (ZT) with chemical potential (μ) and temperature (300, 600, 800, 1000 and 1200 K) to check the thermoelectric performance of *ScPtBi*.

The maximum value of Seeback coefficient is -163 μV/K at 1200 K as seen from Fig. 52.3a. The value of Seeback coefficient is negative indicating the n-type doping.

Fig. 52.2 a Phonon
dispersion curve, **b** Phonon
density of state (PDOS) of
ScPtBi
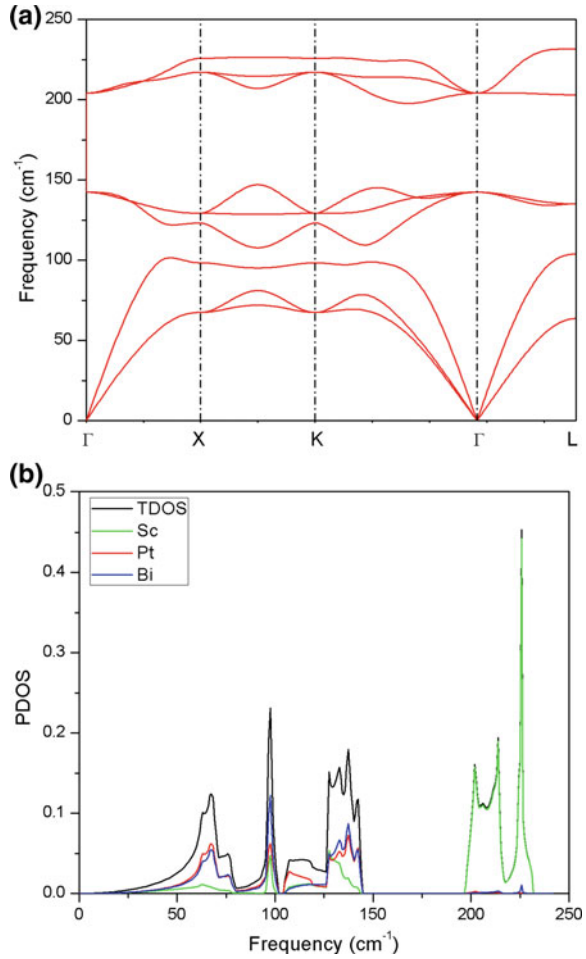
The maximum value of S is obtained at 1200 K shows good thermoelectric perfor-
mance of the material at high temperature. Figure 52.3b shows the variation of elec-
trical conductivity with chemical potential and temperature. The electrical conduc-
tivity slightly decreases with the increase in temperature. This may be attributed due
the increase in the mobility of electrons with temperature.

Figure 52.3c shows the variation of electrical thermal conductivity with chemical
potential and temperature. The electronic thermal conductivity increases with the
increase in temperature due to enhancement in carrier density. The electrical figure
of merit (ZT_e) which determine the electrical part of efficiency of thermoelectric
material as a function of chemical potential is shown in Fig. 52.3d which is given by,

$$ZT_e = \frac{S^2 \sigma T}{\kappa_e}$$
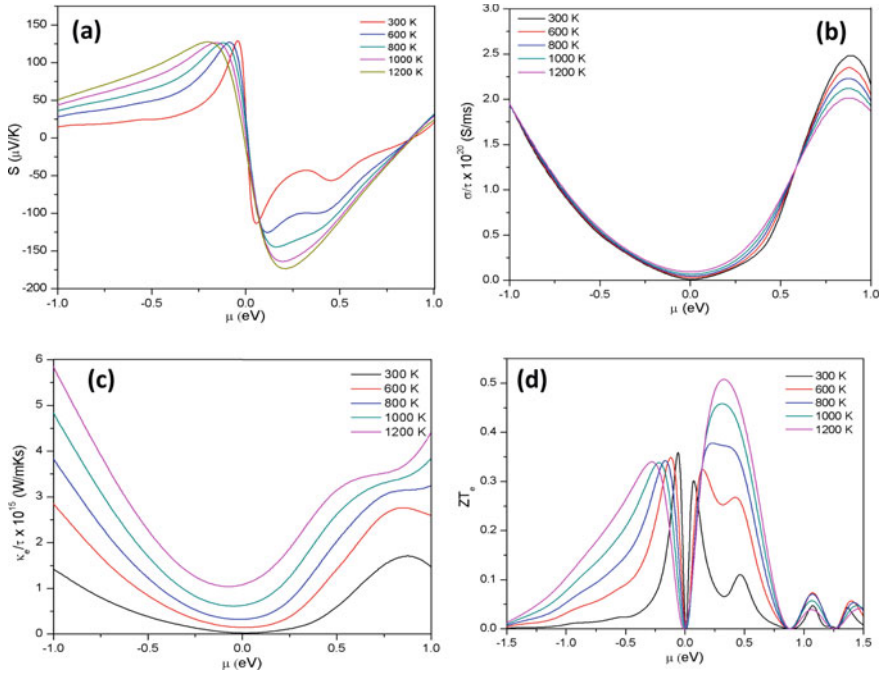
Fig. 52.3 **a** Seebeck coefficient, **b** electrical conductivity, **c** total thermal conductivity, and **d** figure of merit (ZTe) as a function of chemical potential of ScPtBi

where, κ_e is the electrical thermal conductivity. The n-type *ScPtBi* exhibit maximum ZT value of 0.50 at 1200 K and 0.38 at room temperature which is in good agreement with previously reported results [8].

The lattice thermal conductivity (κ_l) is a significant factor that affects the thermoelectric performance of any material, and it is given by Slack's equation as follows [22],

$$\kappa_l = \frac{0.849 \times 3 \times \sqrt[3]{4}}{20\pi^3\left(1 - 0.514\gamma^{-1} + 0.228\gamma^{-2}\right)} \times \left[\frac{\overline{M}\delta\theta_D^3}{\gamma^2 T}\right]$$

where $\overline{M}$ represents the average atomic mass, δ is the volume of one atom in the primitive cell, θ_D is Debye's temperature and γ is Gruneisen parameter. The calculated values of lattice thermal conductivity are 23.96 W/mK and 5.99 W/mK at 300 K and 1200 K temperature, respectively. The κ_l shows the inverse relation with temperature as increase in vibration cause a hindrance to the flow of current. The above calculated transport properties make *ScPtBi* ideal material for thermoelectrical applications due to its high ZT and low lattice thermal conductivity.

52.4   Conclusion

In this work, first-principle calculations have been made on *ScPtBi* in topological phase to compute its structural and vibrational properties by using Quantum ESPRESSO code. The computed value of lattice constant is in good agreement with previously reported experimental and theoretical results. The calculated bulk modulus is high, indicating it is a hard material. Moreover, the lattice dynamical properties are computed for the first time and shows the dynamical stability of material. The thermoelectric properties are estimated using the Boltzmann transport theory employed in the BoltzTraP code and is concluded that *ScPtBi* have maximum Seebeck coefficient in n-type composition. The dimensionless ZT_e value of n-type *ScPtBi* is 0.50 at 1200 K, suggesting better thermoelectrical efficiency at high temperature. The lattice thermal conductivity of *ScPtBi* is also low. Therefore, we conclude that the proposed material in the topological phase has good thermoelectric transport properties, which can be enhanced by doping and applying strain.

References

1. L. Offernes, P. Ravindran, C.W. Seim, A. Kjekshus, J. Alloys Compd. **458**, 47 (2008)
2. A. Erkisi1,5, G. Surucu, Mater. Res. Express **4,** 066504 (2017)
3. J. Tobola, J. Pierre, J. Alloys Compd. **296**, 243 (2000)
4. J. Yang, H. Li, T. Wu, W. Zhang, L. Chen, J. Yang, Adv. Funct. Mater.182880 (2008)
5. H. Xie, H. Wang, C. Fu, Y. Liu, J.G. Snyder, X. Zhao, T. Zhu T, Sci. Rep. 46888 (2014)
6. L. M€uchler, F. Casper, B. Yan, S. Chadov, C. Felser, Phys. Status Solidi RRL **7**, 91 (2013)
7. S. Chadov, X. Qi, J. K€ubler, G. H. Fecher, C. Felser, S.C. Zhan, Nat.Mater. **9**, 541 (2010)
8. K. Kaur, S. Dhiman, R. Kumar, Phys. Lett. A, **381**, 339 (2017)
9. M. Enamul Haque, Anwar Hossain. Results Phys. **10**, 458 (2018)
10. G. Ding, G.Y. Gao, L. Yu, Y. Ni, K. Yao, J. Appl. Phys. **119**, 025105 (2016)
11. P. Giannozzi et al., J. Phys. Condens. Matter **21**, 395502 (2009)
12. J.P. Perdew, A. Zunger, Phys. Rev. B **23**, 5048 (1981)
13. H.J. Monkhorst, J.D. Pack, Phys. Rev. B **8**, 5747 (1973)
14. K.H. Madsen, J. Singh, Comput. Phys. Commun. **175**, 67 (2006)
15. A. Kokalj, J. Mol. Graph. Model. **17**, 176 (1999)
16. F. Birch, Phys. Rev. **71**, 809
17. K.A. Gschneidner, J.C.G. B€unzli, V.K. Pecharsky, *Handbook on the Physics and Chemistry of Rare Earths* (Elsevier, New York, 2007)
18. W. Al-Sawai, H. Lin, R.S. Markiewicz, L.A. Wray, Y. Xia, S.-Y. Xu, M.Z. Hasan, A. Bansil, Phys. Rev. B **82**, 125208 (2010)
19. R.J. Angel, J. Gonzalez-Platas, M. Alvaro, Z. Kristallogr. **229**, 405 (2014)
20. M. Goyal, T. Kaur, M.M. Sinha, in *AIP Conference Proceedings*, vol. 2220 (2020), p. 1
21. M. Goyal, M.M. Sinha, J. Phys. Chem. Solids **153**, 110024 (2021)
22. G.A. Slack, in *Solid State Physics*, edited by F.S. Henry Ehrenreich D. Turnbull (Academic, New York, 1979), p. 1

Chapter 53
Simple Wet-Chemical Synthesis of Ce^{3+} Doped γ-BaAlF$_5$

Vartika S. Singh and S. V. Moharil

Abstract BaAlF$_5$ belongs to family of Alkaline Earth Aluminum fluoride consisting CaAlF$_5$ and SrAlF$_5$ as other members. These materials have recently attracted attention due to its use in PDP applications involving VUV excitation According to literature reviews, BaAlF$_5$ occurs in three polymorphs- alpha, beta and gamma. Among these, only alpha-BaAlF$_5$ phase exists at room temperature whereas beta and gamma are higher temperature phases. In present study, we came to observe that even gamma phase can exist at room temperature. Gamma phase is monoclinic. We have attempted the synthesis of BaAlF$_5$ via simple wet-chemical method. Formation of γ-BaAlF$_5$ is confirmed in our sample. Usually, complex fluorides are prepared by solid state reaction. This conventional synthesis routes needs very lengthy and tedious arrangements involving very high temperatures. Hence, new and much simpler ways are need to be explored. Further in our experiment, as prepared Ce^{3+} doped γ-BaAlF$_5$ showed luminescence which is in good agreement with previous studies.

53.1 Introduction

In 1982, Domesle et al. [1] showed that BaAlF$_5$ consists of three polymorphs and presented the structure of its alpha form which is a most stable low temperature form of BaAIF$_5$ [2]. They proved by DTA and other quenching techniques that the alpha form transforms to its beta- BaAIF$_5$ form. They detected that this transformation initiates at 666 °C slowly and completes at 736 °C. This is irreversible transition. Furthermore, a reversible transition occurs at 789 °C from beta- to gamma-BaAIF$_5$. Bail et al. [3] further defined the structures of beta and gamma phases. Recently, a delta phase also has been reported by Weil et al. [4]. Some luminescence studies such as emission of Eu^{2+} in this host have also been done [5].

V. S. Singh (✉) · S. V. Moharil
Department of Physics, R.T.M. Nagpur University, Nagpur 440 033, India

BaAlF$_5$ belongs to family of Alkaline Earth Aluminum fluoride, where CaAlF$_5$ and SrAlF$_5$ are as other members. These materials have recently attracted attention due to its use in PDP (Plasma Display Phosphors) applications involving VUV (vaccum ultra-violet) excitation [6–8].

53.2   Experimental

Bail et al. [3] obtained the α phase from the stoichiometric [BaF$_2$: AlF$_3$] mixture by heating it for 15 h at 600 °C. The β-phase took 3 days to prepare from the α phase at 740 °C and the γ phase was obtained when β-BaAlF$_5$ was heated continuously for 1 day at 850 °C and then cooled down to 800 °C slowly by stabilizing for 15 min at this temperature. Later on, quenching was done in water. This solid state route of synthesis was very cumbersome and bulky.

As a result, simple one step wet chemical synthesis has emerged as a much generalized method for the synthesis of complex aluminum fluorides.

Chlorides of respective constituent metals of an analytical reagent grade in stoichiometric ratios are dissolved in D.D. water and mixed together to form one solution (chlorides were used as initial materials to avoid hydrolysis during the reaction process). Temperature of the solution was increased upto 85 °C on a hot plate. On reaching 85 °C, drop wise HF(48%) was added to the solution. Usually, HF was used with 10 wt% excess relative to its stoichiometric quantity. Whole process was done in a PTFE container. The resultant precipitate was filtered, washed, dried and collected from the filter paper. As-prepared Ce doped samples showed photoluminescence.

53.3   Results and Discussion

"X-ray diffraction patterns were recorded on a Philips PANalytical X'pert Pro diffractometer. Photoluminescence spectra were recorded on a Hitachi F-4000 spectro-fluorimeter with spectral slit width of 1.5 nm in the spectral range 220–700 nm."

53.3.1   XRD Analysis

Figure 53.1 shows the XRD pattern of BaAlF$_5$ prepared by wet chemical synthesis. In BaAlF$_5$ three forms are reported. The irreversible transition from α → β occurs at 736 °C and reversible transition from β ←→ γ-BaAlF$_5$ occurs at 789 °C. It was found that the XRD lines of our sample matches excellently with ICDD 51-0236 gamma phase of BaAlF$_5$ more, than the other phases. This is rather surprising since gamma form of BaAlF$_5$ is said to be existing only at higher temperatures according to
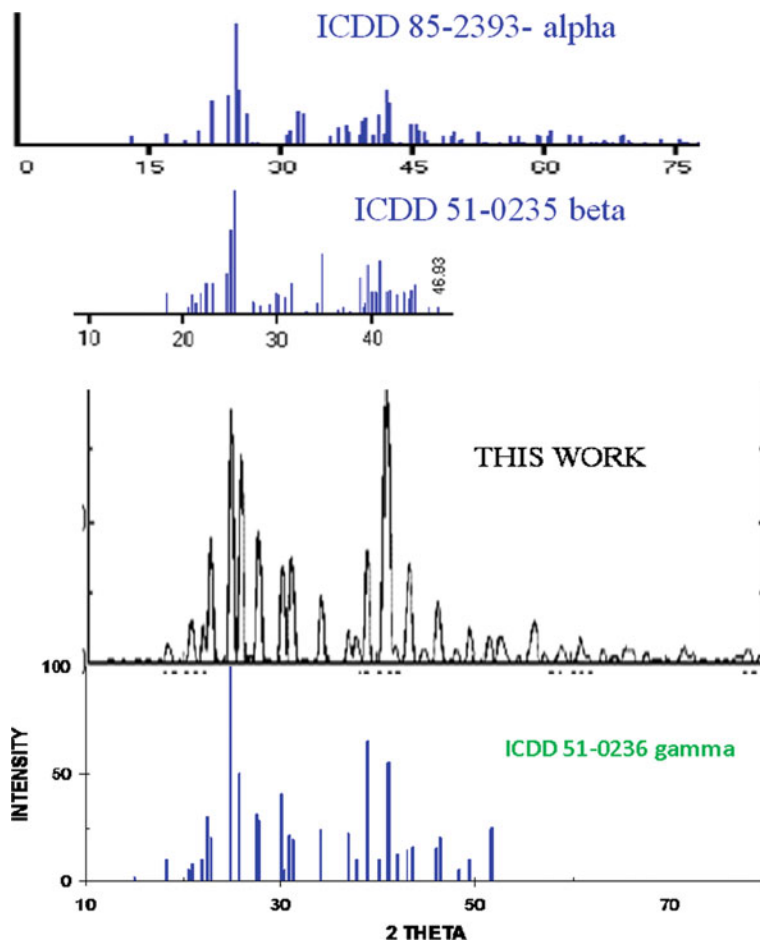
Fig. 53.1 XRD pattern of BaAlF$_5$ prepared by wet chemical synthesis matches well with ICDD 51-0236 (gamma-BaAlF$_5$)

earlier reports. It was expected that only lower temperature alpha form is dominant and stable at the room temperatures. Contrary to this, our work suggests that wet chemical method discussed here can also result in successful formation of phase pure gamma- BaAlF$_5$. The ICDD patterns of the other two forms (alpha and gamma) of BaAlF$_5$ are also given in the figure for better comparison.
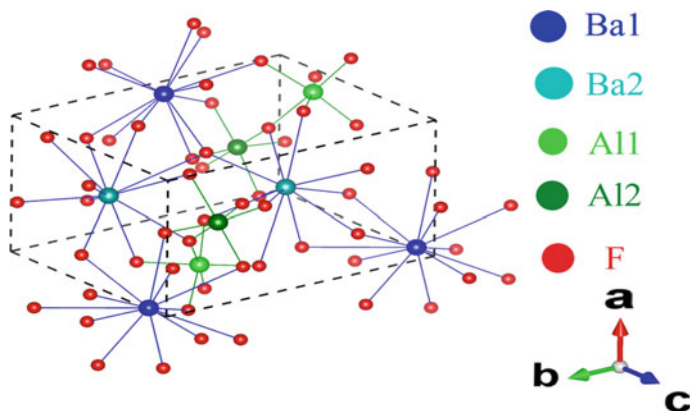
Fig. 53.2 Crystal structure of Gamma-BaAlF$_5$

53.3.2 Crystal Structure

Gamma phase belongs to space groups P2$_1$/m and P2$_1$. Figure 53.2 shows the crystal structure of gamma-BaAlF$_5$.

The three phases (α, β and γ) are made up of the same basic monocapped trigonal prism type units where Al ions enclosed by Ba ions. All these trigonal prisms shares their faces with each other to form infinite oriented octahedral chains. γ-BaAlF$_5$ exhibits the FeB-type structure with quasi- no distortion.

However, beta and gamma are monoclinic. In alpha -BaAlF$_5$, Ba is 12 coordinated (Ba-F from 2.62 to 3.04 Å) in a distorted cuboctahedron (I); in beta –BaAlF$_5$ same polyhedron have Ba(2) with distortion Ba-F from 2.63 to 3.16 Å; and for gamma, it is (Ba-F from 2.65 to 3.30 Å) where other Ba sites do not belongs to defined polyhedra [3].

53.3.3 Photoluminescence of Ce^{3+} in BaAlF$_5$

Formation of pure phase γ -BaAlF$_5$ has been confirmed by comparing the X-ray diffraction pattern with ICDD file. It's remarkable to note that as prepared Ce-doped BaAlF$_5$ synthesized by precipitation method showed Ce^{3+} photoluminescence. Figure 53.3, shows the PL spectra of BaAlF$_5$:Ce(0.5 mol%). Excitation maximum is observed at 254 nm with shoulders at 286 nm and 240 nm at emission wavelength 326 nm which is in good agreement with the previously reported values.

Fig. 53.3 PL spectra of BaAlF$_5$:Ce(0.5%) **a** excitation at λ_{em} = 326 nm with shoulders at 286 and 240 nm, **b** emission at λ_{ex} = 254 nm
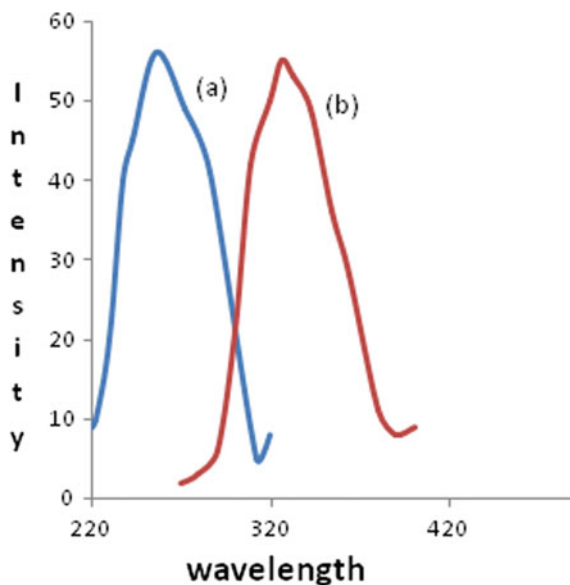
53.4 Conclusion

In the present work, we have shown that even high temperature gamma phase of BaAlF$_5$ can exist at room temperature. From this, we can conclude that formation of phases may depend on the ways of syntheses. Hence, process of syntheses plays a crucial role in the formation of phases for a compound. It is remarkable to note that as prepared Ce^{3+} activated BaAlF$_5$ host showed photoluminescence in our sample. For the first time, photo- luminescence is observed for γ-BaAlF$_5$:Ce^{3+} synthesized via Wet-Chemical process. Luminescence in Eu^{2+} doped BaAlF$_5$ have been already reported in early 70's. Also, other rare earths activated BaAlF$_5$ can be attempted by precipitation method to study and improve further luminescence properties.

References

1. R. Domesle, R. Hoppe, Z. Anorg, Allg. Chem. **495**, 16 (1982)
2. R. Domesle, R. Hoppe, Rev. Chim. Miner. **15**, 439 (1978)
3. A. Le Bail, G. Ferey, A.M. Mercier, A. de Kozak, M. Samouël, J. Solid State Chem. **89**, 282 (1990)
4. M. Weil, E. Zobetz, F. Werner, F. Kubel, Solid State Sci. **3**, 441 (2001)
5. R.A. Hewes, M.V. Hoffman, J. Lumin. **3**, 261 (1971)

6. E. Van Der Kolk, P. Dorenbos, C.W.E. Van Eijk, A.P. Vink, M. Weil, J.P. Chaminade, J. Appl. Phys. **95**, 7867 (2004)
7. A.P. Vink, P. Dorenbos, J.T.M. De Haas, H. Donker, P.A. Rodnyi, A.G. Avanesov, C.W.E. Van Eijk, J. Phys. Condens. Matter **14**, 8889 (2002)
8. N.J.M. Le Masson, A.P. Vink, P. Dorenbos, A.J.J. Bos, C.W.E. Van Eijk, J.P. Chaminade, J. Lumin. **101**, 175 (2003)

Chapter 54
Electronic Solvation (UV-Vis) and NLO Properties of 2-Chloroanthraquinone: An Experimental and Computational Modeling Approach

B. S. Yadav, Ankita Garg, Jayant Teotia, and Shaleen Bhardwaj

Abstract In this present effort, the optical properties of the titled compound have been examined experimentally as well as theoretically by UV-visible spectroscopy. The experimental UV-visible spectra have been recorded in ethanol, acetone, methanol, and DMSO while theoretically examined through time-dependent density functional theory (TD-DFT) computations. The electronic properties, for instance, maximum absorption wavelength (λ_{max}), excitation energy (eV), HOMO/LUMO energies and oscillator strength (f) are measured via time-dependent density functional theory (TD-DFT) through B3LYP hybrid functional along with 6-311++G (d, p) basis-set in gaseous as well as in liquid phase. The non-linear optical (NLO) activity of titled compound like polarizability, electric dipole moment, and also first-order hyperpolarizability have been derived by DFT. All these quantum chemical computational work has been done by the Gaussian 09 W software program package. The findings suggest that the titled chloro substituted Anthraquinone dye can be an applicable aspirant used for photonic and optoelectronic applications.

Highlights

In this present effort, the aim is to learn the substituent effect on geometrical structure, UV-Vis absorption spectra as well as non-linear optical (NLO) properties of 2-Chloroanthraquinone. It is our optimism that the findings may deliver noteworthy information about the compound for designing novel and high performing active material, which is to be used in non-linear optical devices, pharmaceuticals, biological and therapeutic concerns.

B. S. Yadav · A. Garg (✉) · J. Teotia · S. Bhardwaj
Molecular Spectroscopy and Biophysics Lab, Department of Physics, Deva Nagri College, Meerut 250002, India

54.1   Introduction

Through emergent development, a quest for organic materials revealed a huge amount of non-linear optical (NLO) activity in the technological domain of opto-electronics, bio-photonics also photonics, and thereby picking up the benefits in low power non-linear optical appliances. Organic dyes considered as more interesting optical materials for learning non-linear optical activities to understand the photo-physics and forthcoming benefits in up-conversion laser, optical computing, optical limiting, and optical processing [1]. Anthraquinone is a category of organic compounds obtained through aromatic compounds interchanging a uniform number of collections with a suitable order of double bonds, which leads to the conjugation accompanied the aromatic form. Anthraquinone derivatives have valuable usages in the field of synthetic dyes and pigments in addition to the pharmaceutical industry [2–6]. Quantum chemical computations have proposed—"The molecules for instance Anthraquinone" along with conjugated structure and electron donating as well as electron-accepting species are appropriate for learning NLO properties. With the help of quantum chemical calculations, learning of electronic solvation as well as non-linear optical activities of 2-chloroanthraquinone are introduced in a present paper which is to be our information, the compound has not been published yet [7–15].

54.2   Experimental Methodology

The titled compound 2-chloroanthraquinone with a spectroscopic grade purchased from Tokyo Chemical Industry Co., Ltd. (TCI Chemicals, India), used without any extra purification. For electronic transition analysis, UV-Vis absorption spectra observed within the scale of 200–600 nm at 1 nm resolution making use of U-3900 UV-Visible spectrophotometer in several polar solvents like acetone, methanol, ethanol, and DMSO.

54.3   Computational Methodology

All the quantum chemical computational effort of the titled compound was accomplished by the Gaussian 09 program package through DFT/B3LYP as 6-311++G (d, p) basis-set. Optimization of titled compound completed, without making use of symmetry restriction of DFT/B3LYP/6-311++G (d, p) basis-set at a theoretical level. All these input files and data elucidation arranged through Gauss-View 6.0.6. The electronic absorption spectra as well as solvent effect simulated from PCM-TD-DFT method using a similar basis set. Moreover, maximum wavelengths (λ_{max}), oscillator strengths, configuration interaction, and excitation energies were considered

Fig. 54.1 DFT optimized structure of the 2-chloroanthraquinone
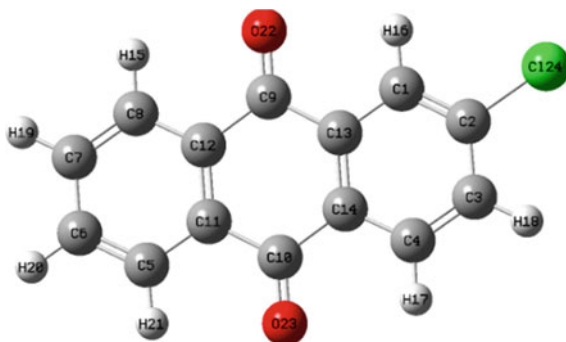
through time-dependent density functional theory (TD-DFT). Theoretical description of the ground state, polarizability (α), dipole moment (μ) including first-order-hyperpolarizability (β), frontier orbital energies were considered by hybrid functional B3LYP/6-311++G (d, p) basis-set.

54.4 Results and Discussions

54.4.1 Optimized Molecular Geometry

All geometric optimization of 2-chloroanthraquinone was done through DFT/B3LYP exchange–correlation along with 6-311++G (d, p) basis set on ground level. Therefore, every atom of a molecule lies in a plane, resulting in the form of geometry to be planar. Figure 54.1 has given here.

54.4.2 UV-Visible Spectral Study: An Experimental and Theoretical Comparison

UV-Visible spectral study shows that quantity of energy is absorbed due to electrons stimulations to excited states. The electronic absorption spectra of 2-chloroanthraquinone are noted in several polar solvents like acetone, methanol, ethanol, and DMSO using the scale of 200–600 nm. The larger value of absorption wavelength (λ_{max}) of the molecule signifies that the electrons charge-transfer transitions arise from bonding to anti-bonding (π-π*) that are recognized by aromatic nuclei and C=C chromophores while a lower value of absorption wavelength (λ_{max}) arises from electron transitions of non-bonding to anti-bonding (n-π*) [15, 16].

The experimental spectra of the titled compound in several polar solvents presented in Fig. 54.2. The theoretical computational predictions of the compound

Fig. 54.2 Experimental absorption spectrum of 2-chloroanthraquinone in acetone, DMSO, ethanol and methanol
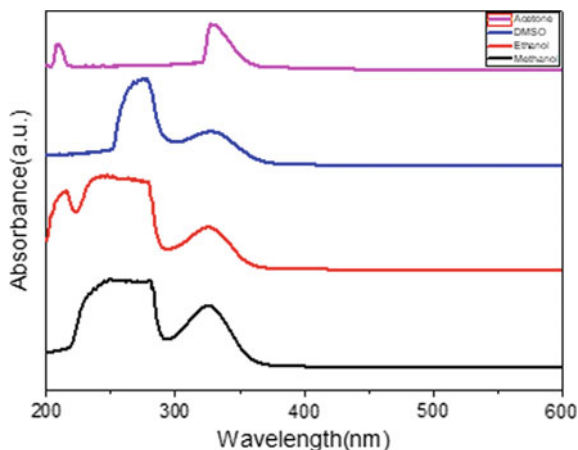
were executed in the solvation model where PCM formalism was taken into account through TD-DFT/B3LYP/6-311++G (d, p) basis-set. According to experimental spectra, absorption bands are noticed at 277 nm, 330 nm in DMSO; at 210 nm, 329 nm in acetone; at 280 nm, 327 nm in ethanol, and at 282 nm, 326 nm in methanol while corresponding calculated peaks are at 358.79 nm, 374.55 nm in DMSO; at 358.19 nm, 375.13 nm in acetone; at 358.35 nm, 374.94 nm in ethanol and at 358.44 nm, 374.72 nm in methanol respectively.

The hypsochromic shift in acetone, hyperchromic shift in methanol, and bathochromic shift in DMSO observed due to the solvent effect. The highest oscillator strength f = 0.0305 is observed in DMSO. Theoretically measured absorption wavelength (λ_{max}), excitation energies (eV), oscillator strengths (f) in different polar solvents applying TD-DFT method are sorted in Table 54.1. For an enhanced explanation of electronic properties, nature of orbitals in the foremost electronic transitions of 2-chloroanthraquinone is given in Fig. 54.3.

54.4.3 Frontier Molecular Orbital Exploration

Frontier Molecular Orbital (FMO) provides essential facts regarding the chemical stability within the molecule related to an energy gap in the middle of HOMO (highest occupied molecular orbital) to LUMO (lowest unoccupied molecular orbital). The green, in addition to red side of HOMO/LUMO designates the positive together with negative charges. The total magnitude of the HOMO/LUMO energy gap denotes the chemical hardness, chemical reactivity, and chemical softness including the polarizability of a molecule that has an influence on the non-linear activity of the compound [16–19].

Moreover, electronegativity (ε), chemical softness (σ), chemical potential (μ), electrophilic index (ω), and chemical hardness (η) are global chemical reactivity

Table 54.1 Experimental and computed absorption wavelengths, oscillator strengths and excitation energies of 2-chloroanthraquinone in gaseous phase, ethanol, acetone, methanol, and DMSO solvents

Phase	Excitation	Expansion coefficient	Calculated wavelength (nm)	Excitation energy (eV)	Oscillator strength (f)	Experimental wavelength λ_{max} (eV)
Gas phase	Excited State 1	Singlet-A″				
	59 → 64	−0.14158				
	61 → 63	0.68724	416.92	2.9738	0.0000	−
	Excited State 2	Singlet-A″				
	59 → 63	0.66806				
	61 → 64	−0.20984	386.60	3.2070	0.0000	−
	Excited State 3	Singlet-A′				
	58 → 63	−0.17406				
	60 → 63	−0.14326				
	62 → 63	0.65836	347.85	3.5643	0.0273	−
Acetone phase	Excited State 1	Singlet-A″				
	57 → 64	−0.13619	406.06	3.0533	0.0000	−
	60 → 63	0.68886				
	Excited State 2	Singlet-A″				
	57 → 63	0.67013	375.13	3.3057	0.0000	329
	60 → 64	−0.20464				
	Excited State 3	Singlet-A′				
	59 → 63	−0.16157	358.19	3.58.19	0.0297	210
	61 → 63	0.14139				
	62 → 63	0.66551				
Ethanol phase	Excited State 1	Singlet-A″				
	57 → 64	−0.13611	405.89	3.0546	0.0000	−
	60 → 63	0.68888				
	Excited State 2	Singlet-A″				
	57 → 63	0.67016	374.94	3.3067	0.0000	327
	60 → 64	−0.20458				

Table 54.1 (continued)

Phase	Excitation	Expansion coefficient	Calculated wavelength (nm)	Excitation energy (eV)	Oscillator strength (f)	Experimental wavelength λ_{max} (eV)
	Excited State 3	Singlet-A′				
	59 → 63	−0.16139	358.35	3.4599	0.0296	280
	61 → 63	0.14098				
	62 → 63	0.66568				
Methanol phase	Excited State 1	Singlet-A″				
	57 → 64	−0.13599	405.67	3.0563	0.0000	–
	60 → 63	0.68892				
	Excited State 2	Singlet-A″				
	57 → 63	0.67020	374.72	3.3087	0.0000	326
	60 → 64	−0.20447				
	Excited State 3	Singlet-A′				
	59 → 63	−0.16232	358.44	3.4590	0.0287	282
	61 → 63	−0.14031				
	62 → 63	0.66558				
DMSO phase	Excited State 1	Singlet-A″				
	57 → 64	−0.13596	405.52	3.0574	0.0000	–
	60 → 63	0.68892				
	Excited State 2	Singlet-A″				
	57 → 63	0.67020	374.55	3.3102	0.0000	330
	60 → 64	−0.20448				
	Excited State 3	Singlet-A′				
	59 → 63	−0.15940	358.79	3.4556	0.0305	277
	61 → 63	0.14024				
	62 → 63	0.14024				

descriptors, taken to recognize chemical properties of the molecule. These are extracted using HOMO/LUMO energy gap values where HOMO energy is denoted such as ionization potential (I_p) and LUMO energy as electron affinity (EA).

Ionization potential (I_p) $= -E_{HOMO}$;
Electron affinity (EA) $= -E_{LUMO}$;
Chemical potential (μ) $= [(E_{LUMO} + E_{HOMO})/2]$;
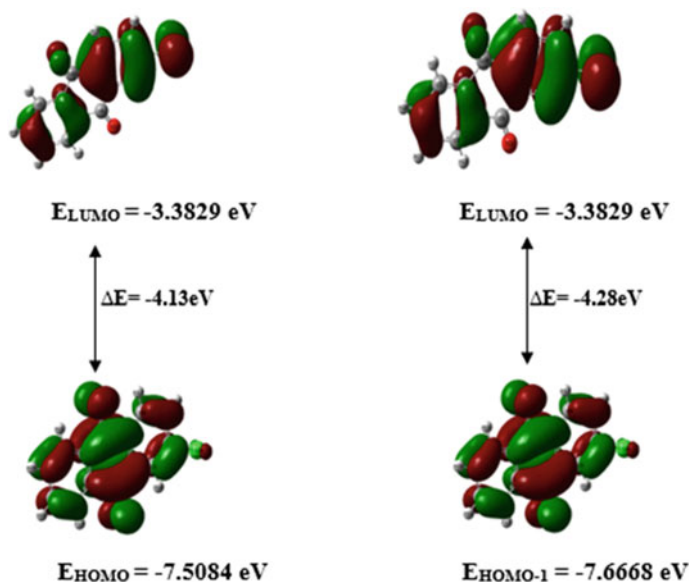
Fig. 54.3 Molecular orbitals of 2-chloroanthraquinone

Chemical hardness $(\eta) = [(E_{LUMO} - E_{HOMO})/2]$;
Chemical softness $(S) = 1/\eta$;
Electronegativity $(\varepsilon) = -\mu$ or $[(Ip + EA)/2]$;
Electrophilicity index $(\omega) = \mu^2/2\eta$.

HOMO, HOMO−1, LUMO and LUMO+1 orbitals belonging to the titled molecule are measured at B3LYP/6-311++G (d, p) basis set. HOMO/LUMO energy gap for lower energy state to first excited state (HOMO → LUMO) transitions and second excitation (HOMO-1 → LUMO) with energy separation are −4.13 eV and −4.28 eV respectively. All these measured values listed in Tables 54.2 and 54.3.

Table 54.2 Calculated HOMO–LUMO energy values of 2-chloroanthraquinone through B3LYP/6-311++G (d, p) basis-set

Energy	E_{HOMO}	E_{LUMO}	E_{HOMO-1}	E_{LUMO+1}	$E_{LUMO} - E_{HOMO}$	$E_{HOMO-1} - E_{LUMO+1}$	E_{TOTAL} (Hartee)
Gas Phase	−0.28	−0.12	−0.28	−0.09	0.16	−0.19	−1148.48
Methanol	−0.28	−0.12	−0.28	−0.09	0.16	−0.19	−1148.48
Ethanol	−0.28	−0.12	−0.28	−0.09	0.16	−0.19	−1148.48
Acetone	−0.28	−0.12	−0.28	−0.09	0.16	−0.19	−1148.48
DMSO	−0.28	−0.12	−0.28	−0.09	0.16	−0.19	−1148.48

Table 54.3 Calculated values of chemical properties (IP, EA, μ, η, σ, ε, ω) of 2-chloroanthraquinone

Parameters	Value (eV)
E_{HOMO}	−0.28
E_{LUMO}	−0.12
Ionization potential (I_P)	0.28
Electron affinity (EA)	0.12
Global hardness (η)	0.08
Chemical potential (μ)	−0.2
Global softness (σ)	12.5
Electronegativity (ε)	0.2
Electrophilicity index (ω)	0.25

54.4.4 Non-linear Optical Properties

Density functional theory (DFT) calculations apply to observe the non-linear optical activity of 2-chloroanthraquinone in terms of polarizability (α), dipole moment (μ), and first-order hyperpolarizability (β) indexes. These elements are outcomes of molecular energy relating to the intensity of the applied electric field [7, 20, 21]. All the calculations were evaluated at DFT/B3LYP/6-311++G (d, p) basis-set accompanied by following equations.

Total dipole moment

$$\mu_{total} = \left(\mu_x^2 + \mu_y^2 + \mu_z^2\right)^{1/2} \tag{54.1}$$

Isotropic mean polarizability

$$<\alpha> = \left(\alpha_{xx} + \alpha_{yy} + \alpha_{zz}\right)/3 \tag{54.2}$$

Anisotropy of polarizability

$$\Delta\alpha = \left\{\left[\left(\alpha_{xx} - \alpha_{yy}\right)^{1/2} + \left(\alpha_{yy} - \alpha_{zz}\right)^{1/2} + \left(\alpha_{zz} - \alpha_{xx}\right)^{1/2} + 6\left(\alpha_{xy}^2 + \alpha_{yz}^2 + \alpha_{zx}^2\right)\right]/2\right\}^{1/2} \tag{54.3}$$

Static first-order hyperpolarizability

$$\beta_{total} = \left(\beta_x^2 + \beta_y^2 + \beta_z^2\right)^{1/2} \ for \ \beta(0, 0, 0) \tag{54.4}$$

where

$$\beta_x = \beta_{xxx} + \beta_{xyy} + \beta_{xzz}; \ \beta_y = \beta_{yyy} + \beta_{xxy} + \beta_{yzz};$$
$$\beta_z = \beta_{zzz} + \beta_{xxz} + \beta_{yyz}$$

All these computed values tabulated in Table 54.4. The components of these parameters show non-uniform charge distribution together with three magnitudes. Polarizability (α) and first-order hyperpolarizability (β) are observed in atomic units (a.u.) and also altered into an electrostatic unit (esu) through conversion factor 0.1482×10^{-24} esu (α) and 8.6393×10^{-33} esu (β). The values of anisotropic as well as isotropic polarizability are equivalent to 3.80×10^{-24} esu and -15.11×10^{-24} esu. Computed static first-order hyperpolarizability β (0, 0, 0) is 4.54×10^{-31} esu. As a result, 2-chloroanthraquinone has characteristics to be an ideal candidate for non-linear optical applications.

Table 54.4 Static polarizabilities, dipole moments, first-order hyperpolarizability elements of 2-chloroanthraquinone at B3LYP/6-311++G (d, p) basis set

Parameters	Values (a.u.)
Dipole moment	
μ_x	0.51
μ_y	−1.78
μ_z	0.00
μ_{total}	1.85
Polarizability	
α_{xx}	−98.89
α_{yy}	−100.91
α_{zz}	−106.06
α_{xy}	−14.34
α_{xz}	0.00
α_{yz}	0.00
$<\alpha>$	−101.96
$\Delta\alpha$	25.65
First-order hyperpolarizability	
β_{xxx}	−5.58
β_{yyy}	−39.73
β_{zzz}	0.00
β_{xyy}	40.66
β_{xxy}	−11.80
β_{xxz}	0.00
β_{xzz}	−4.03
β_{yzz}	9.06
β_{yyz}	0.00
β_{xyz}	0.00
β_{total}	52.66

Fig. 54.4 Mulliken charges of 2-chloroanthraquinone atoms

54.4.5 Mulliken Charges

In Mulliken population analysis, the partial atomic charges are evaluated by Mulliken charges [22]. Mulliken charges have measured using DFT/B3LYP/6-311++G (d, p) in several solvents as methanol, acetone, DMSO, and ethanol as well as in gaseous phase. The calculations executed with the help of quantum computational chemistry, which depends on a linear arrangement of atomic orbitals. These calculations utilize as variables in linear regression measures. Figure 54.4 indicates the positive and negative charge of the atoms in the compound.

54.5 Conclusions

The electronic solvation and non-linear optical activity of 2-chloroanthraquinone were calculated from UV-visible experimental method together with density functional theory. Experimental findings exhibited a good deal with theoretical outcomes. The high values of hyperpolarizabilities indicated that the titled compound is appropriate for non-linear optical materials. The merits of HOMO/LUMO energy gap provide the charge-transfer interaction and chemical stability inside a molecule. Therefore, experimental together with theoretical outcomes of 2-chloroanthraquinone makes it an appropriate electron transport material for various organic electronic devices.

References

1. Y. Atalay, D. Avcı, A. Başoğlu, Linear and non-linear optical properties of some donor-acceptor oxadiazoles by ab initio Hartree-Fock calculations. Struct. Chem. **19**, 239–246 (2008). https://doi.org/10.1007/s11224-007-9278-3

2. S. Ranjitha, V. Aroulmoji, T. Mohr, P.M. Anbarasan, G. Rajarajan, Structural and spectral properties of 1,2-dihydroxy-9,10-anthraquinone dye sensitizer for solar cell applications. Acta Physica Polonica A. **126**, 833–839 (2014). https://doi.org/10.12693/APhysPolA.126.833

3. S. Ranjitha, G. Rajarajan, T.S. Gnanendra, P.M. Anbarasan, V. Aroulmoji, Structural and optical properties of Purpurin for dye-sensitized solar cells. Spectrochimica Acta Part A: Mol. Biomol. Spectr. **149**, 997–1008 (2015). https://doi.org/10.1016/j.saa.2015.04.046

4. Z. MacHatova, Z. Barbierikova, P. Poliak, V. Jančovičová, V. Lukeš, V. Brezová, Study of natural anthraquinone colorants by EPR and UV/vis spectroscopy. Dyes Pigm. **132**, 79–93 (2016). https://doi.org/10.1016/j.dyepig.2016.04.046

5. S.T. Hung, A. Bhuyan, K. Schademan, J. Steverlynck, M.D. McCluskey, G. Koeckelberghs, K. Clays, M.G. Kuzyk, Spectroscopic studies of the mechanism of reversible photodegradation of 1-substituted aminoanthraquinone-doped polymers. J. Chem. Phys. **144** (2016). https://doi.org/10.1063/1.4943963

6. D. Jacquemin, J. Preat, M. Charlot, V. Wathelet, J.M. André, E.A. Perpète, Theoretical investigation of substituted anthraquinone dyes. J. Chem. Phys. **121**, 1736–1743 (2004). https://doi.org/10.1063/1.1764497

7. M.C. Sreenath, I. Hubert Joe, V.K. Rastogi, Third-order optical nonlinearities of 1,5-Diaminoanthraquinone for optical limiting application. Opt. Laser Technol. **108**, 218–234 (2018). https://doi.org/10.1016/j.optlastec.2018.06.056

8. M. Rashidian, D. Dorranian, S. Ahmadi Darani, S. Saghafi, M. Ghoranneviss, Nonlinear responses and optical limiting behavior of Basic Violet 16 dye under CW laser illumination. Optik. **120**, 1000–1006 (2009). https://doi.org/10.1016/j.ijleo.2008.05.001

9. Z. Cai, L. Deng, M. Zhou, J. Gao, Z. Sun, Third-order nonlinear optical studies of new anthraquinone derivatives. Opt. Commun. **283**, 5199–5202 (2010). https://doi.org/10.1016/j.optcom.2010.07.048

10. S. Raghavendra, T.C. Shekhara Shetty, C.S.C. Kumar, S.R. Maidur, P.S. Patil, C.K. Quah, G.S. Ananthnag, S. Chandraju, S.M. Dharmaprakash, Nonlinear reverse saturation absorption, self-defocusing behavior and structure-property relationship of a novel 2,3,4-trimethoxy-4′-nitrochalcone single crystal. J. Mol. Struct. **1193**, 177–184 (2019). https://doi.org/10.1016/j.molstruc.2019.04.102

11. S. Tariq, A.R. Raza, M. Khalid, S.L. Rubab, M.U. Khan, A. Ali, M.N. Tahir, A.A.C. Braga, Synthesis and structural analysis of novel indole derivatives by XRD, spectroscopic and DFT studies. J. Mol. Struct. 127438 (2019). https://doi.org/10.1016/j.molstruc.2019.127438

12. B. Mohan, M. Choudhary, S. Bharti, A. Jana, N. Das, S. Muhammad, A.G. Al-Sehemi, S. Kumar, Syntheses, characterizations, crystal structures and efficient NLO applications of new organic compounds bearing 2-methoxy-4-nitrobenzeneamine moiety and copper (II) complex of (E)-N′-(3,5-dichloro-2-hydroxybenzylidene) benzohydrazide. J. Mol. Struct. **1190**, 54–67 (2019). https://doi.org/10.1016/j.molstruc.2019.04.059

13. L. Mydlova, S. Taboukhat, A. Ayadi, A. Migalska-Zalas, A. El-Ghayoury, A. Zawadzka, M. Makowska-Janusik, B. Sahraoui, Theoretical and experimental investigation of multifunctional highly conjugated organic push-pull ligands for NLO applications. Opt. Mater. **86**, 304–310 (2018). https://doi.org/10.1016/j.optmat.2018.10.017

14. D. Guichaoua, B. Kulyk, V. Smokal, A. Migalska-Zalas, O. Kharchenko, O. Krupka, O. Kolendo, B. Sahraoui, UV irradiation induce NLO modulation in photochromic styrylquinoline-based polymers: computational and experimental studies. Org. Electron. **66**, 175–182 (2019). https://doi.org/10.1016/j.orgel.2018.12.022

15. S. Zafar, Z.H. Khan, M. Khan, Experimental and theoretical investigations of nonlinear optical properties of 1,4-diamino-9,10-anthraquionone. Spectrochimica Acta Part A: Mol. Biomol. Spectr. **114**, 164–169 (2013). https://doi.org/10.1016/j.saa.2013.05.001

16. A.I. Daud, W.M. Khairul, E. Augustine, S. Arshad, I.A. Razak, Synthesis, spectroscopic, structural elucidation, NLO characteristic and Hirshfeld surface analysis of (E)-1-(4-ethylphenyl)-3-(4-(heptyloxy)phenyl)prop-2-en-1-one: a dual approach of experimental and DFT calculations. J. Mol. Struct. **1194**, 124–137 (2019). https://doi.org/10.1016/j.molstruc.2019.05.046

17. C.W. Ghanavatkar, V.R. Mishra, N. Sekar, E. Mathew, S.S. Thomas, I.H. Joe, Benzothiazole pyrazole containing emissive azo dyes decorated with ESIPT core: linear and non linear optical properties, Z scan, optical limiting, laser damage threshold with comparative DFT studies. J. Mol. Struct. 127401 (2019). https://doi.org/10.1016/j.molstruc.2019.127401

18. R.R. Mallah, D.R. Mohbiya, M.C. Sreenath, S. Chitrambalam, I.H. Joe, N. Sekar, Fluorescent meso-benzyl curcuminoid boron complex: synthesis, photophysics, DFT and NLO study. Opt. Mater. **84**, 786–794 (2018). https://doi.org/10.1016/j.optmat.2018.08.012

19. S. Sathiya, M. Senthilkumar, C. Ramachandra Raja, Crystal growth, Hirshfeld surface analysis, DFT study and third order NLO studies of thiourea 4 dimethyl aminobenzaldehyde. J. Mol. Struct. **1180**, 81–88 (2019). https://doi.org/10.1016/j.molstruc.2018.11.067

20. T. Joseph, H.T. Varghese, C.Y. Panicker, T. Thiemann, K. Viswanathan, C. Van Alsenoy, Infrared and Raman spectroscopic analysis and theoretical computation of the first hyperpolarizability of a monoarylated anthraquinone, 1-(4-methoxyphenyl)-4-methylanthraquinone. J. Mol. Struct. **1005**, 17–24 (2011). https://doi.org/10.1016/j.molstruc.2011.07.060

21. T. Joseph, H.T. Varghese, C.Y. Panicker, T. Thiemann, K. Viswanathan, C. Van Alsenoy, T.K. Manojkumar, Spectroscopic (FT-IR, FT-Raman), first order hyperpolarizability, NBO analysis, HOMO and LUMO analysis of 2,4-bis(2-methoxyphenyl)-1-phenylanthracene- 9,10-dione by ab initio HF and density functional methods. Spectrochimica Acta Part A: Mol. Biomol. Spectr. **117**, 413–421 (2014). https://doi.org/10.1016/j.saa.2013.08.016

22. A. Jha, D. Chakraborty, V. Srinivasan, J. Dasgupta, Photoinduced charge transfer in solvated anthraquinones is facilitated by low-frequency ring deformations. J. Phys. Chem. B **117**, 12276–12285 (2013). https://doi.org/10.1021/jp408954p

Chapter 55
A Simple Model for Electron Impact Elastic Cross-section of Complex Bio-molecules for Energies from 20–2000 eV

Pooja Bhowmik, B. L. Ahuja, and Foram M. Joshi

Abstract Track simulations of mono-energetic ionizing particles along with the advancements in mathematical modeling, will elucidate mechanism of DNA damage by ionizing radiations. The theoretical tool to simulate radiation track is Monte Carlo Track Structure code, in which scattering cross-sections of ionizing particles are vital inputs. In addition, electron impact elastic cross-section is key to assess shape of tracks of the secondary electrons. However, electron impact elastic cross-sections of complex bio-molecules are either inadequate or variegated at energies below 100 eV. Thus, in the present report electron impact elastic cross section of DNA bases are presented. Spherical Complex Optical Potential is employed to evaluate scattering cross-section of atoms constituting the molecule. A simple weighing factor based on Minimum Polarizabilty Principle and volume effect of static dipole polarizability; has been introduced in most basic form of Additivity, namely Independent Atom Model (IAM). The factor utilizes polarizabilities of molecules and their constituent atoms to determine cross-section by means of IAM.

55.1 Introduction

Electron collisions with complex biomolecules have important applications in biophysical modeling [1, 2] by simulating radiation track of monoenergetic electrons interacting with the medium. Monte Carlo Track Structure (MCTS) codes is state-of-art that simulates physical interaction of ionizing radiations passing through biological matter and retrieve information on energy deposition upto nanometer scale to model biological cell damage mechanism. These simulations have applications in radiotherapy for diagnosis and computation of dose, and also these are useful for radiation protection purposes [3]. For simulation of track structure, material specific data

P. Bhowmik (✉) · B. L. Ahuja
Department of Physics, University College of Science, M. L. Sukhadia University, Udaipur, Rajasthan 313001, India

F. M. Joshi
G. H. Patel College of Engineering and Technology, Vallabh Vidyanagar, Gujarat 388120, India

are mandatory, especially cross-sections describing the interaction of ionizing radiation like secondary electrons interacting with the molecules of biological media. Till date reliable cross-section data for electron collision with components of DNA and other molecules of biological relevance are partially available [4], because of difficulties encountered in experiments and complicated theoretical methods available to estimate electron impact cross-sections of large polyatomic molecules. Moreover, computational tools for accurate calculations to be used in simulations of track structure are expensive. Thus, semi-empirical models that can generate cross-sections with acceptable accuracies are highly demanded.

Similarly, elastic cross-sections (Q_{el}) by electron impact is its key role in determining spatial distribution of electron tracks in media. However, data of electron impact elastic cross-sections for large polyatomic molecule are not adequate mainly in low incident energy regime. Until now, electron impact elastic cross-sections for DNA/RNA nucleobase are reported by Blanco-Garcia [5] using SCAR formalism at 10 eV to 10 keV energy range; Mozejko and Sanche [6] accounted for the same within energy range of 50 eV to 1 keV using Independent Atom Model (IAM). Recently, Bug et al. [6] have published cross-section data set of DNA analogue namely tetrahydrofuran (THF), trimethylphosphate (TMP), pyrimidine (PY) and purine (PU) in energies between 10 eV to 1 keV. Essentially, pyrimidine is a precursor of DNA nucleobase like cytosine, uracil and thymine; whereas purine is prototype for adenine and guanine. It is to be noted that pyrimidine is profoundly studied target over a wide range of incident electron energy. Earlier work on Q_{el} by electron impact on pyrimidine are reported in Palihawadana et al. [7] within 3–50 eV energy, Sanz et al. [8] used SCAR method to determine Q_{el} upto 10 keV; theoretical calculations by Ferraz et al. [9] within 0.2–500 eV energy, and that from Sinha and Antony [10] in the energy range (10–5000 eV). Nevertheless, Bug et al. [6] has developed model function based on comprehensive set of experimental data and literature review, to calculate integrated elastic cross-section of pyrimidine for energy range of 9 eV to 1 keV.

The simplest procedure of calculating molecular cross-section is Additivity Rule (AR), specifically known as IAM. In IAM, molecular cross-sections are determined by adding cross-sections of atoms comprising the molecule. Besides, IAM ignores geometrical screening of atoms after formation of molecule. Consequently, the results are much higher than the actual molecular cross-sections at low incident electron energies. Later many theories evolved to improvise AR and generate more reliable results. One of them is SCAR [11] that accounts for screening corrections in AR by introducing average overlapping of atomic pairs in the molecule, now it has been successfully implemented on number of large targets for cross-section calculations. The, present work is another effort to extend AR in low energies, where the screening correction is relatively easy to apply for evaluation of Q_{el} by electron impact on large polyatomic molecules.

In the present work, our proposed methodology called Polarizability Based Additivity Rule (PBAR) has been used to calculate elastic cross-section of DNA bases namely pyrimidine ($C_4H_4N_2$), purine ($C_5H_4N_4$), uracil ($C_4H_4N_2O_2$) and adenine ($C_5H_5N_5$). The present cross-sections are compared with corresponding available data.

55.2 Methodology

The procedure of calculating atomic cross-sections using Spherical Complex Optical Potential (SCOP) has been described in previous works [12, 13]. Hence, SCOP is briefly described in the present section. In practice, the interaction potential is represented by optical analogy in SCOP with the potential having real and imaginary parts as expressed below

$$V(r, E_i) = V_R(r, E_i) + i V_I(r, E_i) \qquad (55.1)$$

Here r is the radial distance, V_R is a real part and is the sum of potential arising due static, exchange and polarization processes occurring during the interaction. V_I is the imaginary part of potential because of absorption process due to inelastic channels also known as absorption potentials. The input wave functions taken from the Rothan Hartree Fork are utilized to compute charge density of individual atom and the potentials are modeled through the expressions as described in our previous work [12, 13]. Subsequently, the final form of optical potential is then substituted in Schrodinger equation to derive a complex phase shift. The complex phase shifts are then integrated to construct S-matrix and obtain Q_{el}, total inelastic (Q_{inel}) and total (Q_T) cross-sections of each individual atom. Mathematical formulation of Q_T is as follows:

$$Q_T(E_i) = Q_{el}(E_i) + Q_{inel}(E_i) \qquad (55.2)$$

To obtain the cross-sections of molecule, Additive Rules are applied. IAM is the most basic form of AR to obtain electron scattering cross sections of molecule by summing the cross sections of its constituent atoms. To focus on Q_{el}, the expression for integrated molecular elastic cross-section as per AR is written as,

$$Q_{el}(M) = \sum_{i=1}^{n} Q_{el}^{(i)}(A) \qquad (55.3)$$

In (55.3) n is the number of atoms in the molecule and $Q_{el}^i(A)$ is the total elastic cross section of ith atom in the molecule**.** It is assumed that each atom in the molecule scatters independently. Thus, molecular binding and interaction of constituent atoms in the molecule is neglected in IAM, due to which electron-molecule collision can be

treated as problem of collision with individual atoms. Therefore, at incident energies below 100 eV it fails to generate appropriate results because mutual overlapping of neighboring atoms in the molecule does not come into picture. Hence a weighing factor is introduced in AR which is based on static dipole polarizabilities and named as PBAR. The presently suggested expression for the cross-section becomes

$$Q_{el}(M) = Z\left(\sum_{i=1}^{n} Q_{el}^{(i)}(A)\right) \tag{55.4}$$

wherein

$$Z = \frac{(\alpha_M)}{\sum_{i=1}^{n}(\alpha_A^i)}$$

Here, α_M is polarizability of the molecule, and α_A^i is polarizability of the ith atom constituting the molecule.

The dimensionless Z factor based on polarizabilities relies on some aspects summarized here. Additive models are also used to estimate molecular property from the associated atomic property of atoms comprising the molecule. In other words, the additive model to express a molecular property is the weighted sum of that property associated with the constituent atoms. Nonetheless, AR is also applied to calculate molecular polarizability from the atomic polarizabilities of atoms in free state that forms the molecule. The ratio between actual molecular polarizability as derived from reliable theoretical or experimental methods to the sum of polarizabilities of constituent free atoms should ideally be less than one due to Minimum Polarizability Principle [14]. This principle implies that the polarizability of molecule in equilibrium state is lesser than the polarizability sum of its constituent atoms on free state. Similar additive models are applicable on volumes as well. Evidently, molecular volumes also obey Minimum Volume Principle (MVP) [14]. That means the net molecular volume is always lesser than the sum of the atomic volumes comprising the molecule. It is also an established fact that polarizability has dimensions of volume [15] and directly proportional to atomic or molecular volumes [16]. It can thus be deduced that the ratio 'Z' is percentage contribution of molecular volume in the sum of atomic volumes from which the molecule is formed. Therefore, it is reasonable enough to propose a weighing factor based on static dipole polarizability.

In the present work the ratio Z for the targets pyrimidine, uracil, purine and adenine are 0.726, 0.746, 0.791 and 0.742, respectively. The multiplying factor Z of pyrimidine, uracil, purine, adenine has been derived from their corresponding polarizabilities that are 8.59, 10.09, 9.09 and 13.08 with units in Å^3. Another essential component of Z is atomic polarizability of atoms building the molecule; present molecular targets are composed of carbon, hydrogen and nitrogen atoms. Therefore, standard polarizabilities of carbon, hydrogen and nitrogen used here are 1.760, 0.667and 1.1 respectively with units Å^3 to determine Z. The data of atomic and

molecular polarizabilities are taken from Computational Chemistry Comparison and Benchmark Database (CCCBDB) [17].

55.3   Results

PBAR as defined in previous section has been applied on DNA bases namely pyrimidine, purine, uracil and adenine. We have obtained total elastic cross-section by electron impact at energies from 30 to 2000 eV. Pyrimdine is only extensively studied molecule in the present list of targets and its Q_{el} are reported by various theoretical and experimental groups. Bug et al. [6] have modeled cross-sections of Pyrimidine, that are used as benchmark for underpinning biophysical modeling.

Thus, calculations for Q_{el} of pyrimidine will be outlined first, followed by remaining targets. Numerical values of present Q_{el} for the targets pyrimidine, uracil, purine and adenine are collated in Table 55.1.

In Fig. 55.1, Q_{el} for pyrimidine are plotted and comparisons are done with the theoretical and experimental results available from other publications. A very good agreement has been observed with present Q_{el} and calculations of Bug et al. in the range from 40 to 1000 eV. Below 40 eV the magnitude of cross-sections are higher than the modelled values, yet lies within the range of acceptable accuracy when compared with other published results. Therefore, it can be inferred that the present results and the scheme employed are quite reasonable in deducing Q_{el} of large polyatomic molecules.

Further, in Fig. 55.2 we report cross-sections of uracil. Mozejko and Sanche [6] utilized IAM to calculate Q_{el} of the target and it can be noticed that the cross-sections

Table 55.1 PBAR calculated Q_{el} (in Å^2) for DNA/RNA bases: pyrimidine ($C_4H_4N_2$), purine ($C_5H_4N_4$), uracil ($C_4H_4N_2O_2$) and adenine ($C_5H_5N_5$)

Incident energy (eV)	Pyrimidine	Purine	Uracil	Adenine
20	47.58	62.23	56.56	73.27
30	35.67	47.36	43.41	55.72
40	27.98	37.52	34.60	44.18
50	22.76	30.75	28.50	36.25
70	16.50	22.51	20.99	26.59
100	12.52	17.05	15.89	20.06
200	8.15	11.12	10.13	13.01
300	6.33	8.69	7.92	10.18
500	4.44	6.15	5.64	7.21
900	2.83	3.94	3.66	4.62
1000	2.61	3.64	3.36	4.27
2000	1.47	2.05	1.91	2.41

Fig. 55.1 Electron impact
elastic cross-sections for
pyrimidine: Solid
line-present results,
star—Palihawadana et al.
[7], dashed line—Sanz et al.
[8], dash dot—Sinha and
Antony [10], dotted
line—Ferraz et al. [9], dash
dot dot—Bug et al. [6]
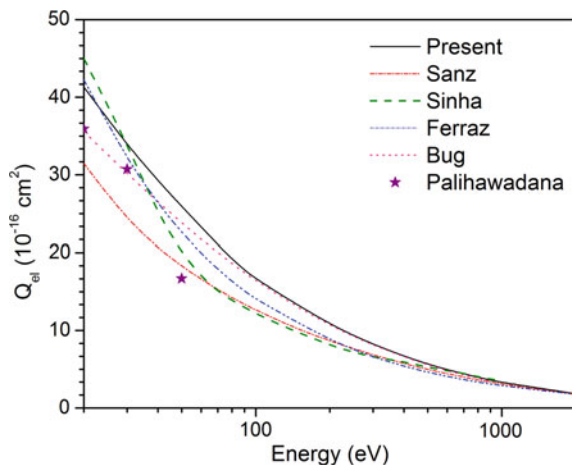
Fig. 55.2 Electron impact
elastic cross-sections for
uracil: Solid line—present
results, dashed line—Blanco
and Garcia [5], dotted
line—Mozejko and Sanche
[6]
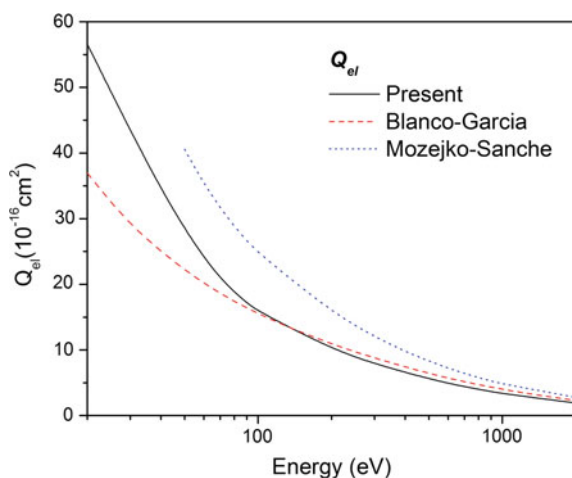
are higher than [5] in the shown energy range below 300 eV. For energies above 70 eV,
the present Q_{el} have reconcile well with calculations reported by Blanco and Garcia
using SCAR [5]; below 70 eV the magnitudes of present calculations are higher.

In Fig. 55.3 presently computed cross-sections of purine are presented along with
those reported by Bug et al. [6]. The authors [6] have deduced Q_{el} of purine by adding
the cross-sections of their molecular composition. The present Q_{el} agrees well with
Bug et al. in the energy range above 200 eV, below incident energies of 200 eV these
are smaller and remarkably shoots up at lower energies. No experimental results of
Q_{el} for purine are available which hinders the experimental validation of present
investigations.

Figure 55.4 shows the electron impact Q_{el} of adenine molecule which has a purine
like base along with those reported by Blanco-Garcia [5], and Mozejko and Sanche

Fig. 55.3 Electron impact elastic cross-sections for purine: Solid line—present results, dashed line—Bug et al. [6]
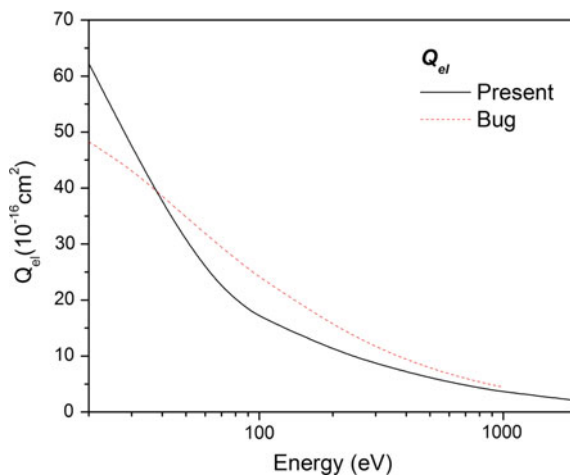
Fig. 55.4 Electron impact elastic cross-sections for adenine: Solid line—present work, dashed line—Blanco and Garcia [5], dotted line—Mozejko and Sanche [6]
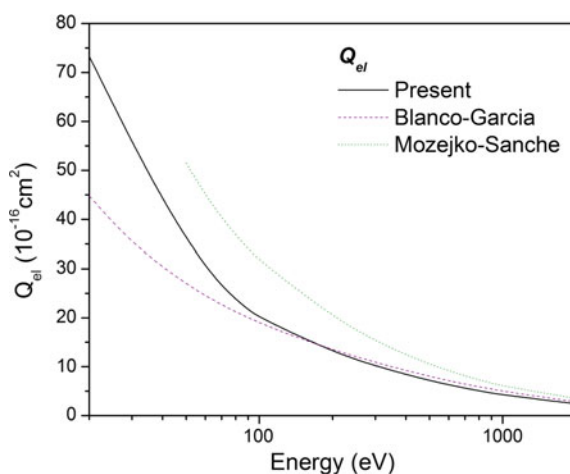
[6]. We observe similarity in behavior of Q_{el} for adenine and uracil molecule. The present Q_{el} are in good agreement with SCAR calculations. It is clear from the figure that presently modified IAM methodology show better values of cross-sections than earlier calculated from IAM scheme [6].

55.4   Conclusions

Electron impact elastic cross-sections of pyrimidine calculated from the proposed PBAR model using IAM technique are in very good agreement with other published results; especially with the data of Bug et al. Simultaneously, presently suggested

method is successfully implemented on other DNA bases namely purine, adenine and uracil to deduce Q_{el} by electron impact for energy range 30–2000 eV. Present work unambiguously depicts that the revised IAM model PBAR generates better results than the original IAM scheme. One can conclude that PBAR scheme is simple and effective method to approximate the cross-sections for large polyatomic molecules. Present cross-section data for elastic process of DNA bases and revised IAM model PBAR are expected to be very useful for coding of electron transport model of track structure.

References

1. H. Nikjoo, D. Emfietzoglou, T. Liamsuwan, R. Taleei, D. Liljequist, S. Uehara, Radiation track, DNA damage and response—a review. Rep. Prog. Phys. **79**, 116601 (2016)
2. I. Kyriakou, D. Emfietzoglou, V. Ivanchenko, M.C. Bordage, S. Guatelli, P. Lazarakis, H.N. Tran, S. Incerti, Microdosimetry of electrons in liquid water using the low-energy models of Geant4. J. Appl. Phys. **122**, 024303–024317 (2017)
3. I.V. Mavragani, Z. Nikitaki, S.A. Kalospyros, A.G. Georgakilas, Ionizing radiation and complex DNA damage: from prediction to detection challenges and biological significance. Cancers **11**, 1789 (2019)
4. L.H. Toburen, Challenges in Monte Carlo track structure modeling. Int. J. Radiat. Biol. **88**, 2 (2012)
5. F. Blanco, G. Garcia, A screening-corrected additivity rule for the calculation of electron scattering from macro-molecules. J. Phys. B: At. Mol. Opt. Phys. **42,** 145203 (2009)
6. P. Mozejko, L. Sanche, Cross section calculations for electron scattering from DNA and RNA bases. Radiat. Environ. Biophys. **42**, 201 (2003)
7. M.U. Bug, W.Y. Baek, H. Rabus, C. Villagrasa, S. Meylan, A.B. Rosenfeld, An electron-impact cross section data set (10 eV–1 keV) of DNA constituents based on consistent experimental data: a requisite for Monte Carlo simulations. Radiat. Phys. Chem. **130**, 459 (2017)
8. P. Palihawadana, J. Sullivan, M. Brunger, C. Winstead, V. McKoy, G. Garcia, F. Blanco, S. Buckman, Low-energy elastic electron interactions with pyrimidine. Phys. Rev. A **84**, 062702 (2011)
9. G. Sanz, M.C. Fuss, F. Blanco, Z. Masin, J.D. Gorfinkiel, F. Carelli, F. Sebastianelli, F.A. Gianturco, G. Garcia, Electron scattering cross section calculations for polar molecules over a broad energy range. Appl. Radiat. Isot. **83**, 57 (2014)
10. J. Ferraz, A. dos Santos, G. de Souza, A. Zanelato, T. Alves, M.-T. Lee, L. Brescansin, R. Lucchese, L. Machado, Cross sections for electron scattering by formaldehyde and pyrimidine in the low- and intermediate-energy ranges. Phys. Rev. A **87**, 032717 (2013)
11. N. Sinha, B. Antony, Electron and positron interaction with pyrimidine: a theoretical investigation. J. Appl. Phys. **123**, 124906 (2018)
12. F. Blanco, G. Garcia, Improvements on the quasifree absorption model for electron scattering. Phys. Lett. A **317**, 458 (2003)
13. F.A. Shelat, K.N. Joshipura, K.L. Baluja, P. Bhowmik, H.N. Kothari, Ind. J. Phys. **85**, 1739 (2011)
14. D. Gupta, R. Naghma and B. Antony, "Elastic and total cross sections for simple biomolecules in the intermediate energy range," AIP Advances **5**, 097159 (2015).
15. S. A. Blair, A. J. Thakkar, Relating polarizability to volume, ionization energy, electronegativity, hardness, moments of momentum, and other molecular properties. J. Chem. Phys. **141**, 074306 (2014)
16. J.D. Jackson, *Classical Electrodynamics*, 2nd edn. (Wiley, New York, 1975)

17. A.D. Becke, E.R. Johnson, Exchange-hole dipole moment and the dispersion interaction: High-order dispersion coefficients. J. Chem. Phys. **124**, 014104 (2006)
18. *Computational Chemistry Comparison and Benchmark Database.* https://cccbdb.nist.gov

Chapter 56
Detection of Water Quality for Purity Assurance Using Optical Means

R. Gupta, M. Tyagi, Deepak, and A. Singh

Abstract Advancement in the technological development ushers undesirable effects, especially on the environment. Water pollution is one of the major concerns in many areas worldwide, resulting in adverse consequences on human hygiene. Therefore, detection of quality of water is the only measure in decimating its adverse effects. Many purifiers are available in the market for improving the quality of water. However, while aiming for cleaner water using modern techniques, the presence of desirable ions in water is compromised, thus improving the quality of water at the cost of drastically reduced content of ions that is required for human consumption. This makes the choice of filter very important. In the present work, four different kind of water i.e. tap water, ground water, candle distilled water and RO water have been studied using two different methods. In first method, the dielectric losses have been studied using Vector Network Analyzer, while in the second method, refractive index of all the samples have been monitored using spectrometer.

56.1 Introduction

Advancement in the technological development usher undesirable effects, especially on the environment. Water pollution is one of the major concerns in many areas worldwide, having adverse consequences on human hygiene [1]. Lack of mass availability of potable water and the related health threats are a major issue of concern all over the world. More people die from drinking unsafe water then from war, accidents or natural calamities put together [2]. Therefore, detection of quality of water is the only measure in decimating its adverse effects. Also, since the contamination present in various sources of water varies significantly from place to place, this emphasizes

R. Gupta
Department of Physics & Astrophysics, University of Delhi, Delhi 110007, India

R. Gupta · M. Tyagi · Deepak · A. Singh (✉)
Department of Physics, Hindu College, University of Delhi, Delhi 110007, India
e-mail: adarshsingh@hinducollege.ac.in

the need for location specific analysis of water quality and use of appropriate method of filtration required specific to a location [1].

The criterion to assess water quality are well researched and documented [3]. Various parameters such as, interferometry, UV spectroscopy have been reported in text for evaluation and analysis of water quality [4–7]. Most of these techniques use high end costly equipment and the said experiments can only be performed in laboratory like monitored conditions and are hence impractical to be used in the interiors or rural areas [8]. The other portable sensors lack broad range sensitivity. The present work uses spectroscopy to determine the refractive index of various water samples. Spectroscopy is a cost effective yet robust tool of consistent sensitivity to estimate the refractive index and is available in most higher secondary schools and undergraduate labs. Refractive index (RI) is a very generic indicator as every substance has a specific refractive index and a mixture of substances will give a bulk value of RI and a dielectric behavior spectrum which is superimposition of dielectric behavior of each individual constituent of the matrix [9–11]. Being a generic sensing concept, dielectric constant and refractive index have a number of advantages for water quality detection. Most water quality sensors that are currently in use are sensitive to only a part of the spectrum of possible contaminations, whereas a refractive index measurement can detect all chemical changes, irrespective of their nature [12]. This is especially the case for many smaller organic molecules, e.g. organic solvents, which are used in industry, and can contaminate water sources and thus form a threat for drinking water.

In the present work an initiative has been sequenced to survey the quality of water available from different sources in Delhi and its analysis for detecting the presence of contaminants using optical techniques. Four most commonly used sources of water in Delhi have been studied, namely, ground water, tap water supplied by the local municipality, candle filter water and RO water. The level of contaminants present in each sample is characterized by the dielectric loss behavior in the infrared spectrum using Vector Network Analyzer (VNA, Model: Agilent) and refractive index values in optical frequencies using spectroscopy. The water quality detection has been carried out as a function of refractive index and dielectric losses.

56.2   Experimental

Four different samples of water namely ground water (S1), candle filter water (S2), tap water (S3) and RO water (S4) have been selected for the present study. The level of contamination has been analyzed firstly using Vector Network Analyzer (VNA). The dielectric losses have been calculated. The optical spectroscopy has also been used by studying the variation in the minimum deviation for different samples of water. The undergraduate experiment of spectrometer has been exploited to extend our study. Initially, the spectrometer has been adjusted and calibrated using Schuster's focusing. Simultaneously to study the behavior of liquid (different sample of water: S1, S2, S3 and S4), a prism assembly has been developed which is hollow from

inside. Before determining the minimum deviation position, the angle of prism was calculated using conventional method. Finally, refractive index of different sample was then calculated by observing the minimum deviation positions for a particular wavelength.

56.3   Results and Analysis

Figure 56.1 shows the dipolar behavior of sample S4 for radio frequencies upto 18 GHz at 300 K. The water molecules behave as coupled mass thermal oscillators forming long chains and oscillate when subjected to RF frequencies. The oscillation produces a torque in the water dipole which results in the orientational polarization of water leading to a relaxation spectrum. Below the natural frequency of oscillation of a water molecule the dipoles oscillate with the frequency of applied field resulting in a constant dielectric behavior and nearly zero losses as seen in 0–2 GHz region in the Fig. 56.1.

As the frequency is increased, a time bound relaxation spectrum is observed since the water molecules gradually stop responding to the applied fields. The relaxation behavior near the natural frequency of water molecule results in dipolar absorption and can be readily observed as dielectric losses [13, 14]. The real part ε' which is plotted in black corresponds to the dielectric constant while the imaginary part plotted in blue represents the dielectric absorption losses. The dipole relaxation time of water is obtained to be nearly 1 cm i.e., in the free space wavelength region as reported by Thakur et al. and Nandedkar et al. [13, 14]. Figure 56.2 shows the dielectric losses (ε'') for different samples with respect to frequency varying from 1 to 18 GHz.

It can be readily seen that the loss curve for ground water shows most erratic behavior and a right shifted absorption peak. On the other hand RO water shows the smoothest curve and a sharp absorption peak. It is well established that the reverse

Fig. 56.1 Real and imaginary part of the dielectric constant for sample S4
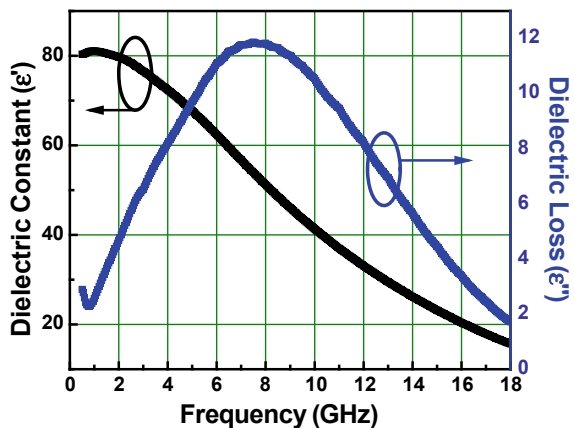
Fig. 56.2 Dielectric loss absorption spectrum of the different samples of water
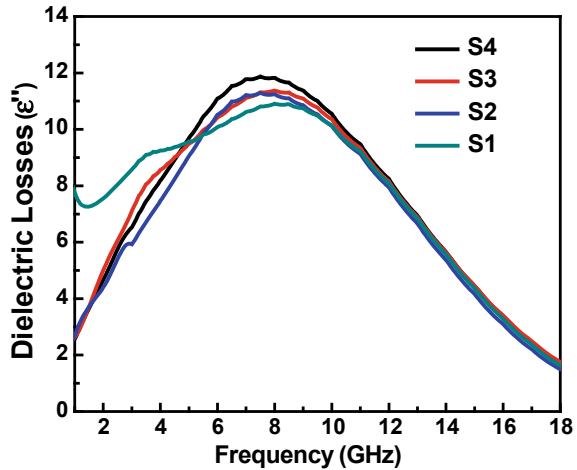
osmosis process of water purification removes not only all impurities from water but also the necessary ions for human consumption thus making the water devoid of all additional compounds. The absorption spectrum of RO water hence shows the dielectric loss behavior of a single compound i.e., nearly pure water. On the other hand in complex materials where a number of compounds are mixed together there would exist several different types of dipoles and hence several different relaxation mechanisms [15, 16]. These mechanisms would depend on the mass of the respective compounds as well as their movement speeds. Heavier atoms and compounds would increase the relaxation time as also would slower speeds [17]. The absorption loss spectra of such a complex material would not then be a smooth curve but a resultant curve obtained from the superimposition of several individual curves corresponding to different atoms/compounds present. The ground water is such a complex material with several ions, elements, minerals and organic matter present. These impurities present though in small amounts as compared to the volume of water, do tend to deviate the water absorption loss curve from being smooth to erratic as clearly seen in the Fig. 56.2. Similar deviations from a sharp smooth curve may also be observed in tap water and candle filter water samples also. However as contamination in these samples is far lower due to filtration, the loss curves of these two samples show a smaller degree of deviation. The right shift in the frequency spectrum of absorption losses of ground water clearly shows presence of heavier mass contaminants. It is seen from the figure that ground water which is the second most used potable water source in Delhi, contains high levels of contamination. Also these contaminants are significantly reduced in tap water and candle filter water, with not a very significant difference between the two.

Figure 56.3 shows the schematic of the set up used for calculating the refractive index of the four different samples. In this setup, a hollow prism has been used as liquid cell. The monochromatic light was incident on the liquid cell through the collimator. The position of the liquid cell was set at the minimum deviation point
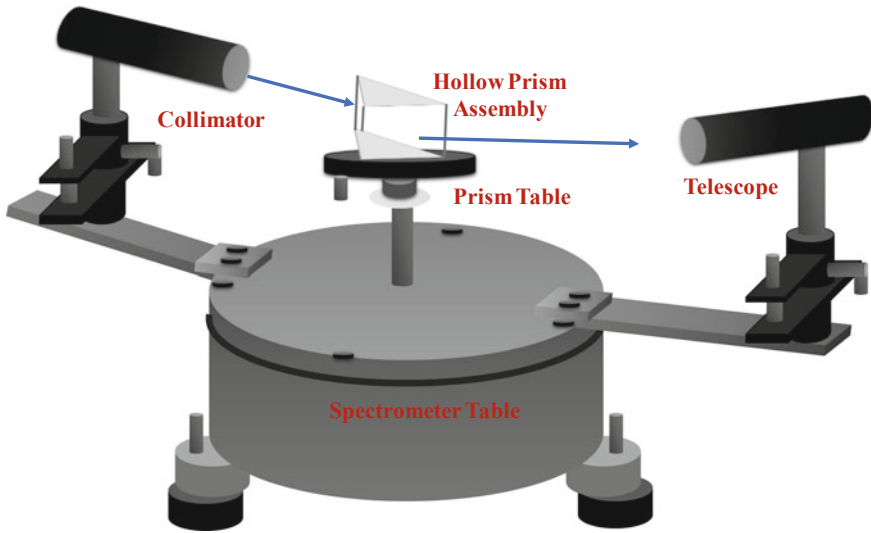
Fig. 56.3 Schematic of the set up used to measuring the refractive index of different samples

where the light ray passing through the prism is parallel to the base of the prism. The light ray gets deviated after passing through the liquid cell. The position of the telescope is set in such a way that the deviated light can be recorded and analyzed as shown in Fig. 56.3.

The refractive index for the different water samples is obtained using spectroscopy and a marked variation is observed (Fig. 56.4). It can be seen that for optical frequencies, ground water shows maximum refractive index. This is attributed to the presence of contaminants like complex compounds, ions, minerals and organic substance to

Fig. 56.4 Refractive index of the different samples of water
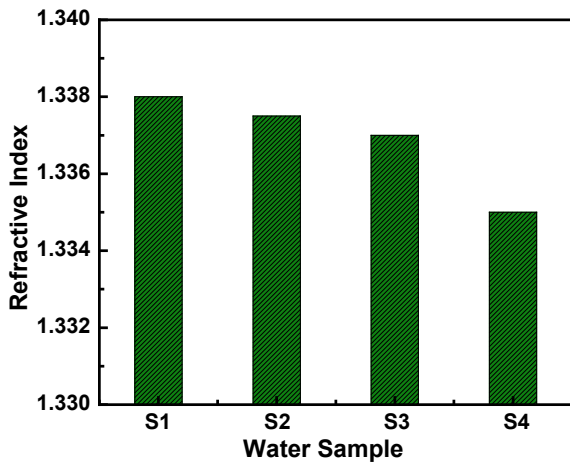
name a few. In this range of excitation electronic polarization is the dominant mechanism contributing to the refractive index [15, 16]. The increased content of heavy mass particles present in the water matrix in sample S1, results in larger contribution to the electronic polarizability as opposed to other water samples. RO water, on the other hand, is devoid of all organic matter, particulate impurities as well as other contaminants thus making its refractive index lowest.

56.4   Conclusion

In the present work, the quality of water from different sources has been surveyed successfully using optical technique, which is a powerful way of determining physical properties of liquids precisely. The analysis has been carried out using the principle of minimum deviation to detect variation in refractive index (μ) using, spectrophotometer, light source and hollow prism. The variations in μ have been studied with temperature for four different samples, namely, ground water, distilled water, tap water and RO water. It has been observed that the μ varied from 1.333 to 1.338 for different samples of water at the fixed temperature of 20°C. The μ was found to be minimum for RO water as expected. The results were also validated by measuring the dielectric losses of all the samples using VNA.

References

1. V. Novotny, *Water Quality: Prevention, Identification and Management of Diffuse Pollution* (Van Nostrand-Reinhold Publishers, 1994)
2. E. Ohno, M. Morisugi, P. Kyophilavong, H. Sao.Measurement of value of statistical life by evaluating diarrhea mortality risk due to water pollution in Laos and Vietnam (2012)
3. K. Onda, J. LoBuglio, J. Bartram, Global access to safe water: accounting for water quality and the resulting impact on MDG progress. Int. J. Environ. Res. Public Health **9**(3), 880–894 (2012)
4. M.H. Mahdieh*, T. Nazari, Measurement of impurity and temperature variations in water by interferometry technique
5. K.H. Chen, S.L. Yang, K.C. Chang, Measurement of small differences in refractive indices of solutions with interferometric optical method. Opt. Laser Eng. **45**, 1071–1076 (2007)
6. Y.L. Jin, J.Y. Chen, L. Xu, P.N. Wang, Refractive index measurement for biomaterial samples by total internal reflection. Phys. Med. Biol. **51**, 371–379 (2006)
7. M. Mahdieh, T. Nazari, Measurement of impurity and temperature variations in water by interferometry technique. Optik **124**, 4393–4396 (2013)
8. A. ElMekawy, H.M. Hegab, D. Pant, C.P. Saint, Bio-analytical applications of microbial fuel cell–based biosensors for onsite water quality monitoring. J. Appl. Microbiol. **124**(1), 302–313 (2018)
9. Phys. Chem. B **104**, 7179–7182 (2000)

10. J. Phys. Chem. B **104**, 7179–7182 (2000)
11. M.N.R. Ashfold, P.W. May, C.A. Rego, N.M. Everitt, Chem. Soc. Rev. **23**, 21–30 (1994)
12. R. Verma, B.D. Gupta, Detection of heavy metal ions in contaminated water by surface plasmon resonance based optical fibre sensor using conducting polymer and chitosan. Food Chem. **166**, 568–575 (2015)
13. O.P. Thakur, A.K. Singh, Anaylysis of dielectric relaxation in water at microwave frequency. Adv. Stud. Theor. Phys. **2**(13), 637–644 (2008)
14. D.P. Nandedkar et al., Analysis of dipole relaxation time for water molecules at temperature of 2930 K. Phys. J. **2**(1), 15–22 (2016). http://www.aiscience.org/journal/pj
15. A.J. Dekker, *Electrical Engineering Materials*, Second Printing (Prentice Hall, Inc, Englewood Cliffe, N.J., 1961)
16. C. Kittel, *Introduction to Solid State Physics*, 1st/2nd Indian edn. (Asia Publishing House, Bombay, 1960) (Original US second edition, Wiley, New York, 1956)
17. A.R. Von HIppel, *Dielectric Materials and Applications* (Technology Press of MIT and Wiley, New York, Chapman and Hall Ltd., London, 1954)

Chapter 57
CDBA-Based Inverse Filter Configuration

Ram Bhagat, D. R. Bhaskar, and Pragati Kumar

Abstract This paper presents a tunable inverse filter configuration which uses two current differencing buffered amplifiers (CDBAs), two capacitors and three/four resistors. The proposed configuration realizes inverse low pass filter (ILPF), inverse high pass filter (IHPF), Inverse band pass filter (IBPF), and inverse band reject filter (IBRF). The validation of the proposed circuit has been established through PSPICE simulations. Simulated results are compared with the theoretical results using MATLAB.

57.1 Introduction

Inverse filters finds applications in communication, control and instrumentation systems to remove the distortion present in the useful signal while processing the signal [1]. In the past various active building blocks (ABB) have been used to realize the inverse active filters with different properties. A brief summary of the earlier works on the design of inverse active filters being tabulated below in Table 57.1.

From Table 57.1, it has been observed that there are very few tunable invers active filters exists in an open literature.

R. Bhagat (✉) · D. R. Bhaskar · P. Kumar
Department of Electrical Engineering, Delhi Technological University, Delhi, India
e-mail: rambhagat@dtu.ac.in

Table 57.1 Comparison with earlier reported inverse filters

References	ABBs used	No. of resistors used	No. of capacitors used	Tunability
[1]	1 NULLOR	4	2	No
[2]	3 CFOA	3–5	2	No
[3]	3 CFOA	2–3	3–4	No
[4]	1 CCII	2	1	No
[5]	4–6 CCII	3–4	2	No
[6]	2 CDBA	3	3	No
[7]	2 CDBA	2–4	2–4	No
[8]	2 CDBA	4/5	2	Yes
[9]	2 CDBA	4	2	No
[10]	2 CDBA	4/5	2	Yes
[11]	3 CDTA	2	2	No
[12]	1 CDTA	1	1	No
Proposed	2CDBA	3/4	2	Yes

Therefore, in this paper authors are presenting a multifunction tunable inverse filter topology with two CDBAs, three/four resistors and two capacitors. The working of the proposed inverse filter topology has been established through PSPICE simulations with CMOS CDBAs. Simulated results are compared with the theoretical results using MATLAB.

57.2 Proposed Inverse Filter Configuration

Figure 57.1 shows the CDBA representation, whose terminal current/voltage relationships are given in (57.1)

Fig. 57.1 CDBA representation
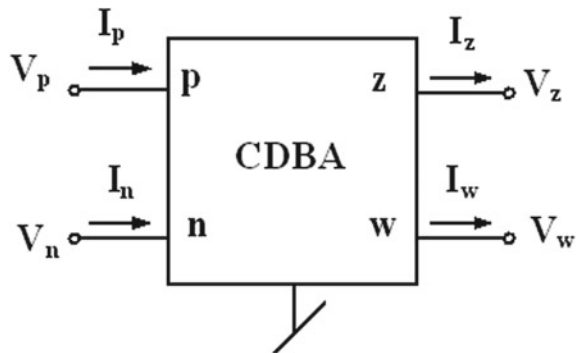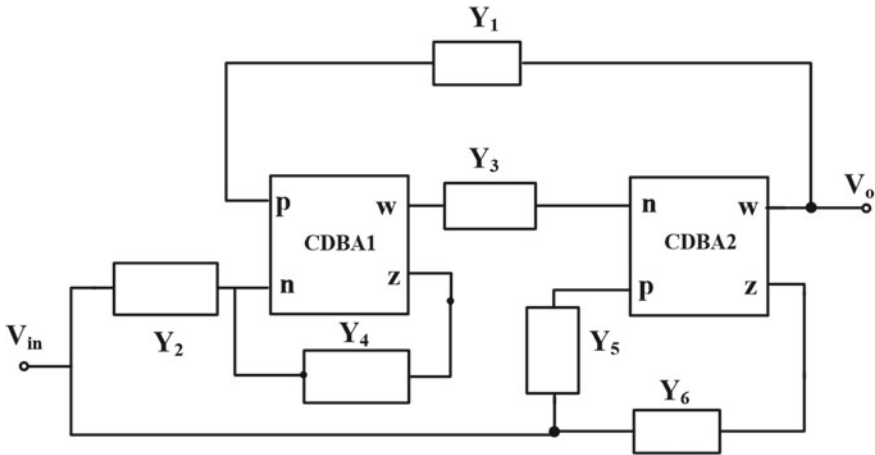
Fig. 57.2 Inverse filter topology

$$V_p = 0 = V_n \; V_w = V_z \text{ and } I_z = \left(I_p - I_n\right) \tag{57.1}$$

Figure 57.2 shows the multifunction inverse filter circuit which realizes ILPF, IHPF, IBPF and IBRF. The transfer function (TF) of which is given by

$$\frac{V_O}{V_{in}} = \frac{2Y_4 Y_6 + 2Y_4 Y_5 + Y_2 Y_3}{2Y_4 Y_6 + Y_1 Y_3} \tag{57.2}$$

The proper choice of branch admittances is going to realize various active inverse filters as shown below in Table 57.2. Table 57.3 shows the cut-off frequency (ω_0), bandwidth (BW)/quality factor (Q) of the inverse filters realized in Table 57.2.

Table 57.2 Transfer function realization of various inverse filters

Type of filter realized	Choice of admittances						Transfer function
	Y_1	Y_2	Y_3	Y_4	Y_5	Y_6	
ILPF	0	$\frac{1}{R_2} + C_1 s$	$C_2 s$	$\frac{1}{R_4}$	$\frac{1}{R_5}$	$\frac{1}{R_6}$	$\dfrac{\frac{1}{\frac{2}{C_1 C_2 R_4 R_6}}}{s^2 + \frac{1}{C_1 R_2} s + \frac{4}{C_1 C_2 R_4 R_6}}$ $\quad for\ R_5 = R_6$
IHPF	0	$\frac{1}{R_2}$	$\frac{1}{R_3}$	$C_1 s$	$\frac{1}{R_5}$	$C_2 s$	$\dfrac{\frac{1}{s^2}}{s^2 + \frac{1}{C_2 R_5} s + \frac{1}{2C_1 C_2 R_2 R_3}}$
IBPF	0	$\frac{1}{R_2}$	$\frac{1}{R_3}$	$C_1 s$	$C_2 s$	$\frac{1}{R_6}$	$\dfrac{\frac{1}{\frac{s}{C_2 R_6}}}{s^2 + \frac{1}{C_2 R_6} s + \frac{1}{2C_1 C_2 R_2 R_3}}$
IBRF	$\frac{1}{R_1}$	$\frac{1}{R_2}$	$\frac{1}{R_3}$	$C_1 s$	$\frac{1}{R_5}$	$C_2 s$	$\dfrac{\frac{1}{s^2 + \frac{1}{2C_1 C_2 R_2 R_3}}}{s^2 + \frac{1}{C_2 R_5} s + \frac{1}{2C_1 C_2 R_2 R_3}}$

Table 57.3 Cut-off frequency, bandwidth/quality factor of the inverse filters of Table 57.2

Type of inverse filter	(ω_0)	BW/Q
ILPF	$\dfrac{2}{\sqrt{C_1 C_2 R_4 R_6}}$	$Q = 2R_2\sqrt{\dfrac{C_1}{C_2 R_4 R_6}}$
IHPF	$\dfrac{1}{\sqrt{2C_1 C_2 R_2 R_3}}$	$Q = R_5\sqrt{\dfrac{C_2}{C_1 R_2 R_3}}$
IBPF	$\dfrac{1}{\sqrt{2C_1 C_2 R_2 R_3}}$	$BW = \dfrac{1}{C_2 R_6}$
IBRF	$\dfrac{1}{\sqrt{2C_1 C_2 R_2 R_3}}$	$BW = \dfrac{1}{C_2 R_5}$

Table 57.4 Sensitivity analysis of inverse filters

Filter	Sensitivity
ILPF	$S_{R4}^{\omega_0} = S_{R6}^{\omega_0} = -\frac{1}{2}$, $S_{R2}^{\omega_0} = 0$, $S_{C1}^{\omega_0} = S_{C2}^{\omega_0} = -\frac{1}{2}$, $S_{C2}^{Q} = S_{R4}^{Q} = S_{R6}^{Q} = -\frac{1}{2}$, $S_{C1}^{Q} = \frac{1}{2}$, $S_{R2}^{Q} = 1$
IHPF	$S_{R2}^{\omega_0} = S_{R3}^{\omega_0} = -\frac{1}{2}$, $S_{R5}^{\omega_0} = 0$, $S_{C1}^{\omega_0} = S_{C2}^{\omega_0} = -\frac{1}{2}$, $S_{C1}^{Q} = S_{R3}^{Q} = S_{R2}^{Q} = -\frac{1}{2}$, $S_{C2}^{Q} = \frac{1}{2}$, $S_{R5}^{Q} = 1$
IBPF	$S_{R2}^{\omega_0} = S_{R3}^{\omega_0} = -\frac{1}{2}$, $S_{R6}^{\omega_0} = 0$, $S_{C1}^{\omega_0} = S_{C2}^{\omega_0} = -\frac{1}{2}$, $S_{C2}^{BW} = S_{R6}^{BW} = -1$, $S_{C1}^{BW} = S_{R2}^{BW} = S_{R3}^{BW} = 0$
IBRF	$S_{R2}^{\omega_0} = S_{R3}^{\omega_0} = -\frac{1}{2}$, $S_{R5}^{\omega_0} = 0$, $S_{C1}^{\omega_0} = S_{C2}^{\omega_0} = -\frac{1}{2}$, $S_{C2}^{BW} = S_{R5}^{BW} = -1$, $S_{C1}^{BW} = S_{R2}^{BW} = S_{R3}^{BW} = 0$

Table 57.3 shows that the proposed inverse filter structure has independent tunability of ω_0, Q-factor and BW.

57.3 Sensitivity Analysis

The sensitivities of (ω_0), (BW) and (Q) of the inverse filters have tabulated in Table 57.4, from where it is observed that these inverse filters are enjoying low passive sensitivities.

57.4 Simulation Results

PSPICE simulations has been used to check the functioning of the inverse filter circuit. Figure 57.3 shows the CMOS implementation of the CDBA [13]. The bias voltages used for simulation is ±2.5 V. The bias current used is 40 μA. All inverse filters are designed for a cut-off frequency of 159 kHz with parameters selected are as $C_1 = C_2 = 100$ pF, $R_2 = 7$ kΩ, $R_4 = R_5 = R_6 = 20$ kΩ for ILPF, $C_1 = C_2 = 100$ pF, $R_2 = 10$ kΩ, $R_3 = 5$k Ω, $R_5(R_6$ for IBRF) $= 7$ kΩ ($R_1 = 10$ kΩ for IBRF) for IHPF,
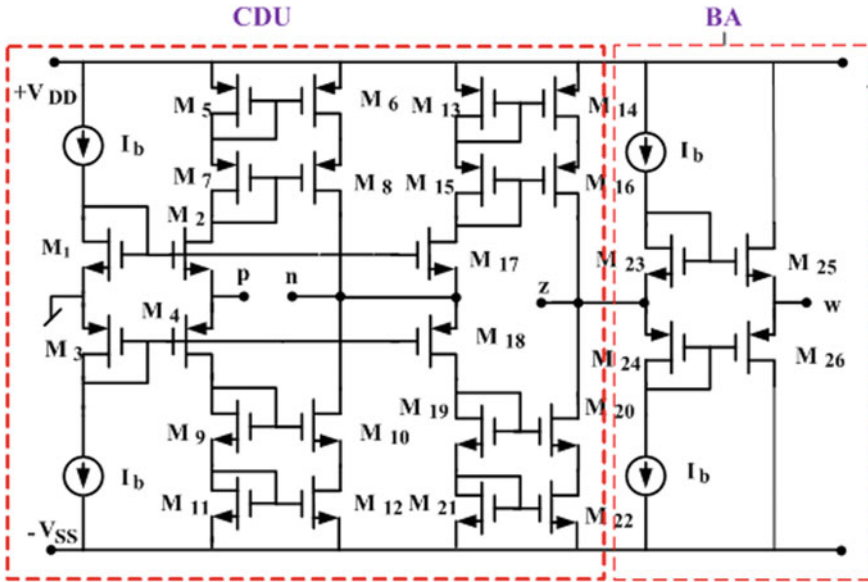
Fig. 57.3 CDBA realization using CMOS [13]

IBPF and IBRF respectively. The simulated frequencies observed for ILPF, IHPF, IBPF and IBRF is 156 kHz, 152 kHz, 157 kHz and 154 kHz respectively, which are in close agreement with theoretical cut off frequency of 159 kHz. Figure 57.4 shows the frequency responses of the proposed inverse filters, where simulated results follows the theoretical results in close agreement. Figure 57.5 shows the tunability of the inverse filters for different cut-off frequencies. Figure 57.6 shows the tunability of the inverse filters for different Q-factors.

57.5 Concluding Remarks

In this paper a tunable inverse filter configuration has been discussed. The presented configuration realizes ILPF, IHPF, IBPF and IBRF using two CDBAs, five/six passive elements. Simulated frequency responses are in close agreement with the theoretical responses. The proposed inverse filter topology enjoys low passive sensitivity.
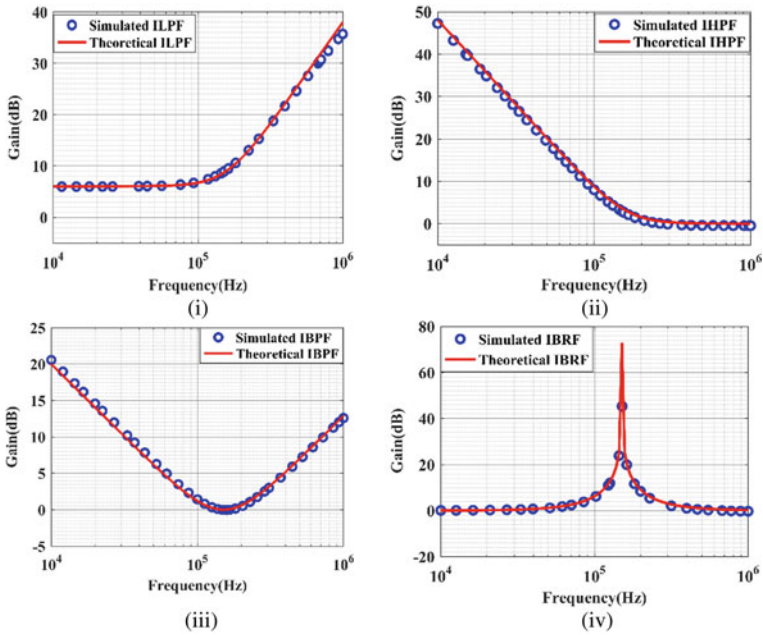
Fig. 57.4 Frequency responses of **(i)** ILPF, **(ii)** IHPF, **(iii)** IBPF, **(iv)** IBRF
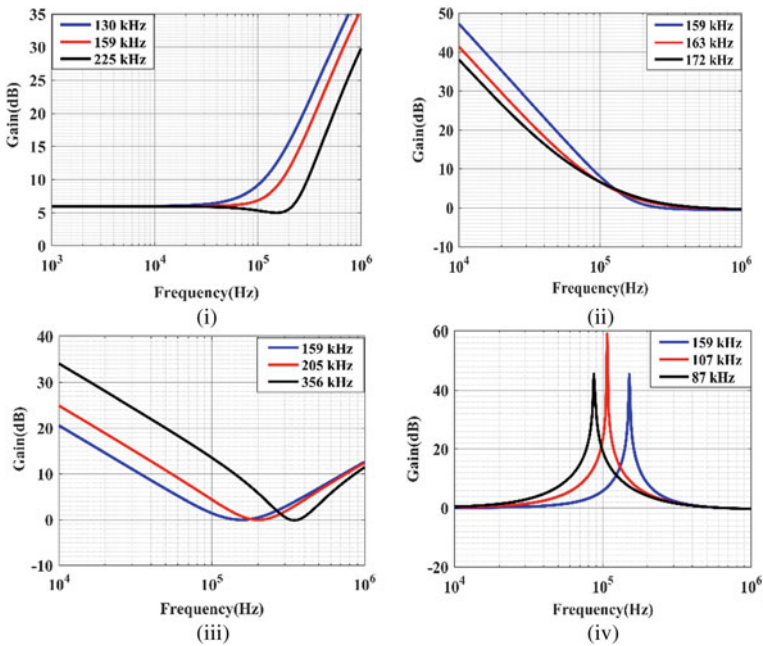
Fig. 57.5 Frequency tunability for **(i)** ILPF, **(ii)** IHPF, **(iii)** IBPF, **(iv)** IBRF
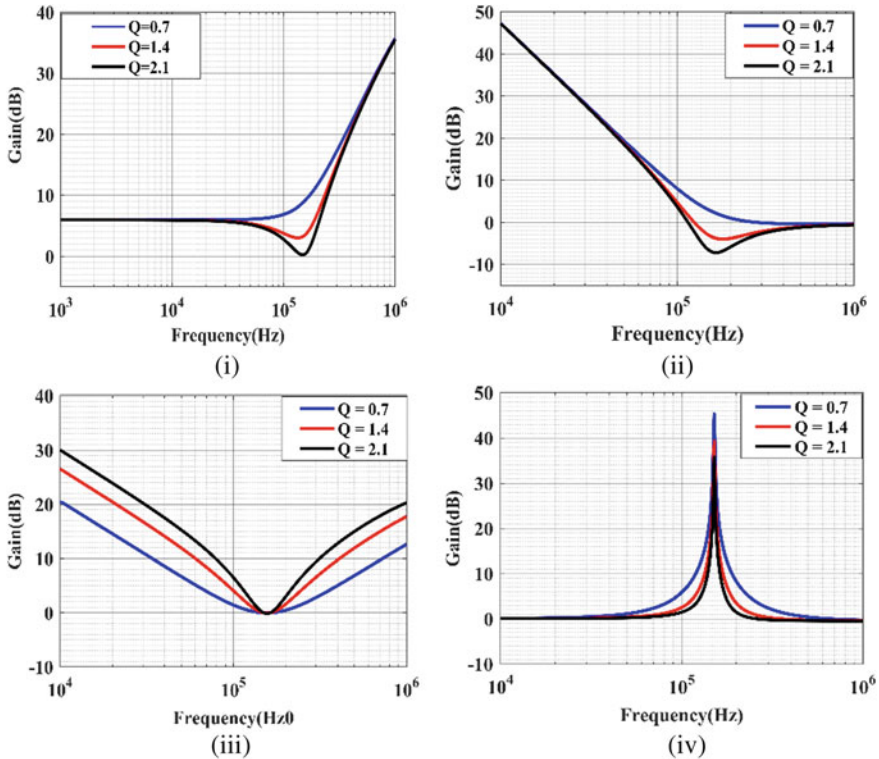
Fig. 57.6 Bandwidth tunability for different value of Q for **(i)** ILPF, **(ii)** IHPF, **(iii)** IBPF, **(iv)** IBRF

References

1. Leuciuc, Using nullors for realization of inverse transfer functions and characteristics. Electron. Lett. **33**(11), 949–951 (1997)
2. S.S. Gupta, D.R. Bhaskar, R. Senani, New analogue inverse filters realized with current feedback op-amp. Int. J. Electron. **9**, 1103–1113 (2011)
3. K. Garg, R. Bhagat, B. Jaint, A novel multifunction modified CFOA based inverse filter, in *IEEE 5th India International Conference on Power Electronics (IICPE)* (2012), pp. 1–5
4. N.A. Shah, M.F. Rather, Realization of voltage-mode CCII-based all pass filter and its inversion version. Ind. J. Pure Appl. Phys. **44**, 269–271 (2006)
5. T. Tsukutani, Y. Kunugasa, N. Yabuki, CCII-based inverse active filters with grounded passive components. J. Electr. Eng. **6**, 212–215 (2018)
6. A.R. Nasir, S.N. Ahmad, A new current mode multifunction inverse filter using CDBA. Int. J. Comput. Sci. Inf. Secur. **11**, 50–52 (2013)
7. R. Pandey, N. Pandey, T. Negi, V. Garg, CDBA based universal inverse filter. ISRN Electron. 1–6 (2013)
8. R. Bhagat, D.R. Bhaskar, P. Kumar, Inverse band reject and all pass filter structure employing CMOS CDBAs. Int. J. Eng. Res. Technol. **08**(09) (2019)
9. R. Bhagat, D.R. Bhaskar, P. Kumar, Multifunction filter/inverse filter configuration employing CMOS CDBA. Int. J. Recent Technol. Eng. **8**(4), 8844–8853 (2019). ISSN 2277-3878

10. R. Bhagat, D.R. Bhaskar, P. Kumar, CMOS CDBA-based inverse filter Structure. Int. J. Innov. Technol. Explor. Eng. **9**(3) (2020). ISSN 2278-3075
11. A. Sharma, A. Kumar, P. Whig, On performance of CDTA based novel analog inverse low pass filter using 0.35 μm CMOS parameter. Int. J. Sci. Technol. Manage. **4**, 594–601 (2015)
12. N.A. Shah, M. Quadri, S.Z. Iqbal, High output impedance current-mode all pass inverse filter using CDTA. Ind. J. Pure Appl. Phys. **46**, 893–896 (2018)
13. A.K. Singh, P. Kumar, A novel fully differential current mode universal filter, in *Circuits and Systems (MWSCAS), 2014 IEEE 57th International Midwest Symposium* (2014), pp. 579–582

Chapter 58
Comparative Study of Polypyrrole/Zinc Oxide Nanocomposites Synthesized by Different Methods

Aasim Hussain, Shumaila, Anju Dhillon, I. Sulania, and Azher M. Siddiqui

Abstract Polymers-inorganic hybrid nanocomposites have attracted enormous research due to their wide range of applications in many fields. In this work, we have synthesized hybrid nanomaterials with unique properties that individual Polypyrrole (PPy) and Zinc Oxide (ZnO) couldn't offer. Firstly, PPy Nanotubes (size ~ 50 nm) were synthesized by a modified chemical oxidative polymerization using Pyrrole monomer and Ammonium Peroxodisulphate (APS) as an oxidant. ZnO urchins (size ~ 50 nm) were prepared by the sol-gel method. The dispersion solution of PPy and ZnO was prepared by using common solvent N-Methyl Pyrrolidine (NMP) and then thin films were grown by the drop-casting method. Secondly, PPy/ZnO nanocomposites were grown by the electrochemical method on the Stainless Steel (grade 304) substrate. Characterizations like XRD, I-V studies, SEM and EDAX were carried out to analyse their structural, electrical properties, surface morphology and chemical composition respectively. Uniform thin films were grown by electrochemical method.

58.1 Introduction

In recent decades, the concept of combining different kinds of materials through cooperative interaction is a successful approach to accomplish specific goals that individual material couldn't achieve. The main objective behind the encapsulation of metal nanoparticles into polymer matrices is to modify the physiochemical properties. Polymers-inorganic hybrid nanocomposites have been attracting enormous consideration due to its unique properties and a wide range of industrial applications

A. Hussain (✉) · Shumaila · A. M. Siddiqui
Department of Physics, JamiaMilliaIslamia, New Delhi 110025, India

A. Dhillon
Department of Applied Sciences, MSIT, New Delhi 110058, India

I. Sulania
Inter University Accelerator Centre, New Delhi 110067, India

[1]. Polymers are one of the widely used classes of materials for industrial applications, due to its various chemical structures availability, lightweight, relatively low-cost fabrication, possible recyclability and durability. A Polymer is first and foremost an insulator. The concept of conduction in polymers was considered irrelevant but after years of research it is revealed that a type of polymers i.e. conducting polymers could conduct electricity and conduction in intrinsic conducting polymers is mainly due to the mobility of delocalized electrons in the conjugated backbone possessing alternate single and double C–C bonds. Conducting polymers can be a substitute for metals and semiconductors while retaining mechanical properties of conventional polymers [2, 3]. Organic semiconductors such as polypyrrole (PPy), Polythiophene (PT) and Polyaniline (PANI) have been studied extensively, reflected by a considerable amount of research publication focusing on its properties and applications. Polypyrrole (PPy), a conducting polymer and its derivatives have attracted enormous attention for their low cost and easy polymerization and good thermal and environmental stability. Currently, Polypyrrole has numerous applications including corrosion protection, fuel cells, biosensors, microsurgical tools, computer displays and drug delivery systems etc. [4, 5]. Conducting polymers and metal oxide composite materials offers excellent thermal stability, retention of charge and enhanced conductivity. Metal oxides namely Zinc oxide (ZnO), Tin (IV) oxide (SnO_2), Tungsten oxide (WO_3), etc. are the extensively studied semiconductors. We chose ZnO, having hexagonal wurtzite structure, whose direct bandgap and excited binding energy is nearly equal to 3.37 eV and 60 meV respectively [6]. ZnO is widely used metal oxide because of the high refractive index, thermal stability, high electron mobility, etc. In-room temperature, it shows stable luminescence properties due to its large excited binding energy. ZnO nanoparticles having a large surface/volume ratio makes it prominent for sensor applications.

In this work, firstly we synthesized Polypyrrole nanotubes by modified chemical oxidation polymerization (*labelled as PPy1*) and zinc oxide nano-urchins were synthesized by the sol–gel method. *PPy1/ZnO* nanocomposites were prepared by solution mixing in N-Methyl Pyrrolidine (NMP) with constant stirring and heating. Thin films were prepared by drop-casting method on asubstrate (glass slide). Secondly, Polyprrole/Zinc Oxide Nanocomposites thin films were prepared by Electrodeposition method (*labelled as PPy2/ZnO*) [7]. Different characterization techniques namely XRD, I-V measurement, SEM and EDAX were performed on nanocomposite thin films to analyze their structural, electrical properties, surface morphology and chemical composition.

58.2 Experimental Details

58.2.1 Materials

Pyrrole monomer(>98% purity), Cetrimonium Bromide [$(C_{16}H_{33})N(CH_3)_3$]Br(CTAB) as surfactant, Hydrochloric acid, Sulphuric acid, Ammonium Peroxodisulphate (APS) as oxidant, Zinc Nitrate, Sodium hydroxide (NaOH),N-Methyl Pyrrolidine (NMP) as common solvent, Ethanol and distilled water.

58.2.2 Modified Chemical Oxidation Method

Preparation of Polypyrrole Nanotubes Preparation of polypyrrole nanotube by modified chemical oxidative polymerization. In this method, we added a determined quantity of CTAB with HCL solution 0.5 M to distilled water while constantly stirring. Once the CTAB completely dispersed, the solution turned from transparent to milky. Then, only APS was added to it and after dispersion solution became transparent again. Now double distilled pyrrole monomer was added to the solution with constant stirring over the whole process. Polymerization occurs from the very first drop of monomer added to the solution reflected by its bluish colour. After stirring 24 h, a dark greenish precipitate formed, which was filtered out and washed several times with ethanol and distilled water to remove un-polymerized and oxidant content rest in solution. Filtered material kept in an oven at 60 °C for 6 h.

Preparation of Zinc Oxide Nanoparticles Zinc oxide nanoparticles were prepared as described by Moghaddam et al., a 0.5 M solution of zinc nitrate and 1 M solution of sodium hydroxide were prepared in distilled water. The Aqueous solution of sodium hydroxide was heated at 55 °C. The Zinc nitrate solution was added dropwise (about 40 min.) to the heated Sodium hydroxide solution with constant stirring (300 rpm) for 2 h. The precipitate of ZnO-NPs was cleaned several times with deionized water and ethanol, dried at 60 °C [8].

Preparation of PPy/ZnO Nanocomposite Polypyrrole and Zinc oxide were mixed to common solvent N-Methyl Pyrrolidine (NMP) and the dispersed solution was prepared by ultrasonication. Thin films were deposited on a glass substrate by the drop-casting method using a micropipette.

58.2.3 Electrochemical Method

PPy/ZnO thin films were synthesized by the Chronopotentiometery technique on Stainless Steel (grade-304) substrate using the CHI660d electrochemical setup,

which consists of three electrodes. We used Graphite as a counter electrode, SS as a working electrode, and standard calomel electrode as a reference electrode [9]. The electrolyte solution composed of 0.2 M pyrrole monomer and 0.2 M H_2SO_4 for pure PPy thin films. During the prepration method, the constant current density $(2\ mA/cm^2)$ was applied to the working electrode for 300 s. The electrolyte solutions for PPy/ZnO thin films was prepared by adding 5wt%, 10wt% of ZnO powder in 0.2 M pyrrole monomer and 0.2 M H_2SO_4.

58.3   Results and Discussion

Structural studies of as grown samples of PPy and PPy/ZnO nanocomposites, synthe-sized by modified chemical oxidation and Electrochemical Polymerization, were done by D-8 X-ray Diffractometer (procured from Bruker AXS Germany) in the range of 10°–60°. It is evident from the broad peak in X-ray diffractograms of PPy thin films depicted in Fig. 58.1a, c that the films are amorphous in nature while after incorporation of ZnO nanoparticles in the PPy matrix there is a considerable enhancement of crystallinity as shown in Fig. 58.1b, d. The number of intermittent sharp peaks indicate short order crystallinity in PPy/ZnO nanocomposites.

Morphological studies were done by FE-SEM: MIRA II LMH from TESCAN. The SEM micrograph reveals the structure of as grown Zinc Oxide nanoparticles which is like urchin having sharp spines of diameter around 50 nm as shown in
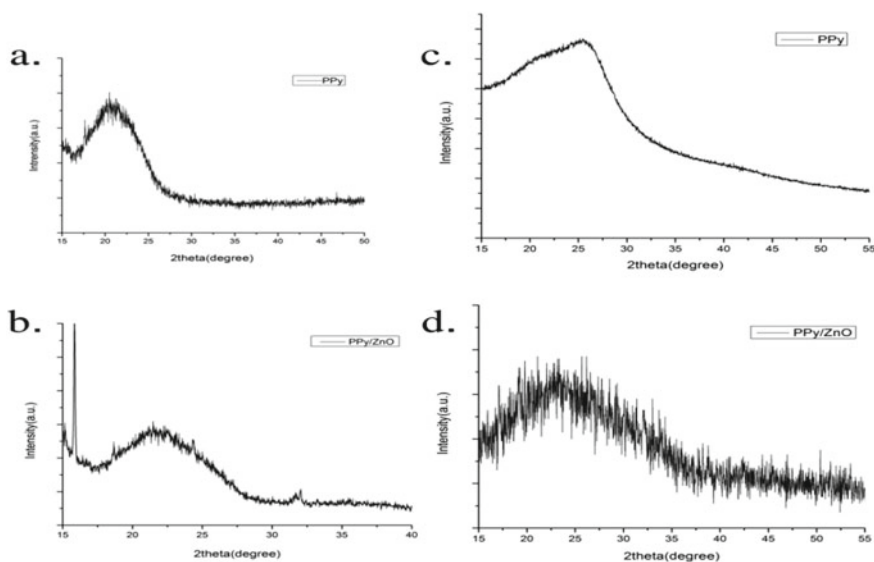
Fig. 58.1   XRD pattern of **a–b** Pure PPy and PPy/ZnO synthesized by modified Chemical oxidation and **c–d** Pure PPy and PPy/ZnO synthesized by Electrochemical method

Fig. 58.2a. The structure of PPy synthesized by modified chemical oxidation is like nanotubes (dia ~ 50 nm) in Fig. 58.2b and the structure of polypyrrole synthesized electrochemically is like cauliflower in Fig. 58.2d. The SEM images in Fig. 58.2c, e clearly show the encapsulation of ZnO nanoparticles within the polypyrrole matrix as the diameter of the PPy got increased after adding ZnO nanoparticles. In Fig. 58.3a–c, EDAX spectrum confirms the chemical composition of synthesized ZnO and PPy/ZnO nanocomposites.

I-V studies were performed at room temperature using Agilent Technologies, B1500A semiconductor device analyzer. In Fig. 58.4, the I-V curve for the range between 0 and 4 V shows linear behaviour. On doping ZnO in modified chemical oxidation method, conductivity decreases while in electrochemical method, conductivity enhances significantly. Figure 58.4e shows the increment in the current of the order 10^4. The lower protonation may be the reason behind lower conductivity of the PPy film. The Dispersion of Zn nanoparticles on the PPy surface enhances conductivity as there is formation of polarons and bipolarons during chain rearrangement while electrochemical deposition [10].
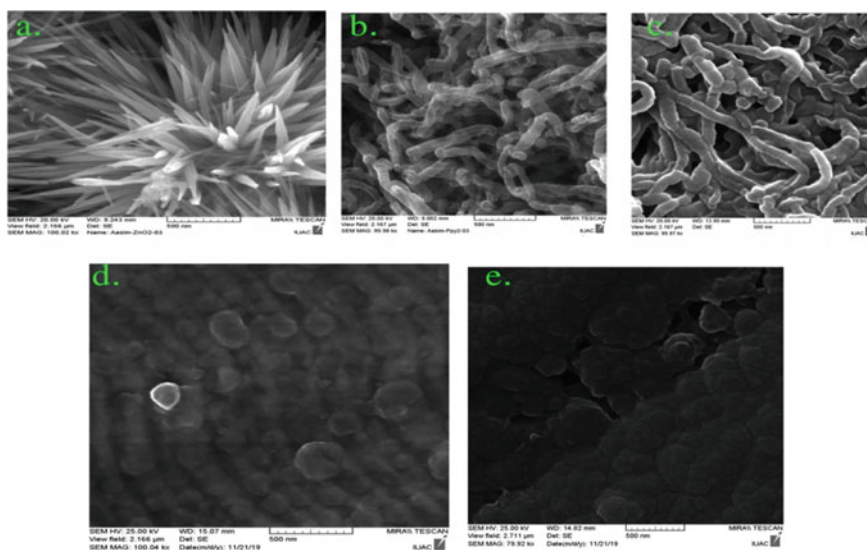
Fig. 58.2 SEM images of **a** Zinc Oxide **b**, **c** Pure PPy and PPy/ZnO synthesized by modified Chemical oxidation **d**, **e** Pure PPy and PPy/ZnO synthesized by Electrochemical method
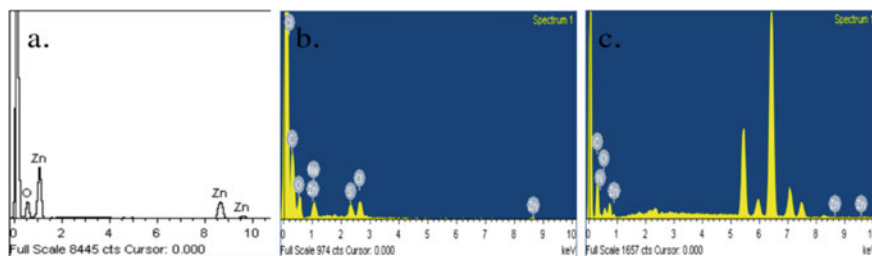
Fig. 58.3 EDAX of **a** Zinc Oxide **b** PPy/ZnO synthesized by modified Chemical oxidation **c** PPy/ZnO synthesized by the Electrochemical method
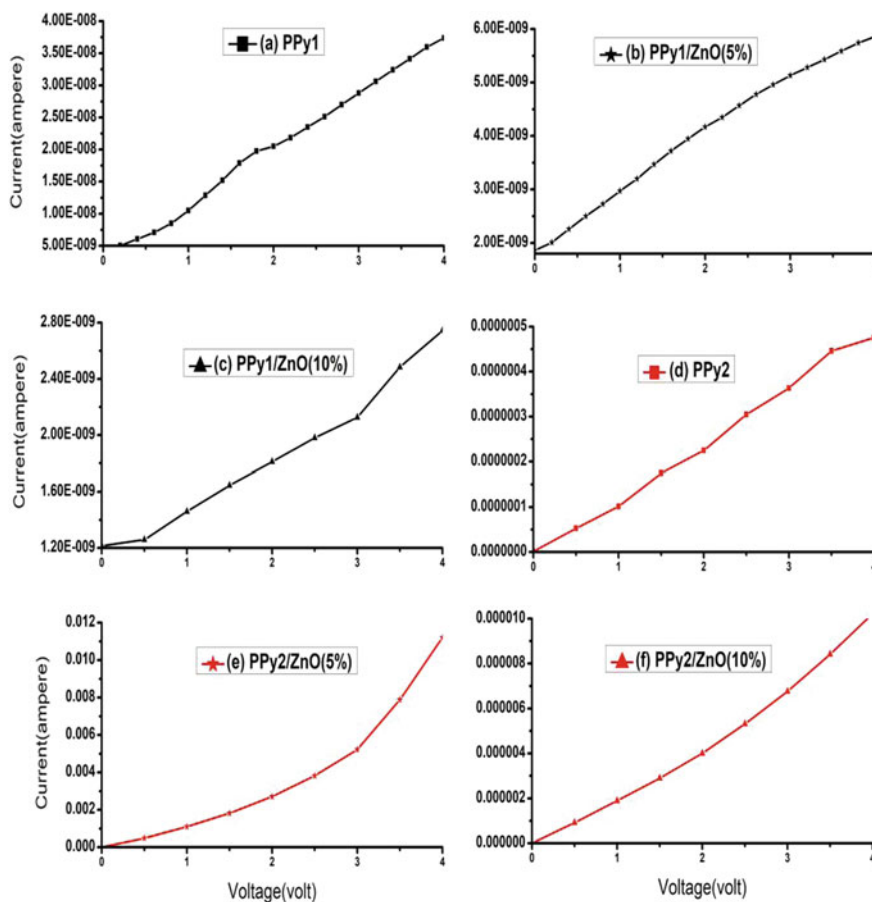
Fig. 58.4 I-V curves of **a–c** Pure PPy and PPy/ZnO synthesized by modified chemical oxidation, **d**, **e** Pure PPy and PPy/ZnO synthesized by electrochemical method

58.4   Conclusion

PPy/ZnO nanocomposites have been successfully synthesized by modified chemical oxidation and electrochemical method. It has been found that after adding ZnO particles significant structural and morphological changes occurred in both synthesized thin films and amorphous nature shifted to semi-crystalline. Electrochemical polymerization is a controlled method than modified chemical oxidation for the synthesis of uniform thin films of PPy/ZnO by adjusting several parameters. I-V graphs shows that 5wt% ZnO is the optimum wt% for conductivity enhancement as there is an increase of conductivity by the order of 10^4 for 5wt% ZnO dispersed in the electrolyte solution, which could give a better response in the field of storage devices and large surface/volume ratio makes it prominent for sensor applications.

References

1. A. Batool, F. Kanwal, M. Imran, T. Jamil, S.A. Siddiqi, Synth. Met. **161**, 2753–2758 (2012)
2. M.A. Chougule, S. Sen, V.B. Patil, Synth. Met. **162**, 1598–1603 (2012)
3. C. Wang, L. Yin, L. Zhang, D. Xiang, R. Gao, Sensors **10**, 2088–2106 (2010)
4. A.S. Kazemi, R. Afzalzadeh, M. Abadyan, J. Mater. Sci. Technol. **29**(5), 393–400 (2013)
5. M. Babazadeh, M. Sheidaei, S. Sattary, Synth. React. Inorg. Met. Org. Chem. **44**, 819–824 (2014)
6. R. Devi, M. Thakur, C.S. Pundir, Biosens Bioelectron **26**, 3420–3426 (2011)
7. V. Kumar, Y. Ali, K. Sharma, V. Kumar, R.G. Sonkawade, A.S. Dhaliwal, H.C. Swart, Nucl. Instrum. Methods Phys. Res. B **323**, 7–13 (2014)
8. A.B. Moghaddam, T. Nazari, J. Badraghi, M. Kazemzad, Int. J. Electrochem. Sci. **4**, 247–257 (2009)
9. R.G. Sonkawade, I.V. Bagal, N.R. Chodankar, M.R. Waikar, P.S. Shinde, A.A. Shaikh, J. Mater. Sci.: Mater. Electron. **29**(13), 11151–11158 (2018)
10. Y. Ali, K. Sharma, V. Kumar, R.G. Sonkawade, A.S. Dhaliwal, Appl. Surface Sci. **280**, 950–956 (2013)

Chapter 59
Investigation of AZO as an Alternative to ITO for Cathode Material in Organic Solar Cells

Vishal Gupta and Lalit Kumar

Abstract A critical part of thin-film solar cells is conduction through the transparent electrode. Currently, the material of choice for the window electrode is Indium Tin Oxide (ITO). However, there is a huge scarcity of indium and also high processing cost is involved in ITO. Zinc based oxides are amazingly alluring alternative materials for ITO because of the colossal characteristic plenitude and low toxic quality of Zn. ZnO can be made conductive by doping with heteroatoms or by presenting oxygen opportunities. The best dopants are Al, Ga and F. In this work we have deposited nanostructured Al-doped ZnO (AZO) as a transparent window on polyethylene terephthalate (PET) substrate through sputtering. AZO thin films have been successfully deposited on PET as well as on glass substrate (1 in. × 1 in.) by sputtering (Mereu et al. in Physica Status Solidi (c) 11(9–10):1464–1467 , [1]; Wang et al. in Vacuum 89:127–131, [2]). AZO films on PET exhibited a marked decrease in resistance with an increase in thickness. Thickness measurement of AZO films deposited on flexible PET was done by Dektak Profilometer which gave the thickness of AZO to be 270 nm, 380 nm, 455 nm and 500 nm for 45 min, 60 min, 90 min and 135 min of sputtering time respectively. On the glass substrate resistivity ~ 30 0hms/sq has been achieved for AZO. Polyaniline a p-type polymer has been successfully deposited on AZO film on the glass. Replacing ITO by aluminum-doped ZnO (AZO) as a cathode material will substantially reduce the cost of organic solar cells (OSC) (AbdulAlmohsin et al. in J Arkansas Acad Sci 66:26–30, [3]; Beek et al. in J. Mater. Chem. 15:2985–2988, [4]; Wang et al. in J. Mater. Chem. 20:862–866, [5]).

59.1 Introduction

We are largely dependent upon fossil fuels for fulfilling our energy requirements. In addition to the fact that fossil fuel reservoirs are limited, many other issues undermine the usage of fossil fuel. These include rising prices and sustain the availability of crude petroleum, its impact on global warming etc. Solar energy which is the most

V. Gupta · L. Kumar (✉)

Department of Physics, Hindu College, University of Delhi, New Delhi, India
e-mail: lalitphysics@hinducollege.ac.in

powerful sustainable energy source available on earth holds promise in addressing these concerns. Even though earth receives only a fraction of the sun's colossal energy, an hour of solar energy is more than the energy consumed by humans in an entire year. The technologies to harvest solar energy can be broadly classified as passive solar and active solar. The passive technology deals with the construction and designing of large structures like buildings that are energy efficient and capable of storing solar energy. On the other hand, active solar technology includes solar thermal collectors and photovoltaic (PV) devices. The PV devices facilitate the fastest and most efficient direct conversion of sunlight into electrical energy. The vast majority of PV devices are based on silicon. Daily new efficiency records are being set by silicon-dominated PV, which has intrigued both the scientific community and industry alike. The most recent one is the efficiency of 32.8% achieved for dual-junction III–V/Si devices. Unfortunately, the commercial realization of such highly efficient Si-based solar cells is witnessing many practical hurdles. The substrates of PV devices contain a thin film of transparent conducting Indium tin oxide (ITO). However, due to limited stock of indium on earth, a multi-fold price rise is there for indium. This has implicitly led to the increased price of solar cells using ITO. There is a great need to develop new materials to develop low-cost photovoltaic devices as there is a huge scarcity of indium and also high processing cost of ITO. Zn-based oxides are amazingly alluring alternative materials for ITO because of the colossal characteristic plenitude and low toxic quality of Zn. ZnO can be made conductive by doping with heteroatoms or by presenting oxygen opportunities. The best dopants are Al, Ga and F. In the present work we propose to develop and deposit nanostructured Al-doped ZnO film as a cathode on PET and glass substrate. This will greatly reduce the cost of an organic solar cell.

59.2 Experimental Details

59.2.1 Materials

Ammonium persulphate (APS) and Hydrochloric acid (HCl) were used as received. Aniline (Thomas Baker) was refined by vacuum distillation prior to utilization. AZO. Sputtering Target (Purity 99.99%, Al_2O_3/ZnO 2/98 wt%) was used as received. Poly (ethylene terephthalate) PET substrates with a thickness of 125 microns were used as flexible substrates.

59.2.2 Investigation of Thermal Stability of PET Substrates

First of all, the thermal sustainability of flexible substrate PET was investigated at different temperatures. PET of thickness 125 μm and size 1 in. $\times$ 1 in. was used for

this purpose. PET substrates were heated on a digital heater in which temperature could be easily controlled. It was observed that there was no bending and the substrate was sustainable without deformity upto 175 °C. At 200 °C, the flexible substrate started bending and the bending enhanced as the temperature was further increased. PET was observed to melt beyond 275 °C. Thus PET is a promising substrate for AZO deposition by sputtering as it is quite stable at operating temperature [6–8]. Figure 59.1 shows the temperature-dependent thermal stability of PET.

XRD of AZO Target XRD of AZO Target is done and it is observed that all the peaks match exactly with the standard peaks of AZO which confirms the purity of the AZO Target. From the XRD spectrogram, it is clear that the AZO target has hexagonal wurtzite structure and no diffraction peaks of Al or Al_2O_3 are observed indicating Zn atoms are replaced by Al atoms effectively. As Al^{3+} replaces Zn^{2+} in the lattice, Al/ZnO solid is formed and the lattice structure of ZnO is maintained. The quantity of Al atoms should not be too large; otherwise, the lattice structure will be destroyed and the performance of AZO targets will be affected. Figure 59.2 shows the XRD pattern of AZO Target.

Fig. 59.1 Temperature-dependent thermal stability of PET (*PET substrates are placed over the paper with PET printed on it*)
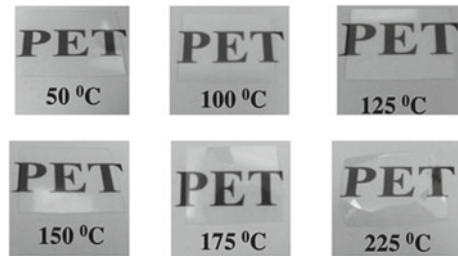
Fig. 59.2 XRD pattern of AZO Target with hkl planes
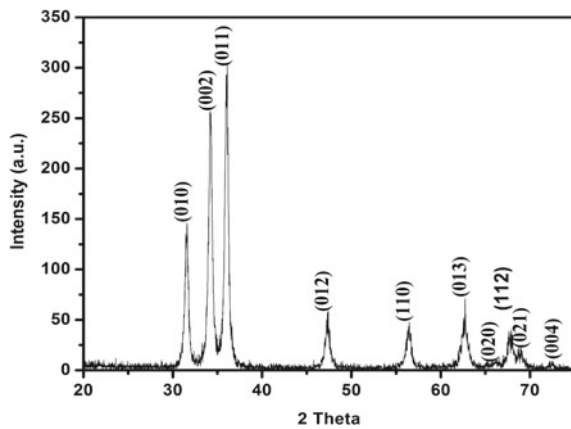
59.2.3 Deposition of AZO Films on PET and Glass Substrates

Deposition on PET Substrate AZO thin films were deposited on PET substrate (1 in. × 1 in.) by DC sputtering. The distance between the AZO target (50.8 mm diameter) and the substrate was maintained at 50 mm. To maintain the inert the atmosphere argon gas was used. The deposition was carried at 28 W for 45, 60, 90 and 135 min at a working pressure of 5.5×10^{-2} mbar. AZO films deposited on PET for different time periods were investigated for I-V characteristics using a Keithley Apparatus. Gold electrodes were used to measure I-V characteristics. I-V characteristics were measured in the range −2 to +2 V and a linear graph was obtained. The resistance of the films was found to be 0.5 MΩ, 190, 115 and 35 KΩ for 45 min, 60 min, 90 min and 135 min deposition time respectively. However, these resistance values were not suitable for further process of device development and hence we tried the deposition on glass substrates.

UV-Visible Characterization UV–Visible characterization through transmittance mode was done for AZO films. Figure 59.3 shows the optical transmittance spectra of AZO films in the wavelength range of 300–900 nm. It was observed that the average transmittance in the visible range(400–800 nm) was larger than 80% for all the samples which are comparable to the transmittance of ITO films and hence AZO can be a promising substitute for ITO [9, 10]. A slight decrease in transmittance with an increase in thickness is observed.

Deposition on Glass Substrate AZO thin films were deposited on Glass substrate (1 in. × 1 in.) by RF magnetron sputtering. The distance between the AZO target (50.8 mm diameter) and the substrate was maintained at 50 mm.

Fig. 59.3 UV-Visible transmittance for AZO films on PET
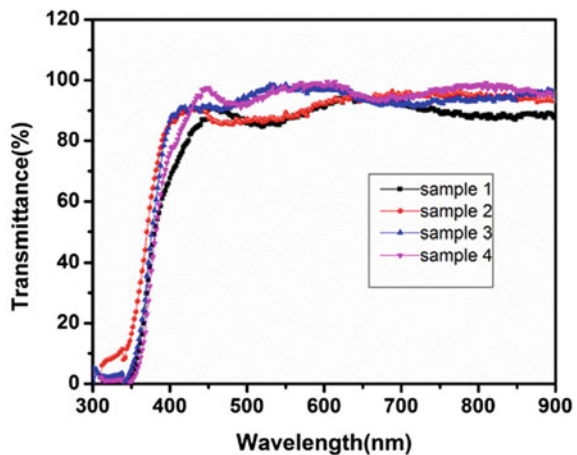
59.2.4 Synthesis of Polyaniline (PANI) and Thin Film Deposition

Synthesis of polyaniline was done by oxidative polymerization of aniline in which HCl acts as a catalyst and ammonium persulphate (APS) acts as an oxidant. 5 ml of 1M HCl and 0.833 ml of aniline were added to 100 ml of distilled water, under continuous stirring. After 30 min, 5 gm of APS was added into the above solution. The reaction vessel temperature was maintained at 0–5 °C during the polymerization process. The precipitates obtained was filtered and dried at room temperature. It was then finely powdered using a mortar pestle and then subjected to washing with HCl and distilled water. Subsequent filtration and drying were done and provided an emeraldine salt(ES) form of polyaniline [11–13]. This emeraldine salt(ES) form of polyaniline was de-doped with 0.1M NH_4OH to obtain an emeraldine base(EB) form of PANI. The dried powder of EB form was then re-doped by mixing with 1 molar camphor sulphonic acid (CSA). It was then dissolved in m-cresol and vigorously stirred for 3 h. The solution obtained after 3 h of stirring was spin-coated on AZO glass at a speed at 3000 rpm for 60 s, then followed by drying at 50 °C, for 5 min. Three layers were deposited by spin coating to obtain PANI film of good conductivity. Au electrode was then deposited using thermal evaporation in a high vacuum, with pressure during evaporation kept at 10^{-5} Pa.

I-V Characteristics The I-V characteristic of the PANI film is shown in Fig. 59.4, which shows an Ohmic characteristic. This is evidence of a good replacement for ITO by AZO. Further work is under consideration for the deposition of n-type material on this pre-deposited p-type PANI film.

Fig. 59.4 IV characteristics of PANI film
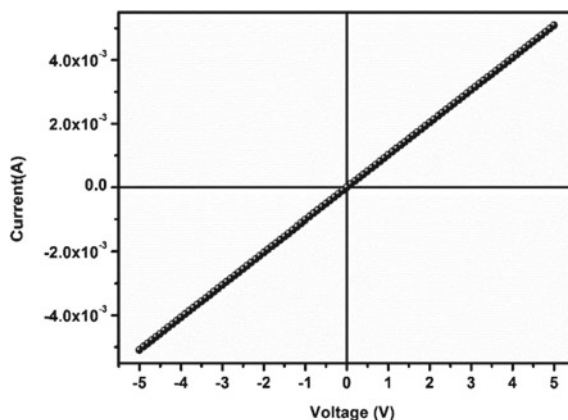
59.3 Conclusions

In summary, we deposited a highly conducting film of AZO on the glass substrate. A thorough investigation of the heat stability of PET substrates was done and revealed its stability upto 175° of heating temperature. On PET substrates we were able to deposit AZO films of different conductivities as a variation of thickness, however, the conductivity as obtained on glass substrates could not be achieved. Further experiments are in progress to achieve the same. On AZO films deposited on glass substrates we successfully deposited, p-type PANI films. PANI films exhibited an Ohmic behavior. Work is under progress to deposit n-type ZnO film, to obtain a p–n junction and to be further explored for solar cell fabrication.

References

1. R.A. Mereu, S. Marchionna, A.L. Donne, L. Ciontea, S. Binetti, M. Acciarri, Optical and electrical studies of transparent conductive AZO and ITO sputtered thin films for CIGS photovoltaics. Physica Status Solidi (c) **11**(9–10), 1464–1467
2. F. Wang, M.Z. Wu, Y.Y. Wang, Y.M. Yu, X.M. Wu, L.J. Zhuge, Influence of thickness and annealing temperature on the electrical, optical and structural properties of AZO thin films. Vacuum **89**, 127–131 (2013)
3. S. AbdulAlmohsin, S.M. Al-Mutoki, Z. Li, Fabrication and Characterization of Aluminum-doped ZnO/PANI Hybrid Solar Cells. J Arkansas Acad Sci **66**(1), 26–30 (2012)
4. W.J. Beek, M.M. Wienk, R.A. Janssen, Hybrid polymer solar cells based on zinc oxide. J. Mater. Chem. **15**(29), 2985–2988 (2005)
5. J.C. Wang, W.T. Weng, M.Y. Tsai, M.K. Lee, S.F. Horng, T.P. Perng, C.C. Kei, C.C. Yu, H.F. Meng, Highly efficient flexible inverted organic solar cells using atomic layer deposited ZnO as electron selective layer. J. Mater. Chem. **20**(5), 862–866 (2010)
6. M.G. Faraj, K. Ibrahim, M.K.M. Ali, PET as a plastic substrate for the flexible optoelectronic applications. Optoelectron. Adv. Mater. **5**(8), 879–882 (2011)
7. F. Villani, P. Vacca, G. Nenna, O. Valentino, G. Burrasca, T. Fasolino, C. Minarini, D. Della Sala, Inkjet printed polymer layer on flexible substrate for OLED applications. J. Phys. Chem. C **113**(30), 13398–13402 (2009)
8. J. You, Z. Hong, Y. Yang, Q. Chen, M. Cai, T.B. Song, C.C. Chen, S. Lu, Y. Liu, H. Zhou, Y. Yang, Low-temperature solution-processed perovskite solar cells with high efficiency and flexibility. ACS Nano **8**(2), 1674–1680 (2014)
9. R.A. Afre, N. Sharma, M. Sharon, M. Sharon, Transparent conducting oxide films for various applications: a review. Rev. Adv. Mater. Sci. **53**(1), 79–89 (2018)
10. F. Maldonado, A. Stashans, Al-doped ZnO: electronic, electrical and structural properties. J. Phys. Chem. Solids **71**(5), 784–787 (2010)

11. Y. Mohd, R. Ibrahim, M.F. Zainal, Electrodeposition and characterization of polyaniline films, in *2012 IEEE Symposium on Humanities, Science and Engineering Research* (IEEE, 2012), pp. 1301–1306
12. S.L. Patil, S.G. Pawar, M.A. Chougule, B.T. Raut, P.R. Godse, S. Sen, V.B. Patil, Structural, morphological, optical, and electrical properties of PANi-ZnO nanocomposites. Int. J. Polym. Mater. **61**(11), 809–820 (2012)
13. Z. Jin, Y. Su, Y. Duan, Development of a polyaniline-based optical ammonia sensor. Sens. Actuat. B Chem. **72**(1), 75–79 (2001)

Chapter 60
Jacobi Elliptic Functions and their Application in Ultra-cold Atomic Gases

Argha Debnath and Ayan Khan

Abstract Recent observation of quantum droplet in ultra-cold atomic gases motivates us to study the theoretical framework of droplet formation. Theoretically, it is understood that the competition of effective mean-field interaction and beyond mean-field interaction actually leads to the stabilization of the droplets which necessarily implies a dynamical equation consisting of cubic and quartic nonlinearity. In this chapter we obtain a set of Jacobi Elliptic Function solutions from a driven cubic-quartic nonlinear Schrödinger equation, where the driving force acts to stabilize the cnoidal solutions. Further, we determine the necessary condition for localized and non-localized solutions.

60.1 Introduction

It is a well-known fact that mathematical functions bear a close relationship with the geometry and one such very common example is trigonometric functions which are defined with reference to a circle. A more general description of closed curve geometry can be derived from the conic sections which particularly leads to an ellipse. The analogous functions derived from these geometries are known as Elliptic functions. These functions were first introduced by Carl Gustav Jakob Jacobi in 1829 [1] and hence they are popularly known as Jacobi elliptic functions (JEF).

The Jacobi elliptic functions carry significant importance in the field of nonlinear optical fiber communication [2] and ultra-cold atomic gases [3]. The ultra-cold Bose gas forming a Bose-Einstein condensate (BEC) is theorized via the Gross-Pitaevskii (GP) equation which falls in the common class of Nonlinear Schrödinger equation (NLSE). A NLSE can be easily mapped to Jacobi Elliptic equation [3] whose solution are known as Jacobi Elliptic functions. These functions can be derived from the amplitude function of Jacobi elliptic integrals [4, 5]. The solutions can be constant, periodic or localized based on the parameter m as $0 \leq m \leq 1$.

A. Debnath · A. Khan (✉)
Bennett University, Tech Zone II, Greater Noida 201310, India
e-mail: ayan.khan@bennett.edu.in

A broad class of the localized solutions are categorized as the solitons which are highly sought after pulse profiles in optical fiber communication for its ability to retain the shape over a large distance [2]. Apart from these, one can also find solitons in Bose-Einstein condensate (BEC) where the localized matter wave is well amenable for atom lithography and atom optics [6, 7].

Off-late, a group of experimentalists have observed a unique droplet-like state in a BEC mixture [8]. This is quite surprising as the conception of the liquid state is mainly derived from van der Waals theory where the liquid state arises when density is quite high due to an equilibrium between attractive inter-atomic forces and short-range repulsion. However, these newly emerged droplets in ultra-cold and extremely dilute atomic gases do not explicitly follow the usual perception [9]. This liquid like state is manifestation of the quantum fluctuations [10, 11]. These droplets are small clusters of atoms self-bound by the interplay of attractive and repulsive forces. The origin of the attractive force can be modeled in the purview of standard mean-field theory whereas the repulsive force originates from the beyond mean-field correction [12, 13]. The underlying theory relies on the Lee-Huang-Yang's (LHY) correction [14] to the mean-field Gross-Pitaevskii (GP) equation [15, 16] which is discussed in great detail in [17].

From the mathematical perspective, the problem boils down to a nonlinear equation where an additional quartic nonlinearity is present along with the usual cubic [17]. Our survey of literature indicate that there exists a significant void in understanding the competition between cubic and quartic nonlinearity. We were only able to find out some discussion in [18], where the authors have studied the existence of soliton in cubic-quartic NLSE (CQNLSE) by using phase portrait analysis. However, no explicit solution was provided. Nevertheless, the recent observation of quantum droplets demands a more thorough investigation of CQNLSE.

In this chapter, our main objective is to derive an analytical solution for CQNLSE in terms of JEF. For this purpose, we consider a pathological case of one dimensional forced CQNLSE. The driving force is required to stabilize this simplistic model. Hence, we systematically investigate an one-dimensional driven Cubic-Quartic-Nonlinear Schrodinger equation (DCQNLSE) for cnoidal solutions and report the findings. We arrange our discussion in the following way, in Sect. 60.2 we discuss the basics of Jacobi Elliptic Equation. We obtain the cnoidal solutions analytically from DCQNLSE in Sect. 60.3. Then we explicate the limiting cases in Sect. 60.4 and draw our conclusion in Sect. 60.5.

60.2 Jacobi Elliptic Equation

Jacobi elliptic functions can be found in diverse systems such as motion of pendulum to electronic elliptic filters. However, here we focus on the quasi one dimensional GP equation, which describes the dynamics of weakly interacting homogeneous BEC at $T = 0$, which is defined as [3],

$$i\hbar\frac{\partial\psi(x,t)}{\partial t} = \left[-\frac{\hbar^2}{2m}\frac{\partial^2\psi(x,t)}{\partial x^2} + g|\psi(x,t)|^2\right]\psi(x,t). \tag{60.1}$$

It can be shown that, via suitable transformation it is possible to write (60.1) in the following form,

$$F''(T) - \lambda F(T) + \kappa F^3(T) = 0, \tag{60.2}$$

where λ relates to chemical potential and κ defines the strength of the two-body interaction potential. T is defined as $x - ut$ where u is the velocity of the matter wave. It is well known that (60.2) poses a variety of solutions in the form of 12 Jacobian elliptic functions as noted in Table 60.1. These functions interpolate between the trigonometric and hyperbolic functions in the limiting cases of m respectively as $m \in [0, 1]$. Among these solutions the most commonly used ones are $\mathrm{cn}(T, m)$, $\mathrm{sn}(T, m)$, $\mathrm{dn}(T, m)$. These three functions are also known as co-polar trio and the other 9 functions can be written it terms of these three in the following manner,

$$\begin{aligned}
\mathrm{cd}\,T &= \frac{\mathrm{cn}\,T}{\mathrm{dn}\,T}; & \mathrm{dc}\,T &= \frac{\mathrm{dn}\,T}{\mathrm{cn}\,T}; & \mathrm{ns}\,T &= \frac{1}{\mathrm{sn}\,T} \\
\mathrm{sd}\,T &= \frac{\mathrm{sn}\,T}{\mathrm{dn}\,T}; & \mathrm{nc}\,T &= \frac{1}{\mathrm{cn}\,T}; & \mathrm{ds}\,T &= \frac{\mathrm{dn}\,T}{\mathrm{sn}\,T} \\
\mathrm{nd}\,T &= \frac{1}{\mathrm{dn}\,T}; & \mathrm{sc}\,T &= \frac{\mathrm{sn}\,T}{\mathrm{cn}\,T}; & \mathrm{cs}\,T &= \frac{\mathrm{cn}\,T}{\mathrm{sn}\,T}
\end{aligned} \tag{60.3}$$

Table 60.1 JEF for $m = 0$ and 1

	m = 0	m = 1
sn(T, m)	$\sin T$	$\tanh T$
cn(T, m)	$\cos T$	$\mathrm{sech}\,T$
dn(T, m)	1	$\mathrm{sech}\,T$
cd(T, m)	$\cos T$	1
sd(T, m)	$\sin T$	$\sinh T$
nd(T, m)	1	$\cosh T$
dc(T, m)	$\sec T$	1
nc(T, m)	$\sec T$	$\cosh T$
sc(T, m)	$\tan T$	$\sinh T$
ns(T, m)	$\csc T$	$\coth T$
ds(T, m)	$\csc T$	$\mathrm{csch}\,T$
cs(T, m)	$\cot T$	$\mathrm{csch}\,T$

The co-polar trios also satisfy the following identities,

$$sn^2(T, m) + cn^2(T, m) = 1$$
$$1 - m^2 sn^2(T, m) = dn^2(T, m)$$

An extensive discussion on this topic can be found in [4, 19]. Here, we will concentrate only on the co-polar trio solutions.

60.3 Cnoidal Solutions for Quantum Liquid

60.3.1 Recent Developments

In the introductory section, we have mentioned about the recent observations of a unique liquid-like phase in BEC. We have also mentioned that the origin of this exotic phase is believed to be the competition between mean-field and beyond mean-field interactions. Here, we plan to elaborate on these interactions and plan to provide a brief theoretical description of the recent experiments.

The mean-field and the beyond mean-field correction proposed by Lee-Huang-Yang (LHY), to the ground state energy of a homogeneous weakly repulsive Bose gas is expressed as [14],

$$\frac{E}{V} = \frac{gn^2}{2}\left(1 + \frac{128}{15\sqrt{\pi}}\sqrt{na^3} + \cdots\right), \tag{60.4}$$

where, n is the density, a is s-wave scattering length and the two body coupling constant $g = \frac{4\pi\hbar^2 a}{m}$, m being the mass of the atom. The second term in the expansion, which can be denoted as $E_{LHY}/V = \frac{256\pi\hbar^2}{m}(na)^{5/2}$, is the LHY correction originating from the zero point motion of the Bogoliubov excitation and is thus manifests pure quantum nature. Till date, in most of the cases, the beyond mean-field correction in the Gross-Pitaevskii equation is introduced heuristically in the spirit of density functional theory. Very recently, we have observed a self-consistent derivation starting from the Heisenberg equation [17].

Based on the recent experiments [8, 11] we can easily divide the physical system in two experimental scenarios where the LHY correction plays crucial role:

- A certain type of fluid which gets strongly magnetized in presence of an external magnetic field is known as ferrofluid. Classically, it has been observed that as magnetization increases, a classical ferrofluid undergoes a Rosensweig instability and creates self-organized, ordered surface structures or droplet crystals [11]. A quantum mechanical counterpart is a dipolar Bose-Einstein condensate. The well known Gross-Pitaevskii equation, also known as nonlinear Schrodinger equation (NLSE), is described as,

$$ i\hbar\frac{\partial \Psi}{\partial t} = \left[-\frac{\hbar^2}{2m}\nabla^2 + g|\Psi|^2 + V(\mathbf{r})\right]\Psi, \tag{60.5} $$

can be modified for long-range dipolar interaction by adding an additional term such that [20]

$$ i\hbar\frac{\partial \Psi}{\partial t} = \left[-\frac{\hbar^2}{2m}\nabla^2 + g|\Psi|^2 + V(\mathbf{r}) + \Phi_{dd}\right]\Psi. \tag{60.6} $$

Equation (60.6) is known as nonlocal NLSE (NLNLSE), where $\Phi_{dd} = \int |\Psi(r', t)|^2$ $V_{dd}(\mathbf{r} - \mathbf{r}')d^3r'$ with $V_{dd}(\mathbf{r}) = \frac{a_{dd}}{4\pi}\frac{1-3\cos^2\theta}{r^3}$. $a_{dd} = \mu^2\mu_0$ is the coupling constant and θ is the angle between the direction of polarization and the relative position of the particles. μ is particles permanent magnetic dipole moment and μ_0 is the permeability in free space. After taking into account the LHY correction the modified equation is written as [21, 22],

$$ i\hbar\frac{\partial \Psi}{\partial t} = \left[-\frac{\hbar^2}{2m}\nabla^2 + V(\mathbf{r}) + \mu_0\left[n(\mathbf{r}), \epsilon_{dd}\right]\Delta\mu\left[n(\mathbf{r}, \epsilon_{dd})\right]\right]\Psi. \tag{60.7} $$

Here, $\epsilon_{dd} = a_{ss}/a$. The usual dipolar BEC experiments are carried out for $\epsilon_{dd} < 1$ as for $\epsilon_{dd} > 1$, BEC is usually unstable. $\mu_0\left[n(\mathbf{r}), \epsilon_{dd}\right] = g|\Psi(\mathbf{r})|^2 + \int |\Psi(\mathbf{r}', t)|^2$ $V_{dd}(\mathbf{r} - \mathbf{r}')d^3r' = gn(\mathbf{r}) + \int d^3r'V_{dd}(\mathbf{r} - \mathbf{r}')n(\mathbf{r}')$ and $\Delta\mu\left[n(\mathbf{r}, \epsilon_{dd})\right] = \frac{32}{3\sqrt{\pi}}gn$ $\sqrt{na^3}F(\epsilon_{dd})$, where $F(\epsilon_{dd}) = \frac{1}{2}\int d\theta_k \sin\theta_k f(\epsilon_{dd}, \theta_k)^{5/2}$ and $f(\epsilon_{dd}, \theta_k) = 1 + \epsilon_{dd}$ $(3\cos^2\theta_k - 1)$.

However, it is possible to study similar effects in lower dimensions as well [23, 24]. A schematic description of a dipolar condensate in quasi one dimension can be viewed in Fig. 60.1. According to the diagram, magnetic dipoles are aligned along the y-axis by an external magnetic field, and with tighter confinement in the yz-plane relative to the x-axis. Therefore, an effective one dimensional equation can describe the droplet formation in dipolar condensate, where the dimensional reduction of the dipolar interaction can be carried out following the prescription of [25].

- The alternative route to study the beyond mean-field effect is to focus on the binary mixtures and as mentioned above very recently, the droplet formation has been reported due to the competition of LHY interaction term and the other interaction terms (i.e. intra-species and inter-species) [8, 12, 26]. The total energy density $\mathcal{E}_{tot}$ is defined as [12],

$$ \mathcal{E}_{tot} = \sum_{j=1,2}\left[\frac{\hbar^2}{2m}|\nabla\Psi_j|^2 + V(\mathbf{r})|\Psi_j|^2 + \frac{1}{2}g_{jj}|\Psi_j|^4\right] + g_{12}|\Psi_1|^2|\Psi_2|^2 + \mathcal{E}_{BMF}, \tag{60.8} $$
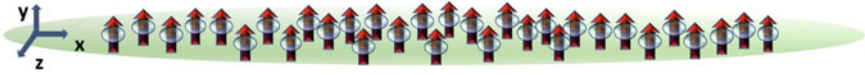
Fig. 60.1 Schematic of the system geometry we plan to focus here. A condensate of atoms with magnetic dipoles aligned along the y-axis by an external magnetic field, and with tighter confinement in the yz-plane relative to the x-axis

where,

$$\mathcal{E}_{BMF} = \frac{8}{15\pi^2}\left(\frac{m}{\hbar^2}\right)^{3/2}(g_{11}n_1)^{5/2}f\left(\frac{g_{12}^2}{g_{11}g_{22}}, \frac{g_{22}n_2}{g_{11}n_1}\right),$$

$$f(x, y) = \frac{1}{4\sqrt{2}}\sum_{\pm}\left[1 + y \pm \sqrt{(1-y)^2 + 4xy}\right]^{5/2}. \tag{60.9}$$

Equation (60.8) throws up several possibilities in studying the collective modes of the system. The nature of intra-species (g_{jj}) and inter-species (g_{12}) can lead to different types of excitations. Addition of beyond mean-field interaction makes the system more intriguing.

The prescribed way to treat (60.8) is by redefining the bosonic fields as $\Psi_j = \sqrt{n_j}\phi(\mathbf{r}, t)$. This assumption actually neglects the inter-component dynamics however, this is a useful assumption as it is able to capture the competition of mean-field and beyond mean-field interactions. The assumption allows us to treat the binary coupled equation as a single component cubic-quartic NLSE. Further it is possible to reduce the system from 3+1 dimension to 1+1 dimension as depicted in Fig. 60.2. Here, the bluish and reddish spheres represent the different species of atoms (atoms in two hyperfine states) distributed in an effectively one dimensional cigar shaped trap. The intra-species interactions are repulsive in nature and the inter-species interaction is attractive. Thus effective mean-field interaction can be tuned to be small and attractive as a result the beyond mean-field interaction can play a pivotal role.

However, it is fair to conclude that the quartic nonlinearity actually destabilizes the system and thereby the existence of quantum liquid was elusive till now. Nevertheless incorporation of beyond mean-field (BMF) corrections in binary BEC or dipolar
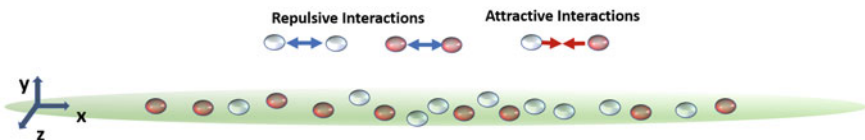
Fig. 60.2 Schematic representation of two component BEC in a cigar shaped trap. The bluish and reddish spheres present atoms in the two different hyperfine states. The intra-species interaction is repulsive and the inter-species interaction is attractive

BEC was instrumental in droplet formation as the BMF effect was stabilized via inter-component BMF and dipolar interaction respectively [26].

As mentioned earlier, we are quite familiar with the fact that one can yield conoidal solution from regular NLSE; nonetheless, based on the above discussions, we are quite motivated to investigate the possibility of finding cnoidal solutions in cubic-quartic NLSE (CQNLSE). In this analysis, based on the above mentioned under-standing, we incorporate a phenomenological force term in the CQNLSE. Such an assumption can be considered only as a pathological case. Though this is not a very accurate prescription nevertheless it allows us to investigate the MF and BMF competition in a relatively simple framework.

We start from the following DCQNLSE,

$$\frac{d^2\phi(x)}{dx^2} + \alpha\phi(x) + \beta|\phi(x)|^2\phi(x) + \gamma|\phi(x)|^3\phi(x) - \eta(x) = 0, \quad (60.10)$$

where, α, β and γ are some constant coefficients and $\eta(x)$ is the driving force. Physically, α corresponds to chemical potential, β is equivalent of two-body mean-field interaction strength and γ is the beyond mean-field contribution. Our next objective is to find cnoidal solutions in terms of coplanar trio for the given DCQNLSE.

60.3.2 "cn" Solution

We assume an ansatz of the form $\phi(z) = A + B\,(\mathrm{cn}(z, m))^\delta$ where z is a dimensionless quantity and defined as $z = \zeta x$, ζ being the inverse of coherence length. We consider the source as $\eta = F\,\mathrm{cn}^{4\delta}(z, m)$. Here, δ is being used as a solution parameter and we plan to determine its value along with other solution parameters. The choice of the function is from the fact that it will help in stabilizing the additional nonlinearity (quartic). Due to the change of variable (60.10) modifies to

$$\zeta^2\frac{d^2\phi(z)}{dz^2} + \alpha\phi(z) + \beta|\phi(z)|^2\phi(z) + \gamma|\phi(z)|^3\phi(z) - \eta(z) = 0. \quad (60.11)$$

Applying the ansatz in (60.11) we obtain a set consistency conditions and solving them we obtain,

$$A^3\gamma + A^2\beta + \alpha = 0$$
$$4A^3\gamma + 3A^2\beta + \alpha + (2m - 1)\zeta^2\delta^2 = 0$$
$$\delta(\delta - 1)(m - 1) = 0, \ A = -\frac{\beta}{2\gamma}, \ A = -\frac{\beta}{4\gamma},$$
$$F = B^4\gamma, \ \delta(\delta + 1) = 0. \quad (60.12)$$

Analysis of the above equations allows us to make the following conclusions: (1) For $\delta = 1$, $m \in [0, 1]$, (2) if $m = 1$ then δ can be any other value. (3) The other possible values of δ is 0 and -1, however, $\delta = -1$ is only possible if $m = 1$. (4) The consistency equation further leads to the fact that for $m = 1$ and $\delta = 1$, $A = -\frac{\beta}{2\gamma}$ whereas for $m = 1$ and $\delta > 1$ (say $\delta = 2$), $A = -\frac{\beta}{4\gamma}$. (5) Considering $A = -\frac{\beta}{2\gamma}$ we obtain $\alpha = -\frac{\beta^3}{8\gamma^2}$, $\zeta = \pm\frac{iB\sqrt{\beta}}{\sqrt{2m}}$ and $B = \pm i\frac{\beta}{\sqrt{\frac{4}{m}-8\gamma}}$. (6) Thus the strength of the driving force can now be evaluated as, $F = \frac{m^2\beta^4}{16(2m-1)^2\gamma^3}$. (7) Since coherence length is a real and positive quantity therefore, $\zeta > 0$ which leads to $\beta < 0$ and $m > 0$. This implies that the cubic nonlinearity is attractive and the sinusoidal modes are strictly prohibited. (8) The solution does not impose any extra condition over the nature of γ i.e., γ can be both attractive and repulsive in nature. However, the applied force must have the same characteristics as γ. (9) Finally, we note that the solution does not exist for $m = 1/2$ as B blows up. Hence, the final cnoidal "cn" type solution for $\delta = 1$ can be written as,

$$\phi(z) = -\frac{|\beta|}{2\gamma}\left(1 \mp \frac{\sqrt{m}}{\sqrt{1-2m\gamma}}\text{cn}(z, m)\right). \tag{60.13}$$

In Fig. 60.3a we plot the solution from (60.13) for two different values of m such as 2/3 and 1/3 which yields oscillatory behavior. The solutions boil down to
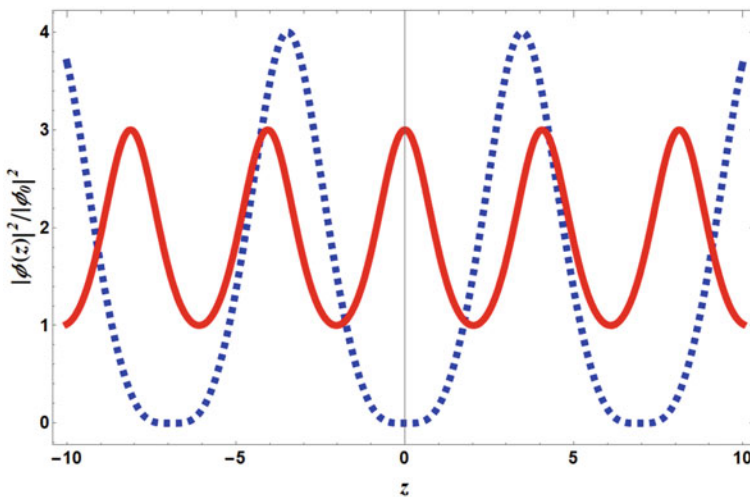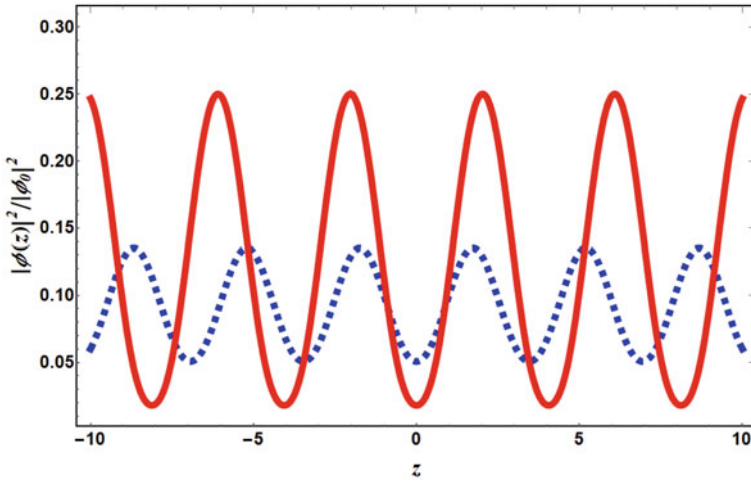

Fig. 60.3 (Color online) The figure depicts the behavior of the obtained "cn" for $0 < m < 1$ from (60.13). The solid line corresponds to $m = 2/3$ and the dashed line is for $m = 1/3$. Here, $\phi_0 = |\beta|/2\gamma$

localized one when we use $m = 1$. Hence, the competition between cubic, quartic nonlinearity as well the effect of applied force result in the generation of nontrivial cnoidal solutions.

60.3.3 "sn" Solution

Next we use, $\phi(z) = A + B\,(\text{sn}(z, m))^\delta$ as ansatz and $\eta = F\,\text{sn}^{4\delta}(z, m)$. Applying the ansatz in (60.11) we obtain a set of equations which result,

$$A^3\gamma + A^2\beta + \alpha = 0$$
$$4A^3\gamma + 3A^2\beta + \alpha + (m-1)\zeta^2\delta^2 = 0$$
$$\delta(\delta - 1)(m - 1) = 0, \; A = -\frac{\beta}{2\gamma}, \; A = -\frac{\beta}{4\gamma},$$
$$F = B^4\gamma, \; \delta(\delta + 1) = 0. \tag{60.14}$$

Further, we obtain $\zeta = \pm\frac{B\sqrt{\beta}}{\sqrt{2m}}$, $B = \pm\frac{\beta\sqrt{m}}{2\sqrt{m+1}\gamma}$, $F = \frac{\beta^4 m^2}{16(m+1)^2\gamma^3}$ and α remains the same. Again we observe that for $m = 0$ the coherence length reduces to zero as $\zeta \to \infty$ which implies the nonexistence of sinusoidal modes. It actually leads to $B \to 0$ which implies the existence of the trivial constant solution. Thus the cnoidal wave solution reads,

$$\phi(z) = -\frac{\beta}{2\gamma}\left(1 \mp \frac{\sqrt{m}}{\sqrt{m+1}\gamma}\text{sn}(z, m)\right). \tag{60.15}$$

In Fig. 60.4b the "sn" solution for $m = 1/3$ and $2/3$ is plotted. It must be noted from (60.15) that, for "sn" solution the cubic interaction requires to be repulsive. This is a stark difference from the "cn" modes. Again the nature of γ actually controls the behavior of the external force. As mentioned earlier, $\text{cn}(z, 1) = \text{sech}(z)$ and $\text{sn}(z, 1) = \tanh(z)$ and applying these results in (60.13) and (60.15) we obtain localized as well as nonlocalized modes. The nonlocalized mode can be characterized by kink soliton as this leads to π phase jump across the center of the soliton [27].

60.3.4 "dn" Solution

$\phi(z) = A + B\,(\text{dn}(z, m))^\delta$ as ansatz and $\eta = F\,\text{dn}^{4\delta}(z, m)$. This yields set of coefficient equations which read,
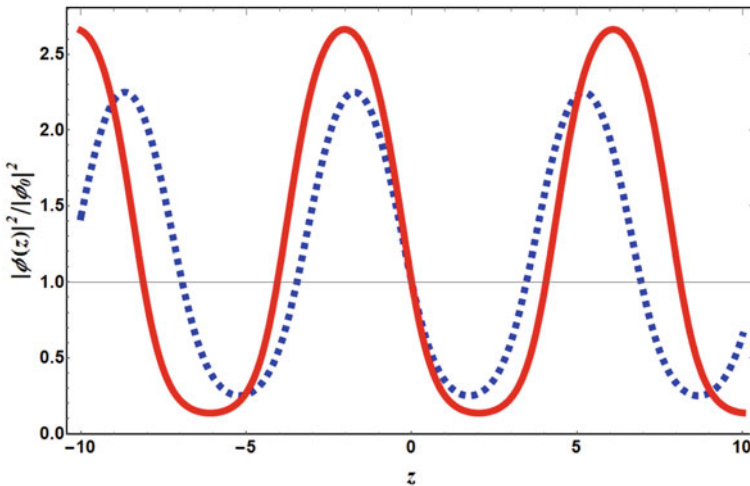
Fig. 60.4 (Color online) The figure depicts the behavior of the obtained "sn" for $0 < m < 1$ from (60.15). The solid line corresponds to $m = 2/3$ and the dashed line is for $m = 1/3$. Here, $\phi_0 = |\beta|/2\gamma$

$$A^3\gamma + A^2\beta + \alpha = 0$$
$$4A^3\gamma + 3A^2\beta + \alpha + (2 - m)\zeta^2\delta^2 = 0$$
$$\delta(\delta - 1)(m - 1) = 0, \ A = -\frac{\beta}{2\gamma}, \ A = -\frac{\beta}{4\gamma},$$
$$F = B^4\gamma, \ \delta(\delta + 1) = 0. \tag{60.16}$$

Equation (60.16) is very much similar to (60.14) except for the second equation. Thus for brevity, we directly consider $\delta = 1$ and solve for B, ζ and F which results, $B = \pm\frac{\beta}{2\sqrt{2-m}\gamma}$, $\zeta = \pm\frac{|\beta|^{3/2}}{2\gamma\sqrt{4-2m}}$ and $F = \frac{\beta^4}{16(2-m)^2\gamma^3}$ respectively. We also note that expression for α does not change from "cn" or "sn" solution. It is worth noting that for "dn" solution, $m = 0$ is acceptable as ζ remains finite. However, we know that $m = 0$ in "dn" leads to a constant solution. We depict "dn" modes for $m = 1/3$ and $2/3$ in Fig. 60.5.

Figure 60.6 depicts the cnoidal solutions for $m = 1$. This clearly suggests the existence of localized and nonlocalized solutions. The red solid line yielded from "cn" solution can be characterized as bright soliton, however the green small dashed line depicting "dn" solution might not imply dark soliton due to the existence of a flat valley instead of a density notch. The blue medium dashed line can be considered as kink soliton due to π phase jump across the soliton center.

Fig. 60.5 (Color online) The figure depicts the behavior of the obtained "dn" for $0 < m < 1$ from (60.15). The solid line corresponds to $m = 2/3$ and the dashed line is for $m = 1/3$. Here, $\phi_0 = |\beta|/2\gamma$
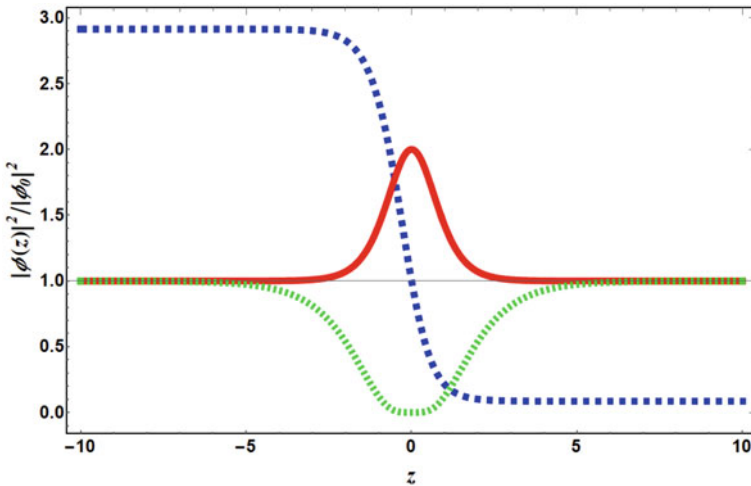
Fig. 60.6 (Color online) The figure depicts the behavior of "cn" (solid line), "sn" (medium dashed line) and "dn" (small dashed line) for $m = 1$. Here, $\phi_0 = |\beta|/2\gamma$

60.4 Localized Modes

Extending the discussion from the previous section, here we elaborate about the localized solutions for DCQNLSE and discuss their physical implications. We consider an ansatz as $\phi(z) = A + B \operatorname{sech}(z)$ and the driving force as $\eta(z) = F \operatorname{sech}^4(z)$. Here, $z = \zeta x$ and ζ being the inverse of coherence length. Applying the ansatz in (60.10) we obtain a set of coefficient equations such that,

$$A^3 \gamma + A^2 \beta + \alpha = 0$$
$$4A^3 \gamma + 3A^3 \beta + \alpha + \zeta^2 = 0$$
$$A = -\frac{\beta}{2\gamma}, \ \ \zeta = \pm i\sqrt{\frac{\beta}{2}} B, \ \ F = B^4 \gamma. \tag{60.17}$$

Solving for B and α, we obtain, $B = \pm \frac{\beta}{2\gamma}$ and $\alpha = -\frac{\beta^3}{8\gamma^2}$ respectively. Thus the strength of the driving force can now be evaluated as, $F = \frac{\beta^4}{16\gamma^3}$.

The physical implications of the obtained solutions are as follows: (1) ζ or the inverse of coherence length must be real and thus $\beta < 0$ which means the two body low energy scattering should be attractive in nature. (2) However, the beyond mean field interaction can be attractive or repulsive. (3) The nature of F depends on the nature of γ, and to ensure $F > 0$, we need to fix $\gamma > 0$ or the BMF interaction is repulsive. Similarly, $F < 0$ when the BMF interaction is attractive in nature. Hence, the static solution can be noted as, $\phi(z) = \phi_0(1 \pm \operatorname{sech}(z))$, where $\phi_0 = \frac{|\beta|}{2\gamma}$, $\zeta = \mp \frac{1}{\gamma} \left(\frac{|\beta|}{2}\right)^{3/2}$.

Figure 60.7 described two distinct situations. If β as well as γ is attractive then we obtain a bright soliton like density peak mode. However, as discussed in [9], for competing interactions, i.e., $\beta < 0$ and $\gamma > 0$, we observe a valley like structure. A flat density profile actually hints at accumulation of self bound states and formation of droplets. Also, we note that unlike bright solitons, the obtained localized density peak solutions does not lead to zero density at the $x \to \pm\infty$ rather saturates at finite background governed by the interactions ($|\phi_0|^2 = \beta^2/4\gamma^2$). Interestingly similar nature has already been reported in the case of soliton generation with two and three-body interaction [28] where the competition between short-range two body and phenomenological three body interaction plays the defining roles.

As we have seen that $\delta = 2$ is also valid provided $m = 1$, hence we check for solution of the type $\operatorname{sech}^2(z)$ and consider an ansatz as $\phi(z) = A + B \operatorname{sech}^2(z)$. As the role of the source is to stabilize the DCQNLSE or more precisely balance the quartic contribution we assume the source is proportional to $\operatorname{sech}^8(z)$. Applying the ansatz in (60.10) we obtain the coefficient equations which lead to the suitable solution as,
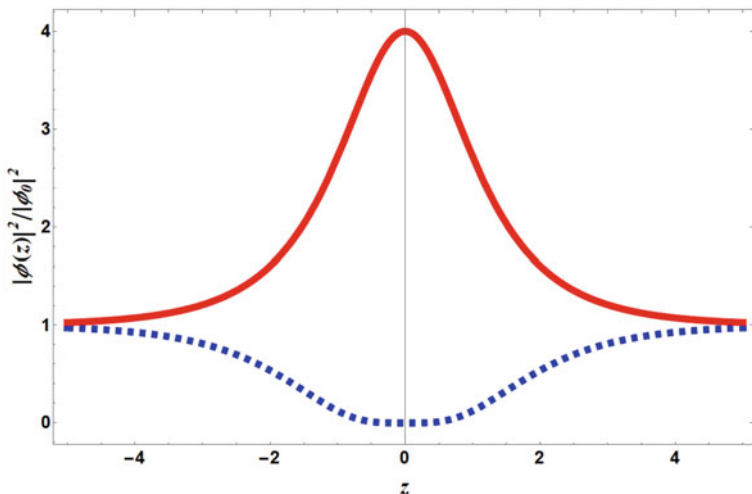
Fig. 60.7 (Color online) Localized modes, as a solution of CQNLSE with a source are depicted here. The dashed line describes a density notch with flatten valley whereas the solid line shows a bright soliton like density peak. Here, $z = \zeta x$ and $\phi_0 = |\beta|/2\gamma$

$$A = -\frac{\beta}{4\gamma}, \quad B = \frac{5\beta}{16\gamma}, \quad \zeta = \pm i\frac{\sqrt{B}\beta}{4\sqrt{\gamma}}$$
$$\alpha = -\frac{3\beta^3}{64\gamma^2}, \quad F = \frac{625\beta^4}{65536\gamma^3}. \tag{60.18}$$

The set of equations described in (60.18) clearly suggests that $\beta < 0$ for a localized solution otherwise the coherence length will be complex which will lead to an unstable trigonometric solution (secant). A significant discretion from the previous solution is that here $|A| \neq |B|$. This actually leads to the possibility of generation of $w-$soliton as depicted in Fig. 60.8. It is also worth mentioning that the coherence length depends on the coefficients of both the nonlinearities for $A + B \operatorname{sech}(z)$ solution however it depends only on β for $A + B \operatorname{sech}^2(z)$ solution. The w-solitons are already been mentioned in strongly coupled BEC [29] where the nonlinearity is quadratic in nature.

60.5   Conclusion

In this chapter, we have explored the existence of different cnoidal solutions in a DCQNLSE. The recent observation of quantum liquid in ultra-cold atomic gases and its subsequent theoretical description via BMF, necessitates a thorough investigation of CQNLSE. Our work is purely based on this motivation and as a starting point,
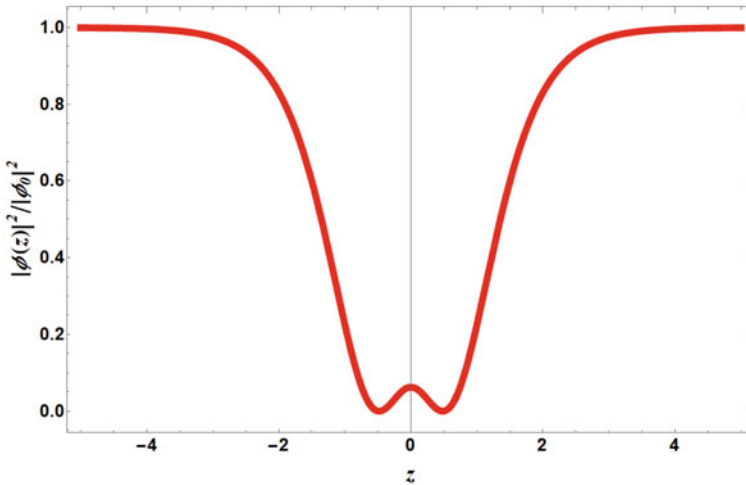
Fig. 60.8 (Color online) Depiction of w-soliton as a solution of CQNLSE with a source. Here, $z = \zeta x$ and $\phi_0 = |\beta|/4\gamma$

we have explored the possible cnoidal solutions. The driving term is inducted in the formalism to stabilize the quartic interaction.

Though the prescription is more pathological in nature nevertheless it allows us to comment on the competing interactions as well as the nature of the solutions which are not too far fetched from the exact experimental discussions. Here, we have derived the solutions in terms of the co-planar trio for DCQNLSE. We observed that these solutions can exist and we can summarize our observation in the following manner, (i) for "cn" and "dn" solutions MF interaction needs to be attractive but this condition is not applicable for "sn" solution. (ii) Nature of the phenomenological force is totally related to the nature of BMF contribution to obtain cnoidal solutions. (iii) $m = 0$ sinusoidal modes are nonexistent, albeit $m = 1$ hyperbolic modes do appear. This leads to the generation of bright and kink type solitons. (iv) The hyperbolic limit of "dn" solution rather interestingly throws up a density valley like structure contrary to our expectation of density notch (dark soliton). (v) We also show the possibility of the existence of w-soliton when $\delta = 2$ and $m = 1$.

There are several new directions that emerges from the current study, which include an investigation of the traveling wave solution and its stability. Here, we have not considered any external potential in the equation of motion and the presence of confinement can lead to interesting results. Considering the nascent age of quantum liquid investigation, we expect our findings will be interesting to a large section of the ultra-cold atomic research community.

References

1. C.G.J. Jacobi, *Fundamenta nova theoriae functionum ellipticarum. Auctore D. Carolo Gustavo Iacobo Iacobi.*. (sumtibus fratrum Borntræger, 1829)
2. G.P. Agrawal, *Fiber-Optic Communication Systems*, vol. 222 (Wiley, 2012)
3. R. Atre, P.K. Panigrahi, G.S. Agarwal, Phys Revi E **73**(5), 056611 (2006)
4. M. Abramowitz, I.A. Stegun, *Handbook of Mathematical Functions: With Formulas, Graphs, and Mathematical Tables*, vol. 55 (Courier Corporation, 1965)
5. S. Takeuchi, J. Math. Anal. Appl. **385**(1), 24 (2012)
6. K.E. Strecker, G.B. Partridge, A.G. Truscott, R.G. Hulet, Nature **417**(6885), 150 (2002)
7. L. Khaykovich, F. Schreck, G. Ferrari, T. Bourdel, J. Cubizolles, L.D. Carr, Y. Castin, C. Salomon, Science **296**(5571), 1290 (2002)
8. C. Cabrera, L. Tanzi, J. Sanz, B. Naylor, P. Thomas, P. Cheiney, L. Tarruell, Science **359**(6373), 301 (2018)
9. I. Ferrier-Barbut, Phys. Today **72**(4), 46 (2019)
10. I. Ferrier-Barbut, H. Kadau, M. Schmitt, M. Wenzel, T. Pfau, Phys. Rev. Lett. **116**, 215301 (2016). https://doi.org/10.1103/PhysRevLett.116.215301
11. H. Kadau, M. Schmitt, M. Wenzel, C. Wink, T. Maier, I. Ferrier-Barbut, T. Pfau, Nature **530**(7589), 194 (2016)
12. A. Cappellaro, T. Macrì, L. Salasnich, Phys. Rev. A **97**, 053623 (2018). https://doi.org/10.1103/PhysRevA.97.053623
13. A. Debnath, A. Khan, Annalen der Physik **533**(3), 2000549 (2021)
14. T.D. Lee, K. Huang, C.N. Yang, Phys. Rev. **106**, 1135 (1957). https://doi.org/10.1103/PhysRev.106.1135
15. E.P. Gross, Il Nuovo Cimento (1955-1965) **20**(3), 454 (1961)
16. L. Pitaevskii, Sov. Phys. JETP **13**(2), 451 (1961)
17. L. Salasnich, Appl. Sci. **8**(10) (2018). https://doi.org/10.3390/app8101998
18. K. Inui, B. Nohara, T. Yamano, A. Arimoto (2009)
19. J.M. Cervero, Am. J. Phys. **54**(1), 35 (1986)
20. T. Lahaye, C. Menotti, L. Santos, M. Lewenstein, T. Pfau, Rep. Progr. Phys. **72**(12), 126401 (2009)
21. F. Wächtler, L. Santos, Phys. Rev. A **93**, 061603 (2016). https://doi.org/10.1103/PhysRevA.93.061603
22. A.R.P. Lima, A. Pelster, Phys. Rev. A **84**, 041604 (2011). https://doi.org/10.1103/PhysRevA.84.041604
23. P.B. Blakie, D. Baillie, S. Pal, arXiv:2004.09859 (2020)
24. M. Edmonds, T. Bland, N.G. Parker, arXiv:2002.07958 (2020)
25. Y. Cai, M. Rosenkranz, Z. Lei, W. Bao, Phys. Rev. A **82**, 043623 (2010)
26. D.S. Petrov, Phys. Rev. Lett. **115**, 155302 (2015). https://doi.org/10.1103/PhysRevLett.115.155302
27. R. Balakrishnan, I.I. Satija, Pramana **77**(5), 929 (2011)
28. U. Roy, R. Atre, C. Sudheesh, C.N. Kumar, P.K. Panigrahi, J. Phys. B: Atom. Mol. Opt. Phys. **43**(2)(2010). https://doi.org/10.1088/0953-4075/43/2/025003
29. U. Roy, B. Shah, K. Abhinav, P.K. Panigrahi, J. Phys. B: Atom. Mol. Opt. Phys. **44**(3), 035302 (2011). https://doi.org/10.1088/0953-4075/44/3/035302

Chapter 61
Analysis of Multimode Interference Based More Sensitive Fiber Optic Methane Gas Sensor Using Bessel Beam with Wave Theory

Sanoj Kumar Yadav, Nabamita Goswami, and Ardhendu Saha

Abstract An idea towards the multimode interference based fiber optic gas sensor based on the wave theory is proposed, designed and simulated where the configuration comprises a multimode fiber with core radius of 62.5 μm and a sensing layer where methane gas is used. The discerned enhanced sensitivity of this wave theory based gas sensor is 4.391 dB/RIU with a resolution of 2.27×10^{-3}, which is a different approach than the reported articles till date. Impact of the mode coupling on performance of proposed sensor is also observed. In areas of chemical, biological and physical sensing the proposed high performance sensor has momentous advantages and applications owing to its ability to provide high sensitivity measurements, small size and large measuring ranges.

61.1 Introduction

Being an important and essential resource of modern industries and plants, gases has attained a very serious concern for disaster management as a result of which optical gas sensors are becoming significant day by day. The devices which sense the presence of gases and often shows its concentration are called gas sensors which has been installed in a specific region. Refineries, industrial plants, fuel stations, waste water treatment facilities etc. are the major key players that employ gas sensors primarily to measure toxic, flammable and asphyxiant gases [1]. Nowadays different types of gas sensor operating on different principles such as semiconductor, electrochemical, photo-ionization detector, catalytic bead, infrared point, optical fiber gas sensor are available in market based on ray theory [2, 3]. Immunity to small size, electromagnetic interference, small sample requirement, remote sensing applications, in situation monitoring, possibility of distributed measurement and low cost are the several advantages that fiber optic gas sensor offer over other traditional gas sensors [4–6]. Fiber optic gas sensor is a great interest area for many researchers as

Sanoj Kumar Yadav · Nabamita Goswami · Ardhendu Saha (✉)
Department of Electrical Engineering, National Institute of Technology Agartala, Barjala, Jirania, Tripura (west) 799046, India

an end product of which a lot of study has been carried to increase the efficiency and performance of optical fiber gas sensor. By using bimetallic layers, addition of extra dielectric layer, incorporation of D shaped, tapered fiber, fiber grating performance of the optical fiber gas sensor can further be improved [7–10]. After stripping the cladding layer, methane is placed which serves the purpose of sensing layer in the proposed configuration. Methane in terms of chemical formula is represented as CH_4 and it is odorless, colorless and the simplest molecule among the hydrocarbon family. 5–10% concentration by volume in air of methane can be explosive. It is highly flammable and have wide range of applications such as fuel for automobiles, turbines, for chlorination, for hydrogen and ammonia production [11].

61.2 Proposed Scheme

The proposed scheme comprises a source which injects Bessel beam in a MMF of 62.5 μm core radius, where the RI of core is 1.4446 and methane is used as a cladding with RI 1.294 at 43 ppm. In terms of overlap integral, power coupling efficiency η_m can be evaluated by input field and various other modal fields [12]:

$$\eta_m = \frac{\left|\int_0^\infty E_s(r)E_m(r)rdr\right|^2}{\int_0^\infty |E_s(r)|^2rdr\int_0^\infty \left|E_m(r)^2rdr\right|} \tag{61.1}$$

where the input field provided and field distribution of the mth guided radial mode are represented by $E_s E_s$ and E_m respectively. Power coupling efficiency can be calculated using Eq. 61.1 [12]:

$$\eta_m = \frac{2\left(\frac{w}{a}\right)^2 \exp\left[-\left(\frac{w^2}{a}\right)\left(\frac{u_m^2}{2}\right)\right]}{J_0^2(u_m) + J_1^2(u_m) + \left(\frac{J_0(u_m)}{K_0(w_m)}\right)^2\left(K_1^2(w_m) - K_0^2(w_m)\right)} \tag{61.2}$$

The formulation of transmission loss along sensor structure leads to [13]

$$L_s(z) = 10\log_{10}\left(\left|\sum_{m=1}^{M} C_m^2 \exp\left(-i\left(\frac{(2m+1)(2m-2)\pi}{L_z}\right)z\right)\right|^2\right) \tag{61.3}$$

where C_m is the field excitation coefficient of each mode, m denotes the radial mode number, L_z represents the self image length and z denotes the propagation distance along the MMF structure.

61.3 Result and Discussion

For simulation a finite difference beam propagation method in commercially available software Lumerical's Mode solutions has been employed and the amplitude distribution of propagating field of Bessel beam is shown in Fig. 61.1. It shows that the incident light from the source is eventually propagated upto the end of the propagation length which is 30 mm chosen through the optimization.

Figure 61.2 shows the power coupling coefficient for the Bessel beam propagating inside MMF with respect to the radial mode number. Here the two most dominating modes are radial mode number 14 ($LP_{0,14} LP_{0,6}$) and radial mode number 15 ($LP_{0,15}$) having coupling efficiencies 19.89% and 18.67% respectively. Inside the fiber the maximum power of injected beam is possessed by the dominating modes
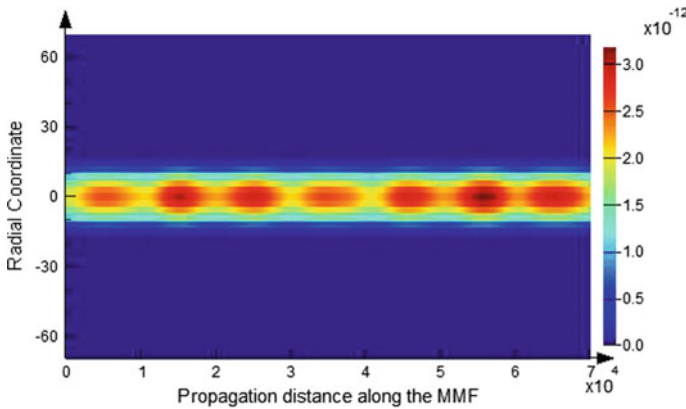
Fig. 61.1 Propagating field distribution within the proposed fiber structure with Bessel beam in Lumerical's Mode Solutions

Fig. 61.2 Power coupling co-efficient as a function of radial mode number inside a MMF
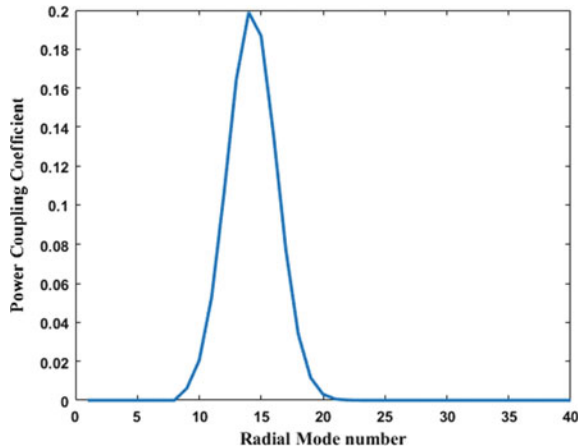
due to the fact of having highest coupling efficiency [14]. Radial mode number 14 in Bessel beam holds the maximum input power coupled to all excited modes inside the MMF of 62.5 μm radius injected with a beam of wavelength 700 nm. For different cladding materials MMF shows variation in multimode interference pattern. As a result of change in surrounding clad the self imaging position also changes. With the Figs. 61.3 and 61.4, the sensitivity of the proposed structure can be analyzed where the transmission loss varies with respect to the change in surrounding clad as well as along the distance of the propagation length. With respect to the wavelength the cladding refractive index is varied from 1.286 to 1.306 to calculate the sensitivity and resolution. According to change in refractive index of cladding the transmission loss is plotted for length of 30 mm of MMF fiber at a specific wavelength of 0.700 μm.

Fig. 61.3 Transmission loss with respect to the variation in refractive index of the sensing layer for length of 30 mm
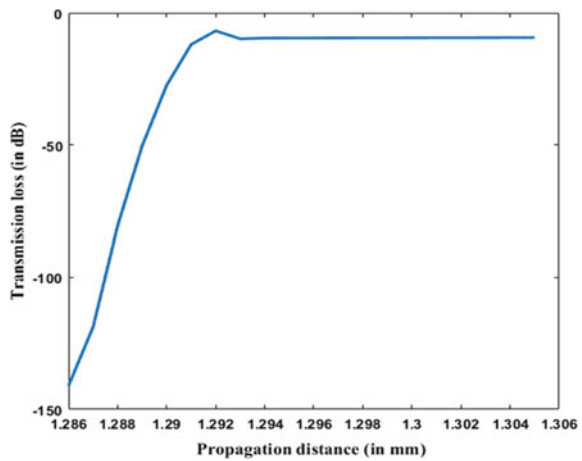
Fig. 61.4 Transmission loss along the propagation distance of the sensing layer
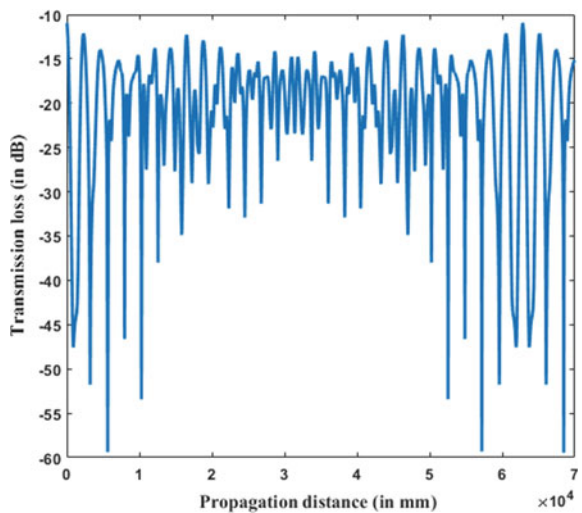
For Bessel beam transmission loss ranges from -141.1 to –9.343 for 30 mm length of MMF. Sensitivity for Bessel beam comes out to be 4.391 dB/RIU. Commercially available power meter has accuracy near to 0.01 dB. Thus the resolution of proposed gas sensor is observed as 2.27×10^{-3}.

61.4 Conclusion

A multimode interference based fiber optic gas sensor is proposed, designed and simulated, where the configuration comprises a multimode fiber with core radius of 62.5 μm and a sensing layer where methane gas is used. The observed augmented sensitivity of this gas sensor based wave theory is 4.391 dB/RIU and with resolution of 2.27×10^{-3}, the mode 14 has the highest coupling coefficient of 19.89%. The suggested idea is a different approach than the reported articles till date. Influence of the mode coupling is also observed on the performance of proposed sensor. For the proposed gas sensor based on wave theory with Bessel beam radial modes number 14 and radial mode number 15 are most dominant modes.

References

1. Honeywell Analytics, "The Gas Book". Retrieved from https://www.honeywellanalytics.com/~/media/honeywell-analytics/documents/english/11296_gas-book_v5_0413_lr_en.pdf?la=en
2. X. Liu, S. Cheng, H. Liu, S. Hu, D. Zhang, H. Ning, A survey on gas sensing technology. Sensors **12**, 9635–9665 (2012)
3. R. Kocache, Gas Sensors. Sens. Rev. **28**, 8–12 (1994)
4. R.C. Jorgenson, C. Jung, S.S. Yee, L.W. Burgess, Multi wavelength SPR as an optical sensor for characterizing the complex refractive indices of chemical samples. Sens. Actuators B **14**, 721–722 (1993)
5. J. Homola, Optical fiber sensor based on surface plasmon excitation. Sens. Actuators B **29**, 401–405 (1995)
6. A.K. Sharma, B.D. Gupta, Absorption based fiber optic surface plasmon resonance sensor: a theoretical evaluation. Sens. Actuators B **100**, 423–431 (2004)
7. N. Goswami, Kamlesh Kumar Chauhan, and Ardhendu Saha, "Analysis of SPR based bimetal coated tapered fiber optic sensor with enhancement sensitivity through radially polarized light." Opt. Commun. **379**, 6–12 (2016)
8. S. Singh, S.K. Mishra, B.D. Gupta, Sensitivity enhancement of surface plasmon resonance based fiber optic refractive index sensor based utilizing an additional layer of oxide. J. Sens. Actuators **193**, 136–140 (2013)
9. B.D. Gupta, R.K. Verma, Surface Plasmon resonance based fiber optic sensors: principle, probe design, and some applications. J. Sens. **2009**, 12 (2009)
10. H. Moayyed, I.T. Leite, L. Coelho, J.L. Santos, D. Viegas, Analysis of phase interrogated SPR fiber optic sensors with bimetallic layers. IEEE Sens. J. **10**, 3662–3668 (2014)
11. P.D. Lundegard, Environ. Forensics, 97–110 (1964)
12. W.S. Mohammed, A. Mehta, E.G. Johnson, Wavelength tunable fiber lens based on multimode interference. J. Light Wave Technol. **22**, 469–477 (2004)

13. A. Datta, A. Saha, Investigation of multimode interference based high sensitivity refractive index sensor realized by shining a zero order Bessel-Gauss beam. J. OSA B **34**, 1327–1338 (2017)
14. Q. Wang, G. Farrell, W. Yan, Investigation on singlemode-multimode-singlemode fiber structure. J. Lightwave Technol. **26**, 512–519 (2008)

Chapter 62
Calculation of Thermodynamic Relations with a Modified and Magnetized Mass in PNJL Model of Cosmology

Anju Dahiya and S. Somorendro Singh

Abstract We present the thermodynamic relations in terms of the equation of state (EOS) described by a model of modified and magnetized quark mass in the PNJL model for two flavor quarks. The calculated thermodynamics relations such as EOS and other parameters has represented in the figures by introducing this modified quark mass. These parameters show very much enhanced results. It indicates the thermodynamic behaviors are also well agreed with the prediction of the mean-field theory of the early universe. Therefore it implies the origin of cosmological studies showing the evidence of forming Quark-Gluon Plasma.

Classifications 25.75.Ld · 12.38.Mh

62.1 Introduction

Quantum chromodynamics (QCD) is an exciting topic in the present day of theoretical physics. It incorporates the peculiar features of asymptotic freedom and confinement. The confinement feature is still challenging to explain and tough to understand. QCD provides a rich phase ranging from quarks bound to hadrons at low temperature and chemical potential to the unbound quark and gluon say quark-gluon plasma (QGP) at the high temperature and high nuclear density. These bound and unbound phases have classified as hadron and quark- gluon plasma. QCD has provided significant contributions to the understanding of the phase diagram at high temperatures. In this paper, we study to follow the thermodynamic relations through the grand canonical ensemble. The canonical ensemble has carried out to the leading order expansion of thermodynamic observables. Then we focus on finding out the equation of state and other thermodynamic parameters using this simple model introducing magnetic field in thermal mass and the PNJL model at finite temperature and zero chemical [1].

A. Dahiya · S. Somorendro Singh (✉)

Department of Physics and Astrophysics, University of Delhi, Delhi 110007, India

e-mail: sssingh@physics.du.ac.in

62.2 Gibbs Free Energy of PNJL Model

In this section, we briefly describe the formation of PNJL model with the introduction of magnetic potential in PNJL model. The thermodynamic potential for two flavor quark in presence of magnetic field PNJL model of cosmology. written as [2].

$$
\begin{aligned}
\Omega(\phi, \phi^*, m; T, \mu) = {} & U(\phi, \phi^*, T) + \frac{(m - m_0)^2}{4G} \\
& - 2N_f \int_\pi d^3 p \, E_p \frac{2}{\pi^3} \\
& - 2N_f eBT \int d^3 p \frac{2}{\pi^3} [Tr \ln(1 + Le^{(E_p - \mu)/T}) \\
& + Tr \ln(1 + L^\dagger e^{-(E_p - \mu)/T})] \\
& - \frac{3(qB)^2}{2\pi^2} [\zeta'(-1, x_f) - \frac{1}{2}(x_f^2) - x_f \ln(x_f) \\
& + \frac{x_f^2}{4}]
\end{aligned}
\tag{62.1}
$$

in which $x_f = \frac{M_f^2}{2q_f B}$, $\zeta'(-1, x_f) = \frac{d\zeta}{dz}|_{z=-1}$, where $\zeta(z, x_f)$ is the Reimann-Hurwitz zeta function. In the above formula $E_p = \sqrt{p^2 + m^2(T, \mu) + 2eB}$ is the Hartree single quasi-particle energy [3]. The thermal mass in presence of magnetic field and cosmological constant is defined as:

$$
m^2(T, \mu) = \frac{81}{8\pi} \frac{T^2}{ln(1 + \frac{B^2}{\lambda^2})}
\tag{62.2}
$$

where $\lambda^2 = 150$ MeV.

The fields ϕ and ϕ^* are different at non-zero quark chemical potential. The fields ϕ and ϕ^* explains the quantum fluctuations of the fields around their mean field values [4]. In this manuscript we use mean field limit where $\phi = \phi^*$. This is normally considered in many literature even though they have finite value of μ.

62.3 Thermodynamic Parameters of Model

Now, we calculate the thermodynamic parameters of QCD viz energy density, pressure, entropy and specific heat for our short paper. The pressure in terms of standard thermodynamic relation is obtained as a function of temperature and chemical potential. The pressure is defined as [5]:

$$
P(T, \mu) = -\Omega(T, \mu)|_{\mu=0}
\tag{62.3}
$$

Energy density is obtained by the second derivative of the Gibbs potential with respect to the temperature.

$$\epsilon(T, \mu) = -T^2 \frac{\partial \left(\frac{\Omega(T,\mu)}{T} \right)}{\partial T} \Big|_{\mu=0} \tag{62.4}$$

Similarly, the entropy density of the system is very much importance in determining the equilibrium state and it helps to find the disordered state of the system. So entropy density as function of temperature and chemical defined as:

$$s(T, \mu) = -\frac{4}{3} T \frac{\partial \left(\frac{\Omega(T,\mu)}{T} \right)}{\partial T} \Big|_{\mu=0} \tag{62.5}$$

In addition to the above thermodynamic relations, we calculate the specific heat, defined by rate of change of energy density. Therefore it's calculation is given by the following formula as:

$$C_v = \frac{\partial \epsilon(T, \mu)}{\partial T} \Big|_{\mu=0} \tag{62.6}$$

The specific heat C_v measures the relevance of conformal symmetry of QCD at finite temperature.

62.4   Results

Figures 62.1, 62.2, 62.3 and 62.4 show energy density, pressure, entropy and specific heat with the variation of temperature in magnetic field for PNJL model of QCD at zero chemical potentials [6].

Fig. 62.1 Energy density as a function of temperature at $eB = (0, 0.8, 1.2, 1.6, 2.0)\,\text{GeV}^2$
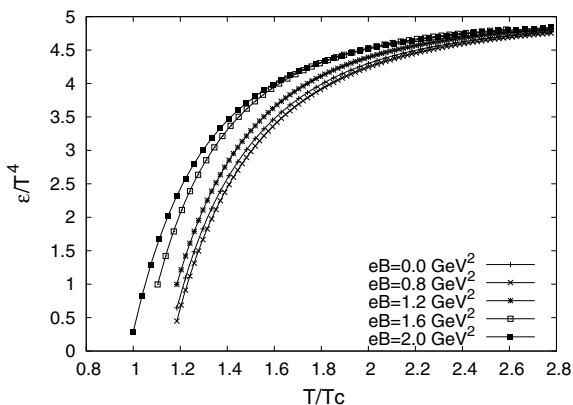
Fig. 62.2 Pressure as a function of temperature at $eB = (0, 0.8, 1.2, 1.6, 2.0)\,\text{GeV}^2$
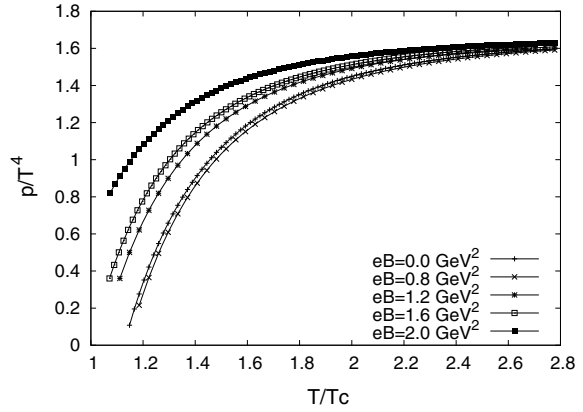
Fig. 62.3 Entropy as a function of temperature at $eB = (0, 0.8, 1.2, 1.6, 2.0)\,\text{GeV}^2$
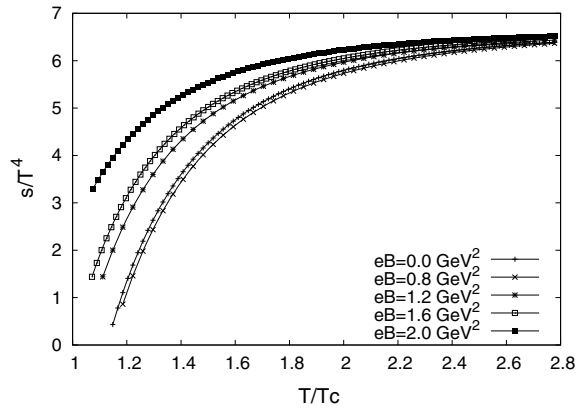
Fig. 62.4 Specific Heat as a function of temperature at $eB = (0, 0.8, 1.2, 1.6, 2.0)\,\text{GeV}^2$
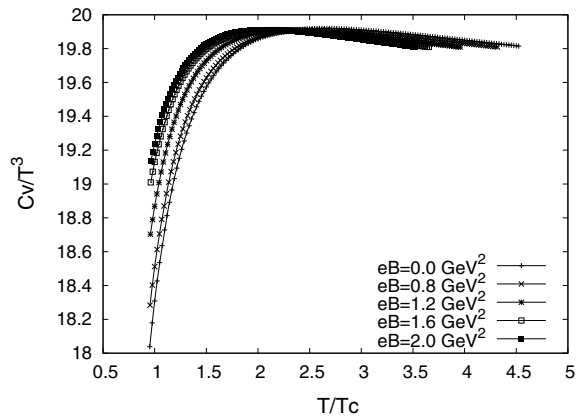
Figure 62.1 shows the value of the energy density keeps increasing with the magnetic field for a particular value of critical temperature. The value of the energy density becomes constant after $T = 2.2T_c$. It implies that energy density is independent of the higher temperature. The energy density for our PNJL model of cosmology has enhanced from the unmagnetized PNJL model [7].

In Fig. 62.2, a similar pattern has shown in the pressure behaviour, and the result is the same with the energy density. Pressure is correspondingly the same in comparison to the energy density in terms of the magnitude of $p = \frac{\epsilon}{3}$ [8].

Figure 62.3, show entropy density, and the result is similar to the other author's works. The results implies that the effect of the magnetic field in PNJL model for cosmology constant has negligible beyond the temperature $2.2T_c$. Moreover, much literature has explained that entropy measurements indicate phase transitions of QGP that the first and second-order phase transition can be obtained by first and second-order derivatives of the Gibbs potential.

In Fig. 62.4, C_v increases with increasing temperature and reaches a peak at 2.0 T c and starts decreasing and becomes constant for the entire range of temperature. So specific heat has risen suddenly, and then it decreases sharply for short-range of temperature. These features differently behave with the increasing magnetic field in PNJL model of cosmology, and it has observed for the entire range of temperature.

62.5   Conclusion

We successfully manage to produce the results of the thermodynamic parameters in the magnetized PNJL model of cosmology. The behaviour in the presence of a magnetic field in the PNJL model of cosmology has represented in figures. However, when we are plotting our results at finite temperatures and zero chemical potential for the magnetized PNJL model of cosmology, our results are enhanced from the unmagnetized PNJL model. The results show that the effect of the thermal mass and the magnetic field is minimum at high temperatures. The effect of the magnetic field in the PNJL model of cosmology is appeared at low temperature and enhanced from the result without a magnetic field. It indicates that the PNJL modelgives the formation of QGP around the temperature $T = (150–170)$ MeV with the increment in thermodynamic parameters in the intermediate range of temperatures $(T_c - 2.2T_c)$. However, the effect of thermal mass and magnetic field boosts the transition temperature from $T_c = 170$ MeV, and it can be around $T_c = (170-200)$ MeV . Due to the effect of the magnetic field in the PNJL model of cosmology, the structure of the QCD model has improved a lot from earlier features of QCD without these factors of magnetic field and thermal mass. It shows that study of QCD phase structure through the magnetized PNJL model of cosmology is good for the exploration of QGP phase transition.

References

1. P.N. Meisinger, M.C. Ogilvie, Phys. Lett. B **379**, 163 (1996)
2. K. Fukushima, Phys. Lett. B **591**, 277 (2004)
3. F. Karch, Phys Lett. B **571**, 67 (2003)
4. C.R. Allton, M. Doring, S. Ejiri, S.J. Hands, O. Kaczmarek, F. Karsch, E. Laermann, K. Redlich, Phys. Rev. D **71**, 054508 (2005)
5. P. Jacobs, X.N. Wang, Nucl. Phys. **54**, 443 (2005)
6. F. Csikor, G. Egiri, Z. Fodor, S.D. Katz, K.K. Szabo, A.I. Toth, JHEP **0405**, 046 (2004)
7. Z. Fodor, S. Katz, K. Szab, Phys. Lett. B **568**, 7377 (2003)
8. C.R. Allton, S. Ejiri, S.J. Hands, O. Kaczmarek, F. Karsch, E. Laermann, C. Schmidt, Phys. Rev. D **68**, 014507 (2003)

Chapter 63
Negative Ion Formation in Electron Collisions with Fullerenes: Fullerene Anionic Catalysis

Z. Felfli, K. Suggs, and A. Z. Msezane

Abstract Negative ion formation in fullerene molecules is explored through low-energy electron elastic scattering total cross sections (TCSs) calculations using our robust Regge-pole methodology. We find that the TCSs are characterized generally by ground, metastable and excited negative ion formation during the collisions, Ramsauer-Townsend minima and shape resonances. The novelty and generality of the Regge-pole approach is in the extraction of the negative ion binding energies of complex heavy systems from the calculated TCSs; for ground state collisions they correspond to the electron affinities. Utility of the fullerene molecular anions is demonstrated in the catalysis of water oxidation to peroxide and water synthesis from H_2 and O_2 using the anionic fullerene catalysts C_{20}^- to C_{136}^-. Density Functional Theory transition state calculations have found the C_{52}^- and C_{60}^- anions numerically stable for both water and peroxide synthesis, C_{100}^- increases the energy barrier the most and C_{136}^- the most effective catalyst in both water synthesis and oxidation to H_2O_2.

63.1 Introduction

The themed collection 'Single Atoms as Active Catalysts' published by the Royal Society of Chemistry to celebrate the International Year of the Periodic Table [1] has motivated this investigation. Here we first explore negative ion formation in the fullerene molecules C_{44} to C_{136} through low-energy electron elastic scattering total cross sections (TCSs) calculations. Then we use the anionic fullerenes C_{20}^- to C_{136}^- to investigate the catalysis of water oxidation to peroxide and water synthesis from H_2 and O_2. The fundamental mechanism underlying atomic negative-ion catalysis was proposed by our group in the context of muon catalyzed nuclear fusion [2, 3]. The mechanism involves anionic molecular complex formation in the transition state (TS), with the atomic negative ion breaking the hydrogen bonding strength. The mechanism has been demonstrated in the synthesis of H_2O_2 from H_2O catalyzed using the Au$^-$

Z. Felfli · K. Suggs · A. Z. Msezane (✉)
Department of Physics and CTSPS, Clark Atlanta University, Atlanta, GA 30314, USA

and Pd⁻ anions to understand the experiments of Hutchings and collaborators [4–6], in the catalysis of light, intermediate and heavy water to the corresponding peroxides [7] and in the oxidation of methane to methanol without the CO_2 emission [8]. Recently, the experiment [6] has used the less expensive atomic Sn for possible water purification in the developing world. In this context here we explore the effectiveness of the fullerene anions C_{20}^- to C_{136}^- in the catalysis of water oxidation to peroxide and water synthesis from H_2 and O_2 hoping to find inexpensive effective negative ion catalysts.

63.2   Method of Calculation

Regge poles formed during low-energy electron elastic scattering become stable bound states. Here we adopt the Regge-pole methodology, also known as the complex angular momentum (CAM) method for the calculation of the electron scattering TCSs. The TCS that fully embeds the essential electron–electron correlation effects is calculated using the Mulholland formula in the form [9] (atomic units are used throughout):

$$\sigma_{tot}(E) = 4\pi k^{-2}\text{Re}[1 - S(\lambda)]\lambda d\lambda$$
$$- 8\pi^2 k^{-2} \sum_n \text{Im} \frac{\lambda_n \rho_n}{1 + \exp(-2\pi i \lambda_n)} + I(E) \qquad (63.1)$$

In Eq. (63.1) $S(\lambda)$ and λ are respectively the S-matrix and the CAM, $k = \sqrt{2mE}$, m being the mass and E the impact energy, ρ_n is the residue of the S-matrix at the nth pole, λ_n and $I(E)$ contains the contributions from the integrals along the imaginary λ-axis; its contribution has been found to be negligible [10].

The incident electron is assumed to interact with the complex atom/fullerene through the potential which accounts for the core-polarization interaction

$$U(r) = -\frac{Z}{r(1 + \alpha Z^{1/3}r)(1 + \beta Z^{2/3}r^2)} \qquad (63.2)$$

In Eq. (63.2) Z is the nuclear charge, α and β are variation parameters. This potential has the appropriate asymptotic behavior, viz. $\sim -1/(\alpha\beta r^4)$ and accounts properly for the polarization interaction at low energies. This potential, extensively studied has five turning points and four poles connected by four cuts in the complex plane. The presence of the powers of Z as coefficients of r and r^2 in Eq. (63.2) ensures that spherical and non-spherical atoms/fullerenes are correctly treated. The effective potential $V(r) = U(r) + \lambda(\lambda + 1)/2r^2$ is considered here as a continuous function of r and λ. The details of the TCSs calculations are found in [9].

63.3   Results

Section 63.3.1 presents the calculated TCSs for selected fullerenes. The generated fullerene negative ions in Sect. 63.3.1 are used in Sect. 63.3.2 to catalyze the oxidation of water to peroxide and water synthesis from H_2 and O_2.

63.3.1   Negative Ion Formation in Low-Energy Electron Collisions with Fullerenes

Representative fullerene TCSs are presented in Fig. 63.1a–d, corresponding to the C_{44}, C_{60}, C_{74}, and C_{100}, respectively. The standard C_{60} TCSs have already been
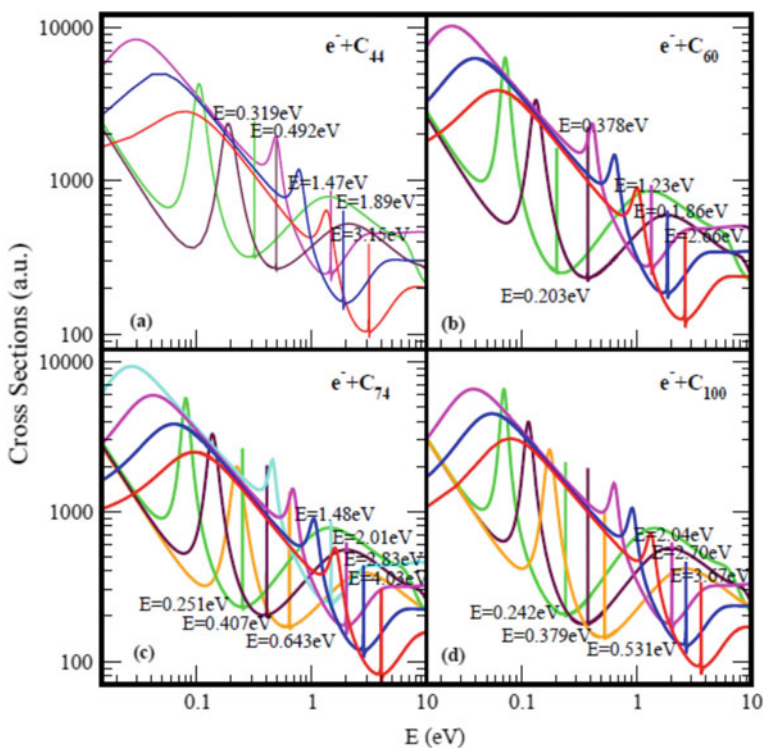
Fig. 63.1 Total cross sections (a.u.) for **a** C_{44}, **b** C_{60}, **c** C_{74} and **d** C_{100}. The red, blue and pink curves represent TCSs for the ground and the metastable (first and second), respectively; for C_{74} the light blue curve corresponds to an additional metastable state. The green and brown curves in (**a**) to (**d**) denote the TCSs for the first and the second excited states, respectively while for C_{74} and C_{100} the orange curves represent additional excited states. The dramatically sharp resonances correspond to the negative ions formed during the collisions

presented in [11, 12] and are taken from there. The C_{44} TCSs were first presented in [13] but with fewer resonances; they have been recalculated here to reveal the additional structures. Dramatically sharp resonances manifesting ground, metastable and excited negative ion formation characterize all the TCSs in the Fig. 63.1. The various anionic binding energies (BEs) can be extracted from the TCSs and contrasted with those of the standard C_{60} fullerene, see also [11, 12].

Clearly seen from the figures is that the ground state anionic BEs located at the absolute minima of the ground state TCSs yield the theoretically challenging to calculate electron affinities (EAs) and demonstrate their wide variation from fullerene to fullerene. The underlying physics in the TCSs has already been explained and discussed in [13, 14]; it is applicable to all the TCSs in the figures. Therefore, it will not be repeated here. These results are consistent with the observation that low-energy electron-fullerene interactions are characterized by rich resonance structures [15, 16] and that the experimentally detected fullerene isomers correspond to the metastable TCSs [17]. They also support the conclusion that the EAs of fullerene molecules are relatively large. This should satisfy part of the requirement to increase fullerene acceptor resistance to degradation by the photo-oxidation mechanism through the use in organic solar cells of fullerenes with high EAs [18]. The extracted EAs from the TCSs could also be used to construct the widely used simple model potentials for the fullerene shells, including endohedral fullerenes. Indeed, the rich resonance structures in the fullerenes TCSs and their large EAs explain the tendency of fullerenes to form compounds with electron-donor anions and their vast applications as well.

63.3.2   Fullerene Negative Ion Catalysis

The utility of the fullerene anions has been demonstrated in the catalysis of water oxidation to peroxide and water synthesis from H_2 and O_2 using the anionic fullerene catalysts C_{20}^- to C_{136}^-. Figure 63.2 demonstrates the Density Functional Theory (DFT) calculated TS energy barriers. DFT and dispersion corrected DFT approaches have been employed for the TS evaluations. Geometry optimization of the structural molecular conformation utilized the gradient-corrected Perdew-Burke-Ernzerhof parameterizations [19] of exchange–correlation as implemented in DMol3 [20]. A tolerance of 1×10^{-3} Ha was used with a smearing value of 0.005 Ha. DFT calculated energy barriers reduction in the oxidation of H_2O to H_2O_2 catalyzed using the anionic fullerene catalysts C_{20}^- to C_{136}^- are shown in the figure. The results in Fig. 63.3 are for the water synthesis from H_2 and O_2 catalyzed using the anionic fullerene catalysts C_{20}^- to C_{136}^- as well. For both water oxidation and water synthesis DFT TS calculations found the C_{52}^- and C_{60}^- anions to be numerically stable and the C_{36}^- and C_{100}^- anions to increase the energy barriers the most in the water oxidation to H_2O_2 and water synthesis using H_2 and O_2, respectively. The C_{136}^- anion has proved to be the most effective in reducing the energy barrier significantly when catalyzing both water oxidation to peroxide and synthesis from H_2 and O_2. Importantly, a single large fullerene such as the C_{136}, or even the C_{74} could replace the Au, Pd and Sn atoms

Fig. 63.2 Transition state energy barriers of anionic fullerenes sizes C_{20}^- to C_{136}^- for catalyzing water oxidation to peroxide

Anionic Fullerene C20-C136 Peroxide Synthesis Transition States via [2+1] Cycloaddition-bonded (02 +2H2O->2H2O2)
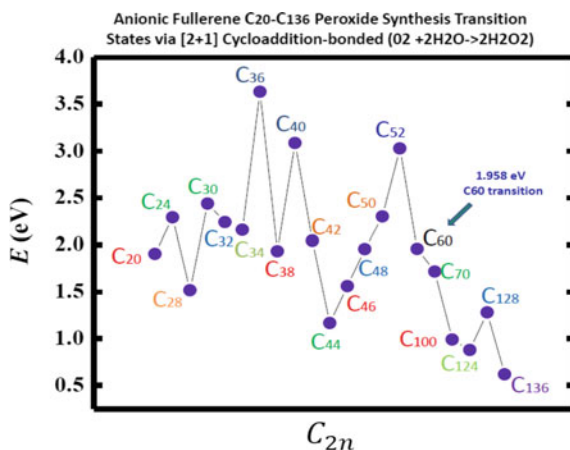
Fig. 63.3 Transition state energy barriers of anionic fullerenes sizes C_{20}^- to C_{136}^- in catalyzing hydrogen and oxygen synthesis to water

Anionic Fullerene C20-C136 Water Synthesis Transition States via [2+1] Cycloaddition-bonded (2H2 +O2->2H2O)
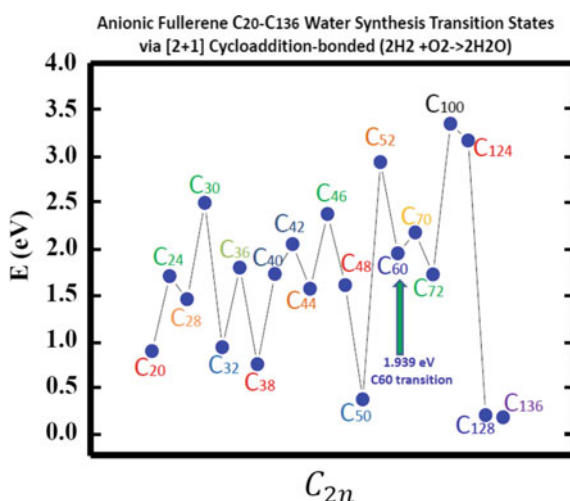
in the catalysis of H_2O_2 from H_2O in the experiments [4–6] acting as a multiple-functionalized catalyst. These fullerenes have their metastable BEs close to the EAs of the used atoms in the experiments. Thus an inexpensive dynamic water purification system for the developing world could be realized [6].

63.4 Concluding Remarks

Our robust Regge-pole methodology has been used to explore negative-ion formation in fullerene molecules through low-energy electron elastic scattering TCSs calculations. The TCSs have been found to be characterized generally by ground,

metastable and excited negative ion formation during the collisions, Ramsauer-Townsend minima and shape resonances. The novelty and generality of the Regge-pole approach is in the extraction of the negative ion BEs of complex heavy systems from the calculated TCSs; for ground states collisions they correspond to the theoretically challenging to calculate EAs. For fullerenes the extracted ground state anionic BEs matched excellently the measured EAs of C_{20} through C_{92} [13, 14]. Indeed, the Regge-pole methodology requires no assistance whatsoever from either experiment or other theory for the remarkable feat. Utility of the fullerene molecular anions has been demonstrated in the catalysis of water oxidation to peroxide and water synthesis from H_2 and O_2 using the catalysts C_{20}^- to C_{136}^-. DFT TS calculations found C_{52}^- and C_{60}^- anions numerically stable for both water and peroxide synthesis and C_{136}^- the most effective catalyst in both water synthesis and oxidation to H_2O_2.

References

1. International Year of the Periodic Table: Single Atoms as Active Catalysts. https://pubs.rsc.org/en/journals/articlecollectionlanding?sercode=nr&themeid=1fc90a67-e081-4265-99eb-2201eb17c286
2. A.Z. Msezane, Z. Felfli, D. Sokolovski, J. Phys. B **43**, 201001 (2010).https://doi.org/10.1088/0953-4075/43/20/201001
3. E.A.G. Armour, J. Phys.: Conf. Ser. **225**, 012002 (2010). https://doi.org/10.1088/1742-6596/225/1/012002
4. J.K. Edwards, A.F. Carley, A.A. Herzing et al., J. Chem. Soc. Faraday Discuss. **138**, 225 (2008). https://doi.org/10.1039/B705915A
5. J.K. Edwards, B. Solsona, P. Landon et al., J. Mater. Chem. **15**, 4595 (2005). https://doi.org/10.1039/B509542E
6. S.J. Freakley, Q. He, J.H. Harrhy et al., Science **351**, 959 (2016). https://doi.org/10.1126/science.aad5705
7. A. Tesfamichael, K. Suggs, Z. Felfli et al., J. Phys. Chem. C **116**, 18698 (2012). https://doi.org/10.1021/jp301861q
8. A.Z. Msezane, Z. Felfli, A. Tesfamichael et al., Gold Bull. **3**(45), 127 (2012). https://doi.org/10.1007/s13404-012-0056-7
9. D. Sokolovski, Z. Felfli, S.Y. Ovchinnikov et al., Phys. Rev. A **76**, 012705 (2007). https://doi.org/10.1103/PhysRevA.76.012705
10. Z. Felfli, A.Z. Msezane, D. Sokolovski, Phys. Rev. A **79**, 012714 (2009). https://doi.org/10.1103/PhysRevA.79.012714
11. A.Z. Msezane, J. At. Mol. Condensate Nano Phys. **5**, 195 (2018). https://doi.org/10.26713%2Fjamcnp.v5i3.1135
12. A.Z. Msezane, Z. Felfli, Eur. Phys. J. D **72**, 173 (2018). https://doi.org/10.1140/epjd/e2018-90121-0
13. A.Z. Msezane, Z. Felfli, Chem. Phys. **503**, 50 (2018). https://doi.org/10.1016/j.chemphys.2018.02.005
14. Z. Felfli, A.Z. Msezane, Euro. Phys. J. D **72**, 78 (2018). https://doi.org/10.1140/epjd/e2018-80420-9

15. O. Elhamidi, J. Pommier, R. Abouaf, J. Phys. B **30**, 4633 (1997). https://doi.org/10.1088/0953-4075/30/20/023
16. J. Huang, H.S. Carman, R.N. Compton, J. Phys. Chem. **99**, 1719 (1995). https://doi.org/10.1021/j100006a013
17. L. Kronik, R. Fromherz, E. Ko, G. Ganteför, J.R. Chelikowsky, Nat. Mater. **1**, 49 (2002). https://doi.org/10.1038/nmat704
18. E.T. Hoke, I.T. Sachs-Quintana, M.T. Lloyd et al., Adv. Energy Mat. **2**, 1351 (2012). https://doi.org/10.1002/aenm.201200169
19. A. Tkatchenko, M. Scheffler, Phys. Rev. Lett. **102**, 73005 (2009). https://doi.org/10.1103/PhysRevLett.102.073005
20. DMol3, Accelrys Software Inc., San Diego, CA (2011)

Author Index